Fraunhofer Institut
Chemische Technologie

Energetic Materials

Analysis, Diagnostics and Testing

31st International Annual Conference of ICT
June 27 - June 30, 2000
Karlsruhe, Federal Republic of Germany

REPORT DOCUMENTATION PAGE

Form Approved OMB No. 0704-0188

Public reporting burden for this collection of information is estimated to average 1 hour per response, including the time for reviewing instructions, searching existing data sources, gathering and maintaining the data needed, and completing and reviewing the collection of information. Send comments regarding this burden estimate or any other aspect of this collection of information, including suggestions for reducing this burden to Washington Headquarters Services, Directorate for Information Operations and Reports, 1215 Jefferson Davis Highway, Suite 1204, Arlington, VA 22202-4302, and to the Office of Management and Budget, Paperwork Reduction Project (0704-0188), Washington, DC 20503.

1. AGENCY USE ONLY (Leave blank)	2. REPORT DATE	3. REPORT TYPE AND DATES COVERED
	June 27, 2000	June 27 – 30, 2000 Final Report

4. TITLE AND SUBTITLE
International Annual Conference (31st) of ICT Held in Karlsruhe, Federal Republic of Germany on July 3-July 6, 2001. Energetic Materials: Analysis, Diagnostics and Testing

5. FUNDING NUMBERS
N000-

6. AUTHOR(S)

7. PERFORMING ORGANIZATION NAME(S) AND ADDRESS(ES)
Fraunhofer-Institut fur Chemische Technologie (ICT)
Joseph-von-Frauhofer-Strasse
Postfach 12 40
D-76318 Pfinztal (Berghausen)

8. PERFORMING ORGANIZATION REPORT NUMBER
ISSN 0722-4807

9. SPONSORING/MONITORING AGENCY NAME(S) AND ADDRESS(ES)
Office of Naval Research,
European Office
PSC 802 Box 39
FPO AE 09499-0039

10. SPONSORING/MONITORING AGENCY REPORT NUMBER

11. SUPPLEMENTARY NOTES
Text in German and English; abstract in English.
This work relates to Department of the Navy Grant issued by the Office of Naval Research International Field Office. The United States has a royalty free license throughout the world in all copyrightable material contained herein.

12a. DISTRIBUTION/AVAILABILITY STATEMENT
Approved for Public Release; Distribution Unlimited.
U.S. Government Rights License. All other rights reserved by the copyright holder.

12b. DISTRIBUTION CODE
A

12. ABSTRACT (Maximum 200 words)
These are presentation and poster session papers presented at the 31st International Annual Conference of ICT held in Karlsruhe, Germany, on June 27-30, 2000.

In recent years the technical progress in synthesis, processing and application of energetic materials was positively influenced by advanced analytical methods, diagnostics and measuring techniques. Efficient screening methods, new sensoring techniques and combinatorical approaches are examples for analytical strategies making accurate data available and allowing their fast evaluation.

The conference objectives include the investigation and characterization of energetic materials by analytical methods, the improvement of existing measuring techniques and the development of new analytical methods and stragegies.

13. SUBJECT TERMS
Chemistry, Foreign reports, Conference proceedings, German language

15. NUMBER OF PAGES

16. PRICE CODE

17. SECURITY CLASSIFICATION OF REPORT	18. SECURITY CLASSIFICATION OF THIS PAGE	19, SECURITY CLASSIFICATION OF ABSTRACT	20. LIMITATION OF ABSTRACT
UNCLASSIFIED	UNCLASSIFIED	UNCLASSIFIED	UL

Herausgeber / Editor:

Fraunhofer-Institut
für Chemische Technologie (ICT)
Joseph-von-Fraunhofer-Straße
Postfach 12 40
D-76318 Pfinztal (Berghausen)

Bundesrepublik Deutschland

Telefon (07 21) 46 40 - 0
Telefax (07 21) 46 40 - 111

Herstellung:

DWS Werbeagentur und Verlag GmbH, Karlsruhe
Printed in Germany

ISSN 0722-4087

U.S. Government Rights License
This work relates to Department of the Navy Grant or Contract issued by Office of Naval Research (ONR) International Field Office-Europe. The United States Government has a royalty-free license throughout the world in all copyrightable material contained herein.

Fraunhofer Institut
Chemische Technologie

Energetic Materials

Analysis, Diagnostics and Testing

31st International Annual Conference of ICT
June 27 - June 30, 2000
Karlsruhe, Federal Republic of Germany

20011130 112

AQ F02-02-0284

31st International
Annual Conference of ICT

Energetic Materials -

Analysis, Diagnostics and Testing

In recent years the technical progress in synthesis, processing and application of energetic materials was positively influenced by advanced analytical methods, diagnostics and measuring techniques. To fulfill the increasing requirements with respect to quality, performance and safety of energetic materials, further improvements of analytical methods and strategies are of utmost importance. Efficient screening methods, new sensoring techniques and combinatorical approaches are examples for analytical strategies making accurate data available and allowing their fast evaluation.

The objectives of the conference include the investigation and characterization of energetic materials by analytical methods, the improvement of existing measuring techniques and the development of new analytical methods and strategies.

The 31st International ICT Annual Conference will act as a forum to review the state of the art, to present new ideas and methods, and to discuss how they assist in the development and processing of energetic materials.

Chairman of the Conference

Dr. Stefan Löbbecke
Fraunhofer ICT, Pfinztal, D

June 27 - June 30, 2000
Karlsruhe, Congress Center
Stadthalle, Weinbrenner-Saal

Federal Republic of Germany

Vorbemerkung

Die Themen unserer Jahrestagung haben wieder ein breites internationales Echo gefunden. Die große Anzahl von eingegangenen Beiträgen machte, wie in den vergangenen Jahren, eine Einteilung in Vorträge und Poster notwendig. Poster ermöglichen eine intensivere Diskussion und eine direkte Rückkoppelung von interessierten Tagungsteilnehmern.

Der vorliegende Tagungsband erscheint zu Konferenzbeginn und enthält die schriftliche Fassungen der Vorträge und Poster. Aus zeitlichen Gründen mußte die Drucklegung vor Eingang sämtlicher Beiträge erfolgen. Nachträglich eingegangene Manuskripte finden sich im Anhang oder wurden durch die Kurzfassung ersetzt.

Prelimentary Remark

The subjects of the annual ICT-Conference have again found wide international response. The vast number of contributions necessitated - as in previous years - a division into oral presentations and posters. Posters enable an intensive discussion and direct feedback from interested conference participants.

The Conference Proceedings are published at the beginning of the conference and contain the written versions of the presentations and posters. Due to the shortage of time, printing had to commence prior to receipt of all contributions. Subsequently received manuscripts are either included in the Annex or the abstract is printed instead

TABLE OF CONTENTS

LECTURES

V 1 **Co-operation between the United Kingdom and France on the assessment of gun propellants**

C. Leach, D. Debenham, J.-Y. Kermarrec, C. Tormo

V 2 **Principles of a STANAG for the estimation of the chemical stability of propellants by heat flow calorimetry**

U. Ticmanis, S. Wilker, G. Pantel, M. Kaiser, P. Guillaume, C. Bales, N. van der Meer

V 3 **Stability of propellants, thermal or functional**

C.A. van Driel, W.P.C. de Klerk

V 4 **Accelerating rate calorimetry experiments on energetic materials: Obtaining time to maximum rate plots on larger samples**

P.F. Bunyan, D.A. Tod

V 5 **Neue Strategien und Verfahren der Inprozess- und Produkte-Analytik in der Treibmittel-Produktion**
New strategies and methods for in-process- and product-analysis in the production of propellants

B. Vogelsanger, B. Ossola

V 6 **Comparison of T-jump/Raman and T-jump/FTIR spectroscopy for high-nitrogen compounds**

T.B. Brill, B.D. Roos

V 7 **Thermal decomposition of secondary nitramines in solutions**

Y. Shu, V.V. Dubikhin, G.M. Nazin, G.B. Manelis

V 8 **Properties of hydrazinium nitroformate (HNF)**

M. van Zelst, A.E.D.M. van der Heijden

V 9 **Comparative investigation of thermal decomposition of various modifications of Hexanitrohexaazaisowurtzitane**

V.V. Nedelko, N.V. Chukanov, B.L. Korsounskii, T.S. Larikova, F. Volk

V 10 **Synthesis and properties of TNAZ**

K. Schmid, D. Kaschmieder

V 11 **A new convenient route to GEM-dinitroalifatic compounds**

N.V. Latypov, A. Langlet, U. Wellmar, P. Goede

V 12 **Cyclodextrin polymer nitrate**

A. Ruebner, G.L. Statton, C. Meyers, B.M. Kosowski, D. Robitelle

V 13 **Zwitterionic amine-nitramines as a new class of energetic materials**

A.M. Astachov, R.S. Stepanov, L.A. Kruglyakova, Y.V. Kekin

V 14 **Synthese und explosive Eigenschaften unempfindlicher energetischer NENA-Sprengstoffe**
Synthesis and explosive properties of insensitive energetic NENA explosives

H. Ritter, M.R. Schäfer, B. Wanders, H.H. Licht

V 15 **Advances in cryogenic solid propulsion**

R. Lo, H. Adirim, S. Poller, N. Eisenreich, V. Weiser, S. Kelzenberg

V 16 **Development of recrystallisation process for superfine PETN from laboratory to full plant scale**

M. du Plessis

V 17 **Preventive approach for managing and removing organic pollutants: The example of NTO**

J. Ouazzani

V 18 **Mechanical characterisation of energetic materials using multi-wave experiments**

G.M. Kavanagh, J. Theobald, D.A. Tod

V 19 **Charakterisierung der Matrix/Füllstoff-Wechselwirkung am Beispiel des Modelltreibstoffsystems GAP/RDX**
Characterisation of the matrix/filler properties of the GAP/RDX propellant system

P. Gerber, C. Hübner, K. Menke

V 20 **Quantitative morphological characterization of high explosive crystal grains by light diffraction and microscopy**

J.T. Mang, C.B. Skidmore, J.F. Kramer, D.S. Phillips

V 21 **Studies of the synthesis and crystallization of CL-20**

R.S. Hamilton, A.J. Sanderson, R.B. Wardle, K.F. Warner

V 22 **The effect of different crystallisation techniques on morphology and stability of HNF**

W.H.M. Veltmans, A.E.D.M. van der Heijden, J.M. Bellerby, M.I. Rodgers

V 23 **The development of analytical methods for a high energy / high elongation propellant**

G.M. Kavanagh, J. Theobald, D.A. Tod

V 24 **Verträglichkeitsuntersuchungen von Nitratestern**
Compatibility investigations of nitrate esters

S. Wilker, G. Pantel, U. Ticmanis, M. Kaiser

V 25 **Humid ageing of polybutadiene based propellants**

S. Torry, A. Cunliffe

V 26 **Influence of slits to the detonation front**

M. Held

V 27 **Initiation threshold of an insensitive underwater high explosive**

W. Arnold

V 28 **Prüfmitteloptimierung im Mittelkaliberbereich für die Aufklärung der Treibladungspulverbett-Dynamik in Unterkaliberpatronen**
Test-equipment optimization in the mediumcaliber-range for the explanation of the propellant-bed-dynamic in subcaliber rounds

E. Rochat

V 29 **Extension of calibrated shock wave test to strong and short shocks**

P. Chabin, J. Groux, S. Lecume

V 30 **Abhängigkeit der Beschussempfindlichkeit von HTPB-gebundenen Sprengstoffen vom Weichmachergehalt im Bindersystem**
Dependence of bullet impact sensitivity of PBX's on mechanical properties

R. Wild, B. Nicklas, T. Keicher

V 31 **withdrawn**

V 32 **Modified ultrasonic method for the study of burning rate characteristics of propellants**

K. Hori, K. Hasegawa, S. Shimose, T. Yamaya, M. Shimoda

V 33 **Einsatzmöglichkeiten von Mikroreaktoren für die Synthese von energetischen Materialien**
The potential of microreactors for the synthesis of energetic materials

S. Löbbecke, J. Antes, T. Türcke, E. Marioth, K. Schmid, H. Krause

V 34 **Clean synthesis of energetic materials using solid-supported reactions and related technologies**

R.W. Millar, M.E. Colclough, R.P. Claridge, J. Hamid, S.P. Philbin, N. Chauhan

V 35 **Nanostructured energetic materials derived from sol-gel chemistry**

R.L. Simpson, T. Tillotson, L. Hrubesh, A. Gash

V 36 **A new low-cost synthesis of PGN**

L.F. Cannizzo, R. M. Hajik, T.K. Highsmith, A.J. Sanderson, L.J. Martins, R.B. Wardle

V 37 **New synthesis of TATB – Scaleup and product characterization**

R.D. Schmidt, A.R. Mitchell, G.S. Lee, M.D. Coburn, P.F. Pagoria, M.D. Coburn, W.T. Quinlan, R. Thorpe, M. Cates

V 38 **Synthesis of precursors to mixed Difluoramine Nitramine energetic materials**

N.J. Trivedi, T. Axenrod, J. Sun, K.K. Das, P.R. Dave, F. Forohar, M. Kaselj, R.D. Gilardi, J.L. Flippen-Anderson

V 39 **Synthesis and properties of salts of dinitroamide (DNA) with various amines**

H. Boniuk, I. Cieslowska-Glinska, M. Syczewski

V 40 **Capillary extrusion rheometry and extrusion of propellants and propellant simulants**

A.C. Hordijk, I. van der Velde, C. Schoolderman, H.W.R. Sabel

V 41 **Experimental determination of ultrafine magnesia particle emissivities at high temperatures**

Y.L. Shoshin, I.S. Altman

V 42 **The heat and products of explosion of aluminized high explosives**

M.N. Makhov

V 43 **Combustion behaviour of pyrotechnic mixture based in ammonium and sodium nitrates with wood particles**

P. Portugal, J. Campos, A. Portugal

V 44 **Chemical and morphological analyses of plasma-treated solid propellant surfaces**

P. Kaste, A. Kinkennon, R. Lieb, A. Birk, M. del Guercio, J. Newberry, M. Schroeder, R. Pesce-Rodriguez

POSTER PRESENTATIONS

P 45 **Synthesis and analyses of N,N′-dinitrourea**

P. Goede, N. Wingborg, H. Bergman, N. Latypov

P 46 **New method of synthesizing K-RDX using dinitrourea (DNU)**

H. Boniuk, W. Pilecki, T. Stawinski, M. Syczewski

P 47 **Triethylenetetramine (TETA) modification – obtaining azidic precursors of energetic mixture binders**

H. Boniuk, T. Stawinski, M. Syczewski

P 48 **Solid acid catalysts: Shape selective nitration of aromatics**

Reddy Damavarapu, Rao Surapaneni, Keerthi Jayasurya, Paritosh R. Dave

P 49 **New energetic propellants for hypervelocity applications: A challenge to the synthesis chemist**

R.L. Simmons

P 50 **The energies of dissociation bonds and efficient energies of interaction in nitroamines**

L.M. Kostikova, E.A. Miroshnichenko, Y.N. Matyushin

P 51 **Energy of interaction NO_2-groups in Nitroderivatives methane and ethane**

Y.N. Matyushin, V.P. Lebedev, E.A. Miroshnichenko,
L.M. Kostikova, Y.O. Inozemcev

P 52 **Synthesis and characterization of azido plasticizer**

D. Drees, D. Löffel, A. Messmer, K. Schmid

P 53 **Glycidyl Azide Polymer Plasticizer – DSC and rheological results**

T. Manzara, R. Hunter

P 54 **Determination of absolute molecular weight of Glycidyl Azide Polymer (GAP) by multi-angle laser light scattering detector in-line with size exclusion chromatography (MALLS/SEC)**

V. Destombes, G. Lacroix

P 55 **Thermal characterization of propellants containing GAP as binder**

Tsao-Fa Yeh

P 56 **Side GAP thermal decomposition reaction**

V.G. Prokudin, V.V. Charskii, A.I. Kuzaev, N.V. Chukanov, B.C. Fedorov, G.M. Nazin

P 57 **Migration of Di-nitro-di-aza-aliphates in Glycidyl-azide-polymer**

M. Niehaus, S. Kelzenberg, G. Bunte

P 58 **Effects of metal powder with different particle sizes on thermal decomposition characteristics of Glycidyl Azide Polymer**

Chen Pei, Zhao Feng-qi, Li Shang-wen, Yin Cui-mei, Yang Dong

P 59 **Effect of gamma radiation on the energetic polymer polyNIMMO**

S.C. Waring, E. Kronfli, J. Akhavan, M.E. Colclough

P 60 **withdrawn**

P 61 **Stabilitätsuntersuchungen von Treibladungspulvern mit neuen Stabilisatoren**
Stability analysis of propellants containing new stabilisers

J. Petrzilek, J. Skladal, S. Wilker, G. Pantel, L. Stottmeister

P 62 **Temperaturabhängigkeit der Zersetzung der Nitrocellulose bestimmt mit Modellierung des TGA-Massenverlusts und Stabilisatorverbrauchs**
Temperature dependence of the decomposition of Nitrocellulose determined by TGA mass loss and stabilizer consumption

M.A. Bohn, N. Eisenreich

P 63 **Erkennen von Wechselwirkungen der Nitramine HMX und CL20 mit Formulierungskomponenten durch Computersimulation**
Exploring of interactions of the nitramines HMX and CL20 with components in formulations by computer simulation

V. Thome, P.B. Kempa, M.A. Bohn

P 64 **Molecular simulation of the morphology of energetic materials**

V. Thome, P.B. Kempa, M. Herrmann, U. Teipel, W. Engel

P 65 **Stabilität von Nitrocelluolse in Anzündmischungèn**
Stability of Nitrocellulose in ignition mixtures

U. Ticmanis, M. Kaiser, M. Künstlinger, K. Redecker

P 66 **Untersuchungen zum Einfluß der Umgebungsbedingungen bei explosiven Komponenten**
Investigations into the influence of ambience conditions on explosive components

A. Keßler, W. Stein

P 67 **Sensitivity properties of spray-dried boron/potassium nitrate granular**

K. Takahashi, N. Asano

P 68 **The study of the sensitivity and the surface characterization of HMX/TATB-based PBX**

Nie Fude, Yang Xenhai, Zhang Ling, Sun Jie, Hua Cheng, Huang Hui

P 69 **Shock sensitivity of HMX based compositions**

A.E.D.M. van der Heijden, R.H.B. Bouma, R.J. van Esveld

P 70 **Estimation of the violence of cook-off tests using PE-4**

A. Bailey, K. DeGraaw, M. Matei, M. Williams

P 71 **Gap test investigation**

M. Held

P 72 **Shelf life evaluation of experimental 155mm charges**

H.G. Schimansky

P 73 **Energy measurement and characterization of Insensitive Munitions (IM) as an experimental method for determination of IM terminal effectiveness for various formulations**

G.J. Ellis

P 74 **The effect of fuel's caloricity on impact sensitiveness of binary oxidizer-fuel compositions**

V.A. Teselkin, A.V. Dubovik

P 75 **Shock compression of liquid Hydrazine – Estimation of detonability and sensitivity to shock loading of its solutions**

I.M. Voskoboinikov, O.I. Voskoboinikova

P 76 **Measurement of the detonation velocity of infinite diameter with small samples**

M. Held

P 77 **A study on detonation characteristics of pressed NTO**

S. Cudzilo, W.A. Trzcinski

P 78 **Detonation of TNT-DINA and DNT-PETN cast charges**

G.D. Kozak, B.N. Kondrikov, Zhou Lin

P 79 **Common shape of dependence of the detonation diameter of detonation on density for TATB example**

G.T. Afanasev, L.N. Akimova

P 80 **Measurement of initiation strength of detonators**

F. Masar, J. Strnad, M. Jungova

P 81 **A theoretical model of detonation process**

Hu Shaoming

P 82 **Detonability of tributyl phosphate and fuming nitric acid**

Y. Nakayama, T. Matsumura, M. Yoshida, S. Fujiwara

P 83 **Application of direct Chemiluminescence to mechanistic and kinetic studies of energetic materials**

J. Kimura

P 84 **Analytical application of thermal methods in the field of explosive materials**

M. Suceska, M. Rajic

P 85 **Effect of some burning catalyst on the thermal decomposition behaviour of an igniter composition**

M.A. Benmahamed, A. Mouloud, N. Ikene

P 86 **Thermal decomposition of nitramine composite solid propellants (N/CSP) based on polyurethane binders**

M.A. Sadek, M.H. Moeen, M.A. Radwan, H.H. Ameen

P 87 **Decomposition of EAK/RDX/Al intermolecular explosive**

Zhao Shengxiang, Zhang Yian, Hu Huanxing, Lu Chunxu

P 88 **Thermochemistry of complex salts of transitive metals with 1,5-diaminotetrazole as ligand**

T.S. Konkova, Y.N. Matyushin, V.P. Sinditskiy, M.D. Dutov, A.F. Fogelzang

P 89 **The thermal decomposition of pentaerythritoltetranitrate studied by GCMS & FTIR**

K. MacDonald, I. Belcher, C. Blackman, J. Bellerby

P 90 **Thermal analysis of selected pyrazines and pyrazoles**

S. Löbbecke, H. Schuppler, W. Schweikert, K. Schmid

P 91 **withdrawn**

P 92 **Chromatographic determination of dinitramid anions in the presence of nitrate**

G. Bunte, H. Neumann, H. Krause

P 93 **Separation and identification of nitro aromatic components by different chromatographic techniques exemplarily for nitronaphthalenes**

G. Bunte, H. Neumann, J. Deimling, W. Schweikert

P 94 **Estimation of the service life of NC propellant by HPLC**

S.A. Shokry, M.E. Husseiny

P 95 **Spectral overlap and absorbance ratio methods for identifying peak purity of explosives in HPLC**

Liu Yonggang, Luo Shunhuo

P 96 **Detection of α-HMX in β-HMX with FTIR diffuse reflection technique**

R. Gjersoe

P 97 **Lattice imperfections of HMX measured with X-ray diffraction**

M. Herrmann, W. Engel

P 98 **Monitoring of nitration reactions in microreactors with FTIR microscopy**

W. Schweikert, T. Türcke, S. Löbbecke

P 99 **IR spectroscopic analysis of energetic materials dissolved in highly compressed gases**

S. Panic, W. Schweikert, H. Krause, S. Löbbecke

P 100 **Mechanical characterisation of energetic materials by applying WLF theory**

G.M. Kavanagh, D.A. Tod, J. Theobald

P 101 **Effects of surface interactions on the mechanical properties of PBXs: Part I. Surface free energy of solids**

Hyoun-Soo Kim, Jung-Seob Shim, Keun-Deuk Lee, Bang-Sam Park

P 102 **Study on the low temperature (-40°C) mechanical properties of high burning-rate HTPB propellants (II) Design and application of the surfactants**

Du Lei, Xiao Jinwu, Yin Ruikang

P 103 **Hydroxyfurazans: Outlook to using**

A.B. Sheremetev, E.V. Mantseva, N.S. Aleksandrova, I.L. Yudin, T.S. Novikova

P 104 **Analysis of hydrazinium nitroformate (HNF)**

J.M. Bellerby, C.S. Blackman, A.E.D.M. van der Heijden, M. van Zelst

P 105 **Characterization of a commercial grade Cl-20: morphology, crystal shape, sensitivity and shock initiation testing by flyer impact**

R.H.B. Bouma, W. Duvalois, A.E.D.M. van der Heijden, A.C. van der Steen

P 106 **Identification and analysis of impurities of HNIW**

G. Jacob, G. Lacroix, V. Destombes

P 107 **Polymorphism and solubility of CL20 in plasticisers and polymers**

S.A. Torry, A.V. Cunliffe

P 108 **Process improvements in CL-20 manufacture**

Rao Surapaneni, Reddy Damavarapu, Rajagopal Duddu, Ajay Kumar, Paritosh R. Dave

P 109 **Polynitrohexaazaisowurtzitane derivatives related to hexanitrohexaazaisowurtzitane (HNIW, WN_6)**

A. J. Bellamy

P 110 **Laboratory testing of HNIW mixtures**

K. Dudek, P. Marecek, P. Vavra

P 111 **Geschäumte Treibladungen mit energetischen Bindern**
Foamed propellants with energetic binders

A. Messmer, A. Pfatteicher, W. Kuglstatter, K. Schmid

P 112 **Water-impregnated explosives containing up to 90% finely dispersed Aluminum**

B.N. Kondrikov, V.E. Annikov

P 113 **Confined explosions of aluminized high explosives**

W.A. Trzcinski, J. Paszula

P 114 **The development of high explosives in CAEP**

Dong Haishan

P 115 **Alternative option for high-performance, IM-compliant, metal accelerating warhead fillings: Pressed PBX technology**

T.T. Nguyen,

P 116 **High-elastic fireconductive cords**

D.L. Rusin, D.B. Mikhalev, D.V. Vetrov

P 117 **Development of cure cast high loaded HMX IHE´s**

D. Cohen, S. Mandelbaum, E. Dreerman, M. Gil

P 118 **The influence of size and shape of the explosive particles on a cure-cast explosive properties**

D. Cohen, S. Mandelbaum, E. Dreerman, M. Gil

P 119 **Screening units for particle formations of explosives using supercritical fluids**

E. Marioth, S. Löbbecke, H. Krause

P 120 **Coating of particulate energetic materials**

T. Heintz, U. Teipel

P 121 **Scale-up of crystallizer for producing spherical crystals of NTO**

Kwang-Joo Kim, Kap-Mo Kim, Jung-Min Lee, Hyun-Soo Kim, Bang-Sam Park, Jun-Wung Lee

P 122 **Recycling and reusing of an aged amine based liquid rocket propellant fuel**

M.H. Sammour

P 123 **Erzeugung von Partikelwolken mit Druckgas und mit Gasgeneratoren**
Generation of particle clouds by means of pressurized gas and gas generators

A. Baier, N. Eisenreich, V. Hell, H. Schmid, H. Schneider

P 124 **Environmental qualification of gas generator systems for automobiles**

T. Reichert, T. Hirth, R. Jakob, J. Cäsar

P 125 **Mathematical simulation of air bag inflation by low temperature gas generator products**

A. Vorozhtsov, S. Bondarchuk, A. Salko, O. Kondratova

P 126 **Gasgeneratorentwicklung für Feuerlöschanwendung**
Gasgenerator development for fire extinguishing purpose

J. Neutz, H. Schmid, D. Schröter, V. Weiser

P 127 **withdrawn**

P 128 **Die Nachprüfung der I-Brenner Methode für die Abschätzung der Verbrennungsinstabilität in Feststoffraketen**
A study of the I-Burner method for the investigation of the combustion instability of solid propellant rockets

K. Matsui

P 129 **Thermodynamical prediction of combustion and detonation properties using modified THOR code**

L. Duraes, J. Campos, A. Portugal

P 130 **Agglomerate and oxide particles generated in combustion of Alex containing solid propellants**

O.G. Glotov, V.E. Zarko, M.W. Beckstead

P 131 **Regularities of combustion of energetic systems containing potassium nitrate**

A.P. Denisjuk, D.L. Rusin, Y.G. Shepelev

P 132 **Burning wave structure and combustion mechanism of glycidyl azide/ nitramine mixtures**

A. Zenin, S. Finjakov

P 133 **Mechanism of vortex formation in flame at non-stationary combustion**

V.P. Samsonov, E.N. Petrova, N.N. Sergeeva, L.A. Shilnikova

P 134 **Upper composition limit of burning of AP-fuel mixtures**

N.N. Bakhman, V.V. Evdokimov

P 135 **UV-spectral analysis of NO in the mixture with other gases**

B. Lurie, A. Mikhno, V. Seregin, S. Smirnov

P 136 **On flame temperature determination by thermal radiation**

I.S. Altman, Y.L. Shoshin, Donggeun Lee, Jae Dong Chung, Mansoo Choi

P 137 **Bestimmung der Temperatur von H_2O_2-Brennstoff-Flammen aus den emittierten NIR-Wasserbanden**
Temperature of the NIR-waterbands from H_2O_2 fuel flames

W. Eckl, V. Weiser, C. Besnard

P 138 **Anwendung der digitalen Particle-Image-Velocimetry (DPIV) zur Vermessung turbulenter Strömungen im Inneren einer luftdurchströmten Brennkammer**
Application of the Digital-Particle-Image-Velocimetry (DPIV) on turbulent airflows in a combustion chamber

J. Backhaus, A. Brock, L. Deimling

P 139 **Strahlungsbeeinflussung der Anzündung und Verbrennung von festen Treibstoffen**
Influence of radiation on ignition and combustion of solid propellants

N. Eisenreich, W. Ehrhardt, S. Kelzenberg, A. Koleczko, H. Schmid

P 140 **The burning property of double-base propellant by using three kinds of common plasticizer and the prospect for the new type plasticizer**

Wang Jiang-Ning, Xu Yu, Wang Ning-Fei

P 141 **The influence of composite catalyst on combustion of Al/HMX/CMDB propellant**

Lu Shuanchang, Xu Yu

P 142 **withdrawn**

P 143 **Abbrandmodelle für Rohrwaffentreibmittel: Abbrandverhalten des Rohrwaffentreibmittels JA2 und Abbrandphänomene poröser Ladungen**
Burning rate models of gun propellants: Burning behaviour of JA2 gun propellant and combustion phenomena of porous charges

T. Fischer, N. Eisenreich, S. Kelzenberg, G. Langer, A. Messmer

P 144 **Abbrandverhalten von CL-20/GAP und HMX/GAP-Festtreibstoffen**
Burning behaviour of CL-20/GAP and HMX/GAP-propellants

V. Weiser, N. Eisenreich, W. Eckl, S. Eisele, K. Menke

P 145 **Burning behaviour of cryogenic solid propellants**

V. Weiser, S. Poller, S. Kelzenberg N. Eisenreich, R. Lo, H. Adirim

P 146 **Ti-Nanopartikel zur Anzündung von Rohrwaffentreibmitteln**
Ti-Nanoparticles to ignite gun powders

V. Weiser, A. Koleczko, N. Eisenreich, S. Kelzenberg, D. Müller

P 147 **Synthetic macromolecular compounds**

M.J. Freiria Gandara

P 148 **ADN – a new oxidizer for smokeless rocket propellants**

C. Lagerstam, P. Sjöberg

P149 **Analysis and test methods for service life prediction of energetic materials**

N. Eisenreich, A. Geißler, E. Geißler, C. Hübner

P150 **Methylsubstituted Hydrazinium Azide derivatives**

T. Habereder, A. Hammerl, G. Holl, T.M. Klapötke, J. Knizek, P. Mayer, H. Nöth

CO-OPERATION BETWEEN THE UNITED KINGDOM AND FRANCE ON THE ASSESSMENT OF GUN PROPELLANTS

Chris Leach[1], David Debenham[1], (UK)
Jean-Yves Kermarrec[2], Christophe Tormo [3] (France)

(1) DERA Fort Halstead, Sevenoaks, Kent, TN14 7BP
(2) DGA DSA/SPNuc, 26 bld Victor 00450 PARIS ARMEES
(3) DGA ETBS, EXT/MBI route de Guerry, 18021

Abstract : So-called "LOVA" propellants are being investigated by a number of nations in order to meet future systems performance needs and Insensitive Munitions or MURAT requirements. These materials promise high energy and low vulnerability coupled to low flame temperatures and predicted low barrel wear. However, as with all new materials it is essential that the appropriate testing methodology is developed in order to fully understand and exploit the material properties. Both France and the United Kingdom have had a strong interest in these new materials and the associated assessment methodology. For many years the governments have collaborated bi-laterally in the general area of defence research under the Anglo French Defence Research Group (AFDRG). The vulnerability and ballistic assessment of gun propellants has been conducted under two AFDRG joint programmes (or Technical Arrangements - TAs) - TA18 and TA47. Both programmes have been highly successful and beneficial to both nations, achieving a greater understanding of these new materials than could have been achieved by totally independent research.

The paper concentrates mainly on the vulnerability testing aspects of the collaboration. Samples were exchanged in order to compare testing methodologies. Although test methods were not identical, the results were comparable and the test results obtained by each nation reinforced those of the other, to the extent that future programmes will be able to benefit from the ability to reduce testing by reading across results between the two nations. It was also possible to conclude that it is feasible to formulate high energy "LOVA" propellants with force constants of 1250 kJ/kg and above, which exhibit low vulnerability to a range of stimuli. The "LOVA" candidates tested in both programmes were found to be less vulnerable than their lower energy baseline counterparts.

The paper highlights the success of this bi-lateral collaboration and emphasises the potential benefits of future joint European research programmes.

1.INTRODUCTION

Weapon designers are faced with the task of defeating ever more challenging armoured targets with high velocity kinetic energy projectiles. As a consequence, higher performance gun propellant charges are required to attain the desired projectile velocities. However, at the same time there is also a growing need to meet NATO Insensitive Munitions, or MURAT, requirements to avoid increasing the vulnerability of our own fighting vehicles or the logistical chain. Thus, the propellant formulator and charge designer need to design and utilise propellants which exhibit both high performance and reduced vulnerability. Invariably, increasing the energy of conventional propellants, based on the nitro-glycerine/ nitro-cellulose matrix, results in an increase in vulnerability. This has prompted a world-wide interest in the alternative technology of so called "LOVA" propellants - composite materials based on high levels of nitramine fillers bound in either an inert or an energetic polymer matrix. These materials promise high energy and low vulnerability coupled to low flame temperatures and predicted low barrel wear. However, as with all new materials it is essential that the appropriate testing methodology is developed in order to fully understand and exploit the material properties. Both France and the United Kingdom have had a strong interest in these new materials and the associated assessment methodology and for many years the governments have collaborated bi-laterally in the general area of defence research under the Anglo French Defence Research Group (AFDRG). In particular. the vulnerability and ballistic assessment of gun propellants has been conducted under two AFDRG joint programmes (Technical Arrangements — TAs).

2. RESULTS

The first Technical Arrangement TA 18, concentrated on the vulnerability assessment of 'LOVA" candidates. Both nations supplied one baseline and one " LOVA " candidate each. The second TA, TA 47, concentrated on ballistic assessment of the previous samples and on vulnerability and ballistic assessment of high energy LOVA propellants.

The UK "LOVA" candidate samples were LOVA 4 for TA18 and LOVA 10 for TA47 both of which are polyNIMMO binder based composite gun propellants. The Fr samples were YH01012, which is an HTPB binder based composite, and XH01501, a GAP binder based composite, for TA18 and TA47 respectively.

Exchanged propellant	LOVA 4	YH01012	LOVA 10	XH01501
Impetus (kJ/kg)	1205	1170	1250	1300
Flame Temperature (K)	3000	2900	3200	3400

Table 1 : Exchanged propellant

2.1 Vulnerability results

The propellants were tested in the web size and physical form (UK slotted tube and Fr multi-tubular) appropriate to that required for the gun system used for the final ballistic assessment, (UK -120 mm, Fr - 105 mm).

The UK vulnerability test results are shown in table 2 below.

	LOVA 4	YH01012	LOVA 10	XH01501
Shaped Charge Attack (mass ratio)	0.19 No significant reaction	0.02 No reaction	0.13 No significant reactions	0.21
Fragment Attack 1783 m/s 1976 m/s 1919 m/s			Zero %TNT 1.2 %TNT 0.4 %TNT No significant reactions	
Shock (ELSGT) Go/No go (mm)	31	71	30	68

Table 2 : UK vulnerability test results

The FR vulnerability test results are shown in table 3,4 and 5 below.

	LOVA 4	YH01012	LOVA 10	XH01501
Velocity (m/s)			581	584
Reaction			No reaction	No reaction
Velocity (m/s)	833	843	856	880
Reaction	No reaction	No reaction	No reaction	No reaction
Velocity (m/s)			983	987
Reaction			No reaction	No reaction

Table 3 : FR 12,7 mm bullet attack results

	LOVA 4	YH01012	LOVA 10	XH01501
Velocity (m/s)			1020	1020
Reaction			No reaction	Combustion
Velocity (m/s)			1513	1530
Reaction			Combustion	Combustion
Velocity (m/s)	2200	2197	1950	1975
Reaction	Combustion	Combustion	Combustion	Combustion

Table 4 : FR fragment impact results

	LOVA 4	YH01012	LOVA 10	XH01501
Attenuator (mm)	0	0		
Reaction	Deflagration	Deflagration		
Attenuator (mm)	20	20	20	20
Reaction	Combustion	Combustion	Combustion	Combustion
Attenuator (mm)	40	40	40	40
Reaction	Combustion	Combustion	Combustion	Combustion

Table 5 : FR shaped charge attack results

Although test methods were not identical, the results were comparable and the test results obtained by each nation reinforced those of the other. Both "LOVA" candidates were found to be less vulnerable than their lower energy, double base baseline counterparts. The main difference between the candidates is that French and UK candidates are based on slightly different formulation methodologies and physical geometry which resulted in both French candidates being slightly more shock sensitive in the expanded large scale gap test (ELSGT) than their UK counterparts. However, all the candidates are less shock sensitive in the form tested than TNT (Go / No go transition - 100mm). It was also possible to conclude that it is feasible to formulate high energy "LOVA" propellants with force constant of 1250 kJ/kg and above, which exhibit low vulnerability to a range of stimuli.

Thermal stimuli were also assessed in the early part of the collaboration. However, response to cook-off was not found to be a particular problem with the conventional baseline candidates tested and thermal testing was therefore not considered a priority with the Lova candidates.

2.2 Ballistic results

Closed vessel firings were carried out for all the candidates, including high pressure firings. The different formulation philosphies adopted by UK and France, mainly relating to choice of filler particle size distribution showed themselves up in different burn rate co-efficients and apparently different pressure exponents.

Ballistic assessment for LOVA 4 and YH01012 was carried out by firings in medium calibre gun systems – a 40 mm high pressure gun designed for research purposes in the UK and a 30 mm gun of the type used on the RAFALE fighter in France. It was concluded that the ballistic behaviour of LOVA gun propellant candidates was different to that for more conventional gun propellants. Although the UK propellant was tested as slotted tube and the French propellant was tested in multi tubular form, the experience gained by both nations was remarkably similar and joint conclusions could be drawn. The firings indicated that the pressure exponent was a function of loading density, decreasing with increasing loading density. Another observation is the very low burn rates at low pressures, which may reduce the efficiency of the propellant in the early stages of the ballistic cycle. One observation made in the French firings was that the barrel erosion found in the YH01012 firings seemed to be greater than with

conventional propellant, althought the results of previous erosion bomb studies, also undertaken in AFDRG, indicated that the rate of erosion should be less. The performance in a gun is less than predicted on the basis of closed vessel firings and by theoretical calculations based on the impetus of the propellant. The precises causes of this lower than expected performance are more difficult to establish. However, a combined assessment points to the influence of mechanical properties, slow gas generation in the earlier stage of the ballistic cycle just after ignition, and irregular burning of the heterogeneous binder/filler matrix as potential reasons for a decrease in the efficiency of the ballistic cycle.

Ballistic assessment for the LOVA 10 and XH01501 was carried out by firings in large calibre gun systems – a 120 mm gun in the UK and a 105 mm gun in France. The results are encouraging, with no ignition delay problems and smooth pressure time curves attained. Although the muzzle velocities were higher than that expected from the conventional baseline propellants (multi base propellants) the velocity attained was lower than might be expected from propellants with a force constant of 1250 kJ/kg and above.

3. CONCLUSION

Both nation were able to learn from the collaboration :

Vulnerability testing methodologies were compared and found to give similar results – future programmes will benefit from the ability to read accross results between the two nations.

Two different "LOVA" formulation approaches were contrasted – something that would have proved prohibitively expensive if undertaken by one nation only.

It is feasible to formulate high energy "LOVA" propellants with force constants of 1250 kJ/kg and above, which exhibit low vulnerability to a range of stimuli.

This collaboration confirmed that the ballistic behaviour of "LOVA" propellants is more complex than conventional propellants based on a nitro cellulose matrix. System performance is not only influenced by propellant energy but by burn rate profiles, mechanical properties and gas dynamics. Such properties need to be fully understood for "LOVA" gun propellants before system performance can be maximised. This collaboration between France and the UK has laid the foundations for this understanding in both nations.

4. ACKNOWLEDGMENTS

The authors would like to acknowledge the contributions of participants in both countries, too numerous to mention personally. Particular mention is made of former national representatives in both countries – Adam Cumming in the UK, and Patrick Lamy and Patrick Gervois in France.

© British Crown Copyright 2000 /DERA
Published with the permission of the controller of Her Britannic Majesty's Stationary Office.

Principles of a STANAG for the estimation of the chemical stability of propellants by heat flow calorimetry

Uldis Ticmanis[0], Stephan Wilker[0], Gabriele Pantel[0], Manfred Kaiser[0],
Pierre Guillaume[▪], Corinne Balès[❖], Niels van der Meer[▲]

[0] WIWEB, ASt Heimerzheim, Großes Cent, 53913 Swisttal (Germany)
[▪] PB Clermont SA, Rue de Clermont 176, 4480 Engis (Belgium)
[❖] ETBS, Route de Guerry, 18015 Bourges (France)
[▲] TNO-PML, Postbus 45, 2280AA Rijswijk (Netherlands)

Abstract

The experimental and theoretical work for establishing a STANAG for the estimation of the chemical stability of propellants by heat flow calorimetry is described. The test criteria are derived assuming worst case conditions in ageing and storage.

Kurzfassung

In dieser Arbeit werden experimentelle und theoretische Arbeiten zur Erstellung einer STANAG, die die chemische Stabilität von Treibladungspulvern abschätzen soll, vorgestellt. Die Prüfkriterien werden von "worst case"-Bedingungen bei Alterung und Lagerung abgeleitet.

1 Introduction

NATO standardisation agreements (STANAG) for the thermal („chemical") stability of propellants describe mutually acknowledged test procedures to facilitate cross procurement by avoiding repeated testing in different countries. Already existing STANAGs on this subject are based on stabiliser consumption in isothermal storage at elevated temperatures [1,2,3,4].

Heat flow calorimetry (HFC) offers a more direct treatment of the problem because here just the quantity that causes the danger of thermal explosion is measured. Moreover, interrupting an HFC experiment shortly before autocatalytical reaction starts and analysing the stabiliser content at this stage yields relevant limits for the stabiliser consumption methods.

2 The risk of thermal explosion of propellants

Some examples for heat flow curves of different propellants, measured in a TAM calorimeter at 89°C are shown in figs. 1 to 4. Depending on the type of stabiliser and the nitroglycerin (NG) content (both marked in the graphs) the shapes vary from no to extremely autocatalytic characteristics. The double base (DB) propellant ("DPA, 40%") detonated in the calorimeter after 11 days. The last part of the signal was lost, but simulation of the measuring system (a steel ampoule with 11 mm inner diameter) resulted in a heat generation of at least 80 mW/g to cause a thermal explosion. This event shows dramatically that the chemical stability of propellants merits a more deeply consideration.

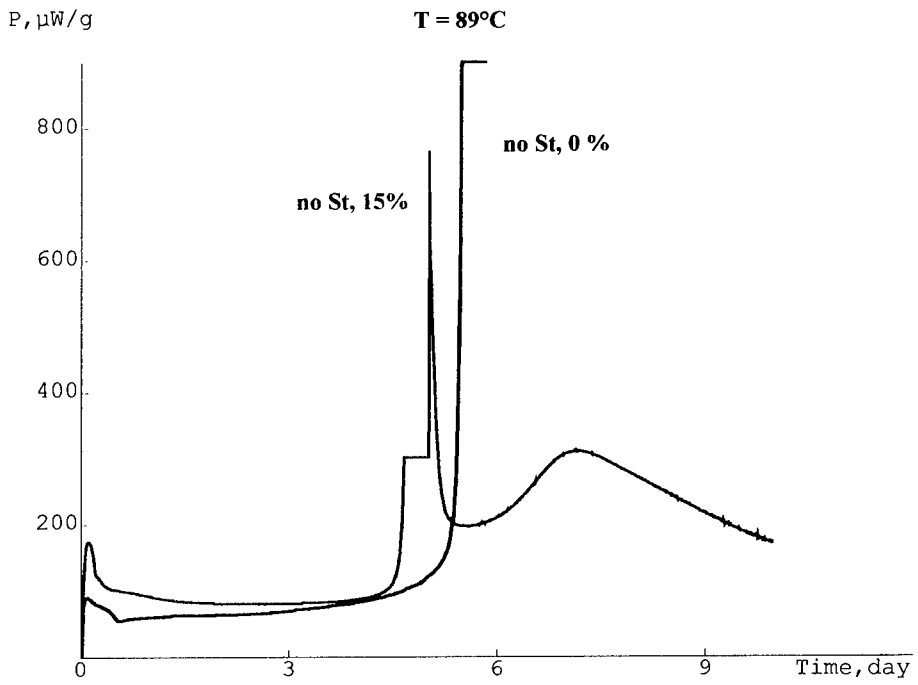

Figure 1. HFC curves of propellants without stabiliser

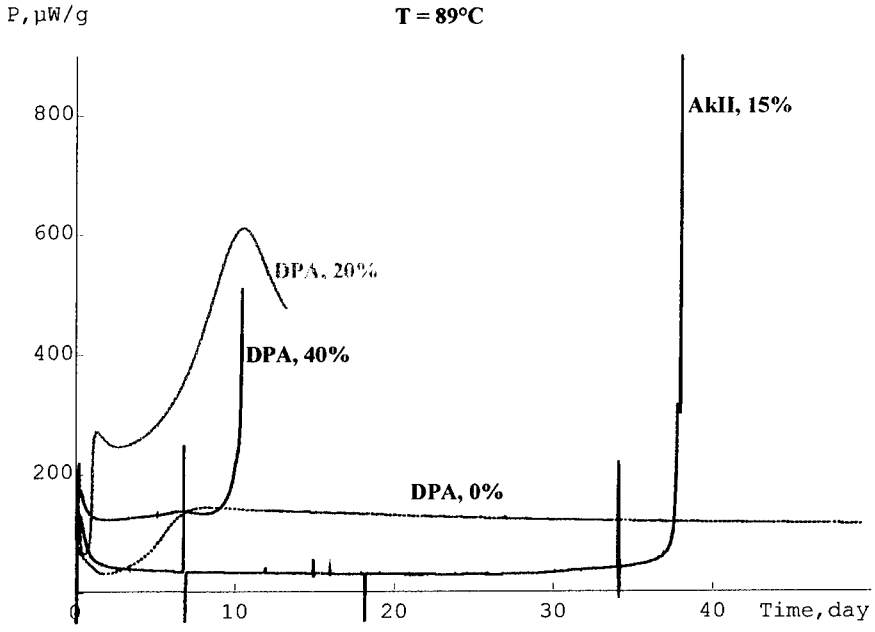

Figure 2. HFC curves of DPA and Akardite II stabilised propellants

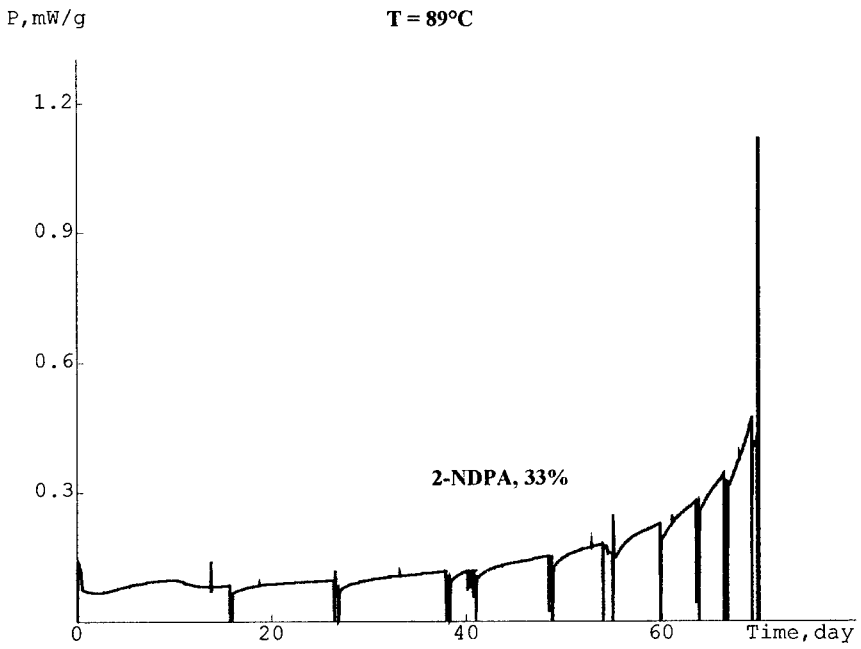

Figure 3. HFC measurement of a 2-NO_2-DPA stabilised propellant

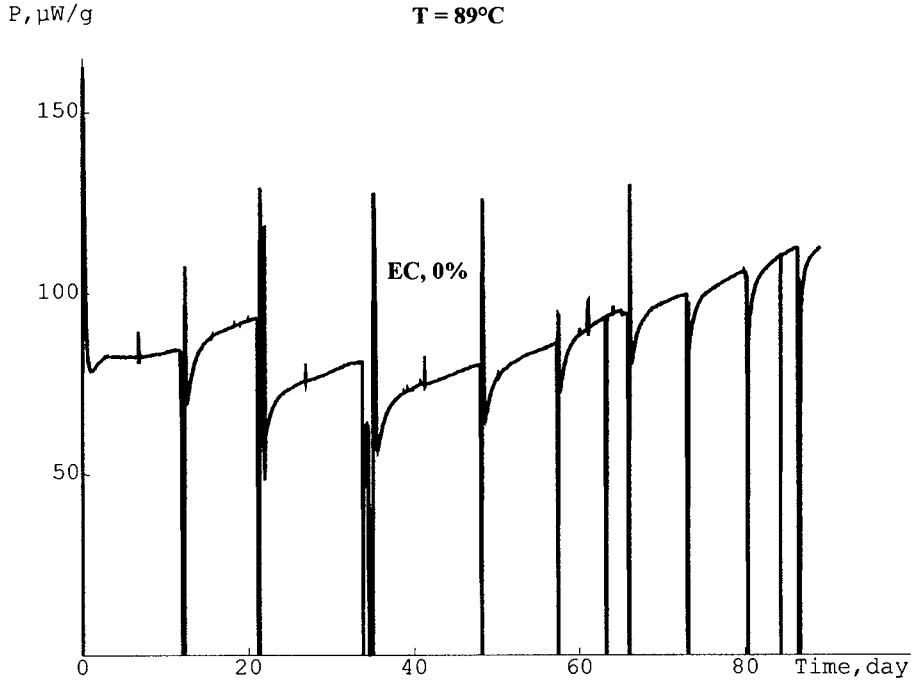

Figure 4. HFC measurement of a propellant stabilised by centralite I.

3 Isothermal ageing theory

The aim of the STANAG [5] is to establish a procedure, based on heat flow calorimetry (HFC), as simple as possible and suitable to ensure chemical stability for a 10-years storage at 25°C. To cover this period in an acceptable measuring duration, the experiments must be performed at elevated temperature. For an extrapolation to ambient conditions we have to consider the temperature dependence of the reactions, characterised by the activation energy (AE). In spite of the quite different shapes of the HFC curves due to nitration and nitrosation of the stabilisers it can be assumed that the temperature dependence will be dominated mainly by the slower decomposition reactions of nitrocellulose and NG. The AE should therefore vary only within a limited range. For the same reason the AE can also be estimated from stabiliser depletion at different storage temperatures.

A lot of storage dates were brought into our NATO "expert working group" while working out the STANAGs based on stabiliser depletion. Former investigations indicated a change in AE in the temperature region around 60°C [6]. Therefore we used the stabiliser depletion dates to test this hypothesis by fitting a n-order reaction below and above this temperature.

$$\ln t = \ln(1/A) + E/RT + \ln[(1 - S/S_0)^{1-n}/(1-n)] \qquad (1)$$

t	=	storage time [d]	R	=	gas constant [0.0083143 kJ/(K · mole)]
A	=	frequency factor [d^{-1}]	n	=	reaction order
E	=	AE [kJ/mole]	S	=	stabiliser content [%]
T	=	storage temperature [K]	S_0	=	stabiliser content before storage [%]

The results are listed in tables 1, 2 and 3.

Table 1. Activation energy from DPA depletion in DB propellants containing up to 15% NG

Storage temperatures	Activation energy	Storage temperature range	Activation energy
[°C]	[kJ/mole]	[°C]	[kJ/mole]
45/50/55	124		
45/50/55	129		
45/50/55	135		
52/60	121	60/65/80	140
52/60	117	60/65/80	153
52/60	109	60/65/80	142
52/60	132	60/65/80	140
52/60	110	60/65/80	140

Table 2. Activation energy from DPA depletion in DB propellants with NG contents from 26 to 43%.

Storage temperatures	Activation energy
[°C]	[kJ/mole]
20/40/50/60	121
20/40/50/60	131
20/40/50/60	126
20/40/50/60	125

Storage temperatures	Activation energy
[°C]	[kJ/mole]
20/40/50/60	127
20/40/50/60	126
20/40/50/60	100

Table 3. Activation energy from 2-NO_2-DPA depletion in DB propellants with NG contents from 20 to 43%.

Storage temperatures	Activation energy	Storage temperature range	Activation energy
[°C]	[kJ/mole]	[°C]	[kJ/mole]
50/60	108	60/70	123
50/60	98	60/70	129
50/60	153	60/70	146
50/60	129	60/70/80	167
50/60	144	60/70/80	163
50/60	132	60/70/80	160
50/60	152	60/70	132
50/60	152	60/70/80	128
-	-	60/70/80	134

The overall mean values

E = 126 kJ/mole (s.d = 15) for temperatures < 60°C and

E = 142 kJ/mole (s.d = 13) for temperatures > 60°C

are not giving a convincing support for a change of AE.

It should however be remarked that the scattering of the dates is high, probably due to unequal sealing of the samples and in consequence a different availability of air. Current investigations in the working group are showing a considerable influence of this factor.

Using hermetically sealed TAM glass ampoules for storage of some DPA stabilised SB propellants we found a continuous change of the AE [6], well described by equation (2):

E_1 = AE dominating at higher temperatures [kJ/mole]

E_2 = AE dominating at lower temperatures [kJ/mole]

$$S = S_0[1-(1-n)(A_1 e^{-E_1/RT} + A_2 e^{-E_2/RT}) * t]^{1/(1-n)} \qquad (2)$$

A_1, A_2 = frequency factors, corresponding to E_1 and E_2 [d^{-1}]

The fittings are shown in figs. 5, 6 and 7, the kinetic parameters are listed in table 4.

Propellant A

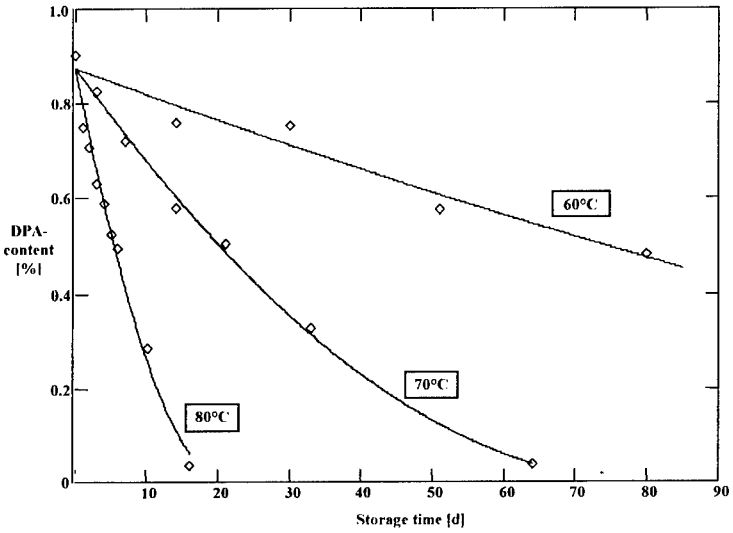

Propellant B

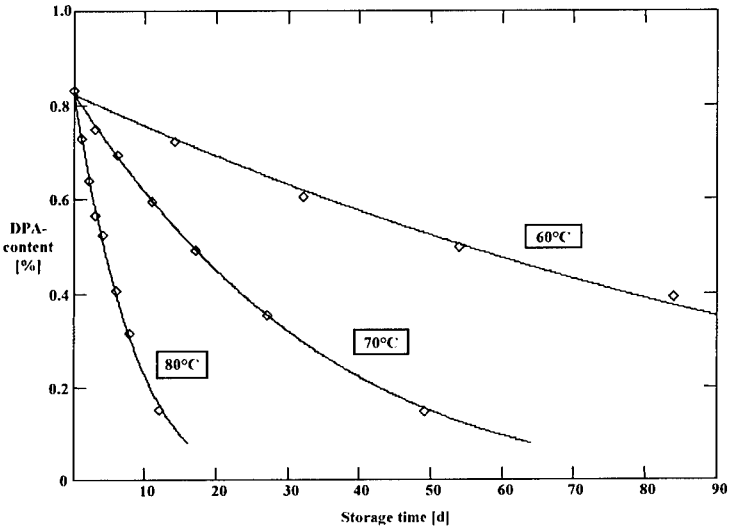

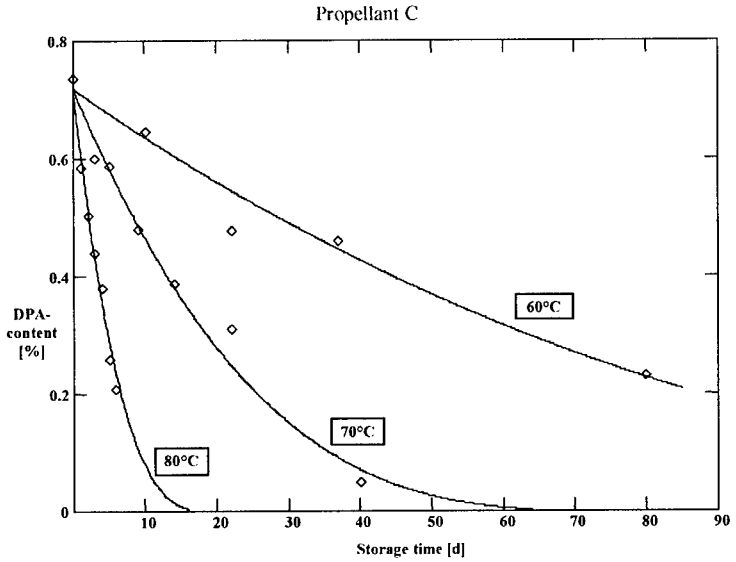

Figures 5-7. Stabiliser (DPA) depletion of some SB propellants in hermetically sealed tubes.

Table 4. Activation energy from DPA depletion in SB propellants using hermetically sealed tubes

Propellant	Lower temperature AE	Higher temperature AE
	[kJ/mole]	[kJ/mole]
A	109	147
B	83	177
C	90	170

From HFC measurements the constance of the AE can be checked using points of equal decomposition degree α (here: equal heat released) at different temperatures and linear regression of

$$\ln t = \ln[\frac{1}{\Delta H * A} * \int_0^Q \frac{dQ}{f(Q/\Delta H)} + \frac{E}{RT}] \qquad (3)$$

Q = heat released [J/g]
ΔH = total reaction heat [J/g]
f(Q/ΔH) = function describing the dependence of reaction rate from reaction degree ("reaction model")

Some plots of AE against the heat released are shown in the figs. 8, 9 and 10 [11]. The first part is dominated by oxidation reactions with the locked-in air, in the following regions near constant values between 120 and 140 kJ/mole are observed. The most informative long time measurements in a temperature range from 50 to 89°C were realised by GUILLAUME [7]. No transition of AE at lower temperatures can be detected from these dates (fig. 11).

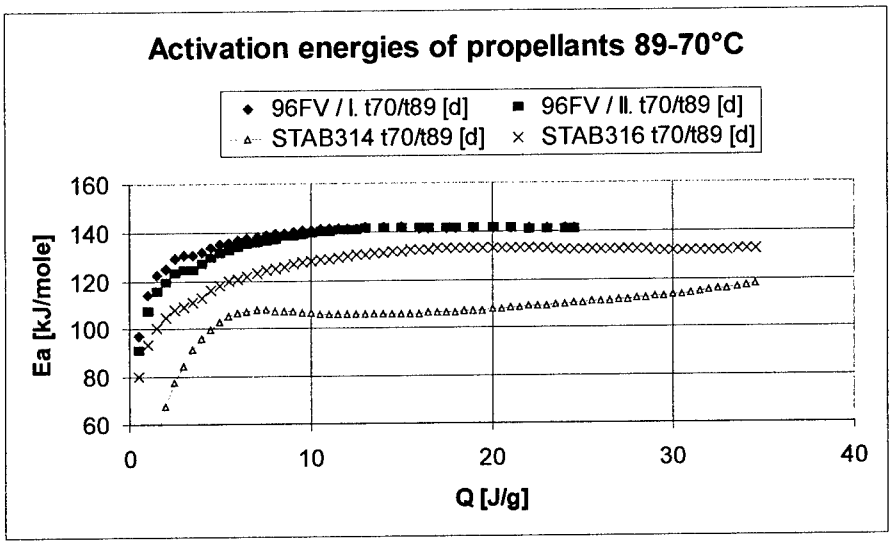

Fig. 8. Activation energies of four DB propellants stabilised with DPA or DPA derivatives.

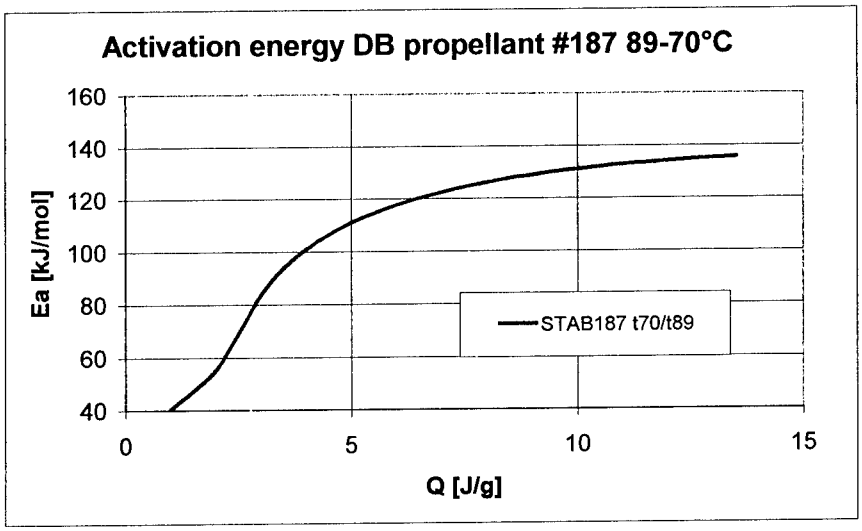

Fig. 9. Activation energy of a DB propellant stabilised by 2-NO_2-DPA [11]

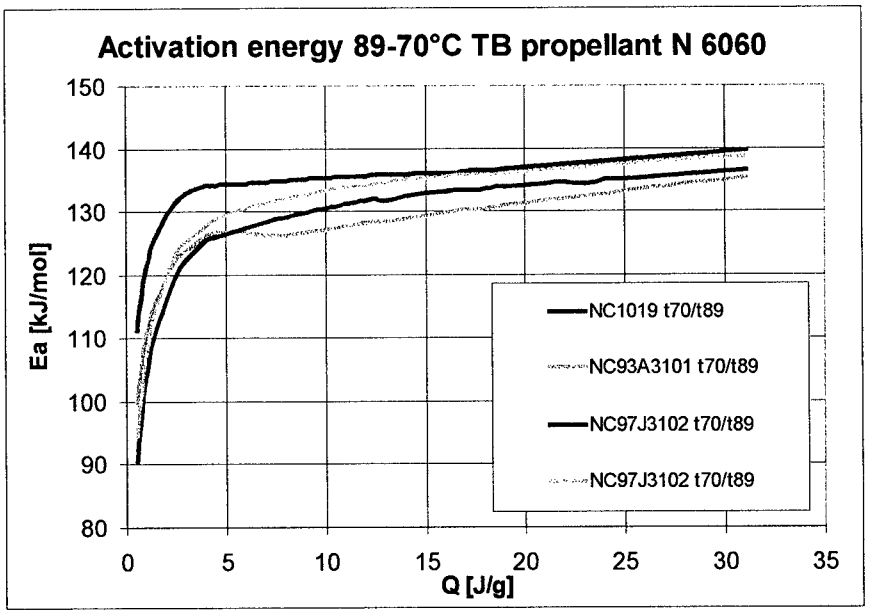

Fig. 10. Activation energy of a TB propellant stabilised by ethyl centralite

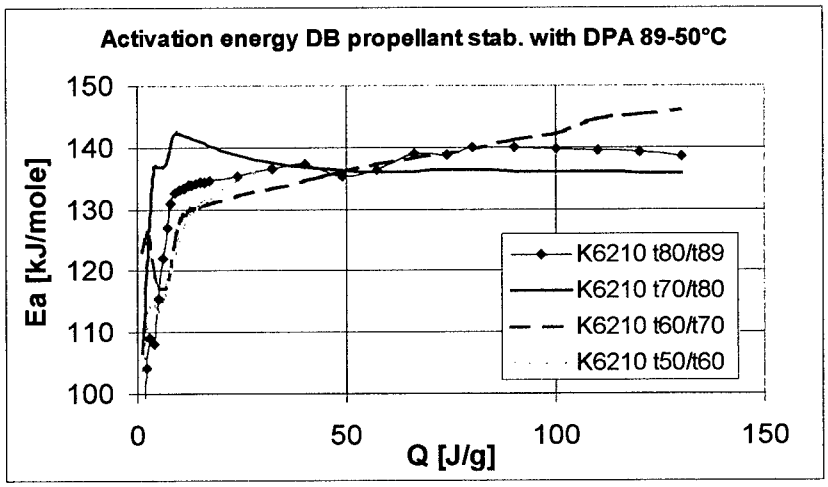

Fig. 11. Activation energy of a DPA stabilised DB propellant between 89°C and 50°C [7]

All HFC measurements reported up to now were carried out starting with fresh samples introduced into the calorimeter at every temperature. Allowing exact "iso-α-evaluation" over a range of decomposition this method is the best. Unfortunately the experiments are extremely time-consuming. An alternative treatment is to age a sample at a higher temperature until a suitable decomposition degree is reached followed by measurements of the same sample at lower temperatures. Since the reaction degree remains nearly constant, the AE can be calculated from temperatures and heat flow values by

$$\ln P = \ln[10^6 * \Delta H * A * f(\frac{Q}{\Delta H})] - \frac{E}{RT} \qquad (4)$$

P = heat flow [µW/g]
A = frequency factor [s^{-1}]

Measurements of this type with DPA-stabilised SB propellants resulted in two different slopes of the plot (see fig. 12, 13 and 14 and table 5).

Table 5. Activation energy from HFC measurements in SB propellants using hermetically sealed tubes (same samples than in table 4)

Propellant	Lower temperature AE	Higher temperature AE	Temperature of transition [a)]
	[kJ/mole]	[kJ/mole]	[°C]
A	88	124	66
B	81	145	65
C	93	136	53

a) Temperature for equal values of both reaction rate constants

Considering all results gained from stabiliser depletion and HFC leads to the conclusion that at least a general transition of AE at lower temperatures is not detectable.

But following the usual philosophy of safety on explosives (If you are not sure, take the worst case) we must assume that a change may exist for some types of propellants. Corresponding to the lowest values found the levels were set at 120 kJ/mole for temperatures above 60°C and at 80 kJ/mole in the range below. Apart from the different temperature dependence the reactions are assumed to be identical below and above 60°C.

The duration of the experiment leading to the same decomposition degree as a ten year's storage at 25°C can then be calculated from [1]

$$t_m = t_{25} * e^{[E_1*(\frac{1}{T_m} - \frac{1}{T_{60}}) + E2*(\frac{1}{T_{60}} - \frac{1}{T_{25}})]/R} \qquad (5)$$

t_m = test duration [days]
t_{25} = duration of storage at 25°C (3652.5 d = 10 years)
T_m = test temperature [K]
T_{60} = temperature of change of the activation energy (AE) (333.15 K = 60°C)
T_{25} = storage temperature (298.15 K = 25°C)
E_1 = AE of the higher temperature range (120 kJ/mole)
E_2 = AE of the lower temperature range (80 kJ/mole)

By introduction of the constant values T_{25} = 298.15 K, T_{60} = 333.15 K and E_2 = 80 kJ/mole eq. 5 simplifies to

$$t_m = t_{25} * e^{E_1/(R*T_m) - C} \qquad (C = 46.713) \qquad (6)$$

Taking into consideration different meanings concerning the test temperature the STANAG allows to choose a temperature in the range from 60 to 90°C.

Eq. (6) is used for calculation of the corresponding test duration (see table 6).

[1] For derivation see appendix 1

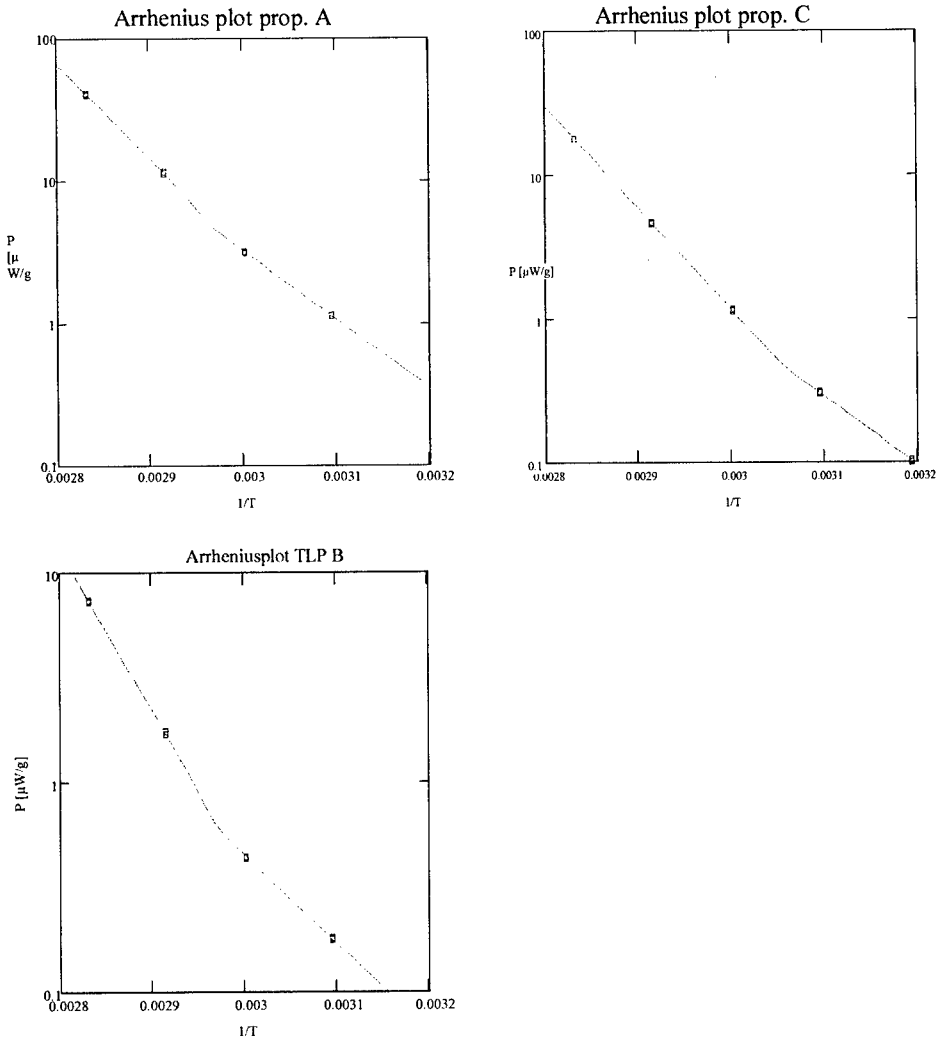

Figures 12-14. Activation energies of three DPA stabilised SB propellants.

Table 6. Test times for different test temperatures

Test temperature [°C]	Test time [days]
60	123
65	57,2
70	34,8
80	10,6
89	3,83
90	3,43

4 Assessments for non-isothermal storage

In practice an isothermal storage will never be realised. However, if a temperature and time profile of storage can be predicted, it is possible to check whether the thermal stress will be less or more than a storage at 25°C. For temperatures below 60°C any storage durations can be added up as storage times equivalent to 25°C. An example is given in table 7.

$$t_{25} = t_s * e^{E_2 (1/T_{25} - 1/T_s)/R} \qquad (7)$$

T_s = storage temperature [K]
t_s = storage duration [y]
t_{25} = storage duration at 298.15 K [y]
E_2 = 80 kJ/mole

Table 7: Calculation of 25°C times for a storage profile

T_s [°C]	t_s [y]	t_{25} [y]
40	0.1	0.47
35	0.4	1.14
30	1.5	2.55
25	3	3.00
20	4	2.31
15	1	0.33
SUM	10	9.80

5 Limitation of the heat generation

Gained from experiments with very small differences of the test temperature and the temperature in the propellant the extrapolation outlined above is also only valid for a likewise ideal storage. Under unfavourable real conditions however (high temperatures, large diameters and isolating packing material of ammunition) the exothermal decomposition may cause a considerable increase of temperature in the inner parts of the propellant and hence an accelerated ageing. The consequence would be, that the reaction degree might exceed the area controlled in the test and reach probably more dangerous regions. This situation is illustrated in fig. 15.

To prevent this risk a heat generation limit has to be fixed to ensure that the temperature increase in the propellant remains small.

As a most unfavourable system we consider a cartridge of 230 mm diameter, thermally well isolated (thermal transfer 0,001 W/(cm²·K), corresponding for example to a polyethylene package of about 4 cm thickness) and set at a temperature of 71°C. Thermal safety simulations were realised using the heat transfer model of THOMAS [8] in an extended version of OPFERMANN [9,10]. The kinetics were modelled for „strong autocatalysis" (comparable to propellant „DPA 40%" in fig. 2), „weak autocatalysis" (related to propellant „DPA 20%" in fig. 2) and a zero-order reaction. The equations and parameters used are listed in Appendix 2.

We started with a series of simulations with the strongly autocatalytic propellant. Fig. 16 shows the behaviour in a very small cartridge (thermal transfer 1 W/(cm²·K), comparable to a

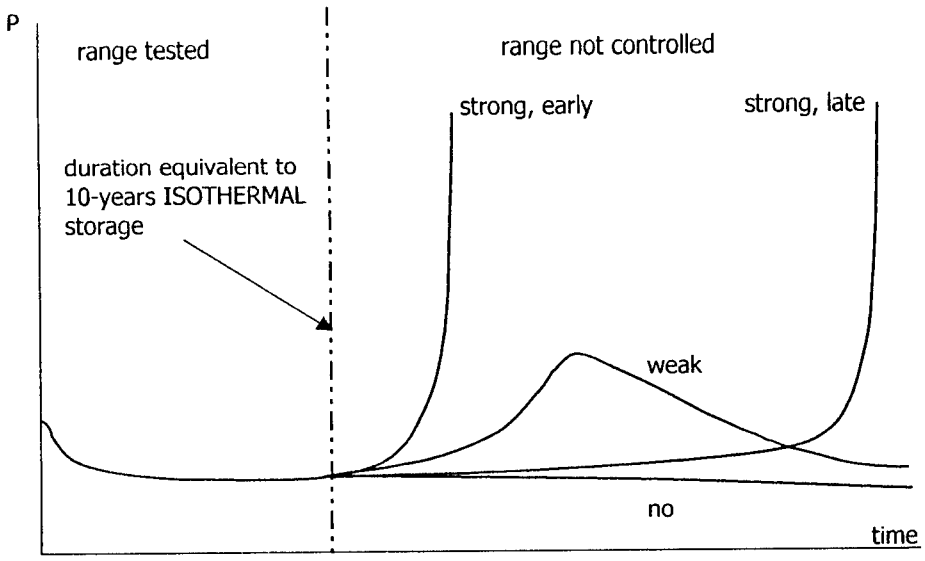

Fig. 15. Possible decomposition mechanisms

HFC experiment) at 89°C. The lines are representing the temperatures in the different distances from the centre (= 0%). Fig. 17 demonstrates the ageing of the same propellant in a large cartidge under the same conditions. The time to explosion is shortened from 11 to 0.6 days. At the highest assumed temperature of 71°C the explosion occurs after more than 90 days (fig. 18). For propellants of this characteristics a thermal explosion can not be excluded, even at lower temperatures. But the safety is yet guaranteed by the long period of time to reach dangerous conditions. E.g. at 47°C the cartridge needs more than 20 years to explode (fig. 19). Assuming the more unfavourable case of an AE of 80 kJ/mole the 20-years-temperature would still be 39°C (fig. 20).

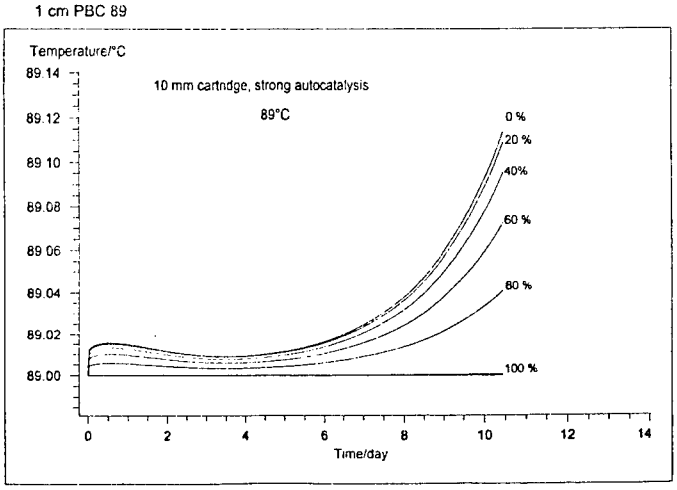

Fig. 16. Simulation of a small cartridge containing an extremely autocatalytic propellant

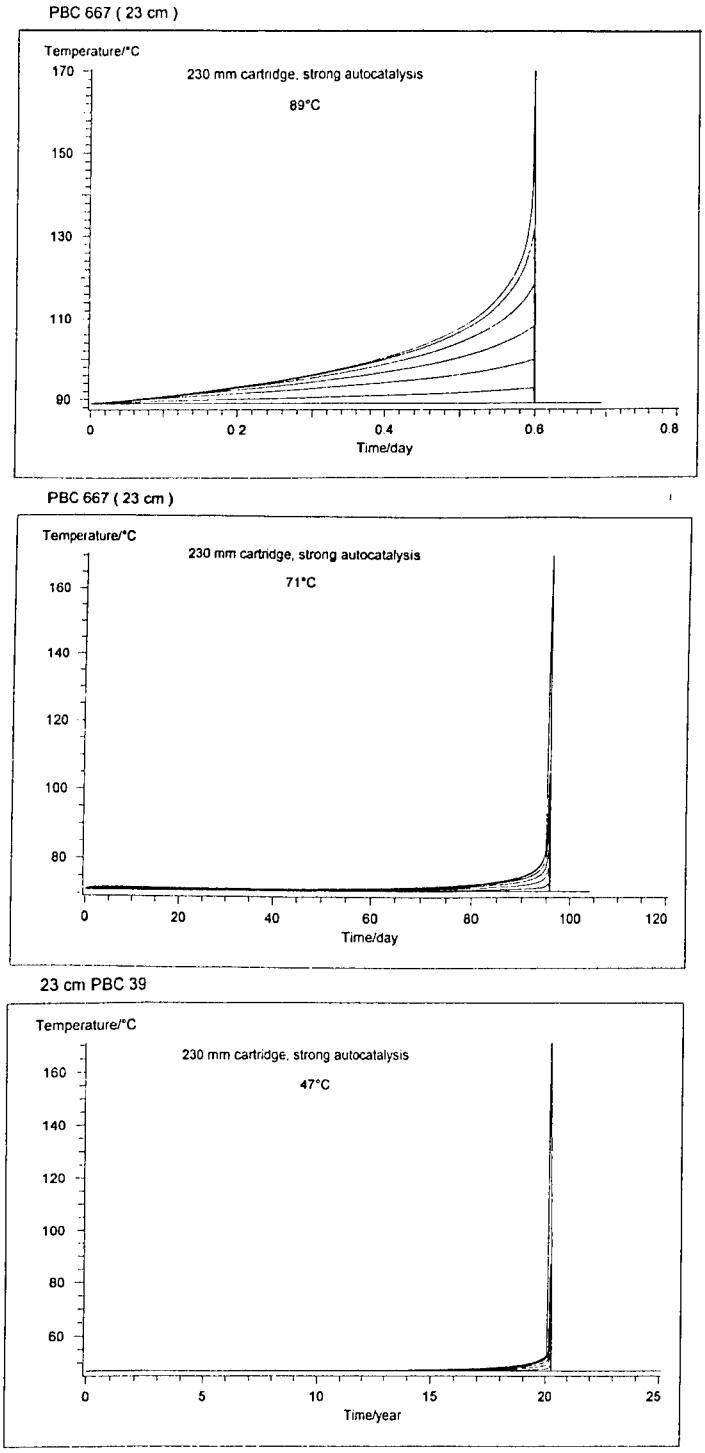

Figs. 17-19. Simulations of a large cartridge containing an extremely autocatalytic propellant

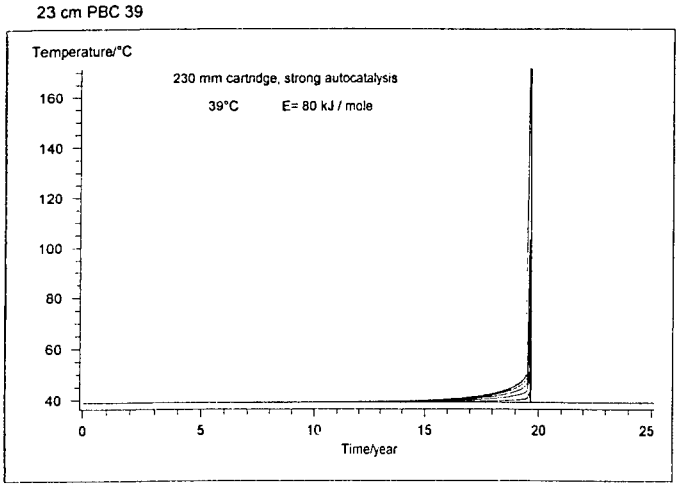

Fig. 20. Simulation of a large cartridge containing an extremely autocatalytic propellant

The propellant of the type „weak autocatalysis" does not explode at 71°C (fig. 21). Critical conditions are not reached until 76°C (fig. 22).

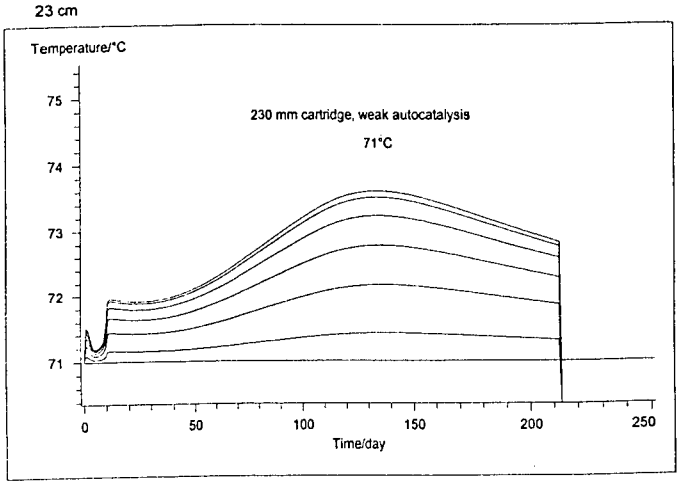

Fig. 21. Simulation of a large cartridge containing a moderately autocatalytic propellant

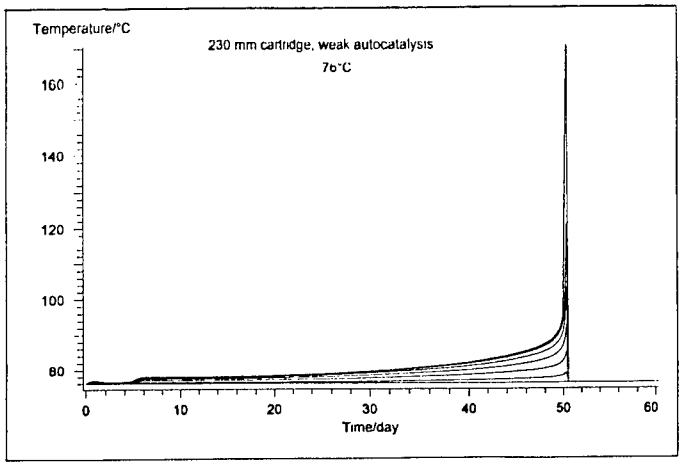

Fig. 22. Simulation of a large cartridge containing a moderately autocatalytic propellant

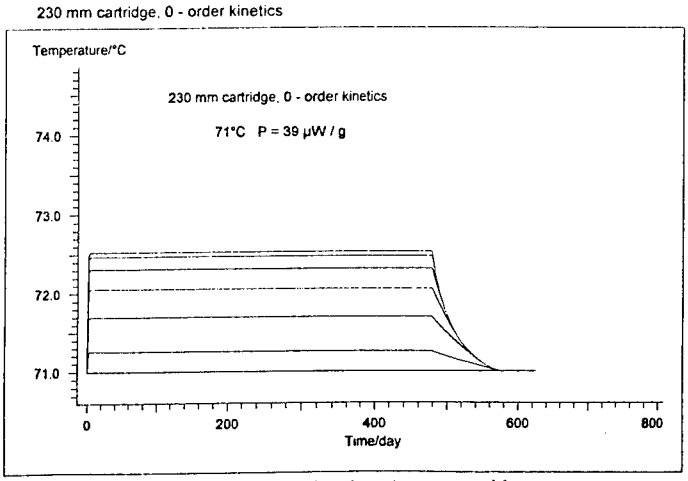

Fig. 23. Simulation of a constant heat generation in a large cartridge

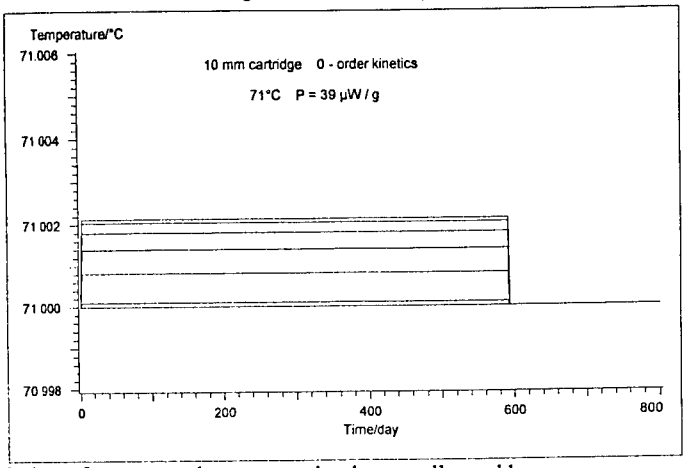

Fig. 24. Simulation of a constant heat generation in a small cartridge

To find a suitable limit for this system the heat generation rate was varied by the frequency factor of the zero order reaction. At a level of 39 µW/g the temperature increase in the inner part of the 230 mm cartridge is about 1.5°C, the time for a total reaction is 480 days (fig. 23), in relation to 590 days for an isothermal ageing (fig. 24). This difference is tolerable. Therefore a heat generation limit of 39 µW/g at 71°C can be accepted as sufficient control of ageing in an equilibrium with the ambient temperature even under worst conditions.

An equivalent limit depending on the test temperature chosen is used as a criterion for sufficient chemical stability of a propellant. It can be calculated by

$$P_l = P_{71} * e^{E_l * \left(\frac{1}{T_{71}} - \frac{1}{T_m}\right) / R} \qquad (8)$$

T_m = test temperature [K]
T_{71} = 344.15 K (= 71°C)
E_l = activation energy (120 kJ/mole)
P_{71} = heat flow limit at 71°C (39 µW/g)
P_l = heat flow limit at T_m [µW/g]

Values for some selected temperatures are given in table 8.

Table 8. Heat generation limits for different test temperatures

T_m [°C]	P_l [µW/g]	T_m [°C]	P_l [µW/g]
60	9.8	80	114
65	18.5	89	314
70	34.5	90	350

In the first part of the measurement some propellants show a fast decreasing exothermic reaction with the locked in air. The total heat of this reaction is small and cannot cause more than a temperature increase of only a few degrees centigrade, even if released momentarily. To disregard this effect the P_l criterion should be used only in the region between the time corresponding to a heat release of 5 J/g and the test time defined by eq. (6). An example of the evaluation of a test is given in fig. 25.

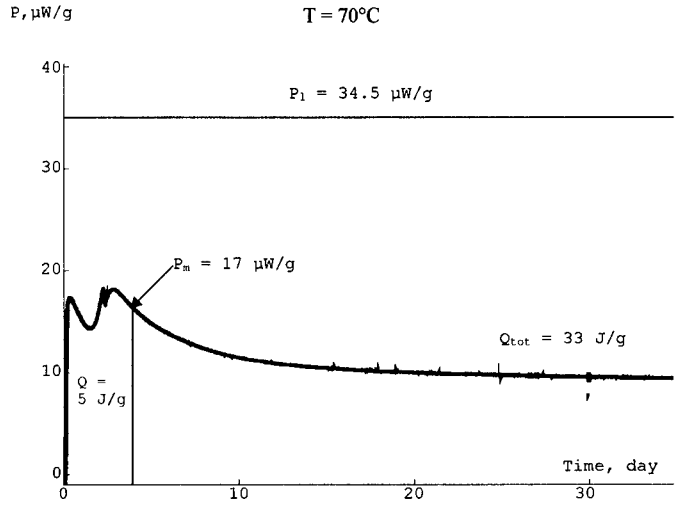

Figure 25. Heat flow curve and evaluation of a DB propellant stabilized with DPA

6 Discussion

While working out this methods some propellants capable of an extremely autocatalytic reaction were found. These propellants can not be expected to remain stable forever, even not if they are used in small calibre ammunition and stored at moderate temperatures. But the saftey is guaranteed for a period much longer than usual service life times. To detect certainly the safety life time two parameters were set on very conservative levels:

1. The assumption of a low AE at lower temperatures means that the test duration will be equivalent to a considerably longer storage time at ambient temperatures than the demanded 10 years.
2. The limitation of the tolerable heat generation of the propellant considering a worst case system is a further guarantee that the stress during the service life time will be smaller than in the test.

In consequence the failing criteria of the test are hard, not far away from unfairness. On the other hand until today no qualified propellant ever was found to fail the test, indicating a good quality of manufacture.

7 References and Notes

[1] STANAG 4527, „Explosives, Chemical Stability, Nitrocellulose based Propellants, Procedure for Assessment of Chemical Life and Temperature Dependence of Stabilizer Consumption", Draft Edn. 1 (**1/98**).

[2] STANAG 4117, „Explosives, Stability Test Procedures and Requirements for Propellants Stabilized with Diphenylamine, Ethyl Centralite or Mixtures of Both", Edn. 3 (**2/98**).

[3] STANAG 4541, „Explosives, Nitrocellulose based Propellants containing Nitroglycerin and Stabilized with Diphenylamine, Stability Test Procedure and Requirements", Edn. 1 (**2/99**).

[4] STANAG 4542, „Explosives, Stability Test Procedure and Requirements for Nitrocellulose based Propellants containing Nitroglycerin and Stabilized with 2-Nitrodiphenylamine", WG Draft (**2/99**).

[5] STANAG 4582, „Explosives, Single and Double Base Propellants, Stability Test Procedure and Requirements using Heat Flow Calorimetry", WG Draft (**4/00**).

[6] U. Ticmanis, G. Pantel, L. Stottmeister, „Stabilitätsuntersuchungen einbasiger Treibladungspulver – Mikrokalorimetrie im Grenzbereich", *ICT-Jahrestagung* 29, 27 (**1998**).

[7] P. Guillaume, M. Rat, G. Pantel, S. Wilker, „Heat Flow Calorimetry of propellants – Effects of sample preparation and Measuring Conditions", *2. TTCP Workshop Leeds* 4/**1999**.

[8] P.H. Thomas, *Trans. Faraday Soc.* 54, 60-65 (**1942**).

[9] J. Opfermann, Manual for the Compter Program „Netzsch Thermal Safety Simulation", Edn. **1993**.

[10] U. Ticmanis, G. Pantel, M. Kaiser, „Simulation der chemischen Stabilität eines zweibasigen Kugelpulvers", *2. Int. Workshop Mikrokalorimetrie WIWEB*, p. 182-195 (**1999**).

[11] J. Petržílek, J. Skládal, S. Wilker, G. Pantel, L. Stottmeister, „Stability analysis of propellants containing new stabilisers – Part I", *ICT Jahrestagung* 31, 61 (**2000**).

Appendix 1

Calculation of the measuring time

A reaction formulated in the heat flow form is given by

$$\frac{dQ}{dt} = \Delta H * f(\frac{Q}{\Delta H}) * A * e^{-E/(RT)} \qquad (9)$$

Q	=	Heat released	ΔH	=	Total reaction heat
t	=	Reaction time	T	=	Temperature of reaction [K]
dQ/dt	=	Reaction rate (heat flow)	Q/ΔH	=	Reaction degree
A	=	Frequency factor	E	=	Activation energy [kJ/mole]
R	=	Gas constant			
f(Q/ΔH)	=	Function of describing the dependence of the reaction rate from the reaction degree			

If T_m is the measuring temperature, Q_m the heat released at the end of the measurement, E1 the AE dominating at higher temperatures, then after separation of the variables, integration at constant temperature and rearrangement the reaction time t_m is obtained by

$$t_m = \frac{1}{\Delta H * A} * \int_0^{Q_m} \frac{dQ}{f(Q/\Delta H)} * e^{E_1/(R*T_m)} \qquad (10)$$

The time t_{60} to reach the same decomposition Q_m at the assumed temperature (T_{60}) of change of AE can equally be calculated from

$$t_{60} = \frac{1}{\Delta H * A} * \int_0^{Q_m} \frac{dQ}{f(Q/\Delta H)} * e^{E_1/(R*T_{60})} \qquad (11)$$

The value of the integral in eqns. 10 and 11 1s unknown but equal. Therefore by division and rearrangement eq. 12 results:

$$t_m = t_{60} * e^{[E_1 \cdot (1/T_m - 1/T_{60})]/R} \qquad (12)$$

If the change of AE is assumed to occur sharply at 60°C an equation similar to eq. 12 is also valid for E_2, the AE dominating the lower temperature range.

$$t_{60} = \frac{1}{\Delta H * A} * \int_0^{Q_m} \frac{dQ}{f(Q/\Delta H)} * e^{E_2/(R*T_{60})} \qquad (13)$$

The corresponding time t_{25} for 25°C (T_{25}) is

$$t_{25} = \frac{1}{\Delta H * A} * \int_0^{Q_m} \frac{dQ}{f(Q/\Delta H)} * e^{E_2/(R*T_{25})} \qquad (14)$$

Division of eqns. 13 and 14 gives after rearrangement

$$t_{60} = t_{25} * e^{[E_2 \cdot (1/T_{60} - 1/T_{25})]/R} \qquad (15)$$

Combination of eq. 12 and 15 results in

$$t_m = t_{25} * e^{[E_1*(\frac{1}{T_m} - \frac{1}{T_{60}}) + E2*(\frac{1}{T_{60}} - \frac{1}{T_{25}})]/R} \qquad (5)$$

Appendix 2

Data used for thermal safety simulations

Kinetics for modelling propellant decompositions

a) n - order reaction $$P = \Delta H * k * 10^6 * [1-(1-n) * kt]^{n/(1-n)} \quad (16)$$

b) 1^{st} *order with autocatalysis* $$P = \Delta H * a^2 * k * 10^6 * \frac{e^{akt}}{(e^{akt} - 1 + a)^2} \quad (17)$$

c) *Avrami – Erofeev reaction* $$P = \Delta H * k * 10^6 * [(1-p)kt]^{p/(1-p)} * e^{-[(1-p)kt]^{1/(1-p)}} \quad (18)$$

d) *Prout – Tompkins reaction* $$P = \Delta H * 10^6 * (\frac{1-Q}{\Delta H})^n * (\frac{Q}{\Delta H})^p * k \quad (19)$$

$$k = A * e^{-AE/RT}$$

For 1^{st} and zero-order reaction: n = 1.0001 and n = 0 in eq. (16).

Kinetics for „strong autocatalysis" were modelled by three independent reactions. For „weak autocatalysis" four reactions were used. Their parameters are listed below.

Type	Reaction (eq)	log A [A in s^{-1}]	AE [kJ/mole]	n	log a	p	ΔH [J/g]
„strong	(16)	14,7817	140	1,0001	-	-	46,0
autocata-	(18)	14,9984	140	-	-	0,67	28,7
lytic"	(17)	9,9119	140	-	5	-	61106
	(16)	5,3743	80	1,0001	-	-	46,0
	(18)	5,5910	80	-	-	0,67	28,7
	(17)	0,5045	80	-	5	-	61106
„weak	(16)	14,0776	136	0,6446	-	-	104,9
autocata-	(16)	13,4177	127	0,1583	-	-	-18,3
lytic"	(16)	14,0484	127	0,5372	-	-	2,7
	(19)	14,1993	139	5,4568	-	0,6821	4000
constant	(16)	variable	140	0	-	-	2000

Other propellant data:

Form of reactor:	cylindrical
Specific heat (C_p):	0,205 + 0,00325 T [J/(g·K)]
Heat conductivity:	0,00122 W/(cm·K)
Loading density:	1 g/cm³
Explosion temperature:	170°C

STABILITY OF PROPELLANTS, THERMAL OR FUNCTIONAL

C.A. (Chris) van Driel[a] and W.P.C. (Wim) de Klerk[b]

TNO Prins Maurits Laboratory
[a] Pyrotechnics and Energetic Materials, [b] Properties Energetic Materials
P.O. Box 45, 2280 AA Rijswijk, The Netherlands
driel@pml.tno.nl, klerk@pml.tno.nl

Abstract

It is well known that the lifetime of conventional gun propellants is limited due to decomposition of nitrocellulose (NC). In general, research on ageing of propellants is mainly focussed on the safety aspects regarding storage of propellants. Decomposition of NC, however, not only leads to heat production that can result in run-away reactions, it also causes a decrease of the mechanical integrity of the propellant grains.

In this investigation various properties of an SB and a DB gun propellant have been determined before and after artificial ageing. A number of parameters is selected from which the safe use of gun propellants can be determined.

It is concluded that the lifetime of conventional gun propellants is not only determined by thermal degradation because changes of the mechanical characteristics may finally lead to unsafe employment.

Introduction

Research on ageing of propellants is in general mainly focussed on the safety aspects regarding storage of propellants. The safe storage lifetime of nitrocellulose (NC) based propellants is limited due to decomposition of NC. The decomposition is suppressed by the application of stabilisers. Many efforts have been put into the understanding of the mechanism of decomposition and behaviour of NC and stabilisers [1–6]. The stability can be predicted by measuring the stabiliser depletion by HPLC [7] or by Heat Flux Calorimetry (HFC)[8].

Decomposition of NC, however, not only leads to heat production that can finally result in run-away reactions, but the decomposition also causes a break-down of the nitrocellulose polymeric chains [9, 10]. This results in a decrease of the mechanical integrity of the propellant grains [11, 12]. In case of gun propellants the mechanical properties affect the ignition behaviour of the propellant grain bed. Embrittlement may lead to enhanced breakage of grains, which in turn leads to an increase of the burning surface area, finally resulting in an accelerated pressure rise and a diminished porosity of the propellant bed during firing. Consequences may be an irregular pressure build-up, pressure waves or increased peak pressures [12].

The aim of this investigation is to gain more qualitative insight in the effects of ageing on the internal ballistic properties of gun propellants and to select a number of parameters that provide indications with respect to the safe use of gun propellants. For this purpose various properties of a single base (SB) and a double base (DB) gun propellant have been determined before and after artificial ageing.

Experimental

propellants

The gun propellants that were used for this study are a 7-hole SB propellant for Howitzer charges, and a flake DB propellant for mortar application. Some characteristic parameters of these propellants are given in Table 1.

Table 1: Characteristic parameters of the investigated propellants.

	SB	DB
bulk density [g/cm^3]	832	1624
calorific value [kJ/kg]	3060	4807
grain shape	tubular, 7 perf.	flake
grain length [mm]	11.03	9.85
grain diameter/thickness [mm]	4.86	1.30
nitrocellulose [%]	83	56
nitroglycerine [%]	–	41
weapon	155 mm Howitzer	120 mm Mortar

artificial ageing

Both propellant types were aged in glass bottles that were closed in order to prevent evaporation of volatile ingredients. The SB propellant was aged for 3 weeks at 85°C, the DB propellant for 10 weeks at 75°C. These conditions simulate an increase of the lifetime of roughly 20 to 30 years. For the present study it is not necessary to know the exact lifetime extension, because the effects of ageing are only determined qualitatively.

heat development and energy content

The heat development of both propellants was examined by microcalorimetry at the same conditions as the artificial ageing. The ageing procedure is performed in the Isothermal Storage Test [1], in closed stainless steel vessels of 70 cm^3, with a sample mass of approximately 5 grams. The advantage of this ageing procedure is that it continuously provides information about the heat generation during the measuring time. Afterwards it is possible to calculate the

energy decrease by integrating the obtained heat versus time curve [2]. The calorific values of the unaged and aged propellants were determined by use of a bomb calorimeter.

chain length NC

The change of polymeric chain length of the propellant samples was determined by means of gel permeation chromatography (GPC). Polystyrene standard samples were used as references for the calculation of the molecular weights. Although the obtained molecular weights are therefore not absolute but relative values, the results provide a good indication of the ageing effect.

morphological changes

In order to investigate possible changes of the microstructure of both propellant types, slices were made from the propellant grains, which were embedded in epoxy resin, sandpapered and polished. These samples were investigated by means of optical microscopy and scanning electron microscopy.

burning properties

Closed vessel (CV) tests were carried out with uncompressed grains as well as grains that were quasi-statically pressed as described below. The obtained pressure-time data are used for the calculation of the dynamic and characteristic vivacity, L and L_k, and the burning rate, r. These parameters are calculated as described in STANAG 4115 [13], the burning rate is only calculated for the uncompressed samples at the pressure interval from 0.2 to 0.8 P_{max}.

mechanical properties: single grains and quasi-static compression test

The effect of ageing on the mechanical properties was investigated by means of uniaxial compression tests or bending tests using single propellant grains as well as quasi-static compression of a propellant bed. Compression and bending tests with single propellant grains were performed at 20°C. The SB 7-hole grains were shortened to a standard length/diameter ratio of 1:1 before subjecting them to the compression test. DB propellant flakes were tested by means of a bending test.

An alternative for tensile testing is the compression of a propellant bed and subsequent firing of the fractured grains in a CV [14]. Quasi-static compression is relatively simple and provides good indications with respect to propellant bed behaviour during the first stages of ignition and combustion in a gun.

For the quasi-static compression test, 300 grams of propellant is quasi-statically pressed for 4 seconds at 300 Bars. The compression is performed at –40°C. After acclimatisation CV tests are performed with a loading density of 0.214. Extrapolation of the change in linear vivacity between 0.2 and 0.7 P_{max} to $P/P_{max} = 0$ results in a value that is a measure of the destruction of the propellant grains. This value corresponds to the relative surface area at the beginning of combustion due to the fractured grains [14], and is sometimes called 'relative surface area'. For various applications one can use specific criteria for the 'relative surface area'.

Results and discussion

chain length NC

The results of the GPC measurements are given in Figure 1a/b. Important data with respect to the polymeric chain length of NC are the (weight average) molecular weight (M_w) as well as the molecular weight distribution. The latter can be determined from the ratio between weight average and number average molecular weight (M_w/M_n). These results of the GPC-measurements are given in Table 2.

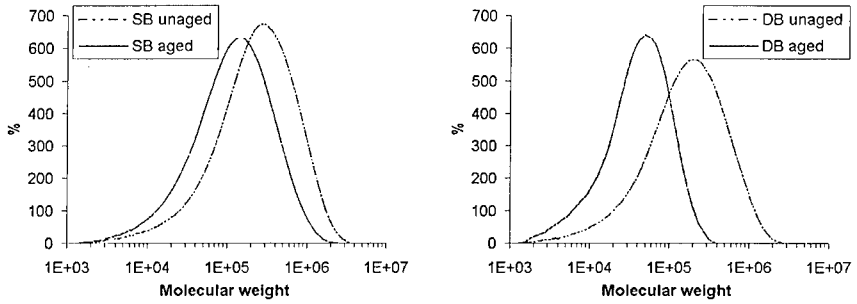

Figure 1a/b: Results of GPC-measurements: molecular weight distributions of unaged and aged SB propellant (left) and DB propellant (right).

Table 2: Results of GPC-measurements.

Sample	Molecular weight M_w (dupl.)	ratio aged/unaged	Width of weight distribution M_w/M_n (dupl.)	ratio aged/unaged
SB unaged	331000	0.53	4.3	0.85
	328000		4.1	
SB aged	176000		3.6	
	173000		3.6	
DB unaged	237000	0.23	4.1	0.58
	245000		4.0	
DB aged	54200		2.4	
	55600		2.3	

The results show that the chain lengths of propellant grains, which were aged for a period that is equivalent to 20 – 30 years, is shortened by 50% (SB) to even 80% (DB). Further the width of the mole weight distributions is decreased as well, by 15% and 40% respectively. It is reasonable to assume that both factors affect the mechanical properties of the propellant grains.

morphological changes

Both SB and DB propellant grains show a change of their colour due to ageing. The SB samples changed from yellow green to yellow brown, DB samples from light yellow to dark brown, which is probably caused by the conversion of primary stabilisers to derivatives. Besides this discolouring, no macroscopic or microscopic changes were observed. SB propellant grains show hair cracks both before and after ageing (see Figure 2a/b), while no obvious increase of their number is observed. DB grains do not show hair cracks.

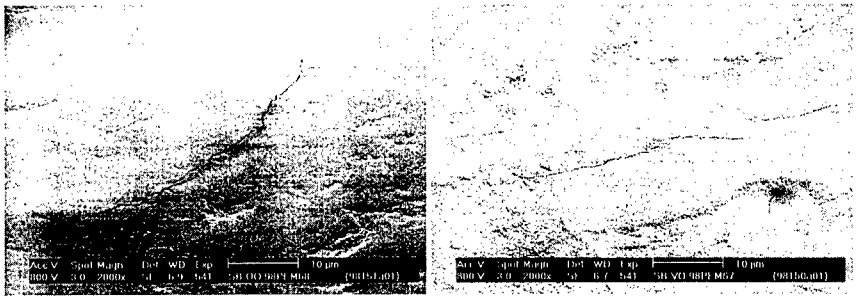

Figure 2a/b: SEM photographs of unaged (left) and aged (right) SB propellant surface, both of them showing a relatively small number of hair cracks.

It should be stated that the samples were aged under confined conditions. This means that evaporation effects are negligible. Under unconfined conditions evaporation may cause the formation of (hair) cracks, which may result in an increased burning rate and consequently an increased peak pressure.

burning properties

The characteristic vivacity, L_k, and the parameters in Vieille's burning law $r = \alpha * P^{\beta}$ that were calculated from the CV test results are given in Table 3. For reasons of comparison the burning rate at the arbitrarily chosen pressure of 150 MPa is given too.

Table 3: Burning properties of unaged and aged propellants.

	L_k [$MPa^{-1}s^{-1}$]	α [$mm\ s^{-1}$]	β [-]	r(150 MPa) [$mm\ s^{-1}$]
SB unaged	1.24	1.96	0.76	86.4
SB aged	1.27	2.35	0.72	85.7
DB unaged	1.71	2.06	0.87	161.1
DB aged	1.70	1.97	0.88	162.0

The results show that the burning properties have hardly changed. The change of the pressure exponent, β, is compensated by the change of α, which is reflected in the calculated burning rate. This means that the burning rate curves of aged and unaged propellants overlap. This applies for both propellant types.

As mentioned above the samples were aged under confined conditions. In another (unpublished) study we have aged the same type of SB propellant in open trays. In that case, L_k showed an increase of 16% while the burning rate increased 10 to 20% as a result of significant changes in both α and β. Simulations indicated that in that case peak pressures in a gun increase by 30%.

mechanical properties: compression test / quasi-static compression test

Typical stress-strain responses are shown in Figure 3a/b. The parameters that have been calculated from the experiments are given in Table 4.

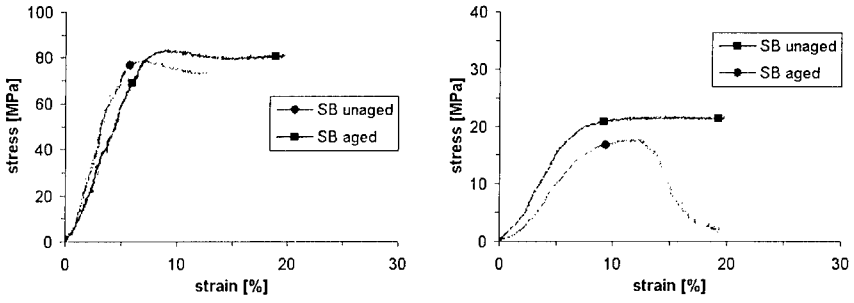

Figure 3a/b: Typical stress-strain responses of compression tests with SB propellant grains (left) and bending tests with DB propellant flakes (right).

Table 4: Compression and bending test results (standard deviations are given between brackets).

	σ_{max} [MPa]	$\sigma_{rupture}$ [MPa]	ε_{max} [%]	$\varepsilon_{rupture}$ [%]	$E_{initial}$ [MPa]
SB unaged	78.9 (3.2)	73.5 (3.0)	10.8 (3.5)	15.7 (4.0)	2027 (337)
SB aged	85.3 (3.0)	79.9 (2.9)	13.4 (3.9)	18.0 (4.4)	1691 (348)
difference	+8.1%	+8.7%	+24.1%	+14.6%	–16.6%
DB unaged	26.2 (3.7)	26.0 (3.6)	27.2 (6.3)	31.1 (6.1)	274 (56)
DB aged	15.3 (1.7)	13.8 (2.1)	19.6 (2.2)	22.9 (2.9)	141 (26)
difference	–41.6%	–41.7%	–65.1%	–48.5%	–65.9%

Table 4 shows that the strength and the strains of aged SB propellant grains are higher than those of unaged grains. The results of the bending tests with DB propellant grains show an opposite result: strength and strains of aged material are lower than those of unaged grains. The initial *E*-moduli of aged SB grains as well as aged DB grains, however, appear to be decreased due to ageing.

These results show that the mechanical properties of NC propellant grains significantly change as a result of ageing. The consequence of this change, in terms of the propellant bed behaviour during the first stages of ignition and combustion in a gun, can hardly be predicted.

The results of CV tests that were performed after quasi-static compression of SB and DB propellant at –40°C are plotted in Figure 4a/b and Figure 5a/b respectively.

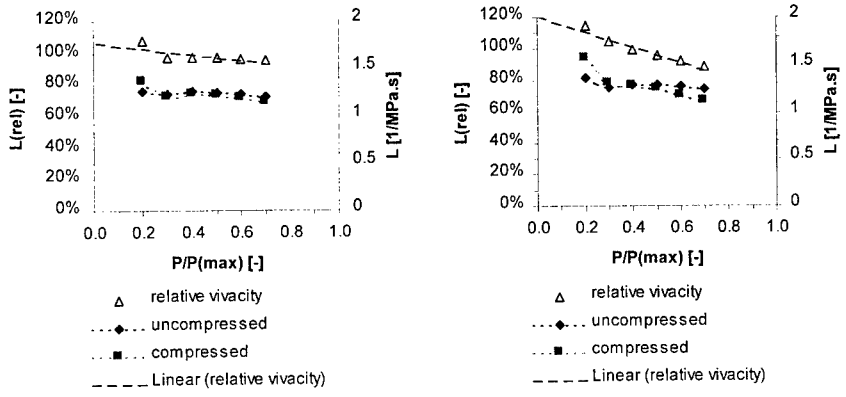

Figure 4a/b: Vivacity curves of unaged (left) and aged (right) SB gun propellant.

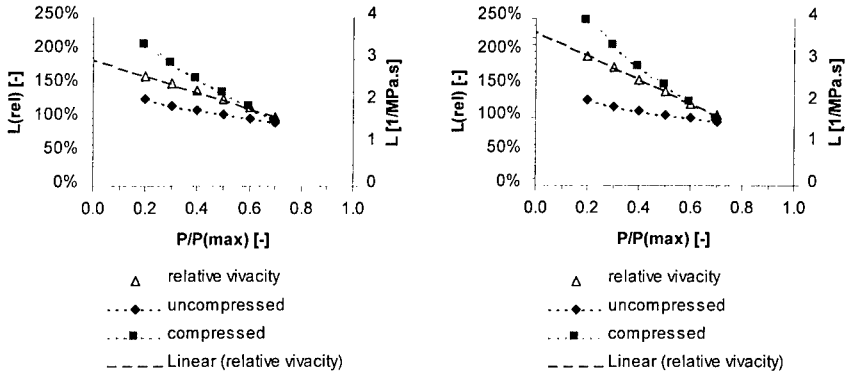

Figure 5a/b: Vivacity curves of unaged (left) and aged (right) DB gun propellant.

The 'relative surface areas' that are derived from the extrapolated relative vivacities are given in Table 5.

Table 5: Results of quasi-static compression: relative surface areas.

	Unaged	Aged	Relative increase
SB propellant	107%	121%	+ 13%
DB propellant	188%	229%	+ 22%

The data in Table 5 show that the mechanical integrity of both propellants decreases significantly due to ageing. The increased surface area of the propellant bed will lead to an accelerated pressure rise during firing while the increased fines fraction results in a diminished porosity. Consequences may be an irregular pressure build-up, pressure waves or increased peak pressures [12].

Criteria for the 'relative surface area' depend greatly on the weapon system for which the propellant is developed. Further, loading density and design peak pressure determine whether problems will arise due to increased 'relative surface area' caused by ageing. Unsafe situations or damage to the weapon as a result of the change in burning behaviour can obviously be expected in the case of high loading densities and when ammunition operates at the maximum allowable peak pressure. In these cases gun simulator tests are recommended to rule out the danger of unsafe application of the propellant.

heat development and energy content

The thermodynamic properties of both propellant types hardly change when aged under confined conditions as shown in Table 6.

Table 6: Change of calorific values due to ageing.

	Microcalorimetry	Bomb calorimeter
SB propellant	– 3%	(change not significant)
DB propellant	– 1.9%	–1.5%

The change of calorific value is often used to determine whether an aged propellant meets the ballistic criteria. Usually the calorific decrease is very small, theoretically resulting in a minor decrease of the muzzle velocity [15]. This is, however, only true if other propellant parameters that are related to the burning behaviour, like the mechanical properties, are unchanged.

discussion

The results described above indicate that a number of parameters significantly change during ageing. These parameters are specifically those that are related to the mechanical properties. Their changes arise mainly from the decrease of the polymeric chain length of the main constituent, NC. Parameters like the energy content, on the contrary, hardly change.

The burning rate appears not to change during ageing under confined conditions. As mentioned above, however, if propellants are aged under unconfined conditions a rather dramatic increase of vivacity and burning rate can be found, probably caused by evaporation effects leading to (hair) cracks and hence an increased surface area.

The safe lifetime of conventional gun propellants is generally derived from propellant parameters that are closely connected to thermal properties. These might be the heat development caused by NC degradation or the content of stabilisers that prevent NC degradation and heat production. In fact, in these cases the safe *storage* lifetime is considered.

The results of this study show that the decrease of mechanical integrity as a result of ageing may lead to unsafe application of propellants. In other words, the safe *ballistic* lifetime may be limited due to loss of mechanical quality.

In order to be able to provide the user with complete information about the conditions of propellant with respect to its lifetime, both the safe storage lifetime and the safe ballistic lifetime should be considered.

A number of parameters that provide good indications with respect to mechanical integrity is mentioned in Table 7. If proper criteria for these parameters are available, the execution of only a small number of these tests will be sufficient.

Table 7: Selection of parameters and test methods.

Parameter	Test method	Remarks
polymeric chain length	GPC	simple and cheap method
mechanical properties	Tensile testing	results are hard to correlate with other parameters
'relative surface area'	Quasi-static compression / closed vessel tests	simple method, clear criteria possible
regularity of pressure build up during ignition / pressure waves	gun simulator	in case of considerable loss of mechanical integrity

Conclusion

The change of polymeric chain length of NC, caused by degradation of NC during ageing, results in a loss of mechanical integrity of propellant grains, while thermal properties and burning behaviour may hardly have changed. The loss of mechanical integrity leads to increased grain fracture during ignition and the first stages of combustion in the weapon. Depending on loading density and design peak pressure, this may lead to unsafe situations with respect to pressure build-up.

It is concluded that the lifetime of conventional gun propellants is not only determined by thermal stability because changes of the mechanical characteristics may finally lead to unsafe employment. Both safe storage lifetime and safe ballistic lifetime should be considered in propellant surveillance. Several test methods are recommended to examine the ballistic lifetime, like GPC, quasi-static compression followed by closed vessel tests, and gun simulator tests.

References

1 J.L.C. van Geel, 'Heat generation measurements for the stability control of nitrate ester propellants', 4th Symposium on chemical problems connected with the stability of explosives, Sweden, 1976.

2 J.L.C. van Geel, 'Self-ignition Hazard of Nitrate Ester Propellants', PhD thesis, Delft University of Technology, 1969.

3 K. Kishore and G. Prasad, 'Ageing studies of solid propellants: A review', in: Indian Institute of Science, 1976, p. 1–56.

4 L. Druet and M. Asselin, 'A review of stability test methods for gun and mortar propellants II: stability testing and surveillance', Journal of Energetic Materials, Vol. 6, 1988, p. 215–254.

5 T. Yoshida, 'Decomposition reaction of nitrate ester', Journal of Society of Industrial Explosives, Japan, Vol. 33, 1972, p. 1-50.

6 B.J. van der Meer and W.P.C. de Klerk, 'Influence of environmental factors on the lifetime of gun propellants investigated with heat flow microcalorimetry', Proceedings of the TTCP workshop on the microcalorimetry of energetic materials, April 1997, Leeds, UK.

7 STANAG 4117, 'Explosives, stability test procedures and requirements for propellants stabilized with diphenylamine, ethyl centralite or mixtures of both'.

8 Draft STANAG, 'Explosives, Nitrocellulose based propellants stabilized with diphenylamine, stability test procedure and requirements using heat flow calorimetry', Working group Draft, september 1999.

9 M.A. Bohn and F. Volk, 'Bestimmung der sicheren Lagerzeit einer plastifizierten Nitrocellulose', 25th International Annual Conference of ICT, June 28 – July 1, 1994, Karlsruhe, Germany.

10 F. Volk and M.A. Bohn, 'Ageing behaviour of propellants determined by mass loss, heat generation, stabiliser consumption, and molar mass decrease', 87th Symposium of the Propulsion and Energetics Panel of the AGARD, 1996, Athens, Greece.

11 F. Volk, M.A. Bohn, and G. Wunsch, 'Determination of chemical and mechanical properties of double base propellants during ageing', in: Propellants, Explosives, Pyrotechnics 1987, Vol. 12, p. 81–87.

12 E.A. Brönnimann, A. Sopranetti, and Ch. Stalder, 'A universal test procedure to predict the shelf life of propellants', Symposium on Chemical Problems connected with the stability of explosives, part 7, Sweden, 1985.

13 STANAG 4115, 'Definition and Determination of Ballistic Properties of Gun Propellants'.

14 W.W. Stein and H. Jahnk, 'Determination of the grain fracture behaviour of propellant beds', 4th Int. Gun propellant & propulsion symposium, 1988, p. V-363.

15 H.P.J. Jongeneelen, 'Ballistic Stability. The relation between the decrease in calorific value and in muzzle velocity', PML report, 1971.

Accelerating Rate Calorimetry Experiments on Energetic Materials: Obtaining Time to Maximum Rate Plots on Larger Samples

P F Bunyan and D A Tod

Defence Evaluation and Research Agency, Fort Halstead, Sevenoaks, Kent, TN14 7BP, UK.

Abstract

A Columbia Scientific accelerating rate calorimeter (CSI-ARC^{tm}) is used by DERA to characterise exothermic reactions in highly energetic materials. Previous work has shown that it is possible to obtain complete runaway curves under adiabatic conditions on propellants and high explosives, yielding data to which conventional ARC algorithms can be applied[1]. However, to achieve a controlled runaway necessitates the use of very small sample masses resulting in an inconveniently high thermal inertia (ϕ) value. This, in turn, leads to undesirably high detectable onset temperatures, shorter temperature ranges being recorded, reduced signal to noise ratio and the collection of a reduced volume of data.

Of course, more favourable ϕ values can be obtained simply by using larger samples. However, due to a combination of the high heat generation rates given when any explosive decomposes and limitations in the rate that thermal equilibrium can be achieved, this invariably results in a catastrophic transition from a relatively slow, controlled reaction to a rapid, explosive reaction at some time during the experiment. Obviously, once this transition occurs, the instrumentation cannot track the exotherm, the system is no longer adiabatic and data gathered during this time cannot be used quantitatively. In particular, a valid, experimental time of maximum rate is not obtained.

This paper presents experimental results obtained from some 'oversized' energetic material samples and describes how partial exotherm data, obtained prior to ignition, may be processed in the absence of experimental maximum rate data and then used to construct time to maximum rate plots.

1 INTRODUCTION AND BACKGROUND

The ARC is an automated laboratory instrument which experimentally determines the temperature, pressure and time relationships of exothermic reactions in a confined, adiabatic environment. It has been used for many years in the chemical industry to evaluate the risk of thermal explosions of self heating materials when stored and used under various conditions. In principle, we can regard many systems found in weapons, such as rocket motors, as systems of this type and therefore suitable for study by the ARC.

Earlier work[1] has shown that, in order to obtain controlled runaway curves from highly energetic solids to which ARC techniques can be applied, it was necessary to ensure that self heat rates were sufficiently small throughout the experiments to ensure that an adiabatic environment was maintained at all times. The practical result of this was that far smaller sample masses had to be used than would be satisfactory for less energetic systems. ϕ factors were therefore rather high, leading to a reduced volume of data and higher onset temperature detection thresholds than desirable, since this resulted in the need to extrapolate the results over a relatively large temperature range.

However, it is possible to record the early part of the runaway reaction using a larger energetic material sample, before ignition occurs, under far more favourable conditions (lower ϕ, lower onset temperature etc.). If a valid estimate of what the time to maximum rate would have been if no transition to ignition reaction had intervened, the equation of the straight line time to maximum rate plot could still be obtained by plotting this partial data.

It can be shown that, in many cases involving decomposition reactions in highly energetic materials of high activation energy, a plot of ln time to maximum rate (tmr) vs 1/T is straight, whereas a plot of ln

(incorrect tmr) plots as a positive curve if the assumed time of maximum rate is too long (e.g. selecting the true time of max rate plus 5 minutes as the time of maximum rate), or a negative curve if the assumed time of maximum rate is too short (e.g. selecting the true time of max rate minus 5 minutes as the time of maximum rate). It follows that it should be possible to obtain valid tmr plots even in the absence of an experimentally measured time of maximum rate by trial and error by plotting a series of tmr curves for different assumed times of maximum rates and then choosing the straightest plot as the correct one.

This paper will test and evaluate this proposal, by applying it to an energetic reaction that is known to be simple and predictable over a wide temperature range[2,3] (polyNIMMO prepolymer decomposition), and also to the decomposition of a more complex, nitrocellulose-based, propellant which is currently in service use (a single base ball propellant).

2 EXPERIMENTATION

2.1 Equipment and Materials

A sample of the energetic polyether, polyNIMMO, blend PPBX210, was supplied by ICI Explosives Division, Stevenston, Ayrshire, Scotland. A sample of single base nitrocellulose ball powder was obtained from existing stock samples. To allow thermal inertia (ϕ) to be calculated, the specific heat of each material was determined with a Mettler DSC-30 differential scanning calorimeter (PolyNIMMO 1.42 $J.g^{-1}.K^{-1}$, Single base propellant 1.40 $J.g^{-1}.K^{-1}$).

Adiabatic thermal runaway curves were recorded using the CSI accelerating rate calorimeter. Samples were contained in 2.54 cm dia. spherical titanium bombs obtained from Thermal Hazards Technology Ltd. Time to maximum rate (tmr) plots of ln (tmr) vs. 1/T were constructed for each experiment and the activation energy estimated from the slope of the regression line, as described by Townsend and Tou[4].

When ϕ was calculated, the assumption was made that the bomb nut and ferrule are heated by the exothermic reaction and not by the jacket heaters (evidence for this was reported at the previous ICT conference[1]), Accordingly, all ϕ values reported in this paper were calculated with the following equation.

$$\phi = \frac{\left(1 + M_b.C_{pb} + M_c.C_{pc} + M_{nf}.C_{pnf}\right)}{M_s.C_{ps}}$$

Where Mb, Mc, Ms are the masses of the bomb, thermocouple clip and sample and Cpb, Cpc and Cps are the specific heats of the bomb, thermocouple clip and sample respectively and Mnf and Cpnf are the mass and specific heat of the stainless steel nut and ferrule.

2.2 PolyNIMMO Experiments

Ten ARC runs were performed on polyNIMMO samples of different masses, ranging from 0.166g, which showed no sign of loss of control, to 0.5005g, which showed a sharp transition to an ignition reaction at 183°C, followed by an effectively instantaneous temperature rise of over 100°C (Fig 1).

In each case a tmr plot was constructed. In the case of the controlled runs (R301, R302) the experimentally recorded time of maximum rate was used to construct the graph which gave the best fit to a straight line, Other plots using the same curve data, but other times, close to, but not at, the experimentally determined time of maximum rate, were curved (Fig 2). Where ignition occurred, the tmr plot curved down if constructed assuming the observed time of ignition was equal to the time of maximum rate (e.g. Fig 3). This suggested that, had control somehow been maintained by the instrument, the true maximum rate would have occurred slightly later. The deduced activation energy was higher than obtained from controlled experiments. A best fit was obtained by assuming a slightly later time to be the time of maximum rate (e.g. Fig 4). In these cases, the deduced activation energy obtained from different experiments, employing different sample masses, were in reasonably close agreement with each other. For higher estimates than that which gave the best straight line fit, the plot had a positive curve (e.g. Fig 5).

Experimental conditions and results from all 10 polyNIMMO experiments are summarised in table 1.

2.3 Single Base Propellant Experiments

Ten ARC runs were performed on propellant samples of different masses. In this case, in order to get any controlled runs at all, the sample mass range had to start with far smaller samples (0.0727g) than could be used in the case of polyNIMMO, up to a maximum of 0.352g, which ignited at 164°C (Fig 6). Note that even a 0.1g sample showed a slight loss of temperature control.

Once again, a tmr plot was constructed for each experiment. Using the experimentally observed time of maximum rate to construct tmr plots gave reasonably good straight line, although only a few data points, gathered at high temperature, were available (Fig 7). With larger samples, where ignition invariably occurred, as in the case of polyNIMMO, a curved line was again obtained if the time of maximum rate was assumed to occur at the time ignition was recorded (e.g. Fig 8). As in the case of polyNIMMO, a best fit was obtained by assuming a later time to be the time of maximum rate, although, in general, a slightly inferior correlation was achieved than with polyNIMMO (e.g. Fig 9).

Experimental conditions and results from all 10 single base propellant experiments are summarised in table 2.

3 DISCUSSION

3.1 PolyNIMMO Experiments

In the case of the fully controlled polyNIMMO ARC experiments, it can be seen that employing the observed time of maximum rate to calculate the tmr plot yields a good straight line and any deviation introduces curvature in a characteristic direction (negative curve for low estimates and positive curve for high estimates).

The same type of results are obtained if the controlled part of the runaway curve from larger samples are processed in the same manner - in this case, it appears reasonable to assume that the time of maximum rate associated with the best fitting straight line would have been realised if the physical limitations on heat transfer in the 'real world' had not caused a loss of adiabatic control by the instrumentation. Supporting evidence for this is given by the level of agreement on the deduced activation energy and associated predictions given by different experiments when this condition is met.

There appears to be a slight progressive increase in deduced activation energy as the sample size is increased. It is possible that the longer period of time spent at elevated temperatures while in the heat/wait/search cycle by very small samples, resulting from the higher onset temperatures due to lower sensitivity, is influencing the reaction by introducing a greater amount of thermal ageing to small samples than to large ones.

3.2 Single Base Propellant Experiments

Although expected to be a more complicated reaction, the same observations made for the polyNIMMO experiments can be made for those conducted on the propellant samples. Of course, in this case there is an even greater requirement to work with data from experiments where ignition occurs, because of concerns about the long extrapolations required from experiments conducted on extremely small samples, which give only a few data points at more elevated temperatures.

The best fit that could be achieved from ARC runs on propellant samples which ignited showed slightly inferior correlation compared to the polyNIMMO runs - the traces were, in fact, slightly 's'-shaped. A clue to why this should be may be given by examining the self heat rate vs. temperature plots illustrated in Figure 10. Both large and small polyNIMMO experiments show no evidence for multiple reactions occurring, whereas the larger propellant sample shows an inflection in the curve around 150°C, which is not apparent in the very small propellant sample, presumably because no self heating above noise had been detected at this point.

This can be interpreted as evidence for a second exothermic reaction occurring at a lower temperature in this material. The controlled experiment obviously had such a small sample mass that this reaction took place during the heat/wait/search cycle without being detected.

Further evidence for this is provided if tmr plots are attempted on the oversize sample run using data gathered entirely below the inflection point at 150°C (Fig 11) or entirely above it (Fig 12). It can be seen that, in both cases, a very good straight line can be obtained by estimating slightly different times to maximum rate for the two sets of data.

3.3 General Discussion

When time of maximumum rate cannot be measured directly, for practical reasons, it still appears possible to obtain quantitative time to maximum rate plots and the information that would normally be derived from them by considering the early part of an ARC experiment in this way. Obviously some of the information which is normally given by a complete ARC run, such as heat of reaction, will still not be available.

Due to financial and safety considerations, this work was conducted on relatively small sample sizes, which could be expected to ignite while confined in an ARC sample bomb without rupturing it and allowing the experiments to be performed in an occupied laboratory. Clearly, a similar approach could be applied to an ARC experiment which was terminated before ignition occurred, allowing the bomb to be filled right up with explosive. The advantages would be far more favourable ϕ values and a further reduction in the need for extrapolation to the temperature of interest. The disadvantage would be that the ARC would need to be located and operated remotely in case of an accidental detonation (caused, for example, if the jacket heaters developed a fault or the maximum experimental temperature was set too high).

4 CONCLUSIONS

It is possible to obtain time to maximum rate plots from data gathered only in the early stages of an ARC experiment by employing an iterative search for a time of maximum rate which gives the best straight line. This will permit the use of larger samples, allowing experiments be conducted on lower ϕ systems and so reduce the need for extrapolation to lower temperatures.

When a straight line is not obtained by this approach, a change in mechanism or the existence of serial reactions should be suspected.

5 ACKNOWLEDGEMENT

The authors wish to thank Dr Peter Barnes and Mr Neil Turner of CESO(N), Bath, UK, for helpful discussion and financial support for this work.

6 REFERENCES

1 P F Bunyan, D A Tod and G Kavanah, *Characterisation of Thermal Runaway Reactions in Energetic Solid Materials Using Accelerating Rate Calorimetry,* Proc. 30th Int. Conf of ICT, Poster Presentation P62, Karlsruhe, Germany, 29th June - 2nd July 1999.
2 J.K.Chen and T.B.Brill, *Thermochimica Acta*, 181,(1991), 71.
3 P F Bunyan, *Thermochimica Acta*, 207 (1992), 147.
4 D I Townsend and J C Tou, *Thermochimica Acta*, 37 (1980), 1.
5 Thermal Hazards Technology, Technical Information Sheet No. 5, *Temperature of No Return: Application of Accelerating Rate Calorimetry Data, Maximum Safe Temperatures and Pack Sizes.*

© British Crown Copyright 2000/DERA

Table 1; Summary of ARC Experimental Results on PolyNIMMO

Experiment identity no.	Mass/g	ϕ	To/°C	Tmr (sys) /°C	Estimated (**e**) or measured (**m**) time of maximum rate/mins	tmr plot - equation of best fitting straight line	R^2	Ea /kJ.mol^{-1}	Te (1000 min)/°C	tnr/°C [a]
R301[b]	0.1660	44.71	143.15	191.34	783.8 **m**	y=16349x-37.223	0.9999	135.9	97.3	129.3
R301[c]	*0.1660*	*44.71*	*143.15*	*191.34*	*773.8* **e**	*y=19919x-45.679*	*0.9928*	*165.6*	*105.6*	*132.7*
R301[c]	*0.1660*	*44.71*	*143.15*	*191.34*	*793.8* **e**	*y=14143x-31.969*	*0.9978*	*117.6*	*90.6*	*126.7*
R302[b]	0.1807	40.83	137.15	199.27	894.9 **m**	y=17664x-40.507	0.9999	146.9	99.4	129.1
R289[b]	0.1723	39.86	146.23	200.8	603.8 **e**	y=17479x-39.624	0.9998	145.3	102.5	133.1
R288[b]	0.2155	32.14	142.99	185.15	583.0 **e**	y=19212x-44.213	1	160.7	102.9	130.4
R292[b]	0.2633	26.5	143.08	183.28	563.5 **e**	y=20830x-47.998	0.9999	173.2	106.2	132.1
R293[b]	0.3239	23.34	136.98	181.98	730.9 **e**	y=20776x-47.943	0.9999	172.7	105.6	131.5
R294[b]	0.3786	20.10	137.18	183.24	662.1 **e**	y=20925x-48.327	0.9999	174.0	105.7	131.4
R295[b]	0.4305	17.86	137.16	181.17	625.6 **e**	y=21707x-50.224	0.9999	180.5	106.8	131.6
R296[b]	0.4692	16.55	134.13	180.35	740.4 **e**	y=21485x-49.656	0.9999	178.6	106.7	131.8
R300[b]	0.5005	15.63	134.17	181.44	649.8 **e**	y=20790x-48.022	0.9999	172.9	105.3	131.1
R300[c]	*0.5005*	*15.63*	*134.17*	*181.44*	*647.6* ***m***	*y=23435x-54.390*	*0.9946*	*194.9*	*109.2*	*132.4*
R300[c]	*0.5005*	*15.63*	*134.17*	*181.44*	*652.0* ***e***	*y=19041x-43.801*	*0.9983*	*158.3*	*102.3*	*130.2*

[a] Critical temperature when contained in a system with a time constant of 30 minutes (e.g. 1 litre laboratory flask[5])
[b] Best fitting straight line obtained from this experiment
[c] *Not the best fitting straight line obtained from this experiment (included here to illustrate the procedure)*

Key to symbols used in tables 1 and 2:

ϕ	Thermal inertia
Ea	Activation energy
R^2	R-squared value (Square of correlation coefficient of trendline)
Te (1000 min)	The predicted ambient temperature required to give an adiabatic time to maximum rate of 1000 minutes
tmr	Time to maximum rate
Tmr	Temperature at maximum self heating rate
Tnr	Critical temperature of no return
To	Temperature at which an exotherm is first detected

The suffix (sys) is used to indicate the entire system comprising the combination of sample and bomb.

Table 2; Summary of ARC Experimental Results on Single Base Propellant

Experiment identity no.	Mass/g	ϕ	To/°C	Tmr (sys) /°C	Estimated (**e**) or measured (**m**) time of maximum rate/mins	tmr plot - equation of best fitting straight line	R^2	Ea /kJ.mol^{-1}	Te (1000 min)/°C	Tnr/°C [a]
R218[b]	0.0715	95.73	150.02	175.10	642.8 **m**	y=24646x-58.016	1	204.9	106.5	128.1
R219[b]	0.0727	95.68	150.06	176.20	642.5 **m**	y=24037x-56.600	0.9997	200.0	105.4	127.5
R319[b]	0.1652	45.65	137.18	193.15	825.8 **e**	y=21864x-51.701	0.9988	181.8	99.9	123.6
R286[b]	0.1872	37.30	138.18	165.21	679.9 **e**	y=22709x-53.577	0.9992	188.8	102.3	125.4
R287[b]	0.2001	34.94	138.07	164.27	677.1 **e**	y=24129x-56.95	0.9994	200.6	104.7	126.7
R285[b]	0.2260	31.13	135.28	164.38	687.9 **e**	y=24193x-57.178	0.9993	201.2	104.4	126.2
R320[b]	0.2505	30.12	134.23	164.42	782.7 **e**	y=23675x-56.034	0.9990	196.8	103.0	125.2
R308[b]	0.2715	28.04	137.15	165.67	560.4 **e**	y=25436x-60.129	0.9980	211.5	106.3	127.2
R318[b]	0.3208	23.96	131.18	163.28	820.1 **e**	y=24782x-58.778	0.9984	206.1	104.1	125.4
R321[b]	0.3519	21.67	131.24	164.02	768.1 **e**	y=24821x-58.851	0.9994	206.4	104.3	125.6
R321[c]	*0.3519*	*21.67*	*131.24*	*164.02*	*765.5 **m***	*y=27821x-66.175*	*0.995*	*231.3*	*107.5*	*126.7*
R321[c]	*0.3519*	*21.67*	*131.24*	*164.02*	*770.7 **e***	*y=22749x-53.781*	*0.9975*	*189.1*	*101.7*	*124.4*

[a] Critical temperature when contained in a system with a time constant of 30 minutes (e.g. 1 litre laboratory flask[5])
[b] Best fitting straight line obtained from this experiment
[c] *Not the best fitting straight line obtained from this experiment (included here to illustrate the procedure)*

Key to symbols used in tables 1 and 2:

ϕ	Thermal inertia
Ea	Activation energy
R^2	R-squared value (Square of correlation coefficient of trendline)
Te (1000 min)	The predicted ambient temperature required to give an adiabatic time to maximum rate of 1000 minutes
tmr	Time to maximum rate
Tmr	Temperature at maximum self heating rate
Tnr	Critical temperature of no return
To	Temperature at which an exotherm is first detected

The suffix (sys) is used to indicate the entire system comprising the combination of sample and bomb.

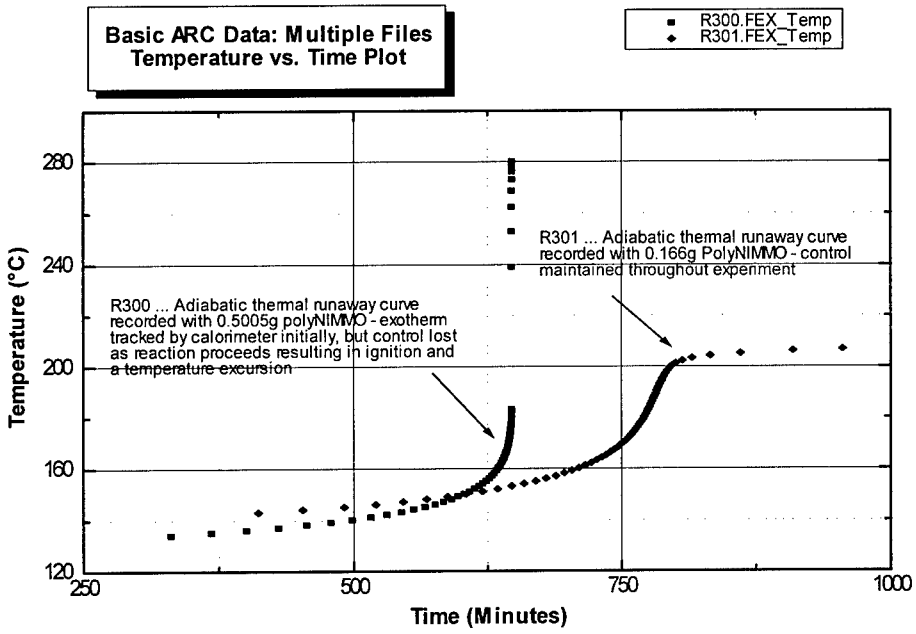

Fig 1 PolyNIMMO ARC Runs - To Show the Effect of Using Larger Sample

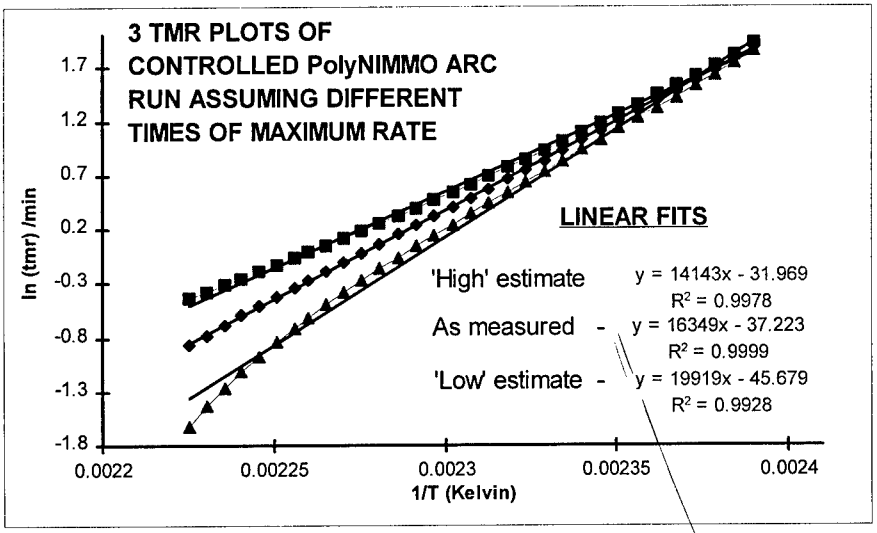

Fig 2 Time to Maximum Rate Plots - Constructed From Fully Controlled ARC RUN Using Different Estimates of Time Of Max Rate (Upper Trace ... 793.85 minutes, Middle Trace ... 783.85 minutes, Lower Trace ... 773.85 minutes)

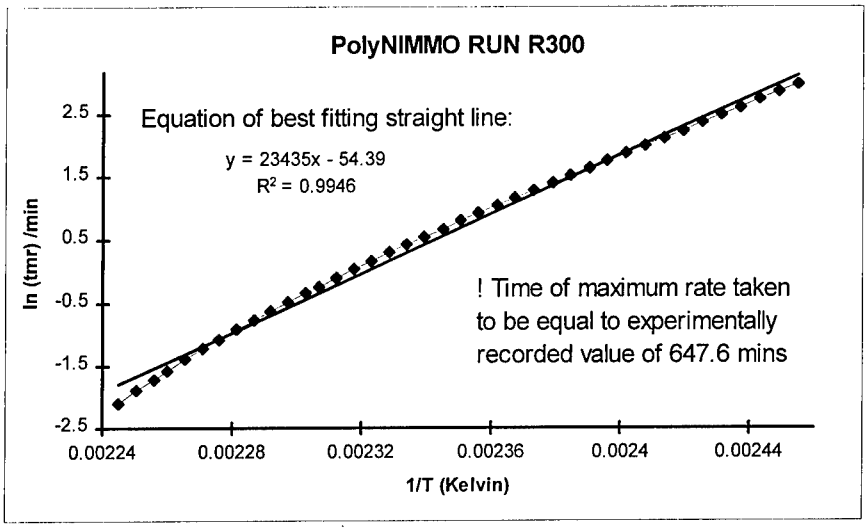

Fig 3 Time to Maximum Rate Plot on Oversize Sample - Selected Time of Maximum Rate Appears Too Low (Shown by Poorly Fitting Straight Line With Negative Curvature) - Despite Being Equal to Observed Time of Explosion.

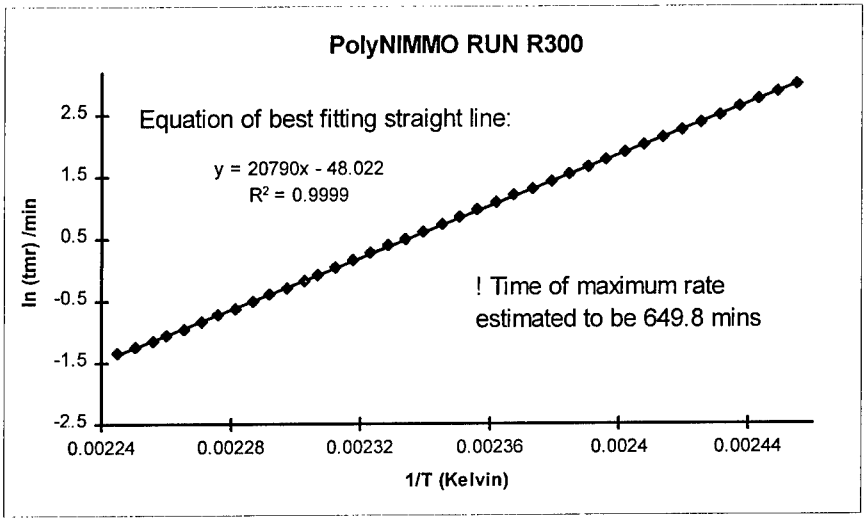

Fig 4 Time to Maximum Rate Plot on Oversize Sample - Time of Maximum Rate Estimated to be Some Time After Ignition Seen - Giving a Good Straight Line Plot

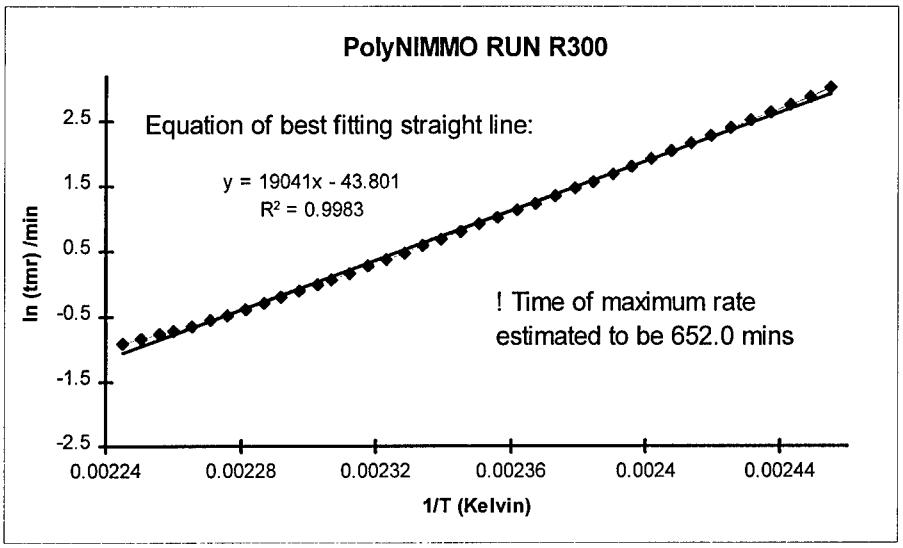

Fig 5 Time to Maximum Rate Plot on Oversize Sample - Estimated Time of Maximum Rate Now Too Long - Giving Poor Straight line Fit With a Positive Curve

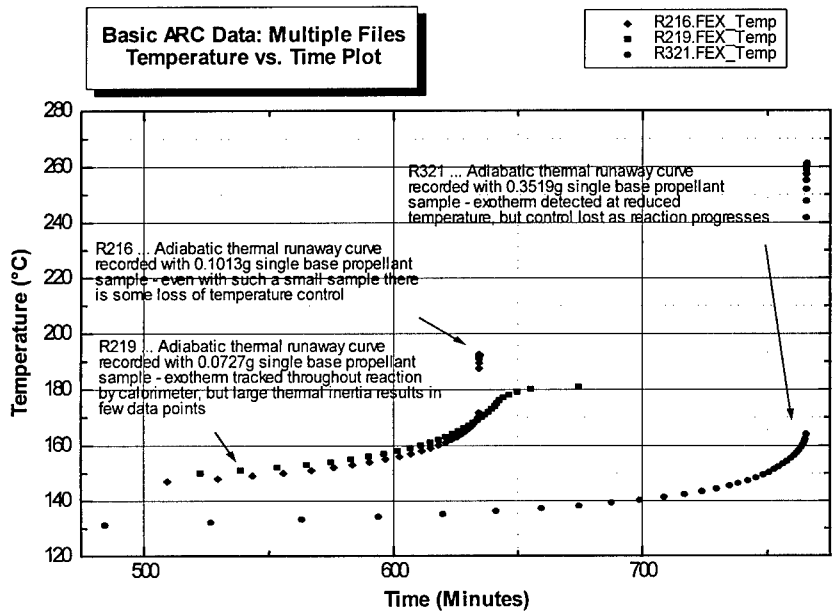

Fig 6 Single Base Propellant ARC Runs - Physical Nature and Geometry of Sample Allows Control to be Maintained Only If Very Small Samples are Employed

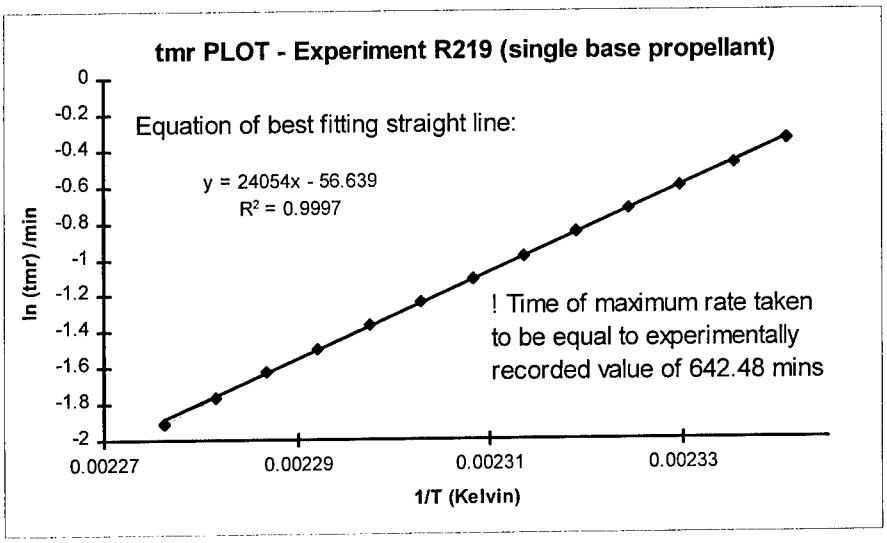

Fig 7 Fully Controlled ARC Run On Small Propellant Sample is Again Reasonably Straight - However, Small Sample Gives Reduced Data at Higher Temperatures

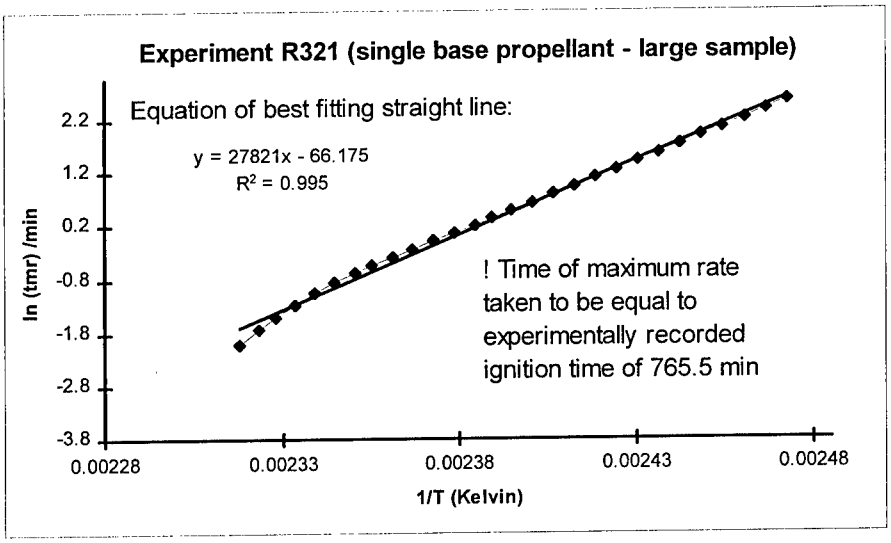

Fig 8 Time to Maximum Rate Plot on Oversize Propellant Sample - Selected Time of Maximum Rate Again Appears Too Low (Shown by Poorly Fitting Straight Line With Negative Curvature) - Despite Being Equal to Observed Time of Explosion.

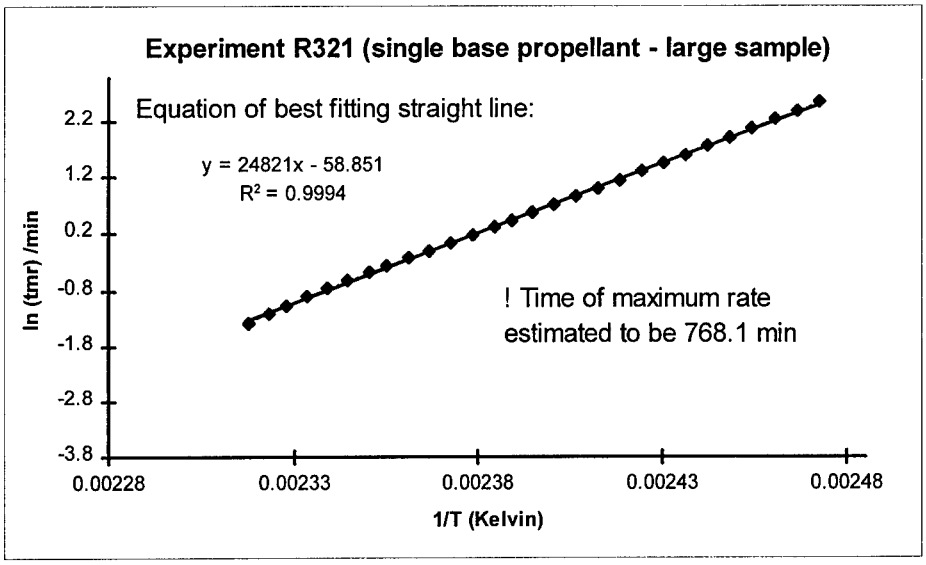

Fig 9 Time to Maximum Rate Plot on Oversize Propellant Sample - A 'Best Fit' to a Straight Line Was Seen When the Effective Time of Maximum Rate was Estimated to be 768.1 Minutes

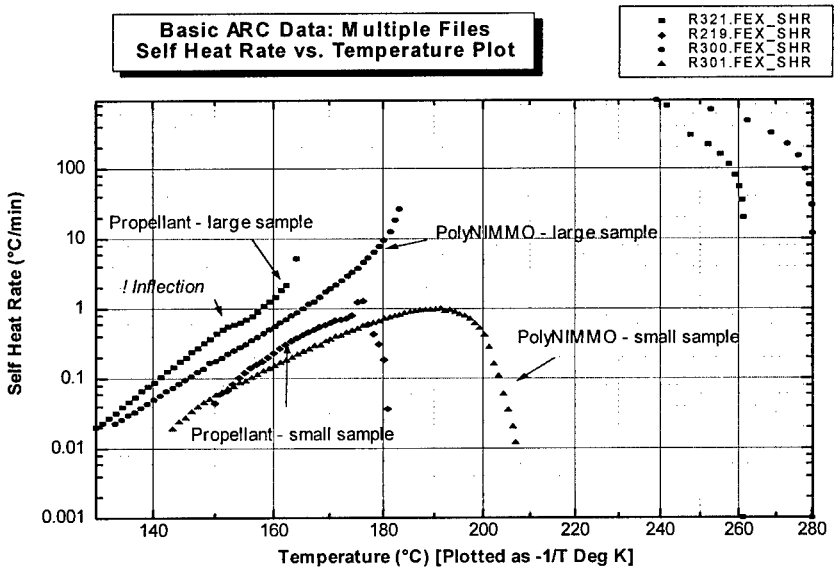

Fig 10 Self Heat Rate Plots on Different Sized PolyNIMMO and Propellant Samples - Note Inflection in Large Propellant Sample Trace at around 150°C

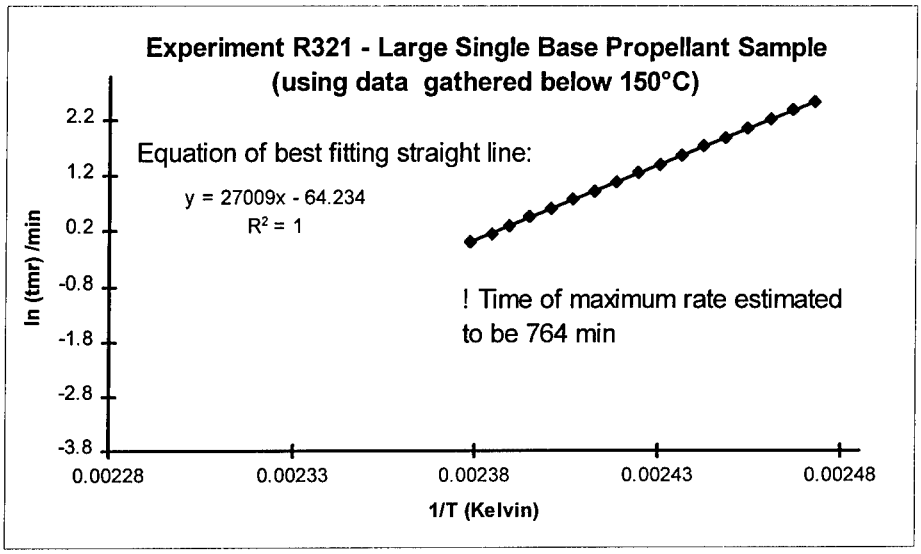

Fig 11 Time to Maximum Rate Plot on Large Propellant Sample - Using Data Recorded Below 150°C

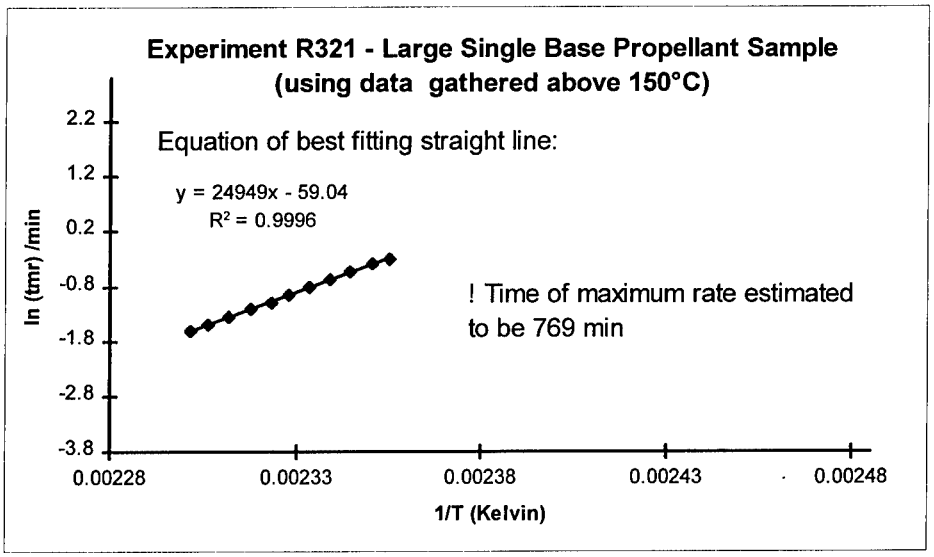

Fig 12 Time to Maximum Rate Plot on Large Propellant Sample - Using Data Recorded Above 150°C

NEUE STRATEGIEN UND VERFAHREN DER INPROZESS- UND PRODUKTE-ANALYTIK IN DER TREIBMITTEL-PRODUKTION

NEW STRATEGIES AND METHODS FOR IN-PROCESS- AND PRODUCT-ANALYSIS IN THE PRODUCTION OF PROPELLANTS

Beat Vogelsanger und Bruno Ossola

NITROCHEMIE WIMMIS AG, CH-3752 Wimmis, Switzerland
Tel: ext - 33 228 13 00 Fax: ext - 33 228 13 30

ABSTRACT

In modern manufacturing processes, quality relevant information has to be available as early as possible. Therefore, a concept for the in-process analysis in the production of propellants was elaborated.

The earliest steps in the manufacturing process, in which the relevant product properties (such as ***composition***, ***chemical stability***, ***degree of nitrocellulose gelatination***, and ***geometry*** of propellant grains) can be determined, have been defined. Furthermore, different analytical procedures to determine those properties have been developed. Three examples for such procedures are discussed in this presentation:

- ***Check of identity of raw materials*** using ***near infrared (NIR) spectroscopy***, combined with multivariate spectrum analysis.
- ***Analysis of propellants under production***, directly or after sample preparation, using ***Fourier transform infrared (FTIR) spectroscopy***, followed by discriminant analysis.
- Determination of ***geometric parameters of propellant grains*** (length, diameter, web size) by ***recording video pictures***, followed by automatic, computer controlled ***image analysis***.

1. Einleitung

1.1 Inprozess-Analytik versus Produkte-Analytik

Die Qualitätssicherung in der Herstellung von Treibladungspulvern und anderen Explosivstoffen stützte sich bis anhin praktisch ausschliesslich auf die ***Analytik der fertiggestellten Produkte***. Mit Hilfe von klassischen, zumeist hochspezifischen Analysenmethoden werden dabei die Rezepturkomponenten und gegebenenfalls weitere Produkteeigenschaften mit hoher Präzision und Richtigkeit bestimmt. Die Durchführung solcher Analysen ist in der Regel zeitaufwendig und teuer. Der wohl grösste Nachteil der Produkte-Analytik ist jedoch die Tatsache, dass die Resultate erst nach abgeschlossenem Herstellungsprozess zur Verfügung stehen, d.h. zu einem Zeitpunkt, in dem allfällig notwendige Korrekturen kaum mehr möglich sind.

Deshalb steuern neuere Analysenstrategien dahin, die qualitätsrelevanten Informationen möglichst früh im Produktionsprozess zu erhalten, d.h. in einem Stadium, in welchem Korrekturen noch möglich sind (Vermeidung von Fehlchargen). Eine solche ***Inprozess-Analytik*** muss eine schnelle und sichere "gut-schlecht-Entscheidung" ermöglichen. Dazu werden heute vorwiegend ***Analysenverfahren mit geringerer Spezifität*** (wie spektroskopische Verfahren) eingesetzt, ***in Kombination mit multivariater statistischer ("chemometrischer") Auswertung***. Dies ist in Abbildung 1 aufgezeigt:

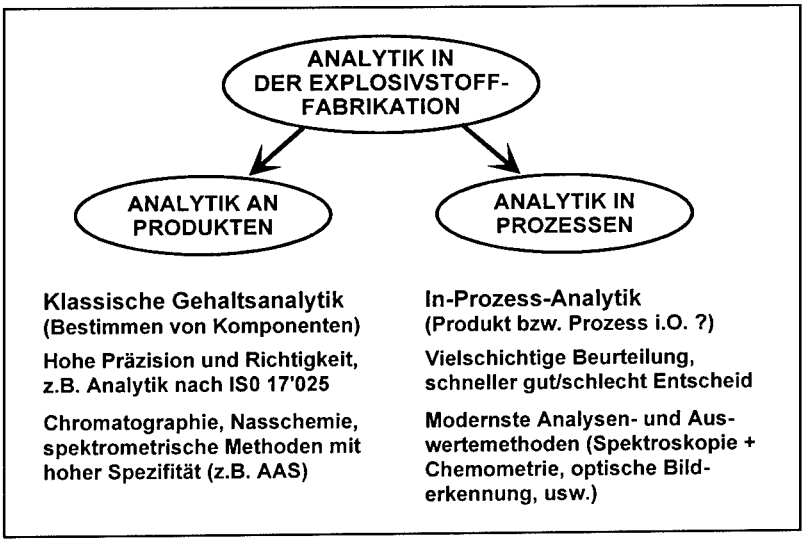

Abbildung 1: Produkte-Analytik versus Inprozess-Analytik.

1.2 Nutzen der Inprozess-Analytik

Der Nutzen einer frühzeitigen Erkennung von Fehlern ist anhand der in Abbildung 2 aufgezeigten Kosten pro Prozessschritt ersichtlich:

- Für ein typisches Mittelkaliber-Treibladungspulver (TLP) machen die Rohmaterialien bereits ca. 50% der Gesamt-Herstellungskosten aus.
- Nach dem Schneiden / Vorsieben sind ca. 70% der Kosten angefallen. Dies ist der letztmögliche Zeitpunkt, bei dem eine Korrektur der Rezeptur noch möglich ist (z.B. bei Fehlen einer Rezepturkomponente durch Zugabe dieser Substanz und Wiederholung der vorhergegangenen Prozessschritte).
- Nach dem Fertigstellen des Produktes sind hingegen bereits 96% der Gesamtkosten verbraucht. Wird also ein signifikanter Produkte-Fehler erst bei der chemischen Schlussprüfung erkannt, so können allenfalls noch die relativ geringen Kosten für die ballistische Prüfung eingespart werden.

Fazit: Die Einführung von geeigneten Inprozess-Kontrollen im Herstellungsprozess von Treibladungspulvern ist deshalb sinnvoll und notwendig.

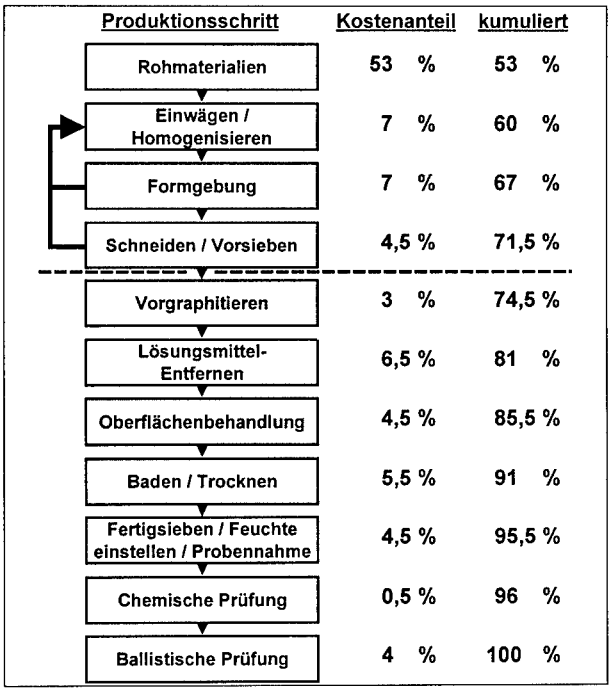

Abbildung 2: Beitrag der einzelnen Prozess-Schritte an die Herstellungskosten eines Loses Mittelkaliber-Treibladungspulver.

2. Prozessanalytik in der TLP-Produktion

2.1 Zu analysierende Parameter und Analysen-Zeitpunkte

Die wichtigsten Produkteeigenschaften von einbasigen Treibladungspulvern sind ***Rezeptur***, ***Gelierungsgrad*** der Nitrocellulose, ***Geometrie*** der TLP-Körner und ***chemische Stabilität***. Die ersten drei Parameter bestimmen das innenballistische Verhalten des Produktes, während die Stabilität als Mass für die Sicherheit bei der Lagerung gilt.

Der jeweils frühestmögliche Zeitpunkt zur Kontrolle dieser vier Parameter im Herstellungsprozess von einbasigen TLP ist in Abbildung 3 aufgezeigt:

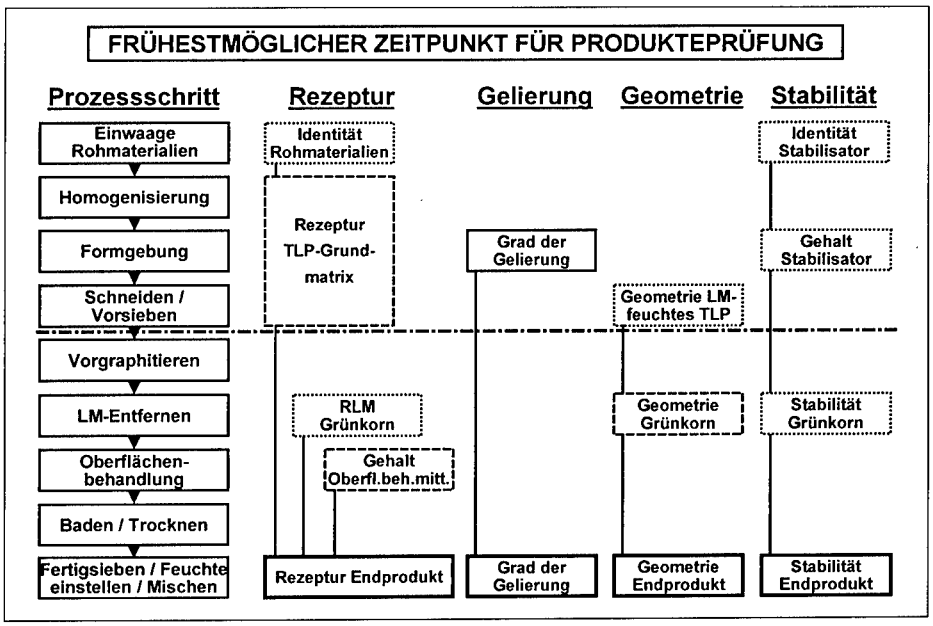

Abbildung 3: Frühestmöglicher Zeitpunkt für verschiedene Produkte-Prüfungen im Herstellungsprozess.

Kontrolle der Rezeptur:

- Bereits bei der Einwaage ist eine ***Identitätskontrolle der Rohmaterialien*** möglich.
- Die ***Rezeptur der TLP-Grundmatrix*** kann direkt am Knetteig oder an den verpressten, ev. geschnittenen Strängen erfolgen. Allerdings treten in den nachfolgenden Prozessschritten noch Veränderungen auf, wie z.B. das Herauslösen von Additiven

im Badeprozess oder der Abbau eines Teils der Stabilisatormenge durch produktionsbedingte thermische Belastungen.

- Die Bestimmung des ***Restlösungsmittel-Gehaltes*** (Alkohol und Ether) am Grünkorn, d.h. direkt nach dem Lösungsmittel-Entfernungsprozess, kann wichtige Angaben über die Effizienz dieses Prozessschrittes geben. Eine Extrapolation auf die im fertiggestellten Produkt noch enthaltene Lösungsmittelmenge ist jedoch nur sehr beschränkt möglich, da in den folgenden Schritten (Oberflächenbehandlung, Baden, Trocknen) noch massive Veränderungen dieses Parameters auftreten.
- Der ***Gehalt an Oberflächenbehandlungsmitteln*** könnte schon nach dem Behandlungsprozess bestimmt werden. Eine gewisse Reduktion dieser Gehalte in den nachfolgenden Prozessschritten ist jedoch ebenfalls zu erwarten.
- Eine ***Rezepturkontrolle am Endprodukt*** liefert die definitiven Gehalte aller relevanten Rezepturkomponenten.

Kontrolle der Gelierung:

- Der Grad der Gelierung der Nitrocellulose im TLP kann bereits nach der Formgebung ("Verpressen") bestimmt werden. Dieser Parameter dürfte sich in den nachfolgenden Prozessschritten nicht mehr ändern.

Kontrolle der Geometrie:

- Die ***Geometrie der Pulverkörner*** kann frühestens ***nach dem Schneiden*** bestimmt werden. Diese Werte eignen sich jedoch nur zur Prozesssteuerung, eine Extrapolation auf die Geometrie des Fertigproduktes ist nur sehr beschränkt möglich. Dies, weil bei der nachfolgenden Lösungsmittelentfernung ein Schwund in Kornlänge und Korndurchmesser auftritt.
- Eine ***Ausmessung des Grünkornes*** (nach dem Lösungsmittelentfernen) ist möglich, jedoch wenig sinnvoll. Dies, weil durch die folgenden Prozessschritte Oberflächenbehandlung und Sieben eine (allerdings geringe) Quellung bzw. eine Veränderung der Korngrössenverteilung auftritt.
- Die ***"definitive Geometrie"*** wird somit erst durch eine Ausmessung des Fertigproduktes erhalten.

Kontrolle der Stabilität:

- Die ***Zugabe des Stabilisators*** kann natürlich, wie oben bei der "Rezepturkontrolle" beschrieben, bereits bei der Einwaage (Identitätskontrolle der Rohmaterialien), im

Knetteig oder an den verpressten, ev. geschnittenen Strängen überprüft werden. Durch die in den nachfolgenden Prozessschritten auftretende thermische Belastung wird jedoch zumeist bereits ein Teil der eingesetzten Stabilisatormenge abgebaut, so dass diese Grösse nicht unbedingt mit dem im Endprodukt vorliegenden Stabilisatorgehalt überein stimmt.

- Die Bestimmung der ***Stabilität des Grünkornes*** kann allenfalls erste Hinweise auf die Stabilität des Endproduktes liefern. Die folgenden Prozessschritte (thermische Belastung, Reduktion des Restlösungsmittelgehaltes) beeinflussen jedoch die Produkte-Stabilität in kaum quantifizierbarem Umfang.
- Auf eine Bestimmung der ***Stabilität des Endproduktes*** kann somit nicht verzichtet werden.

2.2 Momentaner Umfang der Prozessanalytik in der TLP-Produktion

Wie aus Abbildung 4 ersichtlich, wurden bis vor kurzem in der NITROCHEMIE WIMMIS AG von den im Abschnitt 2.1 beschriebenen möglichen Inprozess-Kontrollen lediglich deren zwei auch durchgeführt:

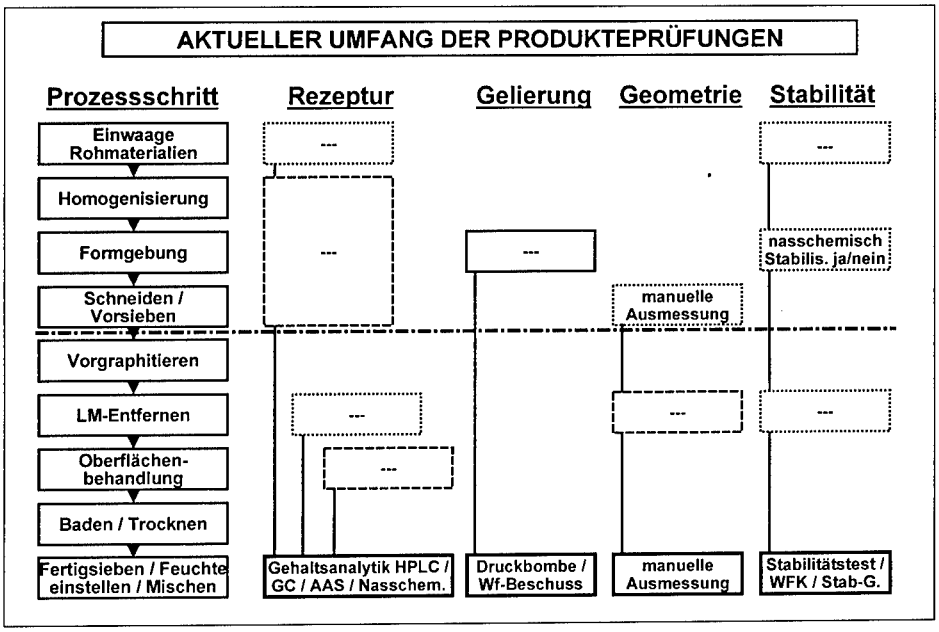

Abbildung 4: Aktueller Umfang der im Herstellungsprozess von einbasigen Treibladungspulvern vorgenommenen Produkte-Prüfungen.

- Durch eine einfache, nasschemische Prüfung (***Stabilisatorprobe***) unmittelbar vor dem Verpressen wurde kontrolliert, ob der Knetteig Stabilisator enthält.
- Mittels ***manueller Ausmessung der frisch geschnittenen Pulverkörner*** wurde eine korrekte Einstellung der Schneidemaschine sichergestellt.

Damit stand die NITROCHEMIE WIMMIS AG jedoch nicht etwa "im Abseits" – unseres Wissens wurden auch in anderen treibmittelproduzierenden Betrieben die Möglichkeiten zur Inprozess-Kontrolle bis anhin kaum genutzt.

2.3 Mögliche Verfahren der Prozessanalytik in der TLP-Produktion

Eine Verstärkung der Inprozess-Analytik (wie sie momentan in den neu erstellten Produktionsanlagen der NITROCHEMIE WIMMIS AG eingeführt wird) bedingt jedoch auch das Vorhandensein der notwendigen Analysenverfahren. Deshalb wurden im Rahmen dieser Arbeit nach geeigneten Analysenverfahren gesucht, bzw. solche erarbeitet. Die Resultate sind in Abbildung 5 aufgezeigt:

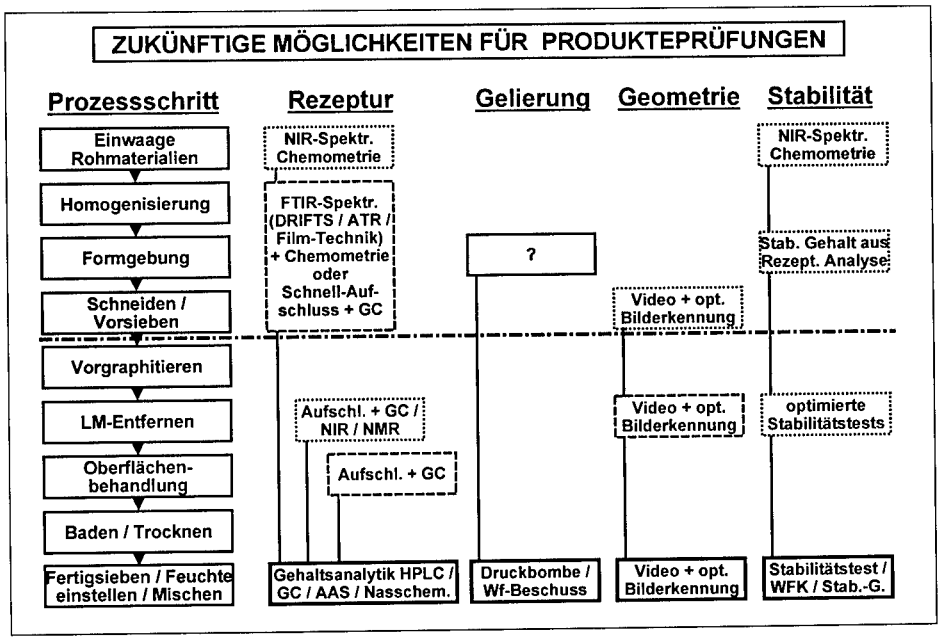

Abbildung 5: Neue Möglichkeiten für Produkte-Prüfungen im Herstellungsprozess.

Kontrolle der Rezeptur:

- Eine ***Identitätskontrolle der Rohmaterialien bei der Einwaage*** kann am einfachsten durch ***Nahinfrarot-(NIR)-Spektroskopie*** erfolgen, verbunden mit ***chemometrischer Spektrenanalyse***. Dabei werden die Spektren mittels einer Lichtleiter-Sonde in wenigen Sekunden aufgenommen - der Messvorgang erfordert keine Probenvorbereitung. Diese Methode wurde in unseren Labors überprüft, für geeignet befunden, und daraufhin in der Produktion eingeführt. Abbildung 6 zeigt auf, wie mit einigen typischen Spektren von jeder der zu analysierenden Substanzen eine schnelle Identitätskontrolle (Klassifizierung) von Rohmaterialen möglich wird.

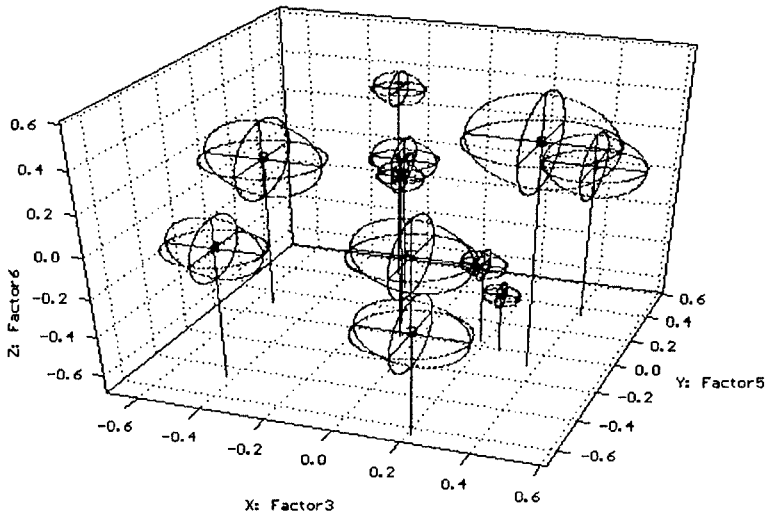

Abbildung 6: Identifikation von Rohmaterialien: Zur Kalibration des Modells wurden von jeweils 5 verschiedenen Mustern der zur TLP-Herstellung verwendeten 11 pulverförmigen Rohstoffen je 3 NIR-Spektren aufgenommen. Aus diesen Spektren wurde das hier abgebildete Modell zur Klassifikation erstellt, dies durch Transformation der Original-NIR-Spektren in ein angepasstes Koordinatensystem mittels Faktoren-Analyse. Jedes Spektrum kann durch einen Punkt in diesem mehrdimensionalen Faktorraum dargestellt werden - das Spektrum ist durch die Koeffizienten der entsprechenden Koordinaten eindeutig definiert. Die Koordinaten von ähnlichen Spektren (d.h. vom gleichen Rohstoff) liegen sehr nahe beisammen und bilden eine "Wolke". In der Abbildung sind für alle 11 Rohstoffe die jeweiligen Toleranzkugeln ("Wolken") eingezeichnet.

Die NIR-Spektren von unbekannten Stoffen werden ebenfalls in diesen Faktorraum umgerechnet – fallen sie in eine Toleranzkugel, so ist der Stoff damit identifiziert, ansonsten wird eine Fehlermeldung "Substanz unbekannt" ausgegeben.

- Die ***Analyse des Knetteiges*** oder der verpressten Masse ist bereits deutlich aufwendiger und bedingt auf jeden Fall eine Probenvorbereitung.[1]

  Durch Auflösen der Proben in einem geeigneten Lösungsmittel (wie z.B. Tetrahydrofuran) und anschliessendem Abdampfen des Lösungsmittels mit einer IR-Lampe auf einem Teflonblock können Filme mit der TLP-Zusammensetzung hergestellt werden. Die Gehalte der einzelnen TLP-Rezepturkomponenten in diesen Filmen werden durch Aufnahme der ***NIR-*** oder ***Fourier Transform Infrarot-(FTIR)-Spektren*** mit ***chemometrischer Auswertung*** bestimmt. Dieser Weg ist prinzipiell gangbar, jedoch deutlich aufwendiger als die oben beschriebene Kontrolle der Rohmaterialien mittels NIR. In Abbildung 7 wird aufgezeigt, wie mittels Diskriminanzanalyse das Vorliegen eines bestimmten Weichmachers im Knetteig überprüft wird.

  Der zweite Ansatz basiert auf einer ***flüssig-*** oder ***gas-chromatographischen Analyse (HPLC*** oder ***GC)***. Dazu müssen Knetteig bzw. verpresste Körner vorgängig aufgeschlossen werden. (z.B. Acetonitril-Aufschluss mit anschliessendem Ausfällen der NC). Dieser Ansatz wäre prinzipiell gangbar, erscheint jedoch für Inprozess-Kontrollen als zu langsam und zu aufwendig (gleicher Zeitbedarf / Aufwand wie bei der Schlusskontrolle).

- Für die ***Bestimmung des Restlösungsmittel-Gehaltes am Grünkorn*** müssen die Restlösungsmittel vor der ***GC***-Analyse durch einen Aufschluss isoliert oder etwas einfacher durch ein Quellmittel aus der TLP-Matrix extrahiert werden. Dieses Verfahren dürfte sich ebenfalls nur beschränkt für Inprozess-Kontrollen eignen, da zu langsam und zu aufwendig.

  Eine Alternative wäre die direkte Bestimmung der Restlösungsmittel mittels ***kernmagnetischer Resonanz NMR***. Diese Technik hat in den letzten Jahren grosse Fortschritte erfahren, so dass nun auch die routinemässige Analyse von Festkörpern (wie TLP-Körnern) möglich ist. Von diesem Verfahren sind kurze Rückantwortzeiten zu erwarten. In Ermangelung eines NMR-Gerätes konnte dieser Ansatz nicht erprobt werden. Vermutlich könnte jedoch auch bei technischer Machbarkeit der hohe Anschaffungspreis eines solchen NMR-Gerätes nicht gerechtfertigt werden.

---

[1] Versuche, den Knetteig direkt, d.h. ohne Probenvorbereitung, mittels NIR- oder FTIR-Spektroskopie (DRIFTS- oder ATR-Technik) zu analysieren, schlugen fehl. Es zeigte sich, dass die stark variierende Lösungsmittel-Konzentration (Ethanol und Ether) im Knetteig die Auswertung verunmöglicht - die Einflüsse der in viel höheren Konzentrationen vorliegenden Lösungsmittel überlagern die spektralen Eigenheiten der Rezepturkomponenten um ein Vielfaches. Selbst unmittelbar nacheinander aufgenommene Spektren des gleichen Knetteiges ergaben beispielsweise bei der Stabilisatorbestimmung um bis zu 100% abweichende Analysenresultate!

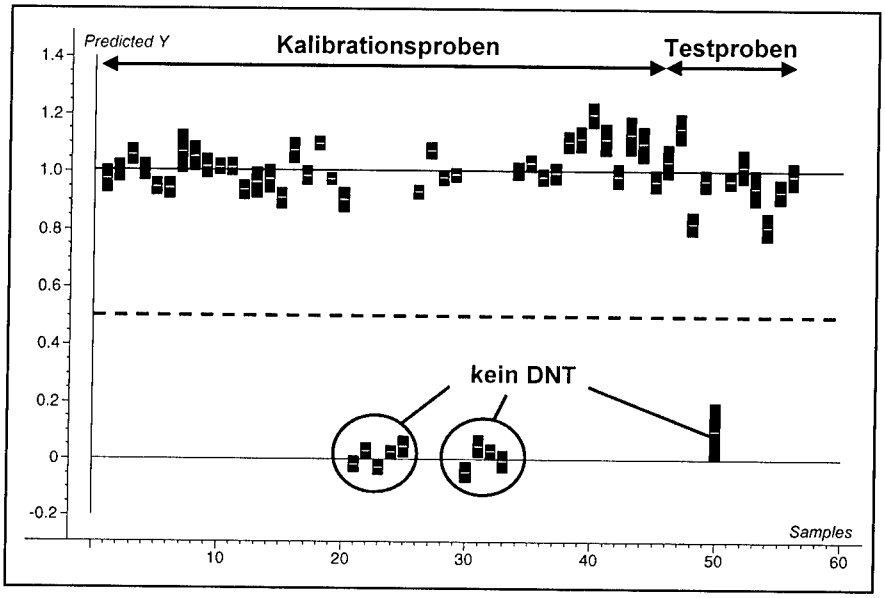

Abbildung 7: Resultat der PLS-(Partial Least Squares)-Diskriminanzanalyse zur Überprüfung der Anwesenheit des Weichmachers Dinitrotoluol DNT im Knetteig. 45 Kalibrationsproben (1 - 45) und 11 Testproben (46 - 56) wurden in Tetrahydrofuran gelöst. Von den nach Abdampfen des Lösungsmittels erhaltenen Filmen wurden FTIR-Spektren aufgenommen. Die 45 Kalibrierproben wurden zur Bildung, die Testproben zur Überprüfung des PLS-Modells verwendet. Ein Ordinatenwert von 1.0 entspricht der Voraussage "DNT ist in spezifizierter Konzentration vorhanden", ein Wert von 0.0 impliziert die Abwesenheit von DNT in der Probe. Die Proben 21 - 25, 30 - 33 und 50 enthalten kein DBP. Wie aus der Abbildung ersichtlich, konnte das Modell alle Proben korrekt zuordnen (klassifizieren).

Die ***Rezepturkontrolle am Endprodukt*** erfolgt durch die bekannten Analysenverfahren wie ***Extraktion*** *oder* ***Aufschluss*** und anschliessender ***Chromatographie, Atomabsorptionsspektroskopie*** *oder* ***nasschemische Bestimmung***.

Kontrolle der Gelierung:

- Trotz der Wichtigkeit dieses Parameters sind bis heute keine einfachen und routinetauglichen Verfahren zur Bestimmung des Geliergrades der Nitrocellulose vorhanden.

- Lediglich die am Schluss des Prozesses durchgeführten innenballistischen Untersuchungen *(**Druckbombe*** und/oder ***Waffenbeschuss**)* erlauben, bei Kenntnis von Rezeptur und Geometrie, einen gewissen Rückschluss auf die Stärke der Gelierung der Nitrocellulose im TLP. Diese Verfahren sind jedoch sehr teuer.

***Kontrolle der Geometrie**:*

- Die ***Geometrie der Pulverkörner*** kann in allen Stadien des Prozesses durch ***Video-Aufnahme*** mit ***optischer Bildanalyse*** bestimmt werden. Die Anwendung dieser Technik zur Kontrolle von Schnittlänge und Korndurchmesser ("äussere Geometrie") ist in Abbildung 8 aufgezeigt. Eine noch ausgereiftere Anwendung ist in der NITRO-CHEMIE ASCHAU GmbH implementiert. Dort wird die optische Bildanalyse auch zur Kontrolle der "inneren Geometrie" von mehrbasigen Pulverkörnern verwendet – sämtliche Web-Stärken und Lochdurchmesser von 7- und 19-Loch Körnern können so automatisch vermessen werden.

***Kontrolle der Stabilität**:*

- Die ***Anwesenheit des Stabilisators*** bei der Einwaage, bzw. dessen Gehalt im Knetteig oder an den verpressten, ev. geschnittenen Strängen kann, wie oben beschrieben, zusammen mit den anderen Rezepturkomponenten bestimmt werden.
- Zur Bestimmung der ***Stabilität von Grünkorn und Endprodukt*** können entweder die konventionellen ***Hochtemperatur-Stabilitätstests*** (basierend auf Gewichtsverlust oder Abspaltung von nitrosen Gasen) oder aber modernere Verfahren wie die ***Wärmeflusskalorimetrie*** verwendet werden. Für allfällige Inprozess-Kontrollen (z.B. am Grünkorn) eignen sich primär Hochtemperaturtests, während für die Schlusskontrolle bevorzugt Prüfungen bei tieferen Temperaturen anzuwenden sind. Dies aufgrund der bekannten Problematik, wonach bei hohen Temperaturen mit kurzer Rückantwortzeit nur eine geringe Aussagenschärfe erzielt wird, wogegen die aussagekräftigeren, bei tieferen Temperaturen vorgenommenen Prüfungen deutlich länger dauern.

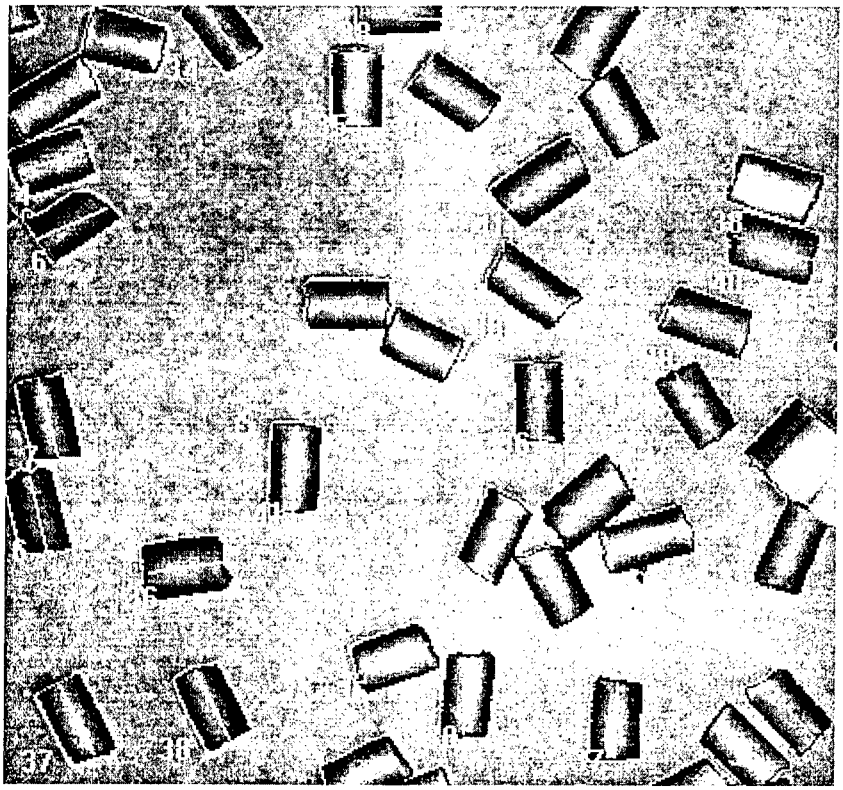

Abbildung 8: Bestimmung von Korn-Durchmesser und Schnittlänge: Zuerst wird das Video-Bild von ca. 20 – 200 auf einer Fläche aufliegenden TLP-Körnern aufgenommen. Dieses Bild wird dann einer automatischen Bildanalyse unterzogen. Hierbei werden im ersten Schritt zusammenhängende Regionen (Objekte) identifiziert – diese können aus einzelnen TLP-Körnern (stehend oder liegend) sowie aus Agglomerationen von Körnern bestehen. Im nächsten Schritt werden die einzelnen Objekte klassifiziert, d.h. aufgrund einer Konturanalyse oder anderer geeigneter Kriterien (wie Fläche und Rundheit) wird festgestellt, welche der Objekte isolierte, liegende TLP-Körner darstellen. Nur diese werden als "zur Ausmessung geeignet" taxiert und einer Grauwertanalyse unterzogen – über den Verlauf der Helligkeit wird die "Zylinderachse" der Körner bestimmt (genau so wie das menschliche Auge aus den Schattierungen / Reflexionen erkennt, wie der Zylinder im Raum liegt). Nun werden Schnittlänge und Durchmesser aller geeigneter Körner gemessen und die Werte in einer Tabelle abgelegt. Der gesamte Vorgang dauert nur wenige Sekunden.

Die obige Abbildung zeigt einen Ausschnitt einer solchen Bildanalyse. Bei allen als "für die Auswertung geeignet" erkannten Pulverkörnern wurde vom System die berechnete Zylinderachse sowie die Schnittlänge (in Anzahl Pixel) eingetragen.

3. Zusammenfassung und Diskussion

Aus den beschriebenen Resultaten und Überlegungen ergeben sich nachstehende Schlussfolgerungen:

- ***Die Inprozess-Analytik ermöglicht eine Überwachung / Steuerung der jeweiligen Prozesse.***
- ***Die Einführung von geeigneten Inprozess-Kontrollen im Herstellungsprozess von Treibladungspulvern ist deshalb sinnvoll und notwendig.***
- ***Die Durchführung von Inprozess-Kontrollen kann jedoch (zumindest im Fall der Treibmittel) die Analytik am fertiggestellten Produkt nicht ersetzen.***
- Im Rahmen dieser Arbeit wurden die bekannten sowie die neu erarbeiteten Analysenmethoden für Inprozess-Kontrollen zusammengestellt bewertet.
- Eine daraufhin durchgeführte ***Kosten-Nutzen-Analyse*** diente als Basis des ***Qualitätssicherungs-Konzeptes*** für die neuen Produktionsanlagen der NITROCHEMIE WIMMIS AG.
- Dieses sieht, neben einer ***lückenlosen Aufnahme der Prozessparameter***, nur ***zwei Inprozess-Kontrollen*** vor, nämlich:
  - Eine ***Identitätskontrolle aller Rohmaterialien*** (inklusive Stabilisator) bei der Einwaage durch ***Nahinfrarot-(NIR)-Spektroskopie mit chemometrischer Auswertung***. Dies in Kombination mit einer Überprüfung der effektiven Zugabe. Damit ist durch das Prozessleitsystem eine Kontrolle und Rückverfolgung von Menge und Identität der eingesetzten Rezepturkomponenten möglich.
  - Eine ***Kontrolle von Schnittlänge und Durchmesser der Pulverkörner*** nach dem Schneiden durch ***Videoaufnahme und optische Bildanalyse***.
- Weiter wurde festgestellt, dass eine ***Überprüfung des Geliergrades*** der Nitrocellulose im TLP ***äusserst hilfreich*** wäre. Zur Zeit steht hier jedoch noch ***kein geeignetes Verfahren*** zur Verfügung. Nach einem solchen Verfahren wird jedoch gesucht.

Würdigung:

Unserem früheren Mitarbeiter Herr Ch. Herren danken wir für das Einbringen von wertvollen Ideen. Bei Herr Dr. Hp. Kellerhals der Fa. Büchi verdanken wir die Durchführung der NIR-Messungen, bei Herr J. Meyer der Fa. Gloor Instruments AG den Aufbau des Systems für die optische Bildanalyse. Der Schweizerischen Gruppe Rüstung GR danken wir für die Mitfinanzierung dieses Projekts im Rahmen des LFP-Vorhabens 35.13 "Analytik an Explosivstoffen / Chemometrie".

COMPARISON OF T-JUMP/RAMAN AND T-JUMP/FTIR SPECTROSCOPY FOR HIGH-NITROGEN COMPOUNDS

Thomas B. Brill and Brian D. Roos
Department of Chemistry and Biochemistry
University of Delaware
Newark, DE 19716 USA

ABSTRACT

Flash pyrolysis of energetic compounds that are nitrogen-rich frequently liberates a large amount of IR-inactive N_2 among the IR-active products. H_2 and O_2 also sometimes form. Therefore, T-jump/Raman spectroscopy was developed to complement T-jump/FTIR spectroscopy and enable completion of the elemental atom balance by adding the IR-inactive gaseous products. Differential Raman scattering cross-sections were determined for commonly released gases from pyrolysis of energetic compounds. The method was demonstrated with HNNF, BAMO, GAP, and 5-NATZ. When at least one of the quantified species is common to both the IR and Raman spectra, the atom-balanced gasification reaction can be obtained with good accuracy.

1. INTRODUCTION

Flash heating of a film of an energetic material is a qualitative "snapshot" simulation of the surface pyrolysis zone during steady combustion at and above atmospheric pressure [1]. Well-controlled flash heating to temperatures resembling those at the burning surface is accomplished by the use of T-jump/FTIR spectroscopy [2-10]. However, several important energetic compounds (*e.g.* azides, nitramines, tetrazoles, etc.) liberate IR-inactive products such as N_2, O_2, and H_2. To complete the stoichiometry of the flash pyrolysis reactions of these energetic materials, it would be helpful to augment T-jump/FTIR spectroscopy with the complementary T-jump/Raman method.

The concentrations from the FTIR and Raman methods can be directly compared provided that the total differential Raman scattering cross-sections and IR absorptivities are known for the common gaseous products. These were determined with the excitation wavelength and collection configuration of the device. The method was demonstrated with varying degress of success using the concentrations of the gaseous products from flash

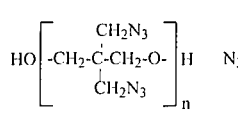

BAMO

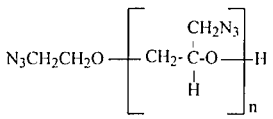

GAP mono-ol

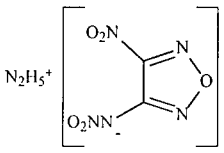

HNNF

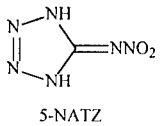

5-NATZ

pyrolysis of hydrazinium [3-nitro-4-nitraminofurazan] (HNNF), poly (bis(3,3'-azidomethyl)oxetane) (BAMO), poly (glycidyl azide) mono-ol (GAP), and 5-nitroiminotetrazole (5-NATZ). The positions of the H atoms in 5-NATZ have been determined by x-ray crystallography [11].

2. DIFFERENTIAL RAMAN SCATTERING CROSS SECTIONS, $\partial\sigma/\partial\Omega$

The total Raman effect for a given vibrational mode represents the sum of the populated rotational and vibrational quantum states at a given temperature. The measured Raman signal intensity is a function of the variables in the eq. 1 [12], *i e.* the laser frequency υ_0, the vibrational frequency υ, the degeneracy of the Raman line g, the temperature T, and the average of the isotropic (α'^2) and anisotropic (γ'^2) elements of the polarizability tensor. "a" is a constant.

$$\frac{\partial\sigma}{\partial\Omega} = \frac{ag(\upsilon_0 - \upsilon)^4(45\alpha'^2 + 7\gamma'^2)}{\upsilon_i(1 - e^{hc\upsilon_0/kT})} \qquad (1)$$

In general, however, the determination of the absolute Raman scattering cross section is difficult [13]. Therefore, the quantitation here is relative to the intensity of N_2. In the present experiment, υ_0 = 532 nm and T = 295 ± 3 K. The integrated Raman signal for a given species x (I_x) relative to N_2 (I_{N_2}) is given by eq. 2, where K is the instrument correction. K fails to

$$\text{Concentration of } x = \frac{I_x K}{I_{N_2}}\left[\left(\frac{\partial\sigma}{\partial\Omega}\right)_{N_2} \Big/ \left(\frac{\partial\sigma}{\partial\Omega}\right)_x\right] \qquad (2)$$

cancel because of the low and high channels of the Holoplex grating that is used in the spectrometer and the non-uniform response across the grating and the CCD camera. These effects were removed from the intensity factors by further manipulation of the measurements.

The calibration cell shown in Fig. 1 was employed to determine $\partial\sigma/\partial\Omega$ for the gaseous species from pyrolysis of energetic materials. The purgable glass tube fitted with pressure-tight end caps had an internal volume of 5.25 cm^3 and could be pressurized to 10 atm. The

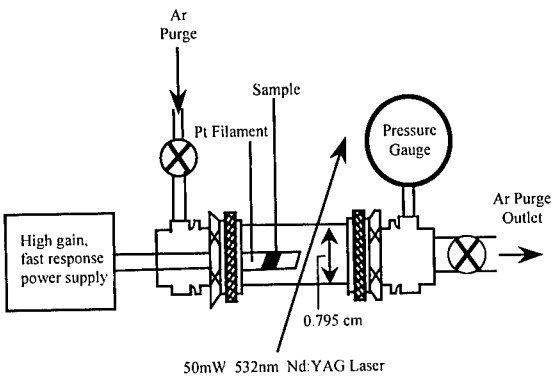

Fig. 1 The T-Jump/Raman spectroscopy cell

cell was housed inside a plastic compartment that also incorporated the laser head so that atmospheric gases could be purged from the collection region by a flow of argon gas. These components were in turn housed inside a light-tight box that eliminated stray background radiation. To determine $(\partial\sigma/\partial\Omega)_x$, a 100 cm^3 steel ballast tank was charged with a known pressure of the desired analyte gas x. A known pressure of nitrogen was then added as an internal standard. Finally argon was added as a diluent to raise the pressure to about 20 atm. The gas mixture equilibrated for 3 hr and a 7.8 atm sample was bled into the cell. The spontaneous Raman scattering spectrum was collected using a Kaiser Optical Systems spectrometer with a CCD detector and a 50mW, frequency-doubled, Nd:YAG CW laser at 532 nm. The average of 10 scans (30 sec/scan) produced the final spectrum. This procedure was repeated four times on new samples having the same partial pressure, which provided an average random error of <5%. Successive addition of argon to the ballast tank diluted the gas mixture until the limit of detection was reached. The entire procedure was repeated to ensure reproducibility. The random error continued to be <5% except near the limit of detection where it was as high as 10%. The spectral sets were converted to an xy file and a suitable baseline with 10% tolerance was subtracted. The spectral band was fit with a Voigt function and the peak height and area were extracted. While peak areas and heights gave comparable results in the higher-pressure data, the heights gave more reproducible results in the lower-pressure range. Figure 2 shows several examples of these Beer-Lambert Law-type calibration curves based on peak height versus pressure. Following eq. 2, the ratio of the slope of the regression line for each analyte to that of N_2 corresponds to the Raman intensity value used to establish the relative concentration.

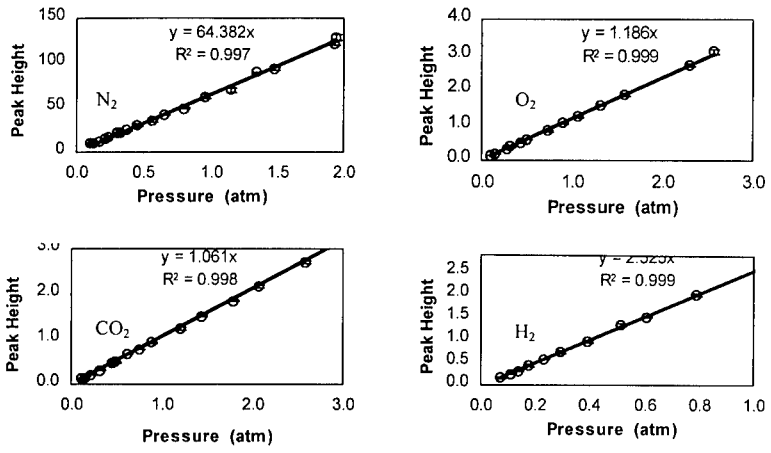

Fig. 2. Beer-Lambert Law Raman calibration plots for selected gases

Table 1 contains Raman scattering intensities determined by the ethods described above. These values resemble those reported elsewhere [12, 14-16] when adjusted to 532-nm excitation used here, and we believe that the concentrations can be trusted to within 2-10%.

Table 1. Differential Raman Scattering Cross Sections of Selected Vibrations Relative to N_2

MOLECULE	BAND	RAMAN SHIFT (CM^{-1})	$\left(\frac{\partial\sigma}{\partial\Omega}\right)/\left(\frac{\partial\sigma}{\partial\Omega}\right)_{N_2}$ THIS WORK
N_2		2331	1
H_2		4155	2.53
O_2		1555	1.19
CO		2143	1.06
NO		1877	0.45
CO_2	υ_s	1388*	1.30
	$2\upsilon_2$	1286*	0.85
N_2O	υ_{as}	2224	0.40
	υ_s	1285	2.11
CH_4	υ(CH)	2915	6.61
C_2H_2	υ(CH)	3372	1.23
	υ(CC)	1973	6.71
C_2H_4	υ(CH)	3020	5.38
	υ(CC)	1624	1.72
	$\upsilon(CH_2)$	1342	2.98
NH_3	υ_1	3334	4.40

* Fermi resonance doublet

3. THE T-JUMP/RAMAN EXPERIMENT

The Raman cell for pyrolysis is the same cell as that shown in Fig. 1. A sample of the energetic material was spread onto the center of the previously calibrated Pt ribbon filament. The optimum sample mass depends on the energetic material, but was about 200 μg for HNNF, 400 μg for BAMO and GAP, and 600 μg for 5-NATZ. By comparison 200 μg is typically optimum for T-jump/FTIR spectroscopy. The filament was then inserted into the Raman cell and connected to a CDS Analytical 1000 control unit. The cell was purged and pressurized to the desired value, and the surrounding plastic case was purged with argon gas to remove the ambient air. The control unit heated the filament at about 2000°C/sec to a chosen set temperature and held it constant for 20 sec. This constant set temperature was maintained by microsecond adjustments of the voltage by the control unit so as to maintain constant resistance in the filament. Rapid voltage adjustment is needed especially during an exothermic event of an energetic material, which occurs at some time during the 20 sec of heating. The duration of the rapid exothermic decomposition is less than 0.5 sec. The energetic materials discussed herein produced a small amount of smoke aerosol. Therefore, up to 5 min was required in some cases to settle this aerosol before the Raman spectrum of the vaporized products could be collected. Five spectra were collected each consisting of an average of 10 scans at 30 sec/scan. The relative concentrations of the gaseous products were determined using the Raman intensity factors that were calculated above.

The T-jump/Raman experiment is used differently than T-jump/FTIR spectroscopy [2-10]. The Raman method provided the final concentrations of the IR-inactive species. The intensities of the gaseous products that can be quantified by both Raman and IR spectroscopy are compared in Table 2 to demonstrate the relative sensitivity of the two methods. The most strongly active vibrational modes in the IR [1] and Raman spectra, when normalized to the intensity of C_2H_2, are directly compared in Fig. 3. Infrared spectroscopy is more sensitive than Raman spectroscopy for detecting the isoelectronic molecules CO_2 and N_2O. Raman spectroscopy is more sensitive to the lower molecular weight hydrocarbon molecules and NH_3. Neither method is particularly sensitive to NO and CO stretching. Because of the much higher S/N in the IR spectrum, IR spectroscopy was generally more useful for quantifying gaseous species, provided of course that the species are IR-active.

Table 2. Comparison of the Raman intensity (relative to N_2) and the infrared intensity (relative to CO_2) for the most intense mid-infrared band.

Molecule	Raman (cm^{-1})	Raman Intensity	Infrared (cm^{-1})	IR Intensity
N_2	2330	1	-	-
H_2	4155	2.53	-	-
O_2	1555	1.19	-	-
CO_2	1388	1.30	2349(R)	1
CO	2141	1.06	2143(R)	0.054
NO	1877	0.45	1876(R)	0.029
N_2O	1285	2.11	2224(R)	0.519
CH_4	2914	6.61	3020	0.083
C_2H_2	1973	6.71	729	0.300
C_2H_4	3020	5.38	949	0.133
NH_3	3334	4.40	968	0.180

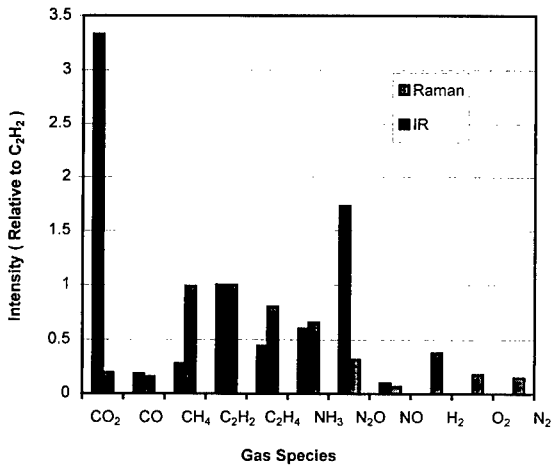

Fig. 3 The comparative sensitivity of IR and Raman spectroscopy for detecting the most intense vibrational mode of the gases shown when normalized to C_2H_2.

A major complication when using Raman spectroscopy for the analysis of pyrolysis gases is the fact that smoke and other aerosols cause elastic (Mie) scattering of the incident laser light. Mie scattering dominates when $\pi D/\lambda > 1$, where D is the particle diameter and λ is the wavelength of the incident light. Complications also arose when quantifying NH_3, CH_4, and C_2H_4 in the Raman spectrum. The concentration NH_3 decreased with time in the

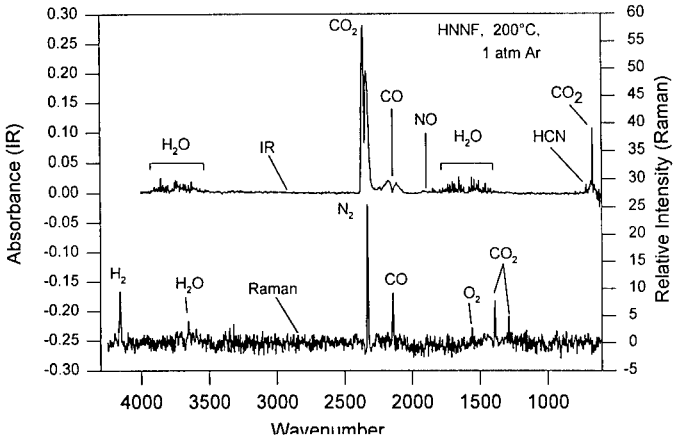

Fig. 4 The IR and Raman spectra of the gaseous products from flash pyrolysis of HNNF at 200 °C and 1 atm Ar.

Raman cell probably because it adsorbed onto the glass wall. The concentrations of CH_4 and C_2H_4 following pyrolysis in the Raman cell were consistently lower than in the IR cell. The concentrations of these species were therefore based on the IR measurement.

4. APPLICATION TO HIGH-NITROGEN COMPOUNDS

In order to use data from T-jump/Raman spectroscopy in conjunction with the T-jump/FTIR data, it is necessary to observe and quantify at least one IR-active species in the Raman spectrum in addition to the IR-inactive species. This enables the concentrations in the IR and Raman spectra to be appropriately scaled to one another. We have previously reported the IR spectra of the gases liberated upon fast heating of the compounds below [10,12,17-20], but the experimental methods and data analysis were somewhat different.

HNNF is useful for validating T-jump/Raman spectroscopy because it liberates N_2, H_2, and O_2, which were all previously detected by mass spectrometry, but not quantified [20]. It was flash-pyrolyzed at a filament set temperature of 200°C under 1 atm Ar and the spectra of the gaseous products are shown in Fig. 4. After quantifying each of the gaseous products in the IR and Raman spectra, the mole fractions were normalized to the amounts of C, H, N and O and then averaged so that the elemental atom balance could be obtained. The global reaction that describes the pyrolysis process is given below:

$$C_2H_5N_7O_5 \rightarrow 3.32N_2 + 0.12HCN + 1.04CO + 0.83CO_2 + 0.28NO + 1.65H_2O + 0.73H_2 + 0.24O_2.$$

The resulting empirical formula is $C_{1.99}H_{4.89}N_{7.05}O_{5.11}$, which is within 2.3% of the formula of the parent HNNF ($C_2H_5N_7O_5$). The stoichiometric coefficients for N_2, HCN, CO, CO_2, and NO in this reaction are the same as found before [20], although the coefficient of N_2 was assumed to make up the difference of N based on the amount of HCN and NO formed. A major variance from the earlier work is in the coefficients previously assumed for H_2O (0.7), H_2 (1.7), and O_2 (0.7). When the concentrations are actually measured as was done in this work, the coefficients are in fact 1.65 for H_2O, 0.73 for H_2, and 0.24 for O_2. This result highlights the value of the Raman analysis in concert with the IR analysis to determine the elemental atom balance with minimal assumptions.

BAMO has the stoichiometry of $C_5H_8N_6O$ when the small contribution of the end groups is neglected. Figure 5 compares the IR and Raman spectra taken at 320°C. Despite its low intensity (Fig. 3) CO proved to be the best product for normalizing the IR and Raman-derived concentrations. The IR spectra have much higher S/N and were therefore used to determine the relative concentrations of most gaseous products. When the concentrations

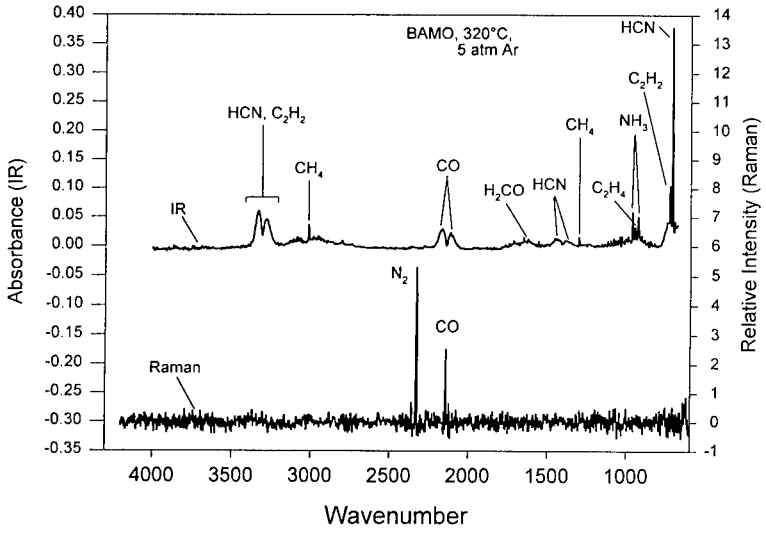

Fig. 5 The IR and Raman spectra of the gaseous products from flash pyrolysis of BAMO at 320 °C and 5 atm Ar.

were normalized to C, H, N, and O and averaged, the resulting equation for the flash pyrolysis is given below and has the product stoichiometry of $C_{4.76}H_{7.86}N_{6.01}O_{1.09}$.

$$-(C_5H_8N_6O)- \approx 1.88N_2 + 1.77HCN + 0.93CO + 0.48NH_3 + 0.59CH_4 + 0.33C_2H_4 + 0.325C_2H_2 + 0.16CH_2O$$

The close resemblance to the parent formulation is consistent with the fact that a small amount of (probably carbon-rich) smoke is formed, which was not taken into account in the mass balance.

GAP mono-ol is $C_3H_5N_3O$ when the end groups are not included. Inclusion of the end groups however has little effect on the empirical formula. Figure 6 shows the IR and Raman spectra of the gaseous products after flash heating of GAP mono-ol at 320 °C under 2 atm of Ar. The previous detailed study of GAP structures by T-jump/FTIR spectroscopy [10] noted

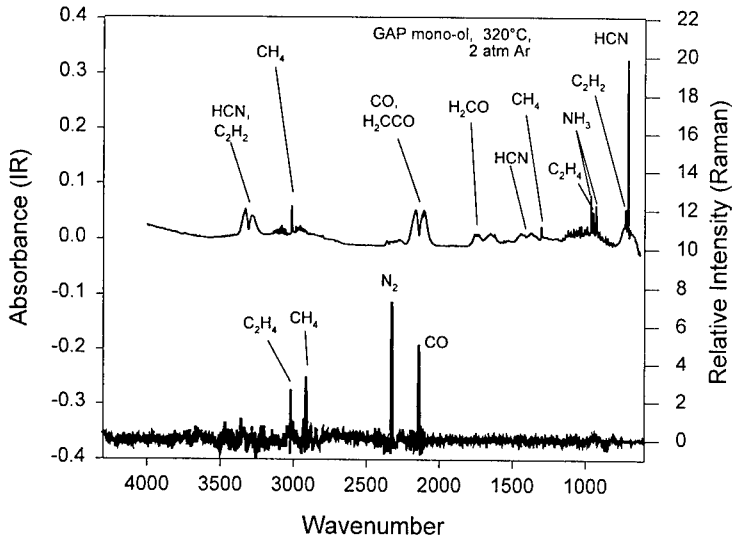

Fig. 6 The IR (top) and Raman (bottom) spectra of the gaseous products from flash pyrolysis of GAP mono-ol at 320 °C and 2 atm Ar.

a large number of gaseous species. The amount of N_2 was estimated by difference before, but is quantifiable now by using the N_2/CO ratio of 1.38 in the Raman spectrum. The resulting equation gives an element atom balance for the gaseous products of $C_{2.905}H_{4.853}N_{3.126}O_{1.022}$, which is within 4.2% of the element ratio of the reactant.

$$-C_3H_5N_3O- \longrightarrow 1.067N_2 + 0.773CO + 0.755HCN + 0.455CH_4 + 0.237NH_3 + 0.231C_2H_4 + 0.177CH_2O + 0.072C_2H_2 + 0.069CH_2CO + 0.004H_2O$$

5-NATZ ($CH_2N_6O_2$) produces the IR and Raman spectra of the gaseous products shown in Fig. 7 when flash heated to 300 °C under 5 atm of Ar. Only the thermodynamically relatively stable products N_2, CO_2, CO, and HCN are detected. It was never possible to detect any product other than a large amount of N_2 in the Raman spectrum. Thus while all of the products except H_2 were detected, none could be seen by both spectral methods, which makes it impossible to scale the IR and Raman spectra to one another. After quantifying the IR-active products, however, the amount of N_2 and H_2 can be estimated by difference, which results in the following reaction:

$$CH_2N_6O_2 \longrightarrow 2.97N_2 + 0.66CO + 0.33CO_2 + 0.52H_2O + 0.04HCN + 0.096NO + 0.5H_2.$$

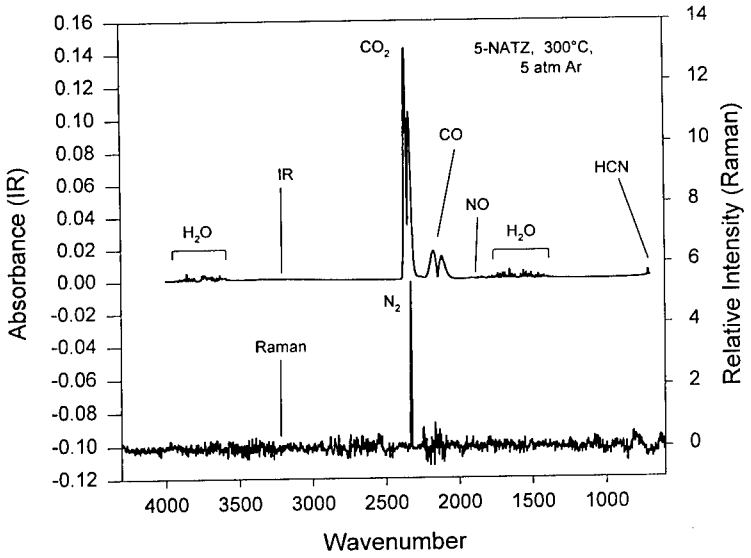

Fig. 7 The IR and Raman spectra of the gaseous products from flash pyrolysis of 5-NATZ at 300 °C and 5 atm Ar.

The gas phase elemental atom balance is $C_{1.03}H_{2.01}N_{6.08}O_{1.94}$, which is within 3.1% or less of the elemental formula of the parent 5-NATZ.

5. CONCLUSIONS

T-Jump/Raman spectroscopy is not as useful as T-jump/FTIR spectroscopy for quantifying the gaseous pyrolysis products of energetic materials. The S/N ratio is lower and smoke complicates the collection of the Raman spectra. The Raman method does successfully quantify IR-inactive products, such as N_2, O_2, and H_2, provided that one IR active product can also be seen in the Raman spectrum. CO proved to be the most useful product for the purpose of normalizing data from the two methods.

6. ACKNOWLEDGMENTS

This work was sponsored partly by the University of Delaware and partly by California Institute of Technology Multidisciplinary University Research Initiative under ONR Grant No. N00014-95-1-1338. The Program Manager is Dr. Judah Goldwasser. HNNF and BAMO (MW ≈ 12000) were gifts from Robert Day and Robert Wardle (Thiokol Corp.), and GAP mono-ol (n = 3-11 giving an average MW of about 700) was a gift from Tony Manzara (3M Corp.).

7. REFERENCES

[1] T. B. Brill, Prog. Energy Combust. Sci. **18**, 91 (1992).

[2] T. B. Brill, P. J. Brush, K. J. James, J. E. Shepherd and K. J. Pfeiffer, Appl. Spectrosc. **46**, 900 (1992).

[3] J. E. Shepherd and T. B. Brill, 10th International Symposium on Detonation, Naval Surface Warfare Center, White Oak, MD, 1993. p. 849.

[4] S. T. Thynell, P. E. Gongwer and T. B. Brill, J. Propuls. Power. **12**, 933 (1996).

[5] T. B. Brill, P. J. Brush and D. G. Patil, Combust. Flame. **92**, 178 (1993).

[6] T. B. Brill, D. G. Patil, J. Duterque and G. Lengellé, Combust. Flame. **95**, 183 (1993).

[7] T. B. Brill, J. Propuls. Power. **11**, 740 (1995).

[8] H. Arisawa and T. B. Brill, Combust. Flame. **106**, 131 (1996).

[9] T. B. Brill, H. Arisawa and P. E. Gongwer, *Challenges in Propellants and Combustion 100 years after Nobel,* Begell House Inc., New York, 1997, p. 3.

[10] H. Arisawa and T. B. Brill, Combust. Flame. **112**, 533 (1998).

[11] A. Gao, A. L. Rheingold and T. B. Brill, Prop. Explos. Pyrotech. **16**, 97 (1991).

[12] A. C. Eckbreth, *Laser Diagnostics for Combustion Temperature and Species,* Abacus Press, Cambridge, MA, 1988, p. 174.

[13] E. S. Yeung in *Chemical Applications of Nonlinear Raman Spectroscopy*, A. B. Harvey, Ed., Academic Press, New York, 1981, p. 174.

[14] A. Weber, *Raman Spectroscopy of Gases and Liquids, Topics in Current Physics* Vol. 11, Springer-Verlag, New York, 1979.

[15] J. M. Cherlow and S. P. S. Porto, *Laser Spectroscopy of Atoms and Molecules*, H. Walther, Ed., Springer-Verlag, New York, 1976, Chapter 4.

[16] W. F. Murphy, H. Holzer and H. J. Bernstein, Appl. Spectrosc. **23**, 211 (1969).

[17] Y. Oyumi and T. B. Brill, Combust. Flame. 65, 127 (1986).

[18] J. K. Chen and T. B. Brill, Combust. Flame. **87**, 157 (1991).

[19] T. B. Brill and P. J. Brush, Phil. Trans. Royal Soc. London A. **339**, 377 (1992).

[20] G. K. Williams and T. B. Brill, Combust. Flame. **114**, 569 (1998).

THERMAL DECOMPOSITION OF SECONDARY NITRAMINES IN SOLUTIONS

Shu Yuanjie, V.V. Dubikhin, G.M. Nazin, G.B. Manelis

Institute of Problems of Chemical Physics, Russian Academy of Sciences,
142432, Chernogolovka, Moscow Region, Russia
Fax: 007(096) 573588 E-mail: nazin@icp.ac.ru

Abstract

Decomposition of RDX and HMX in hydrocarbon solutions (RH) proceeds through the chain mechanism with the following features: inhibition of the reaction when adding inhibitors, H-D isotope effect of solvent, as well as the dependence of the decomposition rate on D(C-H) value in RH. The chain reaction is developed due to the transfer of the free valence from primary N-radicals to R-radicals, weak NO solubility in the liquid phase, absence of condensed products-inhibitors of the chain processes, and instability of intermediate N-nitrosocompounds. The last two conditions being absent, no chain reactions are observed at decomposition of dimethylnitramine (DMNA) and polycyclic compound CL-20.

Introduction

In the studies of RDX thermal decomposition in solutions it has been found that aliphatic-aromatic hydrocarbons with the C-H bond energy from 65 to 85 kcal/mole, as well as alcohols, ketones and some other compounds easily oxidized through the free-radical mechanism increase RDX decomposition rate [1]. Herewith, the deuterium kinetic isotope effect of solvent is observed together with a well-defined dependence of the rate on D(C-H) of the solvent. To explain these facts it has been assumed that a chain process is developed in solutions, the most important stage of which is free valence transfer from primary radicals of N-type formed at the breakage of $N\text{-}NO_2$ bond to C-centered radicals of the solvent.

In chemically inert solvents like, for example, chlorine- and nitro-derivatives of benzene and hydrocarbons with a large molecular mass and strong C-H bonds, RDX decomposition rate decreases as a result of the cage effect, which has been experimentally proved for the first time in [2]. The presence of cage effect by itself indicates that RDX decay in solvents starts with N-NO_2 dissociation, which is reversible

In this paper new evidences have been obtained for the chain mechanism of RDX decay in solutions by introducing inhibitors and analyzing the products formed from the solvent. A more detailed scheme of the process is presented. In addition, just like RDX, decomposition of some other nitramines such as HMX, DMNA and CL-20 has been investigated.

Results and Discussions

Inhibition of RDX decomposition. At decomposition of most explosives free radicals are formed. They can interact with an initial substance and even cause chain decay. However, in the majority of cases chain reactions do not develop being inhibited by decomposition products like NO, NO_2, nitrosocompounds, and nitroxyl radicals. The difference in the activation energy between the reaction of free radicals with NO or NO_2 and that of free radicals with unsaturated molecules comprises no less than 10 kcal/mole, therefore, even at the inhibitor concentration of 10^{-3}-10^{-4} mole per mole of the substance chain reactions will be completely depressed. RDX chain decay in solutions proceeds only owing to low solubility of NO and NO_2 in organic solvents at high temperatures.

Judging by the relatively small increase of RDX decomposition rate in solutions (3 times in toluene, 11 –in glycerin [1]), gaseous inhibitors still affect the reactions despite their low solubility. In case of RDX decomposition only NO is the inert inhibitor to solvents. Therefore NO (under the pressures 2-3 times exceeding NO

pressure at the end of reaction) and solid *para*-dinitrobenzene (*p*-DNB) (which is easily controled) at the concentration of 0.5 wt % were used as inhibitors. Moreover, triphenylmethane, phenol, diphenylamine, NO_2 and molecular iodine were used as inhibitors too.

Fig. 1 shows the effect of NO, NO_2 and *p*-DNB on RDX decomposition in toluene. The rate decreases almost to that in benzene, and at higher ratios of NO/RDX concentration – even below this level. NO, NO_2 and *p*-DNB decrease the rate of RDX decomposition in *p*–xylene and glycerin, just like Ph_3CH does this in *p*–xylene (see Table 1).

Phenol, diphenylamine and I_2 are not inhibitors for RDX. Phenol is involved in the chain reaction like a solvent, diphenylamine accelerates the decay via donor-acceptor interaction mechanism, and I_2 in benzene is inert , but it increases the decomposition rate in toluene acting as an initiator.

Mechanism of RDX decomposition. Nonchain reaction. All possible ways for the initial stage of RDX decomposition have been energetically assessed in[3, 4]. In [5] it has been shown that the kinetic isotope effects observed at decomposition of deuterated DMNA, RDX, HMX [6, 7] are not primary, but secondary or global and, therefore, they have nothing to do with HONO elimination. It can be concluded that in gas phase, in melt or in solid state RDX decomposition starts with breakage of N-NO_2 bond. The following scheme of decay has been proposed in[8, 9] for this case:

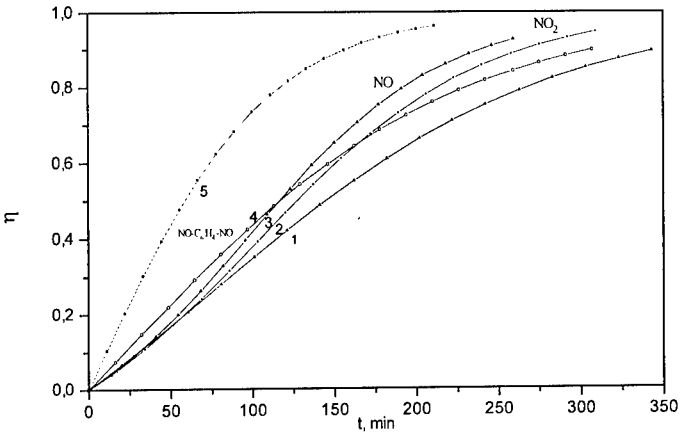

Fig 1. Effect of additives on decomposition of RDX in solutions at 180°C. 1 - benzene, 2 - toluene/NO_2, 3 - toluene/NO, 4- toluene/*p*-DNB, 5-toluene.

Table 1 Effect of additives on RDX thermal decomposition at 180°C

solvent	additives	$k_1.10^4/s^{-1}$	$k_1/k_{benzene}$
benzene	I_2 (4 wt %)	0.54	0.98
benzene	without additive	**0.55**	**1.00**
benzene	*p*-DNB (1.3 wt %)	0.55	1.00
benzene	NO (400 Torr)	0.69	1.25
benzene	Ph_2NH (0.9 %)	2.84	5.16
toluene	NO_2 (400 Torr)	0.45	0.82
toluene	NO (400 Torr)	0.46	0.84
toluene	*p*-DNB (1.54 wt %)	0.76	1.43
toluene	without additive	1.25	2.27
toluene	I_2 (1.44 wt %)	2.55	4.64
p-xylene	NO (400 Torr)	1.52	2.76
p-xylene	*p*-DNB (0.8 wt %)	1.96	3.56
p-xylene	Ph_3CH 40%	2.70	4.91
p-xylene	Ph_3CH 10%	2.89	5.25
p-xylene	without additive	3.09	5.62

Scheme 1

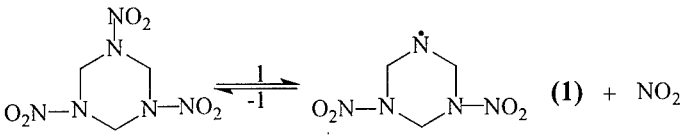

1 $\xrightarrow{2}$ $O_2NNCH_2N(NO_2)CH_2N{=}CH_2$ (**2**)

2 $\xrightarrow{3}$ $CH_2{=}NCH_2N(NO_2)$ (**3**) + $CH_2{=}NNO_2$ (**4**)

3 $\xrightarrow{4}$ $CH_2{=}N$ + **4**

4 $\xrightarrow{5}$ $CH_2O + N_2O$

The scheme can be, of course, adjusted and supplemented. For instance, reaction (2) takes place only owing to the low strength of NCH_2-NNO_2 bond in **1** (18 kcal/mole [4]). This condition is absent in radical **3**. Besides, the yield of N_2O at RDX decomposition comprises not 2 moles, as it follows from the scheme, but only 1-1.5 moles (see [8]). Formation of $N{=}CH_2$ observed in [10] that is followed by HCN formation is not the evidence of reaction (4), because these products can be produced at the decay of $CH_2{=}NNO_2$. Therefore, it may happen that reaction (4) does not take place at all. Instead of this nitramine radical **3** in the presence of nitrogen oxides according to [11] can undergo transformations like

3 + NO $\xrightarrow{6}$ $CH_2{=}N$-CH_2 (**5**) + N_2O + NO_2

3 + NO_2 $\xrightarrow{7}$ **5** + 2 NO + NO_2.

Radical **5** can be easily oxidized to give, for example, $HOCH_2NHCHO$ – one of the products of RDX decay [8]. However, this does not significantly affect the decay rate.

In addition to monomolecular decay to form inert $CH_2{=}N$, radical **1** can react with NO and NO_2. Its reaction with NO is reversible to give nitrosohexogen

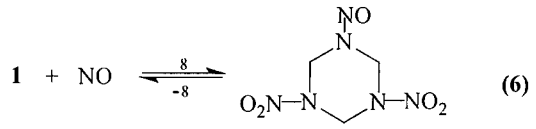

(6)

while that with NO_2 should result according to [12] in opening of the cycle and formation of highly reactive nitrosocompounds

$$\mathbf{1} + NO_2 \xrightarrow{9} O{=}NCH_2N(NO_2)CH_2N(NO_2)CH_2N{=}O \quad (7)$$

and further – of oximes. Their decay gives still more variable products than can be produced from **3**. In particularly, C-nitrosocompounds will promoteNO conversion to N_2. It should be mentioned that compound**7** is an effective chemical trap for free radicals. Probably, compounds **4** and **7** can be destroyed not through monomolecular decomposition, but under the effect of NO or NO_2; if the latters are unsufficient, then they can polymerize and produce nonvolatile products.

Chain decay of RDX in the solutions. Development of the chain and acceleration of RDX decomposition is observed only in those RH solvents, which react with products of RDX decomposition. The scheme of the chain decay takes the form:

Scheme 2

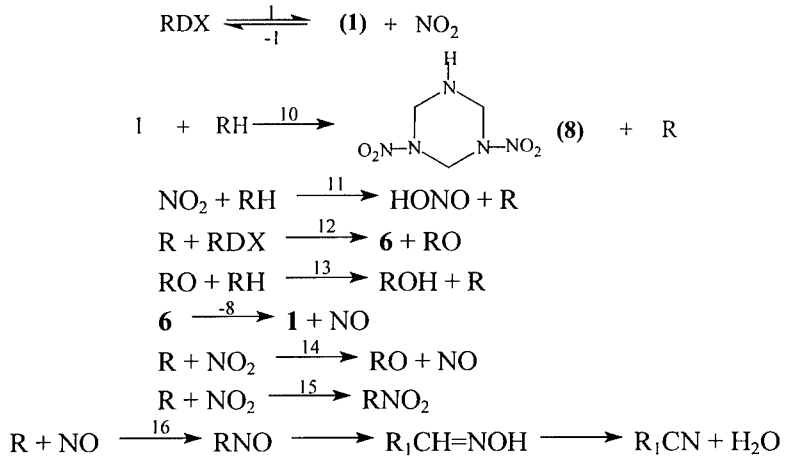

Free valence transfer to the solvent is performed in reaction (10) and (11); herewith, reaction (10) has a significant advantage, because its heat effect is by almost 10 kcal/mole more than that of reaction (11).

Owing to the transfer the death of free valence as a result of intramolecular decay of **1** is avoided. Active C-centered radicals replace radicals ofN-type, which are low active in reactions with nitrogroup. In this stage the isotope effect of solvent arises and, finally, this stage limits upper value of D(C-H), governingcompetition between reaction (10) and reaction (2).

The first condition of chain origination for nitramines is the transfer of the valence to the solvent, and the second condition – origination, herewith, of radicals active in the reaction with nitrogroup.

Radicals R react with NO_2 (that results in partial disappearance of the free valence), die off by reacting with NO and can interact with RDX. In order that reaction with RDX takes place, NO concentration should be 4 orders less than that of RDX. This condition is obeyed, apparently, only due to very low solubility of NO in organic solvents, especially at high temperatures.

It is also evident that the decay products of nitramine should not contain non-volatile and soluble in the liquid phase chemical traps of free radicals, for example, C-nitrosocompounds. This, already third, condition for occuring chain reactions, which is obeyed in the case of RDX. It should be mentioned that reaction (12) limits lower range of bond energy D(C-H), at which solvent preserves its activity.

Scheme 2 assumes that N–nitrosocompounds formed in the intermediate stage are instable and can break to form N-radicals once again. Instability of nitrosocompounds is the forth condition for occuring chain reactions, which is obeyed for RDX too.

The rate of bimolecular reactions for chain continuation should increase, as the external pressure increases. This can be taken as an explanation of the negative

activation volume found in [13] for RDX decomposition in THF, one of the most non-inert solvents.

HMX

The regularities of HMX decay are very similar to those observed at RDX decomposition (Fig. 2, Table 2). There are solvents increasing the decay rate, having the isotope effect and inhibiting influence of NO and *p*-DNB and there exist solvents decreasing the decay rate. HMX has close to RDX retardation effect of solvent depending on the cell effect. Its maximum value comprises 3. Acceleration is somewhat lower than RDX has. Thus, in glycerin the rate of RDX decay increases 11 times as compared to benzene, while that of HMX - 8 times. The activity row of aliphatic-aromatic solvents for RDX ends on triphenylmethane, while that for HMX - on diphenylmethane. This difference is explained by the

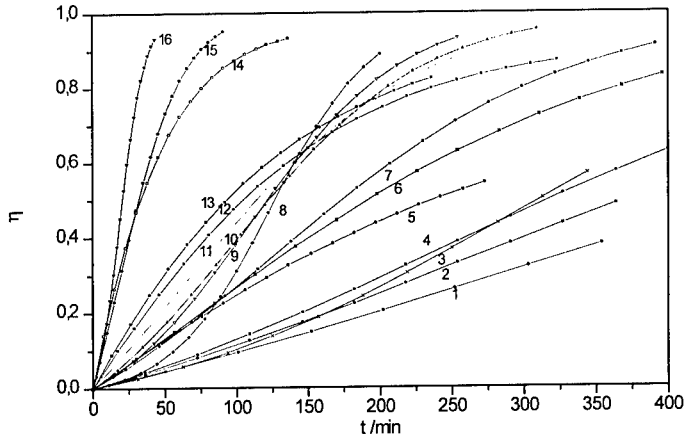

Fig 2. Thermal decomposition of HMX in solutions at 200°C. See curve numbers in Table 2.

Table 2. Effect of solvents on HMX thermal decomposition at 200°C

solvent	$k_1.10^4/s^{-1}$	$k_1/k_{benzene}$	Curve No.in Fig2
triphenylmethane	0.13	0.25	3

biphenyl	0.13	0.25	8
tert-butylbenzene	0.15	0.28	1
ionol	0.17	0.32	2
cumol	0.18	0.34	4
$PhCl_3$	0.36	0.68	7
biphenylmethane	0.39	0.74	9
nitrobenzene	0.43	0.81	6
TNT	0.49	0.92	5
benzene	**0.53**	**1.00**	10
toluene	0.60	1.13	11
triacetin	1.16	2.19	13
m-xylene	1.18	2.23	12
1,4-butanol	2.01	3.79	16
THF	2.27	4.28	15
glycerin	4.39	8.28	14

different structure of nitramine groups in RDX and HMX. N-O bond in planar groups of HMX is stronger than in pyramidal groups of RDX, this leads to a reaction rate decrease of (12).

DMNA

In case of DMNA (Fig. 3 and Table 3) only some solvents (e.g. cumol) increase decay rate as compared to the reaction in benzene. Retardation of decay is observed already in toluene. This is connected with violation of the forth and, virtually, the third conditions for chain developing.Nitrosodimethylamine is more stable than DMNA itself and, therefore, it is not an intermediate, but a final product. In the course of DMNA decay in accordance with the mechanism proposed in [12], unlike monomolecular decay of primary N-radicals for RDX and HMX, disappearance of primary N-radicals for DMNA takes place in the reaction with NO_2 to form a large quantity of nitrosomethane, which is a good inhibitor of chain processes.

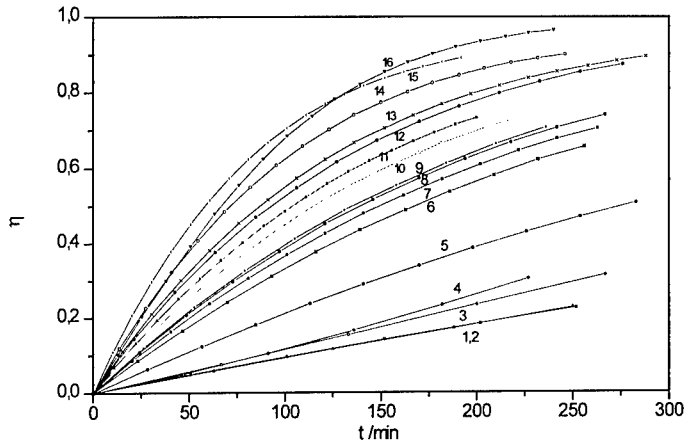

Fig 3. Thermal decomposition of DMNA in solutions at 230°C.
See curve numbers in Table 3.

Table 3 Effect of solvents and additives on DMNA decomposition at 230°C

solvent	$k_1.10^4/s^{-1}$	$k_1/k_{benzene}$	Curve No.in Fig3
glycerin	0.14	0.12	2
triacetin	0.14	0.12	4
1,4-butandiol	0.17	0.15	1
triphenylmethane	0.18	0.16	3
triethylene glycol	0.43	0.38	5
ionol	0.71	0.62	6
diphenylmethane	0.79	0.69	7
m-xylene	0.86	0.75	8
m-dinitrobenzene	0.88	0.77	9
toluene	0.90	0.79	10
benzene	**1.14**	**1.00**	11
m-xylene-d_{10}	1.27	1.11	12
$PhCl_6$	1.34	1.18	16
dipyenyl	1.36	1.19	13
acetic ester	1.68	1.47	14
cumol	2.06	1.81	15

CL-20

CL-20 is the closest analog of RDX in terms of nitramine groups structure and decay rate. But, unexpectedly, in solutions CL-20 behaves like DMNA, rather than RDX or HMX: in all solvents the rate is not higher, but lower than that in benzene (Fig. 4, tabl. 4). Similar to DMNA there is no isotope effect and inhibiting effect of NO and *p*-DNB. The absence of chain decay in this case can be explained by taking into account the third condition of occuring chain.reactions.It is known that at CL-20 decay a great deal (15 wt %) of condensed products, containing C=C, C=N, and C=O bonds, as well as nitroso and nitramine groups[14], are formed. Being dissolved in liquid phase these compounds can play the role of the traps for free radicals and prevent chain development. Maximum retardation effect of CL-20 decay in solutions coincides with that of RDX and comprises 3 times.

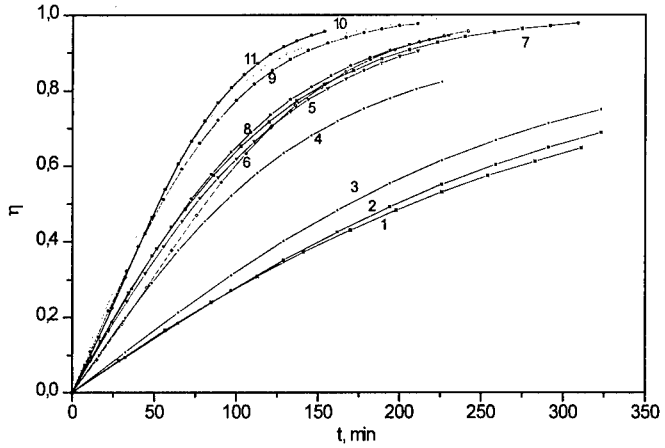

Fig 4 Thermal decomposition of CL-20 in solutions at 160°C
See curve numbers in Table 4.

Table 4. Thermal decomposition of CL-20 in solutions at 160°C

solvent	$k_1.10^4/s^{-1}$	$k_1/k_{benzene}$	Curve No.in Fig4
glycerin	0.57	0.37	1
Ph_3CH	0.63	0.40	2
Ph_3CH/ glycerin =0.1	0.76	0.49	3
m-xylene-d_{10}	1.38	0.88	4
p-xylene	1.34	0.86	5
Ph_3CH/ m-xylene	1.36	0.87	6
m-xylene	0.93	0.60	7
toluene	1.37	0.88	8
benzene	**1.57**	**1.00**	9

Conclusion

In this paper it has been shown that in case of some secondary nitramines including the most important of them, RDX and HMX, conditions are created in solutions for chain reactions to proceed. By means of chain mechanism all experimental facts about deocomposition of RDX and HMX described in literature, for examples, accleration of decomposition rate by some solvents, negative activation volume for decomposition of RDX in THF, intermediate formation of large quantities of N-nitrosoderivatives, can be explained.

Other studied nitramines (DMNA, CL-20) do not have chain reactions at their decomposition. Probability of the chain reactions depends on nitramine structure, mechanism of breakage of the primary N-radical and possibility of forming from it nitrosocompounds or other inhibitors of chain reactions. However, in all cases the first stage of decomposition is always dissociation of $N\text{-}NO_2$ bond.

Acknowledgment

This work has been performed under financial support of the Russian Foundation of Fundamental Research (Project No 98-03-33244)

References

1 Shu Yuanjie, Dubikhin V. V., Nazin G. M., Manelis G. B.; *30th Int. Ann.Conf. of ICT*, June 29-July 2, 1999, P59-1~59-13

2 Oxley J.C., Hiskey M., Naud D., Szekeres R., *J. Phys. Chem.* 1992, **96**, 2505-2509

3 Shaw R., Walker F. E., *J. Phys. Chem.* 1977, **81**, 2572-2576.

4 Melius C. F., Binkley J. S., *23rd JANNAF Combustion Meeting* . V. **I**, 1986, 241-248.

5 Harris N. J., Lammertsma K., *J. Phys. Chem. A.* 997, **101**, 1370-1373.

6 Oxley J. C., Kooh A. B., Szekeres R., Zheng W., *J. Phys. Chem.* 1994, **98**, 7004-7008.

7 Trulove P. C., Champman R. D., Shackelford S. T., *Propellants, Explos., Pyrotech.*, 1994, **19**. 42-58.

8 Schroeder M.A.,*18th JANNAF Combustion Meeting,*V. **I**, 1981, 395- 413.

9 Boggs T. L., *Progress in Astronautics and Aeronautics, V.90: Fundamentals of Solid-Propllent Combustion. Ed. by Kuo K., Summerfied M.,* New York, 1984, 121-175.

10. Morgan C. U., and Beyer R. A.,*Comb. and .Flame*, 1979, **36**, 99-101.

11. Charskii V. V., Pavlov A. N., Nazin G. M., and all. *Russ. Chem. Bull.* 1989, **38**, 794-797

12. Ling Yue, Tang Zehua, Xiao Heming, *Proc. 17th Int. Pyrotech. Semi-nar combined with the 2nd Beijing Int. Symp.on Pyrotech. and Explosives*. V.**I**, 1991, 466-472.

13. Wang J., Brower K.R., *J.Org.Chem.* 1997, **62**, 9055-9060.

14. Korsounskii B., Nedelko V., Chukanov N., et al., *30th Int. Ann. Conf. of ICT,* June 29-July 2, 1999, P64-1~64-20..

PROPERTIES OF HYDRAZINIUM NITROFORMATE (HNF)

van Zelst, Michel; van der Heijden, Antoine E. D. M.

TNO-Prins Maurits Laboratory, Researchgroup Pyrotechnics and Energetic Materials (PE), P.O. Box 45, 2280 AA Rijswijk, The Netherlands

ABSTRACT

Several methods of analysis and testing have been performed on a promising high-performance oxidiser, hydrazinium nitroformate (HNF), which characterise the material. These tests include the friction and impact sensitivity, density, differential scanning calorimetry (DSC), thermo gravimetric / differential thermal analysis (TG/DTA), vacuum stability test (VST) and the determination of hygroscopicity.

Currently, in particular due to the relatively low value for the friction sensitivity, HNF is transported in special containers. In order to avoid the use of these containers, methods to phlegmatize HNF, with the objective to improve the hazard properties of the material, have been investigated. One of these methods is highlighted in this paper.

1. INTRODUCTION

A number of commonly used tests and methods of analysis have been applied to hydrazinium nitroformate ($[N_2H_5^+][C(NO_2)_3^-]$; HNF). HNF is an oxidiser that is very promising for application in high performance solid rocket propellants. It performs better than classic oxidisers like ammonium perchlorate (AP). Furthermore it contains no chlorine, which implies an improved signature and on the other hand this is a good aspect for the environment (no exhaust of hydrochloric acid). For some time now TNO-PML has been studying HNF [3, 9].

Among the properties that have been determined are: the sensitivity to impact and friction, melting point and decomposition temperature from DSC, mass decrease from thermogravimetry (TG), the vacuum stability and hygroscopicity.

The friction sensitivity of HNF must be decreased to pass the criteria for transportation according to the UN guidelines as a material without packaging [1][†]. One way to achieve this is to phlegmatise the energetic material. Several of such methods of desensitization have been investigated for HNF and some of the results will be discussed here.

The analysis were performed on HNF-C and HNF-E grade, whereas the phlegmatising experiments were performed on batch HNF-S grade produced by Aerospace Propulsion Products (APP) in the Netherlands [7].

2. FRICTION AND IMPACT SENSITIVITY TESTING

The impact and friction sensitivity tests were determined according to the UN ST/SG/AC.10/11 directive [1] (BAM standard, see for description for instance [2]). For the impact sensitivity test ~ 40 mm^3 and for the friction sensitivity test ~ 10 mm^3 test material is required.

The results of the sensitivity testing are presented in Table 1.

Table 1: Sensitivity data of HNF-C9.

Property	Value
BAM Impact energy (J)	3
BAM Friction load (N)	16

The friction and impact sensitivity are in a range generally found for HNF batches (friction 12-36 N; impact 2-5 J). The hazard properties are discussed again in section 8 of this paper.

[†] At this moment HNF can be transported up to 333 g as a 1.4 S material in special 'Explosafe' containers from DGM (Dangerous Goods Management).

3. DENSITY

For the Helium pycnometry the volume of the samples was measured with a Micromeritics helium pycnometer. Prior to measuring, the apparatus was calibrated with a calibration standard of a known volume. The density was then calculated. The liquid used for the Liquid pycnometry (at 25 °C) was dodecane.

The results shown in Table 2.3.1 are mean values of two tests.

Table 2: Density (g/cm^3) of two HNF batches, measured with liquid and helium pycnometer.

Batch	Helium	Liquid
HNF-C9	1.87	1.869
HNF-E8	1.83	1.846

Generally TNO considers density measurements by means of liquid pycnometry to be more accurate than those with helium pycnometry. The difference between the density of HNF-C9 and HNF-E8 is relatively large. This might be because HNF-E8 is more porous. The density of HNF has been determined to be 1.872 g/cm^3 by X-ray diffraction [5].

4. DIFFERENTIAL SCANNING CALORIMETRY (DSC)

The DSC traces were measured with a Seiko DSC-220-C-U and the experimental conditions were as follows:

Temperature range	: 25 - 250°C
Heating rate	: 10 °C/min
Atmosphere	: Nitrogen
Flow-rate	: 50 ml/min
Cups used for the sample	: open aluminum cup
Reference cup	: empty aluminum cup

All tests were performed in duplicate. The properties from the DSC (onset of melting, exothermal onset) were determined at the intercept of the extrapolated tangents.

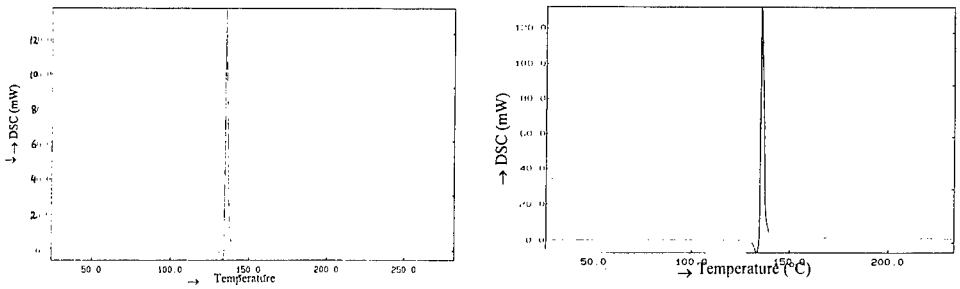

Figure 1: DSC traces of HNF-C9 (left) and HNF-E8 (right).

The difference between the DSC traces of HNF-C9 and E8 is small. Both batches show a clear endothermal peak (melting, see TG/DTA) just before the large exothermal peak appears (decomposition, see TG/DTA). The DSC results are listed in Table 3. Older HNF batches normally did not show this endothermal effect but only an exothermal effect related to decomposition. Apparently the production process of HNF has been improved resulting in a product with a higher purity. Compared to earlier measurements [9] also the onset of decomposition has shifted from a range of 110-124 °C to a temperature of about 134 °C. This could also point to a higher purity of the currently produced HNF grades. However, impurities within a pure material can have the effect of either raising or lowering the apparent peak temperature of a decomposition event (e.g. in an analogous manner to burning rate catalysts sharpening a decomposition profile) [8].

Table 3: Results of DSC measurements.

Sample	Onset of melting (°C)	Onset of decomposition (°C)
HNF-C9	131.0	134.3
HNF-C9	131.0	134.2
HNF-E8	130.8	134.2
HNF-E8	130.7	134.4

5. THERMO GRAVIMETRIC / DIFFERENTIAL THERMAL ANALYSIS (TG/DTA)

The TG/DTA scans were measured with a Seiko TG/DTA-320. The conditions under which the TG/DTA experiments were performed are:

Heating rate	: 10 °C/min
Atmosphere	: Nitrogen
Temperature range	: 25 - 250°C
Nitrogen flow rate	: 50 ml/min
Sample cups	: open aluminum cup
Reference	: empty aluminum cup

The results of the measurements are represented in Figure 2.

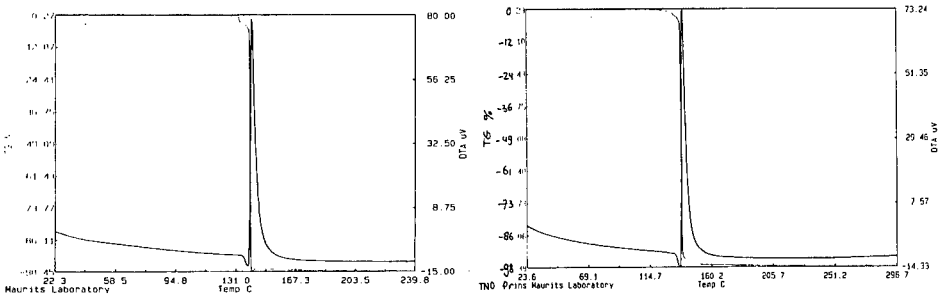

Figure 2: TG plots of HNF-C9 (left) and HNF-E8 (right) at a heating rate of 10 °C/min.

The properties deduced from the measurements are listed in Table 4. The onset of melting was determined from the DTA signal, the decomposition temperature and total mass loss from the TG signal.

Table 4: Results from TG/DTA measurements at a heating rate of 10 °C/min.

	Onset of melting (°C)	Total mass decrease (wt%)	Decomposition (°C)
HNF-C9	131	98.3	134.5
	131	97.9	134.6
HNF-E8	132	97.4	135.7
	131	97.5	134.5

The melting point of HNF is in good order with the DSC data in chapter 4. In general a DSC measurement is more accurate for determining the melting point.

6. VACUUM STABILITY TEST (VST)

For the VST test a sealed and evacuated test tube containing the sample was immersed in a thermostat bath at a temperature of 70 °C during 48 hours. The pressure change in the tube was measured with a Hg column. All samples were tested in duplicate.

The results are summarized in Table 5. From the results it is clear that the amount of gas evolved from the C grade is roughly half that from the C grade.

Table 5: Results of the thermal stability tests (48 hrs @ 70 °C).

Sample	Temperature (°C)	Evolved gas after 48 hours (ml/g)
HNF-E8	70	0.92
		0.93
HNF-C9	70	0.57
		0.59

The TG, DSC and VST measurements provide, among others, information about the thermal stability of HNF. The thermal stability of HNF requires further attention for applications where stability at elevated

temperature is needed. Conventional oxidisers and other well-known energetic materials, like RDX and HMX, are more stable than HNF. However, taking into account an activation energy of ~180kJ/mole calculated by Koroban [4] (reproduced by TNO and APP) HNF is expected not to decompose in significant amounts for hundreds of years at room temperature.

7. HYGROSCOPICITY

To measure the hygroscopic point, a saturated solution of HNF in water was prepared and put in an air tight glass container equipped with a hygrometer (dessicator). The relative humidity (R.H.) could be measured continuously without opening the sealed tube. In this way, the resulting "steady state" R.H. above the saturated solution could be measured, which equals the hygroscopic point of the sample. The hygroscopic point of HNF was found to be 94 %. Which is low in comparison with, for instance, ammonium nitrate which has a hygroscopic point of 62% [6].

Additionally the moisture uptake of HNF was measured at two different relative humidities (R.H. = 20% and R.H. = 65 ± 3%). A sample exposed to both R.H.'s was weighed at regular time intervals. No moisture uptake for HNF could be measured at both R.H.'s. This is in agreement with the hygroscopic point of 94 %., which implies that HNF only starts taking up moisture above a R.H. of 94 %.

8. PHLEGMATIZATION

The phlegmatization experiments have been performed on HNF from batch S8/S9, produced by APP. The mean size of these crystals is ~ 90 µm. Phlegmatization of HNF by means of the addition of a non-solvent (like e.g. RDX/water) is the most obvious method to desensitize an energetic material. Although many different non-solvents were tested, none of them led to a (sufficient) improvement of – in particular – the friction sensitivity. Additional experiments using paraffin wax resulted more promising results.

The deposition of the paraffin wax onto the HNF particles was performed as follows: molten paraffin wax (melting range 54 – 57 °C) was dissolved drop by drop in a mildly stirred slurry of HNF particles in hexane (a non-solvent for HNF) at 60 °C. The slurry/solution was cooled down to room temperature, during which the paraffin wax slowly precipitated. After sedimentation of the HNF particles the hexane is turbid. By evaporation of the hexane, using high-pressure air to shorten the evaporation time, the remaining paraffin wax could precipitate. In this way the total amount of wax added in the beginning is applied to the HNF particles. Afterwards, the sample was further dried for one night at 20 °C and reduced pressure. By changing the relative amounts of materials, different HNF/paraffin wax ratio's can be prepared.

Two different compositions were prepared: 90.2/9.8 and 80.0/20.0 wt% HNF/paraffin wax. The results of the friction measurements to the phlegmatized HNF are summarized in Table 6. The friction sensitivity of both of these samples was found to be increased to a value of 60 N.

Table 6: Compilation of the impact and friction results on unphlegmatized and phlegmatized HNF samples.

Composition	Ratio HNF:phlegmatizer (wt%)	Friction sensitivity (N)
pure HNF S8/S9	-	36
phlegmatized HNF	90.2/9.8	60
phlegmatized HNF	80.0/20.0	60

The UN3 criteria and the corresponding values for pure HNF are listed in Table 7.

Table 7: UN3 test criteria for the impact and friction sensitivity and the thermal stability of an energetic substance [1].

UN3 test series	Criterion	Unphlegmatized HNF
Impact sensitivity	> 2 J	2 – 3 [3]
Friction sensitivity	> 80 N	18 – 20 [3]
Thermal stability (UN3(c) test)	A sample of 100 g stored at 75 °C for 48 hrs. should not exceed a temperature difference of 3 °C compared to the same quantity of a reference substance	Passed

The VST value (48 hours at 60 °C) of the 80 wt% HNF sample was 0.55 ml/g. The VST test value of the pure, untreated, material is 1.03 ml/g, whereas a value of 0.3 ml/g is more common for other HNF grades. It might be so that the treatment of HNF to phlegmatize it caused the evaporation of the small fraction of processing liquids that is present in the pure material. This could have resulted in less gas evolution from phlegmatized HNF compared to the pure untreated S8/S9 batch. Also, it could be so that the wax coating prevents some gas evolution. Furthermore it can be noted that compatibility tests have shown that HNF and the paraffin wax are compatible.

The "coating" of the HNF particles by the paraffin wax turned out not very good. The photographs in Figure 3 illustrate this.

Generally the HNF particles are stuck into a chunk of wax, see Figure 3. The high content wax sample simply shows more paraffin, but the presence of this higher amount of wax does not improve the "coating" of the individual HNF particles. The bad coating properties of this paraffin wax are due to the apolar nature of waxes in general, which apparently only have a very limited interaction with the polar HNF crystal surfaces. Another complicating factor is the needle shape of HNF. A homogenous coating of every HNF particle is possibly required if the contact between individual HNF crystals has to be prevented to drastically improve sensitivity characteristics.

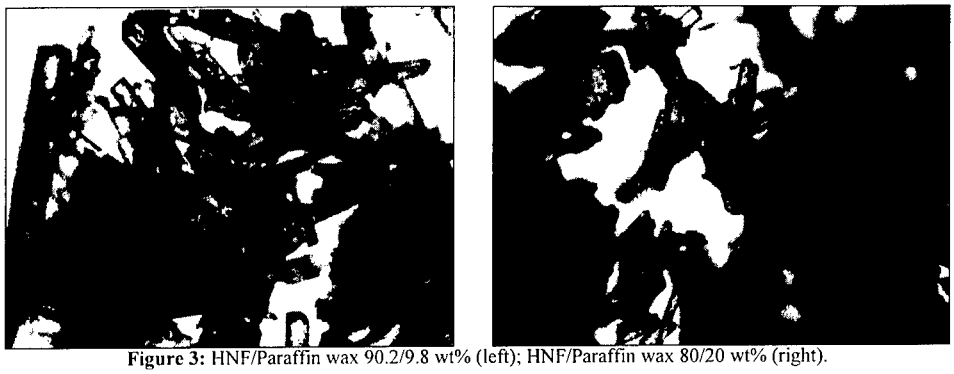

Figure 3: HNF/Paraffin wax 90.2/9.8 wt% (left); HNF/Paraffin wax 80/20 wt% (right).

Furthermore the recovery of the original HNF from the phlegmatized sample proved to be rather difficult. Therefore, this method was not further optimized and scaled up to be used as a means to transport HNF as a 1.1 D material. Research on HNF phlegmatization is still ongoing at the moment.

9. CONCLUSIONS

Two HNF grades produced by different recrystallization techniques have been characterized with respect to their thermal, physical and hazard properties. Compared to older batches of HNF, its stability has been improved as becomes clear from the thermal stability analyses. Furthermore, measurementshave shown that HNF is not hygroscopic. Finally it can be concluded that the addition of paraffin wax has significantly decreased the friction sensitivity of HNF compared to the pure material, however not enough to pass the UN criterion of 80 N and other, more promising, solutions are under investigation.

10. ACKNOWLEDGEMENTS

The authors acknowledge the Dutch Ministry of Defense and the European Space Agency (ESA) for financial support of this work.

11. REFERENCES

[1] *Recommendations on the Transport of Dangerous Goods, Tests and Criteria*, third edition, 1995, United Nations, New York, UN test series 3

[2] Köhler, J. and Meyer, R., *Explosivstöffe*, Wiley-VCH, 9th ed. (1998).

[3] H.F.R. Schöyer, A.J. Schnorhk, P.A.O.G. Korting, P.J. van Lit, J.M. Mul, G.M.H.J.L. Gadiot and J.J.

Meulenbrugge, *Development of hydrazinium nitroformate based solid propellants*, Joint Propulsion Conference and Exhibit, 10 – 12 July 1995, San Diego, CA, USA (AIAA 95-2864).

[4] Koroban, V.A. et al.; *Kinetics and mechanism of the thermal decomposition of hydrazine trinitromethane;* Tr. Mosk. Khim. Tekhnol. Inst. im D.I. Mendekeva, **104;** p.38-44 (1979).

[5] Dickens, B., J. Res. Nat. Bureau stds., 74A: 309-318 (1970).

[6] Weast, R.C., *"Handbook of Chemistry and physics 59th ed."*, CRC Press Inc. (1978).

[7] Zee F.W.M., *"Method of preparing Hydrazine Nitroformate"*, WO 9410104, 1998

[8] Wagstaff, D., Personal communication (April 2000).

[9] Hordijk, A.C. et al., *Properties of hydrazinium nitroformate; a 'new' oxidizer for high performance solid propellants*, paper for the 25th annual conference of ICT, Karlsruhe, Germany (1994).

COMPARATIVE INVESTIGATION OF THERMAL DECOMPOSITION OF VARIOUS MODIFICATIONS OF HEXANITROHEXAAZAISOWURTZITANE

V. V. Nedelko, N. V. Chukanov, B. L. Korsounskii, T. S. Larikova

Institute of Problems of Chemical Physics,
Russian Academy of Sciences
142432 Chernogolovka, Moscow Region, Russia

F. Volk

Fraunhofer-Institute of Chemical Technology (ICT), D-76327 Pfinztal-Berghausen, Germany

Summary

The thermal decomposition of α-, γ- and ε-hexanitrohexaazaisowurtzitane (HNIW) has been investigated by manometric, thermogravimetric, IR-spectroscopic and microscopic methods. Kinetic parameters of the reactions have been determined in terms of the first-order autocatalysis equation. α-Form of HNIW has lowered thermal stability as compared with γ- and ε-forms. The complete thermal phase transitions of α- and ε-polymorphs into γ-HNIW occur already at low decomposition conversions (up to 1%), thus the observed difference in the kinetic behaviour should be explained by physical reasons (such as morphology, particle size, concentration of defects

in the crystals of the decomposing γ-HNIW) and/or by the kinetics of the phase transitions $\alpha \rightarrow \gamma$ and $\varepsilon \rightarrow \gamma$.

Introduction

Hexanitrohexaazaisowurtzitane (HNIW) can exist in various crystal modifications [1]. The thermal decomposition of this substance has been investigated more than once [2-5]. ε-HNIW, the most attractive polymorph for practical use, has been studied widely. Only in one paper we have found the data on β-HNIW [2]. The crystal structure can affect the reactivity and the thermal stability of the substance essentially; in particular such influence was observed for HMX [6]. The present work is devoted to the comparative investigation of the thermal decomposition kinetics of α-, γ- and ε-forms of HNIW.

Experimental

α- and ε-HNIW from Thiocol Corporation (Birgham City, USA) were used in our experiments. γ-HNIW has been obtained by heating of ε-HNIW, as it is known [7] that the thermal phase transition $\varepsilon \rightarrow \gamma$ occurs easily. The sample of ε-HNIW was heated up in an atmosphere of dry pure argon up to 162^0C and was kept at this temperature for 4 hours with simultaneous weight fixing. In these conditions the weight loss of the sample has not exceeded 0,5%.

Kinetics of the thermal decomposition was studied with the use of automatic electronic thermobalance ATV-14M, admitting the measurements as under non-isothermal (programmed heating), and under isothermal conditions. For IR-spectral measurements we used spectrophotometer Specord-75-IR. The spectra of α-, γ- and ε-HNIW samples to be studied were identical to those described in the literature [3,8]. The microscopic observations were carried out on optical microscope MBI-15-2.

Results and Discussion

Under linear heating (heating rate was $2,4^0$C/min) the noticeable thermal decomposition rates of α-HNIW were observed at temperatures above 170^0C, and at 216^0C the substance ignited. The intensive γ- and ε-HNIW decompositions were observed at higher temperatures, and the ignitions occur at 226 and 230^0C, respectively. The data of non-isothermal kinetics demonstrate that the thermal stability of HNIW polymorphs decreases in order $\varepsilon > \gamma > \alpha$.

Even more evident distinctions in decomposition kinetics of HNIW polymorphs were revealed under isothermal conditions. The appropriate data are submitted in a Fig. 1. The kinetic curves are described by the equation for first-order autocatalysis:

$$d\eta/dt = k_1(1 - \eta) + k_2\eta(1 - \eta) \quad (1),$$

where η is the reaction conversion (in gravimetric experiments it is the relation of the weight loss of the sample at time of reaction t to total weight loss), k_1 and k_2 are the rate constants of non-catalytic and catalytic processes,

respectively. In Tables 1 and 2 the activation parameters of the reactions and the rate constants values at 180^0C are presented, and in Figures 2 and 3 the temperature dependences of the rate constants are submitted.

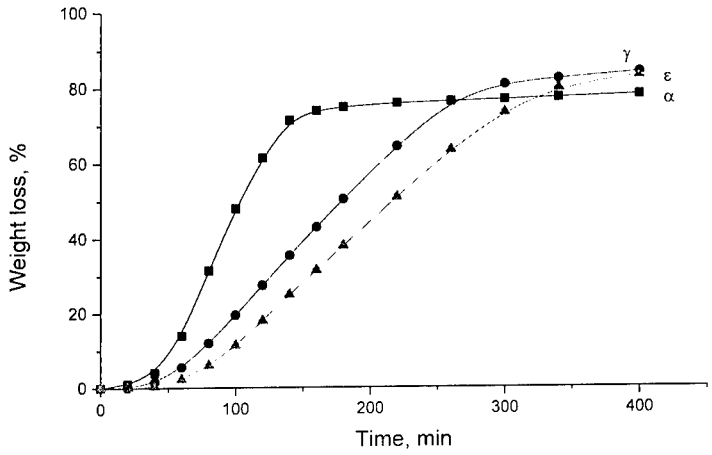

Figure 1. Kinetics of thermal decomposition of various HNIW modifications on air at 194^0C.

From the data obtained it is clear that α-HNIW has the least thermal stability among the investigated HNIW polymorphs. Under non-isothermal conditions α-HNIW ignites at lower temperatures than other HNIW modifications. In isothermal experiments we did not succeed to carry out α-HNIW decomposition at the temperatures above 200^0C. The ε-HNIW sample (10 mg) ignites at 204^0C with the ignition delay 6.5 minutes.

Table 1

Kinetic parameters of non-catalytic stage (k_1) of thermal decomposition of various HNIW modifications

Polymorph	Temperature range, ^{0}C	Kinetic parameters			
		E, kcal/mol	A, s^{-1}	r	k^{180}, s^{-1}
α	166 - 194	35,6 ± 2,6	$10^{11.9\pm1.3}$	0,992	$5{,}3\cdot10^{-6}$
γ	172 - 194	46,7 ± 3,4	$10^{17.7\pm1.6}$	0,995	$1{,}5\cdot10^{-5}$
ε	192 - 211	53,1 ± 1,4	$10^{20.3\pm0.7}$	0,998	$4{,}8\cdot10^{-6}$

Table 2

Kinetic parameters of catalytic stage (k_2) of thermal decomposition of various HNIW modifications

Polymorph	Temperature range, ^{0}C	Kinetic parameters			
		E, kcal/mol	A, s^{-1}	r	k^{180}, s^{-1}
α	166 - 194	55,4 ± 1,9	$10^{23.0\pm0.9}$	0,998	$1{,}9\cdot10^{-4}$
γ	172 - 194	49,4 ± 1,7	$10^{19.6\pm0.8}$	0,998	$5{,}8\cdot10^{-5}$
ε	192 - 211	45,3 ± 2,6	$10^{17.6\pm1.2}$	0,992	$5{,}5\cdot10^{-5}$

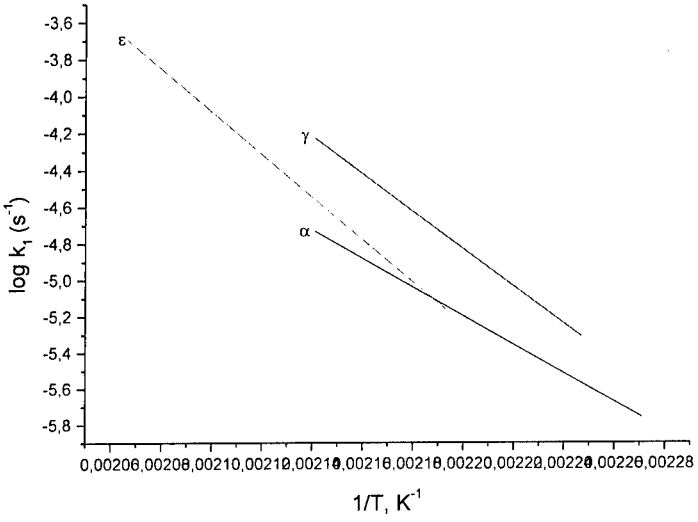

Figure 2. The temperature dependence of the rate constants for non-catalytic stage (k_1) of the thermal decomposition of various HNIW modifications

As it is known [7] the thermal phase transitions in HNIW occur easily. The phase transformations are realized during HNIW thermal decomposition [3,5]. Our IR spectroscopic data show that complete phase transitions into γ-modification takes place already on 1% decomposition of α- and ε-HNIW. Thus, all three kinetic curves shown in a Fig. 1 in fact are related to γ-HNIW decomposition. The different thermal stabilities of α-, γ- and ε-modifications could be caused by different physical characteristics of reacting γ-phase (morphology, particle size, concentration of the defects etc) due to differences in the mechanisms of γ-phase formation.

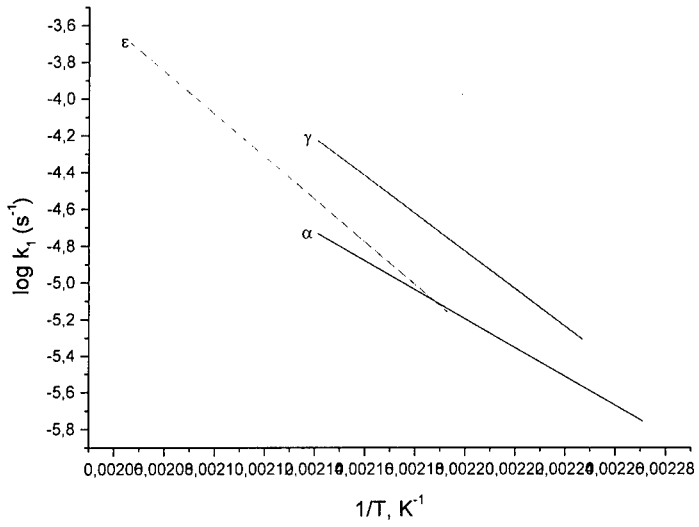

Figure 3. The temperature dependence of the rate constants for catalytic stage (k_2) of the thermal decomposition of various HNIW modifications

According to microscopic observations, in the course of ε → γ transition destruction of ε-HNIW crystals and formation of highly disperse particles of γ-HNIW takes place. In addition, ε → γ transition is accompanied by loss of trace amounts of water (< 0.1 wt %). Pseudomorphs of γ-HNIW after ε-HNIW bear signs of cracking. All these processes can activate substance and supply a smaller thermal stability in comparison with initial ε-HNIW. Certainly, ε-HNIW decomposition is accompanied by phase transition ε → γ. Probably we must take into account the role of the transition time and coexistence of γ-form with the more kinetically stable ε-form at initial stage of ε-HNIW decomposition.

In the previous work devoted to the thermal decomposition of ε-HNIW [5] it was marked that the reaction proceeds topochemically. Therefore the activation parameters of the process can not be related to reactivity of nitramine group. From results mentioned above it is clear that γ-HNIW display a similar behaviour. As to α-form, the activation parameters of non-catalytic reaction with k_1 are close to those, observed at homogeneous decomposition of nitramines [9]. Therefore it is possible that α-HNIW decomposes homogeneously at the earleast stages because of the presence of water in the crystal. However this conclusion should be considered extremely as presumable, because the rate constants k_1 are determined with low accuracy. Really, the analysis of the equation (1) shows, that already at 1% of decomposition of α-HNIW at 180^0C the contribution of catalytic reaction into total rate of the process achieves 26%. It is clear, that this fact can be appreciably affect the accuracy of of k_1 value determination.

References

1. T. P. Russell, P. J. Miller, G. J. Piermarini, S. Block. Pressure/Temperature Phase Diagram of Hexanitrohexaazaisowurtzitane. J. Phys. Chem., 1993, **97**, N 9, 1993 - 1997.
2. D. G. Patil, T. B. Brill. Thermal Decomposition of Energetic Materials, 53. Kinetics and Mechanism of Thermolysis of Hexanitrohexaazaisowurtzitane. Comb. and Flame, 1991, **87**, N 2, 145 - 151.

3. S. Löbbecke, M. A. Bohn, A. Pfeil, H. Krause. Thermal Behavior and Stability of HNIW (CL 20). 29th Int. Annual Conf. of ICT, Karlsruhe, 1998, p. 145-1 - 145-15.
4. J. C. Oxley, A. B. Kooh, R. Szekeres, W. Zheng. Mechanisms of Nitramine Thermolysis. J. Phys. Chem., 1994, **98**, N 28, 7004 - 7008.
5. B. Korsounskii, V. Nedelko, N. Chukanov, T. Larikova. Kinetics of Thermal Decomposition of Hexanitrohexaazaisowurtzitane. 30th Int. Annual Conf. of ICT, Karlsruhe, 1999, p. 64-1 - 64-20.
6. Yu. M. Burov, G. B. Manelis, G. M. Nazin. Thermal Decomposition of 1,3,5,7-tetranitro-1,3,5,7-tetraazacyclooctane in a solid state. Khimicheskaya Fizika, 1985, **4**, № 7, 956 – 962 (in russian).
7. M. F. Foltz, C. L. Coon, F. Garcia, A. L. Nichols III. The Thermal Stability of the Polymorphs of Hexanitrohexaazaisowurtzitane, Part II. Propel., Explosives, Pyrotechn., 1994, **19**, 133 - 144.
8. T. P. Russell, P. J. Miller, G. J. Piermarini, S. Block. High-Pressure Phase Transition in γ-Hexanitrohexaazaisowurtzitane. J. Phys. Chem., 1992, **96**, N 13, 5509 - 5512.
9. G. B. Manelis, G. M. Nazin, Yu. I. Rubtsov, V. A. Strunin. Thermal Decomposition and Combustion of Explosives and Powders. M.: "Nauka", 1996. 223 p. (in russian).

SYNTHESIS AND PROPERTIES OF TNAZ

Schmid Konrad, Kaschmieder Doris

Fraunhofer Institut Chemische Technologie ICT
Joseph-von-Fraunhofer-Straße 7
D-76327 Pfinztal (Berghausen)

Phone: +49(0)721 / 4640-414
Telefax: +49(0)721 / 4640-111

Abstract:

TNAZ, a new, powerful and steam castable strained ring explosive has been synthesised and fully characterized at the ICT.
Since **1997** the research is focused on the synthesis of **TNAZ** in order to enable independent investigations and to prove computational predictions.

1. Introduction

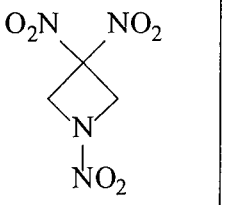

TNAZ

TNAZ (1,3,3-Trinitro-azetidine) was synthesized for the first time in **1984** and became one of the most promising energetic material in the **1990's**. More than fifty publications in recent years concerning to the synthesis and, in an increasing number to the applications elucidate the world-wide interest in this new heterocyclic system.

Due to the combination of strain energy and chemical energy **TNAZ** exhibits unusual and potential valuable properties for applications as castable explosive as well as plasticizer.

	TNAZ	Cl20	HMX	RDX	TNT
density [g/cm^3]	1,84	2,04	1,96	1,82	1,64
mp. [°C]	101	247	>240	204	80,8
decomp. (onset) [°C]	>240	ab 213	>240	204	300
heat of formation [kJ/kg]	280	1049	353	416	185
heat of explosion [kJ/kg]	1900	2200	5711	5757	3335
O_2-balance [%]	- 16,7	- 10,9	- 21,6	-21,6	- 73,5

TABLE 1: ***Comparison of energetic materials***

Computational prediction for **TNAZ** as 'high-energy-TNT-replacement' in composition B shows an 20% increase of the gurney energy. Admixtures with TNT enables to attain any aimed performances by a 'single explosive'.

As ingredient in solid rocket propellants and gun propellants **TNAZ** is supposed to be on the level of the well known CL20.

2. Synthesis

At the ICT since **1997** the research is focused on the synthesis of **TNAZ** in order to enable independent investigations.

In the moment about 7 different synthetic routes are published, from which we selected a 5-step way, original developed by HISKEY [1] [2].
After modifying and optimization in the ICT labs we are now able to produce **TNAZ** in the maximum laboratory scale (**SCHEME 1**)

The synthesis starts with cheap and commercial available materials to form the oxazine **1**. The following ring opening to the γ-aminoalcohol **2** is carried out with conc. HCl in methanol under reflux conditions and subsequent purification by reprecipitation.
The cyclization to the azetidine **3** by the use of DIAD and PPh_3 [Mitsunobu - reagent [3]] incure about 50% of the total chemical costs, which can be reduced by oxidative recycling of DIAD*2H.
Kornblum nitration leads to the dinitro-azetidine, isolated from the reaction mixture after extraction as pure HNO_3-salt **4**.
The finishing step to **TNAZ** utilize the well known procedure for the generating of nitramines from alkylamines in acetic anhydrid at ambient temperature.

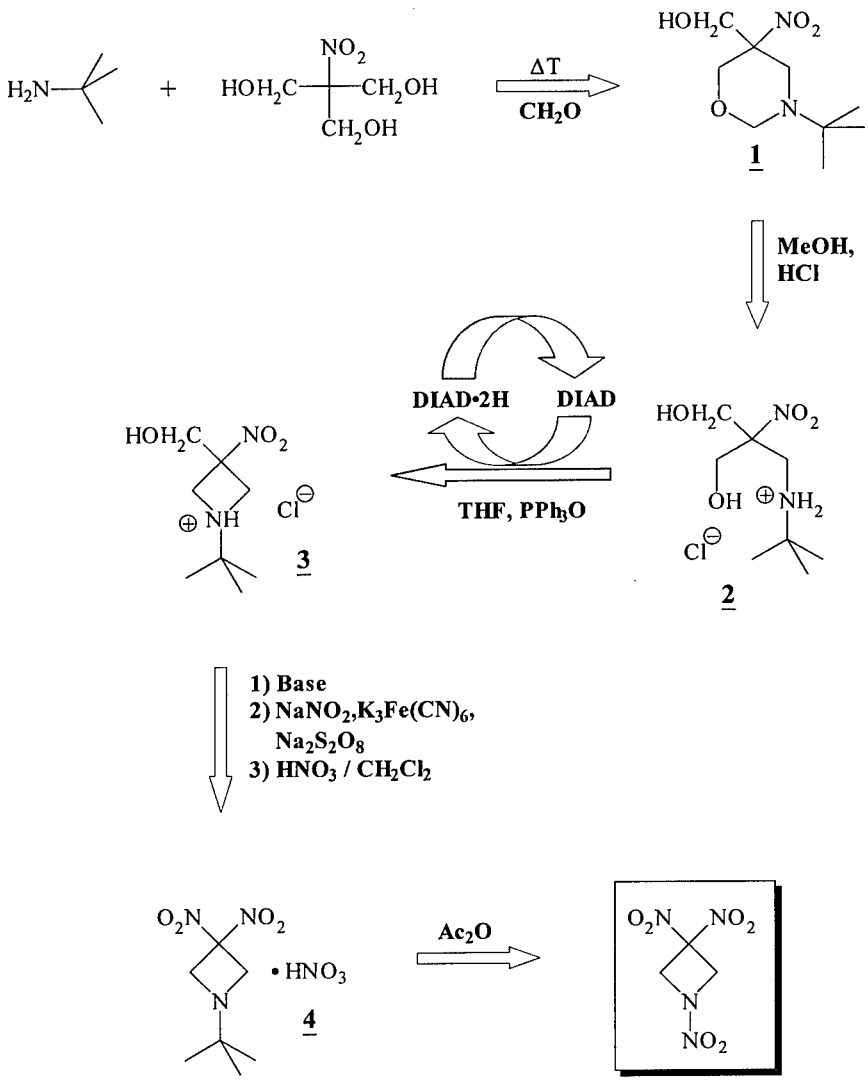

SCHEME 1: *TNAZ-synthesis at the ICT*

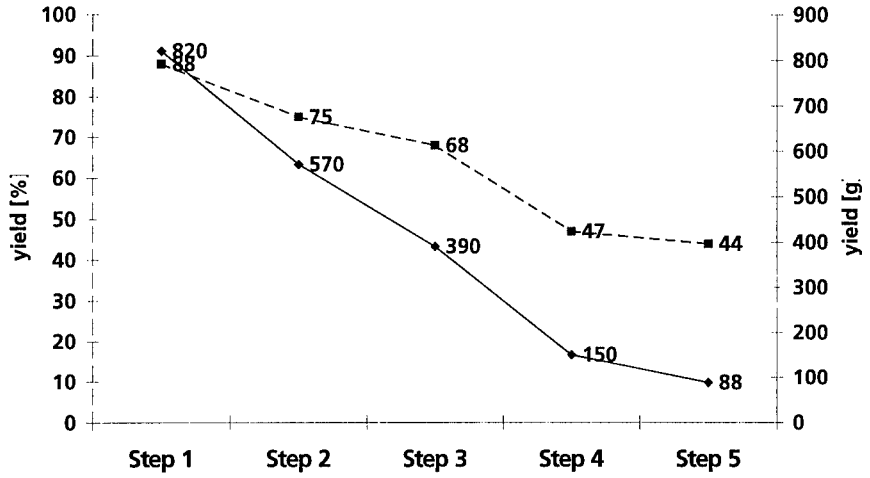

SCHEME 2: *yields of the TNAZ synthesis in laboratory scale*

The overall yield (5 steps) is reproducable in the range of 15-20%. At present about 200 g **TNAZ** per month can be produced, the caused total chemical costs run up to about 5$ per gram.

3. Properties

IR-spectroscopy (FIGURE 1)

TNAZ's high symmetry cauces a decrease of signals in the fingerprint area. Both the expected aliphatic C-H and the N-O / NO_2 vibrations can be clearly identified.

The position of the weak C-H signals over 3000 cm^{-1} is the clue for a high ring tension of this heterocyclic system.

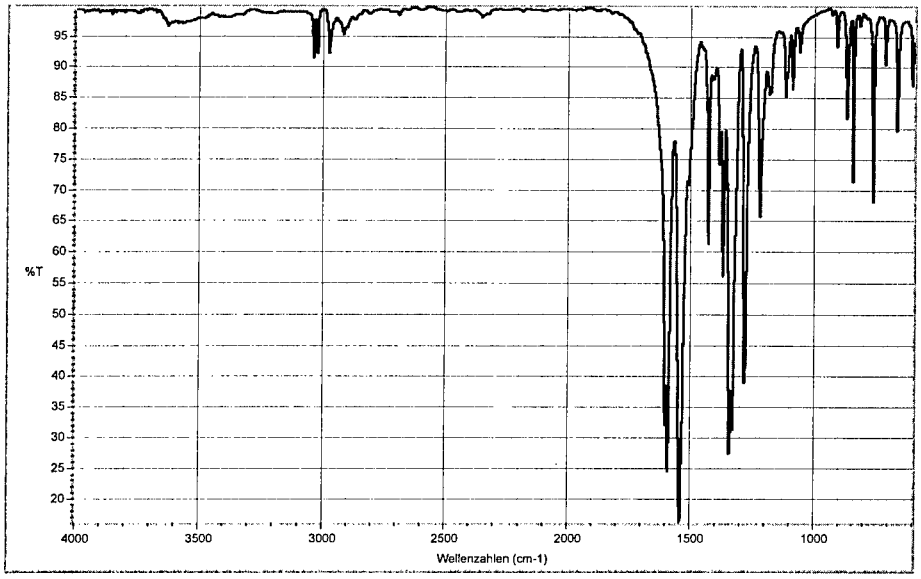

FIGURE 1: ***IR-spectrum [KBr]***

NMR-spectroscopy

The chemical and magnetic equivalent ring protons occure as singlet at δ= 5.30 ppm (**FIGURE 2**)

The secondary ring-carbon atoms show also a single resonance at δ=63.5 ppm. A typical weak signal can be found for the quarternary carbon at δ= 104 ppm (**FIGURE 3**)

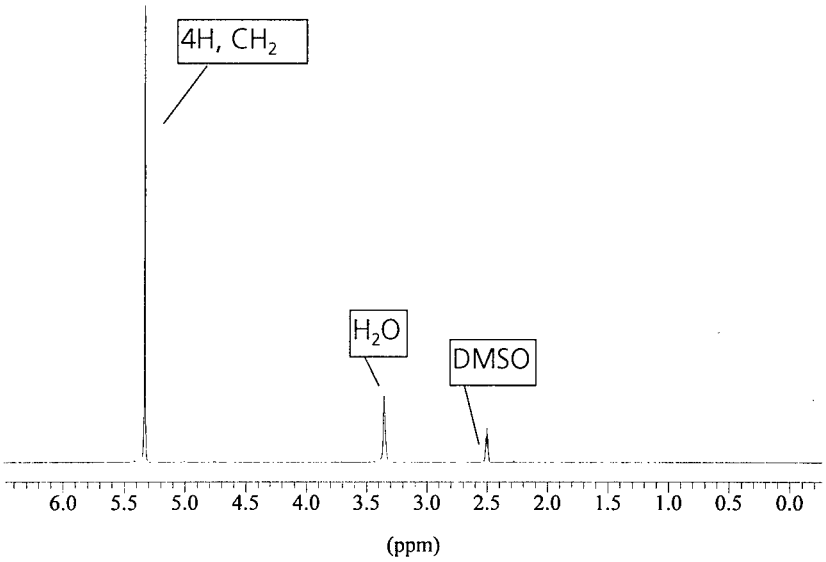

FIGURE 2: ***^{1}H-NMR (DMSO-d6, 250 MHz)***

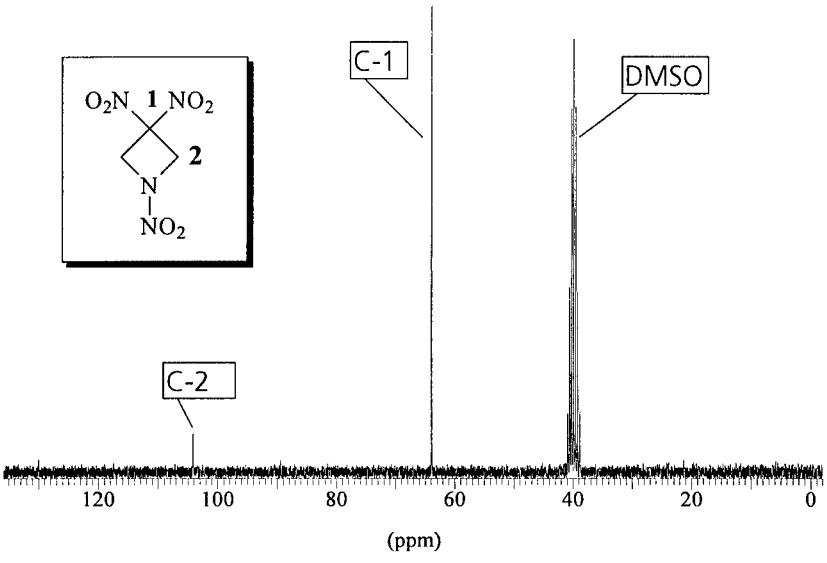

FIGURE 3: ***^{13}C-NMR (DMSO-d6, 69 MHz)***

Differential Scanning Calorimetry

This analysis confirmes the thermal stability of **TNAZ** in a wide temperature range. The conspicuous features in the thermogram (**FIGURE 3**) are the melting endotherm at 100°C and the decomposition exotherm at about 250°C.

Using sample pans with pierced lieds the results differ dramatically (**FIGURE 4**).

The absence of any exothermic peak is explicable by the sublimation of **TNAZ** at temperatures close to the melting point.

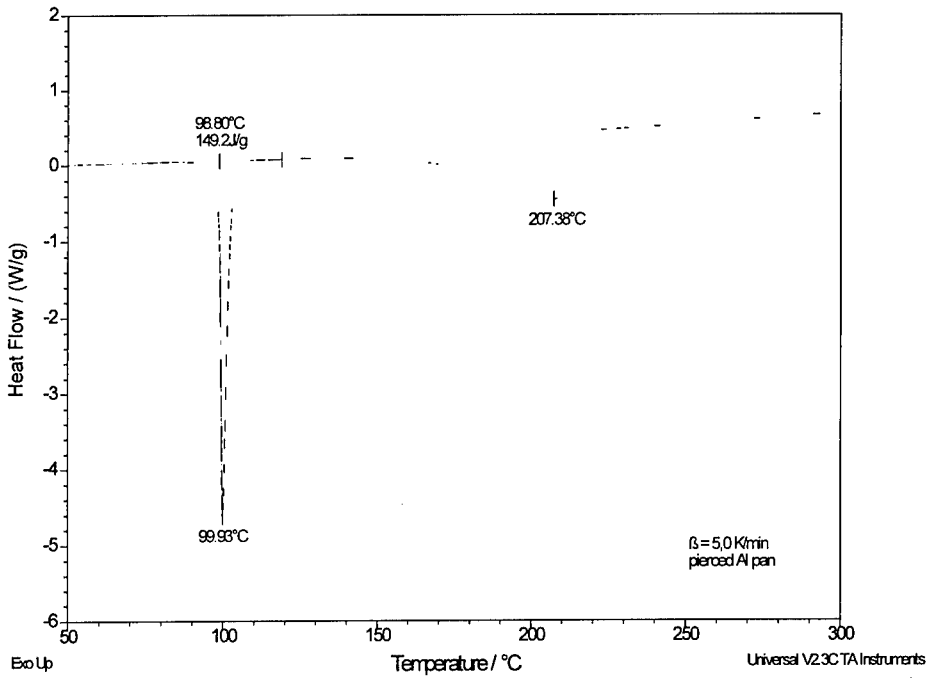

FIGURE 4: DSC (sample pans with pierced lieds)

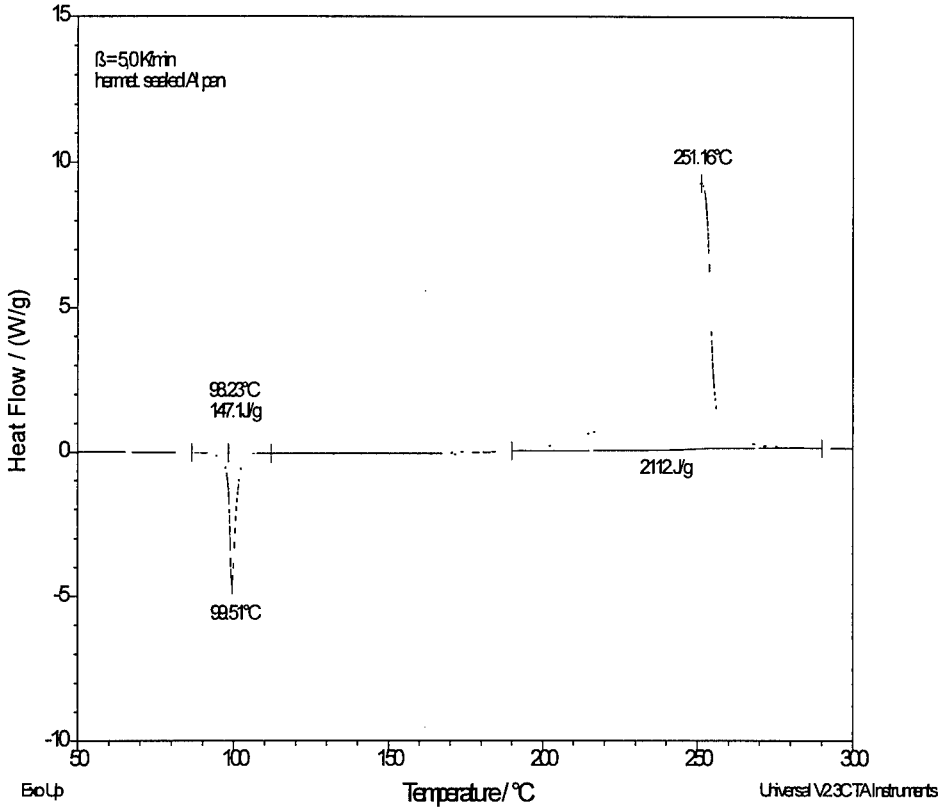

FIGURE 5: ***DSC (sealed sample pans)***

X-ray diffraction

The evaluation proves the phase stability of **TNAZ** in a temperature range from –70°C to 100°C. The lattice parameters were determined and found to be equal to published calculations [4].

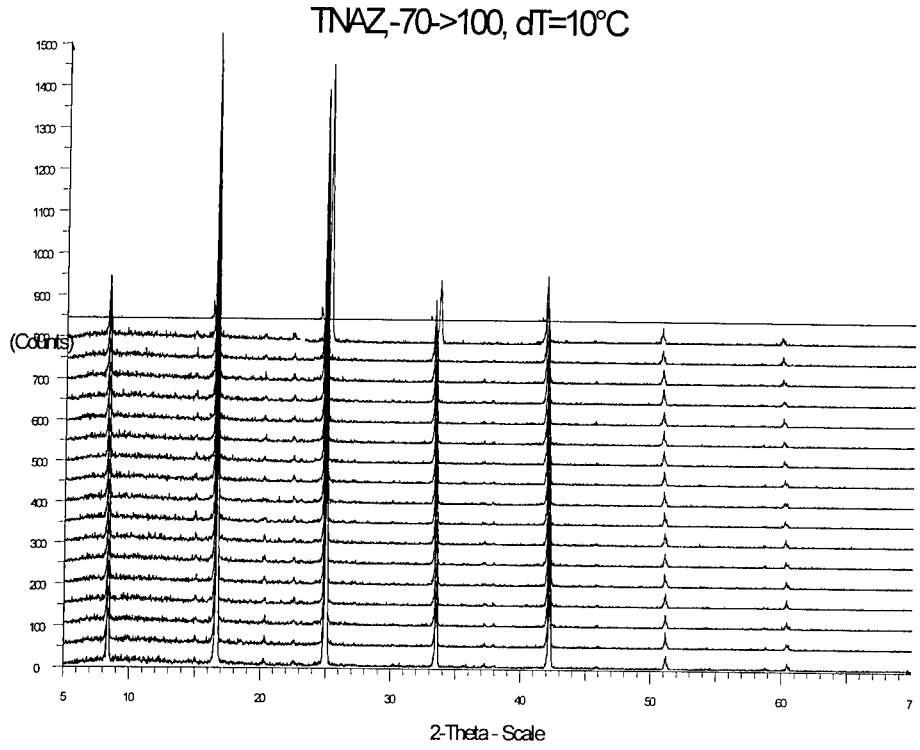

FIGURE 6: *x-ray diffraction*

Accelerating Rate Calorimeter - measurment

The experiment determined a remarkable adiabatic self heating only at about 180°C. In comparison to TNT this indicates an increased thermo-lability, but nearly the same stability as detected for Cl20.

Furthermore the deflagration of **TNAZ** extends on a longer period as other energetic materials used to do. This is a significant benefit for the safety of processing **TNAZ**.

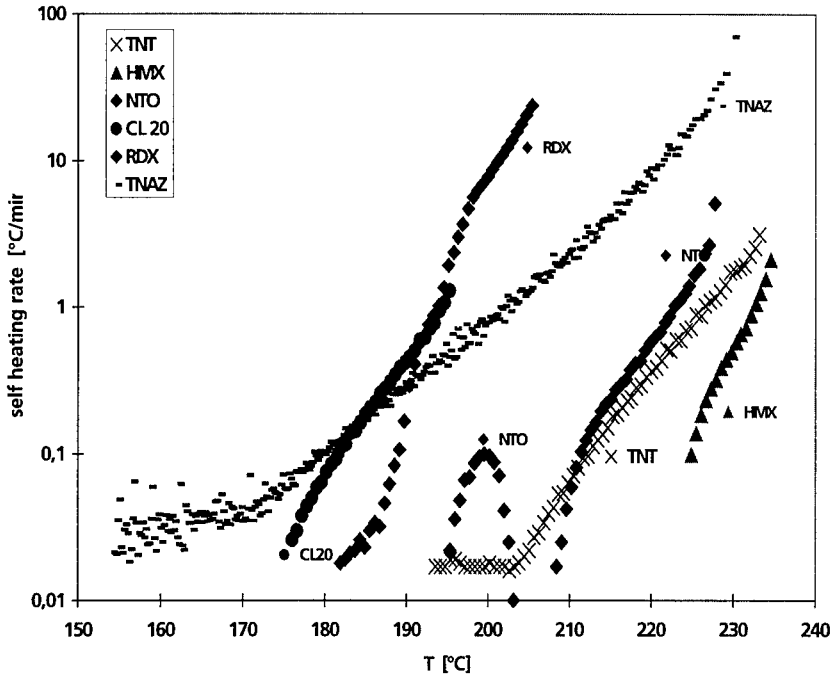

FIGURE 7: ARC-measurement

4. Conclusion

The ICT produces **TNAZ** in the maximum laboratory scale (200 g / month). The technology tranfer to the pilont plant is proposed for the year 2000. The substance is fully characterized, all experimental data correlate well with published spectra.

For the future we intend to develop new synthetic routes in order to shorten the number of steps and to reduce the enormous costs at present.

5. Literature

1) Hiskey, Coburn, US Patent **1994**, Nr. 5,336,784.

2) Hiskey, Coburn, *J. Energet. Mat.* **1998**, *16*, 73-99.

3) Mitsunobu, *Synthesis*, **1981**, 1-28.

4) Archibald, Gilardi, Baum, George, *J. Org. Chem.* **1990**, *55*, 2920-4.

A NEW CONVENIENT ROUTE TO *GEM*-DINITROALIFATIC COMPOUNDS.

Nikolaj V. Latypov, Abraham Langlet, Ulf Wellmar and Patrick Goede
FOA, Defence Research Establishment, Department of Energetic Materials,
S-14725 Tumba, Sweden

Abstract

Nitration of some 2-substituted pyrimidine-4,6-diones in sulfuric acid was studied. The nitration gave several previously unknown 5,5–*gem*-dinitropyrimidine-4,6-diones in high yields. The *gem*–dinitroproducts formed were easily attacked by nucleophiles with the formation of *gem*-dinitroacetyl derivatives, which in turn could be further hydrolysed to the salts of dinitromethane. A new insensitive explosive, guanidine dinitromethane, was synthesized and characterised.

Introduction

There are few examples of direct electrophilic attacks on activated carbon-hydrogen bonds in alifatic systems, leading to the formation of *gem*-dinitro- and trinitro-methylcompounds[1-3]. Some substituted heterocycles, mainly azolones, have been shown to behave in the same way (**Schemes 1-3**)[4-6]:

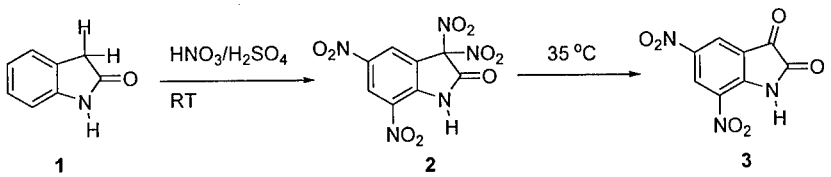

1 **2** **3**

Scheme 1

In those cases where *gem*-dinitration in the heterocyclic ring occurred it was accompanied by nitration either in the condensed aromatic system (**Scheme 1**) or in the substituent (**Schemes 2 and 3**) this made it difficult to follow the sequence of nitration.

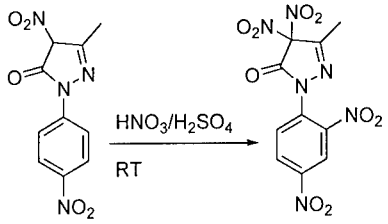

4 **5**

Scheme 2

gem-Dinitro compounds differ significantly in their thermal stability and in some cases their structure was only postulated (**7**).

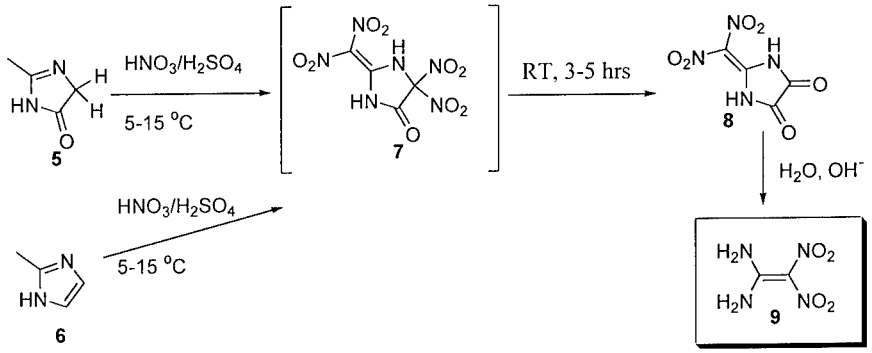

5 **7** **8** **6** **9**

Scheme 3

In an attempt to understand the mechanism of *gem*-dinitration in a heterocyclic molecule and to see if this type of reaction could take place independent of substituents in the same molecule we decided to investigate the nitration of pyrimidinones with only one reaction centre liable to such attacks; (**10**). Sulfuric acid was used as the reaction media, this has previously been found to favour the formation of *gem*-dinitrocompounds[4-6]. The course of the reaction was monitored by UV-spectroscopy.

Discussion

It was found that nitration of (**10**) by pure nitric acid or solutions of nitric acid in organic solvents at room temperature lead to nitration of the substrate in the 5-position; the same results were obtained when solutions of (**10**) in concentrated sulfuric acid (85-95%) were treated with one equivalent of nitric acid, - quick and quantitative formation of mononitrated products (**11**) were observed.

Excess of nitric acid in the reaction mixture (1-2 moles per mole of **11**) and a higher reaction temperature (30-60 °C) caused further nitration of (**11**) in the same position with the formation of 5,5-dinitroproducts(**12**), this was first detected by the appearance of a new maximum in the UV-spectra of the quenched samples (λmax.=355-365nm), in addition to the maximum corresponding to the mononitrated product (λmax.=320-330nm) (**Scheme 4**).

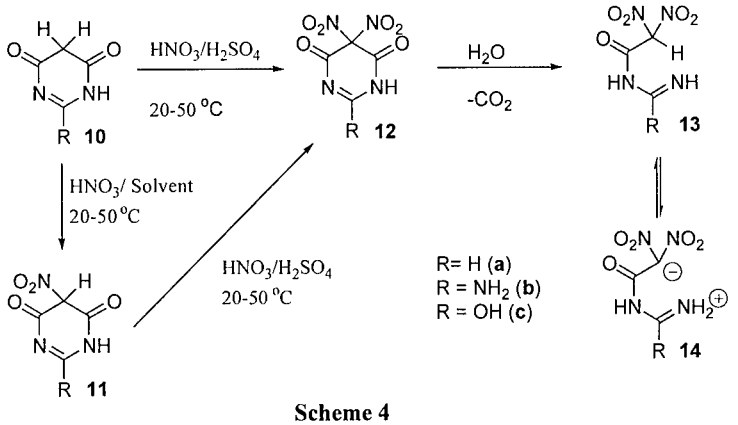

Scheme 4

Reaction times at 30-40 °C varied, depending on the nature of the substituent in the 2-position, from 2 to 20 hrs. These were estimated by the increase of absorbance at ~360 nm. The *gem*-dinitraded products(**12a-c**) proved to be extremely sensitive to nucleophiles, in particular, water. Only one of these compounds(**12a**) was isolated in high yield and characterised, this due to its very low solubility in the nitrating mixtures studied. No N-nitrated products were detected[7], this is possibly explained by the high acidity of the reaction media. Formation of other compounds (**12b** and **12c**) was postulated on the basis of the

structural analyses of compounds obtained during aqueous work-up,-e.g. the reaction mixture produced by nitration of (**10b**) when diluted with water gave directly *gem*-dinitroacctylguanidine(**14b**). No products of type (**12**) or (**14**) were isolated from the nitration of (**10c**). In this case formation of the intermediates (**12c** and **14c**) was deduced from the formation of the dinitromethid-ion (**16**) during alkaline hydrolyses of the qenched nitration mixture.

Isolation of the previously unknown 5,5-dinitrobarbituric acid (**12c**) in pure form made it possible to study its properties and reactions in more detail. The substance is a rather thermally stable solid which decomposes violently at ~150 °C (**figure 1**).

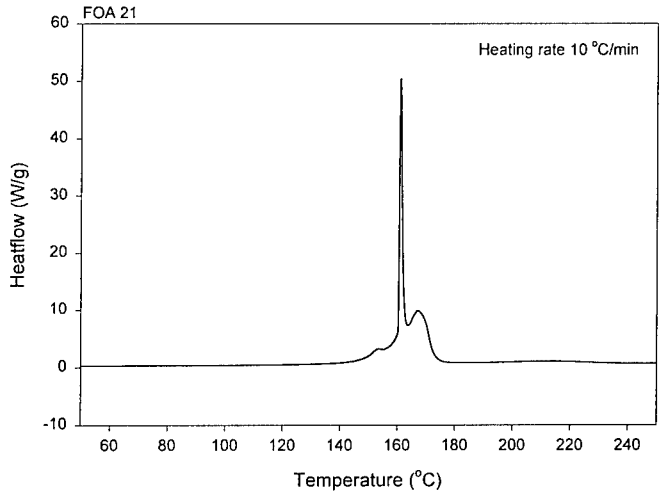

Figure 1, DSC curve for 5,5-dinitrobarbituric acid (**12c**) at heating rate of 10 °C per minute

5,5-dinitrobarbituric acid(**12c**) was very reactive chemically and it was easily attacked at the 4-position by different nucleophiles, e.g. it dissolved readily in cold water forming acidic solutions, from which on standing carbon dioxide evolved, resulting in the precipitation of *gem*-dinitroacetylurea(**14c**). The latter compound is also a strong acid forming rather insoluble salts (potassium,sodium etc.) on careful neutralisation of its aqueous soutions, (**Schemes 4 and 5**)

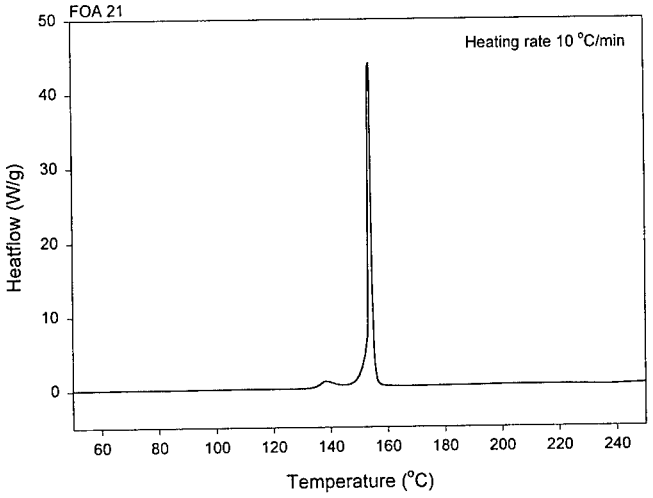

Figure 2: DSC curve for Potassium *gem*-dinitroacetylurea (**15c**) at heating rate of 10 °C per minute

It was also shown that these salts(**15**) are relatively stable thermally (**figure 2**) but can be easily hydrolysed at elevated temperatures in basic media to salts of dinitromethan (**Scheme 5**). This provides a new, efficient and safe method for the preparation of these compounds in comparison with other known methods[8-10] E.g. the overall yield of potassium dinitromethane from barbituric acid is around 80%.

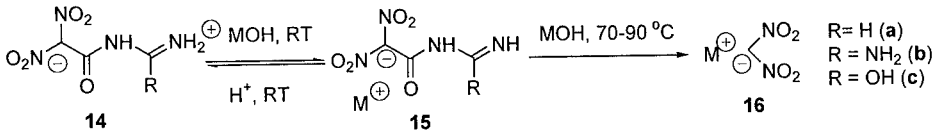

Scheme 5

In addition to the known dinitromethane salts, potassium-, ammonium- etc.- a new compound in this series guanidine dinitromethane(**18, scheme 6**), was obtained by precipitation from an ion-exchange reaction. Unlike other dinitromethane salts, guanidine dinitromethane(**18**) is a relatively thermally stable explosive(**figure3**) with a surprisingly low sensitivity. The impact and friction sensitivities were determined according to the BAM standard which conforms to the UN guideline ST/SG/AC.10/11[11], with one exception: the impact sensitivity was measured with a 2kg drop weight. This study showed guanidine dinitromethane(**18**) to be out of range for the test apparatus: impact sensitivity (cm) >150; friction sensitivity (N) > 350.

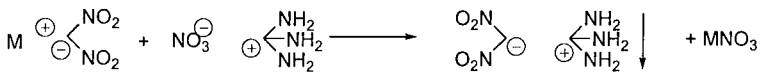

16 **17** **18**

Scheme 6

As well as the dinitromethane salts(**16**), the *gem*-dinitroacetylderivatives(**14**), having several reaction centres look very attractive as synthetic intermediates in the design of new explosives[12]. The chemistry of these interesting compounds is currently under investigation.

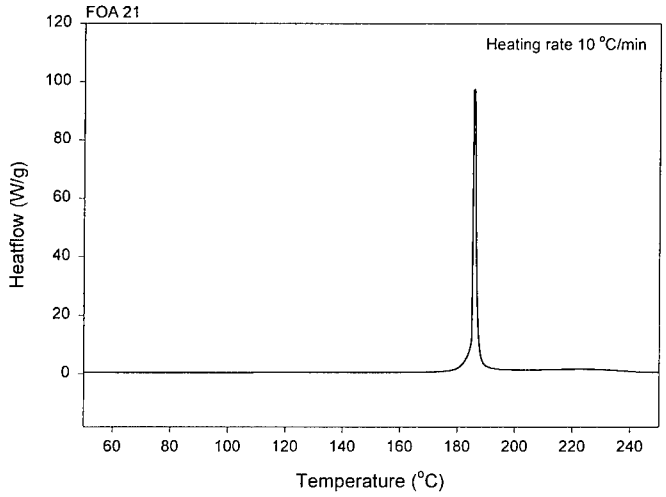

Figure 3: DSC curve for guanidine dinitromethane (**18**) at heating rate of 10 °C per minute

Summary and Conclusions

We have discovered *gem*-dinitration in the pyrimidinone series. This was shown to be an easy and accesible route towards dinitromethane salts as well as other polynitroalifatics. Several new stable multifunctional *gem*-dinitro compounds, which seem to be useful intermediates in the design of new explosives, have been synthesized and characterized. Guanidine dinitromethane is an example of these compounds showing interesting properties as an insensitive and thermally stable explosive.

Experimental

Caution: The *gem*-dinitrocompounds, described in this paper are powerful and sensitive explosives and should be handled with appropriate precautions. Employ all standard energetic materials safety procedures in experiments involving such substances.

5,5-dinitrobarbituric acid(12c)

To a solution of barbituric acid(**10c**) (5.15g, 0.04mol) in 90-95% sulfuric acid (25 ml) was added fuming nitric acid (4 ml, 0.1mol) while the temperature was kept below 25°C. The reaction mixture was then heated to 45°C for 4hrs. The resulting precipitate was filtered off, washed with trifluoroaacetic acid and dried, yielding 5,5-dinitrobarbituric acid(**12c**) as a hemihydrate (8.5g,94%), dec.temp. 150 °C; IR (KBr): 3250 (NH), 1745 (C=O), 1580 (NO_2), 1378 (NO_2); ^{1}H NMR (DMSO-*d6*) δ 11,03 broad; ^{13}C NMR (DMSO-*d6*) δ 113.5, 149.0, 155.1, Anal.calcd.for $C_4H_2N_4O_7$*0,5 H_2O: C, 21.16; H, 1.33; N, 24.67. Found: C, 21.1; H, 1.23; N, 24.89.

***Gem*-dinitroacetylurea(14c)**

Dinitrobarbituic acid(**12c**) (7.2g, 0.032mol) was dissolved at 10°C in 10 ml of water and kept at this temperature for 2 hrs, during this period gas evolution was observed, which resulted in the precipitation of a yellow solid. The solid was filtered and dried at 40°C with changing

colour from yellow to white to give 5.5g (53%) of (**14c**). dec.temp. 130°C. Anal.calcd.for $C_3H_4N_4O_6$: C, 18.75; H 2.08; N, 29.17. Found: C, 18.78; H, 2.26; N, 29.14.

Potassium *gem*-dinitroacetylurea(15c)

Gem-dinitroacetylurea(**14c**) (10g, 0.052mol) dissolved in 50 ml of water was added dropwise to a solution of 2.7 g (0.05mol) KOH in 50ml of water while keeping the temperature at 10°C. A yellow precipitate was immediately formed, which was filtered and dried. Yield 8.2g (77%) of potassium *gem*-dinitroacetylurea(**15c**). ^{1}H NMR (DMSO-*d6*) δ 10.44; 7.66; 7.21. ^{13}C NMR (DMSO-*d* 6) δ 159.15;154.90;134.99. Anal.Calcd.for $KC_3H_3N_4O_6$: C, 15.65; H, 1.31; N, 24.34. Found: C, 15.46; H, 1.28; N, 24.22.

Potassium dinitromethane(16)

10g (0.052mol) of potassium *gem*-dinitroacetylurea(**15c**) was added to the solution of 12g (0.21mol) KOH in 100 ml of water; the resulting mixture was kept at 80°C for 2hrs and then cooled to room temperature. The precipitate of potassium dinitromethane was filtered, washed with 10-15 ml of cold water and dried to give 6.2g (85%) of pure potassium dinitromethane(**16**), which was identified by dec.temp. 220 °C[8] and UV-spectroscopy (λmax. = 363 nm and ε = 20800)[13].

***Gem*-dinitroacetylguanidin (14b)**

3.8g (0.018mol) 2-Aminopyrimidine-4,6-dione(**10b**) dissolved in 40 ml concentrated sulfuric acid were nitrated in conditions analogous to those for (**10c**). After 2hrs the reaction mixture was cooled to room temperature and poured into 200 ml of cold water; the dilution was accompanied by evolution of carbon dioxide and precipitation of a yellow solid, (**14b**) 5.0g (88%). dec.temp. 150 °C. Anal.Calcd. for $C_3H_5N_5O_5$: C, 18.85; H, 2.62; N, 36.65. Found: C, 19.01; H, 2.60; N, 36.57.

Guanidine dinitromethane(18)

6.4g (0.05mol) sodium dinitromethane(**16**) was dissolved in 120 ml water at 70 °C to this was added a solution of 6.1g (0.05mol) guanidine nitrate(**17**) in 30 ml of water. The reaction mixture was cooled to room temperature and a precipitate was formed. The product was

filtered off, washed by water and dried at 40 °C yielding 7.5 g (90%) of guanidine dinitromethane(**18**). dec.temp. 150 °C.

Acknowledgements

The authors would like to thank the Swedish Defence Forces for giving financial support to this project and Mr Lars Bodin for the BAM impact and friction sensitivity test measurements.

References

1)Nielsen, A. T. *Nitrocarbons*; VCH: New York, 1995.

2)Noble, P. J.; Borgardt, F. G.; Reed, W. L. *Chemical Reviews* **1964**, *64*, 19-57.

3)Parker, C. O.; Emmons, W. D.; Rolewicz, H. A.; McCallum, K. S. *Tetrahedron* **1962**, *17*, 79-87.

4)Brimert, T. *Mono- and gem-Dinitrations en route to Heterocycles*; Royal Institute of Technology: Stockholm, 1998, pp 40-41.

5)Latypov, N. V.; Bergman, J.; Langlet, A.; Wellmar, U.; Bemm, U. *Tetrahedron* **1998**, *54*, 11525-11536.

6)Bergman, J.; Bergman, S. *Tetrahedron Lett.* **1996**, *37*, 9263-9266.

7)Runge, J.; Treibs, W. *Journal fur praktische Chemie* **1962**, *4*, 223-227.

8)Grakauskas, V.; Guest, A. M. *Journal of Organic Chemistry* **1978**, *43*, 3485-3488. and references cited therein.

9)Grakauskas, V. *Alkali metal salts of dinitromethane*: US patent 4233250, 1979.

10)Garver, L. C.; Grakauskas, V.; Baum, K. *Journal of Organic Chemistry* **1985**, *50*, 1699-1702.

11)*United Nations: Recommendations on the Transport of Dangerous Goods. Manual of Tests and Criteria ST/SG/AC.10/11/Rev.2.*; 2nd revised ed.; United Nations: New York and Geneva, 1995.

12)Guowei, Y.; Qiwu, X.; Wan, D.; Yu, H. *Journal of the Industrial Explosives Society, Japan* **1982**, *43*, 2-8.

13)Fedorov, Y. A.; Odokienko, S. S.; Selivanov, V. F. *Journal of Applied Chemistry of the USSR* **1979**, *52*, 2201-2202.

CYLODEXTRIN POLYMER NITRATE

Anja Ruebner[1], Gary Statton[1], Danielle Robitelle[2], Curtis Meyers[1]
and Bernard Kosowski[1]

[1]MACH I Inc., 340 East Church Road, King of Prussia, PA 19406, U.S.A.
[2]Air Force Research Laboratory AFRL, Munitions Directorate, 2306 Perimeter Rd, Eglin AFB, FL, 32542

Abstract

The development of the use of cyclodextrin nitrates as possible components of insensitive, high-energy energetics is outlined over a time period of 12 years. Four different types of cyclodextrin polymers were synthesized, nitrated and evaluated regarding their potential use for the military and aerospace community. The synthesis of these novel cyclodextrin polymers and different nitration techniques are shown and the potential of theses new materials is discussed.

1. Introduction

The military and aerospace community has an on-going interest in and need for energetic materials with high energy performance but with low sensitivity characteristics. MACH I, Inc. has completed a Small Business Innovation Research program sponsored by the U. S. Air Force to evaluate nitrated cyclodextrin polymers as possible components of insensitive, high-energy energetics. These materials will also be suitable for components in insensitive, minimum smoke-producing propellants. The U.S. Navy, Naval Surface Warfare Center, Indian Head, MD had a program to evaluate nitrated cyclodextrins. They postulated that the nitrated cyclodextrin can form inclusion complexes with energetic guests similar to

cyclodextrin. However, since the energetic is contained in the inclusion complex, it acts as if partially coated, thus the composition resists detonation due to impact, shock, friction or electrostatic discharge. The included energetic guest does however increase the performance of the system. Consaga et al. [1-2] showed that nitrated γ-cyclodextrin (CDN) is able to encapsulate organic nitrate esters like nitroglycerin (NG) and butanetriol-trinitrate (BTTN). The shock sensitivity of these energetics can be reduced by encapsulation with CDN.

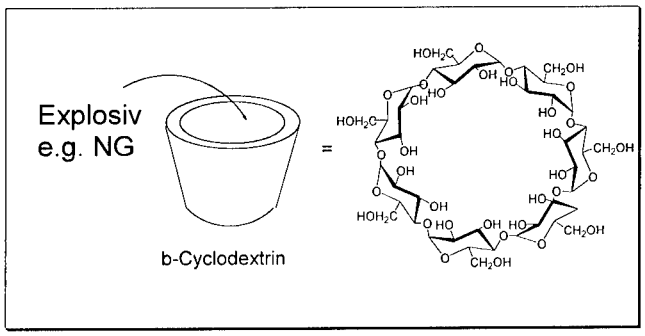

Figure 2: Encapsulation ability of cyclodextrins.

The work on nitration of cyclodextrins at NSWC Indian Head began in 1988. At that time β-cyclodextrin was selected as the candidate for nitration, due to the significant differences in costs. In 1988 the costs for cyclodextrins were as follows: α-cyclodextrin: $200/lb, β-cyclodextrin: $6/lb and γ-cyclodextrin: 2,000/lb. Since then, the price for γ-cyclodextrin has dropped dramatically to $25-30/lb. With this change, more research has been done with γ-cyclodextrin, since this derivative has advantageous encapsulation properties, due to the increased cavity size.

The viscosity of some of the complexes of nitrated esters and the nitrated γ–cyclodextrin monomer is too low however to be used alone without a binder in many

formulations. By polymerizing the cyclodextrin into higher molecular weight versions and nitrating, the processing characteristics should improve measurably and offer explosive chemists new and exciting components.

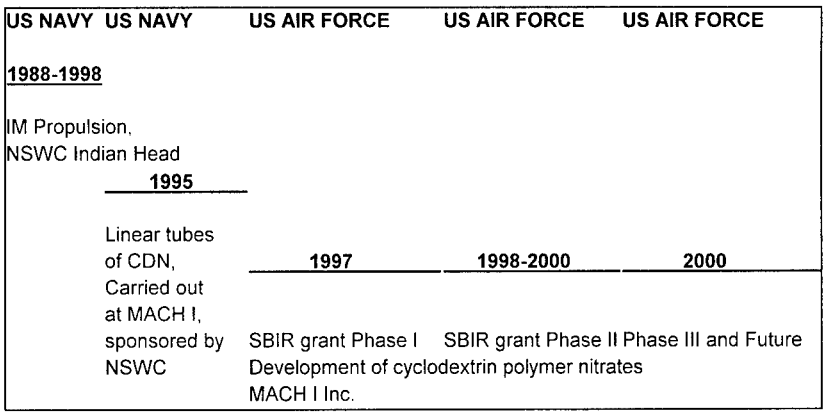

Figure 2: History of cyclodextrin nitrate research.

This paper describes the synthesis, purification and characterization of different types of nitrated cyclodextrin polymers (poly-CDN). All nitrated cyclodextrin polymers provide a high molecular weight for an improved behavior in an explosive formulation, which leads to favorable processing properties. The following polymers, shown in figure 3, were chosen for our investigation: a γ-cyclodextrin polymer crosslinked with 1-chloro-2,3-epoxy propane **1**, a γ-cyclodextrin polymer crosslinked with 4,4'methylene-bis(phenyl isocyanate) **2**, a linear polymer with pendant γ-cyclodextrins **3** and a linear tube, consisting of α-cyclodextrins crosslinked with 1-chloro-2,3-epoxy propane **4**. These polymers were nitrated according to different protocols and the suitability of their nitrated forms as Insensitive Munition (IM) energetic candidates for future use and formulation development was investigated. The 1-chloro-2,3-epoxy propane crosslinked γ-cyclodextrin polymer **1** was selected for scale-up evaluation and further testing.

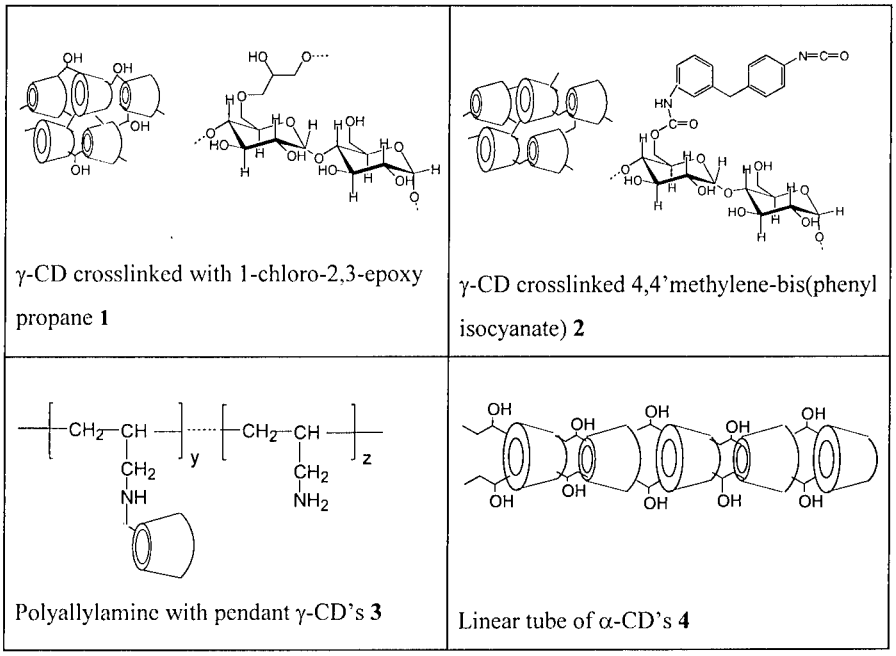

Figure 3: Four different types of cyclodextrin polymers.

3. Results and Discussion

The synthesis of the cyclodextrin polymers shown in figure 3 are in part literature known [3-5]. These four polymers differ in their connection of the cyclodextrin units, due to the use of different crosslinking agents. After crosslinking to a polymer at least two cyclodextrin hydroxyl groups were consumed for the linkage. In case of the hydroxy-propyl linked polymers **1** and **4**, one new hydroxyl group was gained from the linker. Preferably an average of 2.5-3 hydroxyl groups of each D-glucose unit or within the linker were converted to nitrate esters under the condition of nitration. The linear polymer with pendant

cyclodextrins **3**, has its cyclodextrins bound to a polymer backbone by secondary amine linkages. Twenty three hydroxyls are available for nitration for each bound cyclodextrin molecule. The reaction of γ-cyclodextrin with 4,4'methylene-bis(phenyl-isocyanate) yielded polymer **2**. The cyclodextrins are connected by urethane linkages. At least two hydroxyl groups were consumed for the linkage, which left only the remaining hydroxyls of the cyclodextrin available for nitration.

1, 3 and **4** were nitrated using nitric acid, which is a standard nitration technique. Elemental analysis showed nitrogen levels of 11.6 % for the nitrate of **1**, 19.9 % for the nitrate of **3,** and 9.55 % for the nitrate of **4**. Polymer **2** could not be nitrated using nitric acid. Hydrolysis of the urethane linkages occurred under these strongly acidic conditions. Therefore **2** was nitrated in liquid carbon using nitrogen pentoxide [6]. This technique also offers the advantage of an easy purification, since solvent and reagents are volatiles that can be vented leaving the nitrated product pure. However, the costs of nitrogen pentoxide and the lack of scale-up capability, made it difficult to use this technique and the nitration of **2** was not further optimized. The selection of the cyclodextrin polymer to scale up based on the synthesis of the polymer, the properties of the polymer, the nitration of the polymer and properties of the nitrated polymer.

Table 1: Scale-up of Synthesis and Nitration

CD Polymer	Synthesis and Scale-up	Nitration	Scale-up
1	One-step synthesis, 1 lb batches	Nitric acid	1 kg batches
2	One-step synthesis, 100 g batches	Liquid carbon, N_2O_5	1 g scale
3	Three-step synthesis, 100 g scale	Nitric acid	1 g scale
4	Four-step synthesis, 1-10 g scale	Nitric acid	1 g scale

Table 1 shows the scale-up of synthesis and nitration of the different cyclodextrin polymer candidates (**1-4**). The comparison resulted in selecting candidate **1** for further scale-up and testing. A scale up was carried out to produce 1 lb batches. The crude polymer

was purified by tangential flow membrane filtration using a polyethersulfone membrane with a cut-off of 3,000. Molecular weights were determined by GPC and showed a doubling in molecular weight, indicating a complete nitration of all available hydroxyl groups. IR and NMR spectra confirmed this result.

Initial sensitivity experiments were carried out at Eglin AFB, Pensacola, Fl, U.S.A with RDX as an energetic material for encapsulation. The shock sensitivity of RDX was dramatically reduced by encapsulation with the nitrated polymer **1**. Table 2 shows the safety properties of RDX and polymer **1**-RDX complexes at different ratios.

Table 2: Safety properties

Complex -RDX [weight ratio]	**Impact [cm] Bruceton**	**Friction [kg]**	**ESD [Joule]**
RDX	19	9.6	0.0595
1	47	28.8	0.1288
1-RDX 1:1	42	12.8	0.1288
1-RDX 1:5	27	10.8	0.1288
1-RDX 1:10	30	10.8	0.1288

Optical microscopy studies of encapsulated RDX showed a diminishing of the typical RDX crystal structure pattern. The two upper pictures show the typical crystal structure pattern of RDX. The picture identified as Poly-CDN shows the non-crystalline structure of the amorphous cyclodextrin polymer **1**. The lower right picture shows the structure of encapsulated RDX. No discrete crystals of RDX are detectable anymore. This phenomenon explains the significantly improved safety characteristics shown in table 2.

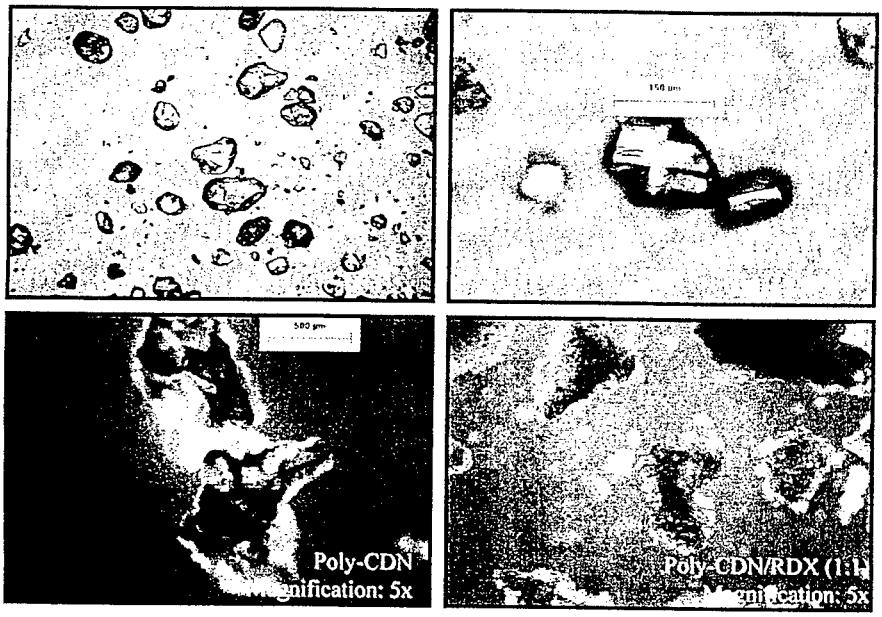

Figure 4: Optical micrograph of RDX (magnification 5x), RDX (magnification 20x), cyclodextrin polymer **1**, RDX encapsulated in **1** (from upper left to lower right).

2. Experimental

Synthesis of cyclodextrin polymers

γ-CD crosslinked with 1-chloro-2,3-epoxy propane 1. 28.7 g (0.72 Mol) NaOH were dissolved in 125 ml water. 50 g (0.038 Mol) dried cyclodextrin and 100 mg $NaBH_4$ were added. The solution was warmed to 50 °C and 35 ml (0.45 Mol) epichlorohydrin were slowly dropped into the solution and stirred for 3 h. After cooling to 4 °C 12.5 ml acetone were added and the mixture was stirred for 1h. The acetone layer was removed by separation and the solution was stirred for another 3 h at 50 °C. After neutralization with 10 N HCl the crude reaction mixture was purified by tangential flow membrane filtration

(Centramate^{TM}, Pall Filtron, cut-off filter 3,000). After freeze drying a pure product was obtained (75 % yield). The average molecular weight was determined by Vapor Pressure Osmometry (M_n = 4185). A cyclodextrin content of 59% was determined with phenol-sulfuric acid [7].

γ-CD crosslinked with 4,4'methylene-bis(phenyl isocyanate) 2. 20 g (0.015 Mol) dried cyclodextrin were dissolved in 200 ml anhydrous DMSO. The solution was heated to 100 °C. 3 g (0.012Mol) 4,4'methylenebis(phenyl isocyanate) (MDI) dissolved in 20 ml anhydrous DMSO were added drop wise. The solution was stirred for 8 h at 100 °C. After cooling to ambient temperature the mixture was precipitated in methanol. The product was filtered, washed with water and dried in vacuum. The average molecular weight is approx. 2,000 (M_n). The cyclodextrin content was determined by NMR to be 81%.

Polyallylamine with pendant γ-CD's 3. The synthesis is described elsewhere [3].

Linear tube of α-CD's 4. The reaction protocol of Harada et al. [4-5] was used.

Nitration

10g cyclodextrin polymer were dissolved in 100 ml nitric acid at 10 °C. The mixture was stirred for 30 min and then precipitated over ice. The product was filtered and washed, dissolved in acetone and re-precipitated in water again. After filtration the material was dried in vacuum. Molecular weights were determined by GPC and showed a doubling in molecular weight, indicating almost complete nitration of all available hydroxyl groups. Elemental analysis showed nitrogen levels of 11.6 % the nitrate of **1**, 19.9 % for the nitrate of **3,** and 9.55 % for the nitrate of **4**.

Nitration in liquid CO_2 with N_2O_5 [6]

1 g Polymer **2** and 5 g sodium fluoride were added to the 600 ml vessel. The nitric acid/dinitrogen pentoxide mixture was added to the 60 ml vessel. The agitator was turned

on and carbon dioxide was slowly added to both vessels until the pressure was 61 atm (1900 psi). The -25° C cooling fluid was pumped through the jackets of both vessels. The 600 ml vessel carbon dioxide addition tube was closed and the valve between the two vessels was opened. For 90 min 1.4 g of carbon dioxide /min was passed through the two vessels. The temperature was -10 ± 2° C. The pressure was slowly released and the product poured into 20 g of sodium bicarbonate in one liter of water. The pressure vessel was rinsed with 700 ml of additional water. The mixture was filtered and the nitrated polymer was washed twice with water. Yield: 0.6 g of a white solid, soluble in acetone. Elemental analysis showed a nitrogen level of 13.6% for the nitrate of **2**.

4. Acknowledgments

This research was financially supported by a SBIR grant from Eglin AFB, Pensacola, Fl, U.S.A., Contract F08630-97-C-0015. We also like to thank Dr. N. Trivedi and Mr. R. Farncomb from Naval Surface Warfare Center, Indian Head Division for carrying out the nitrations in liquid carbon dioxide. We further like to thank Mr. S. Hamilton from Thiokol for carrying out the nitrations using standard nitration technique.

5. References

[1] J. P. Consaga, R. C. Gill, In: Energetic Materials, 29th International Annual Conference of ICT, Karlsruhe, Germany, **1998**, V5-1.

[2] J. P. Consaga, S. L. Collignon, US 5,114,506, **1992**

[3] A. Ruebner, G. L. Statton, M. R. James, in press: *Macromol. Chem Phys.*

[4] A, Harada, J. Li, M. Kamachi, *Nature*, **1992**, 356, 325.

[5] A, Harada, J. Li, M. Kamachi, *Nature*, **1993**, 364, 325.

[6] G. W. Nauflett, R. E. Farncomb, K. F. Mueller, In: Energetic Materials, 29th International Annual Conference of ICT, Karlsruhe, Germany, **1998**, V-9.

[7] In: Methods in Carbohydrate Chemistry, Ed.: R. L. Whistler, M.L. Wolfram, J. N. BeMiller, F. Shafizadeh, Volume I, Analysis and preparation of sugars, Academic press 1962, p. 388.

ZWITTERIONIC AMINE-NITRAMINES AS A NEW CLASS OF ENERGETIC MATERIALS

Alexander M. Astachov[1,2], Rudolf S. Stepanov[2], Ludmila A. Kruglyakova[2], Yuriy V. Kekin[2]

[1]Institute of Chemistry and Chemical Technology RAS (Sib. Div.)
660049, Krasnoyarsk, prosp. K. Marksa, 42, Russia
[2]Siberian State Technological University
660049, Krasnoyarsk, prosp. Mira, 82, Russia

ABSTRACT

Zwitterionic amine-nitramines are proposed as a new class of energetic materials. These compounds simultaneously contain in their molecule both primary nitramine group ($-NHNO_2$) *and nucleophilic centre, which is aminogroup* ($-NH_2$). *Transferring a proton from primary nitramine group to aminogroup leads to a formation of aminoacidic zwitterionic structure:* $H_3\overset{+}{N}-R-\overline{N}NO_2$.

The intramolecular ionic bond increases intermolecular interaction (energy of a crystalline lattice), and as a consequence, thermal stability and density of such a compound. The substances considered can be applied to water-base energetic systems of various assignments.

INTRODUCTION

The application of primary nitramines as energetic materials is limited due to their relatively low thermal stability.

Our systematic research of aliphatic primary nitramines' thermal decomposition, carried out for a number of years, has allowed us to establish the relationship between nitramines' structure and their thermostability, and to reveal the mechanism of decomposition for these compounds in condensed phase. Nitramines' thermal decomposition has autoprotolytic character. The stronger acid

a particular nitramine is, the less stable it is thermally [1,2]. This is due to the fact that known explosoforic groups show electron-acceptor properties:

$$lg\ k_{150°C} = -(0.34\pm0.05)\ pK_a - (1.40\pm0.31) \qquad (1)$$

$$r = -0.942;\ S_y = 0.07;\ n = 8$$

Dinitramide ($O_2N–NHNO_2$) is the most typical example. It has the greatest acidity ($pK_a = -5.62$) and, as a consequence, the lowest stability.

It is clear from equation (1), that attempts to synthesize primary nitramines, which would be more powerful and simultaneously more thermally stable than ethylenedinitramine (EDNA), are unsuccessful. Increasing the nitrogroups number in a molecule in order to obtain more balanced and powerful explosive inevitably results in the increase of acidity and decrease of thermal stability of compounds. For example, detonation parameters of 1,3,5-trinitrazapentane are close to those of oktogen (HMX), but its limited thermostability effectively prevents one from using this compound as explosive. The capacity to somewhat increase thermostability at the expense of growing molecular weight of a substance (for example, by escalating a chain of linear polymethylenepolynitramine $O_2NNH[CH_2N(NO_2)]_nCH_2NHNO_2$), which usually causes the melting point to go up, is limited in this case. Stabilization by the "double protonation" mechanism [1], which is known to work for methylenedinitramine (MEDINA) [3], is suitable only for some substances, not for all. Besides, it does not allow thermostability of compounds to reach even the level of EDNA ($t^{20°C}_{0.02\%}=6\cdot10^2$ years).

So, it seems that search for the new powerful energetic compounds among primary nitramines is hardly promising. It is basically impossible to change an electron-acceptor nature of a nitrogroup, while using buffer electron donation groups results in decreasing the oxygen balance of a substance.

ZWITTERIONIC AMINE - NITRAMINES

If one creates a nucleophilic center $-NH_2$ in a certain part of a molecule that contains a fragment $-NHNO_2$, then protonation on this center is one of the possible ways of stabilization for such a structure:

Scheme 1

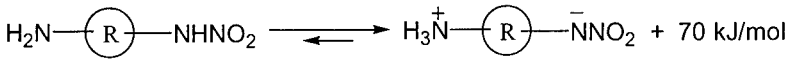

Anion system $R-[NNO_2]^-$ is thermally more stable [1] than $R-NHNO_2$. Additional energy of about 70 kJ/mol (Scheme 1) is required for its thermal decomposition, which follows decomposition mechanism typical for primary nitramines (E_a=106-130 kJ/mol) [1,2]. Energy, necessary for transition of a zwitterion into a molecular amino-nitramine, is obtained from the values of formation heats (ΔH°_f) for amine salts of primary nitramines. This energy includes not only thermal effect of neutralizing, but also the increase of energy of a crystalline lattice caused by the formation of ionic bond.

The information about compounds, which contain in their molecules primary nitramine group and aminogroup simultaneously, is scarce in the literature. Only 1-amino-2-nitraminoethane and 2-amino-3-nitraminopropene are known. These were synthesized in USA in 1950-1954 [4]:

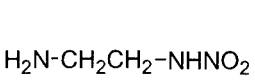

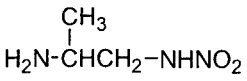

As it was expected, these compounds have zwitterionic structure:

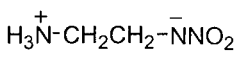

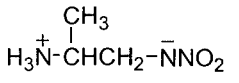

Both compounds are crystalline substances with physical and chemical properties, typical for zwitterionic aminoacid.

Recently, one more similar compound was synthesized [5]:

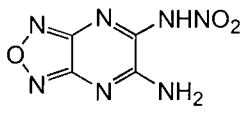

But, judging by its properties, the substance is not a zwitterion. Probably, this is due to the strong electronegativity of furazan cycle (which inactivates the aminogroup) or, may be, due to the nitrimine's structure of this substance.

The thermal stability of 1-amino-2-nitraminoethane was previously investigated by us [1]. The kinetic parameters of thermal decomposition are presented in table 1. Substance exothermally decomposes in a solid phase, without melting. Manometric kinetic curves have an S-shape appearance. We failed to find a region of ratios m/V and S/V for which it would be possible to assume that primary process of decomposition is close to homogeneous. The thermal decomposition rate constants found in dynamic experiments are about 1.5–2 times more than corresponding static values.

Table 1. Kinetic parameters of thermal decomposition of 1-amino-2-nitraminoethane

Method	T, °C	$k_{200°C}\cdot 10^5$, s^{-1}	E_a, kJ/mol	lgA
Bourdon manometric method	185–210	4.66	185.7	16.34
TGA	192–231	13.70	254.2	24.24

Even if parameters of thermal decomposition presented in table 1 are *a priori* overstated, still, thermal stability of 1-amino-2-nitraminoethane considerably exceeds that of the primary nitramines investigated earlier [1,2]. The electron donation ability of the group $H_2NCH_2CH_2-$ is higher than in alkyl substituents.

The value of decomposition rate constant, calculated from equation (1), is 10 times less than that of alkylmononitramines but 100-500 times more than what was calculated based on experimental activation parameters. This proves

zwitterionic structure to contribute substantially to the compound's stabilization. The 1-amino-2-nitraminoethane solid state of aggregation is in itself already a proof of increased intermolecular interaction in an ionic structure. Consider propylnitramine ($C_3H_7NHNO_2$), which is liquid under normal conditions, even though it has a similar molecular mass.

Thus, the increased thermostability of 1-amino-2-nitraminoethane is due to these two factors: the energy of transition of ionic structure into a molecular structure, on one hand, and high electron donation ability of the substituent, on the other. Relatively high values for experimental energy of activation are then a sum of a transition heat and actual activation energy of irreversible decomposition.

The previously known zwitterionic amino-nitramines considered above do not have a practical value as individual energetic substances because of the strongly negative oxygen balance. After confirming experimentally the relatively high thermal stability for zwitterionic amino-nitramine structure, we came to a series of the more balanced energetic compounds:

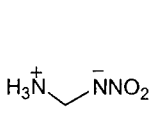

(I)

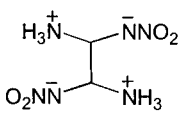

(II)

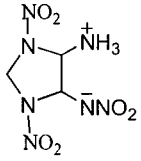

(III)

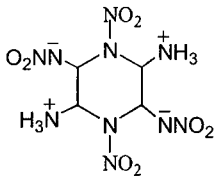

(IV)

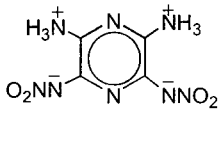

(V)

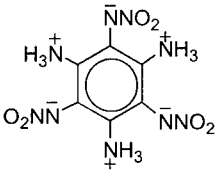

(VI)

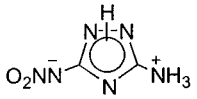

(VII)

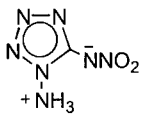

(VIII)

DETONATION CHARACTERISTICS FOR ZWITTERIONIC AMINE-NITRAMINES

Calculated energetic parameters of zwitterionic amino-nitramines (I-VIII) are presented in table 2. Formation heats and densities were calculated by methods of group additions and atomic additions with the use of neural programming principles [6]. Detonation parameters were calculated by thermodynamic method using BKW equation of state (at various sets of parameters [7]) and, also, by simple correlation methods [8]. Table 2 shows averaged converging values obtained by various methods.

Table 2. Some theoretically calculated energetic parameters for I-VIII

	Formula	Mw	Oxygen Bal., %	ρ_0, g/s m^3	ΔH_f^0, kJ/mol	$Q_{expl.}$, MJ/kg	D_{CJ}, km/s	P_{CJ}, GPa
I	$CH_5N_3O_2$	91.1	–43.9	1.62	–160.9	3.7	7.8	21.6
II	$C_2H_8N_6O_4$	180.1	–35.5	1.87	–289.0	3.8	8.6	29.7
III	$C_3H_7N_7O_6$	237.1	–23.6	1.91	–53.9	5.4	9.0	34.4
IV	$C_4H_{10}N_{10}O_8$	326.2	–24.5	1.96	–145.3	5.0	9.1	35.8
V	$C_4H_6N_8O_4$	230.1	–48.7	1.94	–61.3	3.7	8.4	27.7
VI	$C_6H_9N_9O_6$	303.2	–55.4	1.93	–243.6	3.7	8.1	26.1
VII	$C_2H_4N_6O_2$	144.1	–44.4	1.88	40.4	3.6	8.4	27.0
VIII	$CH_3N_7O_2$	145.1	–16.5	1.86	229.9	4.7	9.2	33.7

SYNTHESIS OF ZWITTERIONIC AMINE-NITRAMINES

Compounds (I-VIII) can be synthesized in various ways (scheme 2–5). Hydrolysis of cyclical mononitroureas yields zwitterionic aminonitramines [9]:

Scheme 2

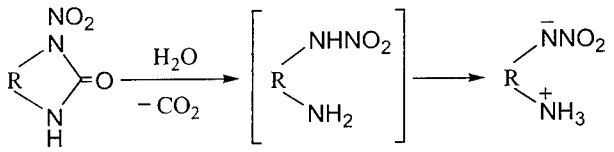

For example, compound (II) can be synthesized by hydrolysis of 1,4-dinitroglycoluril (DINGU):

Scheme 3

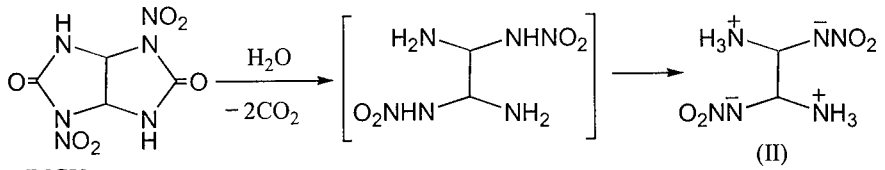

DINGU (II)

1,3,5-Triamino-2,4,6-trinitrobenzene (TATB) serves as initial substance for compound (VI):

Scheme 4

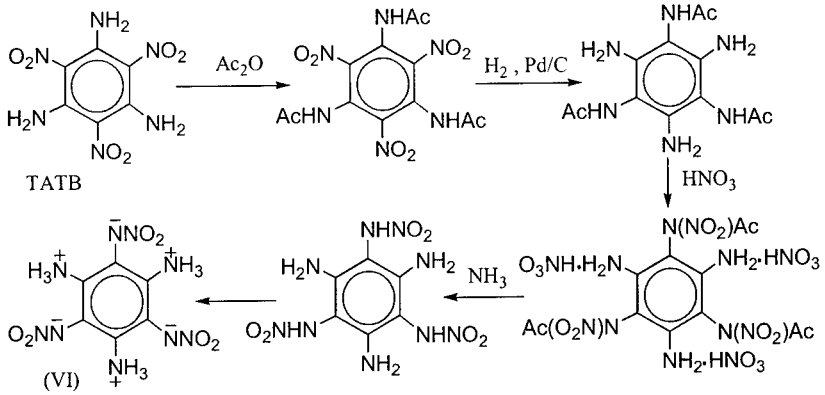

TATB (VI)

N-Nitro-S-methylisothiourea is a starting point for synthesized compound (VII):

Scheme 5

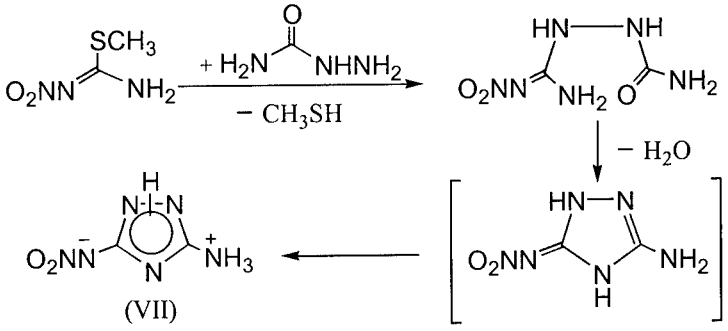

(VII)

CONCLUSION

Certain zwitterionic amine-nitramines physical, chemical, and energetic properties make some of them potentially interesting for use in liquid gun propellants, watery high explosives and various other water-based energetic systems. These properties include solubility in water in the presence of inorganic salts, relatively high content of hydrogen, low temperature of explosion, large volume of detonation products, and so on.

The compounds investigated have relatively small explosion heats (table 2), which is a direct consequence of a loss in neutralization heat when zwitterion formation occurs. It is possible to increase explosion heat by replacing aminogroup by hydrazinogroup:

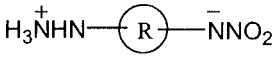

Analysis of the hypothetical zwitterionic hydrazine-nitramines is outside of the framework of this article.

The heterocyclic system can also act as a nucleophilic centre on which protonation occurs. 4-Nitramino-1,2,4-triazole (4-NRTZ) is an example of such a compound. Its zwitterionic structure was originally suggested in 1973 [10] but was only recently confirmed by X-ray analysis [1,11]:

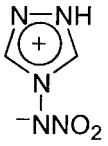

4-NRTZ

REFERENCES

[1] **Astachov A.M.** "Thermal decomposition of the primary nitramines in a condensed phase". Diss., Siberian State Technological University. Krasnoyarsk, 1999.

[2] **Stepanov R.S., Astachov A.M., Kruglyakova L.A.** "Influence of the primary nitramines structure on their thermostability". *Energetic Materials – Production, Processing and Characterization. 29th Intern. ICT-Conference.* **1998**. Karlsruhe. FRG. 128/1–128/7.

[3] **Sauer Ch.W.** U.S. Patent 2,786,078. "Stabilization of Methylenedinitramine". March 19. 1957.

[4] (a) **McKay A.F., Viron S.J.** "The hydrolysis of 1-nitro-4-methyl-2-nitramino-2-imidazoline". *J. Am. Chem. Soc.* **1950**. Vol. 72. N 9. pp. 3965–3966;

(b) **Hall R.H., Wright G.F.** "Reaction of acetyl chloride with 1-nitro-2-nitramino-2-propoxyimidazolidine". *J. Am. Chem. Soc.* **1951**. Vol. 73. N 5. pp. 2213–2216;

(c) **McKay A.F., Weinberger M.A., Picard J.P., Hatton W.G., Bedard M., Rooney H.E.** "The structures of nitroguanidine, 2-nitriminoimidazolidine and 1-nitro-2-nitriminoimidazolidine". *J. Am. Chem. Soc.* **1954**. Vol. 76. N 24. pp. 6371–6374;

(d) **Nilsson L., Noori G., Bergman R., Kesler E., Sterner O., Wickberg B.** "A novel synthesis of β-aminoalkylnitroamines. *rac*-β-Nitroaminoalanine and N-nitroethylenediamine, two reported metabolites from *Agaricus silvaticus*". *Acta. Chem. Scand.* **1983**. B37. N 10. pp. 929–933.

[5] **Starchenkov I.B., Andrianov V.G., Mishnev A.F.** "Chemistry of furazano[3,4-b] pyrazine. V. 1,2,3-Triazolo[4,5-e]furazano[3,4-b]pyrazin-6-oxides". *Khim. Geterotsikl. Soed.* **1997**. N 11. pp. 1565–1570 (in Russian).

[6] **Gorban A.N., Rossiev D.A.** "Neural networks for personal computer". Novosibirsk. Nauka, 1996 (in Russian).

[7] (a) **Mader Ch.L.** "Numerical modeling of detonation". Berkeley-Los Angeles-London. University of California Press, 1979;

(b) **Finger M., Lee E., Helm F.H., Hayes B., Hornig H., McGuire R., Kahara M., Guilry M.** "The effect of elemental composition on the detonation behavior of explosives". *Proc. 6 th Symp. (Int.) on Detonation*, San Diego, California, August 24-27, 1976. S. 1., s.a., pp. 172–181;

(c) **Gubin S.A., Odintsov V.V., Pepekin V.I.** "Thermodynamic calculation of ideal and nonideal detonations". *Fiz. Goreniya Vzryva* (*Combustion, Explosion and Shock Waves*). **1987**. Vol. 23. N 4. pp. 75–84 (in Russian);

(d) **Fried L.E., Souers P.C.** "BKWC: An empirical BKW parametrization based on cylinder test data". *Propellants, Explosives, Pyrotechnics*. **1996**. Vol. 21. pp. 215–223.

[8] (a) **Kamlet M.J., Hurwitz H.** "Chemistry of detonation. IV. Evaluation of a simple method for detonation velocities of C–H–N–O explosives". *J. Chem. Phys*. **1968**. Vol. 48, N 8. pp. 3685–3692;

(b) **Pepekin V.I., Lebedev Yu.A.** "Criterion for evaluation of the detonation parameters of high explosives". *Dokl. Akad. Nauk SSSR*. **1977**. Vol. 234. N 6. pp. 1391–1394 (in Russian);

(c) **Xiong W.** "A simple method for calculating detonation parameters of explosives". J. Energetic Materials. **1985**. Vol. 3. pp. 263–277;

(d) **Stine J.R.** "On predicting properties of explosives – detonation velocity". J. Energetic Materials. **1990**. Vol. 8. pp. 41–73.

[9] **Astachov A.M., Stepanov R.S., Kruglyakova L.A., Kekin Yu.V.** "1-Nitroimidazolidin-2-one and its hydrolysis to 1-amino-2-nitraminoethane". *Zh. Org. Khim.* (*Russ. J. Org. Chem.*). **2000**. Vol. 36. in press.

[10] **Katritzky A.R., Mitchell J.W.** "N-Oxides and related compounds. Part XLIII. Formation of N-nitroimides by base-catalysed nitration". *J. Chem. Soc. Perkin Trans.* I. **1973**. N 21. pp. 2624–2626.

[11] **Vasiliev A.D., Astachov A.M., Stepanov R.S., Kirik S.D.** "4-Nitramino-1,2,4-triazole". *Acta Crystallographica*. **1999**. C55. pp. 853–855.

Synthese und explosive Eigenschaften unempfindlicher energetischer NENA-Sprengstoffe

Synthesis and explosive properties of insensitive energetic NENA explosives

H. Ritter, M.R. Schäfer, B. Wanders, H.H. Licht

INSTITUT FRANCO-ALLEMAND
DE RECHERCHES
Boîte postale 34, F-68301 SAINT LOUIS

DEUTSCH-FRANZÖSISCHES
FORSCHUNGSINSTITUT
Postfach 1260, D-79574 WEIL AM RHEIN

Zusammenfassung

Wir haben durch Kombination von **N**itratoethyl**n**itr**a**minogruppen -$N(NO_2)$-CH_2CH_2-ONO_2 und energiereichen linearen Grundstrukturen die beiden neuen **NENA**-Verbindungen 1,11-Dinitrato-3,5,7,9-tetranitrazaundecan $C_7H_{14}N_{10}O_{14}$ und 1,12-Dinitrato-3,5,8,10-tetranitrazadodecan $C_8H_{16}N_{10}O_{14}$ erhalten. Diese hochenergetischen Explosivstoffe werden mit **TENA 1 und TENA 2** bezeichnet, da sie sowohl **TE**-tranitramine als auch NE-**NA**-Verbindungen sind.

TENA 1 und **TENA 2** sind mit Zersetzungspunkten um 200°C thermostabil und in ihrer Leistung zwischen PETN und RDX einzustufen. Ungewöhnlich gering ist die mechanische Empfindlichkeit: **TENA 2** zeigt erst bei 32 kp Stiftbelastung im BAM-Reibapparat und bei 10 Nm im BAM-Fallhammer die erste Reaktion bei sechs Versuchen, während **TENA 1** bei 36 kp bzw. 25 Nm überhaupt nicht reagiert. Beide Stoffe übertreffen damit in der Handhabungssicherheit sowohl den Nitratester PETN als auch die Nitramine RDX und HMX.

Abstract

By combination of **n**itratoethyl**n**itr**a**mino groups -$N(NO_2)$-CH_2CH_2-ONO_2 and energetic linear structures we obtained the two new **NENA** compounds 1,11-dinitrato-3,5,7,9-tetranitrazaundecane $C_7H_{14}N_{10}O_{14}$ and 1,12-dinitrato-3,5,8,10-tetranitrazadodecane $C_8H_{16}N_{10}O_{14}$.These high explosives are called **TENA 1** and **TENA 2**, being **TE**-tranitramines as well as NE-**NA**-derivatives.

TENA 1 and **TENA 2** are thermally stable (decomposition at 200°C) and their performance is classified between PETN and RDX. Their mechanical sensitivity is unusually low: **TENA 2** exhibits the first reaction at 32 kp with the BAM friction apparatus and at 10 Nm with the BAM drop weight test, whereas **TENA 1** does not react at 36 kp and 25 Nm, respectively. The new explosives exceed both the nitrate ester PETN and the nitramines RDX and HMX in terms of security of manipulation.

1. Einleitung

Verbindungen mit **N**itrato**e**thyl**n**itra**m**inogruppen -N(NO_2)-CH_2CH_2-ONO_2 - die sogenannten **NENA**s - sind als energieliefernde Weichmacher und Bestandteile von Sprengstoffen und Treibladungspulvern bekannt. Neben Diethanolnitramindinitrat **DINA** werden vor allem Methyl-, Ethyl- und Butyl-NENA eingesetzt, die eine energetische NENA-Gruppierung und einen inerten Alkylrest enthalten. Dadurch ist der Energiegehalt dieser Verbindungen wesentlich reduziert.

Eine Erhöhung der Leistung bei vertretbarer Empfindlichkeit kann durch die Kombination von NENA-Gruppierungen mit energiereichen Grundstrukturen erwartet werden. Wir haben uns deshalb das Ziel gesetzt, neue Verbindungen herzustellen, in denen zwei Nitratoethyl-Endgruppen CH_2CH_2-ONO_2 mit vier Nitraminogruppen N-NO_2 enthaltenden linearen Grundstrukturen kombiniert werden. Im Folgenden werden verschiedene Wege zur Herstellung von 1,11-Dinitrato-3,5,7,9-tetranitrazaundecan **1** und 1,12-Dinitrato-3,5,8,10-tetranitrazadodecan **2** diskutiert. Neben der erfolgreichen Synthese werden die charakteristischen Eigenschaften der ersten beiden NENA-Verbindungen beschrieben, die pro Nitratogruppe zwei Nitraminogruppen aufweisen. Wir nennen sie **TENA 1** und **TENA 2**, da sie sowohl **TE**-tranitramine als auch NE-**NA**-Verbindungen darstellen.

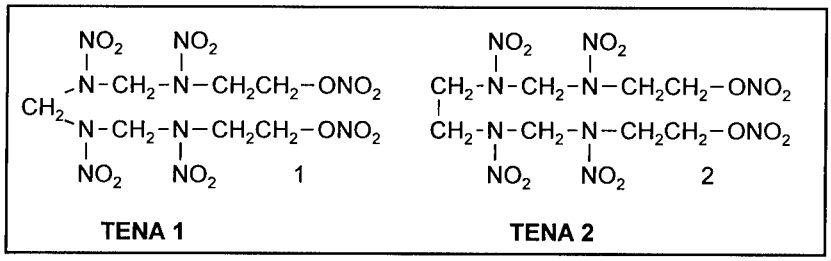

TENA 1 **TENA 2**

2. Synthese von TENA 1

Die Herstellung von NENA-Verbindungen wird meist durch Umsetzung einer entsprechenden Hydroxyethylaminoverbindung mit Salpetersäure durchgeführt, wobei N-H- und O-H-Gruppen nitriert werden. Auf diese Weise werden aus Diethanolamin, Methyl-, Ethyl- und Butylaminoethanol die bekannten Verbindungen DINA, Methyl-NENA, Ethyl-NENA und Butyl-NENA erhalten. Ein analoges Vorprodukt, aus welchem durch mehrfache Nitrierung **TENA 1** entstehen könnte, existiert jedoch noch nicht.

Es ist bekannt, dass die Abbaureaktion von Acetoxymethylnitraminen in saurem Medium zu recht verschiedenen Produkten führen kann. Aus dem durch Nitrolyse von Urotropin oder Tris(hydroxymethyl)hexahydrotriazin erhältlichen 1-Acetoxy-8-nitrato-2,4,6-trinitrazaoctan **3** [1] entsteht der Sechsring Hexogen **4**. Dagegen führt der Austausch der Nitratogruppe gegen ein Chloratom zum 1-Acetoxy-8-chlor-2,4,6-trinitrazaoctan **5** mit völlig veränderter Reaktivität: es ergibt bei der Hydrolyse durch komplexe Abbau- und Rekombinationsreaktionen das 1,11-Dichlor-3,5,7,9-tetranitrazaundecan **6** [2], wie Schema (1) zeigt.

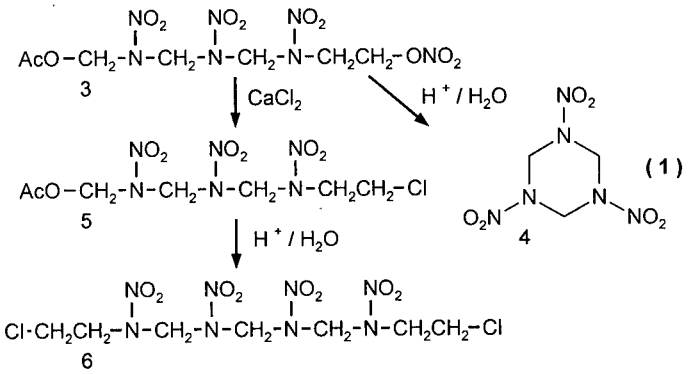

Die Reaktion der Dichlorverbindung **6** mit Silbernitrat stellt eine einfache Möglichkeit dar, um die gesuchte Dinitratoverbindung **1** herzustellen, ohne das Risiko von Nebenreaktionen durch die stark sauren Bedingungen einer Nitrierung einzugehen. Wir erhielten auf diese Weise das Dinitratoprodukt **TENA 1** [3] und konnten bei der chromatographischen Analyse der Reaktionslösung auch das erwartete Zwischenprodukt der Umsetzung, das 1-Chlor-11-nitrato-3,5,7,9-tetranitrazaundecan **7**, isolieren und durch NMR-Spektroskopie identifizieren (2) :

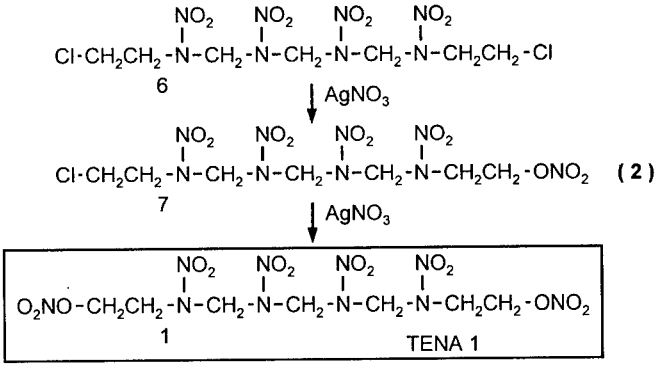

(2)

Zur Herstellung des Dichlortetranitramins **6** wurde ein zweiter Reaktionsweg untersucht, die Umsetzung von Methylendinitramin **8a** mit 1,4-Dichlor-2-nitrazabutan **9** [2]. Es zeigte sich jedoch, daß Produkt **6** hier nur mit Ausbeuten unter 10% gebildet wurde, obwohl das Nebenprodukt Triethylammoniumchlorid mit über 90% Ausbeute isoliert werden konnte (3) :

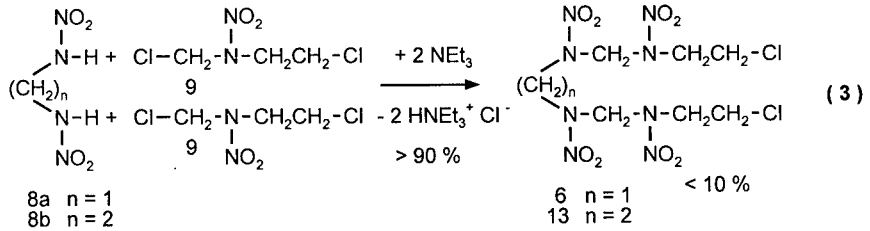

(3)

Da Bromidionen eine deutlich bessere Austrittsgruppe als Chloridionen darstellen, erschien es sinnvoll, die zu **6** analoge, aber bisher nicht bekannte Dibromverbindung herzustellen und mit Silbernitrat umzusetzen, um so das Herstellungsverfahren in Bezug auf Reaktionsdauer und Ausbeute zu optimieren. Hierzu wurde das Trinitraminderivat **3** mit $MgBr_2$ in 1-Acetoxy-8-brom-2,4,6-trinitraza-octan **10** umgewandelt, das bei saurer Hydrolyse das erwartete 1,11-Dibrom-3,5,7,9-tetranitrazaundecan **11** ergab, welches mit $AgNO_3$ zum **TENA 1** umgesetzt werden konnte. Trotz der erhöhten Reaktivität der Dibromverbindung **11** lassen die Ausbeuten von 34% bzw. 11% der ersten beiden Reaktionsschritte diesen Herstellungsweg als weniger geeignet erscheinen (4):

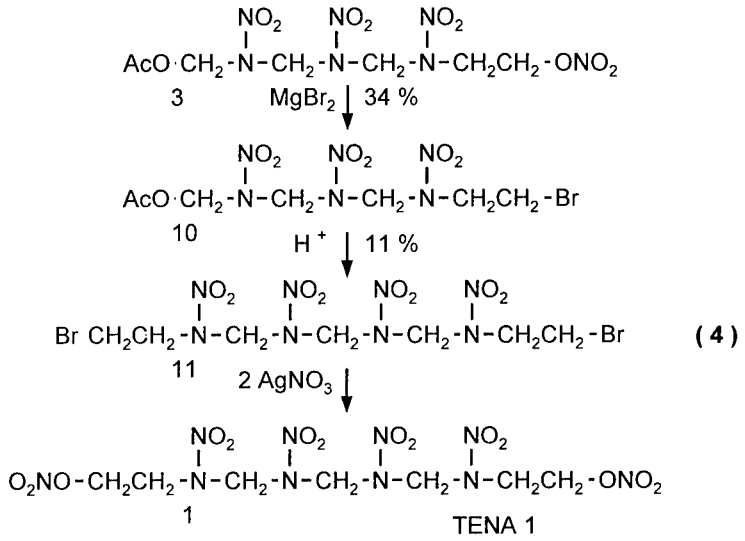

(4)

3. Synthese von TENA 2

Während auch im Falle des **TENA 2** ein nitrierbares Vorprodukt nicht bekannt ist, führt wieder eine Acetoxymethylnitramin-Abbaureaktion zu einer Dichlorvorstufe, die als Ausgangsstoff für die Herstellung von **TENA 2** dienen sollte. Durch saure Hydrolyse entsteht aus 1,6-Diacetoxy-2,5,7,10,12,15-hexanitrazahexadecan **12** [4] ein Tetranitramin mit zwei Chlorethylgruppen, das 1,12-Dichlor-3,5,8,10-tetranitrazadodecan **13** [5], das wir analog wie bei der Herstellung von **TENA 1** mit Silbernitrat über die Chlornitrato-Zwischenstufe **14** in die gesuchte Dinitratoverbindung **TENA 2** überführen konnten [6]. Das ebenfalls aus der Diacetoxyverbindung **12** herstellbare Dibromtetranitramin **15** erwies sich erwartungsgemäß als reaktiver bei der Umsetzung mit Silbernitrat. Aus beiden Dihalogenverbindungen wurde als Nebenprodukt das 1,7-Dinitrato-3,5-dinitrazaheptan **17** isoliert: Seine Bildung erklärt sich dadurch, daß das eintretende NO_3-Ion bei der Zwischenstufe **14** bzw. **16** nicht an der Bindung a unter Halogenid-Abspaltung angreift, sondern an der Bindung b, wie in Schema (5) gezeigt wird:

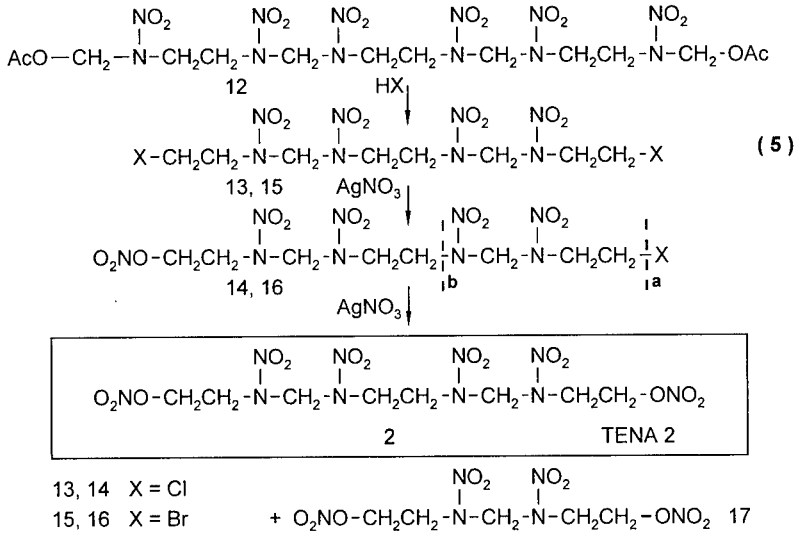

(5)

Der Versuch, das Dichlortetranitramin **13** durch die Umsetzung von Ethylendinitramin **8b** mit 1,4-Dichlor-2-nitrazabutan **9** entsprechend Schema (3) herzustellen, führte nur zu unbefriedigenden Ausbeuten an Verbindung **13** und war deshalb zur Herstellung größerer Mengen nicht geeignet.

4. Charakterisierung von TENA 1 und TENA 2

Bei der Herstellung neuer Verbindungen ist neben der IR-Spektroskopie vor allem die NMR-Spektroskopie dazu geeignet, bestimmte Strukturelemente eindeutig zu identifizieren. So zeigt der Vergleich der IR-Spektren des Dichlor-Tetranitramins **6** und des daraus hergestellten Dinitrato-Tetranitramins **1** (Fig. 2) deutlich neben den Nitraminbanden die Absorptionsbande der Nitratogruppen ONO_2 im **TENA 1**; diese ist auch in den IR-Spektren der Chlornitratozwischenstufe **7** (Fig.3) und des **TENA 2** (Fig.4) zu sehen. Weitere Strukturelemente sind dagegen im IR-Spektrum nur schwer zu identifizieren.

Den eindeutigen Beweis der Struktur dieser Verbindungen ermöglicht dagegen die ^{1}H-NMR-Spektroskopie. Wie Fig. 5 zeigt, treten bei Verbindung **6** aufgrund der symmetrischen Struktur vier charakterische Protonensignale auf: zwei Singuletts (2H und 4H) und zwei Tripletts (je 4H). Verbindung **7** mit einer Chlor- und einer Nitrato-Endgruppe weist eine unsymmetrische Struktur auf: wir erwarten nun drei ver-schiedene Singletts (je 2 H) und vier Tripletts (je 4H), die in Fig. 6 alle zu unterscheiden sind. Die ^{1}H- und ^{13}C-NMR-Spektren von **TENA 1** und **TENA 2** (Tab. 1) beweisen die symmetrische Molekülstruktur der neuen NENA-Verbindungen.

Tab.1: ^{1}H- und ^{13}C-NMR-Daten von **TENA 1** (in DMSO-d_6) und **TENA 2** (in Aceton-d_6)

nucleus	H	H	H	H	C	C	C	C
δ **TENA 1**	4.45	4.90	5.96	6.11	50.4	66.2	67.0	70.8
Integral	4H	4H	4H	2H	2C	1C	2C	2C
splitting	t	t	s	s	t	t	t	t
δ **TENA 2**	4.21	4.26	4.78	5.61	49.3	49.7	67.0	70.0
Integral	4H	4H	4H	4H	2C	2C	2C	2C
splitting	t	t	s	s	t	t	t	t

t = triplett, s = singulett

Die DTA/TG-Diagramme (Differentialthermoanalyse-Thermogravimetrie) von **TENA 1** (Fig. 7) und **TENA 2** (Fig. 8) zeigen die Thermostabilität der Stoffe. Dem Schmelzen bei 147°C bzw. 165°C folgt eine exotherme Zersetzung unter Gewichtsverlust; dabei wird das Maximum des DTA-Signals über 200°C erreicht, was auch bei Nitratoverbindungen wie **DINA** u.a. gefunden wird. Bei **TENA 1** tritt außerdem ein geringes endothermes DTA-Signal um 130°C auf, das wir einer Kristallumwandlung zuordnen.

Wesentlich für die sichere Handhabbarkeit und Verarbeitung eines Stoffs ist eine geringe Empfindlichkeit gegenüber mechanischer Belastung, die bei Nitratestern R-ONO_2 im Allgemeinen nicht auftritt. Bei Messungen mit dem Reibapparat JULIUS PETERS und dem Fallhammer der BAM zeigt bereits **TENA 2** eine geringe Empfindlichkeit gegen Reibung und Schlag mit Messwerten von 10 Nm und 32 kp. Ausgesprochen unempfindlich ist dagegen **TENA 1**: weder im Fallhammer mit dem 5 kg-Gewicht bei 50 cm Fallhöhe noch im Reibapparat bei 36 kp Stiftbelastung wurde bei **TENA 1** eine Reaktion in Form von Knall, Geräusch oder Zersetzung der Probe gefunden (Tab. 2).

Tab. 2: Reib- und Schlagempfindlichkeit von **TENA 1** und **TENA 2** und Vergleichsverbindungen (jeweils erste Reaktion von sechs Versuchen)

Verbindung	PETN	CL-20	RDX	HMX	**TENA 2**	**TENA 1**
Schlagempfindlichkeit (in N m)	3.5	3 [7]	4.5	4.0	**10**	**> 25**
Reibempfindlichkeit (in kp)	6	6 [7]	12	12	**32**	**> 36**

Die in dieser Größenordnung unerwartete Unempfindlichkeit des **TENA 1** verleiht dem reinen Stoff ohne weitere phlegmatisierende Zusätze die Eigenschaft eines IHE (Insensitive High Explosive). Der Vergleich der Strukturformeln des **TENA 1** und des ebenfalls recht unempfindlichen **TENA 2** erlaubt zwei Schlußfolgerungen:

- Nitratoethylnitraminogruppen -$N(NO_2)$-CH_2CH_2-ONO_2 NENA können im Gegensatz zu anderen Strukturen mit Nitratestergruppen –ONO_2 unempfindlich gegen mechanische Belastung reagieren.

- Die alternierende Anordnung von Methylen- und Nitraminogruppen im Grundgerüst des **TENA 1** ist auch ein Strukturelement mit hoher Unempfindlichkeit. Dagegen führt eine Ethylengruppe –CH_2CH_2- zwischen zwei Nitraminogruppen – der einzige Unterschied in der Strukturformel zwischen **TENA 1** und **TENA 2** – bereits zu einer geringen Sensibilisierung.

Da die Brisanz eines Explosivstoffs direkt proportional zu seiner Dichte ist, ist die Dichte eine wesentliche Eingabegröße zur Berechnung seiner Leistung. In Tabelle 3 sind die durch Gaspyknometrie bzw. durch Flotation erhaltenen Meßwerte der in Fig. 1 abgebildeten vier NENA-Verbindungen mit vergleichbarer Struktur angegeben, die zwei Nitratoethyl-Endgruppen und zwei bzw. vier Nitraminogruppen enthalten. Die mit dem Rechencode von STINE [8] berechneten Dichten dieser Verbindungen sind ebenfalls aufgeführt.

Fig. 1: Strukturformeln der NENA-Verbindungen BNE-MEDINA **17**, BNE-EDNA **18**, **TENA 1** und **TENA 2**

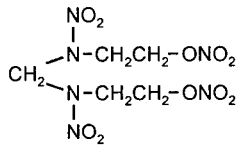

BNE-MEDINA 17

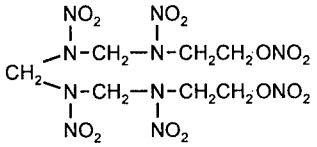

TENA 1

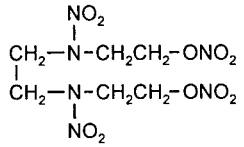

BNE-EDNA 18

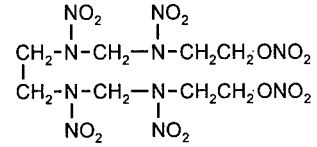

TENA 2

Tab. 3: Dichte von linearen NENA-Verbindungen mit zwei Nitratogruppen O-NO_2 und zwei bzw. vier Nitraminogruppen N-NO_2 (in g/cm^3)
a) berechnet nach STINE [8]
b) gemessen durch Gaspyknometrie bzw. Flotationsverfahren

NENA compound	**BNE-MEDINA 17**	**BNE-EDNA 18**	**TENA 1**	**TENA 2**
formula	$C_5H_{10}N_6O_{10}$	$C_6H_{12}N_6O_{10}$	$C_7H_{14}N_{10}O_{14}$	$C_8H_{16}N_{10}O_{14}$
ρ (calc.)	1.672	1.616	1.696	1.656
ρ (meas.)	1.75	1.65	1.69	1.73

Die berechneten Dichten liegen zwischen 1.62 g/cm^3 und 1.70 g/cm^3. Sie machen deutlich, daß bei NENA-Verbindungen mit vergleichbarer Struktur die Dichte mit der Zahl der Nitraminogruppen NNO_2-Gruppen ansteigt; sie sinkt jedoch durch die Einführung zusätzliche Methylengruppen CH_2.

Die Meßwerte der Dichte liegen bei **BNE-MEDINA**, **BNE-EDNA** und **TENA 2** stets deutlich über den Rechenwerten, was zeigt, daß die Aussage von Rechencodes durch Meßdaten überprüft und korrigiert werden muss. Für **TENA 1** wurde der nach STINE berechnete Wert von 1.69 g/cm^3 gefunden. Während im Falle des **TENA 2** (1.73) der von der Rechnung erwartete Anstieg im Vergleich zu **BNE-EDNA** (1.65), der Modellverbindung mit ähnlicher Struktur, gefunden wird, hat **TENA 1** mit 1.69 entgegen der Rechnung eine deutlich niedrigere Dichte als die Modellverbindung **BNE-MEDINA** (1.75). Es bleibt zu klären, welche Effekte dafür verantwortlich sind.

Detonationsgeschwindigkeit D und GURNEY-Energie $\sqrt{2E_G}$ beschreiben die Fähigkeit eines Stoffs, Beschleunigungsarbeit zu leisten. Anhand der Elementzusammensetzung und weiterer Eingabeparameter können diese Größen mit verschiedenen Codes berechnet werden, auch wenn ein Stoff bisher nicht hergestellt wurde oder keine ausreichende Stoffmengen vorhanden sind. Wir benutzten die Näherungsformel von ROTHSTEIN [9] und von KAMLET & JACOBS [10], um diese Leistungsdaten zu berechnen. Zum Vergleich sind die Daten der Composition B und der Sprengstoffe **PETN** und **RDX** aufgeführt, von denen der eine nur Nitratogruppen enthält, der andere nur Nitraminogruppen.

Tab. 4 : Detonationsgeschwindigkeit D und GURNEY-Energie $\sqrt{2E_G}$ von **TENA 1**, **TENA 2**, **PETN**, **RDX** und **Comp. B**
(berechnet nach ROTHSTEIN [9] bzw. KAMLET-JACOBS [10]

explosive	formula	density (g / cm³)	$\Delta H_f°$ (kJ / Mol)	D (ROTHSTEIN) (m / s)	D (KAMLET) (m / s)	$\sqrt{2E_G}$ (KAMLET) (mm / µs)
TENA 1	$C_7H_{14}N_{10}N_{14}$	1.69	- 100*	8613	8212	2.78
TENA 2	$C_8H_{16}N_{10}N_{14}$	1.78	- 101**	8324	8473	2.85
PETN	$C_5H_8N_4O_{12}$	1.77	- 532	8078	8694	2.91
RDX	$C_3H_6N_6O_6$	1.82	+ 70.6	8940	8869	2.94
Comp. B	$C_{4.58}H_{5.61}N_{4.82}O_6$	1.72	+ 23.3	8103	8020	2.70

* geschätzter Wert (anhand des bekannten Werts von **TENA 2**)
** gemessener Wert [6]

Obwohl die ROTHSTEIN-Formel eine Korrektur für Nitratogruppen enthält, weicht ihr Ergebnis bei **PETN** mit vier ONO_2-Gruppen deutlich von den fundierteren Werten nach KAMLET-JACOBS ab. Wie die Zahlenwerte in Tab. 4 zeigen, sind **TENA 1** trotz seiner relativ geringen Dichte und **TENA 2** in Bezug auf Detonationsgeschwindigkeit und GURNEY-Energie zwischen **PETN** und **RDX**, aber deutlich über Comp. B einzuordnen. Eine Messung der Leistungsdaten ist bisher noch nicht durchgeführt worden.

5. Literatur

[1] A.N.GAFAROV, L.N.PUNEGOVA, G.A.MARCHENKO, S.S.NOVIKOV
Nitrations of the Products of Condensation of Monoethanolamine and Formaldehyde in the Presence of Ammonium Nitrate
Russ.J.Org.Chem. **17**, 623 (1981)

[2] G.A.MARCHENKO, L.N.PUNEGOVA, T.S. SHITOVA, N.A. ROMAN'KO, L.S. EGOROVA, Y. M. KARGIN
Synthesis of N-Acetoxymethylnitroamine Derivatives and Investigation of Their Reactions
Russ.J.Org.Chem. **22**, 33 (1986)

[3] H.RITTER, B.WANDERS, H.H.LICHT
Hochenergetische NENA-Verbindungen. 2. Synthese und Charakterisierung von 1,11-Dinitrato-3,5,7,9-tetranitrazaundecan TENA 1
ISL-Bericht im Druck

[4] F.CHAPMAN, P.G.OWSTON, D.WOODCOCK
Studies on Nitroamines. Part VI. The Nitration of some Aminomethylnitroamines
J.Chem.Soc. **1949**, 1647

[5] V.P.IVSHIN, A.N.GAFAROV, T.N.IVSHINA, L.N.PUNEGOVA
Derivatives of Nitroaminomethanols III. Reactions of 1-Nitroaminomethyl Acetates in Acidic Media
Russ.J.Org.Chem. **17**, 435 (1981)

[6] H.RITTER, E. BUEB, M. SCHÄFER, H.H.LICHT
Synthese und Charakterisierung einer neuen hochenergetischen NENA-Verbindung : 1,12-Dinitrato-3,5,8,10-tetranitrazadodecan TENA 2
ISL-R **112 / 99**

[7] H. WILD
Personal communication

[8] S.R.STINE
"Prediction of Crystal Densities of Organic Explosives By Group Additivity"
Report LA-8920 (1981), Los Alamos Nat. Labs., NM, USA

[9] L.R. ROTHSTEIN, R. PETERSEN
Predicting High Explosive Detonation Velocities from their Composition and Structure
Prop.Expl., **4**, 56 (1979)

[10] M.J.KAMLET, S.J.JACOBS
Chemistry of Detonations. I. A Simple Method for Calculation Detonation Properties of C-H-N-O Explosives
J.Chem.Phys. **48**, 23 (1968)

6. Anhang: IR- und NMR-Spektren, DTA/TG-Diagramme

Fig. 2: IR-Spektren von 1,11-Dinitrato-3,5,7,9-tetranitrazaundecan **TENA 1** und 1,11-Dichlor-3,5,7,9-tetranitrazaundecan **6**

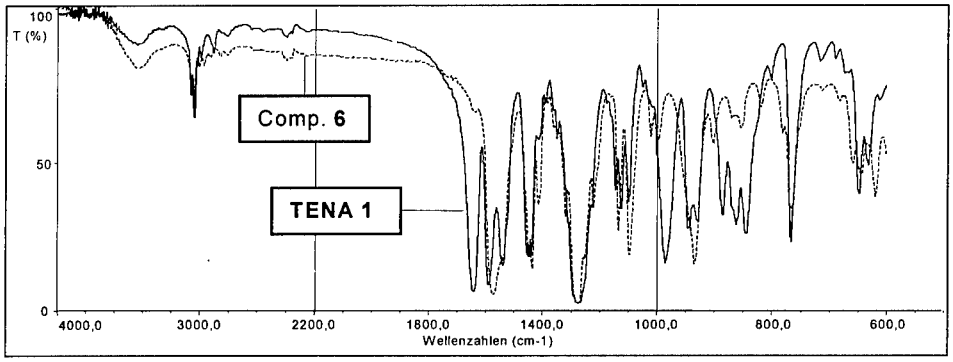

Fig. 3: IR-Spektrum von 1-Chlor-11-nitrato-3,5,7,9-tetranitrazaundecan **7**

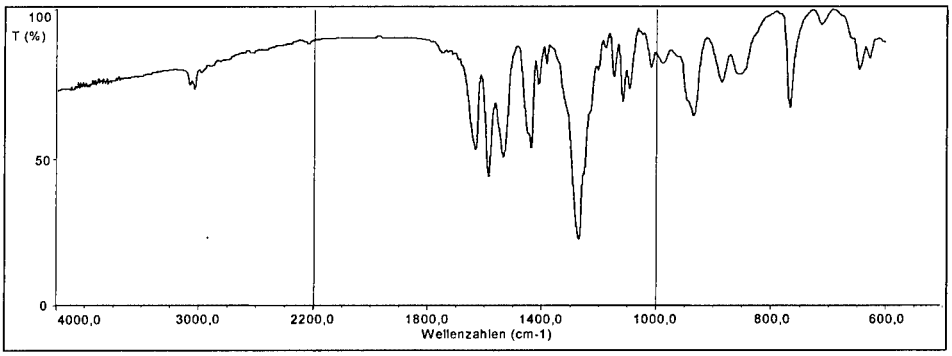

Fig. 4: IR-Spektrum von 1,12-Dinitrato-3,5,8,10-tetranitrazadodecan **TENA 2**

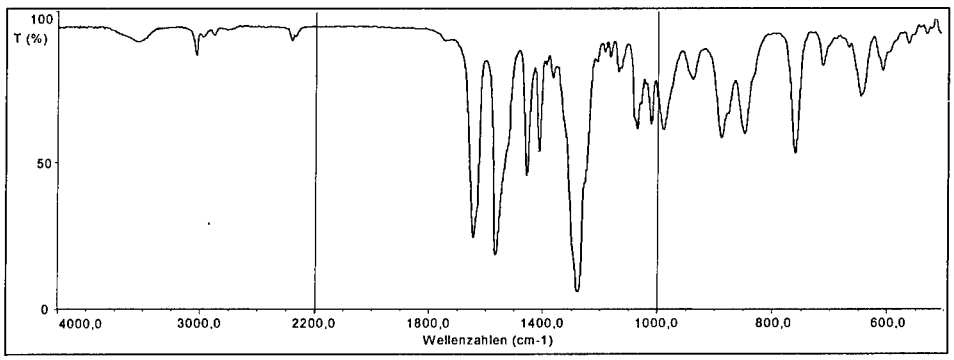

Fig. 5: ^{1}H-NMR-Spektrum von 1,11-Dichlor-3,5,7,9-tetranitrazaundecan **6** in DMSO-d_6

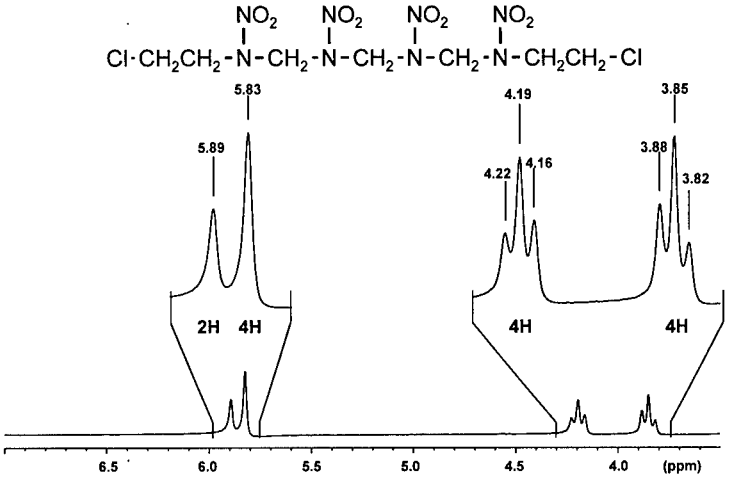

Fig. 6: IR-Spektrum von 1-Chlor-11-nitrato-3,5,7,9-tetranitrazaundecan **7** in Aceton-d_6

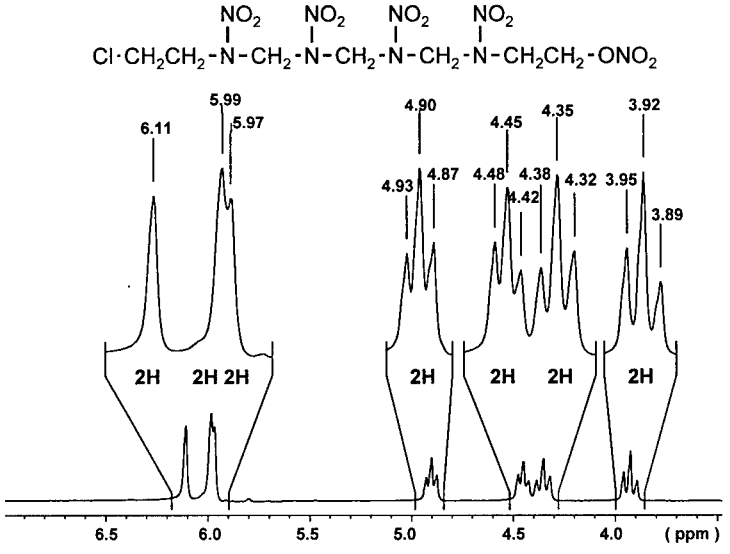

Fig. 7: DTA/TG-Diagramm von 1,11-Dinitrato-3,5,7,9-tetranitrazaundecan **TENA 1**

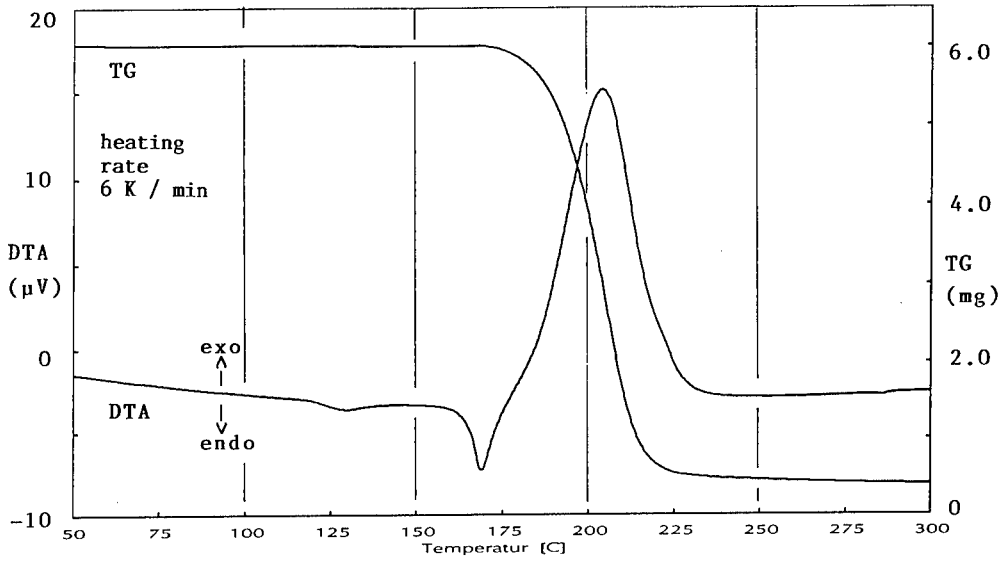

Fig. 8: DTA/TG-Diagramm von 1,12-Dinitrato-3,5,8,10-tetranitrazadodecan **TENA 2**

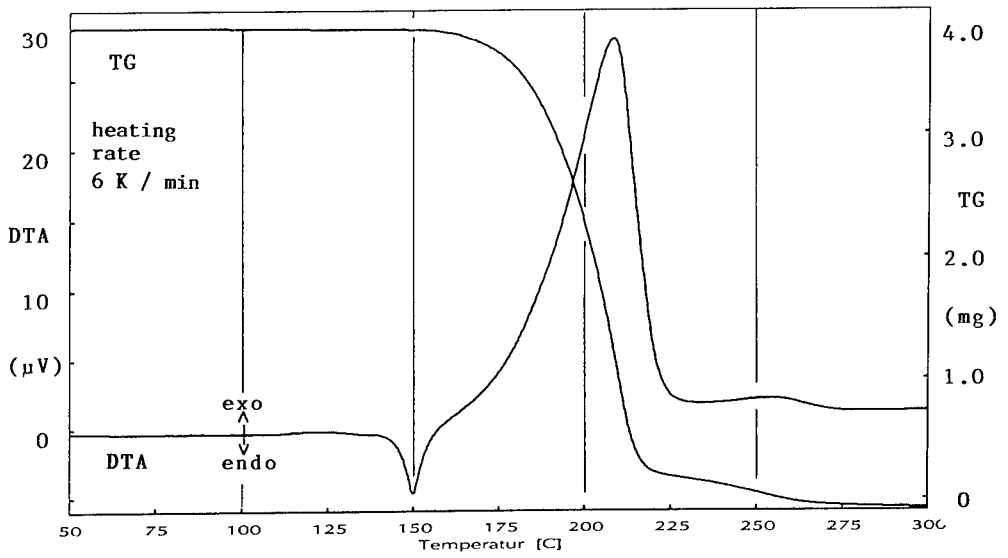

31st Int. Ann. Conf. ICT, June 27 - 30, 2000, Paper V15

ADVANCES IN CRYOGENIC SOLID PROPULSION

R.Lo, H.Adirim, S.Poller,
IRTS, ACE and Technical University of Berlin

N.Eisenreich, V.Weiser, S.Kelzenberg,
Fraunhofer Institut Chemische Technologie (ICT) Pfinztal

1. Abstract

Cryogenic solid propellants (CSP) constitute an entirely new class of chemical rocket propellants. By combining simplicity and reliability of solid propulsion with high Isp performance of liquid propulsion, their potential for propulsion system improvement is unique.
In on-going research since 1996 the feasibility of CSPs has been demonstrated both theoretically and experimentally.
This paper describes the state of the art as of May 2000.
It presents

- an introduction to the main principles and characteristics of CSP
- the status obtained in experimental research
- results of systems analyses concerning CSP effects on the performance of space transportation systems

2. Introduction

As an ideal, the requirements of future launchers call for high performance, low pollution designs of high reliability with competitive costs. The concept of modular cryogenic solid-rocket propellant grains is based on the idea that any conceivable chemical rocket propellant combination (including „green propellants") can be used as solid rocket propellant if the definition of solid propellants is not restricted to ambient temperature. This concept holds marked promises in all of these areas.

High performance in terms of high specific impulse ensures low propellant consumption per unit payload. However, liquid propellant rocket motors achieve high performance through very demanding design constraints such as sophisticated thermodynamic cycles and extremely high combustion pressure. Advanced high performance liquid propulsion needs complicated technology that leads to high cost and reduced reliability. This is a lesson learned in a decade of experience with the Space Shuttle Main Engine. In contrast, a solid rocket motor is simple and therefore reliable. Apart from thrust vector control by nozzle swiveling, that replaces the engine gimbaling of liquid propellant motors, solid propulsion has no moving parts. On the other hand, solid propellant motors are not suited for high chamber pressure. This is also true for CSP-motors. However, simply using frozen liquid propellants at conventional chamber pressures (around 60 bar) yields truly high performance propulsion systems compared with storable solid propellants. More than that, if CSP motors of modular design are used (see fig.1) they are even safer with respect to combustion instability than conventional solids, because quasi-premixed monopropellant combustion is replaced by hybrid type boundary layer combustion.

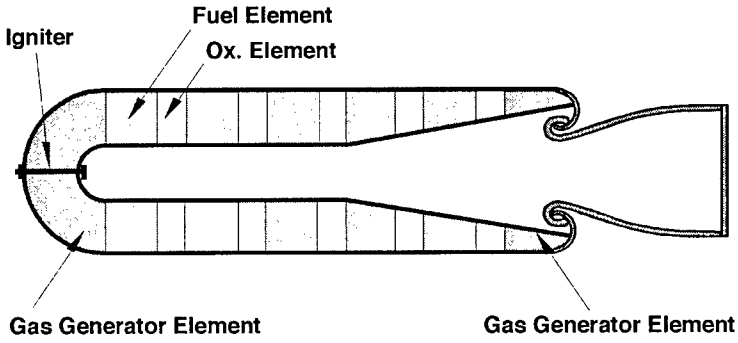

Fig.1: Schematic of solid rocket motor with modular disk stack grain

Low pollution requires careful selection of propellants and a matching design of the vehicle and its mission. Among conventional solid propellants, the compositions used in large amounts in space transportation systems are quite infamous due to their production in large quantities of combustion products that are detrimental to the atmospheric environment (mostly HCl and Al_2O_3). Unfortunately it was shown [see Lit.1,2,3] that there is no such thing as an absolutely environmentally benign rocket propellant. At high altitudes, even simple water vapor is transformed into chemical species that help destroy the ozone layer. However, using CSP systems will have drastic effects on pollution in two ways: first, choosing AP free oxidizers and nonmetallic fuels, alumina smoke and hydrochloric acid will disappear as booster exhaust products and second, for a given total impulse, the lower propellant mass required by CSPs shall reduce the absolute amount of emissions.

Low life cycle costs implicate low development effort, simple vehicle design and operations. CSP technology was independently invented in the 1960ies in the USA [4] and by one of us (Lo [5]). However, since then it has never been subject to any investigations and hence is certainly a new area of R&D. Under these circumstances it would be unrealistic to claim that CSP development was

not good for surprises, including costly ones. However, on-going research indicates a high likelihood that there will be no man-traps in CSP development. While on one side all chemistry and production technology of modular CSPs is much simpler than with conventional solids, there is no reason to believe that CSP cooling and handling should be fundamentally different to cryogenic liquids. In effect, while all CSPs are frozen liquids, their freezing temperatures cover a wide realm between (in principle) kitchen refrigerator and liquid Helium cooling. Applied to reusable space launch vehicles, much will depend on CSP operations. Hence, these are one of the focal points of present research activities.

CSPs are thus a category of chemical propulsion that includes the performance of any liquid propellant combination in use (Isp about 450s 68:1, E) To get beyond this mark, one could use any high energy propellant combination that has ever been suggested, such as liquid bipropellants, tripropellants and metal combustion. More than that, one can also consider super high energy propellants. These are chemical propellant combinations of the highest known values of Isp that approach or even surpass the Isp of nuclear propulsion (900s and beyond).

Many of the propellants in all the classes mentioned above require the use of materials that are unstable in terms of chemistry or mechanical properties (e.g. slurries). The deep temperature solid state of CSPs is very advantageous in both respects. Indeed, some of the more futuristic chemical propellants, such as atomic Hydrogen (Isp about 1800s) rely on solid frozen matrix isolation. Such propellants can either be used in hybrid motors (solid element in combustion chamber burnt with injected liquid component) or in CSPs that use all solid propellants. The former approach is used since 1995 in the High Energy Density Matter program of the USAF. The latter is our approach, that

offers, compared with hybrid combustion, a further degree of freedom and is immune against mixture ratio fluctuation, one of the most inconvenient phenomena of hybrid combustion. As in hybrids, deflagration is also replaced by boundary layer combustion in CSPs. However, the arrangement that was dubbed "Multilayer Internal Hybrid Combustion" promises much better combustion efficiencies and a given mixture ratio can be enforced by proper element size selection.

Thus, the concept opens a whole area of new chemical propulsion research and development.

Cryogenic Solid Propulsion (CSP) is now in its 4th year of theoretical and experimental research under German governmental sponsorship.

3. Burning Behavior of Cryogenic Solid Propellants in Modeling and Experiment

CSP-technology can be realized in two versions:

1. Premixed cryogenic propellants (mono-CSP) follow the burning behavior of solid propellants (see fig. 2).

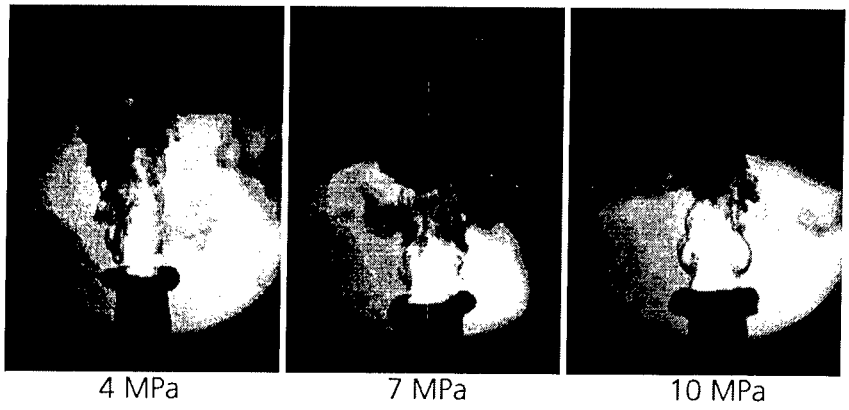

Fig. 2 Steady burning of premixed cryogenic solid propellant observed in a window bomb under various pressures (stoichiometric mixture of methanol and H2O2 70%)

Experiments with mono-CSPs have been carried out under inert pressure conditions in a window bomb using cinematography and spectroscopy. As test materials were used oxidizers like N_2O_4 and H_2O_2 (70%) and fuels like methanol, 2-propanol or isopropylnitrate. Mono-CSPs show stable burning behavior with a constant regression rate which obeys the exponential Law of Vieille under varying pressure conditions. Above the surface, they form a thin liquid layer that has constant thickness under isobaric conditions and decreases with pressure. The use of premixed mono-CSPs is limited to compatible compounds. Their ignition requires more energy due to the low initial temperature and the two phase transitions. The modeling of the burning behavior corresponds to classical mono-propellant modeling of transient burning which includes the heating and phase transitions energies within the condensed phase without a surface reaction. The regression rate is dominated by the heat feedback from the flame which dominates the combustion regime.

2. Another approach is to arrange oxidizer and fuel as separate grains (modular arrangement). This gives the advantage of high safety and provides influencing the burning behavior by grain geometry. Two versions have to be distinguished: externally controlled systems (e. g. by heat from an external gas generator) and self-sustained systems. Up to now only self-sustained systems have been investigated. Examples of simple arrangements consist of a disk stack or a rod-in-matrix burner. An example of the second type is a strand burner with 2-propanol or isooctane fuel rods embedded in a matrix of frozen H_2O_2 (85%) oxidizer (fig. 3).

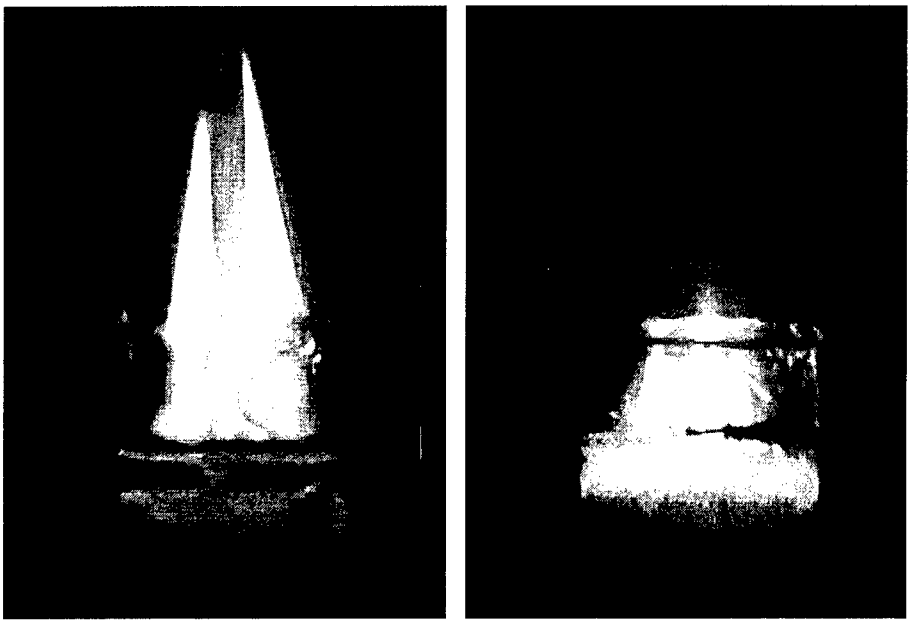

Fig. 3 Rod-In-Matrix configuration of CSPs a) 2-propanol/H2O2 (85%) b) iso-octane/H2O2

Rod diameters were chosen for an overall stoichiometric composition. This particular system shows self sustained combustion in an inert pressure atmosphere. A luminous flame zone stabilizes above a thin melting layer. In the case of 2-propanol (miscible with H_2O_2(85%)) a broad flame is formed, while non-miscible isooctane develops diffusion flames over each fuel rod. Under pressure the overall burning rate of these rod-in-matrix burners is in a similar range as in the case of mono-CSPs. Modeling of modular arrangements also uses heat and mass transfer between hot gaseous reaction zone and condensed phase. Estimations of the heat flux can be based on a burning model of diffusion controlled composite propellants (Summerfield) or more sophisticated on numerical CFD-modeling of reacting gas flows combined with boundary layer effects.

At the next step a linear organ-pipe window-burner with an integrated gas burner is in design. With this system it will be able to simulate a gas generator and to control heatflux to the module surface in a wide range without a feedback mechanism between the gasgenerator burning rate by pressure and propellant flame heatflux. Tests with a first minimal system have performed and show encouraging results (fig. 4)

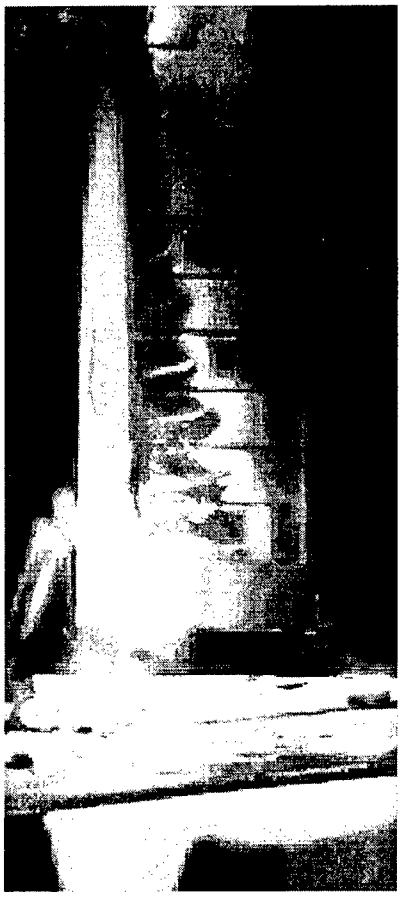

Fig. 4 CSP burning in vertical organ-pipe configuration controlled by a bunsen-type burner

The burning behavior of CSPs is described in more details in [6]. Recent experiments with CSPs resulted in encouraging combustion behavior showing no serious technical obstacles and open a broad spectrum of applications in rocket propulsion.

4. Performance & Cost Modeling of CSP Launchers

So far, ongoing analyses have not shown any insurmountable problems in areas of concern, e.g. cooling equipment and its operation during fabrication and launch; neither were there problems with thrust to weight ratio of uncooled but insulated Cryogenic Solid Boosters (CSBs) which ascend into their trajectory while leaving the cooling equipment at the launch pad.

Performance calculations for new launchers with CSP-replacements of boosters or existing stages were made. ARIANE 5 and a 3-stage launcher with CSP - 1st stage (Fig. 5) served as examples. In a first step, expendable launch vehicles in the payload classes of 6,8 and 12 Mg into GTO were analyzed more deeply. In the second step, based on the results obtained - further launcher categories like semi reusable launch vehicles, small launchers like VEGA, as well as very big ELVs (HLLV-Class) should now also be analyzed.

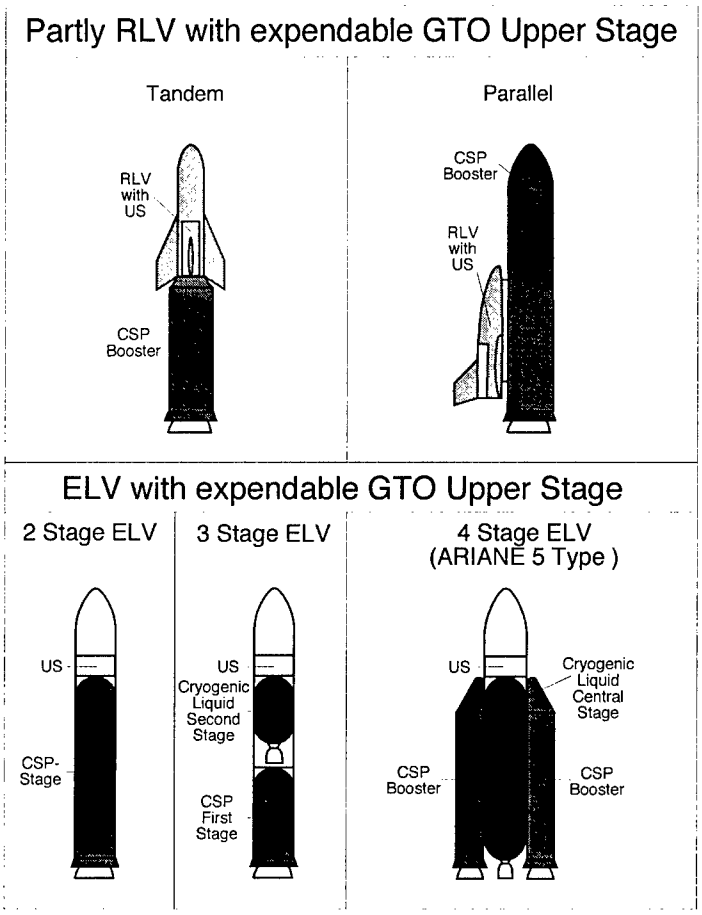

Fig. 5: Possible semi-reusable (RLV) and expandable (ELV) applications of CSP-motors (green)

4.1 Comparability and General Design Process

The goal is to find out which performance improvements result by the substitution of the conventional solid-boosters with boosters using cryogenic solid propulsion (CSPs).

In order to achieve a maximum possible comparability the central stage (EPC) and the upper stage (EPS) remain untouched. This can result in an individual disadvantage for the propellant under consideration, since for example decreasing booster dry mass causes higher acceleration at the end of the flight phase. Assuming that other parts of the rocket remain untouched, the constraints for acceleration, heat-flow-density and dynamic pressure also remain unchanged. However, since all these parameters are coupled with flight-velocity, this leads sooner to critical parameters in lighter rockets than in heavier ones.

The first step of modeling changes comprised replacement of the two solid-boosters EAP with CSP motors. The central-stage EPC and the upper-compartment remained unmodified. This yields two alternative concepts based on ARIANE 5: a launch-system with the same payload-capacity (6,8 Mg in GTO), and a system with the same launch-mass (746 Mg). Because maximum take-off acceleration was chosen as with ARIANE 5, the burning time of the Cryogenic Solid Boosters was not the same as that of the EAP.

4.2 ARIANE 5 / CSP with constant Payload

For same payload-capacity in the reference orbit, the modeling of a rocket system with cryogenic boosters essentially requires a process of iteration, in which the propellant mass is varied as central parameter and - with the help of a CSP mass-model - all other dimensions of the booster are derivedaccordingly. The process is repeated until the payload resulting from

GTO track-optimization corresponds with that of ARIANE 5 in good approximation.

Under the assumptions used, the application of cryogenic SOX/SH_2–boosters lead to a clear reduction of the launch mass. This is essentially caused by the lower propellant mass while the dry-mass is hardly reduced due to the low-density of this bipropellant and the resulting large combustion chamber dimensions. Presumably, hydrocarbon-booster-combinations appear most advantageous from an economic point of view. In particular, solid Methane (SCH_4) and above all frozen kerosene (SRP1) promise very simply handling. The melting region of kerosene lies at a comparatively elevated temperature. This is irrelevant together with SOX (since the coldest material present determines the bulk motor temperature) however, in combination with higher-melting oxidizers it grows much more attractive. Foremost the savings due to lesser insulation equipment should lead to a clear weight-reduction in contrast to the lower melting fuel-combinations.

In the following Fig. 6 (a) an overview of the results with ARIANE 5-versions is presented. Vis-a-vis ARIANE 5 the launch mass of the CSP-launcher with equal payload capacity is decreased by about 30%.

4.3 ARIANE 5 / CSP with the constant Payload

Results obtained with mass modeling of ARIANE 5-derivatives with same launch mass are shown below. Booster diameters were increased to 3,7 m due to the higher optimum CSP propellant mass. Resulting payloads were down-scaled, taking into account the mass changes of propellants and structures of the upper stage EPS, leading to the values shown in Fig. 2 (b).
As Fig. 6 (b) suggests, all launchers are able to lift approximately 10 Mg in GTO._Concerning the structure mass of the boosters, the kerosene-version

yields the best results, followed closely by Methane-CSB. The SOX/SH_2-version shows the highest structure mass and has the largest dimensions. It awaits to be analyzed whether a distribution of the CSP-propellant to three or even four boosters would not yield better results.

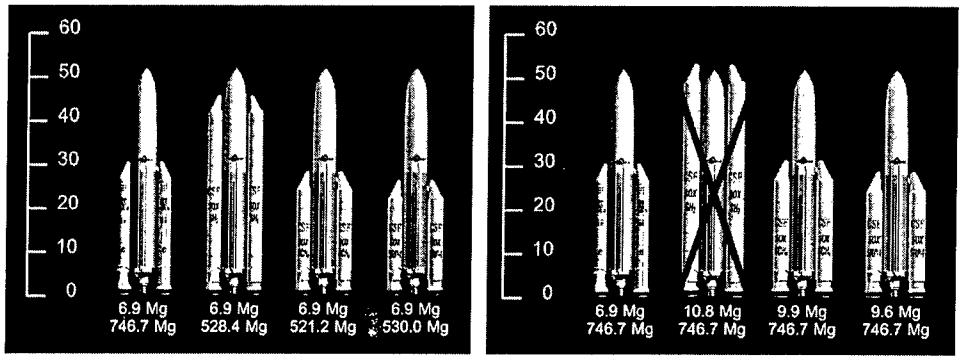

a b

Fig. 6 ARIANE 5 derivatives with constant payload (a) or constant launch mass (b). Height in [m] is shown, from left to right, of: ARIANE 5/EAP, ARIANE 5/CSP-SOX/SH2, ARIANE 5/CSP-SOX/SCH4 and ARIANE 5/CSP-SOX/SPR1.

4.4 Performance Modeling of a 3-Stage Launch Vehicle with CSP-1st Stage

Another concept examined was a purely hypothetical EEELV, European Evolved Expendable Launch Vehicle, based on the assumption that the two solid-boosters EAP of the ARIANE 5 were replaced by a single CSP-1st stage. The second stage was adapted from the ARIANE 5 central EPC just by changing the length of the cylindrical segments. An imperative structure-reinforcement of the EPC was not taken into account in the first step. The Upper Compartment consisting of the upper stage EPS with AESTUS-engine,

VEB, payload and payload-adapter as well as fairing was used without changes.

As a reaction to the trend to higher accelerations as shown above, an adapted thrust-profile was chosen for these stages. Also for this launcher, the payload was calculated through an iteration of the initial value and adapted to the reference-mission of ARIANE 5-EAP. As central parameter the propellant mass was varied and determines all other dimensions of the booster along with the CSP mass-model. The process was repeated until the resulting GTO payload agreed with that of the ARIANE 5 in good approximation after trajectory optimization.

4.5 Staging Optimization

By using a classic staging optimization, the most favorable propellant distribution between first and second stage was determined. It should be considered that in case of larger 1st stages and consequently higher stage-separation the EPC VULCAIN-engine must be ignited in vacuum.

Due to the limited performance of the VULCAIN engine the propellant mass of the second stage had to be kept smaller than the optimized result of approximately 118 Mg. Application of the VULCAIN II engine currently under development would lead closer to the optimum.

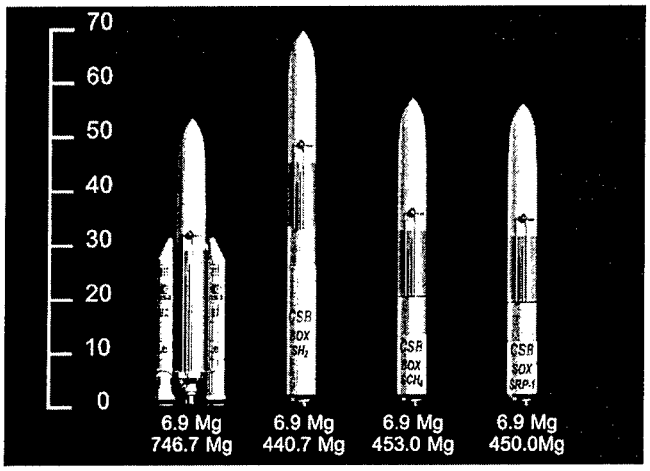

Fig. 6c ARIANE 5 derivatives with constant payload. Height in [m] is shown, from left to right, of: ARIANE 5/EAP, EEELV/CSP-SOX/SH2, EEELV/CSP-SOX/SCH4 and EEELV/CSP-SOX/SPR1.

Clearly, under the assumptions used, the application of CSP-1st stages leads to a substantial reduction of launch mass. Again, this is essentially caused by the reduced propellant mass while the masses of structures remain more or less constant.

4.6 Cost Modeling

Cost modeling was performed under contract as well as in-house work by Daimler Chrysler Aerospace, Space Infrastructure at Bremen (now a subsidiary of ASTRIUM). PRICE-H, a parametric cost estimation tool, was used for calculating costs of flight-hardware and for establishing a set of CERs (Cost Estimation Relationships) for ground infrastructure- and operations costs. The cost modeling is based on a detailed cost break-up. The procedures were developed and applied by DASA within the FESTIP-System study.

The cost estimation includes development, production and operations of the ELVs. The cost for production and operations refer to the first three business years with a mean average of 8 flights per year.

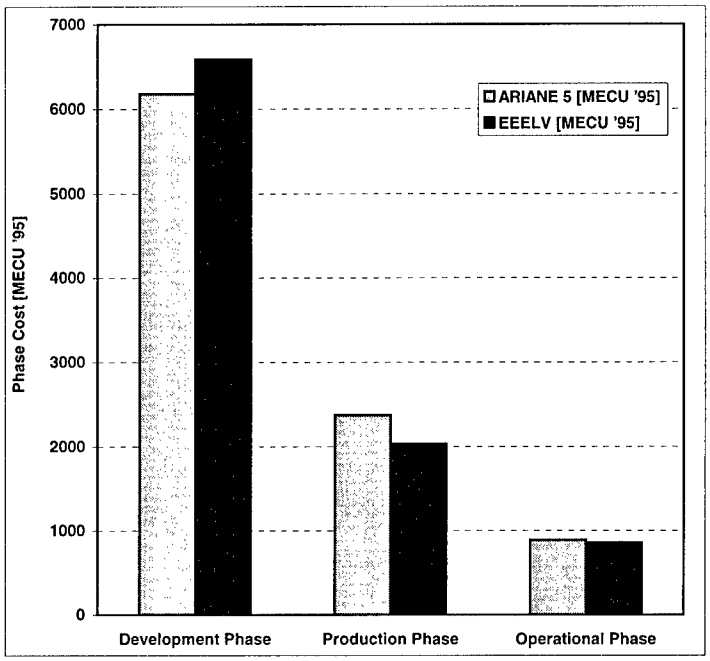

Fig. 7 Total phase cost investigated for ARIANE 5 and EEELV/CSP-SOX/SPR1 derivative with same payload.

As shown in Fig.7 in the first approach the development and production cost of a 3-stage launcher with CSP 1st stage (SOX/SRP1) were calculated and compared with the cost of ARIANE 5. CSP-1st stage is more affordable than ARIANE 5 boosters, even if CSP-propellant costs were assumed pessimistically with SOX/SRP1 propellant prices of up to 94 EURO/kg. The launch-costs of a 3-stage launcher with CSP-1st stage are approximately 12% (15,4 MECU) under the cost of ARIANE 5.

5. Conclusions

Even under conventional assumptions (concerning regression rate in a steel casing with foam insulation), substantial performance gains were calculated when ARIANE 5 was taken as a generic example and its storable solid boosters were replaced by cryogenic ones. CSPs lead to considerably higher performance when the boosters are substituted by a single CSP boost stage (SOX/SH_2, SOX/SCH_4 or SOX/SRP1). Using trajectory simulation and optimization tools, launcher performance calculations have been made. At constant lift-off mass a derivative of ARIANE 5 that has two Cryogenic Solid Boosters instead of the EAPs could lift 10 Mg payload to GTO. Using a single boost stage and a shortened second stage, another derivative that lifts the same payload as ARIANE 5 has, after optimization, a gross take-off weight that is reduced by 30-40%.

In order to identify economic benefits or disadvantages of the CSP propelled launchers in comparison to ARIANE 5 as reference, preliminary cost assessments have been made. As it turns out, any increased costs for production and handling of the CSP engines are outweighed by increased performance. However, many technical issues will have to be solved before costs can be estimated to a higher degree of confidence.

6. Abbreviations

AFOSR	Air Force Office of Sci. Research
CSB	Cryogenic Solid Booster
CSP	Cryogenic Solid Propulsion
EAP	Etage d'Accélération à Poudre
EPC	Etage Principal Cryotechnique
ESA	European Space Agency
GTO	Geostationary Transfer Orbit
GEO	Geostationary Earth Orbit
GTOW	Gross Take-Off Weight
HEDM	High Energy Density Matter
HNF	Hydrazonium Nitroformate
HTPB	Hydroxyl-Terminated Polybutadiene
IAF	International Astronautical Federation
LEO	Low Earth Orbit
LH_2	Liquid Hydrogen
LOX	Liquid Oxygen
MEO	Medium Earth Orbit
MMH	Monomethyl Hydrazine
NTO	Nitrogen Tertroxyde
SH_2	Solid Hydrogen
SHEP	Super High Energy Propellants
SOX	Solid Oxygen
SRP1	Solid Kerosene
TU	Technical University
USAF	United States Air Force

7. Literature

[1] M. E. Voslamber, J. A. Leppich, R. E. Lo: „World Wide Emissions due to Rocket Launches", 21st General Assembly der Geophysical Society, Den Haag, 9.Mai 1996

[2] J. Leppich, R. Lo: „German Data Base of Space Flight Induced Atmospheric Pollution" in „Impact of Emissions from Aircraft and Spacecraft Upon the Atmosphere", U. Schuman, D. Wurzel, Eds., DLR-Mitteilung 94-06, 1994

[3] R. Lo, J. Leppich: "Emissions Due to Space Activities: Facts and Models", Vortrag am EGS XVIII General Assembly der European Geophysical Society, Session OA22/ST19, Wiesbaden May 3-7, 1993

[4] A.V.Grosse, A.G.Streng, Research Inst. of Temple Univ., Philadelphia: "Method of Developing High Energy Thrust", US-Pat. 3.137,127 v. 16.6.1964

[5] R.E.Lo, DVL Lampoldshausen: "Technical Feasibility of Chemical Propulsion Systems with very high Performance" Proceedings of the XVIIIth Astronautical Congress, Belgrad, 25.-29.9.1967, pp. 121-132

[6] V. Weiser; S. Poller; N. Eisenreich; St. Kelzenberg; R. Lo; H. Adirim; Burning behavior of cryogenic solid propellants; 31st International Annual Conference of ICT, 2000, Karlsruhe, pp. 145 (accepted)

8. Further Bibliography

1. M.Thierschmann, R.E.Lo: "Technical Limits Of Using Atomic Hydrogen, Metallic Hydrogen And Electronically Excited Helium As Rocket Propellants", "International Seminar on HEM", 19.-21.11.1996, High Energy Materials Research Laboratory (HEMRL) SUTARWADI, PUNE-411 021 India
2. E.Carrick, Patrick G., USAF, Phillips Lab., Edwards AFB, CA, "Theoretical performance of high energy density cryogenic solid rocket propellants" 31st, AIAA Joint Propulsion Conference and Exhibit, San Diego, CA, July 10-12, 1995, (Jul 1995)
3. R.E.Lo: "Modular Dissected Cryogenic Solid-Rocket Propellant Grains", 49th Int. Astronautical Congress, Melbourne, Australia, Sept.29.1998, Session S.3, Space Propulsion Technology, IAF-98-S.3.10
4. R.E.Lo: „A Novel Kind of Solid Rocket Propellant", Aerospace Science and Technology, Elsevier, 1998.
5. R.Sandri: On the Decomposition Flame of Liquid Ozone-Oxygen Mixtures in a Tube", Combustion and Flame, No 2, 1958.
6. R.E.Lo, J.Leppich, H.Adirim: "Heat Transfer Problems of Cryogenic Solid Rocket Motors", Presentation on the International Scientific Conference "Rocket and Space Technology: Fundamental Problems of Mechanics and Heat Transfer", Moscow, 10-12 November 1998.
7. „IAA Advanced Space Propulsion Concepts Workshop", Final Documentation, El Segundo 1998, Internet: http://www.aero.org/apw/

8. H.D.Froning, R.E.Lo: "Possible Revolutions in Rocket Propulsion", IAA-98-IAA.3.3.03. 1998.
9. R.E.Lo: "Modular Solid Rocket Propellants" German Patent Application No DE 197 56 794 A1, 19.12.1997.
10. R.E.Lo: "Modular Solid Rocket Propellants with Casings, Fill-drain System, Cooling and Suspension" German Patent Application No DE 198 22 845 A1, 22.5.1998.
11. H.Adirim: "System Analysis and Modeling of Cryogenic Solid Propulsion", Dissertation Preprint, Berlin 1999.
12. H.Adirim, R.E.Lo, A.Paatsch: "Next Generation High Performance Low Pollution Launchers: Problems and Solutions", IAA-99-IAA.3.3.01 1999.
13. R.E.Lo, H.Adirim: "Cryogenic Solid Launchers – A New Class of High-Thrust Motors", Meeting of the DGLR Expert Group 4.1 Space Transportation Systems, Nov. 10, 1999 Bremen.
14. R.E.Lo, H.Adirim: "Cryogenic Solid Propulsion for Reusable Space Transportation", 1st FLTP Workshop on Future Reusable Launcher Technologies, November 22/23, 1999 ESTEC.

DEVELOPMENT OF RECRYSTALLISATION PROCESS FOR SUPERFINE PETN FROM LABORATORY TO FULL PLANT SCALE

Melinda du Plessis

Somchem, Division of DENEL (Pty) Ltd, Product Development & Technical Support,
PO Box 187, Somerset West, 7129, South Africa

Abstract

This paper portrays a practical approach to the development of a recrystallisation/ precipitation process for PETN, taking it from laboratory to full plant scale. The purpose of this recrystallisation process was to modify attributing characteristics of the existing PETN crystals regarding processability by altering the size and shape of its crystals. The aim was to produce superfine needle like PETN crystals.

This paper describes experimentation and optimisation on laboratory scale (1 to 2 litres); addresses practical considerations regarding future scale up and evaluating the results. It then deals with experimentation on pilot plant scale (50 to 200 litres) which serves as a test for the workableness of the process on larger scale and confirmation of the laboratory results obtained. Successful experimentation on pilot plant scale provided the foundation for future scale up.

The final step involves implementing the proposed recrystallisation process on full plant scale, submitting the product for final approval and assessing the feasibility of the process for future production.

1 INTRODUCTION

Pentaerytritol tetranitrate (PETN) is a high explosive. The processability and explosive properties of PETN are closely related to the shape, size and porosity of its particles. The final application and utilisation of the PETN dictates the characteristics required for the particles. The request in this instance was to modify PETN from big (150 to 300 μm) raspberry like crystals to superfine (~12 μm) needle like crystals.

A literature study was conducted to gather as much information as possible on the recrystallisation of superfine PETN crystals. The idea was not to rediscover basic principles, but implement basic principles and optimise process conditions to meet product specifications, taking into account plant capabilities available for scale up of the optimised process in future.

This paper portrays a practical approach to the development of a process for the production of superfine PETN on full plant scale. The first step is to identify a practical process feasible for scale up to produce superfine PETN in bulk. A recurring problem in the past was that although an almost perfect or "too good to be true" process would be developed in the laboratory and excellent results generated, the crunch would come during scale up of the process from laboratory to full plant scale. Numerous problems would then crop up and deviating results obtained from that on laboratory scale.

The extent of these problems usually necessitated some minor or major adjustments to the process imposing further optimisation regarding these adjustments. Minor adjustments allowed for minimal optimisation on the plant itself. Major process adjustments though could result in costly optimisation on the plant or suspend development work on plant scale and imply returning to laboratory or pilot plant scale for final optimisation. Whichever, the result remained the same – time schedules and budgets not being met. Superfluous to mention that time is money and to stress the order of magnitude regarding cost of experimentation on plant scale relatively to experimentation on laboratory scale. The importance of the initial thought and thoroughness that goes into the preliminary work on laboratory scale cannot be emphasised enough.

2. PRELIMINARY PHASE

Before any experimental work can commence even on laboratory scale, some basic concepts and principles have to be established. All product specifications, the exact requirements, as well as constraints regarding the process have to be clarified. It provides guidelines and facilitates decision making further down the road concerning process development and scale up. It could only be beneficial to limit any chances of misapprehensions and missteps as early as possible.

2.1 BASIC PRINCIPLES

The literature survey produced lots of information regarding the preparation of superfine explosives, among others PETN, on laboratory scale. After scrutinising this information, it was possible to single out one technique applied repeatedly. It is a recrystallisation/precipitation technique that entails complete dissolution of the PETN in a solvent and redepositing it by mixing it with a non-solvent. The mixing of the PETN solution with the non-solvent initiates the precipitation/recrystallisation of the desired PETN crystals and represents the most critical point in the process.

Conditions regarding the PETN solution, the non-solvent and the mixing thereof determine the characteristics of the crystals deposited. It is possible to modify the characteristics of the crystals to meet product specification by altering the conditions surrounding the dissolution and precipitation of the PETN crystals.

2.2 EXPERIMENTAL DESIGN

The first step is to design an experiment that maps out the consecutive steps required for the preparation of superfine PETN. The experiment in general involves complete dissolution of the PETN in a solvent by applying heat and mechanical stirring and then mixing the warm PETN solution with a cooler non-solvent to initiate precipitation/recrystallisation of superfine PETN crystals. These superfine crystals are then separated from the mixture of solvent and non-solvent by means of filtration. The PETN crystals on the filter are washed with water to get rid of any residual solvent and filtered dry to remove excess water. The product on the filter represents the final product, ready for characterisation and evaluation.

Where future scale up of a process is contemplated, more comprehensive planning is required regarding the design of an experiment. Economics and the impact of the process on the environment are two major concerns that need to be evaluated and addressed. Topics like recycling and the management and disposal of waste become major issues. Due to the scale of operation, economics and waste management necessitate recovery of the solvent from the solvent/non-solvent mixture for re-use to dissolve the next batch of PETN. The waste generated by the process, especially by the filtration step, should be handled responsibly and in such a way as to minimise product loss and costs. Because of the fact that chemicals and a high explosive constitute the major part of this experiment, it highlights the necessity for extra care regarding safety and waste management. Mistakes could not only be expensive, but fatal. A well-thought-out experiment from the onset is essential.

The next step is to look at parameters that could influence conditions regarding the dissolution and in particular, the precipitation/recrystallisation of the desired PETN crystals. Optimisation of the process involves varying these parameters in relation to one another and evaluating the results.

2.3 EXPERIMENTAL CONSIDERATIONS

The choice of solvent was the first major decision. A primary requirement for the solvent is a high solubility for PETN. The other major concerns, especially with the prospect of future scale up of the process, are costs as well as the safety, health and environmental issues regarding the handling and disposal of the chemicals. There is increasing pressure from environmental authorities to limit the use of hazardous chemicals. In view of all these constraints, acetone was identified as the choice of solvent. PETN is highly soluble in acetone (~40g PETN/100g acetone). Acetone is classified as a flammable, but moderately toxic solvent; being freely used on our plants equipped to handle large amounts of acetone. The availability of an acetone distillation column for the recovery of acetone was a major consideration that favoured acetone as a solvent. The volatility and low boiling point (~56°C) of acetone, contributing to a relatively low energy demand regarding distillation, also favoured it from a cost angle.

The primary requirement for the non-solvent is no or low solubility for PETN. Additional requirements like low cost and " environmental friendly" made water the obvious choice.

Another important consideration to take into account when designing an experiment is to identify the parameters for process optimisation and the limits thereof within the capabilities of plant equipment. Be informed of what is available and possible on plant scale. It is senseless and heart-breaking to optimise conditions perfectly on laboratory scale and then only with scale up to discover plant equipment to be inadequate and the process not feasible for scale up. It was for that very reason in this case that preference was given to a batch process despite the benefits represented by a continuous process.

The development of this scale up process for the precipitation/recrystallisation of superfine PETN is best discussed in view of the three scale up steps:

- Laboratory Scale
- Pilot Plant Scale
- Full Plant Scale

3. LABORATORY SCALE

The main purpose of experimentation on laboratory scale was to optimise process conditions for the preparation of superfine PETN that comply with the desired product specification. At this stage there were still a number of unknowns and variables regarding the process that had to be eliminated and narrowed down before the process, that is the design and the conditions, could really be fine-tuned. Laboratory scale represents experimentation with volumes up to two litres.

3.1 EXPERIMENTAL

A statistical approach was used to design the first experiment in the laboratory. The purpose of the statistical approach was to incorporate the maximum number of parameters into a minimum number of experiments and still obtain meaningful results. The goal of the first experiment was primarily to eliminate parameters that do not contribute significantly to process optimisation and single out those that do for further optimisation in a second experiment. The statistical approach, namely the Taguchi Design Experiment that was used, is portrayed in Table 1.

The number 1 and 2 for each parameter represents two different configurations or values. In order to establish definite impacts and tendencies, incremental values were attributed respectively to the 1 and 2. Parameters investigated in the first experiment was:

- Different grades of PETN as raw material
- Percentage of PETN in solution
- Temperature of the PETN solution
- Volume of non-solvent
- Temperature of the non-solvent
- Order of mixing PETN solution and non-solvent
- Stirring speed
- Stirring time

Table 1: Statistical Experimental Design for Process Optimisation on Laboratory Scale

	Parameters identified and varied										
Batch	**1**	**2**	**3**	**4**	**5**	**6**	**7**	**8**	**9**	**10**	**11**
1	1	1	2	2	2	1	1	1	2	2	2
2	2	1	2	1	2	2	2	1	1	1	2
3	2	2	1	1	2	1	2	1	2	2	1
4	2	1	1	2	2	2	1	2	2	1	1
5	2	2	2	1	1	1	1	2	2	1	2
6	1	2	2	1	2	2	1	2	1	2	1
7	2	2	1	2	1	2	1	1	1	2	2
8	2	1	2	2	1	1	2	2	1	2	1
9	1	1	1	1	1	2	2	2	2	2	2
10	1	1	1	1	1	1	1	1	1	1	1
11	1	2	1	2	2	1	2	2	1	1	2
12	1	2	2	2	1	2	2	1	2	1	1

After the elimination of a number of parameters, a different statistical approach was employed in the second experiment to incorporate the remaining parameters that proved to be significant for fine-tuning process conditions. A Full Factorial Design Experiment was used for the second experiment. The second statistical design corresponded to the first in the sense that it also allowed for attributing two different values to the parameters. These values however were chosen with more deliberation than the first time, as the purpose of the second experiment was not eliminating but fine-tuning process conditions. The big difference was that the limited number of parameters in the second design made it possible to correlate parameters' interdependencies.

A few additional aspects concerning scale up like the recovery of the acetone and the handling of the waste generated by the process, were addressed at this stage. Two possibilities were identified for the recovery of the acetone, namely during precipitation/recrystallisation or after separation of the liquid from the product. Since it was impossible at that time to duplicate these exact process conditions in the laboratory, corresponding experiments were conducted in the laboratory to evaluate the major impact thereof on the superfine PETN and develop a so-called feel for the two acetone recovery options.

The waste generated mainly consisted of water containing traces of PETN and certain percentages of acetone. These levels varied in accordance with the option used for acetone recovery. Confirmation of results would only be attainable after implementation of the acetone recovery step on plant scale.

3.2 RESULTS AND DISCUSSION

The PETN batches from the first experiment produced results with average particle sizes that ranged from 11 to 67 μm. The statistical evaluation of the results in accordance with the statistical design of the experiment reported the actual mixing of the PETN solution with the water to be the most significant. Parameters regarding the percentage, volume and temperature also proved to be significant. Results from the first experiment made it possible to eliminate a number of parameters cluttering the optimisation process and single out the significant ones.

The second experiment reported average particle sizes that ranged from 11 to 15 μm, a relatively narrow distribution band of results. These results served as confirmation of the parameters identified and the values attributed. Process conditions were then finalised on account of the optimisation experiments in the laboratory. It paved the way for scale up to pilot plant scale in order to examine the feasibility of the process conditions for scale up.

Before scale up to pilot plant scale and further expenditure, it was only sensible to evaluate the financial side of the process. It was possible to make a few basic cost calculations, relying on a number of assumptions, to get a figure on the profitability of the process. Nobody is interested in a process costing money and not making money. A positive answer in this regard provided the go ahead for scale up.

4. PILOT PLANT SCALE

The purpose of experimentation on pilot plant scale was to investigate the workableness of the process conditions optimised in the laboratory on a larger scale. The average size of the vessels on the pilot plant was 50 to 75 litres which represents an almost fifty fold scale up from laboratory scale.

4.1 EXPERIMENTAL

Due to a number of limitations on the pilot plant as well as time pressure, it was impossible to investigate the recovery of the acetone or address the handling of the waste. The experiment on the pilot plant scale therefor purely served as a verification of the process conditions optimised in the laboratory.

In order to supply a big enough sample to a client for preliminary evaluation of the product, the experiment had to be repeated six times maintaining the same process conditions as far as it was practical possible. The different batches were evaluated separately before being blended into one batch. The scale up experiment as a whole proceeded very smoothly on the pilot plant.

4.2 RESULTS AND DISCUSSION

The six separate PETN batches' average particle size ranged from 11 to 13 μm. These results made it possible to verify the repeatability and robustness of the process conditions, an important aspect for the production of a quality product on plant scale. The process itself was practical and easy to implement on the larger scale and yet maintain process conditions within their limits.

Only one possible restriction was identified. It was the first time that a filter trolley had been used to filter the bigger quantity of superfine PETN when it turned out to take longer than anticipated. The intention was to use the same design of filter trolleys on plant scale. It served as sensitisation for the filtration step to provide well ahead for suitable alternatives should it prove to be necessary. The results from the pilot plant runs however gave the go ahead for implementation on full plant scale.

5. PLANT SCALE

Implementing the process conditions on full plant scale served as the final test for the feasibility of the process for scale up. The volume of the precipitation/recrystallisation vessel on the plant was 3000 litres. It was also the first opportunity to obtain a representative sample of the process for submission of final product approval. The results generated on plant scale were used to draw up a proper mass balance of the process and to determine the profitability thereof.

5.1 EXPERIMENTAL

One of the most outstanding features regarding this final scale up to plant scale was besides the much larger quantities, the long times needed for each consecutive step in the precipitation/recrystallisation process - for example the time it took to fill a tank, the time to transfer the contents from one vessel to another, the time to heat or cool down the contents in a vessel. The retention time of the product exposed to the different process conditions was of a much bigger order. The total exposure time of the superfine PETN to the acetone and heat was longer. It became clear that it was impossible to duplicate these exact conditions on laboratory scale. The dynamics of transferring and mixing the contents were also of another dimension. The effect of these longer exposure times of the product was detected in a slight increase in the average particle size of the superfine PETN – not recommendable for improving product quality.

The process conditions regarding the percentages, volumes and temperatures optimised on laboratory scale were implemented without problems on the big plant scale. The consecutive process steps were logic and practical. The filtration of the superfine PETN in the filter trolleys also proved not to be such a problem as anticipated.

For the first time it was possible to implement and evaluate the acetone recovery step. Both recovery options were implemented and evaluated. Due to practical considerations regarding the handling of bigger volumes and the time involved, the recovery step of the solvent was implemented at the earliest possible opportunity.

A total of sixteen batches was prepared, maintaining the same process conditions. Each batch was evaluated separately. The results of these batches could serve as a test for the repeatability of the process on big scale.

5.2 RESULTS AND DISCUSSION

The scale up to plant scale production produced crystals with an average particle size of 16 µm, an increase of 4 µm compared to pilot plant scale. This increase in particle size can mainly be attributed to the longer exposure times of the PETN to process conditions as well as changes in the dynamics of the stirring and pumping actions on plant scale. Although experience reflects that the PETN crystals are not really susceptible to crystal growth, the longer mixing time of the PETN solution into the non-solvent, had an effect on the formation of the crystals. It has already been identified as the most critical point in the process.

The acetone recovery by distillation as early as possible before filtration benefited the filtration process and lowered the level of PETN in waste water to 5 PPM and lower which is highly beneficial for the treatment of the waste water. The only down side was that it contributed to a slight increase in the average crystal size due to extended exposure of the superfine PETN to the acetone and the changes in the equilibrium that allowed for the crystallisation of not yet precipitated PETN on already crystallised PETN crystals with the effect of crystal growth.

In total the scale up of the process from the pilot plant to the plant scale went according to plan except the slight increase in crystal size results. A possibility to overcome this problem is to modify equipment to shorten the addition and mixing time of the PETN solution to the water. The need for further optimisation however depends on the evaluation of the fine PETN in its specific application.

The results of the sixteen PETN batches produced differences in particle size of only 2 µm that endorsed the findings of the pilot plant experiment, namely that the process is repeatable and robust, even on plant scale.

It can be concluded that the implementation of the process on the plant scale was a big success. Financially the process as employed at present reflects a very good return on investment and can serve as a great motivation to look at further optimisation of the process to attain even smaller crystal sizes. Another option could be to develop a continuous process.

6. CONCLUSION

The development of this process for the precipitation/recrystallisation of superfine PETN from laboratory to plant scale as portrayed in this paper reflects a personal and very much practical approach. It is definitely not an official recipe or the ultimate way to go about it. The practical experience gained with the development of this process, taking it through all the scale up steps, made this an extensive and valuable learning experience. And yet, evaluating the results from the final plant scale reflects that there is room for improvement. Although it is probably unrealistic to expect to implement a scale up without any hitches, it is clear that there is still a lot of experience to be gained.

It is also obvious that each process development for a different product will have its own distinct characteristics that would provide for unique solutions, only to be gained by practical experience.

Preventive Approach for Managing and Removing Organic Pollutants: the Example of NTO

Jamal OUAZZANI
C.N.R.S, Institut de Chimie des Substances Naturelles
Avenue de la Terrasse - 91198 Gif-sur-Yvette, Cedex - FRANCE
Tel : (33) 1 69 82 31 23 - Fax : (33) 1 69 07 72 47
E.Mail : jamal.ouazzani@icsn.cnrs-gif.fr

Introduction

A Large part of man made organic compounds or xenobiotics is intended for widespread use (pesticides, detergents, dyes, pharmaceuticals, explosives...). Their fate in the environment is under the control of abiotic transformations (photodegradation), and microbial degradation. Only biological systems are able to achieve the total transformation of organic compounds into inorganic safe end-products (carbon dioxide, nitrogen, water...). This process called mineralization is catalyzed by various enzymes specialized in the conversion of naturally occurring compounds. Xenobiotics are designed according to expected properties without any care for their ability to be recognized by degradative enzymes. For some particular applications, chemists were interested in increasing the lifetime of xenobiotics. The resulting structures were recalcitrant to biotic or abiotic degradations, and toxic directly or through their derivatives or metabolites.

During centuries, risky compounds were released in the environment without any understanding of their impact on ecosystems and public health. Even those that were recognized hazardous and were withdrawn, still contaminate the environment through leakage from sediments or underground storage thanks. The decision to clean-up polluted sites is generally limited by cost. The concerned areas were highly concentrated which contributed to the eradication of local microflora. The consequence is a limited auto-epuration and a need for costly off site treatments.

Private and institutional operators still engage in ambitious restoration programs for contaminated sites, and evaluate various techniques (incineration, photodegradation, AOPs, Bioremediation...). Unfortunately, only limited efficiency is observed for highly recalcitrant compounds.

The preventive approach

Actually, heavy chemical companies try to avoid environmental disasters that negatively influence their image and business. However, they still produce xenobiotics for new applications or to replace withdrawn compounds. The main objective of our work is to anticipate the environmental impact of compounds that are still under industrial development, and not yet present in the environment in a worrying manner. This strategy tends to offer detection/quantification methods, and remediation processes applicable in the case of accidental pollution, and useful for cleaning industrial wastes. It includes metabolic comparison between microbial and mammalian cells, and the identification of every potential toxic metabolites.

After identification of a target molecule, we started the "well" presented below.

This mutlidisciplinary approach associates cleaning, prevention and valorization processes. It includes:

1 - The synthesis of radio-labeled markers, to follow precisely the outcome of the pollutant and to measure its mineralization, and the synthesis of every potential metabolites and derivatives.

2 - The development of analytical methods for the detection and the quantification of the pollutant and its derivatives, that may form in the environment through biotic or abiotic transformations. These methods are designed either for aqueous or soil contamination.

3 – Investigation of the chemical reactivity of each domain of the compound, and the evaluation of "clean" chemical remediation processes, mainly Advanced Oxidation Processes AOPs.

4 - Microbial degradation of the pollutant to safe derivatives: In this part, we avoid any processing or dilution of the contaminated media to remain close to real situation. We elucidate the enzymatic mechanisms of degradation. The main objective is to optimize the incubation conditions to reach the total mineralization of the pollutant.

5 – Mammalian degradation of the pollutant. We used rat liver cells and various mammalian cell lines. We identify the metabolites of the pollutant, and the enzymes involved in its degradation. This can help to detect reactive and toxic intermediates that may form in the case of accidental ingestion.

6 – The valorization step concerns either the generalization of the biodegradation process to other pollutants, and a screening for beneficial properties of the metabolites.

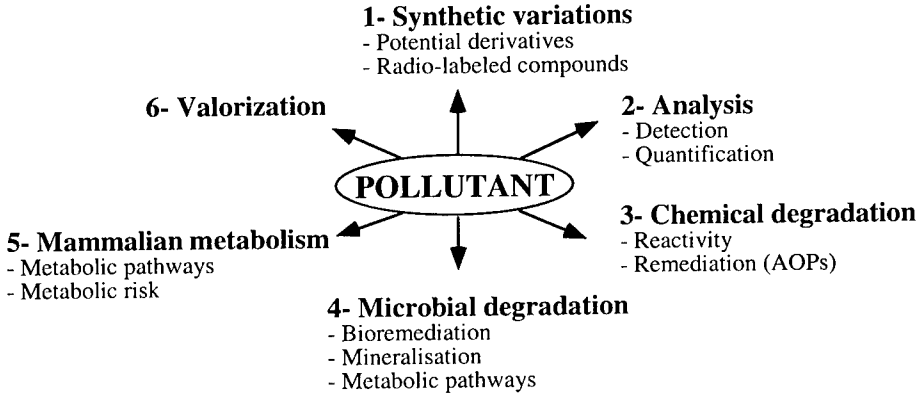

Target Molecule : the example of NTO

Aromatic and heterocyclic nitro compounds are common industrial chemicals. They are associated with many industrial processes and particularly, the ammunitions industry.

There is a great deal of evidence that these recalcitrant compounds are toxic and hazardous. Classical explosives such as TNT, RDX, and HMX are commonly found in soils and waters around manufacturing and disposal sites. Among the physical and chemical remediation techniques available (soil extraction, soil washing, thermal desorption, oxidation processes), the current technology to clean up explosive contaminated soils is incineration. Nonetheless, this method is very expensive and produces large amounts of toxic emissions and ashes. Bioremediation of energetic compounds has received much attention and was largely investigated. However, literature indicates slow and limited microbial mineralization of conventional explosives (TNT, RDX and HMX). The risk that these compounds pose to health and the environment, is now well established. They became less attractive and justify the need for powerful, stable and potentially less toxic explosives. The 5-nitro-1,2,4-triazol-3-one NTO **1** was recently developed as a leader of a new generation of ammunition. It exhibits the same performance as RDX, but a higher stability against physical constraints (pressure, heat, impact, friction ...). This compound has met with considerable interest from both the defense and civilian sectors. For specific military formulations, industrial conditioning of NTO generates acidic waters containing 10-15 g/l of compound. Its recovery as well as its disposal are not actually considered, and the contaminated solutions are stocked until the elaboration of a cost-effective remediation process. The chemical degradation as well as the metabolism of NTO had never been reported before. For these reasons it offers a good opportunity to validate our preventive approach.

1. Chemical Variations

Based on the metabolism of molecules presenting structural similarities with NTO. We made an inventory of the potential NTO metabolites and derivatives (figure 1). These molecules have been taken into account for the calibration of analytical methods.

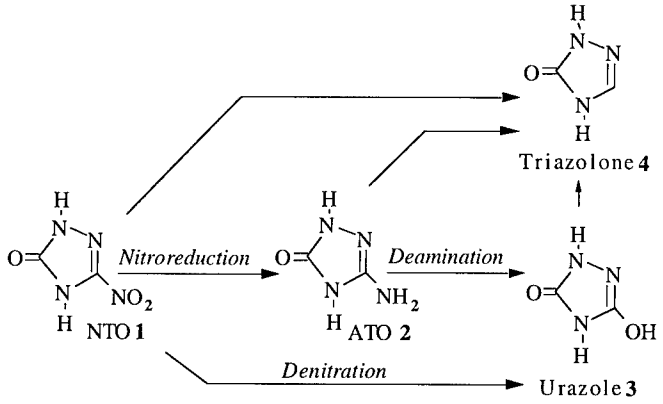

figure 1 : Cyclic potential derivatives of NTO

In order to follow precisely the chemical and biological degradations of NTO, and to propose accurate reaction mechanisms, we synthesized [5-^{14}C]- NTO and [3-^{14}C]-NTO (figure 2). [5-^{14}C]-ATO and [3-^{14}C]-ATO were obtained by nitroreduction of the corresponding labeled NTO.

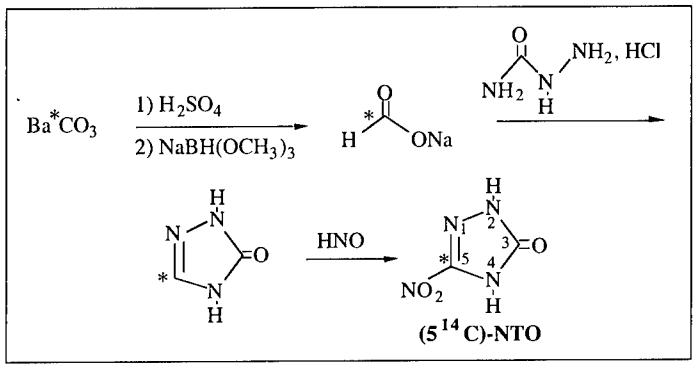

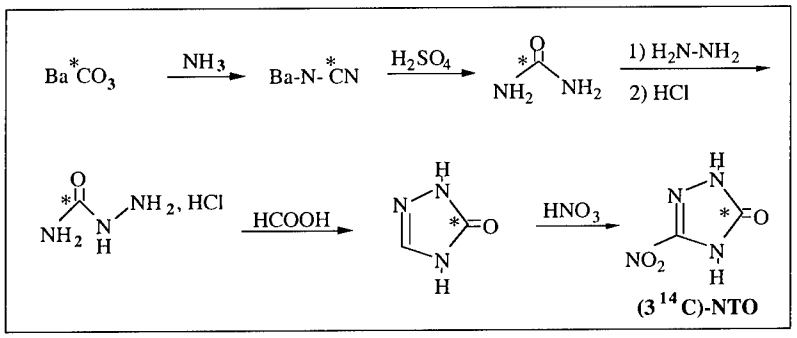

Figure 2 : Synthesis of [5-^{14}C]- NTO and [3-^{14}C]-NTO.

2. Analytical Methods

Polar heterocyclic compounds were not easy to separate by classical chromatographic techniques. Among a variety of chromatographic supports and methods, the best separations for compounds **1** to **4** was obtained by HPLC on a porous graphite column and by capillary electrophoresis (Figure 3).

The HPLC was coupled to radioactivity detection, and used routinely for the quantification of compounds in water and soils. The concentrations detected by HPLC were lower than 5 mg/l in aqueous solutions, and 15 mg/kg of soil.

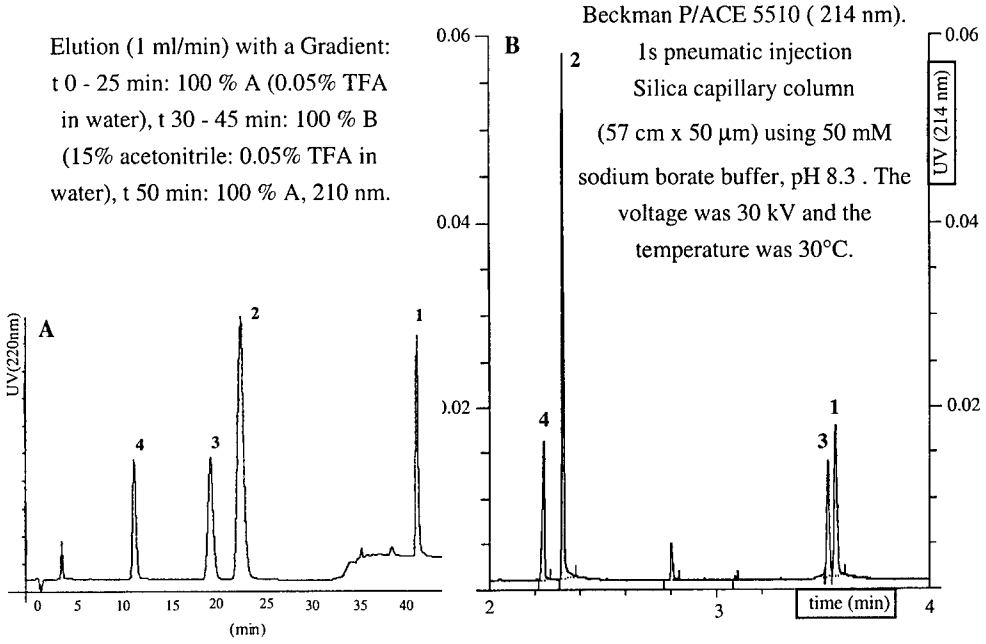

Figure 3 : separations for compounds **1** to **4**. A. HPLC on a porous graphite column.
B. capillary electrophoresis.

3. Chemical Degradation of NTO

3.1. Chemical reactivity

A review on the chemistry of nitrotriazoles, published in 1986, confirms the high stability of the nitrotriazolone ring against drastic reaction conditions.

Contrary to other nitrotriazoles, only two publications reported the chemical transformations of NTO, 1) the nitro-reduction of NTO to the corresponding primary amine ATO, and 2) NTO decomposition in refluxed sulfuric acid. In order to complete our knowledge on the reactivity of substituted triazolones, we investigated the chemical decomposition of NTO and ATO. Target regions in these molecules were the nitro group, the primary amine and the cyclic urea. The nitro group of NTO can be easily reduced either by chemical or microbial nitroreduction (figure 4).

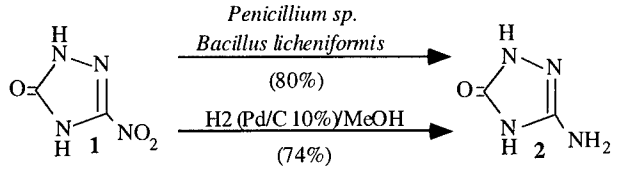

Figure 4 : microbial and chemical nitroreduction of NTO

Hydrolysis of NTO and ATO is presented in figure 5. Drastic acidic conditions only partially degrade the triazolone ring of NTO and ATO.

In alkali (NaOH), urea region of ATO but not NTO, is efficiently hydrolyzed, leading to ring clevage and the formation of a polar compound assumed to be aminoguanidine.
ATO is easily deaminated by dediazotation through unconventional reactions figure 6. The diazo intermediate is not hydrolyzed to the expected urazole, but gives TO **4** or the azide **6** depending on nitrite concentration.

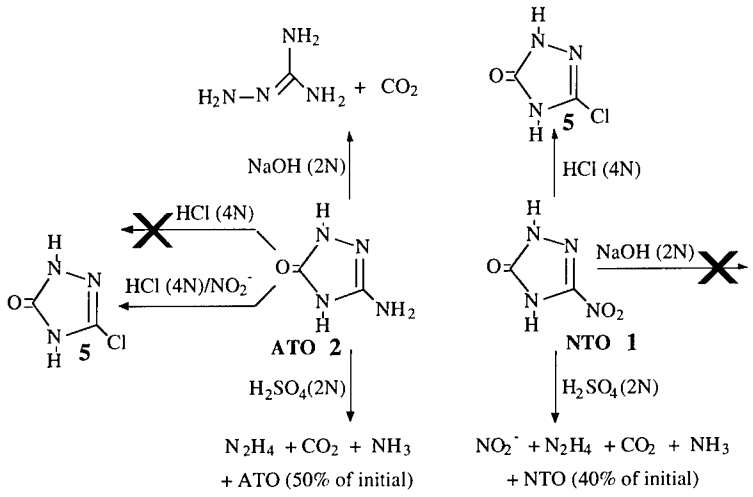

Figure 5 : Hydrolysis of NTO and ATO

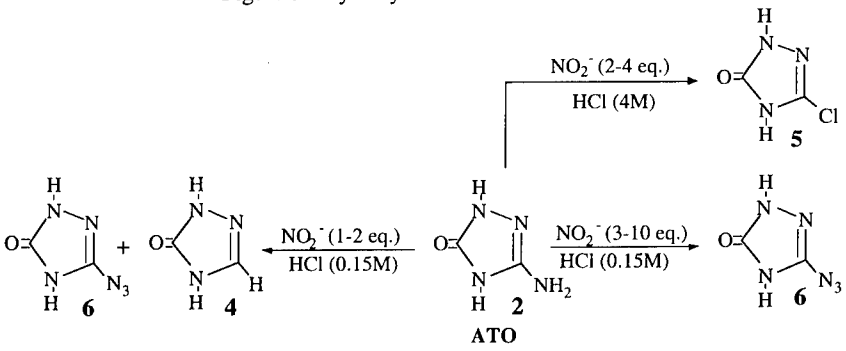

Figure 6 : deamination of ATO

3.2. NTO remediation using Advanced Oxidation Processes

The TiO_2-catalyzed photodegradation (λ>290nm, TiO_2 0.4 g/l, NTO 150 mg/l)) leads to the complete mineralization of NTO in 3 hours. This degradation involves a simultaneous denitrification and ring scission, followed by the total mineralisation of NTO. End products were nitrites, nitrates and carbon dioxide (figure 7). No significant photo-degradation of NTO was detected in the absence of the catalyst. Long term irradiation over one week, leads to a complete degradation of concentrated NTO (5g/l).

Fenton oxidation offers an efficient cost-effective method for NTO remediation. This reaction is faster that the TiO_2-catalyzed photolysis and find application on the mineralization of high concentrations of NTO (15 g/l) (figure 8). Fenton oxidation provokes ring cleavage and subsequent elimination of the two carbon atoms of NTO as CO_2. During this reaction, the nitro group is completely transformed into nitrates. These techniques, and particularly the Fenton oxidation, are perfectly applicable to limpid contaminated solutions containing about 15 g/l NTO. This cost-effective process did not involve any reactive intermediates and leads to harmless end products. We proposed a mechanism of degradation of NTO by OH· presented in Figure 9.

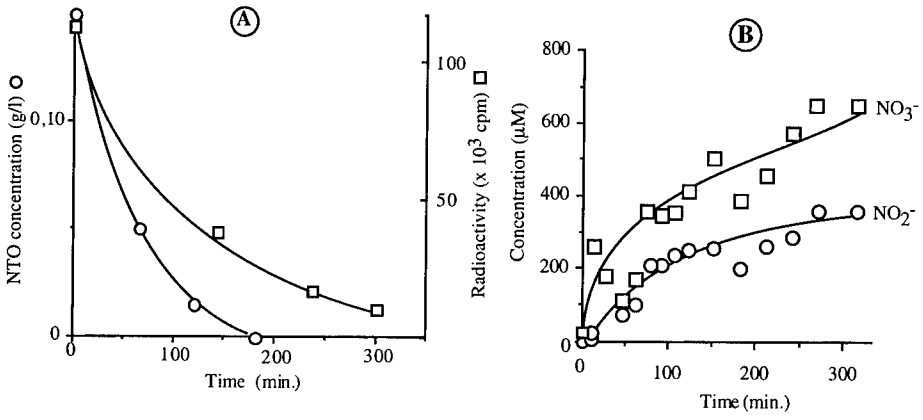

Figure 7 : TiO2 (0.4 g/l) catalyzed photodegradation of NTO (150 mg/l).
A : NTO photodegradation, B : Nitrite and nitrate formation.

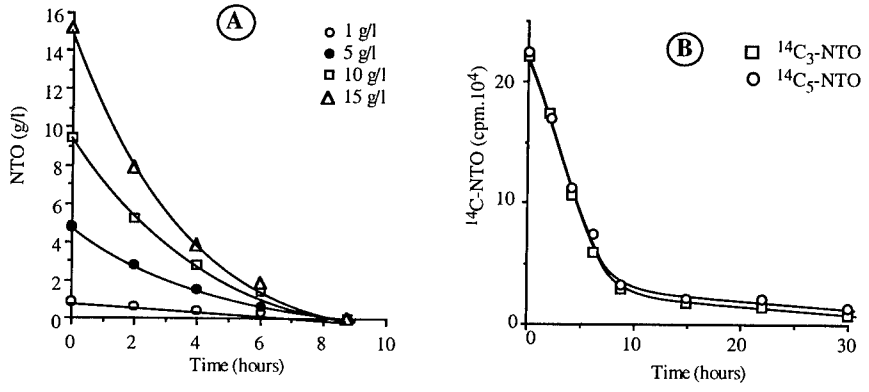

Fig. 8. Degradation of NTO by Fenton oxidation. A. effect of NTO concentration

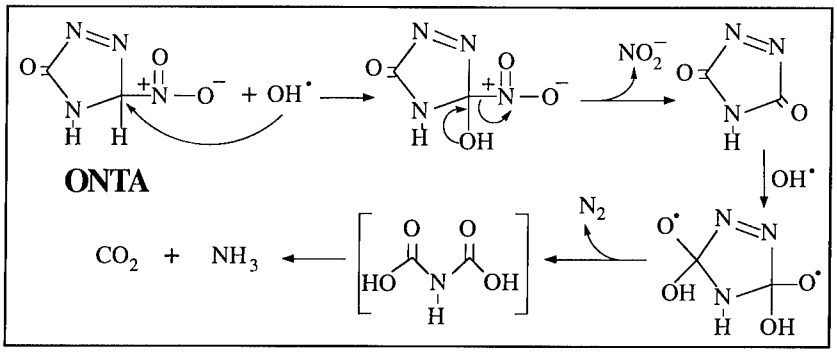

Fig. 9. Proposed mechanism of degradation of NTO by OH·

4. Microbial degradation of NTO

Contrary to other explosives, NTO is well soluble in water and its concentration almost reached 10 to 15 g/l in industrial aqueous wastes. An innocuous microbial strain was isolated from the waste by enrichment techniques, and represented a suitable micro-organism for achieving NTO remediation. This bacteria was identified as *Bacillus licheniformis*. The protocol requires two separate steps: the micro-organism production and the NTO degradation. The first step is a classical culture process, which needs inexpensive nutritional supply and offers large quantities of biomass in three days of growth. This step did not require continuous control or supply and the biomass could be easily recovered. The second step is the incubation of the freshly produced biomass with a waste that contains 15 g/l of NTO. After two weeks of incubation, NTO is totally transformed to urea and a polar compound assumed to be hydroxyurea. Both compounds might be further hydrolyzed by urease-like activities accounting for the 40% mineralization. At the end of the incubation, the biodegradation broth contains biomass, urea and hydroxyurea. NTO transformation by *Bacillus licheniformis* involves two consecutive reactions 1) the nitroreduction of NTO, 2) the hydrolysis of the formed ATO. Optimal conditions for each reaction are represented in figure 10.

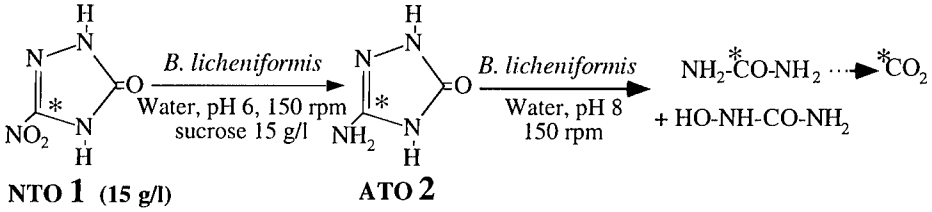

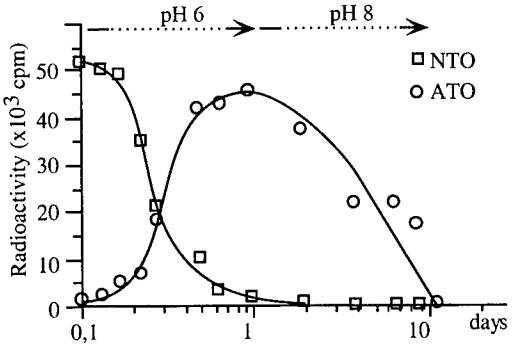

Figure 10 : Biodegradation of NTO by *Bacillus licheniformis*

To elucidate the mechanism involved in the ring fission of ATO, 3-^{14}C-ATO (^{14}C=O) and 5-^{14}C-ATO (^{14}C-NH_2) were synthesized and used to follow the outcome of each region of the molecule. Various results tend to confirm that the "urea" region of ATO is not hydrolyzed. Such hydrolysis provokes a spontaneous release of carbon dioxide from the carbonyl group. When 3-^{14}C-ATO (^{14}C=O)was used in the incubation no mineralization was observed. The labeled carbonyl group was totally recovered as polar compounds. Radioactive urea is not formed in this case. Similar incubations with 5-^{14}C-ATO (^{14}C-NH_2) led exclusively to ^{14}C-urea suggesting that the carbon at position 5 is the site of degradation. Urea may be further degraded to ammonia and carbon dioxide, supporting the 40% mineralization of 5-^{14}C-NTO.

5. Mammalian transformation of NTO by rat liver microsomes:

The potential carcinogenicity of aromatic and heterocyclic nitro-compounds had led to considerable attention being focused on their metabolism in mammals. The general pathway of their biodegradation is nitroreduction which may generate potent cytotoxic intermediates, such as primary amines and hydroxylamines.

The transformation of NTO was principally catalyzed by the microsomal fraction of rat liver cells, from dexamethasone treated rats. This reaction required a NADPH-generating system and led to the formation of two metabolites, 5-amino-1,2,4-triazol-3-one **2** and 5-hydroxy-1,2,4-triazol-3-one **3** (Figure 11). The presence of oxygen did not affect the overall conversion rate of NTO, but considerably altered the proportions of the metabolites. Amine **2** was the major derivative formed under anaerobic conditions, while urazole **3** represented 40% of the metabolites formed under aerobic conditions. 14C-labelled ATO was incubated with dexamethasone-induced microsomes to determine whether urazole **3** derived directly from NTO or from the corresponding amine. 14C-ATO was not transformed by rat liver microsomes into either urazole **3** or any other derivative, even when unlabelled NTO was added to the incubation. This finding suggests that urazole is formed directly from NTO. Nitrite measurement tends to support an oxidative denitrification of NTO rather than an amine oxidase catalyzed reaction.

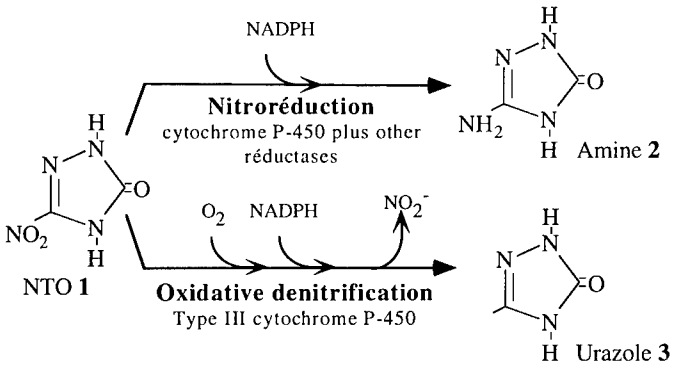

Figure 11 : transformation of NTO by rat liver microsomes

Our results have shown major differences between the mammalian and the microbial metabolism of NTO. Among the reactions observed, nitroreduction of NTO is common to both systems and led to the primary amine ATO. Hepatic microsomal enzymes involved in this reaction are extensively inhibited by oxygen compared to the microbial enzymes.

Nitroreduction is the sole microbial reaction that affects NTO, but the derived amine ATO is subsequently degraded through triazolone ring cleavage. In the mammalian system, besides nitroreduction, NTO undergoes an oxidative denitrification, providing urazole and nitrite.

6- Valorization of the remediation process

ATO could be obtained in large quantities from NTO contaminated wastes. It corresponds to the first step in NTO degradation by *Bacillus licheniformis*. The structure of this molecule reminds some biologically active compounds. According to figure 12 various biological activities were screened. We focused particularly on the herbicidal activity of ATO according to structural similarities with amitrole (amino-imidazole). This widely used compound exhibits low biodegradability and is actually classified as hazardous, because of its potential carcinogenicity. We have shown during our study that ATO is biodegradable and might represent an attractive alternative to amitrole.

Our current projects concern the identification of compounds that might represent recalcitrant pollutants in the near future. We are completing the well, presented at the top of this paper, by investigating the long term toxicity of the retained compounds and the cloning and identifications of the enzymes involved in their biodegradation.

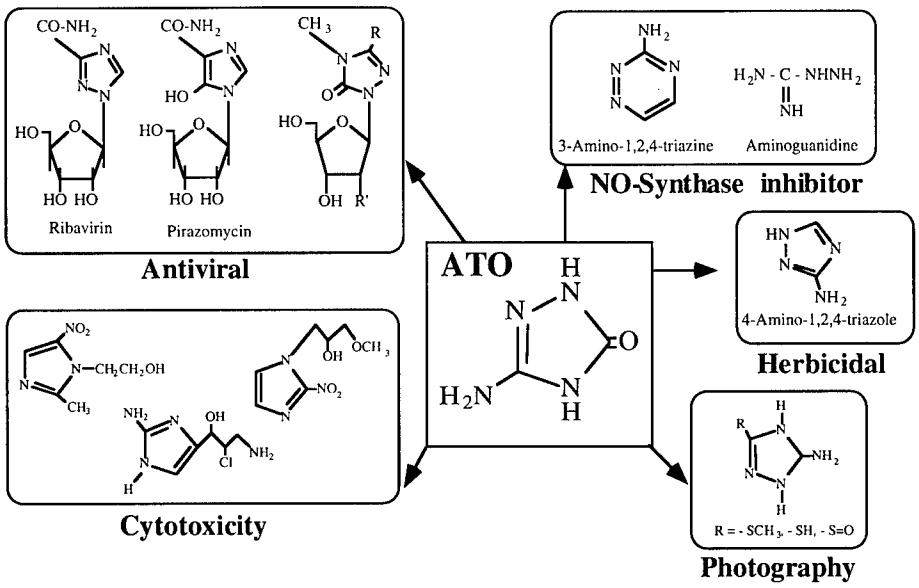

Figure 12 : ATO valorization

References :

L. LE CAMPION, M.T. ADELINE and J. OUAZZANI. Separation of NTO related 1,2,4-triazole-3-one derivatives by a high performance liquid chromatography and capillary electrophoresis. Propellants Explosives pyrothechnics, 22,1-5, **1997**.

L. LE CAMPION, M. DELAFORGE, J.P. NOËL and J. OUAZZANI. Metabolism of ^{14}C-labelled 5-nitro-1,2,4-triazole-3-one by rat liver microsomes : evidence for the participation of cyt P-450. Eur. J. Biochem, **1997**.

L. LE CAMPION, M. DELAFORGE, J.P. NOËL and J. OUAZZANI. Metabolism of ^{14}C-labelled 5-nitro-1,2,4-triazole-3-one (NTO) : Comparison between rat liver microsomes and bacterial metabolic pathways. Journal of Molecular Catalysis B-Enzymatic, 5 (1-4), 395-402, **1998**.

L. LE CAMPION et J. OUAZZANI. La biodégradation des explosifs. Biofutur, 174, 21-24, **1998**.

L. LE CAMPION and J. OUAZZANI. Synthesis of 5-amino-1,2,4-triazole-3-one through the nitroreduction of 5-nitro-1,2,4-triazole-3-one. Comparison between chemical and microbiological catalysis. Biocatalysis and biotransformation, 17 (1), 37-44, **1999**.

L. LE COMPION, S. DE SUZZONI-DEZARD, N. ROBIC, A. VANDAIS, P. VARENNE, J. P. NOEL, and J. OUAZZANI. Synthesis of [3-^{14}C]- and [5-^{14}C]- labelled 5-nitro-1,2,4-triazol-3-one (NTO) and study of its chamical decomposition. Journal of Labelled Compounds and Pharmaceuticals, **1999** (in press).

L. LE CAMPION, C.GIANNOTTI and J. OUAZZANI. Photocatalytic degradation of 5-nitro-1,2,4-triazole-3-one (NTO) in aqueous suspention of TiO_2. Comparison with Fenton oxidation. Chemosphere, 38 (7), 1561-1570, **1999**.

L. LE CAMPION, A. VANDAIS and J. OUAZZANI. Microbial remediation of NTO in aqueous industrial wastes.FEMS. Microbiology Letters, 176 (1), 197-203, **1999**.

MECHANICAL CHARACTERISATION OF ENERGETIC MATERIALS USING MULTI-WAVE EXPERIMENTS

Gaynor M. Kavanagh, John. Theobald & David A. Tod

DERA, Fort Halstead, Sevenoaks, Kent, TN14 7BP, UK

ABSTRACT

Mechanical characterisation of energetic materials is an essential element of the initial qualification process and subsequent surveillance programmes. Dynamic mechanical analysis has been demonstrated to be one of the most effective methods of mechanical assessment in terms of sample usage and experimental time. There is often a reluctance to conduct tests at a variety of frequencies as this increases the sample requirements and expense. A possible way of accumulating more mechanical information is to use a multi-wave experiment.

Some commercially available rheometers have "multi-wave" software available. By using this software experiments can be carried out at several discrete frequencies simultaneously compared to older experiments which monitored mechanical parameters (i.e. G' and G") at one single frequency.

Several energetic materials were investigated by both single frequency and multi-waves experiments and over a range of temperatures. The data extracted from the multi-wave experiments was then compared against the corresponding single frequency results using overlay plots.

Both unaged and aged materials were tested and the results will be discussed.

Keywords:

Characterisation

Dynamic mechanical analysis (DMA)

Multi-wave

Shear Modulus

CHARAKTERISIERUNG DER MATRIX / FÜLLSTOFF-WECHSELWIRKUNG AM BEISPIEL DES MODELL-TREIBSTOFFSYSTEMES GAP / RDX

CHARACTERISATION OF THE MATRIX / FILLER PROPERTIES OF THE GAP / RDX PROPELLANT SYSTEM

Peter Gerber, Christof Hübner, Klaus Menke

Fraunhofer-Institut für Chemische Technologie (ICT), Joseph-von-Fraunhoferstr. 23, D-76229 Pfinztal

Abstract

The mechanical properties of propellants are mainly determined by the filler binder system. With a Particle size > 1µm only a few publications investigate the change of the modulus and loss tangent with different amount of filler and particle size. /1, 2/. Stacer et. al. /1/ for example studied HTPB filled with monosized and bimodal ammonium perchlorate with up to 66 vol.% amount of filler. In this work the binder GAP is crosslinked with N100 and filled with RDX particles with a average particle size of 4 µm. The amount of filler reached 50 vol. %. The dependence of the modulus G* and tan δ from the strain and the frequency is studied. The results were analysed and discussed with a well known power law equations and the relative modulus $G_R = G/G_M$.

Zusammenfassung

Die mechanischen Eigenschaften von Treibstoffen, werden neben der Verarbeitung im wesentlichen vom eingearbeiteten Füllstoff und dem Bindersystem, der Matrix bestimmt. Für Füllstoffe mit einer Partikelgröße > 1 µm existieren nur wenige Arbeiten, welche die Änderung des Moduls und des Verlustfaktores eines Matrix-Füllstoffsystemes bei verschiedenen Füllstoffgehalten und Partikelgrößen bestimmen. /1, 2/. So untersuchte z.B. Stacer, et. al. /1/ HTPB, gefüllt mit monomodalem und bimodalem Ammonium Perchlorat, bei Füllstoffgehalten bis zu 66 vol. %.

In dieser Arbeit wird als Matrix GAP mit N100 vernetzt und mit RDX Partikeln gefüllt. Die mittlere Partikelgröße beträgt 4 µm. Die Füllstoffgehalte wurden zwischen 10 und 50 vol. % variiert. Es wurde die Abhängigkeit des komplexen Moduls G* und des Verlustfaktores tan δ in Abhängigkeit von der Scheramplitude und der Kreisfrequenz bestimmt. Die Ergebnisse werden mit Hilfe des bekannten Potenzgesetzes und des relativen Moduls $G_R = G/G_M$ ausgewertet und diskutiert.

Grundlagen

Bei der dynamisch mechanischen Analyse (DMA) wird eine Probe durch einen oszillatorischen Schwingversuch mit einer sinusförmigen Scherung $\gamma(t)$ mit der Amplitude $\hat{\gamma}$ und mit der Kreisfrequenz $\omega = 2\pi f$ beansprucht.

$$\gamma(t) = \hat{\gamma} \cdot \sin(\omega \cdot t) \qquad (1)$$

Als Materialantwort auf die sinusförmige Scherbeanspruchung kann die daraus resultierende sinusförmige Schubspannung wie folgt dargestellt werden.

$$\tau(t) = \hat{\gamma} \cdot |G^*(\omega)| \cdot \sin(\omega t + \delta(\omega)) \qquad (2)$$

Der Betrag des komplexen Moduls berechnet sich zu:

$$|G^*(\omega)| = \frac{\hat{\tau}(\omega)}{\hat{\gamma}} \qquad (3)$$

Der komplexe Modul G*(ω) ist nach (3) in zwei Anteile separierbar, den Speichermodul G' und den Verlustmodul G''. Der Speichermodul ist ein Maß für die elastisch gespeicherte Energie, der Verlustmodul ist ein Maß für die in der Probe dissipierte Energie. Aus dem Phasenwinkel δ(ω) oder dem Verlustfaktor tan δ(ω) wird der Verlust-und Speichermodul folgendermaßen bestimmt:

$$\delta = \arctan \frac{G''(\omega)}{G'(\omega)} \qquad (4)$$

Die Messungen werden üblicherweise im linear–viskoelastischen Bereich durchgeführt. Hierbei wird lineares Materialverhalten vorausgesetzt, d.h. es gilt nach Gleichung (3) :

$$\hat{\tau} \sim \hat{\gamma} \qquad (\omega = \text{konst.}) \qquad (5)$$

Im diesem Bereich ist der Modul unabhängig von der Scherung γ. Dies gilt für genügend kleine Scheramplituden praktisch für alle Stoffe und Stoffsysteme.

Experimente

Tabelle 1 zeigt die Rohstoffe, welche für die Formulierung eingesetzt wurden. Die Formulierung wurde bewusst auf wenige Rohstoffe begrenzt, um die Einflussgrößen auf das System zu limitieren. Alle Proben basieren auf dem Glycidylazidpolymer-Diol (GAP, Fa. SNPE). Das mittlere Molekulargewicht des Prepolymers beträgt 2058 g/mol, der Polydispersionsindex beträgt 1,09, gemessen mit einem Polypropylenglycol-Standart. Der energetische Binder GAP wurde ausgewählt, weil für ihn nur wenig Informationen hinsichtlich der Matrix/Füllstoffwechselwirkungen vorliegen. Als Füllstoff wurde für diese Untersuchungen Hexogen (RDX, Fa. Dyno) eingesetzt.

Tabelle 1: Rohstoffe

Bezeichnung	Abkürzung	Funktion	Randbedingungen
Glycidylazidpolymer-Diol	GAP	Binder	
aliphatisches Polyisocyanat	Desmodur N 100	Vernetzer	NCO/OH = 1,0
1,3,5-Trinitro-1,3,5-Triazacyclohexan	RDX	Füllstoff	Partikelröße: $x_{50,3}$ = 4µm
Dibutylzinndilaurat	D22	Katalysator	3 Tr. (78 mg)

Die mittlere Partikelgröße wurde mit einem Malvern Mastersizer S zu 4 µm bestimmt. Alle Formulierungen wurden in einen vertikalen Mischer unter Vakuum 2 Stunden lang bei 40 °C gerührt. Nach der Zugabe des Vernetzers wurde die Vergußmasse in eine Form geleert. Durch Zugabe des Katalysators D22 der Firma Merck, kann die Topfzeit so eingestellt werden, daß die Mischung nur wenige Minuten nach dem Vergießen eine gelartige Konsistenz aufweist. Somit kann die Sedimentation der Füllstoffpartikel unterbunden werden. Die Formulierungen wurden über einen Zeitraum von 24 h bei 60°C im Ofen ausgehärtet.

Um die korrekte Zusammensetzung der Proben zu überprüfen wurde nach der Aushärtung von jeder Formulierung die Dichte mit dem Ultrapyknometer 1000 der Firma Quantachrome bestimmt.

Zur Bestimmung des Moduls und des Phasenwinkels wurden die Messungen wurden bei 23°C mit dem ARES Spektrometer der Firma Rheometric Scientific durchgeführt. Die Abmessungen der eingesetzten rechteckigen Probekörper waren 50 mm × 10 mm × 4 mm.

Ergebnisse und Diskussion

Aus Voruntersuchungen durch einen Amplitudensweep mit einer Kreisfrequenz von ω = 1 rad/s über den ist gesamten möglich zu messenden Bereich, welcher bei dieser Probengeometrie $10^{-4} < \gamma < 0{,}6$ beträgt, ist von der Matrix bekannt, daß die Phasenverschiebung unterhalb der Meßgrenze liegt, d.h. die Matrix verhält sich unter diesen Bedingungen elastisch. Auftretende nicht-lineare Effekte bei gefüllten Systemen können somit nicht auf das Matrixverhalten, sonder ausschließlich durch Matrix-Füllstoff und Füllstoff-Füllstoff-Wechselwirkungen erklärt werden.

Bei der Untersuchung bezüglich der Abhängigkeit des Moduls von der Scheramplitude bei gefüllten Materialien ist bekannt /1/, daß der gemessene Modul stark von der Deformationsgeschichte der Proben abhängt. Wenn Proben mit zunehmender oder abnehmender Scheramplitude gemessen werden, oder wenn ein kürzerer oder längerer Zeitabschnitt zwischen zwei aufeinanderfolgenden Messungen lag, waren die Messungen nicht reproduzierbar. Deshalb wurde für die im folgenden vorgestellten Messungen eine Prozedur erarbeitet, der alle Proben unterworfen wurden.

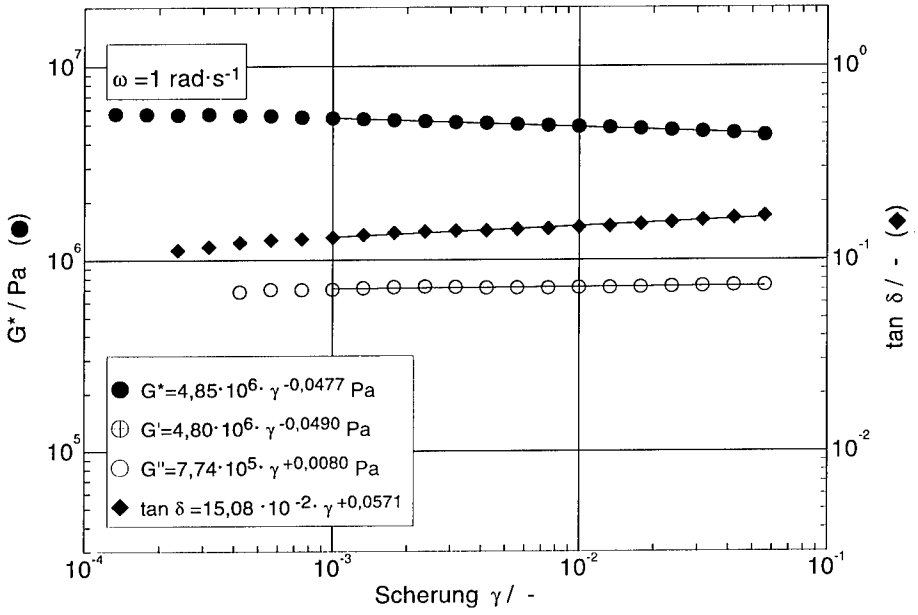

Abbildung 1: Amplitudensweep, Matrix: GAP/N100, c_V = 40 vol. % RDX

Abbildung 1 zeigt beispielhaft für einen Füllstoffgehalt von 40 vol. % den Modul bzw. den Verlustfaktor tan δ in doppelt logarithmischer Auftragung über der Scher

amplitude. Das Nicht-Lineare Verhalten für G* und G' ist gut zu erkennen.
Auffälligerweise ist der viskose Anteil G" unabhängig von der Scheramplitude. Da G' mit zunehmender Amplitude abnimmt, folgt als Konsequenz, daß der Verlustfaktor tan δ mit steigender Scheramplitude zunimmt. Alle weiter untersuchte Füllstoffkonzentrationen zwischen 10 vol.% und 50 vol.% zeigen die gleichen Tendenzen.
Zur Interpretation der Messungen wurde das Potenzgesetz angewendet, welches bereits in vorangegangenen Arbeiten /3/ für die Diskussion von G' und G" benutzt wurde. In dieser Arbeit wird das Potenzgesetz auf G* und tan δ ausgeweitet. Das Potenzgesetz lautet:

$$G^* = G_0^* \cdot \gamma^{-l}$$
$$G' = G_0' \cdot \gamma^{-m} \qquad (6)$$
$$G'' = G_0'' \cdot \gamma^{-n}$$
$$\tan\delta = \tan\delta_0 \cdot \gamma^{-p=-(n-m)}$$

Der Index '$_0$' steht für den jeweiligen Referenzwert bei 1 % Scheramplitude. Die Exponenten l, m, n, und p heißen Nicht-Linearitätsparameter und sind frequenz- und temperaturabhängig.
Abbildung 2 zeigt für den gesamten untersuchten Konzentrationsbereich von 0 bis 50 vol. % den komplexen Modul G* und den Verlustfaktor tan δ in Abhängigkeit von der Scheramplitude. Es ist gut zu erkennen, daß der Modul mit steigendem Füllstoffgehalt zunimmt. Auch sehr kleine Scherungen von 10^{-4} reichen bei dieser Matrix/Füllstoffkombination nicht für den Nachweis eines Linearen Bereiches aus. Der Verlustfaktor ist für c_V = 0 vol. % noch außerhalb des Meßbreiches . Bei 10 vol. % nimmt der Verlustfaktor deutlich zu, und weist eine fallende Tendenz für zunehmende Scheramplituden auf. Für höhere Füllstoffgehalte nimmt der Verlustfaktor mit steigendem Füllstoffgehalt und wachsender Scherung zu. Eine mögliche Erklärung für dieses Verhalten ist die Zunahme von Matrix-Füllstoffablösungen, sowohl bei zunehmender Scherung als auch bei wachsendem Füllstoffgehalt.
Bei einem Verlustfaktor von 0,14 oder kleiner trägt der viskose Anteil G" zum Betrag von G* weniger als 1% bei. In der Literatur werden oft die Größen G' und G" diskutiert. Da bei den durchgeführten Messungen die oben genannte Bedingung für den Verlustfaktor erfüllt ist, gilt:

$$|G^*| \approx |G'| \qquad (7)$$

Der besseren Übersichtlichkeit beschränkt sich diese Arbeit daher auf die Diskussion des komplexen Moduls G* und des Verlustfaktores tan δ.

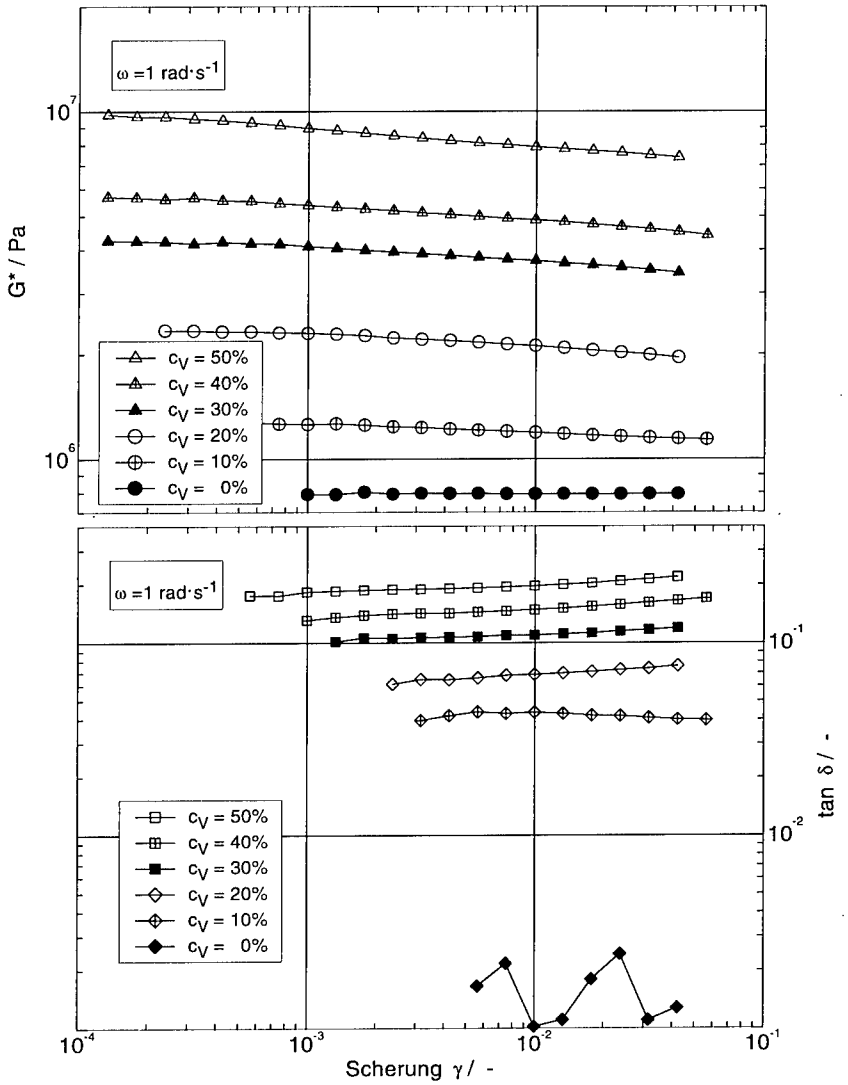

Abbildung 2: Amplitudensweep bei verschiedenen Füllstoffgehalten

Die Nicht-Linearitätsfaktoren (N-LF) hängen neben der Temperatur und der Frequenz von der gewählten Matrix-Füllstoffkombination ab. Als Trend werden in der Literatur beim N-LF eine Zunahme mit zunehmendem Füllstoffgehalt beobachtet. Das gleiche Verhalten zeigt HTPB gefüllt mit AP /1/, oder auch Arbeiten über rußgefüllte Elastomere /4/.

Da der Füllstoff RDX nur aufgrund von elektrostatischen Kräften an die Matrix gebunden ist und keine chemische Bindungen mit der Matrix eingeht, bezeichnet man solche Füllstoffe als nicht-verstärkende Füllstoffe. Für diese Füllstoffklasse ist bekannt, daß der N-LF mit abnehmender Partikelgröße kleiner wird. Bei einer Deformation einer gefüllten Matrix, ist durch die größere spezifische Oberfläche der kleinen Partikel, eine größere Kraft notwendig um die Matrix vom Füllstoff abzulösen. Dies führt zu einer Abnahme des N-LF. Verstärkende Füllstoffe zeigen hingegen, daß der N-LF mit zunehmender spez. Oberfläche zunimmt /1/.

Der N-LF zeigt für RDX 4 µm einen untypischen Verlauf: starke Zunahme des Faktors bis zu einem Füllstoffgehalt von 20%, für höhere Füllstoffkonzentrationen ist der Anstieg des Parameters deutlich flacher wie für niedrige Füllstoffkonzentrationen.

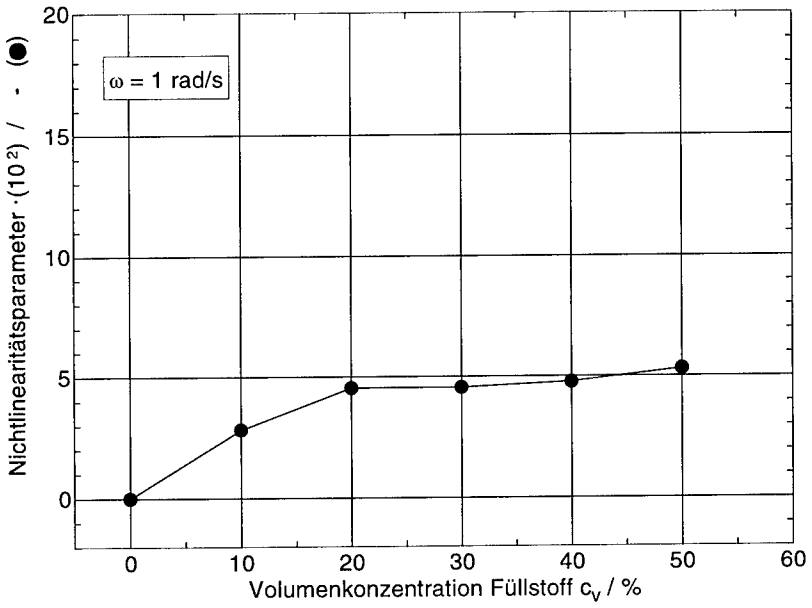

Abbildung 3: Nichtlinearitätsfaktor (I) des komplexen Moduls G*

Um das mechanische Verhalten von gefüllten Polymeren in Abhängigkeit von Füllstoffgehalt zu beschreiben, wird im allgemeinen der relative Modul betrachtet /5, 6/:

$$G_R^* = \frac{G^*}{G_M^*} \qquad \gamma,\ \omega = \text{konst.} \qquad (8)$$

G_R^* : relativer Modul

G^* : Modul des gefüllten Polymers, in dieser Arbeit: G_0^*

G_M^* : Modul der reinen Polymermatrix, ohne Füllstoff

Der Modul G_M^* der Matrix ohne Füllstoffe beträgt bei einer Temperatur von 23°C und einer Kreisfrequenz ω = 1 rad/s: $7{,}8 \cdot 10^5$ Pa.

Bei logarithmischer Auftragung des Moduls über der volumetrischen Füllstoffkonzentration in Abbildung 4, können die gemessenen Punkte gut durch eine Ausgleichsgerade angenähert werden. Pro 10 vol. % Füllstoffanteil erhöht sich der Modul im Mittel um 58%. Dies ist im Vergleich zu 4,8% Modulerhöhung je 10 vol. % Füllstoffanteil beim System HTPB/AP ein sehr hoher Wert. /1/ Die Nichtlinearitätsparameter beim HTPB/AP System nehmen wie beim GAP/RDX Füllstoffsystem mit dem Füllstoffgehalt von 0 bis $6 \cdot 10^{-2}$ zu.

Bei einer Kreisfrequenz von ω = 10 rad/s ist bei der HTPB Matrix (R = 0,95) das viskose Verhalten (tan δ = 0,85) viel stärker ausgeprägt, wie bei der GAP/N100 Matrix (tan δ = 0,01). Mit der sinnvollen Annahme, daß beide Füllstoffe AP und RDX einen wesentlich höheren Modul wie die jeweiligen Matrizes aufweisen folgt, daß die Haftungskräfte der RDX Partikel an der GAP/N100 Matrix wesentlich stärker sind, als bei AP Partikel an einer HTPB Matrix.

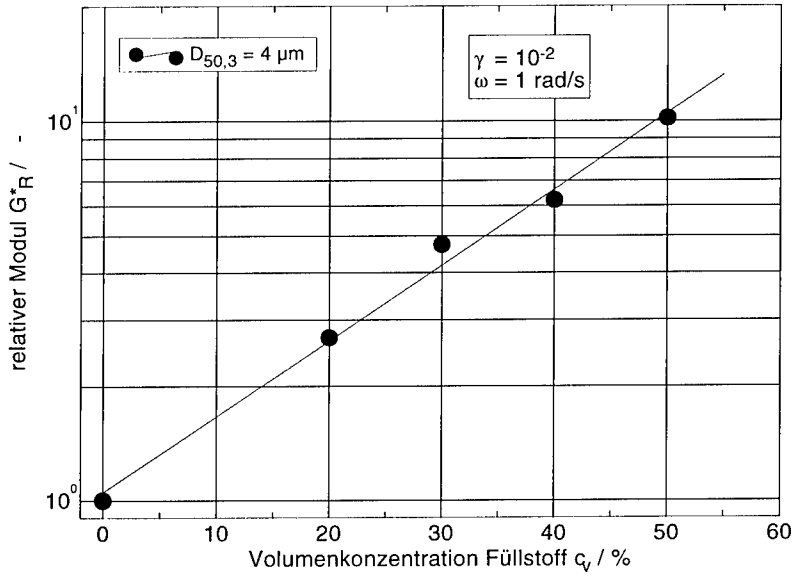

Abbildung 4: Relativer Modul in Abhängigkeit von Füllstoffgehalt

Frequenzabhängigkeit

Für die Diskussion der Frequenzabhängigkeit der Materialeigenschaften ist es notwendig, eine Konvention für den Verlustfaktor tan δ zu treffen. Ein Verlustfaktor von $3{,}5 \cdot 10^{-3}$ entspricht einem Phasenwinkel δ von 0,2° und liegt somit unterhalb des gültigen Meßbereiches der Meßapparatur. Für die weiteren Betrachtungen wird eine meßtechnische Grenze definiert, unterhalb derer der Verlustfaktor gleich 0 gesetzt wird, weshalb für die weiteren Betrachtungen folgende Definition gilt:

$$\tan \delta \equiv 0 \qquad \text{für } \delta \leq 0{,}2 \qquad (9)$$

Die Frequenzabhängigkeit des komplexen Moduls der ungefüllten Matrix ist für den Frequenzbereich von ω = 0,1 rad/s bis ω = 100 rad/s zu vernachlässigen. Die Zunahme des Moduls ist kleiner 3 %. Für höhere Frequenzen steigt der Modul jedoch stark an (ω = 237 rad/s, +16%). Je höher der Füllstoffgehalt, desto ausgeprägter ist die Frequenzabhängigkeit des Moduls. Bei 50% Füllstoffanteil beträgt die Zunahme des Moduls rund 90% (ω = 0,1 rad/s bis ω = 237 rad/s).

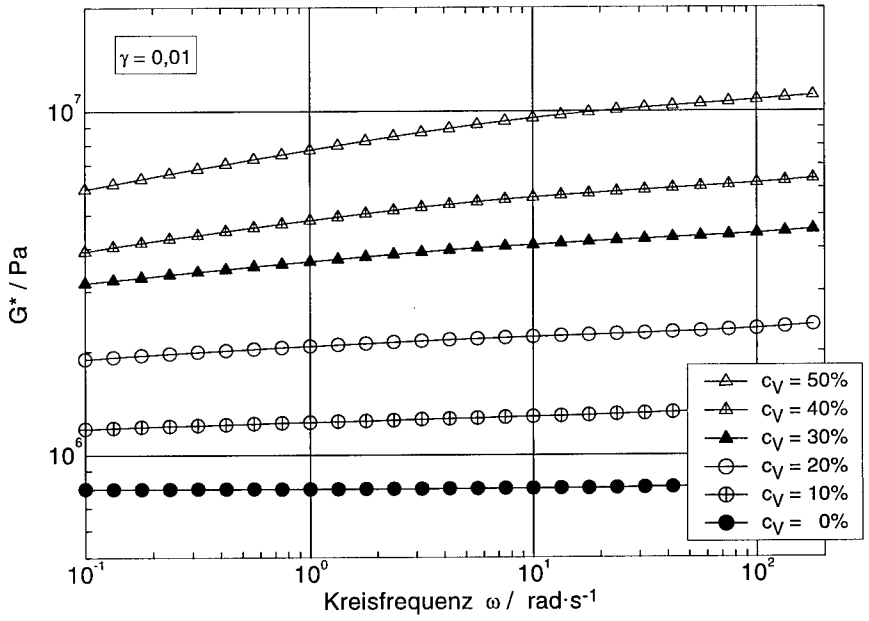

Abbildung 5: Abhängigkeit des komplexen Moduls von der Frequenz

Der Verlustfaktor tan δ ist bei der ungefüllten Matrix für Kreisfrequenzen kleiner 3 rad/s gleich 0. Für höhere Frequenzen nimmt der Verlustfaktor mit steigender

Frequenz zu. Für höhere Füllstoffgehalte durchläuft der Verlustfaktor in Abhängigkeit von der Frequenz ein Minimum. Die Lage des Minimums hängt vom Füllstoffgehalt ab. Im Diagramm ist eine Gerade eingezeichnet, welche die Minima bei verschiedenen Füllstoffgehalten kennzeichnet. Für höhere Frequenzen nimmt der Verlustfaktor mit steigender Frequenz zu, d.h. in diesem Bereich dominiert das Verhalten der Matrix. Für niedrige Frequenzen nimmt der Verlustfaktor mit steigender Frequenz ab. Der viskose Anteil G" durchläuft ebenfalls ein Minimum, während der elastische Anteil G' mit steigender Frequenz stetig ansteigt (hier nicht im Diagramm gezeigt). Eine Ursache für dieses Verhalten liegt in der Wechselwirkung zwischen Matrix und Füllstoff.

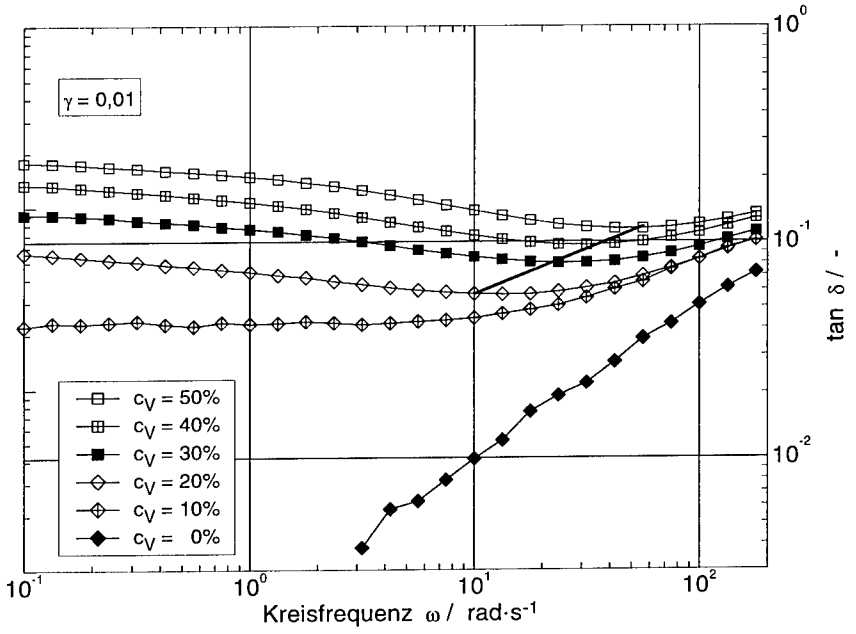

Abbildung 6: Verlustfaktor in Abhängigkeit von der Frequenz

Zusammenfassung

Es wurde die Änderung des Moduls G* und des Verlustfaktores tan δ bei verschiedenen Füllstoffgehalten des Matrix - Füllstoffsystemes GAP / RDX gemessen, und mit den Ergebnissen /1/ des Matrix / Füllstoffsystemes HTPB / AP verglichen. Die Matrix GAP/N100 verhält sich im untersuchten Temperatur- und Frequenzbereich linearelastisch. Die Frequenzabhänigigkeit des Moduls RDX gefüllter Proben nimmt mit dem Füllstoffgehalt zu. Bei Amplitudensweeps läßt sich das nicht lineare Verhalten gut mit dem Potenzgesetz beschreiben.

Die Matrix HTPB (R=0,95) verhält sich bei gleicher Temperatur und Frequenz viskoser wie die Matrix GAP/N100 (R = 1,0). Die Haftkräfte der RDX Partikel an der GAP/N100 Matrix sind wesentlich stärker wie bei AP Partikel an einer HTPB Matrix. Die Ablöseerscheinungen der Partikel von der Matrix bei einem Amplitudensweep sind für beide Martix - Füllstofsysteme von gleicher Größenordnung und lassen sich gut durch den bekannten Potenzansatz beschreiben.

Literatur

/ 1 / Stacer R. G., Hübner C., Husband D. M., Binder, Rubber Chemistry and Technology **63** (4) 488 (1990)

/ 2 / C. Hübner, Dissertation, Universität Karlsruhe (Technische Hochschule), 1994

/ 3 / R. G. Stacer, D. M. Husband, Rheol. Acta, **29**, 152 (1990)

/ 4 / A. R. Payne, R. E. Whittaker, Rubber Chem. Technol. **44**, 440 (1971)

/ 5 / Nielsen L. E., Polymer rheology, Marcel Dekker, New York, 1977

/ 6 / Goodier J. N., Phil. Mag., **22** (1936) 678

QUANTITATIVE MORPHOLOGICAL CHARACTERIZATION OF HIGH EXPLOSIVE CRYSTAL GRAINS BY LIGHT DIFFRACTION AND MICROSCOPY

Joseph T. Mang, Cary B. Skidmore, John F. Kramer, and David S. Phillips
Los Alamos National Laboratory
Los Alamos, New Mexico 87545 USA

Abstract

The morphology and size of crystal grains of high explosive (HE) materials are known to influence their processing characteristics and shock sensitivity. Little quantitative information is available on the morphology of HE grains. Particle size distributions are commonly obtained by light diffraction (LD), assuming a spherical morphology. However, polarized light microscopy (PLM) and scanning electron microscopy (SEM) measurements reveal that such an assumption is often incorrect, thus raising concerns about the validity of the size distributions extracted from LD measurements. While PLM and SEM can add qualitative insight into grain morphology, the limited statistics inhibits quantification. In comparison, LD measurements provide sufficient statistics, but a unique morphological model is difficult to obtain from diffraction data alone. By combining the PLM, SEM, and LD techniques a quantitative measurement of grain size and morphology can be obtained.

Here, we present a series of measurements on the HE materials, HMX, TATB, and PETN. A combination of the PLM, SEM, and LD techniques was employed to quantify their grain size and morphology. Analysis of PLM and SEM images was conducted to provide an initial evaluation of particle sizes and aspect ratios, which served as a basis set for modeling the diffraction data. The anticipated diffraction pattern arising from the basis set was calculated and compared to the measured data. Model parameters (mean size, aspect ratio) were refined in order to obtain the best fit to the diffraction data. Mean aspect ratios of 1.57, 1.51, and 7.50 were measured for HMX, TATB, and PETN, respectively. A comparison was made between grain size distributions derived from LD (assuming spherical grains) alone and those derived from combining LD with PLM and SEM.

I. Introduction

Grain size and morphology are known to affect the shock sensitivity, combustion rate, and processing of high explosive systems [1-4]. Van der Steen and co-workers [1] found that plastic bonded explosives possessing irregularly shaped RDX crystals were more sensitive than PBX's made with smooth grains of a definite morphology. Numerical simulations [2] of the combustion of HE grains have demonstrated the size and morphological dependencies of the combustion rate. Dufort [2] found that, while model systems of monodisperse, spherical grains show a monotonic increase in combustion rate with time, polydisperse systems of irregularly shaped grains displayed large fluctuations and different regions of increase and decrease of combustion rate. When considering the packing of granular beds of HE powders, grain morphology is naturally an important consideration [3]. Several [1,4] authors suggest that morphology influences the mutual interaction of grains in a packed bed and that void formation, caused by the reduced

adherence between the binder and the surface of irregularly shaped grains can partially account for their increased sensitivity.

While previous work [1-4] suggests an important link between HE behavior and grain size and morphology, most characterization work has focused on the grain size alone [5,6]. One of the primary techniques for characterizing HE grain sizes is light diffraction. However, size distributions extracted from these measurements assume that all particles are spherical. We know from previous microscopy work [5,7] that this assumption is not always valid and could lead to erroneous particle size distributions which would adversely influence attempts to model packing parameters and combustion rates.

In order to make a more accurate assessment of the size and morphology of the crystalline grains of HE powders, we have combined data from three different microstructural characterization techniques, polarizing light microscopy (PLM), scanning electron microscopy (SEM), and light diffraction (LD). Three different HE crystalline powders (HMX, TATB, and PETN), having distinct microstructural features, were studied. The microscopy techniques, being limited statistically, were used to provide an initial assessment of the grain morphology and size distribution. A model, reflecting these results was then used to analyze light diffraction data and thus quantify the results. A comparison is made between size distributions derived from this analysis and those obtained by analysis of the LD data assuming that all grains are spherical.

II. Light Diffraction – Fraunhofer Approximation

When a plane wave of monochromatic light impinges upon an aperture (or obstacle), a portion of the incident wavefront is disturbed and diffraction will occur [8]. According to the Huygens-Fresnel principle [8], every point on the undisturbed wavefront serves as an independent source of radiation, each point giving rise to a secondary wavefront. At any point on a distant screen, the resulting irradiance is determined by the interference (superposition) of these secondary wavefronts. The irradiance (intensity) pattern, measured as a function of the angle, θ, from the axis of the incident beam, is characteristic of the size and morphology of the aperture. In the Fraunhofer approximation [8], the intensity pattern is given by the average of the square of the real part of the Fourier transform of the aperture [9]:

$$I(\theta) \propto \left\langle [\mathrm{Re}(\int_{-\infty}^{\infty}\int_{-\infty}^{\infty} F(y,z)e^{ik(Yy+Zz)/R(\theta)}dydz)]^2 \right\rangle, \quad (1)$$

where F(y,z) represents the shape of the aperture and is equal to 1 within the aperture limits and is 0 otherwise, λ is the wavelength of the incident light, and $k = 2\pi/\lambda$.

The application of the above expression is not limited to idealized systems, but can be applied to real systems of powdered materials. Indeed, Eq. 1 forms the mathematical basis for benchtop particle size analysis instruments [10]. However, while real particles are three dimensional, diffraction-based analysis measures only the two dimensional projection of a given particle. We should also note that in the Fraunhofer approximation, the intensity distribution is independent of the particle's index of refraction.

As is done in most introductory Physics texts, Eq. 1 can be readily solved for simple particle (aperture) shapes. For a system of monodisperse spherical particles, having a circular 2-D projection, the diffracted light intensity is given by the well-known expression for a circular aperture [8,9]:

$$I(\theta) = I_0 A^2 \left(\frac{J1(kR\sin(\theta))}{kR\sin(\theta)} \right)^2, \quad (2)$$

where *A* is the area of the circle and R is its radius.

For monodisperse particles having a rectangular cross section, the expression for the intensity distribution appears as [8]:

$$I(\theta) = I_0 A^2 \left(\frac{\sin(kb\sin(\theta)\cos(\phi)/2)}{kb\sin(\theta)\cos(\phi)/2} \right)^2 \left(\frac{\sin(kc\sin(\theta)\sin(\phi)/2)}{kc\sin(\theta)\sin(\phi)/2} \right)^2, \quad (3)$$

where *A* is the projected area of the rectangle, *b* the major axis, and *c* the minor axis. ϕ is the angle of orientation of a particle, with respect to the incident beam. In the case of random particle orientation, Eq. 3 must be averaged over the angle, ϕ [8]:

$$I(\theta) = I_o \int_0^{2\pi} A^2 \left(\frac{\sin(kb\sin(\theta)\cos(\phi)/2)}{kb\sin(\theta)\cos(\phi)/2} \right)^2 \left(\frac{\sin(kc\sin(\theta)\sin(\phi)/2)}{kc\sin(\theta)\sin(\phi)/2} \right)^2 d\phi . \quad (4)$$

Most particulate systems contain some level of size polydispersity. By performing the appropriate population average, the effect of polydispersity on the measured intensity can be accounted for [10]:

$$I(\theta) = I_o \int_0^{\infty} A(a)^2 P(k\theta, a)^2 N(a) da . \quad (5)$$

In the above expression, $P(k\theta,a)$ represents the particle shape factor and N(a) is the number distribution of particles having a dimension between a and a + da.

Figure 1 displays log-log plots of the anticipated diffraction patterns for the simple shapes described above. As can be seen (Fig. 1a), there is little distinction between the intensity distributions for circles and oriented rectangles. However, the distinction is quite clear in the case of randomly oriented rectangular particles, and the distinction becomes dramatic as the aspect ratio ($R \equiv b/c$) increases (Fig. 1b).

III. Experimental

Three different samples of high explosive powders, HMX (lot HOL83L030-050), TATB (dry-aminated lot 12-11-81-0921-264), and PETN (LANL blend 87-16) were investigated. Representative SEM images of each sample are shown in Fig. 2. As can be seen in the figure, there are distinct microstructural differences among the samples, making them well suited for this investigation.

Light diffraction measurements were performed on a Beckman Coulter LS 230 particle size analyzer (size range: 0.04 – 2000 μm), employing the small volume module. Data were collected under flow conditions, using a solid state laser (λ = 750 nm) as the light source. Diffracted light was detected on an array of 126 photodiodes. Samples were prepared by mixing ~ 15 mg of a given material in 6 ml of deionized water. Prior to analysis of the HMX and TATB

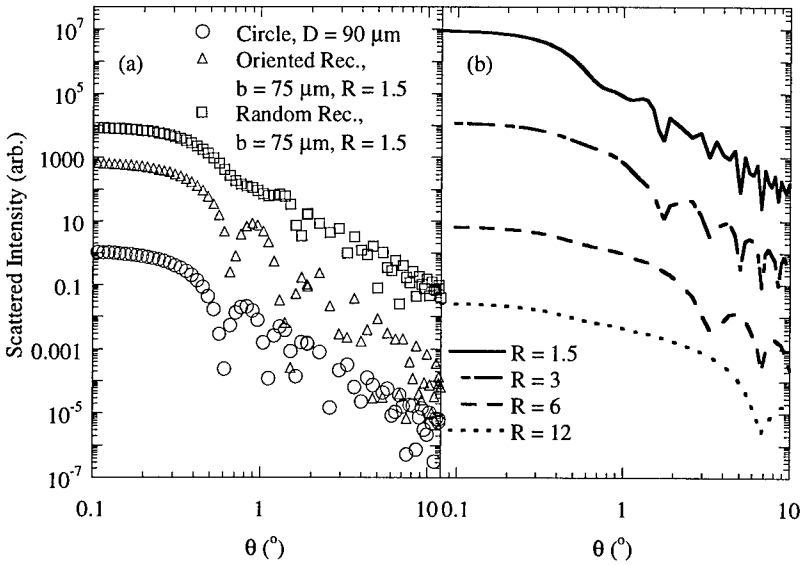

Figure 1: (a.) Comparison of model scattering curves for circular, oriented rectangular, and randomly oriented rectangular apertures. (b.) The effect of increasing *R* on the anticipated scattering from and randomly oriented rectangular apertures.

samples, the suspensions were placed in an ultrasonic bath for one minute in order to reduce the possibility of particle agglomeration. It has been demonstrated that such treatment does not affect the measured size distribution [5,6]. Identical runs were performed, using a small amount of surfactant (Triton X-100), in order to aid sample dispersion. However, no significant differences were found between runs with samples dispersed in water alone and those with samples dispersed in a water/surfactant mixture. Data reported here are for those runs performed in water alone.

Digital images of the crystal morphology for HMX, TATB, and PETN were acquired using light and electron microscopy. A sample of crystals in immersion oil (n=1.518 for HMX, n=1.660 for TATB, n=1.400 for PETN) was observed with transmitted, polarized light. In order to minimize the influence of operator bias, a sequence of images was collected along a line through the sample using a Spot camera (Diagnostic Instruments) and a DMRXA microscope (Leica). The spatial resolution of the microscope optics (NA=0.12 for the HMX and PETN samples, NA=0.25 for the TATB sample) was matched with the camera pixel characteristics to nearly meet the Nyquist limit in each case. Crystal samples were prepared for secondary electron

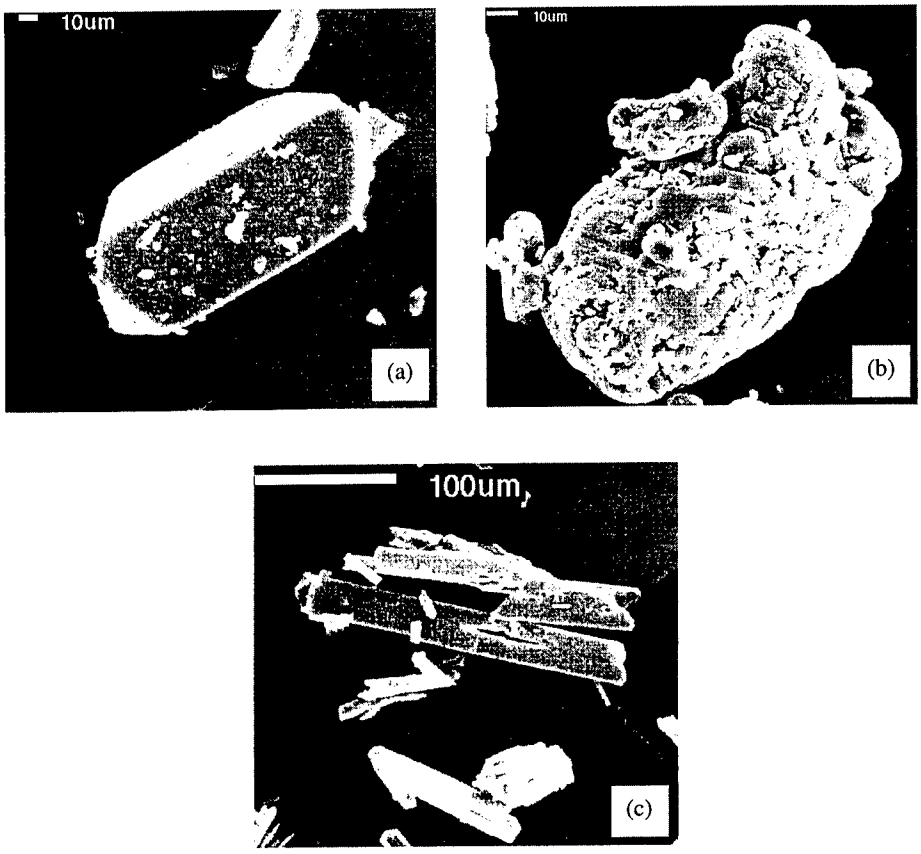

Figure 2: Representative SEM images of (a.) HMX, (b.) TATB, and (c.) PETN

imaging by sputter-coating with a thin layer of gold (~100 angstroms). Images were spatially calibrated and crystal dimensional data were obtained using Image Pro Plus (Media Cybernetics) software.

IV. Results and Discussion

Typically, commercially available instruments, complete with data analysis software, are employed for particle size analysis. With these systems, the data are analyzed according to Eq. 5, assuming that all particles are spherical [10]. This is done because in the case of spheres, Eq. 5 can

be inverted and solved analytically for N(a), thus yielding an unbiased distribution of particle sizes [10]. But in the process, all morphological information is lost. Depending upon the system under study, biasing the morphological content may be as equally unsatisfactory as assuming a functional form for N(a) and thus biasing the resulting size distribution. One solution to avoiding such bias is to have *a priori* knowledge of both the particle morphology and size distribution.

In order to determine an initial grain size distribution and morphological model for subsequent analysis of diffraction data, we performed analysis of digitized PLM and SEM images of all three samples. Preliminary assessment of the images indicated that the crystal grains of all three HE powders were best represented by particles having a rectangular cross section. As automated analysis of PLM and SEM images of HE crystals is complicated because of their inherent structural defects and anisotropic index of refraction, analysis was performed manually. In this way, structural parameters were obtained by circumscribing a given grain with a rectangle. The major axis (b, longer side), minor axis (c, shorter side), and aspect ratio ($R = b/c$) were recorded. The raw data were then binned according to size, thus determining the number distribution. Mean values were determined arithmetically and errors were calculated using Gaussian statistics. Between 300 – 1100 grains of each powder were analyzed in this way. PLM and SEM images were taken in such a way as to maximize the number of grains and resolution at a given magnification. This limited size ranges for the current study to between 2 and 625 μm.

Figure 3 and Table I summarize the results of the image analysis. The distributions displayed in the figures are those obtained from PLM analysis. As we can see from the figures, the statistics were sufficient to provide well-defined distributions. The HMX (Figs. 3a and 3b) and TATB (Figs. 3c and 3d) distributions, while being sharply peaked, possess small shoulders at larger values of b. The prominent peak of the major axis is centered at 14.5 and 12 μm for HMX and TATB, while the peak in the minor axis is centered at 8.5 μm for both materials. In comparison, the PETN (Figs. 3e and 3f) distributions are monomodal and much broader. The major and minor axis distributions are peaked at 90 and 13.5 μm, respectively. In all cases, the distributions show a lognormal profile. Table I shows a comparison of the mean values of the relevant parameters obtained from PLM and SEM analysis. For both HMX and TATB, the average values of b, c, and R obtained from SEM analysis are larger than those obtained from the PLM data. However, in both cases, approximately one third fewer grains were measured for the

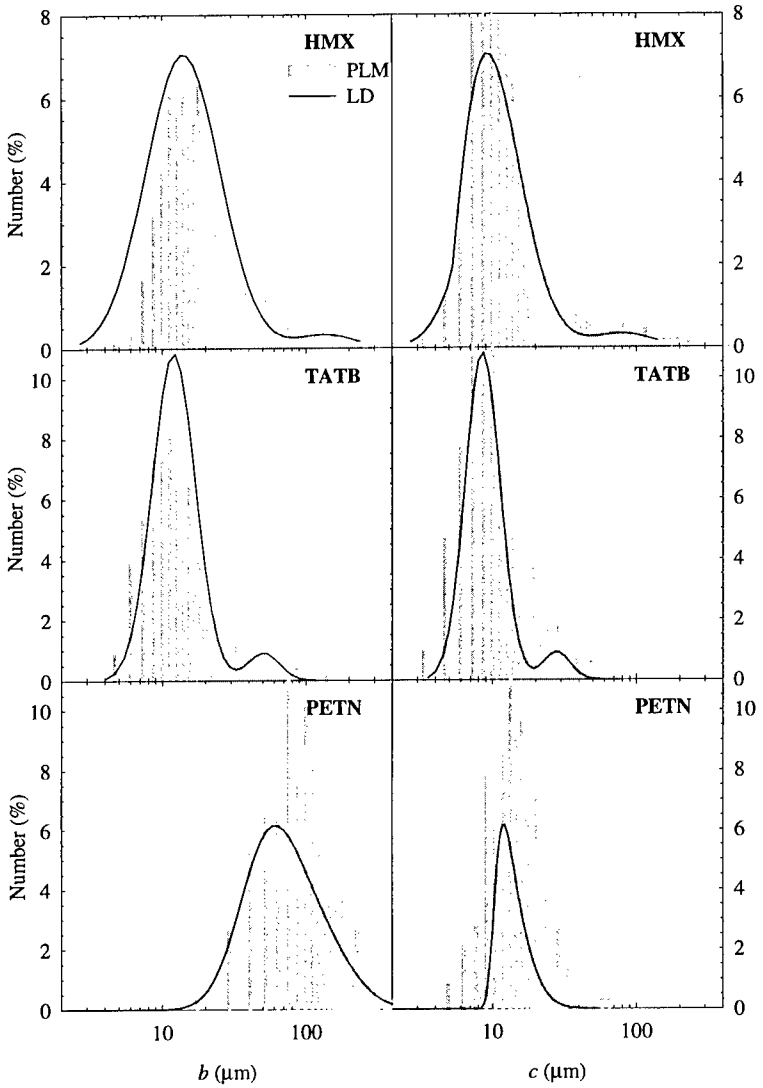

Figure 3: Comparison of number distributions extracted from PLM and LD analysis, employing a model of rectangular grains

SEM analysis. For PETN, an approximately equal number of grains were measured by each technique. In this case, we see that the average values of the relevant parameters are in better agreement, suggesting that the differences found for HMX and TATB are statistical in nature.

Table I: Summary of statistics from PLM, SEM, and LD Analysis

HMX, N_{PLM} = 1181, N_{SEM} = 390							
	Maximum (μm)		Minimum (μm)			Average (μm)	
	PLM	SEM	PLM	SEM	PLM	SEM	LD
Major Axis	292	267	5	3	35 ± 1	45 ± 2	50 ± 6
Minor Axis	232	238	4	2	23 ± 1	29 ± 2	23 ± 1
Aspect Ratio	6.7	6.7	1	1	1.57 ± 0.02	1.62 ± 0.03	
TATB, N_{PLM} = 1101, N_{SEM} = 399							
	Maximum (μm)		Minimum (μm)			Average (μm)	
	PLM	SEM	PLM	SEM	PLM	SEM	LD
Major Axis	139	198	4	4	23.1 ± 0.6	39 ± 2	44 ± 7
Minor Axis	76	118	2	4	14.8 ± 0.3	24 ± 1	30 ± 5
Aspect Ratio	4	3.2	1	1	1.51 ± 0.01	1.62 ± 0.02	
PETN, N_{PLM} = 388, N_{SEM} = 393							
	Maximum (μm)		Minimum (μm)			Average (μm)	
	PLM	SEM	PLM	SEM	PLM	SEM	LD
Major Axis	622	602	21	18	124 ± 4	127 ± 5	101 ± 17
Minor Axis	65	65	5	5	17.0 ± 0.4	21 ± 1	16 ± 3
Aspect Ratio	25	21	2	1.4	7.5 ± 0.2	6.2 ± 0.1	

Considering then the PLM data, we see that the average aspect ratio of 7.5 for PETN is much greater that those measured for HMX (1.57) and TATB (1.51), as anticipated from visual inspection of the images.

Light diffraction data were collected for the same three samples. Log-log plots of the diffracted intensity as a function of detector number are plotted in Figure 4. Through a non-disclosure agreement with Beckman-Coulter, the appropriate conversion between detector number and angle was obtained. This facilitated independent analysis of the data by different morphological models. The lines in the plots are a result of non-linear least-squares fits to model equations, as discussed below. Model calculations were done in the Fraunhofer (far-field) limit, which under the current circumstances is valid for particles as small as 1 μm in size. The fits were limited to data that correspond to the size range of the image analysis.

Data for the HMX and TATB samples were fit according to Eq. 5, for polydisperse, randomly oriented rectangular particles (Eq. 4). Polydispersity (N(a) in Eq. 5) in the major axis of the model system was represented as a bimodal, lognormal distribution, as analysis of the PLM data showed that the derived distributions were best represented in this way. The

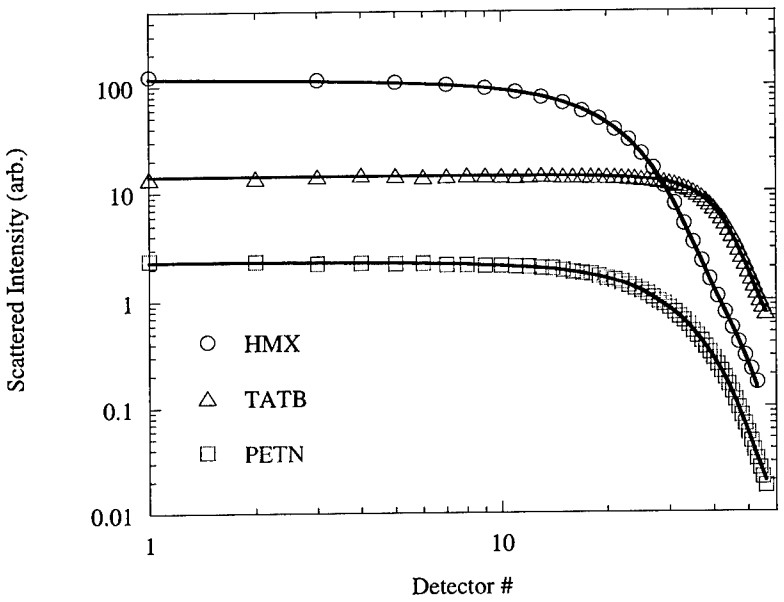

Figure 4: Measured light diffraction data for HMX, TATB, and PETN. The solid lines are fits to the model described in the text.

parameters derived from analysis of the PLM data were used as initial guesses for the model calculations. The distribution parameters (amplitude, center, width) were varied freely during the fitting process. In order to account for polydispersity in the minor axis, the measured aspect ratio was correlated with the major axis. Figure 5 shows plots of the results, where the points represent the average value of R for a given value of b. As can be seen in the plots, the data go to the limiting value of 1 for small b. For HMX, R increases rapidly with b, finally reaching a plateau. For TATB and PETN, R shows a gradual increase over the entire range of the data. In analyzing the PLM and SEM images, one can see many fractured crystalline grains. This fracturing of grains would explain the systematic decrease in R with decreasing b. The solid lines in the plots are the results of fits to an empirically determined relationship, $R = (m1*b^{-m2} + m3)^{-1}$. This relationship was used to calculate the value of c, for a given b value during model calculations. The parameters, m1, m2, and m3 were fixed throughout the model calculations. Good agreement between the model and data was found in both cases (Fig. 4). The solid lines in Figure 3 are the number distributions obtained from the analysis of the diffraction data. These distributions match the PLM distributions very well, showing, that the PLM data were representative of the

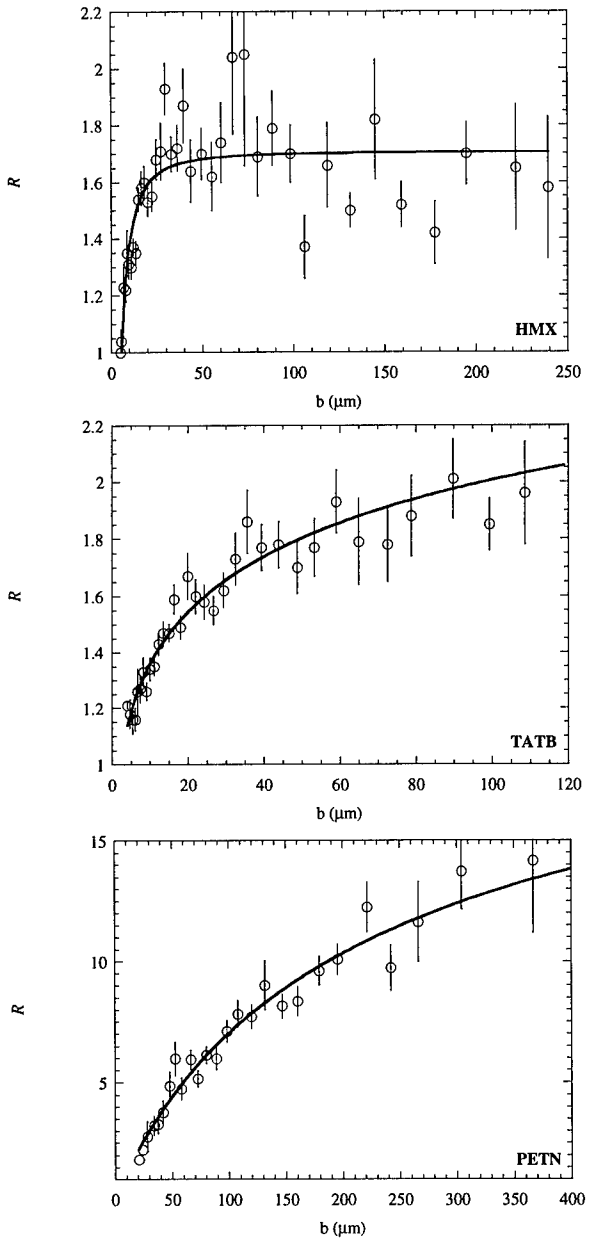

Figure 5: Correlation of R with measured values of b from PLM analysis. An empirical relationship (solid line) was used in model calculations.

population of grains and that the model for the LD data is sound. We would expect, as we are sampling a much larger number of grains ($N_{LD} \sim 10^7$, $N_{PLM} \sim 10^3$), that the distributions extracted from the LD data are more representative of the true population and that differences between the PLM and LD distributions are statistical in nature.

Initial attempts to model the PETN diffraction data followed the same path as that outlined above for HMX and TATB. The number distribution derived from image analysis was used as an initial guess and an empirical relationship between *R* and *b* was determined. However, it was found that this model did not accurately describe the measured data. Since the microscopy data showed that the PETN grains have a high aspect ratio, and, as mentioned previously, the diffraction data were collected under flow conditions, it was necessary to consider the effect of the flow field on the orientation of the crystal grains. Particles of the size studied here can be oriented by very modest shear flow. Helfrich [11]and others have studied the effects of a shear field on the orientation of elliptical particles and have found that in the zero torque (equilibrium) limit, the long axis of the particle will align in the direction of flow, at an angle which is dependent upon the particles aspect ratio [11]:

$$\tan\phi = \frac{c}{b} = R^{-1}. \qquad (6)$$

To account for particle orientation, the data were fit according to Eq. 5, but now the shape factor was that of an oriented particle (Eq. 3). The above expression (Eq. 6) was used to determine ϕ for a given particle. As we see from Figure 4c, the model of oriented particles describes the data very well. A comparison of the distributions extracted from the analysis of the LD data and those from PLM are shown in Figure 3. As we see, the LD distributions, while agreeing in shape and position, with the PLM data, are much sharper. Again, these differences can be attributed to the limited statistics in the PLM analysis.

We have also analyzed the LD data assuming the grains have a circular cross section. A comparison between the distributions extracted for circles and that of rectangles (Fig. 6) shows that, even for the cases of relatively small (~1.5) aspect ratios, the fits assuming circles consistently underestimate the particle sizes. For the PETN data, the circular model is primarily sensitive to the minor axis. Figure 6 demonstrates that accurate morphological models are needed

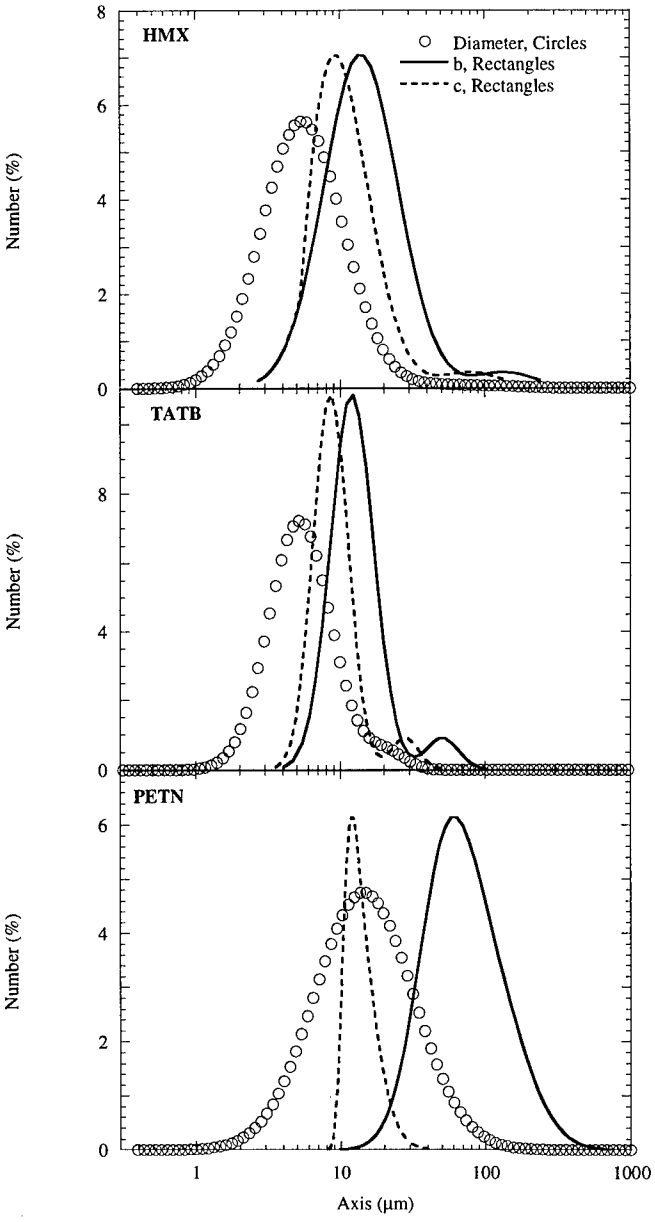

Figure 6: Comparison of the number distributions extracted from analysis of LD data for models of spherical and rectangular grains.

in order to extract the true particle size distributions and suggests that modeling efforts which depend upon particle size distributions as input will be sensitive to the particle morphology.

V. Summary

We have combined the techniques of PLM, SEM, and LD to quantify the size and shape of grains of three different high explosives. Image analysis of the microscopy data was used to provide *a priori* knowledge of the morphology and size distribution of grains. Light diffraction data were then used to refine these distributions. In all cases, we found that the HE powders could best be described as systems of polydisperse grains having a rectangular cross section. In comparing this analysis to a standard analysis, consisting of grains of circular cross section, we found that the latter analysis consistently underestimated the size of the grains. These results are important for modeling the packing of granular beds of high explosives and attempts to accurately model the detonation properties of different HE systems. In future work, we plan to increase the size range by employing higher magnification images and combining the light diffraction data with other techniques, such as small-angle x-ray and small-angle neutron scattering.

VI. References

1. Van der Steen, A.C., Verbeek, H.J., and Meulenbrugge, J.J., *Proceedings of the 9th Detonation Symposium*, p. 83 (1989).
2. Dufort, S., Cherlin, H., and Gohar, P., *Proceedings of the 9th Detonation Symposium*, p. 1271 (1989).
3. Coyne, P.J., Elban, W.L., and Chiarato, M.A., *Proceedings of the 8th Detonation Symposium*, p. 1271 (1985).
4. Borne, L., and Patedoye, J., *Propellants, Explosives, Pyrotechnics*, **24**, p. 255 (1999).
5. Burnside, N.J., Son, S.F., Asay B.W., and Skidmore, C.B., *Proceedings of the 10th APS Topical Group on SCCM* (1997).
6. Bremser, J., and Lee, K-Y., *Proceedings of the 29th International Annual Conference of ICT*, p. 13-1 (1998).
7. Skidmore, C., Phillips, D., and Crane, N., *Microscope*, **45**, 127 (1997).
8. Van De Hulst, H. C., *Light Scattering by Small Particles* (Wiley & Sons, New York, 1957).
9. Hecht, E., and Zajac, A., *Optics*, (Addison-Wesley, California, 1979).
10. Hirelman, D.E., *Liquid Particle Size Measurement Techniques*, (Vol. 2, ASTM, Pennsylvania, 1990).
11. Helfrich, W., *J. Chem. Phys.*, **50**, 100 (1969).

Studies of the Synthesis and Crystallization of CL-20

R. S. Hamilton, A. J. Sanderson*, R. B. Wardle, K, F, Warner
Thiokol Propulsion,
Brigham City, Utah 84302-0707

ABSTRACT

All aspects of the synthesis of the high energy density nitramine, CL-20, have been extensively investigated at Thiokol in order to realize the potential of this exciting new material. The fact that CL-20 can exist in a number of different polymorphs is well known, as is the fact that the material purity, the nature of any impurities, crystal polymorph, crystal morphology and crystal quality can greatly influence the sensitivity of energetic crystals. Therefore, we have been investigating the synthesis and crystallization of CL-20 with three primary objectives:

1 – to develop the optimal large scale synthesis of CL-20;
2 - to develop a practical and reproducible crystallization method for CL-20;
3 – to determine the effect of crystal morphology, purity and quality on CL-20 sensitivity.

Synthesis efforts have investigated a number of nitrolysable precursors to CL-20, including isowurtzitane cages substituted with acetyl, formyl, and nitroso groups and partly unsubstituted cages. Initial crystallization efforts concentrated on using controlled precipitation methods with a variety of environmentally acceptable solvents and non-solvent. We have also investigated the dependence of morphology, crystal size and quality on factors including the purity, type of solvent and non-solvent and crystallization method.

The materials from all of these studies have been characterized by optical and electron microscopy, HPLC, IR, NMR, and particle density distribution and particle size distribution. The effect of crystal purity and morphology on neat powder sensitivity, formulation processing and formulation sensitivity have also been explored.

© 2000, Thiokol Propulsion, A division of Cordant Technologies, Inc.

BACKGROUND

The original route to make CL-20 used tetraacetyldinitrosohexaazaisowurtzitane (TADN) as the precursor to the final nitration[1]. This material is made using either N_2O_4 or a nitrosonium salt. Although the CL-20 made from this route can be very pure, it is not the most economical route and it is either necessary to isolate and handle a nitrosamine or to do the nitrosation and subsequent nitration in one pot. The one pot nitrosation followed by nitration is feasible in the laboratory but cannot practically be scaled up.

The second route to make CL-20 uses tetraacetyldiformylhexaazaisowurtzitane (TADF) as the precursor to the final nitration. Direct nitration gives CL-20 but the formyl groups are hard to remove compared to the acetyl groups. Complete removal takes prolonged vigorous nitration conditions. Under reasonable conditions, some monoformyl (normally $\beta 2\%$) tends to be left. This residual monoformyl material cannot efficiently be removed by crystallization techniques. With the formyl group being electronically and spatially similar to the nitro group this is not altogether surprising. However, it has been suggested that the pentanitromonoformylhexaazaisowurtzitane in the CL-20 crystal lattice, by causing many crystal defect sites, could give rise to high crystal sensitivity. Work to study this effect was conducted in which material was deliberately under-nitrated to leave various amounts of pentanitromonoformyl cage (from 1-10%). This gave rise to no detectable change in powder sensitivity[2] but it did not alleviate the suspicion that somehow the monoformyl cage was responsible for undue sensitivity.

More recently, another practical precursor to CL-20 has been developed[3]. This is the free diamine, tetraacetylhexaazaisowurtzitane (TADA). It has been known for some time and it has been nitrated, but only fairly recently has it been available in large quantities. There are several interesting things to note about this material as a source for CL-20. This first is that as it contains no formyl groups, there can be no formylated impurity in the final product. With no formyl groups one might also expect the nitration to a clean product to be relatively faster than TADF. However, one might expect the nitration of a free amine with mixed acid not to work well[4]. Even if it did work or nitration with another nitrating agent worked well, there could be different impurities in the final product and they may influence crystallization and sensitivity.

EXPERIMENTAL

TADA was nitrated with a number of different nitrating agents, primarily mixtures of nitric acid and another strong acid. With two of these mixtures, different acid ratios were investigated together with different ratios of TADA to acid mixture. In all cases the reactions were followed by ^1H NMR in order to obtain an approximate indicator of the rate of reaction. The NMR samples were prepared by removing an aliquot of the reaction solution, cooling it rapidly and pouring it onto ice. The solid precipitate was filtered off, dried and dissolved in D6-acetone. In addition, in some instances, the final product was isolated and analyzed by HPLC using either comparison against a standard or the method detailed in the draft STANAG 4566 to determine whether the product met STANAG purity requirements. Samples were also crystallized, submitted for small scale hazard testing, polymorph analysis and microscopy.

Typical procedure

In a typical reaction, 10 grams of TADA was dissolved at ambient temperature in 100ml of the nitrating medium being studied. This solution was rapidly heated to a gentle reflux (about 85°C for the nitric/sulfuric acid mixtures). Samples (1-2ml) were removed at intervals, rapidly cooled, quenched on ice, filtered, dried and analyzed by ^{1}H NMR in D6-acetone. At the end of the reaction time, the whole solution was cooled to ambient or below before being carefully poured onto 2 volumes of ice/water. The solid was filtered off, washed with water until the washings were neutral and dried. This product was analyzed by HPLC and ^{1}H NMR.

To recrystallize CL-20, the product from the nitration was dissolved in ethyl acetate and this solution was washed with aqueous sodium bicarbonate solution and then water. It was then dried over magnesium sulfate and concentrated to give a saturated solution at ambient temperature. Three volumes of heptane were then added over 1-2hrs with gentle stirring to effect precipitation of the product. During this process but before the CL-20 started to precipitate, a small amount of epsilon CL-20 seed crystals were added to the solution to ensure the desired polymorph precipitated. The precipitated product was filtered off and dried before being analyzed by FTIR and microscopy. Samples were also subjected to small scale impact, friction and heating tests.

RESULTS

Table 1 shows some of the initial experiments that were conducted with different nitrating media and conditions. The sulfuric/nitric acid system showed the most promising results, so following these experiments optimization of the sulfuric/nitric acid system was investigated. These results are shown in table 2. In order to compare nitration results with those previously conducted with using TADF another set of reactions were conducted using conditions developed for TADF (table 3).

DISCUSSION

The results show that TADA, a free amine, is easily and smoothly nitrated in strongly acidic nitrating media. The mechanism by which this occurs is exceedingly hard to isolate. The reaction is complex, will have multiple, concurrent pathways, and all the intermediates have not been isolated. It is of course probable that the amine is immediately protonated on dissolving in the acid solution. This would normally be expected to prevent subsequent clean nitration. However, nitration of the acetyl substituted positions releases acetyl group into solution that during the course of the reaction will reach fairly high concentrations. It is thus possible that during the latter stages of nitration the reaction medium comes to resemble one in which nitration with acetyl nitrate occurs, a common medium for nitration of secondary amines. In addition, the basicity of the amines will be greatly reduced as the cage is nitrated. This could allow nitration in the same way that other non-basic nitrogens, such as urethanes are nitrated. A further possibility is that the basicity and reactivity of the amines on the piperizine ring of the substituted hexaazaisowurtzitane cage is unusual because of the conformation into which they are locked by the fused ring system.

Despite the observation that most of the amines are cleanly nitrated, there does appear to be a degree of decomposition of the cage during nitration. The yield on nitration from TADF is very nearly quantitative. The yield from TADA is very high but not quantitative, and there are no other isolated products that account for the loss of the precursor. On nitration of TADF there is appreciable NOx evolution presumably because of decomposition of the substituted formyl group. The decomposition of the cage and the deacteylation that occurs from TADA is not accompanied with NOx evolution or obvious gassing. The products therefore must be water soluble, acid stable remnants of the cage that derive from hydrolysis and not oxidation. It is again conjecture, but one could anticipate that they derive from decomposition of the protonated amine in a reaction competing with nitration at these positions.

Good kinetics of the nitration of TADA have not been obtained. ^{1}H NMR or HPLC can be used to observe that the rate of formation of CL-20 but it does not follow an obvious kinetic order. This is to be expected, as during the reaction under the majority of conditions studied precipitate forms that is a mixture of CL-20 and partly nitrated intermediates. The nitration in solution is clearly quite fast. Under optimum conditions, the bulk of the reaction is over in a few minutes. However as the intermediates drop out of solution, the reaction rate becomes more dependant on solubility and the rate of solvation than nitration rate. This is the cause of the somewhat surprising observation that the rate of formation of CL-20 increases with solutions that increase the concentration of nitronium ion only up to a point. This is observed in sulfuric acid where at fairly high concentrations of TADA, the maximum rate of formation of CL-20 is seen in an approximately 75:25 mixture of sulfuric and nitric acids. With higher proportions of sulfuric acid the rate of CL-20 formation slows even though the concentration of nitronium ions is expected to increase. The lack of solubility of the intermediates in mixed acid with a high proportion of sulfuric acid would appear to account for this. This also explains why the rate of CL-20 formation in methanesulphonic acid is higher than one would expect compared to that in sulfuric acid when considering how much weaker an acid it is. Methane sulphonic acid is a much better solvent for the intermediates than is sulfuric acid.

All of these observations add a complication to optimization of nitration conditions. Higher concentrations of TADA can be nitrated rapidly if more sulfuric acid present to maintain high acidity during the reaction but only up to the point where solubility becomes rate determining. Of course, very high rates can be obtained with slightly less sulfuric and more dilute substrate concentrations, but this is less economically desirable. If slower rates are acceptable, efficient reaction with high substrate concentrations are obtained with lower sulfuric acid concentrations. However a greater proportion of nitric acid, the more expensive of the two acids, has to be used.

A detailed study of the crystallization of formyl free CL-20 was started. However crystallization using standard methods that had been developed with CL-20 derived from TADF gave the epsilon polymorph according to FT-IR spectroscopy. These neat crystals had small scale hazard properties that were not distinguishable from TADF derived CL-

20 by our testing methods. Impact and friction sensitivity did not appear to be related to particle size or shape for the materials that we tested under this program.

CONCLUSIONS

The results show that the free amine, TADA can be exhaustively nitrated in good but not quantitative yield in strongly acidic nitrating media. The yield is largely independent of the nitration conditions provided that they are sufficiently reactive to complete the reaction. Absolute figures for yield are hard to determine because of the difficulty of identifying the exact degree of acetylation of the starting material. However, a very pure product that is free from formylated impurities can be obtained by an economically reasonable route.

The results also show that the nitration of TADA is not of a simple kinetic order, in part due to there clearly being a number of steps in the nitration mechanism and in part due to insolubility of the reaction intermediates and the product. However, the reaction rate is clearly very fast compared to the nitration of TADF. The limiting factor to reaction rate is not just the nitronium ion concentration or acidity, but a combination of this and the insolubility of the pentanitromonoacetyl cage.

The polymorphs that can be obtained from formyl-free CL-20 appear to be identical to those obtained from TADF derived CL-20. From these preliminary studies, the crystal morphology and powder sensitivity of the material is also not discernibly different from material containing monoformyl impurities. However, further investigations in this area are continuing.

Table 1. A selection of the experiments conducted to determine optimum nitrating acid, substrate concentrate and approximate rate of reaction.

Substrate	Acid 1	Acid 2	Ratio substrate/acid	Ratio of acid1/acid 2	Time/min	Peak ratio*
TADA	MeSO3H	100%HNO3	0.1	0.25	15	1.9
TADA	MeSO3H	100%HNO3	0.1	0.25	20	5.2
TADA	MeSO3H	100%HNO3	0.1	0.43	10	2.6
TADA	MeSO3H	100%HNO3	0.1	0.43	15	6.5
TADA	MeSO3H	100%HNO3	0.1	0.43	20	24
TADA	MeSO3H	100%HNO3	0.1	0.67	5	1
TADA	MeSO3H	100%HNO3	0.1	0.67	10	4.9
TADA	MeSO3H	100%HNO3	0.1	0.67	15	13
TADA	MeSO3H	100%HNO3	0.1	0.67	20	68
TADA	MeSO3H	100%HNO3	0.1	0.5	5	1
TADA	MeSO3H	100%HNO3	0.1	0.5	10	2.4
TADA	MeSO3H	100%HNO3	0.1	0.5	15	5.2
TADA	MeSO3H	100%HNO3	0.1	0.5	20	13
TADA	P2O5	100%HNO3	0.1	0.05	20	no ppt
TADA	P2O5	100%HNO3	0.1	0.25	2.5hr	1
TADA	HCl	100%HNO3	0.1	0.43	30	no ppt
TADF	MeSO3H	100%HNO3	0.1	0.67	15	1
TADF	MeSO3H	100%HNO3	0.1	0.67	20	1.8
TADA	MeSO3H	100%HNO3	0.1	2.33	15	154
TADA	H2SO4	100%HNO3	0.17	1.5	20	19
TADA	H2SO4	100%HNO3	0.17	1.5	40	22
TADA	H2SO4	100%HNO3	0.2	0.18	30	<1
TADA	H2SO4	100%HNO3	0.33	0.11	60	<1
TADA	-	70%HNO3	0.2	-	5	no ppt
TADA	H2SO4	70%HNO3	0.033	2	10	15.4
TADA	H2SO4	70%HNO3	0.033	2	15	15.4
TADA	H2SO4	70%HNO3	0.033	2	25	15.4
TADA	H2SO4	100%HNO3	0.2	2	10	25
TADA	H2SO4	100%HNO3	0.2	2	15	25
TADA	H2SO4	100%HNO3	0.2	2	20	8

* in these experiments the 1H NMR peak ratio of the smaller CL-20 peak to the largest of any non-CL-20 peak occurring between 7 and 9ppm was used as a crude measure of the extent of reaction and hence reaction rate.

Table 2. Kinetic studies on the nitration of TADA with different ratios of H_2SO_4 to HNO_3.

Ratio H2SO4/HNO3	Time/min	Peak ratio*
0.11	20	72
0.11	25	91
0.11	30	91
0.11	35	97
0.11	40	98
0.25	15	92
0.25	20	100
0.25	25	100
0.25	30	100
0.25	35	100
0.25	40	100
0.43	10	100
0.43	15	100
0.43	20	100
0.43	25	100
0.43	30	100
0.43	35	100
0.43	40	100
0.67	5	91
0.67	10	91
0.67	15	88
0.67	20	100
0.67	25	100
0.67	30	100
0.67	35	100
0.67	40	100
1	10	71
1	15	89
1	20	92
1	30	98

* in these experiments the 1H NMR peak ratio of the smaller CL-20 peak to the largest of any non-CL-20 peak occurring between 7 and 9ppm was used as a crude measure of the extent of reaction and hence reaction rate. At a ratio of 100 the reaction was considered essentially complete.

Table 3. Typical results from the nitration of TADA with an 85:15 HNO_3:H_2SO_4 nitrating mixture

Water (%)	Total Reaction Time (hrs)	Initial Acids Mass (g)	Initial TADA Mass (g)	Max Temp For Reaction Flask	Final CL-20 Mass (g)	Purity by HPLC* CL-20 (%)	Yield (%)
0	4	47.44	5.168	84 C	5.7221	99.0	84.94
7.5	4	45.75	4.998	87 C	5.5030	93.9	84.46
0	2	457.93	49.87	83C	59.6737	101.2	91.79
0	3	450.74	49.12	82C	57.6090	103.4	89.97

* - the HPLC results are relative to a standard CL-20 sample.

[1] A.T. Nielson, US Patent 5,693,794 Caged Polynitramine Compound, 1997.
[2] R. B. Wardle, unpublished results.
[3] Kodama et al, WO/23792, 1996.
[4] T. Urbanski, "Chemistry and Technology of Explosives" vol. 3, Pergamon Press, 1967.

THE EFFECT OF DIFFERENT CRYSTALLISATION TECHNIQUES ON MORPHOLOGY AND STABILITY OF HNF

Willianne H.M. Veltmans[i], Antoine E.D.M. van der Heijden[ii], John M. Bellerby[iii], Michael I. Rodgers[iv]

1 Summary

The solid oxidiser Hydrazinium Nitroformate (HNF) has been identified as a very powerful oxidiser for high performance solid propellants. HNF based propellants have two distinct advantages over presently used Ammonium Perchlorate based propellants: a very high specific impulse and chlorine free combustion products.

In this paper two different crystallisation techniques for HNF and their effect on morphology and stability are described.

The ICI process is a special recrystallisation technique. With this special technique dense agglomerates of very fine primary particles are produced. The technique is especially suitable for co-crystallisation of additives like for instance stabilisers. Optimisation of re- and co-crystallisation of HNF has been performed.

The second recrystallisation technique for HNF discussed in this paper is sonocrystallisation. The application of ultrasound during cooling recrystallisation of HNF has already been shown to have a positive influence on morphology (aspect ratio and particle size) on a small-scale. Scaling up this production technique to pilot-scale showed that the trend of morphology and stability improvement is preserved.

The morphology of the HNF crystals is characterised by microscopic analysis. The stability is not only characterised by vacuum stability tests but also by headspace gas chromatography–mass spectrometry (GC-MS). In this technique samples of HNF crystals are aged in a closed vial at a certain temperature. At different points in time the gas in the vial above the solid HNF is sampled and analysed directly by GC-MS. The stability of HNF can then be characterised by the amount and character of the evolved gases.

[i] Aerospace Propulsion Products bv, P.O. Box 697, 4600 AR Bergen op Zoom, The Netherlands (corresponding author).
[ii] TNO Prins Maurits Laboratory, P.O. Box 45, 2280 AA Rijswijk, The Netherlands.
[iii] Cranfield University, Royal Military College of Science, Shrivenham, Swindon, Wiltshire SN6 8LA, United Kingdom.
[iv] ICI Nobel Enterprises, Ardeer Site, Stevenston, Ayrshire KA20 3LN, United Kingdom.

2 Introduction

In a search for new storable high performance propellants for the European Space Agency (ESA), the solid oxidiser Hydrazinium Nitroformate (HNF) was identified as a very promising ingredient of a new storable composite propellant[1,2]. HNF-based propellants have two distinct advantages over established solid composite propellants: a much higher specific impulse and chlorine free exhaust products[3,4].

A safe synthesis method for HNF on lab scale was established by TNO (The Netherlands Organisation for Applied Scientific Research) in 1990. Since 1993, HNF has been produced on pilot-scale at APP, Bergen op Zoom. Methods were developed and implemented to produce good quality HNF crystals of specific particle size, shape, purity and stability. However, the morphology of the HNF crystals was not yet optimised. In other words, the aspect ratio of the HNF crystals (length over diameter ratio) was still too large to allow the desired high solid load of HNF in the polymer matrix of the final propellant. Furthermore, the high temperature stability of HNF, especially at temperatures higher than 60 °C, still needed important improvement in comparison to established criteria.

This paper describes the effect of two special crystallisation techniques on the morphology and stability of HNF. The special crystallisation techniques are the application of ultrasound during recrystallisation of HNF on pilot scale and the ICI crystallisation process for HNF re- and co-crystallisation.

3 Background

During the development of HNF a number of crystallisation techniques has been applied for (re)crystallisation of HNF to find a method that would give high quality HNF with regard to purity, stability, sensitivity, morphology and would be practical from a production point of view. Techniques that have been tested are for instance precipitation, drowning-out, cooling, evaporation and vapour growth crystallisation. From these techniques drowning-out, cooling and evaporation crystallisation were optimised with regards to solvent[5], cooling/evaporation rate et cetera and implemented as commercial recrystallisation methods for HNF. A summary of the main characteristics of the three commercial grades of HNF (HNF-S, HNF-C and HNF-E) is shown in Table 1.

4 ICI crystallisation

ICI has developed a system for the crystallisation of solid material which results in powders which have very particular types of crystal morphology. This process has been applied to a number of different materials, both explosive and non-explosive, and to mixtures as well as pure compounds. Preliminary work[5] showed that HNF was suitable for the processing method and that HNF could be re- or co-crystallised with this ICI recrystallisation process. As the crystallisation process is of proprietary nature no description will be given of the production method.

Table 1 Summary of HNF characteristics per grade

Parameter		HNF-C	HNF-S	HNF-E
$[HNF]_{acid}$	(w%)	99.8 – 100.8	98.8 – 99.6	99.0 – 100.3
$[HNF]_{HZ}$	(w%)	97.9 – 100.0	97.2 – 99.6	97.8 – 99.3
T_m[1]	(°C)	≥ 116	≥ 115	≥ 115
VTS (60 °C, 48 hrs)	(ml/g)	≤ 0.5	≤ 1.8	≤ 0.2
L/D	(-)	≤ 8	≤ 8	-
$x_{50,n}$	(μm)	400 – 900	50 – 150	-
x_{10}/x_{50}	(-)	≥ 0.5	≥ 0.6	-
x_{90}/x_{50}	(-)	≤ 1.5	≤ 1.4	-
BAM Friction	(Nm)	16-36	16-36	16-36
BAM Impact	(N)	2-4	2-4	2-4

[1] T_m measurement is measured with black body radiation apparatus, which gives melting points 5 – 7 °C lower than when using an oil bath submersion technique and 10 – 15 °C lower than DSC measurements when using heating rates of 5-10 °C/min.

4.1 ICI re-crystallisation of HNF

The variable process parameters have been changed to find the ranges of pure HNF characteristics that were possible to obtain with this production method (see Table 2).

Table 2 Range of several HNF product characteristics obtained by ICI re-crystallisation of HNF

HNF characteristic[1]			Value
Particle size (est.)		(μm)	<1 – 90
Aspect ratio (est.)		(-)	1 – needle shaped
DSC	onset	(°C)	121 – 129
	peak[2]	(°C)	125 – 134
VTS	(48 hrs, 60 °C)[3]	(ml/g)	0.4 – 1.3
	(24 hrs, 80 °C)[4]	(ml/g)	3.4 – 5.4
Impact		(Nm)	<0.5 – 2.5
Friction		(N)	16 – 31

[1] All ranges are based on 14 different batches unless stated otherwise.
[2] Based on 11 batches.
[3] Based on 5 samples.
[4] Based on 2 samples.

These experiments show that with the ICI crystallisation process it is possible to produce very small particles, smaller than with APP's standard production techniques. In general these particles have a very good aspect ratio (~1), only the larger particles (10 – 90 μm) having the tendency to form needles.

Looking at VTS and DSC data a trend can be discerned in that the smaller particles give a lower DSC decomposition temperature and more gas emission (VTS). This is probably due to the increase in surface area. This trend is in accordance with the fact that standard APP material has lower gas emissions.

There is little change in impact and friction sensitivity, although impact sensitivities <2 Nm usually are not measured for standard HNF material.
When comparing these experimental batches with standard HNF material one has to bear in mind that the scale, process optimisation and experience level cannot be compared. Product characteristics as obtained with VTS and DSC can probably be improved significantly for these experimental batches.

4.2 ICI co-crystallisation of HNF with additives

As expected from this recrystallisation process, the use of co-crystallising materials does not significantly affect the nature of the solids produced. The particles sizes produced are comparable to the pure HNF samples. The VTS measurements vary according to the nature of the additive material. Some of the samples show an improvement over pure HNF, while others show either no change or a decrease in stability. The effect on the impact and friction sensitivities is minor. The addition of 4 w% of an additive increases the BAM friction sensitivity from 20-28 to 59 N (the ultrafine HNF remained a sensitive material according to standard criteria).

5 GC-MS

5.1 Experimental

Headspace GC-MS was carried out using a Dani 3950 headspace analyser fitted with a 10 µl sample loop and interfaced to a Fisons GC8000/MD800 gas chromatograph-mass spectrometer. A sample for ageing and analysis was obtained by placing a small amount (approximately 0.5 g) of HNF into a $20cm^3$ crimp top glass vial (Chromacol 20-CV) and then sealing the vial in air with an aluminium crimp cap and butyl rubber/PTFE septum. The loaded vial was then placed in an aluminium block heater (Grant BT3) and aged at a temperature between 40°C and 80°C.

After ageing, the vial was positioned in the headspace unit at a conditioning temperature of 40°C. The headspace in the vial was then sampled and the gas allowed to pass onto the GC column (Chrompack PoraPlot Q; 25 m, 0.25 mm id) which was initially maintained at -80°C using cryogenic cooling. After 5 minutes the column temperature was raised to 150°C at a rate of 15°C per min and held at this temperature for a further 5 minutes. Under these conditions it was possible to achieve complete baseline separation of N_2, O_2, Ar, CO, CO_2, N_2O and H_2O. The separation of argon from the other air gases allows it to be used as an inert internal calibrant against which the increase or decrease in the levels of other headspace gases as a function of time can be compared.

5.2 Results and Discussion

HNF-E

Samples of HNF-E were aged at 40°C, 60°C, 70°C and 80°C and analysed by headspace GC-MS as described above.
At 40°C trace amounts of N_2O were detected after about 300 hours of ageing and the levels of this gas scarcely increased up to 1000 hours when ageing was stopped. No other changes in the composition of the headspace were detected over this period of time at this temperature. A similar situation was

observed at 60°C although in this case N_2O could be detected after about 200 hours and the concentration increased slowly with time.

N_2O was first detected after about 70 hours at 70°C and from about 300 hours levels of this gas in the headspace grew at a rapidly increasing rate. At the same time significant increases in the levels of other headspace gases began to be observed, notably CO_2 and N_2. The levels of H_2O also increased slowly.

At 80°C the evolution of gas from HNF was very rapid and it was necessary to terminate the ageing trials after about 95 hours at this temperature. N_2O was again the major product but levels of N_2, CO_2 and H_2O also increased significantly, particularly after 70 hours. The rapid evolution of gas was accompanied by a change in the appearance of the HNF from an orange crystalline material to a brown slurry.

ICI co-crystallised HNF

Ageing of these materials was undertaken at 60°C and 80°C only. Headspace GC-MS analysis was conducted using the techniques and conditions described above.

In general the results are in close agreement with those for the HNF-E grade. Significant amounts of N_2O are evolved at increasing rates, with smaller amounts of H_2O, N_2 and CO_2 also being observed. However, at both 60°C and 80°C the levels of gas evolved from HNF co-crystallised with a certain additive are lower than those observed using other co-crystallisation agents, the main effect being a reduction in the evolution of N_2O rather than CO_2 or N_2. There is therefore some evidence that this additive is effective in suppressing gas evolution from HNF which is in agreement with the VTS results from ICI (see §4.2).

6 Sonocrystallisation

In the literature[6] it was found that the morphology of crystalline materials, including ammonium nitrate and hydrazinium nitroformate, can be improved by crystallisation while subjecting the solution to a high frequency vibration (ultrasound). More recent publications[7,8] also describe the important effects of power ultrasound, or insonation, in liquid and liquid-solid based systems. In general many of the useful effects of insonation are due to cavitation, the formation and subsequent implosion of gas or vapour bubbles. Cavitation will occur above a certain ultrasound (US) intensity (the so-called cavitation threshold) and corresponding tip amplitude. These cavitational effects of ultrasound in the liquid can be exploited to enhance reaction rates and yields in a wide variety of organic syntheses.

Various reasons for using ultrasound during crystallisation, called sonocrystallisation, are given in the literature[7,8,9,10] and are summarised below:

- initiation of primary nucleation, narrowing the metastable zone width;
- secondary nucleation;
- crystal habit and perfection;

- crystal size distribution;
- reduced agglomeration;
- improved product handling.

The mechanism behind the influence of ultrasound on crystal properties like shape and mean size during crystallisation is not fully understood. Several possibilities are suggested:

- US influences the nucleation behaviour of the crystallisation process by initiating the nucleation process already at a relatively low supersaturation;
- US influences the crystal growth process, disturbing the 'stagnant' boundary layer which exists between the solid surface of the crystal and the bulk of the liquid;
- US leads to breakage of the particles[11];
- a combination of these possibilities.

The part of the sonic spectrum that represents ultrasound ranges from about 20 kHz to 10 MHz. For sonocrystallisation, the frequency is preferably around 20 kHz[12].

6.1 Previous results

On a small-scale (750 ml) sonocrystallisation experiments with HNF have been performed[5,13]. Small scale US equipment has been hired for this purpose that could generate US vibrations with an amplitude up to 8 μm. Insonation led to the deterioration of the aspect ratio of HNF produced by drowning-out recrystallisation, i.e. the aspect ratio increased from 3.0 without insonation to 4.5 with insonation. By using insonation during cooling crystallisation a significant improvement of the morphology of the HNF crystals could be achieved. The aspect ratio of the crystals could be reduced from 3.8 without insonation to 2.0 with insonation. An unexpected result was the improved thermal stability of the HNF crystals (VTS at 60 °C: Figure 1), most prominent from VTS at 80 °C (Figure 2). Summarising the effect of ultrasound on small-scale cooling crystallisation, the best overall HNF quality could be obtained by using the highest ultrasound amplitude possible, which was 8 μm with the test equipment used[14].

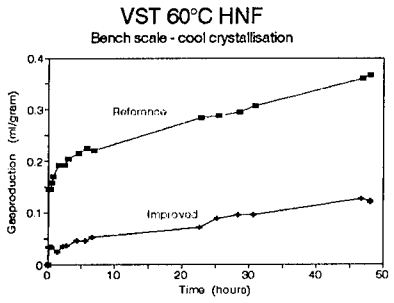

Figure 1 VTS improvement (60 °C) by using US

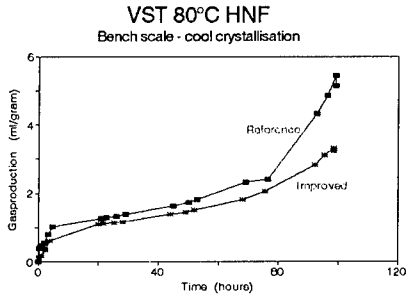

Figure 2 VTS improvement (80 °C) by using US

6.2 Experimental

Based on the results on small-scale sonocrystallisation with a hired probe, larger scale equipment has been purchased (a 1000 Watt US generator with a transducer/converter with two US probes capable of generating 0 to 20 μm amplitude (from tip – to tip) vibrations at the tip of the probe with a frequency of 20 kHz). One probe can be used for bench scale reactor (BSR) experiments while the other can be used on the pilot plant scale. With some minor modifications amplitudes up to 30 μm can be reached.

First BSR scale experiments have been performed with the new US equipment to verify the results obtained with the hired probe, to check the reproducibility and to optimise the sonocrystallisation with regard to period of insonation and US amplitude level. For this goal 11 BSR batches have been produced in which the level of US during seeding and during crystal growth has been varied between 0 and 30 μm. One batch has been produced by adding seeds (standard method).

After the BSR tests, scale-up of the sonocrystallisation to pilot-scale has been performed, using the optimised process parameters of the bench-scale experiments.

The BSR experiments were carried out in a 750 ml reactor, the pilot-scale experiments in a 20 l reactor. Furthermore a standard cooling profile has been applied to all batches to ensure a similar cooling rate for all batches.

6.3 Results and Discussion BSR scale

The results from BSR cooling rate experiments can be summarised as follows.

1. The aspect ratio improves with increasing US amplitude during growth as shown in Figure 3 which has been observed as well in earlier work[5].
2. Lowering the US amplitude after the seeding has been completed, results in a higher aspect ratio. This implies that the intensity of the US during growth has a significant effect on the aspect ratio of the HNF crystals (see also point 1). This influence of US on the crystal growth process has been suggested in the literature (see §6).
3. Particle size reduces with increasing US intensity (shown in Figure 3) which is in agreement with earlier work. If the US amplitude is changed after seeding, this effect is no longer apparent.

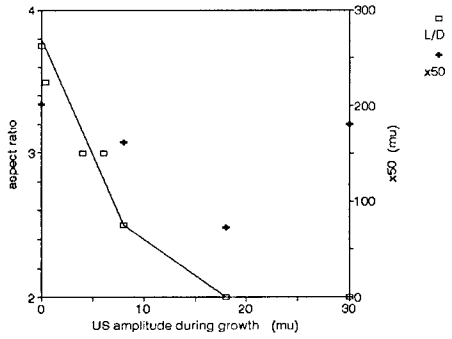

Figure 3 *Morphology for HNF-C batches produced on bench scale as a function of continuous US intensity during growth*

4. Particle size distribution widens by the use of insonation. This had not been observed in previous work, but was expected from the literature as discussed shortly in §6.
5. HNF thermal stability improves when using insonation during cooling recrystallisation, especially above the cavitation threshold. This is shown by a decreased initial gas production in VTS at 60°C (see Figure 4 and Figure 5). VTS at 80°C makes the effect of insonation on thermal stability more apparent, especially after more than 70 hours, as shown in Figure 6. These observations correspond to the earlier results (see Figure 1 and Figure 2).

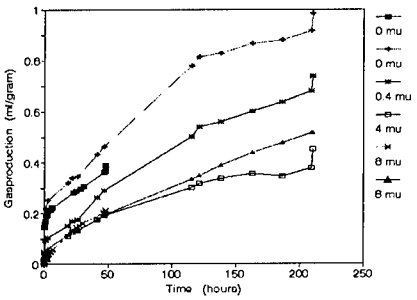

Figure 4 VTS gas production at 60 °C for HNF-C batches produced at bench scale at different lower US intensities.

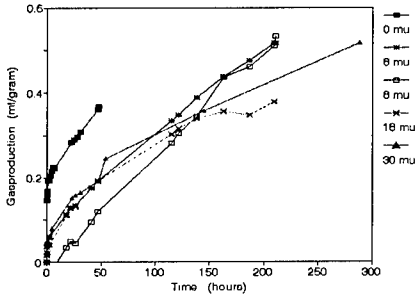

Figure 5 VTS gas production at 60 °C for HNF-C batches produced at bench scale at different, higher US intensities.

6. The level of the US amplitude influences the supersaturation at which spontaneous nucleation occurs (see Figure 7). This is the point at which the first HNF crystals are seen (and formed) in BSR. In general an experiment using HNF seed crystals can be seeded at a supersaturation of approximately 0.5 w% (Figure 7) when seeding. Thus by using insonation above a US amplitude of 8 μm, a lower supersaturation is present during seeding which should facilitate a good start for crystal growth. When the multiple seeding method is used, it is unknown how much of the seed crystals dissolve and how many grow out to mature HNF crystals. These results clearly show that US influences the nucleation behaviour of the crystallisation process as suggested in the literature (§6).

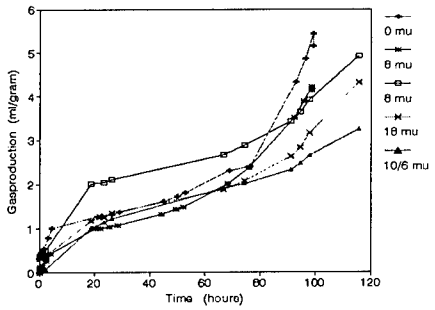

Figure 6 VTS gas production at 80 °C for HNF-C batches produced at bench scale at different US intensities.

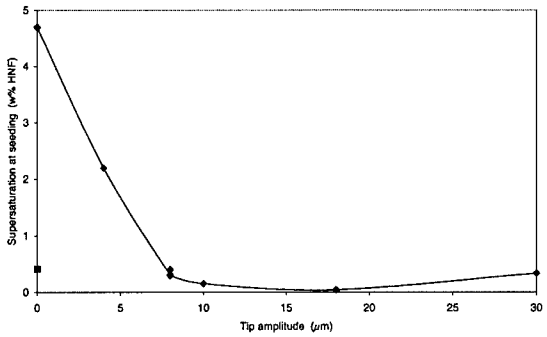

Figure 7 Supersaturation at which the first crystals are formed (spontaneously) for HNF-C batches produced on bench scale as function of US intensity. The point at US amplitude 0 μm, represents an experiment seeded with HNF seed crystals.

7. Changing the US amplitude after seeding is complete, results in a better thermal stability especially at 80 °C (see Figure 6). However, as shown under item 2., the aspect ratio increases at a lower US amplitude during growth.

The results with the new probe verify the most important conclusions from earlier work, i.e.: improved aspect ratio, improved VTS both at 60°C and at 80°C. However, this HNF shows an increased mean crystal size above a US amplitude of 20 μm. Combining all results of cooling crystallisation with ultrasound, a continuous US amplitude of ~20 μm appeared to give the best quality HNF. The introduction of the use of insonation for HNF cooling recrystallisation in the pilot-plant was considered to be justified based on the small-scale experiments. Furthermore it is shown that the mechanism behind the influence of ultrasound on crystal properties consists of at least a combination of the influence of US on the nucleation behaviour and the crystal growth process.

6.4 Results and Discussion pilot-scale

For the evaluation of the sonocrystallisation on pilot-scale three batches have been produced using ultrasound (batch HNF-1, -2 and -3) and these are compared with standard cool recrystallised HNF. The first batch on pilot-scale (HNF-1) was insonated with 20 μm. The morphology clearly improved in comparison to standard HNF-C. However, as batch HNF-1 did not yield HNF crystals with the same morphology as on bench scale, i.e. aspect ratio 2.0, the next batch (HNF-2) has been produced with a US amplitude of 30 μm. BSR experiments showed that increasing the US amplitude, improves the aspect ratio of the HNF crystals. As can be seen from Figure 12, the aspect ratio of HNF-2 was higher than that of HNF-1. This effect has later been checked on bench scale as well. The BSR batch, produced with a US amplitude of 30 μm, showed a similar increase in aspect ratio (see Figure 3). The third batch (HNF-3) was produced with a US amplitude of 20 μm again to check the reproducibility of sonocrystallisation.

Morphology

Photographs of the sonocrystallised batches are given in Figure 11, Figure 12 and Figure 13. Figure 10 is a reference of standard cool recrystallised HNF shown to illustrate the difference in morphology of these batches.

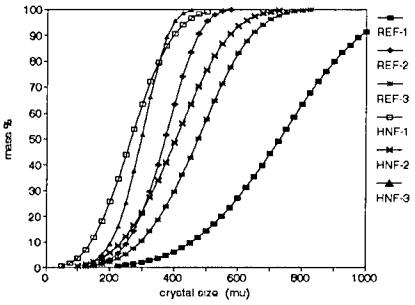

Figure 8 Fit of crystal size distribution for HNF-C batches produced on pilot-scale.

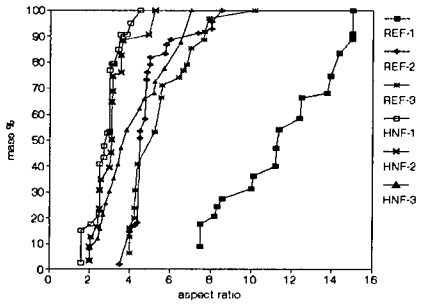

Figure 9 Aspect ratio for HNF-C batches produced on pilot-scale.

To enable a better evaluation of the improvement in the aspect ratio of the HNF crystals, some attention has been given to find a way to determine the range of aspect ratios in a given batch. This has been done by microscopic analysis in a way similar to the determination of the crystal size distribution as shown in Figure 8. Thus aspect ratio distributions have been determined as shown in Figure 9. It should be noted that Figure 8 is a fitted curve, whereas Figure 9 shows real data because no Gaussian distribution has yet been proven applicable in contrast to the x_{50} data. This accounts for the less smooth curves in Figure 9.

These data show that the aspect ratio of HNF crystals improves when using insonation (Figure 9). However, no further improvement in aspect ratio can be obtained by increasing the US amplitude over 20 μm.

The HNF mean crystal size increases when the US amplitude is raised from 20 to 30 μm on pilot-plant scale (Figure 8). This was shown by pilot plant batch HNF-2 and later confirmed by an experiment on bench scale with a 30 μm tip amplitude (Figure 3) as well as by pilot-plant batch HNF-3, which was produced with a 20 μm US amplitude again. The reason why the crystal size decreases as a function of US intensity up to a certain US amplitude (20 μm) and increases above this US amplitude is as yet unclear.

HNF-3 was produced in the same way as HNF-1, i.e. using a US amplitude of 20 μm, apart from a more intense stirring. This was done to suspend the HNF crystals more successfully and ensure a longer residence time for the crystals in the US field, thus yielding the maximum effect of US on growth. However, the aspect ratio of HNF-3 is higher than that of HNF-1. This may be caused by batch-to-batch variations. More sonocrystallised cooling batches should be performed on pilot plant scale to determine the reproducibility of this recrystallisation method.

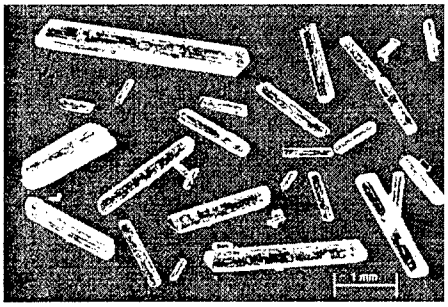

Figure 10 HNF-C ref (C15-01.jpg)
x_{avg} = 520 µm; L/D_{avg} = 4.9

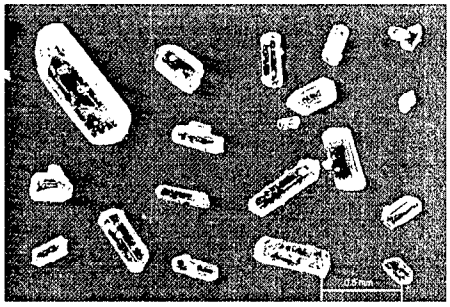

Figure 11 HNF-1 (C17-11.jpg)
x_{avg} = 300 µm; L/D_{avg} = 2.6

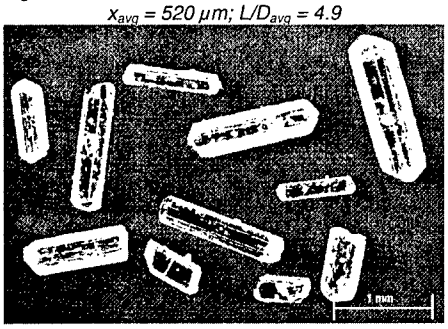

Figure 12 HNF-2 (C18-13.jpg)
x_{avg} = 450 µm; L/D_{avg} = 2.8

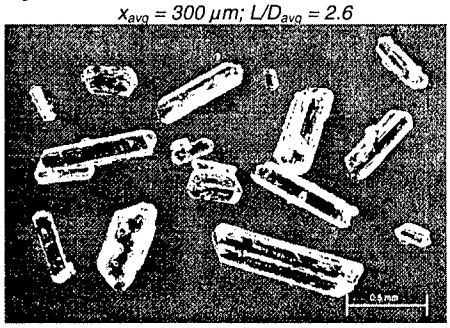

Figure 13 HNF-3 (C19-19.jpg)
x_{avg} = 320 µm; L/D_{avg} = 3.3

The mean crystal size of HNF-3 is in the same range as that of HNF-1, thus the US amplitude may be a good way to control the amount of seeds formed at the start of the batch. However the crystal size distribution of HNF-3 is narrower than that of HNF-1. This may be related to the stirrer intensity but this has to be verified by reproducibility tests.

Thermal stability

The thermal stability of HNF-C produced under ultrasound is better, especially at 80°C, than HNF-C produced without insonation; see Figure 14 for VTS at 60°C and Figure 15 for VTS at 80°C. To enable comparison between sonocrystallised HNF and good quality HNF-C material, produced without insonation, REF-1, REF-2 and REF-3 are shown in these figures.

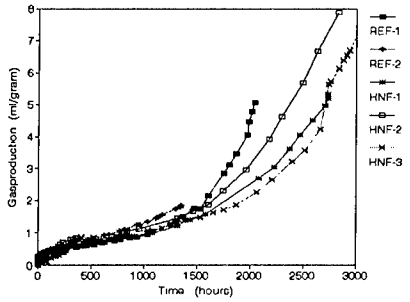

Figure 14 VTS at 60 °C for HNF-C batches produced on pilot-scale with and without insonation.

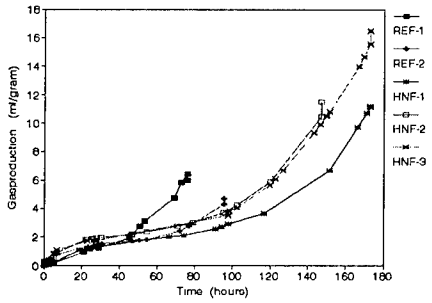

Figure 15 VTS at 80 °C for HNF-C batches produced on pilot-scale with and without insonation.

Sensitivity

BAM Impact and Friction sensitivity were measured for HNF-1, -2 and -3 (see Table 3).

Table 3 BAM impact and friction sensitivity of HNF.

	Impact (N)	Friction (Nm)
HNF-1	3	12 14
HNF-2	2	16 12
HNF-3	-	24
Characteristic value for HNF	2-4	16-36

Given the spread in friction sensitivity values that has been found for numerous HNF batches it is concluded that the HNF batches produced by cooling sonocrystallisation on pilot-scale have the same level of impact and friction sensitivity as standard HNF.

Effect of morphology on solid load in propellants

Both bulk and tap density (after 400 taps) increase when HNF-C is produced under insonation (see Table 4).

Table 4 Bulk- and tap density of pilot-scale HNF-C produced with and without insonation.

	HNF-1	HNF-2	HNF-3	Standard HNF-C
Bulk density (g/ml)	1.03	1.05	0.96	0.9
Tap density (g/ml)	1.24	1.26	1.16	1.06

This is caused by a reduction of the aspect ratio combined with a broadening of the crystal size distribution. A higher tap density will enable a higher solid load in a propellant, according to the following equation:

$$Solid\ load = \frac{\rho_t \cdot \rho_s}{\rho_p \cdot (\rho_s - \rho_t) + \rho_t \cdot \rho_s} \cdot 100\ w\%$$

In which:

ρ_t: tap density HNF (ml/gram)
ρ_s: density HNF = 1.86 g/ml
ρ_p: density polymer, for GAP = 1.3 gram/ml; for HTPB = 0.9 gram/ml

Using the tap densities of HNF-1 and HNF-2 this would imply that a solid load for these batches of respectively 74 w% and 75 w% could theoretically be achieved in HTPB. In a separate programme an experimental solid load of 76 w% HNF-2 in an HTPB propellant has been achieved (however, with limited castability).

7 Conclusions

The ICI crystallisation technique is suitable for re- and co-crystallisation of HNF. Small-scale optimisation resulted in primary HNF particles with an L/D of 1-2 and a particle size of 1-10 μm. Larger particles resulted in higher L/D ratios.

The co-crystallisation of HNF with a number of additives has been performed. One additive showed to be the most promising with regard to stabilising properties although the addition of this additive could not yet improve the stability of ultrafine HNF based on VTS to the level of HNF presently produced by APP.

Scaling-up and optimisation of the sonocrystallisation technique in pilot scale showed that it is very beneficial for the quality of HNF-C material; it improves the HNF morphology (aspect ratio), tap density and thermal stability. Chemical quality and sensitivity to friction and impact is unaffected by the use of US.

8 Acknowledgements

This work was performed under Contract no. 13.239 "Preparation for Industrialisation of HNF Based Advanced Composite Solid Propellants", GSTP-2, Phase 1 from ESA-ESTEC.

9 Acronyms

APP	Aerospace Propulsion Products
BSR	Bench Scale Reactor
DSC	Differential Scanning Calorimetry
ESA	European Space Agency
ESTEC	European Space and Technology Centre
GSTP	General Support Technology Programme
HNF	Hydrazinium Nitroformate
HZ	Hydrazine

TNO	Netherlands Organisation for Applied Scientific Research
VTS	Vacuum Thermal Stability

$[\ ]_{acid}$	Concentration based on acid content
$[\ ]_{HZ}$	Concentration based on HZ content
L/D	Length over Diameter ratio = aspect ratio
T_m	Melting point
x_{10}	particle size for which 10% of total size distribution is smaller
$x_{50,n}$	particle size for which 50% of total size distribution is smaller, particle size based on equivalent spherical diameter
x_{90}	particle size for which 90% of total size distribution is smaller

10 References

1 H.F.R. Schöyer , A.J. Schnorhk, P.A.O.G. Korting, P.J. van Lit, J.M. Mul, G.M.H.J.L. Gadiot and J.J. Meulenbrugge, "High-Performance Propellants Based on Hydrazinium Nitroformate", Journal of Propulsion and Power, **11**, no. 4, pp. 856-869, 1995.

2 H.F.R. Schöyer, A.J. Schnorhk, P.A.O.G. Korting, P.J. van Lit, "First Experimental Results of an HNF/Al/GAP Solid Propellant", AIAA Paper 97-3131, 1997.

3 G.M.H.J.L. Gadiot , J.M. Mul, J.J. Meulenbrugge, P.A.O.G. Korting, A.J. Schnorhk and H.F.R. Schöyer, "New Solid Propellants Based on Energetic Binders and HNF", IAF-92-0633, August 28 – September 5, 1992, Washington, USA.

4 B. D'Andrea and F. Lillo, "Industrial Constraints for Developing Solid Propellants with Energetic Materials", J. Prop. Power **15**, no. 5, pp713-718, 1999.

5 W.H.M. Veltmans , A.E.D.M. van der Heijden, M.J. Rodgers and R.M. Geertman, "Improvement of Hydrazinium Nitroformate product characteristics", Proceedings of 30th Annual International Conference of ICT, June 29 – July 2, 1999, Karlsruhe, FRG, p.55-1.

6 Markels M.Jr., "Process for producing finely divided rounded particles", US patent 3,222,231, 1965.

7 Price C., "Ultrasound - The Key to Better Crystals for the pharmaceutical Industry", Pharmaceutical Technology Europe, Publ. No. 0240, Oct. 1997.

8 Martin P., Cains P., Price C., "Sonochemistry", FCW **6**, Dec. 1997.

9 J. Hofman and V. Roubik, "A study of the crystal growth rate of potassium sulphate for cooling recrystallisation in an ultrasonic field", Material Science Forum Vols. 210-213, pp. 643-648, 1996.

10 S.L. Hem, "The effect of ultrasonic vibrations on crystallisation processes", Ultrasonics, pp. 202-207, October 1967.

11 Somoza C., "Ultrasonic grinding of explosives", US patent 5,035,363, 1991.

12 Perkins J.P., "Power ultrasonic equipment for Sonochemistry Research", article based on paper presented at the Sonochemistry Symposium, Annual Chemical Congress, Warwick University, UK, 8-11 April 1988.

13 W.H.M. Veltmans and A.E.D.M. van der Heijden, "Sonocrystallisation of Hydrazinium Nitroformate to Improve Product Characteristics", 14th International Symposium on Industrial Crystallisation (IChemE), 12-16 September 1999, Cambridge, UK.

14 W.H.M. Veltmans and F.J.M. Wierckx, "HNF crystallisation", Patent application no. 99200592.6

THE DEVELOPMENT OF ANALYTICAL METHODS FOR A HIGH ENERGY / HIGH ELONGATION PROPELLANT

Gaynor M. Kavanagh, John Theobald, David A. Tod
DERA, Fort Halstead, Sevenoaks, Kent, TN14 7BP, UK

ABSTRACT

DERA has a continuing interest in all propellant materials of potential service use and routinely conducts screening tests on candidate materials. Chemical stability and mechanical integrity are of particular concern where a material is being considered for rocket motor applications.

A range of high energy / high elongation propellant materials, with a polyethylene glycol binder are being assessed as part of a general materials evaluation programme. Test materials have been artificially aged under a variety of environmental conditions and compared against natural ageing.

A number of analytical techniques are used to follow the ageing process. Of particular concern is the depletion of stabiliser content on ageing, which is followed using an HPLC method. With this particular class of propellant, using polyethylene glycol as binder, the procedure used to extract the stabilisers has proved to be a critical process. The optimisation of the extraction procedure is presented together with some of the data obtained during the ageing trials.

Keywords:

Analytical method
HPLC
Stabiliser depletion

Verträglichkeitsuntersuchungen von Nitratestern

Stephan Wilker, Gabriele Pantel, Uldis Ticmanis, Manfred Kaiser,
WIWEB-ASt Heimerzheim, Großes Cent, D-53913 Swisttal

Zusammenfassung

Im Rahmen der vorliegenden Untersuchungsserie wurde Nitroglycerin mit verschiedenen organischen und anorganischen Stoffen gemischt und wärmeflusskalorimetrisch untersucht. Dabei zeigte sich, dass Zeitpunkt und Heftigkeit der eintretenden Autokatalyse stark von der Art und der Menge des eingebrachten Kontaktstoff abhängt.

NMR-Analysen des Nitroglycerins und seiner Abbauprodukte bewiesen, dass die Reaktion im wesentlichen durch eine homolytische Spaltung der Nitratgruppe des Nitroglycerins, vornehmlich in Position 2, charakterisiert werden kann. Die Verteilung der Reaktionsprodukte (1,3-Dinitroglycerin und 1,2-Dinitroglycerin) sowie die der weiteren Abbauprodukte (Dinitroglycerincarbonsäure, Mononitroglycerincarbonsäure) wird weder von Art und Menge der eingebrachten Kontaktstoffe noch von der Zeit, die bis zum Erreichen der Autokatalyse abhängt, sondern von der Heftigkeit, mit der die Autokatalyse auftritt, bestimmt.

Einige Zusatzstoffe verändern den Mechanismus der Abbaureaktion. So führt ein Zusatz von Base im wesentlichen zu einer Esterspaltung. Zusatz von Radikalfängern (4-Methoxyphenol) verhindert die Bildung der Nitroglycerincarbonsäuren wirkungsvoll. Wie bereits in anderen Veröffentlichungen beschrieben, führt die Zugabe von Diphenylamin in Mengen über 1% nicht zu einer weiteren Stabilisierung des Nitroglycerins. Andere Stabilisatoren (2-NO_2-DPA, N-NO-DPA) zeigen in der binären Mischung eine besser stabilisierende Wirkung. Stabilisierend wirken auch nicht-reaktive Basen, wie z.B. Carbonate.

Im Vergleich zum Nitroglycerin sind andere Nitratester (Ethylnitrat, BTTN) sehr viel stabiler.

Abstract

In this experimental series nitroglycerin was mixed with different organic and inorganic compounds. The mixtures were investigated by heat flow calorimetry. Time and severeness of the autocatalytic reaction are very dependent on nature and amount of the contact material.

NMR analyses of ngl and its decomposition products prove that the main reaction can be characterised by a homolytic split of the nitrate ester bond, preferably in the center position. The distribution of reaction products (1,3-dinitroglycerin and 1,2-dinitroglycerin) and the further decomposition products (dinitroglycerincarboxylic acid, mononitroglycerincarboxylic acids) is neither dependent on the structure or the amount of contact material nor is it a function of the reaction time. But a dependence on the severeness of the decomposition reaction could be found.

Some contact materials change the mechanism of the decomposition reaction. The addition of basic substances leads to an increase of ester bond hydrolysis. Addition of radical scavengers (4-methoxyphenol) is effectively preventing the formation of nitroglycerincarboxylic acids. As mentioned in other publications, an increase of DPA to over 1% does not result in a stabilising effect. Other stabilisers (2-NO_2-DPA, N-NO-DPA) show a much better stabilising effect in the binary mixture. Also non-reactive bases like carbonates are stabilising nitroglycerin very well.

Compared with ngl other nitrate esters (ethyl nitrate, BTTN) are much more stable.

1 Einführung

Nitratester (Sprengöle) sind grundlegende Bestandteile von Treibladungspulvern und Festtreibstoffen. Neben „altbekannten" Sprengölen wie Nitroglycerin (Ngl) und Diethylenglykoldinitrat (DEGN) gibt es auch „Exoten" wie Butantrioltrinitrat (BTTN), TMETN oder NENAs, die in neuartigen Treibstoffkonzepten Anwendung finden. Alle diese Nitratester sind thermisch nicht sehr stabil und gehen – anders als die daraus gefertigten Treibstoffe – in eine heftige Autokatalyse über, die ein erhebliches Sicherheitsrisiko darstellt.

Das Zersetzungsverhalten dieser reinen Stoffe ist bislang nur in Ansätzen bekannt. Die Stabilität wird in der Industrie in der Regel mit klassischen, nachweislich nicht eindeutigen Tests [1] wie dem Abel-Test überprüft.

Mit Hilfe der Mikrokalorimetrie können binäre und ternäre Gemische aus Nitratestern und Zusatzstoffen bei Temperaturen bis zu 89°C untersucht werden. Die Mikrokalorimetrie bietet gegenüber klassischen Tests mehrere Vorteile:

- Es findet eine permanente Aufzeichnung aller Vorgänge statt.
- Die Versuchsparameter (insbesondere der Füllgrad und die Dichtigkeit der Ampulle und damit die atmosphärischen Bedingungen) lassen sich in weiten Bereichen steuern.
- Der sicherheitsrelevante Parameter (Wärmeentwicklung) wird direkt bestimmt.
- Durch die Messung gleicher Proben bei verschiedenen Temperaturen lässt sich die Aktivierungsenergie bestimmen.

2 Experimentelles

Die Wärmeflussmessungen wurden mit einem „Thermal Activity Monitor" TAM 2277 (Thermometrics, Schweden) durchgeführt. Aus Sicherheitsgründen wurden für diese Untersuchungsreihe die verwendeten 3-mL-Glasampullen nicht komplett gefüllt, sondern Einwaagen in der Größenordnung von 100-250 mg vorgenommen. Eine Übersicht über die durchgeführten Untersuchungen ist Tabelle 1 (im Anhang) zu entnehmen. Die Messungen wurden mit einer Datensammelrate von 5 Minuten bei 89°C bis zum Eintritt in die Autokatalyse durchgeführt.

Die NMR-Spektren wurden bei 400.13 MHz (^{1}H-NMR) und 100.62 MHz (^{13}C-NMR) in Aceton-d_6 mit einem Bruker-DMX 400 MHz-NMR-Spektrometer aufgenommen. Die quantitative Auswertung erfolgte über die Integration der ^{1}H-Spektren.

3 Ergebnisse

Die Messungen wurden nach folgenden Kriterien ausgewertet:

- Auftreten eines ersten Maximums
- Zeitpunkt des Eintretens der autokatalytischen Zersetzung
- Geschwindigkeit der autokatalytischen Zersetzung

Die Ergebnisse sind in Tabelle 2 (in der Anlage) zusammengefasst.

Die Wärmeflussmessung des reinen Nitroglycerins liefert bei 89°C nach etwa 33 Stunden eine heftige Autokatalyse. Charakteristisch für den Zersetzungsverlauf ist auch eine Vorreaktion, die im Falle des reinen Nitroglycerins nach gut 100 Minuten auftritt. Eine vergleichbare Vorreaktion tritt auch bei nicht stabilisierten Pulverrohmassen bzw. –vorkonzentraten auf. Ein wesentlicher Unterschied zu diesen ist jedoch, dass im Fall der PVK/PRM diese Vorreaktion direkt vor der eigentlichen Autokatalyse erfolgt.

Die Zugabe von Wasser (60 mg) zum Nitroglycerin führt zu einer Beschleunigung der Autokatalyse. Gleichzeitig ist der Anfangseffekt nicht mehr sichtbar. Arbeitet man unter sauren Bedingungen (Zugabe von 0,01 N HCl), so unterscheidet sich die Zersetzungskurve von der des reinen Nitroglycerin nicht. Unter basischen Bedingungen (Zugabe von einigen Tropfen 0,01N NaOH) verlängert – gegenüber dem Experiment unter Wasserzugabe – ebenfalls den Eintritt in die Autokatalyse. Abb. 1 zeigt die vier Messkurven.

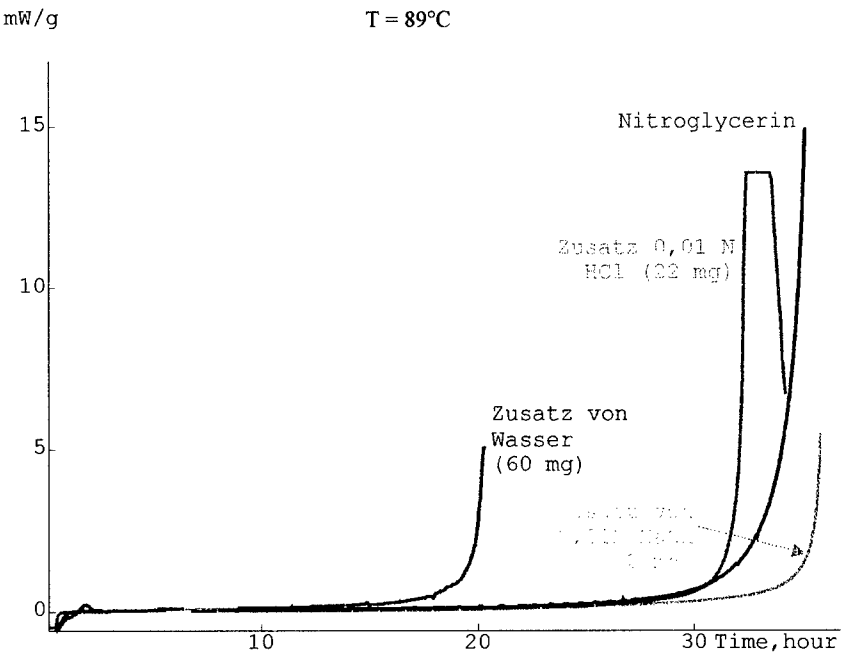

Abb. 1. WFK von reinem Nitroglycerin, Zusatz von Wasser, 0,01 N HCl und 0,01 N NaOH

Vielen TLP wird Kaliumnitrat als Flammendämpfer zugesetzt. Untersuchungen haben ergeben, dass ein erhöhter KNO_3-Anteil in einem zweibasigen TLP zu schnelleren Zersetzungsreaktionen (Zunahme des Frequenzfaktors und Änderung der Zersetzungsmechanismen) führt. Ob dieses Verhalten auch in einem binären Gemisch Nitroglycerin/KNO_3 zu beobachten ist, war Ziel der nächsten Versuchsserie (vgl. Abb. 2). Außerdem wollten wir den Einfluss des Kations (K^+) bzw. des Anions (NO_3^-) auf die Zersetzungsrate ermitteln. Es wurden $Ba(NO_3)_2$, $BaCl_2$, KCl, K_2SO_4 und $NaNO_2$ eingesetzt. Die Ergebnisse dieser Versuchsserie sind – jeweils im Vergleich zu reinem Nitroglycerin und zu mit KNO_3 versetztem Nitroglycerin – in Abb. 3 und 4 zu sehen. Alle eingesetzten Salze wiesen – vom $BaCl_2$ abgesehen – nur geringe Spuren an Feuchtigkeit (ppm-Bereich) auf. $NaNO_2$ reagiert schwach basisch. Alle anderen eingesetzten Salze reagieren in wässriger Lösung erwartungsgemäß neutral.

Sehr wichtig für die Stabilität von TLP bzw. doppelbasigen FTS ist die Anwesenheit von Stabilisatoren. Wir haben einige Untersuchungen zur stabilisierenden Wirkung von aromatischen Aminen bereits veröffentlicht [2]. Auch liegen Untersuchungen des Zersetzungsverhaltens von nicht stabilisierten TLP vor. Die Zugabe von „Standardstabilisatoren" (DPA, Centralit, Akardit) zum Nitroglycerin erfolgte in der Regel im Verhältnis 100:1, beim 2-NO_2-DPA im Verhältnis 100:5. Die Ergebnisse der Untersuchungen sind Abbildungen 5 bis 7 zu entnehmen. Abbildung 5 zeigt den Einfluss von Luftsauerstoff auf die Zersetzungsreaktion.

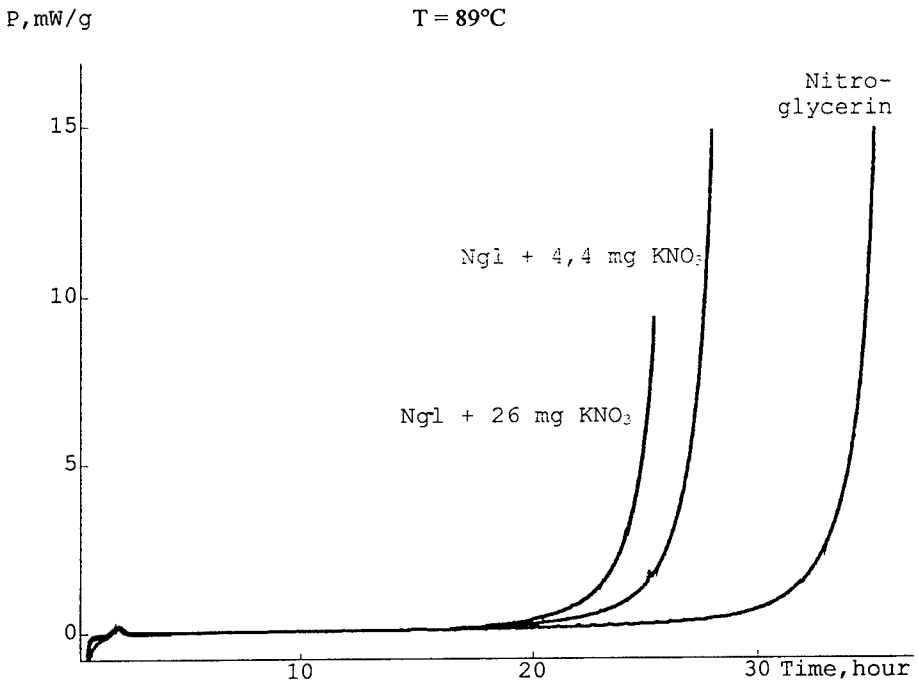

Abb. 2. WFK von reinem Nitroglycerin sowie mit Zusatz von KNO_3 in unterschiedl. Mengen.

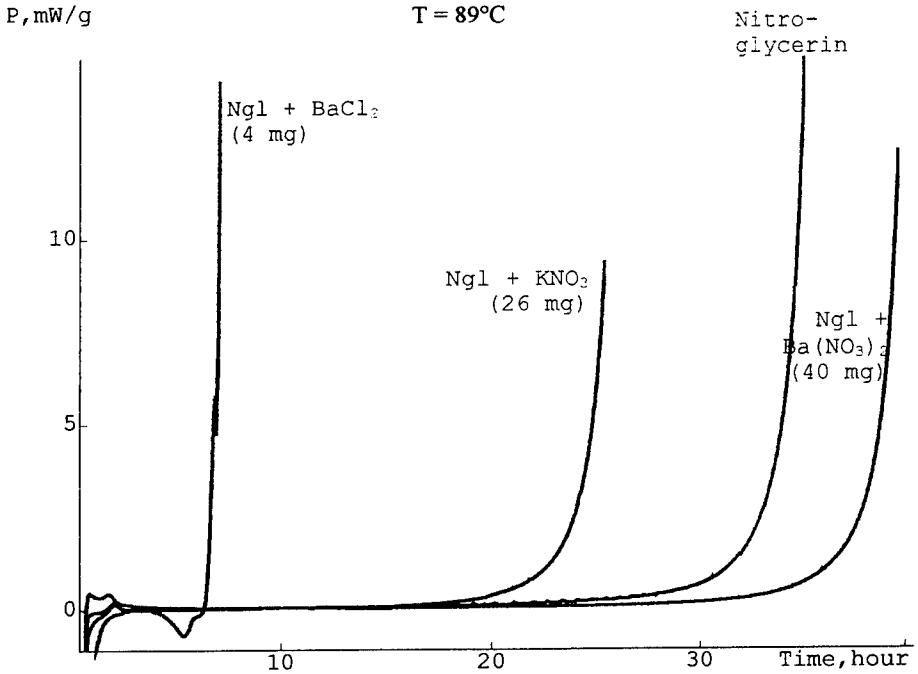

Abb. 3. WFK von reinem Nitroglycerin, Zusatz von KNO_3, $Ba(NO_3)_2$ und $BaCl_2$.

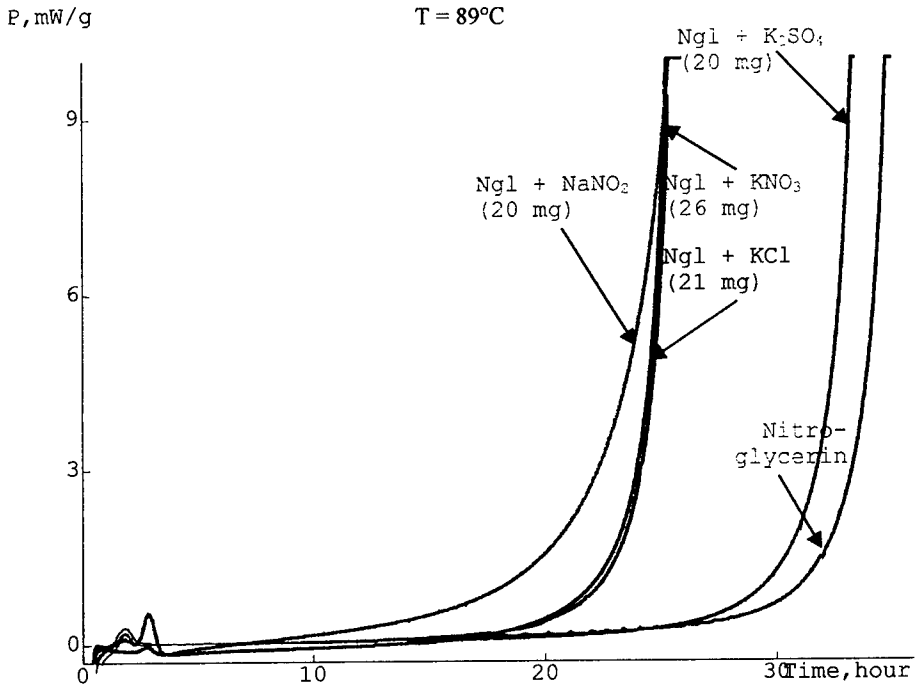

Abb. 4. WFK von reinem Nitroglycerin, Zusatz von KNO_3, KCl, K_2SO_4 und $NaNO_2$.

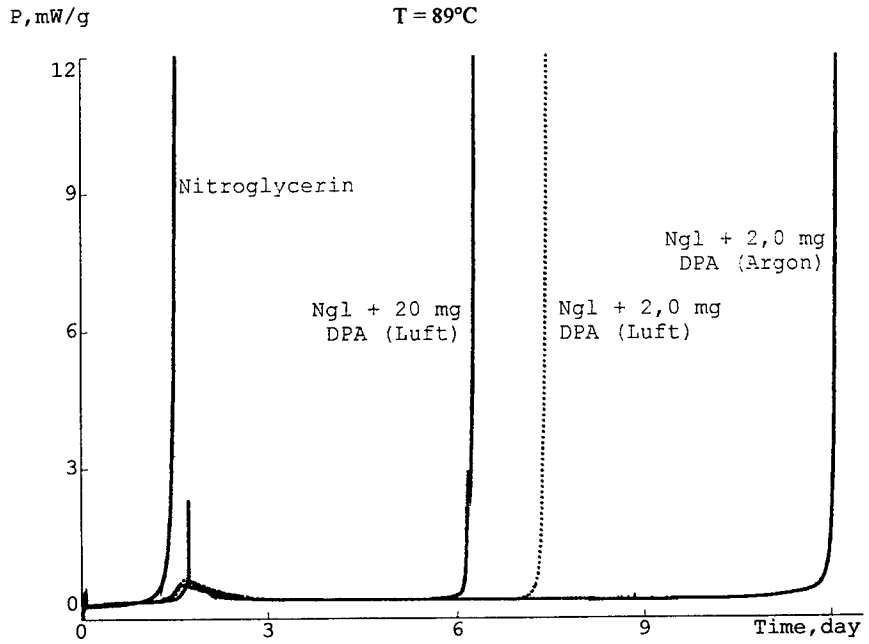

Abb. 5. WFK von reinem Nitroglycerin, Zusatz von DPA (10%), DPA (1%) und DPA (1%, unter Ar).

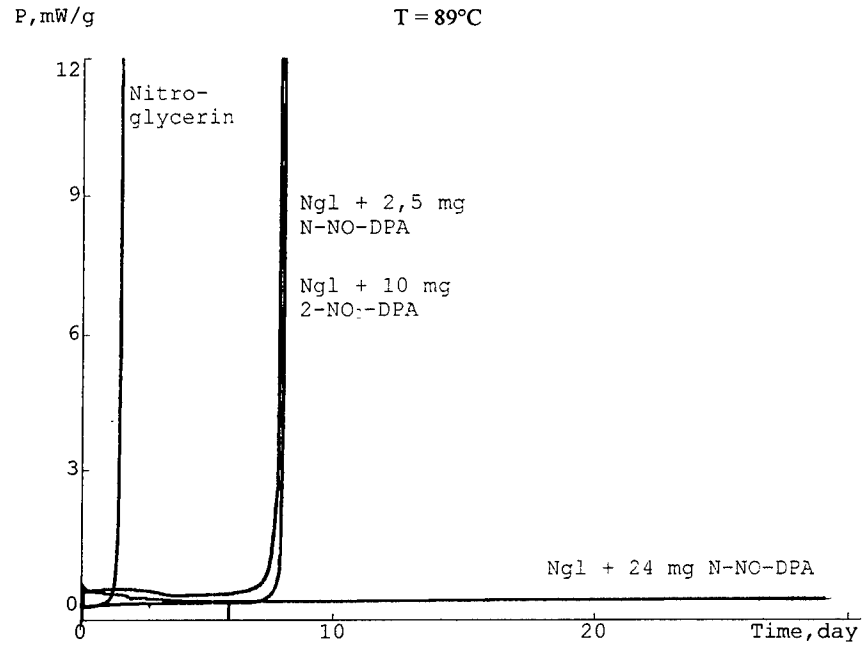

Abb. 6. WFK von reinem Nitroglycerin, Zusatz von N-NO-DPA (10 %), N-NO-DPA (1 %) und 2-NDPA (5 %).

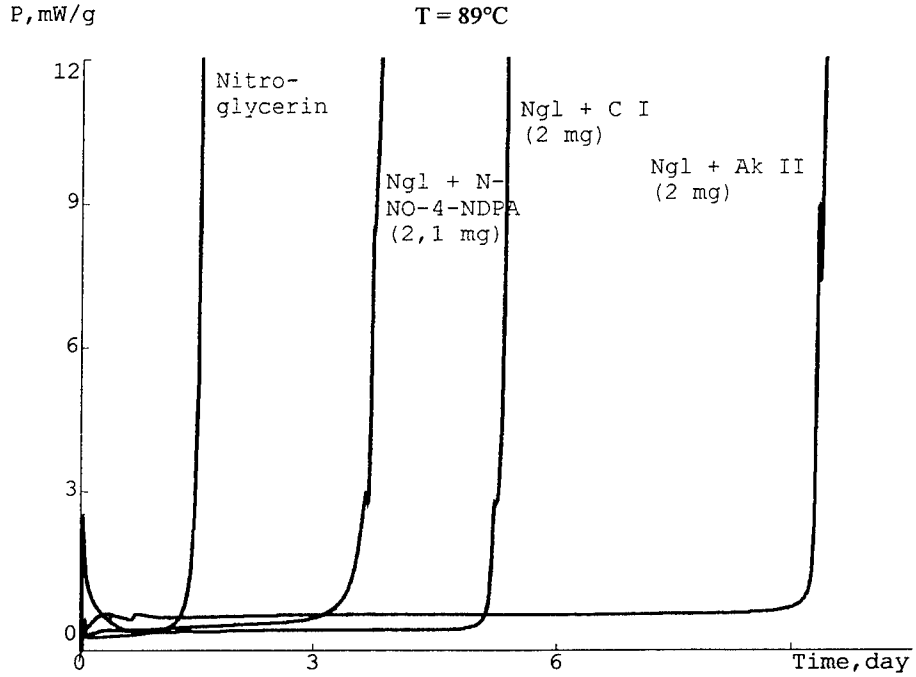

Abb. 7. WFK von reinem Ngl, Zusatz von N-NO-4-N-DPA, Centralit I und Akardit II.

Das Mischen verschiedener Stabilisatoren (z.B. DPA und sein erstes Abbauprodukt, N-NO-DPA) führt teilweise zu erheblich abweichenden Zersetzungsverhalten. Die Auswirkungen des zusätzlichen Einbringens von KNO_3 (was einer Simulation der Verhältnisse in zweibasigen Kugelpulvern wiedergibt) ist Abb. 8 zu entnehmen.

Weitere, bei der Herstellung von Kugelpulvern verwendete Stoffe sind zum einen Carbonate, zum anderen Lösemittel und Weichmacher. Wie sich die binären Gemische dieser Substanzen auf den Zeitpunkt der Autokatalyse des Nitroglycerins auswirken, ist den Abbildungen 9 und 10 zu entnehmen.

In einer vorangegangenen Untersuchungsserie wurde die chemische Verträglichkeit von TLP mit Schwarzpulver untersucht [6]. Eines der Ergebnisse dieser Studie war die Tatsache, dass nur zweibasige TLP Unverträglichkeitsreaktionen zeigten. Daher lag es nahe, dass im Rahmen dieser Untersuchungen auch eine binäre Mischung Nitroglycerin/Schwarzpulver Y 594 untersucht wurde. Die Messkurven sind – wiederum im Vergleich mit reinem Nitroglycerin und der Mischung Nitroglycerin/KNO_3 – in Abb. 11 zu sehen.

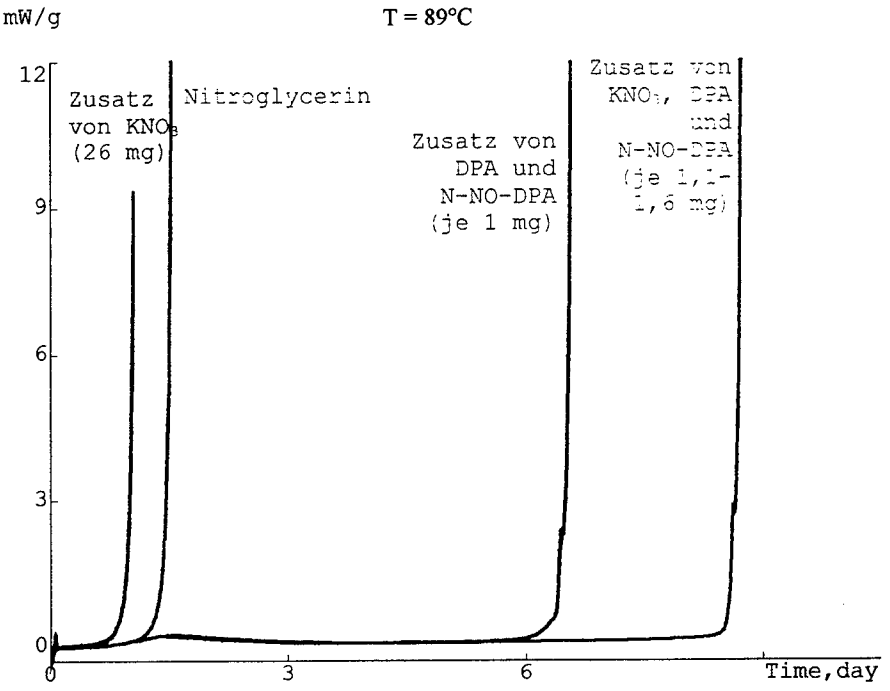

Abb. 8. WFK von reinem Nitroglycerin, Zusatz von KNO_3, und DPA/N-NO-DPA.

Mögliche andere Stabilisatorsysteme können auf der NO_2 abfangenden OH-Gruppe basieren. Es ist seit längerem bekannt, dass z. B. Ethanol im Kontakt mit PVK zu Ethylnitrat umgesetzt wird [2]. Deshalb wurde eine Versuchsserie mit Ethanol-Zusatz geprüft. Desweiteren wurde 4-Methoxyphenol (welches in der Kunststoffindustrie als Radikalfänger eingesetzt wird) in zwei verschiedenen Konzentrationen (die größere entsprach der zum Versuch mit Ethanol äquimolaren Konzentration) mit Ngl gemischt und wärmeflusskalorimetrisch untersucht (s. Abb. 12).

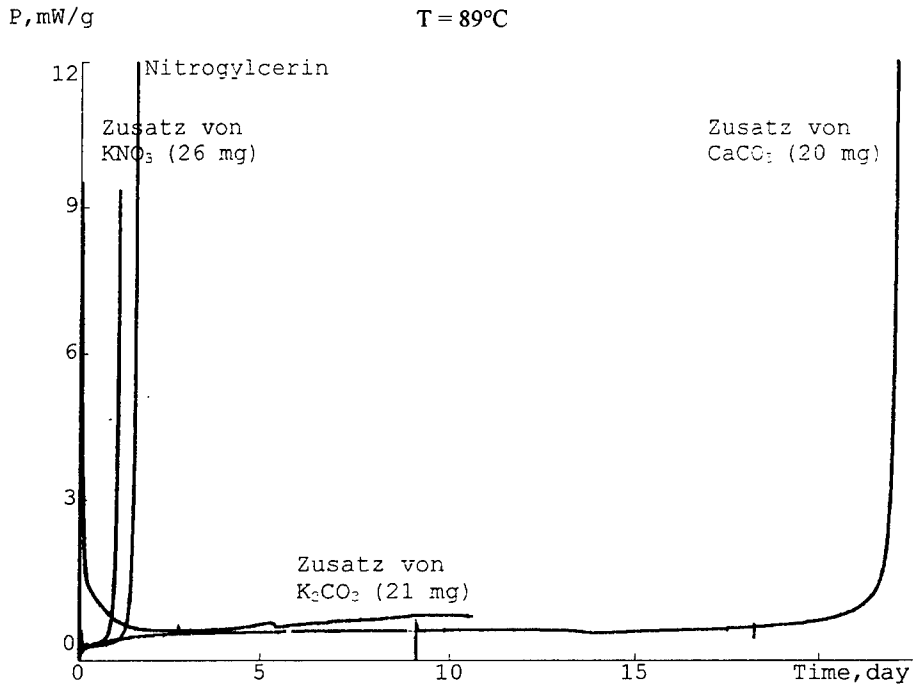

Abb. 9. WFK von reinem Nitroglycerin, Zusatz von KNO_3, K_2CO_3 und $CaCO_3$.

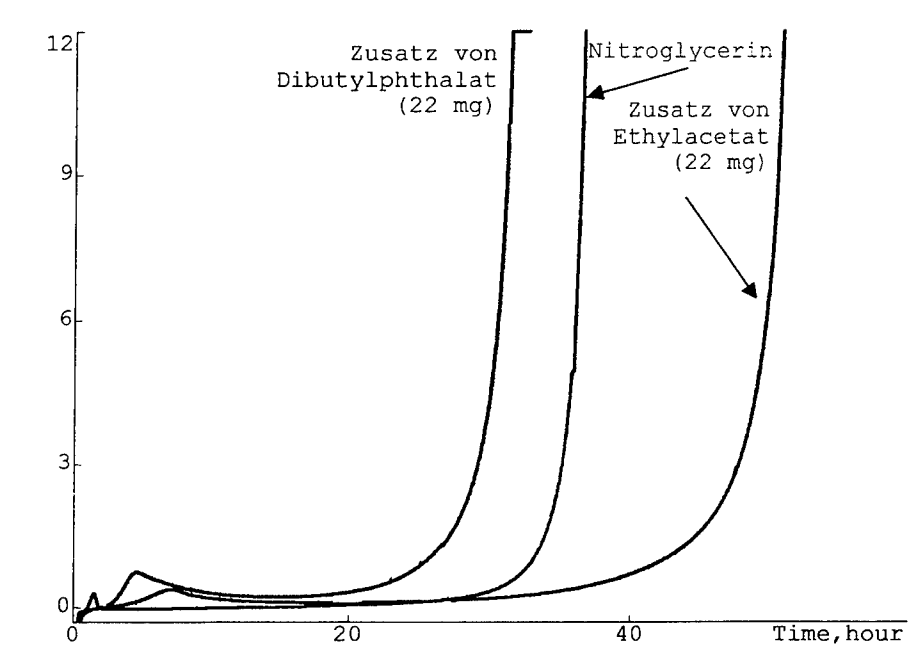

Abb. 10. WFK von reinem Nitroglycerin, Zusatz von Dibutylphthalat und Ethylacetat.

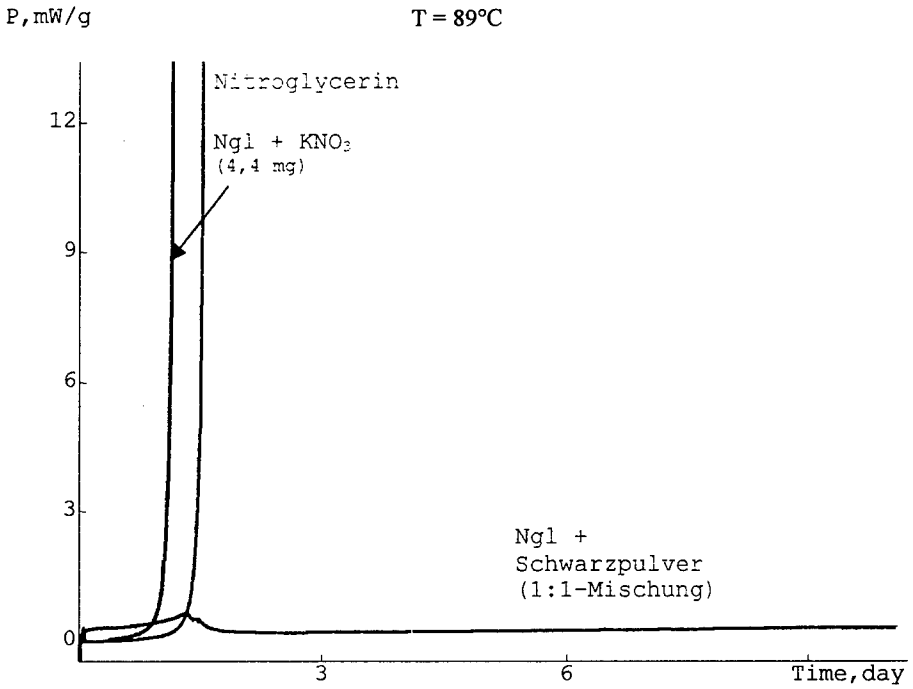

Abb. 11. WFK von reinem Nitroglycerin, Zusatz von KNO_3 und Schwarzpulver.

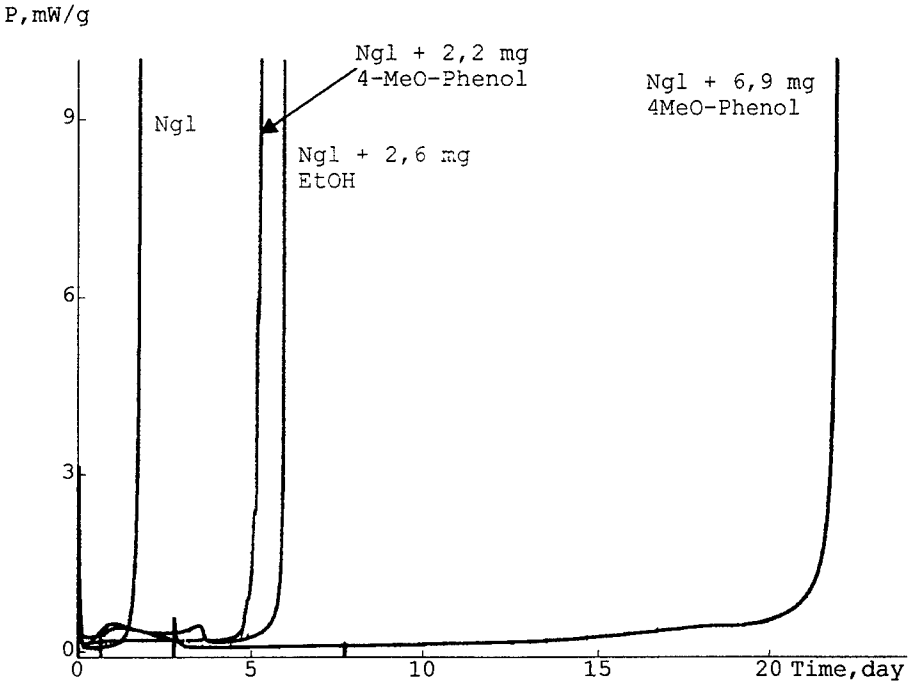

Abb. 12. WFK von reinem Nitroglycerin sowie Gemischen mit EtOH und 4-Methoxyphenol

Andere Nitratester wurden ebenfalls im WIWEB mikrokalorimetrisch untersucht. Da diese Untersuchungen bei 80°C durchgeführt wurden, haben wir zum Vergleich auch das Nitroglycerin bei 80°C vermessen. Die Ergebnisse sind Abb. 13 zu entnehmen.

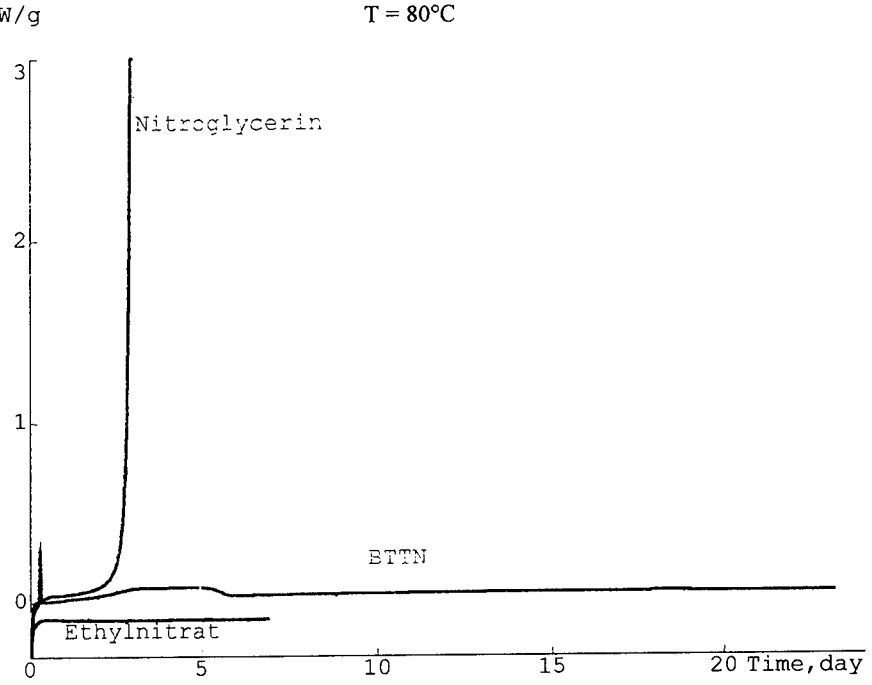

Abb. 13. WFK der reinen Nitratester Nitroglycerin, BTTN und Ethylnitrat bei 80°C.

4 NMR-Untersuchungen

Einige der thermisch belasteten Proben wurden NMR-spektroskopisch nach Abbauprodukten des Nitroglycerin untersucht. Ziel der Untersuchungen war die Frage, ob den durchaus unterschiedlichen Kurvenverläufen auch unterschiedliche Abbaumechanismen zugrunde liegen. Die Erfahrungen bei der Identifikation der NMR-Spektren von Abbauprodukten der Pulvervorkonzentraten [2] kam uns bei der Zuordnung der Signale zugute.

Tabelle 3 (Anlage) gibt die relativen Anteile der Abbauprodukte wieder. Abbildung 14 zeigt ein typisches NMR-Spektrum einer Reaktionsmischung (aus Versuch #24).

5 Diskussion

Wärmeflussmessungen

Die Zersetzung des Nitroglycerins verläuft radikalisch, beginnend mit dem Bruch der zentralen O-NO_2-Bindung, gefolgt von dem Bruch der anderen O-NO_2-Bindungen [7]. Die Zugabe von Wasser verstärkt die Autokatalyse deutlich. Dies hat vermutlich seinen Grund darin, dass die entstehenden autokatalytisch wirkenden Zersetzungsgase in Wasser löslich sind und somit besser auf den Nitratester einwirken können. Dagegen wird beim Zusatz von Base oder Säure die konkurrierende Substitutions- bzw. Esterspaltungsreaktion gefördert. Somit wird die auch

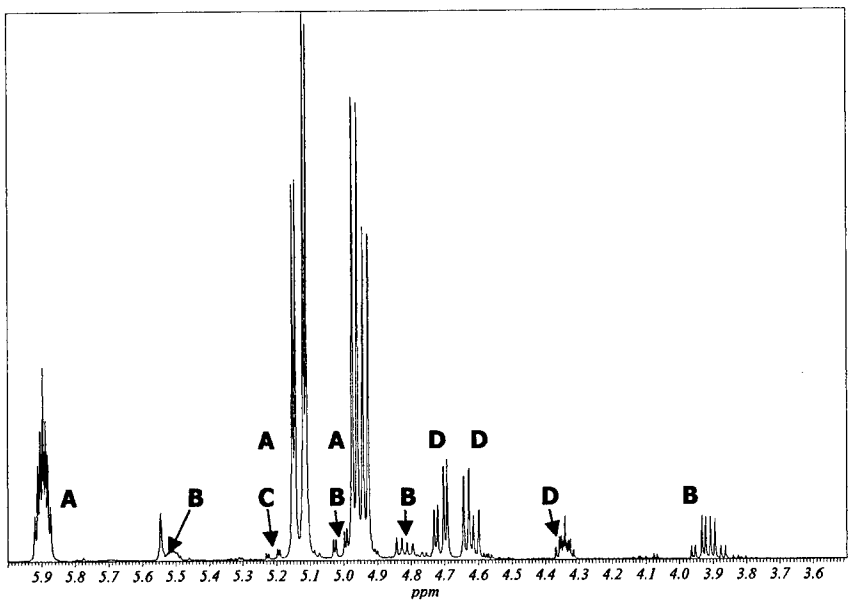

Abb. 14. NMR-Spektrum eines Reaktionsgemischs. Zuordnung der Signale:

A = Nitroglycerin, B = 1,2-Dinitroglycerin, C = 2,3-Dinitroglycerincarbonsäure, D = 1,3-Dinitroglycerin.

hier durch die Löslichkeit der Zersetzungsgase auftretende Verstärkung wieder aufgehoben. Das erklärt den im Vergleich zum Wasserzusatz verzögerten Eintritt in die Autokatalyse.

Das stark oxidierend wirkende NO_2 wird – und das belegen die Erfahrungen anderer Autoren ebenfalls – an organischem Material zu NO reduziert. Die so entstehenden Zwischenprodukte werden durch weitere Einwirkung von NO_2 bzw. durch den vorhandenen Luftsauerstoff zu Carbonsäuren oxidiert. Wenn die Reaktion weiter fortgeschritten ist, kann nicht mehr alles freigesetzte NO_2 reduziert werden. In diesem Stadium setzt die Autokatalyse ein, und bei Ende der Wärmeflussmessungen (3.000 µW/Probe) ist die Atmosphäre über den Proben tiefbraun gefärbt.

Der bei reinem Nitroglycerin zu beobachtende um den Faktor 2,3 (T = 80 bzw. 89°C) verlängerte Eintritt in die Autokatalyse entspricht einer Aktivierungsenergie von etwa 100 kJ/mol und liegt somit unter der der Treibladungspulver [3][4].

Kaliumnitrat verschiebt den Zeitpunkt der Autokatalyse nach vorne. Dabei konnte ein eindeutiger Zusammenhang mit der verwendeten Menge festgestellt werden. Dagegen ist bei Zusatz von Bariumnitrat eine leichte Verzögerung des Eintritts in die Autokatalyse zu beobachten. Im Kontakt mit Bariumchlorid ist dagegen eine sehr heftige und sehr rasche Autokatalyse zu beobachten. Dies dürfte am Wassergehalt des Salzes (es wurde das Dihydrat verwendet) liegen. Ein Zusatz von Feuchtigkeit führt zu einer schnelleren Autokatalyse. Wasserfreie Salze wie Kaliumchlorid und Natriumnitrit zeigen ein dem Kaliumnitrat vergleichbares Verhalten.

Der Zusatz von Stabilisatoren zeigt – wie zu erwarten ist – eine Verschiebung der Autokatalyse zu späteren Zeitpunkten. Interessanterweise verkürzt sich die Zeit bis zur Autokatalyse, wenn der Anteil des Stabilisators DPA von 1% auf 10% erhöht wird. Den gleichen Effekt

konnte man auch bei Stabilisatorabbauversuchen mit verschiedenen Varianten des TLP K 6210 beobachten [5]. Hier zeigte sich, dass bei Erhöhung des DPA-Anteils auch eine Beschleunigung des Abbauvorgangs zu beoachten war. Dies kann nur damit erklärt werden, dass das DPA selbst mit dem Nitroglycerin reagiert und diese (vermutlich bimolekulare) Reaktion mit steigender DPA-Konzentration beschleunigt wird.

Im Rahmen dieser Versuchsreihe wurde auch eine Probe nach gründlicher Entfernung von Luft unter Argon abgefüllt. Der Zeitpunkt der Autokatalyse verschob sich daraufhin um fast 5 Tage. Das dokumentiert den Einfluss, den der Luftsauerstoff auf die Zersetzung des Nitratesters hat. Im wesentlichen dürfte er darin bestehen, dass vorhandendes NO zu NO_2 oxidiert wird, welches dann die autokatalytische Reaktion einleitet.

Überhaupt sind die Reaktionsbedingungen für den Eintritt in die Autokatalyse von entscheidender Bedeutung. Während bei Untersuchungen zum Abbauverhalten von Stabilisatoren in zweibasigen TLP festgestellt wurde [3], dass je nach Füllgrad und Dichtigkeit der Ampulle – was einem unterschiedlichen Sauerstoffzutritt zum TLP hin entspricht – das vorhandene DPA in N-NO-DPA (Luftabschluss) oder in Nitro- und Dinitro-DPA (Luftzutritt) umgewandelt wird. In den vorliegenden Experimenten ist eine rasche Ringnitrierung zu beobachten, da in der nur zu einem geringen Teil gefüllten Ampulle genügend Luftsauerstoff zur Verfügung steht.

Verwendet man den „Stabilisator" N-NO-DPA, so zeigt sich, dass die Verhältnisse umgedreht werden: Je mehr Stabilisator zugegeben wird, desto später tritt die Autokatalyse ein. Bei einem Zusatz von 10% wird – selbst bei einer Versuchsdauer von 29 Tagen – kein Übergang in die Autokatalyse beobachtet. Im Gegensatz zu DPA (und ähnlich wie bei N-NO-4-NO_2-DPA) ist ein vergleichsweise hoher und langanhaltender Anfangseffekt zu beobachten.

Eine Mischung aus DPA und N-NO-DPA (es wurde jeweils ½ % zugegeben) verhält sich in etwa wie ein Zusatz von DPA alleine. Eine stabilisierende Wirkung des zusätzlich eingebrachten N-NO-DPA auf das DPA wird nicht beobachtet.

Die stabilisierende Wirkung von 2-NO_2-DPA ist der des N-NO-DPA vergleichbar. Dasselbe gilt für das Centralit, während Akardit II einen späteren Eintritt der Autokatalyse bewirkt. Das Abbauprodukt N-NO-4-NO_2-DPA führt dagegen schon nach gut 3,6 Tagen zur Autokatalyse. Das bestärkt die Theorie, dass die stabilisierende Wirkung des N-NO-DPA auf dessen Fähigkeit beruht, NO_2 durch eine Nitrierung des aromatischen Rings abzufangen. Ist einer der beiden Ringe schon nitriert (wie im Falle des N-NO-4-NO_2-DPA), so sinkt die Aktivität des Stabilisators drastisch, was dann zu einer erhöhten NO_x-Konzentration über dem Nitroglycerin und damit zur Autokatalyse führt.

Stark basische Zusätze können – wie die Beispiele Kaliumcarbonat und Calciumcarbonat zeigen – die Autokatalyse wirkungsvoll verhindern. Sie können Radikale und Säuren gut abfangen, somit tritt die Zersetzungsreaktion nicht in ihre „gefährliche" Phase.

Indifferent, d.h. wirkungslos, verhalten sich dagegen Stoffe wie Dibutylphthalat oder Ethylacetat. Beide spielen im Produktionsprozess von Kugelpulvern eine große Rolle. Die geringfügig später eintretende Autokatalyse im Falle des Ethylacetats lässt sich u.U. mit einem Verdünnungseffekt erklären.

Nicht erklärbar war zunächst das Verhalten von Schwarzpulver gegenüber Nitroglycerin. Es gab einen berechtigten Verdacht, dass zweibasige TLP und Schwarzpulver (bzw. die Holzkohle aus dem Schwarzpulver) mit Nitroglycerin unverträglich sind. Untersucht man nur die ersten 1,25 Tage, so zeigt sich beim Kontakt Schwarzpulver/Nitroglycerin ein erheblich erhöhter Wärmefluss. Im Gegensatz zum reinen Nitroglycerin steigt dieser aber nur geringfügig an und geht nach diesem kurzen Maximum auf ein relativ konstantes niedriges Niveau über. Detaillierte Untersuchungen am System Schwarzpulver/zweibasige TLP konnten belegen [6],

dass es sich bei der beobachteten Wärmeentwicklung um Adsorptionswärmen an der relativ großen Holzkohle-Oberfläche handelt. Offensichtlich ist also die Holzkohle in der Lage, mit ihrer großen Oberfläche genügend NO_x zu binden und so – das System enthält ja keinen Stabilisator! – eine Autokatalyse über mehr als zehn Tage hinweg zu verhindern.

Im Gegensatz zum Nitroglycerin weist das chemisch sehr ähnliche BTTN auch nach insgesamt 24 Tagen Messzeit bei 80°C keine Tendenz zur Autokatalyse auf. Es ist daher um mindestens den Faktor 8 stabiler als das Nitroglycerin. Die Messung von Ethylnitrat bei 80°C zeigte ebenfalls keine autokatalytische Reaktion innerhalb der Messzeit. Der negative Messwert zeigt, dass diese Substanz bei 80°C flüchtig ist und eine permanente Verdunstung selbst durch die geschlossene Dichtung der Messampulle erfolgt.

Verteilung der Abbauprodukte des Nitroglycerins

Die Verteilung der Ngl-Abbauprodukte kann aufgrund der Tatsache, dass die Messungen jeweils bei der selben Zersetzungsrate beendet worden sind, gut miteinander verglichen werden.

Dass die ermittelten Restgehalte an Ngl keine Funktion der abgegebenen Energie sind, macht Tabelle 3 deutlich. Vergleicht man die Experimente, bei denen ein Salz zugesetzt wurde, miteinander, so zeigt sich kein Zusammenhang zwischen der Energieabgabe und dem aktuellen Ngl-Gehalt. Auch scheint es keinen ursächlichen Zusammenhang zwischen den Versuchszeiten und dem Ngl-Gehalt zu geben. Auffallend ist jedoch, dass der Versuch, der die schnellste und heftigste Autokatalyse zeigte (#7) auch den geringsten Ngl-Anteil und somit den höchsten Anteil an Zersetzungsprodukten aufweist.

Die Verteilung der ersten Folgeprodukte (1,2-Dinitroglycerin (Dngl) und 1,3-Dngl) ist in allen Fällen ähnlich und weist auf einen für alle Experimente ähnlichen Zersetzungsmechanismus hin. Die Abbauprodukte der zweiten Generation (Nitroglycerincarbonsäuren) treten vorzugsweise bei längeren Versuchszeiten (#8, 9, 10) oder besonders heftigen Reaktionen (#7) auf. Das Fehlen der Mononitroglycerine, von Ketonen und Aldehyden im Spektrum der Produktgemische weist auf die stark oxidierend wirkende Atmosphäre über den Proben hin (es traten in allen Experimenten braune Dämpfe auf, und die Proben waren oft tief rotbraun gefärbt). Unter diesen Bedingungen sind nur die Carbonsäuren stabil. Die weiteren Reaktionsschritte wären dann Decarboxylierung und Zerfall in C_2-Körper, vornehmlich Oxalsäure [2].

Interessant ist die Produktverteilung im Falle des Versuchs #15 (NaOH). Hier wird – und es ist das einzige Beispiel – ein im Vergleich zum 1,3-Dngl erhöhter 1,2-Dngl-Anteil gefunden. Dies belegt die Vermutung, dass die Zersetzung – zumindest zum Teil – durch Substitutions- bzw. Esterspaltungsreaktionen gefördert wird. Auch ist der Anteil an Nitroglycerincarbonsäuren deutlich vermindert, was auf eine weniger ausgeprägtes Oxidationspotenzial der Atmosphäre hinweist.

Der wesentlichste Unterschied bei der Verwendung von Stabilisatoren ist die im Vergleich zu nicht stabilisierten Ngl verlängerte Messzeit. Die größeren Messzeiten und die meist deutlich erhöhten freigesetzten Energien bei der Umsetzung führen dennoch nicht zu einem verstärkten Abbau des Ngl. Nur bei der Verwendung von DPA als Stabilisator ist der Ngl-Anteil deutlich vermindert. Hier ist ein deutlich erhöhter Anteil an Dngl und an 2,3-Dinitroglycerincarbonsäure festgestellt worden. Im Vergleich von DPA und 2-NO_2-DPA zeigt letzteres eine deutlich erhöhte Messzeit und einen geringeren Abbaugrad. Dies ist im Einklang mit Untersuchungen, die an doppelbasigen TLP durchgeführt wurden [4].

Im Vergleich zum DPA schlechter ist das N-NO-4-NO_2-DPA. Hier sind kurze Reaktionszeiten und geringer Abbaugrad bis zum Erreichen der Autokatalyse gegeben. Hinzu kommt ein

großer Wert für die freigesetzte Energie. Mit 2-NO_2-DPA gut vergleichbar ist im Hinblick auf Energieabgabe und Zusammensetzung der Reaktionsprodukte Centralit I.

Der Vergleich von Ethanol mit DPA zeigt eindeutige Unterschiede im Reaktionsablauf, obwohl das Spektrum der Reaktionsprodukte und die Versuchszeit sehr ähnlich sind. Unterschiedlich sind vor allem die abgegebene Energie bis zur Autokatalyse und der Verlauf der Induktionsperiode. Insbesondere sprechen das mehrfache Ansteigen und Abfallen der Wärmeproduktionsrate beim Stoffgemisch Ethanol/Nitroglycerin für einen anderen Reaktionsverlauf als bei DPA/Nitroglycerin.

Vergleicht man Ethanol mit 4-Methoxyphenol (#38, 40), fallen die deutlich unterschiedlichen Reaktionszeiten, Wärmeflusskurven und Verteilung der Abbauprodukte auf. Letztere sprechen beim 4-Methoxyphenol für eine eindeutige Verhinderung von Oxidationsreaktionen bis zum Eintritt in die Autokatalyse, da keine Nitroglycerincarbonsäuren nachweisbar waren. Diese anti-oxidante Wirkung des 4-Methoxyphenols wird häufig in anderen Systemen ausgenutzt. Dass 4-Methoxyphenol nicht direkt mit dem Ngl reagiert, beweist die Tatsache, dass eine Erhöhung des 4-Methoxyphenol-Gehalts eine äquivalente Verlängerung der Induktionsperiode nach sich zieht. Somit kann der Zeitpunkt der Autokatalyse eindeutig mit dem 4-Methoxyphenol-Gehalt korreliert werden. Der Vergleich zwischen den Experimenten #38 und #40 (äquimolare Mengen an Ethanol bzw. 4-Methoxyphenol) beweist, dass die stabilisierende Wirkung des 4-Methoxyphenol nicht allein auf seiner Fähigkeit beruht, nitrose Gase durch Bildung eines Nitratesters abzufangen, sondern darüberhinaus Radikale und andere reaktive Komponenten aus dem Reaktionsgemisch wirksam entfernen kann.

NMR-Untersuchungen an thermisch belastetem BTTN ergaben gegenüber ungelagertem BTTN analog zum geringen Stoffumsatz keine sichtbaren Veränderungen, die Hinweise auf die Struktur etwaiger Zersetzungsprodukte geben können.

6 Zusammenfassung

Die durchgeführten Versuche zeigen, dass Ngl in einer thermisch induzierten Reaktion [7] NO_2 abspaltet (dabei ist die zentrale Nitratester-Einheit besonders reaktiv), welches aufgrund seiner oxidierenden und sauren Eigenschaften zu einer Beschleunigung der Zersetzungsreaktion und somit zu einer Autokatalyse führt. Zusätze wie Salze oder unreaktive organische Komponenten beeinflussen Geschwindigkeit oder Verlauf der Zersetzungsreaktion nicht. Findet die Reaktion unter Beteiligung basischer Substanzen statt, so kann sie bis zu einem Faktor von 20 hinausgezögert werden. Wichtig dabei ist, dass die eingesetzte basische Komponente nicht mit dem Ngl reagieren kann (vgl. Versuche #16 mit #14). Dies unterstreicht die Fähigkeit basischer Substanzen, autokatalytische Reaktionen von Ngl wirksam unterbinden zu können.

Organische Basen wie DPA verhalten sich ebenfalls stabilisierend. Ihre stabilisierende Wirkung ist jedoch auf einen kleinen Konzentrationsbereich (< 1%) begrenzt. Fügt man mehr Stabilisator hinzu, werden Nebenreaktionen (die zwischen DPA und Ngl ablaufen) gefördert, was zu einer schnelleren Autokatalyse und damit zu einer verringerten Stabilität des Gemisches führt. Vielfach wird sogar eine Unverträglichkeit von Ngl mit DPA diskutiert [8].

Eine eindeutige Bewertung der stabilisierenden Wirkung von Stabilisatoren auf Nitratester ist schwer durchführbar, da einerseits die entstehenden Stabilisatorabbauprodukte selbst (und zwar teilweise besser) stabilisierend auf Ngl wirken und andererseits die Abbauprodukte des Ngl häufig instabiler sind als Ngl selbst und somit auch die Bildungsrate von NOx im System vom jeweiligen Abbaugrad abhängt.

Somit wird das Zweistoffgemisch DPA/Ngl sehr schnell zu einem komplizierten Vielstoffsystem, in dem verschiedene Reaktionstypen (Radikalreaktionen, Substitutionsreaktionen, Säure-Base-Reaktionen, Oxidationen) nebeneinander ablaufen und in dem die Reaktionsprodukte miteinander in vielschichtiger Weise reagieren können. Teilweise wird der komplexe Reaktionsverlauf auch an Wärmeflusskurven sichtbar, die in einigen Fällen fast periodisch wechselnde Reaktionsraten aufweisen. So ein Reaktionsverlauf wird auch bei 4-Methoxyphenol beobachtet, der vielleicht geeignetsten Substanz zum Abfangen von Radikalen. Zwar wirkt auch DPA als Radikalfänger, die Wirksamkeit von 4-Methoxyphenol ist jedoch ungleich höher. Letztere Substanz hat den weiteren Vorteil, dass sie nicht mit Ngl reagiert (also verträglich ist).

Literatur

[1] R. Böhn, „Kritische Einflußgrößen auf den Abel-Test bei der großtechnischen Herstellung der Salpetersäureester Ethylenglykoldinitrat und Glycerintrinitrat", *Diplomarbeit Univ./GH Siegen*, **1997**.

[2] S. Wilker, U. Ticmanis, M. Kaiser, G. Pantel, G. Holl, K.-F. Elshoff, „Untersuchung der Zersetzung von Pulvervorkonzentrat", *ICT-Jahrestagung* 29, 131 (**1998**); S. Wilker, U. Ticmanis, G. Pantel, M. Kaiser, T. Fox, „Sicherheitslebensdauer von Pulverrohmassen", *ICT-Jahrestagung* 27, 101 (**1996**).

[3] P. Guillaume, M. Rat, G. Pantel, S. Wilker, „Heat Flow Calorimetry of propellants – Effects of sample preparation and Measuring Conditions", *2. TTCP Workshop Leeds* 4/**1999**.

[4] S. Wilker, J. Petržílek, J. Skládal, G. Pantel, L. Stottmeister, „Stability analysis of propellants containing new stabilisers", *ICT-Jahrestagung* 31 (**2000**).

[5] M. Rat, P. Guillaume, S. Wilker, G. Pantel, „Stability Studies of Spherical Propellants", *ICT-Jahrestagung* 27, 16 (**1996**); P. Guillaume, M. Rat, S. Wilker, G. Pantel, „Practical Application of Microcalorimetry to the Stability Studies of Propellants", *1. TTCP Workshop Leeds* 4/**1997**.

[6] U. Ticmanis, S. Wilker, G. Pantel, „Untersuchungen am System Schwarzpulver/sprengölhaltige TLP", *Fachtagung Innenballistik der Rohrwaffen*, Mannheim 1999.

[7] L.E. Paulsson, „Influence of humidity on the stability of propellants", *Symp.Chem. Probl. Connected Stabil. Explos.* 11 (**1998**); I.G. Wallace, S. Westlake, „The use of a Chemoluminescence NOx analyser to study the reaction of propellant stabilisers and their derivatives", *Symp.Chem.Probl.Connected Stabil.Explos.* 5, 19-41 (**1985**); M.H. Sammour, „Competitive Reactivity of stabilisers and ballistic modifiers during simulated aging of propellants", *J. Propul. Power* 14, 152-159 (**1998**); J. Kimura, „Chemiluminescence Study on Thermal Decomposition of Nitrate Esters (PETN and NC)", *Propellants, Explosives, Pyrotechnics* 14, 89-92 (**1989**); H.N. Volltrauer, A. Fontijn, „Low-Temperature Pyrolysis Studies by Chemiluminescence Techniques Real-Time Nitrocellulose and PBX 9404 Decomposition", *Combustion and Flame* 41, 313-324 (**1981**); J. Kimura, „Ageing Kinetics and Mechanism of Nitrocellulose via a Peroxide route", *Symp.Chem. Probl. Connected Stabil. Explos.* 11 (**1998**).

[8] B.S. Svetlov, V.P. Šelaputina, L.D. Maksimova, V.P. Jevtušenkov, „O vsaimodejstvii nitroglicerina s difenilaminom", *Mosk. chim.-technol. Inst. D.I. Mendeleeva, Trudy Moskva*, 83, 35-40 (**1974**); J. Petržílek, „Relations between chemical stability and composition of smokeless powders", doctoral thesis University of Pardubice (**2000**).

ANHANG

Tabelle 1. Durchgeführte Wärmeflussmessungen

Nr.	Sprengöl	Einwaage [g]	Kontaktstoff	Einwaage [g]	T [°C]
1	Ngl	0,231	keiner	-	89
2	Ngl	0,204	keiner	-	89
3	Ngl	0,202	keiner	-	89
4	Ngl	0,600	H_2O	0,059	89
5	Ngl	0,598	H_2O	0,060	89
6	Ngl	0,598	H_2O	0,061	89
7	Ngl	0,211	$BaCl_2 \cdot 2\ H_2O$	0,004	89
8	Ngl	0,203	$Ba(NO_3)_2$	0,040	89
9	Ngl	0,256	KNO_3	0,026	89
10	Ngl	0,207	KNO_3	0,0044	89
11	Ngl	0,201	KCl	0,021	89
12	Ngl	0,204	K_2SO_4	0,020	89
13	Ngl	0,199	$NaNO_2$	0,020	89
14	Ngl	0,201	0,01 N HCl	0,022	89
15	Ngl	0,206	0,01 N NaOH	0,022	89
16	Ngl	0,221	$CaCO_3$	0,020	89
17	Ngl	0,208	K_2CO_3	0,021	89
18	Ngl	0,208	Ethylacetat	0,022	89
19	Ngl	0,204	DPA	0,020	89
20	Ngl	0,201	DPA	0,0020	89
21	Ngl	0,219	DPA (unter Ar abgef.)	0,0020	89
22	Ngl	0,210	N-NO-DPA	0,024	89
23	Ngl	0,215	N-NO-DPA	0,0025	89
24	Ngl	0,217	2-NO_2-DPA	0,010	89
25	Ngl	0,199	N-NO-4-NO_2-DPA	0,0021	89
26	Ngl	0,211	DPA, N-NO-DPA	0,0010, 0,0010	89
28	Ngl	0,215	Centralit I	0,002	89
29	Ngl	0,214	Akardit II	0,002	89
30	Ngl	0,222	DBP	0,022	89
31	Ngl	0,207	KNO_3, DPA, N-NO-DPA	0,0016, 0,0011, 0,0012	89
32	Ngl	0,222	Schwarzpulver	0,226	89
33	Ethylnitrat	0,175	Keiner	-	80
34	BTTN	0,611	Keiner	-	80
35	Ngl	0,163	Keiner	-	80
36	Ngl	0,165	Keiner	-	80
37	Ngl	0,207	keiner	-	89
38	Ngl	0,200	EtOH	0,0026	89
39	Ngl	0,206	4-OMe-Phenol	0,0022	89
40	Ngl	0,199	4-OMe-Phenol	0,0069	89

Tabelle 2. Ergebnisse der Wärmeflussmessungen

Vers.-Nr.	Sprengöl	Kontaktstoff	Messzeit [d]	1. Maximum nach	3 mW/g erreicht nach [d]	Kurventyp
1	Ngl	keiner	1,04	1h42m	1,00	A
2	Ngl	keiner	1,46	1h42m	1,38	A
3	Ngl	keiner	1,50	1h27m	1,46	A
4	Ngl	H_2O	0,83	-	0,75	B
5	Ngl	H_2O	0,88	-	0,88	B
6	Ngl	H_2O	0,83	-	0,83	B
7	Ngl	$BaCl_2 \cdot 2\ H_2O$	0,29	3h00m	0,26	D
8	Ngl	$Ba(NO_3)_2$	1,63	37m, 1h33m	1,58	F
9	Ngl	KNO_3	1,13	1h39m	1,00	A
10	Ngl	KNO_3	1,16	1h43m	1,08	A
11	Ngl	KCl	1,04	42m, 2h45m	1,00	A
12	Ngl	K_2SO_4	1,38	1h50m	1,29	A
13	Ngl	$NaNO_2$	1,08	2h50m	0,92	A
14	Ngl	0,01 N HCl	1,42	2h30m	1,33	A
15	Ngl	0,01 N NaOH	1,50	-	1,46	B
16	Ngl	$CaCO_3$	22,0	-	21,9	B
17	Ngl	K_2CO_3	10,6	1h45m	0,03	C
18	Ngl	Ethylacetat	2,13	7h10m	1,99	A
19	Ngl	DPA	6,29	1d15h	6,21	A
20	Ngl	DPA	7,45	1d16h	7,38	A
21	Ngl	DPA (unter Ar)	12,2	1d18h	12,0	A
22	Ngl	N-NO-DPA	29,3	45m	-	C
23	Ngl	N-NO-DPA	7,98	1h05m	7,79	B
24	Ngl	2-NO_2-DPA	8,48	40m	8,40	A
25	Ngl	N-NO-4-NO_2-DPA	3,83	35m	3,67	A
26	Ngl	DPA N-NO-DPA	6,58	1d11h	6,50	A
28	Ngl	Centralit I	5,33	9h10m	5,25	B
29	Ngl	Akardit II	9,42	7h, 19h	9,25	E
30	Ngl	DBP	1,33	4h	1,21	A
31	Ngl	KNO_3, DPA N-NO-DPA	8,71	1d13h	8,63	A
32	Ngl	Schwarzpulver	10,0	1d8h	-	C
33	Ethylnitrat	keiner	7,0	-	-	C
34	BTTN	keiner	23,7	4d14h	-	C
35	Ngl	keiner	3,23	6h	2,83	A
36	Ngl	keiner	3,00	6h22m	3,07	A
37	Ngl	keiner	1,83	30 m	1,71	A
38	Ngl	EtOH	5,97	25 m	5,92	F
39	Ngl	4-OMe-Phenol	5,31	25 m	5,13	A
40	Ngl	4-OMe-Phenol	22,0	25 m	21,8	A

Kurventypen A: (schnelle) Vorreaktion, danach lange stabile Phase mit heftiger Autokatalyse. B: wie A, ohne Vorreaktion. C: (starke) Vorreaktion, keine Autokatalyse. D: wie A, jedoch fast keine erkennbare Vorreaktion. E: wie A, jedoch deutlich zweistufige Zersetzung. F: wie A, jedoch zweistufige Vorreaktion.

Tabelle 3. Relative Anteile der mittels NMR-Spektroskopie identifizierten Abbauprodukte (Angaben in [%])

Vers.-Nr.	Kontaktstoff	Freiges. Energie [J/g]	Ngl	1,2-Dngl	1,3-Dngl	2,3-Dngl-COOH	2-Ngl-COOH	3-Ngl-COOH
3	keiner	60	81,4	5,2	11,5	1,4	0	0,5
6	H_2O	19	72,3	11,5	15,1	0,7	0,4	0
7	$BaCl_2 \cdot 2\ H_2O$	11	31,9	14,5	24,9	4,0	4,8	20,0
8	$Ba(NO_3)_2$	52	38,5	11,7	19,6	11,5	4,3	14,4
9	KNO_3	34	48,4	9,8	16,4	14,9	2,2	8,4
10	KNO_3	52	52,5	10,4	16,0	12,4	1,9	6,8
11	KCl	36	54,7	11,7	17,2	6,9	1,9	7,6
12	K_2SO_4	55	68,2	4,5	13,0	14,3	0	0
13	$NaNO_2$	109	74,7	5,2	12,1	7,6	0,4	0
14	0,01 N HCl	n.a.						
15	0,01 N NaOH	15	90,9	5,3	3,8	0	0	0
18	Ethylacetat	115	75,9	6,9	11,5	1,9	0	3,8
19	DPA	113	57,0	10,7	16,6	8,5	2,0	5,2
20	DPA	122	58,6	11,1	16,6	8,2	1,2	4,2
24	2-NO_2-DPA	86	76,0	7,9	12,5	2,1	0,3	1,2
25	N-NO-4-NO_2-DPA	243	90,4	2,6	7,0	0	0	0
26	DPA N-NO-DPA	104	66,3	10,0	15,0	1,7	0,9	3,2
28	Centralit I	105	75,4	8,3	12,6	1,8	0,3	1,5
30	DBP	166	47,7	11,9	19,6	10,5	3,3	7,0
31	KNO_3 DPA N-NO-DPA	116	77,7	6,3	13,0	1,9	0	1,2
37	keiner	111	69,8	8,8	15,2	2,6	0,5	3,0
38	EtOH	40	59,1	11,9	19,0	7,8	2,2	0
39	4-OMePhenol	206	84,3	4,8	11,0	0	0	0
40	4-OMePhenol		78,7	009,3	11,8	0	0,01	0

n.a.: NMR-Messung wegen Überlagerung durch großen H^+-Peak nicht quantitativ auswertbar.

Humid Ageing of Polybutadiene Based Propellants

Simon Torry, Anthony Cunliffe

DERA, Fort Halstead, Sevenoaks, Kent TN14 7BP, UK.

Abstract

Due to the unstable nature of energetic materials, weapon systems have finite life spans. All energetic materials undergo ageing processes that affect their performance, reliability, and operational safety. Hence, there is a need to monitor the chemical components in a weapon system so as to maximise its service life.

In this work, two model compositions (cured polybutadiene and cured stabilised/plasticised polybutadiene) and two ammonium perchlorate/polybutadiene based propellants were aged in humid environments. The physical and chemical properties of these materials were studied using sol-gel analysis, nuclear magnetic resonance spectroscopy, FTIR spectroscopy, gas chromatography analysis, thermo-mechanical analysis, and mass uptake experiments.

The effect of humidity on the ageing characteristics of the binder varied considerably with the composition and dimensions of the material. Thick polybutadiene samples aged inhomogeneously – high moisture levels increased the rate of crosslinking and oxidation. The oxidation rates of thin polybutadiene samples decreased substantially when samples were aged in high humidities. Propellants exhibited much faster rates of oxidation that those observed for stabilised/plasticised polybutadiene. High humidity increased the propellant's oxidation rate substantially. Rapid hardening of the propellant was observed in humid ageing trials – the rate of hardening did not correlate with the crosslink density. This suggested that the hardening process was not associated with oxidative cross-linking reactions.

1. INTRODUCTION

Due to the unstable nature of energetic materials, weapon systems have finite life spans. All energetic materials undergo ageing processes, which affect their performance, reliability and operational safety. Hence, there is a need to monitor the chemical components in a weapon system so as to maximise its service life. The benefits to be gained by accurate prediction of service life include reduced whole life-cycle costs, improved safety, improved effectiveness and operational and procurement flexibility. DERA is undertaking a comprehensive programme to predict and extend the service life of energetic materials, including naval munitions. An important part of this is the monitoring of the environmental conditions, particularly temperature and humidity, experienced by systems in service use. In order to make use of this, it is necessary to understand the effects of these conditions on the munitions, and, in particular, to be able to identify and understand critical ageing processes. The effects of temperature and moisture on composite propellants have been identified as important for naval weapons systems.

The service life of a solid rocket motor is a function of a number of variables such as: mechanical properties; chemical degradation; stability of the motor/liner interface; migration/diffusion of plasticisers etc. Lifetime calculations of such a complex system are simplified by estimating the time it takes for one or more critical properties of the propellant composition to reach a defined failure point. Degradation processes can be accelerated by ageing propellant at elevated temperatures and then extrapolating the data to normal operation conditions using the Arrhenius relationship.

A substantial body of work has been devoted to the study of thermal accelerated ageing of polybutadiene based propellants. However, the effects of moisture in the ageing processes have not been studied to any large extent. Hence, in this work, the effects of moisture in the ageing processes of polybutadiene based propellants and its components have been studied by mechanical and chemical analytical techniques. This report represents the ageing characteristics of the propellant's surface fully

exposed to air and moisture. Normally, motors are sealed during manufacturer. Hence, the ageing trials represents the worse case scenario where the motor seal is highly ineffective due to damage or poor design.

2. EXPERIMENTAL

Unfilled Polybutadiene Rubber

Two types of unfilled polybutadiene rubber were prepared (Table 1). The pre-polymer was pre-dried overnight under vacuum at 70°C and then cured with isophorone di-isocyanate at 70 °C for 7 days in a nitrogen atmosphere using a NCO:OH ratio of 0.85:1. Samples were cured in finger moulds (100mm by 6mm by 10mm) and disc moulds (4mm depth, radius 4 mm and 10mm depth by 12.5mm radius).

Ingredients	Unfilled Polybutadiene rubber / Mass %	Stabilised Polybutadiene Rubber / Mass %
Polybutadiene (HTPB R45HT)	93.07	71.90
Isophorone diisocyanate (IPDI)	6.93	5.35
Di-octyl sebacate (DOS)	0	22.00
2,2'-methylenebis(6-tert-butyl-4-methyl phenol) (Calco-2246)	0	0.75

Table 1. Unfilled rubber compositions.

Propellant

State of the art propellant was obtained from Royal Ordnance (Table 2). Propellant was cut into 40 ± 2 mm x 12 ± 1 mm by 3 ± 1 mm strips and aged vertically in glass vials.

Ingredient	HT398	HT341
Ammonium perchlorate (AP)	84	73
Aluminium	0	15
Polybutadiene (R45M)	10	8
Isocyanate (IPDI)	0.7	0.6
Plasticiser (Dioctyl sebacate)	3	3
Antioxidant (CALCO2246)	0.1	0.1
Other components	2.2	0.3

Table 2. Propellant Compositions.

Ageing Conditions

Samples were fully exposed and aged at 50 °C, 60 °C and 70 °C over various saturated salt solutions in sealed glass sample jars. Over the temperature range the relative humidity do not vary more than 3%RH.

NMR Spectroscopy

Nuclear magnetic resonance spectra were measured using an MSL 300 spectrometer fitted with either a 10mm broad band NMR probe or a 5mm 13C/1H probe. Solutions were made up in deuterated chloroform. ^{13}C solid state NMR was performed using a cross-polarisation magic angle spinning (CPMAS) probe. Extracted polymer was swelled in dichloromethane, ground to a crumb and dried in a vacuum. The polymer crumb was loaded into a 7mm zirconium oxide probe. Hydrogen nuclei were decoupled from carbons during FID acquisition.

Thermal Mechanical Analysis (TMA)

TMA analysis was performed using a Mettler TMA40 (Mettler TC15 Controller) running the Star^e (version 4.00) acquisition/analysis program.

Three types of TMA measurements were performed:

- 3mm diameter ball point penetration – sample equilibrated at 50°C for four minutes, 0.001N load applied for 10 minutes, 0.18N load applied for 10minutes;
- elastic deformation –sample equilibrated at 50°C for four minutes, an oscillating load of 0.02 and 0.18N applied per 6 seconds for 5 minutes; and
- bar bending – a load of 0.02N applied for 7 minutes, 0.1N load applied for 15 minutes, 0.02N load applied for 15 minutes at 84°C.

The dynamic elastic deformation test was performed on aged unfilled polymer discs (4mm thick by 4mm radius) sandwiched between two steel plates. Penetration experiments were performed on aged discs of polymer (4mm thick by 4mm radius).

Propellant samples were rigid and hard relative to the unfilled polybutadiene rubber. Hence, both the ball point penetration and dynamic elastic deformation experiments were not suitable methods to assess changes in the mechanical properties of aged propellant. The bar bending experiment was found to be a more appropriate experimental method. A propellant bar of dimensions 20 ± 1mm x 6 ± 1 mm x 3 ±1 mm was loaded into a bar bending sample holder and subjected to a load so that the maximum central deflection was not more than 200 microns. The modulus plots were characterised by two values: the forward modulus and the recovery modulus. The difference between the recovery modulus and the forward arises due to viscoelastic nature of the propellant. In this paper, only the forward modulus has been reported.

Extraction

Aged polybutadiene samples were dried in a vacuum, sliced into 1.5 mm^3 and extracted overnight with dichloromethane using Soxhlet apparatus. Propellant samples were extracted with hexane overnight using Soxhlet apparatus. The solvent was removed from the Sol solutions by rotary evaporation.

GC Analysis

The propellants' antioxidant and plasticiser content was measured using a Perkin Elmer Auto sampler gas chromatogram fitted with a Jencons DB-1 capillary column (30m by ID 0.321mm, film thickness 0.25μm). The temperatures of the injection port, oven and detector port were 300, 250 and 300°C respectively.

Infrared Spectroscopy

Infrared data was acquired using a Nicolet Magna 760 spectrometer, and a Nicplan microscope (fitted with 15 x objectives, motorised stage, and variable apertures). Data was processed using the Omnic 4.1 analytical program. The sample compartment was purged with dry air.

In situ ageing experiments were performed using a Rooc variable temperature FTIR cell fitted with heated sodium chloride windows. The temperature was calibrated with type K thermocouple. Data was analysed using the SERIES Omnic 4.1 software.

3. RESULTS

Unstabilised, Unfilled Polybutadiene Rubber

Aged, thick, unfilled polybutadiene rubber exhibited:

- increases in the crosslink density (sol gel analysis) - oxidative crosslinking, non-Arrhenius;
- increases in the mass uptake - oxidation processes, non-Arrhenius;
- decreases in surface penetration - observe surface hardening, non-Arrhenius;
- increases in elastic modulus - non-Arrhenius.

Polybutadiene rubber oxidised at a faster rate in humid environments. That is to say, the rubber's crosslink density (Figure 1) increased with higher humidity. Additionally, the overall irreversible mass of the samples increased due to reaction with oxygen. The increase in the crosslink density and mass uptake was not reflected in dynamic TMA modulus measurements. Elastic modulus ought to increase

with crosslink density. However, it should be noted that no attempt was made to dry the TMA samples before measurement. Hence, materials aged at 96%RH may be softer than dry aged materials due to plasticisation of the rubber with occluded water.

Arrhenius behaviour was not observed in sol gel, TMA, and mass uptake experiments. This may be due to inhomogeneous ageing processes. FTIR microscopy of a 20-micron thick cross-section of an aged polybutadiene sample confirmed the presence of inhomogeneous oxidation. Severe oxidation, in the form of carbonyl and hydroperoxide species, was observed in the surface layer to depth of 0.2mm. The interior of the sample appeared unchanged. Adam et al [1] noted that oxidised polybutadiene impeded the diffusion of oxygen into the bulk of the polybutadiene rubber. This contributes towards the inhomogeneous ageing of polybutadiene.

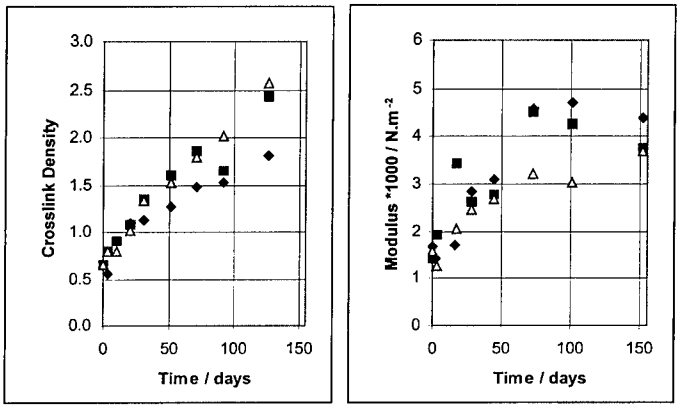

Figure 1. Crosslink density and elastic deformation of unfilled stabilised polybutadiene rubber aged at 70°C (◆ - dry, ■ - 50%RH, ▲ - 96%RH).

In the light of the inhomogeneous ageing profile of thick unstabilised polybutadiene, 20-micron thick samples of polybutadiene rubber were aged in situ in a temperature controlled FTIR cell.

Upon ageing, the alkene IR bands at 970 and 900 cm^{-1} degraded appreciably. Additional bands due to hydroperoxide/hydroxyl and carbonyl oxidation products appeared at 3450 and 1710 cm^{-1} respectively. Broad bands replaced fine peak structures in the finger print region.

The decomposition process was characterised by a sigmoidal curve (Figure 2) - this is typical of polymer radical oxidation reactions. The reaction curve was characterised by an induction period, a rapid oxidation period, and finally a slow oxidation process. During the induction period, the polymer did not appear to change in composition. However, close inspection of the induction period revealed that the polymer did oxidise to small quantities of hydroxyl and carbonyl species - the reaction rate was slow. At a certain critical concentration of hydroperoxide species, the polybutadiene rubber suffered from auto-oxidation reactions. The time to rapid oxidation was described by the Arrhenius process (Table 3). At 96%RH, 50°C, the rapid oxidation period was not observed hence the activation energy is not reported.

Moisture appeared to moderate the oxidation process. The time to rapid oxidation increased as the relative humidity increased. This implies the water is acting as an inefficient antioxidant. That is to say, high humidity impeded the oxidation process. This contradicts measurements performed on thick polybutadiene samples whereby the crosslink density increased with humidity. This will be discussed at the end of this paper.

Humidity / %RH	Activation Energy (maximum rate of oxidation) / kJ K^{-1} mol^{-1}
dry	96
50	160
96	-

Table 3. Activation energy for rapid oxidation process.

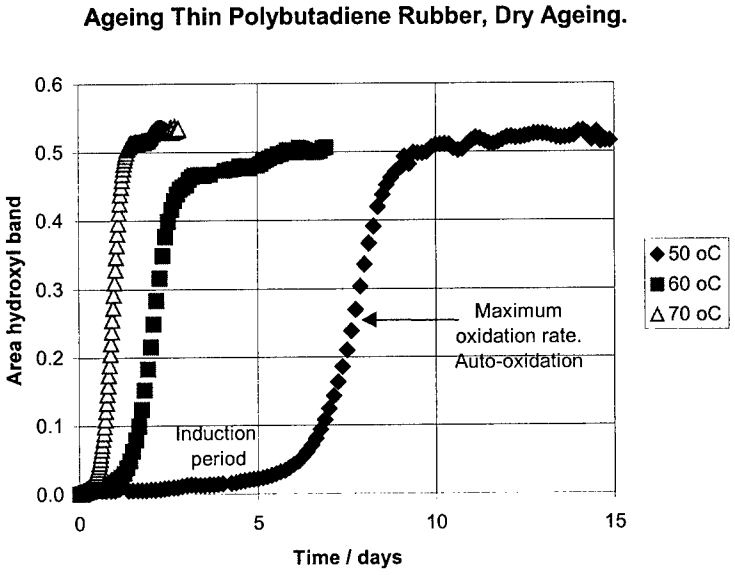

Figure 2. The hydroperoxide band area of aged polybutadiene (dry conditions).

Stabilised, Plasticised Unfilled Polybutadiene Rubber

Upon ageing, stabilised, plasticised, unfilled polybutadiene rubber exhibited:

- increases in crosslink density - little dependence on moisture;
- decreases in mass uptake;
- decreases in DOS plasticiser content - loss of plasticiser depends on moisture;
- decreases in Calco2246 antioxidant content - moisture no effect on rate of consumption;
- increases in elastic modulus due to oxidative crosslinking, non-Arrhenius; and
- decreases in surface penetration decreased due to surface hardening, non-Arrhenius.

According to crosslink density measurements, oxidation of plasticised polybutadiene rubber was not accelerated by the presence of moisture. This was contradicted by elastic deformation measurements. They suggested that samples aged at 70°C in 50%RH were stiffer than those samples aged at 96%RH and under dry conditions (Figure 3). However, this may be due to loss of plasticiser as discussed below.

Oxidation of polybutadiene normally leads to an increase in the mass due to uptake of oxygen. However, in the case of aged, plasticised polybutadiene rubber, there was a net loss. This was attributed to loss and degradation of the plasticiser. Analysis of the rubber extract revealed that the DOS plasticiser underwent hydrolysis during moist ageing trials. A carbonyl peak at 178 ppm (^{13}C NMR

spectroscopy) was associated with the formation of a long chain alkyl carboxylic acid. The rate of DOS consumption depended on relative humidity (Figure 4). Moisture did not appear to affect the rate of consumption of the antioxidant (Figure 4). The Calco2246 consumption at 96%RH was not representative of the general trend, hence the data was excluded from Figure 4.

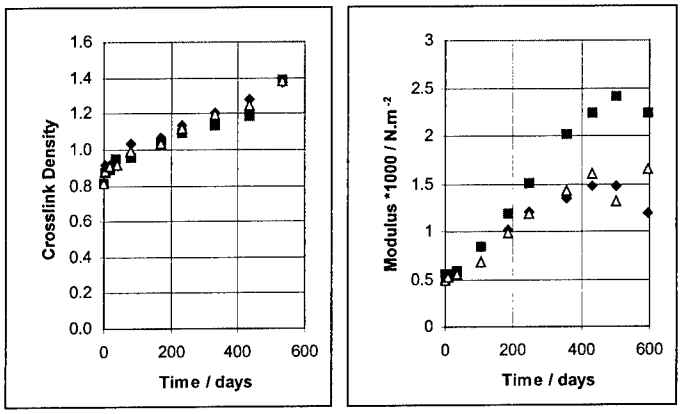

Figure 3. Crosslink density and elastic deformation of plasticised, stabilised polybutadiene rubber aged at 70°C (◆ - dry, ■ - 50%RH, ▲ - 96%RH).

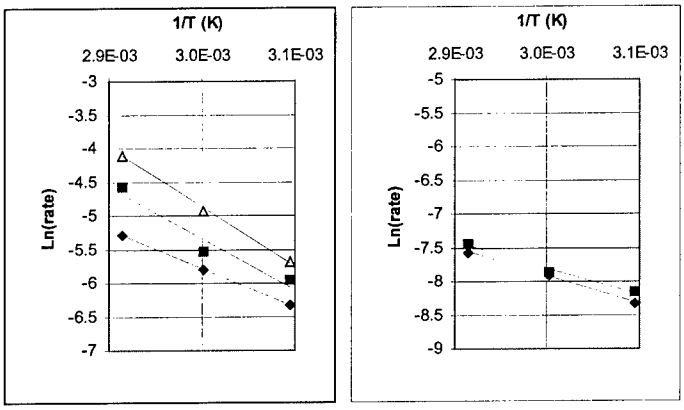

Figure 4. The consumption of DOS (left) and Calco2246 (right) in plasticised polybutadiene at various humidities. (◆ - dry, ■ - 50%RH, ▲ - 96%RH).

Ageing Characteristics of Propellants

Upon ageing propellant samples, there were:

- increases in crosslink density due to oxidative processes;
- decreases in mass uptake due to loss/degradation of plasticiser;
- decreases in antioxidant Calco2246 content; and
- moisture induced 'hardening' which did not correlate with the crosslink density measurements.

Crosslinking/oxidation reactions of both propellants were accelerated by high humidities and high temperatures (70°C, 75 %RH) (Figure 5). The rate of propellant crosslinking was faster than that observed for the unfilled polybutadiene models.

The effect of moisture on the propellant ageing process was opposite to that observed for unfilled materials. The degradation of unfilled, unstabilised polybutadiene was attenuated by moisture. The crosslink density of stabilised/plasticised polybutadiene was not greatly affected by humid environments. In the case of propellants, the oxidation rate was increased in the presence of moisture. Hence, the propellant ageing mechanism appears to be different to that observed for both polybutadiene and stabilised/plasticised polybutadiene rubber.

DOS analysis revealed that, as in the case of plasticised unfilled polybutadiene, the plasticiser underwent hydrolysis in high humidities. It was noted that the rate of DOS degradation was faster in the propellant than in the unfilled plasticised rubber. The hydrolysis may be affected by the presence of ammonium perchlorate. Ammonium perchlorate is a salt of a strong acid and a weak base, hence saturated ammonium perchlorate solutions are acidic in nature. This may accelerate the DOS degradation process.

Moisture markedly affected the antioxidant consumption rate in both propellants. At 70°C in high humidity, all the Calco2246 had been consumed in propellant HT398 after 200 days (Figure 6). The situation was worst in propellant HT341; all the Calco2246 has been consumed after ageing the material for 100 days at 75%RH and 70°C (Figure 6). The rate of consumption of antioxidant in the propellant was very much faster than that measured for the unfilled stabilised/plasticised material. This suggested that the solid fillers, possibly ammonium perchlorate, played a part in the antioxidant consumption process.

Proton and carbon-13 NMR spectroscopy of the extracts did not reveal the nature of the Calco2246 degradation products. Additionally, solid state carbon-13 NMR spectroscopy could not detect the antioxidant crosslinked with the gel network.

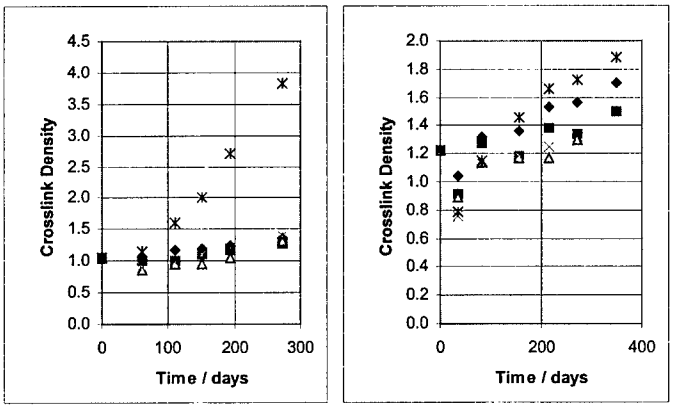

Figure 5. Crosslink density of Propellant HT341 (left) and HT398 (right) aged at 70°C (◆ - dry, ■ - 10%RH, ▲ - 30%RH , X – 50%RH, ✻ - 75%RH).

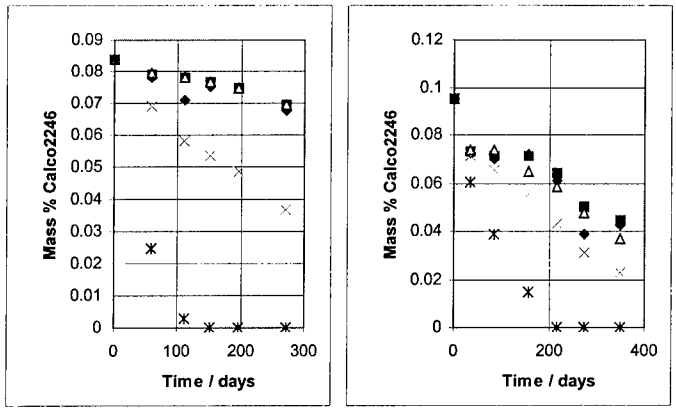

Figure 6. Calco-2246 content in propellants HT341 (left) and HT398(right) at 70°C (◆ - dry, ■ - 10%RH, ▲ - 30%RH , X – 50%RH, ✻ - 75%RH).

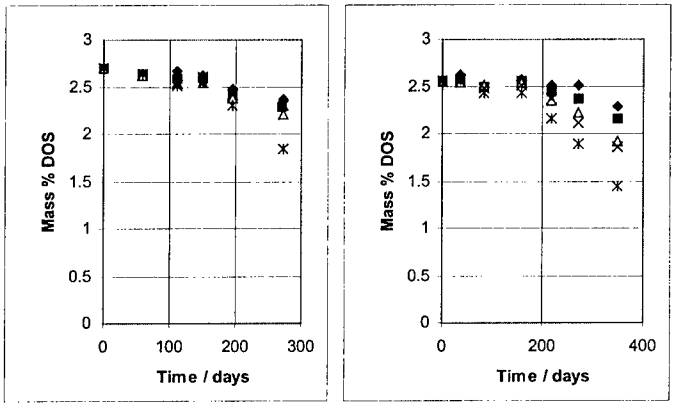

Figure 7. DOS content in propellants HT341 (left) and HT398(right) at 70°C (◆ - dry, ■ - 10%RH, ▲ - 30%RH , X – 50%RH, ✻ - 75%RH).

At high humidities and temperature, both propellants rapidly hardened in the presence of moisture (Figure 8). Note that in case of propellant HT398, the modulus of materials aged at 75%RH were smaller than that of propellant aged at lower humidities. This reflected the plasticisation of the propellant by the water absorbed into the sample. The modulus measurements were made immediately after removal of the propellant from the ageing chamber. No attempt was made to dry the samples prior to measurement, hence measurements reflect propellant saturated with moisture.

As a confirmation of the water plasticisation effect, a sample (HT341, 50°C, 75 %RH aged for 117 days) was dried in situ for one hour. The bar bending experiment was repeated in situ - the modulus was found to increase by 21%.

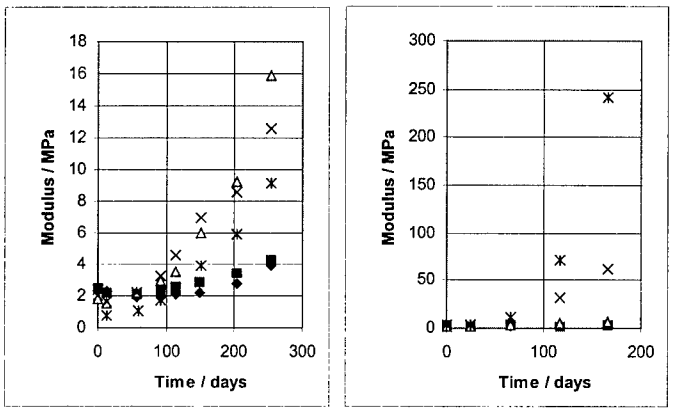

Figure 8. Bar bending modulus of propellant HT398 (left) and HT341 (right) aged at 70°C in various humidities (◆ - dry, ■ - 10%RH, ▲ - 30%RH, X – 50%RH, ✳ - 75%RH).

TMA bar bending experiments suggested that propellant HT341 aged at a much faster rate than propellant HT341. This is probably due in part to the smaller thickness of propellant HT341 samples (HT341 thickness 2.4±0.1mm, thickness HT398 3.4±0.2mm). Additionally, the increase in modulus may reflect different ageing processes accelerated by aluminium in propellant HT341.

Previous work has demonstrated that the mechanical properties of polybutadiene/AP based propellants tend to be sensitive to the crosslinking reactions. Cunliffe et al [2] found that the propellant modulus was proportional to the crosslink density. This assumes that all other conditions are equal - e.g. plasticisation levels stay the same and the ageing process is homogeneous. This was not the case for the samples studied in this work. Samples were not dried before measurement, hence the mechanical properties reflect the plasticisation effects of water. Similarly, DOS was lost during the ageing process, thereby causing hardening of the sample.

Comparison of the mechanical data with the crosslink density data and DOS content data suggests that another process other than oxidation/plasticiser loss was responsible for the hardening of the propellant. The samples appear to harden at a much faster rate than that suggested by the crosslink density data. This effect has also been observed in the moist ageing of other AP based propellants [3]. A prime candidate for the additional hardening is the re-crystallisation of the ammonium perchlorate fines in the bulk of the propellant.

4. DISCUSSION

One of the important factors in the ageing processes of polybutadiene is the ability of the initial oxidation products to propagate. That is to say, the hydroperoxide species in the oxidised rubber have to disassociate and form radicals to propagate the oxidation process. The addition of antioxidants obviously impedes the propagation progress. Additionally, it is reasonable that water could interfere with the dissociation of polybutadiene oxidation species thereby altering the apparent oxidation rate. Ruaya et al [4] has demonstrated that oxidation of thin polybutadiene samples, partially immersed in water, depends on the pH. That is to say, samples subjected to solutions of pH below 3 appeared to resist oxidation. The oxidation rate of samples exposed to solutions of pHs between 7 and 10 appeared to be accelerated. We propose that some of our contradictory results are due to this effect coupled with inhomogeneous ageing processes.

Thick, unstabilised polybutadiene rubber appeared to oxidise at a faster rate in moist environments. However, the opposite occurred for thin polybutadiene samples – moisture attenuated the oxidation process. Polybutadiene has a higher permeability to oxygen than crosslinked, oxidised polybutadiene [1]. We suggest that water attenuates the oxidation process, preventing the formation of a thin, highly crosslinked surface. This allows the oxygen to permeate into the bulk of the sample and thereby causing

greater damage in the interior of the material. Hence, in thick pieces of polybutadiene, the oxidation process accelerates in the presence of moisture.

Unlike unstabilised polybutadiene rubber, moisture did not appear to effect the crosslink density of stabilised, plasticised polybutadiene rubber. Both the plasticiser and the antioxidant moderates inhomogeneous processes in such a way so as to allow oxygen to diffuse into the bulk of the sample. Water is a is a less efficient antioxidant than Calco2246. Hence, its stabilisation effect is not observed. However, humid environments cause the degradation of the ester plasticiser. This causes the rubber to harden. 96%RH humid environments may also temporarily plasticise the rubber.

Oxidation of propellants in moist environments contradicts the above observations. Rather than attenuating the oxidation process, moisture appeared to accelerate it in the propellant samples. There is no doubt that atmospheric oxygen is required for the degradation of the propellant. polybutadiene/AP based materials aged in vacuum do not undergo oxidative crosslinking [3] - the oxygen/oxidising species does not originate from the perchlorate. However, the presence of AP does appear to accelerate the oxidation process. We suggest this be due to the rapid consumption of the antioxidant. However, Calco2246 reaction products were not observed in the propellant extracts. Similarly ^{13}C CPMAS NMR did not provide sufficient resolution and signal to noise, to observed Calco2246 products crosslinked into the gel network. At present, the mechanism of the moisture induced antioxidant consumption is not known. Antioxidant degradation may be accelerated by the acidic pH of the moisture saturated propellant. The DOS plasticiser also appears to decompose at a faster rate in the propellant than in the unfilled stabilised/plasticised polybutadiene rubber. This to may be due exposure of the DOS to the propellant's acidic environment.

It was noted that aluminium filled propellants degraded at a faster rate than non-aluminised material. We do not have any evidence as to the nature of the antioxidant degradation reaction at present.

The chemical degradation reactions clearly demonstrate the binder crosslinks and losses plasticiser. However, these effects do not appear to explain the rapid increase in the modulus of the propellant samples. It is suggested that another mechanism be responsible for the propellants hardening. We propose, that long-term exposure of propellants to humid environments cause the ammonium perchlorate fines to recrystallise in such a way as to increase the modulus of the material.

4. CONCLUSIONS

The ageing characteristics of four types of material (cured polybutadiene, stabilised/plasticised polybutadiene, polybutadiene/AP propellant, and aluminised polybutadiene/AP propellant) in various humidities were investigated.

The Arrhenius model could not describe a number of the ageing processes.

Thick cured polybutadiene materials suffered from inhomogeneous ageing. The outer surface rapidly crosslinked and hardened to an impervious outer layer. The interior of the sample was protected from further oxidation.

The rate of oxidation of thin cured polybutadiene was studied by FTIR. The oxidation process was characterised by an induction period, followed by a rapid oxidation period. This is typical of radical oxidation processes. Moisture substantially retarded the oxidation process. Samples aged at 50°C and 96%RH did not exhibit the characteristic rapid oxidation process despite ageing the sample 15 times longer than dry aged samples.

Unlike unstabilised polybutadiene rubber, moisture did not appear to affect the rate of oxidation in thick stabilised, plasticised polybutadiene bars. The crosslink density of stabilised polybutadiene aged in dry conditions appeared to be similar to material aged in 96%RH. The rate of consumption of Calco2246 was not affected by moisture. The plasticiser, DOS, did suffer from hydrolytic scission (GC and NMR measurements).

The mechanical properties of aged stabilised/plasticised polybutadiene depended on humidity. However, there was no linear trend. The elastic modulus of the material aged at dry, 50 and 96%RH did not appear to fit a trend. The strength of the material aged at 50%RH was greater than that aged under 96%RH and dry conditions. Given the high reversible mass uptake of stabilised/plasticised

polybutadiene at 96%RH, water probably plasticised the polybutadiene and thereby decreased the elastic modulus.

The ageing characteristics of propellant were different to both unstabilised polybutadiene and plasticised/stabilised polybutadiene. The presence of the ammonium perchlorate filler had a marked effect on the ageing characteristics of the polymer binder.

Moisture dramatically effected the crosslink density and Calco2246 content of the propellant. The antioxidant was rapidly consumed at high temperatures and humidity. The crosslink density increased with ageing in moist conditions. This contrasted ageing trials of the unfilled stabilised/plasticised polybutadiene.

As a result of changes in the crosslink density and the antioxidant content, the mechanical moduli of the propellants increased substantially when aged in humid conditions. However, we suggest that chemical changes are not the only driving force for propellant hardening. Moisture induced recrystallisation of AP fines may contribute to the propellants hardening.

5. Acknowledgements

The authors are grateful to Dr. P Barnes (CESO(N)/CINO, MoD, UK) for funding this work.

6. References

1 C. Adam, J. Lacoste, J. Lemaire, Photo-oxidation of Elastomeric Materials. Part 1- Photo-oxidation of Polybutadienes, J. Polym. Degrad. Stab., **24**, 185-200, 1989.

2 A. V. Cunliffe, A. Davis, A. L. Hudd, The relationship between sol content and physical properties of aged rubbery composite propellants, TTCP, Panel W4, Volume 4, paper 4.8, 100-119, 1984.

3 A. V. Cunliffe, A. Davis, A. L. Hudd, The ageing of composite propellant, TTCP, Panel W4, Volume 5, paper 5.21, 320-331, (1984).

4 A. Ruaya, M. T. Shaw, A. Graton, Oxidation of Elastomers in Aqueous Enviroments, Rubber Chem. Technol., 67(5), 775-785, 1994.

INFLUENCE OF SLITS TO THE DETONATION FRONT

M. Held

TDW, 86523 Schrobenhausen, Germany

Abstract

Small slits in high explosives charges perpendicular to the detonation directions give, depending on the width short delay times, still the detonation wave has some build-up distances.

Slits parallel to the detonation direction have a special influence on the detonation waves. A precursor air shock (PAS) is produced in the slit which runs about 50 % faster compared to the detonation wave. This is influencing the detonation front in millimeter ranges around the channels. If the slits have small angles to the detonation direction, the detonation wave is not able to pass, but is running around it. This is changing the detonation front profile in a macroscopic scale.

The partially tricky different test set-ups will be described in detail:

- to get the delay times as a function of the different air gaps arranged perpendicularly to the detonation wave
- to get the detonation profiles visible, although the PAS is running much faster in the parallel slit arrangement
- to get the maximum angle of slits to the detonation direction that the detonation wave can pass without being interrupted.

The used test set-ups and the achieved experimental results are described.

Background

Some special charges, like shaped charges and EFP's, need very symmetric detonation waves to achieve straight jets for large penetrations <1> and exactly symmetric build-up processes for explosively formed projectiles with fins <2>. Gaps and slits in the charges should be generally avoided. Otherwise slits or gaps transverse to the detonation direction should be employed, because this orientation is less disturbing the detonation velocity and therefore the detonation profile. Fig. 1 shows a schematic sketch with possible transverse, longitudinal and oblique gaps in a shaped charge.

In Fig. 2 one test set-up is shown, with which the time delay of the detonation wave and the so-called transition time as a function of air gap distance can be determined in "one" firing. A typical streak record is presented together by the principle analysis of such streak records with the definitions of the transition and the delay times (Fig.3) and finally the achieved test results for two types of sqeeze cast and pressed powerful high explosive charges (Fig. 4) <3>.

The detonation behaviour and the diagnostic technique is much more complex with longitudinal gaps <4>. The so-called "precursor air shocks", shortly PAS, are running much faster in these gaps <5>. To observe the later arriving detonation front, it is necessary to add a block of plexiglass with the same slit profile on the end of the slitted charge, so that the precursor air shock cannot radially expand and cover the end-surfaces before the detonation waves arrive (Fig. 5). For the diagnostic the arrival time measurement technique <6> with a rotating mirror streak camera <7> is used. The arrival time of the precursor air shock can now be seen as light traces, afterwards the arrival time profile of the detonation front as very short flash trace between the porous endsurface of the high explosive charge and the plexiglass block, and finally the expansion of the precursor air shock at the end of the plexiglass block (Fig. 6). Such streak records can be analysed with regard to the detonation velocity along the 40 mm long slit length in the high explosive charge (Fig. 7) and precursor air shock velocities along the 40 mm slits in the HE charge, in the plexiglass and as mean values along both together. The magnified streak records of

the detonation profiles achieved in flash gap technique can be analysed also in great detail (Fig. 10). Surprisingly it was found that under a small angle the detonation wave is not able to pass the slit directly through the slit width, as they are less than 1 mm. The arrival times can be predicted either by the so-called *spherical theory*, that means the detonation wave has no retardation by passing the longitudinal gaps, or by the *gap theory*, which means the detonation wave is running perfectly around the gaps (Fig. 11). The arrival time measurements demonstrate that the *gap theory* must be taken into account for the selected test set-up (Fig. 12).

Now the question arises to what angles and gap widths the detonation wave is following the *gap theory* which means running around the slits.

Oblique slits

The delay times against perpendicular slits and the change of the detonation profile by longitudinal slits through the precursor air shock are discussed already in detail. Now the question is, what slit width under which angle can be passed by oblique detonation waves. The three different possible orientations of slits or gaps are presented in Fig. 13. To get also larger angles a modified test set-up was laid out which is presented in Fig. 14 for the arrangements with 1 mm and 0.3 mm slit width. The distances between the different slits were arranged in such a way that the incident angles were 0°, and then roughly increasing to 10°, 20°, 30°, 40° and finally 50°. The slit length was only 20 mm and therefore the thickness of the plexiglass block was also only 20 mm. The endsurface was observed via a 45° mirror (Fig. 15). Three different charge types were investigated: normally cast TNT/RDX 35/65 charge with about 7.8 mm/µs detonation velocity, normally cast TNT/HMX 35/65 charge with a detonation velocity of around 8.0 mm/µs and a squeeze cast TNT/HMX 15/85 charge with 8.5 mm/µs detonation velocity. The achieved streak records for the 3 different high explosive compositionswith 0.3 mm and 1 mm slit widths are presented in Fig. 16. The information which can be read out from such streak records is specially given in Fig. 17:

a) The first light in the slit is visible, as soon as the detonation wave arrives at the bottom of the slit.
b) The continuation of the light emission comes from the precursor air shock which travels with high velocity along the slit plane.
c) The slightly radial expanding light appears upon the arrival of the precursor air shock on the interface of the HE charge and the plexiglass block .
d) The detonation profile is presented as flash gap traces on the HE/plexiglass interface
e) The expansion of the channel light is given, as soon as the precursor air shock arrives at the end of the plexiglass block and can expand radially.

Analysis

The streak records can be analysed now with regard to different considerations.

One topic is the point from where the spherical detonation wave virtually starts. Typically the detonation begins not exactly in the axis of the 8 mm booster. The first breakthrough of the detonation waves give the lateral deviations ε from the axis The so-called virtual initiation distance VID can be calculated with the equation on top of Fig. 18. The calculated VID is for the normally cast TNT/RDX 35/65 charge 77.5 mm or 2.5 mm in the high explosive charge itself. The normally cast TNT/HMX 35/65 charge is initiated over a small area respectively in the booster in about 2 mm depth. The squeeze cast TNT/HMX 15/85 charge starts roughly 7 mm deep in the booster. These values are true for the given test arrangement, because they depend on the booster dimensions, booster type and, acceptor charge composition, as demonstrated.

The velocities of the precursor air shock (PAS) can be analysed over the 20 mm distance in the high explosive charge alone and over the attached 20 mm plexiglass covering block (Fig. 19). The streak record of the TNT/HMX 35/65 charge with 1 mm air gap was not good enough. Therefore these results are not considered. With the small slit width of 0.3 mm only precursor air shocks are measured to 20° for the

normally cast charges and up to 30° for the squeeze cast TNT/HMX 15/85 charge, which is more sensitive and more powerful. The 1 mm gaps width could be measured up to 40° angle. A surprising result is that the precursor air shock velocity is around 12 mm/µs independent from the angle of the detonation direction and the slit plane. As expected, the PAS velocities along the plexiglass slits are decreasing, for the 1 mm slits more or less from 20° on, with increasing angle (Fig. 19).

The most interesting result are the delay times Δt of the detonation waves around the slits as a function of the angles (Fig. 20). A band is given for the case where the detonation wave has to run around the slit plane (*gap theory*). The band width results from the three different detonation velocities with 7.8 mm/µs, 8.0 mm/µs and 8.5 mm/µs for the three different investigated charge types. The 0.3 mm and 1.0 mm slit widths at 10 mm distance respectively 9.5° oblique angle are not passed by any charge type. At 20° oblique angle the detonation wave runs fully around only for the 1 mm slit width and is passing the 0.3 mm slits independent of the charge types with some delay times. More or less constant delay times are achieved at 30° or 35 mm distance for the 0.3 mm values, whereas the 1 mm values have definitely longer delay times, but are at least also partially passing the slits. The delay times are reduced at the 40° angles (50 mm distance) for both slit widths, 0.3 mm and 1 mm. At 50° the values are strongly scattering and more or less lying around 100 ns delay time, independent of 0.3 mm or 1 mm slit width (Fig. 20).

Summary

A surprising result is that the precursor air shock velocity is constantly around 12mm/µs, independent of the angle of the slit to the detonation direction, also 50% higher compared to the detonation velocities of around 8 mm/µs

0.3 mm air gaps give constant delay times of around 100 ns independent of the investigated charge types, cast TNT/RDX 35/65, normally cast TNT/HMX 35/65 and squeeze cast TNT/HMX 15/85. 1 mm air gaps are not passed up to an angle of 20°. Below 30° the delay times are longer compared to larger angles like 50° or higher. In

this case the trend from the less sensitive high explosive charge TNT/RDX 35/65 is constantly a little larger compared to the TNT/HMX charges 35/65 or squeeze cast 15/85 charges.

These results demonstrate that perpendicular slits are less influencing the detonation profile compared to oblique slits especially under small angles of 10° to 20°, surely depending on the gap width and the charge type, too. Design and layout of precision shaped charges should avoid possible cracks and gaps with small angles to the detonation direction.

References

<1> M. Held "Phenomenological Description of the Function of Shaped Charges" Journal of Explosive and Propellants, - R.O.C -,Taiwan **7**, 1 - 8, 1991

<2> K. Weimann, "Research and Development in the Area of Explosive Formed Projectiles Charge Technology", Propellants, Explosives, Pyrotechnics ***18***, 294 - 298, 1993

<3> M. Held, "Influence of Transverse Air or Inert-Filled Gaps in HE Charges on the Detonation Velocity", Propellants, Explosives, Pyrotechnics ***20***, 70 - 73, 1995

<4> M. Held "Influence of Longitudinal Gaps on the Detonation Front" Propellants, Explosives, Pyrotechnics ***20***, 170 - 177, 1995

<5> C. H. Johannson, *"Detonics of High Explosives"* Academic Press, London, New York, 1970

<6> M. Held "Orthogonal Multi Streak Recording Technique" **9**th Int. Congress on High Speed Photography , 126 - 129, 1970-

<7> Cordin (Corporation), 2230 South 3270 West, Salt Lake City, Utah 84119, USA

Transversal, Longitudinal or Oblique Gaps in Shaped Charges

DaimlerChrysler Aerospace
TDW Gesellschaft für verteidigungstechnische Wirksysteme mbH

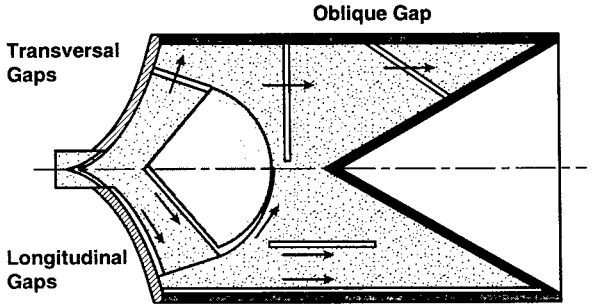

Fig. 1

Transversal - Air Gaps

DaimlerChrysler Aerospace
TDW Gesellschaft für verteidigungstechnische Wirksysteme mbH

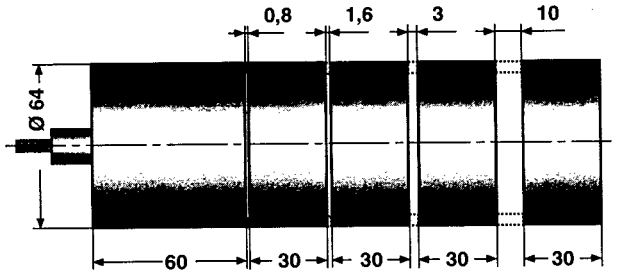

Fig. 2

Streak Analysis of Transversal Gaps

DaimlerChrysler Aerospace
TDW Gesellschaft für verteidigungstechnische Wirksysteme mbH

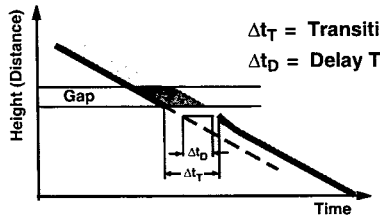

Δt_T = Transition Time
Δt_D = Delay Time

Fig. 3

Transition Δt_T and Delay Times Δt_D

DaimlerChrysler Aerospace
TDW Gesellschaft für verteidigungstechnische Wirksysteme mbH

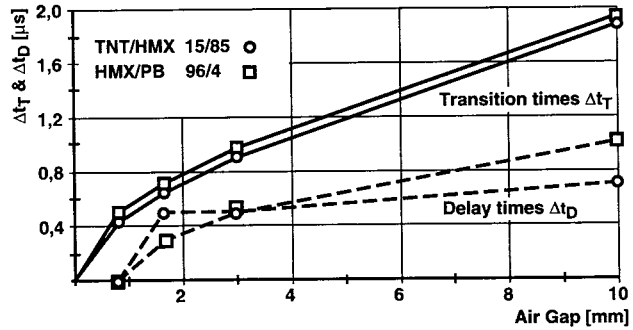

Fig. 4

Longitudinal - Air Gap

DaimlerChrysler Aerospace
TDW Gesellschaft für verteidigungstechnische Wirksysteme mbH

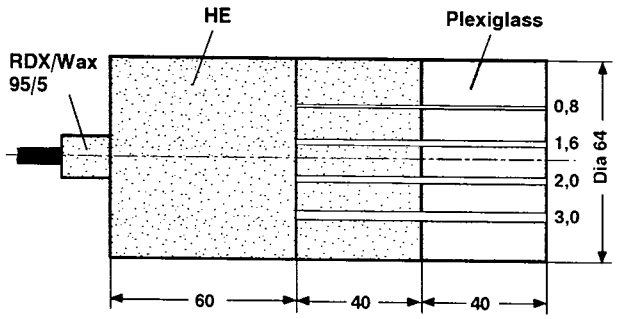

Fig. 5

TDW - Schrobenhausen ICT/2000

Streak Record of Longitudinal Gaps

DaimlerChrysler Aerospace
TDW Gesellschaft für verteidigungstechnische Wirksysteme mbH

HMX/PB 96/4
Air 0.5/1.0/2.0/3.0
Det.-No. 55505

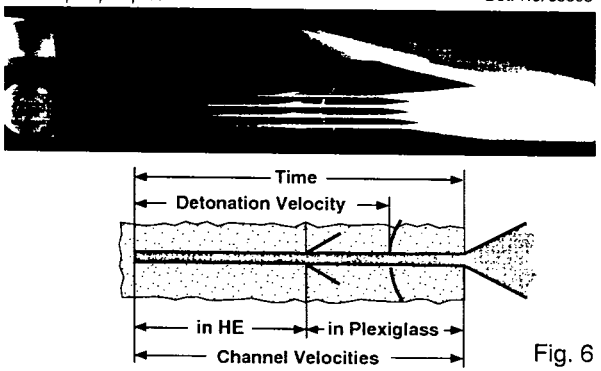

Fig. 6

TDW - Schrobenhausen ICT/2000

Detonation Velocity

DaimlerChrysler Aerospace
TDW Gesellschaft für verteidigungstechnische Wirksysteme mbH

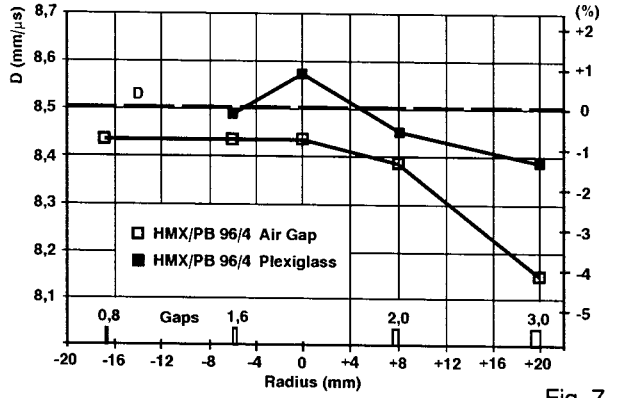

Fig. 7

TDW - Schrobenhausen ICT/2000

PAS - Velocity HMX/B 96/4

DaimlerChrysler Aerospace
TDW Gesellschaft für verteidigungstechnische Wirksysteme mbH

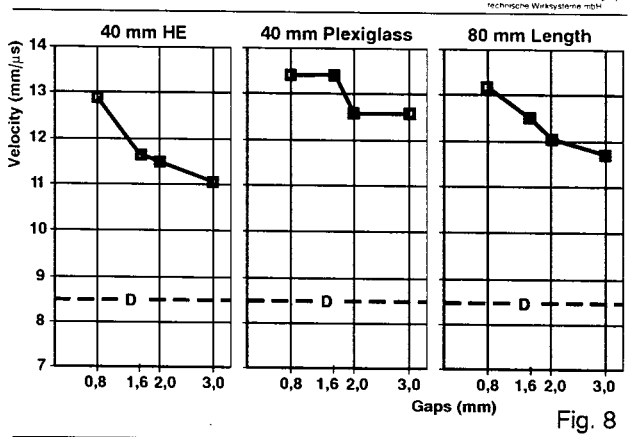

Fig. 8

TDW - Schrobenhausen ICT/2000

Detonation Fine Profile

DaimlerChrysler Aerospace
TDW Gesellschaft für verteidigungstechnische Wirksysteme mbH

TNT/HMX 15/85 Det.-No. 55504

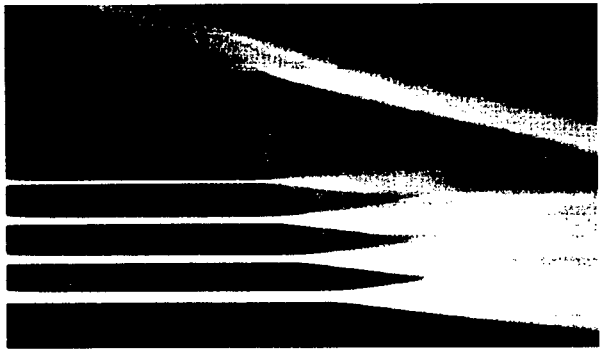

Fig. 9

Detonations - Wave - Profile Air-Gap

DaimlerChrysler Aerospace
TDW Gesellschaft für verteidigungstechnische Wirksysteme mbH

HMX/B 96/4 Det.-No. 55505

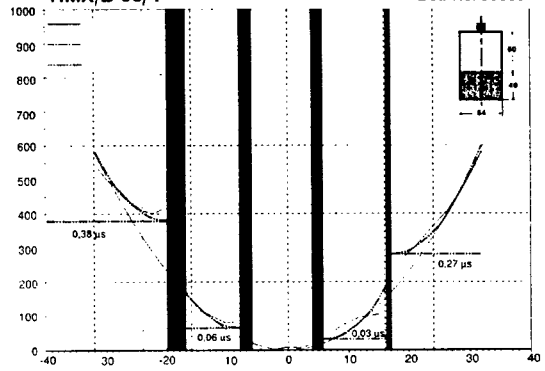

Fig. 10

Longitudinal - Air Gap

DaimlerChrysler Aerospace
TDW Gesellschaft für verteidigungstechnische Wirksysteme mbH

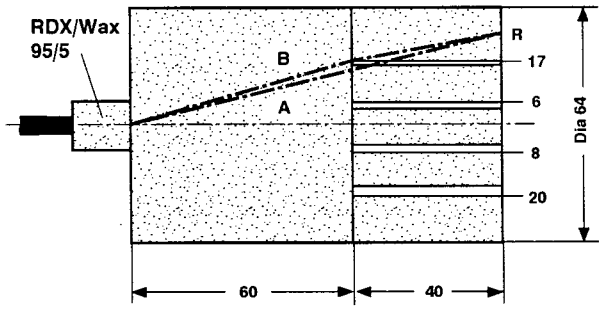

A: Spherical Theory
B: Gap Theory

Fig. 11

Arrival - Time

DaimlerChrysler Aerospace
TDW Gesellschaft für verteidigungstechnische Wirksysteme mbH

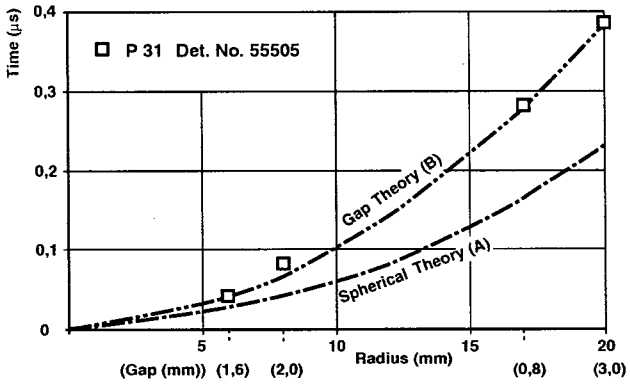

Fig. 12

Influence of Slit Arrangements to the Detonation Wave

DaimlerChrysler Aerospace
TDW Gesellschaft für verteidigungstechnische Wirksysteme mbH

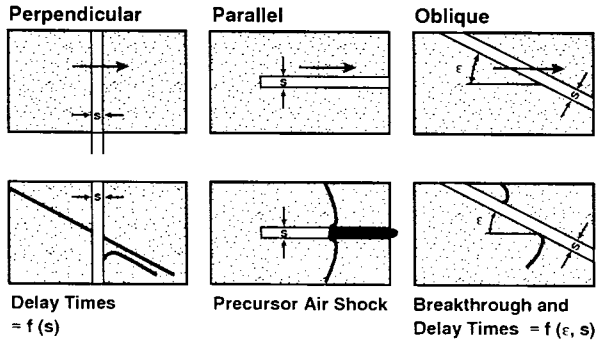

Fig. 13

Slits Under Different Angles

DaimlerChrysler Aerospace
TDW Gesellschaft für verteidigungstechnische Wirksysteme mbH

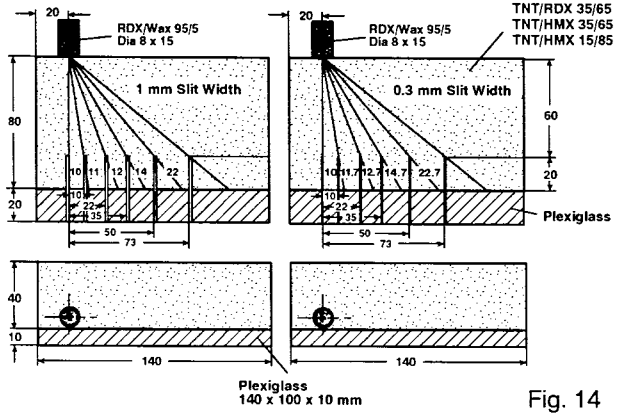

Fig. 14

Test Set-up

DaimlerChrysler Aerospace
TDW Gesellschaft für verteidigungstechnische Wirksysteme mbH

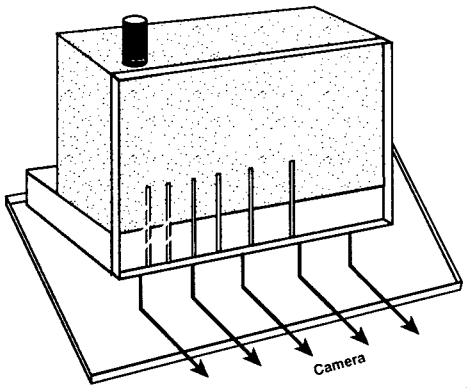

Fig. 15

Slit Tests

DaimlerChrysler Aerospace
TDW Gesellschaft für verteidigungstechnische Wirksysteme mbH

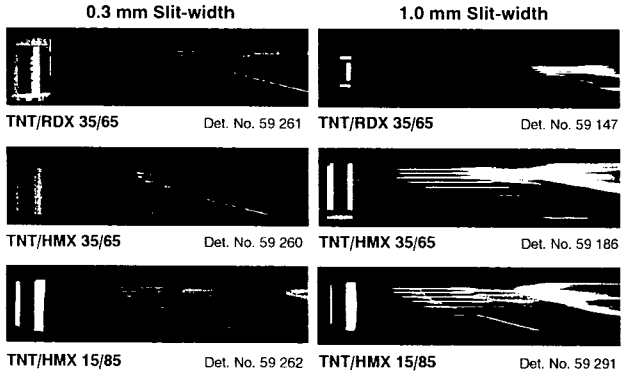

Fig. 16

DaimlerChrysler Aerospace
TDW Gesellschaft für verteidigungs-technische Wirksysteme mbH

Explanation

TNT / HMX 15/85 - 0.3 mm Slit

Still Picture **Streak record** **Det.-No. 59262**

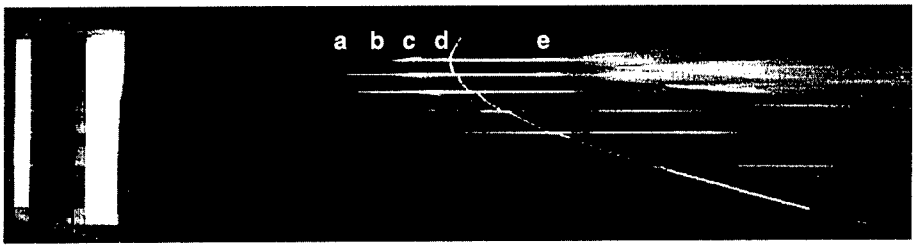

a Detonation wave arrives at bottom of slit
b Precursor air shock (PAS) in HE-slit
c PAS arrives HE/Plexiglass interface
d Detonation wave arrives HE/Plexiglass interface
e PAS in Plexiglass arrives at free surface

Fig. 17

DaimlerChrysler Aerospace
TDW Gesellschaft für verteidigungs-technische Wirksysteme mbH

Virtual Initiation Distance (VID)

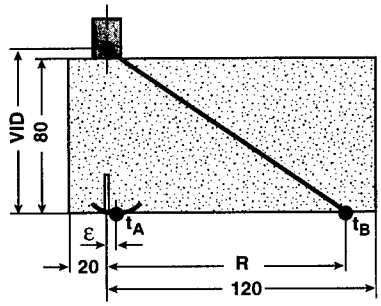

$$VID = \frac{(R - \varepsilon)^2 - \Delta t^2 \bullet D^2}{2 \bullet \Delta t \bullet D}$$

$$\Delta t = (t_B - t_A)$$

HE	D [km/s]	Slit [mm]	Det. No.	ε [mm]	VID [mm]
TNT/RDX 35/65	7.80	0.3	59 261	0	77.8
		1.0	59147	- 4.5	77.2
TNT/HMX 35/65	7.95	0.3	59 260	0	80.8
		1.0	59186	- 3.5	83.1
TNT/HMX 15/85	8.50	0.3	59 262	0	89.8
		1.0	59191	- 2.0	84.6

Fig. 18

Precursor Air Shock Velocities (PAS)

DaimlerChrysler Aerospace
TDW Gesellschaft für verteidigungstechnische Wirksysteme mbH

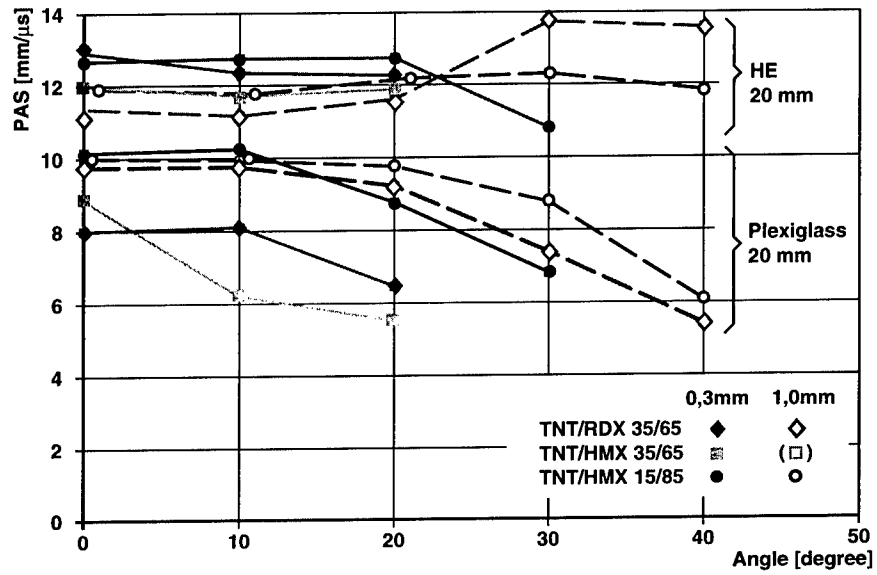

Fig. 19

Δt = f (Angle) of Air Gaps

DaimlerChrysler Aerospace
TDW Gesellschaft für verteidigungstechnische Wirksysteme mbH

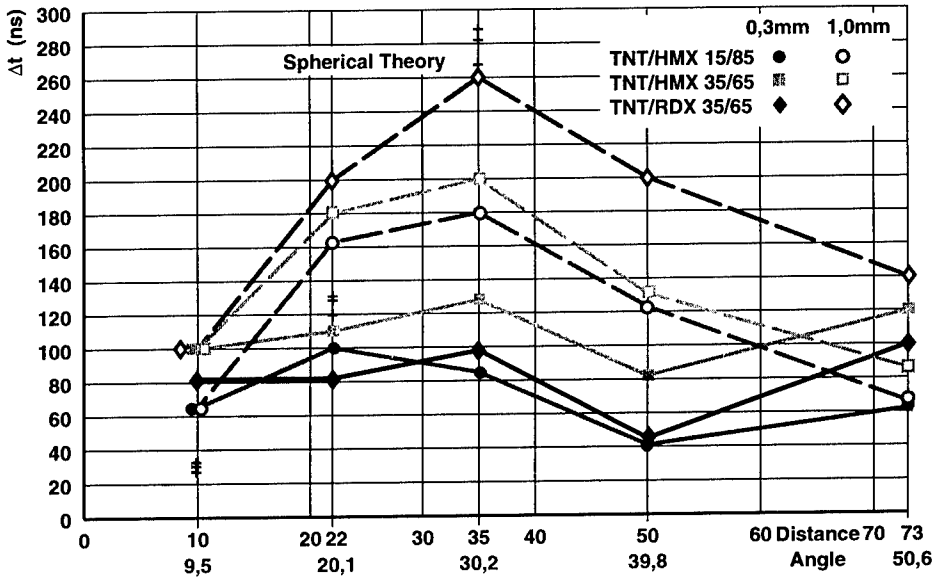

Fig. 20

INITIATION THRESHOLD OF AN INSENSITIVE UNDERWATER HIGH EXPLOSIVE

Werner Arnold

Daimler Chrysler Aerospace AG, TDW – Gesellschaft für verteidigungstechnische Wirksysteme mbH
Postfach 1340, D-86523 Schrobenhausen, Germany

Abstract The initiation threshold of a confined insensitive high explosive (IHE) under shaped charge attack was investigated. The composition of the ammonium perchlorate (AP) containing IHE was AP / RDX / Al / binder, 40 / 24 / 24 / 12 with a density of 1.80 g/cc.This IHE was designed for underwater applications. The initiation threshold was determined by measuring the running times of the reaction wave, the shock pressures, the residual penetration performance of the shaped charge jet in RHA steel plates and the fragmentation behaviour of the steel casing of the IHE charge. The threshold was located very clearly due to the decrease of the reaction velocity and the increase in penetration performance of the jet with decreasing initiation stimulus. The v^2d value of the threshold with 170mm^3/µs^2 was rather high in comparison to conventional high explosives. This high value may be correlated with the large critical diameter of 46mm of the IHE compared to the small jet diameter of only about 5mm.

INTRODUCTION

The initiation of high performance explosive charges by shaped charge jets was reported several times in the past already in technical literature (1). Initiation of these charges can be excellently described using the v^2d criterion. The insensitive high explosive (IHE), loaded with ammonium perchlorate (AP), i.e. AP/RDX/Al/HTPB - 40/24/24/12, and with a density of 1.80g/cc represents a high performance explosive for underwater applications. It reveals non ideal behaviour which means that because of the AP concentration, there are post reactions. Contrary to ideal high performance explosives where often the critical diameter and the build-up to detonation distance of several millimeters typically range in the jet diameters' size, the critical diameter of the present IHE charge is 46mm (2) and by far bigger than the shaped charge jet diameter. The influence on initiability should be investigated. As the AP loaded high explosive displays feeble inherent luminescence also during detonation, it was impossible to apply classical diagnosis methods with a rotating mirror camera.

MEASURING TECHNIQUE

Initiability of HE charges can be determined by measuring the build-up to detonation distance in the Shock Deflagration Detonation Transition (SDDT) phase. For high performance explosives, the detonation break through on the cylindrical surface of the test charge can be recorded using a rotating mirror camera. As the AP explosive charge has low inherent luminescence, diagnosis had to be adapted to this.

Figure 1 shows the measurement set-up. The target is attacked with a caliber 115mm shaped charge from a 2 caliber stand-off. This target consists of a mild steel barrier of variable thickness placed in front of the test charge.

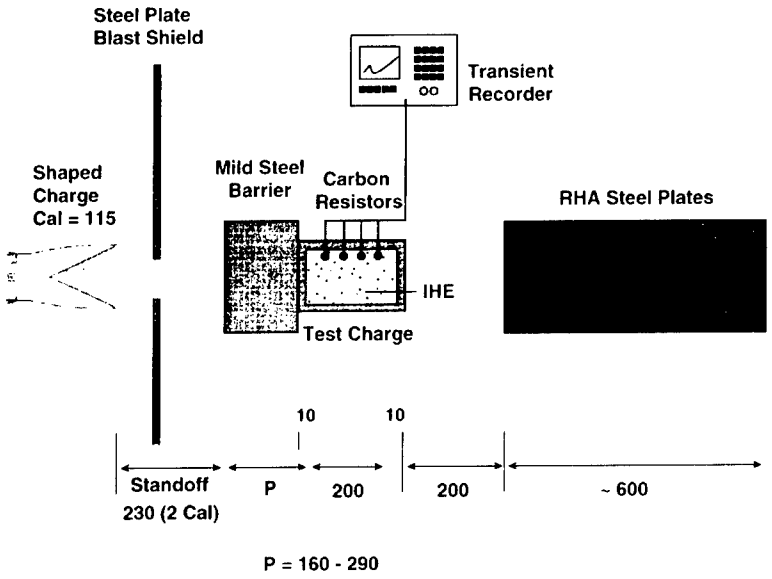

FIGURE 1. Test Set-up

The IHE test charge has a 100mm diameter - which is by far bigger than the critical diameter - and a length of 200mm. Its confinement consists of a 10mm strong mild steel casing. The total steel plate sums up to the barrier thickness P (see Fig.1). 200mm behind the test charge, the residual jet performance is determined in a RHA test pile. Fragment ejection is recorded with witness plates arranged radially in 1.50m distance to the test charge (2.5mm thick mild steel). The test charge's periphery is equipped with four carbon resistors in 25, 75, 125 and 175mm distance each from the charge's front side. They are glued in milled recess holes, flush with the inner steel casing. These carbon resistors not only allow to determine the shock / detonation wave's time of arrival but also to obtain information on the pressure amplitude's level. TDW successfully used them already to measure the performance of explosive trains and the initiability of conventional high explosives under fragment impact (3).

With this equipment, the following parameters are available to perform diagnosis of the initiability:

- Electrical measurements
  - distance / time = velocity
  - shock
- Mechanical measurements
  - residual jet performance
  - impact pattern in witness plates
  - steel casing fragment size

RESULTS

Velocity

With the corresponding thickness P of the mild steel barrier it is possible to provide the following calculation, using the commonly known formulae of the continuous jet,

$$v_j = v_{j0} \cdot \left(\frac{Z}{Z - P} \right)^{\gamma} \tag{1}$$

Z: distance target / virtual point of collaps

$$\gamma = \sqrt{\frac{\rho_t}{\rho_j}} \quad (\rho_t \text{ target density}, \rho_j \text{ jet density}) \tag{2}$$

for the crater bottom velocity in the high explosive:

$$u_j = \frac{v_j}{1 + \gamma} \tag{3}$$

The Cu jet tip velocity is v_{j0} = 9.7mm/µs with a jet diameter of d=5mm. With the measurement results of this work and with (2), the detonation velocity was determined to be D=6.1mm/µs.

The distance/time measurements with the carbon resistors provide a phase velocity because the shock/detonation waves arrive in different angles at the sensors on the IHE charge's cylindrical surface. With a very high stimulus, a detonation spreads from the impact shock front. In the other extreme with a very weak stimulus, the supersonically penetrating jet will entail a Mach stem. No initiation will take place, only the pressure of the shock wave arriving on the cylindrical charge surface is measured. SDDT takes place somewhere between these two extremes.

The result of these measurements is demonstrated in Fig. 2. It shows the comparison of the measured phase velocity and the calculated mean crater bottom velocity of the jet in the IHE. As an abscissa, the jet velocity v_j behind P and the stimulus $v_j^2 d$ were entered complementary to the barrier thickness P. The transition from detonation with low barrier thickness P to a complete absence of a reaction with a high thickness P can be clearly seen. In the latter case, the measured phase velocity of the Mach cone is coherent with the crater bottom velocity expected in theory.

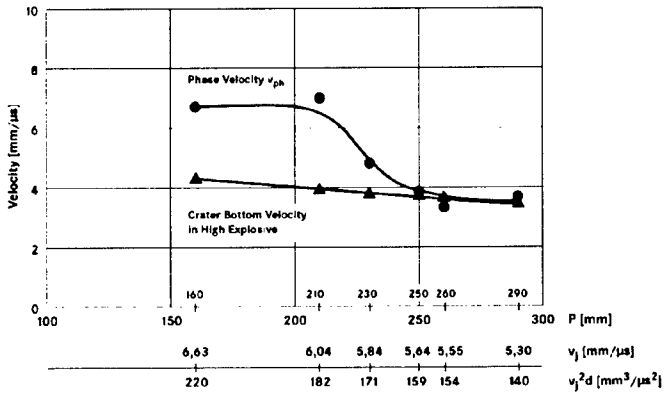

FIGURE 2. Phase velocity and crater bottom velocity of the jet in the IHE charge

Residual Performance

It turned out that, although the barrier thickness P diminished, the residual performance obtained in the RHA steel plates became less. This was caused by the fact that with increasing stimulus the starting reaction of the IHE charge disturbed the jet constantly more and thus impairs the results with respect to residual performance. This can be seen in the pictures of Fig. 3 which serve to compare the RHA pile impact sides at 210mm and 260mm. At 210mm, violent reaction occurs and many jet particles are deviated from their axis.

210mm 260mm

FIGURE 3. Impact side of RHA test pile with barrier thickness 210mm and 260mm

To quantify this loss in residual performance, a relative loss of performance of the jet

$$\frac{\Delta P}{P} \equiv \frac{\sum P_{max} - \sum P}{\sum P_{max}} \tag{4}$$

was defined. The total of all perforated materials ΣP including charge (transformed to steel equiva-lent) was compared to the max. sum ΣP_{max} with non-reaction (P = 290mm). The result is shown as a graph in Fig. 4. The abscissa was structured analogous to Fig. 2.

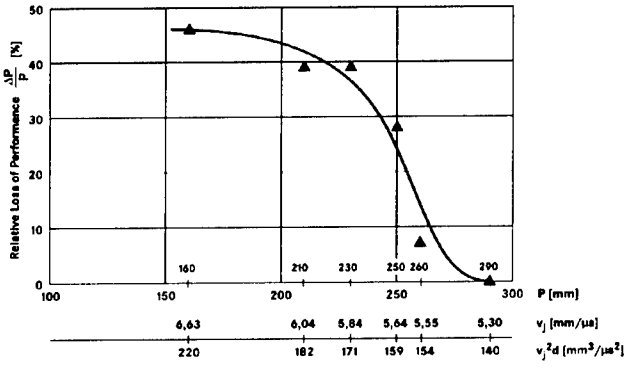

FIGURE 4. Relative loss of jet performance due to IHE reaction

Figure 5 shows a comparison of the graphic differentiation of the phase velocity of Fig. 2 with that of the relative performance evolution in Fig. 4. One can see that the relative loss in performance begins to occur already with a low stimulus compared to that of the phase velocity. This is caused by the fact that localized reactions occuring in the jet tip area already disturb the jet, that these reactions however disappear again on their way to the outer IHE charge surface and thus, are not observed in the phase velocity.

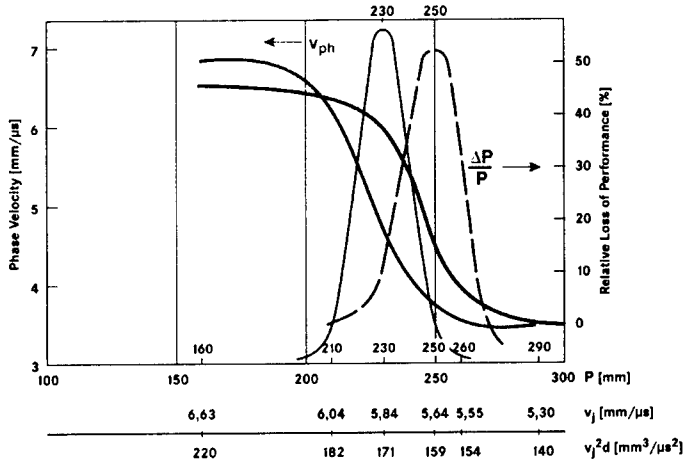

FIGURE 5. Comparison of graphic differentiation of phase velocity and loss of performance

INITIATION THRESHOLD

Fragmentation of the charge casing and the hit patterns in the witness plates did not provide any significant information concerning the SDDT. This is due to the fact that the AP loaded charge is optimized for underwater performance and not for fragment acceleration objectives. This is already shown by the relatively low detonation velocity and thus, also the pertinent low detonation pressure. Fragmentation of the charge casing due to the shock wave created by the jet is similar to that caused by full detonation.
On the other hand, the increase of pressure measured with the carbon resistors delivered complementary information and simplified categorization into the various Explosive Reaction Levels (ERL) as a function of stimulus (Fig. 6) acc. to MIL-STD-2105B. The initiation threshold of the confined, AP loaded underwater charge is

$$v_j^2 d = 170 \text{ mm}^3/\mu s^2.$$

This threshold could be defined in a very exact manner using the

- Velocity / pressure measurements (carbon resistors)
- Residual performance in RHA test pile

For the purpose of comparison, measurement results (4) for the unconfined charge attacked with a caliber 44mm shaped charge are also indicated. As already noted several times (1), a higher stimulus compared to the one of an unconfined charge is required, despite the available confinement, as shock wave effects occuring early due to the confinement might reduce sensitiveness.

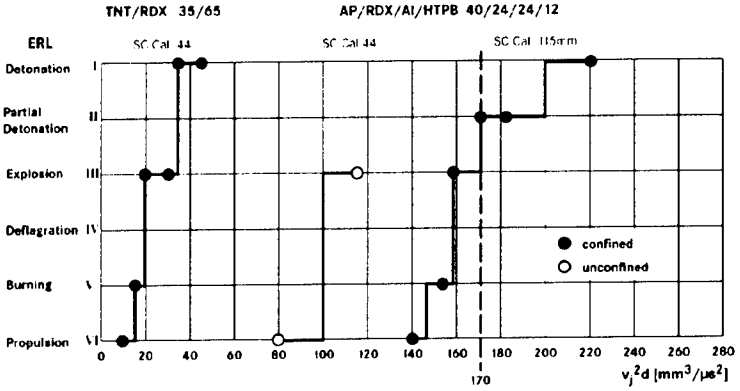

FIGURE 6. Initiation threshold for confined and unconfined high explosives

CONCLUSIONS

Measurement of the phase velocity and of the shock wave pressure using carbon resistors and of the residual performance in an RHA pile permitted precise determination of the initiation threshold under shaped charge attack. This is a method to measure the SDDT also in case of detonations with a weak inherent luminescence. The initiation threshold for the confined charge is higher than that of the unconfined one due to the preceding shock wave effects.

The initiation threshold of the AP loaded underwater charge $v_j^2d=170mm^3/\mu s$ is well above that of conventional charges like RDX/TNT 65/35 (see Fig. 6). This confined charge detonates at about $v_j^2d=30mm^3/\mu s^2$, i.e. with a stimulus 6 times lower. Gap test results obtained in this respect show less initiation difference. For the gap test, the receiver charge's surface subjected to pressure has a diameter of 50mm and is thus superior to the underwater charge's critial diameter of 46mm. In comparison to this, the dimensions of the jet with about 5mm diameter are far below that value. This could explain the very high initiation threshold. A deviation from the v_j^2d rule was already noted in (5), as soon as the critical diameter of the charge is superior to the dimensions of the jet.

ACKNOWLEDGEMENTS

This work was performed by TDW under the auspices of the German Military Department of Procurement BWB, contract No. T/W11G/T0053/M1511.

REFERENCES

1. Held, M., "Reaction Threshold in Unconfined and Confirned Charges", in Proceedings *Survivability in a Peacetime Environment*, Meeting #471, Williamsburg, 1994, pp. 338-351.
2. Rottenkolber, E., and Eichler, J., "Shock Sensitiveness and Critical Diameter of KS57/5", DASA-TDW report TN-AG3341-3511-64/88, 1988
3. Held, M., "Initiation Threshold by Fragment Impact" in Proceedings *Combustion and Detonation*, 28th International Annual Conference of ICT, Karlsruhe GE, 1997, pp. 24-1 to 24-13
4. Held, M., "Diagnostics of the Reaction Behaviour of Less Sensitive High Explosives under Jet Attack", *Propellants, Explosives, Pyrotechnics*, Vol. 16, 1991, pp. 131-139
5. Lawrence, W., and Starkenberg, J., "The Effects of the Failure Diameter of an Explosive on its Response to Shaped Charge Jet Attack", *Int. J. Impact Engng.*, Vol.20, 1997, pp.499-510.

PRÜFMITTELOPTIMIERUNG IM MITTELKALIBERBEREICH FÜR DIE AUFKLÄRUNG DER TREIBLADUNGSPULVERBETT-DYNAMIK IN UNTERKALIBERPATRONEN

Etienne Rochat
Oerlikon Contraves Defence,
Pyrotec AG
CH-8845 Studen, Switzerland

Abstract

The goal of the investigation was to find a testbed fixture for diagnosing the igniter to propellant interactions in the mediumcaliber-range.

1. Einleitung

Mit zunehmender Leistungssteigerung der Unterkalibermunition im Mittelkaliber-Bereich tritt die Pulverbettdynamik des Treibladungspulvers als gewichtiger Parameter in Erscheinung.
Der Kerbeinfluss an der Verbindungsstelle Patronenhülse zum Geschoss und die Querkräfte auf das weit in die Patronenhülse reichende Pfeilgeschossheck beeinflussen die Innen- und die Abgangsballistik.
Abhängig von der örtlichen und zeitlichen Anzündung der Treibladung bildet sich eine unterschiedlich ausgebildete Gas/Festkörper-Mischphase, welche hinter dem beschleunigten Geschoss nacheilt und dieses ungünstig beeinflussen kann.

2. Beschreibung der Problemstellung

Die 25mm - 35mm Unterkalibermunition zeigt folgende Problempunkte:

- Ladungseinstellung ->-> abnehmender v- und p-Zuwachs bei hohen Füllgraden
- Rohrerosion ->-> exzessiver Rohrausbrand ganz hinten im Rohr
- Beschädigung von Pfeilflügeln, Kernbruch, Trefferbildverzerrungen
- Thermischer Wirkungsgrad tiefer als erwartet

Diese Effekte lassen sich mit der klassischen Prüfinfrastruktur nur schwer erklären.
Entscheidend scheinen die Einflüsse zu sein, welche zeitlich zwischen dem Durchlaufen des Körnerstosses im Treibladungspulver und dem Einpressen des Geschosses in den Zügen des Rohres liegen.
Ziel unserer Arbeit war die Entwicklung und Validierung einer Laborprüfeinrichtung, die Auskunft zu den oben festgestellten Parametern gibt. Dazu wurde eine Hülsenbombe mit unterschiedlich langen Stummelläufen bestückt. Durch eine massive Gasentlastung im Rohr wurde das Treibladungspulver gelöscht und das Geschoss zusammen mit dem nacheilenden Treibladungspulverbett nach dem Mündungsaustritt fotografiert. Die Druckverteilung in der Patronenhülse wurde in 2 Achsen registriert.
Die Versuche erfolgten mit den Originalpatronenhülsen, -Pfeilgeschossen und -Treibladungen. Die Treibladungsanzündung wurde variiert.

3. Einsetzbare Prüfgeräte

Charakterisierung der TLP und Treibladungsanzünder im Labor

Mittels Laboranalysen lassen sich Explosionswärme, chemische Zusammensetzung, mechanische Eigenschaften, Oberflächenbehandlung, Korn-Dimensionen usw. bestimmen. Stofftransportprobleme innerhalb und aus dem Pulverkorn können überprüft werden. Ebenfalls können gelöschte, thermisch gealterte und vorbelastete Treibladungspulverkörner untersucht werden.

Optische Bombe und Beschuss ins Freie

Der Beschuss von Treibladungsanzündern in einer optischen Bombe oder ins Freie ermöglicht die optische Beobachtung der Reaktion und das Messen von Flammvolumen, Temperaturen und Gasgeschwindigkeiten.

Ballistische Bomben

Der Pulverabbrand in der geschlossenen Bombe liefert Treibladungspulverdaten zur Lebhaftigkeit, Brisanz, Brennzeit und zum maximalen Druck.

Thermochemische Berechnungen

Aus diesen Simulationen ergeben sich wertvolle Informationen zur Flammtemperatur, zum Molekulargewicht, zum voraussichtlichen Maximaldruck, zum erwarteten Arbeitsvermögen und zu der Identität der zu erwartenden Reaktionsprodukte.

Erosionsbombe

Der Versuch in der Erosionsbombe gibt vergleichende Aussagen über die Erosivität von Treibladungspulvern.

Treibladungsanzünder-Prüfbombe [Lit. 1,3]

Die TLANZ werden nach Wunsch laboriert und in der Prüfbombe abgefeuert, wobei die Initiierungsbedingungen, das Innenvolumen und die Prüftemperatur variiert werden können. Unsere Bombe hat ein grosses Längen- / Durchmesserverhältnis. Dadurch erhalten die brennenden Partikel eine Freiflugstrecke. In der Mitte ist eine Düse platziert, um Ablöscheffekte zu provozieren. Die Druckmessungen können im Treibladungsanzünder und im Verbrennungsraum vor und nach der Düse erfolgen.

Ziele der Messungen sind:

- Istwertaufnahmen
- Reproduzierbarkeiten und Abhängigkeiten ermitteln
- Gasvolumenbestimmungen
- Ablöschneigungen bei negativen Druckgradienten erkennen.

Treibladungsanzünder-Prüfbombe

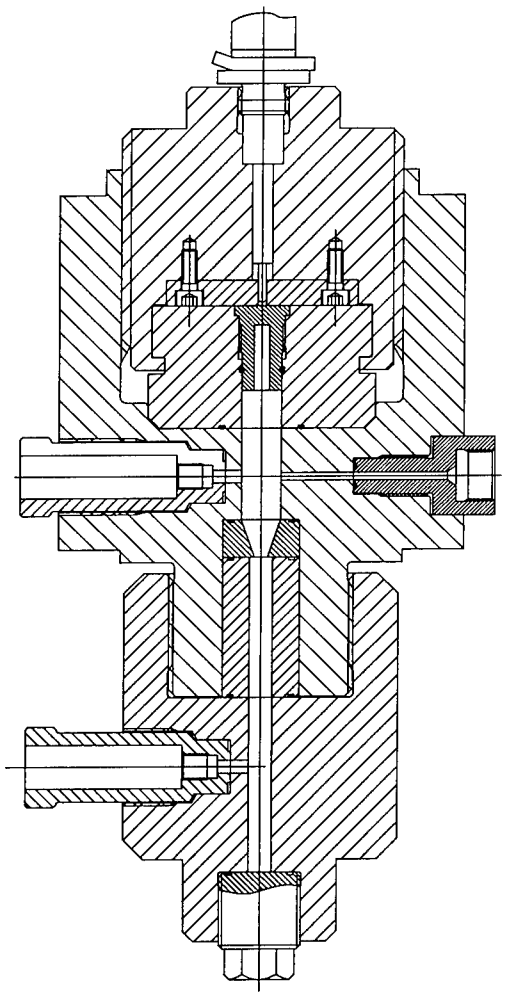

Patronenhülsen-Prüfbomben [Lit. 2,3,4]

Bei diesen Prüfgeräten handelt es sich um die wichtigsten Prüfbomben. Die Konfiguration der eingesetzten Munitionskomponenten ist identisch wie bei der späteren Verwendung.
Für alle Mittelkaliberpatronenhülsen existieren separate Prüfbomben. Die Patronenhülsen können mit einem Geschoss oder mit unterschiedlich starken Berstscheiben versehen werden. Die Initiierungsbedingungen, die Prüftemperatur, die Ladedichte, die Kerbung bzw. der Ausziehwiderstand können variiert werden. Die Prüfungen erfolgen bei Temperaturen von -54°C bis +71°C. Die maximal 6 fache Druckmessung erfolgen am Hülsenboden, bei der Hülsenmitte und am Hülsenmund. Ziele der Messungen sind:

- TLANZ-Schwadendurchgriff quantifizieren
- Treibladungspulverbett-Dynamik messen
- Geschosskerbungseinfluss quantifizieren
- Reproduzierbarkeiten und Abhängigkeiten ermitteln
- Abstimmen der Anzündung vor Drucklauf- und Waffenbeschüssen
- Vorabklärungen bei der Überprüfung der ballistischen Stabilität, aus Sicherheitsgründen vor dem Waffenbeschuss und Abtasten von Grenzgängigkeiten

Löschbombe

Bei diesem Prüfgerät handelt es sich um eine spezielle Patronenhülsen-Prüfbombe für Patronenhülsen ohne Schulter, ausgerüstet mit unterschiedlich starken Berstscheiben. Das brennende Treibladungspulver wird durch eine schlagartige Druckexpansion gelöscht und im Wasserbecken aufgefangen.

- Überprüfen der Sprödbruchanfälligkeit
- Abstimmen der Treibladungspulveranzündung an die Eigenschaften der Treibladung
- Erkennen von frühzeitigem Kernzonenausbrand im Treibladungskorn
- Überprüfen der Formfunktion des Abbrandes

Gasdruckmesser (Drucklauf) und Waffenbeschuss

Im Gasdruckmesser erfolgt die innenballistische Messung und die Präzisionsbeurteilung.
In der Waffe erfolgt die Funktions-, Lebensdauer- und Leistungsprüfung.

Patronenhülsen-Prüfbombe

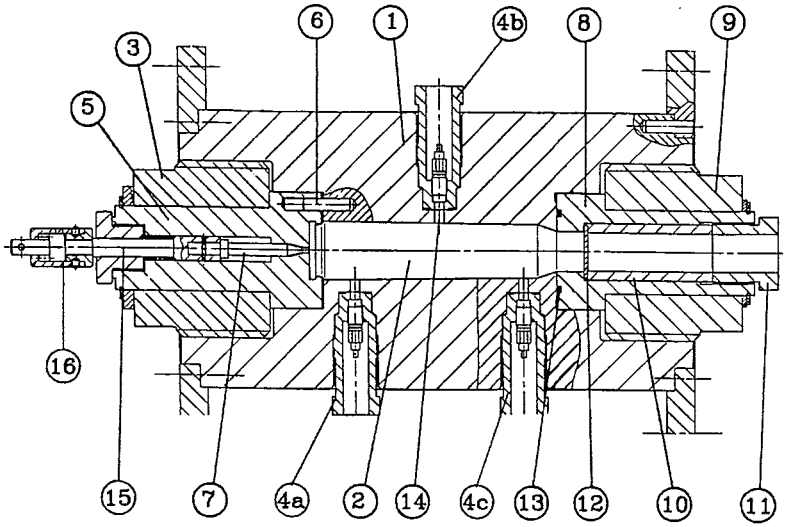

Mit Berstscheiben-Variante

Einbau der Positionen 8, 10,11,12

Gelochter Stummel-Lauf

Austausch der Positionen 8, 10,11,12

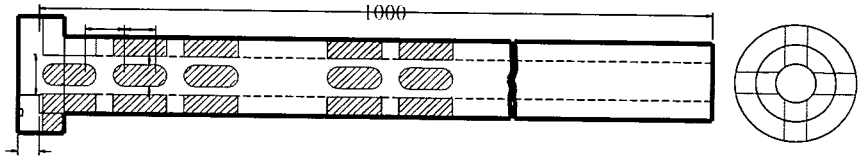

4. Messmittel

Druckmessung

Die Druckmessung erfolgt mit der Piezotechnik. Die Versuche im Gasdruckmesser (Drucklauf) und die Waffenbeschüsse werden mit 10 kHz gefiltert, die Bombenmessungen werden ungefiltert registriert und auf dem Rechner nachbearbeitet.

Optische Abbildungen, Mündungsfeuerbeobachtung

Optische Abbildungen erfolgen mit Röntgen, Video und Hadlandkamera.

Weitere Messmittel

Dazu zählen Wegmessungen am Geschütz und am Geschoss, aber auch einfachste Hilfmittel wie Zeugenbleche, Fliesspapierscheiben oder Fangnetze. Das Ausmessen der Rohre zeigt die örtliche Rohrerosion.

5. Gegenüberstellung der Prüfgeräte

Prüfmethode	Charakterisiert	'Artefakte'
Chemische und physikalische Charakterisierung im Labor	Explosionswärme, Identität, Oberflächenbehandlung, Korn-Dimensionen, Alterung, chemische Stabilität	Nur statische Aussagen
Thermochemische Berechnungen	Flammtemperatur, Kappa, Molekulargewicht, maximaler Druck, Arbeitsvermögen	Nur statische Aussagen
Optische Bombe und Beschuss ins Freie	Flammenvolumen, Temperaturen und Gasgeschwindigkeiten	Arbeitsdruck zu tief, Volumen nicht realistisch, kein mechanischer Widerstand vor dem Treibladungsanzünder
Ballistische Bomben	Lebhaftigkeit, Brisanz, Brennzeit=f(p), maximaler Druck=f(delta), Abbrand-Stabilität von L=f(delta), ballistische Stabilität	V=const, zu tiefer Druck für die meisten Abbrennzonen des Pulverkornes Anzündung nicht Original, Brenngeschwindigkeit tief

Prüfmethode	Charakterisiert	'Artefakte'
Erosionsbombe	Mittlere Erosivität eines Pulvers, Einfluss von Flammtemperatur, Explosionswärme, Pulverkorndimensionen, Molekulargewicht	Nur eine Aussage über das ganze Korn und die durchschnittliche chemische Zusammensetzung möglich, Einfluss von Rohrschonungsadditiven und Oberflächenbehandlung nicht deutlich
Treibladungsanzünder-Prüfbombe	Output mit p(t), Zündverzüge, Gassäulenschwingungen, Ausbreitungsgeschwindigkeit, Gasvolumenbestimmungen, Ablöschneigungen bei negativen Druckgradienten erkennen.	Arbeitsdruck zu tief, Volumen nicht realistisch, kein mechanischer Widerstand vor dem Treibladungsanzünder, Überlappende Gasproduktion vom angezündeten TLP nicht vorhanden
Patronenhülsen-Prüfbomben	TLANZ-Schwadendurchgriff gegen Treibladung quantifizieren, TLANZ-Schwadendurchgriff gegen Inertpulver quantifizieren, Anzündvorgang quantifizieren, Druckdifferenzen messen, Treibladungspulverbett-Dynamik messen, Anzünder Design optimieren	Berstscheiben beeinflussen Vorgang, keine zu beschleunigende Masse als Verdämmung, kein Ausziehwiderstand. Es tritt mit dem Einreissen der Berstscheibe sofort eine Gasdruckentlastung ein
Patronenhülsen-Prüfbomben mit Gasentlastungsrohr, und Stummellauf-Kanonen	Dito Patronenhülsen-Prüfbomben, Geschossform-, Geschossgewichts- und Geschosskerbungseinfluss quantifizieren, Erkennen von nicht angezündeten Treibladungspulverzonen	Es fehlen die Werte für den Maximaldruck und die Mündungsgeschwindigkeit. Die Temperaturkoeffizienten sind nicht bestimmbar
Löschbombe	Sprödbruchanfälligkeit, Formfunktion des Abbrandes, Kornbruch und Korndeformation	Zerstörung der gelöschten Treibladungskörner beim Auffangen möglich

Prüfmethode	Charakterisiert	'Artefakte'
Gasdruckmesser (Drucklauf)	Innenballistische Messung, Präzisionsbeurteilung p- und v- Beurteilung der Temperaturunabhängigkeit, Temperturunempfindlichkeits-Beurteilung	Waffenkinematik und Zuführschock fehlt, Gasleakage nicht original, kein Seriefeuer möglich
Waffenbeschuss	Funktions-, Lebensdauer- und Leistungsprüfung, Waffenkinematik, Zuführkinematik, Rohrzustandseinfluss	Zu viele interferierende Parameter, schwierige Interpretation

6. Optimierung der Patronenhülsen-Prüfbombe [Lit. 5,6,7]

Für die wirklichkeitsnahe Analyse der Treibladungspulverbettdynamik versuchte man wiederholt Prüfgeräte zu konstruieren, die ein Geschoss verschiessen und das Treibladungspulverbett abbilden lassen.

Im Picatinny Arsenal (USA) wurde mit einem 25mm-Simulator mit einem transparenten Kunststoffmantel an Stelle der Patronenhülse aus Metall gearbeitet. Die Versuche endeten mit dem Erreichen des Berstdruckes des Kunststoffmantels bei ca. 700bar.

In unserer Firma bildete man mittels Röntgenblitztechnik den Mündungsbereich von Gasdruckmessern ab, die mit stark gekürzten Rohren verschiedener Länge versehen wurden. Bei dieser Technik ist der Treibladungspulverabbrand im Zeitpunkt der Röntgenblitzaufnahme schon weit fortgeschritten.

Wir versuchten mit unseren Versuchen eine Testeinrichtung für 25mm M242 / KBA Munition zu entwickeln, die das Prüfen von Originalpatronen erlaubt. An der Patronenhülse wird an 6 Messstellen der Druckverlauf gemessen. Sobald das Geschoss die Patronenhülse verlassen hat wird der Treibladungspulverabbrand möglichst schnell unterbrochen. Das Geschoss wird zusammen mit der nacheilenden Gas/Festkörper-Mischphase mit einer Hadlandkamera fotografiert. Das Geschoss muss während dem Ablöschenprozess des Treibladungspulvers in einem gelochten Rohr geführt werden, damit es sich nicht unkontrolliert überschlägt.
Eine bestehende Patronenhülsenbombe wurde mit Stummelläufen versehen, in die grosse Löcher zur Erzielung einer massiven Gasentlastung eingefräst wurden. Es zeigte sich, dass der Gasdruck bei Rohrlängen unter 300 mm viel zu hoch wird. Das verbleibende Pulverbett hinter dem Geschoss wird nach dem Verlassen des Rohres durch die Expansion des Restgasdruckes auseinandergerissen und das Hadlandbild wird durch die noch aktive Treibladungspulver-Abbrandflamme überstrahlt.
Über 10 Optimierungsrunden wurde laufend das Rohr verlängert, die Gasentlastung verstärkt und so nahe wie möglich an den Patronenhülsenmund positioniert. Die am Schluss ausgewählte Konfiguration verfügt über ein 1000 mm langes Rohr, welches nur noch eine ungehemmte Beschleunigung des Geschosses über ca. 13mm erlaubt. Die Gasentlastung wurde auf der ganzen Löschstrecke, so weit dies mit der mechanischen Festigkeit des Rohres vereinbar war, maximiert. Der Maximalgasdruck gemessen in der Patronenhülse, erreicht bei gekerbten Patronen aber immer noch 2500 bar!

25mm Pfeilmunition auf der Patronenhülsen-Prüfbombe mit einem 1000mm Gasentlastungsrohr, Vergleichsbeschüsse mit und ohne Flashtube.

oben: ohne Flashtube, 1x p_1 , 2x p_1 , 3x p_3

unten: mit Flashtube, 1x p_1 , 2x p_1 , 3x p_3

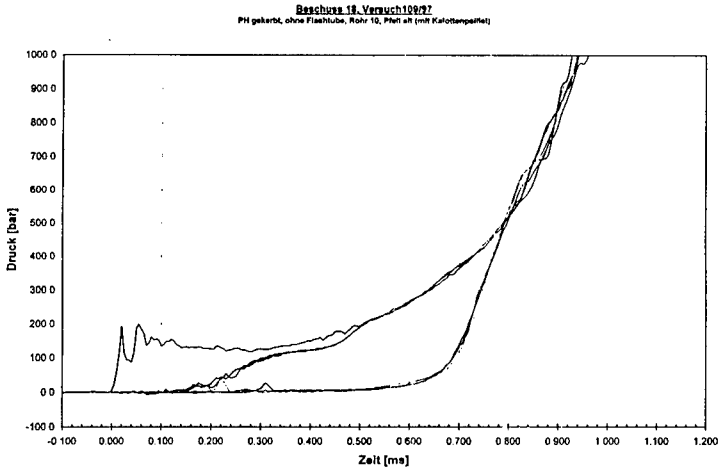

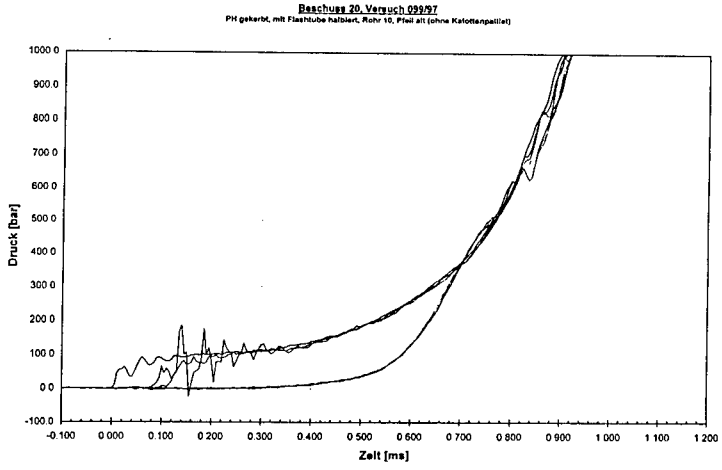

25mm Pfeilmunition auf der Patronenhülsen-Prüfbombe mit einem 1000mm Gasentlastungsrohr, Vergleichsbeschüsse mit verschiedenem Treibladungspulver-Typ

oben: TLP (singlebase), 1x p_1 , 2x p_1 , 3x p_3

unten: EI-TLP (semi doublebase), 1x p_1 , 2x p_1 , 3x p_3

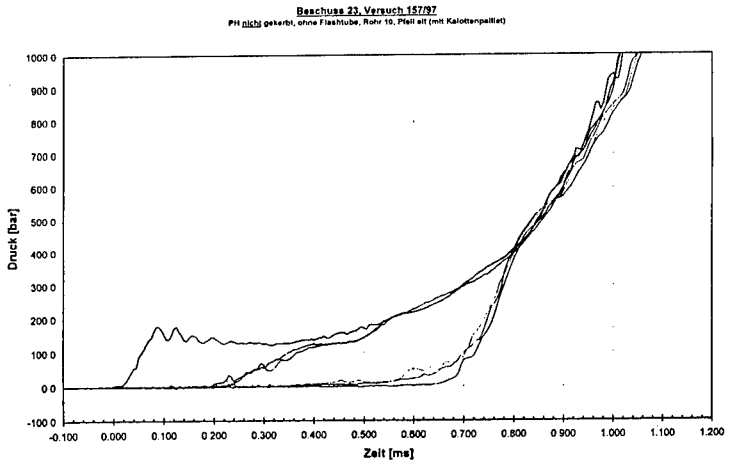

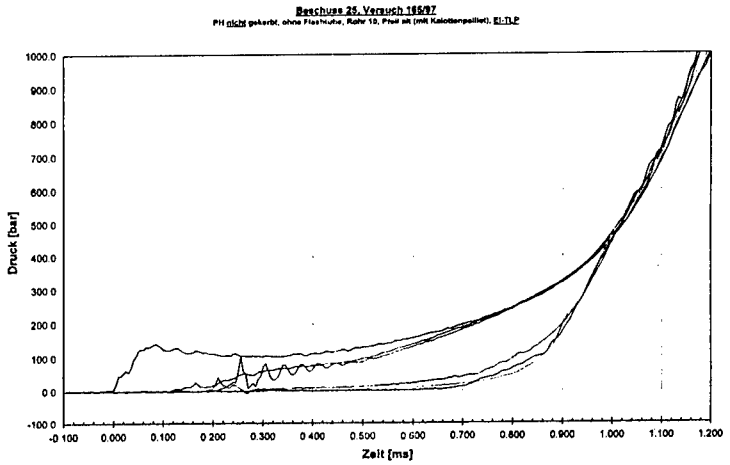

Hadlandbilder nach der Löschstrecke

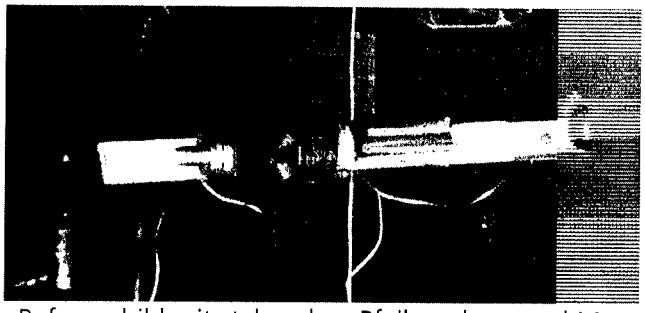

Referenzbild mit stehendem Pfeilgeschoss und Massstab

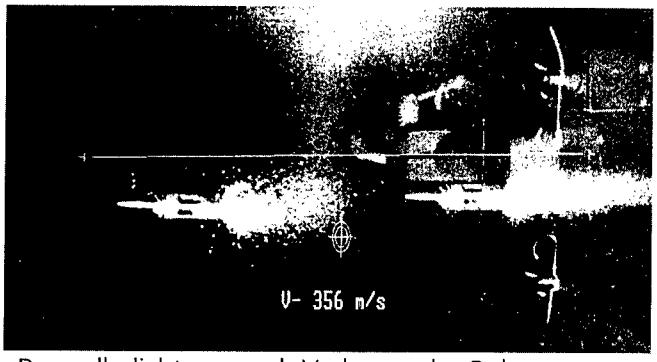

Doppelbelichtung nach Verlassen des Rohres

Geschoss mit grossem Treibladungspulver-Pfropf am Heck

8. Zusammenfassung und Diskussion

Die beschriebene Patronenhülsen-Prüfbombe mit Gasentlastungsrohr steht jetzt für systematische Untersuchungen, Optimierungen und Produkte-Entwicklungen zur Verfügung. Die Arbeiten werden auf weitere Kaliber ausgedehnt. Zur Diskussion steht die zusätzliche Instrumentierung mit einem Geschossbewegungs-Sensor und die Weiterentwicklung einer Geschossauffangeinrichtung.

Sehr wichtig ist die Einsicht, dass nur mit einem breit abgestützten Instrumentarium ein brauchbares Verständnis erzielt werden kann. Jedes Prüfverfahren schränkt die Einflussparameter spezifisch ein und überlagert das Messergebnis mit Artefakten. Absolut wahre Messungen sind unmöglich und nur die mit Sachverstand zusammengestellte Kombination verschiedener Teilresultate bringt uns weiter.

9. Literatur

1 Rochat Et., Berger.B.
Unempfindliche Anzündmischungen für moderne Treibladungen
30 International Annual Conference of ICT, Karlsruhe, 1999

2 Rochat Et., Lagler J.
Analyse der Anzündung von Mittelkalibermunition im Labor
17 International Annual Conference of ICT, Karlsruhe, 1986

3 Rochat Et., Lagler J.
Labormethode zur Messung der Anzündzeit in Rohrwaffenmunition
Fourth International AVL-Symposium on Ballistic Measurement,
Ochsenboden Switzerland 1989

4 Briggen HR., Brönnimann E., Daume E., Rochat Et
Anzünduntersuchungen im Rahmen innenballistischer Leistungssteigerung von Mittelkalibermunition
16 International Annual Conference of ICT, Karlsruhe, 1985

5 Flückiger R., Rochat Et.
Test methods for investigating the ignition phenomena of solid gun propellants
Fourth International AVL-Symposium on Ballistic Measurement,
Ochsenboden Switzerland 1989

6 Freymond P., Pulverdynamik I
Technische Notiz MUN-SB 45/83, Werkzeugmaschinenfabrik Oerlikon-Bührle AG,

7 Stiefel L.,
Studies of the early portion of the pressure-time curve of ignition of 25mm insensitive propellant charges, JANNAF workshop on ignition of low sensitivity gun propellant charges, Pennsylvania State University, 1988

Dank: Ich danke speziell Herrn U. Theiler vom ballistischen Labor für die Durchführung und Aufarbeitung der Experimente sowie Hr. J. Lagler für die kompetente Durchsicht des Manuskriptes.

EXTENSION OF CALIBRATED SHOCK WAVE TEST TO STRONG AND SHORT SHOCKS

Philippe Chabin, Jacky Groux, Serge Lécume

SNPE
Centre de Recherche du Bouchet (C.R.B.)
91710 Vert le Petit
France

ABSTRACT :

This study allowed us to develop a Calibrated Shock Wave test in the domain of strong shocks (> 15 Gpa) and short time duration (100 ns<) at low and room temperatures, with the Impulse Electric Launcher developed at the SNPE. Two heterogeneous explosive compositions with NTO have been tested, the Electric Launcher data have been compared to those obtained with a classical Calibrated Shock Wave test carried out in the same conditions of temperature. These Electric launcher data confirm that the iso-energy criterion (Puτ) is not adapted to the two tested explosive compositions. Nevertheless, the evolution of the critical energy seems to be well represented by two criteria (James and Peugeot-Quidot) in all the pressure-time domain. The low temperature tests (-55°C) performed with the Impulse Electric Launcher confirm that the low temperatures have practically no effect on the shock initiation threshold of the two heterogeneous explosives used in this study

1. INTRODUCTION

Characterization of an explosive composition pertaining to the insensitive munition family in the short and strong shock domain, is essential for the forecast of its behavior with respect to a high level of aggression, such as shaped charges, light and high speed fragments, and to optimize potential firing units systems.

All these compositions generally based on NTO, have an energy threshold curve clearly above the classical compositions, and thus require means able to solicit them to very high pressure levels, allowing a chemical decomposition under shock.

The aim of this present study is to extend the field of application of the classical calibrated Shock Wave Test (1), by the use of Impulse Electric Launcher (L.E.I.) at room and low (-55°C) temperature (2).

This test has been applied on two compositions at ambient temperature. These compositions belong to the explosive family with inert binder (B2248A) and with energetic binder (B3110B), the mass percentage of each component are given hereafter :

- B2248A (42 % HMX/ 46 % NTO/ 12% inert binder)
- B3110B (29 % HMX/ 30% NTO/ 16 % Al/ 25% energetic binder)

The influence of a low conditioning temperature (-55°C) on the sensibility has been studied only on the B2248 A composition.

2. REMINDER OF THE PRINCIPLE AND THE PERFORMANCES OF L.E.I.

2.1 PRINCIPLE :

The L.E.I. consist of an energy bank with 12 capacitors, linked to a flat line, itself composed by two electrodes (figure 1). At the end of the flat line, we find the "barrel" on which the experimental setup is put.

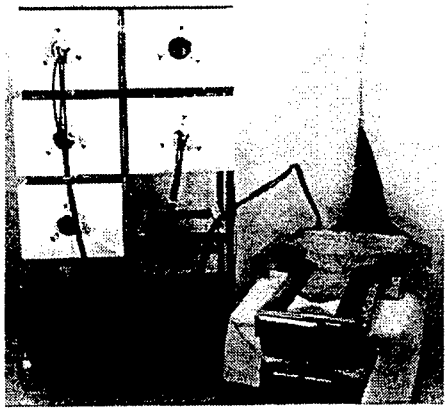

Figure 1 : L.E.I : photography of the capacitor bank and the flat line

The principle diagram is shown in figure 2. The electric current, generate by the discharge of the capacitors, is deposited on a thin bridge foil in a very short time, causing the foil to explode. The plasma so created acts as a propulsing gas on a thin dielectric flyer plate (Mylar) which compose the projectile. By the release of the plasma and the magnetic forces, this foil will reach a velocity of several kilometers per seconds over a few millimeters.

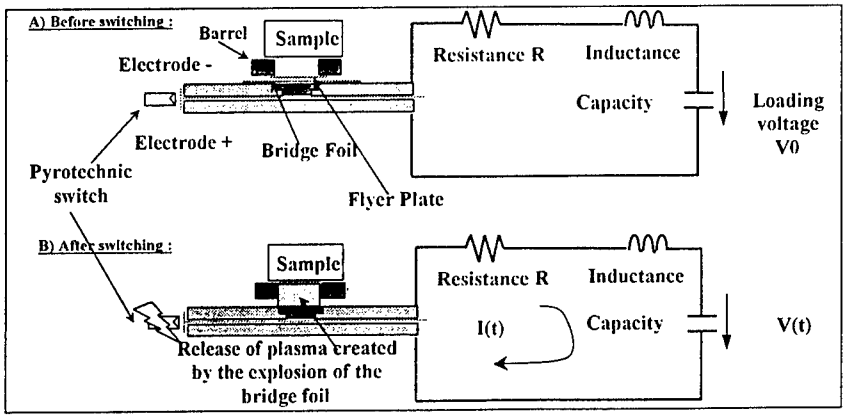

Figure 2 : principle

A pyrotechnic switch has been developed especially for this application with very low externals effects.

2.2 PHYSICALS AND ELECTRICALS CHARACTERISTICS OF THE L.E.I.

An optimal transformation of the aluminium foil require a very fast discharge (10^{12}A/s) of the capacitors. This transformation depends directly on electric characteristics R, L, C of the L.E.I. :

- Resistance R must be lower to limit dissipative effect,
- Inductance L must be small to facilitate the speed of the discharge,
- Capacity C must be important to store as much energy as possible.

These characteristics were determined experimentally on our installation. Results presented this below are expressed according to the number ***n*** of used condensers

* The maximal capacitor charge is variable between 0 and 50 kV

* Capacity :	C	: C = nC0	with C0 : 15.75 μF
* Resistance	R	:R = R0 + R1/n	with R0 : 3.25 mΩ et R1 : 47.35 mΩ
* Inductance	L	:L = L0 +L1/n	with L0 : 18.67 nH et L1 : 348.33 nH

so for the complete configuration of our installation, namely for 12 condensers:

$$R = 7.2\ m\Omega - L = 47.7\ nH - C = 189\ \mu F$$

What represents an energy available maximum, for a charging voltage of 50 kV

$$E = \tfrac{1}{2} CU^2 \quad : \text{Emax} = 240\ \text{kJ}$$

According to the tested explosive, to the amplitude and to the duration of the shock looked for, the terminal part of the launcher may be modified. The main parameters and their associated domain of variation are presented in table n°1:

Table n°1 :

Parameter	Domain of variation
Projectile diameter / bridge width	5 to 50 mm
Projectile thickness	50 μm to 1 mm
Barrel length	1 to 10 mm

2.3 CALIBRATION

The knowledge of the flyer plate velocity is important, for the analysis of experiments and for the forecast of shots according to the experimental configuration used. However on the L.E.I., during a shot, a direct measure of the velocity is not easy because the dimensions of the barrel (h = 5 mm) as well as the position of the explosive target, prevent a visualization of the flyer plate.
For this, we used a simple model of prevision of the velocity, based on the knowledge of the electric characteristics of the L.E.I., on the geometry of the flyer plate and on the initial charge voltage.

This model is an extension by TUCKER (3) of GURNEY's model used in the drive by explosive :

$$Vp\left(\frac{M}{C} + \frac{1}{3}\right) = \sqrt{2(kJ_e^n)}$$

with Vp : Flyer Plate velocity (m/s)
M/C : Specific mass ratio : flyer plate / foil
Je : Current density at the explosion of the foil (A/m2)

Several experiments associating a measure of velocity of the flyer plate, *Vp* (figure 3), and a measure of current at the explosion, *Ie* with *Je= f(Ie)* (figure 4), allowed us to adjust the two coefficients *k* and *n* of the model. The value of the current density *Je* can also be obtained by a simulation of the R.L.C. circuit of the L.E.I. a comparison between measured and calculated current is shown in figure 4.

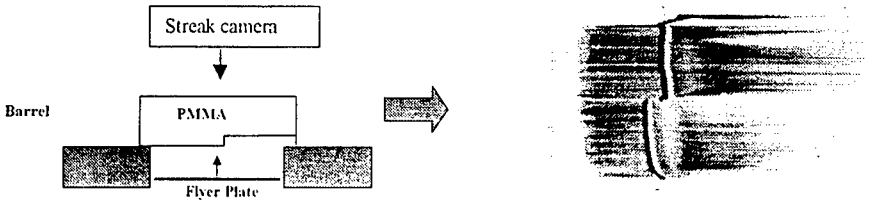

Figure 3 : Flyer plate velocity and planarity measurements

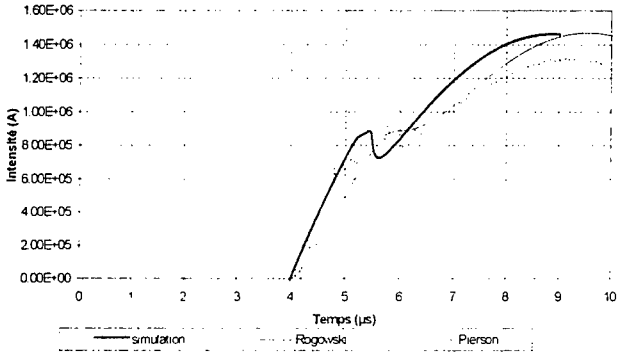

Figure 4 : calculated and simulated current.

The calibration used in this study, relative to a 5 mm long barrel, is presented in figure 5.

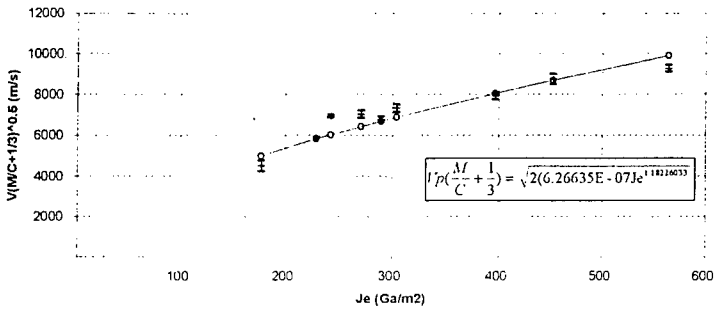

Figure 5 : L.E.I. Calibration (5 mm long barrel)

3. EXTENSION OF CALIBRATED SHOCK WAVE TEST

The general principle of the classical Calibrated Shock Wave Test was resumed. Experimental assembly consist of a cylindrical sample of explosive put on the barrel of the launcher with an anvil witness stuck on the explosive (figure 6). During the shot the witness plate is recovered in a chamber, filled with rags, placed over the assembly.

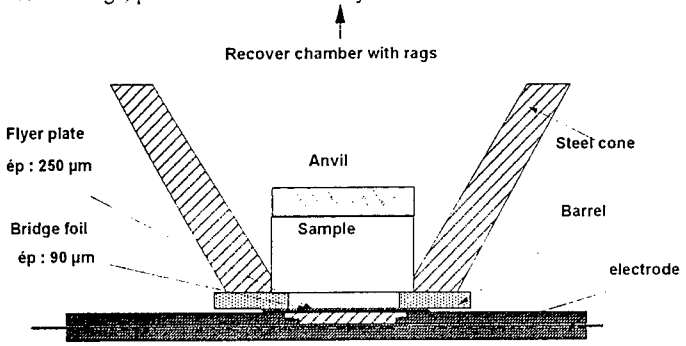

Figure 6 : experimental setup at room temperature

Diagnosis detonation / non-detonation is based on the exam of the target witness. Impact pressure is estimated by crossing the unreactive Hugoniot of the flyer plate and that of the explosive sample. For B2248A and B3110B, we used the unreactive Hugoniot determined by the mixing rule table n°2. The duration of solicitation is obtained from an analytical calculation which only takes into account the pressure maintained during the incident shock.
Regarding the determination of the impact velocity, the search for the detonation threshold is performed with the calibration. Once this threshold is determine, another shot is performed under the same experimental condition and without sample, the velocity of the flyer plate is measure with a streak camera (figure 3) and the pressure values and the impact duration are calculated accurately.
The impact planarity was estimated from the same type of recording, a tilt lower than 5 mrad on a 30 mm diameter of the flyer plate is measured. Curvature beyond this diameter becomes so important as one can consider that it does not interfere any more with the initial impact.
So, from a 50 mm diameter of flyer plate, only a monodimensional zone equivalent to a 30 mm diameter is really sollicitate. However, this 30 mm diameter is always superior to the critical dimensions of the explosives samples (Table n°3)

Table n°2 :

Compositions	Unreactive Hugoniot coefficients			Observations
	Density ρ (kg/m³)	C_0 (m/s)	S	
B 2248A	1685	2365	2.272	Mixing rule
B 3110B	1840	2050	2.512	Mixing rule
Mylar	P (Pa) = 1400(2184+2.72u-0.000722u²+9.31^{e-08}u³)u u (m/s)			Polynôme degree 3 Ref (7)

3.1 DEFINITION OF THE SHOT ASSEMBLY

The dimensions of samples were defined in two ways. Firstly, to observe the detonation or no detonation reaction without ambiguity, and secondly with the B2248A, for the shots performed at low temperature, to facilitate thermal homogeneity in the zone sollicitate by the incident shock.

The high critical dimensions of the non-ideal compositions impose a work with an important flyer plate diameter. Table n°3, summarizes experimental conditions adopted for the two tested compositions.

Table n°3 : flyer plate / sample dimensions

	Flyer plate geometry		Sample geometry		
Composition	Diameter (mm)	Thickness (μm)	Diameter (mm)	Explosive thickness (mm)	Critical diameter (mm)
B 2248A	50	250	55	30	11
B 3110B	25	250	30	15	< 15

The dimensions of the anvils witnesses were optimized experimentally by means of attempts with detonation provoked for every composition. The objective was, in case of detonation, to be able to recover fragments of significant size (figure 7). Experiments were all performed with a 5 mm long barrel.

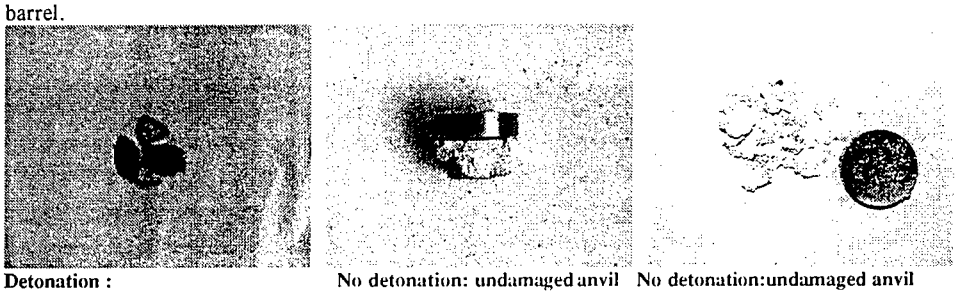

Detonation : Recovered fragments of the anvil | **No detonation: undamaged anvil Cracked sample** | **No detonation:undamaged anvil Fragmented sample**

Figure 7: Anvil photography after a shot

3.2 TEMPERATURE CONDITIONING :

Constraints linked to the realization of the calibrated shock wave test at low temperature on the Impulsionnal Electric launcher are the following ones:

- Final temperature in the sample of -55°C,
- Thermal homogeneity in the sample,
- No voltage breakdown because of the low temperature, as well in the phases of the loading voltage of the flat line as the discharge of capacitors in the bridge foil,
- Any frost between the flyer plate and the target (5 mm long barrel)
- Important delay between the implantation of the sample and the shot linked to the safety of use of the Impulsionnal Electric Launcher and to the check of the instrumentation.

The temperature conditioning is performed in 3 phases:

- Phase 1) Contitioning of the sample and the anvil in a conditioning chamber,
- Phase 2) Conditioning of the terminal part,
- Phase 3) Putting the sample into place and preservation of the temperature until the shot.

The final configuration corresponding at the shot is the following one (figure 8):

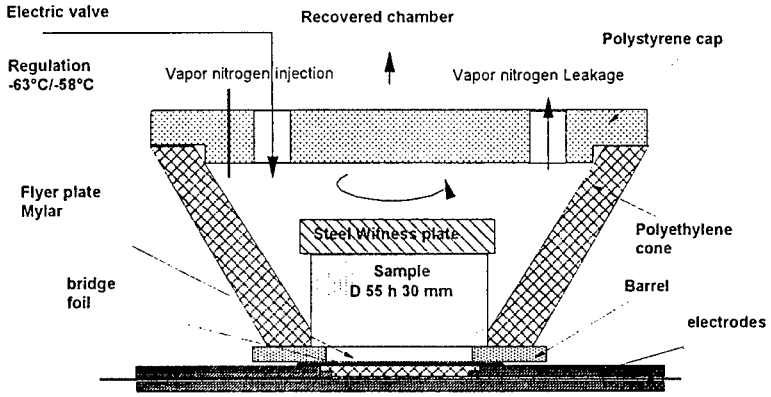

Figure 8 : Montage en température

10 thermocouples were inserted into samples for the control of the temperature, result obtained at the end of 20 minutes with this mode of conditioning is shown in figure 9 for the evolution of the temperature according to time in the sample, and in figure 10 for the estimation of the distribution of the temperature in the sample.

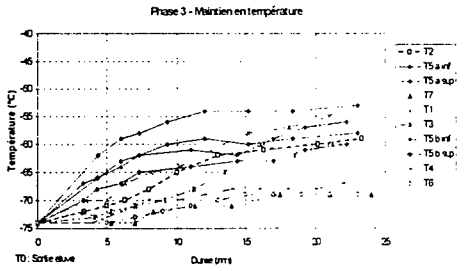

Figure 9: T° evolution

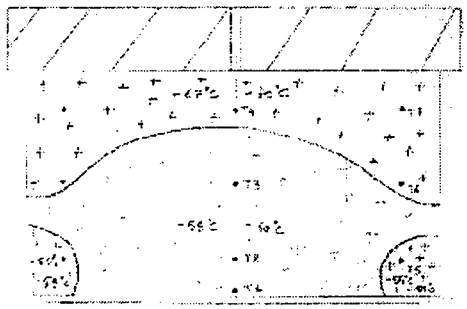

Figure 10: T° distribution

In absolute value, the pressure gradient of temperature is 15°C between the impact face (-55°C /-54°C) and the back face of the sample (-68°C /-69°C). However we see, in figure 10, that 2/3 of the sample, so the monodimensional zone sollicitated by the incident shock, are at a temperature between -55°C and -60°C, which justifies the 30 mm thickness of the sample.

For the exploitation of experiments at low temperature, it is necessary to know the unreactive Hugoniot of B2248A at -55°C. The coefficients of this one were chosen by taking into account following points:

- Impact experiments performed during a previous study (4) on B2248A at -30°C temperature, showed that temperature variation does not affect the value of the unreactive Hugoniot coefficients C0 and s,
- The evolution of the density with the temperature may be estimated with the linear coefficient of dilatation α : 70^{e-06} ($°C^{-1}$), by making the hypothesis that volumic dilatation β is equal to 3α.

Considering the previous remarks, a density ρ = 1.717 g / cm3 was calculated at - 55°C, so a variation of 1.53 % with regard to the density at room temperature can be noticed. The expression of unreactive Hugoniot at -55°C for B2248A is :

$$P(Pa) = 1.717(2365 + 2.272u)u$$

4. RESULTS :

4.1 L.E.I. RESULTS

The results obtained for the two compositions are regrouped in tables n ° 4, 5 and 6.

Table n°4 : B3110B at room temperature

N° shot	Loading voltage (kV)	Current (kA)	ϕ Flyer plate/ ϕ target (mm/mm)	Flyer plate velocity (m/s)	Impact pressure (Gpa)	Shock duration (ns)	Energy (J/cm²)	Diagnosis
83	22.5	396	25/30	3578	16.1	87	210	No-détonation
84	21.5	413	25/30	3684*	17	85	224	No détonation
82	23	498	25/30	4165*	20.6	79	283	Détonation
81	25.6	550.8	25/30	4457	23	75	320	Détonation

Table n°5: B2248A à température ambiante

N° shot	Loading voltage (kV)	Current (kA)	ϕ Flyer plate/ ϕ target (mm/mm)	Flyer plate velocity (m/s)	Impact pressure (Gpa)	Shock duration (ns)	Energy (J/cm²)	Diagnosis
79	20.6	381	25/30	3490	15.1	67.4	196	No détonation
80	26.8	480	25/30	4072 *	19.2	61.3	266	No détonation
78	27.4	497	25/30	4167 *	20	59.4	277	Détonation
77	26.3	540	25/30	4397	21.8	52.7	310	Détonation

Table n°6 : B2248A à -55° C

N° shot	Loading voltage (kV)	Current (kA)	ϕ Flyer plate/ ϕ target (mm/mm)	Flyer plate velocity (m/s)	Impact pressure (Gpa)	Shock duration (ns)	Energy (J/cm²)	Diagnosis
159	29	797	50 / 55	3670	161	81.45	209	No détonation
157	35	850	50 / 55	3830	171	79.6	225	No détonation
160	35	915	50 / 55	4025	184	77.56	247	No détonation
162	32	980	50 / 55	4211*	195	75.3	266.4	No détonation
161	35	1100	50 / 55	4547*	220	72.41	308.2	Détonation
158	40	1300	50 / 55	5083	260	67.74	376.6	Detonation

* Streak camera measurement

For each composition, at room temperature and at -55°C, the (P,τ) points obtained on the L.E.I. were placed in Pressure - time diagrams (figures 11, 12 and 13) where are also presented results from classical calibrated shock wave test performed in the same experimental conditions.

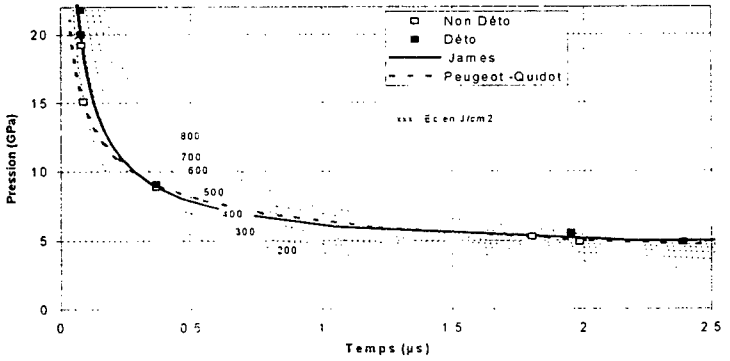

Figure 11 : B 2248 at room temperature - L.E.I. points + Classical CSWT.

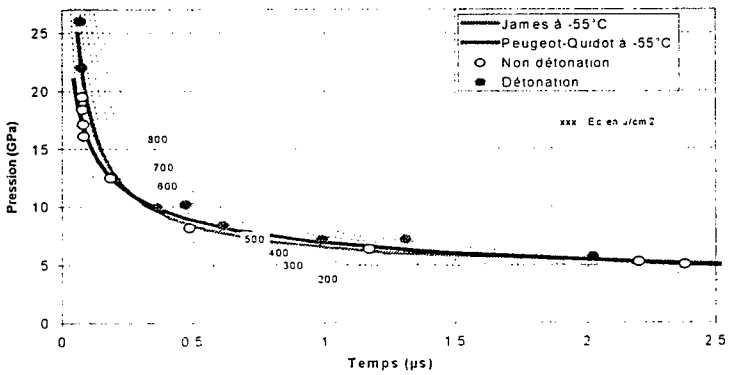

Figure 12 : B 2248 T°:-55°C - L.E.I. points + Classical CSWT

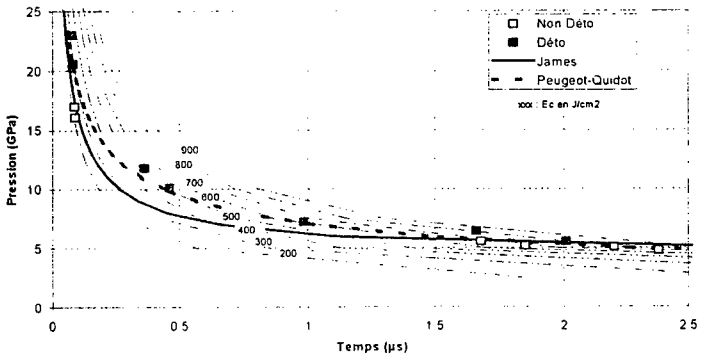

Figure 13 : B 3110B at room temperature - L.E.I. points + Classical CSWT

From experiments performed on the L.E.I. one can confirm that in the domain of strong shocks of short duration, necessary energy to initiate the explosive composition decreases, and it which that are conditions of temperature

So for the whole studied domain we can see that the criterion of iso-energy threshold is not adapted. The common interpretation of this type of result consists in saying that the more pressure is important, the more number of hot spot sites activated in the explosive becomes important. The efficiency on the transformation of the shock energy in activation energy grows and the total energy required to the initiation decreases.

4.2 ENERGY THRESHOLD CRITERION :

In order to reproduce as well as possible this decrease of energy threshold in the field of the strong shocks of short duration, two developed criteria one by James (5), the other by Peugeot-Quidot (6), were used to fitted the experimental results. These criteria are both derived from the original relation developed by Walker and Wasley, but are better adapted to the pressure time field reached by the L.E.I.

According to the criterion used, the variation of energy threshold can be described by the following relationships:

Peugeot - Quidot (6) : $E = \frac{K}{\rho_0 U} P^{2-n}$ K, n coefficients

James (5) : $\Sigma = \frac{Ec}{2\rho_0 U \tau} + \Sigma_c$ Ec, Σ coefficients

These criteria were applied to compositions tested in this study, at room and low temperature (figures 11 , 12 and 13). One can so notice, that the two criteria reproduce correctly the evolution of the energy threshold. The criterion of James seems however better adapted to the domain reached by the L.E.I..

The values of the coefficients of each used model, for each composition and temperature, are put back in the table n°7, this below:

Table n°7 : Coefficient values for the James and Peugeot-Quidot criteria

		James		Peugeot - Quidot	
Composition	Experiment temperature	Ec	Σ_c	K	n
B 2248	20°C	2.4	0.19	200	2.86
B 2248	-55°C	2.8	0.19	220	2.80
B 3110B	20°C	2	0.2	100	2.37

4.3 TEMPERATURE INFLUENCE :

Results from the - 55°C L.E.I. and classical calibrated shock wave test experiments were compared with those obtained at room temperature (figure 14).

We see that, in spite of an important decreasing of experiment temperature (in order of 75 °C), one does not observe significant gap between initiation threshold at low and room temperatures. More

particularly in the domain tested with the L.E.I., the energy threshold values are almost identical between the two temperatures.

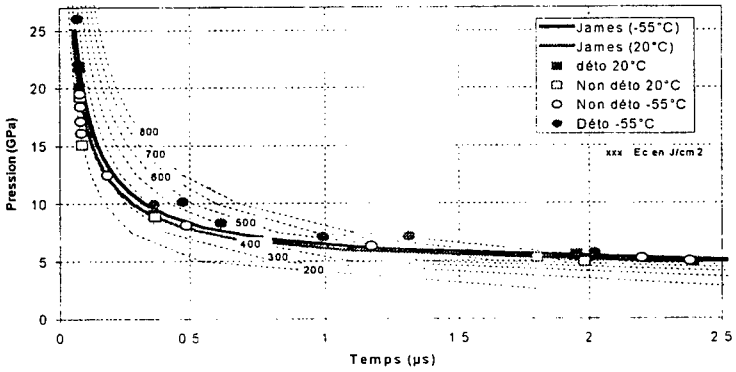

Figure 14 : Comparison between room and temperature shots

These experiments performed on the L.E.I. confirm the results obtained on the classical calibrated shock wave test at -30°C temperature on this composition (4).
The weakness of gaps noticed on the initiation thresholds could be attributed to the weak porosity of the tested heterogeneous explosive, what makes that the hot spot size and so their efficiency is less susceptible to be affected by the decrease in temperature.
It is necessary however to note that the dimensions of the tested explosives are widely higher to their critical diameters (table n°3). In the case of compositions with strong critical diameters and\or for samples of size close to critical dimensions, the influence of the temperature can become important and create a strong interaction with the initiation process.

5. CONCLUSIONS :

This study allowed us to develop a Calibrated Shock Wave Test in the domain of strong shocks and short duration by the use of the Impulsional Electric Launcher. This test was also adapted to the realization of experiments at low temperatures.

Two compositions with NTO, B 3110B and B2248A, were tested at ambient temperature, the influence of the temperature (-55°C) was studied on B2248.
The results were compared to those obtained from the classical calibrated shock wave test performed under the same experimental conditions.

From these works, it appears that :

- the points obtained on the L.E.I. confirm that the iso energy criterion is not adapted, in the studied domain of temperature between -55°C and 20°C.
- the criteria of James and Peugeot-Quidot seem to reproduce correctly thresholds obtained in the classic domain and in the strong shocks of short duration domain.
- the results obtained on this study confirm that for tested compositions, temperature variation does not seem to have of significant influence on the initiation thresholds.

REFERENCES

(1) Description d'un mode opératoire standard pour l'étude de la sensibilité des explosifs condensés à l'onde de choc - Application à une composition coulée.
Rapport ISL N°19/74 du 22/05/74
Y. de Longueville

(2) Lanceur Electrique de laboratoire adapté à l'étude des compositions peu sensibles.
5ème Journées détonique Tome 1.47- Brives - 7.8.9 juin 1994.
P.Chabin - P.Clément - P. Gimenez - J. Groux - P. Mouton

(3) Electrical Gurney energy : a new concept in modeling of energy transfer from electrically exploded conductors.
Sand 75-0244, may 1975
T.J.Tucker - P.L.Stanton

(4) Influence de la température sur l'amorçage des explosifs composites
4ème symposium international hautes pressions dynamiques - HDP IV - 5-9 Juin 1995 - Tours
J.Mala - J.Groux - P.Chabin

(5) An extension to the critical energy criterion used to predict shock initiation thresholds
Propellants, Explosives, Pyrotechnics 21, 8-13, 1996
H.R. James.

(6) Threshold energy: a dimensionnal extension of the critical energy for jet attack application
Propellants, Explosives, Pyrotechnics 23, 188-192, 1998
F.Peugeot - M.Quidot

(7) LASL Shock Hugoniot Data
S.P.Marsh

Abhängigkeit der Beschussempfindlichkeit von HTPB-gebundenen Sprengstoffen vom Weichmachergehalt im Bindersystem

Roland Wild, Thomas Keicher, Burkhard Nicklas

Juni 2000

Abstract

The dependence of bullet impact (cal 0.5) sensitivity of HTPB-bonded HMX-explosives on the plasticizer content was investigated. Though the elastic moduli of the specimen differed about a factor 9, none of them reacted. This leads to the conclusion, that this class of explosives is generally insensitive to such a stimulus. A simple theoretical model, based on thermal properties, was developped, which could, within some restrictions, explain this behaviour.

1 Einleitung

Moderne Sprengstoffe bestehen in der Regel aus einer energetischen Komponente (Hexogen, Oktogen) und einem Bindersystem, sehr oft auf der Basis von hydroxylterminiertem Polybutadien (HTPB). Die elastischen und thermischen Eigenschaften derartiger Sprengstoffe werden unter anderem durch den Weichmachergehalt im Bindersystem bestimmt.

Die Beschußempfindlichkeit von Sprengstoffen hängt sehr stark von diesen Eigenschaften ab. Ein spröder Stoff hat zum Beispiel eine höhere Empfindlichkeit gegenüber derartigen Belastungen als ein weicherer Stoff. Im folgenden wird über die durchgeführten Untersuchungen berichtet.

2 Probenmaterial und Untersuchungsumfang

2.1 Probenmaterial

Für die Untersuchungen wurden mit HTPB-gebundene Oktogensprengstoffe verwendet. Als Weichmacher diente Dioctyladipat. Um den nötigen Füll-

stoffanteil zu erreichen wurde das Oktogen in einer bimodalen Korngrößenverteilung verwendet. Die einzelnen Formulierungen sind in der folgenden Tabelle zusammengefaßt.[1]

Füllstoffgehalt	Weichmacheranteil			
	0	20	40	60
80	HX 361	HX 366	HX 367	HX 362
84	-	HX 365	-	-
86	-	-	HX 365	-
88	-	-	-	HX 271

2.2 Untersuchungsumfang

2.2.1 Mechanische und thermische Eigenschaften

Die elastischen Eigenschaften der Proben wurden mittels Dynamisch Mechanischer Analyse (DMA) im Temperaturbereich von -100 °C bis 80 °C bestimmt. Die Versuche wurden mit drei verschiedenen Frequenzen (100 Hz, 10 Hz und 1 Hz) durchgeführt. Die thermischen Eigenschaften, Wärmeleitfähigkeit λ und spezifische Wärmekapazität c_p, wurden mit der TPS (Transient Plane Source)-Methode in einer Apparatur der *Fa. Hot Disk, Schweden*, gemessen. Diese Untersuchungen wurden nur bei Raumtemperatur durchgeführt.

2.2.2 Beschußversuche

Für die Beschußversuche wurden zylindrische Proben (Durchmesser 50 mm, Länge 100 mm) in ein Stahlgefäß, das an den Stirnseiten mit Kappen verschraubt war, eingeschlossen. Die Wandstärke des Stahlzylinders betrug 5 mm, die Stirnflächen der Kappen hatten eine Stärke von 4 mm. Die Abbildung 1 zeigt eine Skizze des Beschußgefäßes. Der Beschuß erfolgte mit 12,7 mm (cal. 0.5) Geschossen (mit einem Stahlkern) und 7,62 mm NATO-Munition. Die Auftreffgeschwindigkeit der 12.7 mm Geschosse betrug $\approx 900\frac{m}{s}$, die der 7,62 mm Geschosse $\approx 780\frac{m}{s}$. Mit der 12,7 mm-Munition wurden je zwei Versuche bei Raumtemperatur und -40 °C, mit der 7,62 mm Munition nur ein Versuch bei Raumtemperatur durchgeführt.
Mit Hilfe einer Hochgeschwindigkeitskamera wurde schließlich die Austrittsgeschwindigkeit der 12,7 mm Geschosse aus den Beschußproben gemessen.

3 Ergebnisse

3.1 Mechanische und thermische Eigenschaften

mechanische Eigenschaften Die Ergebnisse aus den DMA-Messungen (E-Modul) sind in der folgenden Tabelle und im Diagramm 1 der Anlage zu-

[1] Alle Angaben sind in Prozent. Die Prozentsätze beim Weichmachergehalt beziehen sich auf den Anteil im Bindermaterial.
Die Proben wurden vom ICT, Pfinztal-Berghausen hergestellt.

sammengestellt. Der E-Modul wurde bei 100 Hz und 20°C gemessen.

Stoff	HX 361	HX 365	HX 366	HX 364	HX 367	HX 271	HX 362
E-Modul/MPa	57,6	45,4	31,6	28,2	17,1	13,4	6,5

Man erkennt deutlich wie der E-Modul mit zunehmendem Weichmachergehalt abnimmt.

thermische Eigenschaften Die erhaltenen Werte sind in der nachstehenden Tabelle zusammengestellt.
Wärmeleitfähigkeit λ in $\frac{Watt}{m*K}$:

Stoff	HX 361	HX 365	HX 366	HX 364	HX 367	HX 271	HX 362
	0,38	0,39	0,36	0,40	0,36	0,40	0,35

spezifische Wärmekapazität c_p in $\frac{Joule}{g*K}$:

Stoff	HX 361	HX 365	HX 366	HX 364	HX 367	HX 271	HX 362
	1,01	0,96	1,1	0,96	0,99	0,91	0,97

Wie man aus den Ergebnissen ersieht, ist die Abhängigkeit der thermischen Eigenschaften von der jeweiligen Formulierung nicht sonderlich ausgeprägt. Allenfalls bei der Wärmeleitfähigkeit kann man eine schwache Abnahme mit zunehmendem Weichmachergehalt feststellen (siehe auch Diagramme 2 und 3).

3.2 Ergebnisse aus den Beschußversuchen

Bei allen Versuchen wurden die Proben glatt durchschlagen, eine Reaktion des Sprengstoffes wurde nicht beobachtet. Die Abbildung 2 zeigt eine typische Aufnahme des Beschußgefäßes nach dem Versuch. Die Abbildung 3 zeigt das Austreten des Geschosses aus dem Beschußgefäß. Hierbei handelte es sich um eine Doppelbelichtung. Aus dem Abstand der beiden Geschoßabbildungen und der Zeit zwischen diesen beiden Aufnahmen läßt sich dann die Antrittsgeschwindigkeit des Geschosses errechnen. Sie lag im Mittel bei $650\frac{m}{s}$ (12,7 mm Munition).

4 Diskussion der Ergebnisse

Allgemeines Eine Reaktion des Sprengstoffs kann beim Beschuß durch eine Stoßwelle oder durch eine thermische Entzündung ausgelöst werden. Eine Stoßwellenauslösung ist bei den relativ niedrigen Auftreffgeschwindigkeiten

unwahrscheinlich, so daß im vorliegenden Fall, wenn überhaupt eine Reaktion eingeleitet wird, dies durch eine thermische Entzündung geschieht. Bei diesem Vorgang spielen dann die elastischen und auch die thermischen Eigenschaften des Sprengstoffs eine maßgebende Rolle. Durch den Aufschlag des Geschosses wird das Gefüge des Sprengstoffs zerstört. Je spröder der Sprengstoff ist, desto kleiner werden die Partikel sein, und falls diese entzündet werden, desto höher die Abbrandgeschwindigkeit. Auf diese Weise kann dann eine mehr oder heftige Reaktion ausgelöst werden. Sprengstoffe mit einem hohen E-Modul sollten daher empfindlicher gegenüber Beschuß sein als solche mit einem niedrigen E-Modul (weichere Sprengstoffe). Die E-Module der untersuchten Proben unterschieden sich zwar ungefähr um den Faktor 9 (58 MPa zu 6,5 MPa). Unterschiede im Reaktionsverhalten konnten jedoch nicht beobachtet werden. Selbst bei -40 °C kam es zu keiner Reaktion.

mechanische Eigenschaften Dieses oben beschriebene Verhalten kann man sich erklären, wenn man berücksichtigt, daß die E-Module bei relativ kleinen Verformungen gemessen wurden. Maßgebend ist aber vor allem das Verhalten bei sehr schnellen und großen Verformungen. Um dies abzuschätzen wurden Sprengstoffproben (17 mm Durchmesser und 25 mm Länge) mit einer Geschwindigkeit von ca. 160 $\frac{m}{s}$ gegen eine Stahlplatte geschossen (Friability-Test) und die Bruchstücke begutachtet. In der Abbildung 4 sind die Bruchstücke des härtesten Stoffes (HX 361) und des weichesteten Stoffes (HX 362) dargestellt. Die Bruchstücke unterscheiden sich nicht signifikant von einander. Hieraus ist zu folgern, daß die Unterschiede in den gemessenen elastischen Eigenschaften auf das Bruchverhalten bei schnelleren Verformungen keinen großen Einfluss haben.

thermische Eigenschaften Die thermische Auslösung soll anhand des nachfolgenden, noch recht einfachen, Modells diskutiert werden.

- Es wird ein unendlich langer zylindrischer Körper angenommen der gegenüber der Umgebung thermisch isoliert ist
- das Geschoß wird als bewegte Wärmequelle, die sich in der Zylinderachse bewegt, modelliert.

Unter diesen Voraussetzungen wurden von *Rosenthal und Cameron* [1]die räumliche und zeitliche Temperaturverteilung angegeben. Sie läßt sich näherungsweise mit folgender Beziehung beschreiben:

$$T = \frac{q}{\rho c_p \pi a^2 v}\left(\frac{R}{2} * \frac{e^{-R(\beta+\sqrt{\beta^2+\alpha^2})}}{\sqrt{\beta^2+\alpha^2}} + e^{-R(\beta+\sqrt{\beta^2+1})}\right) \qquad (1)$$

mit

T= Temperaturdifferenz zur Ausgangstemperatur
q=eingekoppelte Wärme pro Zeiteinheit
a= Radius der Probe
ρ= Dichte der Probe
λ = Wärmeleitfähigkeit

c_p= spez. Wärmekapazität
v = Geschwindigkeit der Wärmequelle
$\beta = \frac{x-vt}{a}$
$\alpha = \frac{r}{a}$ $\qquad R = \frac{avc_p}{2\lambda}$
Der maßgebende Parameter ist R, da hier die Wärmeleitfähigkeit und die Geschwindigkeit der Wärmequelle eingehen.

Für die Rechnungen ist zunächst abzuschätzen welche Wärme das Geschoß beim Durchdringen des Sprengstoffs abgibt. Hierzu kann man folgende Abschätzung machen:
Das Geschoß durchschlägt zunächst die Stahlkappe an der Vorderseite, der Energieverlust kann anhand der Thorformeln [2] abgeschätzt werden. Bei einer Auftreffgeschwindigkeit von etwa 900 $\frac{m}{s}$ beträgt die Restgeschwindigkeit ca. 780 $\frac{m}{s}$. Dies ist also die Geschwindigkeit der bewegten Wärmequelle. Der Wärmeinhalt des Geschosses ergibt sich dann aus der Differenz der kinetischen Energien. Die Reibungsverluste im Sprengstoff sind minimal, denn entsprechend [2] ist die Restgeschwindigkeit nach Durchschlagen der hinteren Kappe ca. 650 $\frac{m}{s}$, dies entspricht ungefähr der gemessenen Restgeschwindigkeit; hieraus folgt, daß eine Reibung im Sprengstoff sehr wenig zum Geschwindigkeitsabfall beiträgt. Mit den Werten:

$$\lambda = 0.4\frac{Watt}{m * K} \qquad c_p = 1.0\frac{Joule}{K * g} \qquad q = 3,5 * 10^6\frac{Joule}{s}$$

läßt sich nun die Temperaturverteilung (Differenz zur Ausgangstemperatur) für den Zeitraum zwischen dem Eintritt und dem Austritt des Geschosses berechnen. Man erhält die im Diagramm 4 dargestellte Temperaturverteilung. Die Koordinate ß = -4 entspricht der x-Koordinate Null im Laborsystem , die Temperaturverteilung zwischen ß = 0 und -4 stellt demnach die Verteilung im Sprengstoffkörper dar. Die Temperatur bei r = 35 μm erreicht zwar einen maximalen Wert von ungefähr 350°C, fällt jedoch innerhalb von $10\mu m$ auf die Ausgangstemperatur des Körpers ab. Eine Reaktionseinleitung ist unter diesen Bedingungen recht unwahrscheinlich.
Eine endgültige Beurteilung dieser Modellrechnung ist jedoch **noch nicht möglich**, da ein realistisches Anzündmodell zur Zeit nicht zur Verfügung steht. Qualitative Aussagen sind aber möglich. Erniedrigt man bei sonst gleichen Bedingungen die Geschwindigkeit der Wärmequelle z.B. auf 700 $\frac{m}{s}$ so steigt die berechnete Temperatur auf ungefähr 1750°C an. Dies mag erklären weshalb bei niedrigeren Geschwindigkeiten manchmal eine höhere Beschußempfindlichkeit gefunden wird. Umgekehrt sinkt die Temperatur mit abnehmender Wärmeleitfähigkeit, wie man aus dem Diagramm 5 erkennen kann. Dies würde bedeuten, daß mit kleiner werdenden Wärmeleitfähigkeiten der Sprengstoff beschußunempfindlicher wird.

5 Zusammenfassung

Es wurde über Untersuchungen der Abhängigkeit der Beschußempfindlichkeit von HTPB-gebundenen Oktogensprengstoffen vom Weichmachergehalt (und damit von den mechanischen und thermischen Eigenschaften) berichtet. Al-

le Proben, unabhängig vom Weichmachergehalt, erwiesen als unempfindlich gegenüber dem Beschuß mit 12,7 mm und 7,62 mm Munition. Hieraus kann man folgern, daß HTPB-gebundene Sprengstoffe in aller Regel unempfindlich gegen derartigen Belastungen sind.
Weiterhin wurde ein erstes theoretisches Modell vorgestellt, das mit einigen Abstrichen, das Verhalten erklären kann.

Literatur

[1] ROSENTHAL, D. CAMERON, R.H. *Trans. Americ. Soc. Mech. Engrs.* ***69*** *1947 p.961*

[2] HEALY,J.J. WEISSMANN, S. *16th Minutes Explosives Seminar 1974, pp 1107-1142*

Autoren:
Roland Wild
Dr. Burkhard Nicklas
WIWEB, Großes Cent, 53913 Swisttal
Dr. Thomas Keicher
ICT, Fraunhoferstraße 1, 76327 Pfinztal-Berghausen

Anlage

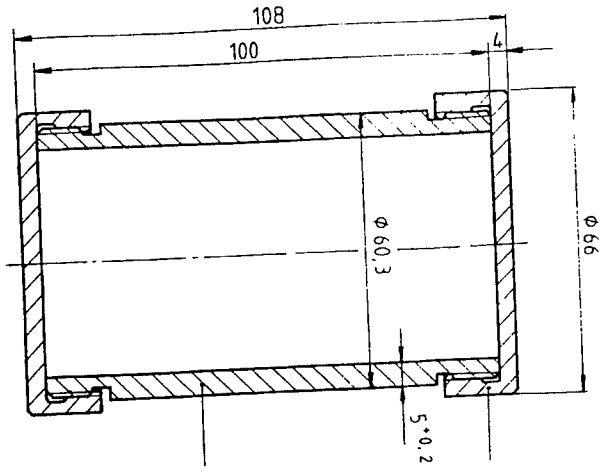

Abbildung 1: Skizze des Beschußgefäßes

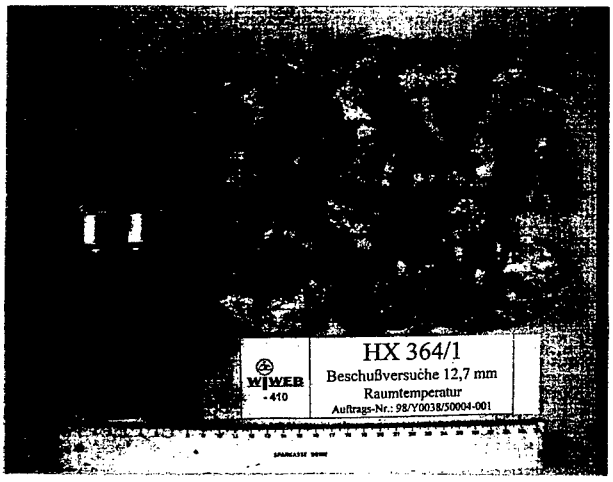

Abbildung 2: Beschußgefäß nach dem Versuch

Anlage

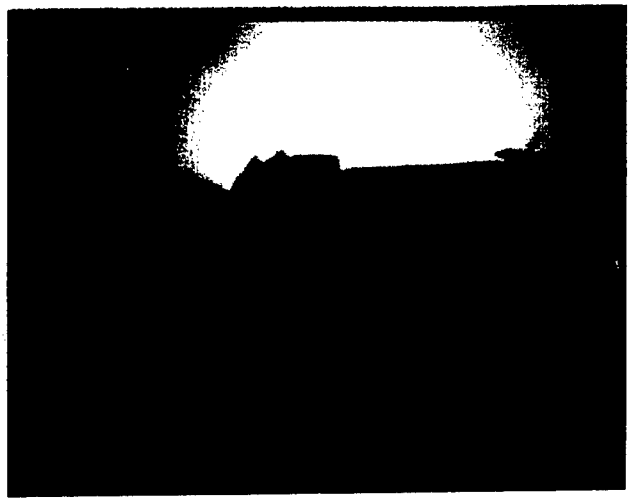

Abbildung 3: Austritt des Geschosses aus dem Beschußgefäß

HX 361/2 HX 362/13

Abbildung 4: Proben nach dem Aufschlag (links HX 361, rechts HX 362)

Anlage

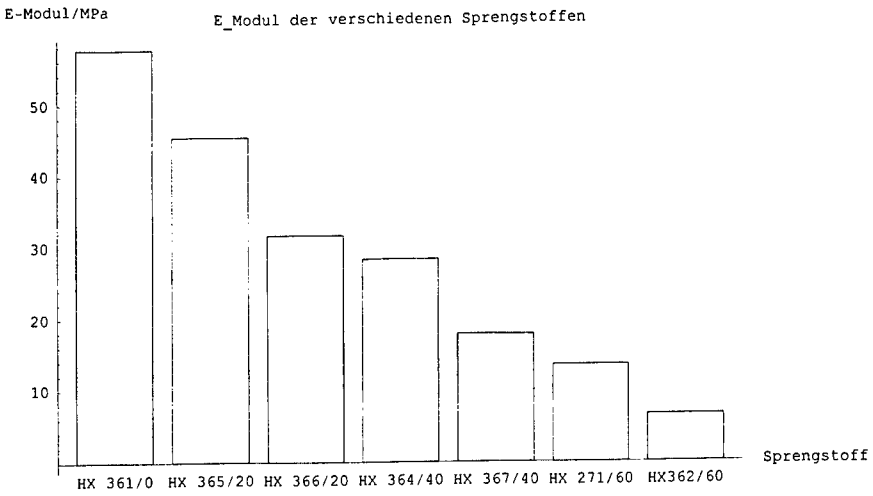

Diagramm 1: E-Moduli (20°C, 100Hz)

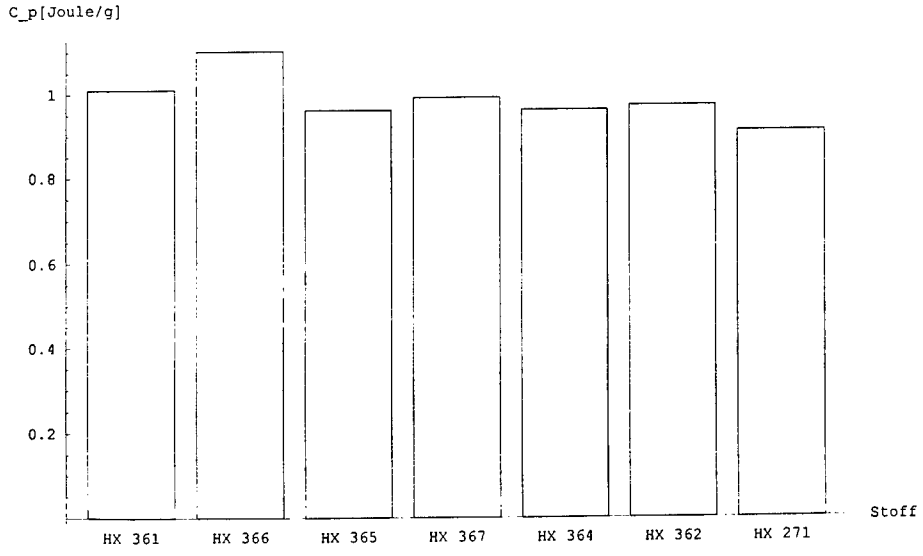

Diagramm 2:Spezifische Wärmekapazität

Anlage

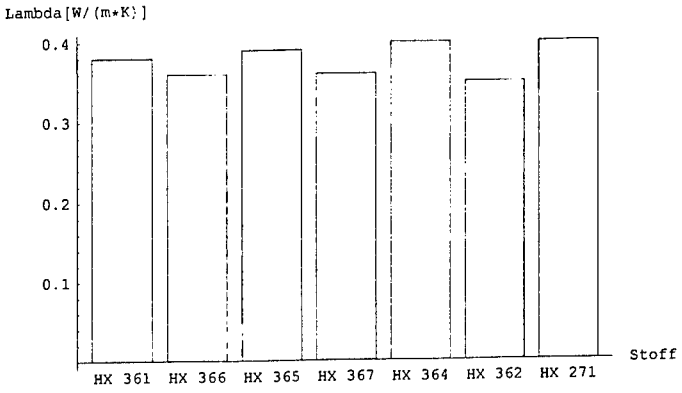

Diagramm 3: Wärmeleitfähigkeit

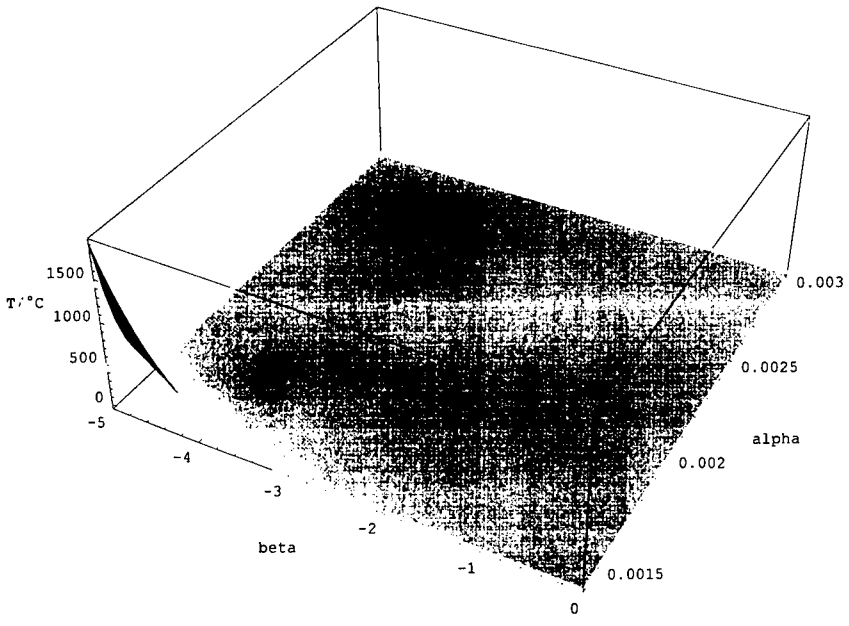

Diagramm 4:Räumliche und zeitliche Temperaturverteilung
(Differenz zur Ausgangstemperatur)

Anlage

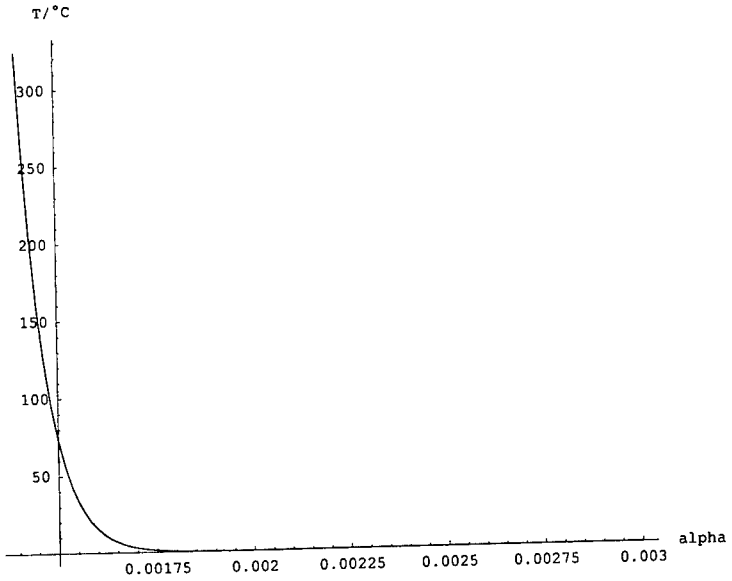

Diagramm 5: Temperaturverlauf bei ß = -4 als Funktion von alpha

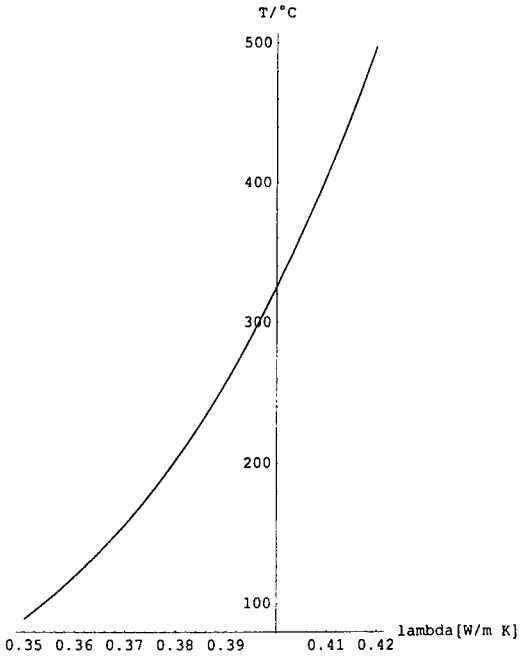

Diagramm 6: Abhängigkeit der Temperatur bei ß = -4 und alpha = 0,0014 von der Wärmeleitfähigkeit

MODIFIED ULTRASONIC METHOD FOR THE STUDY OF BURNING RATE CHARACTERISTICS OF PROPELLANTS

Keiichi HORI, Katsuya HASEGAWA, Shigeru SHIMOSE, Toshio YAMAYA and Masataka SHIMODA

The Institute of Space & Astronautical Science (ISAS), Ministry of Education, Science, Sports & Culture, JAPAN.

3-1-1 Yoshinodai Sagamihara Kanagawa 229-8510, JAPAN.

ABSTRACT

Ultrasonic method for the burning rate measurement of propellants was developed by ONERA, and their device, EDUM (Electronic Device for Ultrasonic Measurement) is widely accepted and used to study the burning rate characteristics of propellants in several institutes and universities in Europe and USA. EDUM has two sophisticated functions; mask function and auto-gain control function, and these functions enable the precise and easy measurement of burning rates of propellants under wide range of dP/dt.

However, this method needs the coupling material which protects the ultrasonic sensor from high pressure and temperature of the combustion chamber and, further, the matching of acoustic impedance between coupling material and propellant sample. Therefore, the measurements are limited to specially designed chambers and the sample length is up to 6~7cm even if the matching of acoustic impedance is enough.

We have made some modifications to the ultrasonic method making use of Doppler effect and Wavelet Analysis. Ultrasonic signal is emitted from the ultrasonic sensor which is attached directly to the metallic combustion chamber, and it propagates through the chamber wall and end-burning propellant grain. Ultrasonic signal reflects from the burning surface and the ultrasonic sensor receives the signal. The frequency of the observed signal departs from the original due to Doppler effect, because the burning surface of the sample propellant is moving towards the sensor. This departure of frequency is analyzed by Wavelet method and the instantaneous burning rate is obtained using sonic speed within the sample propellant. For the Wavelet analysis, much smaller signal output comparing to the one needed in the ONERA method is available, which makes the maximum sample length longer, and some technical improvements enable to exclude coupling material. Although, our method needs experience, this is expected to be useful to measure the burning rate of propellants in full-scale motors with further improvements.

1. INTRODUCTION

It is essential to understand burning rate characteristics of propellant fully before its application to rocket or gas generator, and the lack of the knowledge about it under rapid pressure excursions sometimes causes a serious trouble. Especially, the understanding of such transient burning rate characteristics is indispensable for HEM (High Energy Materials), because HEM is often applied to gas generator.

Linear burning rate characteristics of solid propellants are generally investigated with strand-burner, however, this method can only provide burning rate under steady conditions. Ultrasonic technique is unique to provide the information about the transient burning characteristics so far, therefore, lots of attention have been paid to this technique. This technique was eventually proposed by ONERA and developed by them [1), (2)], and their device, EDUM (Electronic Device for Ultrasonic Method) is widely accepted and used for the study of both steady and transient burning rate characteristics of solid propellants [(3), (4)]. Typical experimental setup of the measurement is shown in Fig. 1. Coupling material, usually epoxy resin, is inserted between transducer and propellant sample for the protection of the transducer from high pressure and temperature in the combustion chamber.

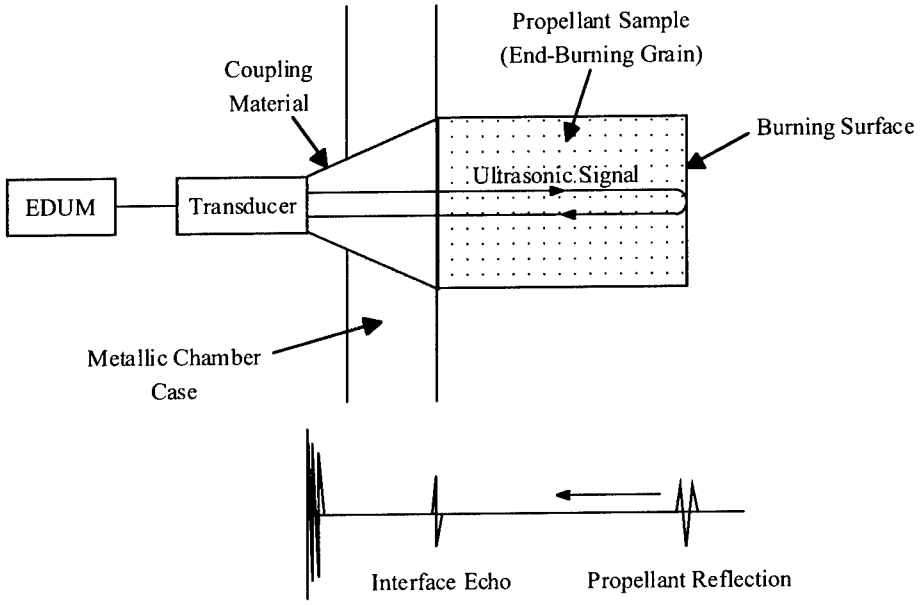

Fig. 1 Typical Setup of Burning Rate Measurement with Ultrasonics

EDUM which acts as both generator and receiver of ultrasonic signal sends ultrasonic pulse towards the propellant sample, and the pulse traverses through coupling material and sample. This

pulse is partially reflected at the interface between the coupling material and propellant sample, and matching the acoustic impedance of the two materials minimizes this echo. The second echo reflects from the burning surface and goes back to the transducer. EDUM measures the propagation times of these two echoes, and the difference of them and the sonic speed within the propellant sample give the double of the instantaneous propellant length. Thus, web thickness of propellant sample as a function of time can be measured, and the instantaneous burning rate is obtained as the slope of this curve.

Experiments are usually conducted with MHz order transducer pulsed at the frequency of several kHz. The frequency of pulse being high, the measurement of transient burning rate is possible. This is considered to be the most significant advantage of the ultrasonic technique. In addition, burning rate can be obtained over a wide range in a single test with a closed bomb, which is important practically. These two merits let many researchers pay lots of attentions to ultrasonics irrespective of following difficulties included in this technique.

(1) Precise calibration of sonic speed in the propellant sample as functions of pressure, temperature, dP/dt is necessary. The influence of dP/dt, however, is not clear yet.
(2) Matching of acoustic impedance between coupling material and propellant sample is necessary. Using epoxy resin as a coupling material with some additives, it is easy to adjust acoustic impedance to that of conventional composite propellants. However, if the acoustic impedance of a sample is low, the matching is very difficult.
(3) Even if the matching is enough, the length of propellant sample is limited up to 6~7cm.
(4) Ultrasonic pulse traverses through surface reaction zone, where temperature abruptly increases from initial temperature to around 700K. This may have some effect on ultrasonic signal, however, the estimation of the effect is very difficult and considered to be small, therefore, the effect is always neglected.
(5) The effect of surface roughness, microstructure is still in study [3].
(6) Measurements under extremely high pressures are impossible becausé coupling material cannot withstand high pressures due to stress concentration at some points.

For the basic research, experimental setup using a specially designed chamber with coupling material and end-burning propellant grain less than 6~7cm long is enough. However, our final goal is to obtain the information about how propellants burn in real motors at various conditions. For this purpose, we paid efforts and present our status here.

2. MODIFICATION

2.1 Elimination of Coupling Material

The first attempt we made is the elimination of coupling material. Fig. 2 shows our experimental setup. Ultrasonic transducer is directly attached to metallic motor case and propellant sample is set on the opposite surface of the metal case (inside the motor). Propellant sample is adhered to metal case with RTV rubber, therefore, the situation is not far from real motor.

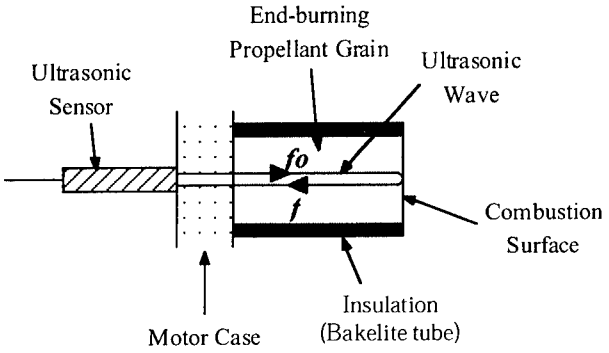

Fig. 2 Experimental Setup

As is well known, the matching of the acoustic impedance between propellant sample and metal is not enough, therefore, the energy of the ultrasonic pulse which enters propellant sample is very small. Further, weak attenuation of the pulse within the metallic material makes the signal so noisy as shown in Fig. 3, which makes it impossible to detect the echo from the propellant surface.

To overcome this difficulty, we employed the ODC (Oscillation Deadner Circuit). ODC receives the first echo from metal surface and generates the inverse signal of the first echo, and sends this signal. The inverse signal cancels the second echo from metal surface significantly, therefore, the noise in the important region after the first echo from metal surface is fairly diminished (Fig. 4).

Although the situation is improved by ODC, S/N ratio is still poor and it is difficult to detect the echo signal from propellant burning surface automatically. The detection of the signal is done by human efforts at the present stage. Therefore, round trip time method employed in EDUM cannot be used here. The reason is as follows; EDUM provides the round trip time trace automatically, however, the trace includes the inherent error of time axis and usual digitization error. Therefore, before taking the slope, smoothing step (usually interpolation) of the trace is necessary. This means that although only two successive data provide instantaneous burning rate theoretically, lots of data points are necessary in practical and such a data acquisition by human efforts is time consuming (For the steady burning rate measurement, every 10ms data acquisition is enough, however, it is not satisfactory for the transient burning rate measurement).

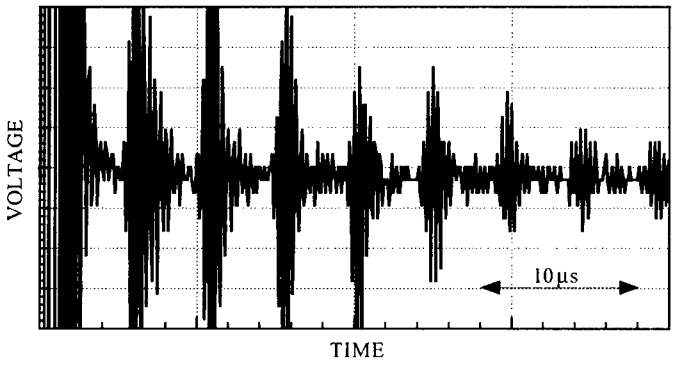

Fig.3 SIGNAL PATTERN (ORIGINAL)

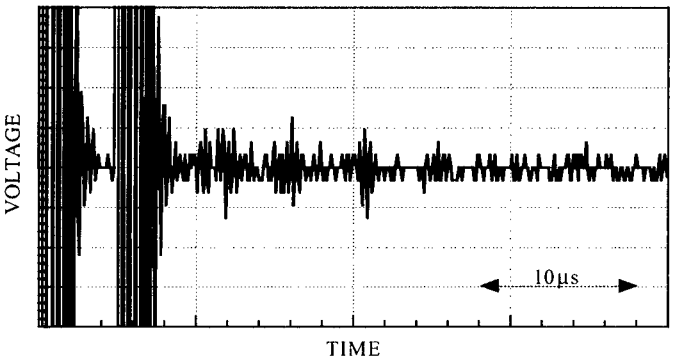

Fig.4 SIGNAL PATTERN (with ODR)

As long as echo signal from propellant burning surface is detected discretely by human efforts, we have to rely on the analytical method presented in the following section at the present stage.

2.2 Analysis

2.2.1 Doppler Effect

Propellant sample burns towards the ultrasonic transducer one-dimensionally, the frequency of the received signal f must be higher than that of original signal fo (Fig. 2). This change is due to Doppler effect, and the frequency of the received signal is given in eq. (1)

$$f = fo \times \frac{C + r}{C - r} \tag{1}$$

Here, C is sonic speed in the propellant sample and r is linear burning rate. The frequency of original signal fo is of course known and C is experimentally pre-measured. Accordingly, precise measurement of f in a burning test provides r.

2.2.2 Wavelet Analysis

Sonic speed in solid propellant is very large comparing to the linear burning rate of propellant, and frequency change $(f - fo)$ is very small, therefore, frequency analysis of the received signal must be done so carefully.

To determine f, we employed "Wavelet Analysis". Wavelet wave is multiplied to the received wave varying frequency and phase. The integration of the multiplication should be maximum when the frequency and phase of wavelet wave are equal to those of the received signal. This principle is shown in Fig. 5 schematically and this procedure corresponds to search the frequency of the summit of the curved surface of the integration in Fig. 6.

The advantage using this method is that the magnitude of the signal can be very small comparing to that needed for round trip time method, and this makes maximum sample length longer.

2.2.3 Data Processing

The first step is the detection of the echo signal from the surface of propellant sample. To make the detection easier, the noise in high frequency and low frequency regions is cut off with low pass filter and high pass filter leaving the vicinity of fo. Then, the detection is done by human efforts as described above.

Overall signal flow is summarized in Fig. 7. As is shown, gate circuit controls ultrasonic pulse generation and ODC.

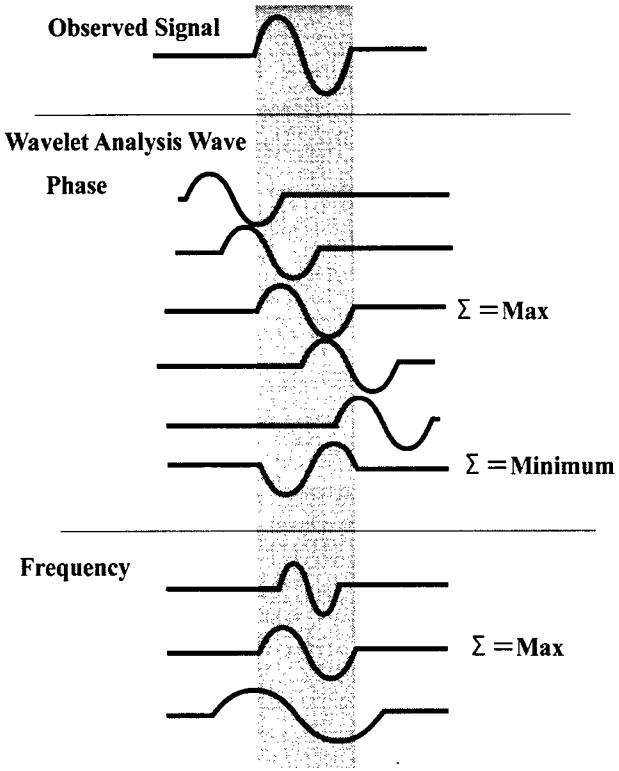

Fig.5 Principle of Wavelet Analysis

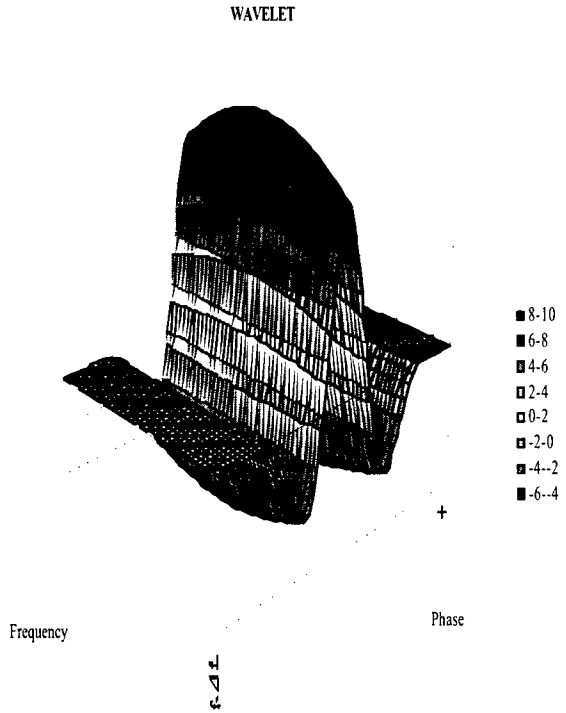

Fig.6 Curved Surface of the Integration in Wavelet Analysis

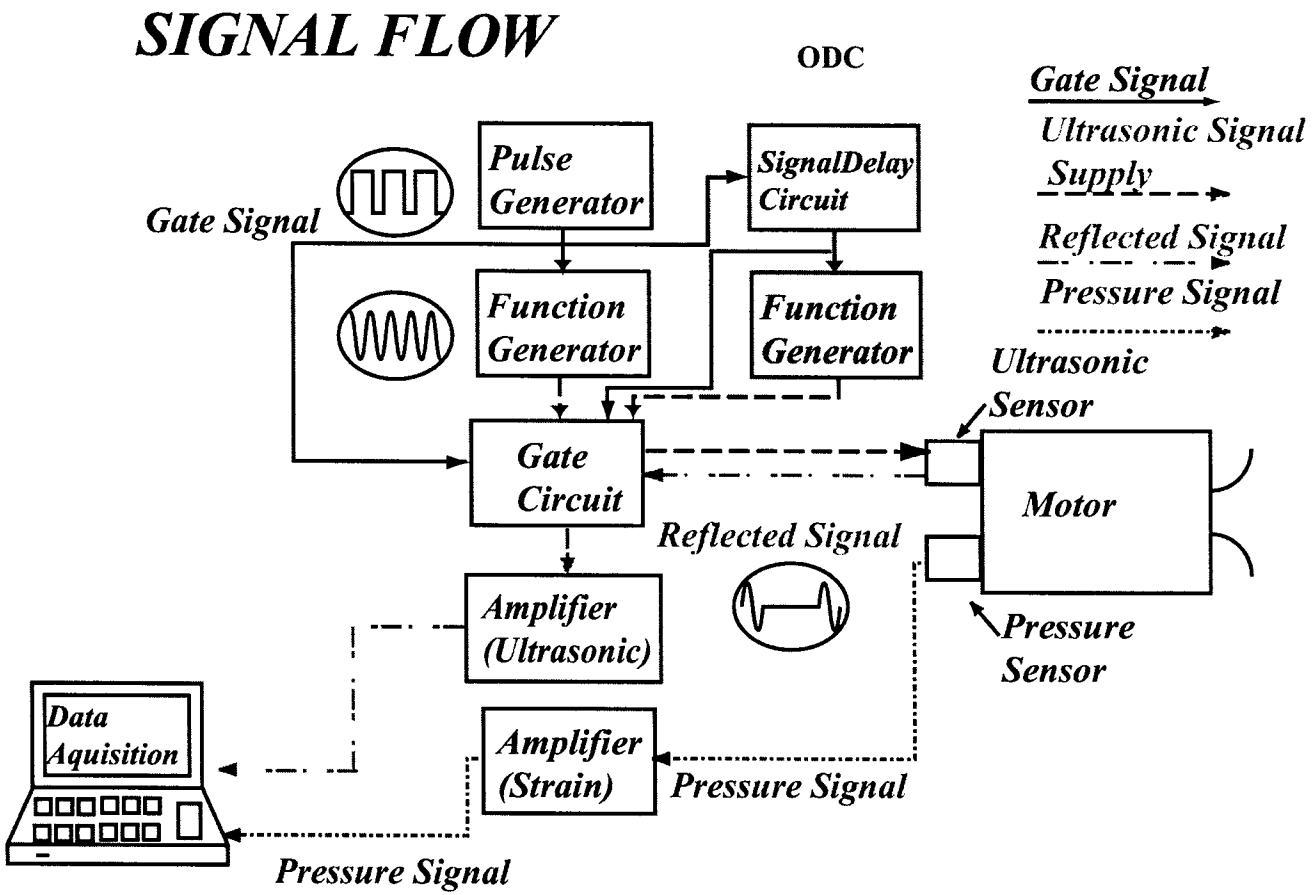

Fig.7 Signal Flow of the Ultrasonic Technique

3. EXPERIMENTAL & RESULT

3.1 Propellant Sample

Conventional composite propellant was chosen as a sample propellant. The composition is 68mass% of AP, 16mass% of Al and 16mass% of HTPB and its linear burning rate is expressed as $r = 2.60P^{0.52}$ (@20℃). Propellant was cured into ϕ40mm bakelite tubes and made as end-burning grains.

Pressure calibration of sonic speed in the propellant sample was done before the burning test. Figure 8 shows the sonic speed as a function of pressure. Sonic speed is around 1800m/s and slightly increases with pressure.

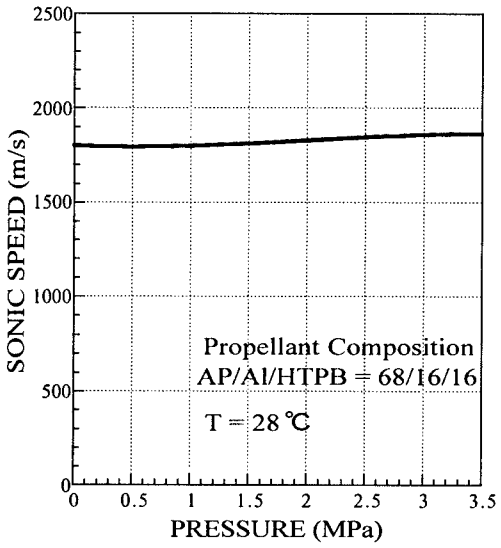

Fig. 8 Sonic Speed in the Propellant Sample as a function of Pressure

3.2 Burning Test

Experimental setup is shown in Fig. 9. Ultrasonic sensor is attached to 10mm thick stainless steel motor case and coupling material is not used. Ignition is established with an igniter ball to realize a weak ignition, which enables to extend the pressure range in one burning test. A pressure pattern of 10cm length sample is shown in Fig. 10.

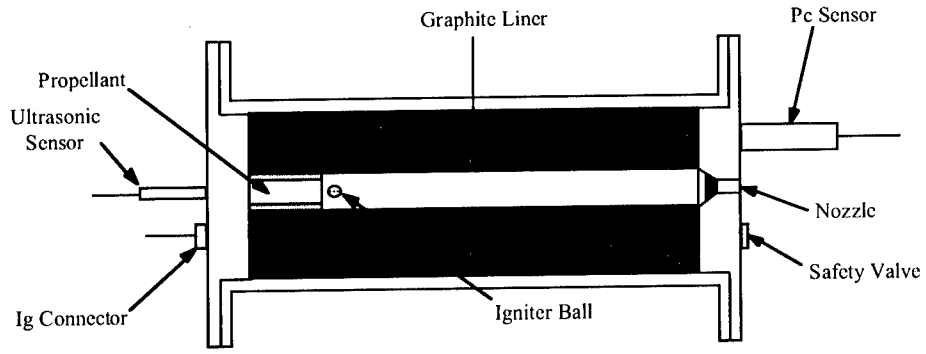

Fig.9 Experimental Setup of Burning Test

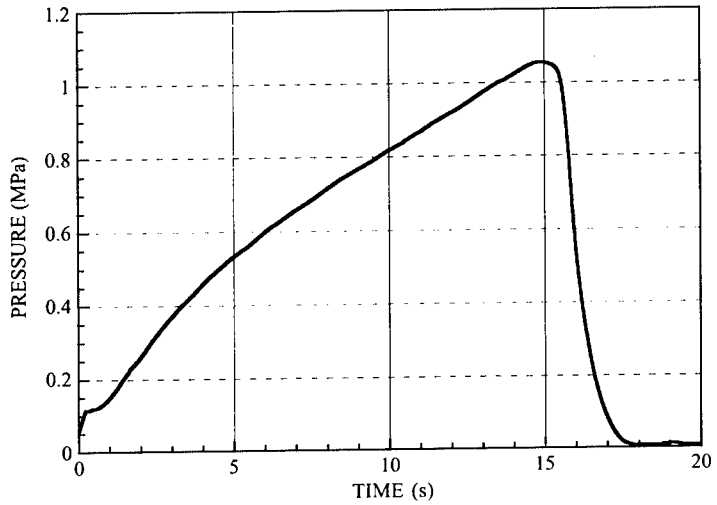

Fig.10 Typical Pressure Pattern of Burning Test

3.3 Linear Burning Rate

Wavelet analysis was applied to the observed signal and two examples at the optimum phases are shown in Fig. 11. These two curves show that frequency change is 0.60Hz for Pc = 0.28MPa and 0.71Hz for Pc = 0.44MPa.

Linear burning rates are shown in Fig. 12 along with those obtained by strand burner. The data obtained by ultrasonics is at 28℃ and the data by strandburner is at 20℃. This shows that the data by ultrasonic is slightly higher than that by strandburner (the effect of temperature change 8℃ may be small), however, the further improvements in sonic speed calibration, data acquisition system may make them closer.

4. SUMMARY

Ultrasonic technique for the linear burning rate measurement was modified. Coupling material was eliminated and maximum propellant sample length was prolonged by means of oscillation deadner circuit and wavelet analysis.

Further improvements will make it possible to apply this ultrasonic method to full-scall motors.

5. REFERENCES

(1) Kuentzmann P. et al., "Ultrasonic Measurements of Solid Propellant Burning Rate" LaRecherche Aerospatiale, 1, 55(1979).

(2) Traineau J. et al., "Ultrasonic Measurements of Solid Propellant Burning Rates in Nozzleless Rocket Motors", J. of Propulsion, 2, 215(1986).

(3) McQuade W. et al., "Determination of the Ultrasonic Burning Rate Technique", AIAA Paper 98-3555.

(4) Murphy J.J. and Krier H., "Ultrasound Measurements of Solid Propellant Burning Rates: Theory and Application", AIAA Paper 98-3556.

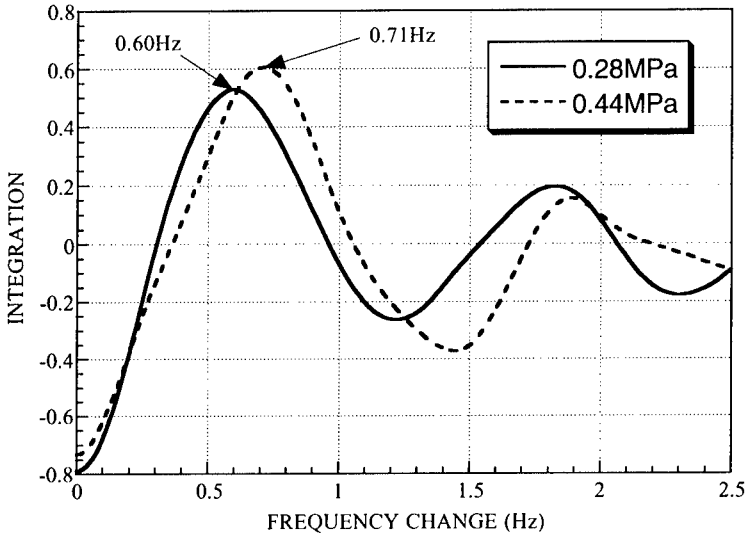

Fig. 11 Integration Curves in Wavelet Analysis

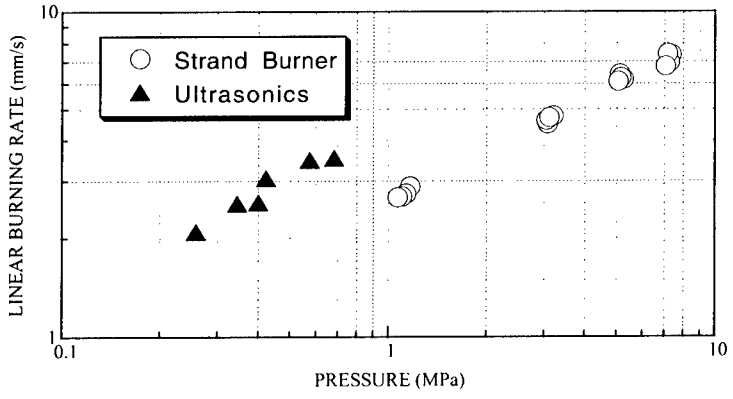

Fig. 12 Comparison of Linear Burning Rate between Ultrasonics and Strandburner

The Potential of Microreactors for the Synthesis of Energetic Materials

S. Löbbecke, J. Antes, T. Türcke, E. Marioth, K. Schmid, H. Krause

Fraunhofer-Institut für Chemische Technologie ICT
P.O. Box 12 40, 76318 Pfinztal, Germany

Introduction

In recent years microreactors have received an increasing interest as useful devices for chemical reactions and processes.
Microreactors can be manufactured in different materials (metals, polymers, silicon, glass, ceramics) with very different geometries and internal structures depending on the specific application they are made for. Common features of microreactors are their internal volumes in the sub-milliliter range and channel widths of less than 1000 µm. These geometries result in very high surface-to-volume ratios which provide for much better heat exchange than that in macroscopic batch or flow-through reactors (up to 15 times higher). Hot spots or accumulated reaction heats being responsible for large numbers of secondary, consecutive and decomposition reactions can be suppressed in microreactors. As a consequence, higher selectivities, yields and product qualities can be obtained.
Furthermore, by using highly miniaturized microreactors the hazardous potential of highly exothermic or explosive reactions can be significantly reduced. Safe operation is also achieved for reactions applying toxic materials or for processes under high pressures.
Other technological advantages of microreactors enabling a more accurate processing of chemical reactions are the short retention times of the reactants combined with good mass transfer performances and a continuously driven process.

The sum of all these features makes microreaction technology very interesting for the synthesis of energetic materials. Both safe operation and a more precise processing

concerning selectivity, yield and product quality are ubiquitous challenges whenever explosives, propellants and other energetics have to be synthesized.

The main objective of this work is to show the application potential of microreactors for the synthesis of energetic materials. Nitrations which belong to the most important reaction steps in the field of energetic materials synthesis were chosen as test reactions.

Experimental

Three different kinds of microreactors were used for the nitration experiments.
A commercially available micromixer enabling the multilamination of the educt streams was supplied by the Institute of Microtechnology Mainz IMM, Germany (Fig. 1). A second, flat micromixer made of silicon and based on a split-and-recombine structure was supplied by the Technical University of Ilmenau, Germany (Fig. 2).

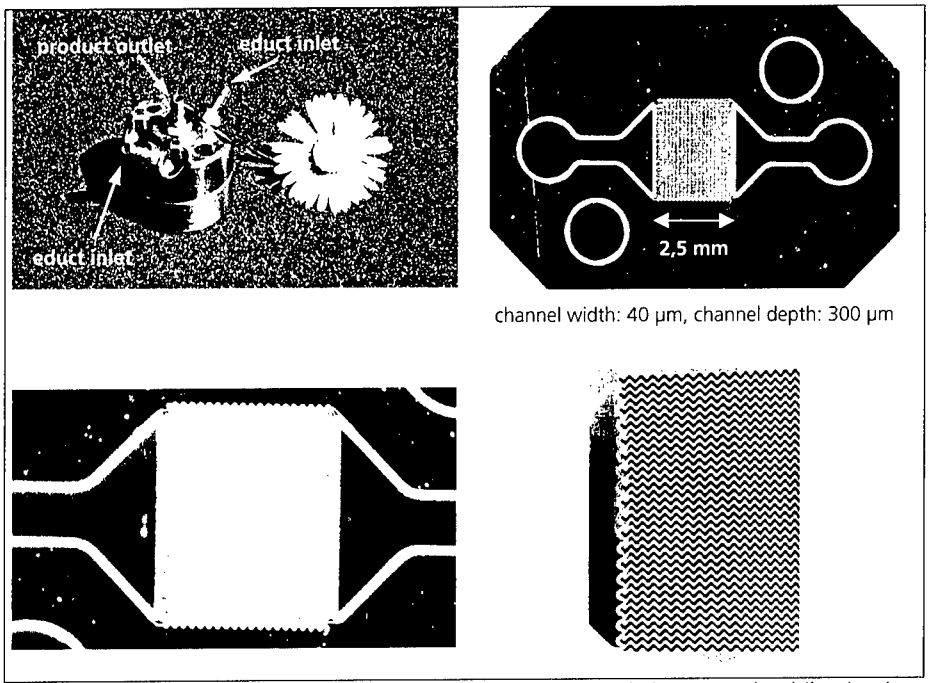

Fig. 1: micromixer made of silicon in a stainless steel housing (multilamination structure, IMM)

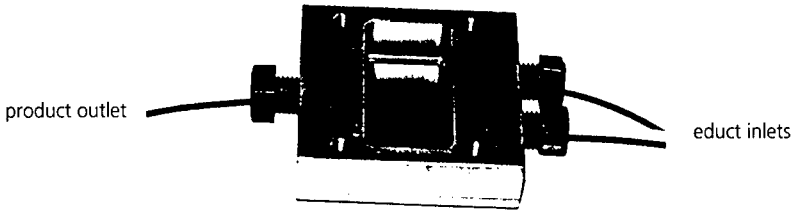

Fig. 2: micromixer made of silicon in an Al housing (split-and-recombine structure, TU Ilmenau)

In addition, a tailor-made microreaction device made of glass was constructed in cooperation with mikroglas technik Mainz, Germany which contains 20 reaction channels in parallel with educt mixing zones and an integrated cooling structure as well (Fig. 3).

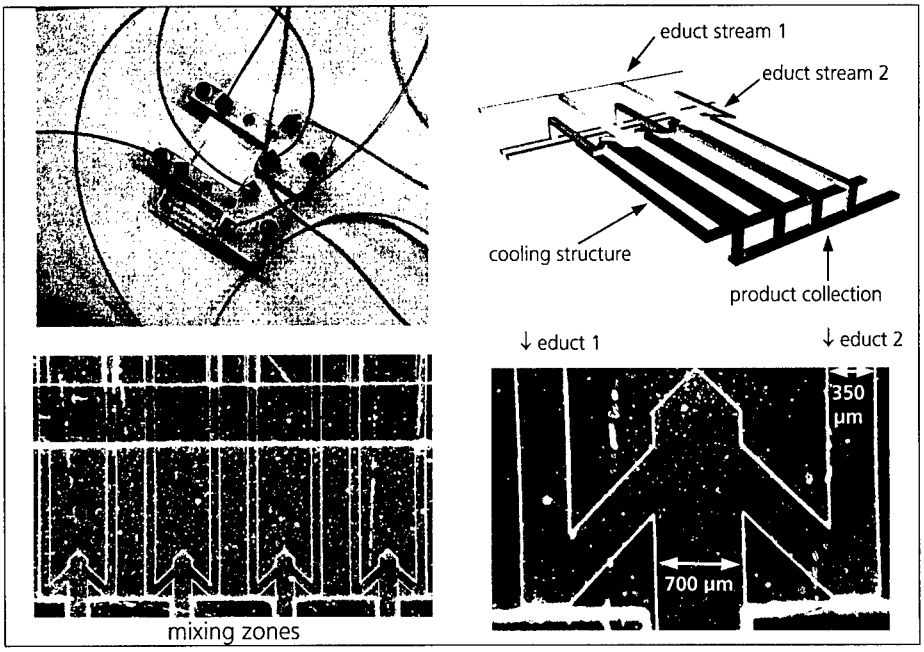

Fig. 3: microreactor made of glass consisting of 20 reaction channels in parallel and an integrated cooling structure

Nitrating agents and educts were mixed inside the microreactors (resp. micormixers) and then passed through a reaction capillary (resp. PTFE tube) of up to 150 cm length. Nitrations were carried out in a continuous mode at temperatures between -10°C and +50°C realizing variable residence times between 15 s and 45 s. The reaction mixture eluting out of the microreaction system was quenched in water, extracted and passed to NMR, HPLC or gaschromatography with mass-selective detection for analysis. In addition, FTIR microscopy was used for online analytical investigations of nitrations in silicon microreactors [1].

Different nitrating agents were used for the microreaction experiments. Beside fuming nitric acid (HNO_3) diluted in dichloromethane (CH_2Cl_2) dinitrogen pentoxide (N_2O_5) was used as a less acid nitrating agent. N_2O_5 was either dissolved in CH_2Cl_2 as well or used as a gaseous reactant (sublimation of solid N_2O_5 or in-situ production: $N_2O_4 + O_3$).

Since nitrating agents are highly corrosive media suitable materials had to be identified for the microreactors used. Microstructured devices made of silicon, titanium or glass were proved to be suitable for nitration processes. Other materials like stainless steels did not withstand corrosion processes inside of the microstructures. Figure 4 shows as an example blockages inside a metallic microstructure due to corrosion effects.

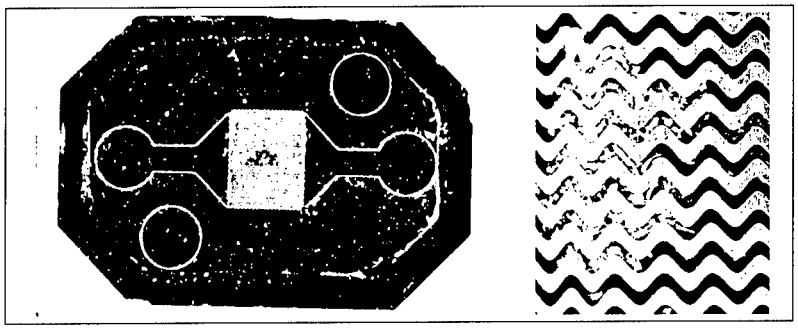

Fig. 4: corrosion and blockages inside a metallic microstructure caused by nitrating agents

Beside investigating chemical compatibility microreactors were also characterized with respect to their mixing performance applying a modified VILLERMAUX / DUSHMAN reaction of potassium iodate with potassium iodide [2 - 5]. This empirical method is

based on concurrent parallel reactions after the mixing of two solutions (*solution A*: 0.1374 mol/L HCl, *solution B*: 0.0319 mol/L KI in 1.33 mol/L NaAc + 0.00635 mol/L KJO_3^- in 1.33 mol/L NaAc):

$$HCl + NaAc \leftrightharpoons HAc + NaCl \text{ (very fast)}$$

$$5\ I^- + IO_3^- + 6\ H^+ \leftrightharpoons 3\ I_2 + 3\ H_2O \text{ (fast)}$$

$$I_2 + I^- \leftrightharpoons I_3^-$$

The mixing quality of the reactors (resp. static mixers) is inversely proportional to the I_3^- concentration which can be measured by UV/Vis spectroscopy at a wavelength of 290 nm.

In figure 5 mixing qualities of the microreactors applied for nitration reactions are compared with that of a conventional T-mixer showing a significant better mixing behavior of the microfluidic devices. The experimental data were determined with high repeatabilities.

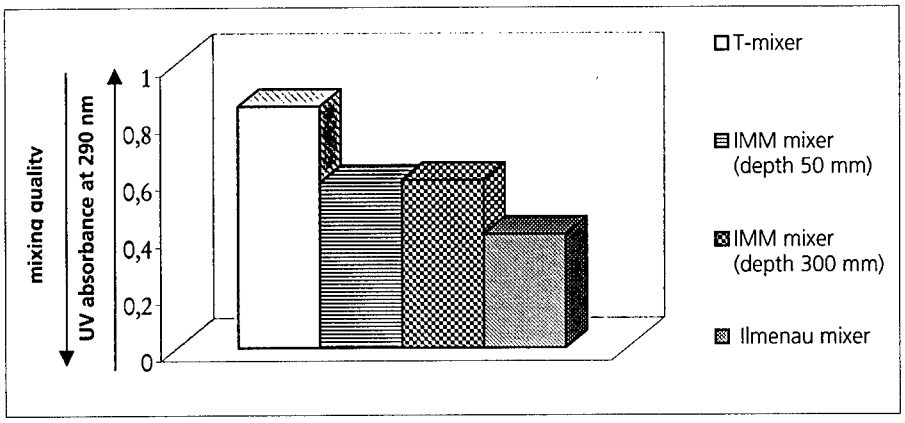

Fig. 5: mixing quality of different static micromixers (microreactors) empirically determined by a modified VILLERMAUX / DUSHMAN reaction

The mixing performance of the glass reactor was additionally characterized by neutralization reactions (1 M HCl_{aq} + 1 M $NaOH_{aq}$) using bromothymol blue as an indicator. The neutralization was observed under a light microscope at different flow rates of the acid and the base (0.1 to 3.0 mL/min). Figures 6 and 7 show photographs taken during the continuously driven neutralization reaction indicating clearly a laminar flow behavior of the educt streams and thus a diffusion controlled mixing of the reactants (blue resp. dark color inside of the microchannels = neutralized reaction product). At higher flow rates (here: 3.0 mL/min) complete mixing is only achieved at the end of the reaction channel confirming the necessity of a 40 mm long reaction zone. At lower flow rates complete mixing is achieved much more earlier. These experimental data desribing the mixing performance of the glass reactor could be confirmed by CFD simulations (CFD: Computional Fluid Dynamics; ACE+ 6.0 from CFDRC, Huntsville, Alabama) as it is illustrated in fig. 8 and 9.

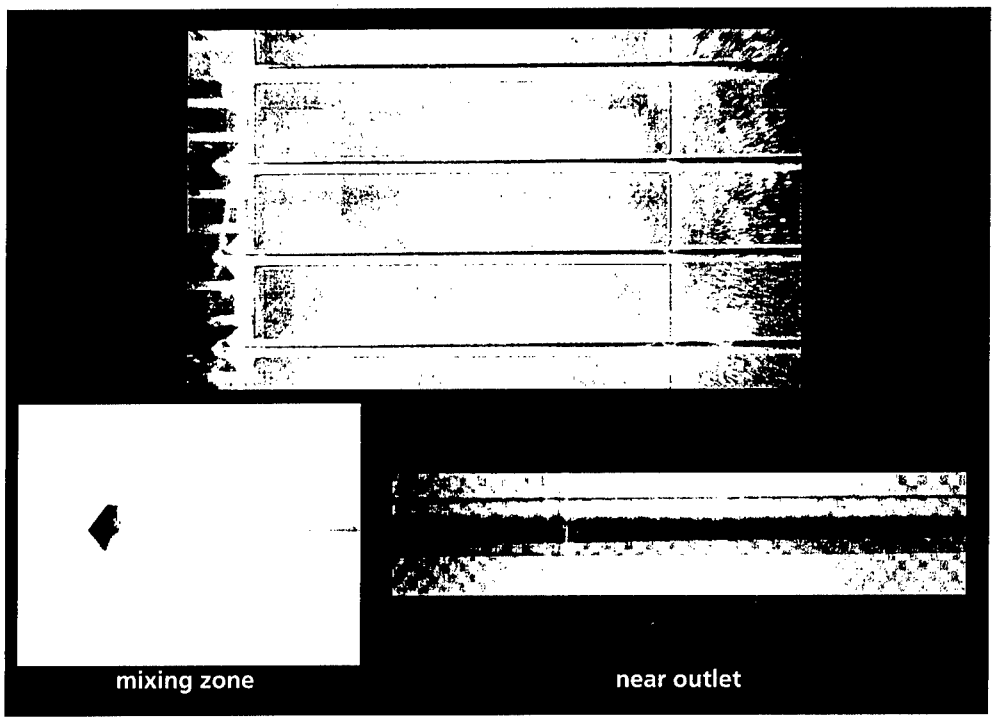

Fig. 6: microscope photos of an acid/base neutralization carried out in the glass microreactor (flow rate: 3.0 mL/min)

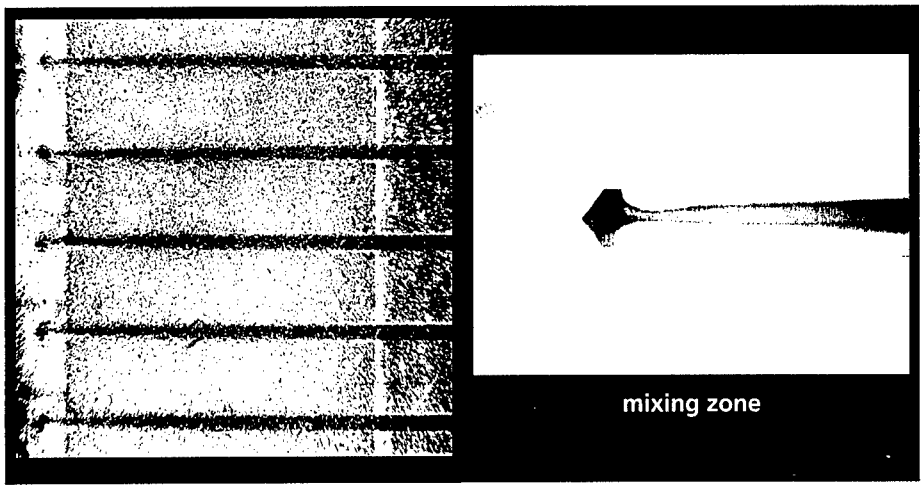

Fig. 7: microscope photos of an acid/base neutralization carried out in the glass microreactor (flow rate: 0.3 mL/min)

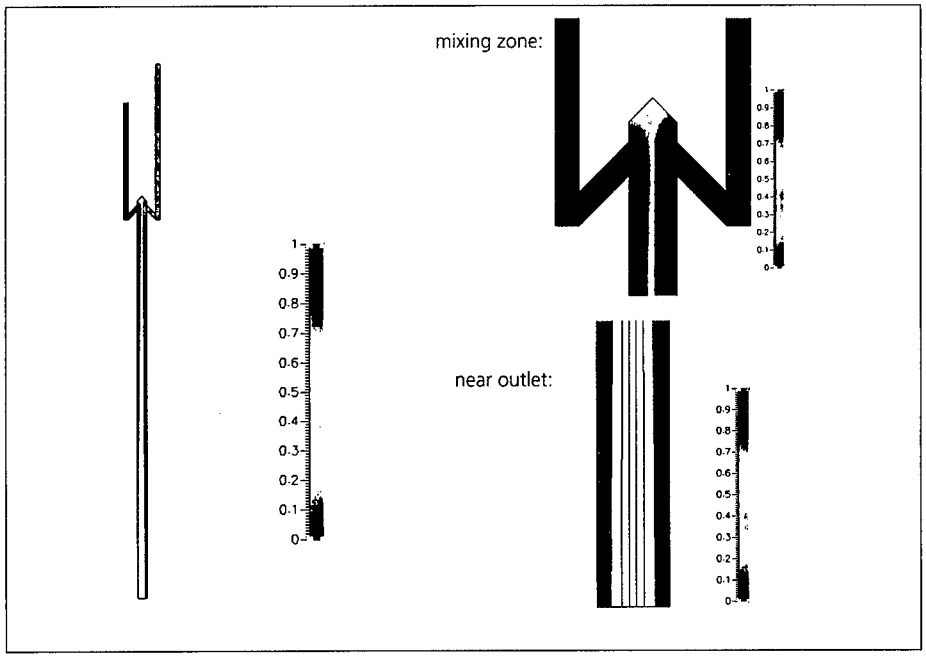

Fig. 8: CFD simulation of mixing two fluids in the glass microreactor (T = 273 K, velocity at entrance: 0.001 m/s, density of both fluids: 1 kg/m^3, kinematic viscosity: 10^{-6} m^2/s)

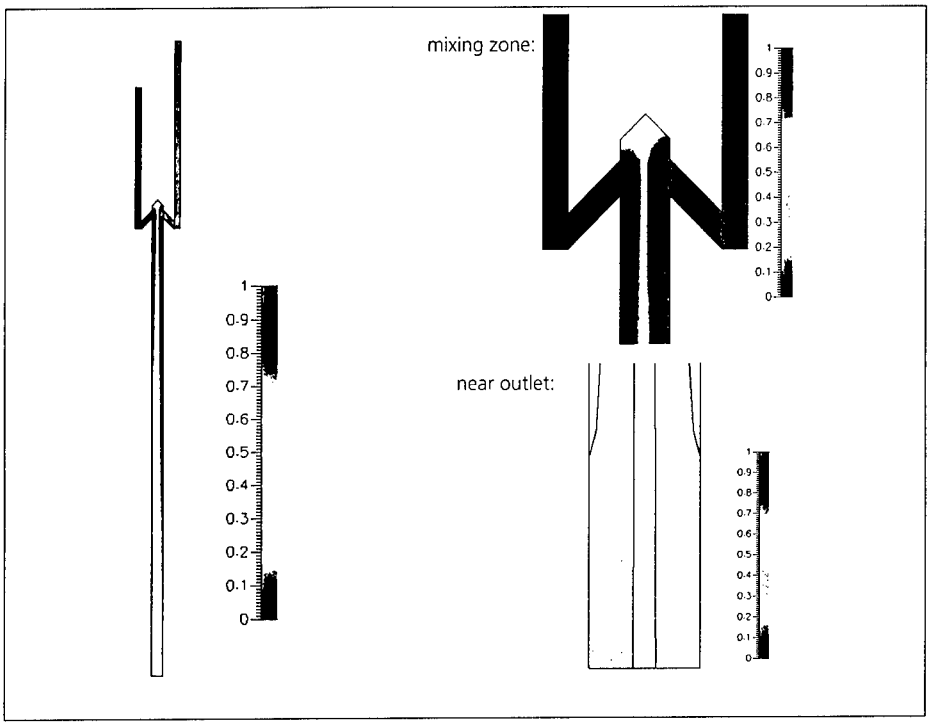

Fig. 9: CFD simulation of mixing two fluids in the glass microreactor (T = 363 K, velocity at entrance: 0.0005 m/s, density of both fluids: 1 kg/m^3, kinematic viscosity: 10^{-6} m^2/s)

Exemplary results

The nitration of naphthalene with gaseous dinitrogen pentoxide respectively N_2O_5 dissolved in dichloromethane was chosen as a first test reaction. From macroscopic batch reactions it is known that - depending on the process conditions applied - several products can be obtained differing in number and position of their nitro groups (Fig. 10).

By applying continuously operating microreactors short residence times combined with good mass transfer performances are achievable for nitration processes [6 - 8]. Therefore, main nitration products obtained from microreaction experiments were mono- and dinitro naphthalenes in contrast to a significantly broader product spectrum

obtained from macroscopic batch reactions containing also tri- and tetranitrated products beside numerous isomers of lower nitrated naphthalenes.

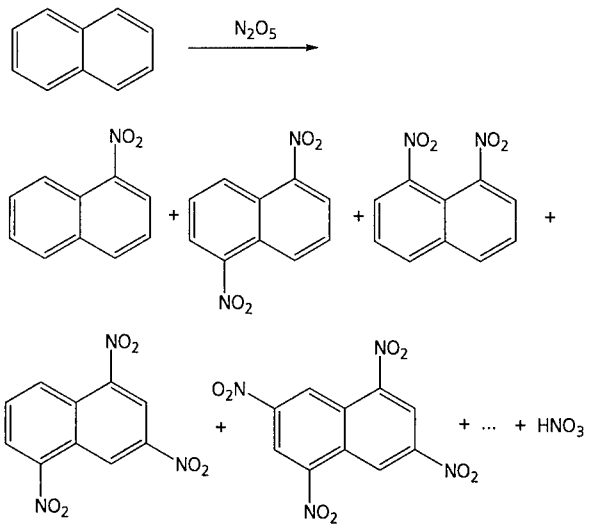

Fig. 10: nitration of naphthalene: possible reaction products

Figure 11 compares the nitration products obtained in the three different microreactors when gaseous N_2O_5 is used in a 6-fold excess. In contrast to macroscopic nitrations which require intensive cooling (approx. -50°C to -20°C) microreactions were carried out at 30°C with flow rates of 1 mL/min and a retention time of 3 s. The data confirm the preferential formation of mono and dinitro naphthalenes when microreactors are used. Different conversions can be observed when microreactors with different geometries and internal structures are applied. The highest conversion is obtained when the IMM reactor is used. Dinitro naphthalenes are the main products in this case. In contrast to this, by applying the glass reactor 1-mononitro naphthalene is the main reaction product whereas only few amounts of dinitro naphthalenes are formed.

When fuming HNO_3 is used as a nitrating agent the selectivity for mononitro naphthalenes can be significantly enhanced. Figure 12 shows that the selectivity is more than 95% for each of the three microreactors. By using the glass reactor 1-mononitro naphthalene is again the product with the highest yield.

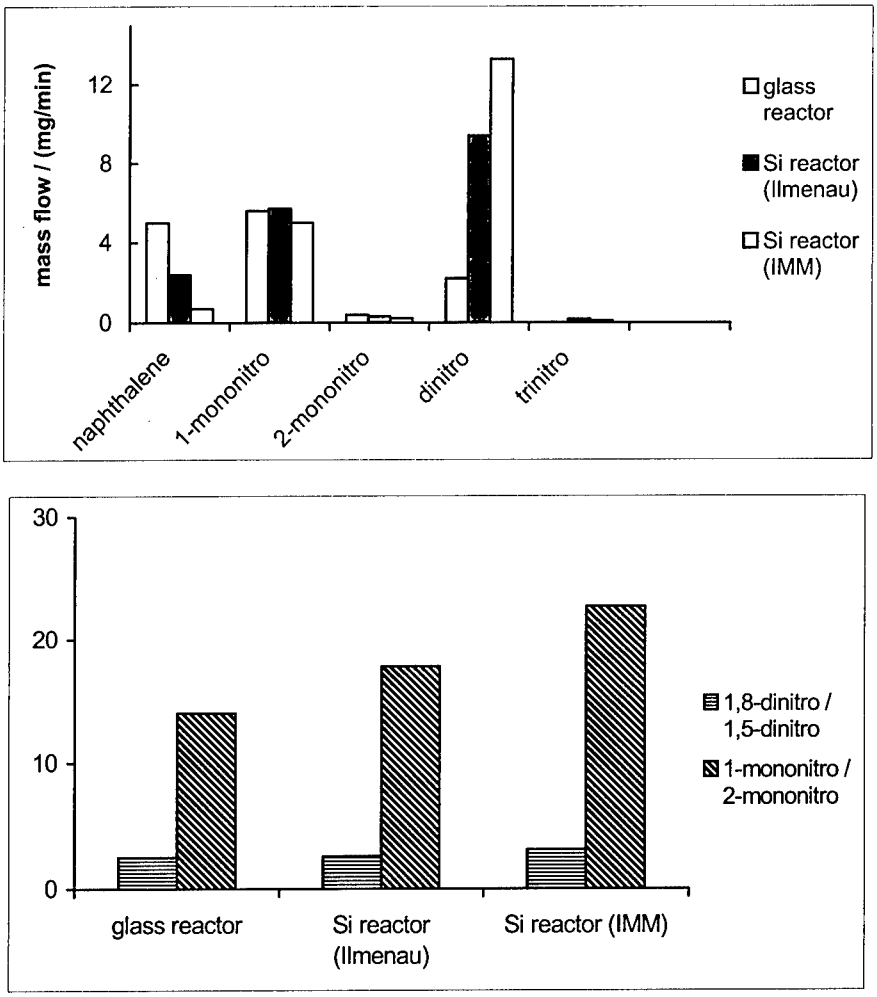

Fig. 11: nitration of naphthalene in microreactors using gaseous N_2O_5 (6-fold excess, 30°C, 1 mL/min, retention time: 3 s)

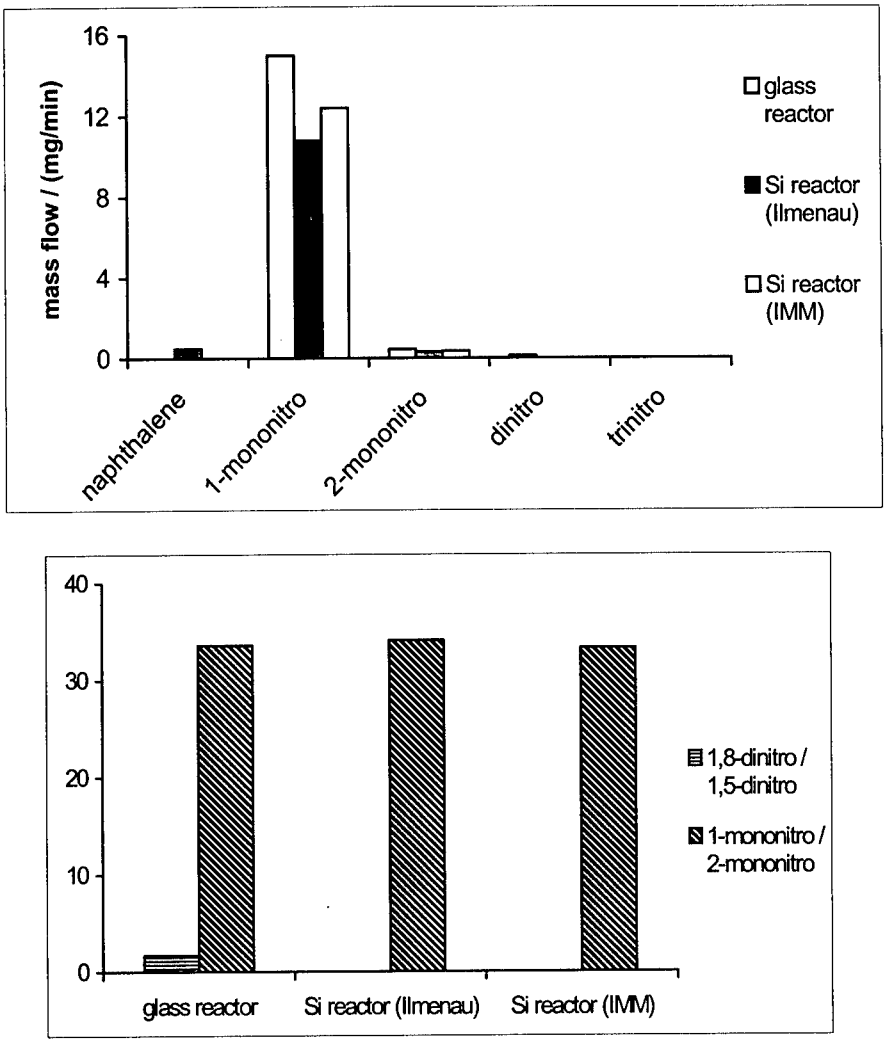

Fig. 12: nitration of naphthalene in microreactors using fuming HNO_3 diluted in CH_2Cl_2 (6-fold excess, 20°C, 1 mL/min, retention time: 45 s)

Beside controlling the nitration degree (number of nitro groups) the good heat exchange and mass transport in microreactors make also changes of isomeric ratios possible (Fig. 11 - 13). For example, the isomeric ratio of 1,5-dinitro naphthalene to 1,8-dinitro naphthalene was found to be almost constant in macroscopic batch reactions at different process conditions:

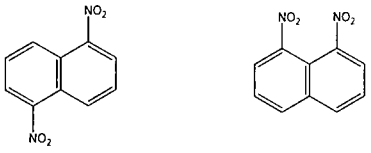

1,5-dinitro naphthalene : 1,8-dinitro naphthalene ≈ 1 : 3.6 (macroscopic reactor)

By applying microreactors the amount of the unfavored 1,5-dinitro isomer could be significantly increased (Fig. 13) resulting in an isomeric ratio of:

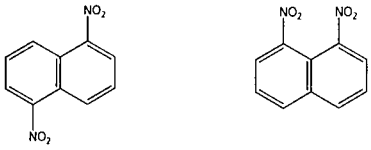

1,5-dinitro naphthalene: 1,8-dinitro naphthalene ≈ 1 : 2.8 (microreactors)

Another example for changing isomeric ratios of nitration products when microreactors are used is the ratio of 1-mononitro naphthalene to 2-mononitro naphthalene (Fig. 11, 12 and 14). In industrial processes ratios of 20:1 are achieved:

1-mononitro naphthalene : 2-mononitro naphthalene ≈ 20 : 1 (batch/industrial process)

By using microractors and fuming HNO_3 as nitrating agent (Fig. 12) this ratio could be dramatically increased to more than 30:

1-mononitro naphthalene : 2-mononitro naphthalene ≈ 32 : 1 (microreactors)

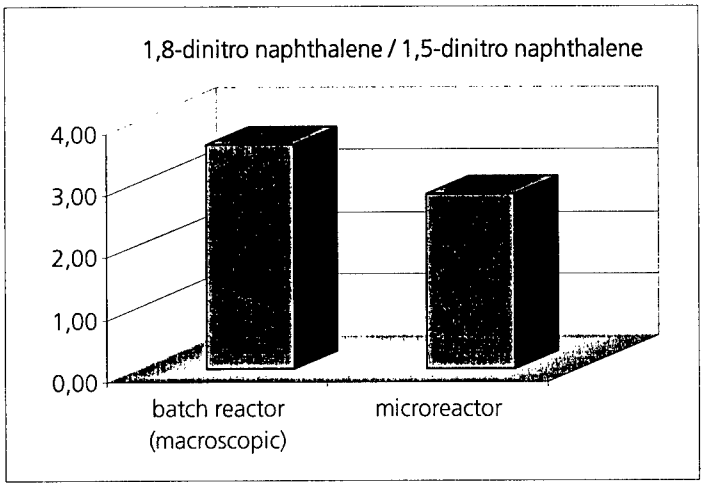

Fig. 13: changes in isomeric ratios of dinitro naphthalenes by using microreactors

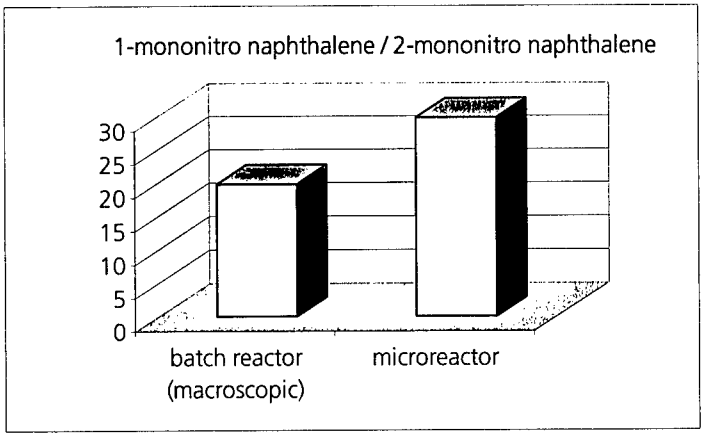

Fig. 14: changes in isomeric ratios of mononitro naphthalenes by using microreactors

All results received from the nitration experiments of naphthalene show that carrying out nitrations in microreactors permit several interesting advantages regarding selectivity, yield and purity of products. In comparison with macroscopic batch reactions 100% conversion within less than one minute is achievable. Furthermore, a more precise targeting of the nitration process is possible in microreactors. Preferably mono

and dinitro naphthalenes are the main reaction products, the formation of higher nitrated derivates is neglectable. In addition, isomeric ratios of nitration products can be significantly changed in comparison with industrial or other macroscopic batch processes. A further tuning of the reaction process can be achieved by changing the reactor type and/or the nitrating agent.

Another reaction carried out in microreactors is the nitration of N,N'-diethyl urea (Fig. 15). N,N'-dinitro N,N'-diethyl urea is an important precursor for the synthesis of the energetic plastiziser DNDA.

In macroscopic batch reactions at temperatures between -20°C and -10°C the synthesis of N,N'-dinitro N,N'-diethyl urea is accompanied with concurrent reactions like the thermal decomposition of the nitrated products due to accumulated heat in the batch reactor.

It is assumed that the synthesis of dinitro urea is based on a two step mechanism with the formation of the mononitro derivate being the first reaction step. Unfortunately, in macroscopic reactions N-mononitro N,N'-diethyl urea is suspected to react quite quickly with the nitrating agent and can thus not be isolated.

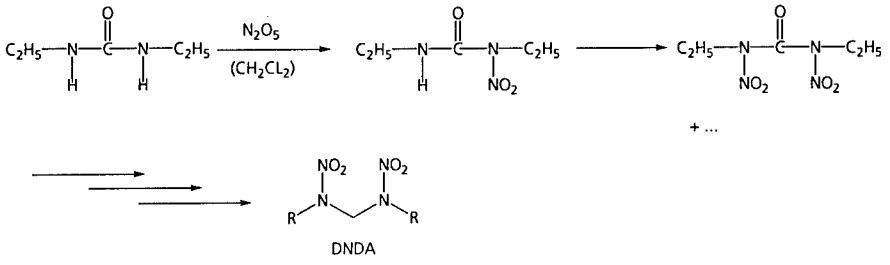

Fig. 15: nitration of N,N'-diethyl urea

By carrying out the nitration of N,N'-diethyl urea in continously operating microreactors a more deliberate synthesis of N-mononitro N,N'-diethyl urea can be achieved.

In all experiments using dissolved and gaseous (sublimated and in-situ produced) N_2O_5 as nitrating agent the mononitrated intermediate was obtained as the main reaction product with yields up to 75%. N-mononitro N,N'-diethyl urea could even be

synthesized at room temperature due to the short retention times of the reactants combined with the good heat and mass transfer performance of the microreactors.
Hence, microreactors are suitable tools for a safe and more controllable processing of N,N'-dinitro N,N'-diethyl urea synthesis. The selective synthesis and isolation of the mononitrated urea would allow a "step-by-step" nitration of the final product.
Furthermore, the deliberate synthesis of the mononitrated urea may also give an access to new products which are based on syntheses using N-mononitro N,N'-diethyl urea as a new precursor.

Beside the nitration of naphthalene and diethyl urea, microreactors have been also successfully used for other nitration reactions, for example those of simple hydrocarbons like methane or hexane using gaseous N_2O_5.
The high exothermicity of these reactions still requires many efforts to keep them safe and reliable in technical processes. In microreactors methane and hexane have been successfully nitrated by reducing dramatically the hazardous potential of these processes. However, process conditions have not been optimized until now for the microreactor nitrations, so that the number of unwanted byproducts (particularly in the case of hexane) was only slightly decreased in comparison with macroscopic processes.

Conclusions

Different examples have shown that microstructured reaction devices are suitable tools for nitration processes in both gaseous and liquid phase and can thus be applied to the synthesis of energetic materials ensuring a safe and reliable process.
Since heat, mass transfer and residence time can be controlled very precisely in microreactors, both the selective single or multiple nitration of substances and the selective nitration of particular positions in a molecule are achievable. In comparison with macroscopic batch or continous processes the product spectrum of nitrations can be significantly varied.
The use of microreactors thus permits higher product selectivities, the isolation of intermediates and an access to previously unknown products.

References

[1] W. Schweikert, T. Türcke, S. Löbbecke, 31st Int. Annu. Conf. ICT (2000), (Energetic Materials - Analysis, Diagnostics and Testing), 98, 27 - 30 June 2000, Karlsruhe, Germany *[this proceeding]*

[2] S. Dushman, J. Phys. Chem., 8, (1904) 453

[3] J. Villermaux, L. Falk, M.C. Fournier, AIChE Symp. Ser. 90 (1994) 299, 50-54

[4] M.C. Fournier, L. Falk, J. Villermaux, Chem. Eng. Sci. 51 (1996) 22, 5053-5064

[5] W. Ehrfeld, K. Golbig, V. Hessel, H. Löwe, Th. Richter, Ind. Eng. Chem. Res. 38 (1999) 1075-1082

[6] J.R. Burns, C. Ramshaw, P. Harston, 2nd Int. Conference on Microreaction Technology (IMRET 2), 8-12 March 1998, New Orleans, USA

[7] J. Antes, T. Türcke, E. Marioth, K. Schmid, H. Krause, S. Löbbecke, 4th Int. Conference on Microreaction Technology (IMRET 4) , 5-9 March 2000, Atlanta, GA, USA

[8] J.R. Burns, C. Ramshaw, 4th Int. Conference on Microreaction Technology (IMRET 4) , 5-9 March 2000, Atlanta, GA, USA

CLEAN SYNTHESIS OF ENERGETIC MATERIALS USING SOLID-SUPPORTED REACTIONS AND RELATED TECHNOLOGIES

Ross W. Millar, M. Eamon Colclough, Robert P. Claridge, Javid Hamid, Simon P. Philbin and Naren Chauhan

Defence Evaluation & Research Agency (DERA), WS3 Dept.,
Fort Halstead, Sevenoaks, Kent TN14 7BP, United Kingdom

ABSTRACT

This paper describes progress in the development of clean nitration and azidation methods, based upon the use of solid supports such as clays and zeolites. These cleaner synthetic routes will be necessary to meet the increasingly stringent demands of environmental legislation in the new century. Various routes to achieve these goals are described, the principal subdivisions being: a) nitrations using solid-supported nitrating agents; b) nitrations using catalytic solids, and c) solid-supported azidating agents. Nitrations in clean solvents such as liquid/supercritical carbon dioxide have also been carried out. Using all of these approaches, several chemical classes of precursor molecules, including aromatics, alcohols and amine derivatives have been nitrated, and various types of energetic materials (nitrate esters, nitramines, aromatic nitro compounds and aliphatic azides) have been successfully synthesised. The results show promise for the development of workable methodologies which will overcome the limitations imposed by present and anticipated environmental legislation.

1.0 INTRODUCTION

In previous papers [1-3] the need for cleaner routes for the synthesis of energetic materials, both known and novel, was stated, particularly from the perspective of UK research at DERA. Such work utilises the integrated research facilities in WS3 Department, where disparate disciplines including molecular modelling, chemical evaluation and testing, formulation, scale-up and of course bench synthesis are amalgamated to enable new products and methodologies to be evaluated within the same department. In the work reported here, attention is focussed upon key reactions for the introduction of energetic groups into molecules, namely nitration and, to a lesser extent, azidation. The general strategy is to initially prove the concept of these novel reactions with non-energetic 'model' compounds, with extension in successful cases to energetic counterparts, be they energetic liquids for plasticiser use, solids (e.g. TNT) or energetic polymer precursors (e.g. BAMO, BNMO).

Traditional methodologies for effecting nitration reactions have required the use of strong acids as reagents and reaction media, and it is difficult to dispose of or recycle such media without damaging the environment [4]. Likewise, azidations carried out by current methods require the use of highly polar solvents such as dimethylformamide (DMF) or dimethylsulphoxide (DMSO) which are environmentally unfriendly. Whilst the nitration methodologies developed at DERA [5,6] and based on the use of dinitrogen pentoxide in chlorinated hydrocarbon (CHC) solvents have gone some way towards alleviating these problems, there nevertheless remain unsolved problems connected with the use and disposal of such solvents, which are known to be ozone depleters and therefore detrimental if allowed to escape into the atmosphere. An aim of this presentation, therefore, is to show how, by suitable choice of methodologies for effecting nitration and azidation reactions, the current dependence on environmentally unsatisfactory media and reagents can be minimised, or in some cases eliminated entirely.

2.0 NITRATIONS

2.1 Solid-Supported Nitrations

2.1.1 General

The principles involved in carrying out reactions on solid supports have been detailed elsewhere [7]. Essentially, two classes of reaction system may be employed: a) those where the nitrating agent is bound onto the solid support, or b) those where the solid acts as a catalyst, with the nitrating agent in solution. In either case it is important to realise that the reaction occurs on the surface of the support, not in the bulk solution, a factor which gives these systems a decisive advantage in enabling the use of environmentally benign solvents, e.g. hexane (which are usually poor solvents for nitro compounds and their precursors). In the majority of the work reported here, systems of type a) are employed, although some catalytic zeolite systems have also been studied (see section 2.1.5).

2.1.2 Claycop

In work reported earlier [2], the system comprising an anhydrous transition metal nitrate (copper(II) nitrate) supported on a K10 montmorillonite clay - 'claycop' - first described by Laszlo [8], was evaluated to assess its efficacy in producing energetic compounds, particularly nitrate esters, nitramines and polynitroaromatic compounds. Although this system permitted nitrations to be carried out in an environmentally benign solvent, hexane, the scope of its utility was severely limited, being applicable only to a few nitrate esters with constraints on their structure (i.e. secondary or, better, tertiary nitrate esters). No nitramines could be synthesised and the reagent required additional nitric acid to effect polynitration in aromatic systems. Furthermore, the finding that, in aromatic nitrations, similar results were obtained in the absence of the transition metal nitrate indicated that claycop was not, in fact, the active species in the second nitration step [9]. This work was therefore discontinued and attention turned to the dinitrogen pentoxide (DNPO) systems reported below.

2.1.3 Clay-DNPO

In an attempt to eliminate the use of CHC solvents which had hitherto always been used in DNPO nitrations (DNPO is insoluble in straight-chain hydrocarbons and incompatible with all other known non-halogenated solvents of low polarity), it was decided to investigate the adsorption of gaseous DNPO directly onto K10 montmorillonite clay. This, if successful, would generate a solid nitrating agent with moderated power and enhanced stability compared to DNPO alone. To our satisfaction this turned out indeed to be the case, and K10 clays containing 10-20% by weight of DNPO were readily prepared in this way. These solids were used in several series of nitration reactions, carried out in hexane: firstly with alcohols (Scheme 1) where yields of up to 99% of the nitrate ester products **2a-d**, **4** & **6a** were obtained from the corresponding alcohols (**1a-d**, **3** & **5a**) after reaction periods of 30 min.- 1 hr at the temperatures shown. Workup was simple with mere filtration followed by washing of the spent clay with a solvent compatible with DNPO (currently dichloromethane is used but it is intended to replace this with an

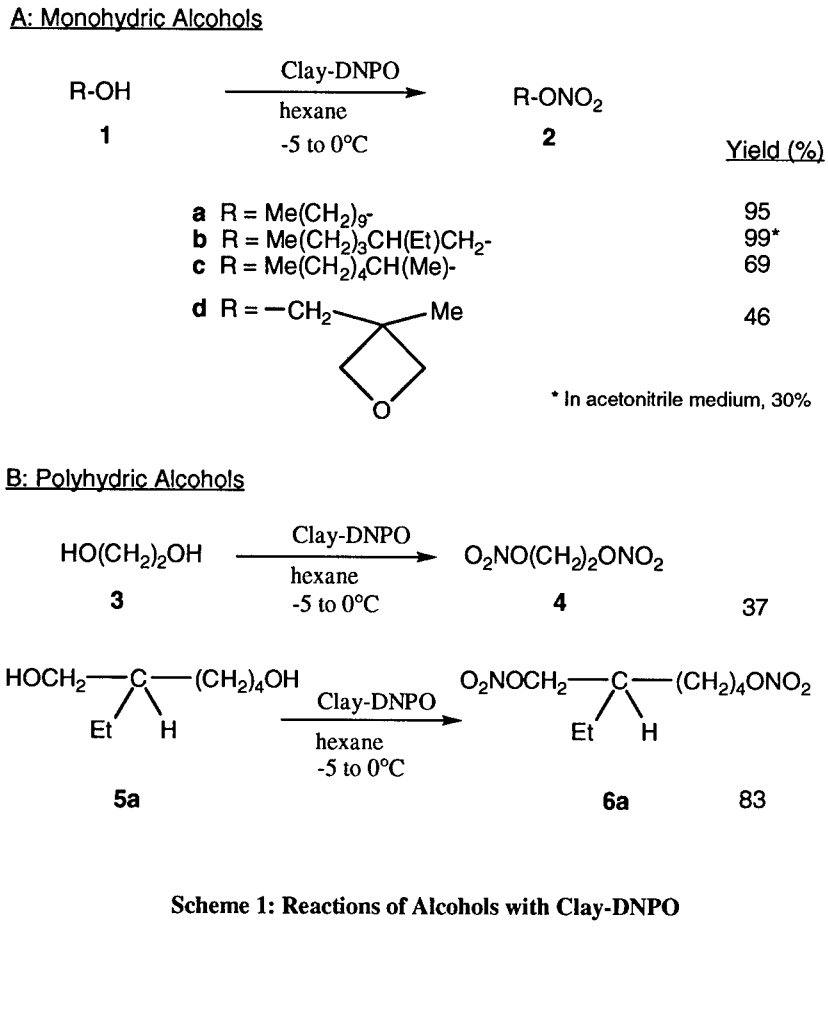

Scheme 1: Reactions of Alcohols with Clay-DNPO

environmentally-benign solvent such as a perfluorocarbon). Notably, when a polar solvent, acetonitrile, was used as reaction solvent yields were diminished, suggesting that effects arising on the surface of the clay are important in promoting the reaction, although the nature of these effects is at present unclear.

The clay-DNPO system was also useful in the synthesis of nitramines, and the mononitramine N-nitromorpholine (**8**) was synthesised in up to 58% yield (cf. 0% in the corresponding reaction with

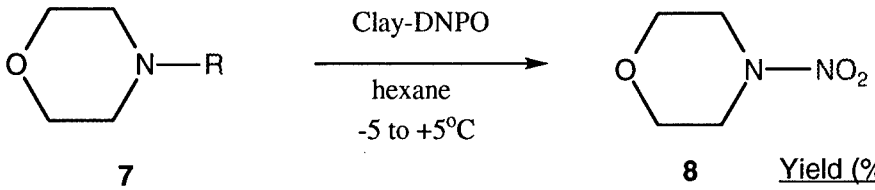

7

a R = COMe
b R = $SiMe_3$

8 Yield (%)*

58
49

* cf. DCM reaction: 80%[6]

Scheme 2: Synthesis of a Nitramine using Supported DNPO

claycop [2]), from either the N-acetyl or N-trimethylsilyl precursors, **7a** and **7b** (Scheme 2). It is hoped to extend this work to polynitramines at a future date.

Finally, a polynitroaromatic, *m*-dinitrobenzene (**10**), was also synthesised from the hydrocarbon precursor (**9**) using clay-DNPO (Scheme 3):

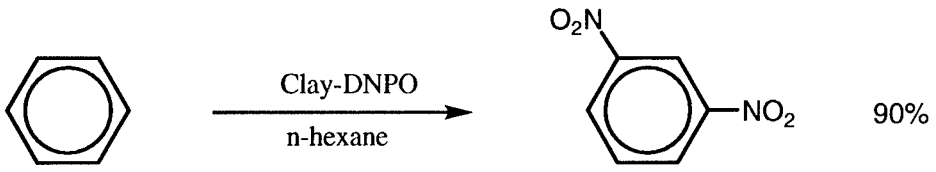

9 **10**

Scheme 3

Therefore these reactions represent a milestone in nitration chemistry whereby for the first time, to the authors' knowledge, a variety of nitrated materials have been made without requiring the use of strong acids or environmentally-unfriendly solvents as the main reaction medium. With further optimisation these reactions should be scaleable and meet the requirements of anti-pollution legislation expected in the next few years. The extension of the system to a second type of solid support, zeolites, is now described.

2.1.4 Zeolite-DNPO

In a similar manner to that described in section 2.1.3 above, DNPO was adsorbed onto a small-pore zeolite, H-ZSM-5. Reaction with alcohols in hexane medium gave a variety of nitrate esters in up to 86% yield (Scheme 4). In some cases better yields of nitrate esters were obtained than with clay-DNPO,

A: Monohydric Alcohols

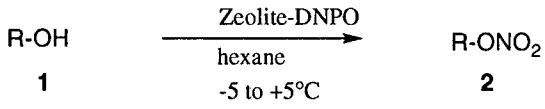

1 2

	Yield (%)
b R = $Me(CH_2)_3CH(Et)CH_2$-	77
c R = $Me(CH_2)_4CH(Me)$-	86
e R = $Me(CH_2)_7$-	78

B: Polyhydric Alcohols

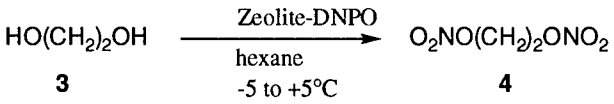

3 4 84

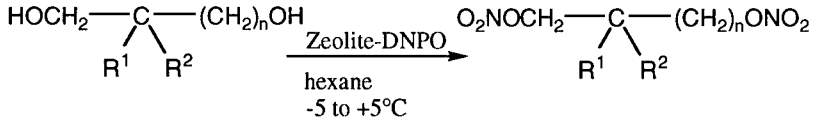

5 6

a R^1 = Et, R^2 = H, n = 4	44
b R^1,R^2 = -CH_2OCH_2-, n = 1	24

Scheme 4: Reactions of Alcohols with Zeolite-DNPO

e.g. ethyleneglycol dinitrate (**4**), whilst in others the reverse was the case. Thus the two methods can be considered to be complementary.

In the attempted synthesis of nitramines using this system, however, none of the desired products have been obtained to date, possibly owing to adsorption in the pores of the zeolite. It is intended to re-investigate the synthesis using a medium-pore zeolite of the faujasite type. Aromatic nitration was not investigated with the zeolite-DNPO system (but work on aromatic nitration by DNPO in dichloromethane in the presence of faujasite-type zeolites is described in section 2.1.5). The same comments apply to the exploitation of this chemistry as were made for clay-DNPO (section 2.1.3).

2.1.5 Catalytic Zeolytic Systems

In this section, work is described where the zeolite, of faujasite (protonic) or H^+-β type, is considered to act primarily as an acid catalyst and thus promote the nitration reactions (aromatic in all cases), rather than as a carrier of the nitrating agent *per se*. Also, the environmental friendliness of these systems is more open to question with the requirement to use CHC solvents (especially dichloromethane, DCM) to dissolve DNPO (faujasite work), or acid anhydrides (especially trifluoroacetic anhydride, TFAA) in conjunction with 100% nitric acid to generate the nitrating species (β work). Nevertheless, the promise of increased regioselectivities from these systems, which by creating fewer by-products may outweigh to some extent the shortcomings of the solvents, means that these systems are still worthy of consideration in the green context.

To focus on one reaction out of many carried out which is exemplifies the points mentioned above, the nitration of toluene to 2,4-dinitrotoluene is considered. The two discrete steps **11** → **12** and **12** → **13** (Scheme 5) were investigated separately, then a combined "one-pot" synthesis of **11** → **13** was

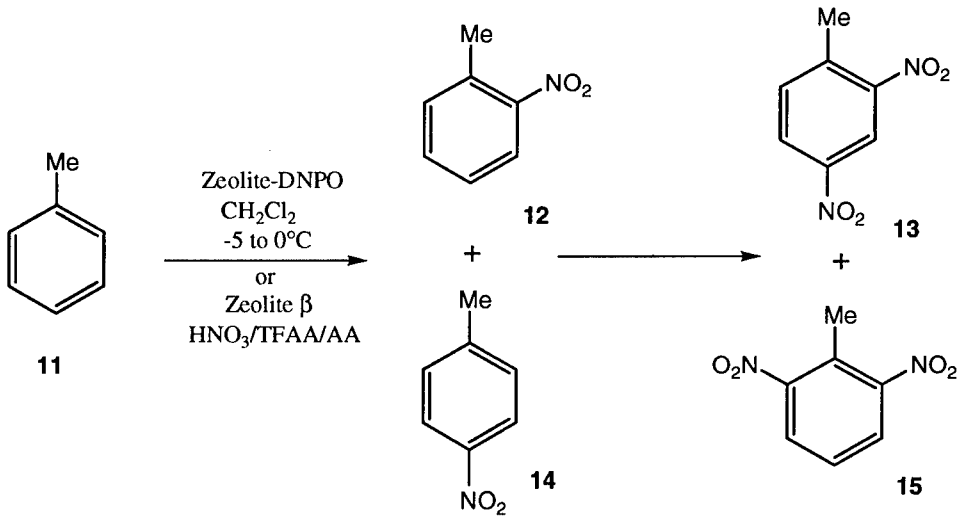

Scheme 5: Nitration of Toluene by Zeolite 720-DNPO or Zeolite β-TFAA/AA

studied using both the faujasite/DNPO/DCM and zeolite β/nitric acid/anhydride systems. Initially, the dinitration step (**12** → **13**) is considered as this poses the greatest problem in finding reagents of suitable nitrating strength and also regioselectivity in the position of nitration.

Zeolite H-faujasite 720 (supplied by Zeolyst Ltd.) was found to exhibit the greatest regioselectivity in the dinitration step using DNPO, with a ratio of **13**:**15** of 4.3:1 attainable (at 0°C, 3 min. reaction time, 94% yield). Taking into consideration the preferred formation of 4-nitrotoluene in the first stage (**14**:**12** = 0.8 to 0.9; cf. mixed acid *ca.* 0.5), this meant that in the overall process the desired product **13** was formed in preference to **15** in a ratio of 10:1. These effects are rationalised in terms of the dimensions of the pores in the zeolite which are comparable to the molecular dimensions of the benzene ring, thus disfavouring the formation of the more bulky *ortho*-nitrated products [7,10].

A more dramatic influence on the regioselectivity of the reaction (Scheme 5) was observed when the zeolite H^+-β was used in conjunction with the nitric acid-TFAA system, in the presence of added acetic anhydride (which enhances the selectivity by retarding the reaction rate). Under these conditions, values of the **13**:**15** ratio of up to 17:1 were obtainable (at -10°C, 2 hr. reaction time, 99% yield). Combined with the selectivities obtainable in the first step (using acetic anhydride only [11]), this meant that selectivities resulting in an overall **13**:**15** ratio of up to 70:1 were attainable where TFAA was added only in the second stage (or 25:1 if it was used throughout).

Thus, as suggested above, the increased regioselectivities obtainable using these systems outweigh to some extent the environmental limitations of the solvents and, moreover, with fewer by-products to dispose of at the end of the respective syntheses, they can still be considered in the green context.

2.2 Nitrations in Supercritical Fluids

In earlier work [2], the syntheses of several nitrate esters and one nitramine were reported in liquid CO_2 using DNPO. Selected reactions have now been optimised, and further new reactions studied. In the nitrate ester series, the use of incremental addition of the nitrating agent, DNPO, raised the yield of n-decyl nitrate (**16**), from the corresponding trimethylsilyl ether, from 5% to 65%. Also, a new substrate, ethyleneglycol (**17**) was nitrated to ethyleneglycol dinitrate (**18**) in 85% yield in a similar procedure.

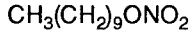

16

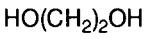

17

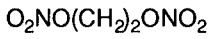

18

Improvements were also obtained in the yields obtainable in nitramine syntheses, in particular by modifications to work-up procedures. Thus yields in the range 45-65% were now routinely obtainable,

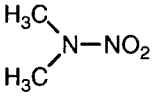

19

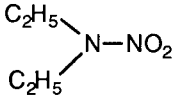

20

and two additional nitramines, N,N-dimethyl- (**19**) and N,N-diethyl- (**20**) nitramines, were accessible by this technology. Although it had been thought [2] that the addition of solvent modifiers, e.g. acetonitrile, to the CO_2 system might improve yields further (observation of the reactions has indicated that they are generally heterogeneous), such modifications were found to have no perceptible effect.

In an extension to the study, the synthesis of a polynitramine, RDX (**21**), was attempted from the triacetyl precursor, TRAT (**22**). DNPO was found to be insufficiently powerful to cleave the N-acyl

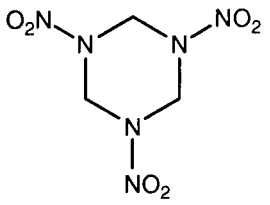

21

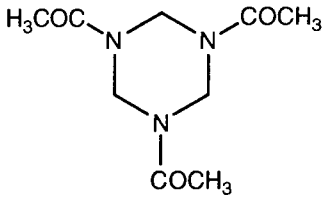

22

functions, so attention was turned to the nitronium salts NO_2BF_4 and NO_2SbF_6. With the former reagent, a very low yield (*ca.* 1%) of RDX was obtained; thus it is concluded that this does not appear to be a viable route for the synthesis of RDX.

3.0 AZIDATIONS

The desirability of replacing strongly polar solvents such as DMF and DMSO in azidation reactions was mentioned above (Section 1.0). Such media are necessary to promote ionisation of the alkali metal azides (e.g. sodium azide) commonly used in the nucleophilic displacement of halides to produce these materials [12]. However, it was felt that in the microenvironment of clay particles, where strong electric field gradients are present [7], such essentially ionic reactions would be facilitated and, indeed, it was found to be feasible to load a K10 montmorillonite clay with sodium azide in a similar way to that employed with transition metal nitrates or DNPO, the novel material so generated being called 'clayzide'.

When clayzide was reacted with molecules containing replaceable halide, organic azide products were formed (Scheme 6). Thus compounds inert to nucleophilic substitution such as 1-chloroadamantane (**23**) or chlorobenzene (**24**) did not undergo substitution, but activated halides such as the benzylic compounds **25** & **26** gave the corresponding azides (**27** & **28**) in high yield in ethanolic medium. It was

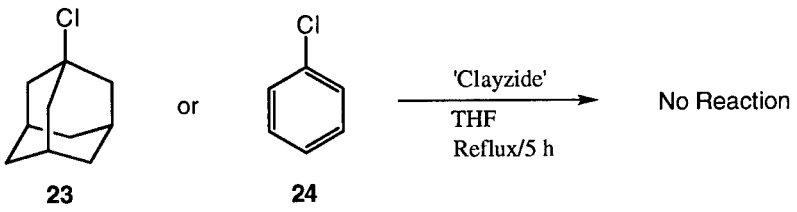

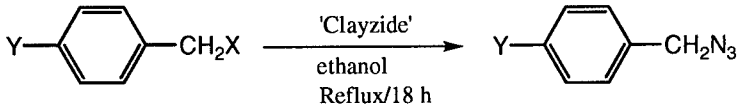

25	X = Br, Y = NO_2	**27**	85%
26	X = Cl, Y = H	**28**	78%

Scheme 6: Azidations by Clay-Supported Azide Reagent ('Clayzide'): Model Compounds

also possible to extend the scope of the reaction to energetic polymers or their precursors (Scheme 7): thus polyepichlorohydrin (**29**) could be converted to the GAP pre-polymer (**30**), and bis-(bromomethyl)-

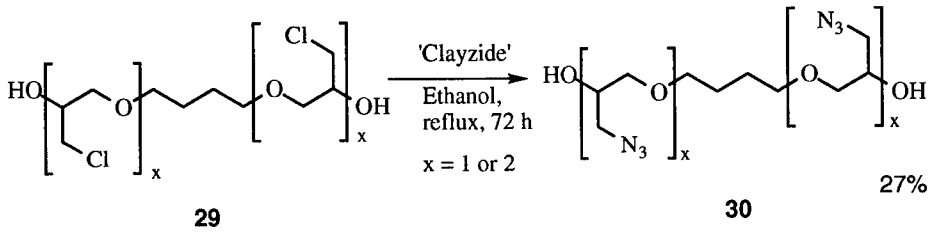

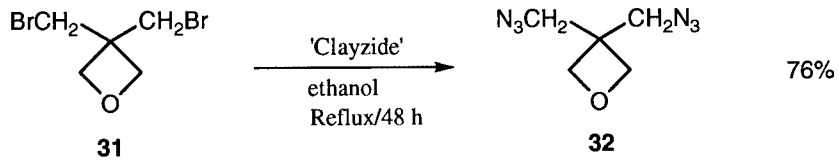

Scheme 7: Azidations by Clay-Supported Azide Reagent ('Clayzide'): Oligomers and Polymer Precursors

oxetane (**31**) gave BAMO (**32**), both reactions again being carried out in ethanol, albeit in somewhat lower yields than the benzylic substrates.

Coincidentally with this work a report appeared of a similar methodology being developed by Varma's group [13], where the clay was first modified by incorporation of a surfactant (creating a pillared clay). This modified clay was then treated with azide and reacted with active halides similarly to the small molecule work detailed above, except that hexane was used throughout as solvent. It is the authors' opinion that, whilst this methodology (essentially under phase-transfer catalysed conditions) may suffice for small molecule reactions, more polar solvents such as ethanol or THF will invariably be required to solubilise macromolecules and their precursors; the two approaches may therefore be regarded as being complementary.

4.0 CONCLUSIONS

A number of approaches towards the cleaner synthesis of energetic materials have been investigated, with the thrust, both in nitration and azidation chemistry, being to eliminate where possible the use of solvents which are harmful to the environment, particularly strong acids, ozone depleters and highly polar solvents. Processes also need to be atom economic [14], i.e. virtually all of the active species on a reagent should be incorporated into the product, so that large excesses of reagent are not required, and if regioselectivity in position of attack (e.g. in aromatic systems) can be achieved, then so much the better. An alternative statement of the penultimate point above is to say that the waste-to-product ratio, as defined by Sheldon [15], should be minimised.

Many of the above aims have now been realised in the work reported here, although further work remains to be done. Specifically, the ability to now perform nitrations, using clay- or zeolite-supported dinitrogen pentoxide, in a medium as inert as hexane is a signal achievement, and the syntheses of further energetic nitrate esters will be investigated/optimised using this methodology. The extension of nitramine syntheses using solid-supported reagents to polynitramines remains a challenge, as does the ability to achieve efficient trinitration of benzene derivatives. Polynitration of benzene derivatives (to the dinitro products) *has* been achieved on solid surfaces but using the solid (zeolite) as a catalyst rather than as a solid-supported reagent. This methodology incurs the penalty of requiring environmentally-unfriendly solvents/co-reactants (e.g. dichloromethane, trifluoroacetic anhydride), and although high regioselectivities are attainable in the position of nitration, which may be beneficial in the synthesis of chemical intermediates e.g. for pharmaceutical or agrochemical application, in the defence context such considerations are of lower importance.

The utility of liquid or supercritical carbon dioxide as a medium for the synthesis of nitrate esters, including polynitrates (e.g. ethyleneglycol dinitrate), and simple nitramines has now been amply demonstrated, although with this medium of course there are limitations to the severity of conditions that

can be employed, since the use of dinitrogen pentoxide dictates that temperatures be kept below 20°C, which is a sub-critical temperature for CO_2 (i.e. supercritical conditions cannot be employed). Also, the scale-up beyond laboratory scale of such reactions remains problematical, with large capital investment being required for process plant.

Finally, in azidations a positive contribution to the environmental friendliness of these reactions has been made through an elimination of the requirement hitherto to use strongly polar solvents such as dimethylformamide or dimethylsulphoxide. The method, using a novel clay-supported azide ('clayzide') is applicable to the synthesis of energetic polymers and their precursors.

5.0 ACKNOWLEDGEMENTS

The authors gratefully acknowledge the contributions of the following:- Prof. Keith Smith and Miss Tracy Gibbins, University of Wales, Swansea; Drs Roy Moodie and John Sandall and Mr Llewellyn Lancaster, University of Exeter.

6.0 REFERENCES

1. A New Route to Nitramines in Non-Acidic Media, R. W. Millar, presented at International Symposium on Life Cycles of Energetic Materials, Del Mar, Calif. USA, 12-16 Dec. 1994.

2. Clean Synthesis of Energetic Materials, M. E. Colclough, R. W. Millar, R. P. Claridge, J. Hamid & N. Chauhan, presented at 1998 Life Cycles of Energetic Materials Conference, Fullerton CA, U.S.A. 29 March - 1 April 1998.

3. A. S. Cumming and N. C. Paul, *Waste Management*, **1997** 17(2/3), 129.

4. *Chemistry of Waste Minimisation*, Ed. J. H. Clark, Chapman & Hall 1995.

5. Novel Syntheses of Energetic Materials Using Dinitrogen Pentoxide, R W Millar, M E Colclough, H Desai, P Golding, P J Honey, N C Paul, A J Sanderson and M J Stewart, presented at 209th ACS National Meeting, Anaheim CA 2-5 April 1995 (*ACS Symp. Ser. 623*, "Nitration: Recent Laboratory & Industrial Developments", Eds. L. F. Albright, R. V. C. Carr & R. J. Schmitt, Ch. 11. Washington DC: American Chemical Society, 1996).

6. R. W. Millar & S. P. Philbin, *Tetrahedron* **1997**, 53(12) 4371.

7. *Solid Supports and Catalysts in Organic Synthesis*, Ed. K. Smith, Ellis Horwood 1992.

8. A. Cornelis & P. Laszlo, *Synthesis* **1980** 849.

9. N. L. Lancaster, R. B. Moodie & J. P. B. Sandall, *J Chem. Soc. Perkin Trans. 2* **1997** 847.

10. N. L. Lancaster, R. B. Moodie, J. P. B. Sandall, R. W. Millar & R. P. Claridge, "Zeolite Catalysis of Aromatic Nitrations with Dinitrogen Pentoxide", *J Chem. Soc. Perkin Trans. 2* **1999** 1815.

11. K. Smith, A. Musson and G. A. DeBoos, *J Org. Chem.* **1998** 63 8448.

12. *Derivatives of Hydrazine and Other Hydronitrogens Having N-N Bonds*, P. A. S. Smith, Benjamin 1983, Ch. 6.

13. R. S. Varma & K. P. Naicker, *Tetrahedron Letters* **1998**, 39 2915.

14. B. M. Trost, *Science* **1991** 254 1470.

15. R. A. Sheldon, *Chem. Ind.* **1997** 12; *ibid.* **1994** 38.

© British Crown Copyright 2000/ DERA Farnborough, Hants. U.K.

Nanostructured Energetic Materials Derived From Sol-gel Chemistry

Randall L. Simpson, Thomas M. Tillotson, Lawrence W. Hrubesh, and Alexander E. Gash
Energetic Materials Center
Lawrence Livermore National Laboratory
Livermore, CA 94550
United States

Abstract

Initiation and detonation properties are dramatically affected by an energetic material's microstructural properties. Sol-gel chemistry allows intimacy of mixing to be controlled and dramatically improved over existing methodologies. One material goal is to create very high power energetic materials which also have high energy densities. Using sol-gel chemistry we have made a nanostructured composite energetic material. Here a solid skeleton of fuel, based on resorcinol-formaldehyde, has nanocrystalline ammonium perchlorate, the oxidizer, trapped within its pores. At optimum stoichiometry it has approximately the energy density of HMX. Transmission electron microscopy indicated no ammonium perchlorate crystallites larger than 20 nm while near-edge soft x-ray absorption microscopy showed that nitrogen was uniformly distributed, at least on the scale of less than 80 nm. Small-angle neutron scattering studies were conducted on the material. Those results were consistent with historical ones for this class of nanostructured materials. The average skeletal primary particle size was on the order of 2.7 nm, while the nanocomposite showed the growth of small 1 nm size crystals of ammonium perchlorate with some clustering to form particles greater than 10 nm.

Introduction

It is known that the mechanical, acoustic, electronic, and optical properties are significantly and favorably altered in materials called "nanostructures", which are made from nanometer-scale building blocks (usually 1 to 100 nm). This approach enables the formation of new materials, generally having improved, exceptional, or entirely new properties. Modern technology, through sol-gel chemistry, provides an approach to control structures at the nanometer scale. In general, initiation and detonation properties of energetic materials are dramatically affected by their microstructural properties. Here, we exploit sol-gel chemistry as a route to process energetic materials and we describe four specific approaches to fabricating energetic nanostructured materials.

Since the invention of black powder the technology for making solid energetic materials has remained either the physical mixing of solid oxidizers and fuels (e.g., black powder) or the incorporation of oxidizing and fuel moieties into one molecule (e.g., 2,4,6-trinitrotoluene). The basic distinctions between these energetic composites and energetic materials made from monomolecular approaches are as follows. In composite systems, desired energy properties can be attained through readily varied ratios of oxidizer and fuels. A complete balance between the oxidizer and fuel may be reached to maximize energy density. Current composite energetic

materials can store energy as densely as 23 kJ/cm^3. However, due to the granular nature of composite energetic materials, reaction kinetics are typically controlled by the mass transport rates between reactants. Hence, although composites may have extreme energy densities, the release rate of that energy is below that which may be attained in a process controlled by chemical kinetics.

In monomolecular energetic materials the rate of energy release is primarily controlled by chemical kinetics and not by mass transport. Hence, monomolecular materials can have much greater power than composite energetic materials. A major limitation with these materials is the total energy density achievable. Currently the highest energy density for monomolecular materials is approximately 12 kJ/cm^3 (about half that achievable in composite systems). The reason for this is that the requirement for a chemically stable material and the current state of the art synthetic procedures limit both the monomolecular oxidizer-fuel balance and the physical density of the material.

We have developed a new synthesis approach to form energetic materials, specifically explosives, pyrotechnics, and propellants, using the chemical sol-gel methodology [1,2]. In energetic nanocomposites we can control oxidizer-fuel balances at the nanometer scale. Sol-gel chemistry involves the reactions of chemicals in solution to produce nanometer-sized primary particles, called "sols". The "sols" can be linked to form a three-dimensional solid network, called a "gel", with the remaining solution residing within open pores. Solution chemistry determines the resulting nanostructure and composition, which in turn determine the material properties. Controlled evaporation of the liquid phase results in a dense porous solid, "xerogel". Supercritical extraction (SCE) eliminates the surface tension and in so doing the capillary forces of the retreating liquid phase that collapse the pores. The results of SCE are highly porous, lightweight solids called "aerogels" [3]. A typical gel structure is characteristically very uniform because the particles and the pores between them are on the nanometer size scale. Such homogeneity ensures uniformity of the material properties, which is one of the key reasons for synthesizing energetic materials using the sol-gel methodology.

The sol-gel approach to energetic materials offers the ability to precisely control the composition and morphology of the solid at the nanometer scale, a result that is difficult or not possible to achieve by conventional techniques. With sol-gel chemistry the process may, in some cases, be carried out with equipment no more complicated than a beaker. We believe that such control of the nanostructure could enable the creation of entirely new energetic materials with desirable properties. One promising result from this work, that supports the our previous contention, is a *decrease* in the impact sensitivity of sol-gel derived energetic nanocomposite materials. For example, we have shown that energetic ingredients processed by conventional methods exhibited drop-hammer impact sensitivities less than 10 cm, whereas the same constituents processed with sol-gel chemistry showed more than 130 cm sensitivity. This finding, with its implications to the safety of energetic materials, may be important in and of itself.

In addition to providing fine nanostructural and compositional control, sol-gel methodology offers other safety advantages in energetic material processing. For example, ambient temperature gelation and low temperature drying schemes prevent degradation of the

energetic molecules, and the water-like viscosity of the sol before gelation allows easy casting to near-net shapes, which may be preferred to the alternatives.

Although sol-gel chemistry is a well-known means of producing nanostructured materials, it was not proposed as a route to create energetic materials until our effort [4]. We have developed four new classes of energetic materials that can be derived through the sol-gel method. Figure 1 graphically depicts the four material classes and their general structures.

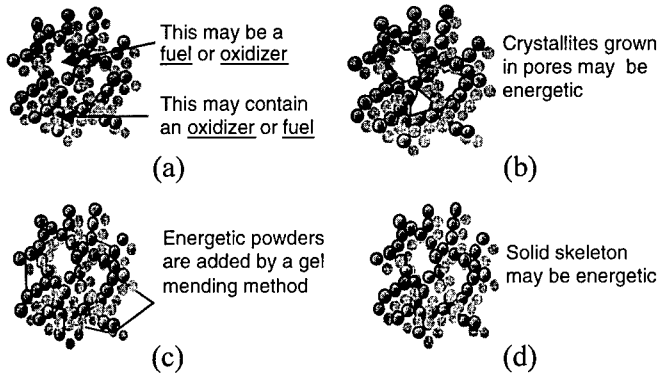

Figure 1. Classes of sol-gel derived energetic materials. (a) Energetic nanocomposite structures. (b) Energetic nanocrystalline materials. (c) Powder addition energetic materials. (d) Energetic skeletal structures.

Energetic Nanocomposites

Using a sol-gel procedure first described by Pekala **[5]** to make aerogels, a porous hydrocarbon solid matrix, was prepared by the polycondensation of resorcinol with formaldehyde (RF) in water. Subsequent crystallization of an oxidizer, ammonium perchlorate (AP), within the pores of the gel matrix, completes the synthesis. The oxidizer was first dissolved in water, then added to the reacting RF sol prior to gelation. Gelation of the RF sol occurred first. Crystallization of the AP was then induced by exchanging the liquid residing in the pores for a solvent in which the oxidizer was insoluble. The final step of removing the pore fluid was done by either a slow evaporation, resulting in a dense solid, or by supercritical extraction with carbon dioxide leading to a low density, highly porous material.

Transmission electron microscopy (TEM) was performed on a nanocomposite synthesized using the procedure described above and is shown in Fig. 2. Inspection of Fig. 2 shows a solid structure composed of interconnected clusters of nanometer-size primary particles, and AP crystallites smaller than 20 nm. Near-edge x-ray absorption was also performed on this nanocomposite. This technique creates an image by scanning a monochromatic x-ray beam, from a synchrotron source, across the sample and recording the near-edge x-ray absorption intensity of nitrogen. Since the only source of nitrogen in the material is AP the distribution of the oxidizer in the nanostructured material can be examined. The results are shown in Fig. 3. It can be seen that that nitrogen is uniformly distributed in the material on a scale less than 43 nm,

which was the limit of resolution for the instrument. These results for the nanostructure were consistent with other published reports on the structure of sol-gel derived materials [6].

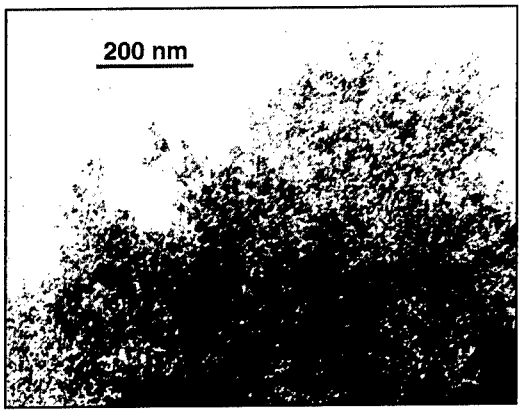

Figure 2. Transmission electron micrograph of a dried resorcinol-formaldehyde sol-gel containing crystallites of ammonium perchlorate showing only nanometer-size particles.

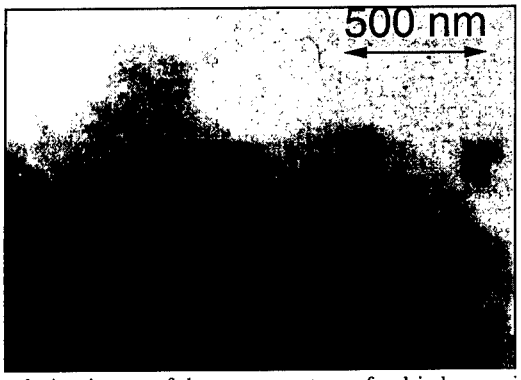

Figure 3. High-resolution image of the nanostructure of a dried resorcinol-formaldehyde sol-gel containing crystallites of ammonium perchlorate produced by near-edge x-ray absorption microscopy. This indicates the uniform distribution of nitrogen within the material. Resolution is 43 nm.

Small-angle neutron scattering (SANS), a non-destructive method for characterizing nanostructures, was also performed on this material. This technique, which measures the neutron scattering intensity as a function of incidence angle, derives information about the average size of scattering particles from the change in slope of a log-log plot of intensity versus momentum transfer. The results, shown in Fig. 4, for the fuel-only (RF) specimens is consistent with other SANS data for gels, which typically give average primary particle sizes of a few nanometers [8,9]. By comparison, the results for the RF-AP nanocomposite bulk material and thin films, indicate extremely small, ≈1 nm particles (probably oxidizer crystals that have grown within the

gel pores), as well as a significant portion of particles larger than 10 nm in diameter. These larger particles are presumed to be larger oxidizer crystals that have grown to occupy several pores. The sol-gel chemistry ultimately offers a means to control the distribution and size of crystals within the gel matrix.

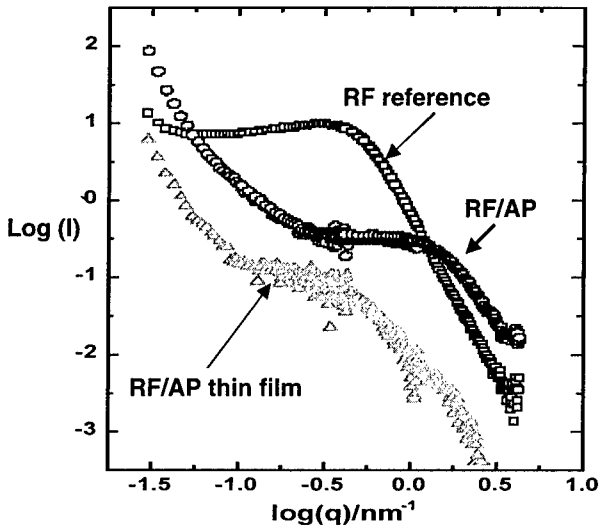

Figure 4. A log-log plot of the intensity of scattered neutrons versus the scattering wave-vector by SANS, is used to characterize the average sizes of scattering particles.

The surface area of the RF-AP nanocomposite was measured using standard BET (Brunauer-Emmett-Teller) adsorption isotherm techniques. The highest surface areas ever recorded on ultralow density, pure RF aerogels are 700-1000 m^2/g [5]. The RF/AP energetic nanocomposite had a measured surface area of 292 m^2/g. This surface area is six or more times greater than the highest surface areas of conventional explosive powders.

The characterization described above shows that the RF-AP material is nanostructured. To determine whether the material was energetic differential scanning calorimetry (DSC) was performed. DSC plots for neat ammonium perchlorate and the RF-AP nanocomposite are compared in Figs. 5a and 5b. The trace for the RF-AP nanocomposite shows a large exotherm beginning at about 250°C, indicating that it is indeed energetic. In contrast, the DSC of pure AP has significantly less integrated decomposition enthalpy in the absence of the gel skeletal fuel (RF). Hence, the RF-AP nanocomposite is indeed energetic.

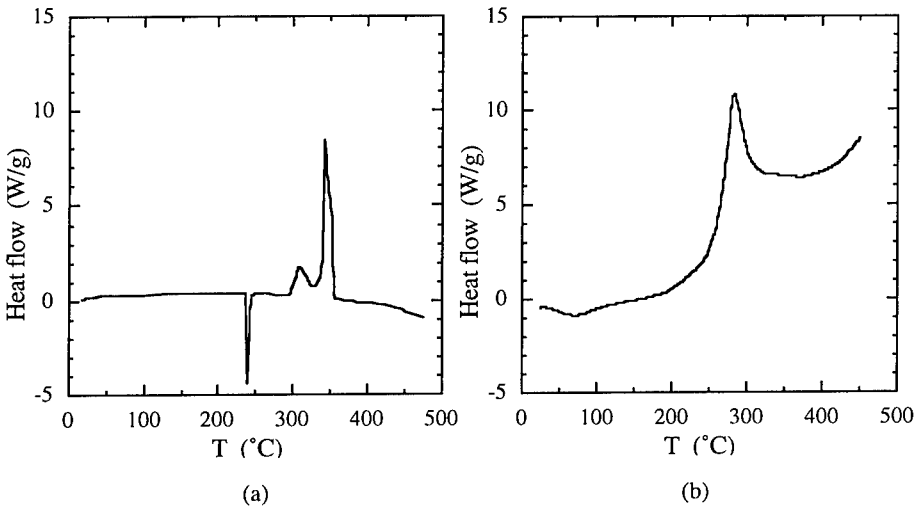

Figure 5. (a) Pure AP showing no significant energy release. (b) RF-AP nanocomposite releasing significant energy above 250°C. The sweep rates were 10°C/min.

Safety of Nanostructured Materials

All of the four classes of sol-gel derived energetic materials have been tested for sensitivity to impact. In the nanostructured energetic materials tested to date the impact sensitivities were found to be significantly less than those observed for analogous conventional materials. For example, a 90wt% PETN/10% SiO_2 xerogel made by the powder addition method (Fig. 1c) resulted in a drop hammer H_{50} value of 133 cm, much greater than with the result for neat PETN, which has an H_{50} value of 17 cm. These results are intriguing because conventionally mixed powders generally exhibit increased sensitivity with the addition of silica powders. PETN-based compositions made by blending with fumed SiO_2 were found to have impact H_{50} values less than 17 cm. The reason for the decrease in impact sensitivity in the sol-gel-derived materials is not fully understood. There are several hypotheses. First, the impact test is essentially a frictional ignition and burn propagation test. Pure aerogels and xerogels have very low convection and conduction thermal transport properties. These characteristics may impede deflagration. Second, whereas most energetic materials have mechanical stress-risers on the order of microns the sol-gel materials have structures on the nanometer scale, hence, impact stresses will be more uniformly distributed. What hot spots are made are likely to be smaller than those that would be generated in conventional materials. At the initial stage of impact induced stress localization the ratio of thermal dissipation to chemically driven thermal generation of the hot spots will be larger with the nanocomposites than with conventional materials. Thus it is more likely that the nanocomposites will have ignition sites below the critical size required for ignition. Decreased sensitivity is one exciting example of the new and different properties attributed to the nanostructured nature of these energetic materials.

Conclusions

The development of sol-gel nanostructured energetic materials appears very promising. We are just beginning to explore the possibilities. A new class of energetic materials may be obtained with improved properties using chemistry that doesn't require complex equipment and processing techniques. Some of the property enhancements of sol-gel derived materials include desensitization and safe processing and handling. The homogeneity may lead to more precise performance. Accurately controlling the crystal size might allow one to tailor the power output in high-energy composite energetic materials.

References and Notes

1. R.L. Simpson, R.S. Lee, T.M Tillotson, G. Fox, R.W. Swansiger and L.W. Hrubesh, patent applied for 1997.
2. T.M. Tillotson, R.L. Simpson, L.W. Hrubesh, second patent applied for 2000.
3. C.J. Brinker and G.W. Scherer, Sol-Gel Science, Academic Press, San Diego, CA, 760 (1990).
4. T.M. Tillotson, L.W. Hrubesh, R.L. Simpson, R.S. Lee, R.W. Swansiger and L.R. Simpson, *J. Non Crystalline Solids* **225**, 358 (1998).
5. R.W. Pekala, *J. Mater. Sci.* **24**, 3221 (1989).
6. G.C. Ruben, R.W. Pekala, T.M. Tillotson and L.W. Hrubesh, *J. Mater. Sci.* **26**, 134 (1991); R. Pahl, U. Bonse, R.W. Pekala, and J.H. Kinney, *J. Appl. Cryst.* **24**, 771 (1991); D. W. Schaefer, R.W. Pekala, and G. Beaucage, *J. Non-Crystalline Solids* **186**, 159 (1995).
7. T.M. Tillotson and L.W. Hrubesh, *J. Non-Crystalline Solids* **145**, 44 (1992).
8. C.J. Merzbacher, J.G. Barker, K.E. Swider, J.V. Ryan, R.A. Bernstein, D.R. Rolison, *Journal of Non-Crystalline Solids,* **225** (1995) 234.
9. C.J. Merzbacher et al., ACS Symposium, Anaheim, CA, (Mar. 21-24, 1999), in press.
10. G. Poelz and R. Riethmueller, *Nucl. Instr. Meth.,* **195** (1982) 491.
11. T.M.Tillotson, I.M. Thomas and L.W. Hrubesh, in Better Ceramics Through Chemistry III, edited by C.J. Brinker, T.E. Clark, and D.R. Ulrich (Materials Research Society, Pittsburgh, 1988) 685.

Acknowledgements

We would like to acknowledge Drs. L. Terminello and W. Meyer-Ilse, of the Lawrence Livermore National Laboratory, for performing the near-edge x-ray absorption microscopy at the Lawrence Berkeley National Laboratory. Mr. M. Wall, also of the Lawrence Livermore National Laboratory, provided outstanding transmission electron microscopy. The neutron scattering work was carried out by Dr. C.J. Merzbacher of the Naval Research Laboratory. Our thanks are given to Dr. Merzbacher for not only the scattering data but for many important discussions about its interpretation.

A NEW LOW-COST SYNTHESIS OF PGN

Louis. F. Cannizzo, Robert. M. Hajik, Thomas. K. Highsmith, Andrew. J. Sanderson, Laura. J. Martins, Robert. B. Wardle
Thiokol Propulsion,
Brigham City, Utah 84302-0707
Email:sandeaj@thiokol.com

Poly Glycidyl Nitrate (PGN) is the most energetic practical elastomeric binder currently available for propellant, explosive and pyrotechnics development. This has prompted a great deal of research to be conducted into its synthesis and characterization. Unfortunately, the two methods for the synthesis of the monomer that have been developed so far (N_2O_5 nitration of glycidol and ring opening of epichlorohydrin with nitric acid followed by ring closure with a strong base) are arguably not ideal due to cost and safety considerations. We have developed a new route to glycidyl nitrate by treating glycerin with nitric acid followed by ring closure of ring closure with sodium hydroxide (scheme 1).

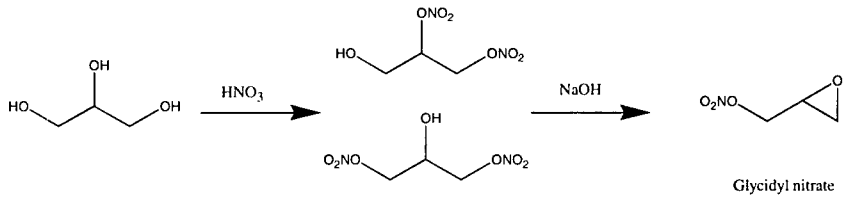

Scheme 1. The synthesis of glycidyl nitrate from glycerin

No purification steps are required to provide a monomer of sufficient purity to polymerize using standard cationic techniques. As the reagents used in this synthesis are cheap and commercially available this procedure greatly reduces the cost of PGN and increases the viability of PGN as a propellant and explosive ingredient. Curing studies and formulation of the PGN made using monomer from this synthesis have been conducted, together with end group modification and extensive characterization and analysis.

Keywords: PGN, energetic binder, synthesis, characterization.

© 2000, Thiokol Propulsion, a division of Cordant Technologies

Introduction

Poly(glycidyl nitrate) (PGN) is a hydroxyl terminated, energetic, poly-isocyanate curable poly ether. When cross-linked with isocyanates it forms tough rubbery materials. Having also a high oxygen balance and high density combined with a moderate heat of formation, it is attractive as a binder for propellant, explosive and pyrotechnic applications. Chemically it behaves as one would expect for a material containing both a polyether backbone and pendant nitrate ester groups.

PGN has been the subject of considerable research and development effort since it was first made some 40 years ago because of the high performance it offers.

Synthesis of the monomer, glycidyl nitrate

According to Urbanski[1], the first synthesis of PGN was conducted in the USA using the route shown in scheme 2:

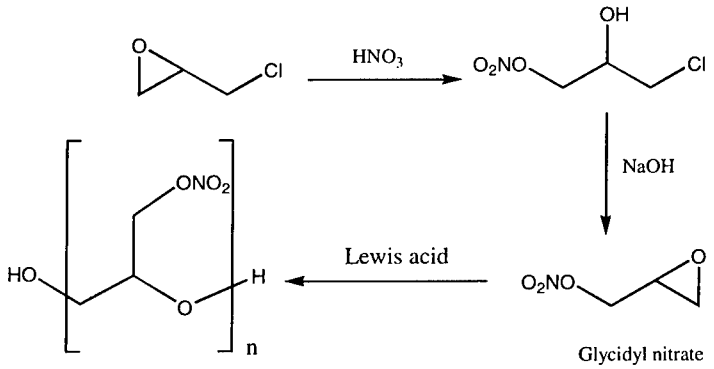

Scheme 2. The synthesis of glycidyl nitrate from epichlorohydrin

The polymer molecular weight was hard to control and tended to be low. It was also hard to obtain sufficiently pure monomer. Although the material looked promising, it was not developed into a practical product at this time.

In the UK in the late '80s, an alternative synthesis of the monomer was developed using N_2O_5 and glycidol. This synthesis was very clean and the monomer could be used directly from the nitration for polymerization. The polymerization was also studied and an alternative method used that reproducibly gave a controllable moderate molecular weight product[2]. It was realized however that on curing there was a tendency for reaction of the polymer chain at the cross-links to occur that resulted in chain scission and softening of the rubber. A solution for this problem was developed in which the prepolymer end groups were modified so that this reaction no longer occurred[3].

At the same time a synthesis was developed at Thiokol, Elkton with a similar polymerization to that used in the UK, but with the monomer made using the epichlorohydrin route. In this instance the monomer was purified by distillation[4].

Another method of preparing the monomer, glycidyl nitrate (GN) was published many years ago but does not appear to have been investigated recently[5]. In this reaction, dinitroglycerine (DNG) is reacted with a strong base and ring closed to the epoxide (scheme 3):

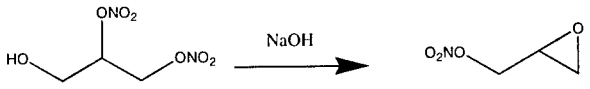

Dinitroglycerine Glycidyl nitrate

Scheme 3. The synthesis of glycidyl nitrate from dinitroglycerine

Dinitroglycerine is not a commercially available material, however it is simply prepared from the reaction of glycerine with nitric acid (scheme 4, see following page):

We thought that it could be possible to conduct these reactions successively in one reactor and so obtain the monomer for PGN from very cheap starting materials. We found that this procedure can indeed be made to work and GN obtained in high purity (figure 1). This GN was polymerized using the published procedures and found to be sufficiently pure for good molecular weight control to be obtained.

In this one-pot synthesis, if a short contact time without a large excess of base is used in the hydrolysis step, the yield of GN is high but significant amounts of NG and DNG remained in the reaction mixture (figure 2). It was found that pure GN, free of nitroglycerine (NG) and DNG could be obtained after prolonged contact with the strong base and but that significant decomposition of the GN also occurred under these conditions. The hydrolysis products were water-soluble so that the GN obtained was pure, but the yield was less than optimal. In the course of optimising the conditions for this reaction, we attempted to polymerize the unpurified GN. Somewhat surprisingly, we found that the same product could be obtained from the GN, NG, DNG mixture that we obtained from pure GN, and thus our nitration/hydrolysis reactions could be optimized so as to maximize the yield of GN without being concerned about NG and DNG impurities.

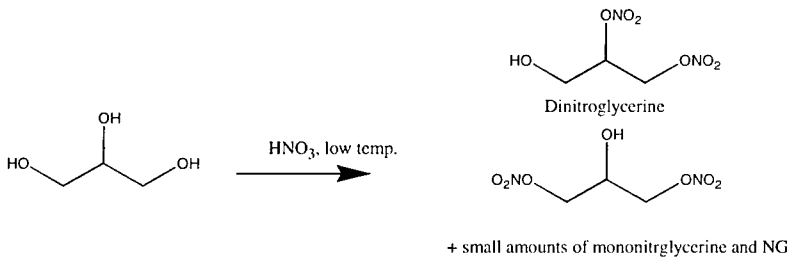

Scheme 4. The synthesis of dinitroglycerine from glycerine

Polymerization of glycidyl nitrate

The polymerization of oxiranes with pendant electron withdrawing groups has been studied but has been found to be more problematic than most other strained ring oxygen heterocycles. The polymerization of GN is no exception to these observations. The best, published polymerizations have resulted only in moderate molecular weights. We have investigated many polymerization conditions, initiators and catalysts, and found that moderate molecular weight and reasonably narrow dispersivity can be obtained from cationic polymerization catalysts and pseudo active-monomer conditions, but that high molecular weight PGN is elusive.

Typical analysis of PGN from out reactions are shown in figures 3-5 (GPC, ^{1}H and ^{13}C).

Characterisation of polyglycidyl nitrate

One of the most challenging aspects of PGN synthesis has been the characterization of the polymeric product. Each unit in the polymer has a chiral center, and this combined with the coupling in the ^{1}H nmr spectrum (figure 4) leads to very broad peaks from which it is not possible to easily determine functionality or molecular weight. The ^{13}C spectra are clearer as there is no coupling to contend with. However, quantitative ^{13}C spectroscopy to analyze the polymer is also extremely difficult.

Typically with hydroxyl functional it is common to give hydroxyl equivalent weight as a polymer characteristic. However we have found that this to is not a parameter to measure or interpret. The usual method we use to determine hydroxyl equivalent weight is to react the polymer with an excess of tosyl isocyanate (TsNCO) and titrate the urethane formed. However it was noticed that the value that this method gave was highly dependant on sample concentration (table 1). It appears that PGN can promote reaction of isocyanates with themselves or urethanes to give allophanates. This is known to be a potential problem with some other polyethers, but it appears to be exacerbated with PGN due to the relative unreactivity of the hydroxyl groups. Further evidence that this can happen is furnished by the observation that crosslinked rubbers can be obtained from PGN with a functionality of ≤ 2 and a difunctional isocyanate like HDI.

Sample size (g)	0.117	0.219	0.550	0.963	2.04
Apparent OH equivalent weight	371	588	1014	1328	1835

Table 1. Variation of apparent OH equivalent weight of PGN by TsNCO method.

We are investigating the common alternative method to determine hydroxyl equivalent weight of reacting the end groups with acetic anydride and titrating with base. This method is known to be more subject to operator variability and is slower than the TsNCO method but we thought that it would not be prone to the same errors. Unfortunately, even if this method gives a number that may be true hydroxyl equivalent weight, it is not necessarily related to the best value to use when conducting curing reactions with isocyanates. Depending on the polymer concentration in a mixture with polymers and solids, and the nature of any catalysts used, the catalysis of the isocyanate side reactions will occur and change the OH to NCO ratio from that calculated.

We routinely use GPC to characterize the polymers we make. GPC studies of our PGN normally return molecular weights and dispersivity relative to a standard. Typically we are able to

consistently obtain polymers with an Mn up to 4500 and Mw of 7000 relative to a polystyrene standard (previous reports give Mn "up to 3500"). This is useful for comparing the product from different reaction conditions. However in the light of the difficulty of quantitative end group and molecular weight analysis by other methods it would be useful if GPC could be used to give absolute values. We are currently in the process of conducting parameterization experiments on a light scattering detector in order to attempt to obtain absolute molecular weight values with GPC.

The eventual use of PGN is as a cross-linked binder. Therefore whilst other quantitative analytical methods for PGN are being developed, we decided that cure studies would determine whether our material is useable. We also considered this to be important in the light of the decuring that has been seen with PGN. To date we have shown that our PGN cures well with or without the presence of plasticisers and solids. It shows much less tendency to decure than other difunctional material that we have tested and it will cure with pl/po ratios of 3. We have not yet determined why our polymer does not appear to decure as previous materials have, but it has been a repeatable observation.

Future studies

We have found a simple route to PGN that gives a very attractive product from inexpensive starting materials. We have scaled our route to 1kg batches and plan to scale up further in the near future and we are conducting curing and formulation studies in propellant and explosive compositions. A primary area for study is the characterization of PGN as we scale up the synthesis in order to maintain product quality and understand process variables. Another area that we will continue to investigate is the curing and aging of gumstocks and formulations.

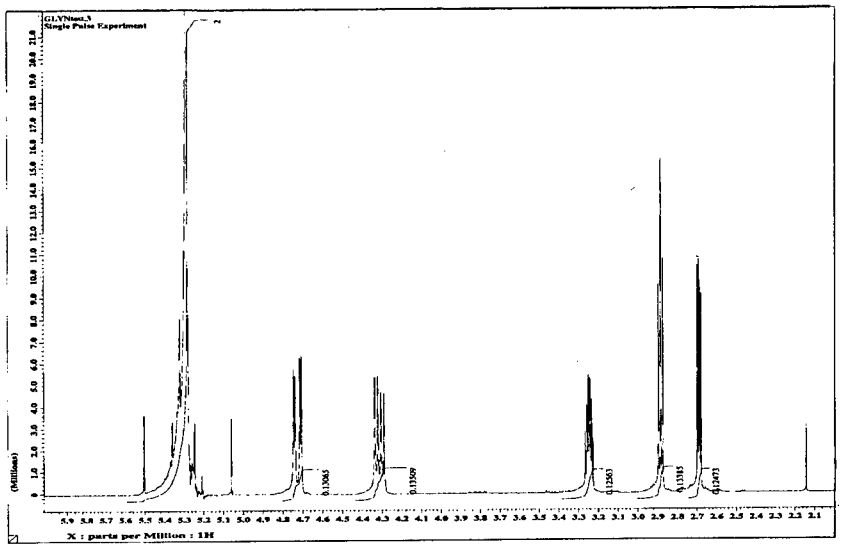

Figure 1. The ^{1}H nmr spectrum of glycidyl nitrate and methylene chloride in CDCl3

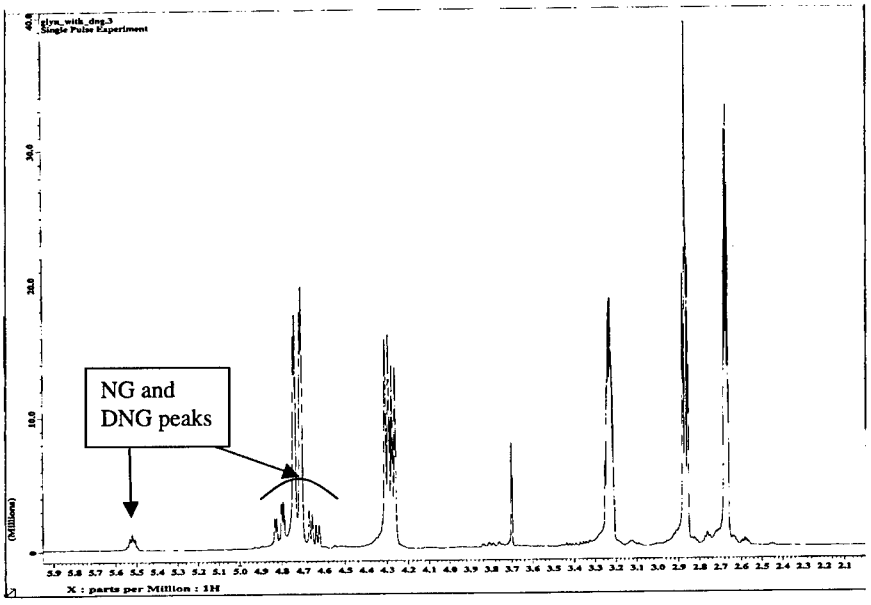

Figure 2. The ^{1}H nmr spectrum of glycidyl nitrate with nitroglycerine and dinitroglycerine in CDCl3.

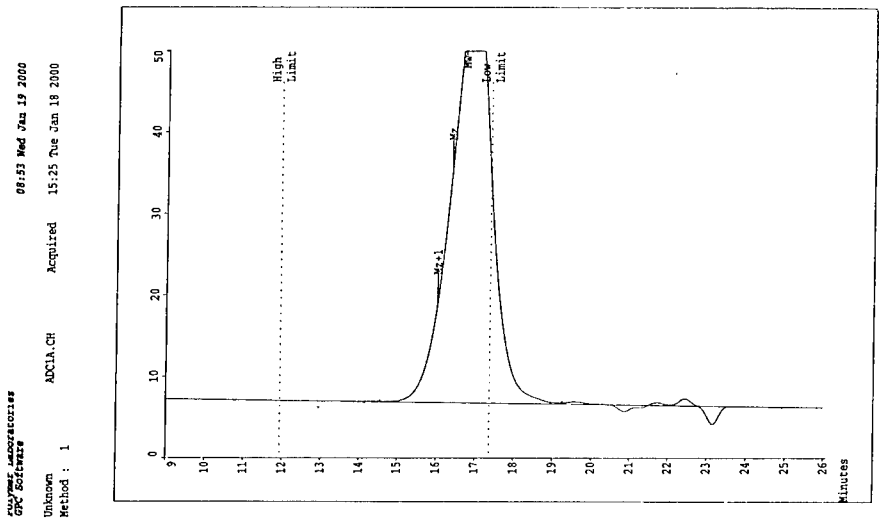

Figure 3. The GPC trace from PGN, Mn=3500 (polystyrene calibration).

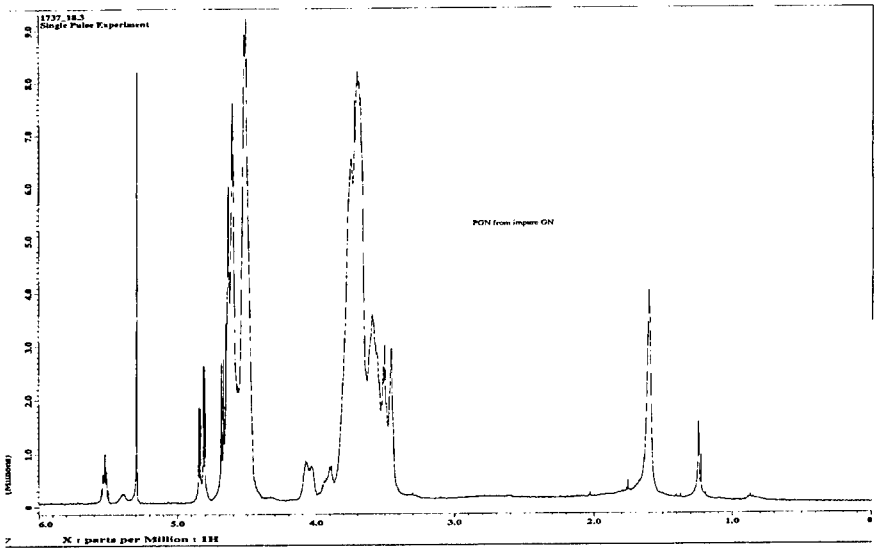

Figure 4. The ^{1}H nmr spectrum of PGN made from impure GN before removal of NG/DNG in CDCl3.

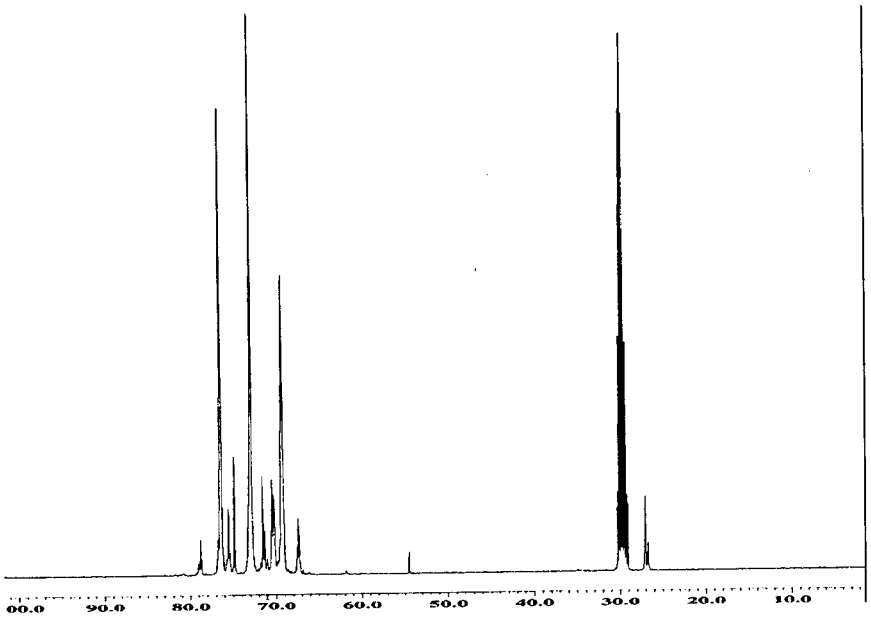

Figure 5. The ^{13}C nmr spectrum of PGN made from impure GN before removal of NG/DNG in CDCl3.

[1] T. Urbanski, "Chemistry and Technology of Explosives" vol 4, Pergamon Press, 1964.
[2] H. J. Desai et al, Polymer vol 37 no.15, pp. 3471-3476, 1996.
[3] W. B. H. Leeming et al, "An investigation into polyGLYN stability", paper 99, 27th International Annual Conference of ICT, 1996.
[4] R. B. Willer, R. S. Day, and A. G. Stern, US Patent US5,120,827, 1992.
[5] Ph. Naoum, "Nitroglycerin u. Nitroglycerinspregstoffe", Springer, Berlin, 1924.

NEW SYNTHESIS OF TATB. SCALEUP AND PRODUCT CHARACTERIZATION*

Robert D. Schmidt, Alexander R. Mitchell, Gregory S. Lee, Michael D. Coburn, Philip F. Pagoria

Lawrence Livermore National Laboratory, Energetic Materials Center

Livermore, California 94551, USA.

W. Timothy Quinlan, Raymond Thorpe, Monty Cates

Mason and Hanger, Co., Pantex Plant

Amarillo, Texas 79120, USA

ABSTRACT

At the 29th International Annual Conference of ICT (1998), we described the results of laboratory-scale process development studies for a new synthesis of 1,3,5-triamino-2,4,6-trinitrobenzene (TATB). This new synthesis approach—which uses vicarious nucleophilic substitution (VNS) methodology—converts picramide to TATB in high yield, and potentially at lower cost and with fewer environmental effects than existing synthetic approaches. In this report we describe results of our work on producing TATB by the VNS method at the pilot plant scale. We will discuss structure and control of impurities, changes in yield/quality with reaction conditions, choice of solvents, workup and product isolation, safety, and environmental considerations. Product characterization (particle size, DSC, HPLC, etc.) as well as small-scale safety and performance testing will also be discussed.

INTRODUCTION

The high degree of thermal and shock stability of 1,3,5-triamino-2,4,6-trinitrobenzene (TATB) is well known, and this compound is often used as a benchmark for comparing insensitive explosives.[1] These remarkable characteristics of TATB favor its use in military[2] and civilian applications[3] when insensitive high explosives are required. Additionally, TATB is a precursor to the intermediate benzenehexamine,[4-8] which has been used in the preparation of

ferromagnetic organic salts[8] and in the synthesis of new heteropolycyclic molecules such as 1,4,5,8,9,12-hexaazatriphenylene (HAT) that serve as strong electron acceptor ligands for low-valence transition metals.[5,7] The use of TATB to prepare components of lyotropic liquid-crystal phases for use in display devices has also been described.[9]

The conventional techniques for producing TATB are expensive and relatively complex, since they rely on environmentally hazardous intermediates and use relatively harsh reaction conditions. Several years ago, we reported a novel approach to the synthesis of TATB which utilizes relatively inexpensive starting materials and mild reaction conditions.[10-12] This new process relies on amination of nitroaromatic starting materials using a reaction known as Vicarious Nucleophilic Substitution (VNS) of hydrogen.[13] Scheme 1 outlines the approach.

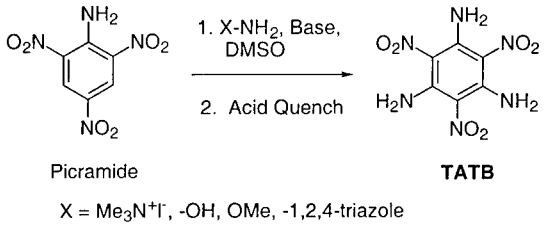

Scheme 1. VNS Synthesis of TATB from Picramide.

We have been working on the scale-up of this new synthesis with the goal of developing a new production of TATB. Our initial studies showed that 1,1,1-trimethylhydrazinium iodide (TMHI) was the most efficient aminating reagent available for the VNS synthesis of TATB.[10-12,14] However, use of TMHI in larger scale work proved impractical. During the process, large amounts of the corrosive, noxious gas trimethylamine are produced, and purity problems are encountered in the product TATB at higher scales.

Consequently, the use of other VNS aminating reagent--such as hydroxylamine and 4-amino-1,2,4-triazole (ATA)--was investigated. This paper examines the results of our work on

the scale-up of TATB synthesis using these reagents, including the effect of reaction conditions on yield, purity, small-scale performance and morphology of the TATB product.

PROCESS STUDIES WITH HYDROXYLAMINE AS THE VNS AMINATING REAGENT

Initial Studies

Hydroxylamine is the earliest known example of a VNS aminating reagent,[15] although the term "VNS" was not coined until many decades later.[13] Our earliest work in aminating picramide with hydroxylamine was disappointing since the reaction only provided DATB containing trace amounts of TATB at best.[11] The poor reactivity of hydroxylamine was independently confirmed by Seko and Kawamura who were unable to aminate nitrobenzene using hydroxylamine.[16] However, the low cost of hydroxylamine as an aminating reagent initiated further investigation and we found that hydroxylamine will in fact aminate picramide to TATB at elevated temperature (65-90°C. One example of successful reaction conditions is outlined in Scheme 2.[17]

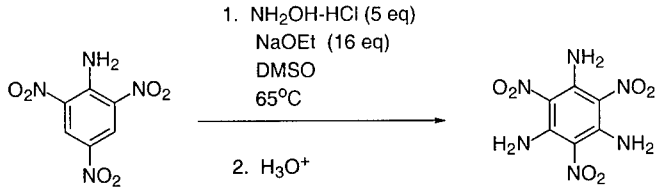

Scheme 2. VNS Synthesis of TATB using Hydroxylamine Hydrochloride.

The relatively low cost of hydroxylamine salts makes this option very attractive.

Studies on Varying Reaction Conditions

In an earlier report[18] we discussed the effects of decreased solvent and reagents on the synthesis of TATB using TMHI. Similar studies were done for hydroxylamine, and it was found that the reaction will run efficiently up to 0.2 M picramide and using 5 eq. of hydroxylamine hydrochloride. The reaction requires twice as much base as with other VNS aminating reagents, since the accompanying hydrochloride moiety needs to be neutralized for the reaction to work. As a result, the reaction mixture forms a rather thick slurry, which makes mixing more difficult. In small-scale tests, the reaction under these conditions produced a 70% yield of TATB, in ~97% purity.

An anomaly has been the formation of an unusual impurity at higher-scale reactions. It was found that as the reaction scale was increased, the product TATB had an increasingly green tint to it. In extreme cases, the product was a distinct drab green. Based on spectroscopic evidence (FTIR and MS) and theoretical calculations, it is believed that the impurity is 1-nitroso-3,5-dinitro-2,4,6-benzenetriamine (Figure 1). Such a compound might result from partial reduction of TATB by hydroxylamine.). It was estimated that this impurity is present in the TATB in up to 10% concentration.

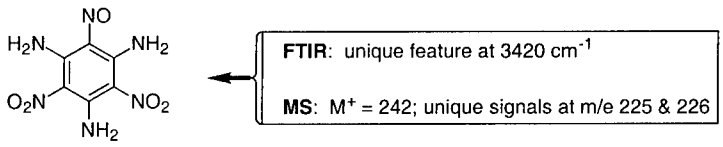

Figure 1. Structure of 1-nitroso-3,5-dinitro-2,4,6-benzenetriamine.

Experiments are currently being conducted to attempt to eliminate the formation of this impurity by introducing oxidants or radical scavengers to the reaction mixture.

In Situ Generation of Hydroxylamine

In order to reduce the thickness of the slurry, attempts were made to pre-neutralize the hydrochloride, filter off the resulting NaCl, and thus generate salt-free hydroxylamine for use in the reaction. Curiously, application of this method failed to produce any TATB, and in fact only small amounts of DATB were detected in the product. The reasons for this failure remain unclear.

PROCESS STUDIES WITH 4-AMINO-1,2,4-TRIAZOLE AS THE VNS AMINATING REAGENT

Due to the difficulties encountered in aminating picramide with hydroxylamine, we investigated a third VNS aminating reagent--4-amino-1,2,4-triazole (ATA). The use of ATA in the amination of nitroaromatics was first reported by Katritzky.[19] As with hydroxylamine, our initial studies using ATA were conducted at room temperature, and we similarly found that ATA only produced DATB under these conditions. However, upon reinvestigation, we found that at elevated temperature (65-70°C), ATA reacts very well with picramide to furnish TATB in excellent yield. Scheme 3 summarizes typical reaction conditions using ATA as the VNS aminating reagent.

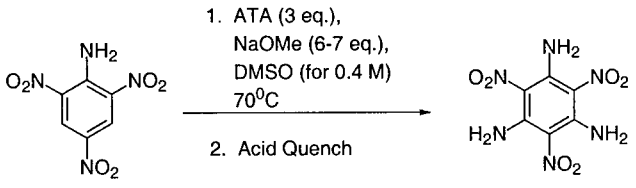

Scheme 3. VNS Synthesis of TATB using ATA.

Several advantages with using ATA soon became apparent. First, the concentration of picramide in the reaction solution can be significantly increased while still retaining excellent

yield and product quality. We have conducted successful, small-scale experiments at up to 0.6M picramide using ATA. Second, the reagent is free of halides, thus ensuring the elimination of such contaminants from the product TATB. Third, the conversion of picramide is complete, and the purity of the product TATB is >99.9%. Product color is also very good, without any trace of the green tint found with hydroxylamine, nor the brown coloration sometimes seen with TMHI. The single disadvantage with ATA at this time is its relatively high cost. However, this is due to a low market demand; when ATA was made in large quantities, its cost was around $13/lb, and synthesis of ATA is simple.[20,21]

Because of these many advantages, ATA was selected as the reagent that we would use in our scale-up of the VNS TATB synthesis. In the lab, we conducted reactions of up to 100 grams, with high yields (92%) and very good product quality (>99.5% pure, golden yellow TATB). Small scale performance testing indicated that this TATB was essentially identical to that produced by traditional methods: highly insensitive to spark, friction and impact; sharp DSC exotherm at 370°C; and satisfactory CRT measurement.

With these results in hand, the process was repeated at our pilot plant facility at a 1 kg scale. Initial results at this scale were encouraging, although some technical difficulties were encountered which resulted in green discoloration (as seen with hydroxylamine) and a somewhat reduced yield. A subsequent experiment resolved most of these problems, and further trials are in progress. Details of these experiments will be presented.

METHODS OF QUENCHING THE REACTION

Upon completion, the reaction solution must be quenched with an acid or other proton source to induce precipitation of TATB. In early work, it was found that use of either aqueous mineral acid solutions or water to quench the reaction results in TATB with a very small particle size, on the order of 0.2-1 μm[18]. Use of organic acids, and quenching at elevated temperature, both increase the product TATB particle size. Thus far, the largest TATB

particles have been obtained by quenching the reaction at 65°C with a solution of salicylic acid in DMSO. See Table 1 for summary of results.

Entry[1]	Acid	Temperature	Particle Size
1	Mineral Acids, Water	25°C	< 1μm[1]
2	Acetic Acid	25°C	1-5 μm[1]
3	Acetic Acid (vapor)	25°C	10-30 μm[1]
4	Citric Acid/DMSO	25°C	5-10 μm[1]
5	Salicylic Acid/DMSO	25°C	5 μm[2]
6	Salicylic Acid/DMSO	65-70°C	25-29 μm[2]

Notes: 1. Particle size estimated by Scanning Electron Microscope photographs.
2. D[v, 0.5], as measured by Malvern Particle Analyzer.

Table 1. Effects of quenching method on TATB particle size.

PRODUCT ANALYSIS

Since TATB is nearly insoluble in most solvents, simpler forms of chemical analysis such as NMR or Gas Chromatography are not practicable. Therefore, other techniques which allow analysis of the solid were investigated. The first of these attempted was Fourier Transform Infrared Spectroscopy (FTIR). The amine N-H stretching modes in TATB produce two characteristic absorptions at approximately 3225 and 3325 cm^{-1}, while those for DATB occur at 3360 and 3390 cm^{-1}. By using Nujol mull or KBr pellet preparations ofTATB samples, we have found that DATB can be reliably detected at concentrations of 1% or greater. Additionally, as mentioned above, the green impurity found in some product TATB samples (suspected to be the mononitroso-analogue of TATB) can be detected by its N-H stretch absorption at 3420 cm^{-1}.

Another technique for TATB product analysis which we are using is direct insertion solids probe mass spectrometry (DIP-MS). In this technique, a solid sample of TATB is placed in a sample holder at the end of a probe. The probe tip is inserted into a mass spectrometer, and is heated to cause the solid sample to evaporate into the MS ion volume,

thereby allowing analysis of solids. Compounds with differing volatilities will evaporate at different times (a process known "probe distillation") and can thus be resolved to some extent by the MS detector. We have found that DATB can be reliably detected in a TATB sample at 1% concentration, and in some cases in concentrations as low as 0.1%.

In order to compare the TATB from this VNS process to that from more traditional processes, we have also conducted DSC, CRT, DH_{50}, spark and friction sensitivity tests on this material. The results of these measurements compare favorable with TATB produced by the traditional methods.

PURIFICATION OF TATB

Because TATB is nearly insoluble in even the strongest solvents, it is not practical to purify it on a large scale using standard recrystallization methods. However, because of the impurities seen in our earlier TATB synthesis studies, we developed a new method for the purification of TATB. A very general procedure is outlined in scheme 4.

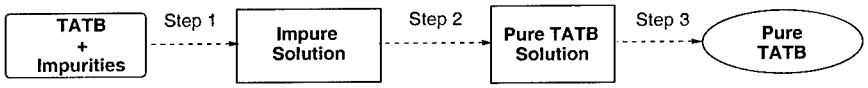

Scheme 4. Purification of TATB by derivatization.

At this time, the details of this method have been submitted for patent protection, and so cannot be included in this paper. However, we hope to be able to present these details in the near future.

ACKNOWLEDGEMENTS

This work was performed under the auspices of the U.S. Department of Energy by Lawrence Livermore National Laboratory under Contract No. W-7405-ENG-48.

REFERENCES

1. Rice, S. F. and Simpson, R. L., "The Unusual Stability of TATB: A Review of the Scientific Literature," Lawrence Livermore National Laboratory, Livermore, CA, Report UCRL-LR-103683 (July, 1990).

2. Dobratz, B.M., "The Insensitive High Explosive Triaminotrinitrobenzene (TATB): Development and Characterization - 1888 to 1994," Los Alamos Scientific Laboratory, Los Alamos, NM, Report LA-13014-H, (August, 1995).

3. Voreck, W.E., Brooks, J.E., Eberhardt, J.R. and Rezaie, H.A., **U.S. Patent 5,597,974**, "Shaped Charge for a Perforating Gun Having a Main Body of Explosive Including TATB and a Sensitive Primer," January 28, 1997.

4. Kohne, B. and Praefcke, K., "Isolierung farblosen Benzolhexamins," *Liebigs Ann. Chem.*, **1987**, 265.

5. Rogers, D.Z., "Improved Synthesis of 1,4,5,8,9,12-Hexaazatriphenylene" *J. Org. Chem.*, **1986**, *51*, 3904.

6. Kohne, B., Praefcke, K., Derz, T. Gondro, T. and Frolow, F., "Benzotri(imidazole) - a New Ring System Derived from Benzenehexamine," *Angew. Chem. Int. Ed. Engl.*, **1986**, *25* , 650.

7. Nasielski-Hinkens, R., Benedek-Vamos, M., Maetens, D. and Nasielski, J., "A New Heterocyclic Ligand for Transition Metals: 1,4,5,8,9,12-Hexaazatriphenylene and its Chromium Carbonyl Complexes,"*J. Organomet. Chem.*, **1981**, *46*, 179

8. Breslow, R., Maslak, P. and Thomaides, J.S., "Synthesis of the Hexaaminobenzene Derivative Hexaazaoctadecahydrocoronene (HOC) and Related Cations," *J.Am. Chem. Soc.*, **1984**, *106*, 6453.

9. Praefcke, K. and Kohne, B., "Amido Compounds as Components of Lyotropic Liquid-crystal Phases," Ger. Offen. DE 3,612,238; *Chem. Abstr.*, **1988**, *108*, 159109n.

10. Mitchell, Alexander R.; Pagoria, Philip F.; Schmidt, Robert D. " A New Synthesis of TATB Using Inexpensive Starting Materials and Mild Reaction Conditions," in *Energetic Materials-Technology, Manufacturing and Processing*, Keicher, T., Ed., Proc. 27th Int. Annual Conf. of ICT. Karlsruhe, Germany, **1996**, 29.1-29.11.

11. Mitchell, A. R.; Pagoria, P. F.; Schmidt, R. D., **U.S. Patent 5,633,406**, "Vicarious Nucleophilic Substitution Using 4-Amino-1,2,4-triazole, Hydroxylamine or O-

Alkylhydroxylamine to Prepare 1,3-Diamino-2,4,6-trinitrobenzene or 1,3,5-Triamino-2,4,6-trinitrobenzene", May 27, 1997.

12. Mitchell, A. R.; Pagoria, P. F.; Schmidt, R. D., **U.S. Patent 5,569,783**, "Vicarious Nucleophilic Substitution to Prepare 1,3-Diamino-2,4,6-trinitrobenzene or 1,3,5-Triamino-2,4,6-trinitrobenzene", October 29, 1996.

13. Makosza, M. and Winiarski, J. "Vicarious Nucleophilic Substitution of Hydrogen", *Acc. Chem. Res.*, **1987**, *20*, 282.

14. Pagoria, P. F.; Mitchell, A. R.; Schmidt, R. D., "1,1,1-Trimethylhydrazinium Iodide: a Novel, Highly Reactive Reagent for Aromatic Amination *via* Vicarious Nucleophilic Substitution of Hydrogen", *J. Org. Chem.* **1996**, *61*, 2934.

15. J. Meisenheimer, J. and Patzig, E., "Directe Einführung von Aminogruppen in den Kern aromatischer Körper", *Ber.*, **1906**, *39*, 2533

16. Seko, S. and Kawamura, N., "Copper-Catalyzed Direct Amination of Nitrobenzenes with O-Alkylhydroxylamines," *J. Org. Chem.*, **1996**, *61*, 442.

17. Mitchell, A. R., Pagoria, P. F. and Schmidt, R. D, U.S. and Foreign Patent Applications have been filed.

18. Schmidt, Robert D.; Mitchell, Alexander R.; Pagoria, Philip F. " New Synthesis of TATB. Process Development Studies" , in *Energetic Materials-Production, Processing and Characterization*, Proc. 29th Int. Annual Conf. of ICT. Karlsruhe, Germany, **1998**, 49.1-49.11.

19. A.R. Katritzky, K.S. Laurenzo, *J. Org. Chem.*, **1986**, *51*, 5039; **1988**, *53*, 3978.

20. Goe, G. L.; Scriven, E. F. V.; Keay, J. G.; Huckstep. L. M. **U.S. Patent 5,099,028**, "Process for the Synthesis of 4-amino-1,2,4-(4H)triazole derivatives", March 24, 1992.

21. Private Communication, Riley Tar and Chemical Corp., 9/26/95.

SYNTHESIS OF PRECURSORS TO MIXED DIFLUORAMINE NITRAMINE ENERGETIC MATERIALS[§]

Theodore Axenrod,[*,a] Jianguang Sun,[a] Kajal K. Das,[a] Paritosh R. Dave,[*,b] Farhad Forohar,[b] Mira Kaselj,[b] Nirupam J. Trivedi,[*,c] Richard D. Gilardi[d] and Judith L. Flippen-Anderson[d]

Contribution from

Department of Chemistry, The City College of CUNY, New York, NY 10031; GEO-CENTERS, INC. at ARDEC, Bldg. 3028, Picatinny Arsenal, NJ 07806; Laboratory for the Structure of Matter, Naval Research Laboratory, 4555 Overlook Avenue, SW, Washington DC 20375; and Energetic Materials Research and Technology Department, Naval Surface Warfare Center - Indian Head Division, 101 Strauss Avenue, Indian Head, MD 20640.

Abstract

Energetic Materials with mixed difluoramine and nitramine functionalities are of interest due to their potential as oxidizer ingredients to provide high energy density and performance characteristics. The synthesis of several precursors to a six-membered ring NF_2-analog of RDX will be presented. Three synthetic routes to 5-substituted-1,3-diazacyclohexane derivatives will be reported. The first method involves treatment of 1,3-diaminopropan-2-ol with paraformaldehyde to yield 5-hydroxy-1,3-diazacyclohexane. A second method is based on the condensation of 2-bromo-2-nitro-1,3-propanediol with t-butylamine and formaldehyde to yield 1,3-di(t-butyl)-5-bromo-5-nitro-1,3-diazacyclohexane. The third method relies on the cycloalkylation of methylenebisacetamide with 3-chloro-2-chloromethyl-2-propene to provide 5-exomethylene-1,3-diacetyl-1,3-diazacyclohexane. Functional group manipulations of the initial derivatives provide a number of novel 1,3-diazacyclohexanes functionalized at the 5-position.

Introduction

The design and synthesis of small[1] and medium-ring[2] nitrogen-containing heterocycles have been investigated in these laboratories as part of a continuing program to prepare novel high density energetic materials with improved sensitivity properties.[3] The chemistry of 1,3-diazacyclohexanes has attracted considerable interest in recent years, since appropriately functionalized compounds of this ring system either serve as

[§] Portions of this paper has been accepted for publication in *J. Org. Chem.*

[a] CUNY
[b] Geo-Centers, Inc.
[c] NSWC-IHD, E-Mail: TrivediNJ@ih.navy.mil
[d] NRL

crucial synthetic precursors or are themselves important members of this class of heterocycles. Examples include 1,3,5-trinitro-1,3-diazacyclohexane and 1,3,5,5-tetranitro-1,3-diazacyclohexane whose syntheses were achieved by the nitrolysis of the Mannich condensation product from nitromethane, formaldehyde and t-butylamine[4-7] as well as by the cyclocondensation of a nitroguanidine.[8] While the parent 1,3-diazacyclohexane,[9] 5-hydroxy-1,3-diazacyclohex-1-ene[10] and more recently 5-exomethylene-1,3-dialkyl-1,3-diazacyclohexane[11] have been reported, general methods for the syntheses of 1,3-diazacyclohexanes derivatives which have been functionalized at the 5-position with other than C-nitro groups, are lacking. In this report, we describe three such approaches to 5-substituted 1,3-diazacyclohexanes that allow for the incorporation of various substituents at the 1,3 and 5-positions, including access to the hither-to-fore unknown 1,3-disubstituted 1,3-diazacyclohexan-5-ones, which are key intermediates for the introduction of a variety of substituents at the 5-positon. Additionally, the facile synthesis of a new energetic material, 1,3-dinitro-5-nitrato-1,3-diazacyclohexane **17**, as well as the chemistry leading to a number of related 5-substituted derivatives of this ring system are described.

Results and Discussion

The construction of the 1,3-diazacyclohexane ring system has been achieved by three pathways. These approaches are depicted below in scheme 1.

In our first method, the ring closure reaction of 2,2-substituted-1,3-diaminopropane with formaldehyde gave the 5,5-substituted 1,3-diazacyclohexane ring which was further derivatized in the 1,3- positions by a variety of reagents. The second method involved the reaction of readily available 2-bromo-2-nitropropan-1,3-diol with t-butylamine and formaldehyde to give the 1,3-diazacyclohexane ring in one step. The reaction of methylenebisacetamide with 3-chloro-2-chloromethyl-2-propene **27** was the basis of our third method to construct the 1,3-diazacyclohexane ring structure.

Scheme 1

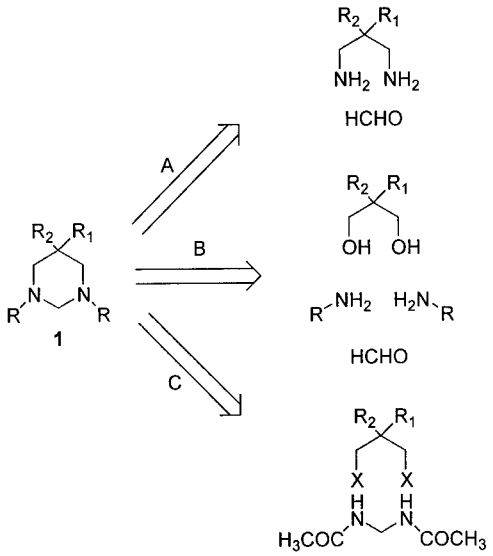

The synthesis of 5-substituted 1,3-diazacyclohexanes by method A described above is elaborated in Scheme 2. Treatment of 1,3-diaminopropan-2-ol **2** with paraformaldehyde in methanol solution affords 5-hydroxy-1,3-diazacyclohexane **3** in 88% yield as a water-soluble hygroscopic colorless crystalline solid.[12] In refluxing 1,2-dichloroethane **3** reacts with acetic anhydride to yield the completely acetylated derivative **10** or with acetic anhydride in potassium carbonate to yield the selectively diacetylated 1,3-derivative **4**. Similarly, propionic anhydride and di-*tert*-butyl dicarbonate convert **3** to the corresponding dipropionyl and di-BOC derivatives, **5** and **6**, respectively. Reduced water solubility and ease of isolation of products derived from the propionyl and butoxycarbonyl derivatives make them in some instances preferable to the acetyl derivatives as reactants. The reaction of **3** with *para*-toluenesulfonyl chloride in presence of potassium carbonate gave 1,3-ditosyl-5-hydroxy-1,3-diazacyclohexane **7** in excellent yield. Analogous reaction of **3** with methanesulfonyl chloride gave the corresponding 1,3-di(methanesulfonyl)-5-hydroxy-1,3-diazacyclohexane, **8**. 1,3-Diamino-2-propanol **2** was also conveniently acetylated in refluxing ethyl acetate to give

1,3-diacetaminopropan-2-ol **9**. The latter on treatment with formaldehyde in acetic acid containing sulfuric acid undergoes a Mannich ring-closure to also produce **10**, albeit in rather poor yield.[13] Selective hydrolysis of **10** by aqueous potassium carbonate also readily affords **4**.

Scheme 2

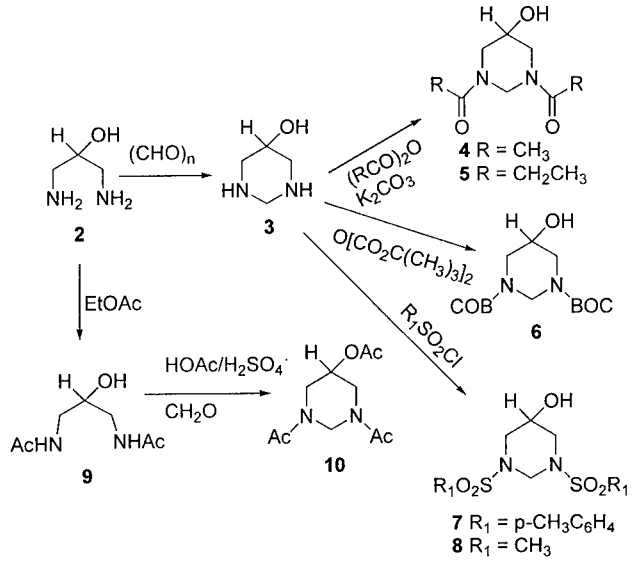

With 5-hydroxy-1,3-diazacyclohexane **3** and related compounds readily available, the synthesis of 5-keto derivatives was investigated as potential key intermediates for the further functionalization of the 1,3-diazacyclohexane ring system at the 5-position. However, attempts to transform the 5-hydroxyl group in either **4** or **5** to the corresponding ketone by various oxidation procedures were unsatisfactory. In our hands, when these materials were subjected to PCC, Jones reagent, Swern oxidation conditions and acetyl nitrate supported on montmorillonite[14] , the corresponding ketone could not be isolated. The failure of the oxidations was attributed to the solubility of the starting materials/products in water which led to the hydrolysis of the aminal group leading to water-soluble ring-opened products. This view is at least partially strengthened by the finding, outlined in Scheme 3, that 1,3-ditosyl- and 1,3-dimesyl-1,3-diazacyclohexane-5-

ol derivatives **7** and **8,** water-insoluble materials, were readily converted by oxidation with Jones reagent to the corresponding ketones **14** and **15**. Although ketones **14** and **15** were found to readily form stable hydrates, the ketone forms were easily recovered by dehydration of the hydrate using azeotropic distillation with benzene or toluene. Reaction of ketone **14** with ethylene glycol in the presence of acid readily converted it to the ketal derivative, 1,4-dioxa-7,9-ditosyl-7,9-diazaspiro[4.5]decane **16**.

Scheme 3

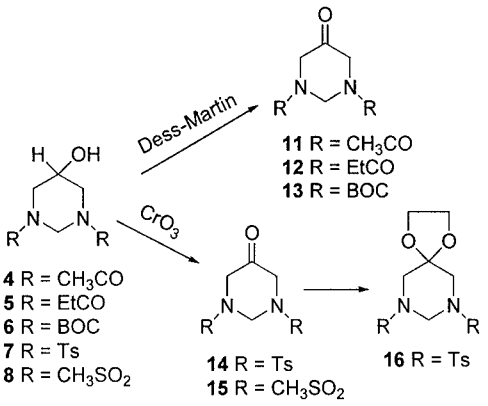

We now report that the Dess-Martin procedure[15] cleanly oxidizes diacylated 5-hydroxy 1,3-diazacyclohexanes to ketones in excellent yields using the preformed 1,1,1-triacetoxy-1,1-dihydro-1,2-benziodoxol-3(1H)-one periodinane reagent in methylene chloride solution. To avoid hydrate formation, product isolation was simplified by a non-aqueous work-up. Addition of ethyl ether to the reaction mixture precipitated the iodobenzoic acid and the organic layer was passed through a short column of silica gel. Elution with ethyl acetate afforded the corresponding ketones **11**, **12** and the di-BOC derivative **13** in yields of 87%, 83% and 100%, respectively.

It is well-established that cyclic polynitramines are important energetic materials.[16] With reasonable quantities of these acylated ketones and related 5-hydroxy-1,3-diazacyclohexane compounds in hand, attention turned toward further functionalization of the ring system to prepare new high energy density materials. 5-

Hydroxy-1,3-diazacyclohexane **3**, when treated with 100% HNO_3 and P_2O_5, produces the 1,3-dinitro-5-nitrato-1,3-diazacyclohexane **17**, in 80% yield. X-ray crystallographic analysis confirms this structure and the crystal density is found to be 1.76 g/cc[3]. The ORTEP diagram for **17** is shown in Figure 1.

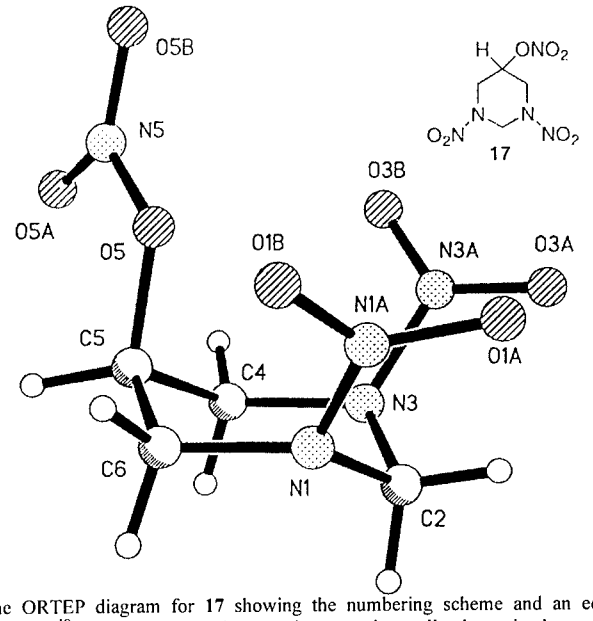

Figure 1. The ORTEP diagram for **17** showing the numbering scheme and an edge-on view of the molecular structure.[19] The figure was drawn using experimentally determined coordinates and thermal ellipsoids represented at the 20% probability level.

When compound **10** was subjected to nitrolysis using either nitric acid and trifluoroacetic anhydride in methylene chloride or nitric acid and P_2O_5 the N-acetyl groups were replaced by nitro groups to give the dinitramino acetate **18**. Hydrolysis of **18** with 5% HCl readily furnished the dinitramino alcohol **19.** Attempts to oxidize the dinitramino alcohol **19** to the desired dinitramino ketone **20** were unsuccessful (Jones, Dess-Martin), perhaps due to the instability of the product during the work-up, but the dinitramino ketone **20** could be prepared from the 1,3-dipropionyl ketone **12**. Thus, treatment of the 1,3-dipropionyl ketone **12** with nitric acid and trifluoroacetic anhydride

in methylene chloride furnished the desired nitrolysis product, 1,3-dinitro-1,3-diazacyclohexan-5-one **20**. These transformations are summarized in Scheme 4.

A second pathway (Method B, Scheme 1) to access this ring system, based on the condensation of 2-bromo-2-nitro-1,3-propanediol **21** with t-butylamine and formaldehyde to yield 1,3-di(t-butyl)-5-bromo-5-nitro-1,3-diazacyclohexane **22**, was examined and is shown in Scheme 5.

Scheme 4

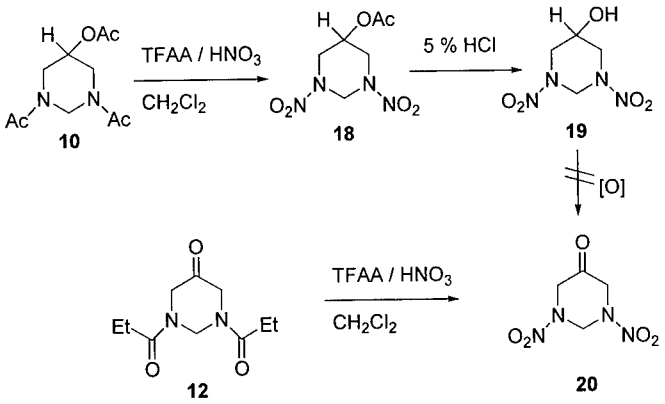

Scheme 5

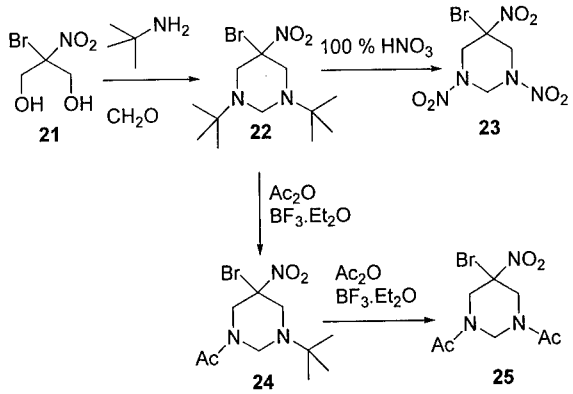

Compound **22** was obtained in 81% yield as a pale yellow crystalline solid. The nitrolysis of **22** with 100% nitric acid gave a 54% yield of 1,3,5-trinitro-5-bromo-1,3-diazacyclohexane **23.** Further transformations involving acylative dealkylation of **22** by reaction with acetic anhydride and BF_3-etherate to afford the corresponding 1-acetyl-3-t-butyl-5-bromo-5-nitro-1,3-diazacyclohexane **24** and 1,3-diacetyl-5-bromo-5-nitro-1,3-diazacyclohexane **25** have been successfully carried out.[17]

The third general approach (Method C, Scheme 1) to the 5-substituted 1,3-diazacyclohexane system is outlined in Scheme 6.

Scheme 6

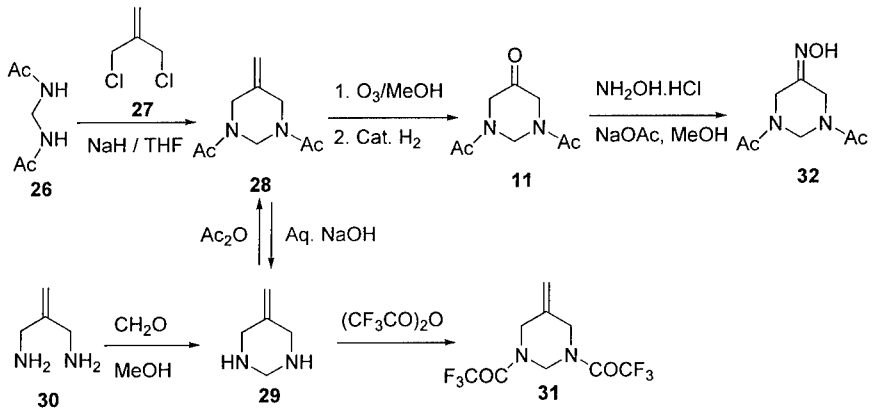

The treatment of the readily available methylenebisacetamide **26** with two equivalents of sodium hydride in THF followed by alkylation with 3-chloro-2-chloromethyl-2-propene **27** resulted in the formation of 5-exomethylene-1,3-diacetyl-1,3-diazacyclohexane **28**. Hydrolysis of the amide functions was achieved by treatment with aqueous alkali to give 5-exomethylene-1,3-diazacyclohexane **29**. The same product was also obtained by the treatment of 3-amino-2-aminomethyl-2-propene **30** with formaldehyde. Alkylation and acylation of the amine functions of **29** provides a general method for the synthesis of 1,3-disubstituted 5-exomethylene-1,3-diazacyclohexanes. This is exemplified by acylations with acetic anhydride to give **28** as well as with

trifluoroacetic anhydride to provide **31**. In order to synthesize the 1,3-diazacyclohexan-5-one system, ozonation of the exomethylene unit in **28** was investigated. Ozonolysis of **28** under various conditions followed by work-up with dimethylsulfide failed to afford isolable product. But, ozonation in methanol followed by catalytic hydrogenation to decompose the ozonide provided 1,3-diacetyl-1,3-diazacyclohexan-5-one **11** in modest yield (50%). It was necessary to monitor the hydrogenation because prolonged exposure to hydrogen resulted in the reduction of the carbonyl function to afford alcohol **4** (scheme 2). Conversion of **11** to the corresponding oxime **32** was accomplished by treatment with hydroxylamine hydrochloride/sodium acetate.

In conclusion, three general approaches to the synthesis of 5-keto-1,3-diazacyclohexane and related 1,3-diazacyclohexanes, all versatile intermediates for further functionalization of the 1,3-diazacyclohexane ring system at the 5-position, have been developed. A number of 5-substituted 1,3-diazacyclohexanes including new energetic materials have been prepared.

Acknowledgment. We thank the Office of Naval Research, Mechanics Division, for financial support of this work.

References:

1. Axenrod, T.; Watnick, C.; Yazdekhasti, H.; Dave, P.R. *J.Org Chem.*, **1995**, *60*, 1959.
2. Dave, P.R. ; Forohar, F.; Axenrod,T.; Das, K.; Qi, L.; Watnick, C.; Yazdekhasti, H. *J.Org Chem.*, **1996**, *61*, 8897.
3. Miller, R.S. *Research on New Energetic Materials*, in *Decomposition, Combustion and Detonation Chemistry of Energetic Materials*; Brill, T.B.; Russel, T.P.; Tao, W.C.; Wardle, R.B. Eds., Materials Research Society Symposium Proceedings: Pittsburgh, PA, **1996**, Vol *418*, pp 3-14.
4. Levins, D.A.; Bedford, C.D.; Staats, S.J., *Propellants, Explos. Pyrotech.*, **1983**, *8*, 74.
5. Cichra, D.A.; Adolph, H.G. *J.Org Chem.*, **1982**, *47*, 2474.
6. Boileau, J.; Piteau, M.; Jacob, G. *Propellants, Explos. Pyrotech.*, **1990**, *15*, 38.
7. Ritter, H.; Licht, H.H. *Propellants, Explos. Pyrotech.*, **1985**, *10*, 147.
8. Yao, G; Xu, Q.; Wan, D.; Yu, Y. *Kogyo Kayaku*, **1982**, *43*, 2.
9. Brown, D.J. in *Pyrimidines and Their benzo Derivatives*, Vol *3*, part 2B, Boulton, A.J. and McKillop, Eds.; in *Comprehensive Heterocyclic Chemistry*, Katritzky, A.R. and Rees, C.W. Eds.; Pergamon Press, NY, 1984.

10. Spry, D.O.; Aaron, H.S. *J.Org Chem.*, **1966**, *31*, 3838.
11. Barluenga, J.; Canteli, R. M.; Florez, J. *J.Org Chem.*, **1996**, *61*, 3646.
12. In the presence of excess formalin, 1,3-diaminopropan-2-ol is reported to give 1-formyl-5-hydroxy-3-methylhexahydropyrimidine which presumably arises from an intramolecular hydride transfer process involving a methyleneamino intermediate. See: Bagga, M.M.; Everatt, B.; Hinton, I.G. *J. Chem Soc., Chem. Commun.*, **1987**, 259.
13. Vail, S.L.; Moran, C.M.; Moore, H.B. *J.Org Chem.*, **1962**, *27*, 2067.
14. de Oliveira Filho, A.P.; Moreira, B.G.; Moran, Paulo J.S.; Rodrigues, J. Augusto R.; *Tetrahedron Lett.*, **1996**, *37*, 5029.
15. a) Ireland, R.E.; Liu, L. *J.Org Chem.*, **1993**, *58*, 2899. B) Dess, D.B.; Martin, J.C. *J. Am.Chem.Soc.*, **1991**, *113*, 7277.
16. Nielsen, A.T; Chafin, A.P.; Christian, S.L.; Moore, D.W.; Nadler, M.P.; Nissan, R.A.; Vanderah, D.J.; Gilardi, R.D.; George, C.F.; Flippen-Anderson, J.L. *Tetrahedron*, **1998**, *54*, 11793.
17. Dave, P.R.; Kumar, K.A.; Duddu, R.; Axenrod, T.; Dai, R.; Das, K.K.; Guan, X.P.; Sun, J.; Trivedi, N. J., Gilardi, R. in this issue.
18. X-ray crystallographic analysis and ORTEP diagrams are included in the supporting information for this article. Crystallographic data (including structure factors) for the structures reported in this paper have been deposited with the Cambridge Crystallographic Center. Copies of available material can be obtained, free of charge, on application to the Director, Cambridge Crystallographic Data Center, 12 Union Road, Cambridge CB2 1EZ. UK (fax: +44-(0)1223-336033 or e-mail: deposit@ccdc.cam.ac.uk).
19. Sheldrick, G. M., SHELXTL Version 5 Software Reference Manual (1994 Release). Siemens Energy and Automation, Inc., Madison, WI 53917-1173, USA.
20. Noyes, W.A.; Forman, D.B., *J. Amer. Chem. Soc.*, **1933**, *55*, 3493.
21. Schulze, V.K.; Winkler, G.; Dietrich, W.; Muhlstadt, M. *J. Prakt. Chem.* **1977**, 463.

Henryka Boniuk, Iwona Cieślowska-Glińska, Michał Syczewski

Division of Highenergetic Materials, Faculty of Chemistry,
Warsaw University of Technology (Politechnika)
Noakowskiego 3, 00-664 Warsaw, Poland

SYNTHESIS AND PROPERTIES OF SALTS OF DINITROAMIDE (DNA) WITH VARIOUS AMINES.

Abstract

Salts of DNA were prepared in the reaction of pure DNA or its ammonium salt with amines. Thermal stability, susceptibility to hydrolysis and sensitivity to mechanical stimuli of prepared compounds were determined. Some of the salts showed good or satisfactory thermal stability and low susceptibility to hydrolysis, and therefore their use as explosives or components of energetic mixtures would be taken into consideration. For example, salt of triethylenetetramine (TETA) with dinitroamide - $TETA(DNA)_4$ is not susceptible to hydrolysis and its explosive strength is comparable with that of RDX (on ballistic mortar). A salt of ethylenediamine with DNA shows similar properties. Identity and purity of synthesised compounds were determined using elemental analysis, DTA-TG and spectrophotometric methods.

Keywords: dinitroamide salts, ammonium salts

Introduction

Being a strong acidic radical, hydrogen dinitramide (DNA), ever since it's detection has been used to synthesise different salts, also those with substituted ammonium bases [1,2]. The properties of these salts differ highly in stability and hygroscopicity. These features, as well as heat resistance and energetic characteristics, decide about the possible practical use of these salts as components of energetic materials.

Amine salts can theoretically be utilised not only as oxidisers but also as independent explosives. Depending on the type of amine, its

dinitramide salt may have a different oxygen balance and therefore different energetic characteristic.

This work compiles the thermochemical characteristics of chosen salts, whose stability, heat resistance, spontaneous decomposition temperature and energetic characteristics seem promising as far as future practical uses are concerned. The selected dinitramide salts were obtained, purified and identified. Their thermochemical properties, friction sensitivity and in some cases also working capacity have been determined.

Experimental

The salts were synthesised mainly through the neutralisation of a hydrogen dinitramide solution ($HN(NO_2)_2$) with pure organic bases. The $HN(NO_2)_2$ solution was obtained through the following reaction:

$$MN(NO_2)_2 + HCl \longrightarrow HN(NO_2)_2 + MCl\downarrow$$

where M is a metal, whose chloride does not solubilize in the used solvent (e.g. anhydrous ether). The treatment of the $MN(NO_2)_2$ suspension was conducted with a substantial excess of HCl, which guaranties full chemical change of the salt into free DNA. The amount of the solvent should be significant enough, that the concentration of the forming $HN(NO_2)_2$ acid not exceed 60% or otherwise intensive decomposition may take place (even accompanied by an explosion).

The reaction of salt formation proceeds according to the following equation:

$$HN(NO_2)_2 + R_nNH_{3-n} \longrightarrow R_nNH_{4-n}\cdot N(NO_2)_2$$

Yields were as high as 98-100%. The purity of the product – based on analysis of the UV spectrum and the results of elemental analysis - was so high, that the salt frequently did not require crystallisation.

In the case of strong bases, that is those whose pK_a is higher than that of NH_3, the salts were obtained by heating $NH_4N(NO_2)_2$ with a free base:

$$NH_4N(NO_2)_2 + R_nNH_{3-n} \longrightarrow R_nNH_{4-n} \cdot N(NO_2)_2 + NH_3$$

The UV spectra (to determine the amount of the dinitramide anion) were recorded on the Specord UV VIS Carl Zeiss Jena spectro-photometer.

DTA -TG analysis was recorded on the Derivatograph PC MOM Budapest and the sample was brought to full decomposition.

Sensitivity to mechanical stimuli (friction) was tested on the BAM friction sensitivity apparatus (Julius Peters KG, Berlin, Germany) and through the working capacity ballistic mortar method.

Results and Discussion

Some of the salts were excluded from detailed study due to their high hygroscopicity and low stability even in STP conditions (e.g. salts with hydroxylamine, urea, hydrazine etc.). Table 1 compiles salts, whose properties promise practical utilisation.

Table 2 compiles the results of elementary analysis of chosen salts. The high conformity of the results of elementary analysis and presumed composition of the salt confirm the observed almost 100% yield of the neutralisation reaction, especially in the case of strong organic bases. This is why all of the ($HN(NO_2)_2$) acid (e.g. salt 3 Table 1) is attached to the amine, if there exists a deficiency of the acid.

Table 1

No	Salt	solvent recryst	mp decomp.p	friction sensitivity	oxygen balance
			°C	[kG]	[%]
1	2	3	4	5	6
1	$NH_2C_2H_4NH_2 \cdot 2HN_3O_4$	i-C_3H_7OH	125 136	11.76	-5.8
2	$NH_2(CH_2CH_2NH)_2CH_2$ $CH_2NH_2 \cdot 4HN_3O_4$	CH_3OH	159 163	4.7	-19.5
3	$NH_2(CH_2CH_2NH)_2CH_2$ $CH_2NH_2 \cdot 3HN_3O_4$	CH_3OH	oil 173,5	7.8	-36
4	$(O_2NOCH_2CH_2)_2NH \cdot$ HN_3O_4	CH_3OH	114 135	18.4	- 15.9
5	$H_2NC(NH)NH_2 \cdot HN_3O_4$	CH_3OH	148 176	>23.5	-9.6
6	$H_2NC(NH)NHNH_2 \cdot HN_3O_4$	C_2H_5OH	94 180	18.4	- 13.3

Table 2

No	Salt	Chemical analysis					
		C [%]		H [%]		N [%]	
		teoret.	exper.	teoret.	exper.	teoret.	exper.
1	2	3	4	5	6	7	8
1	$H_2NCH_2CH_2NH_2 \cdot 2HN_3O_4$	8.76	8.95	3.65	3.62	40.88	40.32
			8.99		3.68		40.59
2	$H_2N(CH_2CH_2NH)_2CH_2CH_2NH_2 \cdot$ $4N_3O_4$	12.54	12.65	3.83	3.80	39.02	38.48
			12.58		3.83		38.59
3	$H_2NC{=}NHNH_2 \cdot HN_3O_4$	7.23	6.94	3.61	3.64	50.06	49.52
			6.99		3.57		49.59
4	$H_2NNH_2 \cdot HN_3O_4$	-		3.6	3.56	50.36	49.16
					3.66		49.20

Some of the parameters given in Table 1 derived from the DTA-TG study, the results of which are presented in Fig. 1-5. The heating rate of the samples was equal 2°C/min. It must be pointed out, that the melting point and decomposition point (in Table 1) are given for the maximum peak of DTA, (not for the onset point). According to these determinations ammonium salt possesses m.p.≈ 96°C and decomposition point≈ 127°C.

Ethylene diamine salt with two $HN(NO_2)_2$ molecules (Fig. 1) can serve as a model salt. By the course of the TG we can tell that neutralisation of both amine groups ensures good thermostability of the salt up to its melting point. Above the melting point the fast exothermic decomposition occures accompanied by rapid mass decrement of the sample. We observe a similar course of the DTA-TG in the case of a DNA salt with triehylenetetramine (Fig. 2), when all the amine groups undergo neutralisation. When the amount of DNA used suffices only to neutralise three amine groups, the product shows an apparent deterioration in stability (Fig. 3). We can observe slow decomposition starting from normal temperature up to the temperature of spontaneous breakdown ($\Delta TG \neq 0$), although the temperature is higher, than the breakdown temperature of fully neutralised triethylenetetramine. The sensitivity of the not fully neutralised salt is much lower.

The DTA has a more complex course in the case of guanidine salt, where there are two endothermic peaks (at 107°C and 149°C) despite repeated crystallisation of the product. Explaining the change at 107°C requires further study. It is possible that the main product along with trace impurities (e.g. NH_4NO_3) forms eutectic (which melts at 107°C). We can observe a similar situation in the case of guanidine nitrate [3].

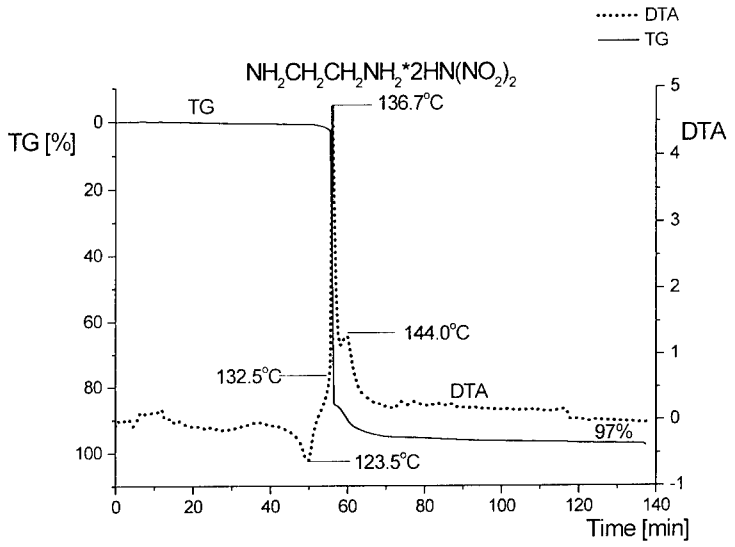

Fig.1 Thermogram $NH_2CH_2CH_2NH_2 \cdot 2HN(NO_2)_2$; mass of simple= 44.30mg; air atmosphere; heating - 2°/min.

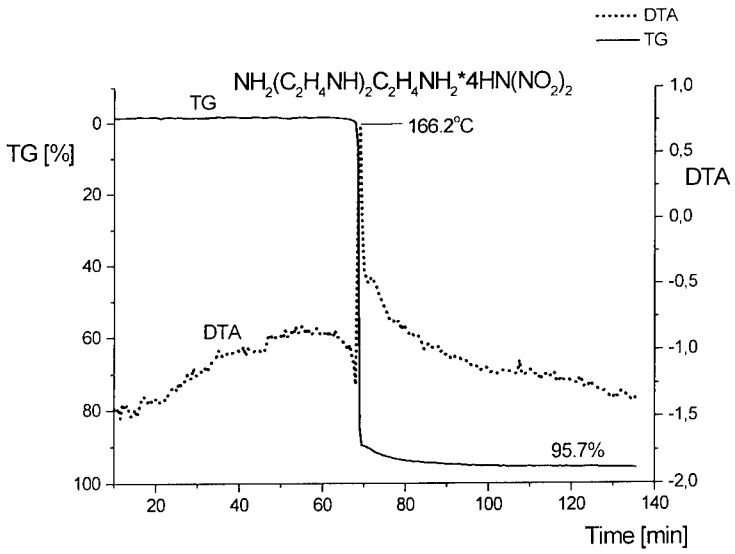

Fig.2 Thermogram $NH_2(C_2H_4NH)_2C_2H_4NH_2 \cdot 4HN(NO_2)_2$; mass of simple= 15.62mg; air atmosphere; heating - 2°/min.

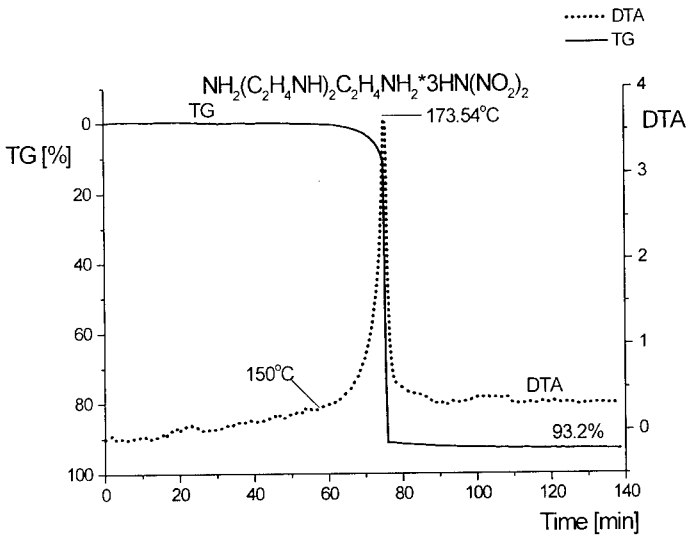

Fig.3 Thermogram $NH_2(C_2H_4NH)_2C_2H_4NH_2 \cdot 3HN(NO_2)_2$; mass of simple= 32.90mg; air atmosphere; heating - 2°/min.

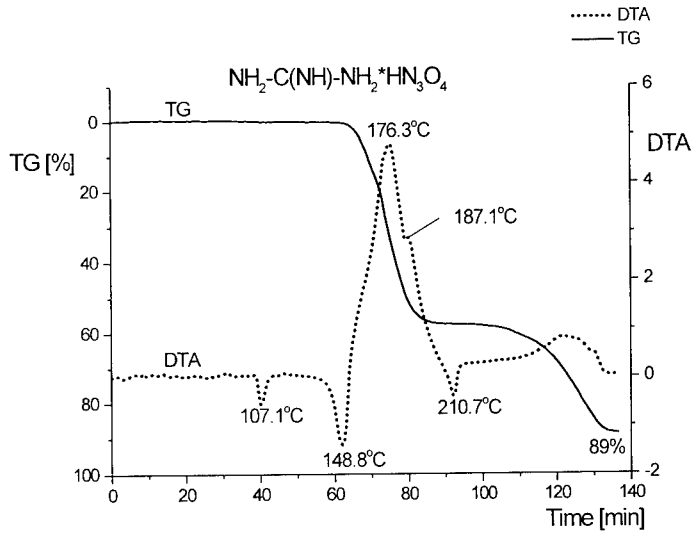

Fig.4 Thermogram $NH_2\text{-}C(NH)\text{-}NH_2 \cdot HN(NO_2)_2$; mass of simple= 43.90mg; air atmosphere; heating - 2°/min.

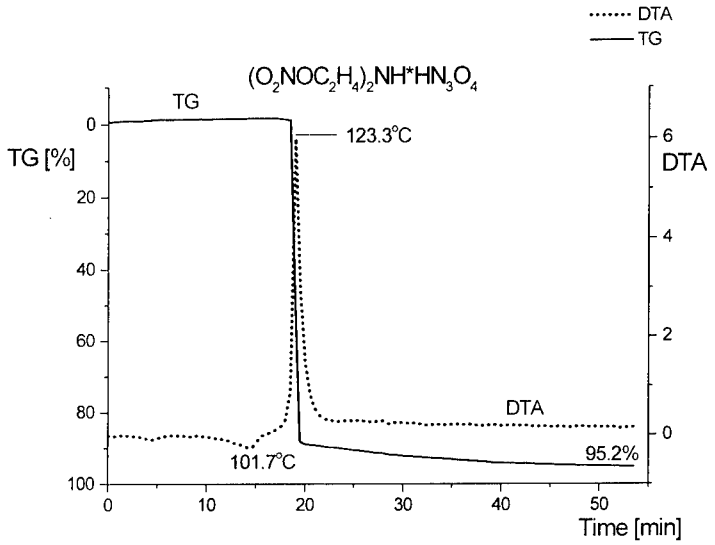

Fig.5 Thermogram $(O_2NOC_2H_4)_2NH\ HN(NO_2)_2$; mass of simple= 12.63mg; air atmosphere; heating - 5°/min.

Despite containing ester groups, DNA salt with diethanoloamine trinitrate (Fig. 5) shows good stability up to the temperature of spontaneous breakdown.

Useful properties of the studied salts

Sufficiently high thermostability of the studied salts, their unhygroscopicity and positive oxygen balance, seem to suggest, that these substances can be used as independent high-energetic materials, as well as components of compound energetic materials. For example, the working capacity of salt No 2 (Tab. 1) (determined through the ballistic mortar working capacity method) is exactly equal that of RDX. We can therefore conclude that for salts with a better oxygen balance, the work-

ing capacity will be even higher. It is a well-known fact that triethylenetetramine is used for hardening epoxide resins. It has turned out that its salt together with DNA also possesses the ability to crosslink (reticulate) epoxide resin, raising the energetic characteristics of such a binder at the same time.

Thanks to the fact, that it contains ester nitrate groups, salt No 4 (Tab.1) can plasticize nitrocellulose. It can therefore be an active component of smokeless powder.

Financial support from the State Committee for Scientific Research (KBN - Project Nr 0 T00A 032 16) is gratefully acknowledged

REFERENCES

1. O.A.Łakianow, A.R. Agewnin, A.A. Lejczenko, N.M. Seregina, W.A.Tartakowskij; Izw. Akaad.Nauk.Ser.Chem. 1995, 113
2. I.Cieślowska-Gińska, M. Syczewski - Wiadomości Chemiczne (in prep)
3. T.Urabański; Chemistry and Technology Explosives V2, Pergamon Press PWN-Polish Scientific Publishers Warszawa 1956

31 st International Annual Conference of ICT

CAPILLARY EXTRUSION RHEOMETRY AND EXTRUSION OF PROPELLANTS AND PROPELLANT SIMULANTS

by Aat C. Hordijk, Inge van der Velde, Casper Schoolderman and Rob Sabel
TNO Prins Maurits Laboratory, P.O. Box 45, 2280 AA The Netherlands

Summary

At the TNO Prins Maurits Laboratory work has been done on extrusion for several years and recently on extrusion rheometry. Because of an international trend towards the development and application of propellants using energetic TPE's like AMMO/BAMO (USA) and GAP-based TPE's (Canada), we started four years ago with non-energetic TPE's to obtain experience with the processing characteristics.
Three different TPE's have been tested and two were selected for further experimental work. Processing characteristics have been determined using a Rosand twin bore capillary extrusion rheometer (CER).
It was quickly found out that solventless processing of a highly filled TPE at about 60 to 90 °C exceeds the safety limits for extrusion and an optimum amount of solvent had to be determined using inert and energetic fillers.
CER experiments with live propellants and various amounts of solvent were performed. The results were recalculated to head pressures to be expected. The calculated pressures correspond well with those measured.

Propellants based on a TPE have been produced on a small scale and tested. The results in terms of processing characteristics and mechanical properties are presented.

Keywords
Flow characterisation, Rheometry, TPE, processing,

2. Introduction

At the TNO Prins Maurits Laboratory work has been done on extrusion [1, 2] and now recently on extrusion rheometry [3]. We started four years ago with nonenergetic TPE's to obtain experience with the processing characteristics, prior to the use of energetic TPE's like AMMO/BAMO (USA) [4, 5] and based on GAP Canada) [6] which are advantageous because of their increased performance, their environmental friendliness (less solvent and decreased propellant spill) and the possibility of recycling after the service life time has been passed.

The compositions discussed in this paper, contain an energetic filler or a mimic thereof and a compounded TPE binder. Three major aspects are discussed:

- the selection of a suitable TPE,
- the effect of solvent for a given composition,
- an estimation of extruder head pressures to be expected based on rheological data.

Some of the above mentioned aspects also influence the properties of the composition after processing, for instance the mechanical properties and the performance.

The processing of PBXs at TNO-PML is carried out using

- a small scale 300 ml IKA mixer for preliminary processing characterisation,
- a larger HKV 5 (max 3 liter) and HKV 25 (10 liter capacity) mixer for casting of larger test items and
- a twin screw extruder [1].

The compositions described here are based on TPE's. The TPE's used are non-energetic and of the polyStyrene /polyButadiene type. Unfilled TPE's behave as visco-elastic fluids when tested at temperatures above their softening point and they are processed at temperatures of 10 to 100 °C above this point. By mixing the filler is introduced into the TPE matrix. The filler-binder interaction is based on physical-chemical forces.

The rheological behaviour may be measured with:

- a Haake RT 10 Rheometer to determine the visco-elastic properties [2] of the TPE,
- a Rosand twin bore Capillary Extrusion Rheometer and
- a Thermal Mechanical Analyser and a draw-bench to determine the mechanical properties of the extruded compositions [2].

This paper deals with extrusion, with product and preproduct characterisation and with the recalculation of rheological data to head pressures to be expected.

3. Characterisation of TPE's

The various types of TPE tested are described in table 1. Presented are the composition of the TPE's compounded with various percentages and types of plasticiser as obtained from Wittenburg BV in The Netherlands.

Table 1 Overview of TPE's tested

TPE type	Composition	MFI (°C)
4427	SEBS – di and tri blocks	8 g / 10 min. (200)
3718	SIS + < 5% plasticiser + resin	3.5 g / 10 min. (230)
2747	SEBS + 50 % plasticiser	16 g / 10 min. (190)

The softening points have been determined with the Haake RT 10 performing a temperature sweep and with TMA (TMA /SS-150 from Seiko). The T_s values found with both methods are presented in table 2 and agree very well.

Table 2 Comparison of softening temperature as determined with Haake and TMA

Compounded TPE code	TMA ; T_s (°C)	Haake; T_s (°C)	TMA; T_g (°C)
2747	67	61	- 62
3718	51	63	
4427	83	-	-

The TPE's have been tested in the Capillary rheometer at various temperatures. The apparent shear stresses found are corrected for the entrance effect giving a corrected shear stress as a function of apparent wall shear rate. The typical results of the TPE 4427 are shown in figure 1.
From fig 1. it is learned that

- a yield stress probably exists at temperatures near to T_s
- slip occurs at higher apparent shear rates ($\dot{\gamma} > 100\ s^{-1}$) and stresses higher than about 600 kPa; the velocity at the wall is no longer zero
- the rheological behaviour may be described by the Herschel-Bulkley equation in between these shear rates and
- this behaviour changes towards a power fluid with increasing temperature

The Herschel-Bulkley equation reads as follows

$$\tau = \tau_0 + K \dot{\gamma}^{n} \quad (0 < n < 1) \qquad \text{(eq. 1)}$$

in which τ_0 is the yield stress. This equation represents the stress contribution of a power fluid and a yield stress to the total stress.

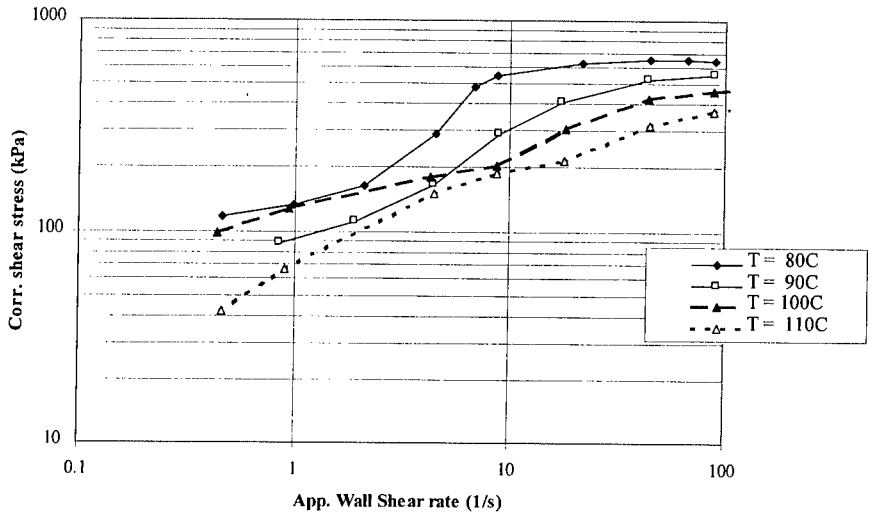

Fig 1. TPE 4427 at various temperatures.

4 Extrudable compositions based on TPE

It was found out [2] that the stresses to be applied to force an extrudable propellant mix to flow are in the range of about 3 kPa or much more. These stresses agree well with those found by others [7]; stresses of 18 – 22 kPa are needed in a shear rate range of 20 – 70 s^{-1}. In a twin screw extruder as used at TNO-PML the maximum shear stresses are limited to values in between 100 and 200 kPa [1] to guarantee save processing of highly energetic materials.

4.1 TPE – preliminary experiments with inert filling

Small samples were made with powdered sugar and the TPE 2747 by swelling and dissolving the TPE in cyclohexane, mixing the sugar with this mixture and allowing it to dry. The powdered sugar with a mean diameter of 45 micron as determined with a Malvern Particle Sizer, is a substitute for energetic fillers as RDX or HMX which may lead to self-heating followed by a deflagration due to viscous heating while extruding.

Tests are carried out with solid loads of 50 wt % and 70 wt % powdered sugar at 80 and 90 °C [3]. The results of tests at 90 °C are presented in figure 2 with the unfilled TPE as a reference.

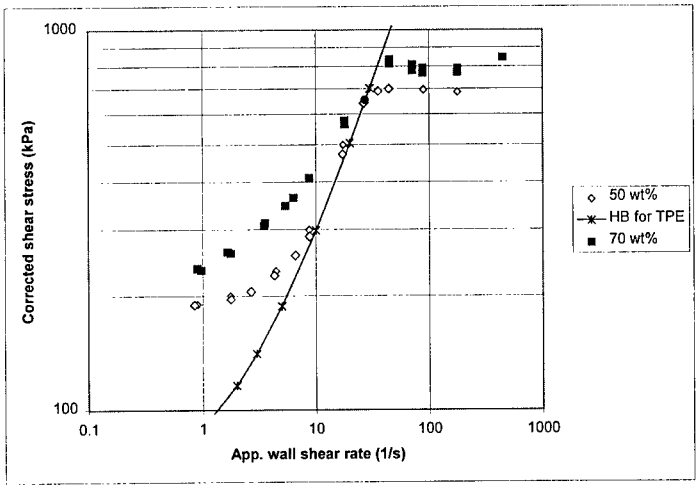

Figure 2 *Capillary Rheometer results of TPE and sugar filled TPE at 90 °C.*

Figure 2 demonstrates that only at lower apparent wall shear rates the measured curves satisfy the Herschel-Bulkley equation. Due to the filling large yield stresses become evident and the corrected shear stresses at which wall slip occurs shift from about 500 kPa to about 700 kPa at about the same apparent wall shear rates.

Moreover it is shown, that the stress safety limit of 200 kPa is exceeded already at relatively low shear rates. In order to decrease the shear stress and improve the flow properties, a solvent can be used.

4.2 Extrusion trials with TPE/sugar and solvent

Tests were carried out with TPE 2747, powdered sugar as a filler and cyclohexane as a solvent. The first 3 barrels - of a total of 8 - had a temperature of 120 °C in order to soften the TPE. The other 5 barrels as well as the extrusion head had temperatures of 70 °C. Measured are the product temperature and head pressure (peak and constant values). The product quality was of less importance because an optimisation of the die had yet to be carried out. Samples of the extrudate were taken and tested in the CER.

In table 3 the results of five runs are described. Under die swell is understood the extrudate diameter as compared to the die diameter.

Table 3 – results of extrusion trials with a TPE and an inert filler.

Run no	Solvent (wt %)	mass flow (kg/hr)	P (bar)	T (°C)	die swell (%)
1	7.2	5	11	66	17
2	3.8	5	18	70	18
3	2.2	5	23	78	15
4	7.0	10	15	69	5
5	7.6	7.5	13	69	11

The samples taken are rheologically characterised at 80 °C. The results are presented in figure 3. From these results it can be concluded that the stresses are higher than the stress safety limit of 200 kPa for a 70 wt % of sugar at 80 °C. Furthermore, the effect of solvent is considerable, because

- the onset of slip occurs shifts to higher shear rates and
- yield stresses become more evident at shear rates below 5 s^{-1}.

Between the shear rates of 5 and about 30 s^{-1} the Herschel-Bulkley equation is obeyed. It is concluded that even for a solvent content as high as 5 wt % the stress safety limit of 200 kPa is exceeded.

5. Extruder die pressure – calculations and measurements

In this chapter results are compared obtained either by direct measurement of the head pressure or calculated from CER experiments. The experiments have been performed with a live propellant using various percentages of solvent.

5.1 Pressure measurement

A live propellant has been prepared in the extruder and because of the better die design given form in a ram extruder. The composition is presented in table 4.

Table 4 Composition of a live propellant

Component	wt %
TPE 3718	16
HE , 5 and 25 micron	83
additives	1
solid load	84

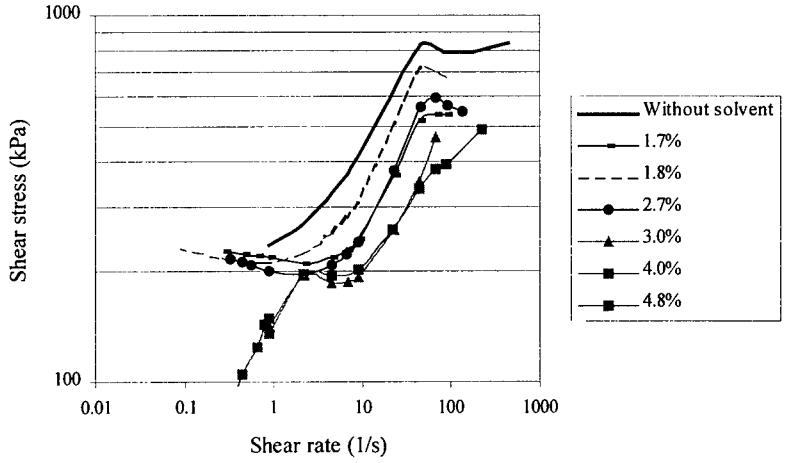

Fig. 3 Effect of solvent on rheological behaviour of the TPE/sugar mix at 80 °C.

The propellant has been shaped into a 7 holes grain through a die having a die-land length of 20 mm, a diameter of 7.50 mm and 7 pins with a diameter of 0.90 mm. During the shaping of the propellant the pressure and the mass flow have been measured as a function of the various solvent contents. The results are presented in figure 4.

5.2 Calculation of the head pressures.

Calculations have been carried out using the equation proposed by Benbow et al. [9] and Graczyk [10] and which reads as follows

$$P_{tot} = \ln (A_0 / A)\, f(v) + (B / A)\, g(v) \qquad \text{(eq 3)}$$

In this way the head pressure is divided into two parts; a part related to the entrance effect, f(v), and one to the capillary, g(v). This equation gives the opportunity to change the die land parameters (diameter and length) and those of the entrance (diameter changes) and to calculate the resulting pressure change. The parameter changes are presented in table 5.

Table 5 The parameters for CER and ram extruder die

	ln (A_0 / A)	**B / A**
capillary die	4.605	64
die ram extruder	5.103	22.28

The first step is to obtain the f(v) and g(v) functions for the propellant with various solvent contents (3 – 8 wt %). As it is assumed that these functions are independent of the test or processing method,

and that shear heating may be neglected, the pressure may be recalculated for the extruder die. The results are presented in figure 4 and may be compared with the measured values given in the same figure.

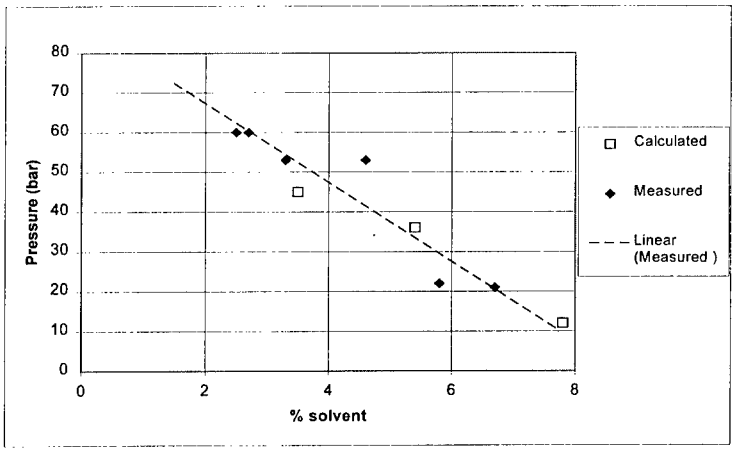

Figure 4 – Comparison of Measured and calculated die-pressuresfor a live propellant at 70 ℃

From figure 4 it is concluded, that the measured and calculated pressures are similar and that the equation proposed by Benbow gives good results for these kind of pastes.

6 Mechanical properties

As stated in the Introduction the parameters influencing rheology affect the mechanical properties as well. In table 6 some mechanical data are presented of the compositions as determined with a tensile tester using the tensile and compression mode at 20°C. It is remarked that castable compositions are tested using tensile stresses and extruded ones in compression, both with a shear rate of 0.01 s^{-1} (only the compression data are presented).

Table 6 Tensile and compression data of several compositions(20 ℃, 0.01 s^{-1}).

Mechanical Prop.		**RU 130-1**	**RU 133**	**TPE**	**TPE**	**IBK 1010**
processing		Cast	extruded	extruded	Extruded	extruded
modality		Mono RDX	mono RDX	mono Sugar	Mono Sugar	RDX/TAGN
part. size	(micron)	180	180	45	45	5 – 25
Solid load	(wt%)	65	86.2	51	69	85
Compress E	(MPa)	6.4	80	7	8	40
Stress	(MPa)	1	4.4	-	-	4.8
Strain	(%)	16.1	22	-	-	37
Stress at 60	(MPa)	4.8	4.5	5.5	-	-

It appears that for the monomodal cast cured batches the maximum stress, the strain at max. stress and the strain at rupture decrease with increasing particle size. Extruded, curable compositions like the RU 133, show a high Young modulus. The TPE binder shows Young' moduli and strengths which are comparable with those of the cast compositions like the RU 130, which may be advantageous with regard to high speed impact behaviour.

The TPE and TPE sugar mixes were tested with the TMA as well with a load of 5 gram and a heating rate of 5 °C/min. The results are presented in table 7.

Table 7 –TMA results of the TPE and TPE/sugar mixes

	T_s (°C)	T_g (°C)
TPE 2747	67	- 62 ± 1
with 50 wt % sugar	71 ± 1	- 61
with 70 wt % sugar	64 ± 4	- 65
with 80 wt % sugar	54 ± 1	nd

It is concluded that the softening temperature changes with the solid content, but the glass transition temperature does not change.

Conclusions

- The Capillary Extrusion Rheometer has proven its value for the determination of the flow behaviour of TPE's and highly filled systems based on TPE's.
- The head pressures calculated using rheological data and measured for a live propellant based on a TPE as a function of solvent content, agree well.
- The use of TPE's as a binder result in acceptable Young moduli and max. stresses
- The softening temperature of a TPE with sugar filler changes with the solid content, but the glass transition temperature does not change.

Acronyms

CER	Capillary extrusion rheometer	
MFI	Melting Flow Index	(g/ 10 minutes)
PBX	Plastic Bonded eXplosives	
PS	(mean) particle size	(micron)
PSD	particle size distribution	
RDX	a commonly used energetic filler (explosive)	
SI	solid load (wt percentage of filler)	(wt%)
SBS	styrene-butadiene-styrene tri block polymer	
SEBS	styrene- ethylene-butadiene-styrene tri block	
SIS	styrene-isoprene-styrene tri block	

TPE	Thermoplastic Elastomer	
TMD	theoretical maximum density	(g/cc)
A	cross sectional area – of barrel (A_0) or die	(m^2)
B	surface area of capillary	(m^2)
D	diameter of die	(m)
G'	shear storage modulus	(Pa)
G"	shear loss modulus	(Pa)
L	length of die-land	(m)
n	pseudo-plasticity index	(-)
T_s	softening point	(°C)
T_g	glass transition point	(°C)
v	extrudate velocity	(mm/s)
γ	shear rate	(s^{-1})
τ_0	yield stress or critical stress	(Pa)
τ	stress	(Pa)

Acknowledgement

The authors wish to thank Mr. Jan van Gool and the Ministry of Defence for their support.

Literature

[1]	Sabel, H.W.R.	Extrusion trails with a TSK045 twin screw extruder
	Schonewille, E	ICT 1998
[2]	Hordijk, A.C.	The application of Rheological equipment for improved processing of
	Sabel, H.W.R.	HTPB based PBXes
	Schonewille, E.	ICT 1996, V3
[3]	Hordijk, Aat C.	Processing of Higly filled prepolymers or TPE's by casting or extrusion
		RAPRA Polymer Rheology '99 conference
[4]	Cannizzo, L.F.	The plasticization of Energetic Thermoplastic Elastomer
	Edwards, W.W.	IM & EM symposium 1999 – Florida
[5]	Scott Hamilton, R.	A fully recyclable Oxetane TPE Rocket propellant
	Mancini, V.E.	ICT '99
[6]	Ampleman, G,	Synthesis and production of Energetic co-polyurethane TPE
	Marois, A. et al	based on GAP. V-6; ICT '98
[7]	Müller	Verarbeitung von LOVA-TLP in Doppelschnecken Extruder,
		ICT, 1990, V 22
[8]	Cogswell, F.N.	Polymer Melt Rheology
		Woodhead Publ. Limited, Cambridge, UK 1997
[9]	Benbow, J.	Paste flow and Extrusion
	Bridgwater, J.	Clarendon Press (Oxford) 1993
[10]	Graczyk, J.	Capillary rheometry for characterisation of ceramic pastes by extrusion
		British Ceramic Proceedings no 60, June 1999

EXPERIMENTAL DETERMINATION OF ULTRAFINE MAGNESIA PARTICLES EMISSIVITIES AT HIGH TEMPERATURES

Yuriy L. Shoshin, Igor S. Altman

Institute of Combustion & Advanced Technologies, Odessa State University, Dvoryanskaya 2, Odessa 65026, Ukraine, e-mail: vov@ictg.intes.odessa.ua

This paper is devoted to the study of ultrafine magnesia formed during the single Mg particle combustion in air. This investigation is of interest because the properties of oxide particulate determine the radiation heat transfer during the combustion of the volatile metals.

The interferometry technique for the measurement of ultra-fine particle volume fraction is offered. The interferograms of the single Mg particle burning in air are obtained using the Mach-Zehnder type interferometer specially adjusted for highly emitting and scattering flame. The spatial distribution of ultra-fine magnesia volume fraction in Mg particle flame is restored. The gas temperature in the region without smoke is determined. The ultra-fine oxide particle emissivity is obtained. It is found that this emissivity is on 3 orders greater than the theoretically calculated value. The natural gas convection velocity is obtained. The correlation between the relative gas-particle motion and the emissivity of Mg particle flame is discussed.

INTRODUCTION

Volatile metals are widely used in solid propellants and explosives, and thus volatile metal combustion processes are of great practical importance. Combustion of volatile metals is accompanied by strong radiation. It is generally recognized that a radiation heat transfer can play an essential role as in volatile metal dust cloud combustion as in single metal particle combustion. For example, recent experiments showed that the radiation heat losses during a single Mg particle (radius *0.5mm÷1.3 mm*) combustion in air is about 40 % from the total heat

release [1] independently on the initial particle radius. In difference from the radiation of heterogeneously burning metals, the radiation of volatile metal flames is still badly understood. While in a flame of heterogeneously reacting metals burning particles themselves are main radiators, in a volatile metal flame the radiation can originate also from ultrafine oxide particles formed in the flame and from molecules of gaseous oxides. Particularly, in [1] the contribution of ultrafine oxide particles into total energy emitted by Mg particles burning in air was estimated to be not less than 95%. Therefore, for correct modeling of magnesium flames radiation the emitting properties of ultrafine oxide particles formed in the flame should be known. Note that unlike the large particle, the emission properties of ultra-fine particle should be described by the ratio of particle emissivity to the particle radius, because the radiation power of an ultrafine particle is proportional to its volume [2,3]. This ratio q_0 is determined by the dielectric function $\varepsilon=\varepsilon'+i\varepsilon''$ of the particle material at wavelength λ:

$$q_0 = \frac{24\pi}{\lambda} \frac{\varepsilon''}{\left(\varepsilon' + 2\right)^2 + \left(\varepsilon''\right)^2}. \qquad (1)$$

In case when a flame does not absorb noticeably its own radiation the total radiation power emitted by ultarfine particles is the sum of radiation powers of all individual oxide particles and, therefore, it is proportional to a total volume of ultrafine oxide in the flame region. For such a flame value q_0 *can* be determined if total flame radiation power, total ultrafine volume in the flame emitting region and temperature of oxide particles are known. In present work value q_0 is experimentally determined for the particular case of single Mg particle flame in air. As it was shown in [1] the flame like studied one in the present work practically does not absorb its own radiation.

The total volume of ultrafine oxide in the flame emitting region and flame temperature was obtained by interferometry technique. It is known that the interferometric methods allow obtaining spatial distribution of the local refractive index of media. Both gas molecules and ultrafine oxide particles contribute into local refractive index. The contribution of ultra-fine particles into the local media refractivity is proportional to their volume fraction [3] and, therefore, the knowledge of this contribution allows to calculate the particle volume fraction. For the flames studied the regions of oxide smoke locations and regions free of smoke were identified by obtained interferograms. In the smoke regions the contribution Δn_g of gas into local refractive index was found to be much less than contribution Δn_{ox} of ultrafine oxide

particles. Therefore, measured local refractivity in smoke regions could be attributed only to ultrafine particles, and volume fraction distribution of oxide particles could be obtained. Total volume of oxide particles in the flame region was found using obtained spatial distribution of oxide particles volume fraction.

In flame regions free of smoke gas temperature profiles were obtained by measured refractive index. The temperature of emitting ultrafine particles was supposed to be close to maximum gas temperature obtained in a position very close to smoke region. This temperature was used for the calculation of ultrafine oxide particle emissivity.

The flame radiation power was determined by the empirical dependence of total radiation energy of a single Mg particle flame upon the initial particle mass, which found in [1]. These radiation energies were measured for the same Mg particle flames as studied in the present work.

The velocity of the natural gas convection above the burning Mg particle is restored using the measured ultrafine oxide volume fraction. The corelation between the gas convection velocity and the emissivity of single Mg particle flame is discussed.

APPARATUS AND PROCEDURE

Experiments were carried out with single Mg particles having radius *0.5 mm÷1.3 mm* burning in air. The boron fiber (*120 μm* diameter) with tungsten core supported the particle. The particle ignition was via the small propane diffusion flame. The photodiode, connected with the oscilloscope, registered particle burning time.

The specially designed Mach-Zehnder type interferometer was used to obtain the interferograms of Mg particle flame. Schematic of interferogram registration is shown in Fig.1. The single-mode *25 mW* He-Ne laser (λ=*632 nm*) was used as a light source. The interferometer had the rhomb

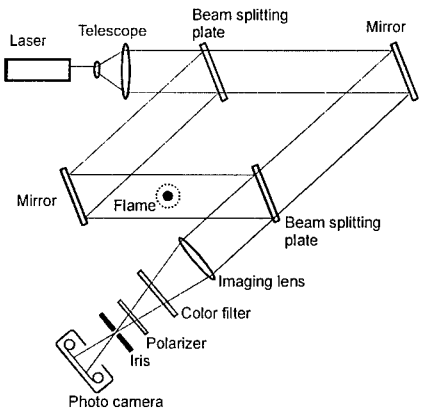

Fig.1. Schematic of flame interferogram registration.

configuration unlike the traditional rectangular one. This configuration allows to use the maximal area of available mirrors. The beam splitting plates had reflection factor *0.65*. Due to this the intensity of signal beam at the interferogram registration plane was about four times greater than the intensity of reference beam (in the absence of flame). The nonsymmetrical light intensity division was necessary to compensate the signal beam attenuation by Mg flame due to the light scattering and absorption by the ultra-fine magnesia particles. Using the experimental result of the light extinction measurement in the same flame [1] it was estimated that the interferogram picture contrast, determined as the ratio of light intensity in neighbor maximums am minimums in the interferometric picture, was not less than 6 in the whole registration field. The *35 mm* photocamera with removed issue lens registered interferogram. The *14 cm* focus lens was placed before the camera to form the focused image of the flame region on the film. Thus each laser ray, deflected due to the refractive index gradient within the flame, returned to its corresponding position in the interferogram registration plane. An iris diaphragm was placed in the focus plane of the lens to filter the own flame radiation and scattered laser radiation. For the additional filtering of flame radiation a color filter and a polarizer were used. The interferograms were registered at the moment approximately corresponding to half particle burning time. The exposure time was *1/500 s*.

Many of the obtained interferograms were not axi-symmetrical, because of the irregular deformation of Mg particle after ignition. The mostly symmetrical interferograms were chosen for the analysis. Fig.2 shows an example of obtained interferograms. The shadow of the oxide smoke is seen on the interferogram. It is seen that interference fringes curves down in the region of shadow. This distortion is caused by the increase of the mean media refractive index due to the presence of ultra-fine magnesia particles.

Fig.2. Interferogram of a burning magnesium particle.

Using the interferometric fringe pattern the light phase profiles were obtained at the different horizontal levels. From these profiles the differential local refractive index Δn was restored by the inverse Abel transform [4]. Fig.3 shows the example of the restored differential refractive index profile corresponding to the level of the burning Mg particle center. Using the restored refractive index we formally calculated the temperature profile in assumption that only gas contributes into the refractive index. In this calculation Gladstone-Dale's ratio and the ideal gas law were used. This temperature profile is also shown in Fig.3. In the outer region where the oxide particles are absent the calculated temperature profile corresponds to the real gas temperature. As it is seen in the inner region the formally calculated temperatures are unrealistic. The smallness of these temperatures is caused by the contribution of the ultra-fine oxide smoke into the local refractive index, which was not taken into account in the temperature calculation. So for the correct interpretation of the interferogram it is necessary to separate the relative contributions of oxide particles and of gas into the local refractive index. It is not possible to make this separation basing only on the interferogram. When treating the interferogram we made the additional assumption about the studied flame, which seems to be quite natural. The gas temperature within the smoke region (shadow in the interferogram) was supposed to be not less than the maximal calculated gas temperature (Fig.3). The background of this assumption is that the ultra-fine particles can only enlarge the local refractivity and therefore the real gas temperature should be not less than the formally calculated one. Then the value of Δn_{ox} we determined putting Δn_g to be equal to its value at the maximal formally calculated gas temperature. In this case the estimated absolute error of obtained value of Δn_{ox} does not exceed 7% from its maximal value.

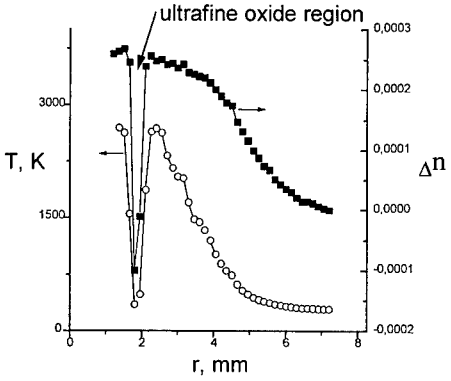

Fig.3. Radial profiles of local refractive index and formally calculated temperature. Initial particle radius 0.9 mm.

The ultra-fine oxide volume fraction f_v was restored according to the formula:

$$\Delta n_{ox} = \frac{3}{2} f_v \frac{\varepsilon' - 1}{\varepsilon' + 2}, \qquad (2)$$

which follows from the known equation for the suspension permittivity [3].

RESULTS AND DISCUSSION

Ultra-fine oxide particle volume fraction

In accordance with the described above procedure the radial profiles of the ultra-fine oxide particles volume fraction at different levels were restored. Fig.4 shows some of the f_v profiles restored by the interferogram.

For all Mg particles studied in the lower part of the flame ($h \leq 0$) ultra-fine oxide particles were within the narrow spherical layer of radius about twice the initial Mg particle radius. The thickness of this layer was estimated as a width of distinct shadow of oxide smoke in this region. This thickness was about 50μm for all the flames studied. This value is in a good agreement with our result obtained during spatially resolved light extinction measurements [1]. The phase profile has very large gradient in this zone. The analysis of fringe pattern did not provide the spatial resolution enough to restore this rapid change of the phase profile. That is why, the correspondent condensed oxide volume fraction profiles restored by the fringe pattern at $h \leq 0$ (for example profile at $h=0$ in Fig.4) had width about *300 μm*. Special analysis was made which has showed that the integral of f_v along radial coordinate was not sensitive for particular choice of phase profile gradient during f_v restoration. As only this integral is important for the further analysis of the obtained experimental data, the smoothing of f_v profile does not influent the conclusions made below. We estimated the real value of f_v in the lower part of the

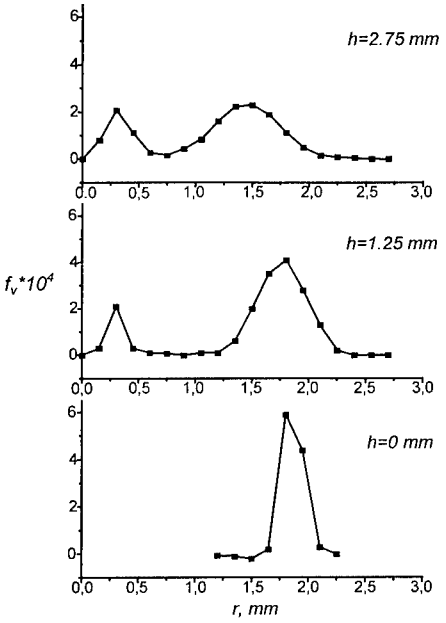

Fig.4. Restored by the interferogram ultrafine oxide volume fraction profiles at different heights from the burning particle center. Initial particle radius 0.9 mm.

flame multiplying the restored peak values f_v to the ratio of width of oxide smoke layer obtained by the fringe pattern analysis and by the shadow in the interferogram. The estimated value f_v at $h=0$ was about $4 \cdot 10^{-3}$, $3 \cdot 10^{-3}$ and $2 \cdot 10^{-3}$ for the flames of Mg particles of initial radius *0.65 mm*, *0.9 mm* and *1.3 mm* correspondingly.

Above the burning Mg particle the second peak in f_v profile presents closer to the flame symmetry axis (profiles $h=1.25$ *mm* and $h=2.75$ *mm* in Fig.4). Therefore in this region the oxide smoke localizes within two coaxial layers. The external peak of f_v smoothes above the burning Mg particle and peak value of f_v decreases. So the spatial resolution provided by fringe pattern analysis becomes enough to restore real profiles f_v in the upper part of the flame.

Apparently, the thin spherical smoke layer in the lower part of the flame coincides with the surface of zero Stefan flow. The Stefan flow is directed toward this surface from both sides resulting in the ultra-fine oxide particles storage within narrow layer near this surface. Due to the natural convection oxide particles move upward within this layer and then abandon the spherical surface and form the external peak of f_v profile above the burning Mg particle. Probably, the inner peak of f_v profile above the particle is formed by ultra-fine oxide particle produced in the upper part of the flame, after oxide particles produced in the lower part of the flame abandon the spherical layer. However it is not clear why oxide smoke above the burning Mg particle forms the distinct inner circular layer, but not evenly distributes within the external smoke layer.

Emissivity of ultra-fine magnesia particles in flame

The ultra-fine oxide particles emissivity in the flame region was estimated using the restored by interferogram oxide volume fraction and measured [1] integral Mg particle flame radiation energy. For this estimation the flame emitting region was modeled by the spherical surface of radius $2r_0$. It was supposed that the flame radiation is not absorbed noticeably within the flame region. The correctness of these assumptions is based on our recent experimental results on spatially resolved light extinction/radiation measurements in single Mg particle flame. These results will be reported in the separate paper.

Almost all the radiation energy of Mg particle flame is emitted by ultra-fine oxide particles 1,5]. As in accordance with our supposition this radiation not absorbs within the

flame region, the integral flame radiation power P is approximately the sum of radiation powers of all ultra-fine oxide particles within the flame region. Therefore

$$P = \sigma T^4 \sum \varepsilon_i S_i = 3 q_0 \sigma T^4 \sum V_i = 3 q_0 \sigma T^4 V \qquad (3)$$

here σ is Stefan-Boltzmann constant, T is the flame emitting zone temperature, S_i is the surface and V_i is the volume of the individual ultra-fine oxide particle, V is the total ultra-fine oxide volume within the flame emitting zone. Getting Eq.(3) we used the known [3] connection between the ultra-fine particle emissivity ε_i and its radius r_i: $\varepsilon_i = q_0 r_i$.

Value V can be written as $V = f_s S$, where f_s is the average volume of ultra-fine oxide per unit of the flame emitting surface $S = 4\pi(2r_0)^2 = 16\pi r_0^2$:

$$f_s = \frac{\sum V_i}{S} = \frac{\int f_v dV}{S}. \qquad (4)$$

The integration in Eg.(4) is within the emitting zone. In assumption that the emitting ultra-fine particles are localized within thin zone Eq.(4) can be reduced to the form:

$$f_s = \int f_v^0(r) dr, \qquad (5)$$

where index *"0"* denotes that integration is within zone at $h=0$.

The power of flame radiation was estimated as

$$P = \frac{0.4 m_0 Q}{\tau_b}, \qquad (6)$$

where m_0 is the initial Mg particle mass, Q is heat of the reaction $Mg(cond) \rightarrow MgO(cond)$, τ_b is the measured particle burning time. The factor 0.4 is taking from our work [1] where the total radiation energy during Mg particle combustion was directly measured.

Using Eqs.(3)-(6) we obtain

$$q_0 = \frac{m_0 Q}{120 \pi r_0^2 \sigma T^4 \tau_b \int f_v^0(r) dr}. \qquad (7)$$

For the calculation of q_0 by formula Eq.(7) we used the peak temperature $T = 2700$ K at $h=0$ restored by the interferogram. Note that this value is in a good agreement with the single Mg particle flame temperature measured by spectral methods [5]. The calculated value of q_0 was within diapason $(1.5 \div 2) \cdot 10^5$ m^{-1} for the flames of Mg particles of different initial diameters.

For the comparison we estimated value of q_0 using the experimental data on magnesia conductivity at high temperatures [6] and the known [3] relation between the conductivity σ and imaginary part of dielectric function: $\varepsilon''=\sigma\lambda/(2\pi c\varepsilon_0)$. The value of q_0 obtained by this estimation is about $200\ m^{-1}$ that is on *3* orders smaller that the experimentally restored one. The possible reason of this discrepancy is nonequilibrium concentration of electrons in conductivity band of magnesia during ultra-fine oxide particle condensation growth. As it was theoretically predicted in [7] the electron can be exited due to the great energy release during MgO molecules condensation. Note that the analogous discrepancy is discussed for alumina ultra-fine particles in the rocket plume [8].

Gas convection velocity

The ultra-fine oxide particles formed within the flame are removed from the flame emitting zone due to the natural convection. Therefore the volume of emitting ultra-fine particles V is determined by the rate of oxide particle production in the flame and by the velocity of natural convection. The mean rate W of ultra-fine oxide volume production is about

$$W=\frac{0.8m_0}{\rho\tau_b}\nu_{st}, \qquad (8)$$

where ρ is magnesia density and ν_{st} is the stoichiometric coefficient. The factor *0.8* corresponds to the measured [1] part of initial magnesium transformed into oxide smoke during the combustion of Mg particles.

The total ultra-fine oxide volume within the flame can be estimated as $V=h_f W/v_c^f$, where $h_f\approx 4r_0$ is the height of the emitting region and v_c^f is the mean convection velocity in this region. Then the value of f_s can be estimated as

$$f_s\equiv\frac{V}{16\pi r_0^2}=\frac{m_0}{5\pi r_0\rho v_c^f\tau_b}\nu_{st}. \qquad (9)$$

The measured value τ_b is proportional to r_0^2. Taking into account that m_0 is proportional to r_0^3 we conclude that f_s is inversely proportional to the mean gas convection velocity in the flame region.

The simple relation is between the value f_s and Mg particle flame emissivity ε_f. As the flame radiation power $P=\varepsilon_f\sigma T^4 S$ and $V=f_s S$ we have from Eq.(3)

$$\varepsilon_f = 3q_0 f_s . \tag{10}$$

Therefore the flame emissivity as well as f_s is inversely proportional to the mean convection velocity in the flame region.

Using the obtained oxide volume fraction we restored the natural convection gas velocity in the smoke region above the burning Mg particle where the condensation processes are completed. In this region we can write the continuity equation along the vertical coordinate h for smoke:

$$v_c f_h = W , \tag{11}$$

where

$$f_h = \int_0^\infty 2\pi f_v(r) r dr \tag{12}$$

is the the ultra-fine oxide volume per unit of height and v_c is the mean convection velocity of smoke jet at the corresponding level. Using Eqs. (8), (11), (12) we restored the dependencies of v_c upon h . These dependencies for different initial Mg particle radiuses are shown in Fig.5

The continuity equation is not applicable within the flame region where the condensation of MgO vapor occurs. However we can suppose that the restored value of convection velocity in the region near to Mg particle (where condensation is completed) is close to the mean convection velocity in the flame emitting region v_c^f. Fig.6 shows the mean convection velocities at height $h=4r_0$ for the particles of different initial radiuses. It is seen from this figure that the convection velocity is nearly proportional to the initial Mg particle radius. On

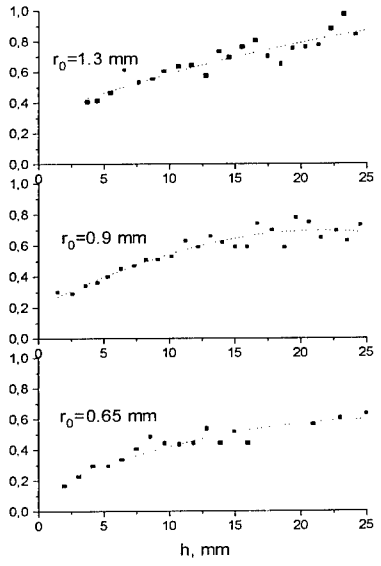

Fig.5. Gas convection velocity v.s. height above the burning particle center for different initial particle radiuses

this base we can think that v_c^f is also proportional to r_0. In this case Eq.(10) gives the inversely proportional dependence of Mg particle flame emissivity upon the initial radius. The same dependence of the flame emissivity upon the initial Mg particle radius was obtained by the flame radiation energy measurements [1]. So we can conclude that the change of the convection velocity is the reason of the change of the flame emissivity dependently on the initial Mg particle radius.

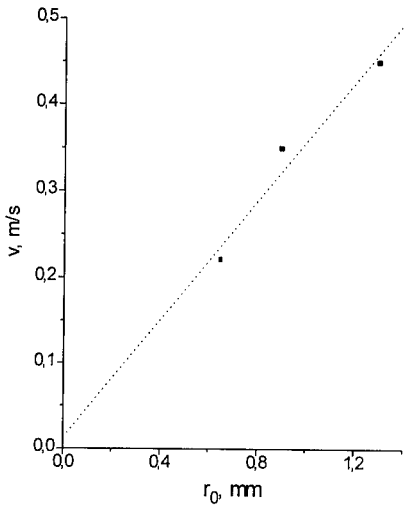

Fig.6 - Gas convection velosity at height $h = 4r_0$ above the burning particle center v.s. initial particle radius

CONCLUSIONS

For the first time the interferometry technique was applied for the ultra-fine particle volume fraction measurements. The spatial distributions of the ultra-fine magnesia volume fraction were obtained for the single Mg particle burning in air. The gas temperature was restored in the region free of smoke. Using our previous experimental results on the single Mg particle flame radiation and the volume fractions obtained in the present work we estimated the emissivity of the ultra-fine oxide particles in the flame. The obtained value of emissivity is on 3 orders greater than the theoretically calculated one.

The natural gas convection velocity above the burning Mg particle was restored with the help of the obtained interferograms. The analysis of the relation between the flame emissivity and the convection velocity is given.

The conclusion is made that the natural gas convection controls Mg particle flame emissivity. In case of the volatile metal dust combustion the similar influence of the relative gas-particle motion in flame front on the burning particle radiation can be expected.
Therefore the influence of the relative gas-particle motion should be taken into account when describing of radiation heat transfer of both the burning single metal particles and metal dust clouds.

ACKNOWLEDGEMENTS

This work is partially supported by INTAS (Project 96-2334).

REFERENCES

1. Shoshin, Yu.L., and Altman, I.S, 17-th ICDERS, Germany, 1999, CD poster 107.
2. Bohren, C.F., and Huffman, D.R., *Absorption and Scattering of Light by Small Particles*, Wiley, New York, 1983.
3. Landau, L.D., and Lifshitz, E.M., *Electrodynamics of Continua* (in Russian), Nauka, Moscow, 1982.
4. Vest, C.M., *Holographic Interferometry*, Mir, Moscow, 1982
5. Florko, A.V., Zolotko A.N., Kaminskaya, N.V. and Shevchuk, V.G., Fizika Goreniya i Vzryva, 18(1): 17-22 (1982).
6. Samsonov G.V., *Physical and Chemical Properties of Oxides,* Handbook (in Russian), Metallurgiya, Moscow, 1969.
7. Altman, I.S., *Combustion, Explosion and Shock Waves*, 34(4): 411-413 (1998).
8. Pluchino, A.B., and Masturzo D.E., *AIAA Journal*, 19(9): 1234-1237 (1981).

THE HEAT AND PRODUCTS OF EXPLOSION OF ALUMINIZED HIGH EXPLOSIVES.

M. N. Makhov.

N. N. Semenov Institute of Chemical Physics, Russian Academy of Sciences.
4, Kosygin Street, Moscow, 117977, Russia. E-mail: makhov@polymer.chph.ras.ru

Abstract

The results of measurements of the explosion heat and the composition of products for a series of mixtures, containing high C-H-N-O explosives and aluminum, are presented in the paper. This investigation was made with the aim of studying the dependence of the explosion heat and the composition of products on the charge diameter, the particle size of ingredients, the oxygen content of the basic explosive, the initial concentration of aluminum. The semi-empirical method for predicting the explosion heat and the composition of products was developed by processing the total body of experimental data.

Introduction

The addition of Al to high explosives is known to enhance their total energy. This is the generally recognized way of formulating energetic compositions for use in various fields of practice. The explosion heat (EH) is the fundamental parameter, characterizing the total energy and the potential ability of an explosive to do work. However, there is little information on investigations of EH and explosion products (EP) of aluminized explosives in the literature. EH values and EP compositions have been measured under different conditions only for several individual mixtures [1 -3]. The results of the thermodynamic calculation of EP compositions, carried

out by using the Tiger Code BKW, show significant disagreement between calculated and experimental values [1]. The aim of the work presented was to measure EH values and EP compositions for a series of aluminized high explosives and on the basis of obtained data to study the influence of the casing, the charge diameter, the loading density, the particle size of components, the initial Al concentration, the oxygen content of the basic explosive. Furthermore, the problem was stated to develop a semi-empirical method for predicting EH and the EP composition for aluminized mixtures.

According to the method of measuring EH the charge of an explosive is placed into the casing [4-6]. The object in using the casing is to increase the extent of completeness of reactions in outer layers of charges. Furthermore, it is known, that EP of unconfined charges are shocked considerably by reflections from calorimetric bomb walls and new equilibrium of products is frozen under conditions of low pressure. The casing attenuates the secondary heating of EP, as the energy of EP of heavily confined charges is largely converted to kinetic energy of the casing [5-9]. It is shown in [5, 6], that for pure high explosives, such as TNT and HMX, the use of the copper casing, making the mass ratio: the casing / the explosive be more than 4, prevents re-equilibration of EP. The value of EH, obtained under this conditions, doesn't depend on the thickness of the casing, corresponds to the EP composition, frozen on the C-J isentrope, and can be considered as the parameter, characterizing the total energy content of an explosive. This value is a function only of the loading density. The EH values for 16 pure explosives, presented in the work [4], were obtained under this conditions (the charge diameter and the thickness of the copper casing were 20 and 7 mm respectively). If the mixture tested consists of high explosives with particle sizes of several tensμm, above mentioned values of the charge diameter and the thickness of the copper casing, as a rule, ensure the completion of reactions on the stage, preceding the freeze-out temperature range. However, the presence of insensitive substances in a mixture, such as Am-

monium Nitrate, Ammonium Perchlorate, Potassium Perchlorate and the like, increases the time of interaction between mixture components. Incomplete reactions can take place, when such systems are detonated [10]. It is yet more difficult to provide conditions for complete reactions in the case of the mixtures, containing metal powders.

Experimental methods and results.

Mean particle sizes of Al powders used were 0.1, 20, 50 and 200 μm. The content of active Al of powders with particles 20, 50 and 200 μm in size was not less than 0.98. The ultra fine powder of Al (0.1 μm) was produced by application of the condensation-in-flow technique in Institute of Energy Problems of Chemical Physics RAS. The content of active Al of the ultra fine powder was about 0.9. Mixtures were prepared by the prolonged mixing of the components in the cylindrical steel container, filled an inert liquid. Ceramic balls, placed into the container, accomplished additional comminution of an explosive. After this procedure the particle size of explosives in mixtures varied from ten to several tens μm. Charges were manufactured by pressing.

The values of EH were measured using two calorimeters with the bombs of 2 and 5 liters in volume. The mass of the charge detonated was changed from 12 to 45 grams. Prior to a test the bomb was blown out with argon and pumped out. The bomb with a charge was placed in a vessel with a calorimetric liquid (distilled water). The calorimeter temperature was monitored by the measuring system with a resistor thermometer. Energy equivalents of the calorimeters were measured in special runs in which benzoic acid was burned in excess of oxygen. The EH value of the detonator used was also measured. The error of EH measurements was 1 %. The gas analyses were carried out using Infrared Spectrophotometer. The equations of mass and heat balances were also used for determining EP compositions.

The results of studying EH for the mixture, containing 2,4,6-trinitrotoluene (TNT) and Al in the proportion 80/20 by mass, made it possible to ascertain the group of factors, affected EH of aluminized high explosives. The EH values obtained are summarized in Table 1. In Table 1: d - the mean particle size of Al,ρ - the loading density, Q - the EH value (H_2O - gaseous). The EH values of pure TNT are also presented in Table 1 (rows 9 - 12). The charge diameter and the thickness of the casing were 10 and 5 mm respectively.

Table 1. Experimental EH values of TNT-based mixtures

No	d, μm	ρ, g/cm^3	Q, kJ/kg	ΔQ, kJ/kg
1	0.1	1.68	6260	1940
2	20	1.71	6200	1840
3	50	1.72	6070	1710
4	50	1.35	5730	1800
5	200	1.72	5250	890
6	200	1.66	5650*	1360
7	50	1.70	5330**	1000
8	50	1.72	4980***	
9		1.20	3930	
10		1.45	4220	
11		1.51	4290	
12		1.57	4360	

*) the charge diameter is 20 mm, the thickness of the casing is 7 mm;
) the particle size of TNT is 1.5 mm; *) the casing is absent.

First of all, the results are shown that EH depends on the loading density (rows 3, 4). The increase of the loading density results in the increase of the EH

value, but the EH gain, corresponding to the lower density, slightly higher than that of the greater density. The EH value of the unconfined charge is considerably lower than that of the heavily confined charge (rows 3, 8). The influence of the charge diameter is more pronounced for the mixture with Al of 200μm (rows 5, 6). Differences in the particle size between Al and explosives also influence EH. If the explosive particle size is considerably more than Al particle diameter, the EH value becomes less than the expected value due to the fact that Al particles aggregate between more large explosive particles (rows 3, 7). As one would expect, the increase of the Al particle size results in the decrease of the EH value (rows2, 3, 5). However, the mixture, containing ultra fine Al, has slight advantage over the mixture with Al of 20 μm (rows 1, 2). The last effect is probably caused by the difference in particle size between TNT and ultra fine Al and also by the thick oxide layer on the surface of particles and the relatively low content of active metal of mentioned Al.

The investigation of aluminized mixtures, containing different high explosives, has been made with the aim of studying the influence of the oxygen content of the basic explosive on EH values and EP compositions. The oxidizer/fuel balance is expressed by the oxygen factor. The oxygen factor is the ratio of the oxygen amount in an overall molecule of the mixture $C_aH_bO_cN_dAl_f$ to the oxygen amount needed to oxidize the combustible elements: $\alpha = c/(b/2 + 2a + 1.5f)$. The oxygen factors of the explosives investigated cover a wide range of values. The oxygen factor of TNT is 0.364, Cyclotrimethylenetrinitramine (RDX) - 0.667, Petaerythritol Tetranitrate (PETN) - 0.857, Bis(2,2,2-trinitroethyl)nitramine (BTNENA) - 1.4. The mean particle size of Al was 20 μm. The Al concentration was varied in the range: 0 - 45 % by mass. The results are accumulated in Table 2. In Table 2:β - the initial Al fraction; ΔQ - the EH gain over the EH value of a pure explosive. The calculated values are also presented in Table 2.

Table 2. Experimental and calculated EH values

Explo-	β	ρ, g/cm^3	Q, kJ/kg	ΔQ, kJ/kg	Q_{calc}, kJ/kg
TNT		1.60	4390		4380
	0.10	1.66	5270	900	5340
	0.30	1.76	6660	2350	6820
	0.35	1.78	6920	2650	6860
	0.40	1.80	6820	2570	6760
RDX		1.70	5610		5570
	0.10	1.75	6570	1010	6530
	0.20	1.80	7280	1740	7390
	0.30	1.84	7980	2460	7940
	0.35	1.87	7980	2470	8030
	0.40	1.89	7850	2360	7930
	0.45	1.90	7710	2250	7830
PETN		1.70	5900		5930
	0.20	1.79	7850	1930	7940
	0.35	1.85	9210	3310	9130
	0.40	1.88	9480	3600	9380
	0.45	1.92	9440	3560	9290
	0.50	1.95	9320	3440	9150
BTNENA		1.90	5230		5230
	0.20	1.98	9310	4080	9100
	0.30	2.00	9890	4660	9980
	0.40	2.01	10580	5350	10660
	0.45	2.03	10420	5190	10500

The semi-empirical relations, suggested in [4, 11] for calculating EH, are valid solely for pure high explosives. For estimating EH values of aluminized mixtures the same approach as previously were used. The relation derived specifies the dependence of the coefficient of maximum permissible heat (Q_{max}) realization on the oxygen factor. Q_{max} is calculated by a hypothetical reaction equation written in conformity with the following order of formation of the products: Al_2O_3 (+ AlN), H_2O, CO_2, C (or O_2). The probability of AlN arising is taken into account when the oxygen amount is not enough to oxidize aluminum completely (high initial Al concentrations and low oxygen factors of explosives). The following expression was derived by processing the total body of experimental data:

$$\mathbf{Q/Q_{max} = Q_1/Q_{max\,1}[1 - 0.25(1 - \alpha/\alpha_1)/\ \alpha_1^{0.5}]}$$

The index "1" corresponds to the pure explosive. The relation obtained is valid for the examined ranges of the Al concentration (0 - 45 %) and the oxygen factor of the explosive (0,36 - 1.40), for particle sizes of Al and explosive, averaging 20μm, and for the relative charge density in excess of 0.9.

Figure 1 presents the results of the calculation, carried out for the compositions, which contain, besides above mentioned explosives, following compounds: 2,4,6-trinitrobenzene (TNB), Cyclotetramethylenetetranitramine (HMX), 1,3,3-trinitroazetidine (TNAZ), 2,4,6,8,10,12-hexanitro-2,4,6,8,10,12-hexaaza-isowurtzitane (CL-20), Hexanitrobenzene (HNB). The oxygen factor of TNB is 0.444, HMX - 0.667, TNAZ - 0.75, CL-20 - 0.8, HNB - 1.0.

The experimental and calculated results show that the addition of Al to high explosives considerably enhances EH. Since among oxygen-containing products O_2 is the most effective oxidizer of Al and the reaction of Al with O_2 proceeds with the greatest energy release, the maximum EH gain corresponds to the explosive, containing excess oxygen in its molecule (BTNENA). However, Al concentrations,

corresponding to maximum EH values, lie within narrow limits (33 - 43 % by mass). As follows from the results (Table 2), the maximum EH gain of RDX is lower than that of TNT in spite of the fact, that RDX exceeds TNT in the oxygen factor. The fact is that products of TNT (small oxygen factor) contain the larger amount of CO and the smaller amount of CO_2 and H_2O in comparison with EP of RDX, and the heat of reaction of Al with CO (for one mole of Al_2O_3) is higher than the heat of reactions of Al with CO_2 (to CO) and H_2O. The results of the calculation corroborate the experimental findings. Figure 2 exhibits the dependence of calculated values of the EH gain on the oxygen factor of the basic explosive. Numbering in Figure 2 is saved the same as in Figure 1. As follows from Figure 2, values of the EH gain for the relatively wide range of oxygen factors (0.36 - 0.80) are slightly differ from each other.

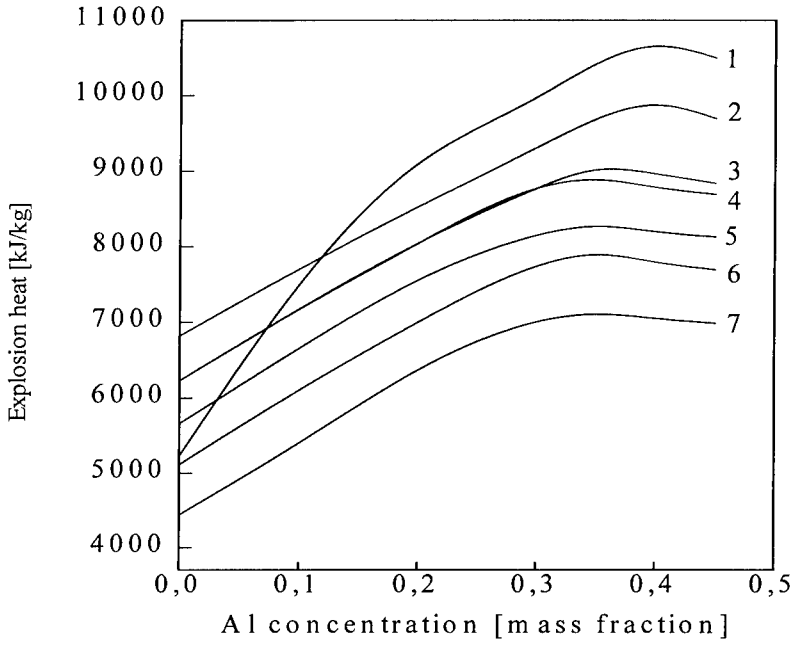

Figure 1. The EH value versus the Al concentration; 1 - BTNENA, 2 - HNB, 3 - TNAZ, 4 - CL-20, 5 - HMX, 6 - TNB, 7 - TNT

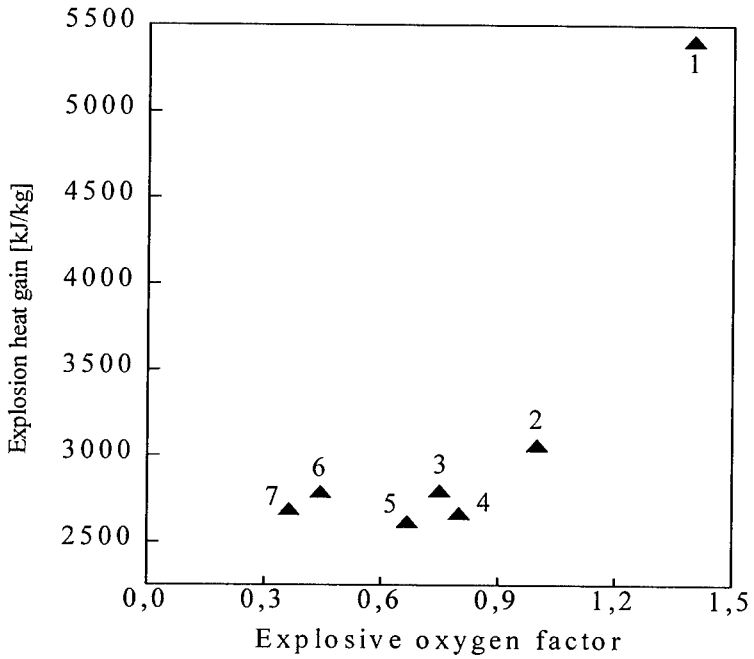

Figure 2. The EH gain versus the explosive oxygen factor

The results of studies of EP exhibit that Al reacts with all oxygen-containing products. As already noted, Al is mostly oxidized by free oxygen, if O_2 is present in EP. In the absence of free oxygen Al actively reacts with CO_2 and H_2O and partially with CO. On condition that O_2 is absent and products contain small amounts of CO_2 and H_2O, Al actively interacts with CO. The calculation of the EP composition reduces to determining the fraction of oxygen, containing in the i-th product, consumed to oxidize Al (k_i). The major equation is of the form:

$$\partial k_i/\partial k = m_i/\sum m_i$$

In the equation: k - the amount of oxygen needed to oxidize Al. To calculate m_i the following relations have been derived with the use of experimental data:

$$m_{O2} = 12n_{O2};$$

$$m_{CO2} = \{1 - [n_{O2}/(n_{O2} + n_{CO2})]^2\}\, n_{CO2};$$

$$m_{H2O} = \{1 - [n_{O2}/(n_{O2} + n_{H2O})]^{0.15}\}\, n_{H2O};$$

$$m_{CO} = 0.4\{1 - [n_{O2}/(n_{O2} + n_{CO})]^{0.1}\}\{1 - [(n_{CO2} + n_{H2O})/(n_{CO2} + n_{H2O} + n_{CO})]^2\}\, n_{CO};$$

where: n_i - the instantaneous magnitude of the concentration of the i-th product.

The method for estimating the EP composition ignores the formation of AlN. For the AlN formation to be taken into account, additional studies need to be conducted. The EP composition can be calculated on condition that either the EH value is known or Al burnt fraction is given. As an illustration, Table 3 lists experimental and calculated (under row) concentrations of EP for two mixtures. In Table 3:γ is the Al burnt fraction. Concentrations of EP are expressed in moles per kilogram of a mixture. The EP composition of the basic explosive was estimated by using the method suggested in the work [12].

Table 3. Experimental and calculated values of EH and EP concentrations

Explosive	β, %	ρ, g/cm^3	Q, kJ/kg	CO_2	CO	H_2O	Al_2O_3	γ
RDX	20	1.80	7280	1.37	6.17	3.98	2.91	0.79
			7390	1.27	6.15	3.88	3.01	0.81
PETN	35	1.85	9210	0.80	5.77	0.98	5.44	0.84
			9130	0.85	5.80	1.06	5.37	0.83

Thus, calorimetric values of EH, obtained under uniform conditions, allow us to compare aluminized high explosives on the energy content. The values, being

calculated by using the method suggested, can serve for the same purpose. The results of calorimetric measurements can be used to provide the boundary conditions for numerically modeling of detonation processes in explosives.

References

1. Volk F., Bathelt H., Schedlbauer F. and Wagner J., Preprint. 8th International Symposium on Detonation. Albuguergue. New Mexico, 1985. V. 1. P. 330.
2. Volk F., Schedlbauer F., Proceedings. of 10th International Symposium on Detonation. Boston. Massachusetts. ONR 33395-12, 1993. P. 601.
3. Deiter J.S., Wilmot G.B., Proceedings of 10th International Symposium on Detonation. Boston. Massachusetts. ONR 33395-12, 1993. P. 619.
4. Pepekin V.I., Makhov M.N., Lebedev Iu.A., Dokl. Akad. Nauk SSSR, 1977. V. 232. No 4. C. 852 (in Russian).
5. Makhov M.N., Pepekin V.I., Proceedings of the 9th All-union Symposium on Combustion and Explosion ("Detonation"). Chernogolovka. USSR, 1989. P. 23. (in Russian).
6. Makhov M.N., Khim. Fiz., 2000. V. 19. (to be published, in Russian).
7. Ornellas L.D., Carpenter J.H., Gunn S.R., Rev. Sci. Instrum., 1966. V. 37. No7. P. 907.
8. Ornellas D.L., J. Phys. Chem., 1968. V. 72. No 7. P. 2390.
9. Ornellas D.L., Combustion and Flame, 1974. V. 23. No 1. P. 37.
10 McGuire R.R., Ornellas D.L. and Akst I.B., Propellants and Explosives. 1979. V. 4. No 2. P. 23.
11. Makhov M.N., Arkhipov V.I., Fizika Goreniya Vzryva, 1989. V. 25. No 3. P. 87 (in Russian).
12. Makhov M.N., Pepekin V.I., Polish Journal of Chemistry, 1981. V. 55. P. 1381.

COMBUSTION BEHAVIOUR OF PYROTECHNIC MIXTURE BASED IN AMMONIUM AND SODIUM NITRATES WITH WOOD PARTICLES

Paula Portugal*, José Campos[+] and António Portugal[++]

Lab. of Energetics and Detonics
[+]Mech. and [++]Chem. Eng. Deps. - Fac. of Sc. and Tech. – Univ. of Coimbra - 3030 Coimbra
** Polytechnic Inst. of Tomar – 2300 Tomar - PORTUGAL*

Abstract

Ammonium nitrate is the base component of a recent family of gas generators and pyrotechnic composite mixtures. Those mixtures have generally the same plastic binder (hydroxyl terminated polybutadiene) of the classic ammonium perchlorate based composite propellants, but they have lower pollutants concentration. The disadvantages of this kind of mixture come from its low flame temperature and combustion instabilities, at atmospheric pressure. Previous work, related to the model of combustion of ammonium nitrate based propellants, proves the influence of pressure and phase transition on the stability of flame regression. In the present work, the prediction of the combustion characteristics of a pyrotechnic mixture of ammonium and sodium nitrates (respectively of ~ 69 and ~ 10% - mass percent), using dimethylformamide (~ 4%) as a partial solvent, mixed with wood particles (from ~ 1.2 to 2.4 %) and enclosed in an expanded two component polyurethane binder solution (~15%), was performed using THOR code. The experimental mixture was produced by an original twin screw mixing system, allowing the final expansion inside the cylindrical test confinement. The existence of void cavities, by binder expansion, closing nitrate particles, allows the combustion of nitrates with an increase of thermal insulation and local pressure. The observation of flame, during combustion at atmospheric pressure, proves also the influence of wood particles (inside polyurethane void cavities), absorbing liquid nitrates after its phase transition and stabilising of the flame regression (with measured values of ~ 0.5 mm/s). The presented experimental results prove the great influence of binder cavities and the existence of polyurethane pyrolisis during combustion phenomena of this kind of mixture.

1. INTRODUCTION

The environmental aspects of combustion products are, nowadays, one of the more important characteristics of a new pyrotechnic mixture. Efforts have been made in order to find clean oxidizers that can take the place of the classical ammonium perchlorate (AP). In some kind of applications, ammonium nitrate (AN) is the base component of a recent family of gas generators and pyrotechnic composite mixtures, as a candidate to substitute AP. However, in spite of several favorable attributes, AN presents also some disadvantages. Besides its high hygroscopicity and phase transitions, the burning characteristics of AN are not comparable to

the burning characteristics of AP. Experimental results, from decomposition processes of pure ammonium nitrate, show significant influence (Kolaczkowski, 1980) of endothermic dissociation above 169 °C ($NH_4NO_3 \rightarrow HNO_3 + NH_3$); exothermic elimination of N_2O on careful heating at 200 °C ($NH_4NO_3 \rightarrow N_2O + 2H_2O$); exothermic elimination of N_2 and NO_2 above 230 °C ($4\ NH_4NO_3 \rightarrow 3N_2 + 2NO_2 + 8H_2O$); and exothermic elimination of nitrogen and oxygen, sometimes accompanied by detonation ($NH_4NO_3 \rightarrow N_2 + 1/2\ O_2 + 2\ H_2O$), in a good agreement with theoretical predictions (Duraes et al., 1996).

Previous work, related to the model of combustion of ammonium nitrate based propellants (Carvalheira et al., 1995), proves the influence of pressure and phase transition on the stability of flame regression. The works done at our Laboratory to increase oxidiser effect and density of the mixtures, based in ammonium nitrate, led us to use mixtures of ammonium nitrate (AN) and sodium nitrate (SN) (Campos et al., 1991; Pires et al., 1996) and to optimise the ratio AN/SN to the constant value of 86/14 % (in mass). The mixture uses also the same binder type (a polyurethane solution system - PUR) of the hydroxyl terminated polybutadiene of the classic ammonium perchlorate based composite propellants, very well justified in previous works (Carvalheira et al., 1995). The required concentration, near 20 %, due to the rheological properties, implies now the selection of a solvent of the AN/SN mixture, without water content, in order to achieve a better mixed final composition. The selected solvent (dimetil-formamide - DMFA) was used to solublize AN and SN as much as possible. In previous works it was also shown the effect of melting transition of AN in the combustion phenomena (Pires et al., 1996, Carvalheira et al., 1995). The proposal, in the present study, was to use wood fine particles, mixed with AN/SN crystals, to ensure an absorption effect of melted AN/SN (keeping these oxidisers inside PUR cavities). Concluding, our pyrotechnic mixture is formed by ammonium and sodium nitrates, using dimethylformamide as a partial solvent, mixed with wood particles (from ~ 1.2 to 2.4 %) and enclosing this oxidiser system in an expanded two-components polyurethane binder solution. The concentrations were selected in order to study the influence of wood (1.2 and 2.4%) and PUR concentrations (17, 19 and 21%) in combustion phenomena.

2. MIXTURES COMPOSITION AND THERMODYNAMIC PROPERTIES

Six pyrotechnic compositions are selected and presented in Table 1. The thermochemical properties of the components of the pyrotechnic mixtures are presented in Table 2. The presented values are from literature or from our direct measurements.

Mixture	NA/NS	Treated Wood Particles	DMFA	PUR
1	77.49	1.16	4.23	17.10
2	75.70	1.14	4.13	19.00
3	73.90	1.11	4.03	20.97
4	76.60	2.30	4.18	16.92
5	74.70	2.5	4.07	18.76
6	72.92	2.42	3.98	20.69

Table 1– Tested pyrotechnic compositions (values in mass percent).

Component	Global formula	ρ (kg/m^3)	C_p (J/mol K)	H_f (kJ/mol)
AN	NH_4NO_3	1725	137.6	-351
SN	$Na\ NO_3$	2261	103.2	-445.9
DMFA	C_3H_7NO	949	152.8	-242.4
PUR	$C_{5.14}\ H_{7.50}\ N_{0.19}\ O_{1.76}$	1180	627	-397.1
TREATED WOOD PARTICLES	$CH_{1.44}O_{0.66}$	233	52.3	-599.5

Table 2 – Thermochemical properties of the components of the pyrotechnic mixtures.

3. THEORETICAL COMBUSTION PREDICTION

The theoretical combustion prediction and evaluation starts with the prediction of combustion products, using THOR code, based on theoretical work of Heuze et al., 1985, and later modified (Campos, 1991, Duraes et al., 1995, 1997). Several equations of state can be used, namely BKW, Boltzmann, H9, H12 and H_L (Duraes et al., 1995, 1997).

The classical combustion system is generally a CHNO system, but in our case it has been introduced the Na element of sodium nitrate (SN). In THOR code it is possible to consider up to m atomic species (m<20) and to form n chemical components with these atomic species (n<40), assuming between these n chemical components, m are considered "basic" chemical components and n-m "non basic". The selection "ab initio" of the "basic" chemical components depends on the equivalence ratio r of the mixture, related to the stoichiometry (r=1), and they are those that are expected to have significant concentrations in final products composition. For our system m=5 *(C, H, N, O* and *Na)* it has been selected:

- CO_2, H_20, O_2, N_2 and NaO_2 for poor mixtures (r<1),

- CO_2, H_2, H_20, N_2 and *NaOH*, for rich mixtures (r>1) of initial low density and *C(s)*, CO_2, H_2O, N_2 and *NaOH* for rich mixtures of initial high density (initial condensed or solid components).

The mass balance yields a linear system involving m equations. The left n-m equilibrium equations are determined by the method of Lagrange multipliers or the equilibrium constants. In order to determine the chemical concentration of the n components, for imposed P and T conditions, it is assumed the minimum value of global Gibbs free energy $G = \Sigma\ x_i\ \mu_i$, being

the Gibbs free energy of each component $\mu_i = G_{Oi}(T) + R\ T\ \ln P + R\ T\ \ln (x_i)$. The values of $G_{Oi}(T)$ are the Gibbs free energy as a function of temperature. They can be obtained from JANAF Thermochemical Tables, 1971, and from polynomial expressions of Gordon and McBride, 1971. The solution of the composition problem involves simultaneously:

- the thermodynamic equilibrium, obtained with the mass and species balance, and the equilibrium condition $G=G_{min}$ (P,T,x_i), previously described, generally applying to the condensed phase the model proposed by Tanaka, 1983,
- the thermal equation of state (EoS),
- the energetic equation of state, related to the internal energy $E = \Sigma x_i e_i(T) + \Delta e$, $e_i(T)$ calculated from JANAF Thermochemical Tables, 1971, and from polynomial expressions of Gordon and McBride, 1971,
- the combustion regime, being $P_b=P_O$ constant for the isobare adiabatic combustion (equal final and initial total enthalpy $H_b=H_O$).

The used values for calculations are presented in Table 2. The calculations were performed for a constant ratio of AN/SN (86/14%), changing the concentration in polyurethane binder, for an equivalence ratio r (related to the stoichiometry) from 0.9 until 1.2, assuming that the existing excess of PUR (related to the imposed r) was pyrolised. The mass concentration of wood was also changing – it is presented the calculations for wood mass concentrations of 1.2 and 2.4%. The influence of $\Gamma=dH/dE)_S$ and its relationship with $\gamma=c_p/c_v$, proves the validity of selected EoS (H_L) for our calculations (vd. Duraes et al.,1997).

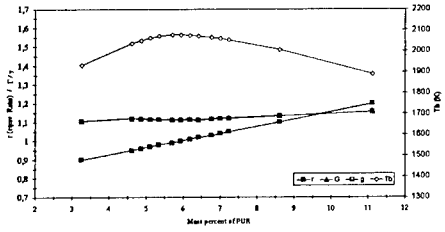

Figure 1 – Calculated values of r (equiv. ratio), Γ, γ and Tb, as a function of mass percent of PUR for a constant percent mass of 1.2% of wood.

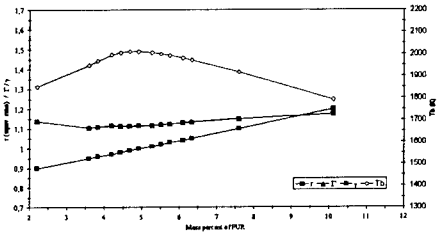

Figure 2 – Calculated values of r (equiv. ratio), Γ, γ and Tb, as a function of mass percent of PUR for a constant percent mass of 2.4% of wood.

Calculated results (vd. Figures 1 to 4) show the maximum calculated combustion temperatures (Tb~2100 K and Tb~2000 K for 1.2 and 2.4% of wood) obtained for r~1 (assuming a global reaction between components). The composition of combustion products

is presented in Figures 3 and 4. It proves the possibility of a PUR pyrolisis regime for highest PUR concentrations.

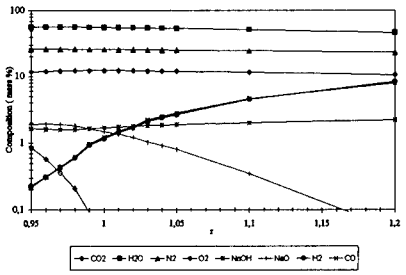

Figure 3 – Mass percent composition of combustion products for 1.2% of wood.

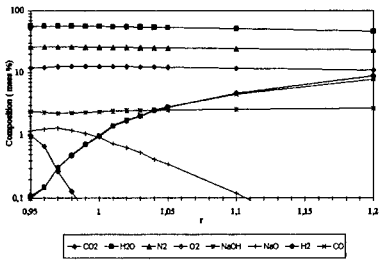

Figure 4 – Mass percent composition of combustion products for 2,4% of wood.

4. COMPONENTS AND MIXTURES

AN (Ammonium Nitrate)

It is a crystalline white solid, colourless, very hygroscope, and highly water-soluble. It is usually sold as prills due to his strong water affinity. This component shows five different physical solid sate phases in the temperature range (–18) - (+125) °C. The AN used in this work was tested by DCS/TGA techniques (Figure 5). The three first peaks in thermogram correspond to the following phase changes: solid phase IV directly to solid phase II (T~53°C); solid phase II to solid phase I (T~125°C); and melting point (T~169°C), which means that we worked with PSAN (Phase Stabilised Ammonium Nitrate). PSAN is AN with Ni, Cu, or Zn oxides, which promote the phase IV changing directly to phase II, avoiding the large volume expansion that occurs when phase IV changes to phase III at 32 °C. The fourth peak corresponds to AN thermal decomposition at 210°C, with nitrogen oxides and ammonia formation and release.

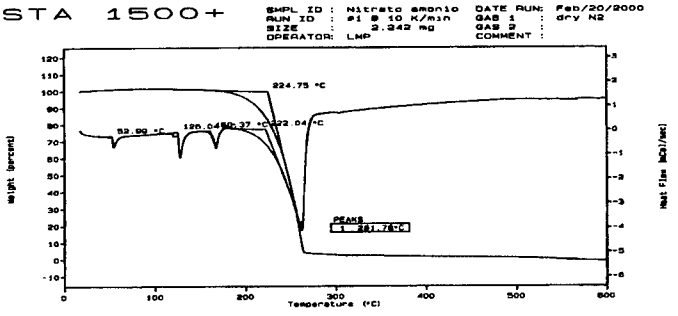

Figure 5 – AN thermogram by DSC/TGA techniques.

SN (Sodium Nitrate)

It is a crystalline white solid, colourless, very hygroscope, and highly water-soluble. SN produces a characteristic yellow flame due to the presence of Na chemical element. This salt melts at 306.8 °C and decomposes at 380 °C, releasing oxygen and converting into nitrite. SN is also usually sold as prills due to his strong water affinity.

Prills of AN and SN were mixed in the 86% AN to 14% SN ratio (as it was explained before). Then, they were reduced together to a fine powder, which can be seen in the picture b) - Figure 6.

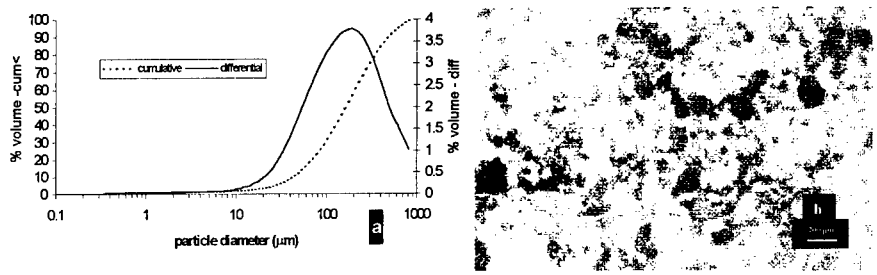

Figure 6 – Granulometric curves (a) and optic microscope picture (b) from the AN/SN crystal mixture.

DMFA (N,N-dimetil-formamide)

DMFA was used to solublize AN and SN as much as possible and to promote these salts diffusion into the wood particles. Solubility tests were made previously with DMFA and other solvent candidates, such as ethanol and methanol. DMFA presented better solubility results for both AN and SN: 63g AN / 100g DMFA and 15.8 g SN /100g DMFA at 60°C. It was observed an interesting result from these solubility tests, which was the recristallization of AN and SN (when their DMFA solutions cool to the room temperature). In fact, the new crystals have the needle appearance, that can be seen in Figure 7, and no morphology changes were then observed, even during months, to light exposure.

PUR (Polyurethane)

This component was used not only as combustible but also as a binder for good rheological properties of the final mixture. The polyurethane is an well known synthetic polymeric material, resulting from the reaction between a prepolymer with molecules hydroxyl terminated and a diisocyanate. In this work it was used a commercial polyurethane foam (obtained from two liquid solutions, mixed in the ratio 100/110). A free expansion (without any filler material) of this material results in a foam with 0.032 density.

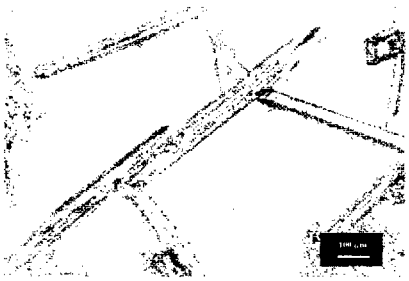

Figure 7 – AN crystals from recrystallization of AN/DMFA solution, obtained by temperature variation from 60°C to room temperature.

Wood (pine) treated particles

Wood is essentially composed by cellulose, hemicelluloses, lignin and minor components. In this work we wanted to reduce the apparent and bulk densities of pine particles, undersize 125 μm (Figure 8), by removing part of these constituents. So, the particles were treated with 1% NaOH water solutions (following the Soda treatment process, used in the pulp industry) for a 4% solid/liquid ratio, during a time range 2 - 135 min. No morphological changes were observed between the treated and non-treated particles, but the samples had a medium mass loss of 25% for all the treatment time duration. The mass reduction was due to lignin and minor components extraction. The observed time no dependence is related to the used very small particle size (the chemicals diffusion into the particle porous became a not controlling step). The granolumetric distribution changes are negligible (Figure 8), but the objective was achieved: the bulk density was reduced 25%. This density value was obtained by mercury intrusion porosimetry analysis technique (Porosizer 9320 from Micromeritics). The bulk density seems only to be reduced by its apparent density parameter (bigger porous dimensions) due to the observed no morphological or no granulometric changes. Table 2 presents the main properties of these particles.

Mixing procedure

The mixture preparation process is a very important step, even decisive, to the final mixture combustion results. Several procedures were tested. The following steps compose the optimised procedure in order to achieve the best-mixed mixture:

- after adding all DMFA to half mass of the crystal AN/SN mixture, and mixed it very well, it was added one of the components of the polyurethane solution system;
- after all wood particles were added and mixed again;

- finally, it was introduced the left AN/SN crystal half mixture and the other PUR component, mixing only during a short time, in order of not allowing the reticulation reactions develop during this last mixing process.

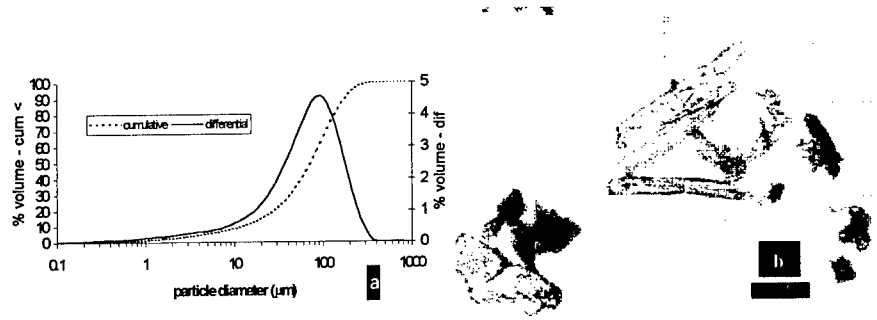

Figure 8 – Granulometric curves (a) and optic microscope picture (b) from the pine treated particles.

The experimental mixture was mixed using an original twin screw mixing system, with two intermeshing screws without any metal to metal contact, and injecting the mixed composition directly inside the test confinement (5 x 5 cm diameter PVC test-tube), where the expansion phase occurs (Figure 9). The obtained final densities are presented in Table 3. The test-tube is PVC made because it does not burn during the combustion tests (this would wrongly change the mass evaluation, introducing experimental errors). The Figure 10 shows an optic microscope picture of a pyrotechnic composition prepared by the previous process.

(MASS PERCENT) PUR ↓ PINE→	1,2	2,4
17	0.600	0.907
19	0.436	0.630
21	0.410	0.426

Table 3 – Global apparent density of experimental mixtures.

Figure 9 – Cure process: a) expanding mixture b) complete expanded mixture c) mixture final appearance before tests (mass excess eliminated).

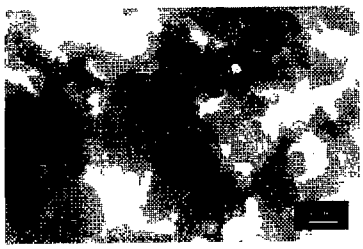

Figure 10 – Optic microscope picture from a prepared pyrotechnic mixture.

DSC/TGA techniques were used to obtain the thermograms of the mixtures (Figure 11). It can be concluded, from the thermograms, that the thermal decomposition of these compositions is a complex process, with many stages. In fact, it can be observed more than 3 slops, in the mass loss curve, for all the studied compositions, which indicates that we are in the presence of more than 3 series reaction systems, with gas generation. Another important observation is the endothermic AN decomposition (Figure 11), at 210°C, to be completely covered by the heat release of the mixture decomposition (so it is only observed an exothermic process).

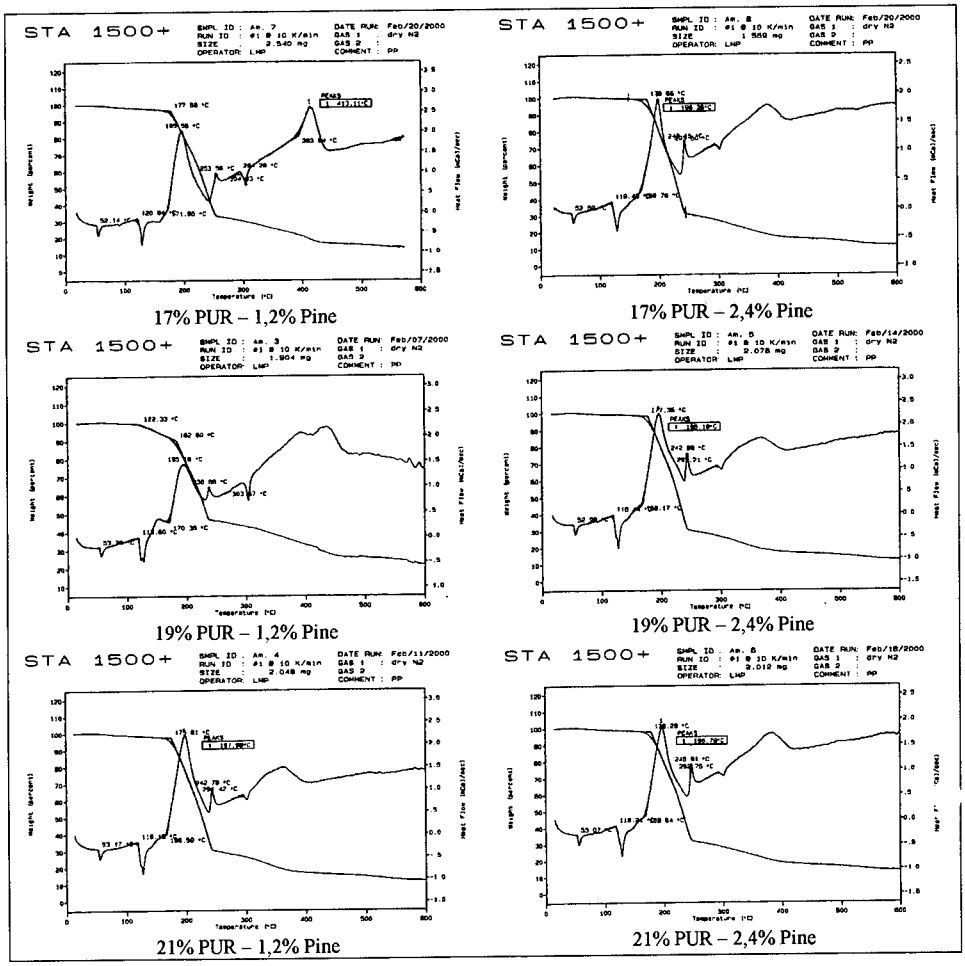

Figure 11 – Thermogram curves of the pyrotechnic mixtures, obtained by DSC/TGA techniques.

5. EXPERIMENTAL RESULTS AND DISCUSSION

The used experimental apparatus (Figure 12) allows the:

- *-Temperature recording and thermal determination of regression velocities.* It was used two Cr/Al thermocouples (Thermocoax TKI 10/10/NN), shown in Figure 13, connected to a digital signal analyser (Tektronix TDS 320);
- *Mass loss recording, as a function of time (gravimetric analysis).* It was used a digital 0.001g precision balance (Mettler), connected to a data acquisition system;
- *Video-crono-photography.* It was used a video camera of 50 fps and second time resolution, recording directing the flame front from a reflecting mirror, in order to get the upper plan of the flame combustion with the minimum optical deformation.

The ignition procedure was performed spreading ethanol in the top of the mixture and igniting this system with an external flame source.

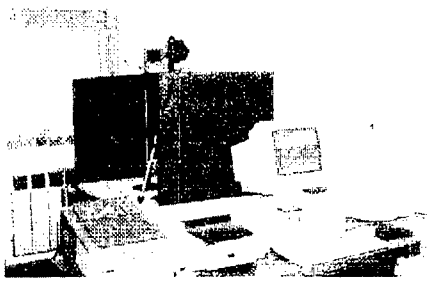

Figure 12 – Experimental apparatus.

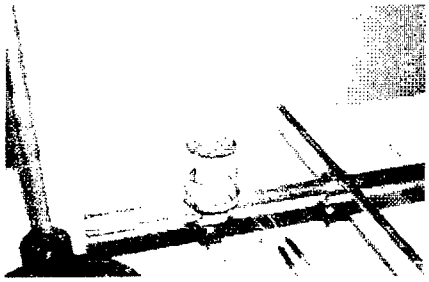

Figure 13 – Support, combustion plate and cylindrical test-tube with the attached thermocouples.

The video record of the flame (Figure 14), during combustion, allows to observe many heterogeneities. A video treatment (by solarized effect) proves the existence of hot spots, where the combustion is very much intense and generating points of dispersing flames (vd. Figure 15). The existence of void cavities, by binder expansion, closing nitrate particles, allows the combustion of nitrates with an increase of thermal insulation and local pressure. The observed flame starts with a typical yellow colour, showing the existence of Na. It progress generates pockets of melted AN/SN crystals, that seem to be partially absorbed by the wood particles. These phenomena allow to keep the melted AN/SN enough time to ensure a more perfect combustion with the polyurethane (or with pyrolised polyurethane material).

Figure 14– Flame aspects.

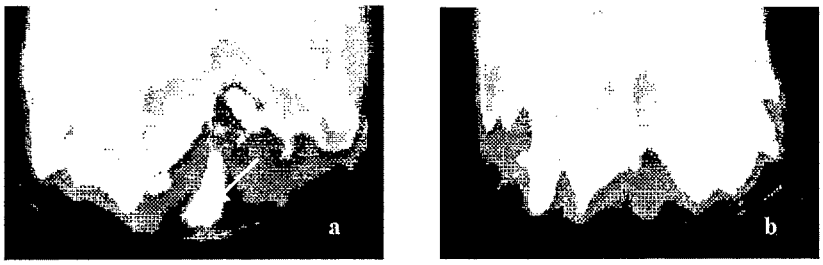

Figure 15 – Flame aspects, optical treated by solarized effect, showing the local and temporary hot spots.

The used equipment allows the record, in real time, of measured temperature from the two thermocouples (vd. example in Figure 16). These records allow the evaluation of the mean temperatures of combustion, as a function of the PUR and wood concentrations (Figure 17).

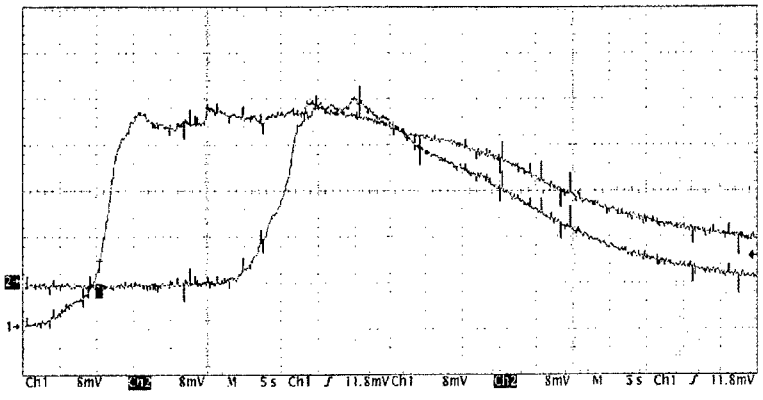

Figure 16 – Example of experimental temperature records (190.5 °C/ vertical div.), as a function of time (5s/ horizontal div.).

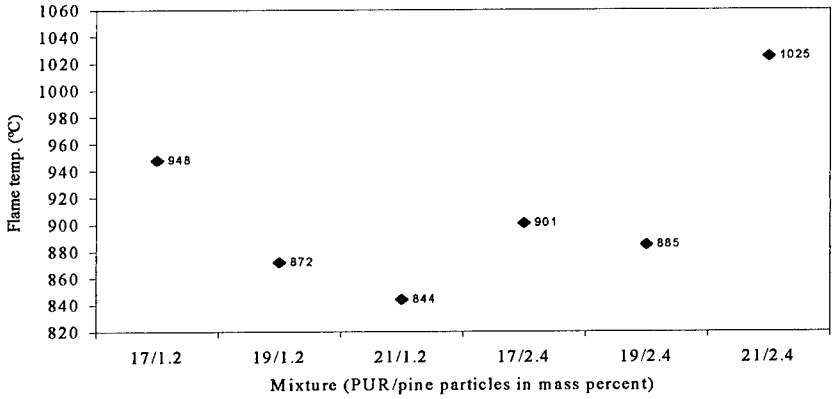

Figura 17 – Experimental mean flame temperatures, as a function of mass percent of PUR /wood.

The record of mass loses, by gravimetric analysis, as a function of time (Figures 18 and 19) allows the direct evaluation of mass regression rate.

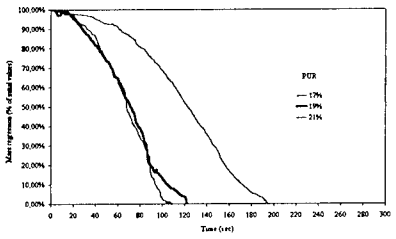

Figure 18 – Mass regression, as a function of time, for wood concentration of 1.2 %.

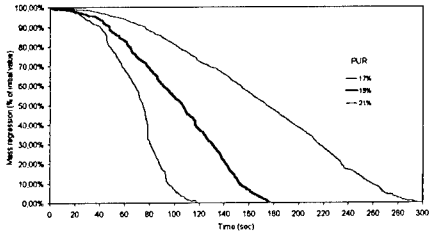

Figure 19 – Mass regression, as a function of time, for wood concentration of 2.4 %.

The evaluation of regression rate of the used mixtures can also be obtained from the definition of regression velocity V_F , with $M_i \frac{dm}{dt} = \rho A_F V_F$, where dm/dt represents the mean values of mass loses, as a function of time, during the time between 0.2 and 0.8 of total time of the combustion phenomena (reducing the ignition and extinction delays) from the temperature records. The correlation of mass regression, from temperature records, with those obtained of gravimetric analysis (Figure 20), shows a good agreement and proves not only the global stable behaviour of flame propagation, but also the small scale of observed flame hot spots.

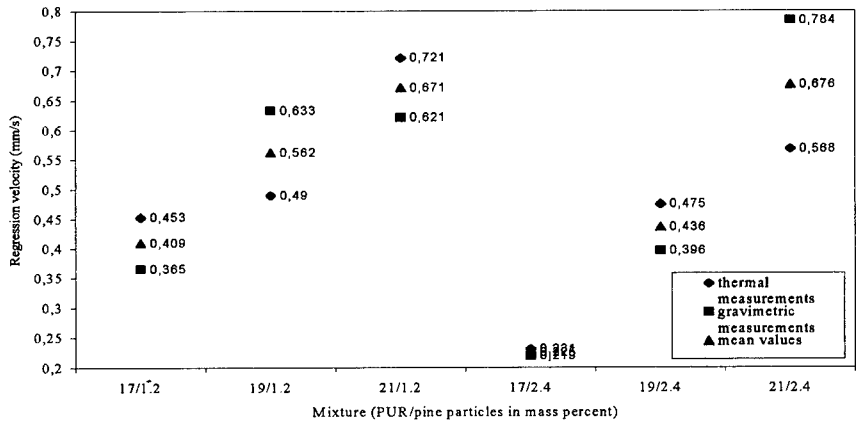

Figure 20 – Regression velocities (thermal and gravimetric measurements and mean values), as a function of PUR/wood concentrations.

6. CONCLUSIONS

In the present work, the pyrotechnic mixture of ammonium and sodium nitrates is prepared using dimethylformamide as solvent, mixed with wood (pine) particles and binded by an expanded two components polyurethane solution. The existence of treated wood particles, in this media, reduces also the agglomeration of nitrate particles. The theoretical calculations allow the evaluation of effective contribution of components in the combustion. The existence of void cavities, by binder expansion, closing nitrates particles, allows the combustion of nitrates with an increase of thermal insulation and local pressure. The observation of flame, during combustion at atmospheric pressure, proves the existence of hot spots and the influence of wood particles (inside polyurethane void cavities) absorbing liquid nitrates, after its phase transition, increasing the stability of the flame (with measured velocity values of ~ 0.5 mm/s). The presented experimental results prove the great influence of binder cavities and the existence of polyurethane partial pyrolisis during the combustion phenomena.

REFERENCES

Campos, J., "Thermodynamic Calculation of Solid and Gas Combustion Pollutants Using Different Equations of State", *Proc. of 1st International Conference on Combustion Technologies for a Clean Environment*, Vilamoura, Algarve, Portugal, pp. 30.4-1-30.4-11, (1991).

Carvalheira, P., Campos, J., and Gadiot, G., "Burning Rate Modifiers for NA/HTPB-IPDI Composite Solid Propellants for Gas Generators", *Proc. of the 26th International Annual Conference of ICT*, pp. 69.1-69.14, (1995).

Durães, L. et al., "Combustion and Detonation Modelling Using THOR Code", *Proc. of the 28th International Annual Conference of ICT*, pp. 89.1-89.10, (1997).

Durães, L. et al., "New Equation of State for the Detonation Products of Explosives." *Proc. of 1995 APS Topical Conference on Shock Compression of Condensed Matter*, Seattle, WA, USA, pp. 385-388, (1995).

Durães, L. et al., "Thermal Decomposition of Energetic Materials Using THOR Code", *Proc. of the Twenty Second International Pyrotechnics Seminar*, Fort Collins, Colorado, pp. 497-508, (1996).

Gordon, S., McBride, B.J., "Computer Program for Calculation of Complex Chemical Equilibrium Compositions, Rocket Performance Incident and Reflected Shocks and Chapman-Jouguet Detonations", *Report NASA SP 273*, NASA Lewis Research Center, (1971).

Heuzé, O. et al., "The Equations of State of Detonation Products and Their Incorporation into the Quatuor Code", *Proc. of the 8th Symposium (International.) on Detonation*, Albuquerque, New Mexico, pp. 762-769, (1985).

Janaf, *Thermochemical Tables*, 2nd Edition, National Bureau of Standards, Washington DC., (1971).

Kolaczkowski, A., *Samorzutny Rozklad Saletry Amonowej*, Wydawnictwo Politechniki Wroclawskiej, Wroclaw, (1980).

Pires, A. et al., "Incineration of Explosives in a Fluidised Bed", *Proc. of the 27th International Annual Conference of ICT*, pp. 80.1-80.14, (1996).

Tanaka, K., "Detonation Properties of Condensed Explosives Computed Using the Kihara-Hikita-Tanaka Equation of State", *Report from National Chemical Laboratory for Industry*, Ibaraki, Japan, (1983).

Chemical and Morphological Analyses of Plasma-Treated Solid Propellant Surfaces

P. Kaste, A. Kinkennon, R. Lieb, A. Birk, M. Del Guercio, J. Newberry, M. Schroeder, R. Rodriguez
U.S. Army Research Laboratory, AMSRL-WM-BD, APG, MD 21005-5066, USA

ABSTRACT

The morphological and chemical characterization of M30 propellant grains recovered after conventional or plasma ignition in interrupted closed bomb experiments has been performed. The capillary material used during plasma ignition was either poly-ethylene (PE) or polyethylene terephthalate (Mylar). Propellants were extinguished at pressures between 35 and 100 MPa. The samples are of interest due to previous reports of apparent burning rate augmentation with plasma ignition of M30, compared to conventional ignition, in non-interrupted closed bomb experiments [1]. In the current work, differences between extinguished grains from conventional and plasma ignition were primarily physical or morphological in nature. For the extinguished grains from PE plasma ignition there appeared to be a stripping of NQ crystals in the perforations. Along the outer surfaces of the grain ignited with plasma evidence of embedded particles and increased surface area were observed; the melt layer was immeasurably thin. Although extensive chemical characterization has been performed, there appears to be very little chemical difference between the burned surfaces of the plasma and conventionally ignited samples. The SEM analysis of grains recovered after plasma ignition using PE capillaries showed that NQ depletion in the perforations was most evident at the lowest blowout pressure used (35 MPa) and seemed to diminish at higher pressure, apparently becoming obscured by "normal" burning processes. Thus, it appears that plasma-propellant interactions and associated effects occur only very early during ignition. This is consistent with the fact that few differences in the chemical composition are observed for plasma and conventionally ignited samples. SEM analysis of grains recovered from plasma ignition with Mylar capillaries was also performed, and compared to conventional ignition [2]. The grains from conventional ignition exhibited normal progressive burning. However, grains recovered from plasma ignition had pits, gouges and cracks in the surfaces. These features provide unprogrammed surface area increases which could contribute to the apparent burning rate augmentation.

INTRODUCTION

The interaction of plasmas with solid propellants is being investigated using an interrupted closed chamber capable of either plasma or conventional black powder ignition. The ultimate goal is to understand plasma-propellant interactions so that plasma ignition may be used for improved gun systems. Low-density plasmas offer the potential for enhanced gun performance through short ignition delays, efficient ignition of high energy density charges, and the ability to tailor the mass generation rate of solid gun propellants. Replacing conventional igniters could also improve vulnerability properties. In previous, non-interrupted,

closed bomb analyses, the effect of plasma ignition on propellant burning rate was investigated, and it was reported [1] that for M30, a 33% increase in burning rate over the range of 100–220 MPa occurred with plasma ignition, relative to conventional ignition with black powder. Apparent burning rate augmentation is also observed for M30 using plasma ignition with Mylar capillaries, but to a lesser extent. The plasma augmentation of JA2 burning rate was insignificant. Researchers in the international community have also reported augmentation of the burning rate with nitramine-based composite propellants [3].

In this work, interrupted burn experiments with conventional or plasma ignition have been performed for the dual purpose of: a) determining whether the increase in burning rate for M30 was intrinsic to the propellant or the result of an increase in surface area due to, for example, fracture [4] or porous burning; and b) characterizing extinguished grains to understand the ignition and combustion chemistry that occurs with the two igniters. The approach was to repeat key experiments from Del Guercio [1] with M30 and JA2 propellant but interrupt the burning at 35, 75, and 100 MPa and collect the extinguished propellant for physical examination and chemical analysis. The interrupted closed bomb experiment offers a means of studying basic plasma-propellant interactions under well-defined conditions of plasma energy and power input, pressure profile, and proximity of the grains to the plasma. Since the blowout pressure can be varied, the grains can be studied after ignition when plasma-propellant interactions would be dominant, or at higher blowout pressures when the propellant burning would be dominant. Morphological and chemical characterization of residual propellant from both plasma and conventionally ignited samples has provided a method for studying differences in plasma and conventional closed bomb ignition.

EXPERIMENTAL

1. Closed Bomb Firings. Propellant samples for closed bomb analysis consisted of seven-perforated grains of M30 or JA2 with a diameter, length, and perforation diameter of nominally 0.75, 1.5, and 0.07 cm, respectively. Closed bomb analyses of M30 and JA2 were performed in a 3.81-cm inner diameter (ID) closed bomb with a volume of 129 cm^3. For all firings, a typical propellant charge weighed 32 gm. For interrupted burn experiments, the addition of an interface from the bomb to the evacuation chamber yielded a total closed bomb area of 150 cm^3 (Figure 1). The expansion chamber consists of a 240-liter tank with a 2.5-cm-diameter blowout area interfaced to the closed bomb. Rapid extinguishment of the propellants occurred due to the sudden expansion into the evacuated tank. Soft capture of the propellant was achieved with a lining of thermally resistant polyurethane foam. In the case of plasma ignition, a perforated straw with holes was used to facilitate uniform distribution of the plasma around the propellant (Figure 2). In the conventional mode, an electric match was used to ignite 0.6 gm of black powder confined in a plastic straw with the propellant distributed in two tiers concentrically positioned around the straw (Figure 3). The plasma was generated by an electrical pulse to a nickel fuse wire, which was rapidly vaporized. This resulted in ionization of the capillary liner (PE or Mylar), and a high current discharge was sustained. The time interval for injection was between 0.9 and 1.2 ms. The electrical pulse was generated with a 400-kJ capacitor-

based pulse-forming network, with a charging voltage of 4 kV and an output energy of up to 29.3 kJ. The chamber was equipped with one or two 607-C4 Kistler pressure transducers.

2. High-Pressure Liquid Chromatography (HPLC)-UV Analysis. HPLC was used to quantify the components, except for nitrocellulose (NC), of virgin and extinguished grains of JA2 and M30. For JA2 propellant, levels of the plasticizers (nitroglycerine (NG) and diethylene glycol dinitrate (DEGDN)) and its stabilizer, Akardite II, were determined. For M30, NG and the crystalline oxidizer nitroguanidine (NQ) were determined. Virgin samples of JA2 and M30 were used to prepare the calibration curves and were prepared in duplicate. The chromatographic parameters are listed in Table 1. M30 samples were run with a detector monitoring both 260 nm for the NQ analysis and 210 nm for the NG analysis. NQ elutes with the extraction solvent, but at 260 nm, only NQ was detected, which improved the error in the analysis.

Table 1. Chromatographic Parameters for JA2 and M30 Component Analysis

Chromatograph	Isco Model 2350 Pump
Stationary Phase	Alltech C18 Econosphere 5u Cartridge
Mobile Phase	CH_3CN:H_2O, 60:40
Flow	Rate 0.5 ml/min
Injection	10- ul Fixed-Loop Injector
Detector	Spectra Physics FOCUS @ 210 nm; 260 nm for NQ
Data Collection	ThermoSeparation Products PC1000 Software

3. Liquid Chromatography-Mass Spectroscopy (LC-MS). LC-MS was used to investigate decomposition of the components of JA2 and M30. A Hewlett-Packard 1090 liquid chromatograph was used with a 59980B LC-MS interface and 5989B mass spectrometer. Outer shavings of the propellant grains were extracted overnight. Extraction solvents were ether (for JA2) and 2:1 methanol:water (for M30). Both solvent systems were chosen to exclude NC in the extract. The ether was evaporated, and the JA2 extracts were re-dissolved in 2:1 methanol:water. Samples were passed through cellulose filters (0.2 μm) prior to injection of 25 μL aliquots. A C18 microbore column (100 x 2.1 mm; 5 μm bead size) was used in the separation. The elution solvent was 50:50 MeOH:water at 0.3 ml/min. The mass spectrometer was run in the electronic ionization mode and ions between 34 and 200 m/z ratio were monitored.

4. Scanning Electron Microscopy (SEM). Micrographs of virgin and extinguished grains were examined to establish any morphological differences between grains ignited by conventional or plasma sources. The grains were cold-fractured along the longitudinal grain axis to expose the burned surfaces of the perforations, a cross-section of the burning surfaces, and the unburned propellant below this surface. The lateral exterior burn surfaces were also examined. The prepared specimens were sputter coated with gold-palladium for 20 to 30 sec at 30 mA. An International Scientific Instruments SEM, model ISI-SS-40, was used with a 10 keV electron beam. The images were captured on Polaroid Type 52 black and white film.

5. FTIR Analysis. Micro-reflectance FTIR was used to obtain spectra of the propellant surface (i.e., about top 10 μm) with no modification of the sample. FTIR analyses were performed using a Mattson Polaris spectrometer operating at a resolution of 4 cm^{-1}. The reflectance spectra were obtained using a Spectra-Tech (Shelton, CT) microreflectance attachment with 32X IR objective and signal averaging 200 scans. Aluminum foil was used to collect the background spectra. Data were reduced with FIRST (Mattson) software; the Kramers-Kronig transformation algorithm was performed on the transmittance spectrum to obtain spectra in absorbance units. Samples for micro-reflectance must be flat, since curvature may distort the focus. Typically, JA2 samples were cut with a razor; M30 samples were prepared by microtoming.

6. X-Ray Fluorescence (XRF) Spectroscopy. XRF spectroscopy was performed on the extinguished grains in order to identify metals present in the plasma that may be incident on the propellant samples. Before obtaining XRF spectra, the propellant grains were cooled to dry ice temperature, split with a knife blade and coated with carbon. Spectra were obtained using a Kevex model 3600-0374 XRF detector interfaced to a Kevex Delta Class Analyzer with Kevex Quantex software, version V. The XRF was interfaced to a JEOL 820 scanning electron microscope (SEM).

RESULTS

1. Closed Bomb Firings. Initial, non-interrupted experiments in which the propellant was completely burned showed that the apparent plasma burning rate augmentation of M30 was greater for the PE capillary compared to the Mylar capillary (Figure 4). The power curve was considered when evaluating each trial with plasma ignition. For burning rate determination, comparable plasma energies and rise times were desired. Figure 5 shows four plots for which the initial rise is similar, but the areas under the curves are much different, yielding input energies of about 18 kJ for the M30 samples and 29 kJ for the JA2 samples. The initial rise is comparable for all samples, so that the strain rates applied to the propellants would be expected to be comparable. Excessive strain rates that might cause fracture as an artifact were thereby avoided.

The P-t curves for the M30 and JA2 samples ignited by plasma are shown in Figure 6, for blowout pressures of nominally 35 and 100 MPa. P-t curves for conventionally ignited M30 are also shown, and are evident from the longer time-to-burst of about 10 ms at 60 MPa. Also apparent is the uniform curvature due to the regular mass generation of the conventionally ignited propellant. In contrast, propellants ignited by plasma show a sharp increase in pressure within the first 1-2 milliseconds due to the sudden plasma impulse, followed by a more typical pressure increase when normal propellant burning takes over. In the case of JA2, early experiments with the PE capillaries were used for plasma generation, and curves with

overlying traces for the initial pressure rise were obtained. However, because none of the many firings with PE yielded overlapping curves for M30, Mylar capillaries were used for the M30 series.

Originally, it was hoped that a propellant burning rate could be computed using BRLCB [5] for each closed bomb trial using the P-t curves and the changes in the dimensions of grains [6]. However, the fact that the P-t curves of the plasma-ignited grains showed an initial rapid pressurization made the analysis more complicated. Therefore, for a given propellant, two firings were selected that had similar plasma power conditions and pressure-time histories, but were extinguished at two different pressures. (See Figure 6, ETC curves for M30 or JA2.) The recovered grains from both firings were measured to determine the extent of regression between the two blowout pressures. The regression between the two blowout pressures was also calculated assuming conventional burn rate parameters. Comparison of the calculated and measured regression distances gave an indication of the extent of the intrinsic post-plasma burning rate augmentation. Typically, during the plasma pulse the pressure would rise to about 30 MPa for PE capillaries and about 20 MPa for Mylar capillaries. It is noted that pressures comparable to the 20-30 MPa initial pressure spikes were generated in analogous closed bomb trials in which no propellant was used, showing that the pressure increases are due to generation of the plasma [7].

For both M30 and JA2, no was evidence was found of burning rate augmentation after the plasma event (i.e. the measured grain regression was consistent with that calculated using conventional burn rate parameters for these propellants). Thus, it appears that the post-plasma burn rates are not intrinsic. For both M30 and JA2, grain regression at 35 MPa was consistently greater than predicted based on conventional burning rates, which is evidence that there is burning rate augmentation (40-120%) during the plasma event. Details of this analysis are provided in [6].

Burning occurred to a greater extent in the samples ignited with black powder than with the plasma due to the fact that, with plasma-ignited samples, a significant fraction of the total pressure was due to plasma injection, rather than propellant burning. This initial plasma pressurization occured rapidly, leaving a shorter effective time for propellant burning to occur (about 4-6 msec at 60 MPa), compared to conventional ignition (about 11 msec at 60 MPa; see Figure 6). This occurred whether Mylar or PE capillaries were used in the plasma ignition. For M30 grains recovered at nominally 35 and 60 MPa, the grain regression measured for plasma ignited samples (Mylar capillaries) was 0.23 and 0.33 mm respectively, while for conventionally ignited samples, the regression measured for the same blowout pressures was 0.37 and 0.62 mm respectively.

2. HPLC. Virgin and extinguished samples of JA2 and M30 from conventional and plasma (PE-based capillary) ignition were analyzed by HPLC. The components of JA2 (the plasticizers, NG and DEGDN, and stabilizer, Akardite II) and M30 components (NG and crystalline NQ) were analyzed. No decomposition products were detected from either virgin or extinguished grains. Moreover, no significant difference in the

plasticizer (NG, DEGDN) levels of virgin for extinguished JA2 propellant (either from conventional or plasma ignition) was observed. Nor does M30 show any difference between the virgin and extinguished grains.

3. LC-MS. The extinguished samples of JA2 and M30 at various blowout pressures were analyzed; virgin samples were included as references. Only the outer surfaces of the grains were sampled in order to obtain the greatest possible concentration of any decomposition products present. The LC-MS chromatograms obtained for virgin and conventionally ignited JA2 were indistinguishable. For the plasma-ignited sample, an early eluting peak (less than 1 min) is observed with the plasma sample. Although the peak overlaps a methanol impurity peak (determined from a separate analysis of methanol; not shown), the peak is too large to be due to this component alone. Major peaks in the mass spectrum of this unknown were 63, 77, 120, and 148 m/z. It is noted that the nitrate esters (e.g., DEGDN and NG) typically yield a 46-m/z fragment, presumably due to ONO, and this fragment was not detected in the unknown. Thus, if it is a decomposition product of the NG or DEGDN, it would apparently be totally denitrated. The chromatograms of the M30 components were also virtually identical, and no decomposition product was detected.

4. Scanning Electron Microscopy. Extinguished surfaces have been studied previously [8], and it has been noted that many combustion features are preserved on surfaces that undergo a rapid pressure reduction. The flame is rapidly blown away from the surface, which quickly solidifies, leaving most of the burning surface features intact. SEM micrographs from this study revealed several interesting features. The exterior lateral surfaces of many of the extinguished grains from both the plasma (PE capillary) and conventional ignition sources appeared very similar except for one feature. In plasma ignition, the grains showed evidence of burning caused by hot particles being sprayed onto the grain surface, as shown in Figure 7, 90X. Also, several grains showed very irregular, nonprogrammed burning (Figure 7, 5X). These phenomena would increase the surface area, and would give the appearance of a higher burning rate during the early stages of the propellant combustion. However, since the augmentation is caused by increased surface area, the apparent burning rate will be lowered in later stages of burning, as the resulting surface area is reduced due to the intersection (burn through and crossing) of burning surfaces.

Another interesting feature was noted on the burning surfaces within the perforations. Most burning surfaces of extinguished propellant appeared as shown in Figure 8, which depicts a conventionally ignited grain. Note that the surface is smooth, indicating melting. However, in Figure 8 there seemed to be no indication of melting with plasma ignition. Moreover, there appeared to be a series of grooves that conformed to the size of NQ particles (about 5 μm in diameter, 50-200 μm long). Stereoscopic pictures confirmed the presence of grooves. This suggests a different process for the plasma-ignited samples that caused the NQ crystals to vacate the matrix. It is noted that the grooves were much less prominent at higher pressure (100 MPa, not shown) and the surface appeared more like the conventional. This is consistent with the burning mechanisms returning to similar processes at higher pressures.

SEM analysis of grains extinguished from plasma ignition using Mylar capillaries was also performed, and compared with those ignited with black powder. The analysis of these grains was more detailed than those described above. Prior to the closed bomb analysis, the grains were scored in a specific manner which enabled reconstruction of their relative position, including orientation relative to the igniter, in the original charge. Mapping of the entire grain was performed for several representative grains. The results for a grain recovered after black powder ignition is shown in Figure 9. The surfaces were smooth and evenly-burned, with no unusual deformities. In contrast, a grain recovered from plasma ignition with Mylar capillary is shown in Figure 10. Cracks and depressions, yielding surface areas greater than normally-burned surfaces, are obvious.

5. FTIR Analysis. Microreflectance FTIR analysis of propellant grains was performed to determine differences in chemistry with plasma vs. conventional ignition. The lateral, external surfaces of JA2 grains ignited with plasma or black powder showed evidence of aldehyde formation (appearance of a carbonyl band at 1735 cm^{-1}) due to denitration of the nitrate esters (Figure 11). The carbonyl formation was detected at the higher blowout pressures but was not apparent at 35 MPa (Figure 11). Thus, denitration appears to be related to extent of burning, not to the type of ignition.

Since, for M30, NQ depletion in the perforations was observed in the SEM analysis, the microreflectance spectra of both the perforated regions and lateral surfaces of the extinguished M30 grains were obtained. The results for the lateral surfaces are shown in Figure 12a. The NQ diminished with increasing pressure in both conventional and plasma-ignited samples. Conventionally ignited samples at 75 MPa burned (i.e., regressed) the most, and for these samples NQ at the surface is virtually eliminated. Thus, the depletion of NQ at the surface at pressures up to 100 MPa appears to be related to extent of regression, rather than to the ignition method. This trend was the same whether the plasma ignition was initiated with a PE or Mylar capillary.

The microreflectance spectra of the M30 perforated regions were also obtained. Figure 12b shows the results for PE capillary plasma ignition, which are similar to those for the lateral surfaces (i.e. greater NQ reduction occurs at higher pressure). This trend was the same whether plasma or conventional ignition was used.

This is seemingly in contrast to the SEM results (previous section), which showed that, particularly at 35 MPa, NQ particles appeared to be stripped from the perforations. The SEM and FTIR results can be resolved by the fact that the NQ crystals are locally concentrated and aligned along the direction of extrusion near the surface of the perforations. Previous SEM results [9] have shown that bundles of NQ crystals align along the perforation axis, thinly coated in binder, with each crystal being approximately 5 μm

in diameter. Thus, it is very feasible that after the outer NQ crystals are removed, the new surface generated is equally rich in NQ crystals. At low pressure blowout (35 MPa), regression due to normal burning has apparently not removed the crystals. The micro-reflectance spectra are proportional to the concentration of NQ crystals in about the top 10 μm of the surface. Thus, the FTIR spectra are comparable for virgin and plasma-treated samples, whereas the SEM, with topological capability, detects the NQ crystal loss [9]. It is also noted that surface alignment of the NQ crystals does not occur to the same extent along the outer, lateral surfaces, so that such NQ stripping is specific to the perforated regions.

6. XRF Spectroscopy. XRF was used to detect metals from the closed bomb hardware which may impinge on the sample. The XRF results for the outer, lateral surfaces and for the perforated surfaces of the extinguished grains were examined. Iron from the closed bomb hardware was found on the outer surfaces for both plasma (PE capillary) and conventionally ignited samples. The results for M30 are shown in Figure 13, inserts. In addition, Cu from caps on the electrodes was deposited on the plasma-ignited samples. The results for the perforated regions were quite different for conventional vs. plasma ignition (Figure 13, b and c). As had been observed on the outer surface, the plasma-ignited sample shows the presence of Fe and Cu inside the perforations. However, although Fe was found on the outer surface of the conventionally ignited sample (Figure 13, insert), it is not observed inside the perforations. The spectrum of a virgin grain shows no significant Cu or Fe present (Figure 13a).

The presence of metals inside the perforations in the case of plasma ignition, while none is found with black powder ignition, may suggest a greater force penetrates inside the perforations during plasma ignition. This is consistent with SEM results that show that NQ in M30 is stripped by plasma ignition, and not by conventional ignition.

CONCLUSIONS

In order to better understand the basic mechanisms of plasma-propellant interactions, the morphological and chemical characterization of extinguished M30 propellants from conventional and plasma (PE and Mylar) ignition has been performed. The ultimate goal of this work is to develop design rules for plasma ignition of propellants so that increased performance and reduced vulnerability may be realized. Although few differences between conventional and plasma ignition were detected in the chemical analyses, important physical and morphological differences were observed. An initial rapid pressure increase was evident in the P-t traces for plasma ignition, resulting in the blowout pressure being achieved more quickly, so that there was less time for the propellants to burn. Thus, extinguished grains from conventionally ignited samples regressed to a greater extent than those ignited with plasma. Moreover, the initial pressure rise might have resulted in a shock formation in the closed bomb. A similar system in which the plasma was generated with an ablating capillary has been modeled for open expansion into air [10]. The model

revealed an underexpanded jet, with a precursor shock, a barrel shock that reflects at a triple-point and a Mach disk. Although differences exist between the open-air and closed bomb systems, including boundary and electrical characteristics, it seems reasonable that some sort of shock or force occurs that modifies the solid propellant, and is greater for plasma than for black powder ignition. Dynamic compressive mechanical properties testing [11,12] has shown that M30 is more brittle than JA2. Thus, it has been proposed [13] that the apparent burning rate augmentation of M30 was due to grain fracture. Nonetheless, no widespread fracturing were observed. This is important in that propellant fracture has severe adverse implications for gun systems.

Several other observations related to the propellant surface are consistent with an increased interaction of the plasma with the propellant, compared to black powder:

a) NQ crystals appear to be stripped from the perforation axes in plasma-ignited M30 propellants. The normal melt layer observed for conventionally ignited samples is not observed with plasma ignition.

b) Metals from the closed bomb hardware are apparent in the perforations of the plasma-ignited samples (PE), but are not found in the conventionally ignited samples.

c) Irregular burning is found on the lateral surfaces of some plasma-ignited M30 propellant grains, possibly due to ablation.

Although extensive chemical characterization has been performed, including D-GC-MS, LC-UV, LC-MS, and FTIR analyses, there appear to be very few chemical differences between the burned surfaces of the plasma and conventionally ignited samples. Efforts to isolate products promptly after sampling were undertaken to improve the sensitivity of the analyses; nonetheless, few specific differences between conventional and plasma ignition were identified.

In fact, it may be that any differences in chemical interactions that occur initially with plasma and conventional ignition are obscured by later burning processes, so that there are few decomposition products remaining on the extinguished propellant surfaces. This is supported by the SEM analysis, which show that NQ depletion in the perforations was most evident at the lowest blowout pressure used (35 MPa) and seemed to diminish at higher pressure, apparently becoming obscured by "normal" burning processes. Thus, plasma-propellant interactions, and associated effects, may occur only very early during ignition. This is consistent with the results reported by Birk [6] that the increase in burning rate due to the plasma occurs during, not after, the plasma event. It is also consistent with a greater force (evidenced by the initial high slope of the P-t curve) or possible shock (analogous to the open air plasma formation) occurring early in the plasma process).

Birk has also analyzed the vivacity curves from the closed bomb trials of the samples studied in this work. Vivacity curves [14] that slope upward with increasing pressure indicate progressive burning, as would be expected from 7-perforated grains. Downward- sloping curves indicate regressive burning, which if

observed for 7-perforated grains implies an increase in surface due to some mechanism other than normal grain burning. Birk has found that JA2 grains appear to burn progressively, while M30 appears to burn regressively. An increase in surface area is consistent with regressive burning.

The source of the increased surface area is being investigated. Kooker [13] has performed simulations showing that the shape and magnitude of the burning rate curves deduced from ETC closed-chamber experiments were reproduced with a modest amount of grain fracture. It is feasible that an increase in surface area by means other than grain fracture (e.g., surface ablation, embedded particles, microcracks etc.) could yield similar results. The SEM mapping of the grains recovered after plasma ignition with Mylar capillaries showed extensive surface area generation not typical of normal burning of perforated grains. It is feasible that such surface area generation could significantly increase the apparent burning rate. A depletion of NQ in the perforations might also contribute to a true burning rate augmentation (in the case of plasma ignition with PE capillaries) through chemical reactions. However, a true chemical burning rate augmentation as the only mechanism for the M30 non-interrupted behavior (Figure 4) would not be consistent with regressive burning.

The plasma dependence on capillary composition is also being further investigated through experiments (7) and modeling (15). The peak pressure measured in empty chamber trials, given comparable plasma energy, is less for Mylar [7] than for PE capillaries. The physical phenomena that might account for this observation are complex. Compared to PE, Mylar produces a more dense plasma, but with lower exit velocity; the calculated temperatures of the effluent for Mylar and PE are comparable (15). Thus, in spite of their different elemental composition, the gas dynamics for PE and Mylar capillary plasmas may be similar. A more detailed analysis is planned.

The capillary residue is clearly different for the two materials. Mylar generates significantly less residue, presumably because Mylar contains oxygen, which assists in the conversion of carbon and hydrogen to permanent gases. Hot particles formed during the generation of the residue may contribute to a true burning rate augmentation, which occurs during the plasma event by processes that could include an increase in surface area due to embedded or erosive particles, increased heat conduction, or other mechanisms.

SUMMARY

In extinguished closed bomb analyses, burning rate augmentation of solid propellants with plasma ignition was found to occur during, but not after, the plasma event. An initial rapid pressure rise, detection of metals in the perforations, stripping of NQ from M30 propellants, irregular surface burning (possibly due to ablation), and hot embedded particles have been observed with plasma, but not with conventional ignition, suggesting a more forceful process for plasma ignition. Significant surface area generation was observed

for grains which were well-mapped in the SEM, which would be expected to increase the mass generation rate. Nonetheless, gross fracture was not observed in grains extinguished after plasma ignition. Moreover, chemical analyses of extinguished grains have not revealed any identifiable differences between plasma and conventional ignition, very possibly because any early chemical interactions are obscured by normal burning processes occurring later. Experimental and modeling efforts are in progress to further understand plasma-propellant interactions, including the effects of heat conduction by hot particles, the influence of shock and thermal waves, and radiation effects. .

ACKNOWLEDGMENTS

Dr. D. Kooker (ARL, APG, MD) spent much time in helpful discussions and his technical insights are very much appreciated. Dr. Michael McQuaid (ARL, APG, MD) is thanked for his consultations in the area of capillary physics. Dr. Michael Nusca (ARL, APG, MD) is thanked for his discussions regarding plasma flow and shock formation.

FIGURES

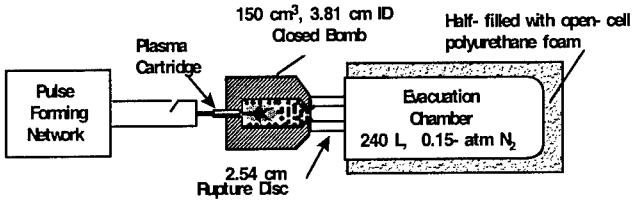

FIGURE 1. Apparatus for Extinguished Closed Bomb Experiments with Propellant Soft-Capture.

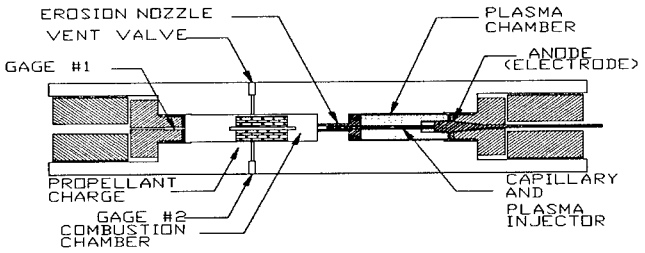

FIGURE 2. Schematic of the Plasma Igniter.

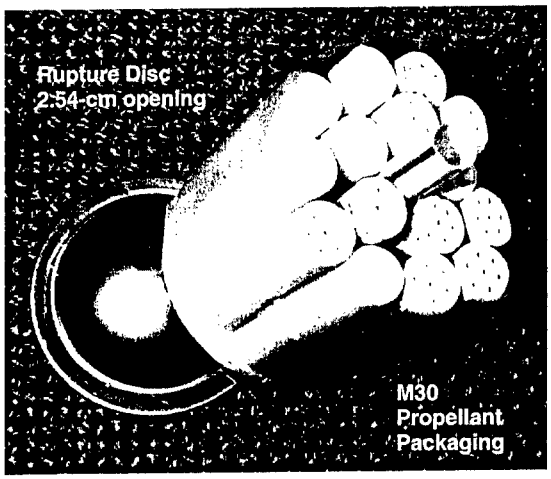

FIGURE 3. Rupture Disk and an M30 Charge Used in Closed Bomb Experiments.

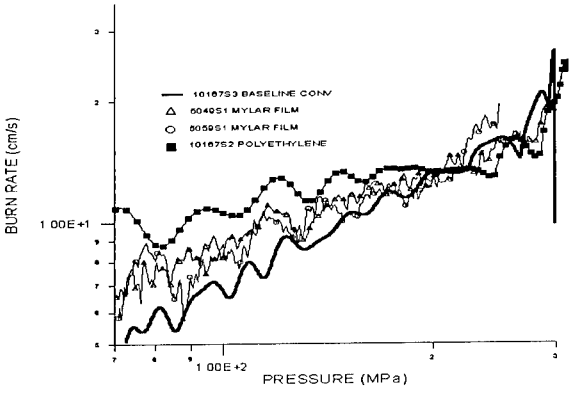

FIGURE 4. Apparent Burning Rates of M30 Ignited with Mylar- or PE-Based Plasmas in Non-Interrupted Closed Bomb Trials.

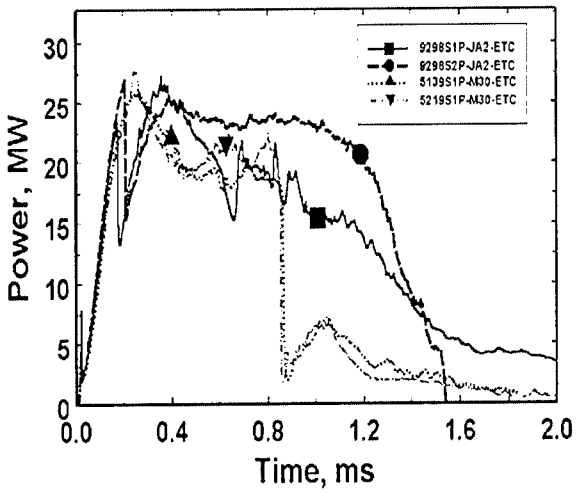

FIGURE 5. Electrical Power Curve for Two Plasma Ignition Trials Yielding Different Input Energies (18.4 kJ and 29.3 kJ).

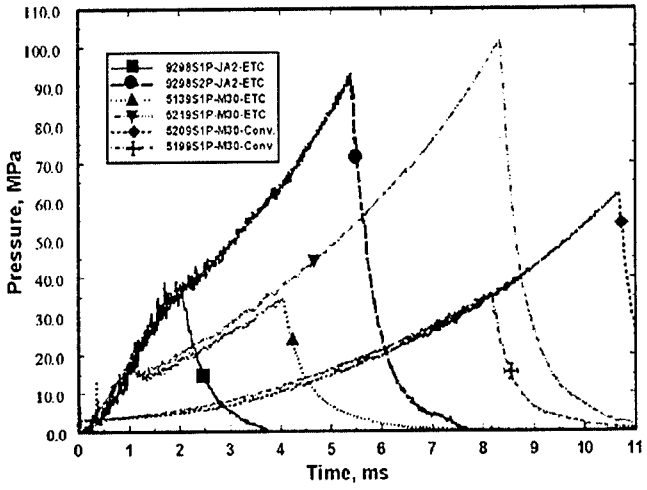

FIGURE 6. Pressure-Time Curves for Plasma-Ignited M30 (Mylar Capillary) and JA2 (PE Capillary) Firings, and Conventional Firings for M30, for Interrupted Closed Bomb Trials.

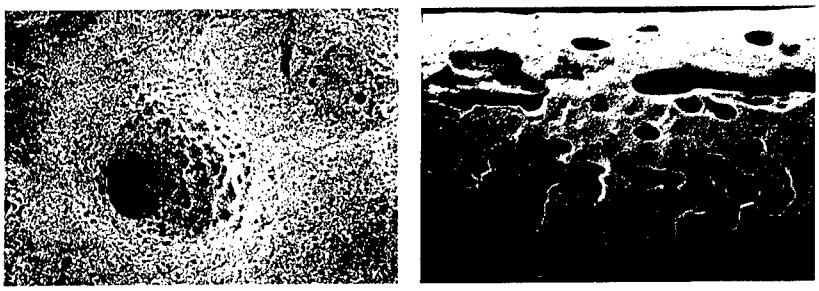

(90X) (5X)

FIGURE 7. Micrograph of the Extinguished Grain Exterior Showing Evidence of Hot Particle Spray from the PE Plasma Igniter (100 MPa).

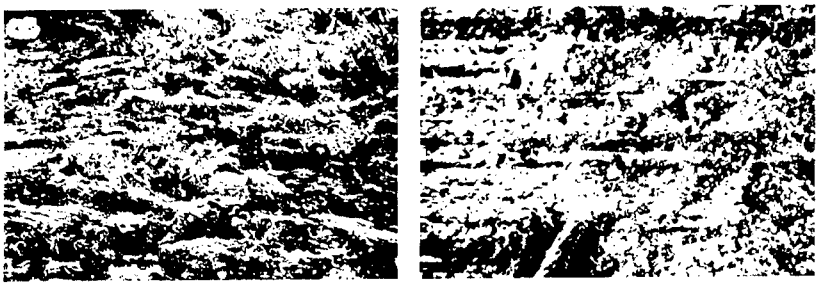

Conventional Ignition
(70 MPa, 850X)

Plasma Ignition
PE Capillary (35 MPa, 850X)

FIGURE 8. Micrograph of the Burning Surface of the Extinguished Grain Perforation Showing Different Features Between Ignition Methods

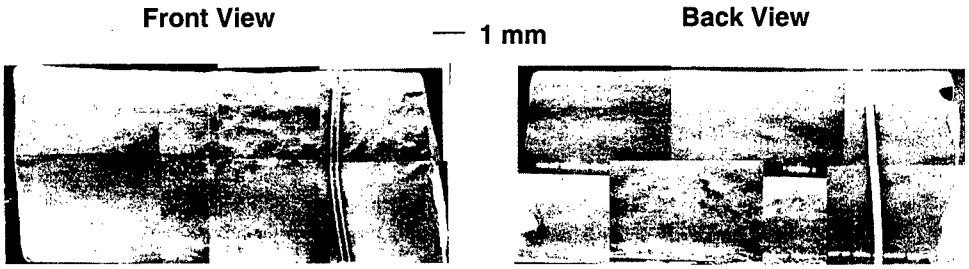

FIGURE 9. SEM Maps of the Outer Surfaces of a Grain Recovered After Black Powder Ignition.

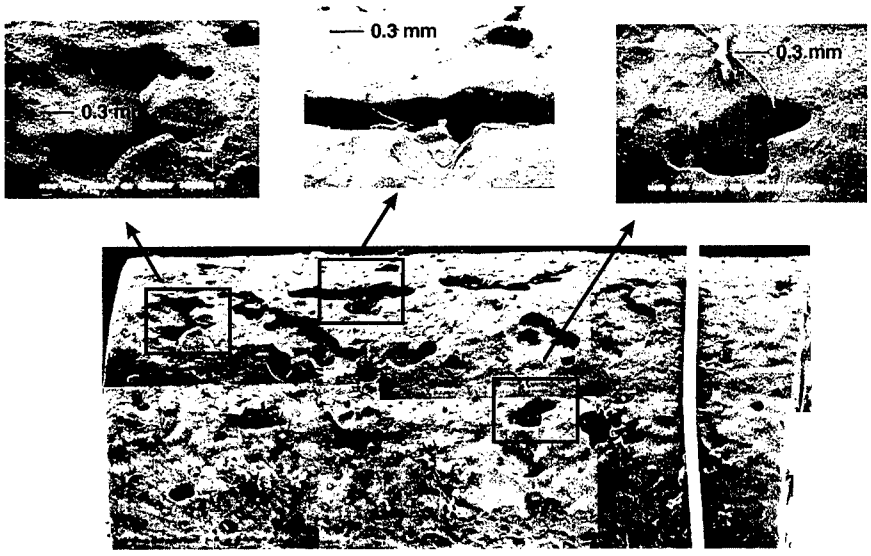

FIGURE 10. SEM Mapping of a Grain Recovered from Plasma Ignition with Mylar Capillary.

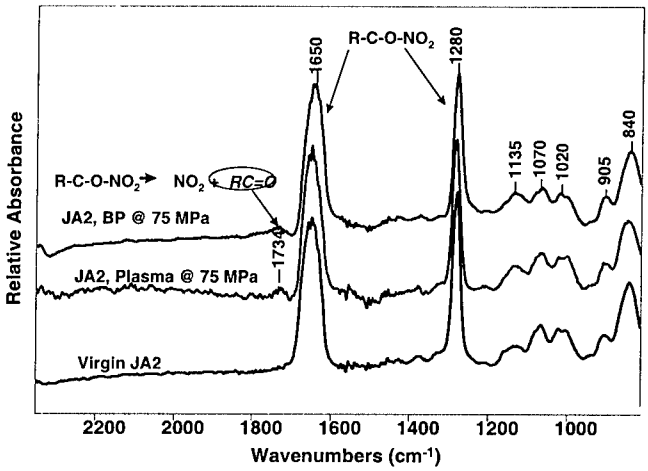

FIGURE 11. FTIR Spectra of JA2 Showing Aldehyde Formation Due to Denitration of the Nitrate Ester Groups for Extinguished Samples.

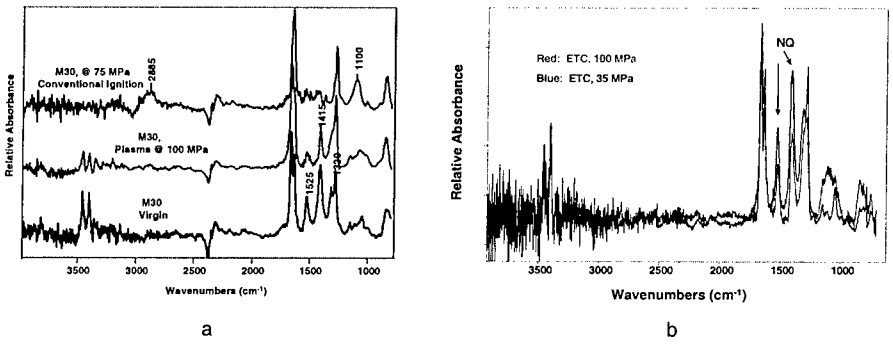

FIGURE 12. Surfaces of Extinguished M30 Propellant Grains: a) Lateral Surfaces; b) Perforated Surface.

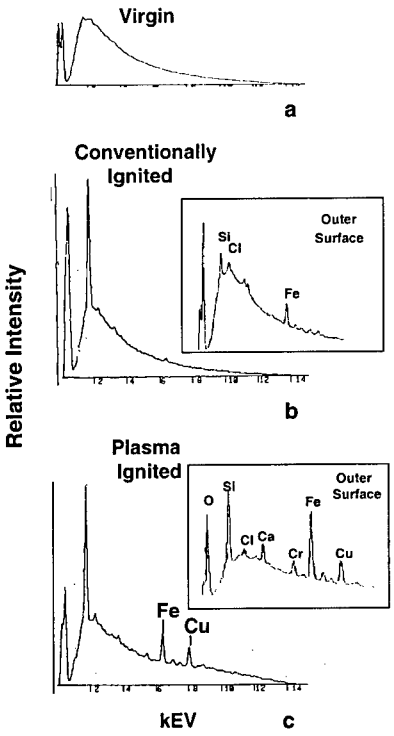

FIGURE 13. XRF Analysis of M30 Grain Perforations: a) Virgin, b) Ignited with Black Powder, and c) Ignited with Plasma.

REFERENCES

1. Del Guercio, M. "Propellant Burn Rate Modification by Plasma Injection." 34th JANNAF Combustion Subcommitte Meeting, Vol. 1, pp. 35–42, West Palm Beach, FL October 1997.

2. A. Kinkennon, Birk, A., M. Del Guercio, P. Kaste, R. Lieb, J. Newberry, R. Pesce-Rodriguez, M Schroeder, "SEM Characterization of Extinguished Grains from Plasma-Ignited M30 Charges", JANNAF PDCS Meeting, , NASA Kennedy Space Center, FL, May 2000 (in press).

3. Woodley, C. R., and S. Fuller. "Apparent Enhanced Burn Rates of Solid Propellants Due to Plasmas." 16th International Symposium on Ballistics, pp. 153–162, San Francisco, CA, 23–28 September 1996.

4. D. E. Kooker. "Burning Rate Deduced form ETC Closed-Chamber Experiments: Implications for Temperature Sensitivity of Gun Systems." 35th JANNAF Combustion Subcommittee Meeting, Dec.1998.

5. Oberle, W., and D. Kooker. "BRLCB: A Closed-Chamber Data Analysis Program." ARL-TR-36, U.S. Army Research Laboratory, Aberdeen Proving Ground, MD, January 1993.

6. Birk, A., M. Del Guercio, A. Kinkennon, D. E. Kooker, & P. J. Kaste. "ETC Closed-Chamber Interrupted-Burning Tests with JA2 and M30 Solid Propellants." 36th JANNAF Combustion Mtg, FL, 18-22 Oct. 1999.

7. Del Guercio, M. "Electrothermal-Chemical Closed Chamber Characterization of Plasma Capillaries." 36h JANNAF Combustion Meeting, NASA Kennedy Space Center, FL, 18-22 October 1999.

8. Lieb, R., and C. Gillich. "Morphology of Extinguished Monolithic JA2 Grains Fired in a 30-mm Solid Propellant Electrothermal-Chemical (SPETC) Gun." ARL-TR-606, U.S. ARL, APG MD, November 1994.

9. Lieb, R., "Nitroguanidine Morphology in Extruded Gun Propellant," Technical Report BRL-TR-2812, US Army Ballistic Research Laboratory, APG, MD, June 1987.

10. Nusca, M. J., and M. J. McQuaid. "Modeling the Open-Air Plasma Jet from an ETC Igniter Using a Multi-Species Reacting Flow CFD Code." 35th JANNAF Combustion Subcommittee Mtg, October 1999.

11. Gazonas, G. A. "The Mechanical Response of M30, XM39 and JA2 Propellants at Strain Rates from 10^{-2} to 250 Sec-1." BRL-TR-3181, U.S. Army Ballistic Research Laboratory, APG, MD, January 1991.

12. Lieb, R. J., and M. G. Leadore. "Mechanical Failure Parameters in Gun Propellants." Technical Report, BRL-TR-3296, U.S. Army Ballistic Research Laboratory, Aberdeen Proving Ground, MD, November 1991.

13. Kooker, D. E. "Burning Rate Deduced From ETC Closed-Chamber Experiments: Implications for Temperature Sensitivity of Gun Systems." 35th JANNAF Combustion Meeting, Tucson, AZ, Dec. 1998.

14. Klingaman, K.W., and J.K. Domen. "The Role of Vivacity in Closed Vessel Analysis." JANNAF Propellant Development and Characterization Subcommittee Meeting, Patrick AFB, FL, April 1994.

15. McQuaid, M. A., "Characterization of the Discharge from an Ablating Capillary Arc Ignition System Equipped with a Poly(Ethylene Terephthalate) Liner)." ARL Report, in press.

SYNTHESIS AND ANALYSES OF N,N'-DINITROUREA

Patrick Goede, Niklas Wingborg, Helena Bergman and Nikolaj V. Latypov
National Defence Research Establishment, S-147 25 Tumba, Sweden.

Abstract

N,N'-Dinitrourea was prepared through nitration of urea at low temperature in mixed acids. The prepared material was pure and found to be stable at room temperature. The properties of N,N'-dinitrourea were analysed by: TG, DSC, Ignition test in Wood's metal bath, MS, gaspycnometry and BAM impact and friction sensitivity tests.

Introduction

There has been a recent interest in N,N'-dinitrourea as a component in Mannich reactions[1] and in the synthesis of 2-oxo-1,3,5-trinitro-1,3,5-triazacyclohexane (keto-RDX)[2]. In the keto-RDX synthesis N,N'-dinitrourea is prepared in situ without isolation of the compound, to optimize the reaction conditions a request for N,N'-dinitrourea was phrased[3]. N,N'-dinitrourea is also a precursor to nitramide a useful starting material for the synthesis of aliphatic nitramines[4]. In an earlier article dealing with the preparation of N,N'-dinitrourea, it was claimed to be unstable[5]. We have prepared pure and stable N,N'-dinitrourea and studied its properties.

Synthesis of N,N'-dinitrourea

N,N'-Dinitrourea was obtained by nitration of urea in a 50:50 mixture of sulphuric acid and nitric acid at low temperature, **scheme 1**. While our work was in progress an almost identical approach to N,N'-dinitrourea was published[5]. In that article the authors reported that N,N'-dinitrourea undergoes decomposition, which may lead to spontaneous ignition at room temperature. We believe this behaviour is due to trace amounts of acid in their final product. The N,N'-dinitrourea we obtained was washed

with trifluoracetic acid to remove all acidic impurities and we found it to be stable for several weeks in a dessicator over silica gel at room temperature.

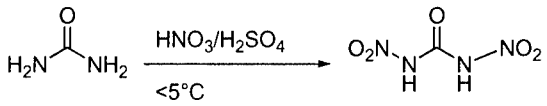

Scheme 1: Synthesis of N,N'-dinitrourea

Experimental

Caution: N,N'-dinitrourea is a powerful and sensitive explosive and should be handled with appropriate precautions. Employ all standard energetic materials safety procedures in experimental operations involving such a substance.

10.9ml 95% Sulphuric acid was added to 13.2ml (0.14mol) 100% nitric acid and then cooled to 0 °C. 3g (0.05mol) Urea was then added to the reaction mixture for about 30 minutes. Care was taken that the temperature of the reaction mixture wasn't allowed to rise above 5 °C. After the addition the reaction mixture was allowed to stand for another 30 minutes at 0° C, during this time a white precipitate formed. The white crystal mass was filtered off on a glass-funnel and then washed with trifluoroacetic acid (5*5 ml). The product was dried over vacuum giving 5.0g (0.033mol, 67%) of N,N'-dinitrourea. IR (KBr): 1684 (CO), 1544, 1419 (NO_2), 1224 (NO_2); Anal. Calcd. for $CH_2N_4O_5$: C, 8.00; H, 1.34; N, 37.34. Found: C, 7.94; H, 1.39; N, 37.26.

Analyses

Differential Scanning Calorimetry, DSC

The DSC used was a Mettler DSC 30 with a ceramic sensor. Every experiment as well as the calibration was performed in a nitrogen atmosphere. The flow of nitrogen was approximately 50 ml/minute. The DSC was calibrated with indium (Mettler Calibration Standard) and evaluated according to Mettler's recommendations[6]. The samples were put in aluminium cups with pierced lids.

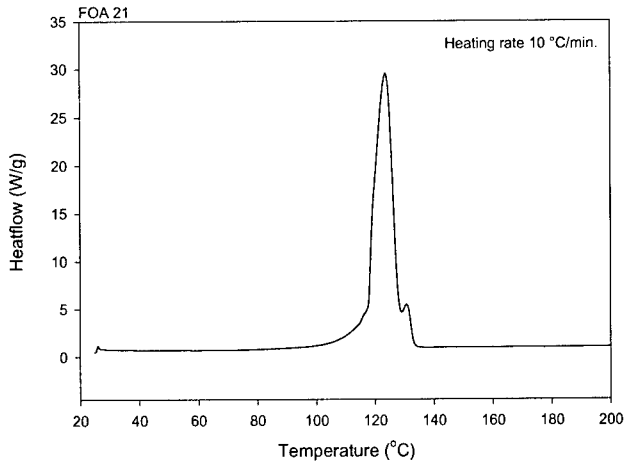

Figure 1: DSC curves for N,N'-dinitrourea at a heating rate of 10 °C per minute.

At a heating rate of 10 °C/minute an exotherm starts smoothly at approximately 100 °C and becomes very steep at 120 °C, **figure 1**. By measuring the temperature at were the peak occured at different heating rates, the activation energy could be calculated, according to ASTM E 698 – 79, by plotting $-\ln(\beta/T^2)$ versus 1000/T were β is the heating rate in °C/minute and T is the peak temperature in K, **figure 2**.

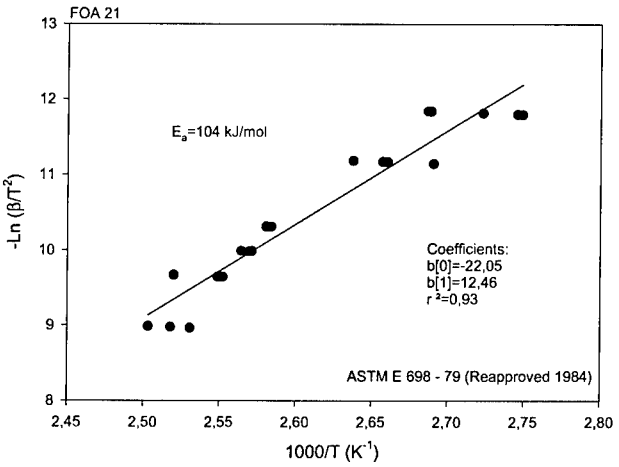

Figure 2: -Natural logarithm of β/T^2 versus 1000/T.

The activation energy was then calculated by fitting a straight line to the data and by using **equation 1**.

$$E_a = R\frac{d - \ln(\beta / T^2)}{d(1/T)} \quad \textbf{Equation 1}$$

By this method the activation energy was found to be 104 kJ/mol.

Ignition test in Wood's metal bath

In the ignition test the time to ignition was measured as a function of the temperature. This was done by immersing a test tube with the sample in a bath of Wood's metal at a certain temperature. The time to ignition was then measured with a chronometer. In all cases the mass of the sample in the test tube was 24-28 mg. The temperature of the bath was increased in steps of approximately 5 °C. 34 samples were tested, usually four at each temperature. The ignition temperature is defined to be in the interval between the maximum temperature at which no reaction occurs within 300 seconds and the lowest temperature where a reaction does occur, in at least one of the four samples, within 300 seconds. The method is not very accurate since the time is

measured manually. The measurements were started just below the temperature at which ignition was suspected from DSC data at a heating rate of 10 °C/minute.

The ignition temperature for N,N'-dinitrourea was found to be between 91 °C and 93 °C (four reactions) which was lower than expected from the DSC data. To calculate the activation energy, E_a, for the ignition of N,N'-dinitrourea, the natural logarithm of the ignition time was plotted versus the reciprocal temperature, **figure 3**.

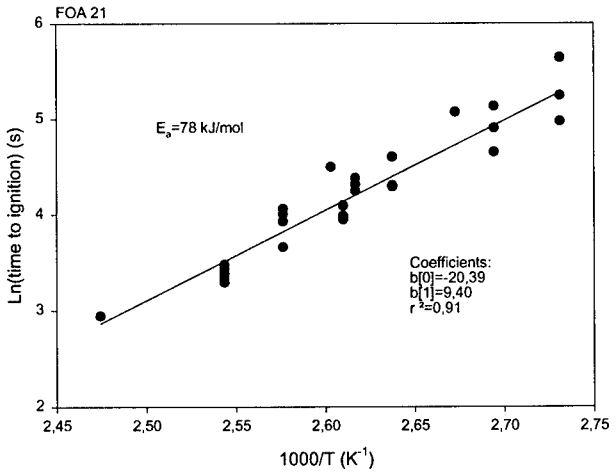

Figure 3: Natural logarithm of time to ignition versus 1000/T.

The activation energy was then calculated by fitting a straight line to the data and by using the Arrhenius equation. By this method the activation energy was found to be 78 kJ/mol between 93 and 131 °C. This value was lower than that determined by DSC, **Figure 2**. A similar discrepancy between activation energies determined by DSC and ignition test in Wood's metal bath was found for ADN and N-guanylurea-dinitramide[7]. The explanation offered in that case was that the compound had either different decomposition reaction orders or different decomposition mechanisms in the two experiments.

Thermo Gravimetry, TG

The TG used was a Mettler TGA 850. The test was performed in a nitrogen atmosphere at a heating rate of 10 °C/minute. The samples were put in alumina cups and the flow of nitrogen was approximately 80 ml/minute. Prior to the testing, the TG was calibrated according to Mettler's recommendations[6]. The results of the measurements are shown in **figure 4**.

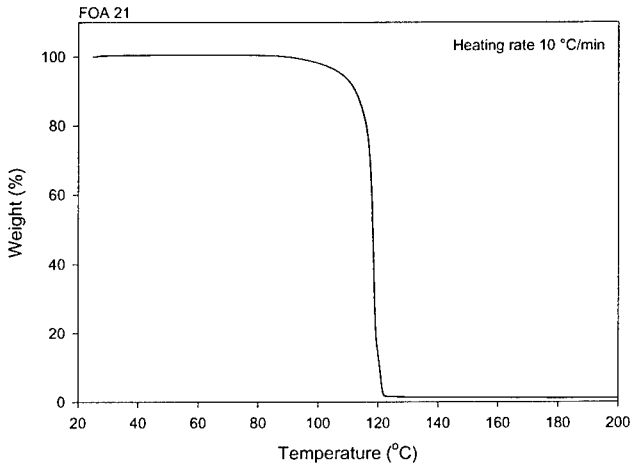

Figure 4: TG plot of N,N'-dinitrourea at a heating rate of 10 °C/min.

As can be seen in **figure 4**, the weight started to decrease between 80 and 90 °C followed by a steep mass loss between 110 and 120 °C. The N,N'-dinitrourea decomposition as measured in the TG correlated clearly to the exothermal decomposition found in the DSC, **figure 1**.

Mass spectroscopic data

It has been shown earlier[8] that the thermal fragmentation path of a substance shows similarities to its mass spectral fragmentation. A mass spectroscopic study is thus a natural starting point for acquiring new information about the decomposition mechanism.

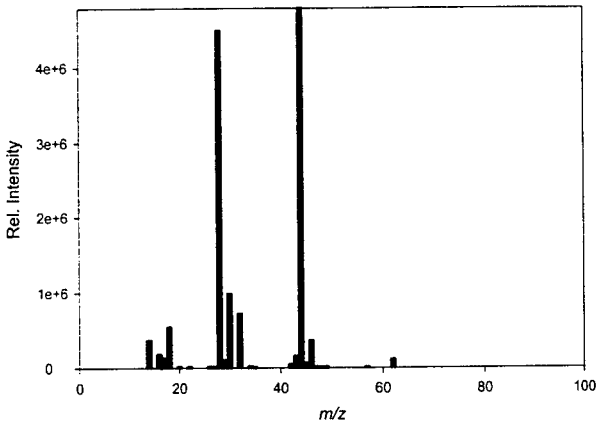

Figure 5. N,N'-dinitrourea at 70 eV

The mass spectroscopic study was conducted on a JEOL 300D double-focusing magnetic sector instrument equipped with a PC-based computer system utilizing Technivent Vector/2 software for data analysis. All mass spectra were obtained by using the solid sample inlet and the heating rates were varied. Electron impact spectra at both 70 eV and 20 eV were acquired.

It was observed that N,N'-dinitrourea did not show a molecular peak (*m/z* 150) neither at 70 eV nor at 20 eV. We could from this conclude that N,N'-dinitrourea was not as thermally stable as FOX-7[9] or NTO[10]. At 20 eV the most significant *m/z* were 18, 28, 30, 32, 42, 43, 44, 46 and 62. By far the most intense mass peak in the spectra was *m/z* 44. The spectra at 70 eV was very similar to that at 20 eV, a slight increase in secondary fragments like m/z 26, 27 (CN/HCN) could be detected but the major peaks were still m/z 18, 28, 30, 32, 42, 43, 44, 46 and 62. An example of a recorded spectrum at 70 eV is displayed in **figure 5**. In **table 1** is a summary of the decomposition peaks found at 70 eV with tentative assignments. To get a full understanding of the thermal decomposition path for N,N'-dinitrourea a more

thorough investigation is needed. One of the mechanisms involved seemed to be the breakdown of N,N'-dinitrourea with the concomitant formation of NH_2NO_2 and CO_2. This would require the presence of H_2O, and consequently *m/z* 18 was observed in the spectra. Since NH_2NO_2 thermally decomposes to N_2O and H_2O only very small amounts of water need to be present to initiate this decomposition chain which thus would be autocatalytic.

Table 1. Observed m/z in the 70 eV N,N'-dinitrourea spectra and possible assignments.

m/z	Possible assignment
18	H_2O
26	CN
27	HCN
28	CO, N_2
29	HCO
30	NO
32	H_2NO
42	NCO, H_2N_2C
43	HNCO?
44	H_2NCO?, CO_2, N_2O
45	
46	NO_2
62	NH_2NO_2

Density

The volume of the sample was measured with a Micromeritics helium pycnometer. Prior to measuring, the apparatus was calibrated with a calibration standard of a known volume. The density was then calculated. The density of N,N'-dinitrourea was found to be 1.98 g/cm^3. By the same method the density of NaCl was found to be 2.16 g/cm^3 which is very close to the literature value (2.17 g/cm^3)[11].

Sensitivity

The impact and friction sensitivities were determined according to the BAM standard which conforms to the UN guideline ST/SG/AC.10/11[12], with two exceptions. One: the impact sensitivity was measured with a 2kg drop weight. Two: the impact and friction testing was done by using an up-and-down method on both sides of the 50 % probability level. The results where then calculated at 16.7 % (1 of 6) and 50 % probability. The number of samples tested were 25 in both tests.

Table 2: Sensitivity data evaluated at 50 and 16.7 % probability.

Probability (%)	50	16.7 (1 of 6)
Impact energy (J)	5	3
Friction load (N)	76	27

According to the results shown in **table 2,** N,N'-dinitrourea is very sensitive to friction. According to the UN guideline ST/SG/AC.10/11[12] if the friction load is less than 80 N or the impact energy is 2 J or less at a probability of 16.7 % (1 of 6), then a substance is considered to be too dangerous to transport in the form in which it was tested. N,N'-dinitrourea does not meet the UN criteria with respect to friction sensitivity and it can thus not be transported without special arrangements such as use of explosive safe containers or being phlegmatised.

Summary and Conclusions

N,N'-dinitrourea has for the first time been synthesized in pure form and in acceptable yield. It was found to be stable in a dessicator for several weeks without decomposing. It has a high density (1.98 g/cm^3) and a very high positive oxygene balance (+21,33%) this should make it interesting as an energetic material. It is, however, sensitive to friction and impact, has a low thermal stability and is chemically labile. All this taken into consideration we consider that N,N'-dinitrourea

should preferably be used as a starting material towards more stable energetic materials than an energetic material in its own right.

Acknowledgements

The authors would like to thank the Swedish Defence Forces for giving financial support to this project. Mr Lars Bodin for the BAM impact and friction sensitivity test measurements and the ignition test measurements in Wood's metal bath.

References

(1) Zhang, Y.; Yu, M.; Li, W. *Propellants, Explosives and Pyrotechniques* **1997**, *22*, 279-283.

(2) Meihong, X.; Qizheng, Y. In *International Autumn Seminar on Propellants, Explosives and Pyrotechniques*; Feng, C., Ed. 1997, p 180-184.

(3) Zhang, Y.; Yin, H.; Li, P.; Li, W. In *24 th International Pyrotechnic Seminar* 1998, p 637-645.

(4) Raszewski, Z.; Syczewski, M. *Proppellants, Explosives and Pyrotechniques* **1999**, *24*, 366-370.

(5) Syczewski, M.; Cielowska-Glinska, I.; Boniuk, H. *Propellants, Explosives and Pyrotechniques* **1998**, *23*, 155-158.

(6) Mettler Toledo Operating Instructions STAR^e Software, Version 5.0 1997, p 10-1 - 10-24.

(7) Bemm, U.; Östmark, H.; Bergman, H.; Langlet, A. In *Insensitive Munitions & Energetic Materials Technology Symposium* San Diego, 1998, p VB-4-1 - VB-4-11.

(8) Stals, J. *Transactions of the Faraday Society* **1971**, *6*, 67.

(9) Bergman, H.; Östmark, H.; Pettersson, A.; Pettersson, M.-L.; Bemm, U.; Hihkiö, M. In *1999 Insensitive Munitions and Energetic Materials Technology Symposium* Tampa, 1999, p 346-351.

(10) Östmark, H.; Bergman, H.; Åqvist, G. *Thermochimica Acta* **1993**, *213*, 165-175.

(11) *The Merck Index*; Merck & CO., Inc.: Rahway, 1976.

(12) *United Nations: Recommendations on the Transport of Dangerous Goods. Manual of Tests and Criteria ST/SG/AC.10/11/Rev.2.*; 2nd revised ed.; United Nations: New York and Geneva, 1995.

Henryka Boniuk, Witold Pilecki, **Tomasz Stawiński**, Michał Syczewski

Division of Highenergetic Materials, Faculty of Chemistry,
Warsaw University of Technology (Politechnika)
Noakowskiego 3 00-664; Warsaw Poland

NEW METHOD OF SYNTHESIZING K-RDX USING DINITROUREA (DNU)

Abstract

Known methods of synthesizing 2-oxo-1,3,5-trinitro-1,3,5-triazacyclohexane (K-RDX) require relatively expensive reactants, therefore research into improved methods remains a current need.

This study explored the possibilities of using dinitrourea in K-RDX synthesis.Using raw DNU or the DNU remaining in the mixture obtained at the end of the reaction, a complex process of hexamine nitrolysis involving condensation of developing fragments of nitroaminomethylal compounds with DNU was conducted.

As a result of the experiments, two manners of conducting this process were observed: the first one was preceded by the extraction of DNU from the postreaction mixture, the second - entailed conducting the process using the DNU synthesis postreaction mixture without the extraction of DNU itself.

Purification of K-RDX is rendered more difficult due to the fact that it is susceptible to hydrolysis. The identity and purity of the product were tested using the following methods: DTA-TG, Elementary Analysis, IR, NMR.

Key words: K-RDX, dinitrourea, K-6 synthesis

Introduction

2-oxo-1,3,5-trinitro-1,3,5-triazacyclohexane (K-RDX, K-6) is a fairly new explosive from the heterocyclic nitroamine group. This compound is very interesting due to its good energetic characteristics:
density =1.932 g/cm^3, detonation velocity exceeding 9000m/s and power higher than that of octogen by 3-5% [1].
The K-6 synthesis methods described in literature usually consist of several stages and the required materials are expensive and inaccessible. The use of trifluoroacetic acid anhydride [1,2], with it being difficult to attain, highly toxic and expensive, can serve as an excellent example. Despite using easily accessible materials, the method of obtaining K-6 proposed by Russian researchers [3] is also somewhat unuseful due to its low yield (18%). The synthesis methods described briefly by Chinese researchers seem interesting, but little information about them doesn't allow an objective comparison and evaluation [4,5].

In recent years attention has been brought to the possibility of utilising dinitrourea (DNU) as an intermediate product in the synthesis of other stable nitroamines. Due to its very high reactivity and susceptibility to hydrolysis, dinitrourea will surely not be used as a independent highenergetic material, but thanks to the accessibility of raw materials, simplicity of synthesis with high yield and low price it can be taken into consideration as an intermediate product in the synthesis of other explosives. The below described method of obtaining K-RDX can serve as example of such utilisation of DNU. The basis of this process is the reaction of dinitrourea with hexamethylenetetramine (with simultaneous nitration). The application of acetic anhydride or trifluoroacetic anhydride is excluded and the nitration process is conducted in a mixture of sulfuric acid and nitric acid. The regeneration and application of waste acids in

this case is no different than the processes widely used in factories that produce nitro compounds.

This new K-RDX synthesis method can be applied practically in two variations. The first – by obtaining dinitrourea, diluting it in an excess of HNO_3 and then by gradually adding hexamethylenetetramine in a temperature of below 0^0C. The second – by obtaining dinitrourea, solubilising it in HNO_3 and then adding dinitrourea salt with hexamethylenetetramine in a temperature of below 0^0C.

The first variation of the new method is not complicated and can be conducted in one reactor. However, the product obtained this way is contaminated with RDX in the amount of about 30% and the maximum yield of the reaction is equal 45% (based on crude product). The second variation consists of two steps conducted in separate reactors. In the first stage dinitrourea salt with hexamethylenetetramine is obtained by adding DNU to an aqueous solution of hexamethelenetetramine. In the second the obtained salt is closed to a slurry of DNU in nitric acid. This process is more complicated and requires handling dinitrourea that separated from spent acids, which is relatively dangerous. However the product obtained this way contains less RDX (about 15%) and the reaction has a higher yield – 55%.

Experimental

Synthesis of 2-oxo-1,3,5-trinitro-1,3,5-triazacyclohexane from dinitrourea and hexamethylenetetramine.

Dinitrourea was obtained form 10g of urea and 40 cm^3 of nitrating mixture [6]. The product was not separated, but its solubility was increased by adding 35 cm^3 of 96% HNO_3 in a temperature of below

$(-5)^0$C. To sustain the required temperature 7g of hexamethylenetetramine were added in portions and with simultaneous intensive stirring to the slurry of (partially solubilised) DNU, which was cooled to a temperature of $\leq (-10)^0$C. The suspension was stirred for 1h in 0^0C and later for 20 min. in 10^0C. The resulting suspension was poured into an ice-water mixture, filtered and washed, m.p. 162^0C.

$$O{=}C(NHNO_2) + C_6H_{12}N_4 \xrightarrow{HNO_3} \underset{45\%}{3\,K-6}$$

Synthesis of dinitrourea salt with hexamethylenetetramine

A solution of 35g of hexamethylenetetramine in 500 cm^3 of water was prepared in a beaker equipped with an agitator and thermometer and cooled to 0^0C. Dinitrourea (obtained from 30g of urea) was added in portions with intensive stirring to the solution. The designated temperature of 0^0C was maintained at all times. The precipitated salt was filtered off and washed with CH_3OH and 69g of the salt were obtained (m.p. 20^0C). The general chemical equation is as follows:

$$C_6H_{12}N_4 + OC(NHNO_2)_2 \longrightarrow \underset{72\%}{C_6H_{12}N_4 * OC(NHNO_2)_2}$$

Synthesis of 2-oxo-1,3,5-trinitro-1,3,5-triazacyclohexane form dinitrourea and dinitrourea salt with hexamethylenetetramine

The proper reaction was preceded by obtaining DNU form 5g of urea and 20 cm^3 of nitrating mixture. The DNU slurry was diluted by adding 33 cm^3 of 96% HNO_3 in a temperature of below $(-5)^0$C. Next, it was cooled to $(-10)^0$C and at this temperature 12g of dinitrourea salt with hexamethylenetetramine were gradually added. The salt was added very

slowly with intensive stirring (leaving the salt on the surface of the acid leads to its decomposition). After adding all of the salt the reaction was conducted for 1h at 0^0C and later for 20 min. at 10^0C. Once the reaction ended the content of the flask was poured into an ice-water mixture, the product was filtered off and washed with a vast amount of water, m.p. 165^0C.

$$2OC(NHNO_2)_2 + C_6H_{12}N_4{*}DNU \xrightarrow{HNO_3} 3\ K\text{-}6$$

Purification, identification and properties of K-6

The crude product was purified by recrystalization from ethyl acetate and acetonitrile – m.p. 184-185^{0}C (with decomposition) The product obtained this way was tested through DTA -TG (Fig 1), ^{1}H NMR, IR and elementary analysis.

Elementary analysis after recrystalization showed good compliance with the calculated theoretical composition:

Anal.Calcd. for $C_3H_4N_6O_7$: C - 15.25; H - 1.71; N - 35.60

Found: C-15.73,15.86; H-1.66,1.57; N - 35.42,35.37.

^{1}H - NMR (CD_6COCD_6): δ=6,328 (s, 4H).

IR 3056, 1768,1604,1284,1224, 1152 [cm^{-1}].

The above given results match the values shown in literature [items 2,3] and confirm the structure of the obtained K-RDX. Despite fairly good results of identification with the above described methods, the course of TG with thermogravimetric testing shows a very characteristic, partial, two-step mass decrement before the main step of spontaneous decomposition.

An exothermic peak corresponding to the product is apparent on the DTA curve. However the chemical change begins at 144^{0}C on the TG

curve. This can be a result of the hydrolysis of K-RDX taking place along side heating and under the influence of traces of humidity.

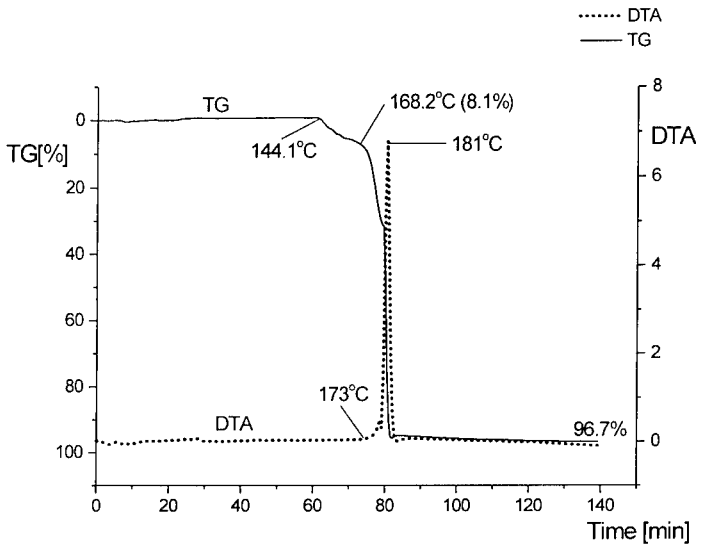

Fig. 1. Thermogram of K-RDX (heating 2^0C/min; m= 25.90mg)

Chosen physico-chemical properties of the product and its susceptibility to hydrolysis were also tested. The explosion force of K-RDX (tested on the ballistic mortar) was equal 102% that of hexogen. Sensitivity to impact was tested on the Kasta hammer with a 5kg weight and designated lower and upper explosive limits at 11 and 27 cm. The sensitivity of K-6 to friction was tested on the BAM friction sensitivity apparatus and established the lower and upper limits of sensitivity at 9,6 and 16 kg. The results seem to show, that K-RDX is fairly sensitive to mechanical stimulus, but its sensitivity is lower than suggested in literature [1,2]. With such sensitivity K-6 can be utilized practically only in phlegmatized form.

The results of tests on the susceptibility of K-RDX to hydrolysis are given in Table1.

Table 1 Susceptibility of K-6 to hydrolysis

condition of hydrolysis	Mass decrement [%] / time	
H_2O, 25^{0}C	4 / 4day	11 / 11 day
H_2O, 50^{0}C	6 / 3h	17* / 10h
H_2O, 100^{0}C	Full decomposition of the sample in 0,5h	
1% HNO_3, 50^{0}C	7 / 3h	
1% NaOH, 50^{0}C	79 / 3h	

*Reaction with fresh water

The above given results suggest that K-6 is not resistant to water. An apparent hydrolysis takes place already in 25^{0}C. Boiling water causes full decomposition in 0,5 h. A comparison of hydrolysis in an acidic and base environment shows, that K-RDX is less resistant to alkalis. The mass decrement of the sample in an alkaline environment is 10 times greater than in an acidic environment, with the same exposure time and temperature. The obtained results suggest that contact between K-RDX and humidity should be limited, especially in high temperatures.

Conclusion

Tests on the new method of K-RDX synthesis give the following conclusions:

- Dinitrourea, thanks to its low price and simplicity of synthesis with a high yield, can be a worthy intermediate product in the synthesis of other nitroamines.
- The new method of 2-oxo-1,3,5-trinitro-1,3,5-triaza-cyclohexane preparation can be implemented in two ways, using dinitrourea and hexamethylenetetramine (45% yield) or dinitrourea salt with hexamethylenetetramine (55% yield) as parent substances.
- The new methods of K-RDX synthesis require widely used, cheap and accessible materials.
- The obtained product is contaminated with RDX: 30% for hexamethyleneamine as a parent substance and 15% for dinitrourea salt with hexamethylenetetramine as parent substances.
- K-RDX is susceptible to hydrolysis, which takes place especially easily in an alkaline environment.
- K-RDX is susceptible to mechanical stimuli and should be phlegmatized for practical use.

Financial support from the State Committee for Scientific Research (KBN - Project Nr 0 T00A 032 16) is gratefully acknowledged

References

1. A.R. Mitchell, P.F. Pagoria i inni., *Propellants, Explos., Pyrotech.*, **19**, 232 (1994).
2. D. Hunag, U.S. Patent 5, 391, 736, 1995.
3. A.C. Ermakow, C.A. Serkow, W.A. Tartakowskij i in., *Chimija geterocikliczeskich sojedienij*, **8**, 1129 (1994).
4. Z. Yueiun, X. Chunping, Chemical Abstracts, vol. 127, **250216**.
5. X. Meihong, Y. Qizheng, Chemical Abstracts, vol. 128, **142796**.
6. M. Syczewski, I. Cieślowska-Glińska, H. Boniuk - Propellants, Explosives, Pyrotechnics **23**, 155 (1998)

Henryka Boniuk, Tomasz Stawiński, Michał Syczewski

Division of Highenergetic Materials, Faculty of Chemistry,
Warsaw University of Technology (Politechnika)
Noakowskiego 3; 00-664 Warsaw Poland

TRIETHYLENETETRAMINE (TETA) MODIFICATION - OBTAINING AZIDIC PRECURSORS OF ENERGETIC MIXTURE BINDERS.

Abstract

Epiazydohydryne (EAH) was used in the synthesis of new curing agents for epoxide resins production. Reactions of triethylenetetramine with EAH were conducted using the following molar ratios TETA:EAH=1:2; 1:4 and 1:6.

Subsequently, the obtained compounds were transformed into salts of inorganic and organic acids. The thermal stability of products from the reactions of EAH with TETA, stability of the salts from these substances and mixtures with energetic materials (TNT, AP, HMX) were tested. The experiments covered the determination of the decomposition temperature [T_m] and the loss of mass in the sample [TG].

Keywords: azide derivatives triethylenetetramine, curing agents for epoxide

Results of synthesis and investigation

Epiazydohydryne (***EAH***-Fig.1a) was synthesized and in turn used in the synthesis of triethylenetetramine azide derivative (***TETA***-Fig.1b).

The addition of EAH to TETA had a quantitative course until a ratio of TETA:EAH = 1:6 was achieved.

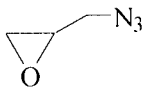

EAH

a)

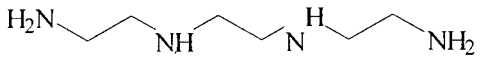

TETA

b)

Fig.1

The reaction between ***TETA*** and ***EAH*** was conducted using the following molar rations:

TETA:EAH:= 1:2 – ***2AT***,

TETA:EAH =1:4 – ***4AT***

TETA:EAH =1:6 – ***6AT***.

The product containing full substitution (***6AT***) can be represented with the following formula (Fig. 2).

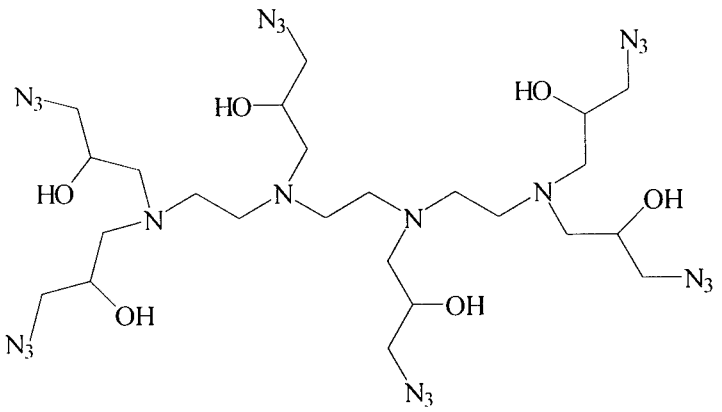

Fig. 2

When substitution is not full, a mixture of isomers can form. These were not separated. The results of elementary analysis and determination of the percentage fraction of azide groups in the products (titrimetric method) are shown in Tabel 1.

Tab. 1: Elementary analysis and determination of percentage fraction of azide groups in the products: ***2AT***, ***4AT*** oraz ***6AT***

Chemical analysis	Mixture						EAH	
	2AT		4AT		6AT			
	exper.	cal.	exper.	cal.	exper.	cal.	exper.	cal.
C [%]	40.95	41.32	39.60	39.82	38.54	38.91		
H [%]	8.14	8.20	6.94	7.06	6.45	6.53		
N [%]	39.90	40.26	40.90	41.32	41.10	41.60		
azide group contents [% by weight]	24.15	24.40	29.80	30.10	33.75	34.05	42.00	42.03

Salts with the following acids: HNO_3, $HClO_4$. 2,4,6-trinitrophenol (***TNF***), 2,4,6-trinitroresorcine (***TNR***), 2,4,6-trinitrophloroglucin (1,3,5-trihydroxy-2,4,6-trinitrobenzene, ***TNG***) and 4,4,4-trinitrobutyric (***TNB***) were obtained from derivatives of ***TETA*** (***2AT***, ***4AT*** and ***6AT***).

The salts were obtained through neutralizing amines to pH=7.
In the obtained salts, irrespective of the type of acid and azide group contained in the amine, the molar ratio of acid to derivative of ***TETA*** was equal 2.6 : 1.

The termostability of the obtained materials was studied through the DTA-TG method. The compounds showed good and satisfactory stability up until spontaneous break-down temperature (exothermic break down temperature) (e.g. thermogram Fig.3 and Fig.4).

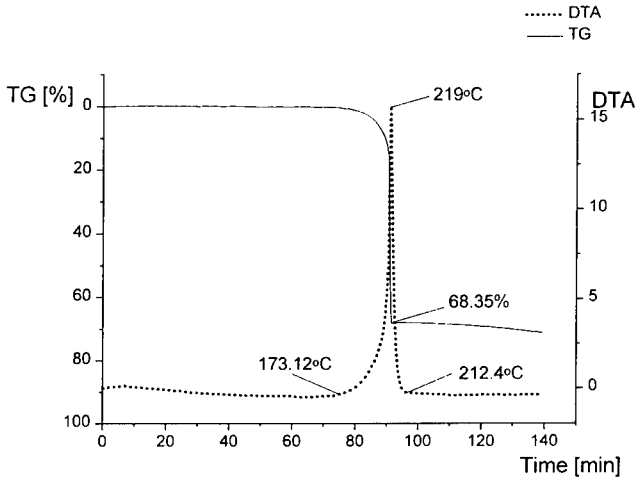

Fig. 3. Thermogram amine ***6AT***, mass of simple = 98.11mg; Ar atmosphere; heating 5°/min;

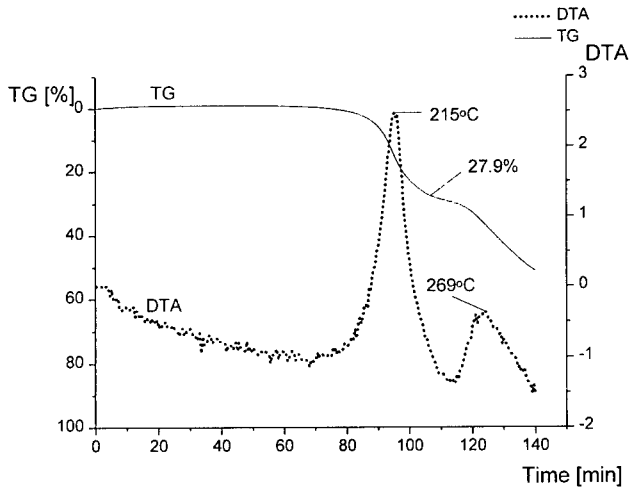

Fig. 4. Thermogram salt ***6AT***x$HClO_4$; mass of simple = 80.52 mg
Ar atmosphere; heating 5°/min;

Salts of ***TETA*** derivatives were found to be compatible with explosives such **RDX**, **HMX** and **NC**. The retained ability of these salts to harden epoxy resins means they can be used as a component of binders in energetic mixtures.

Partial financial support from the State Committee for Scientific Research (KBN - Project PBZ 019-12) is gratefully acknowledged

SOLID ACID CATALYSTS : SHAPE SELECTIVE NITRATION OF AROMATICS .

Reddy Damavarapu, Rao surapaneni
U.S.Army Armaments Research,Development and Engineering Center
Picatinny Arsenal,NJ 07806-5000
Keerthi Jayasurya and Paritosh Dave
Geocenters Inc. at Picatinny Arsenal NJ 07806

The nitration of aromatic compounds is an important process in both industrial and academic research.[1] In particular, the nitration of toluene is found to be useful for producing military explosives such as 2,4,6-trinitrotoluene (TNT) and pharmaceutical intermediates such as para-aminobenzoic acid (PABA). The conventional methods for nitration of aromatic compounds require corrosive nitric and sulfuric acids that afford a mixture of mono and poly-nitroaromatics.[1c] Under these conditions, the nitration of alkyl substituted aromatics such as toluene or xylenes, often leads to oxidation of the alkyl side groups, and this could produce a mixture of by-products. Developments in solid acid catalysts such as Nafion and other polysulfonic acid resins have reduced the corrosive nature and by-product formation of the exisiting process.[2] However, the separation and removal of unwanted isomers from the product stream can be costly. Unfortunately, these sulfonic acid resin catalysts offer no significant contribution toward controlling regioselection in mononitration of alkyl aromatics such as toluene. The para-nitrotoluene isomer is highly desirable over the ortho and meta isomers because of its high commercial value.[3]

In this paper we report a method for catalytic mononitration of toluene using H-ZSM-5 zeolite and n-propyl nitrate that produces the para isomer with remarkable selectivity.The meta isomer which is the contributing factor to the formation of red water is totally eliminated. Our approach is two fold. We performed computational analysis to determine the pore and channel sizes of various zeolites that affords the minimal size for the reactants to diffuse into the zeolite channels. Based on the analysis, we have selected H-ZSM-5 as an acid catalyst to attempt the nitration of toluene. We have also used Dinitrogenpentoxide and Nitric acid as nitrating agents and obtained similar results with varying yields.

We have carried out ab-initio self-consistent field (SCF) molecular orbital calculations to determine the molecular dimensions of toluene and its three mononitro isomers. The shape selective characteristics of H-ZSM-5 can be determined by calculating the molecular dimensions of the reactants and products. The geometries of toluene, n-propyl nitrate, and three mononitrated isomers of toluene were optimized at 4-31G basis set level using Guassian 92 program.[5] The elliptical diameter of H-ZSM-5 is about 5.1-5.6 Å. Toluene, which is cylindrical in shape with a kinetic diameter of about 5.25 Å, fits rather closely inside the channels .Due to the spatial restrictions inside the zeolite channels, only the para position is available for an electrophilic attack by the nitronium ion, NO_2^+ . The other two isomers have a much larger kinetic diameter of about 6.7 Å, which is clearly much larger than the size of the pores of H-ZSM-5 catalyst. Therefore, the free movement of these two isomers is not permitted, hence excluded by shape selective characteristics of the catalyst.

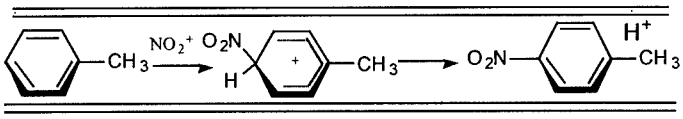

The nitration reactions were performed as a slurry mixture where toluene and n-propyl nitrate were stirred over the catalyst. The n-propyl nitrate is an ideal nitrating agent because generation of NO_2^+ ion only occurs in the presence of acids.[2] Also, this reagent is safe to handle.

The nitration of toluene using H-ZSM-5 catalyst with Si/Al ratio of 30 gives a mixture of mononitrotoluenes with the isolable yield of 43%. Unlike in the conventional nitration process, the o:m:p product distribution under these conditions is 32:1:67, respectively . The total yield of nitrotoluene was improved by increasing the amount of H-ZSM-5 catalyst used in the reaction while maintaining the product distribution. Increasing the temperature to reflux temperature of toluene (116^{o}C) appeared to play a significant role on the total yield of the reaction. At room temperature, the reaction is very slow requiring 7 days to achieve 20% conversion. The isolable yields are consistently high and selectivity favors the para isomer as the catalyst concentration and temperature increased. At higher catalyst concentrations with respect to the nitrating agent (>6:1), we have observed the formation of a mixture of normal and iso-propyl methylbenzenes as by-products with major by-product being 1-isopropyl-4-methylbenzene. It is possible that prolonged heating may cause decomposition of the nitrating agent at reflux temperature. We did not observe any brown fumes in the nitrating reaction to suggest the formation of nitrogen oxides as a by-product resulting from the decomposition of the nitrating agent.

There is a significant effect on the total yield and para selectivity of the reaction when we used a H-ZSM-5 catalyst with different Si/Al ratios. For example, H-ZSM-5 catalyst with Si/Al ratio of 80 increases the total isolable yield to 61% at 90°C and the o:m:p product distribution is 29:1:70, respectively. A preparative scale reaction was performed using 5 g. of n-propyl nitrate and 30 g. of H-ZSM-5 catalyst at reflux temperature and the isolable yield was 68% . An isolable yield of 50% was obtained after 8 hours of the reaction without affecting the o:m:p product distribution. Under comparable conditions, the isolable yield increased when the reaction was carried out for 16 hours. Prolong reaction time does not affect the product distribution. Using H-ZSM-5 catalyst with Si/Al ratio of 1000, the selectivity of the para isomer improved significantly to over 90% of the product mixture but the isolable yield was 15%. At reflux temperature the isolable yield was 18% with the same selectivity favoring the para isomer. We were able to overcome this low yield by increasing the amount of catalyst used in the reaction and under comparable reaction conditions the isolable yield increased to over 50%. The best o:m:p product distribution recorded was 5:0:95, respectively and no by-products were observed. For comparison, the o:m:p product distribution in the conventional nitration process is 56:5:39, respectively.[6] The yield determined by GC using 2,4-dinitrotoluene as an internal standard gives 67% under comparable reaction conditions (Si/Al = 1000, reflux temperature) with o:m:p distribution of 7:0:93, respectively . The fact that the yield obtained by GC is higher than the isolable yield suggests that we may be removing some products inadvertently in the process of stripping the solvent during the work up of the reaction.

Based on the several nitration reactions carried out using H-ZSM-5 with different Si/Al ratios the following observations are noteworthy:

(1) When we used a large amount of H-ZSM-5 with high Al content (Si/Al=30), methylpropylbenzene was found as a by-product with 1-isopropyl-4-methylbenzene as the major component in the mixture by GC/MS.

(2) We have made an attempt to investigate the possibility of nitrotoluene, particularly ortho and meta isomers, remain trapped within the pores of the zeolite. It is known that the H-ZSM-5 framework has low stability in base.[7] A sample of H-ZSM-5 (Si/Al = 1000) collected after the reaction was treated with saturated NaOH solution in an attempt to destroy the rigid structure of

the zeolite and release the trapped compounds. The liquid mixture was separated from the slurry and extracted with hexanes and analyzed for nitrotoluene using GC method. Only a small amount p-nitrotoluene isomer was found in the GC analysis.

(3) It is possible that coking of the zeolite is limiting its reactivity thus reducing the yield of nitration products. For example, addition of extra quantity of n-propyl nitrate after 16 hours of reaction time did not increase the yield of the reaction.

(4) The spent catalyst has been regenerated by recalcination under atmospheric conditions at 550°C for about 16 hours. The reactivity profile of a regenerated catalyst was tested under comparable conditions and the isolable yield was 49% with the o:m:p product distribution 9:0:91, respectively .The regenerated catalyst has regained the activity completely.

Conclusion

The results presented in this investigation show the reactivity pattern expected from conventional nitration process can be completely reversed by using a suitable catalyst. This has been achieved by the shape selective characteristics of H-ZSM-5 during the catalytic nitration of toluene. In addition, we believe that controlling the relative number of active sites outside the channels can regulate the product distribution. Case in point is that over 90% regioselectivity for the para isomer can be achieved by using a catalyst that contains a proportionately large number of active sites in the interior regions of the channels. Surprisingly, few researchers in this area have addressed this point as a possible explanation for zeolite catalyzed reactions where only modest regioselectivity is achieved. Nagy et. al. have addressed this by chemically modifying the zeolite to deactivate the outer active sites.[4] We believe external modification of zeolites would be an important consideration for future design of more sophisticated shape selective catalysts. Finally, we plan on investigating other aromatic substrates and electrophilic type reactions catalyzed by H-ZSM-5, in search of similar regioselectivity.

References

1. (a) Olah, G. A.; Malhotra, R,; Narang, S. C. *Nitration: Methods and Mechanism*; VCH: New York, 1989; pp.5-7.

(b) Borman, S. *Chem. Eng. News* **1994,** Jan.17, p.18.
(c) Schofield, K. *Aromatic Nitration*; Cambridge Univ.: Cambridge, 1980.
2. (a) Olah, G. A.; Malhotra, R.; Narang, S. C. *J. Org. Chem.* **1978**, 43, 4628.
(b) Olah, G. A.; Malhotra, R,; Narang, S. C. *Nitration: Methods and Mechanism*; VCH: New York, 1989; pp. 36-40.
3. De Laude, L.; Laszlo, P.; Smith, K. *Acc. Chem Res.* **1993**, 26, 607.
4. Nagy, S. M.; Yarovoy, K. A.; Shakirov, M. M.; Shubin, V. G.; Vostrikova, L. A.; Ione, K. G. *J. Mol. Catal.* **1991**, 64, L31.
5. Gaussian 92, Revision A; Frisch, M. J.; Trucks, G. W.; Head-Gordon, M.; Gill, P. M. W.; Wong, J. B.; Foresman, J. B.; Johnson, B. G.; Robb, M. A.; Schlegel, E. S.; Replogle, E. S.; Gomperts, R.; Andres, J. L.; Raghavachari, K.; Binkley, J. S.; Gonzalez, C.; Martin, R. L.; Fox, D. J.; Defrees, D. J.; Baker, J.; Stewart, J. P.; Pople, J. A., Guassian, Inc., Pittsburgh, PA. 1992.
6. Olah, G. A.; Malhotra, R; Narang, S. C. *Nitration: Methods and Mechanism*; VCH: New York, 1989; pp. 9-15.
7. Gates, B. C. *Catalytic Chemistry*; John Wiley & Sons: New York, 1992; pp. 268-272.

New Energetic Propellants for Hypervelocity Applications: A Challenge to the Synthesis Chemist

Ronald L. Simmons
Naval Surface Warfare Center
Indian Head, MD 20640

ABSTRACT

As the combustion gas molecular weight (MW) is lowered to gain impetus (without increasing the flame temperature), gamma (γ) increases, which adversely affects chemical energy and offsets the gain in impetus. This paper shows how to change the C-H-O-N stoichiometry to alter the combustion products to increase both Cp and Cv, thereby reducing gamma. Increasing the concentration of poly-atomic species, and decreasing the concentration of di-atomic species increases Cp and Cv, which decreases gamma. Guidelines are presented showing how it is theoretically possible to attain simultaneously low gas molecular weight (high gas output), high impetus, and low gamma (i.e., high chemical energy). These new guidelines should help the synthesis chemist to devise new molecules with the proper C-H-O-N stoichiometry and heat of formation.

INTRODUCTION

Certain facets of gun propulsion are moving into the hypervelocity regime, where in some instances, it is desired to launch projectiles at velocities of 1800-2000 meters/second or more, i.e., >Mach 5-7. These hypervelocities may require radically new propellants of very high impetus (> 1300 Joules/gram) and very high chemical energy (> 5500 Joules/gram), where chemical energy is defined as impetus/γ-1.

For example, the current JA-2 propellant, a hot (Tv ~ 3500°K) double-base propellant used in 120mm tank ammunition (in both Europe and the US), has an impetus of 1157 Joules/gram and a chemical energy of 5142 Joules/gram. The gas output is 40.26 moles/kg for an average gas MW of 24.84. To increase the impetus beyond 1300 Joules/gram (without increasing Tv), the average MW of combustion gases needs to be reduced to 22.0. And if the impetus is increased beyond 1400 Joules/gram (at the same Tv), then the gas MW must be further reduced to 20.4 or below.

Such a decrease in gas MW is rather substantial, especially when no loss of chemical energy is desired. Unfortunately, as the impetus is increased via lowering the gas MW, the chemical energy does not increase because gamma (γ) also increases ... negating high chemical energy, and in some instances actually reducing the chemical energy available (Figure 1).

Figure 1 Chemical Energy vs Impetus

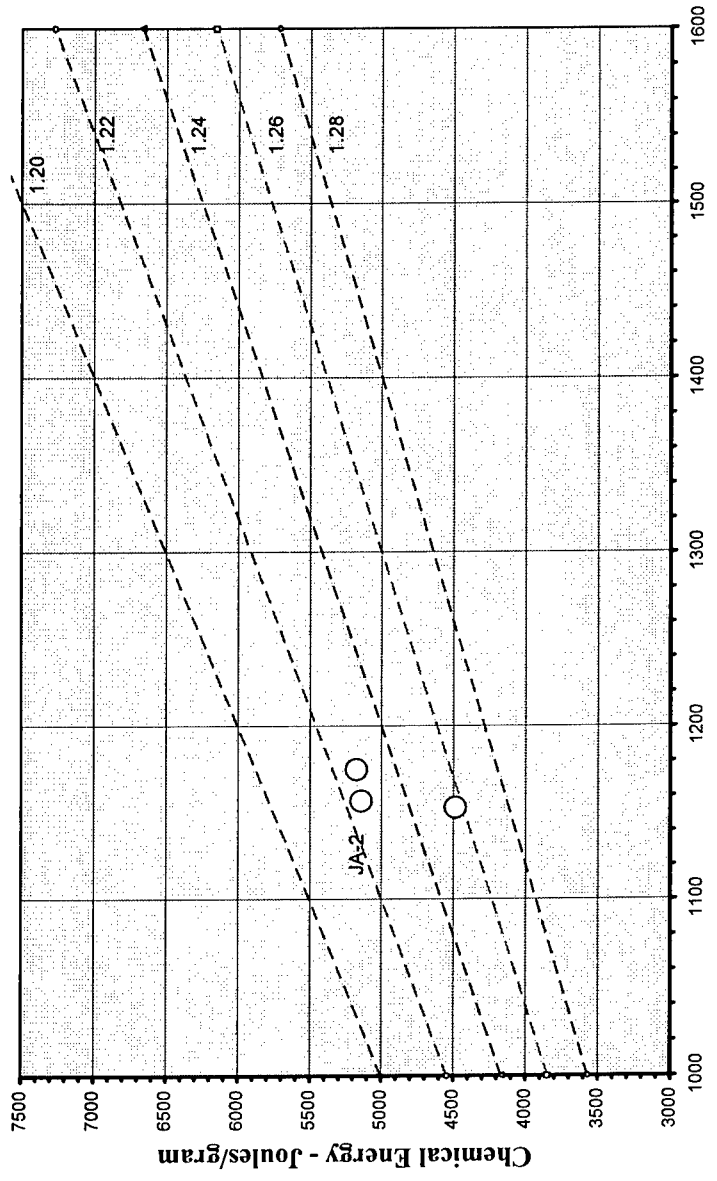

Current high impetus gun propellants have inherently high γ values (compared to JA-2 and other conventional NC-based propellants), which is of concern. Examples are as follows:

Propellant	Impetus Joules/g	Gas MW	γ	Energy Joules/g
JA-2 reference	1157	24.84	1.225	5142
76% RDX in CAB/NC	1153	21.61	1.257	4486
76% RDX in TPE	1175	19.87	1.275	4273
78% CL-20 in TPE	1320	22.32	1.262	5038

Consequently, propellants of substantially lower γ (as well as higher impetus) are needed to achieve higher chemical energy.

At least for NC-based propellants, γ is also a function of flame temperature; decreasing as temperature increases. However, current gun barrel technology will not tolerate flame temperatures higher than that of current JA-2 propellant (~3500°K). Therefore, it is imperative to seek means to reduce γ while simultaneously reducing gas MW (increasing gas output) and increasing impetus without increasing flame temperature.

DISCUSSION

Gamma is defined as Cp/Cv, where Cp is the isobaric heat capacity, and Cv is the isochoric heat capacity of the combustion gases. Thus lowering γ means increasing Cv, while Cp = Cv + R. For most solid propellants, Cv of the combustion gas is essentially constant at 0.35 cal/g/deg K.

Examination of heat capacity tables reveals that diatomic molecules such as H_2, CO, and N_2 have substantially higher γ values than polyatomic molecules such as H_2O, CO_2, HCN, NH_3, and CH_4. For example (at 298°K):

	Gas	Cv cal/°K/mole	Gamma γ
Diatomic:	H_2	6.893	1.405
	CO	6.965	1.399
	N_2	6.932	1.399
Polyatomic:	H_2O	6.044	1.329
	CO_2	6.887	1.289
	HCN	6.584	1.302
	NH_3	6.534	1.304
	CH_4	6.538	1.304

Variation of γ with temperature is shown in Figure 2.

Figure 2 Gamma vs Temp

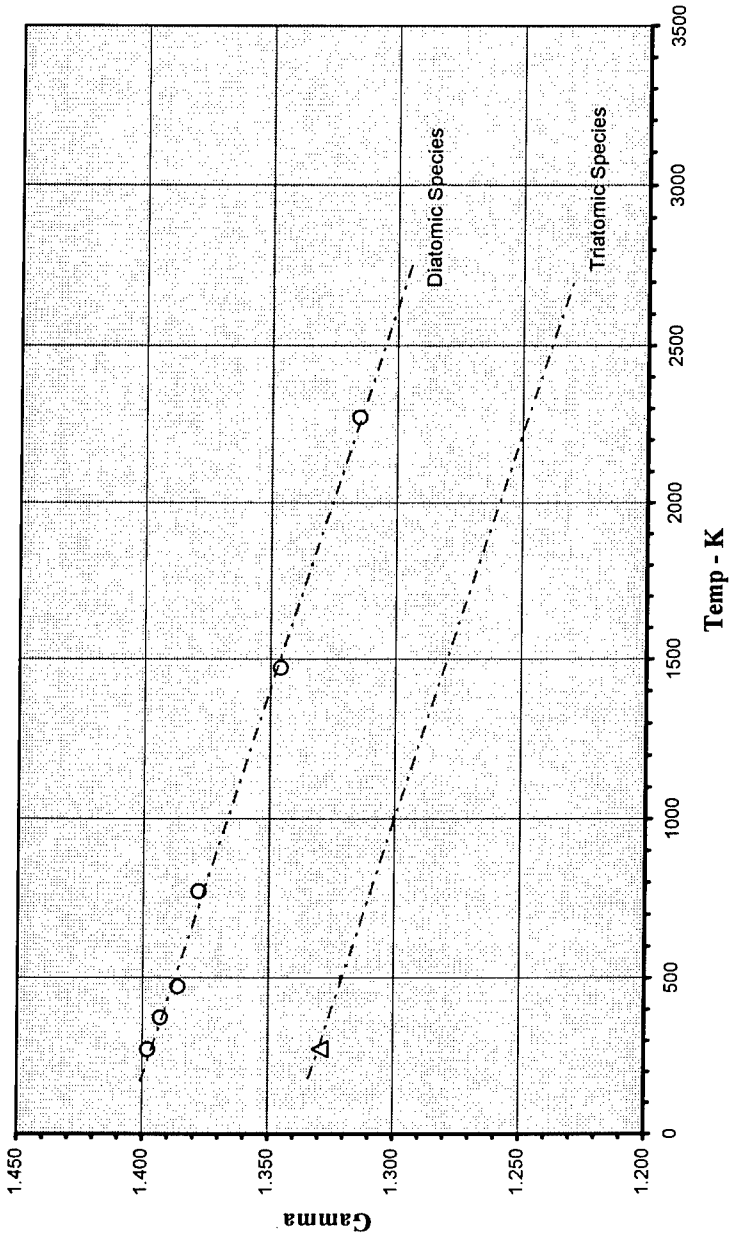

From kinetic theory of gases and definition of γ, the following are obvious:

$$\gamma = Cp/Cv \text{ and } Cp = Cv + R$$

$$\therefore \gamma = \frac{Cv + R}{Cv} = 1 + R/Cv \text{ for one mole of gas} = 1 + nR/Cv \text{ for "}n\text{" moles of gas}$$

Thus as "n" increases (to increase impetus $F = nRTv$), and Cv is essentially constant (at 0.35 cal/g/deg K) for most gun propellants, it is obvious that γ increases by definition ... which directly affects chemical energy ($F/(\gamma-1)$). As illustrated in Figure 3, it is important to find ways to increase Cv as the gas output increases (and gas MW decreases) to achieve lower values of γ.

The kinetic theory of gases shows that monatomic molecules have a limiting $\gamma = 5/3 = 1.667$, while diatomic molecules have a lower limiting $\gamma = 7/5 = 1.400$, and triatomic molecules have an even lower limiting γ. The cause of this lies in the fact that when the molecule contains more than one atom, it possesses rotational energy and vibrational energy in addition to simple translational energy. These additional energies increase both Cp and Cv, which lowers the value of γ.

Thus it is clear that the route to lower values of γ lies in increasing the concentration of polyatomic molecules in the combustion products, namely H_2O, CO_2, HCN, NH_3, and CH_4, which in turn increases the value of Cv. Unfortunately, most gun propellants have diatomic species dominating, i.e., CO, H_2, and N_2, with polyatomic species in a minor role.

For most gun propellants, the dominant polyatomic species is H_2O, with CO_2 usually present in a lesser amount, while HCN, NH_3, and CH_4 are minor species comprising < 0.1% of the total gas output. Other minor species comprise < 0.01% of the total, and can safely be ignored.

In order to address the problem of how to increase Cv (and thus decrease γ), a number of C-H-O-N stoichiometries were examined for this paper producing about 50 moles gas/kg, or a gas MW near 20. Heats of formation (ΔHf) were arbitrarily altered to keep Tv near 3400°K ($\approx$ Tv of JA-2). Several hundred calculations were made using the Blake code at a loading density of 0.20 g/cc.

To summarize the findings, at a constant Tv ~ 3400°K and gas MW ~ 20, the following effects were noted:

Figure 3 Gamma vs Gas MW

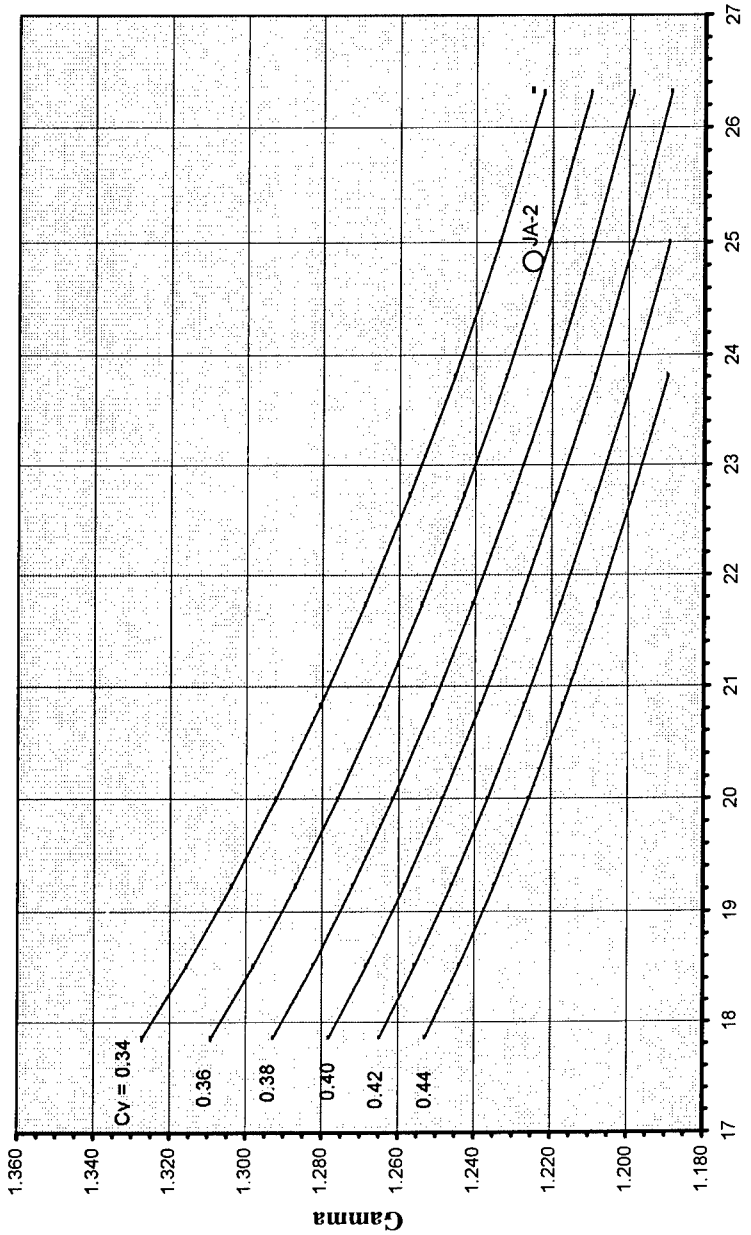

Parameter	Constant N/C Increasing O/C	Constant O/C Increasing N/C
ΔHf (to maintain Tv)	Must increase	must decrease
H/C ratio (to maintain gas MW)	Must increase	must increase
Wt % N	Decreases	Increases
Fraction polyatomic species	Increases	Decreases
Fraction H_2O	Increases	Decreases
Cv	Increases	Decreases
γ	Decreases	Increases
Covolume	Decreases	Increases
OB	Increases	Increases
Qex	Increases	Decreases

Obviously to reduce γ, the route of choice is to increase O/C ratio (while maintaining nearly constant N/C ratio) to form more H_2O. At the same time, to achieve low gas MW, the H/C ratio must be high. To minimize the formation of CO (because it is diatomic) and CO_2 (because it is heavy with a gas MW of 44), the carbon content of the propellant should be minimal.

The route to more H2O:
- Increase O/C ratio
- Reduce C wherever possible
- Increase H/C ratio ⇒ low gas MW
- N is better than C ...
  - even though N_2 weighs same as CO ... do not want CO_2
- But if N/C > 1, more hydrogen and more oxygen are needed
  - otherwise, diatomic species increase and γ increases.

Some of the outstanding C-H-O-N stoichiometries (with associated ΔHf values) were the following seven (listed in increasing O/C ratio):

C	H	O	N	ΔHf (cal/mole)
1	2.30	1.5	1.0	zero
1	2.59	1.5	1.5	+7,500
1	2.75	1.5	2.0	+14,000
1	3.20	2.0	1.0	-15,000
1	3.66	2.0	2.0	-1,500
1	4.11	2.5	1.0	-31,000
1	4.57	2.5	2.0	-17,000

Thermochemical calculated output values are shown in Table 1. Note that #6 gives the lowest γ (1.228) and highest chemical energy (6307 Joules/g) at 3400°K.

Table 1 ... Selected Outstanding C-H-O-N Stoichiometrics.							
Input:							
C	**1**	**1**	**1**	**1**	**1**	**1**	**1**
H	**2.30**	**2.59**	**2.75**	**3.20**	**3.66**	**4.11**	**4.57**
O	**1.50**	**1.50**	**1.50**	**2.00**	**2.00**	**2.50**	**2.50**
N	**1.00**	**1.50**	**2.00**	**1.00**	**2.00**	**1.00**	**2.00**
Hf - cal/mole	0	7,500	14,000	-15,000	-1,500	-31,000	-17,000
Output:							
MW	52.335	59.631	66.795	61.242	75.712	70.159	84.629
Hf - cal/g	0.000	125.774	209.596	-244.931	-19.812	-441.856	-200.877
Wt % N	26.76	35.23	41.94	22.87	37.00	19.96	33.10
O/C ratio	1.500	1.500	1.500	2.000	2.000	2.500	2.500
H/C ratio	2.300	2.590	2.750	3.200	3.660	4.110	4.570
stoich gas/kg	50.64	51.06	50.53	50.62	50.59	50.67	50.63
mob	1.650	1.795	1.875	1.600	1.830	1.555	1.785
OB	-50.44	-48.16	-44.91	-41.80	-38.67	-35.46	-33.75
delta n	0.675	0.853	1.063	0.700	1.085	0.723	1.108
delta nRT	399.92	505.08	629.50	414.73	642.83	428.06	656.16
HCP - cal/mole	172616.6	190022.5	201987.9	188359.2	217572.1	203443.4	233156.3
HCV - cal/mole	173016.5	190527.6	202617.4	188773.9	218214.9	203871.5	233812.5
HCV - cal/g	3305.9	3195.1	3033.4	3082.4	2882.2	2905.9	2762.8
Qex - cal/mole	61905.5	69652.3	76354.9	81029.9	94982.7	99157.8	113610.6
Qex - cal/g	1183	1168	1143	1323	1255	1413	1342
BLAKE calcs @ 0.20 g/cc:							
Impetus - J/g	1431	1442	1429	1443	1433	1438	1435
Tv - K	3404	3402	3408	3422	3407	3408	3406
Moles gas/kg	50.57	50.97	50.43	50.73	50.58	50.74	50.68
% of stoich	99.9	99.8	99.8	100.2	100.0	100.1	100.1
Gas MW	19.77	19.62	19.83	19.71	19.77	19.71	19.73
Gamma	1.251	1.254	1.256	1.237	1.243	1.228	1.235
Covolume - cc/g	1.157	1.177	1.184	1.091	1.129	1.035	1.081
F/gamma-1 - J/g	5701	5677	5582	6089	5897	6307	6106
Cv - cal/deg/g	0.4003	0.3987	0.3914	0.4253	0.4136	0.4422	0.4285
Cp - cal/g/deg K	0.5008	0.5000	0.4916	0.5261	0.5141	0.5430	0.5292
Gas Composition (moles/kg):							
CO	17.69	15.65	14.03	14.22	11.78	11.69	10.03
CO2	1.32	1.01	0.84	2.06	1.38	2.54	1.76
H2	13.44	13.99	13.58	11.77	12.13	10.35	10.89
H2O	8.25	7.41	6.69	14.19	11.78	18.72	15.87
N2	9.48	12.49	14.88	8.12	13.15	7.09	11.77
CH4	0.01	0.01	0.01				
NH3	0.08	0.09	0.10	0.06	0.08	0.04	0.06
HCN	0.06	0.07	0.07	0.02	0.03	0.01	0.01
NO	0.01	0.01	0.01	0.01	0.01	0.01	0.01
other	0.23	0.24	0.22	0.28	0.24	0.29	0.28
Total =	50.57	50.97	50.43	50.73	50.58	50.74	50.68
Diatomic	40.62	42.14	42.50	34.12	37.07	29.14	32.70
Tri or higher	9.72	8.59	7.71	16.33	13.27	21.31	17.70
Fraction Tri +	0.1922	0.1685	0.1529	0.3219	0.2624	0.4200	0.3493
Fraction H2O	0.1631	0.1454	0.1327	0.2797	0.2329	0.3689	0.3131
H2O/Poly	0.8488	0.8626	0.8677	0.8690	0.8877	0.8785	0.8966
Fraction di	0.8032	0.8268	0.8428	0.6726	0.7329	0.5743	0.6452
							RLS

Guidelines to lowering γ while decreasing the gas MW (to increase impetus) by paying attention to the concentration of polyatomic species in the combustion products, are as follows:

1) Adjust C-H-O-N stoichiometry to produce the desired gas MW ... example 20;
   Can be done ... not especially difficult;
   BUT ... limitations may exist especially near extremes of H/C, O/C, N/C;
   Limitations are not well defined; and
   May not be able to formulate to desired stoichiometry if near limits.

2) Adjust ΔHf to produce Tv ~ 3400°K;
   May be extremely difficult;
   As O/C increases -- ΔHf must decrease ... otherwise too hot;
   As N/C increases -- ΔHf must increase ... otherwise too cool;
   A very delicate balance exists -- may be beyond our current capabilities;
   Relationship between ΔHf and chemical structure (for energetic compounds) needs to be improved/expanded.

3) Caution – as N/C increases (as we move towards higher N compounds) ...
   More N_2 is formed ... diatomic species ... undesirable for low γ;
   More difficult to increase polyatomic species.

Note that these are stoichiometric goals for the propellant ... not individual ingredients. And that high N is not necessarily desirable. Low C + high H/C + high O/C ratio are key parameters. Ingredients need to be synthesized and formulated into propellant such that the proper overall C-H-O-N stoichiometry and Hf are attained ... using guidelines in this paper.

CONCLUSIONS

New propellants and concepts are needed for hypervelocity guns. It is hoped that guidelines in this paper will help stimulate chemical research for new organic molecules of proper C-H-O-N stoichiometry and ΔHf (heat of formation) to attain high impetus and high chemical energy. Both factors are critical: C-H-O-N stoichiometry determines the gas output (gas MW), gas composition (polyatomic species), Cv, and γ, while ΔHf determines the flame temperature.

ACKNOWLEDGEMENTS

For the many discussions and conversations regarding energetic chemistry, thermochemistry, and hypervelocity gun ballistics, the author would like to thank especially the following:

Alfred Stern, Bill Koppes, Michael Sitzmann, Randy Cramer, and Susan Peters of NSWC/Indian Head; Arpad Juhasz, Gloria Wren, Tom Minor, Andy Brant, and Joe Heimerl of ARL/Aberdeen Proving Ground; Fred Robbins formerly of ARL/Aberdeen; Woody Waesche of SAIC/McLean; Fred Y. Su of SAIC/San Diego; E. Hays Zeigler of Alliant/Radford; Richard S. Miller formerly of the Office of Naval Research; Gerry Winchenbach of Eglin AFB; Fritz Schedlbauer, Thomas Keicher, and Fred Volk of Fraunhofer ICT/Pfinztal, Germany; Rudi Heiser of Fraunhofer Institut fur Kurzeitdynamik/Weil-am-Rhein, Germany; Beat Vogelsanger of NitroChemie/Wimmis, Switzerland, and Tatyana S. Pivina of Zelinsky Institute of Organic Chemistry/Moscow, Russia.

SELECTED BIBLIOGRAPHY

1. R. L. Simmons, *Guidelines to Higher Energy Gun Propellants*, 27th International Annual Conference of ICT, Karlsruhe, Germany, June 25-28, 1996.

2. B. Finck and H. Graindorge, *New Molecules for High Energetic Materials*, 27th International Annual Conference of ICT, Karlsruhe, Germany, June 25-28, 1996.

3. A. Cumming, *Next Generation Propellant Research in the UK*, Solid Propellant Chemistry, Combustion, and Motor Interior Ballistics Conference, X'ian, China, June 14-17, 1999.

4. F. Volk and H. Bathelt, *Influence of Energetic Materials on the Energy-Output of Gun Propellants*, 28th International Annual Conference of ICT, Karlsruhe, Germany, June 24-27, 1997.

5. E. Robson and J. Kendrick, *Molecular Modelling of Novel Energetic Mat*erials, 27th International Annual Conference of ICT, Karlsruhe, Germany, June 25-28, 1996.

6. E. Robson, J. Kendrick, W. Leeming, G. Leiper, A. S. Cumming, and C. Leach, *Molecular Modelling of Novel Energetic Materials,* Life Cycles of Eneregtic Materials, Williamsburg, VA, October 6-9, 1996.

7. A. V. Evtushenko, M. S. Molchanova, B. B. Smirnov, and V. A. Shlyapochnikov, *Computer Search for New C-H-N-O-containing Energetic Compounds*, X'ian, China, June 14-17, 1999.

8. R. L. Simmons, *A Road Map to Very High Impetus Gun Propellants – Some Intriguing Possibilities*, 29th International Annual Conference of ICT, Karlsruhe, Germany, June 30 to July 3, 1998.

9. R. L. Simmons, *Guidelines to Selecting Compounds Generating Low MW Gases – A Few Simple Rules*, 28th International Annual Conference of ICT, Karlsruhe, Germany, June 24-27, 1997.

10. S. T. Peters and N. Almeyda, *An Analytical Test of the Hypothesis that Low Molecular Weight Combustion Gases will Facilitate Achievement of Hypervelocity*, 30th International Annual Conference of ICT, Karlsruhe, Germany, June 29 to July 2, 1999.

11. P. Vavra, *Procedure for Selection of Molecular Structures of Explosives Having High Performance*, 30th International Annual Conference of ICT, Karlsruhe, Germany, June 29 to July 2, 1999.

12. J. E. A. John, Gas Dynamics, Allyn and Bacon, Boston, 1969.

13. M. J. Zucrow and J. D. Hoffman, Gas Dynamics, John Wiley & Sons, New York, 1976.

14. M. E. Levy and M. Visnov, *Hypervelocity Solid Gun Propellants*, Frankford Arsenal Phase Report R-1786, December 1965.

15. H. Bergman, H. Ostmark, M-L. Petersson, U. Bemm, and H. Hihkio, *Some Initial Properties and Thermal Stability of FOX-7*, NDIA Insensitive Munitions and Energetic Materials Technology Symposium, Nov 29 to Dec 2, 1999, Tampa, FL.

16. D. Mueller, *New Gun Propellant with CL-20*, Propellants, Explosives, Pyrotechnics, Number 24, 1999.

17. D. A. Geiss, S. M. Nicolich, M. Mezger, K. E. Lee, and R. L. Hatch, *Additional Characterization of High Performance CL-20 Formulations*, NDIA Insensitive Munitions and Energetic Materials Technology Symposium, Nov 29 to Dec 2, 1999, Tampa, FL.

18. P. Braithwaite, D. Backes, A. Haaland, R. B. Wardle, T. Manning, L. Harris, and K. Klingaman, *Characterization of Thermoplastic-Elastomer (TPE) Gun Propellants*, NDIA Insensitive Munitions and Energetic Materials Technology Symposium, Nov 29 to Dec 2, 1999, Tampa, FL.

19. C. Leach, D. Debenham, J. Kelly, and K. Gillespie, *Gun Propellants Based on Poly-NIMMO and Poly-GLYN Binders*, NDIA Insensitive Munitions and Energetic Materials Technology Symposium, Nov 29 to Dec 2, 1999, Tampa, FL.

20. Y. Longevialle, M. Golfier, H. Graindorge, and G. Jacobs, *The Use of New Molecules in High Performance Energetic Materials*, NDIA Insensitive Munitions and Energetic Materials Technology Symposium, Nov 29 to Dec 2, 1999, Tampa, FL.

21. L. F. Cannizzo, R. S. Hamilton, T. K. Highsmith, A. J. Sanderson, and B. A. Zentner, *Furazan-Based Energetic Ingredients*, NDIA Insensitive Munitions and Energetic Materials Technology Symposium, Nov 29 to Dec 2, 1999, Tampa, FL.

22. H. Ostmark, *FOX-7 – A New Explosive With Low Sensitivity and High Performance*, 11th International Symposium on Detonations, Snow Mass, CO, Aug 30 to 4 Sep 1999.

GLOSSARY

Term	Definition
C	Carbon
H	Hydrogen
O	Oxygen
N	Nitrogen
H/C	Hydrogen/carbon ratio
MW	Molecular weight
N/C	Nitrogen/carbon ratio
O/C	Oxygen/carbon ratio
OB	Oxygen balance to $CO_2 + H_2O + N_2$
F	Impetus also known as force constant (Joules/gram)
ΔHf	Heat of formation (isobaric)
γ	Gamma
Tv	Isochoric flame temperature (°K)
E	Chemical energy (Joules/gram)
K	Temperature in degrees Kelvin
R	Universal gas constant (8.31434 Joules/gram)
C_p	Heat capacity at constant pressure (isobaric)
C_v	Heat capacity at constant volume (isochoric)
n	Moles of gas per gram

THE ENERGIES OF DISSOTIATION BONDS AND EFFICIENT ENERGIES OF NTERACTION IN NITROAMINES

L.M.Kostikova, E.A.Miroshnichenko, Y.N.Matyushin

Semenov Institute of Chemical Physics, Russian Academy of Sciences
117977 Kosygin Str. 4, Moscow, RUSSIA
Fax: (095) 938 2156. E-mail: ynm@polymer.chph.ras.ru

ABSTRACT

On the base of experimental measurements and analysis literary data the enthalpies of formation of the row primary and secondary nitroamines are recommend. The enthalpies of formation of the row nitromines radicals are determined using experimental data on the kinetics and semiempirical calculation methods, which together with the available data on the enthalpies of formation the free radicals have allow get the energies of dissotiation bonds C-H, C-C, C-N, N-H and N-N in the nitroamine compounds. The regularites of changing of the received dissociation energies comparatively these energy in corresponding to the construction of skeleton aminoes and hydrocarbons are determined.

The contributions of the nitramine groups in the enthalpies of formation in the gas phase and in the enthalpies of atomization are determined. The efficient energies of interaction nitramine groups in polynitroamines are calculated.

EXPERIMENTAL

For the determination of the enthalpies of formation the nitroamines from the enthalpies of combustion in the standard condition semimicrocalorimetric method was used. The enthalpies of formation of substances is received from energies of their combustion in the calorimetric bomb at the abundance of oxygen. The energies of combustion are measured on the hermetic calorimeter with the magnetic stirrer developed in ICP RAS specially for researches of energetic materials [1]. The calibration of the calorimeter is executed on burning the reference standard - benzoic acid of the mark K-1, certificated in D.I.Mendeleev Institute of Metrology. The absence of the systematic error of the measurements on the given calorimeter is confirmed by burning of the secondary reference standard – succinic and hippuric acids. The calorimeter allows to measure the thermal effects of the combustion reactions of the substances with the error 0.02 - 0.03%. The bases of a technique of burning of energetic materials are stated in work [2].

With calculation of the combustion enthalpies the amendments on heat exchange of the calorimetric vessel with the cover, on the incendiary energy and the combustion energy of auxiliary substance, on the thermal effect of formation of the nitric acid, Washburn and work of expansion of gases are entered.

With calculation of the standard enthalpies of formation the following the enthalpies of formation of the combustion products are used:

$\Delta_f H^\circ [CO_2] (g) = - 393.51$ kJ·mol^{-1} [3]

$\Delta_f H^\circ [H_2O] (l) = - 285.83$ kJ·mol^{-1} [3].

Purity of the nitroamines was characterized by the chromatographic methods

and their element composition was check by the analysis on C, H and N by the analyzer "Carbo Erba".

RESULT AND DISCUSSION

On the base of the analysis literary date following enthalpies of formation the radicals are recommend: $\bullet CH_3$ – 146,9; $\bullet H$ – 218,0; $\bullet NH_2$ – 190,0; $\bullet NHCH_3$ – 177,4; $\bullet N(CH_3)_2$ – 161,1; $\bullet NO_2$ – 33,1; $\bullet CH_3NNO_2$ – 139,0. $kJ \cdot mol^{-1}$

The enthalpies of formation in the standard condition, $\Delta_f \mathbf{H}^o$, the enthalpies of vaporizations, $\Delta_v \mathbf{H}$, and the enthalpies of formation in the gas phase, $\Delta_f \mathbf{H}^o_g$, of the row nitroamines are listed in Table 1.

For the calculation of enthalpies of formation of the amine and the nitroamine radicals additive-group approach and method of substituting are used. The enthalpy of formation of the radical $\bullet HNNO_2$ is estimated by the method of substituting using the enthalpy of formation the radical methylnitroamine. At the calculation of enthalpies of formation of the radical $\bullet N(NO_2)_2$ was expect that effect of substituting CH_3 group on NO_2 group for methylamines and corresponding to radicals is equal. From enthalpies of formation dimethylnitroamine (-7,5 $kJ \cdot mol^{-1}$) and methyldinitroamine (53,5 $kJ \cdot mol^{-1}$) the effect of substitution CH_3 group on NO_2 group is composed 61,0 $kJ \cdot mol^{-1}$. From the enthalpies of formation $\bullet CH_3NNO_2$ (138,9 $kJ \cdot mol^{-1}$) possible to value the enthalpy of formation $\bullet N(NO_2)$ equal 200,0 $kJ \cdot mol^{-1}$. Similar image, as well as with use group method the others values of the enthalpies of formation the radicals are calculated from experimental data (Table 2).

The energy of dissociation of bonds in nitroamines is calculated by usingthe enthalpies of formation of the nitroamines from Table 1 and the radicals from Table 2 on the equation (1)

$$\mathbf{D(R_1 - R_2) = \Delta_f H^o(R_1) + \Delta_f H^o(R_2) - \Delta_f H^o(R_1 - R_2)} \qquad (1)$$

The values of the energies of dissociation of bonds were compare with values of the lengths of bonds in amines calculated for the some compounds by the semitheoretical method MNDO [6]. Results are led in the Table 3.

From Table 3 is seen that for getting a correspondence tothe energy of dissociation bonds and accounting geometric parameters of molecules ofenergetic materials, necessary to complete method MNDO contributions, taking into account the interaction between the electronegative groups.

Table 3 show that the energy of dissociation bond C–N in nitroamines considerably lower than in the methylamines. This agree geometry of molecules: the length of bond C–N in the nitroamines more, than in methylamines.

The chemical modification nearest environment considerably changes the energy of dissociation of bond N–NO_2 (from 230 before 118 kJ·mol^{-1}). The energies of dissociation of bond N–C noticeably below in the nitroamines in contrast with methylamines. The bonds N–C, being between two nitroamine groups, are changed most greatly. Bonds N–H in the nitroamines in contrast with methylamines are greatly lower. The bonds of the second surrounding, in particular, C–H in the nitroamines, practically such, as in amines, but noticeably lower then in the alkanes. The bonds C–C, being between methylnitroamine groups, nearly on 62 kJ·mol^{-1} more weak the bonds C–C in the hexane (the energies of dissociation of bonds in the alkanes take from the work [7] with provision for enthalpies of formation the radical CH_3 equal 146,9 kJ·mol^{-1}).

Table 1. Thermochemical properties of nitroamines, 298 K, kJ·mol^{-1}

COMPOUND	$-\Delta_f H^\circ$	$\Delta_v H$	$-\Delta_f H^\circ$ g
NH_2NO_2(c)	63,5 ± 0,8	56,0 ± 0,8	7,5 ± 1,2
CH_3NHNO_2(c)	73,2 ± 1,2	74,5 ± 0,3	-1,3 ± 1,3
$CH_2(NHNO_2)_2$(c)	62,8 ± 1,2	141,0 ± 3,0	-78,2 ± 4,0
$(CH_2NHNO_2)_2$(c)	103,8 ± 1,2	148,0 ± 2,6	-44,2 ± 4,0
$(CH_2)_6(NHNO_2)_2$(c)	212,0 ± 1,2	-	-
$(CH_3)_2NNO_2$(c)	75,0 ± 1,2 [4]	67,4 ± 0,4	7,6 ± 2,0
$(C_2H_5)_2NNO_2$(l)	106,0 ± 8,0 [5]	53,0 ± 3,0 [4	53,0 ± 10,0
(н-$C_3H_7)_2NNO_2$(l)	163,0 ± 3,0	57,0 ± 1,2	106,0 ± 4,0
$CH_3NNO_2CH_2NNO_2CH_3$(c)	51,6 ± 0,5	102,5 ± 0,4	50,9 ± 0,4
$CH_3NNO_2(CH_3)_2NNO_2CH_3$(c)	-41,5 ± 0,8	-	-
$CH_3NNO_2(CH_2)_2NNO_2CH_3$(c)	94,0 ± 1,5	110,5 ± 0,8	-16,6 ± 2,0
$CH_3NNO_2(CH_2)_6NNO_2CH_3$(c)	199,6 ± 3,0	125,6 ± 2,0	74,0 ± 4,0
$CH_3N(NO_2)_2$ (l)	-1,7 ± 0,8	52,0 ± 0,4	-53,7 ± 1,0
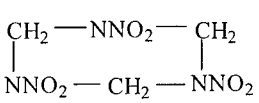 (c)	-70,7 ± 2,5	128,0 ± 2,1	-198,7 ± 3,3
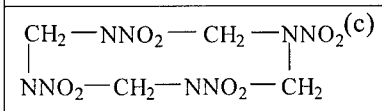 (c)	-85,8 ± 1,7	174,9 ± 3,6	-261,9 ± 4,2
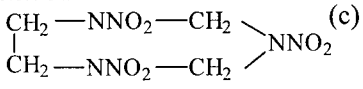 (c)	-41,0 ± 2,5	124,7 ± 1,2	165,7 ± 3,0
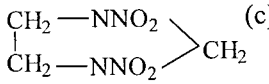 (c)	1,7 ± 2,5	105,4 ± 0,8	103,8 ± 2,9

Table 2.

Enthalpies of formation of amine and nitramine radicals, 298K, kJ·mol^{-1}

RADICAL	$\Delta_f H^\circ$	RADICAL	$\Delta_f H^\circ$
$\bullet CH_2NH_2$	155,2	$\bullet H_2CN(NO_2)_2$	210,5
$\bullet CH_2NHCH_3$	149,8	$\bullet H_2CCH_2N(NO_2)CH_3$	144,3
$\bullet CH_2N(CH_3)_2$	136,8	$\bullet H_2CN(NO_2)CH_2N(NO_2)CH_3$	202,1
$\bullet HNNO_2$	162,3	$\bullet H_2CN(NO_2)(CH_2)N(NO_2)CH_3$	173,2
$\bullet O_2NNNO_2$	200,0	$\bullet CH_3NCH_2N(NO_2)CH_3$	185,4
$\bullet H_2CNHNO_2$	164,8	$\bullet CH_3N(NO_2)CH_2CHN(NO_2)CH_3$	164,0
$\bullet H_2CN(NO_2)CH_3$	149,4	$\bullet CH_3N(NO_2)CH_2CHN(NO_2)CH_3$	147,7

Table 3.

Lengths and the energies of dissociation of bonds in the nitroamines, 298K, kJ·mol^{-1}

COMPOUND	Bond length, °A		Energy of dissociation	
	N – N	**C – N**	**N – N**	**C – N**
NH_2NO_2	1,41	-	230,0	-
NH_2CH_3	-	1,46	-	359,8
CH_3NHNO_2	1,40	1,48	209,2	297,1
CH_3NHCH_3	-	1,44	-	342,7
$(CH_3)_2NNO_2$	1,40	1,49	163,2	292,0
$(CH_3)_3N$	-	1,45	-	331,8
$CH_3N(NO_2)CH_2N(NO_2)CH_3$	1,40	1,48	167,4	293,3

Thus, in the nitroamine compounds of the most strong bonds several are weaken (N–C, N–H, C–C, C–H), then most weak bond $N–NO_2$ in the primary nitroamines saves its the energy of dissociation at a level of the hydrazine bond in the alkylhydrazines [7]. In the dialkylnitroamines the energy of dissociation of the bond $N–NO_2$ several falls. In methyldinitroamine because of the interaction nitrogoups the energy of dissociation of the bond $N–NO_2$ considerably decreases (118 $kJ \cdot mol^{-1}$).

The energy of dissociation of the bonds in the nitroalkanes are changed otherwise as against from the nitroamines, so the energy of bonds C–H in nitroalkanes stay close to corresponding to values in alkanes, but the energies of dissociation of the bonds C–C even are strengthening.

Listed in the Table 1 the thermochemical characterizations of the nitroamines enable analyse particularities of energy of the nitroamines group depending on constructions of molecules and developcalculated methods of estimation and forecastings of thermochemical properties. The enthalpies of atomization of the nitroamines were calculated on the base data for the formation enthalpies of the nitroamines in the gas phase and the formation enthalpies of the atoms. Group parameters of work [5] for the calculation of contributions hydrocarbon-amine part of molecules allow calculate parameters, accounted for nitroamine group. Contributions of groups in the enthalpy of formation in the gas phase and in the enthalpy of atomization, $\Delta_f H^\circ a$, have listed in the Table 4.

The contributions of the nitroamine groups in the enthalpy of atomization (formation in the gas phase) under identical nearest environment do not depend from the amount and mutual location them in the molecule and equal for line and cyclic structures. Thus, nitroamine groups in polynitroamines do not interact intramolecular. The specifics of influence of the molecular interactions on the enthalpy characterizations of the nitroamines in the standard condition possible to value, analysing, for instance, the enthalpies of combustion. For the

Table 4.

Contributions of groups in the enthalpy of formation in the gas phase and in the enthalpy of atomization, 298K, $kJ \cdot mol^{-1}$

GROUP	$\Delta_f H^\circ g$	$\Delta_f H^\circ a$
$C-(C)(H)_3$	-42,3 [5]	1411,3 [5]
$C-(C)2(H)_2$	-20,6 [5]	1171,6 [5]
$C-(N)(H)_3$	-42,3 [5]	1411,3 [5]
$C-(N)(C)(H)_2$	-26,9 [5]	759,6 [5]
$C-(N)_2(H)_2$	-11,5	1162,5
$N-(C)(H)(NO_2)$	46,9 ± 2,5	1615,0 ± 2,5
$N-(C)_2(NO_2)$	75,3 ± 1,7	1368,2 ± 1,7
$N-(C)(NO_2)_2$	92,9	2322,1

determination of contribution separate nitroamine groups are use data from Table 1. Calculation has show that contributions to the enthalpy of combustion in the standard condition of the nitroamine groups from the compounds, in which these groups are divided two or more methylene footbridges, are render equal within the error of the experimental data and for groups $NHNO_2$ and NNO_2 have composed 220,1 ± 1,7 and 222,6 ± 0,8 $kJ \cdot mol^{-1}$. In the Table 5 the experimental and calculated values of the enthalpies of combustion in the standard condition of the polynitroamines of the different construction are compared. The different between the experimental and calculated values of the enthalpies of combustion in the standard condition are adopted as the efficient energies interaction of nitroamine groups:

$\mathbf{E = \Delta_c H^0 (calc) - \Delta_c H^0(exp)}$;

Marking in the Table 5:

$\mathbf{\Delta_c H^0(exp)}$ and $\mathbf{\Delta_c H^0(calc)}$ - experimental and calculated enthalpies of combustion;

E - a full efficient energies interaction of the molecule or the energy to destabilizations:

$\mathbf{E_1}$ - an energy, relatively refer to 1 pair interacting groups.

From Table 5 is seen that experimental values the enthalpies of combustion of the polynitroamines greatly exceed calculated values, received from the analysis of the enthalpies of combustion of the mononitroamines and dinitroamines with the distant friend from friend the nitroamine groups. As it was shown above, in the gas phase the nitroamine groups do not interact between itself, so received efficient energies interaction are to be bound only with specifics of intermolecular interaction of nitroamine groups in polynitroamines. Possible expect, that in the case of polynitroamines, not each group of the molecule nitroamine can completely realize that energy with which interact nitroamine groups in mononitroamines.

Thus, efficient energies interaction in polymethylenenitroamines can be cause by the incomplete intermolecular interaction in the standard condition. Depending on specifics of substanses efficient energies interaction of nitroamine are significant changed and reach in cyclic compound 100 $kJ \cdot mol^{-1}$.

Possible conditionally separate a general energy of the interaction on the amount of the nitroamine groups, divided by the one methylene group. Significant differencre of these values (from 8 before 36 kJ) shows that difficult create sufficiently sure and simple scheme of calculation of the polynitroamines

Table 5.

Efficient energies interaction of nitroamine groups in the standard condition, 298K, $kJ \cdot mol^{-1}$

COMPOUND	$-\Delta_c H^\circ$ (exp)	$-\Delta_c H^\circ$ (calc)	E	E_1
$NHNO_2CH_2NHNO_2$	902,9	893,7	9,2	9,2
$CH_3N(NO_2)CH_2N(NO_2)CH_3$	2279,4	2258,9	20,5	20,5
$CH_3(NNO_2CH_2)_2NNO_2CH_3$	2961,9	2935,1	26,8	13,4
$CH_3(NNO_2CH_2)_3NNO_2CH_3$	3648,9	3611,2	37,7	12,5
$(CH_2NNO_2)_3$	2107,9	2028,0	79,9	25,5
$(CH_2NNO_2)_4$	2805,0	2703,7	101,3	25,5
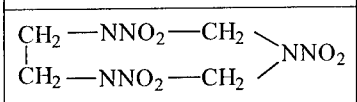	2758,5	2679,9	18,8	9,4
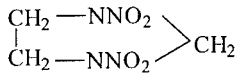	2036,4	2003,7	32,6	32,6

in the standard condition unlike the gas phase. Obviously accounting scheme for nitroamines, must be combined, i.e. containing together with thermochemical parameters, coefficient connected with the physicist-chemical properties of under study compounds and reflect specifics of interamolecular interactions of each compounds.

This research was supported by the Russian Fondation of Fundamental Investigations (Grant № 00-03-32196a).

REFERENCES

1. Matyushin Yu. N.; Vorobev A. B.; Konkova T. S. et al. *Pat USSR* 1221568, **1986** (in Russian).

2. Lebedev Y. A.; Miroshnichenko E. A.; Knobel Y. K. *Thermochemistry of the Nitro Compounds*, Nauka, Moscow, **1970**, 168. (in Russian).

3. Cox J. D.; Vagman D. D.; Medvedev V. A. (Eds.) *Codata Key Values for Thermodynamics*, New-York – Washington, **1989**.

4. Matyushin Yu. N.; Vjunova I.B.; Pepekin V.I.; Apin A.Ya.. *Izv. Akad. Nauk SSSR, Ser. Khim.*, **1973**, *45*, 2354 (in Russian).

5. Cox J.D.; Pilcher G. *Thermochemistry of organic and metalloorganic* compounds. London – New-York: Acad. Press, **1970**, 643 p.

6. Clark T. *Handbook of Computational Chemistry.* Willey & Sons, Germany, **1990**.

7. Gurvich L.V., Karachevcev G.V., Kondratjev V.N. et al. *The Energies of Chemical Bonds. Ionization Potentials and Affinity to Electron.* Moscow, Nauka, **1974**, 351 p, (in Russian).

ENERGY OF INTERACTION NO_2-GROUPS IN NITRODERIVATIVES METHANE AND ETHANE

Y.N.Matyushin, V.P.Lebedev, E.A.Miroshnichenko,
L.M.Kostikova, Y.O.Inozemcev

Semenov Institute of Chemical Physics, Russian Academy of Sciences
117977 Kosygin Str. 4, Moscow, RUSSIA
Fax: (095) 137 8297, E-mail: ynm@polymer.chph.ras.ru

The efficient energy of interaction (EEI) between molecules of the nitro-groups reaches the greater values and can be safely evaluated in the high-nitrated compounds, where greater number NO_2-groups are disposed on near distance. EEI of the nitrogroups presents itself a variety of potential energy of molecule, so its value is valued as the difference between two fixed energy levels – the experimental value to enthalpies offormation the compound and calculated value at the condition of absence of interactions between nitrogroups.

EEI of the functional groups (on the molecular level) possible conditionally consider as an analogy of potential energy. Value EEI influences on the stability of substance to different physical and chemical influences, in many defines durability its chemical bonds (particularly most weak bond in the molecule), energy, density, thermostability, sensitivity to mechanical influence and etc. So study of reasons, causing arising this energy, and regularities of its change will enable optimize the process of searching for energetic material with given property.

EEI nitrogroups are determined on the grounds of received in this working experimental data and published by the authors of the earlier work in rows methane-tetranitromethane end ethane-hexanitromethane. The regularities of changing this energy depending on numbers and positionsnitrogroups are installed. The influence EEI on the values of the formation enthalpies and the dissotiation energies of the bonds C – N and C – C is shown.

INTRODUCTION

The study of thermochemical characteristics nitrocompounds and factors, act upon changing these characteristics, presents scientific and practical interest.

Analysis of values of enthalpies of formation C-nitrocompounds has show that in low-nitrated compounds, where nitrogroups are removed friend from the friend on the greater distance and practically do not interact between itself, is observe constancy numerical contributions of the nitrogroups in the enthalpy of formation, i.e. it is keep rule of additivity of contributions. Inthe high-nitrated compounds additivity rule is break that is stipulate by the appearance in molecules of the compounds the additional energy, which reason is the interaction of the nearsituated nitrogroups. This the efficient energy of interaction (EEI) of the nitrogroups in the polynitrocompounds reaches the greater values and can be safely evaluated.EEI is component part of the enthalpies of formation (energy) of the molecule. It will be realize at the decomposition of molecule in reactions of combustion or explosive conversion. This energy influences on physical and chemical characteristics nitrocompounds and so deserves a close examination.

The thermochemical values of chemical compounds, including the standard enthalpies of formation, enthalpies of formation from atoms and others, are relative and is calculated comparatively fixed level.EEI functional groups possible conditionally to consider as a variety of potential energy, which value can be calculated as a difference of energy of two fixed levels. In this instance value EEI functional groups is evaluated asthe difference of two energy levels - between the experimental measured the enthalpy of formation

of the compound and calculated on the additive contributions for the hypothetical condition, when interaction of functional groups is absent.

The enthalpy of formation for the hypothetical condition ofthe molecule is evaluated by the method of substituting: forthe enthalpy of formatuon of the compound in the gas phase is installed energy effect of substitutingthe atom of hydrogen in the methane (ethane) on NO_2 group. Since in the hypothetical condition the interaction of the nitrogroups is absent, the calculated enthalpy of formation in the gaseous condition, for instance, fortetranitromethane is enthalpies of formation of the methane plus 4 energy effects of changing an atom of hydrogen on NO_2 group.

EXPERIMENTAL

The reliable determination of the enthalpies of combustion and formation of the energetic material, to which C-nitrocompounds is pertain, because of their the specific properties (difficulties of syntheses and cleaning, low thermostability, high sensitivity to mechanical influences) is technically complicated in the experimental plan by the process. In the laboratory of Thermochemistry ICP RAS the method and technique of experiment specially for the energetic materials study and series of calorimetric instruments were designed [1,2].

Received by authors experimental values of the enthalpies of formation nitroderivatives methane and ethane in condensed and gaseous condition, required for undertaking the thermochemical analysis, are provide in the Table 1.

Table 1.

The enthalpies of combustion and formation of the nitroderivatives methame and ethane, 298 K, kcal/mol

№	COMPOUND	$-\Delta_c H^\circ$	$\Delta_f H^\circ$	$\Delta_f H^\circ(g)$
1.	CH_4 (g)		-17.9 [3]	-17.9 [3]
2.	CH_3NO_2 (l)	169.5	-28.5	-19.3
3.	$CH_2(NO_2)_2$ (l)	137.3	-25.2	-14.3
4.	$CH(NO_2)_3$ (c)	117.6	-10.7	5.8
5.	$C(NO_2)_4$ (l)	103.2	9.2	19.7
6.	C_2H_6 (g)		-20.2	-20.2
7.	$C_2H_5NO_2$ (l)	324.5	-34.4	-24.5
8.	$(NO_2)CH_2CH_2(NO_2)$ (c)	282.0	-42.7	-23.2
9.	$(NO_2)_2CHCH_3$ (l)	289.0	-35.7	-21.1
10.	$(NO_2)_3CCH_3$ (c)	263.6	-27.0	-9.8
11.	$C_2(NO_2)_6$ (c)	207.1	19.0	33.8

The values EEI of nitrogroups in the rows methane - tetranitromethane and ethane - hexanitroethane are evaluated on the base of data presented in the Table 1. This values are provided in the Table 2.

The consequent introduction nitrogroup in the molecule of methane in the row methane – tetranitromethane brings about increase values EEI from 0 before 37 kcal/mol. The values EEI increases from 0 before 80 kcal/mol in the row ethane - hexanitroethane. In nitroderivatives ethane EEI depends not only from the number nitrogroups in the molecule, as well as from the place of joining. Such a picture of the change EEI is observe also in the polynitrobenzene.

In high-nitrated compounds EEI reaches values comparable to strong (energy) chemical bonds and exsert the essential influence upon physical, chemical and thermodynamic properties of the compounds.

Table 2.

The efficient energy of interaction NO_2-groups in rows methane-tetranitromethane and ethane-hexanitromethane

NITRODERIVATIVES METHANE					
Compound	Nitro-ethane	1,2-Dinitro-ethane	1,1-Dinitro-ethane	1,1,1-Trinitro-ethane	
$\Delta_f H^o(g)$ exp	-17.8	- 9.2	5.8	19.7	
$\Delta_f H^o(g)$ calc	-17.8	-17.7	-17.6	-17.5	
EEI	0	8.5	23.4	37.2	
NITRODERIVATIVES ETHANE					
Compound	Nitro-ethane	1,2-Dinitro-ethane	1,1-Dinitro-ethane	1,1,1-Trinitro-ethane	Hexanitro-ethane
$\Delta_f H^o(g)$ exp	-24.5	-23.2	-21.1	-9.8	33.8
$\Delta_f H^o(g)$ calc	-24.5	-27.8	-28.8	-33.1	-46.0
EEI	0	5.6	7.7	23.3	79.8

The received results allow to analyse the influence of the value EEI nitro-groups on the energy of dissociation C - NO_2 and C – C bonds in the nitro-derivatives of methane and ethane. The energies of dissociation these bonds is calculated on the equation

$$D(R_1 - R_2) = \Delta_f H^o(R_1) + \Delta_f H^o(R_2) - \Delta_f H^o(R_1 - R_2), \qquad (1)$$

where:

$D(R_1 - R_2)$ – the energy of dissociation bond, kcal/mol;

$\Delta_f H^o(R_1)$ and $\Delta_f H^o(R_2)$ – enthalpies of formation the radicals in the gaseous phase, kcal/mol;

$\Delta_f H^o(R_1 - R_2)$ – the enthalpy of formation of the compound in the gaseous phase, kcal/mol.

At the calculation of energies of dissociation bonds in the nitrocompounds the enthalpies of formation of the radicals take from work [4].

The values of the dissociaton energy of the bond and corresponding to it EEI nitrogroups in nitroderivatives methane and ethane are brought in the Table 3.

Table 3.

The dissotiation energies of the bonds and the efficient energy of interaction NO_2-groups in rows methane-tetranitromethane and ethane-hexanitroethane

NITRODERIVATIVES METHANE					
Compound	Nitro-ethane	1,2-Dinitro-ethane	1,1-Dinitro-ethane	1,1,1-Trinitro-ethane	
EEI	0	8.5	23.4	37.2	
$D(C - NO_2)$	60.8	52.2	45.1	42.2	
NITRODERIVATIVES ETHANE					
Compound	Nitro-ethane	1,2-Dinitro-ethane	1,1-Dinitro-ethane	1,1,1-Trinitro-ethane	Hexanitro-ethane
EEI	0	5.6	7.7	23.3	79.8
$D(C - NO_2)$	58.3	-	50.5	42.7	35.8
$D(C - C)$	94.7	93.8	99.3	98.3	73.8

From the Table 3 is seen that increasing an amount nitrogroups in the compound brings about the growing of the value EEI. Herewith reduction of the energy of dissociation of C – NO_2 bond is observed. The energy of dissociation of C – C bond in the ethane equals 90.3 kcal/mol, that noticeably lower, than in mono-, di- and trinitroderivatives ethane. Thereby, introduction nitrogroups in the molecule ethane brings about strengthening C – C bond, however, value of energy of this strengthening depends as well as from the place of joining nitrogroup. In 1,2-dinitroethane value of this energy on 5.5 kcal/mol lower, than in 1,1- dinitroethane, that is stipulate by 1-2 the interactions of the nitrogroups. In hexanitroethane 1-2 interactions of the nitrogroups (sum total 9) brings about significant reducingvalue of C – C bond in contrast with ethane – on 16.5 kcal/mol.

The efficient energies of interaction nitrogroups in nitroderivatives methane and ethane bring about reducing the energy of dissociation C – NO_2 bond with increasing the amount nitrogroups. Influence of amount and places of joining nitrogroups can bring both to increase, and reducingthe value of the dissociation energy C – C bond in nitroderivatives ethane.

This research was supported by the Russian Fondation of Fundamental Investigations (Grant № 00-03-32196a).

REFERENCES

1. Lebedev V.P., Miroshnichenko E.A., Matyushin Y.N. et al. *Jurn. Phiz. Chim.* **49,** 1928, 1975.
2. Matyushin Yu. N., Vorobev A. B., Konkova T. S. et al. *Pat USSR* 726442, **1980** (in Russian).
3 J. D. Cox, G. Pilcher, *Thermochemistry of organic and organometallic compounds*, Acad. Press, L.- N.Y., **1970**, 643 p.
4. Gurvich L.V., Karachevcev G.V., Kondratjev V.N. et al. *The Energies of Chemical Bonds. Ionization Potentials and Affinity to Electron.* Moscow, Nauka, **1974**, 351 p, (in Russian).

Synthesis and characterization of azido plasticizer

Detlef Drees, Dieter Löffel, Angelika Messmer, Konrad Schmid

Fraunhofer Institut für Chemische Technologie
D-76327 Pfinztal-Berghausen (Germany)

Synthese und Charakterisierung von Azidoweichmachern

Summary

In order to get a good compatibility with azidopolymers plasticizers are required with a similar chemical structure. The energetic plasticizers EGBAA, DEGBAA, TMNTA and PETKAA were synthesized and characterized. They are liquid and the glass transition temperatures are between –70.8 and –34.1°C. The differential scanning calorimetry (DSC) analysis shows an acceptable thermal stability for practical applications.
The infrared spectrum shows distinctly the functional groups C-N_3, ester, carbonyl and nitrate. The elemental analysis and NMR agree with the molecular structures. As a practical example, EGBAA was combined with the energetic binder PolyNimmo. The viscosity, glass transition point and stability of 50% mixtures were investigated.

Um eine gute Verträglichkeit mit Azido Polymeren zu erhalten, sind Weichmacher mit einer ähnlichen chemischen Struktur erforderlich. Die energetischen Weichmacher EGBAA, DEGBAA, TMNTA und PETKAA wurden synthetisiert und charakterisiert. Sie sind flüssig und die Glasübergangspunkte liegen zwischen –70,8 und –31,4°C. Die DSC Analyse zeigt eine akzeptable thermische Stabilität für praktische Anwendungen.
Das Infrarot Spektrum zeigt deutlich die funktionellen Gruppen C-N_3, Ester, Carbonyl und Nitrat. Die Elementaranalyse und die NMR-Daten stimmen mit den Molekülstrukturen überein. Als ein praktisches Beispiel wurde EGBAA mit dem energetischen Binder PolyNimmo kombiniert. Die Viskosität, Glasübergangspunkt und die Stabilität einer 1:1 Mischung wurden untersucht.

1 Introduction

In the field of energetic binders the investigation of azidopolymers began at the beginning of the 80th. However, until now the mechanical properties of azidopolymers are problematic, but could be solved by the development of suitable plasticizers. In order to get good compatibility with the azidopolymers, plasticizers are desired having azido groups as similar structural elements. Besides a good compatibility, the azido plasticizers would have the advantage of delivering extra energy on combustion combined with minimum smoke. During their exothermic decomposition they exclusively give smokeless burning products with a high amount of nitrogen.

The requirements above triggered the development of azido plasticizers also to be used in binders other than azidopolymers. In this study the synthesis and characteristics of some representative azido plasticizers are presented. The plasticizers in this investigation have the follow general formula:

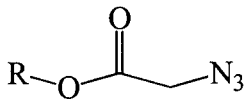

As a further important requirement, the azidoplasticizers should substitute known nitrateester plasticizers, e.g. TMETN and BTTN:

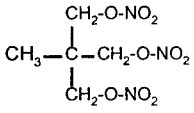

TMETN

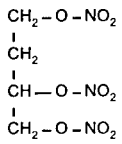

BTTN

Compared to nitrateesters the azido plasticizers are more stable and are compatible with binders like GAP or PolyNimmo. Besides the low viscosity the plasticizer promise a good workability.

In this investigation the new energetic plasticizers in Figure 1 EGBAA, DEGBAA, TMNTA and PETKAA are described and, as an application, the 1:1 mixture of EGBAA and PolyNimmo characterized.

EGBAA 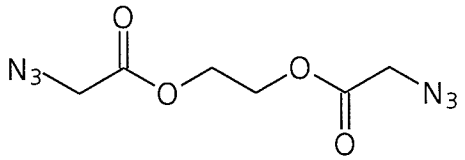 Azido-acetic-acid-2-(2′-azido-acetoxy)-ethylester	**DEGBAA** 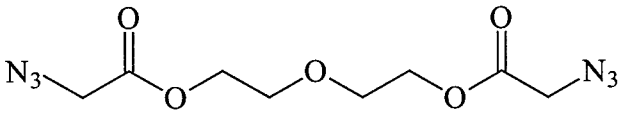 Azido-acetic-acid-2-[2′-(2″-azido-acetoxy)-ethoxy]-ethylester
TMNTA 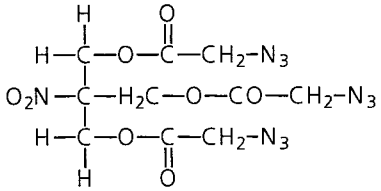 Azido-acetic-acid-3-(2′-azido-acetoxy)-2-(2′-azido-acetoxymethyl)-2-nitro-propylester	**PETKAA** 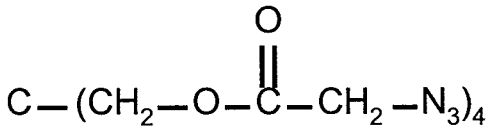 Azido-acetic-acid-3-(2′-azido-acetoxy)-2,2-bis-(2′-azido-acetoxymethyl)-propylester

Figure 1. Structure formula and chemical names of the azido plasticizers

2 Synthesis

EGBAA is taken as an example to describe the synthesis of the 4 plasticizers. The starting material is Glycol which reacts with two molecules of chloroacetic acid. From this reaction chloroaceticacid-2-(2-chloro-acetoxy)-ethylester is obtained which reacts with sodiumazide to the desired product.

All reactions follow this general scheme:

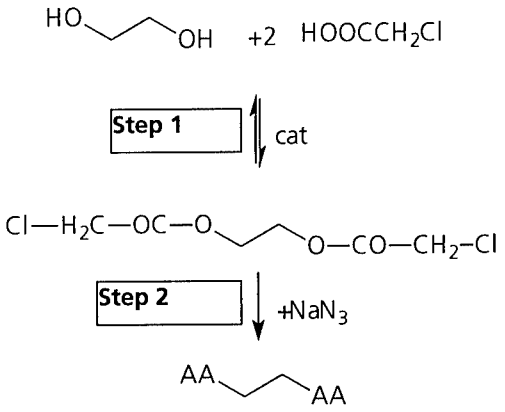

AA = —O—CO—CH_2–N_3

Table 1a and 1b show the reaction conditions used. The first reaction step was carried out in toluene. The water, which is formed by the reaction is removed by hetero-azeotrope-distillation. The intermediate has a yield between 80-100%. The second step, the reaction with sodiumazide, were carried out in the solvents DMSO and 2% water. On these conditions the reaction to TMNTA has a reaction time of 72 h and the yield is about 50%.

Table 1a. Reaction of Alkohol with Chlor-acetic-acid

Edukt	Solvent	Time of Reaction [h]	Temperature [°C]	Yield [%]
ETHYLENGLYCOL	Toluene	5	Reflux[1]	80
DIETHYLENGLYCOL	Toluene	10	Reflux[1]	100
TRIMETHYLOLNITROMETHANE	Toluene	8	Reflux[1]	80
PENTAERYTHRITE	Toluene	6	Reflux[1]	97

1 hetero-azeotrope-distillation

Table 1b. Reaction of the intermediate with sodiumazide

Product	Solvent	Time of reaction [h]	Temperature [°C]	Yield [%]
EGBAA	DMSO, 2% Water	24	40	70
DEGBAA	DMSO, 2% Water	24	40	85
TMNTA	DMSO, 2% Water	72	40	50
PETKAA	DMSO, 2% Water	24	40	75 bis 95

3 Identification of the plasticizer

Table 2 lists relevant physical and thermal properties.

Table 2. Physical Properties

Compound	Density [25°C/ g*cm^{-3}]	O_2-balance [%]	Heat of Combustion [kJ/mol]	Enthalpy of Formation [kJ/mol]
EGBAA	1.34	-84.15	3344.3	-167.36
DEGBAA	1.00	-99.92	4540.5	-328.86
DEGN	**1.385**	**-40.79**	**2297.4**	**-426.8**
TMNTA	1.45	-71.95	5435.0	-230.54
PETKAA	1.39	-88.82	7202.0	-215.20

	Viscosity (20°C) [mPa*s]	Viscosity (25°C) [mPa*s]
EGBAA	23.4	19.3
DEGBAA	29.2	-
DEGN		
TMNTA	1288	749
PETKAA	2880	1612

DEGBAA has a similar structure when compared to the nitrateester plasticizer DEGN:

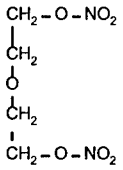

The results in Table 2 show that the nitrateester plasticizer have a better oxygen balance (–40.8%) with respect to the azidoplasticizer and the enthalpie of formation is more negative (EGBAA= -328.9 kj/mol; DEGN = -426.8 kj/mol). Among the azidoplasticizer synthezised EGBAA has the highest enthalpie of formation and the lowest glass-transition-point.

Table 3. Thermal Properties

Compound	DSC (Onset) [°C]	TG (Dpeak)[°C]	Glass-Transition-Temperature (Midpoint)[°C]
EGBAA	206.4	218.0	-70.8
DEGBAA	215.0	212.0	-63.3
TMNTA	217.2	207.7	-34.1
PETKAA	221.5	212.0	-35.4

Table 3 summarizes the thermal properties of the samples synthezised. They are thermally very stable and the glass-transition points are low, the lowest point being –70.8°C. The DSC and TG values demonstrate that the azido plastizicers can be applied up to 150°C.

Table 4. Stability properties

Compound	Deflagration point [°C] (5K/min)	Weight loss [%] (90°C, ca. 80 Days)	Dutch-Test [%] (110°C, 72h)
EGBAA	232	0.9	0.26
DEGBAA	235	0.48	0.14
TMNTA	214	0.25	0.24
PETKAA	234	-	0.57

Compound	Impact sensitivity [Nm]	Friction sensitivity [N]
EGBAA	5.5	165
DEGBAA	>10	160
TMNTA	16	192
PETKAA	60	360

The stability and sensitivity values in Table 4 determined by dutch-test, impact- and friction sensitivity show that the azido plasticizers are very stable. For example, the weight loss values are < 2%.

Table 5. Elemental Analysis, Infrared spectra and NMR-Spectra

Substance	**C [%]**	**H [%]**	**N [%]**
EGBAA	**31.38**	**3.46**	**36.87**
Calculated	31.58	3.51	36.84
DEGBAA	**34.6**	**4.36**	**30.85**
Calculated	35.29	4.41	30.88
TMNTA	**29.82**	**2.97**	**34.66**
Calculated	30.0	3.0	35.0
PETKAA	**33.4**	**3.57**	**34.29**
Calculated	33.33	3.42	35.90

The elemental analysis shows a good agreement between the calculated values and the measured values in Table 5. The nitrogen contents are between 30-36%. The components were identified by IR- and NMR-spectroscopy. The IR spectra are compared in Figure 2.

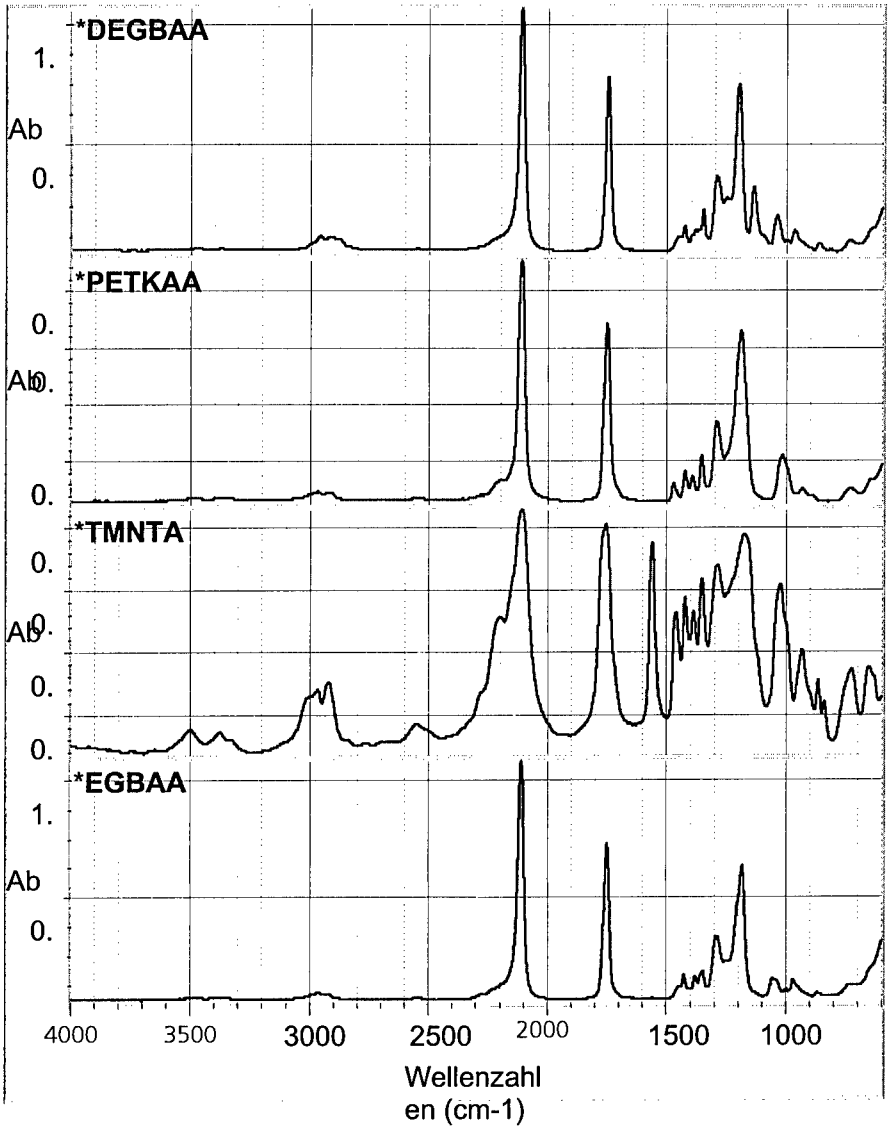

Figure 2. IR-Spectra of the azido plasticizers

The characteristic peaks of the functional groups are located at 2110 cm^{-1} (azido), 1750 cm^{-1} (ester), 1180 cm^{-1} (C=O) and 1580 cm^{-1} (nitro).

The ^{1}H-NMR- spectrum in Figure 3-6 shows the typical resonances expected for the different CH_2-groups.

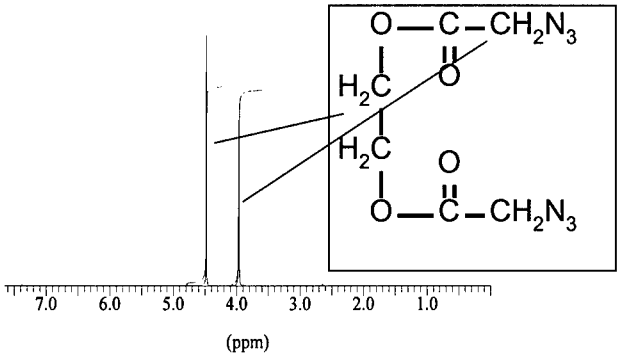

Figure 3. EGBAA (^{1}H)

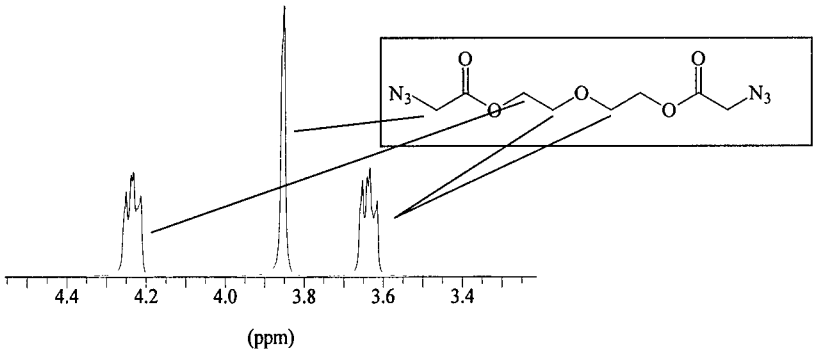

Figure 4. DEGBAA (^{1}H)

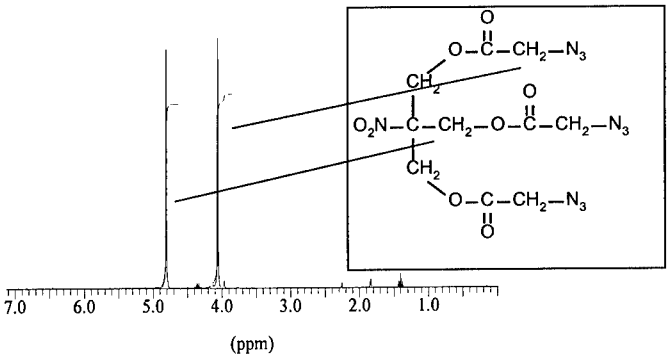

Figure 5. TMNTA (^{1}H)

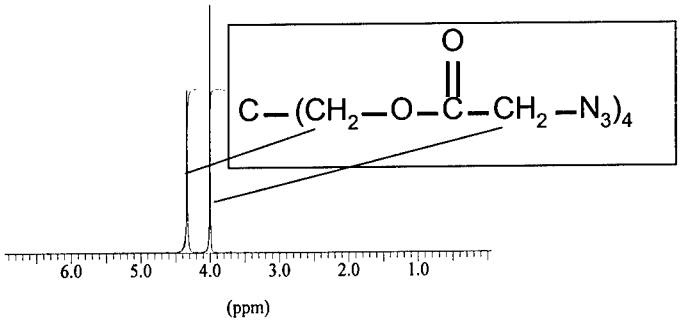

Figure 6. PETKAA (^{1}H)

Whereas EGBAA, TMNTA, PETKAA exhibit two singlet peaks, DEGBAA in contrast shows peaks consisting of two triplet and one singlet according to the different structure. The fact that no other peaks are observed in the NMR spectra confirms the purity of the samples.

Applications

Table 6 summarizes the results on tests on the mixture EGBAA/ PolyNimmo in the ratio 50:50. The results are compared with those obtained for the nitrate esters TMETN and BTTN.

Table 6. Stability at 50% Contents of plasticizer

	Dutch-Test (105°C, 72 h) ≤ 2%	**Deflagration-Temperature (20°C/min)**
100% PolyNimmo	0.45%	193°C
TMETN	1.50%	188°C
EGBAA	0.60%	201.5°C

As a result, EGBAA is more stable than TMETN represented by the dutch test weight loss of 0.6% versus 1.5%. In addition, the deflagration temperature measured at 201.5°C is higher than that of the nitrate ester mixture causing a better cook-off behaviour.

Table 7. Glass-Transition-point of PN with 50% plasticizer

	100% PN	TMETN	BTTN	EGBAA
DSC (10°C/min) MidPoint [°C]	-15.1	-45.2	-52.6	-66.7

Table 8. Viscosity of PolyNimmo with 50% plasticizer

	100% PN	TMETN	BTTN	EGBAA
Viskosity (Pa*s)	234.80	5.12	2.253	0.399

Table 7 compares the glass transition points of the mixtures. That for the EGBAA mixture is at -66.7°C and is lowest with respect to those of the nitrate esters demonstrating the good plasticizing ability. Furthermore, EGBAA reduces significantly the viscosity (Table 8) of PolyNimmo making processing much easier enabling higher filler loading.

Conclusions

Four different new azido plasticizers were synthezised and characterized by elemental analysis, IR and NMR. The new compounds have a high chemical and thermal stability. In a test mixture with PolyNimmo the azidoplasticizer EGBAA shows promising results with respect to compatibility, stability and processibility.

Enlightning discussions with Thomas Keicher are gratefully acknowledged.

Glycidyl Azide Polymer Plasticizer - DSC and Rheological Results

Tony Manzara and Rob Hunter
3M Performance Materials
St. Paul, MN 55144-1000 USA

Abstract: Plasticizers are commonly used in polymeric binder systems for energetic materials to improve processing results, and to improve low-temperature mechanical properties. Glycidyl Azide Polymer Plasticizer (GAP-0700) has been shown to lower the glass transition temperature of several useful polymers. It also decreases their viscosity at elevated temperatures suitable for processing energetic materials.

Introduction: GAP Plasticizer has been used to increase the energy, increase the burning rate, and improve the processing of polymers used as binders in energetic formulations. (1,2,3) At the last ICT Annual Meeting, we reported on compatability studies of GAP-0700 with numerous polymers, as well as thermal stability of the blends via Thermogravimetric Analysis. (4) We have continued that study by selecting ten thermoplastics which could serve as polymeric binders, and determining the effect of the GAP-0700 on their glass transition temperatures and their mechanical behavior. Eight of the polymers gave useful blends. 3M's GAP-0700 has average molecular weight of about 700, viscosity near 100 centipoise at 25 °C, density of 1.23 g/cc, heat of formation estimated at +330 calories/gram, molecular formula $C_3H_5N_3O$, and is virtually free of hydroxyl groups.

Experimental: Tests were done on high molecular weight thermoplastic polymers by making a solution of the high polymer and GAP Plasticizer at a ratio of one part by weight polymer and one part by weight GAP in ethyl acetate (plasticizer to polymer ratio Pl/Po was 1:1). This solution was dried to a film.

The films were observed by Differential Scanning Calorimetry in the temperature range of -100 to + 140 °C. The material was cooled to -70 °C, then heated at the rate of 20 °C per minute to 140 °C, cooled at the rate of 40 °C per minute to -70 °C, and heated again to 140 °C at 20 °C per minute. This procedure will relax any crystallization induced by solvent casting the films. The viscosity of each plasticized polymer was determined on a Rheometric Scientific SR-5 Universal Stress Rheometer at 75 and 100 °C, using pressed films 1 mm thick and 25 mm diameter, an oscillatory frequency of 1 Hz, and a stress level of 1000 dynes/cm^2. The viscosities (Eta*) in the table are reported in Kilopoise. Results: The results are shown in the table.

Discussion: It is clear from the data that GAP-0700 Plasticizer markedly lowers the glass transition temperature (Tg) of all of the tested polymers. The effect is enough to allow flexibility throughout the expected range of environmentally encountered conditions. The polymer viscosities are also reduced, and will allow processing via pressing or via extrusion, depending on the amount of binder in the formulaton. The Cellulose Acetate Butyrate blend had a higher viscosity at the higher temperature, while the Estane* 5713 thermoplastic polyurethane blend had high viscosity at 75 °C and low viscosity at 100 °C, a desireable

Glass Transition Temperatures and Viscosities of High Molecular Weight Polymers Blended 1/1 with GAP-0700

Polymer Type	Source	Catalog# (*=tm)	Kp, 75°C	Kp, 100°C	Tg 1/1GAP	Tg Unplasticized
Acrylic Ester	Zeon	Nipol* AR 53L	73	50	-50 °C	-39 °C
Acrylic ester	Zeon	Hytemp* 4454	76	57	-63 °C	-38 °C
Cellulose Acetate Butyrate	Eastman	CAB- 381-20	213	300	-53 °C	141 °C
Nitrocellulose	Hercules	Aqualon* 2000			-46 °C	120 °C
Poly(butyl methacrylate)	Aldrich	18,152-8	14	2	-63 °C	15 °C
Poly(ethyl methacrylate)	Aldrich	18,208-7	233	195	-47 °C	63 °C
Poly(methyl methacrylate)	Aldrich	18,223-0	301	81	-38 °C	114 °C
Thermoplastic polyurethane	BF Goodrich	Estane 5713P	402	87	-60 °C (a)	-43 °C
Ethylene-vinyl acetate	Bayer	Levapren* 400	lost plasticizer (b)		-65 °C	-28 °C
Hydroxypropyl cellulose	Aldrich	43,500-7	lost plasticizer (b)		1.5 °C	57 °C

notes: (a) also exhibits a transition at 113 °C (b) these films were hazy and the plasticizer separated at 75 °C from the polymer

To contact the authors: rwhunter@mmm.com (+1-651-458-2254)

or apmanzara@mmm.com (+1-651-458-1392).

References

1. US Patent 5,507,891 Zeigler to Alliant Techsystems
2. US Patent 5,616,883 Hamilton and Baglini to OEA, Inc.
3. US Patent 4,288,262 Flanagan and Gray to Rockwell International
4. Rob Hunter and Tony Manzara, Interaction of GAP Plasticizer with Other Polymers, ICT Proceedings, 1999

TITLE:

DETERMINATION OF ABSOLUTE MOLECULAR WEIGHT OF GLYCIDYL AZIDE POLYMER (GAP) BY MULTI-ANGLE, LASER LIGHT SCATTERING DETECTOR IN-LINE WITH SIZE EXCLUSION CHROMATOGRAPHY (MALLS / SEC).

AUTHORS: *V. DESTOMBES – G. LACROIX*

SNPE Propulsion- CRB BP N'2
F-91710 VERT LE PETIT (France)

ABSTRACT:

GAP production is usually controlled by size exclusion chromatography (SEC). This technique does not give absolute data and needs molecular weight calibration. Evolution of parameters of SEC analysis, as column aging, involved significant deviation of molecular weight measurements, and thus sometimes gives erroneous results.
The recent development of absolute molecular weight detector, multi-angle laser light scattering detector (MALLS detector), in-line with a size exclusion chromatograph, allowed us to study a new method to determine absolute molecular weight of GAP.

In this paper, we describe this new method and we detail:
- comparative results between classical method of molecular weight determination by SEC/PPG calibration and the new one by SEC/MALLSD
- comparative results of functionality calculation with absolute molecular weight and functionality determination by experimental method (gel point method).

KEYWORDS: GAP, light scattering, MALLS, steric exclusion chromatography, SEC, functionality.

Topic of the study

GAP production is usually controlled by size exclusion chromatography (SEC). The basic objective of SEC is to break a polymer-sample into its size fractions. In a "traditional SEC mode", column calibration is followed by converting size separation into equivalent mass distribution. From these, one may calculate the number and weight average molecular weights of a sample, $\overline{Mn}$ and $\overline{Mw}$.

$$\overline{Mn} = \frac{\Sigma hi}{\Sigma\left(\frac{hi}{mi}\right)} \quad \text{and} \quad \overline{M_W} = \frac{\Sigma hi \times mi}{\Sigma hi}$$

where :
- (hi) is the height (concentration) of fraction fi, on the mass calibration curve
- (mi) is the mass of fraction fi, on the mass calibration curve

Each column must be calibrated in reference to a set of mass-standards. Evolution of parameters of SEC analysis as column aging, can be observed. This evolution involves deviation of molecular weight measurements and thus, sometimes, give erroneous results.
The recent development of absolute molecular weight detector, multi-angle laser light scattering detector (MALLS detector), in line with a size exclusion chromatograph has allowed to develop a new method to determine absolute molecular weight of polymer as GAP.

1 – DESCRIPTION OF GAP

The chemical structure of Glycidyl Azide Polymer is :

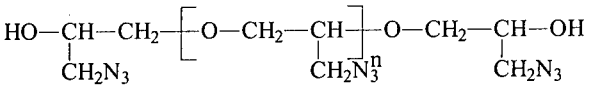

2 – MALLS MEASUREMENT PRINCIPLE

The MALLS technique allowed the deduction of absolute molecular weights directly without the need of calibration standards and independently from molecular structure effects. The incident light is scattered by macromolecule in a direction determined by a given angle θ°, versus the direction of the incident ray.

The relationship linking the intensity of the scattered light, the scattering angle and the molecular properties is simply

$$\Delta R(\theta°) = \frac{K.C}{\frac{1}{Mwi} + 2A_2.C}$$

Where :

* $\Delta R(\theta°)$:($R_{macromolecule.solution} - R_{solvent}$) : is the intensity of the scattered light at angle $\theta°$.

* C : is the sample concentration

* Mwi : is the molecular weight of the size fraction fi

* A_2 : is the second Virial coefficient .It characterizes polymer/solvent interactions; it is often ignored because of its low value.

* K is an optical parameter relative to

$$n^2 \times \left(\frac{dn}{dc}\right)^2$$

where : - n is the refractive index of the sample

- $\left(\frac{dn}{dc}\right)$ is the refractive index increment between solution and solvent

These 2 parameters greatly influence the response coefficient (power 2 in the MALLS relationship).

Then, number and weight average molecular weights of the polymer sample, $\overline{Mn}$ and $\overline{Mw}$, are obtained by traditional SEC relationship (cf. topic of the study),

$$\overline{Mn} = \frac{\Sigma hi}{\Sigma\left(\frac{hi}{Mwi}\right)} \text{ and } \overline{Mw} = \frac{\Sigma hi.Mwi}{\Sigma hi}$$

2.1. – <u>Interest of MALLS / SEC compared to the traditional SEC Mode</u>

1 – Absolute molecular weight deducted from light scattering measurement is independent of analysis parameters like column aging.

2 - MALLS detector gives an important scattering response in high size molecule area (at the beginning of chromatogram peak) where the traditional SEC detector (Refractive Index detector) is not sensitive: this characteristic is important for the functionality characterization.

2.2. – <u>Parameters affecting response of MALLS detector</u>

1 - The first one is the refractive index increment $\frac{dn}{dc}$. The table n° 1 shows us the decreasing MALLS response when $\frac{dn}{dc}$ falls down. This parameter is found in literature or is obtained experimentally.

Table n° 1 : $\frac{dn}{dc}$ *vs MALLS response percent*

$\frac{dn}{dc}$	*% response MALLS vs Ref (PS)*
0.185 (PS*)	100 (Ref.)
0.13	50
0.10	< 30
0.09 (GAP)	30 < % R. GAP < 20
0.08	# 20
0.06	# 10

(*) = Polystyrene standard

2 - The second one is the scattering angle. Table n° 2 shows us the variation of MALLS response with scattering angle. Figure n° 2 represents MALLS chromatograms of GAP at the three angles 45°, 90° and 135°

Table n° 2 : *angles θ° vs MALLS response (signal / noise ratio)*

θ°	*MALLS response (S/N : arbitrary units)*	*(- %) / Réf.*
90	9.5	Ref.
135	4.5	- 50
45	2.8	- 70

We have chosen to work only on 90° data because of the best signal over noise ratio of the 90° chromatogram compared to the two others.

3 – DESCRIPTION OF INSTRUMENTATION AND EXPERIMENTAL CONDITION OF ANALYSIS

3.1. – Analytical instrumentation

Figure n° 3 presents a schematic arrangement of laboratory SEC system, incorporating a mini DAWN MALLS unit.

- the on-line degasser is a ERMA INC, ERC 3000 model. It's useful to eliminate noise arising from solvent bubbles ,
- the pump and the injector are put together into the SEC system, Waters 150 C,
- four PL Gel SEC columns are used : L = 30 cm, particles diameter = 5 µm and porosity is 10^5, 10^4, 100 and 50 Å,
- refractive index detector, model Waters 410 is placed in series with the mini-Dawn (following it),

- MALLS detector is the mini DAWN unit from Wyatt Technology. The 3 angles outputs are transmitted to an analog to digital converter. The RI signal is transmitted alternatively with LS signal to the computer converter.

3.2. – Experimental condition of analysis

The eluent used is an HPLC quality tetrahydrofurane (THF), degassed and filtered before crossing the MALLS cell.
- flow rate = 0.9 ml/min
- solvent, injector and columns temperature is 30°C
- injected volume is 250 µl
- GAP concentration is 4.5 mg/ml
- PS standard concentration is 1mg/ml for $PS_{(M=19600)}$ standard and 3 mg/ml for $PS_{(M3250)}$ standard. Those two PS standards are used to adjust :
  - RI et MALLS detectors shift
  - RI constant
  - MALLS constant

4 – MASS RESULTS

Figures n° 4,5 and 6 show the different graphic representation of RI and MALLS combined data of dihydroxyl GAP.

- **Figure n° 4** : presents molecular weight versus elution volume distribution of a dihydroxyl GAP sample. Refractive index chromatogram and MALLS (θ=90°) chromatogram of a dihydroxyl GAP, represented on this figure, illustrate the different response coefficient of this type of polymer.

- **Figure n° 5** : presents the differential molecular weight distribution of a dihydroxyl GAP (differential weight fraction, hi, vs molecular weight, Mwi)

- **Figure n°6** : presents the cumulative molecular weight distribution of a dihydroxyl GAP (cumulative weight fraction Wn-i (0 to 100 %) vs molecular weight, Mwi)

Five GAP samples have been analyzed by :

* the traditional SEC method in which columns are calibrated in reference to a set of polypropylene glycol standards (PPG) from mass 200 to mass 4000, in two different laboratories (the control laboratory and the Research center laboratory).

* the light scattering SEC method described in paragraph n° 2 and paragraph n° 3.

All the mass results obtained in the five GAP samples are collected in table n° 3.

Table n° 3 *: mass results of five GAP samples*

GAP N°SEC / METHODS	1		2		3		4		5	
	$\overline{Mn}$	$\overline{Mw}$	$\overline{Mn}$	$\overline{Mw}$	$\overline{Mn}$	$\overline{Mw}$	$\overline{Mn}$	$\overline{Mw}$	$\overline{Mn}$	$\overline{Mw}$
SEC (PPG) Production unit	1820	1990	1720	1880	-	-	1670	1810	1800	1940
SEC (PPG) Research Center	2020	2180	2020	2210	1950	2190	1990	2210	-	-
SEC (MALLS)	2370	2480	2480	2630	2460	2640	2580	2740	2470	2590

Table n° 4 shows the mass result average for the five GAP samples and mass deviation calculation between :

- the two SEC (PPG) methods, product unit and research center one,
- the two SEC methods, PPG and MALLS one.

Table n° 4 : *mass results average of the five GAP samples and mass deviation calculation between the different SEC methods.*

Mass results average and deviation / SEC methods	$(\overline{Mn})_{n=5} \pm \sigma(n-1)$	$(\overline{Mw})_{n=5} \pm \sigma(n-1)$
SEC (PPG) Prod. Unit (P.U.)	1752 ± 70 (dispersion = 4 %)	1905 + 78 (dispersion = 4 %)
SEC (PPG) Research Center (R.C.)	1995 ± 33 (dispersion = 1.6 %)	2197 ± 15 (dispersion = 0.7 %)
SEC (MALLS)	2478 ± 75 (dispersion = 3 %)	2616 ± (dispersion = 3.6 %)
SEC (PPG) [R.C. – P.U]	243 ± 10	292 ± 10
SEC (MALLS) –SEC (PPG) [R.C]	480 ± 14	419 ± 12

Each mass value corresponds to the average of three successive tests. We observe a mass deviation of 245 to 300, with a 4 % dispersion between production control results and research center results. This deviation is significative because it is superior to the standard deviation method, which is plus or minus 10 % of the result value (# 180 to 200, in GAP case). This mass deviation is caused by the different evolution of the 2 chromatographic systems (especially, column ageing) and can't be controlled.

The mass deviation observed in the same chromatographic system, between the two SEC methods (traditional and MALLS one): 420 to 480 with a 3 % dispersion, is explained by the fact that calibrated method involves chemical behavior differences between standards and samples, which don't exist in absolute method.
When MALLS molecular weight is known for a polymer family, it doesn't evolve, because the given mass result is independent from molecular structure effects.

Actual specification of SNPE standard diol-GAP molecular weight is

$$\boxed{\begin{array}{l}\overline{Mn} = 1700 \pm 300 \\ \overline{Mw} = 2000 \pm 300\end{array}}$$

based on SEC (PPG) analysis.

The use of SEC / MALLS as production control of GAP requires specification modifications.

MALLS molecular weight results obtained in the five GAP samples allow us to propose new specifications on number and weight average molecular weights of standard dihydroxyl GAP:

$$\boxed{\begin{array}{l}\text{Mn (MALLS)} = 2400 \pm 200 \\ \text{Mw (MALLS)} = 2600 \pm 200\end{array}}$$

5 – FUNCTIONALITY CHARACTERIZATION

5.1. – Measurement principle

There are two methods:

5.1.1. – Calculation method by multiplying number average molecular weight $\overline{\text{Mn}}$ by hydroxyle rate [OH], measured by chemical analysis.

$$\boxed{\text{F (OH)} = \overline{\text{Mn}} \text{ x } [\text{OH}] \text{eq/kg}}$$

5.1.2. – Experimental method, called gel point method, developed by Oberth*. Its principle is to visually detect a gel formation in a mixture of hydroxyled polymer and diisocyanate, with different $\frac{\text{NCO}}{\text{OH}}$ ratios.

The functionality is determined by the following relationship :

$$\boxed{F(OH) = \frac{2Fx}{Fx + \left(\frac{[trihydroxyl]}{[dihydroxyl]} * (Fx - 2) \right)}}$$

where Fx = $2 \left(\frac{\text{OH}}{\text{NCO}} \right)$, is the trihydroxyl agent functionality, determined by the same method of gel point detection with various NCO/OH ratios.

(*) A.E. Oberth, " Functionality determination of hydroxyl-terminated prepolymers", AIAA Journal, vol. 16, N° 9, p. 919-924, september 1978.

5.2. – Functionality results

Functionality of the five GAP samples has been determined by the two methods. Results are collected in table n° 6.

Table n° 6 *: functionality results of the five GAP samples*

GAP N°	[OH] RATE (eq/kg)	F (OH) (PPG / P.U)	F (OH) (PPG / R.C)	F (OH) (MALLS)	F (OH) (Gel.Pt)
1	0.770	1.4	1.55	1.82	1.92
2	0.780	1.34	1.57	1.93	1.90
3	0.823	-	1.6	2.03	1.94
4	0.775	1.3	1.54	2.00	1.94
5	0.780	1.4	-	1.93	1.90
				$M[F(OH)_{MALLS}]$ = 1.94 ± 0.08 % dispersion = 4%	$M[F(OH)_{gel\ Pt}]$ =1.92 ± 0.02 % dispersion = 1%

The comparison of functionality results obtained by calculation with $\overline{Mn}$(MALLS) and experimentally by Gel point method shows a high similarity, which is a real advancement in functionality characterization because Gel point method, the only known until now, as being an accurate method is a really long and tedious experimental method.

CONCLUSION

Molecular weight and functionality results obtained by SEC / MALLS in five dihydroxyl GAP samples show the exactitude of molecular weight value of this technique applied to hydroxyl GAP. The use of this technique allows us to propose new specifications for dihydroxyl GAP production control, independent from molecular structure effects.

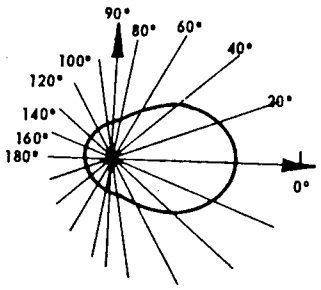

Figure n° 1 : scattering angle distribution curve of light scattered by macromolecule.

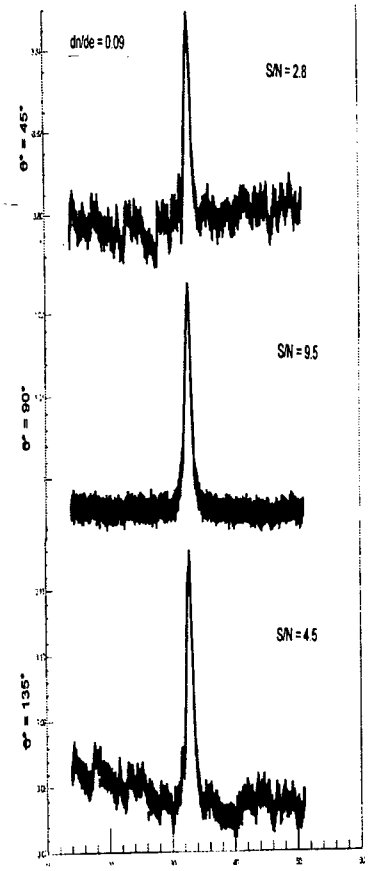

Figure n° 2 : MALLS chromatograph of dihydroxyl GAP

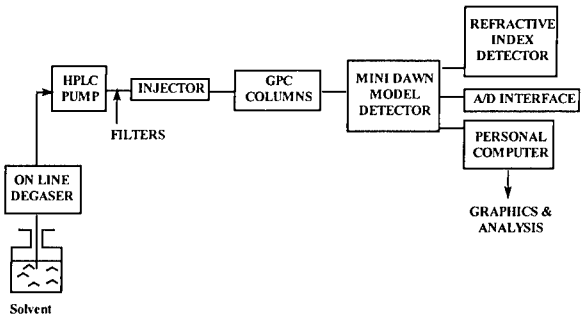

Figure n° 3 : SEC system configuration incorporating mini.DAWN MALLS

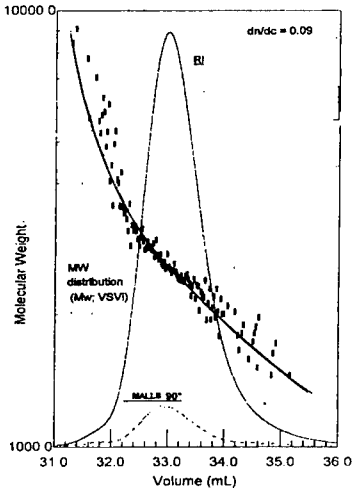

Figure n° 4 molecular weight versus elution volume distribution of a dihydroxyl GAP

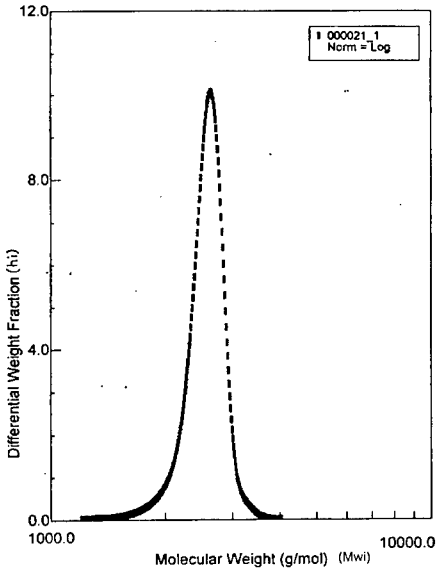

Figure n° 5 : molecular weight distribution of a dihydroxyl GAP

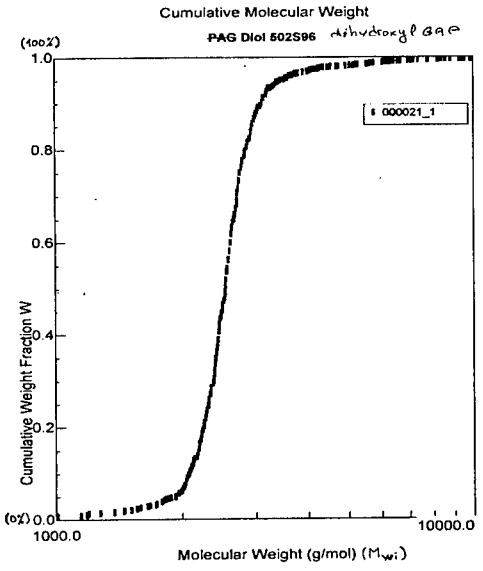

Figure n°6 : cumulative molecular weight distribution of a dihydroxyl GAP

THERMAL CHARACTERIZATION OF PROPELLANTS CONTAINING GAP AS BINDER

Tsao-Fa Yeh
Department of Applied Chemistry
Chung Cheng Institute of Technology
Tahsi, Taoyuan 33509, Taiwan, R.O.C.
tfyeh@ccit.edu.tw

Abstract:

The binder of propellants used in this study was Glycidyl azide polymer (GAP), Ammonium nitrate (AN), potassium/ammonium nitrate eutectic mixture (AK), ethylene diamine dinitrate (EDDN), EDDN/AK eutectic mixture (EAK), cyclo-1,3,5-trimethylene-2,4,6-trinitramine (RDX), and RDX/EAK eutectic mixture (REAK) were used as oxidizers of propellants.

Thermal decomposition of propellants were carried out by simultaneous Thermogravimetric Analysis-Differential Thermal Analysis (TGA/DTA) and Differential Scanning Calorimetry (DSC) with four heating rates and under nitrogen pouring with a flow rate 100 mL/min. The results of thermal decomposition of propellants were compared with GAP/AN propellant as standard. The compatibilities and kinetic parameters of propellants were also studied.

SIDE GAP THERMAL DECOMPOSITION REACTION

Vladimir G. Prokudin, Vladimir. V. Charskii, Anatoly I.Kuzaev,
Nikita V. Chukanov, Boris C. Fedorov, Gennady M. Nazin

Institute of Problems of Chemical Physics, Russian Academy of Sciences,
142432 Moscow region, Chernogolovka (Russia)
FAX: (096) 515 3588
E-mail: prokud@icp.ac.ru

Abstract

Glycidyl azide polymer (GAP) samples synthesized by polyepichlorhydrine (PECH) azidation were shown to have a side reaction in the early decomposition phase. At 80-115°C this reaction can be controlled due to heat emission and gas products (N_2) evolution. The gas evolution rate is 10-20 times greater than calculated value for the decomposition of pure GAP, and the conversion degree by N_2 yield doesn't exceed 0.1-0.5%. Also the side reaction is observed for purified and cross-linked samples. The most probable mechanism of side reaction is the decomposition of an unstable structural element of GAP polymer chain - $OCH{=}CHCH_2N_3$ type, formed in a small amount during PECH and then GAP producing.

Introduction

A great number of papers is devoted to the GAP thermal decomposition (see references in [1]). The data of different authors agree well, and the rate constant of the first order is described with a good accuracy by equation:

$$k = 10^{14.4} \cdot \exp(-39000/RT),\ c^{-1} \qquad (1)$$

In accordance with this equation the time of 0.1% decomposition at 110°C comprises 19.5 hours. This conversion degree corresponds to the evolution of 0.224 cm^3/g of N_2 (under normal conditions). In reality, as our preliminary tests

of several GAP samples showed, such gas evolution was achieved in3-6 hours. That is the evidence of the side reaction taking place in the early phases of decomposition process.

The literature data are also available pointing to a side process.Five GAP samples differing in synthesis conditions and molecular weight were investigated in paper [2]. The thermogravimetry technique (TG) was used. It has been shown that at 74°C for 24 hours weight loss is 0.37-1.94%, while at 100°C the side process proceeds with a slowing rate for at least 100 hours. Paper [3] informs that at 74°C the cross-linked GAP looses 1.13% of its weight.A more detail investigation of the early phase of GAP decomposition has been made in the work presented. Calorimetric and manometric methods were used instead of thermogravimetry which had to be adjusted for evaporation.

Experiment and Results

Four GAP samples $-[OCH_2CH(CH_2N_3)]_nOH$ (I-IV)
and PAG-3/15 sample $C_2H_5C\{CH_2[-OCH_2CH(CH_2N_3)]_nOH\}_3$ (V),
GAP sample (VI), cross-linked by toluylenediisocyanate (TDI) with glycerine assistance and sample (VII), purified by Al_2O_3 have been investigated. The data given below include: sample number, average molecular weight, synthesis temperature (°C), and the time of polyepichlorohydrine (PECH) azidation, (hours).

I: 500, 80, 64. II: 500, 105, 10.

III: 1000, 80, 70. IV: 2300, 115, 8.

V: 1630, 80, 50. VI: Sample IV, cross-linked.

VII: Sample IV, purified by Al_2O_3.

Fig. 1-4 show the kinetic curves of gas evolution and fig. 5 – heat generation during initial decomposition phases. One can see from the figures that all samples have the side decomposition reaction. By the data of gas chromatography nitrogen was the only side reaction product.

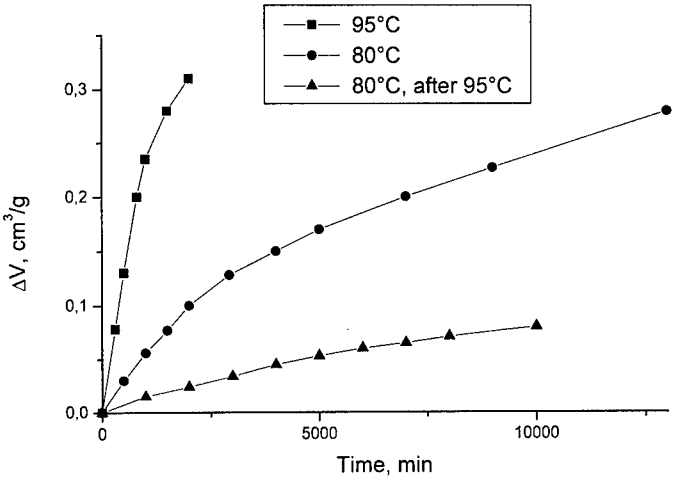

Fig. 1. The kinetic curves of gas evolution from GAP sample IV.

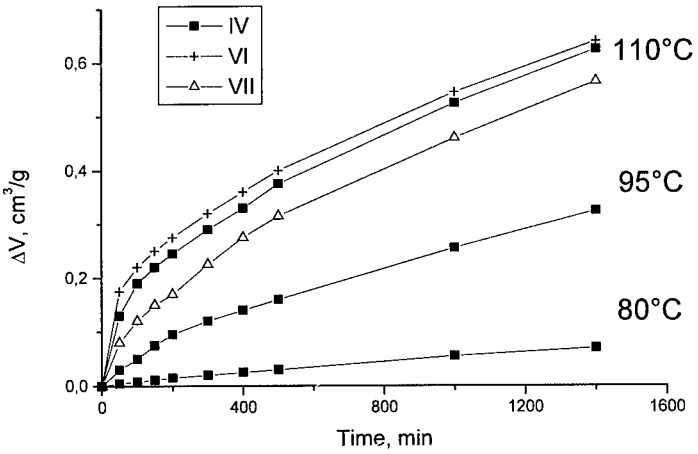

Fig. 2. The kinetic curves of gas evolution from GAP samples.

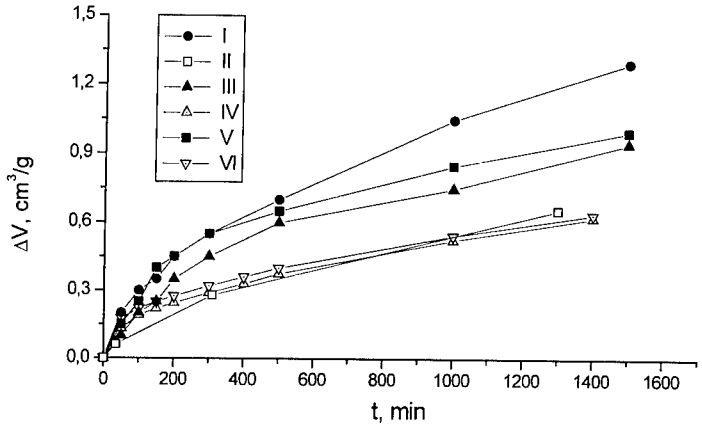

Fig. 3. The kinetic curves of gas evolution at 110°C from GAP samples.

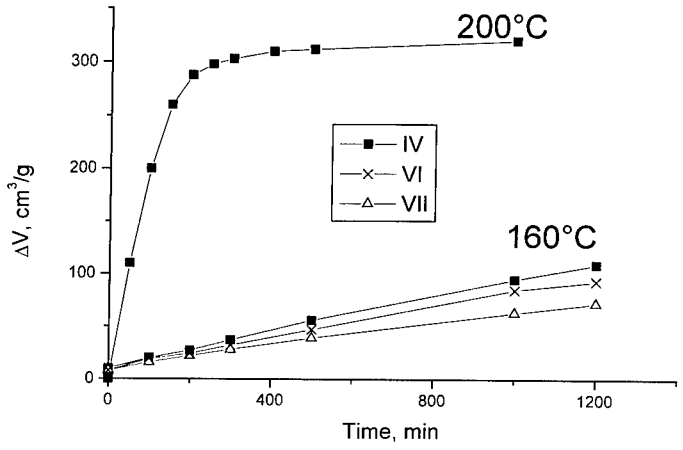

Fig. 4. The kinetic curves of gas evolution at 160°C and 200°C from GAP samples.

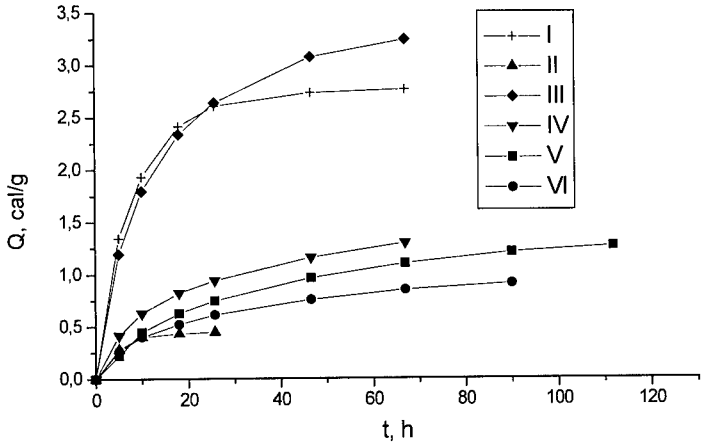

Fig. 5 The kinetic curves of heat generation from GAP samples at 105°C.

The conversion degree achieved as a result of this reaction varies from 0.1 to 0.5% or $(1\text{-}5)\cdot10^{-5}$ mol N_2 per 1 g of substance. The difference between samples is rather small, therefore it is hard to define whether GAP molecular mass or synthesis temperature or duration of azidation PECH during GAP producing affect the intensity of the side reaction. The detection of such dependences is interfered by a particularity that both GAP synthesis and side reaction of its decomposition proceed in the same temperature range., that is simultaneously. Thus, when PECH azidizing runs more intensive, the side product is decomposed in the greater degree.

At 110 °C the side reaction completed within 10 hours, then GAP monomolecular decomposition is observed. The period of half-transformation for side reaction is about 2 hours. The side reaction does not affect the rate of GAP decomposition at 110 °C or higher temperatures. For sample IV the time of 0.1 cm^3/g of gas products evolution ($\tau_{0.1}$) has been defined at the temperatures of 80-115°C. The following expression has been obtained:

$$\lg(\tau_{0.1})\ (\text{min}) = -20.3 + 8333/T \qquad (2)$$

At 60 and 80°C $\tau_{0.1}$ is equal to 35 and 1.5 days, respectively. These time periods are 20 times less than one would expect for the pure GAP monomolecular decomposition. Special experiments conducted have shown that admixtures of water and DMFA, as well as GAP purification in a column with Al_2O_3 do not affect the side reaction. It is also not affected by cross-linking with TDI and glycerine. Using the absolute value of $\tau_{0.1}$ it is possible to conclude that the side reaction does not restrict GAP practical usage significantly, includingsamples of VI type.

Special experiments conducted have shown that admixtures of water and DMFA, as well as GAP purification in a column with Al_2O_3 do not affect the side reaction. It is also not affected by cross-linking with TDI and glycerine (sample VII). Therefore, a conclusion can be made that side reaction is not an admixture decomposition, but it is a decomposition of unstable structural element of GAP polymer chain formed in the stage of GAP synthesis.

It is known [3] that aliphatic azidocompounds stability greatly varies at introduction double bond C=C (vinylazides) or C=O (benzoylazides) or trivalent nitrogen in an α-location for azide group. Very probably that ethereal atom O can influence as the atom N. Therefore we try to detect double bonds C=C and C=O was made in GAP samples.

Using IR spectroscopy in a thick layer (1 mm) we discovered for a sample IV a weak absorption band of carbonyl group, however it was not enough clear that we observed absorption for GAP but not for DMFA impurity. The double bonds C=C analysis by ozonization method was given the more certain results. We found, that all GAP samples have double bonds with concentration within $(1\text{-}5)\cdot10^{-5}$ mol/g, that is it corresponds to amount N_2, evolved as a result of side reaction. Also we found the same amount of double bonds in PECH samples, from which GAP samples were produced. For example, in sample IV amount of double bonds was equal $5\cdot10^{-5}$ mol/g and in parent PECH - $4.9\cdot10^{-5}$ mol/g. Thus

C=C double bonds are formed during PECH synthesis and then are conserved in GAP.

Typical kinetic parameters are E = 27.5 Kcal/mol и lgA = 14.5 (s^{-1}) [4] for thermal decomposition of vinylazides. The time of half-transformation vinylazides at 110 °C is equal 2 min, that is 60 times less, than for side reaction of GAP degradation. On the contrary the structures with double bonds C=O, C=N (and, apparently, C=C) in a β-location for azide group are too stable for side reaction. Their decomposition rates only are 3 times more, than for alkylazides [5]. The structure $-OCH=CHCH_2N_3$ have intermediate position and can appear as a probable source of side reaction.

It is quite clear how this fragment is produced during GAP synthesis. ECH cation polymerization runs using the catalyst - $Et_2O{\cdot}BF_3$. In this case oligomers with end-chain groups OBF_2 are formed in some small amount and its hydrolysis

$$-OCH_2CHOBF_2 + H_2O \text{ -----> } -OCH_2CHOH + HOBF_2$$

is followed by elimination

$$-OCH_2CHOBF_2 \text{ -----> } -OCH=CHOH + HOBF_2$$

The part and role of elimination reaction is increased when molecular weight oligomer is increased, because in viscous media diffusion of water to the reactionary centre is less effective. So it is possible to explain absence of the certain correlation between efficiency of side reaction and a number of end-chain groups (namely M_w) in GAP samples.

Conclusion

During GAP synthesis an unstable fragment (structural impurity) of a polymer chain containing C=C double bond is formed. GAP thermal decomposition for first reaction phases is degradation such fragments when from 0.1 up to 0.5 % N_2 contained in azide groups is evolved from different GAP samples.

Acknowledgments

The authors wish to thank prof. I. V. Tselinskii and dr. V. P. Sinditskii for synthesis some GAP samples.

The work has been performed under financial support of the Russian Foundation of Fundamental Research (Project No 99-03-33244).

References

1. H. Arisawa, and T. B. Brill, "Thermal Decomposition of Energetic Materials. 71: Structure-Decomposition and Kinetic Relationship in Flash Pyrolysis of Glycidyl Azide Polymer (GAP)",*Combustion and Flame*, 1998, Vol 112, Iss 04, pp. 533-544.
2. Li Changqing, Wang Ping, Huang Yue, at al. "Investigation of Glycidyl Azide Polymer " Proc of the 17th Int. Pyrotechnics Seminar Combined with the 20th Beijing Int. Symp. on Pyrotechnics and Explosives., October 23-31, 1991. Beiyng. China.Beiyng Inst. of Technology Press. 1991; Vol. 1, P. 451-459.
3. Zhang Xiaoyi, Cheng Xuening. "Investigation of Decomposition Kinetics and Reaction Mechanism of Organic Azide Polymer GAP" Proc of the 17th Int. Pyrotechnics Seminar Combined with the 20th Beijing Int. Symp. on Pyrotechnics and Explosives., October 23-31, 1991. Beiyng. China.Beiyng Inst. of Technology Press. 1991; Vol.1, p 542-546.
4. A. Hassner, N. H. Wiegand, and H. E. Gottlieb, "Kinetics of Thermolysis of Vinyl Azides. Empirical Rules for Formation of Azirines and Rearranged Nitriles", *J. Org. Chem.*, 1986, 51, 3176-3180.
5. G.B. Manelis, G.M. Nazin, Yu.A. Rubtzov, V.A. Strunin "*Termicheskoe razlozhenie i gorenie vzryvchatyh veshestv i porohov*" - M.: Nauka, 1996. -223 s.(In Russian)

Migration of Di-Nitro-Di-Aza-Aliphates in Glycidyl-Azide Polymer

M. Niehaus, St. Kelzenberg, G. Bunte
Fraunhofer Institut für Chemische Technologie (ICT)

Abstract

Softening agents like di-nitro-di-aza-aliphates significantly influence the mechanical properties of polymer binders. Hence, by adding softeners the ballistic performance of propellants may be adjustet properly. However, the diffusion of the substances during long-time storage may affect the shelf life of the propellant. Therefore the diffusion of a mixture of 2,4-di-nitro-di-aza-pentane, 2,4-din-nitro-di-aza-hexane and 3,5-di-nitro-di-aza-hexane (DNDA 57) in glycidyl-azide-polymer (GAP) was determined by using high performance liquid chromatography (HPLC). Experiments give evidence that DNDA 57 migrates in the matrix by means of a Case-II mechanism. The diffusion coefficients estimated range between 10^{-11} m²/s and 10^{-10} m²/s at temperatures ranging from -50 °C to 50 °C.

1 Introduction

It is well known in literature that deterrents as well as softeners influence the ballistic properties of propellants. For example the initial burning rate of propellants may be modified be treating the surface of the energetic material with substances like di-butyl-phthalate (DBP), di-octyl-phthalate (DOP) or camphor /1, 2, 3/. With respect to conventional nitrocellulose (NC) based energetic materials, propellants comprising NC as well as 2,4-di-nitro-di-aza-pentane (DNDA 5), 2,4-di-nitro-di-aza-hexane (DNDA 6) and 3,5-di-nitro-di-aza-hexane (DNDA 7) show a superior ballistic performance /4/. Recently it has been shown that also compositions of certain glycidyl-azide (GAP) binders with a mixture of DNDA 5, DNDA 6 and DNDA 7 (DNDA 57) and RDX have a high potential as propellants /5/.

The migration of DNDA 57 may affect severly the burning characteristics of the propellant and therefore requires determination of the diffusion coefficients. Assuming that the rate of transfer of diffusing substance through unit area is proportinal to the concentration gradient measured normal to the section for a long circular cylinder the diffusion equation becomes /6/:

$$\frac{\delta c}{\delta t} = \frac{1}{r} \cdot \frac{\delta}{\delta r}\left(r \cdot D \cdot \frac{\delta c}{\delta r}\right) \qquad \text{Equation 1}$$

where c is the concentration of the diffusing substance, r is the radius of the cylinder and D is the Diffusion coefficient. If in the cylinder of radius a the conditions are

$c = c_0$	$r = a$	$t \geq 0$
$c = c_1$	$0 < r < a$	$t = 0$

the solution may be approximated by /6/:

$$\frac{m_t}{m_\infty} = 1 - \frac{4}{b^2} \cdot \frac{J_0(0\,\alpha_1) - J_0(b\,\alpha_1)}{\alpha_1^2 \cdot (J_0(0\,\alpha_1 + J_0(b\,\alpha_1))} \cdot \exp(-D\,\alpha_1 t) \qquad \text{Equation 2}$$

where $m_{(t)}$ denotes the quantity of diffusing substance which has entered or left the cylinder in time t and m_∞ the corresponding quantity after infinite time. α_n is defined as:

$$\alpha_n = \sqrt{\left|J_0(r\,\alpha_n) Y_0(0\,\alpha_n) - J_0(0\,\alpha_n) Y_0(r\,\alpha_n)\right|}$$

with J_0 and Y_0 beeing Bessel functions of first and second order respectively.

2 Experimental

Bifunctional GAP (ICT) with an aquivalent weight of 1,22 g/mmol was cured 12 hours at 50 °C with hexamethylene-tri-isocyanate having an aquivalent weight of 0,195 g/mmol. The cylindrical samples having a diameter of 21 mm and a length of 10 mm were kept within a DNDA 57 solution up to 148 hours at –50 °C as well as 23 °C and 50 °C. After treating the samples with DNDA 57 the concentration of the softener in the polymer was determined using HPLC. In order to eliminate the influence of side effects only the middle of the sample was examined.

3 Results

Figure 1, 2 and Figure 3 show the relationship between fractional uptake and treating time at temperatures of –50 °C as well as 23 °C and 50 °C. The sorption of DNDA 57 is clearly non Fickian as the fractional uptake in the first 125 hours is a linear function of time /7/. Yet with increasing impregnation time a growing difference between the linear regression curve and the experimental occurs. In contrast to Fickian (case I) diffusion a case II mechanism is characterised by a very rapid migration of the diffusant compared with the relaxation process of the polymer structure.

In such systems a front which marks the boundary between swollen gel and glassy core advances with constant velocity. In a long cylinder the boundaries advance radial to the longitudinal axis and will consequently meet at the center. At this point a sharp break in slope of the fractional uptake/time curve yields.

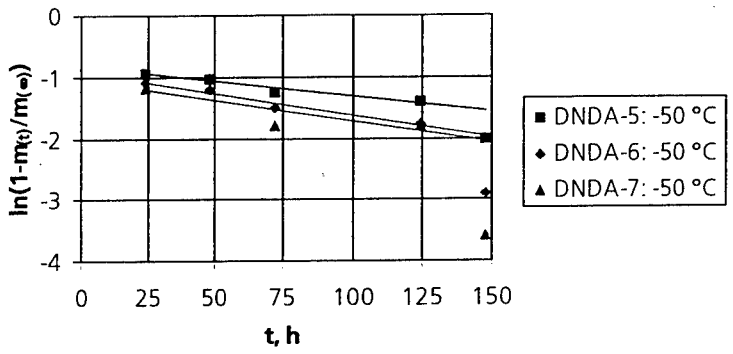

Figure 1: Sorption of DNDA 57 in GAP/N100 versus time at –50 °C

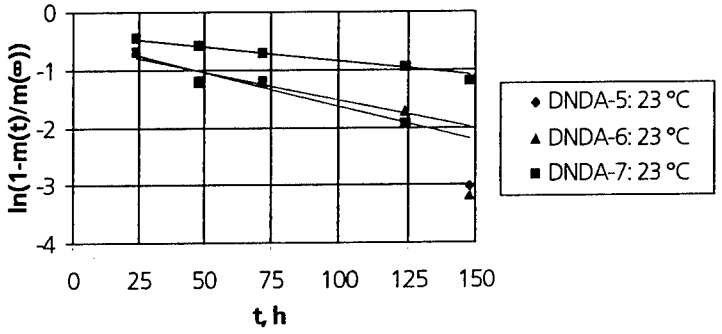

Figure 2: Sorption of DNDA 57 in GAP/N100 versus time at 23 °C

Therefore the observed relationship between fractional uptake of DNDA 57 and time is consistent with diffusion by case II mechanism. According to literature the time at which slope break occurs agrees well with the time for complete penetretion of the grain by the softening agent /7/. Hence, the penetration time for the GAP/DNDA 57 system is estimated to be in the order of magnitude of 125 hours.

In Figure 4 the relation between the swelling of the polymer and penetration time of DNDA 57 is given. Especially at 50 °C and 23 °C a large swelling of the sample with time occurs which at longer time intervalls results in cracking of the grain. This gives further evidence that DNDA 57 migrates by a case II diffusion mechanism.

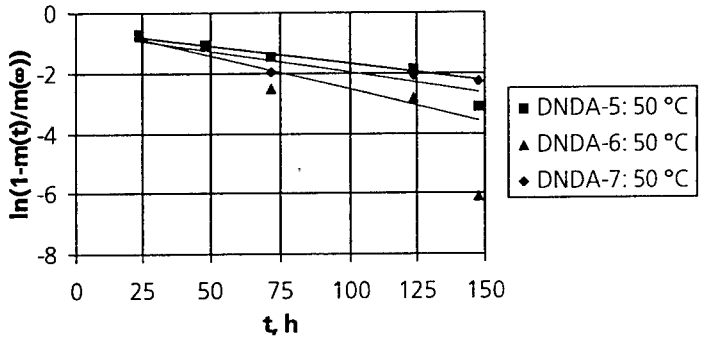

Figure 3: Sorption of DNDA 57 in GAP/N100 versus time at 50 °C

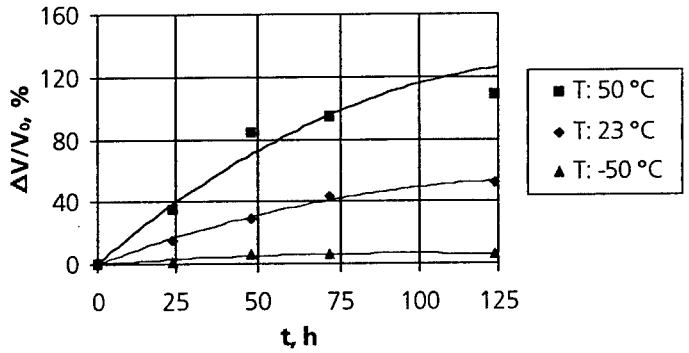

Figure 4: Increase in volume of GAP versus time

The effective diffusion coefficients of DNDA 5 as well as DNDA 6 and DNDA 7 may be estimated by applying equation 2. As the data clearly indicate (s. table 1), increasing temperature will increase the rate of DNDA 57 sorption. Also 3,5-di-nitro-di-aza-hexane migrates much slower than DNDA 5 and DNDA 6.

Table 1: Effective diffusion coefficients of DNDA 5, DNDA 6 and DNDA 7

	Diffusion coefficient, m^2/s		
T, °C	DNDA-5	DNDA-6	DNDA-7
-50	$9{,}43 \cdot 10^{-11}$	$1{,}66 \cdot 10^{-10}$	$7{,}08 \cdot 10^{-11}$
23	$1{,}84 \cdot 10^{-10}$	$2{,}22 \cdot 10^{-10}$	$1{,}55 \cdot 10^{-10}$
50	$2{,}33 \cdot 10^{-10}$	$3{,}02 \cdot 10^{-10}$	$1{,}45 \cdot 10^{-10}$

There are no other data in literature regarding the migration of diffusants in GAP. But in comparison to common NC/diffusant systems, having diffusion coefficients in the order of magnitude of 10^{-15} m^2/s /2, 8/ the diffusion coefficients for the migration of DNDA derivates in GAP are much larger. The large mobility of DNDA 57 in GAP may be attributed to the comparatively small volume of the molecules. Also it is likely that the mobility of DNDA 57 is increased by the large swelling of the GAP matrix.

4 Conclusion

Experiments suggest that the diffusion of DNDA 57, a mixture of mixture of 2,4-dinitro-di-aza-pentane, 2,4-din-nitro-di-aza-hexane and 3,5-di-nitro-di-aza-hexane, in glycidyl-azide-polymer (GAP) can be correlated with a moving boundary model (case II diffusion). For the system given the penetration time of DNDA 57 the penetration time can be estimated to be in the order of magnitude of 125 hours. The diffusion coefficients for the system range between 10^{-11} m^2/s and 10^{-10} m^2/s at temperatures ranging from -50 °C to 50 °C. The large mobility of DNDA 57 in GAP may be attributed to the small volume of the molecules. Also the experiments indicate that the mobility of DNDA 57 in the polymer might be increased by the large swelling of the GAP matrix.

5 Literature

1 E. J. Kirschke, S. K. Canova, W. L. O'Meara, Plasticizer Concentration Gradient as an Aid to Interior Ballistic Modelling of Ball Powder Propellant, JANNAF Propulsion Meeting, San Diego, USA 1987

2 B. Vogelsanger, B. Ossola, E. Brönnimann, The Diffusion of Detergents into Propellants Observed by FTIR Microspectroscopy - Quantification of the Diffusion Process, Propellants Explosives Pyrotechnics, 21, 330-336, 1996

3 K. Ryf, Antriebssysteme höchster Leistung für Rohrwaffenmunition, 19th Int. Ann. Conf. ICT, 4/1-4/18, Karlsruhe, 1988

4 D. Müller, M. Helfrich, Treibladungspulver für Rohrwaffen mit LOVA-Charakteristik bei verbesserten mechanischen Eigenschaften, ICT-Bericht 28, 1995

5 M. Niehaus, Experimentalpulver auf NC/GAP Basis, ICT-Symposium Explosivstoffe, Karlsruhe, 1999

6 J. Crank, The Mathematics of Diffusion, Oxford University Press, Second Edition, 1975

7 D. Winkler, A. Starks, The Non-Fickian Diffusion of Deterrents into a Nitrocellulose-Based Propellant, J. Applied Polymer Science, 35, 51-62, 1988

8 H. Meier, D. Bösche, G. Zeitler, E. Zimmerhackl, W. Hecker, Bestimmung von Konzentrationsprofilen oberflächenbehandelter Treibladungspulver mittels Radionuklidtechnik, Forschungsbericht aus der Wehrtechnik, 1983

Effects of Metal Powder with Different Particle Sizes on Thermal Decomposition Characteristics of Glycidyl Azide Polymer

ZHAO Feng-qi CHEN Pei Yang Dong* LI Shang-wen YIN Cui-mei

(Xi'an Modern Chemistry Research Institute, Xi'an 710065, Shaanxi, P.R. China)
(Nanjing University of Science and Technology, Nanjing 210094, Jiangsu, P.R. China)*

Abstract: The effects of nanometer metal powders(Cu□Ni)□superfine metal powders(Al□Ni) and normal metal powders(Cu□Al) on the thermal decomposition characteristics of glycidyl azide polymer (GAP) were investigated by DSC and DTG. The results showed that nanometer-Cu powder made the apparent activation energy and the peak temperature of the thermal decomposition of GAP decrease 35.6kJ/mol and 33.2□ respectively. The influence of nanometer-Cu on the thermal decomposition behavior of GAP was larger than normal metal Cu powder. The other metal powders had little influences on the thermal decomposition characteristics of GAP, whether their particle sizes were big or small. In the pressure of 0.1□2□6MPa, the decomposition behavior of GAP/nanometer-Cu mixture was different with that of GAP. In GAP/nanometer-Cu mixture, the influence of nanometer-Cu on the thermal decomposition behavior of GAP became weak with the decrease of nanometer-Cu content. The action mechanism of nanometer-Cu affecting the thermal decomposition process of GAP was analyzed.
Keywords: GAP, metal powders with different particle sizes, namometer-Cu, thermal decomposition

1 Introduction

Owing to some excellent properties, the research of GAP/AN composite propellants have become a hot spot [1-3], but GAP/AN propellants still have some shortages that do not adopt to the rocket motor.

Nanometer material that has some special properties can be used as a novel catalyst to improve the combustion characteristics. The applications of nanometer material in solid propellants have be reported recently [4-6], but there is no research in GAP/AN propellant. So the effects of metal powders with different particle sizes on the thermal decomposition of GAP are investigated, which contributes to provide some useful data for finding suitable burning rate catalyst from the point of views of thermal decomposition.

2 Experiments

2.1 Characterizing GAP and metal powders

GAP with molecular weight 3070 and hydroxyl value 6.54molKOH/g used in our experiment is a multipolymer of epichlorohydrin and amylene oxide (epichloroh-ydrin : amylen oxide=80 : 20), which was produced in our Institute.

The average particle size of metal powders was measured by JSM-5800 scanning electron microscope (SEM) made in Japan and LIMK-ISIS energy spectrometer (sharpness of separation is 3.5nm) made in English. The results showed in Table 1.

Table 1 Average diameter of metal powders used in our experiment

Nanometer-Cu powder	Nanometer-Ni powder	Superfine Ni powder	Superfine Al powder	Normal Cu powder	normal Al powder
90nm	80nm	1.1um	1.5um	3um	4um

2.2 Thermal analysis experiment

The thermal decomposition experiment was carried out by DSC190S made in American TA Company. The experiment condition was as follows: sample mass, less 2.00mg; heating rate, 10□/min; atmosphere , static nitrogen. The TG/DTG curve was obtained from TGA2950 thermogravimetric analyzer meter. The conditions of TG measurement were as follows: normal pressure, the flow rate of nitrogen, 50ml/min.

2.3 Photoelectron spectrum determination

The valence state of Cu powder in sample was determined by PHI5400 photoelectron spectrometer made in American PE Company.

3 Results and Discussion

3.1 The effects of different metal powders on the thermal decomposition of GAP

3.1.1 DSC results of sample containing different kind of metal powder

The thermal decomposition data of the samples are listed in Table 2. The DSC curves are showed in Fig 1. From Table 2 and Fig 1, the following observations may be made: (1) The shape of exothermic decomposition peak of GAP becomes sharp due to the effect of nanometer-Cu; while, the other metal powders have little effects on the peak shape of GAP. (2)Under the existence of nanometer-Cu and normal Cu, the decomposition peak temperature of GAP shifts 33.2□ and 12.9□ downwards respectively. However, other metal powders, whether their particle sizes were big or small, have little effect on it. (3) At the presence of nanometer-Cu and normal Cu, the onset temperature (T_e) of thermal decomposition of GAP shifts 22.5□ and 9.6□ downwards respectively, and the values of T_e shift 14.1□ and 10□ upwards respectively for adding the superfine and normal Al in GAP. But nanometer and normal Ni have no effect on it. (4) The values of ΔT decrease when Cu powders and Al powders exist. In the two kinds of metal powders, the effect of nanometer-Cu is more serious than that of normal Cu, the effect of superfine Al is more obvious than that of normal Al , too. But the effects of Ni powders on ΔT are little.

In a word, both the classification and the particle size of metal powders have effects on the thermal decomposition of GAP. The effects of nanometeer-Cu on the peak temperature, onset temperature andΔT of GAP are larger than that of normal Cu. For Ni powders, they have little effects on the thermal decomposition of GAP, whether their particle sizes are big or not. Al powders with different particle sizes have similar effects on GAP, both of them make the onset temperature of GAP shift to high temperature. From fig.1, it can be seen that nanometer-Cu narrows the peak width, increases the decomposition heat of GAP, enhances the decomposition rate of GAP. These facts show that nanometer-Cu can increase the burning rate of GAP propellants.

Table 2 The effects of different metal powders on the thermal decomposition of GAP

Samples	Decomposition Peak		ΔT^*/□
	T_p/□	T_e/□	
GAP	253.7	184.4	69.3
GAP/Cu(90nm)	220.5	161.9	58.6
GAP/Cu(3um)	240.8	174.8	66.0
GAP/Ni(80nm)	253.7	184.3	69.4
GAP/Ni(1.1um)	252.2	181.1	71.1
GAP/Al(150nm)	254.1	198.5	55.6
GAP/Al(4um)	253.6	194.4	59.2

* $\Delta T = T_p - T_e$

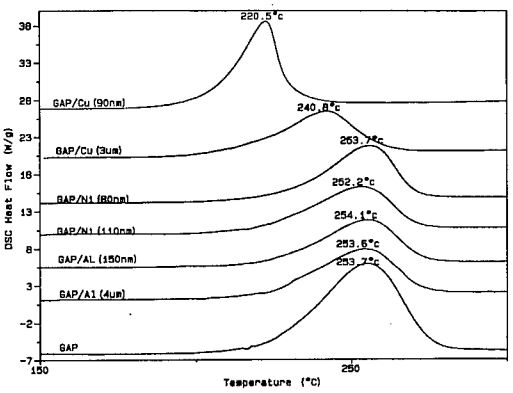

Fig.1 DSC curves of GAP and GAP/metal powders mixtures.

3.1.2 TGA results of sample containing different metal powder

The TG results of the samples containing different metal powder are showed in Table 3. At the stages of mass loss, comparing GAP, the TG onset temperature and DTG peak temperature of mixtures, GAP/nanometer-Cu and GAP/ normal Cu, shift to lower temperature. DTG peak temperature of GAP/nanometer-Cu shifts 30□ to low temperature, which coincides with DSC data of GAP/nanometer-Cu mixture. Comparing the mass loss of the samples of GAP/metal powder, it can be seen that, at the first and second mass loss stages, the mass loss of GAP are 39.3% and 57.8% respectively. Because it was impossible for lose mass of metal powders, the mass loss of all the samples only comes from the thermal decomposition of GAP. So the mass loss of GAP/metal powder mixture is due to the decomposition of GAP. In Table 3, at every a mass loss stage, the mass loss of GAP/metal powder are about 24% and 34% respectively, after they are converted to that of GAP, the value are 40% and 56.7% respectively, which approximates to the mass loss of GAP sample. The results indicates that metal powder do not change the decomposition process of GAP; nanometer-Cu only advances the temperature of the thermal decomposition of GAP.

Table 3 Data of GAP and 1.5/1.0 -GAP/metal powder mixture obtained by TGA

Samples	the first stage of decomposition			the second stage of decomposition		
	DTG	TG		DTG	TG	
	T_{p1}/□	T/□	mass loss/%	T_{p2}/□	T/□	mass loss/%
GAP	238.7	277.7	39.3	337.3	850.0	57.8
GAP/Cu(90nm)	207.7	249.2	24.0	281.6	850.0	34.6
GAP/Cu(3um)	229.1	268.5	23.0	321.4	850.0	35.3
GAP/Ni(80nm)	240.8	276.2	24.9	314.3	850.0	33.8
GAP/Ni(1.1um)	240.8	288.8	24.8	329.8	850.0	34.6
GAP/Al(150nm)	242.3	274.5	26.0	330.0	850.0	33.5
GAP/Al(4um)	242.2	279.0	24.8	330.2	850.0	33.7

3.2 The effects of Nanometer-Cu powder on the thermal decomposition of GAP

From above experiment results, it can been seen that nanometer-Cu was a every effective

catalyst, so some detail effects of nanometer-Cu on GAP were studied.

3.2.1 The effects of nanometer-Cu powder on the kinetic parameters of thermal decomposition of GAP

At 0.1MPa,DSC experiments are carried out at four heating rates of 5,10,20,and 30□/min. The DSC curves illustrated that, with heat rate increasing there is an upward shift in the temperature of the exothermic peaks and a increase in the values of ΔH.

The apparent activation energy in Table 4 is calculated by Kissinger method, where k is reaction rate constant, T is reaction temperature. The decomposition rate can be judged with the Arrhenius equation. The results show that, the apparent activation energy of thermal decomposition of GAP greatly decreases due to the effect of nanometer-Cu. As a result, the peak temperature of GAP in the sample of GAP/nanometer-Cu shifts downward and the peak shape become sharp.

Table 4 Kinetic parameters of thethermal decomposition of GAP and GAP/nanometer-Cu mixture at 0.1MPa

Sample	r	Ln(A/s^{-1})	Ea/kJ·mol^{-1}	Arrhenius equation
GAP	0.999	28.45	144.55	lnk=28.45-17386.9/T
GAP/nanometer-Cu	0.999	21.86	108.98	lnk=12.38-13108.5/T

3.2.2 The effects of nanometer-Cu on GAP in the condition of pressure

DSC curves of GAP and GAP/ nanometer-Cu mixture are showed in Figs 2 and 3 Comparing these curves, the following two different aspects can be seen: (1) With pressure increasing, the change of the peak shape of GAP is different. The peak shape of GAP/nanomeetr-Cu has nothing to do with pressure. But, the front peak of GAP is smooth at 0.1MPa, while, at 2MPa and 6MPa, which appears steps in wider temperature range. It is known that pressure increasing hinders the reactions producing gas from going on. Because the initial decomposition of GAP begins from the break of nitrine bond and produces NO_2, the high pressure holds up the decomposition of GAP and makes the induction period become long. These factors result that the steps appeared on DSC curve of GAP. (2) With pressure increasing, the peak temperature of GAP gradually shifts downward; that of GAP/nanometer-Cu also shifts downward from 0.1MPa to 2MPa, however, when pressure increased again, the peak temperature of GAP/nanometer-Cu mixture has no change basically.

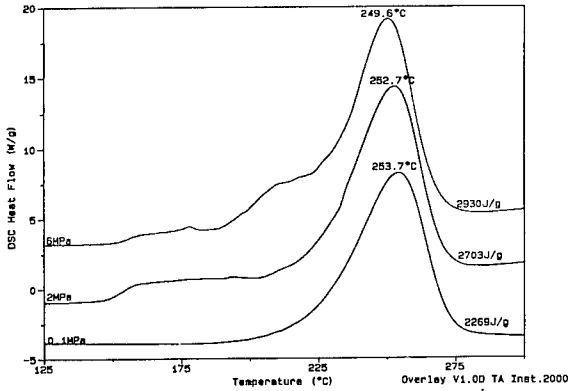

Fig. 2 DSC curves of GAP at different pressures

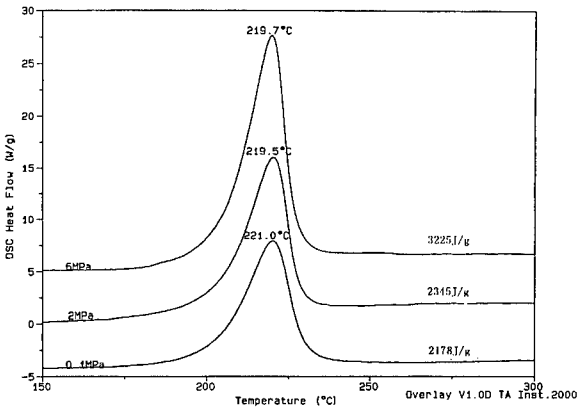

Fig. 3 DSC curves of GAP/nanometer-Cu mixture at different pressures

3.2.3 Effects of the content of nanometer-Cu on the thermal decomposition of GAP

Table 5 Results of GAP and different ratio-GAP/ nanometer-Cu mixture obtained by DSC

Sample	Decomposition Peak		ΔT^*/□
	T_p/□	T_e/□	
GAP	253.7	184.4	69.3
1.5/1GAP/Cu	220.5	161.9	58.6
5/1GAP/Cu	222.6	163.7	58.9
15/1GAP/Cu	234.6	165.3	69.3
20/1GAP/Cu	237.1	166.5	70.6

* $\Delta T = T_p - T_e$

From Table 5, it can be seen that with decreasing of the content of nanometer-Cu, the peak temperature□onset temperature and ΔT of GAP/nanometer-Cu mixtures gradually shift upward. The decomposition rate of GAP is getting slow. When the ration of GAP to nanometer-Cu changes from 5□1 to 15□1, the peak temperature and ΔT of GAP decomposition have a sudden change. However, the leap of peak temperature is only 2-3□ from 1.5□1 to 5□1 and from 15□1 to 20□1, the leap scope of ΔT were only 0.3-3□,too. This shows that the content of nanometer-Cu was not linear relationship with the effect degree of nanometer-Cu on the decomposition peak temperature of GAP.

3.2.4 The mechanism of nanometer Cu on the thermal decomposition of GAP

It is possible to assume that the apparent activation energy of GAP is decreased by the complex forming between GAP and nanometer-Cu. Based on the experiment results, it is holed that the complex forming in GAP liquid. The reasons are as follows:

(1) If the interaction between nanometer-Cu and GAP takes on in GAP liquid phase, TG temperature of GAP/nanometer-Cu mixture will be lower than that of GAP. The data in Table 2 are so indeed. That shows that nanometer-Cu interacts with GAP in liquid phase. Besides, from DTG peak temperature in Table 3, it also can be seen that the interaction between GAP and nanometer-Cu is in the initial stage of decomposition, which made DTG peak temperature

of GAP in the first stage shift downwards, correspondingly, that of the second stage also does so.

(2) GAP is a kind of viscous liquid, which easily sticks on metal powder. When the GAP/nanometer-Cu mixture is heated, the simply physical absorption will change to the complicated chemical one. It is to say, the activated complex is formed between the molecule or atom of GAP and the active center on metal powder surface, which can decrease the activation energy of GAP to promote the decomposition of GAP. It is reported that, N_2, C≡O,RC≡N and RN≡C have a special tendency to from transition metal complex by single end group or double end groups, only in less case, the position of two end groups is closed or formed the complex with two transition metal atoms (2Ni) by double lateral groups[7].According to the view, it is deduced that the complex is formed between the triazo group in GAP molecule and copper atom by single end group, and the coordinate bond (Cu-N(1)≡N(2)-N(3)-R) is formed between copper atom and nitron atom, which weakens the bond between N(2) and N(3) and makes it break easily. As a result, the decomposition of GAP is accelerated, correspondingly, the peak temperature shifts downwards, too. Although copper atom and nickel atom have the similar electron configuration, both N (1) and N (2) participate in forming the complex with two nickel atoms by double lateral groups. The sketch map is N(1)=N(2)-N-R.

↓ ↓
Ni Ni

It is known that the space occupied by -R chain is much bigger than triazo groups in GAP molecule. -R chain hinders triazo from combining nickel atom due to sterilely hindered effect, nickel does not accelerate the decomposition of GAP. Aluminum is not transition metal and can not form the complex with GAP, therefor, Aluminum does not promote the decomposition of GAP, too. Comparing with normal Cu, nanometer-Cu has much larger specific area and more active site. The coordinate bond is much more easily formed between nanometer-Cu atom and triazo group of GAP molecule, so the catalysis effect of nanometer-Cu is more significant than that of normal Cu.

4 Conclusions

(1) Among these metal powders, the effects of Cu powders on the thermal decomposition of GAP is the greatest, furthermore, the effect of nanometer-Cu powder is much larger than that of normal one, and nanometer-Cu makes the peak temperature and onset temperature of GAP shifts 33.2□□22.5□ downwards respectively and narrows the peak width. But , for over three respects, the value of normal Cu are 12.9 □□9.6 □ and 3.3□ respectively. The other metal powders have little effect on GAP.

(2) With pressure increasing, the change of the peak temperature and the shape of GAP and GAP/nanometer-Cu mixture are different.

(3)With nanometer-Cu content decreasing, both the decomposition peak temperature and the onset temperature of GAP/nanometer-Cu mixture shift downwards, and the peak width (ΔT) becomes wide. But the content of nanometer copper is not liner relationship with the effect degree of nanometer Cu on the peak temperature of GAP decomposition.

(4) The complex forming between nanometer copper and liquid GAP molecule decreases the activation energy of the decomposition GAP, and results in the decomposition GAP at lower temperature. The complex can not be formed between nickel or aluminum and GAP, so they have little effects on the thermal decomposition of GAP.

References

1. Akira IWAMA. et al. GAP/AN/AP/Al-Mg propellants for low pollution and waste cost and their application to 70mm motor. 23rd Int Annu Conf of ICT, 26/1-26/14(1992)
2. Yoshio Oyumi. et al. Insensitive munitions(IM) and combustion characteristics of GAP/AN propellants. Propellants, Explosives, Pyrotechnics,21, 271-275(1996)
3. Tokui.H. et al. Synthesis and physical-chemical properties of GAP and the application of GAP/AN based propellants to a small motor. 21st Int Annu Conf of ICT, 7/1-7/14(1990)
4. Li Quan,Zeng Guangfu, Xi Shiquan. Nanometer-sized particles. HUANXUE TONGBAO. 1995(6)□29
5. Lian Shunhua. The Effect of Superfine Grain Oxidant on Improvement of Burning Performance of Solid Propellants. Journal of Propulsion Technology. 1992(3)□72
6. Tian Deyu,Zhu Hui, Chen Li. Effect of Copper- Containg Catalysts on Combustion Characteristics of RDX/HTPB Composite Propellants. Journal of Propulsion Technology. 1995(6)□72
7. K.Jones et al. J. Amer. Chem. Soc. 98,74(1976)

EFFECT OF GAMMA RADIATION ON THE ENERGETIC POLYMER POLYNIMMO

S C Waring, E Kronfli J Akhavan & M E Colclough*

Department of Environmental and Ordnance Systems
Cranfield University
Royal Military College of Science
Shrivenham, Swindon, SN6 8LA, UK

Defence Evaluation & Research Agency*
Fort Halstead
Sevenoaks, Kent, TN14 7BP, UK

ABSTRACT

Energetic binders used in propellants such as the prepolymer polyNIMMO [poly(3,-nitratomethyl-3-methyl oxetane)] contains labile groups, such as a nitrate ester and an ether linkage. Nitrate esters are known to degrade naturally with time, a process which is accelerated by heat and/or light. When used in explosives and propellants it is important to be able to predict a binder's limitations and service life.

The effect of gamma radiation on the prepolymer polyNIMMO was investigated. PolyNIMMO was irradiated in air and in an inert atmosphere at various dose rates, up to a total dose of 100 kGy. These samples were analysed by Gas Chromatography /Mass Spectroscopy (GC-MS) to look at permanent gases, as well as Infra-Red spectroscopy (IR), carbon 13 Nuclear Magnetic Resonance (NMR), Ultra Violet and visible spectroscopy (UV-vis), Electron Spin Resonance (ESR) and Gel Permeation Chromatography (GPC), in order to characterise the effect of radiation on polyNIMMO. The results from ESR showed that radicals were being formed which, was also confirmed by using a radical trap, diphenyl picryl hydrazyl (DPPH). Short-lived radicals were difficult to identify but a structure was suggested for the long-lived radicals. The results from GPC showed a cyclic variation in molecular weights and intrinsic viscosities at specific radiation doses, suggesting chain scission and chain coupling was taking place.

At doses above 100 kGy IR revealed a shoulder developing at 1729 cm^{-1} attributed to a carbonyl group, which increased in intensity with an increase in radiation dose. For radiation doses around 750 kGy a second peak appeared at 1550 cm^{-1}, which was attributed to a nitro group stretch. These peaks increased in intensity with increasing radiation dose.

Keywords
energetic polymers, polyNIMMO, gamma radiation, polymer bonded explosives, degradation

Stability analysis of propellants containing new stabilisers

– Part I –

Stephan Wilker[•], Jan Petržílek[□], Jan Skládal[□], Gabriele Pantel[•], Lutz Stottmeister[•]

[•] Wehrwissenschaftliches Institut für Werk-, Explosiv- und Betriebsstoffe, Großes Cent, D-53913 Swisttal, Germany

[□] AliaChem a.s., Div. Synthesia, Research Institute for Industrial Chemistry, CZ-532 17 Pardubice-Semtín, Czech Republic

Abstract

This work – which is the first part of a series of publications – deals with the influence of different stabilisers on the decomposition behaviour of DB propellants. By systematically varying stabiliser types and concentrations and by using and combining different analytical methods an overview on the reactivity and reactions of different types of stabilisers and their decomposition products was obtained. For example, an increase in DPA or C I content leads to a decrease of propellant stability. In case of 2-NO_2-DPA the opposite effect could be observed.

The main reactions that stabilisers show are capture of radicals and nitration reactions. But they can be overwhelmed by direct interactions between the stabiliser and the nitrate esters, namely nitroglycerin. In this „mixture" of reactions the stability and reactivity of the individual radicals is of big importance. „Reactive" stabilisers like DPA are used up fast. As long as they are present in the propellant they can prevent autocatalytic decomposition reactions and save the chain scission of the nitrocellulose which is important for good ballistic properties. If the DPA is used up its daughter products (mainly N-NO-species) take over the stabilising activity. To study this some samples only stabilised with N-NO compounds are manufactured and studied.

Zusammenfassung

In dieser Arbeit – die den Beginn einer Serie von Veröffentlichungen darstellt – wird der Einfluss verschiedener Stabilisatoren auf die Zersetzung von zweibasigen TLP studiert. Durch systematische Variation der Stabilisatortypen und –gehalte sowie die Anwendung und Kombination zahlreicher Untersuchungsmethoden wurde eine Übersicht über die Wirkungsweisen der unterschiedlichen Stabilisatoren und ihrer Abbauprodukte erhalten. So konnte gezeigt werden, dass eine Erhöhung des Stabilisatorgehalts (DPA, C I) zu einer Destabilisierung des TLP führt. Bei 2-NO_2-DPA ist der gegenteilige Effekt der Fall.

Die Hauptwirkungsweisen der Stabilisatoren (Abfangen von Radikalen, Nitrierung) können durch Wechselwirkungen zwischen dem Stabilisator und dem Nitratester (Nitroglycerin) überlagert werden. Dabei kommt der Stabilität der beteiligten Radikale und ihrer Reaktivität eine große Rolle für die Geschwindigkeit der jeweiligen Reaktionen eine große Rolle zu. „Reaktive" Stabilisatoren, wie das DPA werden schnell verbraucht, und können – so lange sie im TLP enthalten sind – autokatalytische Zersetzungsreaktionen und das Abbrandverhalten von TLP beeinflussende Kettenabbaureaktionen der Nitrocellulose wirksam verhindern. Ist das DPA verbraucht, so müssen die Abbauprodukte des DPA (vornehmlich N-NO-Spezies) die Funktion des Stabilisators zu übernehmen. Zu diesem Zweck wurden einige nur mit N-NO-Verbindungen stabilisierte TLP hergestellt und untersucht.

1. Introduction

The influence of the structure and the amount of the stabiliser used in gun propellants on the ageing behaviour is of great interest. In many countries the service life of propellants is checked by stabiliser consumption. But a close correlation between stabiliser reactions both with nitric oxides as well as with the nitrate esters is missed. In this paper (which is the first part of a series of publications) the ageing behaviour of double base propellants with different mostly common stabilisers is investigated. The forthcoming publications will focus on propellants stabilised with substituted DPAs to show in detail the influence of substitution patterns on weight loss, heat flow calorimetry and stabiliser depletion. To reach this aim a series of about 50 different experimental propellants stabilised with DPA derivatives or urea derivatives has been manufactured by Synthesia. All of the propellants derive from the same nitrocellulose batch. That eliminates the influence of different nc qualities on the decomposition behaviour and gives clearer insight into the reactions of the stabiliser and the interactions between stabiliser and the nitrate esters.

2. Experimental

Sample list

Table I shows the samples that were produced by AliaChem/Synthesia and are discussed in this article

Sample Nr.	Stabiliser	amount [%]
319	DPA	0.38
225	DPA	0.55
282	DPA	2.55
305	N-NO-DPA	0.43
301	N-NO-DPA	0.87
306	N-NO-DPA	2.11
226	2-NO_2-DPA	0.73
187	2-NO_2-DPA	2.64
D073	2,4-DNO_2-DPA	0.66

Sample Nr.	Stabiliser	amount [%]
304	3-NO_2-DPA	0.49
293	3-NO_2-DPA	1.11
229	Akardite II	0.86
230	Akardite II	2.87
224	Centralite I	0.84
160	Centralite I	2.61
309	Centralite I	5.95
253	N-NO-N-EA [a)]	0.76
130	No stabiliser	0.00

a) N-Nitroso-N-ethylaniline

Two further samples (307 and 308) were also manufactured. They were stabilised with N-NO-2-NDPA and N-NO-4-NDPA, respectively. These two stabilisers decomposed in parts during manufacturing into the corresponding mono-nitro DPAs.

All samples contain about 14 % nitroglycerin. Samples 224, 225, 226, 229, 230 and 253 additionally contain 0.9 % 2,4-DNT. In addition some of the DPA, N-NO-DPA and 2-NO_2-DPA stabilised samples contain traces of further decomposition products.

For the investigation by classical high temperature tests further samples were manufactured. They contain up to 10 % of DPA, 2-NO_2-DPA, Centralite I or Akardite II.

Microcalorimetric measurements were conducted with a Thermal Activity monitor („TAM“) from Thermometric AB, Sweden. The measurements were exclusively performed in completely filled and sealed 3-ml-ampoules. The sample amount was around 3 g. Measuring

temperatures were 89 °C and 70 °C. Usually the measurements were carried out until endothermic gas evolution peaks occur.

HPLC analyses were performed using a Gynkotek HPLC system under following conditions: Column: Lichrospher 100 RP 18, 5 µm, 250/20/4 mm, solvent: MeOH/H_2O 67:33 (unless otherwise stated), flow rate: 1.2 ml·min^{-1}, Temperature: 25°C.

Different types of high temperature tests were performed:

The determination of the chemical stability of single and double base propellants by means of vacuum stability test (VST) was conducted according to ref.[1]. The method is based on heating the sample under a lowered pressure at 115 °C for 5 hours (double base propellant) or at 125 °C for 4.5 hours (single base propellant). In this time decomposition of the propellant and gas evolution occurs. Measurements were performed in automatic equipment of "STABIL" type.

Determinations of chemical stability of single and double base smokeless powders by means of methylviolet test were conducted according to MIL-STD-286B[2]. Bergmann-Junk test at 132 (BJ132) or 120 °C (BJ120) was conducted according to ref.[3]. The measure of chemical stability was the quantity of nitric oxide released from 5 g sample. Determination of chemical stability at 100 °C (HT100) was conducted according to ref.[3] and the measure of chemical stability was the time interval up to occurrence of brown fumes above the conditioned sample. Chemical stability by weight loss test at 89 °C with single base powders was conducted according to ref.[3], the principle being based on gravimetric determination of time interval up to the beginning of progressive decomposition of the propellant.

3. Microcalorimetric Results

3.1 DPA and N-NO-DPA stabilised propellants

Figure 1 shows heat flow curves of DPA and 2-NO_2-DPA stabilised propellants.

Sample 225 shows a very typical „DPA stabilised propellant" heat flow curve[4] with a first maximum, a sharp change of the slope followed by a broad first minimum. Afterwards an increase into the second maximum that is reached after 4.4 days can be observed. After about 8.8 days the pressure-built-up in the ampoule was too high, so endothermic gas evolution peaks appeared. Up to this point 82 J.g^{-1} were released. In detail the shape of the curve differs from that of the DB propellants of the K 6210 type. So, for example, the first minimum of sample 225 shows a slow increase of the heat generation whereas K 6210 remains more or less constant. Also the shape of the second maximum is different. In the case of sample 225 (and 282) a clear change of the slope after 3.0 days (value 100 µW.g^{-1}) is observed. This change of slope is absent in K 6210. In general the heat flow values are much smaller in sample 225 than in K 6210 with a comparable DPA and nitroglycerin content.

Very comparable to K 6210 is the fact that an additional stabiliser content leads to higher heat flows[5]. But a faster disappearance of DPA (meaning a later second maximum) could not be observed, although the increase of DPA from 0.7 to 3 % does not shift the second maximum by a factor of four. **Sample 282** has the highest average heat production of all samples containing „usual" stabilisers (12.2 J.g^{-1}.day^{-1}).

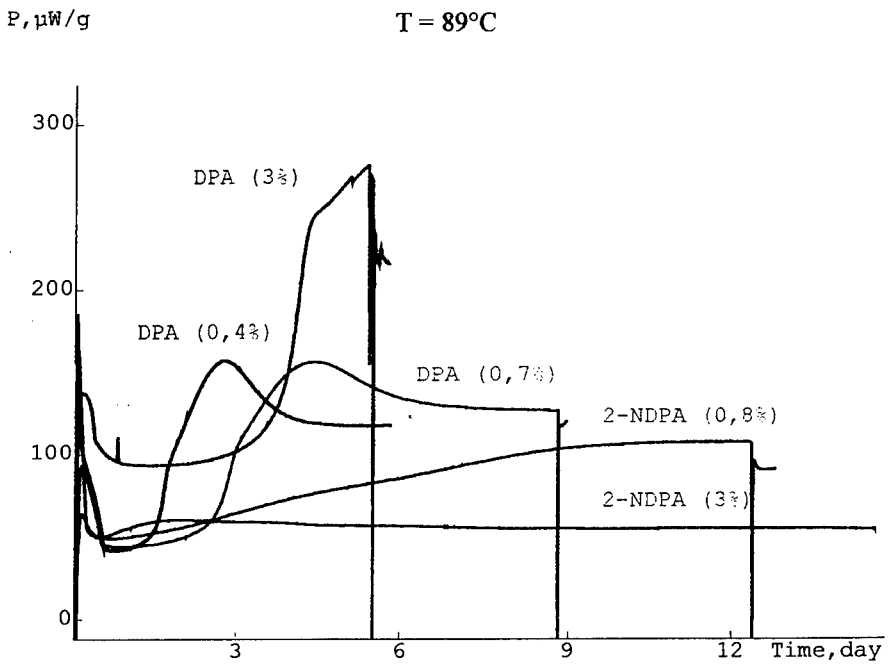

Figure 1 HFC curves of DPA and 2-NO_2-DPA stabilised propellants

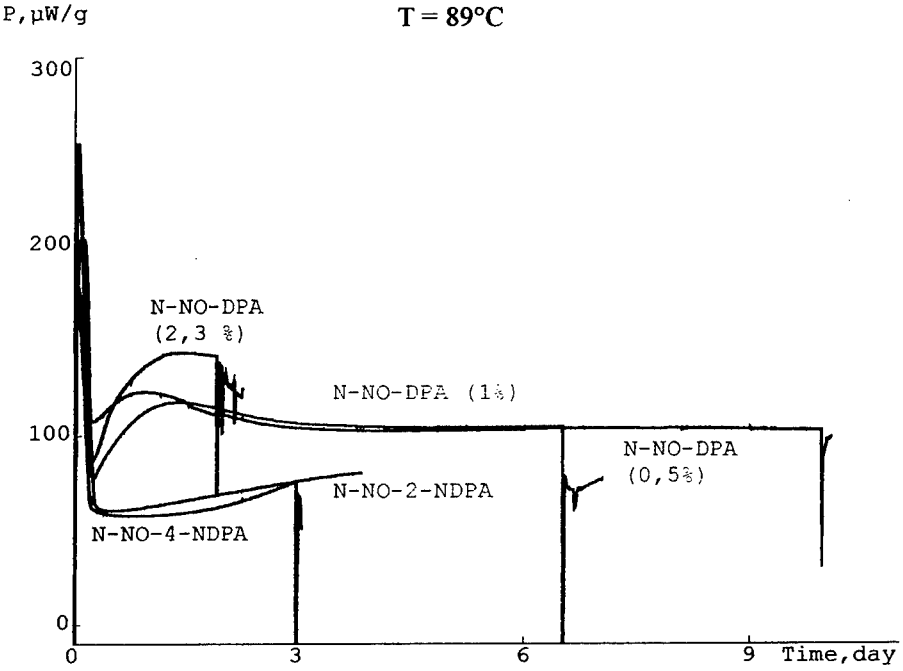

Figure 2 HFC curves of N-NO-DPA and N-NO-NO_2-DPA stabilised propellants

Sample 319 (with only 0.38 %DPA) has the same shape of the curve than sample 225. It even shows the same heat flow in the second maximum. The only difference is that this maximum appears earlier.

The N-NO-DPA stabilised **sample 301** has a different shape of the curve. After the first maximum a sharp miniumum could be observed which leads to a slow but steady increase of heat flow into a broad second maximum after 1.3 days. After that a slow decrease is taking place until the value becomes nearly constant. After 6.5 days endothermic gas evolution peaks occur. Up to this point 60 $J.g^{-1}$ were produced. The change of the stabiliser amount from 1 % to 0.5 % does not affect the shape of the curve. So **sample 305** shows nearly the same curve. The increase from 1 to 2.3 % **(sample 306)** is related with an increase in heat flow and earlier gas evolution peaks.

The N-NO-N-DPA stabilised **samples 307 and 308** were partially de-nitrosated during manufacture of the propellants. Their HFC curves are thus a „mixture" of N-NO-DPA and NO_2-DPA stabilised samples.

Propellants stabilised with 2-, 3- and 2,4- substituted DPA

A third type of curve is present in the 2-NO_2-DPA stabilised **propellant 226**. After a first maximum that reaches 165 $\mu W.g^{-1}$ (13 $\mu W.g^{-1}$ lower than sample 301) a minimum is observed. After this a very long slow increase into a constant heat flow is observed. This constant period lasts for more than 3 days before endothermic gas evolution peaks occur. The heat flow curves are presented in Figs. 1 and 3.

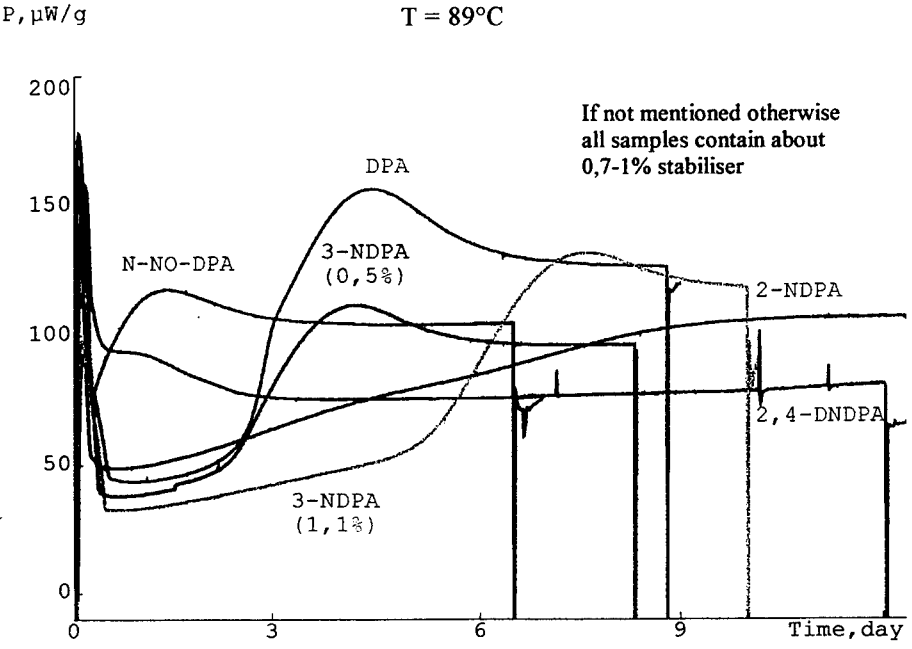

Figure 3 HFC curves of DPA, N-NO-DPA, 2-NO_2-DPA, 3-NO_2-DPA, and 2,4-DNO_2-DPA stabilised propellants

Interestingly, an increase in stabiliser content does also lead to lower heat flows and later gas evolution peaks. **Sample 187** (see Figure 1) demonstrates this. This indicates a better „compatibility" of 2-NO_2-DPA with nitroglycerin than DPA.

Sample D073 is stabilised with 2,4-dinitro-DPA. The heat flow curve shows a first maximum and afterwards a decrease into a nearly constant heat flow. The double determination shows a surprisingly high deviation. Leaking of the ampoule does not occur before 8 days. An increase into a second maximum could not be observed but is likely to happen after maybe 10 days. The energy release after 9 days is 63 $J.g^{-1}$.

Completely different to sample 226 is the heat flow curve of **sample 293**. It contains the „unusual" stabiliser 3-NO_2-DPA. The shape of the curve is very similar to that of the DPA stabilised sample 225. Only the change in the slope during the increase into the second maximum is absent. Compared to sample 225 the second maximum appears later (7.5 instead of 4.4 days). Also the average value of the heat flow is smaller in the sample 293. So until gas evolution occurs some 6.3 $J.g^{-1}$ are released per day, whereas sample 225 shows a heat generation of 9.3 $J.g^{-1}.day^{-1}$. The first maxima are very comparable (92 $\mu W.g^{-1}$ sample 293, 93 $\mu W.g^{-1}$ sample 225). The shape of the curve of sample 293 seems to show the decomposition behaviour as it is with pure DPA, where the first maximum indicates an oxidation reaction, and the second maximum appears at the same time when the primary stabiliser is used up and N-NO-species are dominating.

A decrease in stabiliser content (0.49 instead of 1.11 % 3-NO_2-DPA, **sample 304**) leads to a heat flow curve with the same shape but with an earlier second maximum. This behaviour could be expected because the second maximum indicates the time when the primary stabiliser is used up.

3.2 Centralite, substituted aniline and Akardite stabilised propellants

Sample 224 (stabiliser: Centralite I) shows a significant first maximum. The heat flow falls a little bit during the first 3 days to about 100 $\mu W.g^{-1}$. After that a slow increase occurs. After 9 days the specific heat production rate is 113 $\mu W.g^{-1}$. At this point 77 $J.g^{-1}$ are generated, according to an average of 9.2 $J.g^{-1}.day^{-1}$. Two experiments of the triple determination had to be finished earlier due to severe endothermic gas generation peaks. They are usual for Centralite containing propellants which also manifests in high weight losses in the Dutch test.

Sample 160 which contains Centralite I in higher concentrations shows a very high initial effect (maximum 227 $\mu W.g^{-1}$) and higher heat flows thereafter. Gas evolution starts after 7½ days. So it seems that the higher Centralite content leads to a higher reactivity. **Sample 309** with an even higher centralite content shows again an increase in heat flow, in initial effects and in severeness of gassing.

N-NO-N-ethyl-aniline is a decomposition product of Centralite I[6]. It is the stabiliser used for **sample 253**. It also shows a first maximum (200 $\mu W.g^{-1}$). Afterwards a constant level (96 $\mu W.g^{-1}$) is reached. Gas evolution occurs after 4 days. The average energy release is very high (9 $J.g^{-1}.day^{-1}$).

Sample 229 contains Ak II as stabiliser. It is the sample with which the longest heat flow measurement was made (38 days). After a first maximum (130 $\mu W.g^{-1}$) a long period of low heat generation is observed. So it is very surprising that the heat flow rises very fast after about 37 days and leads into a severe autocatalysis, which is completely different to other types of propellants[7]. The measurement was stopped, when the max. heat flow (30 mW/sample) was reached. Even at these high rates only 3.1 % of the sample weight was lost.

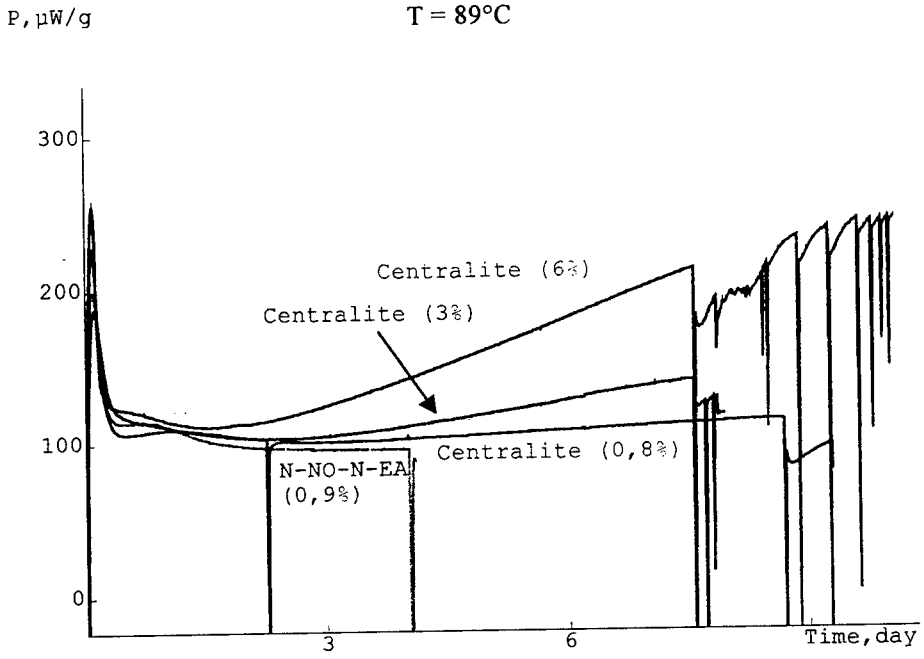

Figure 4 HFC curves of propellants stabilised with centralite and N-NO-N-ethyl aniline

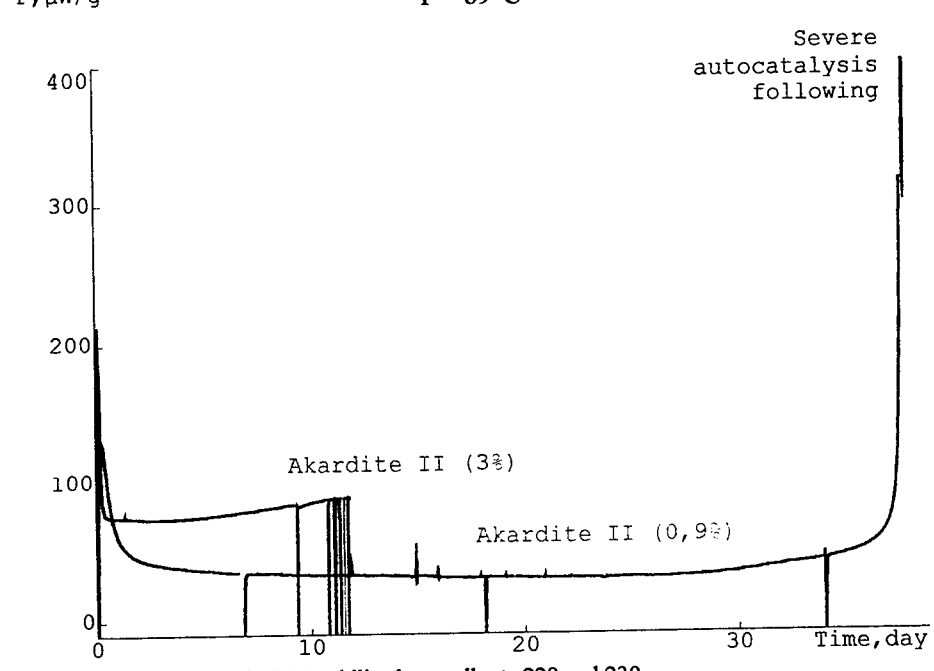

Figure 5 HFC curve of Ak II stabilised propellants 229 and 230

If the Ak II content is increased (**sample 230**) all heat flows are increasing, the first maximum appears much faster. The autocatalysis is not reached due to severe gas evolution peaks that occur from the 9th day on. The average energy release is 6.9 $J.g^{-1}.day^{-1}$, which means an increase of exactly 50 % compared to sample 229.

3.3 Unstabilised propellant (sample 130)

Another severe autocatalysis could be observed by measuring **sample 130**. It does not contain any stabiliser. The first maximum shows a value of 175 $\mu W.g^{-1}$. After that a broad minimum (80 $\mu W.g^{-1}$) is reached before after 4.5 days the heat flow increases very rapidly into the autocatalysis. After the autocatalysis had occured a second maximum of the reaction happens between the 6th and the 9th day. A lower loading density (300 mg) leads to the surprising result that the autocatalysis happens much faster (1.0 day) than in the completely filled ampoule. This is in contrast to many other experiments we conducted with non-stabilised nitrate esters[8]. After the reaction the nitrocellulose was degraded so much that it was completely soluble in the acetonitrile/methanol/water mixture used for the preparation of the HPLC analyses. Table 2 shows all the results of the heat flow measurements.

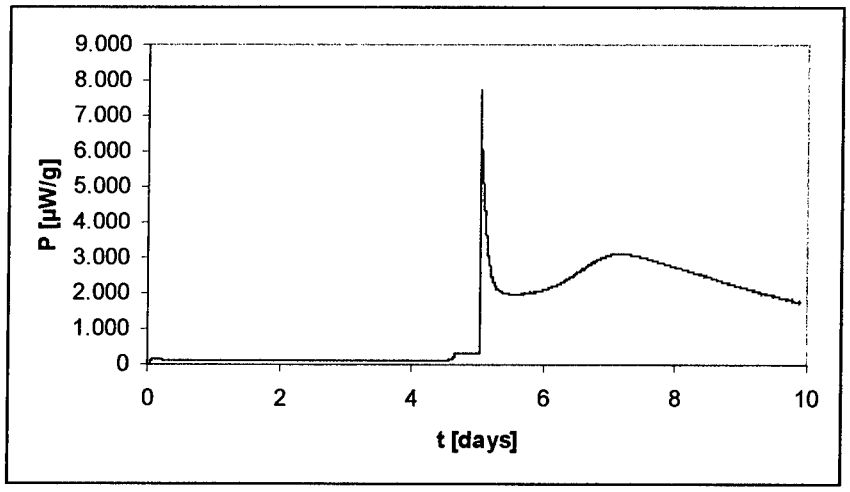

Figure 6 HFC curve of unstabilised propellant 130

3.4 Activation energies calculation

From the measured values at 89°C (Table II) and at 70°C activation energies (Table III) at iso-α stages were calculated (t70/t89 = from the time until α is reached, P89/P70 = from the values at α). Usually the Ea (t) values are much lower than the corresponding Ea(P) values. This is due to the heating-up process of the samples in the beginning of the measurement.

Table II Results of HFC measurements at 89°C

Sample nr.	Stab.	Amount [%]	1. Max. [μW/g]	2. Max. [days]	2. Max [μW/g]	t_{end} [days]	P_{end} [μW/g]
319	DPA	0.38	184	2.7	156	5.9	117
225	DPA	0.55	93	4.4	156	8.8	126
282	DPA	2.55	137	5.1	267	5.4	275
305	N-NO-DPA	0.43	203	1.0	123	10.0	103
301	N-NO-DPA	0.87	178	1.4	118	6.5	105
306	N-NO-DPA	2.11	253	1.5	143	1.91	142
226	2-NO_2-DPA	0.73	165	12.3	107	12.4	105
187	2-NO_2-DPA	2.64	64	2.1	60	14.7	53
307	N-NO-2-NO_2-DPA	0.35	233	10.9	95	14.3	91
308	N-NO-4-NO_2-DPA	1.15	168	N/A	N/A	3.0	72
D073	2,4-DNO_2-DPA	0.66	155	N/A	N/A	9.0	78
229	Ak II	0.86	130	N/A	N/A	38.0	9440
230	Ak II	2.87	211	N/A	N/A	10.8	88
224	C I	0.84	188	N/A	N/A	8.7	113
160	C I	2.61	227	N/A	N/A	7.9	139
309	C I	5.95	255	N/A	N/A	12.7	288
253	N-NO-N-EA	0.76	200	N/A	N/A	4.02	96
304	3-NO_2-DPA	0.49	106	4.1	102	8.0	88
293	3-NO_2-DPA	1.11	92	7.5	125	9.8	112
130	no stab.	0.00	175	-	-	9.9	1730

The end of measurement is defined here as the beginning of gas evolution peaks.

Table III Calculation of activation energies

Sample nr.	Stabiliser	Q [J/g]	Ea (t) [kJ/mole]	Ea (P) [kJ/mole]
225	DPA	5.8	104	120
224	C I	7.7	98	123
187	2-NO_2-DPA	13.5	136	147

4. „Classical" high temperature tests

4.1 Vacuum stability test

It is obvious from the shape of the curves (Figure 7) that in the initial phases of the test DPA causes a significant decrease in the rate of quantity of the released gas (this part of the curve is called *"induction period"*). A period follows characterised by a vigorous increase in gas volume growth rate (this part of the curve is called *"the period of accelerated decomposition"*).

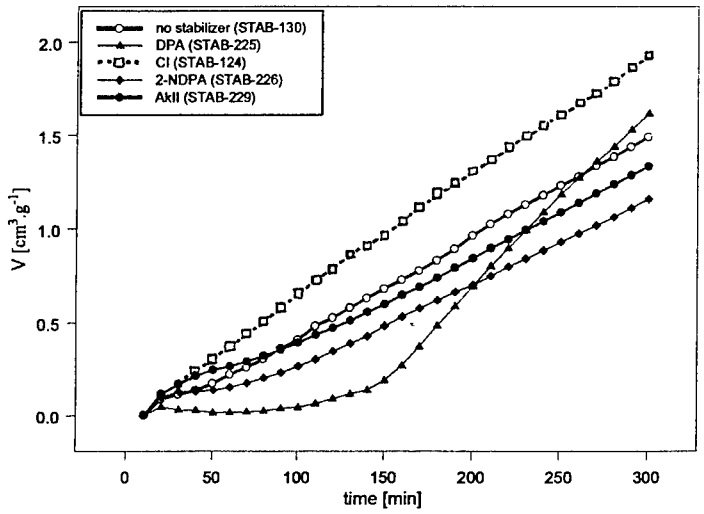

Figure 7 Released gas volume / time dependence for selected samples

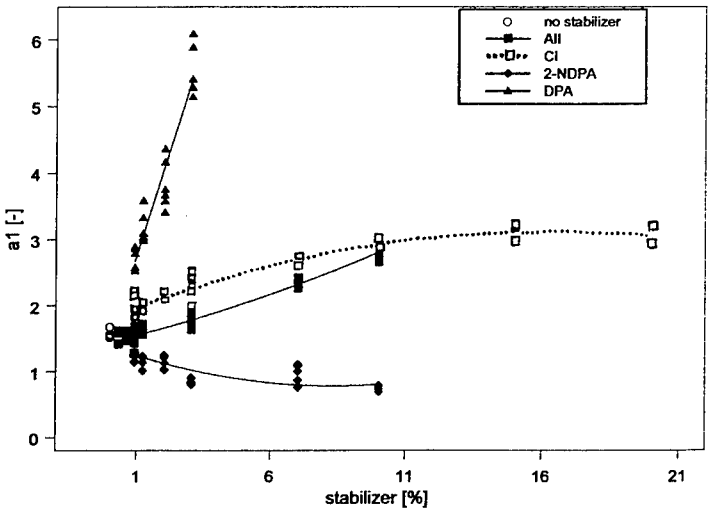

Figure 8 Relative gas evolution rate after the induction period measured for propellants stabilised with different concentrations of DPA, 2-NO_2-DPA, Ak II or CI

An increase of DPA also leads to an increase of the induction period. But this relation is not linear and reaches a limit when the DPA content is 2 % or more. It is also obvious that the growth of the gas volume above the sample is not generally linear time dependent. For further

statistical processing of measurement results new procedures have been developed of evaluation of curves measured by means of vacuum tests[9].

It has been proven by chemical analysis that the end of induction period occurs when DPA concentration is nearing zero. This conclusion follows also from the measurement of DPA concentration in pure nitroglycerin[10].

Surprising conclusion follows from the above results (Figure 7, 8) that propellant without stabiliser does not give the worst vacuum test results as expected but, on the contrary, the rate rise of released gas volume is increased by adding of CI, AII and DPA stabilisers. Directly these stabilisers or their daughter products enable progress of such undesirable chemical reactions that lead to gas releasing from a propellant. On the contrary, 2-NO_2-DPA stabiliser decreases the rate of gas releasing. Vacuum tests of N-NO-DPA, N-NO-N-EA, 2-NO_2-DPA, and 2,4-DNDPA stabilised model propellants have proven that these daughter products are not capable of increasing gas release rate when compared with propellant without stabiliser.

4.2 Methylviolet test

Measured test values grow linearly with initial stabilisers concentrations in case of DPA and 2-NO_2-DPA in a propellant, in case of a series of propellants with CI the dependence of test results on concentration is not statistically significant. From methylviolet test point of view CI does not act as a stabiliser.

If we compare methylviolet test results to vacuum and BJ120 tests results it is obvious that methylviolet test proceeds for relatively short time – about 90 to 120 minutes. During its course there is probably a non zero DPA concentration existing in the sample when the quantity of released gas is at minimum (it is a matter of analogy to the induction period of the vacuum test). This fact may prove its positive effect on methylviolet test results. With increase of DPA concentration both the induction period duration and methylviolet test results are higher. But the possibility cannot be excluded that prolongation of time period up to test paper discoloration is positively effected by DPA or 2-NO_2-DPA ability to sublime from the propellant and to act as stabiliser directly on test papers.

4.3 Bergmann-Junk-test

BJ120 tests were performed with model double base propellants, stabilised with 0 to 10 % DPA, 2-NO_2-DPA, Ak II, or CI stabilisers (the same propellants that had been tested by VST before). The results are graphically represented in Figure 9.

In cases of all stabilisers there is an obvious decrease in BJ120 test results when 0.9 % stabiliser is added, that is followed by a moderate but statistically significant growth in case of further increasing of initial CI and 2-NO_2-DPA concentration, by stagnation in case of Ak II and by stagnation followed by vigorous growth with DPA. In case of DPA stabiliser it is obvious that with its initial concentrations of 7 to 10 % the test result exceeds several times the values for the propellant without stabiliser. In the course of test of these samples test heavy nitrogen dioxide fumes were also observed above those samples.

There is a mutual conformity between the results of vacuum test and BJ120 test in case of DPA stabilised propellants. Temperature is by 5 °C higher in the course of BJ120 test and duration of the test is the same as with vacuum test. On the basis of knowledge of DPA depletion rate during vacuum test we can state that during BJ120 test exhaustion of DPA in the propellant occurs. By analogy to the accelerated period of vacuum test the gas is then released that leads to high values of BJ120 test.

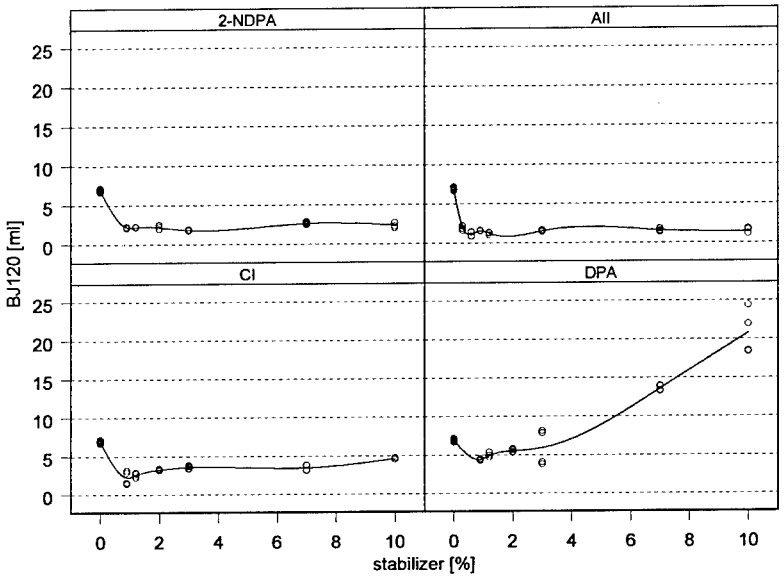

Figure 9 Effect of type and initial concentration of stabiliser on the values of BJ120 test results for D073 type propellants, the point are interlined by smoothing spline

The comparison of BJ120 test results for model double base propellants primary stabilised with the same initial concentration (0.9 %) of stabilisers or some of their daughter products (N-NO-DPA, 2,4-DNDPA) have proven that addition of any of compounds discussed brings about statistically significant decrease in test results values.

The comparison of BJ132 test results for single base Ak II, CI, DPA or 2-NO_2-DPA stabilised model propellants leads to similar conclusions as in case of BJ120 test.

4.4 Chemical stability at 100 °C

Application of HT100 test to model double base propellants and initial Ak II, CI, DPA or 2-NO_2-DPA stabilisers concentration from 0 to 3 % (the same propellants that had been tested by vacuum test and BJ120) led to results depicted in Figure 10. With further increase of stabilisers' concentration the test results do not show a linear growth.

It is obvious that HT100 values for CI show the slowest growth with increasing stabiliser concentration, for DPA and 2-NO_2-DPA this growth is more rapid. The highest growth increase is observed for Ak II. The conclusions that follow from the tests of single base Ak II, CI, DPA or 2-NO_2-DPA stabilised propellants are in accordance with the results found at double base propellants.

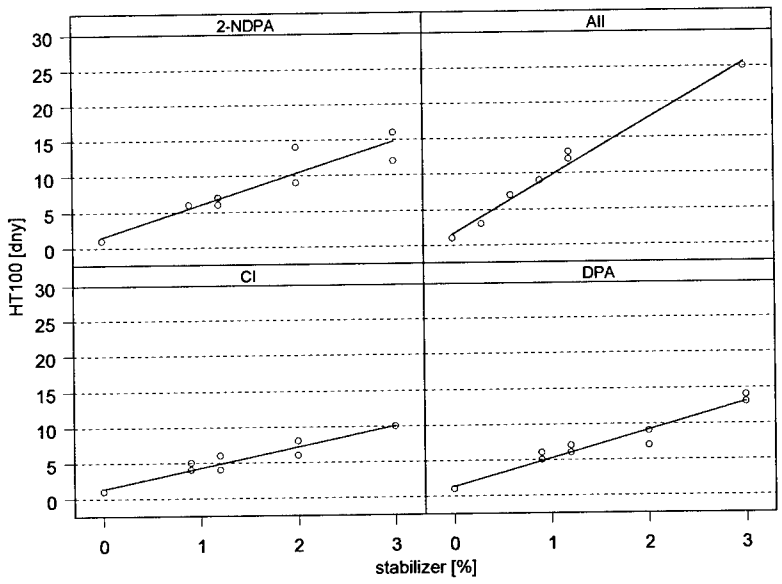

Figure 10 Effect of type and initial stabiliser concentration on values of HT100 test results for D073 type propellants; the points are interlined by regression lines

HT100 test results provide quite different information than the above given tests (vacuum test, BJ120 test, MV test). Not only that this test is capable of differentiating the propellant without stabiliser but its results also show best correlation with initial quantity of stabiliser and to considerable extent they are not affected by the type of stabiliser used. Differences between the results of this test and those of the others, above discussed tests, are unambiguously given by its different principle – it is the time up to accelerated decomposition what is observed and not only the quantity of products released in the course of a limited time period. Duration of this test is therefore much longer than in case of the other, above discussed tests and its expressive capacity reflects best actual chemical stability defined as "capability of the propellant to be stored without acute danger of self-ignition". From the viewpoint of assessing the measure of danger of accelerated decomposition and possible self-ignition this test is possible to be considered as most informative among the tests discussed in this chapter.

From the HT100 point of view, of the tested stabilisers most effective is Ak II. DPA and 2-NO_2-DPA are on the same level, and least effective is CI. The same effectiveness of DPA and 2-NO_2-DPA is an interesting phenomenon if we consider that 2-NO_2-DPA contains less free positions to hold nitro and nitroso groups than DPA and therefore we could suppose that DPA will be able to prevent from autocatalysis for longer time than 2-NO_2-DPA. The fact that it is not so will be obviously caused by the ability of DPA to accelerate reactions proceeding in the propellant (which follows from kinetic studies in[9] and also from the results of vacuum test given above in this Chapter). The problems that are reflected in acceleration of rise of the released gases volume after induction period in the course of vacuum test or in increase of values of BJ120 test with increasing of DPA initial concentration in the propellant, do not reflect themselves in shortening the time before the accelerated decomposition starts, but they

reflect themselves only in decreasing of slope of HT 100 results dependence on the initial DPA concentration in the propellant. So the DPA caused problems observed during vacuum test and BJ120 test are probably overcome by stabilising capabilities of DPA daughter products (N-NO-DPA and DPA nitroderivatives) and from the viewpoint of self-ignition they need not, under common storage conditions, represent a high risk. They can be, however, of significant influence on ballistic stability.

HT100 test results for model propellants primarily stabilised with the same initial concentration of stabilisers (0.9 %) or some of their daughter products (N-NO-DPA, 2,4-DNDPA, N-NO-N-EA) have proven that all the used compounds prolonged significantly the time period up to the beginning of accelerated decomposition. This capability growths in the order: 2,4-DNDPA and N-NO-N-EA, CI and N-NO-DPA, DPA and 2-NO_2-DPA, the highest values have been achieved in case of the Ak II stabilised propellant sample.

To verify the assumption of universality of the above given conclusions the above discussed tests have been performed with model propellant sample sets with different densities, with nitrocelluloses of different origin (wooden or cotton linters) or with combinations of above discussed stabilisers. It has been proven that influence of propellant density and nitrocellulose type has only a little effect to the stability tests results. The effects of the individual stabilisers are of additive nature.

4.5 Weight loss at 89 °C

Model propellants stabilised by Ak II, CI, DPA, 2-NO_2-DPA (0.9 %), or CI (6 %) have been subjected to weight loss test at 89 °C, the results of which are given in Figure 11. The propellant with 6 % CI has shown the course of weight loss quite different from the above mentioned samples – the accelerated decomposition has been reached after 36 days of conditioning, in the course of which a uniform weight loss proceeded. Total weight loss had been 8.7 % before the beginning of autocatalysis.

The results of weight loss testing are in accordance with the results published by Volk[11]. The order of stabilisers set up according to its effectiveness in retarding accelerated decomposition (CI, DPA, 2-NO_2-DPA and Ak II) is coincident with the order found at HT100 tests. A vigorous increase in weight loss rate of the propellant with increase in the initial CI concentration is in accordance with vacuum tests results.

5. Stabiliser depletion

HPLC analyses were performed after HFC measurements. This means that not a complete set of stabiliser depletion was performed. The aim was to see to what extent the original stabiliser has been consumed and which daughter products were formed.

In case of the DPA stabilised samples a complete dissapearance of DPA was observed when the heat flow measurement was stopped after the second maximum. This is in accordance with the findings in[4]. The main reaction products are N-NO-DPA and N-NO-4-N-DPA. The higher the released energy is, the higher is the ratio N-NO-NDPA/N-NO-DPA. Also traces of 2-NO_2-DPA and DNDPAs could be detected.

In contrast to that the N-NO-DPA stabilised samples still contain some of the original stabiliser even after long heat flow experiments. In another series of stabiliser depletion experiments with DB ball propellants[12] it was found that even with energy losses of more than 300 $J.g^{-1}$ still a – nearly constant – amount of N-NO-DPA and N-NO-4-NDPA remains in the sample.

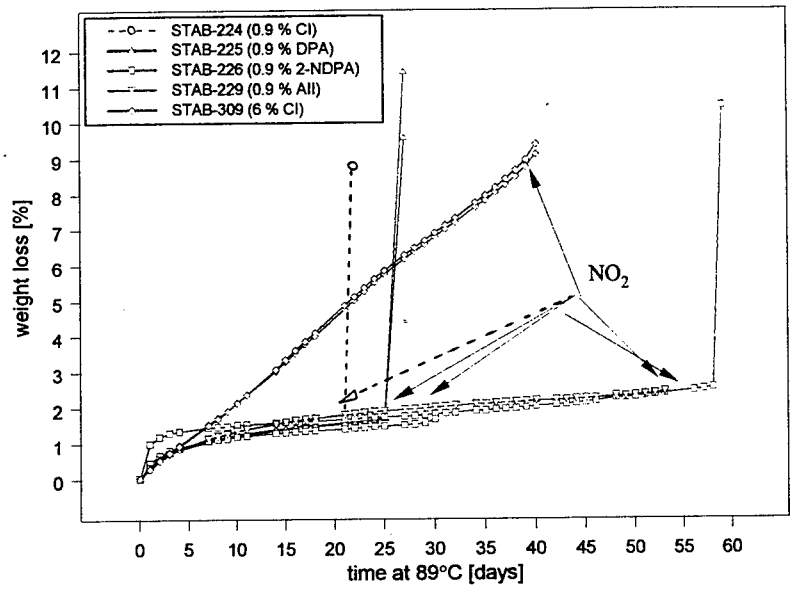

Figure 11 Weight loss measurements at 89°C (double determinations)

2-NO_2-DPA stabilised propellants tend to keep its original stabiliser much longer. But finally, after an energy release of 90 $J.g^{-1}$ (sample 226) all of the 2-NO_2-DPA had disappeared and DNDPAs are formed. Sample D073 still contains about half of the original stabiliser content after 63 J/g energy release. The rest of it had been transformed into TNDPAs.

The 3-NO_2-DPA stabilised propellants do not show any residual 3-NO_2-DPA after the HFC measurements which is in accordance with the fact that the second maximum has passed.

Akardite stabilised propellants still contain Ak II after the heat flow experiments. It has the ability to be split up into DPA and gaseous products. So a constant low amount of DPA is present in the sample and, as it is much more reactive than Ak II itself, it is the active stabilising agent in sample 229 and 230. Of course, DPA reaction products can also be found in the sample. When arriving into autocatalysis, no Ak II is left anymore and about 0.4 % 2,2',4,4'-TeNDPA are present as the only stabiliser product.

The depletion of centralite in propellants is somewhat comparable to that of 2-NO_2-DPA concerning the depletion rate. It as well depends also on the original content of CI. Higher original contents are relatively faster used up (when looked at the same heating time). The decomposition path of CI is divided into two directions[6]:

1. Nitration of one (or two) aromatic rings,
2. Split of the molecule and formation of N-NO-N-EA.

Both ways can be observed in samples 224, 160 and 309.

Tables IVa-IVc collect the results of the HPLC analyses of the samples.

Table IVa HPLC analyses after HFC measurements (DPA derivatives)

Stab.	Sample	Orig. content	T [°C]	Q [J/g]	N-NO-DPA	N-NO-NDPA	N-DPA	DN-DPA	TN-DPA
DPA	225	0.55	89	32	0.67	0.07	0.05	-	-
	225	0.55	89	88	0.36	0.43	0.01	0.06	-
	282	2.55	89	66	2.14	0.45	0.16	-	-
N-NO-DPA	305	0.43	89	93	0.04	0.14	-	0.06	0.03
	301	0.87	89	60	0.40	0.73	0.02	0.10	-
	306	2.11	89	26	2.02	0.14	-	-	-
2-NO_2-DPA	226	0.73	89	90	X	-	-	0.17	0.32
	187	2.64	70	14	X	0.37	2.17	0.04	-
	187	2.64	89	70	X	0.03	0.20	1.94	0.03
2,4-D-NDPA	D073	0.66	89	63	X	X	X	0.50	0.12

Table IVb HPLC analyses after HFC measurements (Ak II derivatives)

Stab.	Sample	Orig. content	T [°C]	Q [J/g]	Ak II	DPA	N-NO-DPA	N-NO-NDPA	TeN-DPA
Ak II	229	0.86	89	173	-	-	-	-	0.41 [a)]
	230	2.87	89	74	1.25	0.03	1.00	0.02	-

a) sample in autocatalysis

Table IVc HPLC analyses after HFC measurements (C I derivatives)

Stab.	Sample	Orig. content	T [°C]	Q [J/g]	C I	N-C I	DN-C I	N-NO-N-EA
C I	224	0.84	89	77	-	0.14	Nq	Nq
	160	2.61	89	80	1.73	-	-	0.18
	309	5.95	89	202	0.91	0.02	-	0.99
N-NO-N-EA	253	0.76	89	36	X	X	X	0.63

Explanations to tables IVa-IVc: X not possible derivative. Orig. content in [%]. Nq: not quantified. The sum of all stabiliser reaction products might be bigger in some cases than the original stabiliser content. The reason for this is that some propellants originally contain some depletion products which are not given in this table or in table 1.

6. Discussion

The principal reaction of DPA in propellants or with nitrate esters could be determined by its basicity. Lurie's hypothesis[10] is based on the ability of DPA to react with nitroglycerin under the formation of N-NO-DPA and 1,3-propanediole-1,3-dinitrate-2-one and subsequent alkaline hydrolysis under formation of salts of formic and oxalic acid with DPA.

The published results of acidobasic properties of DPA[13] derivatives stand, however, against this theory. It follows from these results that DPA is not able to cause alkaline hydrolysis and to form oxalic and formic acids salts. The equilibrium constant of DPA protonation (the protonised form is on the right side of the equation) of 5.78 has been determined (that means in 0.1M sulphuric acid environment 54 % of DPA will be dissociated). In case of 3-NO_2-NDPA stabilised propellant the induction period has been, however, also observed in VST and HFC experiments. But its dissociation constant given in[13] is 0.053 (in 0.1M sulphuric acid environment only 1 % of 3-NO_2-NDPA will be dissociated). Against the Lurie's theory stands also the given smaller sensitivity of DPA depletion rate to substitution on benzene ring than would accord with the acidobasic nature of the reactions. The assumption of formation of carboxylic acids in the course of induction period (which is a strongly exothermic reaction) is also in contradiction with low measured released heat flows. The explanation seems to be more acceptable of the phenomena observed based on presumption of radical course of reactions.

Thermal decomposition of nitroglycerin leads to initiation of reactions described in ref.[14]. The DPA present is able to react with nitrogen dioxide but it can also, by reacting with other radicals, form stable DPA$^{\bullet}$ radicals (the presence of which has been proven by means of EPR[10,15]). This reaction causes terminations of decomposition reactions because the DPA$^{\bullet}$ radical is little reactive and its cumulation in the propellant occurs. For this reason the DPA stabilised propellants show the lowest nitrocellulose molecular weight loss[16]. In this way also stabilisation of peroxide radicals R-OO$^{\bullet}$ to R-OOH occurs that would, without presence of DPA, succumb to disproportionation to aldehyde and alcohol. Stabilisation of peroxidic radicals by DPA has been described by Varlamov[17]. Accumulation of hydroperoxides is the result of dynamic equilibrium of their formation and decomposition that is influenced by conditioning temperature and actual DPA concentration in the propellant. For this reason the intensity of gas release in the course of accelerated period of decomposition is dependent on the conditioning temperature at which DPA degradation in the propellant had proceeded[9]. DPA, however, effects also as antioxidant that blocks oxidations of aldehydes to carboxylic acids by bonding nitrogen dioxide or oxygen. Simultaneously DPA is able to prevent the increase of acidity of the environment by reactions with nitrous or nitric acids. It has also been proven that DPA is able to remove formic acid as well by reaction to N,N-diphenylformamide[9]. In the propellant the accumulated DPA$^{\bullet}$ radical is little reactive associated with a high selectivity. It can be then supposed that the DPA$^{\bullet}$ radical (that can be considered to be a cation) will be attracted by nitrate groups of nitroglycerin with partial negative charge. The result can be initiation of nitroglycerin decomposition. The released nitrogen oxides are subsequently effectively trapped by DPA. The activation energy of the process of DPA concentration decrease in the propellant is therefore lower than would be adequate to thermal decomposition of nitroglycerin. The decreased order of the reaction characterising decrease of DPA concentration in the propellant[9,18] can be explained by increase in environment reactivity in the course of DPA depletion partly by the effect of DPA$^{\bullet}$ radical accumulation partly by higher reactivity of nitroglycerin decomposition products. It follows from measuring of EPR spectra[15] that N-NO-DPA is in equilibrium with nitric oxide and DPA$^{\bullet}$ radical, which can also explain the increase in heat flow due to N-NO-DPA in the propellant.

In case DPA substituted in benzene ring will be used as stabiliser the electrondonor substituents will increase stability and selectivity of the radical and to decrease its reactivity. Electronacceptor substituents will, on the contrary, decrease its stability and increase its reactivity. In case of 3-NO_2-NDPA the concentration of its radical in the propellant will be small and also its selectivity will not be high. The result will be the observed decrease in rate of 3-NO_2-NDPA depletion compared to the not substituted DPA. 2-NO_2-DPA stabiliser, however, due to steric hindrances will not almost stabilise a possible radical, which will result in the fact that this stabiliser will not cause acceleration of the decomposition of nitrate esters and also it is not able to terminate radical reactions. This will reflect itself in absence of induction and accelerated periods.

In the next publication of this series[19] a huge amount of numbers of samples all containing substituted DPAs as stabilisers will prove the influence of I and M effects on reactivity and selectivity of the stabilisers.

Centralite stabilised propellants show a steady increase in heat flow and gassing when the centralite content is rising. Even the initial effect is affected in the same direction. In addition N-NO-N-EA has the same shape of curve and thus a comparable stabilising effect than CI itself.

Increasing Ak II concentration has the same effect than CI or DPA (→ higher heat flow, bigger first maximum, earlier gassing). A low Ak II content in a propellant actually stabilises the propellant very well. It needs about 38 days to be completely consumed but if it is once used up, a severe autocatalysis happens. This behaviour is not the same than in DPA stabilised propellants. It could be explained by the relative slow decomposition of Ak II into DPA[11,20]. So a constant low DPA content is present in the propellant and – because DPA is much more reactive towards NO_x – it is used up and transformed into higher nitrated derivatives. This reaction is going on until no Ak II is present anymore. The remaining DPA derivatives (mainly tri- and tetranitro-DPAs) are so weak in their stabilising activity that the NO_x produced by the propellant decomposition cannot be „neutralised" anymore. This leads to the severe autocatalysis, which can also be observed with the unstabilised sample 130.

Weight losses/pressure increases follow the same pattern. In principle the only difference is the atmosphere above the propellant which can have a remarkable effect on the reaction/ decomposition mechanism[21]. In presence of oxygen the first decomposition products of DPA (N-NO-DPA and its nitro-derivatives) are readily oxidised and thus faster nitrated. This leads to earlier and more severe autocatalysis (e.g. sample 225 after 24 days).

7. Conclusion

It is obvious from literary research[9] and the results given in this work that when assessing the actions proceeding in the course of ageing of propellants it is necessary to realise that this is a matter of a complex set of parallel and subsequent chemical reactions. The preference of each individual reaction is influenced by the initial composition of a propellant and the conditions of ageing. The main factor to affect the preferences of the reactions proceeding is the type of the stabiliser used and a possibility of oxygen access to the propellant sample. All the tested stabilisers are capable of effective prevention from nitrous acid, nitric acid, and nitrogen di-oxide accumulation. By this way they can delay the accelerated decomposition of a propellant and thus ensure long storage life of propellants. However, it has been proven that functioning of stabilisers in a propellant is not restricted to trapping of the products of the decomposition of the nitrate esters. It has been proven in cases of DPA and CI that thermal decomposition of nitrate group does not represent the main primary decomposition reactions in a propellant.

Under the temperatures studied (55 – 115 °C) the most rapid action of nitrate esters' decomposition is their direct reaction with these stabilisers or with their reaction products[9].

In case of DPA it has been proven that this compound is capable of changing preferences of the subsequent reactions in such a way that it blocks oxidation reactions of aldehydes to carboxylic acids and formation of gaseous products, terminates radical reactions by formation of stable radicals and causes accumulation of unknown compounds with high enthalpy of formation[9]. These capabilities make DPA minimise the extent of undesirable reactions during the time of its presence in the propellant that lead to splitting of polymeric nitrocellulose chains, which leads to assurance of high ballistic stability of DPA stabilised propellants. DPA (just as CI) is capable of effective functioning also as an antioxidant in a propellant. At the moment when DPA has been spent a vigorous decomposition processes occur both due to decomposition of accumulated compounds with high enthalpy of formation and due to the effect of little effective stabilisers system present in the propellant in this stage of decomposition (the main stabilising compound being N-NO-DPA). These reactions result in a vigorous decrease in nitrocellulose molecular weight, which consequently leads to deteriorating of ballistic properties of the propellant. This fact restricts the service life of DPA stabilised propellants to the time period during which the primary stabiliser is present in the propellant. This finding is roughly equivalent to the experiments made at PB Clermont[12] where it could be shown that at a stage of decomposition which is twice the time of DPA consumption the ballistic properties are beginning to drop below the acceptance limit. This period is, however, relatively short due to direct reactions of nitrate esters with DPA or its reaction products namely in the cases when the propellant contains nitroglycerin.

In the case that CI is used as a stabiliser in concentration up to 1 % the stabilisation of the propellant proceeds predominantly by bonding of nitrogeneous products of primary decomposition of the nitrate esters into the aromatic rings of the stabiliser. At initial CI concentrations of three and more per cent in a propellant the preference of urea skeleton splitting occurs probably due to a change in propellant structure, which results in gradual acceleration of primary decomposition of nitrate esters as a result of effect of some CI reaction products[9].

Considering the fact that the main stabiliser products are capable of further stabilising the propellant, the problems associated with the incompatibility of DPA and CI with nitrate esters do not seem to be serious for safe storage. These problems, however, have a negative effect on service life period.

In case of 2-NO_2-DPA stabilised propellants no acceleration of primary decomposition processes of nitrate esters were observed that were caused by this compound. 2-NO_2-DPA functions as a stabiliser in a propellant above all by trapping nitrogeneous reaction products of nitrate esters' decomposition, its antioxidising capabilities are small, however. How Ak II works as a stabiliser has not been studied in such a great details as it has been in the cases of DPA, 2-NO_2-DPA and Centralite I. Its high capability follows, however, from the performed tests and literary research of long-term prevention from accelerated decomposition of a propellant. Acceleration of reactions has been, however, proven when the initial Ak II concentration in a propellant is increased to 3 %. From high values of volume of released gas in the initial stages of measurement with corresponding heat flow increase it is possible to presume a small capacity of Ak II to function as an antioxidant and to terminate radical reactions, which may result in its restricted ability to effectively prevent from nitrocellulose chains splitting.

From the viewpoint of inspection methods used to determine the safety storage of propellants it is appropriate to use tests in the course of which accelerated decomposition is initiated and this decomposition is registered either by observing of fumes or by accelerated weight loss. To assess the measure of danger of accelerated decomposition it is possible to use also

measurement of heat flow at relatively high temperature (e.g. 89 °C) for a period of several (e.g. 5 - 10) days. On the contrary, the tests that are based on detection of released gas in the course of conditioning (BJ120, BJ132, MV) are not appropriate for this purpose because interpretation of their results is considerably complicated and requires a detailed knowledge of chemical composition of the propellant. For the same reason the use of vacuum test is not appropriate for estimation of measure of hazard either. In addition, it has been proven in case of MV test that its results significantly depend on the quality of testing papers[9].

From the chemical stability point of view the method that is giving most reliable results are heat flow measurements. When the kinetics (and activation parameters) of the decomposition reactions are known a very good prediction of the chemical stability can be made[7].

References and Notes

[1] ČSVN 26 910, vydáno 16.6.**1989**.

[2] MIL-STD-286B, Method 404.1.2, „Heat test (120° and 134.5 °C)".

[3] ČSN 66 8102, 28.3.**1978**, část 31.

[4] P Guillaume, M Rat, S Wilker, G Pantel, „Practical Application of Microcalorimetry to the Stability Studies of Propellants", *TTCP Workshop Leeds* 4/**1997**.

[5] M Rat, P Guillaume, S Wilker, G Pantel, „Stability Studies of Spherical Propellants", *ICT-Jahrestagung* 27, 16 (**1996**).

[6] WA Schroeder, MK Wilson, C Green, PE Wilcox, RS Mills, KN Trueblood, „Chromatographic Investigations of Smokeless Powder", *Ind.Eng.Chem.* 42, 539-546 (**1950**), BT Fedoroff, OE Sheffield (eds.), *Encycl. Explos. Related Items,* Vol. 2, S. C135-C136 (**1962**), R Ammann, H Hilty, HR Pfeiffer, W Rauber, „Methods to evaluate the chemical stability of propellants using HPTLC and HPLC", *Symp.Chem. Probl. Connected Stabil.Explos.* 5, 127-161 (**1979**), L Druet, J Angers, „LC/MS Studies of Ethyl Centralite Stabilized Propellants", *Propellants, Explosives, Pyrotechnics* 13, 87-94 (**1988**), F Volk, „Determination of the Lifetime of Gun Propellants Using Thin Layer Chromatography", *Propellants and Explosives* 1, 90-97 (**1976**), T Lindblom, „Determination of Stabilizer and its Nitroderivatives in Double Base Powders by HPLC", *Symp.Chem. Probl.Connected Stabil.Explos.* 5, 107-125 (**1979**), JW Brook, B Kelso, I Neil, N MacLeod, „An Investigation of some Aspects of the Stability Testing of Nc-based Propellants", *Symp.Chem.Probl.Connected Stabil.Explos.* 5, 435-457 (**1979**), M Frey, „Über neuere Verfahren in der Treibmitteluntersuchung (III) – Vorausbestimmung der Lebensdauer von Nitratestern", *Explosivstoffe* 15, 97-105 (**1967**), L Druet, M Asselin, A Bolvari, „Stability Testing of Gun and Mortar Propellants", *Symp.Chem.Probl. Connected Stabil.Explos.* 7, 233-247 (**1985**), V Kučera, „Untersuchung der Zersetzungskinetik von rauchlosen Pulvern", *Explosivstoffe* 19, 49-57 (**1971**), NJ Curtis, P Berry, „Derivatives of Ethyl Centralite in Austrailian Gun Propellants", *Propellants, Explosives, Pyrotechnics* 14, 260-265 (**1989**).

[7] U Ticmanis, G Pantel, M Kaiser, „Simulation der chemischen Stabilität eines zweibasigen Treibladungspulvers", *2. Int. Workshop Stabilität/Mikrokalorimetrie WIWEB* März **1999**., S. 182-195.

[8] S Wilker, M Kaiser, G Pantel, B Ditz, „Verträglichkeitsuntersuchungen von Nitratestern", *ICT Jahrestagung* **31** (2000).

[9] J Petržílek, „Relations between chemical stability and composition of smokeless powders", doctoral thesis University of Pardubice (**2000**) and further references therein.

[10] B Lurie, T Lindblom, LE Paulsson, „Kinetics and mechanism of chemical processes in nitro-ester propellants containing diphenylamine", *LCEM Conference*, Fullerton, CA, USA (**1998**).

[11] F Volk, „Determining the Shelf Life of Propellants", *Propellants and Explosives.* 1, 59-65, (**1976**).

[12] U Ticmanis, P Guillaume, A Fantin, G Pantel, J-P Marchandise, L Stottmeister, S Wilker, „Ballistische Untersuchungen an thermisch belasteten TLP", *3. Forum Explosivstoffe WIWEB* **2000**.

[13] O Pytela, P Vetešník, „Dissociation constants of monosubstituted diphenylamines and optimized construction of acidity function", *Collect. Czech. Chem. Commun., 48*, (**1983**), 2363.

[14] J Quinchon, J Trachant, M Nicolas, „Les poudres, propergols et explosifs", Vol. 3, Technique et Documentation, Paris (**1982**).

[15] T Mrzewiński, T Urbański, „Change of Diphenylamine in Single Base Propellants", *Symp.Chem.Probl.Connected Stab Explos.* 6, 317, (**1982**).

[16] A Sopranetti, E Brönnimann, R Stähli, „Effects of different stabilisers on single-base and double-base propellants", *Symp.Chem.Probl.Connected Stab. Explos.* 6, 83 (**1982**).

[17] VT Varlamov, *Izv. Akad. Nauk SSSR, Ser. Khim.* 3, 549 (**1989**), VT Varlamov, *Izv. Akad. Nauk SSSR, Ser. Khim.* 8, 1750 (**1989**), VT Varlamov, *Kinet. Catal.* 30 (5), 1079 (1989), VT Varlamov, *Izv. Akad. Nauk SSSR, Ser. Khim.* 4, 743 (**1990**).

[18] J Petržílek, „Kinetic study of stabilizer consumption in spherical propellants", *2. Int. Workshop Stabilität/Mikrokalorimetrie WIWEB* März **1999**., S. 32-50.

[19] J Petržílek, J Skládal, S Wilker, G Pantel, L Stottmeister, „Stability analysis of propellants containing new stabilisers – Part II", *ICT Jahrestagung* 32 (**2001**).

[20] M Rat, „Stabilité des poudres double base GBPa (0,15) – Mécanisme d'action de l'acardite II", *SNPE-Bericht* NT N° 130/**91**/CRB/NP.

[21] P Guillaume, M Rat, G Pantel, S Wilker, „Heat Flow Calorimetry of propellants – Effects of sample preparation and Measuring Conditions", *2. TTCP Workshop Leeds* 4/**1999**.

Temperaturabhängigkeit der Zersetzung der Nitrocellulose bestimmt mit Modellierung des TGA-Massenverlusts und Stabilisatorverbrauchs

Temperature dependence of the decomposition of nitrocellulose determined by TGA mass loss and stabilizer consumption

M.A. Bohn und N. Eisenreich

Fraunhofer-Institut für Chemische Technologie, ICT
Postfach 1240
D-76318 Pfinztal-Berghausen, Germany

Kurzfassung

Die temperaturabhängige Zersetzung der Nitrocellulose (NC) ist ein komplexer Vorgang, da mehrere Hauptzersetzungsreaktionen parallel ablaufen, wobei deren Aktivierungsenergien sehr unterschiedlich sind. Daher kann es zu scheinbar widersprüchlichen Ergebnissen kommen, je nach verwendetem Temperaturbereich. Mit Daten zur Zersetzung von NC allein (N-Gehalt=13,3 Mass.-%) erhalten mit TGA-Massenverlustmessungen zwischen 140°C und 175°C und mit Daten zur NC-Zersetzung erhalten aus dem Stabilisatorverbrauch eines mit DPA stabilisierten einbasigen Treibladungspulvers zwischen 65°C und 90°C wird diese Temperaturabhängigkeit gezeigt.

1. NC-Zersetzungskinetik ermittelt mit Stabilisatorverbrauch

Die typischen Zersetzungsreaktionen der Nitrocellulose, welche mit üblichen NC-Stabilisatoren wie Diphenylamin (DPA), Akardit II (Ak II) oder Ethylcentralit (EC I) verlangsamt werden können, sind im Reaktionsschema Gl.(1) gezeigt. Die primäre Zersetzung kann an der Salpetersäureestergruppe thermolytisch (homolytisch) mit NO_2-Abspaltung und hydrolytisch als Esterverseifung erfolgen. Beide Reaktionen bilden autokatalytisch wirksame Produkte: NO_2, N_2O_4, HNO_3, welche über viele Reaktionen miteinander gekoppelt sind. Daher wird als Approximation nur ein autokatalytisch wirksames Produkt P im Reaktionsschema eingeführt. Die eingesetzten Stabilisatoren haben Radikalfängerfunktion und können das Radikal NO_2 abfangen. Sie sind auch basisch und können die Salpetersäure HNO_3 abpuffern. Alle Stabilisatoren haben auch stabilisierend wirkende Folgeprodukte, die in diesem Reaktionsschemea nicht berücksichtigt sind, jedoch in einer anderen Arbeit enthalten sind /1,2/. Wenn der primäre Stabilisator viel reaktiver als seine Folgeprodukte im Abfangen des autokatalytischen Produkts P ist, ist diese Näherung nach Gl.(1) möglich. DPA ist z.B. sehr viel reaktiver als alle seine Folgeprodukte /1,2/. Zur Bestimmung der kinetischen Parameter wird das Reaktionsgleichungssystem Gl.(2) verwendet (RS I). Es enthält nur eine Reaktionsgeschwindigkeitskon-

Paper 62 on the 31st International Annual Conference of ICT, June 27 to June 30, 2000, Karlsruhe, Germany, organized by Fraunhofer-Institut für Chemische Technologie (ICT).

stante k_{NC}, da von vornherein nicht gegeben ist, daß die nötige Information über beide Zersetzungsarten in den Meßdaten enthalten und auch 'extrahierbar' ist. Zudem ist aus /1,2/ bekannt, daß Stabilisatorverbrauchsdaten keine Information über die autokatalytische Zersetzungsreaktion der NC enthalten, da der Stabilisator gerade diese Reaktion verhindert. Folglich kann man sie weglassen oder man muß einen Wert für k_{NCauto} festlegen. Wie in /1,2/ wurde auch hier $k_{NCauto} = 10 \cdot k_{NC}$ gesetzt. Die Werte der Reaktionsgeschwindigkeitskonstanten ändern sich fast nicht, wenn von $k_{NCauto} = 10 \cdot k_{NC}$ zu $k_{NCauto} = 0$ gegangen wird /2/.

	$NC \xrightarrow{k_{NC,T}} P + R$	primäre Zersetz., -ONO_2-Thermolyse
	$NC \xrightarrow{k_{NC,H}} P + R$	primäre Zersetz., -ONO_2-Hydrolyse
(1)	$NC + P \xrightarrow{k_{NCauto}} P + R$	autokatalytische Zersetzung
	$DPA + P \xrightarrow{k_{DPA}}$ Folgeprodukt	Stabilisierungsreaktion

Reaktionsgleichungssystem RS I

$$\frac{dx_{NC}}{dt} = -k_{NC}x_{NC} - k_{NCauto}x_{NC}x_P$$

(2)
$$\frac{dx_P}{dt} = +k_{NC}x_{NC} + k_{NCauto}x_{NC}x_P - k_{DPA}x_{DPA}x_P$$

$$\frac{dx_{DPA}}{dt} = -k_{DPA}x_{DPA}x_P$$

Das Differentialgleichungssystem Gl.(2) wird numerisch intergriert und mit anschließender Parameteranpassungsrechnung werden k_{NC} und k_{DPA} bestimmt. Dies wird solange zyklisch wiederholt, bis die optimale Anpassung erreicht ist. Die Meßdaten wurden im ICT mit einem einbasigen, DPA-stabilisierten Treibladungspulver (TLP) durch Temperaturlagerung bei 65°C, 70°C, 75°C, 80°C, 85°C und 90°C und HPLC-Bestimmung des Stabilisatorgehalts in einem Dichlormethanextrakt erhalten /3/. Die Tabelle 1 zeigt die nach Gl.(2) bestimmten Reaktionsgeschwindigkeitskonstanten k_{NC} und k_{DPA}. KK ist der Korrelationskoeffizient der Anpassungs-

Tabelle 1: Reaktionsgeschwindigkeitskonstanten k_{NC} und k_{DPA} in einem einbasigen TLP bestimmt mit RS I bei $x_P(0) = 0{,}0075$ mol/(mol ONO_2) und $k_{NCauto} = 10 \cdot k_{NC}$ als Funktion der Temperatur ermittelt aus mit HPLC bestimmten Stabilisatorverbrauchsdaten /3/.

T [°C]	k_{NC} [1/d]	k_{DPA} [1/d]	KK
65	3,976 E-5	24,68	0,9907
70	7,921 E-5	40,17	0,9939
75	1,623 E-4	233,68	0,9951
80	3,043 E-4	309,51	0,9868
85	7,898 E-4	205,64	0,9956
90	1,307 E-3	807,1	0,9974

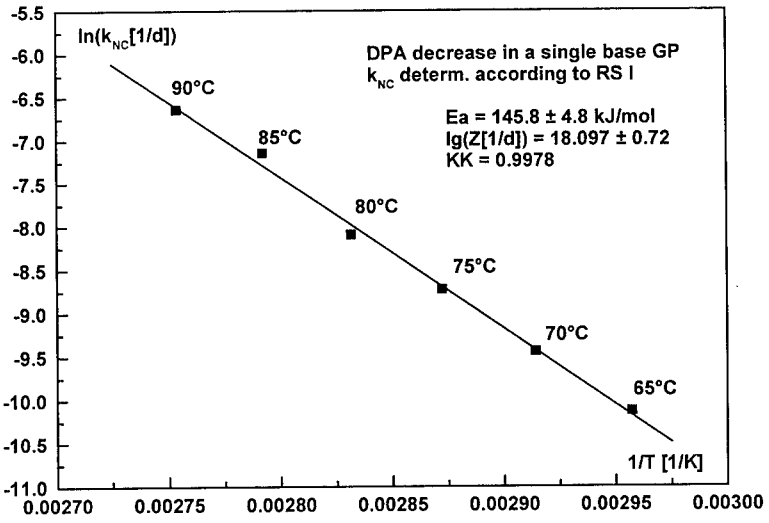

Abb. 1: Arrhenius-Plot der Reaktionsgeschwindigkeitskonstanten k_{NC} aus Stabilisatorverbrauchsdaten.

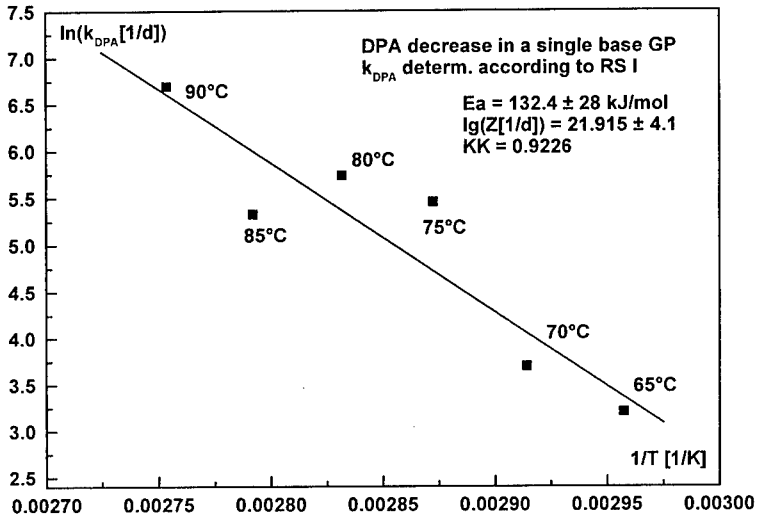

Abb. 2: Arrhenius-Plot der Reaktionsgeschwindigkeitskonstanten k_{DPA} der DPA Reaktion mit dem autokatalytisch wirksamen Produkt P.

rechnung. Wie in /1,2/ ausführlich begründet, ist die Anfangskonzentration $x_P(0)$ von P ungleich null, sie wurde hier zu $x_P(0)$ = 0,0075 mol/(mol ONO_2) gesetzt. Die Abb.1 und Abb. 2 zeigen die Arrhenius-Darstellungen der beiden Reaktionsgeschwindigkeitskonstanten k_{NC} und k_{DPA}. Die Korrelation ist bei k_{NC} mit KK=0.9978 recht gut, die k_{DPA}-Werte streuen.

2. NC-Zersetzungskinetik ermittelt mit TGA-MV

Zur Beschreibung von Massenverlustdaten (MV-Daten) mit kinetischen Ansätzen wurde schon eine systematisierte Vorgehensweise präsentiert /4,5,6/, welche der einfacheren Zugänglichkeit halber hier in Kürze angegeben wird. Gl.(3) zeigt den allgemeinen Ansatz einer autokatalytischen Zersetzung. Das Reaktionsprodukt B reagiert in einer zweiten Reaktion mit A und beschleunigt dessen Verbrauch. C steht für alle gasförmigen, S für alle festen Produkte. Daneben kann noch eine nichtreagierende Komponente N vorliegen.

$$A \xrightarrow{k_1} B + C + S \qquad \text{primäre Zersetzung}$$

(3) $$A + B \xrightarrow{k_2} 2\,B + C + S \qquad \text{autokatalytische Zersetzung}$$

Die Stoffmenge in mol an B(t,T) wird nach Gl.(4) aus A(t,T) gebildet.

(4) $$B(t,T) = B(0) + A(0) - A(t,T)$$

Insgesamt gilt dann für die Abnahme von A die Gl.(5), wobei für die primäre Zersetzung eine Reaktion 1. Ordnung angesetzt wird. In Gl.(5) wurde mit dem Anfangsgehalt A(0) an A, hier ist A = NC, normiert.

(5) $$\left.\left(\frac{d\left(\frac{A(t,T)}{A(0)}\right)}{dt}\right)\right|_T = -k_1(T)\cdot\frac{A(t,T)}{A(0)} - k_2(T)\cdot A(0)\cdot\frac{A(t,T)}{A(0)}\cdot\left(\frac{B(0)+A(0)-A(t,T)}{A(0)}\right)$$

Die Umformulierung zu Massen wird mit $M_A = A / m_A$ und analog für die anderen Reaktionspartner durchgeführt, wobei m_i die Molmasse der Komponente i ist. In Gl.(6) ist die Geschwindigkeitsgleichung für die normierte Masse von A, $M_{Ar}(t,T) = M_A(t,T) / M_A(0)$ angegeben. Die zugehörigen Reaktionsgeschwindigkeitskonstanten sind in Gl.(7) definiert. Ein Anfangsgehalt B(0) kann berücksichtigt werden.

(6) $$\left.\left(\frac{dM_{Ar}(t,T)}{dt}\right)\right|_T = -k^1_{ML}(T)\cdot M_{Ar}(t,T) - k^2_{ML}(T)\cdot M_{Ar}(t,T)\cdot\left(F + 1 - M_{Ar}(t,T)\right)$$

(7) $$k^1_{ML}(T) = k_1(T) \quad \text{und} \quad k^2_{ML}(T) = k_2(T)\cdot A(0) \quad \text{und} \quad F = \frac{M_B(0)}{M_A(0)}\cdot\frac{m_A}{m_B}$$

Die Integration der Gl.(6) mit der Anfangsbedingung $M_{Ar}(0)=1$ ergibt die Gl.(8).

$$(8) \quad M_{Ar}(t,T) = \frac{k^1_{ML}(T) + (F+1)\cdot k^2_{ML}(T)}{k^2_{ML}(T) + \left(k^1_{ML}(T) + F\cdot k^2_{ML}(T)\right)\cdot \exp\left(\left(k^1_{ML}(T) + (F+1)\cdot k^2_{ML}(T)\right)\cdot t\right)}$$

Gl.(8) wird als Modell '1. Ordnung-autokatalytisch' bezeichnet.

Selbst bei reinen Substanzen kann es einen Unterschied zwischen der Meßgröße M(t,T) und der gesuchten Größe $M_A(t,T)$ geben, da sich M(t,T) nach Gl.(9) zusammensetzt.

$$(9) \quad M(t,T) = M_N + M_A(t,T) + M_B(t,T) + M_S(t,T)$$
$$= M(0) - M_C(t,T)$$
$$\text{mit} \quad M(0) = M_N + M_A(0) + M_B(0) + M_S(0)$$

Für die Masse $M_B(t,T)$ gilt Gl.(10).

$$(10) \quad M_B(t,T) = B(t,T)\cdot m_B = M_B(0) + \frac{m_B}{m_A}\cdot\left(M_A(0) - M_A(t,T)\right)$$

Analog zu B(t,T) gilt C(t,T) = A(0) - A(t,T), woraus für $M_C(t,T)$, die Gl.(11) mit $m_C = m_A - m_B - m_S$ folgt.

$$(11) \quad M_C(t,T) = C(t,T)\cdot m_C = \frac{m_A - m_B - m_S}{m_A}\cdot\left(M_A(0) - M_A(t,T)\right)$$

Mit Gl.(11) erhält man aus Gl.(9) die Gl.(12), wobei die mit M(0) normierte Masse $M_r(t,T)$ mitangegeben ist.

$$M(t,T) = M(0) - \frac{m_A - m_B - m_S}{m_A}\cdot\left(M_A(0) - M_A(t,T)\right)$$

(12)

$$M_r(t,T) = \frac{M(t,T)}{M(0)} = 1 - \frac{m_A - m_B - m_S}{m_A}\cdot\frac{M_A(0)}{M(0)}\cdot\left(1 - M_{Ar}(t,T)\right)$$

In Gl.(12) wird Gl.(8) eingesetzt. Zu Anwendung kommt Gl.(13) für den Massenverlust MV.

$$(13) \quad MV(t,T) = O + 100\%\cdot\frac{M(0) - M(t,T)}{M(0)} = O + 100\%\cdot\left(1 - M_r(t,T)\right)$$

In /7/ sind TGA-Massenverlustmessungen (TGA-MV) an reiner Nitrocellulose mit einem N-Gehalt von 13,3 Mass.-% im Temperaturbereich 140°C bis 175°C durchgeführt und nach obigem Modell ausgewertet worden. Die Reaktionsgeschwindigkeitskonstanten zeigt die Tabelle 2. Nur die Anfangsdaten der Messungen wurden

benutzt, da sich NC mit zunehmender Zersetzung nach einem komplexeren Mechanismus zersetzt, auch bei niedrigeren Temperaturen /4,5,6,7,8/.

Tabelle 2: Reaktionsgeschwindigkeitskonstanten k_{NC} der primären NC-Zersetzung und k_{NCauto} der autokatalytischen NC-Zersetzung bestimmt aus TGA-Massenverlustmessungen /7,8/.

T [°C]	k_{NC} [1/d]	k_{NCauto} [1/d]	KK
140	0,2341	1,547	0,922
150	0,5858	5,988	0,986
160	1,970	16,934	0,988
165	3,802	27,289	0,998
175	11,405	91,584	0,993

Die Abbn 3 bis 6 zeigen die Arrhenius-Darstellungen der Reaktionsgeschwindigkeitskonstanten k_{NC} und k_{NCauto}, wobei in den Abbn 5 und 6 nur der Temperaturbereich 150°C bis 175°C verwendet wurde. Die Korrelation der Daten ist gut. Allerdings ergibt die zweie Auswertung schon deutlich andere Arrhenius-Parameter, so daß die Messung bei 140°C als nicht konsistent mit den Messungen bei den anderen Temperauren angesehen werden kann. Eine mögliche Erklärung ist das schon Wirksamwerden der zweiten Zersetzungsreaktion nach Gl.(1), welche mit niedrigerer Aktivierungsenergie abläuft, siehe Abschnitt 3. In der zweiten Auswertung sind die Unterschiede zwischen primärer und autokatalytischer Zersetzung deutlich ausgeprägt. Der Wert der Aktivierungsenergie der primären Zersetzung liegt mit dann Ea = 188,0 kJ/mol im Bereich, den auch andere gefunden haben /9,10/.

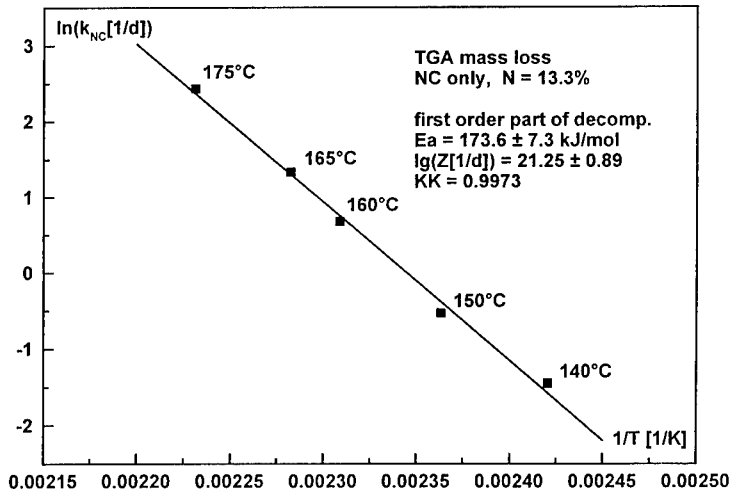

Abb. 3: Reaktionsgeschwindigkeitskonstante k_{NC} der primären NC-Zersetzung erhalten aus TGA-MV-Messungen zwischen 140°C und 175°C.

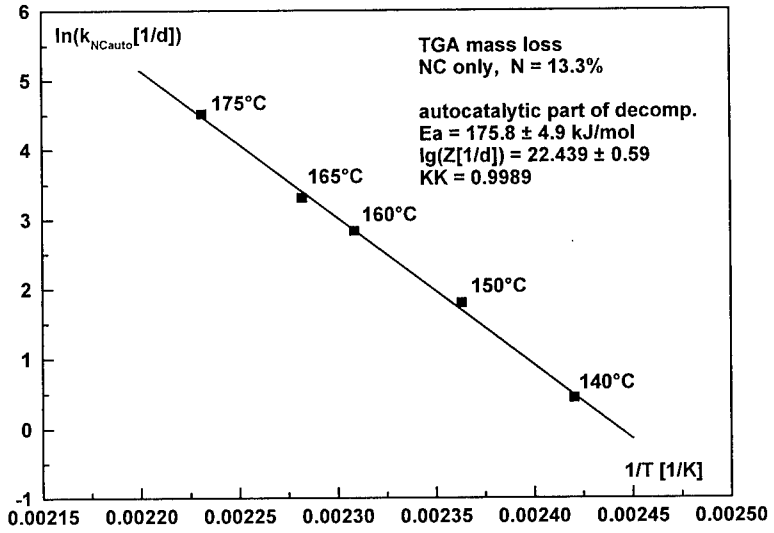

Abb. 4: Reaktionsgeschwindigkeitskonstante k_{NCauto} der autokatalytischen NC-Zersetzung erhalten aus TGA-MV-Messungen zwischen 140°C und 175°C.

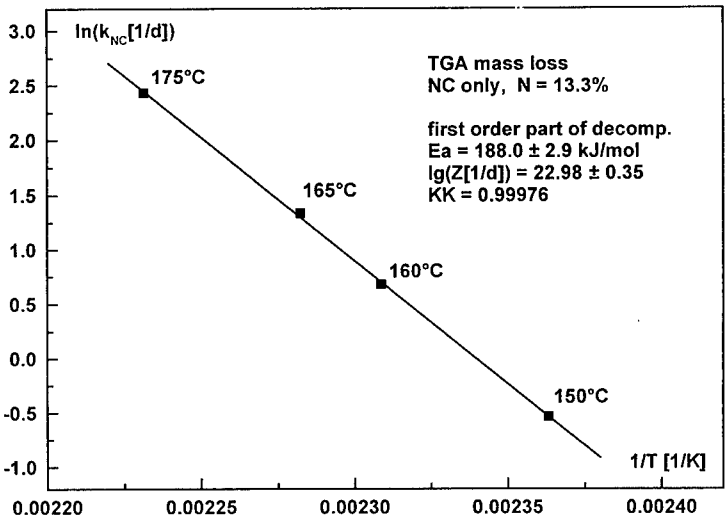

Abb. 5: Reaktionsgeschwindigkeitskonstante k_{NC} der primären NC-Zersetzung erhalten aus TGA-MV-Messungen zwischen 150°C und 175°C.

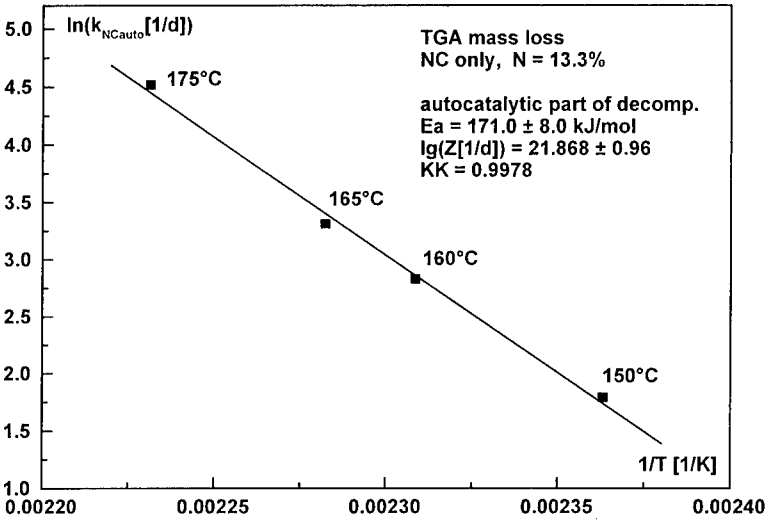

Abb. 6: Reaktionsgeschwindigkeitskonstante k_{NCauto} der autokatalytischen NC-Zersetzung erhalten aus TGA-MV-Messungen zwischen 150°C und 175°C.

3. Diskussion und Schlußfolgerung

Nach Abb. 1 ist die Aktivierungsenergie der NC-Zersetzung mit Ea = 145,8 kJ/mol im Temperaturbereich 65°C bis 90°C deutlich niedriger als im Hochtemperaturbereich 150°C bis 175°C mit Ea = 188,0 kJ/mol, Abb. 5, oder Ea = 173,6 kJ/mol im Bereich 140°C bis 175°C, Abb. 3. Die Interpretation ist, daß im unteren Temperaturbereich durch anteilige Hydrolyse der Salpetersäureestergruppe mit geringerer Aktivierungsenergie die bestimmbaren Zersetzungsraten eine niedrigere Aktivierungsenergie haben als es dem Wert für die Homolyse der CO-NO_2-Bindung mit einer Bindungsenergie um 170 kJ/mol entspricht. Nach /11/ hat die Hydrolyse der Salpetersäureestergruppe eine Aktivierungsenergie um 100 kJ/mol. In der Abb. 7 sind alle k_{NC}-Werte im Arrhenius-Diagramm aufgetragen. Die Aktivierungsenergie wird zu Ea = 139,5 kJ/mol bestimmt. Doch ist trotz guter Gesamtkorrelation zu erkennen, daß die Hochtemperaturwerte nicht ganz so gut auf der Geraden liegen. Ein sog. Knick in der Arrhenius-Darstellung ist daher vom Hoch- zum Mittel- bis zum Niedertemperaturbereich feststellbar. Auch für den Stabilisatorverbrauch und für die Molmassenabnahme der NC in einem einbasigen oberflächenbehandelten Treibladungspulver wurden solche Änderungen in Arrhenius-Diagramm festgestellt /12/, wobei im Niedertemperaturbereich der Molmassenabbau der NC

den sehr niedrigen Wert von Ea = 58,7 kJ/mol erreicht, was der Hydrolyse der glucosidischen Bindung der NC-Kette zugeordnet wird. Im Mitteltemperaturbereich von 70°C bis 100°C wird für den NC-Kettenabbau Ea = 144,0 kJ/mol gefunden, was dem Wert für k_{NC} zwischen 65°C und 90°C entspricht, Abb. 1.

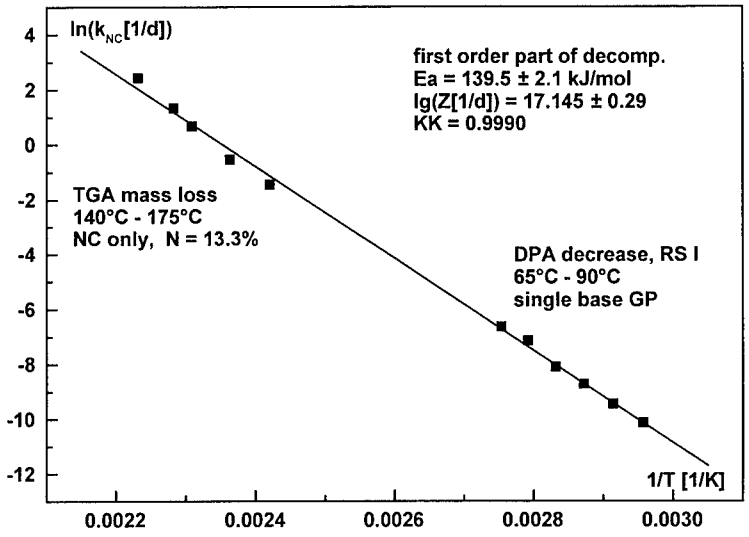

Abb. 7: Reaktionsgeschwindigkeitskonstante k_{NC} der primären NC-Zersetz-Zersetzung zwischen 65°C und 175°C, Kombination der Daten aus TGA-MV- und Stabilisatorverbrauchsmessungen.

5. Literatur

/1/ M.A. Bohn, N. Eisenreich
Kinetic modelling of the stabilizer consumption and the consecutive products of the stabilizer in a gun propellant
Propell. Expl. Pyrot. 22, 125-136 (1997).

/2/ M.A. Bohn, N. Eisenreich
Kinetische Modellierung der Stabilisatorkonzentrationsabnahme und der Stabilisatorfolgeproduktkonzentrationen in einem Treibladungspulver zur erweiterten Voraussage der sicheren Einsatzzeit
Bericht 18/96 für BMVg, Dezember 1996,
Fraunhofer-Institut für Chemische Technologie (ICT).

/3/ F. Volk, H. Neumann, M.A. Bohn
Untersuchungen an einem einbasigen TLP
Fraunhofer-Institut für Chemische Technologie (ICT).

/4/ M.A. Bohn
Systematische Darstellung der Alterung von Rohrwaffentreibmitteln und Raketenfesttreibstoffen
Paper 109 in Proceed. of the 28th Internat. Annual Conference of ICT 1997, pages 109-1 to 109-46, June 24 - 27, 1997, Karlsruhe, Germany. Fraunhofer-Institut für Chemische Technologie (ICT).

/5/ M.A. Bohn
Kinetic Modelling of the Ageing of Gun and Rocket Propellants for the Improved And Time-Extended Prediction of Their Service Lifetime
Proceed. of the 4th Conference on the 'Life Cycles of Energetic Materials', pages 188 to 225, March 29 to April 1, 1998, Fullerton, California, USA. Ed.: J.A. Sanchez, Los Alamos National Laboratory, Los Alamos, NM, USA.

/6/ M.A. Bohn
Modellierung von Meßgrößen zur quantitativen Beschreibung der Alterung von Rohrwaffentreibmitteln, Raketenfesttreibstoffen und Komponenten
Bericht 13/97_99 für BMVg, Mai 1999,
Fraunhofer-Institut für Chemische Technologie (ICT).

/7 N. Eisenreich
Beitrag zur Kinetik thermischer Zersetzungsreaktionen - Thermoanalytische Auswertung der Zersetzung von Nitrocellulose
Dissertation, Technische Universität München, 1978.

/8/ N. Eisenreich, A. Pfeil
Non-linear Least-Squares Fit of Non-Isothermal Thermoanalytical Curves. Reinvestigation of the Kinetics of the Autocatalytic Decomposition of Nitrated Cellulose
Thermochim. Acta 61, 13 (1983).

/9/ G.B. Manelis, Y.I. Rubtsov, L.B. Smirnov, F.I. Dubovitskii
Kinetics of the Thermal Decomposition of Pyroxilin
Kinetika i Katalis (Kinetics and Catalysis) 3, 42 (1962).

/10/ H.N. Volltrauer, A.Fontijn
Low-Temperature Pyrolysis Studies by Chemiluminescence Techniques - Real Time Nitrocellulose and PBX 9404 Decomposition
Comb. Flame 41, 313-324 (1981).

/11/ B. Lurie, Z. Valishina, V. Malchevski ICT-JT 1993
Kinetics and Mechanism of the Cellulose Nitrate Denitration and Degradation at the Thermal Decomposition and Hydrolysis
Proceed. 24th Internat. Annual Conference of ICT 1993, pages 57-1 to 57-19, June 29 - July 2, 1993, Karlsruhe, Germany,
Fraunhofer-Institut für Chemische Technologie (ICT).

/12/ M.A. Bohn, F. Volk
Aging behavior of Propellants Investigated by Heat Generation, Stabilizer Consumption and Molar Mass Degradation
Propell. Expl. Pyrotech. 17, 171-178 (1992).

Erkennen von Wechselwirkungen der Nitramine HMX und CL20 mit Formulierungskomponenten durch Computersimulation

Exploring of interactions of the nitramines HMX and CL20 with components in formulations by computer simulation

V. Thome, P.B. Kempa, M.A. Bohn

Fraunhofer-Institut für Chemische Technologie, ICT
Postfach 1240
D-76318 Pfinztal-Berghausen, Germany

Kurzfassung

Chemische Reaktionen sind für den Gebrauch von Treibmitteln, Explosivstoffen, Anzündmitteln und Gaserzeugungsformulierungen oft einsatz- und nutzungsbegrenzend. Die Kombination von Komponenten in solchen Formulierungen ist daher entscheidend für die Entwicklung solcher Stoffsysteme. Zur Zeit gibt es keine methodische, unmittelbare Voraussage möglicher Unverträglichkeiten und einsatzzeitbegrenzender chemischer Reaktionen. Zur Bewertung des Stabilitätsverhaltens sind umfangreiches Fachwissen und die experimentellen Bestimmungen zwingend. Die Möglichkeiten der Simulation von Wechselwirkungen zwischen Molekülen sind soweit entwickelt, um die Geeignetheit für diese Problematik untersuchen zu können. Es wird ein Weg diskutiert, mögliche chemische Reaktionen mit semiempirischen quantenchemischen Berechnungen zu erkennen. Als kristalline energetische Hauptkomponenten werden β-HMX (β-Oktogen) und ε-CL20 (ε-HNIW, Hexanitro-hexaaza-isowurtzitan) genommen. Reaktive Formulierungskomponenten sind der energetische Binder GAP (Glycidylazid Polymer) und Guanidin als Träger von NH_2-Gruppen.

1. Einleitung

Zwei Hauptgruppen quantenchemischer Berechnungsmethoden werden eingesetzt: 'ab initio'-Methoden und semiempirische Methoden. Prinzipiell benötigen 'ab initio'-Methoden keine experimentell bestimmten Atom- und Moleküleigenschaften. Von grundlegenden Ansätzen ausgehend werden alle Eigenschaften berechnet. Doch ist der Aufwand für die hier betrachteten Systeme und die Zielsetzung immer noch außerordentlich groß. Semiempirische Methoden verwenden genäherte Ansätze in der Beschreibung der Systeme. Diese enthalten Parameter, welche durch Anpassen an experimentelle Daten von Atomen zu bestimmen sind. Eine der ersten erfolgreichen Methoden war der MNDO-Ansatz (Modified Neglect of Diatomic Overlap) /1/. Eine wichtige Weiterentwicklung ist die AM1-Methode (Austin Model 1) /2/. Die verbesserte Anpassung der Modellparameter an die ex-

Paper 63 on the 31st International Annual Conference of ICT, June 27 to June 30, 2000, Karlsruhe, Germany, organized by Fraunhofer-Institut für Chemische Technologie (ICT).

perimentelle Daten und die Korrektur der weitreichenden Abstoßungen der Innerschalenwechselwirkung erlaubten, den Hauptnachteil der MNDO-Methode zu überwinden, die Beschreibung von Wasserstoffbindungen. Zudem wurde die Gesamtoptimierung der Parameterisierung verbessert. Die Parameterisierung ist sehr entscheidend für die Qualität einer semiempirischen Methode. Sie ist immer sehr aufwendig, besonders wegen des Auffindens des globalen Minimums der Parameteranpassung. Anfang der 1980iger Jahre entwickelte Stewart /3/ ein effektiveres Optimierungsverfahren, mit dem gleichzeitig sehr viele Parameter an die Daten vieler Atome in realisierbaren Rechenzeiten angepaßt werden konnten. Damit wird von vornherein das Auffinden des globalen Minimums erleichtert. Er nannte diese Methode mit neuer Parameterisierung PM3 (Parametric Method three). PM3 basiert auf der MNDO-Methode mit einer verbesserten Beschreibung der weitreichenden Wechselwirkungen, ähnlich wie bei AM1. In dieser Arbeit wird die PM3-Methode eingesetzt.

2. Vorgehensweise zum Erkennen reaktiver Wechselwirkungen

Um reale Komponentensysteme zu beurteilen, wird von aktuellen in Formulierugen eingesetzten Kristallisationsphasen der energetischen Stoffe ausgegangen, hier somit von β-HMX (β-Oktogen) und ε-CL20 (ε-HNIW, Hexanitro-hexaazaisowurtzitan). Die Kristallflächen mit ihrem Anteil an der Gesamtoberfläche des Kristalls sind festzustellen. Die prinzipiellen Reaktionsmöglichkeiten zwischen den Komponenten sind mit chemischer Kenntnis zu ermitteln. Die Erreichbarkeit der betreffenden Gruppen für eine reaktive Wechselwirkung ist zu bestimmen. Schließlich werden die realen Molekülkonfigurationen erstellt, welche die Eingangsdaten für die semiempirische quantenmechanische Rechnung sind.

Als Molekülbildner wurde das Programmsystem Cerius$^{2(TM)}$, Version 4 der Firma Molecular Simulations, Inc. (MSI), San Diego, Kalifornien, USA verwendet, welches auf einer Octane$^{(TM)}$-Workstation von Silicon Graphics Computer Systems, Inc., Mountain View, Kalifornien, USA betrieben wird. Damit wurden die Kristallstrukturen der β-Phase des HMX und der ε-Phase des CL20 erstellt. Die Oberflächen dieser Kristallstrukturen sind darstellbar und die Erreichbarkeit reaktiver Stellen beurteilbar. Mit Cerius$^{2(TM)}$ wurden dann die 'Supermoleküle' zusammengebaut, also die reaktive Anordnung zwischen Substrat-Molekül (β-HMX oder ε-CL20) und der gewählten Formulierungskomponente. Diese Supermoleküle sind der Ausgang für die PM3-Rechnungen, wozu das Programmsystem Win-MOPAC Version 2 eingesetzt wurde, welches auf der Großrechnerversion MOPAC 97 basiert. Das Programmsystem MOPAC (semiempirical Molecular Orbital Program /4/) wurde von Stewart entwickelt und wird von Fujitsu Limited, Japan angeboten. WinMOPAC wird auf einem MS-Windows$^{(TM)}$-Rechner betrieben.

Zum Beurteilen der Reaktivität zwischen den aktiven Stellen der Moleküle wird so vorgegangen, daß mit den Supermolekülen eine MOPAC-PM3-Rechnung zur Bestimmung der neuen optimalen Geometrie durchgeführt wird. Diese berechnete Geometrie wird verglichen mit der nach Cerius$^{2(TM)}$ erstellten Ausgangsgeometrie. Abstandsänderungen in den reaktiven Gruppen werden zur Beurteilung herangezogen. Damit die Kristall- und Formulierungssituation in der MOPAC-PM3-

Rechnung erhalten bleibt, werden die Koordinaten der Atome des Supermoleküls fixiert bis auf jene der reaktiven Gruppen. Von Interesse bei der Ermittlung möglicher reaktiver Wechselwirkungen sind die Partialladungen der einzelnen Atome, die Erreichbarkeit der Atome und Atomgruppen auf den kristallographischen Oberflächen, die Konfiguration, die geometrischen Koinzidenzen in Atomgruppen und grundsätzliche chemische Reaktivitäten. Davon sind bis auf den letzten Punkt die Daten mit den genannten Programmsystemen unmittelbar erhältlich.

In der Abb. 1 ist ein Beispiel für die molekulare Konstruktion eines reaktiven Angriffs zu sehen, erstellt mit mit Cerius$^{2(TM)}$. Das Guanidin, der Molekülteil ganz oben in der linken Hälfte der Abbildung, greift mit zwei seiner positivierten H-Atome eine Nitrogruppe des ε-CL20 auf dessen 011-Fläche an. Man erkennt erstens die gute Zugänglichkeit der Nitrogruppen auf dieser Oberfläche des ε-CL20 und zweitens die Koinzidenz der Abstände zwischen den H-Atomen des Guanidin und den O-Atomen der Nitrogruppe.

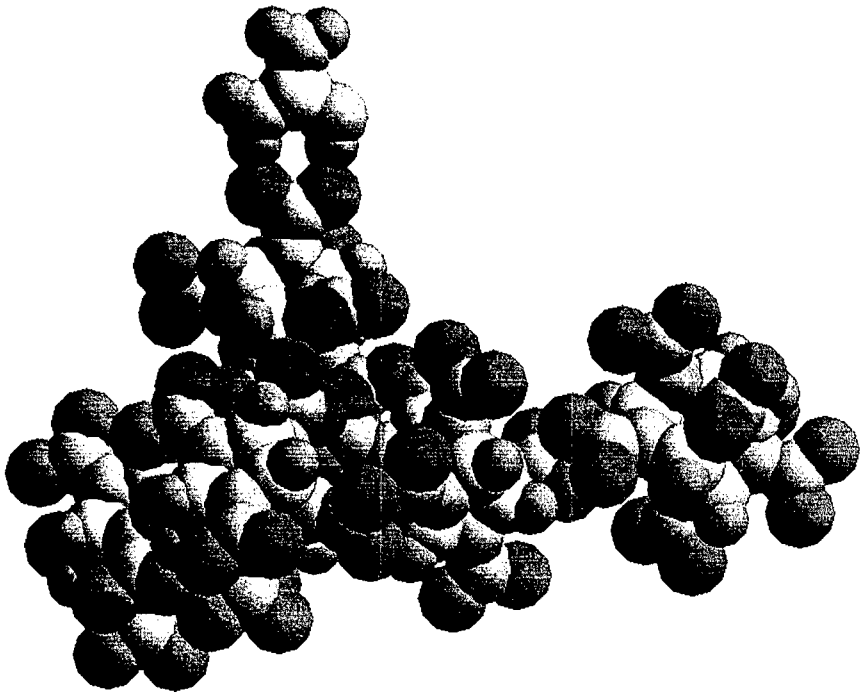

Abb. 1 Angriff des Guanidin (ganz oben, linke Hälfte) mit zwei seiner positivierten H-Atome auf die negativierten O-Atome einer Nitrogruppe des ε-CL20 auf dessen 011-Fläche.

3. Verwendete Komponenten und ihre Daten

Für neue leistungsgesteigerte Formulierungen sind die kristallinen Komponenten β-HMX (β-Oktogen) und das relativ neue ε-CL20 (ε-HNIW, Hexanitro-hexaaza-isowurtzitan) von Interesse. Untersuchungen mit ε-CL20 bestätigen ihm zwar eine gute thermische Stabilität als Einzelkomponente /5/, doch scheint es in Kontakt mit Formulierungskomponenten reaktiver als β-HMX zu sein. Manche Unterschiede könnten der noch nicht optimalen Produktqualität des ε-CL20 zugeordnet werden, doch es gibt Anzeichen für prinzipielle Unterschiede in der Reaktivität der beiden Stoffe. Als reaktive Formulierungskomponenten wurden der energetische Binder GAP (Glycidylazid Polymer) und Guanidin wegen der NH_2-Gruppen ausgewält. GAP als Polymer wird durch ein Fragment der Kette simuliert, welches die wesentlichen Komponenten des Polymeren wiedergibt. Zur Konstruktion des ε-CL20 wurden die kristallographischen Daten nach /6/ verwendet, für die des β-HMX nach /7/.

3.1 Konfiguration der Komponenten

In den Abb. 2 bis 5 werden die Moleküle in ihrer verwendeten Konfiguration gezeigt. In den Abbn. 2a, 2b und 3 sind ε-CL20 und β-HMX zu sehen, in den Abbn. 4 und 5 das GAP-Fragment bzw. GAP-Simulat und das Guanidin.

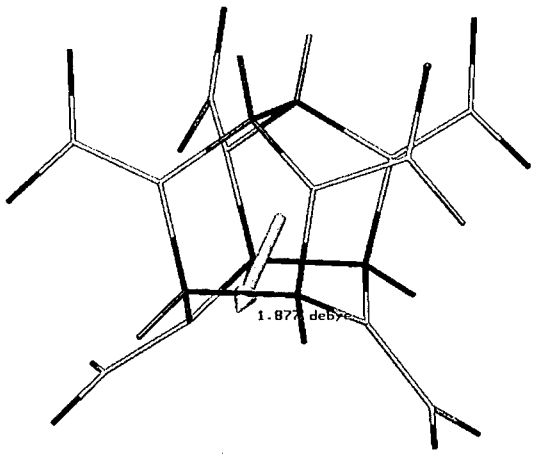

Abb. 2a: Stabmodelldarstellung des CL20-Moleküls in der ε-Phasengeometrie /6/, erstellt mit Cerius$^{2(TM)}$. Das ε-CL20 bildet ein molekulares Dipolmoment (dicker Pfeil als Dipolmomentvektor) aus. Der Wert von 1,877 D und die Richtung wurde mit einer PM3-Rechnung erhalten.

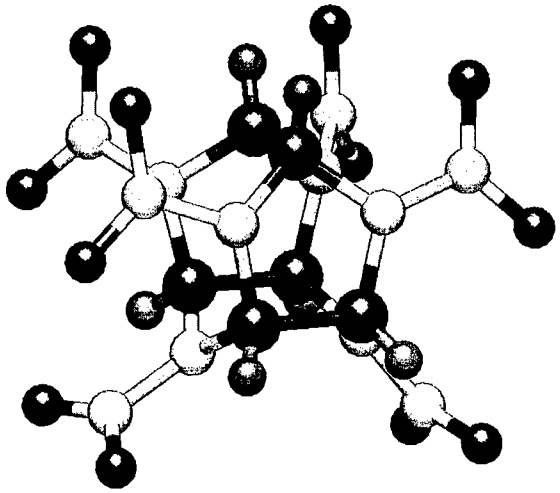

Abb. 2b: Wie Abb. 2a, aber in der Kugel-Stabmodelldarstellung, die einen besseren räumlichen Eindruck vermitteln kann. Ohne Darstellung des Dipolmomentvektors.

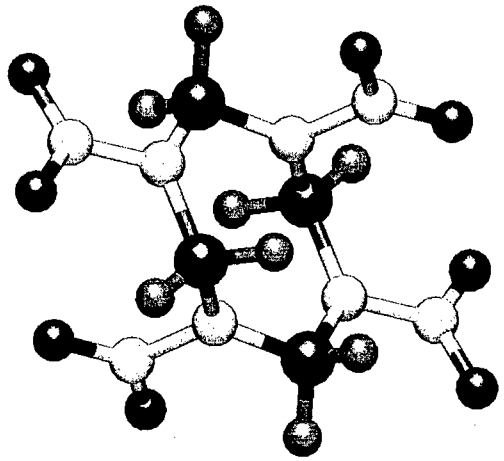

Abb. 3: HMX-Molekül in der β-Phasengeometrie /7/, erstellt mit Cerius$^{2(TM)}$. β-HMX bildet kein molekulares Dipolmoment aus.

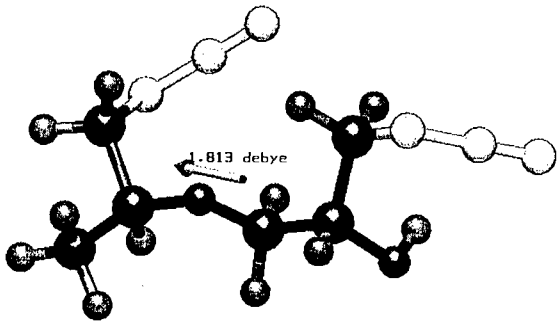

Abb. 4: GAP-Fragment in der optimierten Geometrie nach Cerius$^{2(TM)}$. Das molekulare Dipolmoment von 1,813 D wurde mit einer PM3-Rechnung erhalten.

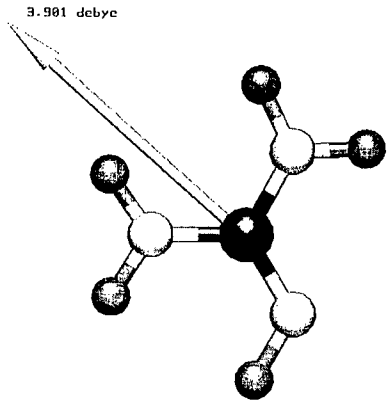

Abb. 5: Guanidin in der optimierten Geometrie nach Cerius$^{2(TM)}$. Das molekulare Dipolmoment von 3,901 D wurde mit einer PM3-Rechnung erhalten.

3.2 Partialladungen, Abstände und Bindungsordnungen

In den folgenden Abbildungen werden die Partialladungen P auf den Atomen, die Abstände d zwischen den Atomen und die Bindungsordnungen BO der Bindungen zwischen den Atomen angegeben. Partialladung und Bindungsordnung wurden mit MOPAC-PM3 für die Einzelmoleküle bestimmt, bei HMX und CL20 in deren β- und ε-Phasen-Konfiguration. Partialladungswerte sind vom Programmsystem bzw. von der Methode ihrer Bestimmung abhängig. Die Abstände sind die nach Cerius$^{2(TM)}$ entsprechend den Kristallstrukturdaten und nach den standardisierten Regeln des Aufbaus organischer CHNO-Moleküle.

3.2.1 ε-CL20

Beim CL20 sind zwei Gruppen von Atomen interessant, die NO_2-Gruppierung der Nitramingruppen, welche als Abgangsgruppe in Form von NO_2 oder HNO_2 fungieren kann, und die einzelnen H-Atome an den C-Atomen des Käfigs. Die sechs Nitramingruppen und die drei CH-CH-Gruppierungen haben alle etwas verschiedene interatomare Abstände, Partialladungen und Bindungsordnungen. Für die Nitramingruppen und die CH-CH-Gruppierungen werden je zwei in den Abb. 6 und 7 bzw. Abb. 8 und 9 angegeben.

3.2.2 β-HMX

Wie beim CL20 sind zwei Gruppen von Atomen interessant, die NO_2-Gruppierung der Nitramingruppen und die H-Atome an den C-Atomen des Achtrings. Die vier Nitramingruppen und die vier HCH-Gruppierungen bilden zwei Untergruppen mit je etwas unterschiedlichen Daten, aber innerhalb der Untergruppen sind die Daten gleich. Im Gegensatz zum ε-CL20 unterscheiden sich beim β-HMX die beiden H-Atome in ihren Partialladungen sehr.

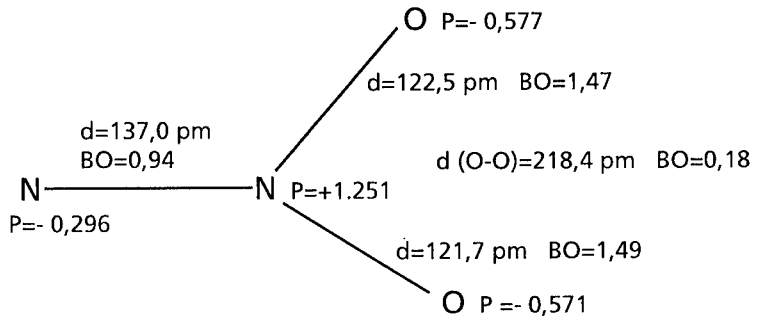

Abb. 6: Eine der vier oberen Nitramingruppen in Abb. 2 der sechs CL20-Nitramingruppen.

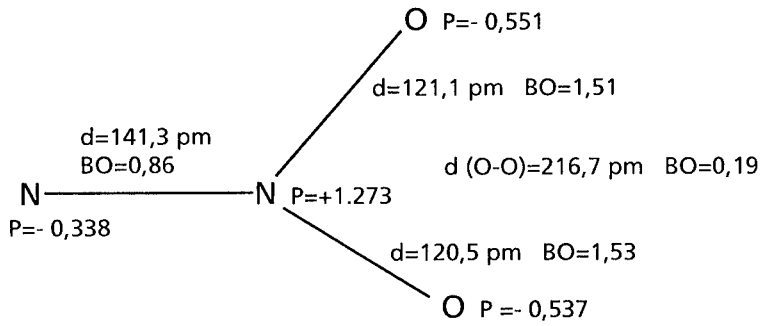

Abb. 7: Eine der zwei unteren Nitramingruppen in Abb. 2 der sechs CL20-Nitramingruppen.

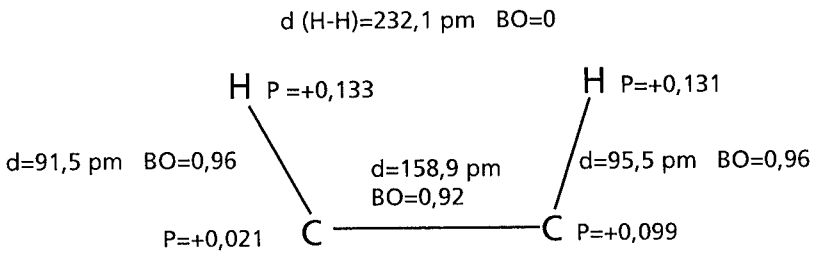

Abb. 8: Die in Abb. 2 obere der drei CL20-CH-CH-Gruppierungen des CL20.

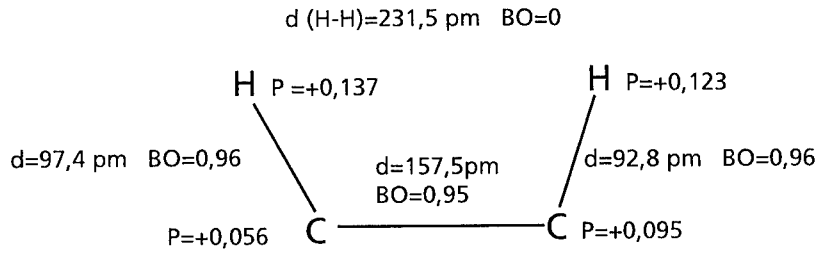

Abb. 9: Eine der in Abb. 2 zwei unteren der drei CL20-CH-CH-Gruppierungen des CL20.

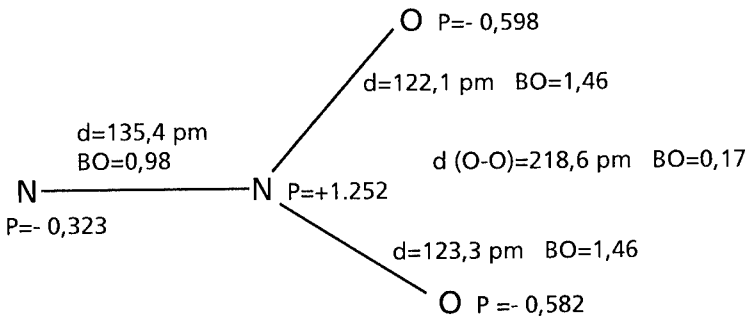

Abb. 10: Erste Untergruppe mit zwei der vier HMX-Nitramingruppen.

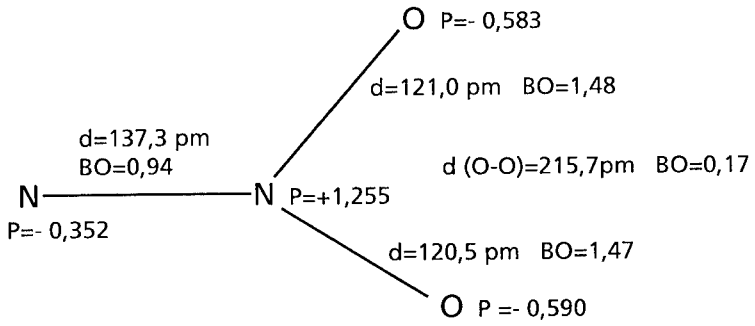

Abb. 11: Zweite Untergruppe mit zwei der vier HMX-Nitramingruppen.

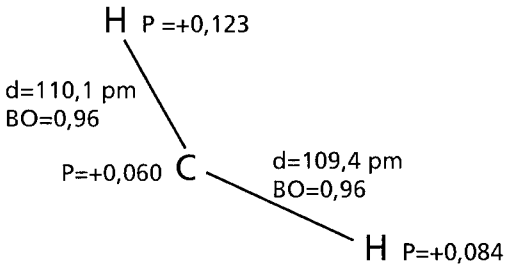

Abb. 12: Erste Untergruppe mit zwei der vier HMX-HCH-Gruppen.

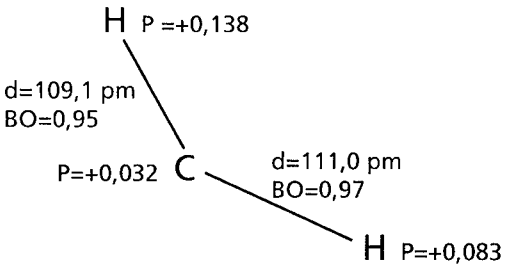

Abb. 13: Zweite Untergruppe mit zwei der vier HMX-HCH-Gruppen.

3.2.3 GAP-Simulat

Beim GAP sind die Azidgruppen ein reaktiver Molekülteil. Das GAP-Simulat enthält zwei C-N_3-Gruppierungen mit je etwas unterschiedlichen Daten, hier wird nur eine Gruppe mit ihren Daten in der Abb. 14 gezeigt.

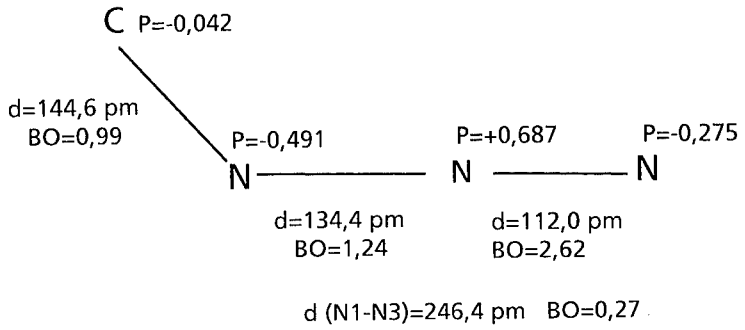

Abb. 14: Daten der C-N_3-Gruppe des GAP-Simulats.

3.2.4 Guanidin

Die Daten des Guanidin sind in der Abb. 15 zu sehen.

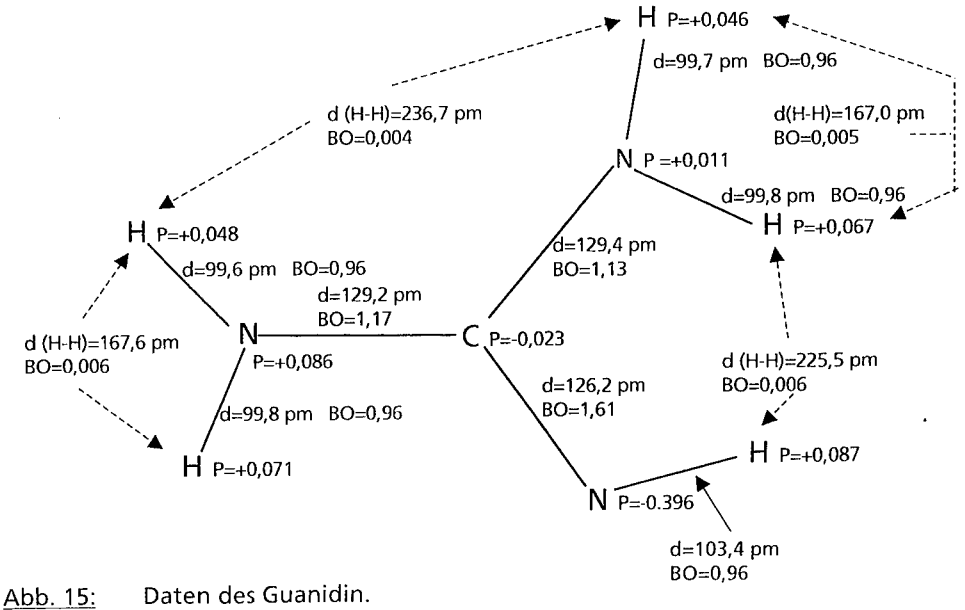

Abb. 15: Daten des Guanidin.

3.3 Flächenanteile und Gruppenzugänglichkeit des ε-CL20-Kristalls

Die Tabelle 1 und die Abb. 16 zeigen den Anteil der Flächen des ε-CL20-Kristalls an dessen Gesamtoberfläche als Funktion der Dielektrizitätskonstanten der Umgebung.

Tabelle 1: Anteil der Flächen des ε-CL20-Kristalls an der Gesamtoberfläche als Funktion der Dielektrizitätskonstanten DK.

DK	1	1,5	2	2,5	3	4	5	10	20	40
Fläche	Flächenanteil in %									
1 1 0	50,4	51,9	52,8	53,1	53,3	52,0	50,6	44,6	39,1	35,8
1 1 -1	12,2	12,6	12,7	12,5	12,2	11,4	10,8	9,2	7,9	7,0
1 2 0	6,9	4,6	2,7	1,4	0,6	0,0	0,0	0,0	0,0	0,0
1 1 -2	7,3	6,7	6,1	5,5	5,1	4,2	3,7	1,7	0,6	0,2
0 2 0	2,0	1,4	1,3	1,1	0,9	0,8	0,8	0,8	0,6	0,4
0 1 1	8,9	10,3	11,9	13,4	14,7	17,3	18,9	25,1	30,6	33,8
0 0 2	12,4	12,5	12,7	12,9	13,1	13,4	13,6	13,3	12,0	10,8
1 0 -1	0,0	0,0	0,0	0,0	0,0	0,9	1,7	4,9	7,8	9,7
1 0 1	0,0	0,0	0,0	0,0	0,0	0,0	0,0	0,0	0,0	2,2
1 1 1	0,0	0,0	0,0	0,0	0,0	0,0	0,0	0,0	0,0	0,0

Die Daten sind mit einer Elementarzelle erstellt worden, deren Oberflächenenergie mit der DK als Parameter energieminimiert wurde. Beim Kristallwachstum in

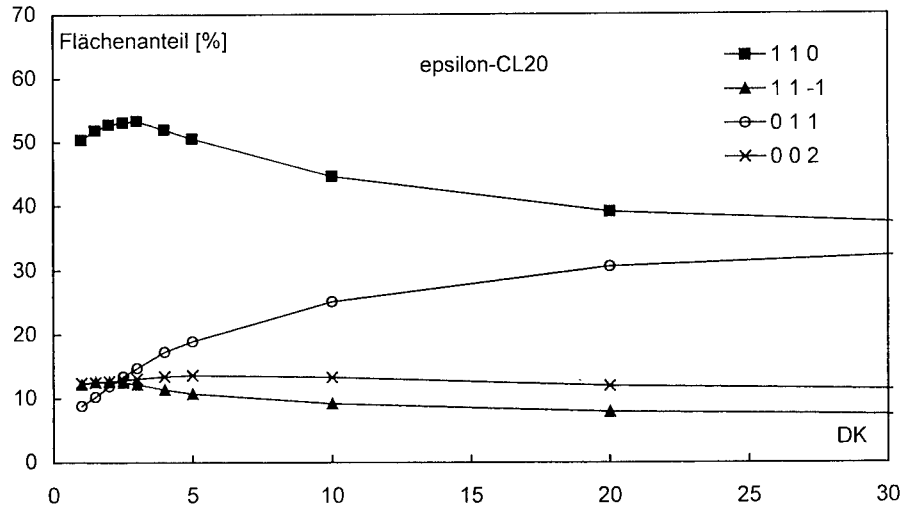

Abb. 16: Flächenanteile an der Gesamtoberfläche des ε-CL20-Kristalls als Funktion der Dielektrizitätskonstanten DK der Umgebung. Es sind nur die Flächen mit den größten Anteilen gezeigt.

der jeweiligen DK-Umgebung und alleiniger Kontrolle durch die elektrostatisch bestimmte Kristalloberflächenenergie stellen sich diese Flächenanteilverhältnisse

ein. Diese Daten wurden mit dem Programmsystem MSI- Cerius$^{2(TM)}$ erzeugt. Der Vergleich mit der experimentellen Kristallstruktur ergibt ein Flächenanteilverhältnis wie bei etwa DK = 4. Die Fläche 110 hat den weitaus gößten Anteil, gefolgt von den Flächen 11-1, 011 und 002 mit je etwa 12% bis 15% Anteil. Die 011-Fläche nimmt mit der DK zu, die 110-Fläche nimmt analog dazu ab. Auf der 110-Fläche sind die NO_2-Gruppen nach außen gerichtet und gut erreichbar. Die Wasserstoffatome der CH-CH-Gruppierung sind beide gut zugänglich. Die 110-Fläche zeigt für alle diskutierten Wechselwirkungskonfigurationen gute Zugänglichkeit. Die 011-Fläche bietet an den NO_2-Gruppen eine gute Möglichkeit für einen Guanidin-Angriff, siehe Abb. 1, aber weniger für GAP. Auf 002 und 11-1 ist ein Zugang zu den H-Atomen und auch die Möglichkeit für Guanidin, die NO_2-Gruppen zu erreichen.

3.4 Flächenanteile und Gruppenzugänglichkeit des β-HMX-Kristalls

In der Tabelle 2 und der Abb. 17 sind der Anteil der Flächen des β-HMX-Kristalls an dessen Gesamtoberfläche als Funktion der Dielektrizitätskonstanten der Umgebung dargestellt. Zur Erzeugung dieser Daten gilt das schon in Abschnitt 3.3 Gesagte. Mit der experimentellen Kristallstruktur kann eine DK = 3 bis 5 zugeordnet werden. Die Fläche 011 hat den weitaus gößten Anteil, gefolgt von den Flächen 11-1 und 020 mit je etwa 35% und 15% Anteil. Beim β-HMX können auf der 011-Fläche fast alle hier diskutierten Angriffsmöglichkeiten realisiert werden, allerdings oft geometrisch nicht so gut wie beim ε-CL20. Ein wichtiger Unterschied zum ε-CL20 ist, daß der Angriff an zwei H-Atomen eines Moleküls gleichzeitig nicht möglich ist. Zudem ist von der HCH-Gruppierung immer nur ein H-Atom erreichbar.

Tabelle 2: Anteil der Flächen des β-HMX-Kristalls an der Gesamtoberfläche als Funktion der Dielektrizitätskonstanten DK.

DK	1	1,5	2	3	4	5	10	20	40
Fläche	Flächenanteil in %								
1 1 -1	29,5	30,5	31,4	32,3	32,7	33,1	34,2	34,9	34,8
2 1 -1	0,1	0,0	0,0	0,0	0,0	0,0	0,0	0,0	0,0
1 0 0	0,0	0,1	0,0	0,0	0,1	0,2	0,7	1,4	2,0
1 1 1	0,6	0,0	0,0	0,0	0,0	0,0	0,0	0,0	0,0
0 2 0	2,8	5,1	7,8	10,6	12,1	13,1	15,4	16,4	17,0
0 1 1	67,0	64,4	60,8	57,1	55,1	53,6	49,8	47,1	44,9
1 0 -2	0,0	0,0	0,0	0,0	0,0	0,0	0,0	0,0	1,3
110	0,0	0,0	0,0	0,0	0,0	0,0	0,0	0,0	0,0

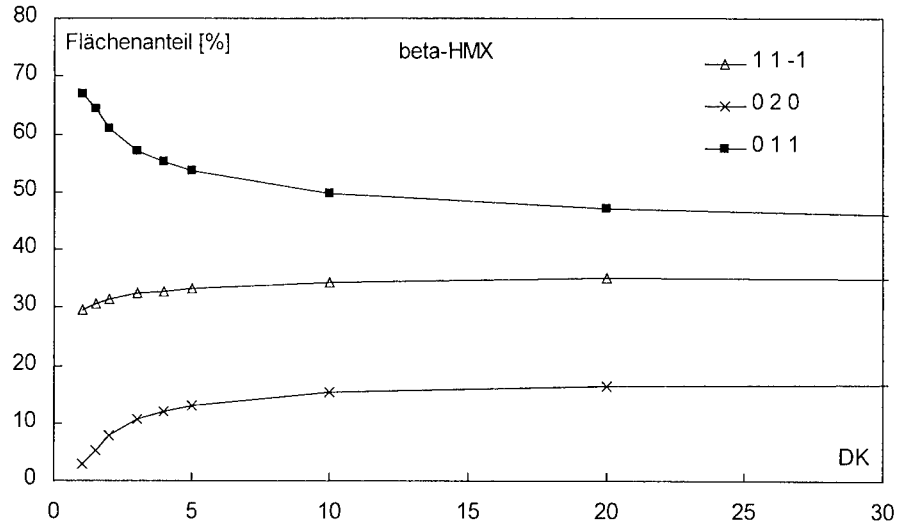

Abb. 17: Flächenanteile an der Gesamtoberfläche des β-HMX-Kristalls als Funktion der Dielektrizitätskonstanten DK der Umgebung. Es sind nur die Flächen mit den größten Anteilen gezeigt.

3.5 Mögliche reaktive Konfigurationen

Reaktive Konfigurationen zeigen die Abb. 18 bis 23. Die Partialladungen an den Atomen führen zu möglichen Anordnungen. Wenn die geometrischen Abstände in etwa übereinstimmen, können die elektronischen Wechselwirkungen zur Umverteilung der Bindungen hin zu energetisch günstigeren Atomkonfigurationen führen, was eine chemische Reaktion bedeutet. Die N_3-Kette mit ihren beiden negativierten N-Atomen liegt im Abstandsbereich der H-Atome der CH-CH-Gruppierung des ε-CL20. Analog koinzidieren die Abstände der anderen Konfigurationen in der Abb. 20 und der Abb. 21. Drei reaktive Konfigurationen sowohl mit GAP als auch mit Guanidin wurden formuliert.

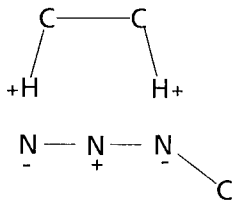

Typ GAP-DNH

Abb. 18: Angriff der N_3-Kette des GAP auf die positivierten Wasserstoffatome der CH-CH-Gruppierung des ε-CL20.

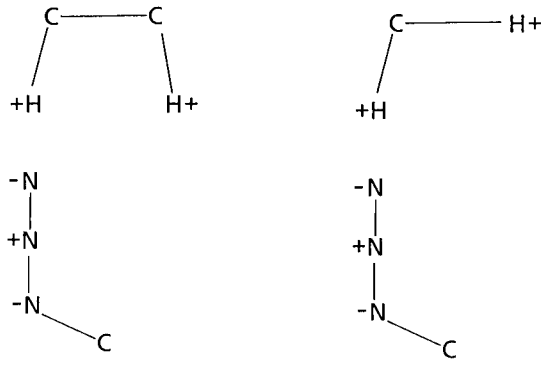

Typ GAP-NH

Abb. 19: Angriff der N_3-Kette des GAP auf ein positiviertes Wasserstoffatom der CH-CH-Gruppierung des CL20 oder der HCH-Gruppierung des HMX.

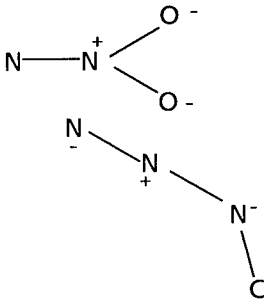

Typ GAP-Dipol

Abb. 20: Dipolarer Angriff der N_3-Kette des GAP auf den lokalen Dipol der NO-Gruppierung der Nitramingruppen.

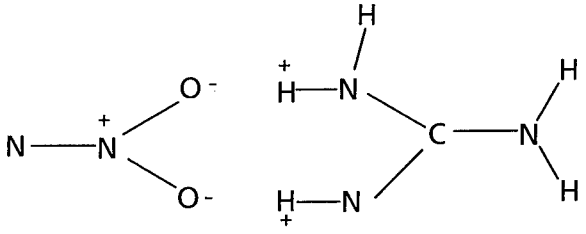

Typ Gua-DHO

Abb. 21: Angriff des Guanidins mit benachbarten positivierten Wasserstoffatomen auf die negativierten Sauerstoffatome der Nitramingruppen.

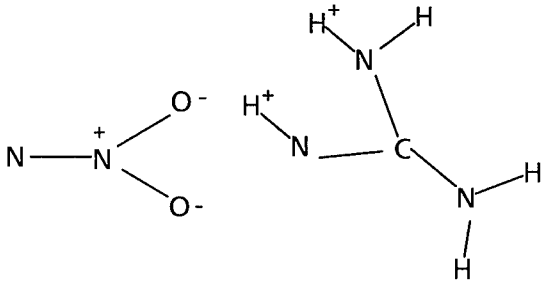

Typ Gua-HO

Abb. 22: Angriff des Guanidins mit einem positivierten Wasserstoffatom auf die negativierten Sauerstoffatome der Nitramingruppen.

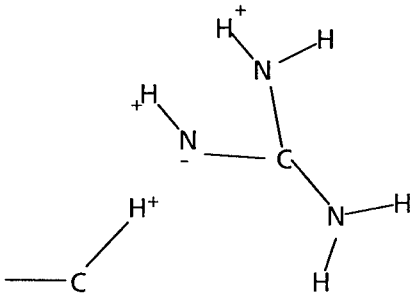

Typ Gua-NH

Abb. 23: Basischer Angriff des Guanidin auf ein positiviertes Wasserstoffatom der CL20 - CH-CH - oder der HMX - HCH -Gruppierung.

4. Ergebnisse und Diskussion

Die Bewertung, ob eine reaktive Wechselwirkung vorliegt, basiert auf den Abstandsänderungen zwischen den Atomen in den reaktiven Gruppen. Sie wird immer im Vergleich zur Ausgangssituation durchgeführt.

4.1 ε-CL20

4.1.1 Reaktionen mit GAP

Alle drei reaktive Konfigurationen sind zwischen ε-CL20 und GAP möglich. Beim Typ GAP-DNH wird eine Bindungsverlängerung einer C-H-Bindung in der CH-CH-Gruppierung um 5,5% gefunden, was als eine Tendenz zur H-Atomübertragung auf die Azidgruppe interpretiert wird. Diese Tendenz ist beim Typ GAP-NH noch

vorhanden. Dort beträgt die C-H-Bindungsverlängerung allerdings nur etwa 2,5%. Der Typ GAP-Dipol läßt eine Wechselwirkung erkennen, welche die Tendenz zur NO_2-Abspaltung zur Folge hat.

4.1.2 Reaktionen mit Guanidin

Die drei oben angegebenen reaktiven Konfigurationen mit Guanidin sind bei ε-CL20 möglich. Der Typ GUA-DHO erzeugt eine Tendenz zur NO_2-Gruppenabspaltung. Der Angriff auf die N-NO_2-Gruppe ist direkt möglich, es gibt keine Hinderung durch Nachbarbereiche. Die N-NO_2-Gruppe und Guanidin können in einer Ebene liegen. Guanidin wirkt mit den NH- / NH_2-Gruppen als Reduktionsmittel für die Nitramingruppe. Auch beim Typ Gua-HO zeigt sich der selbe Effekt. Der Typ Gua-NH wirkt auf die C-H-Gruppierung protonenabziehend, was als C-H-Bindungsverlängerung bemerkbar ist.

4.2 β-HMX

4.2.1 Reaktionen mit GAP

GAP kann mit β-HMX nur in zwei der angegebenen Weisen in Wechselwirkung treten, nach Typ GAP-NH und Typ GAP-Dipol. Beim Typ GAP-NH kommt es zwar zu einer analogen reaktiven Konfiguration wie bei ε-CL20, aber die C-H-Bindungsverlängerung ist reaktiv nicht signifikant, sie beträgt nur 1,4%. Zudem kann nur ein H-Atom der HCH-Gruppierung erreicht werden. Die Konfiguration GAP-Dipol ist wirksam, aber nicht so ausgeprägt wie beim ε-CL20. Insgesamt sind die reaktiven Wechselwirkungen zwischen GAP und β-HMX nur schwach ausgeprägt.

4.2.2 Reaktionen mit Guanidin

Alle drei Typen konnten realisiert werden. Beim Typ Gua-NH ist der Zugang zum H-Atom hier besser möglich als beim ε-CL20, eine Reaktion zwischen Guanidin und β-HMX ist daher wahrscheinlicher als zwischen Guanidin und ε-CL20. Der Typ Gua-HO erzeugt wie beim ε-CL20 die Tendenz zur NO_2-Gruppenabspaltung, doch ist dies beim ε-CL20 ausgeprägter. Der Angriff des Guanidin beim Typ Gua-DHO auf die β-HMX-NO_2-Gruppen ist in keinem Fall geometrisch so gut möglich wie beim ε-CL20. Auch hier kann man noch eine mögliche Tendenz zur NO_2-Gruppenabspaltung erkennen, aber ε-CL20 erscheint wiederum reaktiver als β-HMX.

5. Schlußfolgerung

Mit der Simulation der Wechselwirkungen der Nitramine β-HMX und ε-CL20 mit den Komponenten GAP und Guanidin wurden reaktive Konfigurationen über Bindungslängenänderungen zugeordnet. Für GAP wurde ein repräsentatives Ket-

tenteil als Simulat eingesetzt. Guanidin wirkt bei beiden kristallinen Substanzen in vergleichbarer Weise reaktiv, jedoch mit höherer Tendenz bei ε-CL20. Nach den benutzten Kriterien zeigt GAP mit ε-CL20 eine erhöhte Reaktivität im Vergleich zu β-HMX. Die positiven Partialladungen der H-Atome sind im Mittel beim ε-CL20 größer als beim β-HMX, zudem ist mindestens ein C-Atom der CH-CH-Gruppe beim ε-CL20 positivierter, was die H-Abspaltung beim ε-CL20 gegenüber β-HMX erleichert. Die vorgestellte Methode ist noch nicht absolut einsetzbar. Man ist zunächst immer auf chemische Kenntnis über mögliche Reaktionsmechanismen angewiesen, desweiteren muß sie im Vergleich eingesetzt werden. Weitere Ansätze zur Beurteilung reaktiver Wechselwirkungen sind zu untersuchen, z.B. das Verfahren des Übergangszustands.

6. Literatur

/1/ M.J.S. Dewar, W. Thiel
J. Am. Chem. Soc. 99, 4899ff und 4907ff (1977).

/2/ M.J.S. Dewar, E.G. Zoebisch, E.F. Healy. J.J.P. Stewart
J. Am. Chem. Soc. 107, 3902 (1985).

/3/ J.J.P. Stewart
J. Comput. Chem. 10, 209 (1989).

/4/ J.J.P. Stewart
QCPE 455 (1983).

/5/ S. Löbbecke, M.A. Bohn, A. Pfeil, H.H. Krause
Thermal Behavior and Stability of HNIW (CL20)
Paper 145 in Proceed. of the 29th Internat. Annual Conference of ICT 1998, pages 145-1 to 145-15, June 30-July 3, 1998, Karlsruhe, Germany.
Fraunhofer-Institut für Chemische Technologie (ICT), D-76318 Pfinztal.

/6/ Cambridge Cristallographic Data Center (CCDC), Cambridge CB2 IEZ, UK
Crystal data of CL20 phases, CCDC-Nr 124 947 to 124 950
Authors: Loic Toupet, Université de Rennes, France,
Louis Ricard, Ecole Polytechnique de Palaiseau, France,
G. Jacob, G. Cagnon, SNPE, Vert-fe-Petit, France.

/7/ C.S. Choi, H.P. Boutin
Acta Cryst. B26, 1235-1240 (1970).

MOLECULAR SIMULATION OF THE MORPHOLOGY OF ENERGETIC MATERIALS

Volker Thome, Paul Bernd Kempa, Michael Herrmann, Ulrich Teipel, Walter Engel

Fraunhofer Institut für Chemische Technologie / Joseph-von-Fraunhofer-Straße 7
D-76327 Pfinztal / Berghausen

Introduction

Computer simulation is used to study crystals and crystallization processes. Understanding and controlling of such processes is of interest for industry, as numerous examples in chemical and pharmaceutical industries show, that crystal morphology affects milling, grinding, filtration, dissolution rate, density and texture optimization. Crystal morphology, for example spherical or plate-like crystals, could influence the mechanical properties of products. In the same way the morphology of energetic ingredients is an important parameter for processing highly filled polymer matrices, which are used for solid propellants. β-HMX and ammonium nitrate, phase IV, were chosen to demonstrate, that the prediction of their morphologies is possible with computer simulation.

Method

A MSI Octane station with the program Cerius 4.0 was used for simulating the morphology using the atomic data and the charge distribution of any system with special fields of force.

First step: geometric approach

In a first step the morphology was calculated after the method of Bravais Friedel Donnay Harker (BFDH), which uses the crystal lattice and the symmetry to calculate the relative growth rates of the crystal faces. Generally, observed crystal morphology is found to be

dominated by lower-order faces. The relationship between centre to face distance and lattice plane spacing is given by:

$D \sim 1/d_{hkl}$

D = centre to face distance

d_{hkl} = lattice plane spacing

Second step: energetic approach

In a second step the morphology was calculated after the attachment energy method, which takes inter- and intramolecular energies (coulomb and van der Waals forces) of the system into account. The attachment energy is calculated for a series of suitable slices, found with the BFDH method. From the energy calculation and the growth rate a centre to face distance is assigned to each face. The attachment energy E_{att} is defined as the energy release on the attachment of a growth slice to a growing crystal surface.

$E_{att} = E_{latt} - E_{slice}$

E_{latt} = lattice energy of a crystal

E_{slice} = energy of a growth slice of thickness d_{hkl}

The charge distributions of β-HMX and ammonium nitrate, phase IV, were calculated after the charge equilibrium method (QEq) [1] and used together with the Universal Force Field (UFF) [2] for estimating the lattice energy. For this procedure an approximation is implemented for nonbonded interactions between atoms at large distances using a spline function or, alternatively, an Ewald summation.

With β-HMX, possessing no dipole moment (see fig. 1), the lattice energy consists mainly of van der Waals forces. Therefore the interaction treatment of energies between the atoms of β-HMX was summed for separation within a spline on radius. Interactions at larger separations are also summed, however, with reduced magnitude according to a spline function. The spline function decays to zero at a spline-out radius such that larger separations may be ignored.

The results of HMX are presented in fig. 2 – 4. Fig. 2 shows a crystal built up by a geometric approach. The crystal in fig. 3 has been refined using the energetic approach. The SEM photograph in fig. 4 represents a crystal prepared experimentally for comparison.

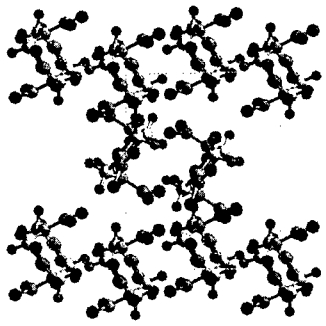

Fig. 1: Crystal structure of β-HMX
carbon grey, hydrogen green, oxygen red, nitrogen blue

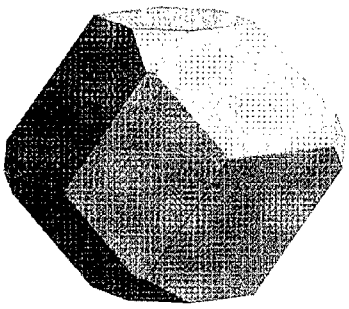

Fig. 2: Morphology of β-HMX, geometric approach after BFDH method

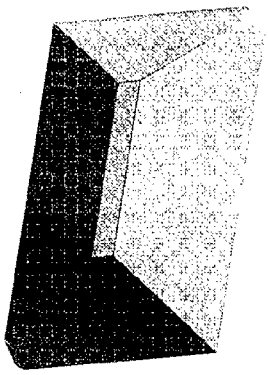

Fig. 3: Morphology of β-HMX, energetic approach calculated with a spline function

Fig. 4: Morphology of β-HMX, purchased from Dyno Industrier

In contrary to β-HMX the ammonium nitrate phase IV lattice energy is dominated by coulomb forces (see fig. 5). For such an ionic system an Ewald summation [3] is recommended. This method uses the Ewald reciprocal space sum for calculating the energy and force contribution of all atoms within the elementary cell. The results of the geometric and the following energetic approaches are represented in fig. 6 and 7. The crystal in fig. 7 represents a better

approach to experimentally found needles, elongated in the a-axis, which occurs at supersaturations above 2% [4].

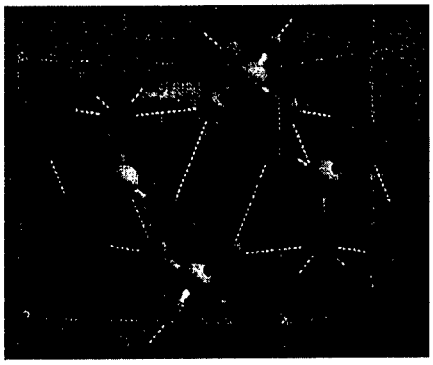

Fig. 5: Crystal structure of ammonium nitrate IV
yellow: H-bonds

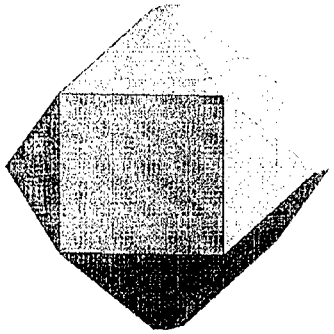

Fig. 6: Morphology of ammonium nitrate IV
geometric approach after BFDH method.

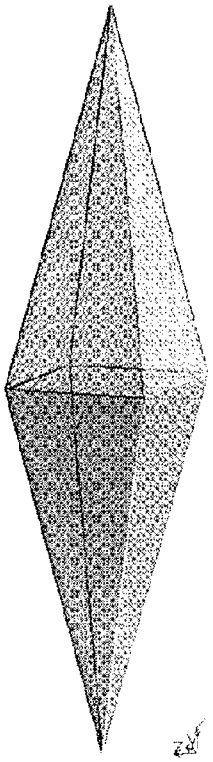

Fig. 7: Morphology of ammonium nitrate IV
energetic approach calc. with Ewald summation

Conclusions

The results show the relevance of choosing the appropriate approximation method. The accurate morphology is only obtained when the calculation is done with a spline function for β-HMX and an Ewald summation for ammonium nitrate, phase IV.

The BFDH morphology applied to ammonium nitrate, phase IV, failed to predict a needle like shape, whereas the attachment energy method succeeded, if the interaction energies were

treated with the appropriate approximation method. Therefore the choice of an Ewald summation for morphology prediction of an organic molecule, which is predominated by van der Waals forces, would lead to inaccurate results.

References

[1] Anthony K. Rappe, W. A. Goddard III; „Charge Equilibration for Molecular Dynamics Simulations"; *J. Phys. Chem.* 1991, *95*, 3358-3363

[2] C. J. Casewit, K. S. Colwell and A. K. Rappe; „Application of a Universal Force Field to Organic Molecules"; *J. Am. Chem. Soc.* 1992, *114*, 10035-10046

[3] N. Karasawa and W. A. Goddard III; *J. Phys. Chem.* 93, (1989), 7320;

[4] Roger J. Davey, Peter D. Guy, Barbara Mitchell, Andrew J. Ruddick and Simon N. Black; „The Growth of Phase IV Ammonium Nitrate Crystals and their Transformation to the Phase III Structure"; J. Chem. Soc. Faraday Trans 1, 1989, 85(7), 1795-1800

Stability of nitrocellulose in ignition mixtures

Uldis Ticmanis [1], Manfred Kaiser [1], Michael Künstlinger [1], Klaus Redecker [2]

[1] Wehrwissenschaftliches Institut für Werk-, Explosiv- und Betriebsstoffe, Ast Heimerzheim, Großes Cent, 53913 Swisttal (Germany)
[2] Dynamit Nobel GmbH Explosivstoff- und Systemtechnik, Standort Stadeln, Kronacher Str. 63, 90785 Fürth (Germany)

Abstract

Three pyrotechnics compositions were examined for thermal stability of their nitrocellulose binder by TGA and DTA. The resulting non-autocatalytic kinetics indicated a high stability at ambient temperatures.

1 Introduction

Thermal stability is not generally a problem of mixtures containing primary explosives or pyrotechnics compositions used for ignition. If not used in perfectly sealed systems their, ageing will be determinated more by oxidation reactions with water or air. Pure thermal stability of some organic primary explosives (e.g. tetrazene and diazodinitrophenol) were examined in the past and found to be sufficient to withhold the stress expected in the service life time [1, 2, 3]. In many compositions nitrocellulose (NC) is used as binder and based on experience on propellants [4, 5] we assumed that this compound may considerably limit the stability of these mixtures as well. For this reason three compositions containing different amounts of NC were selected for investigations of decomposition kinetics (table 1).

Table 1 Composition of the ignition mixtures

Low NC content	Medium NC content	High NC-content
$PbCrO_4$	$BaCrO_4$	ZnO_2
$KClO_4$	$KClO_4$	PbO_2
Sb	W	Ti
NC (~ 1%)	$BaSiF_6$	Fe
	SiO_2	B
	NC (~ 2%)	NC (~ 6%)

The mixtures L (Low NC content) and M (Medium NC content) are used for ignition time delay in a delay element and in a detonator. Mixture H (High NC content) serves to ignite a propellant charge. The compositions do not contain just the same type of NC but all are relatively low nitrated (about 12% nitrogen).

2 Estimation of activation energy

Values of the activation energy in the total decomposition range were gained from simultanous DTA/TG measurements using low heating rates and aluminium crucibles slightly closed with a lid in order to achieve favourable conditions for autocatalytic reactions. Due to the different NC contents the experiments were carried out with sample weights of about 150, 100 and 20 mg for the mixtures L, M, and H. The heating rates (in K/min) are marked in the graphs (fig. 1, 2 and 3). Composition M shows a secondary reaction of NC (fig. 1), the second TGA step in fig. 3 is due to the decomposition of zinc peroxide.

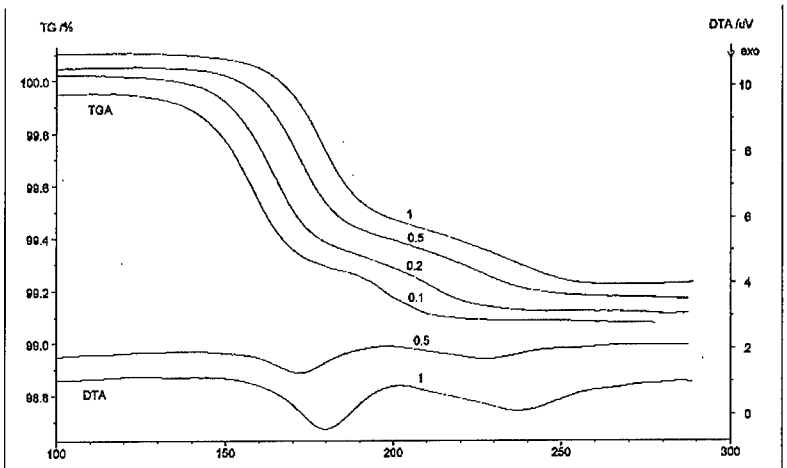

#-INSTRUMENT	DATEI	VERSUCHS-ID	PROBE	DATUM	MASSE	SEGM.	BEREICH	ATMOS.	KORR
1 - STA 429	A9593K01.SST	A9593K01.SST	AZM 09593	18.02.2000	152.610 mg	3/ 3	77 °C/0.1(K/min)/275 °C		000
2 - STA 429	A9593K02.SST	A9593K02.SST	AZM 09593	18.02.2000	137.350 mg	3/ 3	77 °C/0.2(K/min)/290 °C		400
3 - STA 429	A9593K05.SST	A9593K05.SST	AZM 09593	22.02.2000	153.020 mg	3/ 3	77 °C/0.5(K/min)/285 °C		000
4 - STA 429	A95931C.GST	A9593K1c.SST	AZM 09593	22.02.2000	153.710 mg	3/ 3	77 °C/1.0(K/min)/290 °C		400

Figure 1 Dynamic DTA/TG of composition L

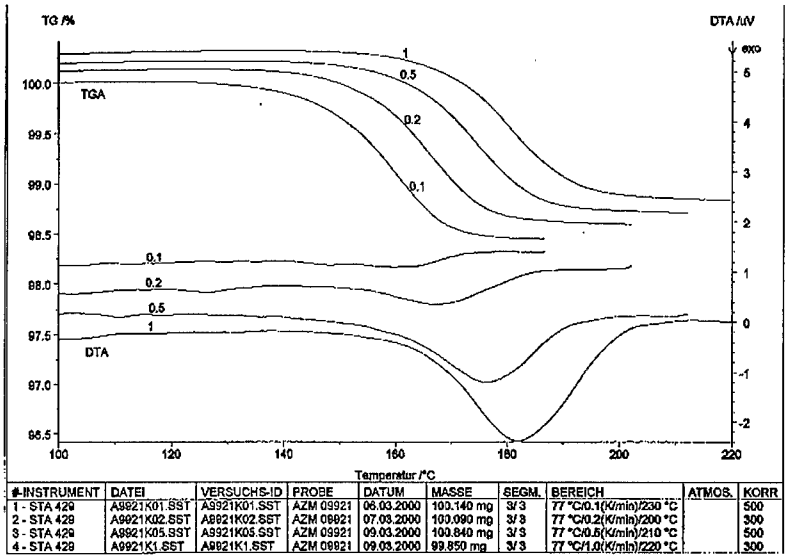

#-INSTRUMENT	DATEI	VERSUCHS-ID	PROBE	DATUM	MASSE	SEGM.	BEREICH	ATMOS.	KORR
1 - STA 429	A9921K01.SST	A9921K01.SST	AZM 09921	06.03.2000	100.140 mg	3/3	77 °C/0.1(K/min)/230 °C		500
2 - STA 429	A9921K02.SST	A9921K02.SST	AZM 09921	07.03.2000	100.090 mg	3/3	77 °C/0.2(K/min)/200 °C		300
3 - STA 429	A9921K05.SST	A9921K05.SST	AZM 09921	09.03.2000	100.840 mg	3/3	77 °C/0.5(K/min)/210 °C		500
4 - STA 429	A9921K1.SST	A9921K1.SST	AZM 09921	09.03.2000	99.850 mg	3/3	77 °C/1.0(K/min)/220 °C		300

Figure 2 Dynamic DTA/TG of composition M

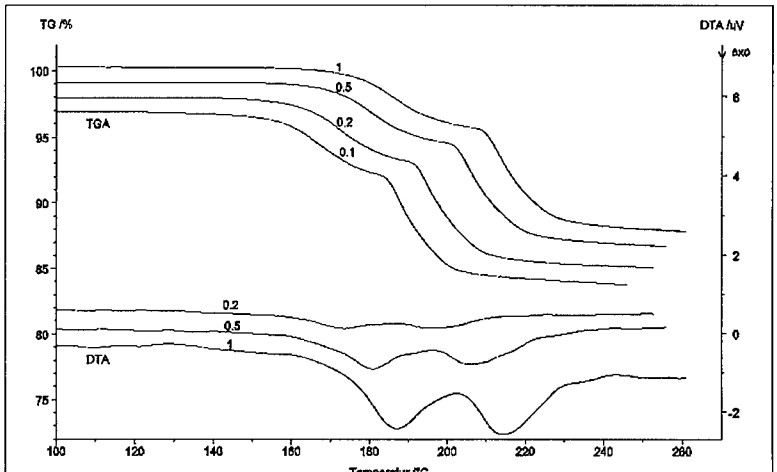

#-INSTRUMENT	DATEI	VERSUCHS-ID	PROBE	DATUM	MASSE	SEGM.	BEREICH	ATMOS.	KORR
1 - STA 429	09661K01.SST	09661K01.SST	AZM 09661	22.11.1998	20.060 mg	1/1	25 °C/0.1(K/min)/245 °C		400
2 - STA 429	09661K02.SST	09661K02.SST	CL 20 S	20.11.1998	20.000 mg	1/1	25 °C/0.2(K/min)/260 °C		300
3 - STA 429	09661K05.SST	09661K05.SST	AZM 09661	21.11.1998	20.360 mg	1/1	25 °C/0.5(K/min)/255 °C		500
4 - STA 429	09661K1.SST	09661K1.SST	AZM 09661	21.11.1998	20.290 mg	1/1	25 °C/1.0(K/min)/280 °C		300

Figure 3 Dynamic DTA/TG of composition H

For checking the activation energy in the whole decomposition region, we used the isoconversional („iso-α“) method of Kissinger [6]

$$\ln\frac{H}{T_\alpha^{\,2}} = A' - \frac{E}{RT_\alpha} \qquad (1)$$

H = heating rate [k/min]
T_α = Temperature for equal reaction degree (here : mass loss) at different heating rates
A‘ = constant value for iso-α-points
E = activation energy [kJ/mole]
R = gas constant [=0.0083143 kJ/mole·K]

The results are plotted in the figures 4, 5 and 6:

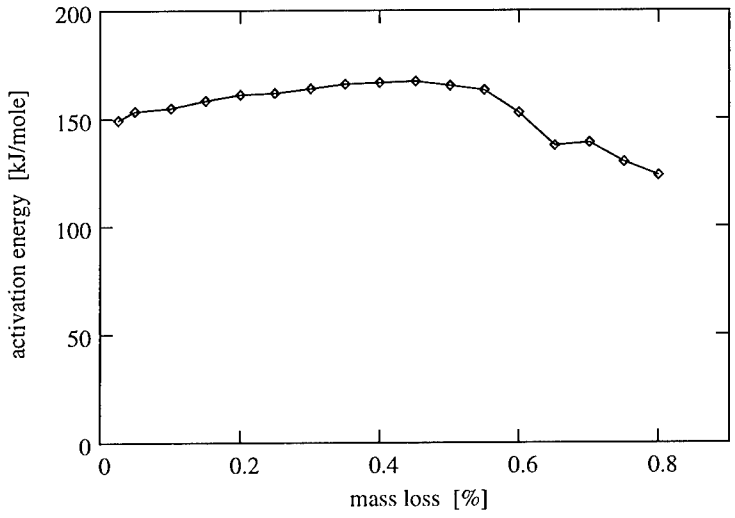

Figure 4 Activation energy of NC decomposition in mixture L

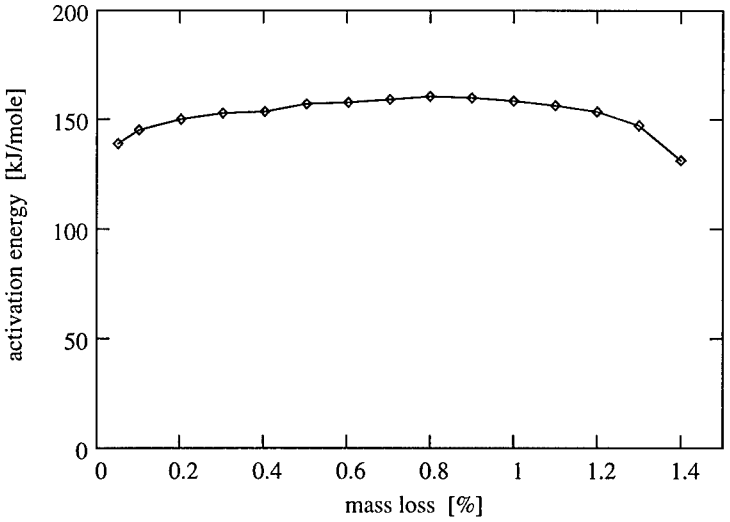

Figure 5 Activation energy of NC decomposition in mixture M

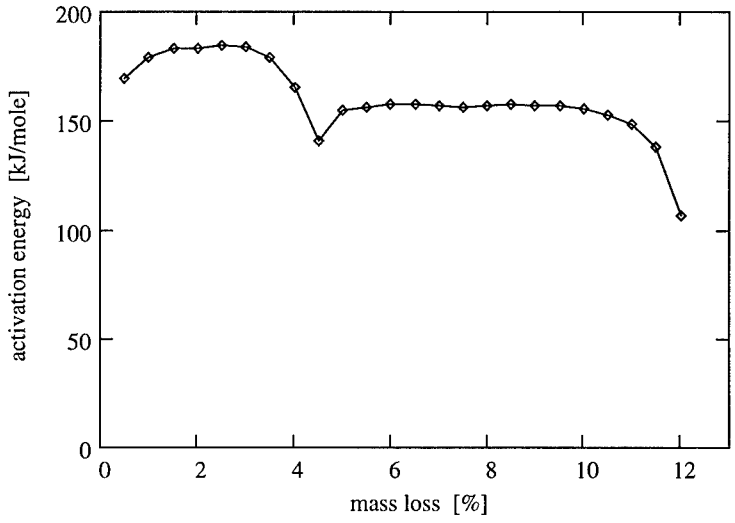

Figure 6 Activation energy of the decomposition of NC and ZnO_2 in mixture H

Mixture L (fig. 4) shows a nearly constant level up to a mass loss of 0.6% (mean value 161.4 kJ/mole) followed by a decrease due to the dominance of the secondary reaction. Fig. 5 indicates only relatively small differences in the whole reaction area (mean value 154.5 kJ/mole) of composition M. The third mixture H (fig. 6) is characterized by two levels corresponding to the reaction of NC and zinc peroxide (mean value of NC decomposition 178.6 kJ/mole).

3 Determination of the reaction model

The type of a reaction can be detected more easily by isothermal TGA. Therefore in addition we made some measurements at constant temperature calculated for a time for total reaction of about 1000 min from the dynamic experiments [1].
It was found that in all three cases the decomposition of NC follows a first order reaction (eq. 2) with high precision.

$$G = G_e(1-e^{-kt}) \qquad (2)$$

G = mass loss [%]
G_e = mass loss after complete reaction [%]
k = reaction rate constant [s^{-1}]
t = reaction time [s]

The fittings (fig. 7, 8 and 9) demonstrate the excellent correlation of calculated and measured (marked points) values.

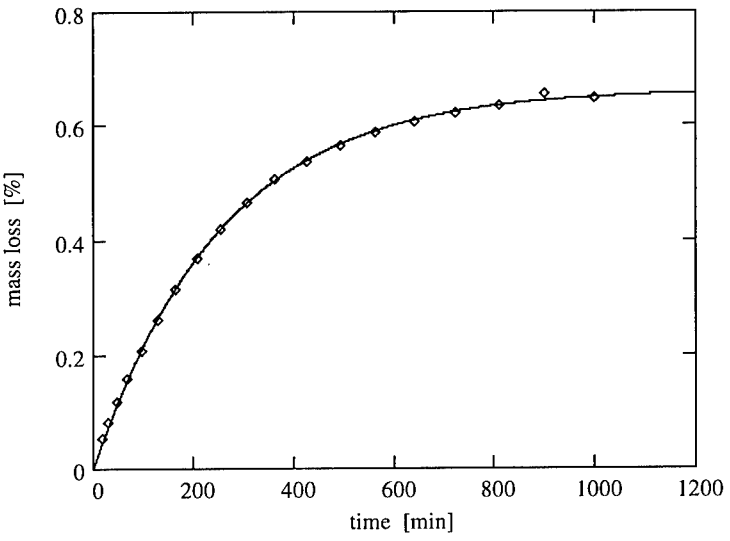

Figure 7 First order fitting of NC decomposition at 150.2 °C in mixture L

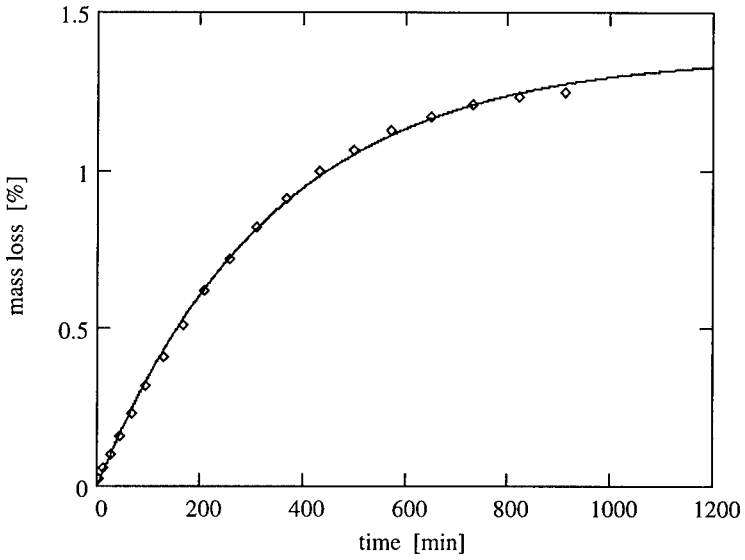

Figure 8 First order fitting of NC decomposition at 150.2 °C in mixture M

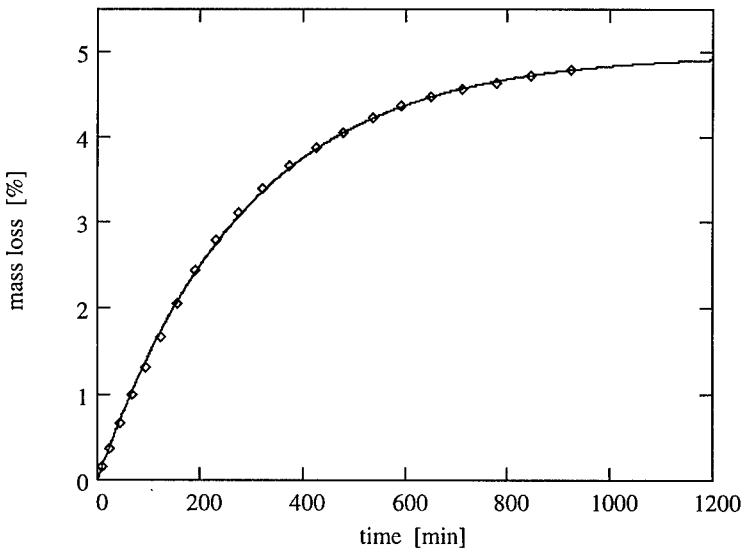

Figure 9 First order fitting of NC decomposition at 159.6 °C in mixture H

Using the obtained values for the reaction rate constants and the mean activation energy values mentioned above, the frequency factors (A) can be calculated from

$$A = k \cdot e^{E/RT} \qquad (3)$$

The parameters of the first order reactions are listed in table 2

Table 2 First order reaction constants

Composition	Activation energy [kJ/mole]	Frequency factor [s^{-1}]	Total mass loss G_e [%]
L	161.4	5.4317×10^{15}	0.663
M	154.5	5.6638×10^{14}	1.370
H	178.6	2.1125×10^{17}	4.9851

4 Extrapolation tests

To check the validity of the kinetics at lower temperatures and in a closed system the compositions L and H were stored in hermetically sealed glas ampoules for 38 days (L) and 34 days (H). Even assuming highly conservative extrapolation theories this means a thermal stress equivalent to a storage at 25 °C for at least 100 years [7]. Figures 10 and 11 show the TGA of the mixtures before and after storage. The observed mass loss difference (0.06%) of the primary reaction of mixture L (fig. 10) is equal to the measured difference (0.27%) of the sum of both reactions (decomposition of NC and zinc peroxid) is higher then calculated for NC (0.05%). Moreover, the separation step is considerably reduced. The reason may be the autocatalytic decomposition characteristics of zincperoxid. These Prout-Tompkins type reactions own a well calculable „memory effect" which means that after storage at lower temperatures, with decomposition below a detectable limit the reaction is accelerated in a following high temperature test.

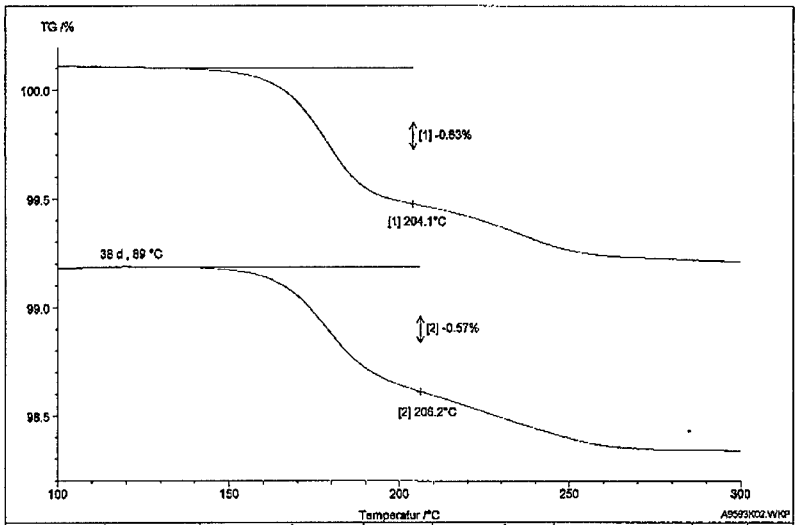

#-INSTRUMENT	DATEI	VERSUCHS-ID	PROBE	DATUM	MASSE	SEGM.	BEREICH	ATMOS.	KORR
1 - STA 429	A9593K1B.SST	A9593K1b.SST	AZM 09593	19.02.2000	135.420 mg	1/1	25 °C/1.0(K/min)/400 °C		600
2 - STA 429	A9593K1G.SST	a9593K1g.SST	AZM 09593	16.05.2000	134.350 mg	1/1	29 °C/1.0(K/min)/330 °C		300

Figure10 Dynamic TGA (1K/min) after long time storage of mixture L

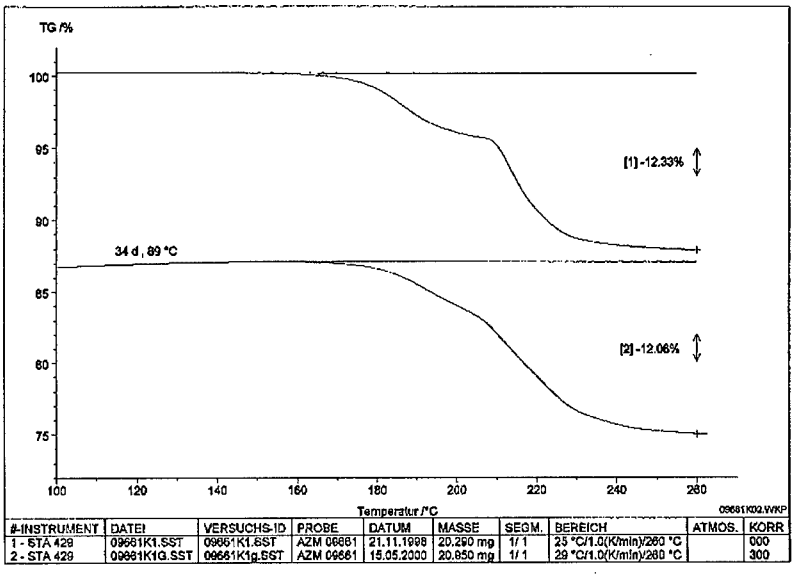

#-INSTRUMENT	DATEI	VERSUCHS-ID	PROBE	DATUM	MASSE	SEGM.	BEREICH	ATMOS.	KORR
1 - STA 429	09661K1.SST	09661K1.SST	AZM 09661	21.11.1999	20.290 mg	1/1	25 °C/1.0(K/min)/260 °C		000
2 - STA 429	09661K1G.SST	09661K1g.SST	AZM 09661	15.05.2000	20.850 mg	1/1	29 °C/1.0(K/min)/260 °C		300

Figure11 Dynamic TGA (1K/min) after long time storage of mixture H

5 Discussion

As a consequence of the investigations we had to revise our somewhat hasty opinion that a NC-binder generally limits the thermal stability of pyrotechnics compositions. Even by assuming a decomposition degree of 2% of the original NC content to be critical for burning charactristics, the obtained kinetics indicate that this value will be reached after a 10 years storage at temperatures between 50 and 60 °C. Of course this high stability may be not realised for bad quality NC and for compositions with internal incompatibility of this compound.

References

[1] M. Kaiser, U. Ticmanis, Thermochim. Acta 250 (1995) 137

[2] S. Wilker, G. Pantel, M. Kaiser, U. Ticmanis, ICT-Jahrestagung 26, 84 (1995)

[3] M. Kaiser, W. Scheunemann, U. Ticmanis, ICT-Jahrestagung 26, 30 (1995)

[4] U. Ticmanis, G. Pantel, L. Stottmeister, ICT-Jahrestagung 29, 27 (1998)

[5] U. Ticmanis, S. Wilker, G. Pantel, M. Kaiser, P. Guillaùme, C. Balès, N. van der Meer, ICT-Jahrestagung 31, 2 (2000)

[6] H.E. Kissinger, Anal.Chem. 29 (1957) 1702

[7] STANAG 4582, „Explosives, Single and Double Base Propellants, Stability Test Procedure and Requirements using Heat Flow Calorimetry" Draft (4/00).

RHEINMETALL
W&M

UNTERSUCHUNGEN ZUM EINFLUSS DER UMGEBUNGSBEDINGUNGEN BEI EXPLOSIVEN KOMPONENTEN

Dr. Almuth Keßler und Wolfgang Stein
RHEINMETALL W&M GmbH, Heinrich-Ehrhardt-Straße 2
29345 Unterlüß

Abstract

In the course of various investigations the question of how ambience conditions influence explosive components arose. In this context the moisture of the components and how it changes when assembling the ammunition, storing it subsequently and finally firing it from the weapon plays a decisive role.
In this respect investigations were made which identify and describe the interdependence of the components and the ambience conditions as well as their interrelations.
The results of these investigations are discussed by example of a double-base propellant as well as 120 mm combustible cartridge cases.

Zusammenfassung

Im Rahmen verschiedener Untersuchungen traten Fragen bzgl. des Einflusses der Umgebungsbedingungen auf explosive Komponenten auf. In diesem Zusammenhang spielt unter Umständen die Feuchtigkeit der Komponenten und deren Änderung bei der Laborierung von Munition, der anschließenden Munitionslagerung und schließlich bei dem Beschuß in der Waffe eine entscheidende Rolle.

RHEINMETALL W&M

Zu diesem Thema wurden Untersuchungen durchgeführt, die die Abhängigkeiten der Komponenten von Umgebungsbedingungen sowie deren Beziehungen untereinander nachweisen und beschreiben.

Die Ergebnisse der Untersuchungen werden am Beispiel von 2-basigem Treibladungspulver (DB-TLP) sowie von 120mm verbrennbaren Hülsenmaterialien (VBH-Material) erörtert.

Einführung

Bei Rh W&M GmbH werden im Labor für Chemie unter anderem routinemäßig Feuchtigkeiten von Explosivstoffen mittels Karl-Fischer Titrationen durchgeführt (Abb.1), wobei teilweise Schwankungen der Explosivstofffeuchtigkeiten je nach vorherrschenden klimatischen Bedingungen zu beobachten waren. Um die Begebenheiten unter anderem im Hinblick auf fertigungstechnische Anforderungen genauer bewerten zu können, wurden verschiedene Untersuchungen zu diesem Thema durchgeführt. Dabei war von Interesse, ob bzw. und in welcher Größenordnung sich Bezüge der Explosivstofffeuchtigkeiten von den klimatischen Bedingungen nachweisen lassen und inwieweit sich daraus weitere Abhängigkeiten ergeben.

Resultate und Diskussion

Typische Hygroskopizitätskurven eines zweibasigen TLP zeigen erwartungsgemäß eine deutliche Abhängigkeit der Pulverfeuchte von den vorherrschenden Umgebungsbedingungen (Abb. 2, Temperatur T = 21°C).
Basierend auf diesen Ergebnissen wurden Lagerungen mit unterschiedlichen Probenmaterialien durchgeführt (Abb.3). Man erkennt einen deutlichen Unterschied bzgl. der Feuchtenänderungen der eingesetzten Materialien, wobei sich Abhängigkeiten der Feuchtenänderung zum einen vom untersuchten Materialien als auch vom Sprengöl- und Nitrocellulose-Gehalt nachweisen lassen. Auch diese Daten beziehen sich auf die Feuchtigkeiten im Gleichgewichtszustand bei Lagertemperaturen von T = 21°C.

Die Abb.4 verdeutlicht den Einfluß der Temperatur auf die Feuchtigkeit von TLP, wobei die Endwerte der ermittelten Pulverfeuchte als Funktion der Umgebungsfeuchtigkeit aufgetragen wurden. Man erkennt eine deutliche Abhängigkeit der Feuchtigkeiten von den Lagertemperaturen.

Die bislang vorgestellten Ergebnisse beziehen sich lediglich auf Einzelkomponenten.
Es stellt sich die Frage, inwieweit diese Ergebnisse auf Praxisbedingungen, d.h. auf Munition übertragbar sind. Zudem befinden sich in Verpackungen u.U. Inertmaterialien mit teilweise nicht unerheblichen Feuchtemengen. In diesem Zusammenhang wurden Patronenlagerungen simuliert, deren Versuchsaufbau in Abb.5 skizziert ist.
Bei den gelagerten Komponenten handelt es sich um TLP, VBH, Kunststoff sowie Pappe (Verpackungsmaterial), welche unter definierten Bedingungen gelagert wurden. Abb.6 gibt einen Auszug der Ergebnisse wieder.
Dabei zeigt schon eine Lagerung ohne Temperaturbelastung bei T = 21°C eine Änderung sämtlicher Komponentenfeuchtigkeiten. Erwartungsgemäß erkennt man zudem eine Abhängigkeit der Feuchtenänderungen je nach Lagertemperatur.

Vor dem Hintergrund dieser Ergebnisse ist der Wassergehalt einer verpackten Patrone skizziert (Abb.7). Obwohl das TLP und VBH-Material im Vergleich zum Verpackungsmaterial Pappe massenbezogen den weitaus größeren Faktor darstellen, beinhaltet die Pappe über 70% der gesamten Wassermenge in der Verpackung und ist damit bei einer Betrachtung des Wasserhaushalts auf jeden Fall zu berücksichtigen.

Als weiteren Aspekt muß man sich mit dem Einfluß der Pulverfeuchte auf die Innenballistik beschäftigen. Man erkennt am Beispiel von 2-basigem und 3-basigem TLP eine deutliche Abhängigkeit der Lebhaftigkeit von der Pulverfeuchte, wobei die Lebhaftigkeit bei sinkender relativer Feuchtigkeit ansteigt (Abb.8).

RHEINMETALL
W&M

Schlußfolgerung

Zusammenfassend läßt sich sagen, daß die Feuchtigkeiten der Munitionskomponenten bzw. der gesamte Wasserhaushalt in der Patrone eine wichtige Rolle in der Entwicklung, Fertigung, Lagerung von Munition und vor allem auch für deren bestimmungsgemäße Verwendung spielt. Aufgrund der nachgewiesenen Wechselwirkungen muß eine sorgfältige Abwägung der Komponenten erfolgen, wobei auch Inertmaterialien wie Verpackungsmaterial unter Umständen eine entscheidende Rolle spielen.

RHEINMETALL
W&M

Karl-Fischer Titrationseinheiten

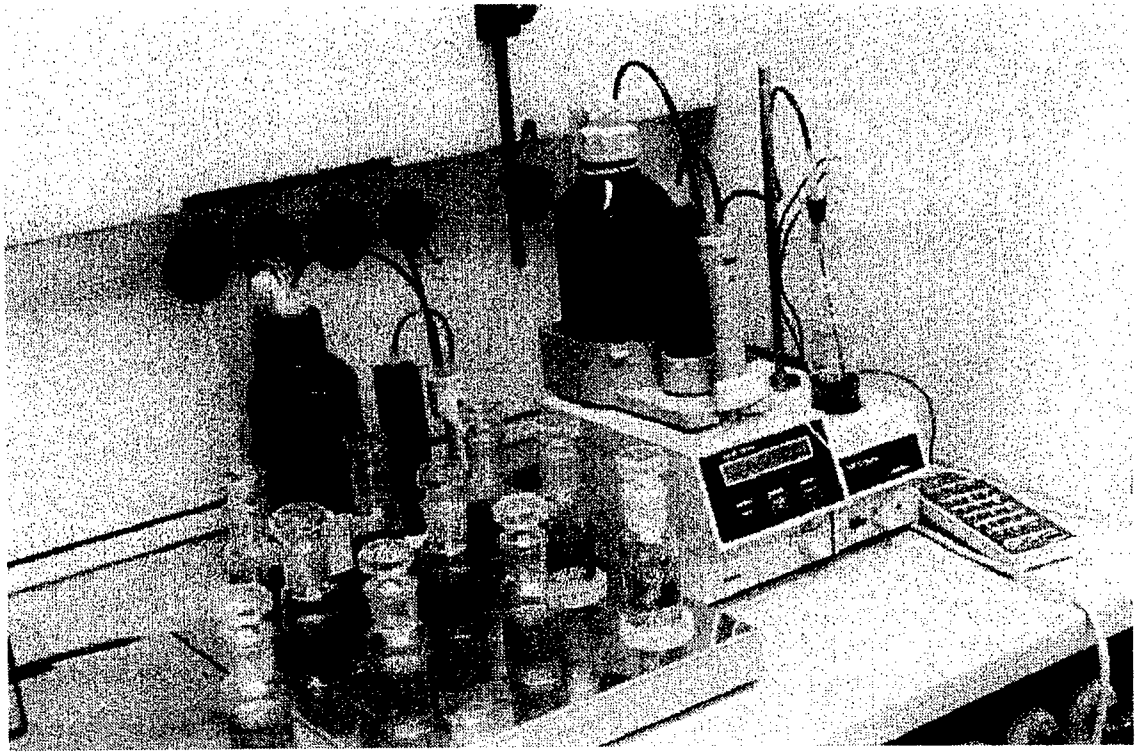

Abb. 1

Copyright by Rheinmetall

RHEINMETALL
W&M

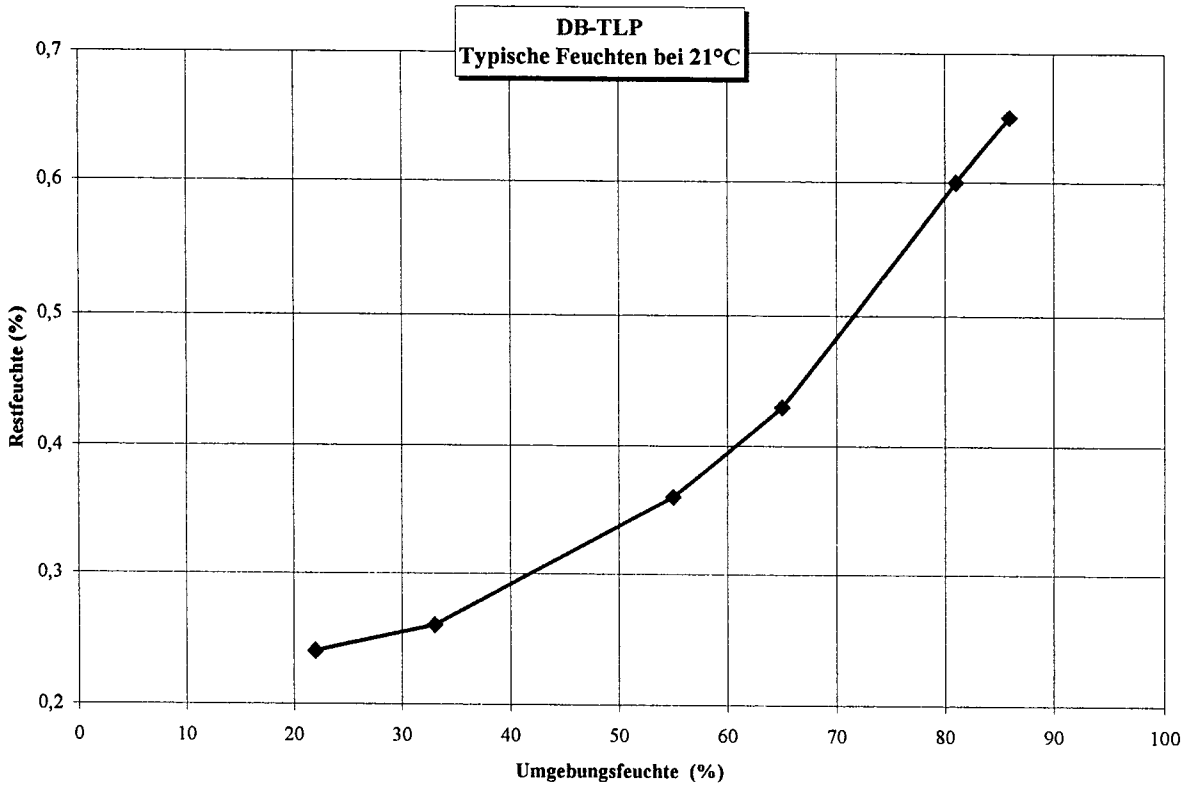

9 - 99

Abb. 2

Copyright by Rheinmetall

EG0020Dr. Keß

RHEINMETALL W&M

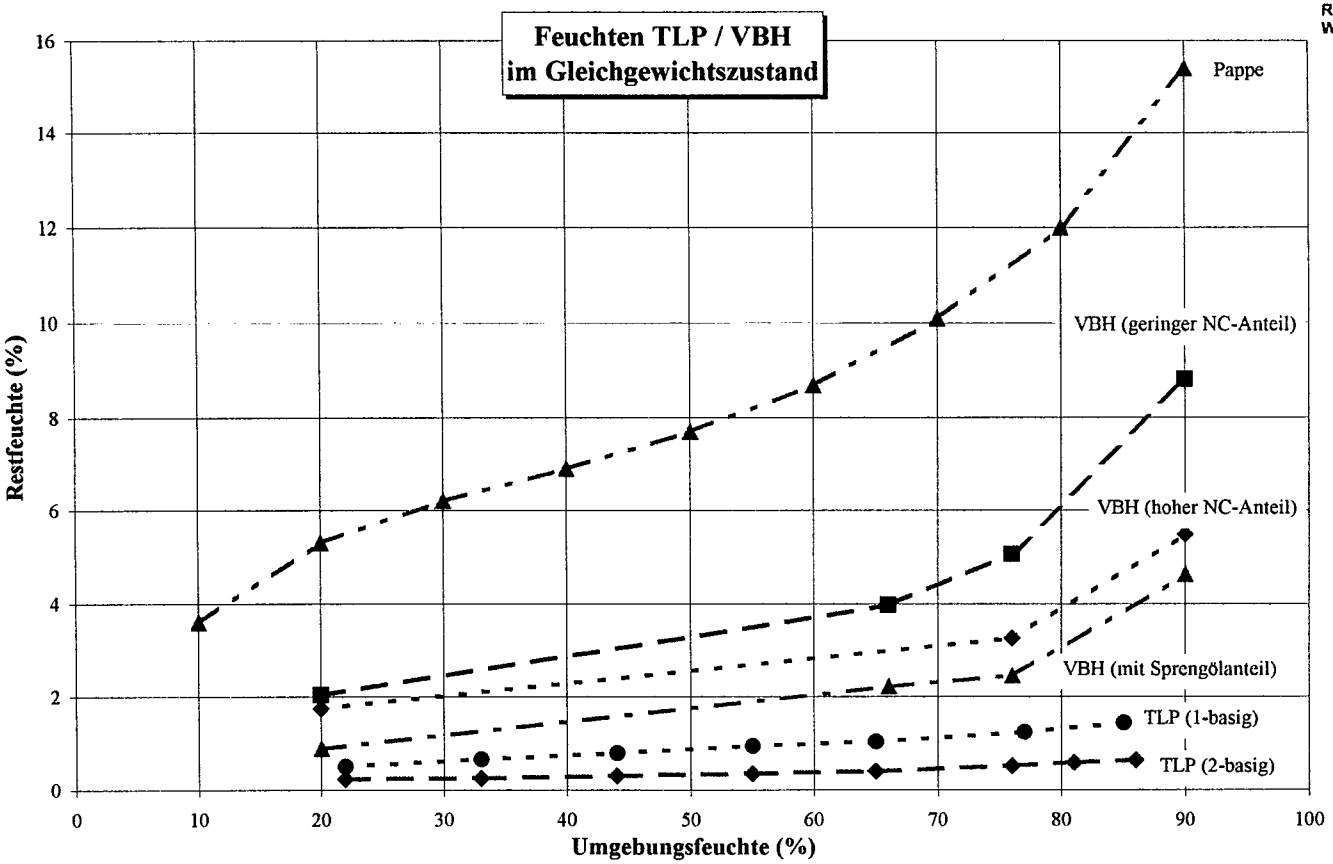

Abb. 3

Copyright by Rheinmetall

EG0021Dr. Keß

RHEINMETALL
W&M

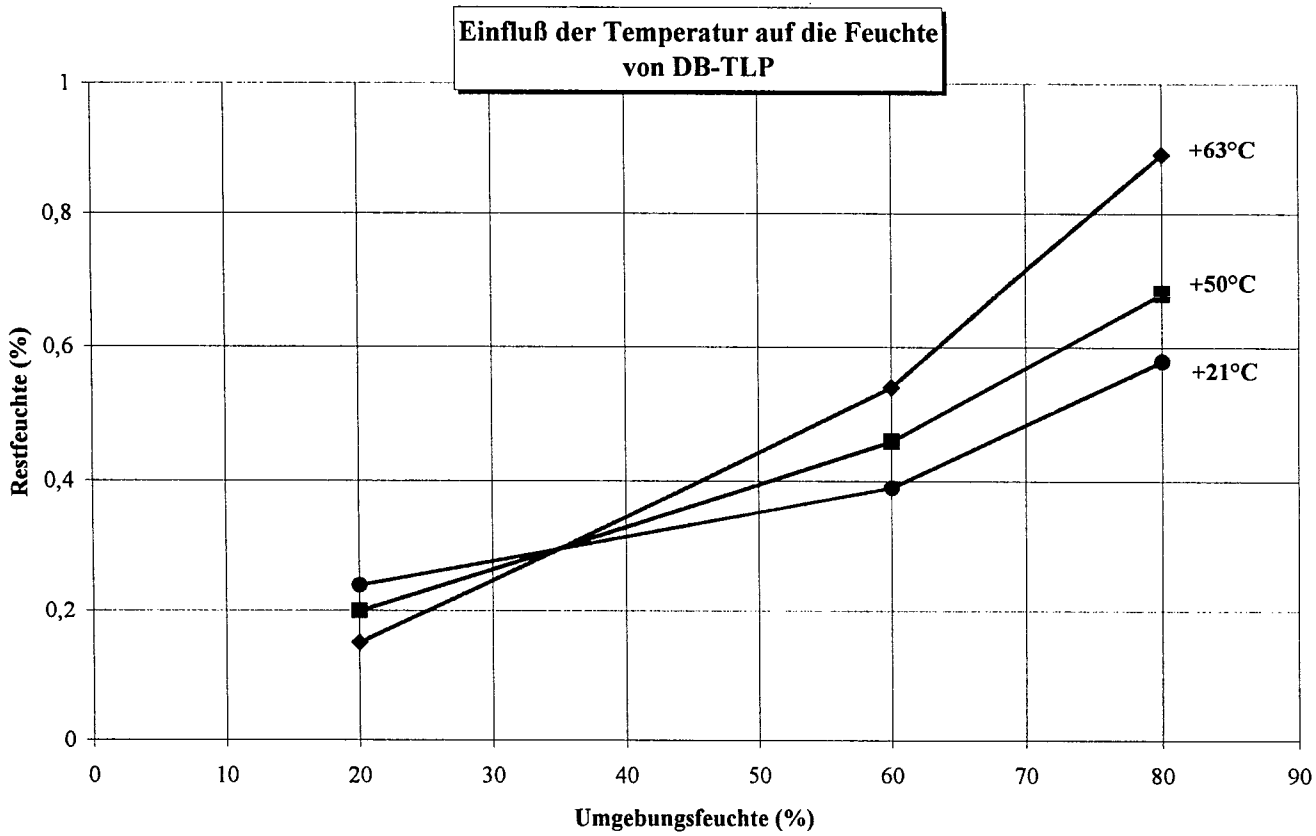

Abb. 4

8 - 99

Copyright by Rheinmetall

RHEINMETALL
W&M

Versuchsaufbau

"Wechselwirkung in Verpackung"

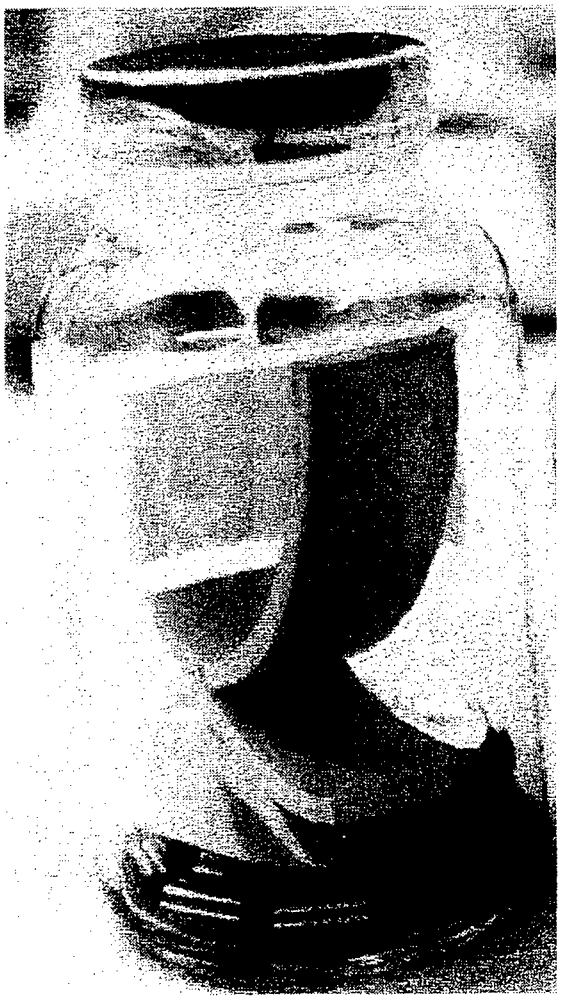

Abb. 5

Copyright by Rheinmetall

RHEINMETALL
W&M

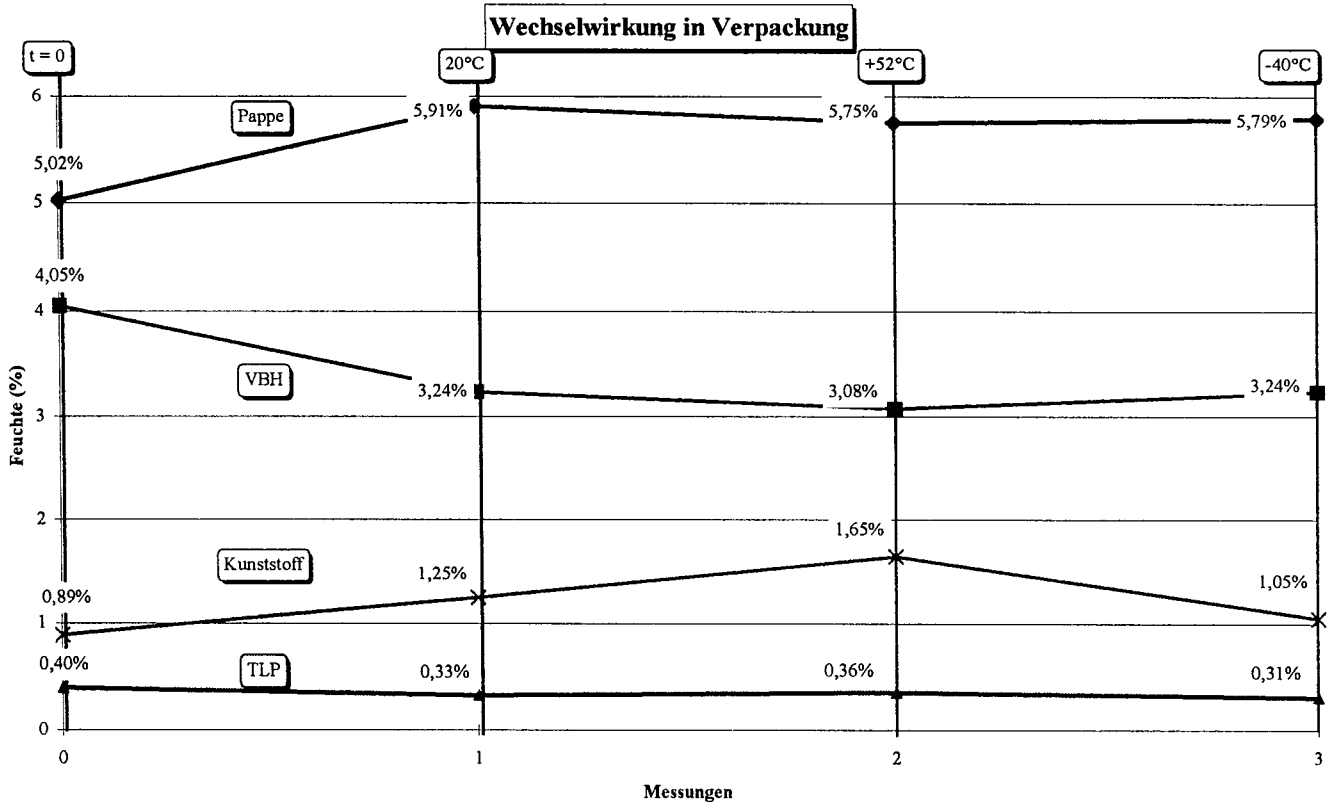

Abb. 6

Copyright by Rheinmetall

EG0027Dr. Keß

RHEINMETALL
W&M

Wassergehalt in der Patrone

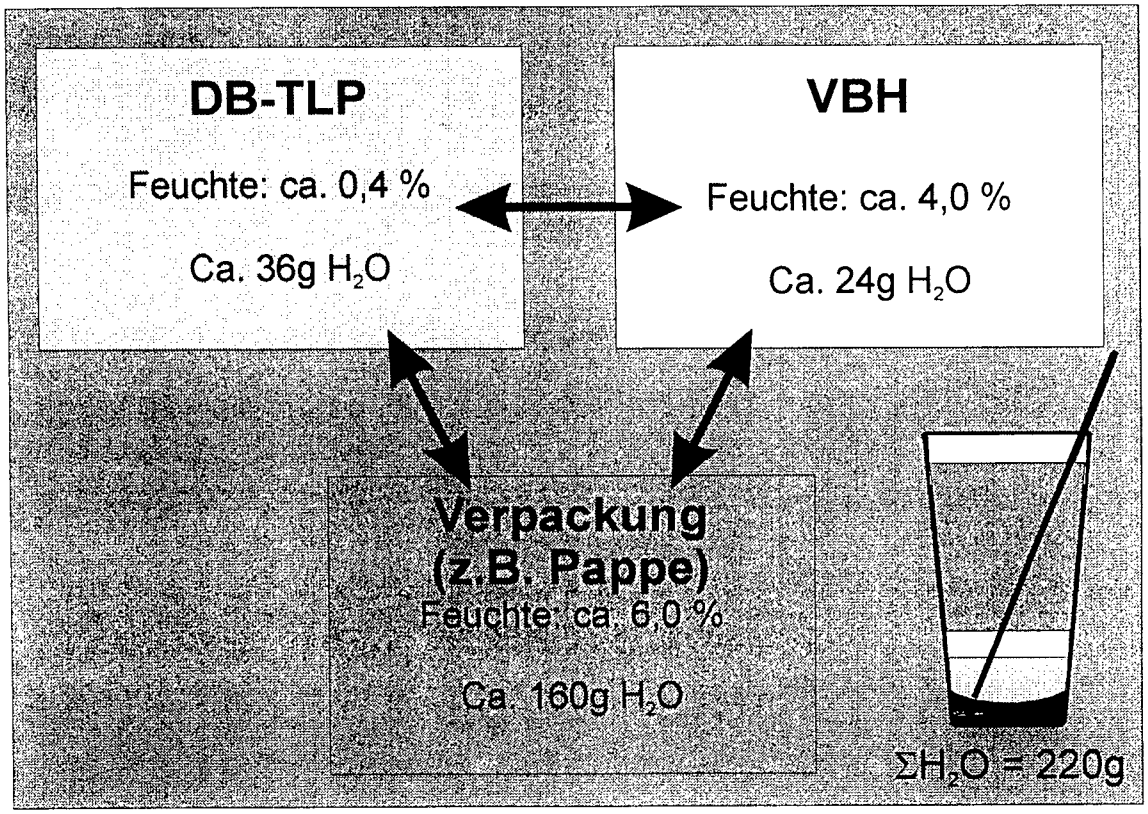

Abb. 7

Copyright by Rheinmetall

RHEINMETALL
W&M

Relative Lebhaftigkeitskennwerte
Einfluß Feuchte

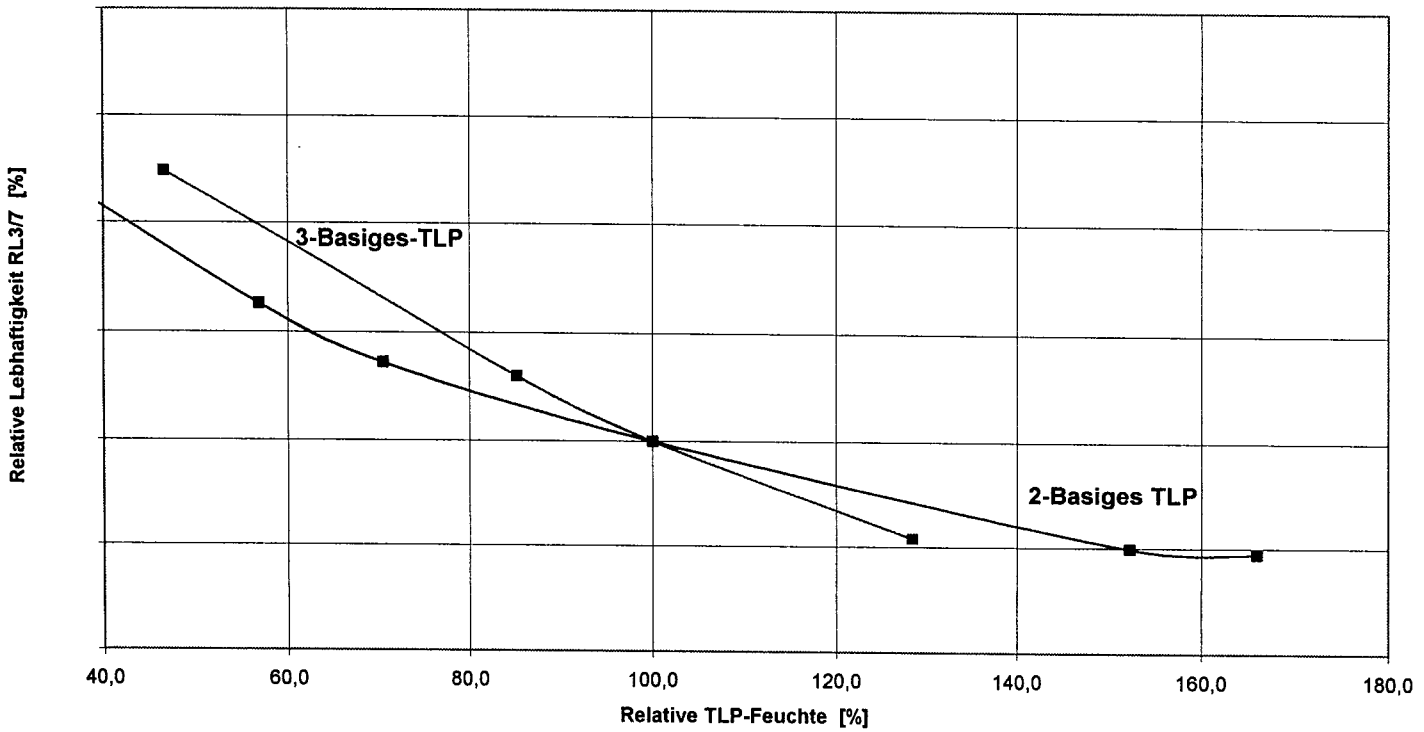

Abb. 8

Copyright by Rheinmetall

Sensitivity properties of spray-dried boron/potassium nitrate granular

Katsuhiko Takahashi and Nobukazu Asano

NOF Corporation

61-1 Kitakomatsutani, Taketoyo-cho, Chita-gun, Aichi 470-2398, Japan

Abstract

In order to understand sensitivity properties of spray-dried boron/potassium nitrate granular (Spray-BKNO3), thermal, mechanical and electrostatic sensitivity test was carried out. For comparison with sensitivity properties of Spray-BKNO3, sensitivity properties of boron/potassium nitrate granular manufactured by conventional manner(Conv-BKNO3) was also measured.

In this study, It is found that sensitivity of Spray- BKNO3 is lower than that of Conv-BKNO3 as follows.

(1)Onset temperature for decomposition of Spray-BKNO3 and Conv-BKNO3 by DSC measurement is about 540 and 390 °C, respectively. Temperature, which ignites Spray-BKNO3 and Conv-BKNO3 at 4sec by Krupps' ignition point test is 517 and 417 °C,respectively.

(2)Friction sensitivity class both of Spray-BKNO3 and Conv-BKNO3 is in class 7. Drop hammer sensitivity of Spray-BKNO3 and Conv-BKNO3 is class 8 and class 4,respectively.

(3)The minimum ignition energy of Spray-BKNO3 and Conv-BKNO3 by electrostatic discharge is about 5.3mJ and 3.3mJ, respectively.

1. Introduction

Boron/potassium nitrate (hereinafter called "BKNO3") granular is popularly used as booster in many type of inflators, usually placed between squibs and gas generants or charged into the squibs, to ignite the gas generants with predetermined output rate at wide range temperature conditions. BKNO3 is a well known ignitor composition and many companies have been manufacturing this composition for many years. The conventional manufacturing process for BKNO3 granular is a

batch process and basically consists of four processes, namely, blending, granulation, sieving and drying, which process requires much manpower. In addition, the conventional process is hard to increase the batch size because of BKNO3's high sensitivity and its violent burning characteristic [1]. From those reasons, the BKNO3 granular manufactured by the conventional process is quite difficult to drastically reduce the cost.

In recent years, many different azide free gas generating formulations have been developed to replace the azide based formulations. Those azide free formulations are generally hard to ignite compared with the azide based formulations. It is considered that the mild burning property of BKNO3, which means the slower burn rate with sufficient calorific output, will help the azide free formulations to be ignited within the prescribed time frame.

Therefore, for customer's satisfaction, the development program to manufacture BKNO3 granular by spray-dry process has been completed. The advantages of the use of spray-dried process to manufacture BKNO3 granular are mainly; 1) High productivity and low manufacturing cost, 2) Perfect remote control process, 3) Consistency of properties and performance and 4) Easy recycling. Spray-dry process and safety countermeasures has been described in our report [2].

In this study, thermal, mechanical and electrostatic sensitivity test of Spray-BKNO3 was carried out to understand basic sensitivity properties of Spray-BKNO3 for safety handling. For comparison with sensitivity properties of Spray-BKNO3, sensitivity properties of Conv-BKNO3 was also measured.

2. Experiments

2.1 Sample preparation

Amorphous boron with less than 0.8μm in average diameter and potassium nitrate with about 30μm in average diameter was used for sample preparation. And purity of boron and potassium nitrate was more than 90% and 99%, respectively.

Manufacturing process for spray dried boron/potassium nitrate granular (hereinafter called "Spray-BKNO3") is described in our report [2]. Laboratory scale spray dryer(L8 type spray dryer manufactured by Ohgawara Kakoki Co. Ltd.) was used in this study. Spray-BKNO3 was prepared according to the following process.

Water slurry with amorphous boron and potassium nitrate was prepared by using mixer and this slurry was supply to laboratory scale spray dryer. And then, spherical Spray-BKNO3 was obtained. Sample properties of Spray-BKNO3 used in this study is summarized in table 1.

For comparison, BKNO3 granular prepared by the conventional process was also used as sample. This conventional BKNO3 granular(hereinafter called "Conv-BKNO3") was prepared by four process, namely, blending, granulation, sieving and drying. A binder(i.e. polyester resin, nitrocellulose or "viton") should be added to make a favorable granular. Viton was added to Conv-BKNO3 in this study. Properties of Conv-BKNO3 is also summarized in table 1.

Table 1 Properties of Spray-BKNO3 and Conv-BKNO3

Properties		Spray-BKNO3	Conv-BKNO3
Formulation	B (wt.%)	22.4	27.2
	KN (wt.%)	77.6	67.9
	Viton (wt.%)	-	4.9
Average Diameter (μm)		60-100	500-600
Apparent Density (g/cm^3)		0.98	0.70

note1) Here, KN represents potassium nitrate.

2.2 Experiments

2.2.1 Thermal sensitivity

To obtain the information regarding thermal stability of BKNO3 granular, Sealed cell Differential Scanning Calorimeter (SC-DSC) and Krupps' ignition point measurements were carried out.

(a) SC-DSC measurements

DSC apparatus of type SSC-5000 manufactured by Seiko Instruments Inc., was used for SC-DCS measurements. Sample of about 1 mg was put into stainless steel vessel. And then, SC-DSC measurements was conducted under the condition with heating rate of 10°C/min and nitrogen atmosphere.

(b) Krupps' ignition point test

Krupps' ignition point test was conducted according to ES-11(1) "Ignition temperature test (1)" in Industrial explosives society standard [3].

Temperature, which ignites sample at 4 sec(hereinafter called "4sec Ignition temperature") was observed by using Krupps' ignition point apparatus. After putting the sample of a few decades milligram into steel cylinder with predetermined temperature, ignition delay time was measured. And then, with a reciprocal number of temperature(K) and a logarithm of ignition delay time, 4sec Ignition temperature was determined.

2.2.2 Mechanical sensitivity

Drop hammer sensitivity test and friction sensitivity test was carried out according to ES-21 "Drop hammer sensitivity test method (1)" and ES-22 "Friction test" in Industrial explosives society standard, respectively [3].

(a) 5kg Drop hammer sensitivity test

5kg iron hammer was dropped on the test sample gripped between two cylinder rollers placed on the anvil of the test rig. Sensitivity of a sample was determined by the relationship between the height of hammer and explosion or no explosion. Test was carried out at suitable drop height and from obtained 1/6 'explosion point', drop hammer sensitivity was indicated by the class shown in table 2.

Table 2 Classes of drop hammer sensitivity

Drop hammer sensitivity class	1/6 'explosion point' (cm)
Class 1	Under 5
Class 2	More than 5 and less than 10
Class 3	More than 10 and less than 15
Class 4	More than 15 and less than 20
Class 5	More than 20 and less than 30
Class 6	More than 30 and less than 40
Class 7	More than 40 and less than 50
Class 8	More than 50

(b) Friction sensitivity test

Test apparatus has the same configuration of BAM method. After repeating the same load six times in succession and observing the load limits for an explosion of sample, 1/6 'explosion point' was determined. Friction sensitivity was indicated by the class shown in table 3.

Table 3 Classes of friction sensitivity

Friction sensitivity class	1/6 'explosion point' (N)
Class 1	Less than 9.8
Class 2	More than 9.8 and less than 19.6
Class 3	More than 19.6 and less than 39.2
Class 4	More than 39.2 and less than 78.5
Class 5	More than 78.5 and less than 156.9
Class 6	More than 156.9 and less than 353.0
Class 7	More than 353.0

2.2.3 Electrostatic sensitivity

The electrostatic sensitivity of BKNO3 layer and dust in various conditions was measured in accordance with the test method determined by Research Institute of Industrial Safety, Ministry of Labor, Japan.

(a) Electrostatic sensitivity test of BKNO3 layer

Test apparatus diagram and the configuration around a discharging electrode is shown in figure 1 and 2, respectively. Ignition energy of BKNO3 granular was measured with a few milligrams quantity at various discharging resistance. Input energy into BKNO3 granular was calculated by using equation (1) from measured current and voltage history.

$$\text{Input energy} = \int_0^t I \cdot V \cdot dt \qquad (1)$$

Here, t, I and V are measured time, current and voltage, respectively.

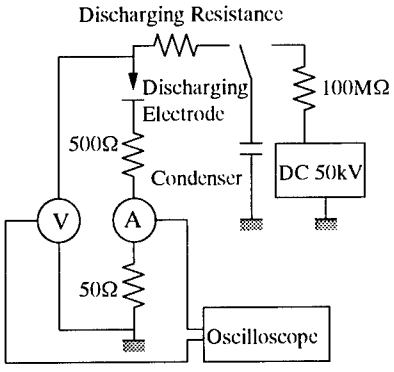

Fig.1 Test apparatus diagram

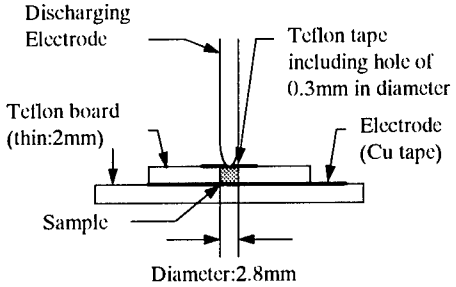

Fig.2 Configuration around discharging electrode

(b) Electrostatic sensitivity test of Spray-BKNO3 dust

The minimum ignition energy measurement apparatus (MIKE 3) manufactured by A.Kühner Co., ltd. was used to obtain electrostatic sensitivity of Spray-BKNO3 dust. Sample dust within the range from 150 to 3500mg was dispersed in 1.2L explosive chamber (Hartman type) and fixed discharging energy (1mJ, 3mJ, 10mJ, 30mJ, 100mJ and 1J) was adopted. Test at the same condition (namely, same sample weight and same discharging energy) was repeated 5 times and even if ignition occurred only one times in 5 trial at the same condition, sample dust at that condition was judged as 'ignition'.

3. Results and Discussion

3.1 Thermal sensitivity

3.1.1 SC-DSC measurements

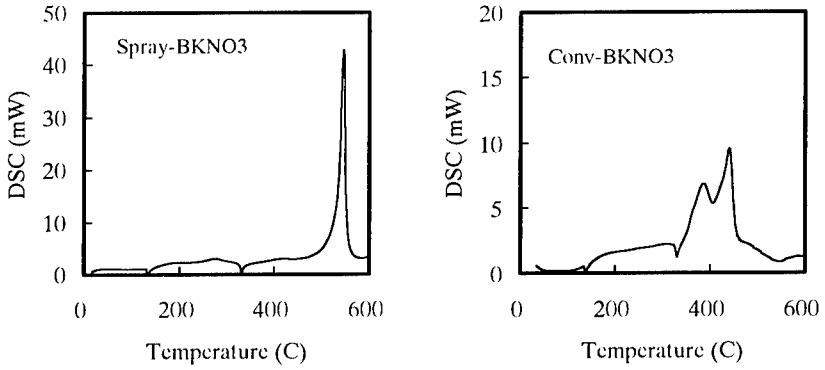

Fig.3 DSC curves of Spray-BKNO3 and Conv-BKNO3

SC-DSC results of Spray-BKNO3 and Conv-BKNO3 is shown in figure 3. DSC results represent that both of Spray-BKNO3 and Conv-BKNO3 has endothermic peak due to phase transition of potassium nitrate at about 138°C and melt of potassium nitrate at about 331°C, respectively. Onset and peak temperature due to decomposition of Spray-BKNO3 is 543°C and 560°C,respectively. On the other hand, Onset and peak temperature due to decomposition of Conv-BKNO3 is lower about

100-200℃ than that of Spray-BKNO3. Specially, exothermic reaction of Conv-BKNO3 occurs as soon as potassium nitrate is melted. It is considered that this low onset temperature of Conv-BKNO3 is due to reaction between Viton as a binder and potassium nitrate.

3.1.2 Krupps' ignition point test

Krupurs' ignition point test results is shown in figure 4-a and 4-b. Ignition delay of Conv-BKNO3 is faster than that of Spray-BKNO3, because onset temperature due to decomposition of Conv-BKNO3 is lower than that of Spray-BKNO3. From relation between a logarithm of ignition delay and a reciprocal number of temperature, it is found that 4sec Ignition temperature of Spray-BKNO3 and Conv-BKNO3 is 517 ℃ and 417 ℃ , respectively. And also, from a slope of a logarithm of ignition delay versus a reciprocal number of temperature, calculated activated energy of Spray-BKNO3 and Conv-BKNO3 is 188kJ/mol and 163kJ/mol, respectively.

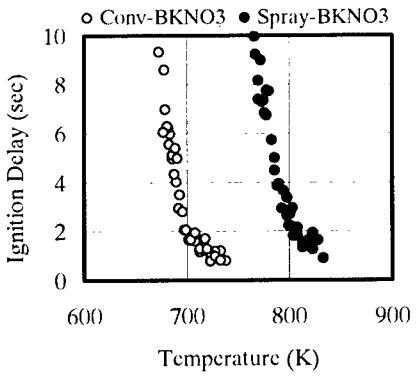

Fig.4-a Ignition delay versus temperature

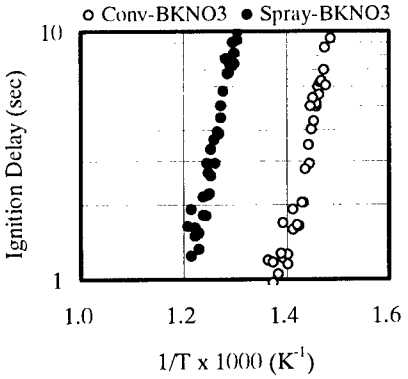

Fig.4-b Logarithm of ignition delay versus reciprocal number of temperature

3.2 Mechanical sensitivity

Results of Mechanical sensitivity is summarized in Table 4. From experimental results, it is shown that friction sensitivity of Conv-BKNO3 is the same as that of Spray BKNO3. On the other hand, drop hammer sensitivity of Conv-BKNO3 is more sensitive than that of Spray-BKNO3. It is

considered that this difference is also due to the difference of thermal stability between two ignitor powder.

Table 4 Mechanical sensitivity

Item	Drop hammer sensitivity	Friction sensitivity
Conv-BKNO3	Class 4	Class 7
Spray-BKNO3	Class 8	Class 7

3.3 Electrostatic sensitivity

In order to determine the minimum ignition energy of BKNO3 layer and dust, electrostatic sensitivity test was carried out and those experimental results are shown in figure 5 and figure 6. Figure 5 shows that the minimum ignition energy of Conv-BKNO3 and Spray-BKNO3 layer by electrostatic discharge is about 3.3mJ and 5.3mJ, respectively. So, the minimum ignition energy of Spray-BKNO3 layer by electrostatic discharge is about 36% lower than that of Conv-BKNO3. Nakano[4] experimentally represented that electrostatic discharge sensitivity of PETN depends on its particle diameter and its loading density. Namely, the ignition energy of PETN increases with increase of particle size of PETN and decreases with increase of loading density of PETN. In this study, it is considered that the reason why electrostatic sensitivity of Spray-BKNO3 is lower than that of Conv-BKNO3, is mainly due to particle size effects, because primary particle size of Conv-BKNO3 is a few decades micrometer and on the other hands, particle size of Spray-BKNO3 is about 80μm.

Figure 6 shows electrostatic sensitivity of Spray-BKNO3 dust. In this figure, solid line shows the minimum ignition energy line. From this results, it is found that the minimum ignition energy of Spray-BKNO3 is more than a few hundred millijoule. This ignition energy and the minimum ignition dust concentration of Spray-BKNO3 is higher than that of non-explosives materials such as cornstarch powder and so on [5]. However, when boron potassium powder is ignited, severe damage will be happened. So, it is necessary to carefully handle this powder.

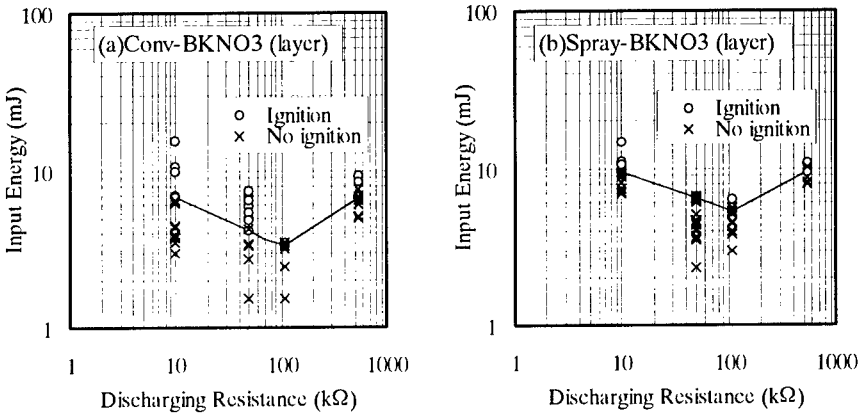

Fig.5 Electrostatic sensitivity of layered Conv-BKNO3 and Spray-BKNO3

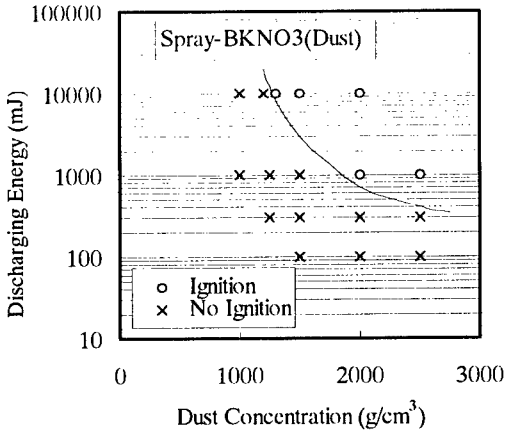

Fig.6 Electric sensitivity of dusted Spray-BKNO3

4.Conclusion

In order to understand sensitivity properties of Spray-BKNO3, several sensitivity test such as thermal, mechanical and electrostatic sensitivity, was carried out. For comparison with sensitivity of Spray-BKNO3, sensitivity tests of Conv-BKNO3 was also carried out.

As a results, It was found that sensitivity of Spray- BKNO3 is lower than that of Conv-BKNO3 as follows.

(1)Onset temperature for decomposition of Spray-BKNO3 and Conv-BKNO3 by DSC measurements is about 540 and 390 ℃, respectively. 4sec Ignition temperature of Spray-BKNO3 and Conv-BKNO3 at 4sec by Krupps' ignition point test is 517 and 417 ℃.

(2)Friction sensitivity class both of Spray-BKNO3 and Conv-BKNO3 is in class 7. Drop hammer sensitivity of Spray-BKNO3 and Conv-BKNO3 is class 8 and class 4,respectively. So, totally mechanical sensitivity of Spray-BKNO3 is more insensitive than that of Conv-BKNO3.

(3)The minimum ignition energy of Spray-BKNO3 and Conv-BKNO3 by electrostatic discharge was about 5.3mJ and 3.3mJ. respectively.

It is considered that the above differences between Spray-BKNO3 and Conv-BKNO3 is due to the effects of particle size and binder.

References

[1] J. M. Smallwood, "Electrical Discharge Insensitivity to a Pyrotechnic Powder", The 18th. International Pyrotechnic Seminar (1992)

[2] K.Takahashi, N.Asano and K.Ochi, "Properties of spray-dried boron/potassium nitrate granular" in Energetic Materials Production, Processing and Charcterization,29th International Annual Conference of ICT, Karlsruhe,June30-July 3, pp68-1-68-12 (1998)

[3] The industrial explosives society, Japan, 'Industrial explosives society standard, 3rd edition', 1988

[4] Y.Nakano, "Electrostatic discharge sensitivity of explosives", Proceedings of the industrial explosives society, Japan, May, pp13-14 (1968)

[5] Toei Matsuda, 'The technical assessment of materials liable to dust explosion", in Safety Document of Research Institute of Industrial Safety, RISS-SD-90-1 (1990)

THE STUDY OF THE SENSITIVITY AND THE SURFACE CHARACTERIZATION OF HMX/TATB-BASED PBX

Nie Fude Yang Xuehai Zhang Ling
Sun Jie Hua Cheng Huang Hui

(Institute of Chemical Materials,China Academy of Engineering Physics,
P.O.Box:919-311,Mianyang Sichuan 621900,China)

Abstract In order to obtain a formulation with high energy output and low sensitivities,the influence of the amount and the process of wax used in the HMX/TATB based molding powders on the sensitivities were studied.The results show that the amount of wax on the mechanical sensitivity ,such as impact test,friction test,and H_{50} is very large,but has little influence on the thermal sensitivitiy such as 5s exploding point and 1000s thermal exploding critical temperature.At the same time the surface characterization of the molding powders was studied by scanning electric microscopy(SEM) and X-ray photoelectron spectroscopy (XPS),the relation of the surface properties and the sensitivities was discussed too.

1 Introduction

With safety issues playing a dominant role in the present-day energetic materials technology,concern is growing about the safety of explosives subjected to unexpected external stimuli.explosive researchers pay more and more attention to the study of insensitive high explosives(IHE)and insensitive munition(IM)[1,2,3].

HMX is extensively used in plastic bonded explosives(PBX),shaped charges and casting explosives.In order to reduce the sensitivities of HMX, sometimes a large amount of desensitizing agents such as wax was added in the formulation, but the large addition of the desensitizing agents is not only reduce the energy of the formulation,but also influence the mechanical properties .

The objective of this investigation is to examine the effect of the amount and the way of wax added in the HMX/TATB based PBX formulation on the mechanical and thermal sensitivity.At the same time the surface characterization was analysis by

scanning electric microscope(SEM) and X-ray photoelectric spectroscopy(XPS).

2 experimental

2.1 Design of formulations

Six PBX formulations containing 95.8%energetic materials were designed.The composition of the formulations was given in Table 1.The total amount of wax and binder kept constant.

Table 1. Composition of Formulations(weight %)

	HMX/TATB	BINDER	WAX
PBX-1	95.8	3.0	1.2
PBX-2	95.8	3.3	0.9
PBX-3	95.8	3.6	0.6
PBX-4	95.8	3.9	0.3
PBX-5	95.8	4.2	0
PBX-6	95.8	3.3	0.9

All the molding powders were prepared by modified water-solvent slurry mothed.The process to produce PBX-1 and PBX-2 molding powders is different from that of the rest. In the process to prepare PBX-3,PBX-4 and PBX-6 molding powders,all the wax was added after the formation of the molding powders.But in the process to produce PBX-1 and PBX-2 molding powders,wax was added at twice.

2.2 Measurements

The friction sensitivity,the impact sensitivity(exploding probability method and H50),the 5s exploding point and the 1000s thermal exploding critical temperature of the formulations were respectively determined according to CHINA GJB 772A-97-602.1,610.1,601.2 606.1 and 607.1.

SEM and XPS respectively measured the surface figuration and the content of the surface elements.

3 Results and Discussion

3.1 Mechanical and Thermal Sensitivity

Table 2. Mechanical and Thermal Sensitivity Test Results

	PBX-1	PBX-2	PNX-3	PBX-4	PBX-5	PBX-6
Friction sensitivity(%)	4	12	12	48	44	2
Impact sensitivity(%)	0	8	44	76	96	0
Impact sensitivity(H50 cm)	79.4	42.1	/	/	/	49.9
5s Exploding point (℃)	342	342	343	346	343	340
1000s Thermal exploding critical temperature (℃)	262	262	262	262	262	262

The friction sensitivity and the impact sensitivity increase rapidly along with the reduction of wax in the formulation.Although PBX-4 has more 0.3%wax than PBX-5,the friction sensitivity of PBX-4 and PBX-5 is almost equal.it means wax has no desensitization to the friction sensitivity when the amount of wax in the formulation is less than 0.3%.At the other hand the impact sensitivity of PBX-4 is less 20% than that of PBX-5wax,it means that wax has largely desensitization to impact sensitivity.Although the exploding probability of PBX-1 and PBX-6 under friction or impact is almost the same,H_{50} of PBX-1 is higher 30cm than that of PBX-6,it means PBX-1 is more insensitive than PBX-6.

The results that PBX-6 is more insensitive than PBX-2 shows it would have more desensitization effect when all wax was coated on the molding powder surface if the amount of wax in the formulation is the same.

At the same time,the results show that wax have no effect on the 5s exploding point and the 1000s thermal exploding critical temperature.

3.2 Surface Analysis

The surface of PBX-1 and PBX-6 molding powder is regular and smooth(figure 1 and figure 6),there are less explosive particles exposed in the surface.The less wax used in the formulation,the more explosive particles exposed in the surface.This results are accordance with the increase of the Nitrogen element content in the surface(table 3).It seems that the explosive particles exposed in the surface react more easily under the friction or impact.The more explosive particles exposed in the molding powder surface,the more sensitive the formulation under mechanical action.

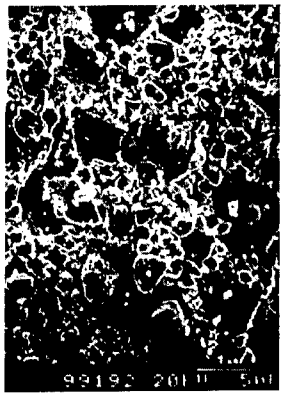

Figure 1 SEM picture of PBX-1

Figure 2 SEM picture of PBX-2

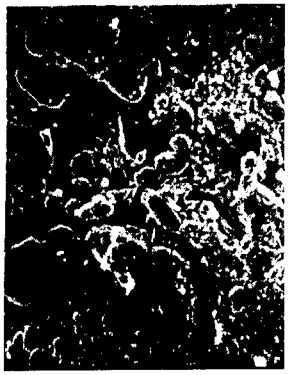

Figure 3 SEM picture of PBX-3

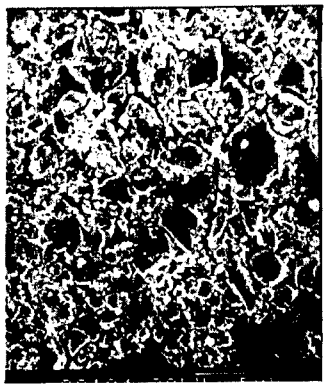

Figure 4 SEM picture of PBX-4

Figure 5 SEM picture of PBX-5

Figure 6 SEM picture of PBX-6

Table 3. Summary of XPS data for TATB,HMX,PBX-1,2,3

	C	O	N	F	Cl
TATB	35.8	31.9	32.3		
HMX	30.6	34.6	34.8		
PBX-1	77.6	8.8	5.3	6.0	2.3
PBX-2	69.0	11.2	7.7	8.6	3.5
PBX-3	60.8	12.2	9.0	14.0	4.0

4 Conclusion

(1) The amount of wax has large influence on the mechanical sensitivity ,such as impact sensitivity,friction sensitivity,and H_{50},but has little influence on the thermal sensitivity such as 5s exploding point and 1000s thermal exploding critical temperature.

(2) Wax has no desensitization to the friction sensitivity when the amount of wax in the formulation is less than 0.3%.

(3) It would have more desensitization effect when all wax was coated on the molding powder surface if the amount of wax in the formulation is the same.

(4) The formulation containing 1.2%wax is not sensitive to impact and friction.

Reference

1 Air Senoir Nation Representative Long Term Technology Project on Insensitive explosives(IHES).27th International ICT conference ,KARLSRUHE GERMANY,1996.

2 P.A.Urtiew et al Shock sensitivity of IHE at Elevated Temperature.UCRL-JC-111337.

3 R.R.McGuire,R.P.Guarienti.DOE HARZARD CLASSIFICATION for INSENSITIVE HIGH EXPLOSIVES(IHE).UCRL-91420.

SHOCK SENSITIVITY OF HMX BASED COMPOSITIONS

A.E.D.M. van der Heijden °, *R.H.B. Bouma* * *and R.J. van Esveld* *

TNO Prins Maurits Laboratory, ° *Research Group Pyrotechnics and Energetic Materials,* * *Research Group Properties of Energetic Materials, P.O. Box 45, 2280 AA Rijswijk, The Netherlands*

Abstract

One of the parameters which determines the shock sensitivity of explosives is the defect structure of the energetic filler material. In a cooperation between the Fraunhofer Institut für Chemische Technologie (ICT) and TNO Prins Maurits Laboratory, the crystallisation and characterisation of HMX has been subject of investigation since 1995. In particular, the influence of the internal defect content of the HMX crystals on the shock sensitivity of compositions containing HMX particles, differing in size and crystal quality, has been studied.

This paper focusses on the assessment of the shock sensitivity of compositions containing HMX particles which are suspended in a fluid with the same density as that of the HMX particles. The density of the fluid can be controlled by preparing a proper mixture of two separate, high density liquids. The reason for using a suspension with a practically homogeneous density is to minimise binder-particle interactions – which may influence the shock sensitivity – present when using a polymer bonded explosive composition. Suspensions of several sieve fractions of (in-house) recrystallised HMX batches were tested with respect to their shock sensivity. The shock sensitivity is assessed with help of the Mega Ampere Pulser (MAP) test set-up, with which relatively small samples can be studied. The results of the shock sensitivity tests and their relation with the internal quality of the suspended HMX crystals will be presented and discussed.

1. Introduction

In 1995, a two year cooperation between the Fraunhofer Institut für Chemische Technologie (ICT) and The Netherlands Organisation for Applied Scientific Research (TNO Prins Maurits Laboratory) started on the subject of nitramine crystal defects, in particular HMX. Intermediate results on this cooperation have appeared in references [1-4]. One of the aspects which were investigated within a follow-up study in 1998/99 was an improved method to characterize crystalline defects in HMX [4]. After characterizing several of the recrystallised and as-received batches, the shock sensitivity of four different HMX based compositions has been determined in order to determine whether the presence of crystalline defects and the mean crystal size of the particles influences the sensitivity to shock. The results of these tests are presented in this paper.

Section 2 describes the experimental part of the research. In section 3 the results of several of the characterisation analyses, as well as the shock sensitivity results are presented and discussed. The conclusions are given in section 4.

2. Experimental

2.1 Background

In contrast to testing the shock sensitivity of 'standard' polymer bonded explosives (PBX's) based on the use of a cured binder system like HTPB, it was decided to use a liquid with a density equal (or very close) to the mean crystal density of the HMX crystals. In this way the HMX particles neither sink nor float. The advantage of testing these kind of samples is that the influence of the particle/binder interaction on the shock sensitivity can be minimized; moreover, the reflections of the shock wave when passing through the sample will be reduced since there are hardly any changes in density within the sample. The occurrence of these reflections cannot be completely suppressed, since this also depends on the velocity of sound in a certain medium. In this way it is possible to test the HMX crystals 'stand alone' and possible influences of the binder and particle/binder interactions (*e.g.* the presence of voids at the interface between particle surface and binder) can be reduced, provided that the crystals are sufficiently wetted by the suspending liquid.

The suspension had to satisfy the following criteria:

- A relatively high density, since the density of HMX is quite high (theoretically 1.904 g/cm^3);

- A density which can be modified, depending on the mean crystal density of the HMX particles to be suspended;
- A sufficient wetting of the particles by the liquid.

This led to the use of a mixture of two liquids, L1 and L2. By changing the mixing ratio, the density of the mixture could be matched with that of the mean crystal density of the HMX particles.

2.2 Preparation of HMX samples

As-received HMX (supplied by Dyno AS, Norway) was recrystallised in order to obtain batches of different qualities with regard to crystalline defects. Details about the recrystallisation method can be found in [2]. Four batches were compiled from several recrystallisation batches. From each one of these batches, two sieve fractions were retrieved: one fraction consisting of fine particles in the range of 106-180 μm and a coarse fraction of 355-425 μm. Also the as-received HMX was sieved in a fine and coarse fraction.

The mean crystal density of the sieve fractions was determined by means of liquid pycnometry. Mixtures were prepared using the liquids L1 and L2 in a mixing ratio corresponding to the measured mean crystal density of the sieve fractions. For both sieve fractions, the same solid load should be used in order to avoid an influence of this parameter on the shock sensitivity. The maximum solid load which could be achieved with either the fine or coarse fraction was used to prepare the samples for the shock sensitivity tests. The particles and the liquid mixture were mixed and stirred in order to obtain a homogeneous suspension.

2.3 Shock sensitivity tests

The Mega Ampere Pulser (MAP) has been developed at the TNO Prins Maurits Laboratory in order to extend the possibilities to investigate the shock initiation properties of explosives. The MAP discriminates itself compared to other shock initiation tests by the fact that a well-defined pulse with a relatively short pulse width is applied, which allows one to study the influence of the pulse duration on the initiation behaviour of the explosive as well. This shock pulse is transferred to the sample by impact of a flyer plate with the sample. A more detailed description of the experimental set-up can be found in ref. [5].

The sample holders for the shock sensitivity tests consist of PVC cups with an internal diameter of 20 mm and a height of 25 mm; the thickness of the PVC cup is 2 mm. The cup is closed with a 25 µm thick kapton foil. The thickness of the kapton flyer plate is 250 µm. Per test series, approximately 10 samples are required in order to determine the shock initiation pressure.

The samples are prepared by mixing the appropriate amounts of crystals and liquids, depending on the required solid loads of the samples.

3. Results and Discussion

3.1 Mixture of liquids

The density of the mixture could be described theoretically with the following equation:

$$\rho = [f_1/\rho_1 + f_2/\rho_2]^{-1}$$

where f_1 and f_2 are the mass fractions of the two liquids, and ρ_1 and ρ_2 the densities of the pure liquids. This prediction is based on the assumption that no volumetric changes occur after mixing, *i.e.* the total volume is the sum of the two volumes that are mixed (it is a well-known fact that this is not true for a mixture of water and ethanol). The difference between the theoretical and the experimentally found values were found to be smaller than 0.20% for the densities of interest for HMX ($1.880 < \rho < 1.900$ g/cm^3). The experimental results and their comparison with the predicted values according to the equation given above are listed in table 1.

Table 1: Calculated and measured densities of the liquid mixture L1/L2 as a function of the mixing ratio. Within the density range of interest for HMX ($1.880 < \rho < 1.900$ g/cm^3) the difference between calculated and measured density is smaller than 0.20%.

Mixing ratio L1/L2 [wt%]	ρ (calculated) [g/cm^3]	ρ (measured) [g/cm^3]	Deviation [%]
0 / 100.0	1.9523	1.9497	0.13
5.0 / 95.0	1.9229	–	–
10.0 / 90.0	1.8944	–	–
11.4 / 88.6	1.8865	1.8836	0.15
13.8 / 86.2	1.8732	1.8700	0.17
15.0 / 85.0	1.8667	–	–
15.7 / 84.3	1.8628	1.8582	0.25
100.0 / 0	1.4950	1.4899	0.34

3.2 Characterisation HMX batches

The recrystallised and as-received HMX batches were characterized – after sieving – with regard to mean crystal density by means of liquid pycnometry and sensitiviness towards impact. The results are given in table 2. The corresponding mixing ratio of the liquids L1/L2 is also included in this table. A selection of these batches were also characterized with help of confocal scanning laser microscopy and scanning electron microscopy. These observations showed that in particular the as-received HMX crystals contained a large number of micro-inclusions with a size of the order of 2 μm. Such micro-inclusions were only rarely found in the recrystallised batch. More details can be found in ref. [4].

Table 2: Summary of the HMX batches which were used for the shock sensitivity tests. The fine and coarse fractions from the batches #2 and #3 originate from the same source batch.

#	HMX batch	Sieve fraction [μm]	ρ (measured) [g/cm^3]	Impact [Nm]	Remark
1	TL 633/99	355-425	1.900	15 / 15	Recrystallised; stirrer rate 360 rpm
2	TL 634/99	106-180	1.895	25 / 7.5	Recrystallised; stirrer rate 450 rpm
3	TL 635/99	355-425	1.895	20 / 15	Recrystallised; stirrer rate 450 rpm
4	TL 106/95A	355-425	1.885	10 / 7.5	As-received batch

The mean crystal density of the batches is higher for the recrystallised HMX than for the as-received batch. Batches #2 and #3, originating from the same source batch but corresponding to a fine and coarse sieve fraction, respectively, show the same density. Assuming that the mean crystal density is determined, for its major part, by the inclusion content in the crystals, this indicates that for this batch the inclusion content of the crystal sizes investigated with these two sieve fractions is similar.

The impact sensitivity of the batches was determined in duplicate, according to the UN directive UN ST/SG/AC.10/11. Usually there is a difference of plus or minus one level in impact sensitivity. However, the difference in impact sensitivity found for batch #2 is quite large. It is unclear at the moment what could have caused this difference. The impact sensitivity is in a range which is normally found for HMX at TNO.

The yield after sieving the fine fractions (106-180 μm) from batches #1 and #4 was too low taking into account the amounts required for the shock sensitivity tests. These fractions were therefore not further characterized.

3.3 Shock sensitivity tests

The results of the MAP tests are summarized in table 3. The MAP tests were started with the reference material (TL106/95A) in a 50/50 wt% HMX/L1-L2 mixture. This solid load was chosen since this was the highest solid load which could be achieved with the HMX batch consisting of the fine fraction from 106 to 180 μm. By having a constant solid load for all the samples, the results of the shock initiation tests can be compared and conclusions can be drawn about the differences between internal crystal quality aspects and the fine and coarse sieve fractions used. It is expected that if the crystal quality plays a role in the shock sensitivity, this will be reflected in a different shock initiation pressure as determined from the MAP experiments.

Several tests showed that the sample with the reference material did not initiate, even not at the maximum flyer plate impact velocity. Apparently, the solid load was too low to sustain an initiation and detonation or the diameter of the sample was lower than the critical diameter. Therefore, it was decided to increase the solid load to the maximum feasible filling level with the coarse sieve fraction (355 – 425 μm), which was determined to be 63 wt%. This increase in solid load appeared to be sufficient to successfully initiate the samples with the reference material. However, the consequence of an increased solid load of the coarse fraction, was that the shock initiation tests using the fine fraction with the same solid load of 63 wt% (TL634/99) could not be performed, since a solid load as high as this value was not feasible with this grade.

Using the Hugoniot of the sample and that of the flyer plate (kapton), the detonation pressures can be calculated. In figures 1 to 3 the initiation characteristics (initiation distance *vs.* initiation pressure) are shown for the three different batches. A typical example of the results of a MAP test is given in figure 4.

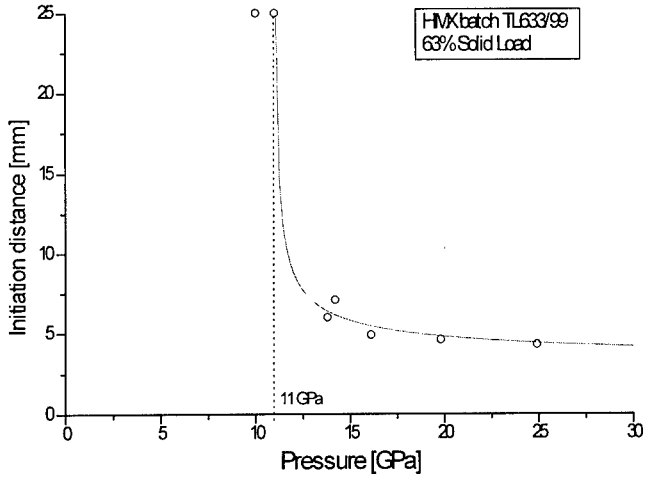

Figure 1: *Initiation characteristic of batch #1, TL633/99.*

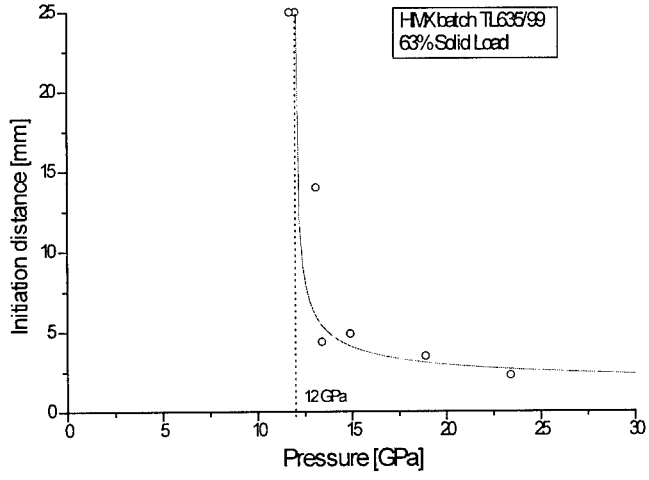

Figure 2: *Initiation characteristic of batch #3, TL635/99.*

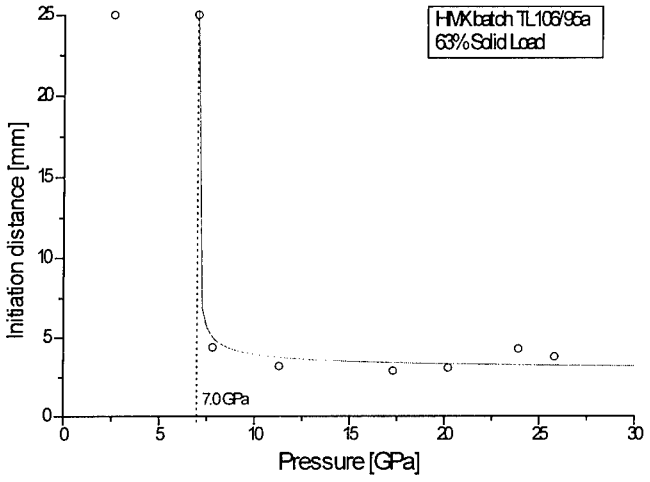

Figure 3: *Initiation characteristic of batch #4, containing the reference batch of HMX, TL106/95A.*

The detonation pressure for the TL106/95A reference batch (#4) was found to be 7.0 GPa. For the recrystallised batch TL633/99 (#1) this was 11 GPa, clearly indicating that this batch is much less shock sensitive than the reference batch. For TL635/99 (#3), also consisting of a recrystallised HMX batch, the shock sensitivity was determined at 12 GPa. Looking at the crystal densities, in particular the reference batch has a relatively low density (see table 2). The difference between the densities of the recrystallised is much more close, and also the initiation pressures found for these batches are quite close. During the preparation of the samples it was noted that the sample containing the reference material (TL106/95A) was opaque, whereas TL633/99 was practically transparant and TL635/99 even more transparant than TL633/99. This points at a lower scattering of light possibly as a result of a lower number of imperfections in the crystals. Another explanation could be based on the rather rough crystal surfaces of the reference material compared to the recrystallised batches, as shown earlier by means of optical microscopic observations [1]. This might also have caused the more opaque nature of the sample as a result of the scattering of light at these rough crystal surfaces.

These results point at a relation between the shock initiation pressure and the internal quality (expressed as the mean density of the HMX crystals) of the crystals. This effect is illustrated in figure 6, in which the detonation pressure is plotted *vs.* the crystal density of the particles in the suspension. A similar effect was found with HMX/HTPB based PBX's in the past by both ICT and TNO [2]. The difference with these new results is that these have been obtained with samples in which the influence of the 'binder' is suppressed as much as possible by using a liquid of matching density rather than a polymer matrix. In this way the shock impedance is practically similar for both the explosive particles and the surrounding medium.

Table 3: Summary of the shock initiation tests of the four HMX batches.

#	HMX batch	Sieve fraction [μm]	Mixture HMX/L1-L2 [wt%]	Detonation pressure [GPa]	Mean detonation velocity [km/s]
1	TL 633/99	355-425	50 / 50	Not determined	–
			63 / 37	11	5.98
2	TL 634/99	106-180	50 / 50	Not determined	–
			Higher solid load not feasible with this grade		
3	TL 635/99	355-425	50 / 50	Not determined	–
			63 / 37	12	6.20
4	TL 106/95A	355-425	50 / 50	No initiation	–
			63 / 37	7.0	6.78

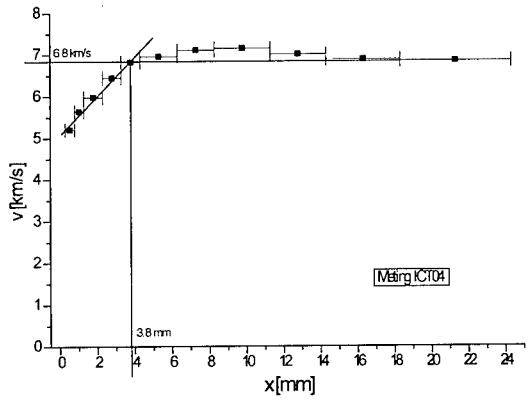

Figure 5: *Typical example of the data obtained with a flyer impact initiation test on samples containing the reference HMX material (63 wt% solid load).*

The mean detonation velocity of the samples is of the order of 7 km/s, although a slightly lower value was found for both the recrystallised batches (see table 3). This might be related to a critical diameter effect. Additional tests with longer samples and a larger diameter should be able to clarify this result.

Due to the fact that samples containing the fine fraction (TL634/99, #2) could not be tested using a solid load of 63 wt%, similar to that of the coarse sieve fraction, no conclusions can be drawn on a possible difference between the shock sensitivity of the fine and coarse fraction, originating from the same batch, especially since both sieve fractions showed the same mean crystal density.

The finding that the reference batch is much more sensitive towards a shock initiation might be related to the fact that especially this reference batch contains a large number of micro-inclusions. These were only rarely found in the recrystallised batches [4]. Apart from a much lower crystal density, probably due to the presence of macro-inclusions, the presence of the much smaller micro-inclusions might have enhanced the susceptibility to shock initiation of the reference batch compared to that of the recrystallised batches.

4. Conclusions

In this paper the results of shock initiation MAP tests on HMX suspended in a liquid mixture of matching density are presented and discussed. The data point at a clear relationship between the shock sensitivity and the internal crystal quality of the particles in the suspension: the higher the mean crystal density (used as a measure of the internal crystal quality), the less sensitive the suspension. This set of data confirms earlier results obtained with HMX/HTPB based PBX's.

Acknowledgements

The authors acknowledge financial support from the Dutch Ministry of Defence.

List of abbreviations

CSLM Confocal Scanning Laser Microscope

GC Gas Chromatography

ICT Fraunhofer Institut für Chemische Technologie

FOP Fiber Optic Probe

HMX $C_4H_8N_8O_8$

HTPB Hydroxy-Terminated PolyButadiene

MAP Mega Ampere Pulser

PBX Plastic Bonded eXplosive

PVC PolyVinyl Chloride

RDX $C_3H_6N_6O_6$

SEM Scanning Electron Microscopy

TNO Netherlands Institute of Applied Scientific Research

UN United Nations

References

[1] A.E.D.M. van der Heijden and W. Duvalois, *Characterisation of the internal quality of HMX crystals*, Proceedings of the 27th Annual International Conference of ICT, June 25-28, 1996, Karlsruhe, FRG, p. 32-1

[2] A.E.D.M. van der Heijden and R.H.B. Bouma, *Shock sensitivity of HMX/HTPB PBX's: relation with HMX crystal density*, Proceedings of the 29th Annual International Conference of ICT, June 30 – July 3, 1998, Karlsruhe, FRG, p. 65-1

[3] U. Teipel and H. Kröber, *Formation of HMX crystals with high internal quality by cooling crystallisation*, Proceedings of the 29th Annual International Conference of ICT, June 30 – July 3, 1998, Karlsruhe, FRG, p. 66-1

[4] A.E.D.M. van der Heijden, W. Duvalois and C.J.M. van der Wulp, *Micro-inclusions in HMX crystals*, Proceedings of the 30th Annual International Conference of ICT, June 1999, Karlsruhe, FRG

[5] W. Prinse, M. van Rooijen, J. Mul, *Shock sensitivity and the TNO Mega Ampere Pulser*, Proceedings of the 25th International Annual Conference of ICT, June 28 – July 1, 1994, Karlsruhe, FRG

Estimation of the Violence of Cook-off tests using PE-4

Alan Bailey, Keith DeGraaw, Mariana Matei, Mike Williams
Cranfield University
RMCS, Shrivenham, Swindon, Wilts
UK, SN6 8LA

ABSTRACT

The ODTX cook-off test for small spherical samples of energetic materials is well known. The temperature of a pair of hot anvils is controlled and the effect of this on the time to event is measured. Apparent activation energies can be calculated. The controlled surface temperature and geometry allows relatively simple modelling. Current interest lies in estimating how the violence of cook-off changes with temperature. Previous workers have measured the increase in the void volume of the anvils caused by an event. Specially constructed anvils with a strain gauge bonded to the base have also been used. We have tried to advance this work so that the violence of each event can be estimated quickly for little extra cost on a routine basis.

We have used spheres of PE4 plastic explosive for this work at temperatures from 200 to 250 deg C.

A pressure gauge inserted in the lower anvil, connected to the charge space by a drilled capillary, responded to the pressure rise during an event but increased the time to event by adding to the void volume and did not survive more than three firings.

A simple four-parameter scale based on post-event observation of the anvils suggested that the greatest damage was caused at the lowest

temperatures. It was also noted that a microswitch, which responded to the closing of the press, was "bounced" by the shock waves passing through the apparatus. The frequency and duration of the oscillations of the switch also gave an indication of event violence.
A strain gauge was inserted between the lower anvil support and the frame of the apparatus. This was "squeezed" when there was an event.
The initial responses were greatest and had the most rapid rise times for intermediate temperatures. The speed of the sound waves in air (timed over 1 metre) did not vary significantly.
The activation energy for PE4 was 35 kcal/mole, corresponding to the activation energy for the gas phase decomposition of RDX given by Kuo and Summerfield.

1. Introduction

The ODTX has been used for many years to measure the time to explosion for small spheres of explosive heated at a constant external surface temperature. The data obtained has been used in modelling of time to explosion for different regimes.
In a series of papers [1, 2, 3, 4] researchers at Lawrence Livermore National Laboratory (LLNL) have reported measurements of the time to explosion in spheres of various high explosives following a rapid, uniform increase in the surface temperature of the sphere. Due to the spherical symmetry, the time-dependent properties of the explosive (temperature, chemical

[1] Catalano,E.;McGuire,R.;Wrenn,E.;Ornellas,D;Walton,J.In Sixth Symposium (International) on Detonation; Ofice of Naval Research ACR-221:Colorado, CA, 1976; pp214-22.
[2] Tarver,C.M.;McGuire, R.R.; Lee,E.L.;Wrenn, E.W.;Brein, K.R. In Seventeenth Symposium (international) on Combustion; The Combustion Institute: Pittsburgh, 1978; pp 1407-1413.
[3] McGuire, R.R.;Tarver, C.M. In Seventh Symposium (International)on Detonation;Naval Surface Wepons Center NSWC MP 82-234: Annapolis, 1981; pp56-64
[4] Tarver, C.M.;Chidester, S.K.;Nichols, A.L. J.Phys. Chem. 1996, 100, 5794-4799

composition, etc.) are functions of the radial spatial coordinate only; thus the name "one-dimensional time-to-explosion".The purpose in developing this experimental approach was to allow utilisation of the experimental results in fixing various parameters in the chemical reaction model so that calculational predictive methods could be applied more widely and with a greater measure of confidence.

In assessing the cook-off hazard of a munitions, it is important to know not only when to expect an explosive response, but also to have some measure of its violence. In ODTX experiments important differences in anvil damage have been observed as a function of the temperature applied to a given explosive.

From post reaction visual inspection of the anvils and the explosive sample, the authors of Paper[1] describe two distinct types of events.

"A low order event, probably a rupture of the seals caused by gas pressure, yields little or no damage to the anvils; indeed the copper ring is generally still in place and the majority of the explosive unconsumed though charred...

A high order event, on the other hand, causes considerable metal flow in the aluminium anvil and twisting and fragmentation of the copper seal."

In the UK, some attempts have been made to estimate the violence of the event in ODTX machine by measuring the relative anvil deformation and by studying the dynamic strain of the anvils[5].

Our work has been directed at finding a method of measuring the violence of the cook-off event in ODTX, which is convenient, easy to apply, and which can be used on a routine basis during a series of trials.

---

5 I Belcher, R C Drake, K A Fleming and R H Roberts, Thermal Modelling of Confined Explosive Systems, British Crown Copyright 1991/MOD

Several tests with PE-4 have been performed in the ODTX in order to measure the time duration for when an explosive event occurred with respect to a set temperature and to measure the extent of the violence when an explosive sample reacts. The ODTX apparatus used was primarily designed to perform one function, to measure the time to explosion. This is considered a fundamental aspect when investigating cook-off with many explosive compositions and the ability to computer model them.

There have been numerous studies that describe the pressure rise rate dp/dt with respect to time from explosive gases. Bailey, Lee and De Graauw [6] agreed that under heavily confined conditions used in by ODTX apparatus, dp/dt would be an indication of the level of violence that an explosive yields. A method to capture the pressure gradient with respect to time by placing a pressure transducer in such a way that it had a direct path to the cavity were the explosive sample is located has been used. However, after the third trial the pressure transducer was virtually blown out of the aluminium anvil and permanently damaged and, as a result, a method of estimating the violence of the event that is non-invasive, non-destructive (of the apparatus) and is easy to apply for a series of runs (up two dozen experiments) has been developed. We have used:

1. Post-event visual inspection of the anvils with a simple ranking method
2. A strain gauge clamped between the support table and the frame of the apparatus
3. The effect of the explosion on the microswitch placed on the top anvil which determined the position of the piston
4. The time arrival of the sound wave from the event at the microphone

2. Experimental

The One Dimensional Time to Explosion was designed at Lawrence Livermore National Laboratory as a well-controlled, heavily confined test environment with constant temperature boundary conditions on the outside of the sphere.

In ODTX experiments a small sphere of explosive is placed between two pre-heated aluminium anvils with hemispherical cavities that are maintained at the selected temperature. Reaction and decomposition of the explosive generates gas that is kept in the cavity by a copper ring seal. The two anvils are held together by a hydraulic ram and explosion is defined when the pressure in the cavity pushes the two anvils apart, but slow decomposition of the explosive may also generate enough pressure to separate the anvils. The retained gases are often intermediate products in the chemical reaction scheme, and react with the original explosive, modifying the reaction rate.

The principal measurement is the time to "explosion", which is measured from the closure of the anvils.

For a given explosive or composition, the ODTX test allows the determination of the following:

-The relation between the time to explosion (t) and the test temperature (T)

-The critical temperature below which no reaction occurs

[6] Bailey,A; Lee, P.R and De Graaw, K. Meeting at RMCS 2 Jun 98

2.1 Method and Equipment used to Capture Pressure Data

By placing the transducer into the lower anvil, in direct path to the cavity were the explosive is located, enabled measurement of the pressure gradient with respect to time (dp/dt). This would mean that the pressure transducer would virtually capture the pressure rise and fall with little to no distortion. The method that was proposed and adopted can be seen in the figure 1.

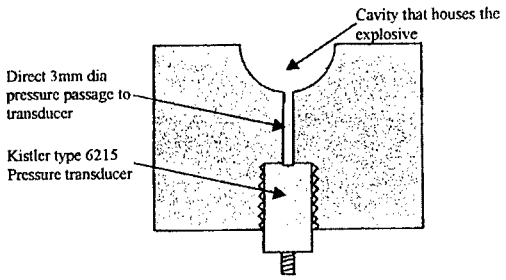

Figure 1 – Lower Anvil with Pressure Transducer

The pressure transducer that was used is a Kistler quartz high-pressure sensor type 6215. It has the ability to measure the pressures up to 600 MPa (equal to 6000 bar) and is suitable to operate at heated temperatures of 200 $^{\circ}$ C. The pressure rise with respect to time data was captured on a Nicolet Pro20 digital oscilloscope. In line with the pressure transducer and oscilloscope was a Kistler type 5009 charge amplifier. There were only four trials conducted as the pressure gauge mal-functioned after being damaged in the third trial and it was blown out of the aluminium anvil and destroyed.

2.2 The estimation and violence of the reaction

The violence of the event has been determined by post inspection of the anvils. Previous workers with this apparatus in the UK have made estimation of the violence of the event by looking at the pattern of

damage and by trying to measure an increase in the volume of the cavity. This was done by filling it with water, or mouldable substance, and weighing[5].

2 .2. 1 Observation

A subjective method of estimating the damage to the anvils has been developed. A number that describes the violence of the event has been given within the levels of 1 to 3, where 1 is slight and 3 being extreme. This has been done for four categories, Products, State of the Copper Ring, Cavity size and Surface damage.

Products:	3-no product left
	2-brown residue
	1-explosive residue
Copper ring:	3-broken/fragmented
	2-twisted
	1-all there
Cavity:	3-bent/deformed
	2-undamaged
	1-clear
Surface:	3-metal scoured
	2-damaged
	1-clear/smooth

2 .2. 2 Microswitch

A microswitch type V3, 16 A Long Lever was placed on the top holder anvil as a means of determining if the press had closed successfully. However it was noted that it "bounced" (switched off/on) when an event occurred.

2. 2. 3 Strain gauge

A strain gauge type BI-Morph (vibration) Element was placed between the lower anvil assembly and chassis frame, from which ΔV strain and rise time from the very first pressure recorded on the Nicolet oscilloscope have been measured.

2. 2. 4 Thermocouple

In order to determine if it is any self heating into the anvil, one hole for a thermocouple type K was drilled into the flat lower anvil at 5 mm distance from the bottom of the cavity.

2. 2. 5 Microphone

The event the marks the endpoint caused by the violent rupture of the confinement is sensed by a microphone that is placed at 1 m distance from the closure of the anvils.

The signals of the thermocouple, strain gauge, microswitch and microphone were recorded on a Nicolet Odyssey during the firings.

3. Times to explosion

For a given explosive or composition, the ODTX test allows the determination of the following:

- The relationship between the time to explosion (t) and the test temperature (T)
- The critical temperature below which no reaction occurs

The trials were conducted on PE-4 (RDX/plasticiser/oil, 88/11/1 parts by weight) over a temperature range that includes the melting point.

For example, the results obtained with PE-4 are presented in figure 2.

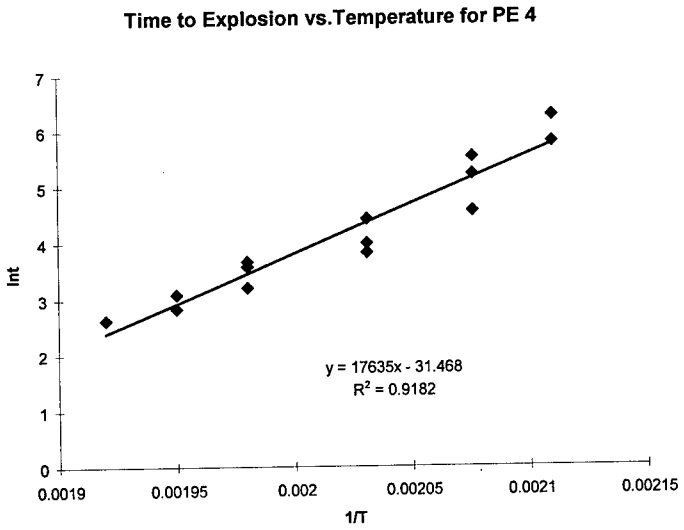

Figure 2 - Measured Times to Explosion in the ODTX Apparatus for PE-4 over a Temperature Range that Includes Melting Point.

We have represented them as a straight line while the initial portion of the curve is fairly linear but they take on considerable curvature at lower temperature. Activation energy of 35.02 kcal/mole was calculated from the induction time/temperature relationship of the explosion initiation proposed by Roginsky and Sapozhnikov and Semenov[7].

$$\ln t_{ind} = \text{const.} + (E_A/R)\,(1/T_o)$$

[7] A.G.Merzhanov, Combust. Flame (1967), 201-21

In theory the log (t) = f (1/T) graph is composed of three parts (1, 2, 3,)[8]:

1. If the test temperature is close to the critical temperature, time to explosion becomes long
2. At the intermediate temperatures, the explosives samples reach thermal equilibrium and the reaction develops at the centre of the sphere according to cook off phenomenon
3. The temperatures are high. The samples do not reach thermal equilibrium and the reaction develops on the sphere boundary.

These different behaviours between high and low temperatures show the kinetic parameters cannot be deduced simply from these plots. Especially activation energy for zeroth order Arrhenius kinetics cannot be directly determined from the linear part of the curves because conduction effects are of great importance in this range of test temperatures.

However, these results are useful to compare the thermal sensitivity of different explosives and to test the validity of the kinetics of decomposition used in the numerical simulations. This latter point is one of the main interests of the ODTX test.

4. Pressure Rise Rate related to the violence of cook-off

The pressure rise rate *dp/dt* with respect to time throughout a burning process indicates the rate at which the pressure of the gases surrounding the explosive are acting on it when in a confined condition. Considering that an explosive event's pressure rise and fall can occur within 2 milli seconds, and can reach pressures as high as 400MPa from a small sample of only 1.7 gram gives an indication of how quickly the forces from the hot expanding gases travel over the unconsumed propellant within a confinement.

[8] C. Castille, D. Bainville, P. Reyner, and R. Belmas, Commissariat a L'Energie Atomique, Centre D'Etudes de Vaujours, Moronvilliers, France

The degree of violence can be in increments such as deflagration, rapid deflagration or detonation. From these statements, it can be deduced that the steeper the gradient of the slope generated by the pressure rise with respect to time the greater the rate at which the explosive is burning.

Analysis of recorded pressure-time data

Three trials were conducted under different heating temperatures at, 220 ° C, and respectively 250 ° C. A general indication of pressure gradients was sought, and not a finite plot or capture of peak pressure. The data capture rate was set in microseconds. The main part of the pressure rise and fall generally lasted for two milliseconds.

Figure 3 shows the data from the three firings super-imposed on top of each other and synchronised to the time when the pressure reached 100 bar. The reason for this is that each firing had a slow pressure rise over different time intervals before the event pressure rapidly rose. Thus in order to get some realistical starting point, 100 bar seemed best from the data recorded for the three firings.

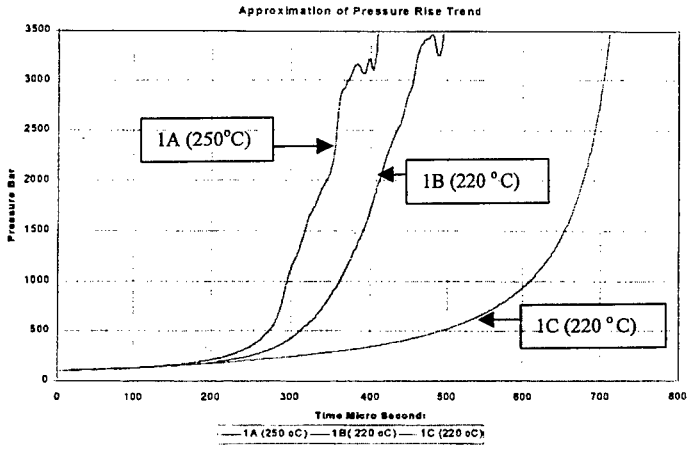

Figure 3 – Pressure Time Plots for Three ODTX Firings

A peak pressure of 3923.3 bar (392.33 MPa) was measured at 220 ° C, which is slightly higher than firing 250 ° C. As stated earlier, the peak pressure values are considered as an indication only, and not the absolute value. The level of the event was lower that firing A conducted at 250 ° C and considered as a rapid deflagration. Slope of this curve is the second steepest of the three graphs.

5. A comparison between the damage of the anvils and the data from the Nicolet recordings from the microswitch and strain gauge

5.1 Damage

Table 1 presented below gives the severity of the event by summing the characteristics presented above (2.2.1):

Temperature (° C)	Products	Copper Ring	Cavity	Surface	Sum
200	2	3	3	3	11
210	3	3	2	2	10
220	2	3	1	3	9
230	1	2	1	3	7
240	2	1	1	3	7
250	1	1	3	2	7

The system applied does not always gives estimations of violence that are either all low or all high for all four categories but the trend of the sum of all of the categories is from high violence for low temperatures to low violence for high temperatures.

The damage is caused over all of the events that take place in one trial. Some trials had three events. All must contribute something to the anvil damage.

5.2 Microswitch

As mentioned above a microswitch, was located on the top anvil holder to show that the press had closed successfully, "bounced" (switched off/on) when an event occurred. There seemed to be a pattern to these bounces. There were many bounces spread over a long period (miliseconds) at low temperatures (see Table 2). Table 2 also shows the duration over which the microswitch "bounced".

5.3 Strain gauge

The dynamic strain experienced by an anvil during an explosive event in the ODTX apparatus was measured by a strain gauge placed between the block that supports the lower anvil assembly and the chassis frame (2.2.3). The peak strain voltage and the time from the initial development of the strain to the peak strain were measured.

Table 2 presented below shows the correlation between the damage of the anvil and the recordings from the microswitch and strain gauge.

T (° C)	Damage	Bounces for a single event (microswitch)	Duration (ms)	ΔV strain gauge	Rise time strain gauge (μs)	No. of bangs
200	11	16	9.29	-5.24	319	1
210	10	7	8.53	-9.09	335	2
220	9	5	8.31	-10.9	141	1
230	7	3	5.70	-8.04	172	1
240	7	2	5.26	-8.51	149	3
250	7	1	3.62	-6.83	184	1

All the microswitch data indicated that there is a direct link between the duration of the major event and the number of bounces and the damage to the anvils.

The peak strain voltage and the rise times from the first event in any recording shows that the violence at the strain gauge is possibly greatest in the mid temperature range, where a higher compression was generated over a shorter period of time.

6. Temperature Profile during Heating in ODTX test

Another main objective of this study was to measure the temperature history throughout the charge and to determine the approximate location where the runway exothermic first occurred.

In this case a central hole was drilled into the lower anvil and the thermocouple was fixed into the centre of the charge. Another thermocouple was placed outside the cavity.

Figure 4 below shows the temperature profile at the very end of the run under cook-off conditions on PE-4. The temperature history of the thermocouple was recorded on the Nicolet oscilloscope.

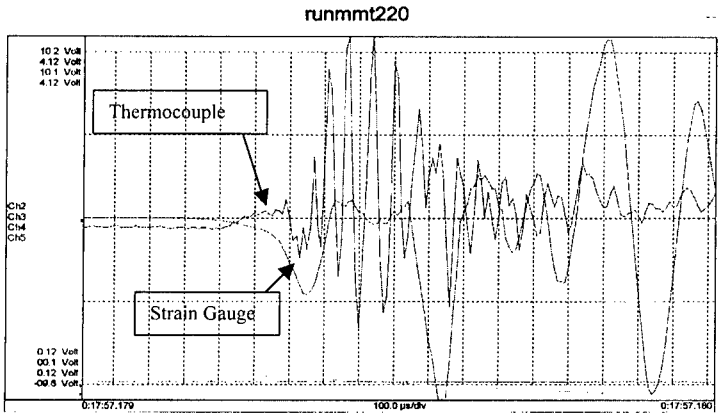

Figure 4 – The signals recorded on the Nicolet Channels during the Firings from the Thermocouple and Strain Gauge

The charge was placed on the thermocouple in the cavity at room temperature, the press closed and the temperature ramped to 220 °C.

The interior thermocouple records temperature of only 201 ° C when the event occurs that can be contrasted with the outer one that reached 210 ° C. The temperature is higher at the edge of the cavity and probably held at 201 ° C inside by the latest heat of fusion as PE-4 melts. The rise in temperature of the central thermocouple was about 31 ° C in 177 μs coinciding with the start of the event (as captured by the strain gauge) but the thermocouple normally does not respond this fast. The later temperature profile (the oscillations) of the central thermocouple might be considered as a result of the plasma phenomena or RDX evaporation or both.

7. Summary and Conclusions

- The instrumented laboratory scale thermal-ignition test (ODTX) was used to obtain dynamic measures of reaction growth, to support developments towards quantitatively modelling the violence of cook – off munitions
- The initial Pressure-Time data suggests that there is a correlation between the gradient of the pressure rise slope and the degree of violence in which the explosive reacts
- The activation energy is in line with RDX gas phase reaction suggested by R. R. McGuire and C.M. Tarver
- The damage to anvils was greatest at low temperatures
- Duration of first event was longest at low temperatures
- Power at the strain gauge is greatest at mid range temperatures
- At 210 ° C, slow heat, dT/dt is rapid at ignition temperature that is probably the melting point of PE 4

ICT 2000

GAP TEST INVESTIGATION

M. Held

TDW, 86523 Schrobenhausen, Germany

Abstract

Flash X-ray pictures of gap test arrangements show that the material of the gap, in this investigation disks of plexiglass, will disperse and destroy unconfined acceptor charges, if the shock is not strong enough to get a prompt or at least a very fast initiation.
The initiation location and/or the direction of the detonation wave of the donor charge to the gap material and acceptor charge or inverse, is under the investigated test conditions from very small influence to the behaviour of the acceptor charge.

Erfahrungen bei dem Zwischenlagentest

Zusammenfassung

Röntgenblitzbilder von Gaptestanordnungen zeigen auf, daß das Zwischenlagenmaterial, in dieser Testserie Plexiglasscheiben, die unverdämmten Empfängerladungen zerlegen, wenn die Stoßwelle nicht stark genug war, die Empfängerladung spontan oder zumindest sehr schnell zu initiieren.
Die Initiierungsart der Geberladung, in Richtung des Zwischenlagenmaterials und der Empfängerladung, oder entgegen, hat bei den gewählten Testbedingungen einen sehr kleinen Effekt auf das Verhalten der Empfängerladung.

Introduction

For a tandem system with two fragment warhead sections the acceptor high explosive charge of the second warhead section should not react or should not be disturbed if the high explosive charge of the first warhead section or the donor charge detonates 1 ms to 2 ms earlier. For this reason a donor and an acceptor charge arrangement was layed out to proof this in a survivability test.

A gap test arrangement is typically used to test the "initiability" (after the definitions of the author) (<1> or <2>) of the different high explosive charges. This means, they give the pressure limits of the used arrangements between the initiation and reaction. This test is also used only partially to get the sensitivity of the high explosive charge between no reaction and reaction (<3> and <4>). Under the given requirements the acceptor charge can at least react slightly. It is only necessary that the second warhead section is able to detonate fully after a time difference of 1 ms to 2 ms. For this reason some tests were arranged which did not show the wanted possibility but they showed interesting results which, in the author's opinion, are worthwhile to be presented and to be discussed.

Test Setup

This investigation started with a typical gap test set-up arrangement with a donor charge of 96 mm diameter and 100 mm length of an unconfined pressed high explosive charge HMX/Wax 94,5/4,5/1. To get less pressure to the barrier and the acceptor charge, the initiation of the donor charge was arranged from the bottom so that the detonation wave ran away from the barrier or in the opposite direction compared to usual gap test layouts (Fig. 1). For the initiation a normal number 8 detonator was used which initiated a booster of pressed RDX/Wax/Graphite 94/5/1 of 20 mm diameter and 20 mm length from the side. The booster and the detonator was installed in a 10 mm thick Polyamid disk of 120 mm diameter. A number of 20 mm thick plexiglass disks ,also 120 mm diameter, followed. With the number of the plexiglass disks, the gap length can be easily changed as for the card gap tests <5>.

On the end a 10 mm Polyamid disk was attached again . The acceptor charge, also existing of pressed HMX/Wax/Graphite charge 94,5/4,5/1 of 100 mm length and 96 mm diameter, followed then. A bar of 5 mm plexiglass with 20 mm width was added at the end surface, in which 3 carbon resistors were arranged. In addition three carbon resistors were installed on the edges of the acceptor charge to the plexiglass every 120°. The aim of these pressure gauges was to measure the arrival times of the shock wave, the incoming pressure and then the reaction wave or the reaction pressure of the acceptor charge. The achieved signals did not give conclusive results. Therefore these results of the additional diagnostic tool will not be discussed

A copper wire of 2 mm thickness, respectively a 0.5 mm copper foil of 10 mm width were used along the side of the acceptor charge.

A picture of the gap test arrangement in front of the protecting wedge for the film cassette is shown in Fig. 2 in which 5 disks of 20 mm plexiglass were used. Therefore the total gap length was with the 2 additional 10 mm Polyamid disks of inert material between the donor and acceptor charge was 120 mm.

A picture of the test set-up in front of the flash X-ray cassette is given in Fig. 3. The distance of the axis of the gap test charges, with the total high explosive weight of the donor and the acceptor charge of 2.6 kg, to the protecting cassette was 600 mm respectively 3000 mm to the flash X-ray tube. To achieve a good protection against the blast wave of the at least detonating donor charge a plywood wedge of 60° was arranged between the charge and the protecting cassette <6>. This Fig. 3 shows on the left side the protecting cassette for the film cassette with the wooden edge in front of the gap test charge and on the right side the windows for the X-ray tube again protected by 10 mm aluminum plate. This was the typical arrangement of this test series.

Test results

In the following descriptions several subsequent tests are presented. Every test received a new layout based on the result of the previous test.

Test 61745

.Under the given test layout with the unconventional initiation against the direction to the acceptor charge, it was expected that 120 mm gap length of plexiglass, gives at least a partial survivability of the acceptor charge in the time difference of 2 ms. A so-called static picture of the test arrangement by the flash X-ray was taken (Fig. 4 - top).. It shows the donor charge on the left side, the 120 mm thick plexiglass layers and the acceptor charge with the 2 mm copper rod and 0.5 x 10 mm copper foil on top and on the bottom and finally the plexiglass bar with the 3 carbon resistors on the right side. The carbon resistors themselves are not, but the connecting wires are visible.

The gained FXR-picture after 2000 µs demonstrates that the acceptor charge was totally gone or maybe partially detonating (Fig. 4 - down).

Det 61758

After this result the length of the inert gap was increased from 120 mm to 200 mm with 9 x 20 mm plexiglass disks and 2 x 10 mm Polyamid disks.

The flash X-ray picture shows that after the 2 ms delay time at least a part of the acceptor charge reacted again or was at least strongly pushed by the moving gap material (Fig. 5). Portions of the high explosive acceptor charge can still be seen. The rear front face moved 57 mm which gives a mean velocity of 28 m/s of the end surface. This picture demonstrates that not only a shock wave passed through the Plexiglass disk. The plexiglass plates were accelerated and acted like a piston against the acceptor charge. This totally unconfined acceptor charge had no

remarkable strength and was axially and radially pushed away alone under the load of the "Moving Piston". as the plexiglass disks are, not taken large shock pressure loads into account, which are relatively small by the given gap length of 200 mm

Det 61809

To reduce further the shock load and the velocity of the plexiglass plates which were pushed against the acceptor charge a 20 mm steel plate of 140 mm diameter was installed in the middle instead of a plexiglass disk. The total gap length was again 200 mm built of 8 x 20 mm plexiglass disks, 1 x 20 mm thick steel plate and 2 x 10 mm thick Polyamide disks. Between the last 3 layers of plexiglass 0,1 mm copper foils were also installed in order to see better the movement of these disks in the FXR picture.

The comparison of the static to the dynamic picture after 2 ms delay time is presented in Fig. 6. The 20 mm thick steel disk was not deformed but it flew with a velocity of about 50 m/s, whereas the end surface of the last plexiglass disk or the attached surface of the high explosive moved a distance of 62 mm, respectively had a velocity of 31 m/s. The plexiglass disks were broken into pieces and radially squeezed out. The high explosive was also pushed forward and also radially squeezed out. This can be exactly examined, as the end face of the acceptor charge is lined up to the FXR axis.

Det 61810

Up to now the time difference of the detonation of the donor charge and the flash X-ray pictures was 2 ms. Since this test, this time difference has been reduced to 1 ms in order to see the earlier stage of the behaviour of the acceptor charge under those conditions. In addition a series of steel spheres, alternating from a 7 mm sphere to 2 times 5 mm spheres etc. were installed on the upper edge of the acceptor charge. On the lower side was again a 0.5 mm thick and 10 mm wide copper foil and a

Det. 61811

The same arrangement was fired with and end-on initiation of the donor charge with the same time difference for the FXR-picture to see the influence between a rearward and a forward detonation to the barrier and to the acceptor charge (Fig. 10).

The analysis of the FXR-pictures (Fig. 11) shows that the steel plate, installed in the centre of the plexiglass disks, flew with 72 m/s 22 % faster compared to 59 m/s, but the end surface of the acceptor charge had nearly the same displacements of 29 mm and therefore the same velocities. The displacements of the 7 mm and 5 mm fragments were also very similar.

The first and the second large fragments were on top, whereas the smaller fragments were a little beneath, what means slower. It seems that the larger 7 mm fragments slipped on the smaller 5 mm fragments and were therefore radially pushed a little bit more. The reaction of the acceptor charge and the dispersion of the high explosive material in both initiation modes were more or less equal.
This is expressed in the very similar displacements of the spheres in these two tests (Fig. 12).

Conclusion

This series of gap tests involved with the diagnostic technique of flash X-ray demonstrates the interlayer or that the gap material pushed the acceptor charge which will be destroyed mechanically without the high explosive material to high order reaction. The axially and radially expanding high explosive material is good visible in the FXR-picture. The radial dispersing expansions can be very well seen on the copper foil of 0.5 mm thickness and 10 mm width, as it does not have any remarkable strength. This is different to the 2 mm copper wire which has its own bending strength and which therefore flies independently after some acceleration and does not represent the contour of the radial expanding explosive material. This

is similar to the spheres which were pushed and accelerated by the first forces and which flew then independently, partially interacting with their neighbours, their own trajectories.

This mechanically damaging effect by the pushed inert gap material against the high explosive charge should be in mind if somebody uses gap tests against confined and unconfined acceptor charges.

References

<1> M. Held, "Initiierung von Sprengstoffen ein vielschichtiges Problem der Detonationsphysik", Exlosivstoffe **5**, 2-17, 1968

<2> M. Held, "Initiation of Explosives: A Multi-Layered Problem in Detonation Physics", Translation of <1> by LLL, Reference 02973, 1980

<3> Test Serie 7 of "Recommendation of the Transport of Dangerous Goods, Test and Criteria", Second Edition, United Nations, New York, 1990

<4> M. Held, "Reaction Threshold in Unconfined and Confined Charges", Proceedings of Insensitive Munitions, Technology Symposium, Meeting #471, 338-351, 1994

<5> P.R. Lee, "Gap Tests", Chapter 8.5.1 in the book "Explosive Effects and Applications", J.A. Zukas and W.P. Walters, ISBN 0 – 387 – 98201 – 9, 1997

<6> J. E. Backofen, W.F. Schola and D. J. Bütz, "A Flash Radiograph Cassette Shielding Technique for Studying Cased Shaped Charges", Journal of Ballistics **6**, 1591-1608, 1982

1. Gap Test Arrangement

DaimlerChrysler Aerospace
TDW Gesellschaft für verteidigungstechnische Wirksysteme mbH

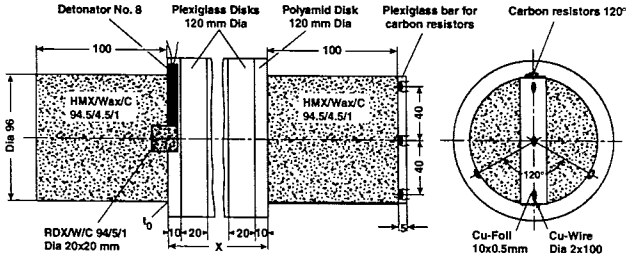

Fig. 1

1. Gap-Test Arrangement

DaimlerChrysler Aerospace
TDW Gesellschaft für verteidigungstechnische Wirksysteme mbH

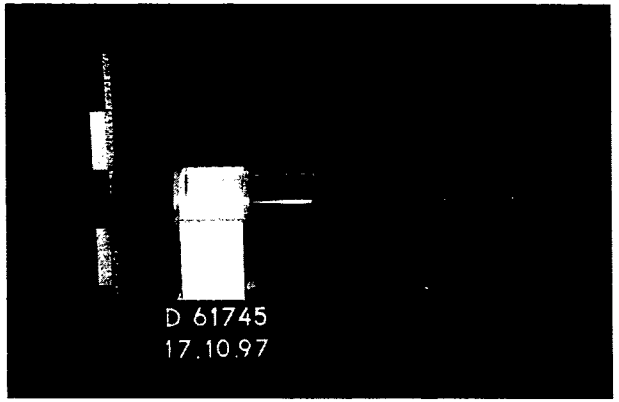

Fig. 2

Gap-Test Arrangement with FXR-Diagnostic

DaimlerChrysler Aerospace
TDW Gesellschaft für verteidigungstechnische Wirksysteme mbH

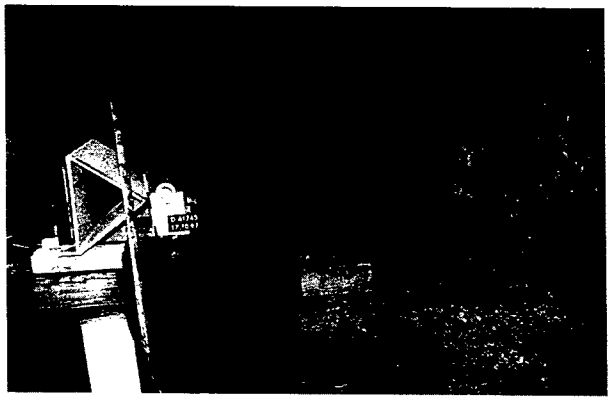

Fig. 3

Still and Dynamic FXR Pictures of the 120 mm Plexiglass Gap Length

DaimlerChrysler Aerospace
TDW Gesellschaft für verteidigungstechnische Wirksysteme mbH

(1. Gap Test Arrangement)

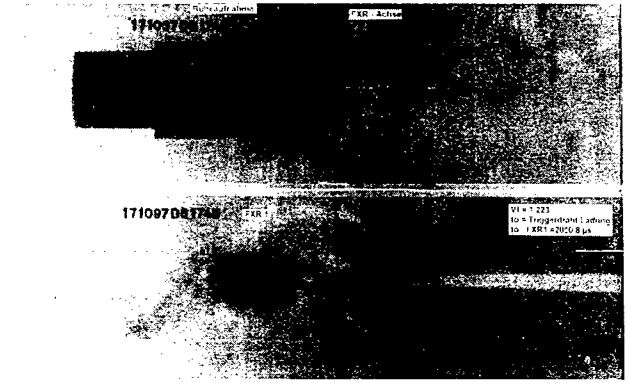

Fig. 4

Still and Dynamic FXR Pictures of the 200 mm Plexiglass Gap Length

DaimlerChrysler Aerospace
TDW Gesellschaft für verteidigungstechnische Wirksysteme mbH

(2. Gap Test Arrangement)

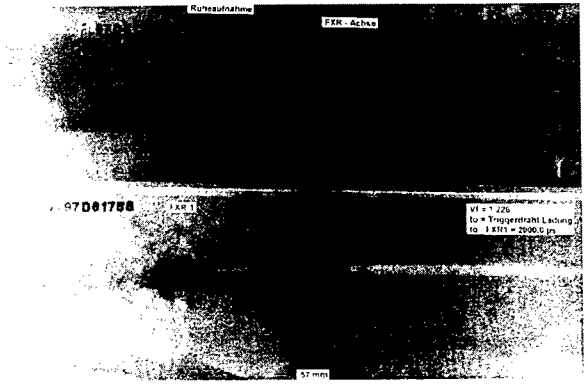

Fig. 5

Still and Dynamic FXR Pictures of the 3. Gap Test Arrangement

DaimlerChrysler Aerospace
TDW Gesellschaft für verteidigungstechnische Wirksysteme mbH

(Composite Gap Material with 8 x 20 mm Plexiglass / 2 x 10 mm Polyamid and 1 x 20 mm Steel (in the Middle) Disks)

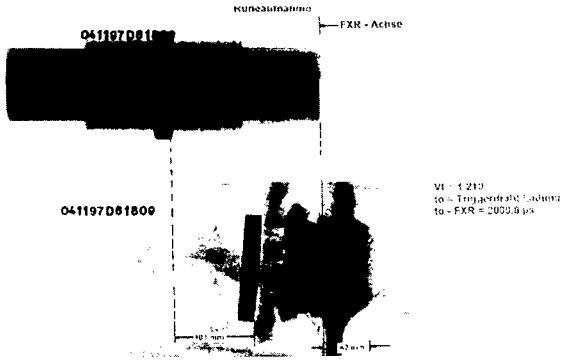

Fig. 6

4. Gap Test Arrangement Det. 61 810

DaimlerChrysler Aerospace
TDW Gesellschaft für verteidigungstechnische Wirksysteme mbH

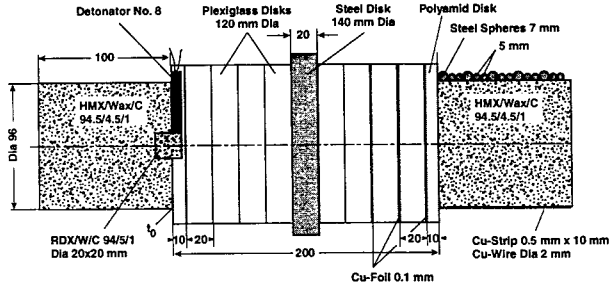

Fig. 7

4. Gap Test Setup

DaimlerChrysler Aerospace
TDW Gesellschaft für verteidigungstechnische Wirksysteme mbH

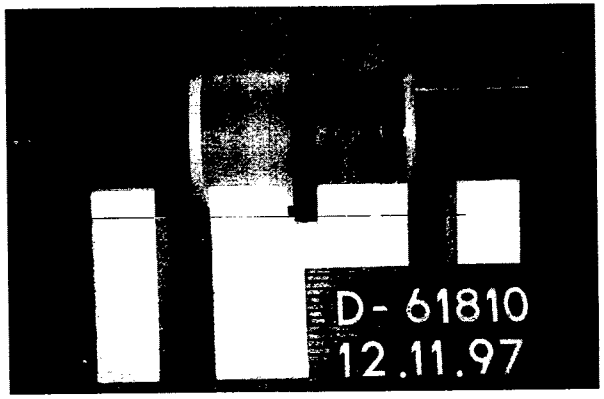

Fig. 8

Still and Dynamic FXR Pictures of the 4. Gap Test Arrangement

DaimlerChrysler Aerospace
TDW Gesellschaft für verteidigungstechnische Wirksysteme mbH

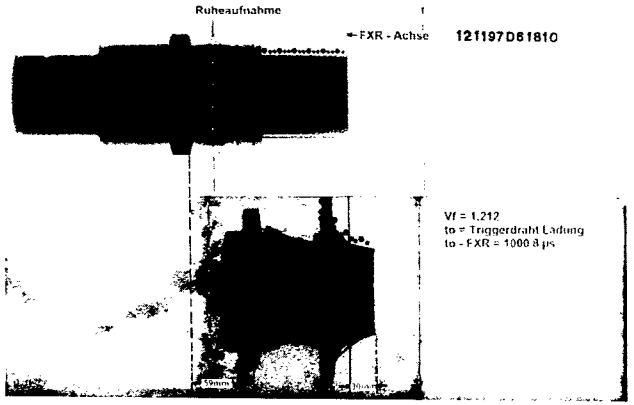

Fig. 9

5. Gap Test Arrangement Det. 61 811

DaimlerChrysler Aerospace
TDW Gesellschaft für verteidigungstechnische Wirksysteme mbH

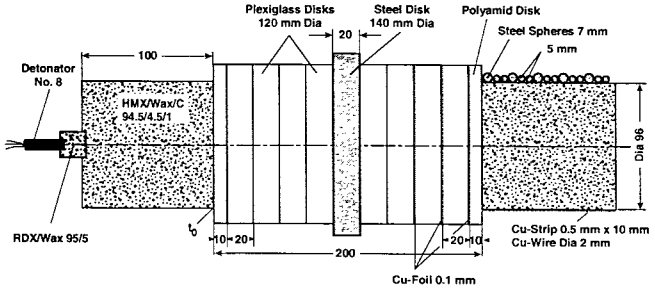

Fig. 10

Still and Dynamic FXR Pictures of the 5. Gap Test Arrangement

DaimlerChrysler Aerospace
TDW Gesellschaft für verteidigungstechnische Wirksysteme mbH

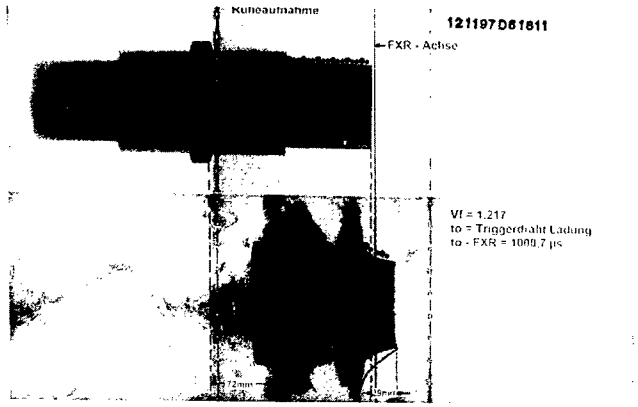

Fig. 11

Displacement of Spheres on the Acceptor Charge

DaimlerChrysler Aerospace
TDW Gesellschaft für verteidigungstechnische Wirksysteme mbH

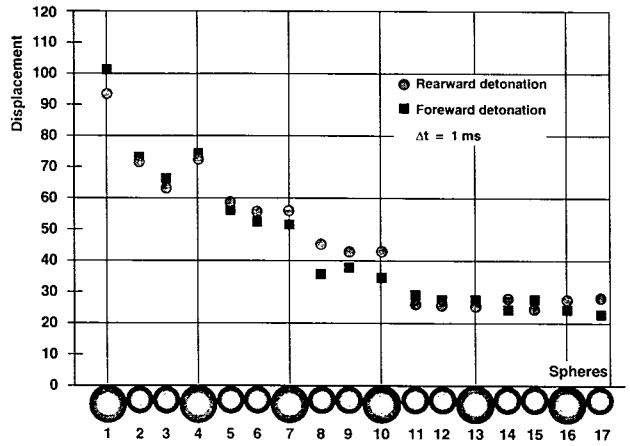

Fig. 12

SHELF LIFE EVALUATION OF EXPERIMENTAL 155mm CHARGES

Helge Gisa Schimansky

Somchem, Division of DENEL, (Pty), Ltd, Gun Propulsion – R & D,

Abstract

In order to develop a test procedure for the specific determination of shelf lives of 155mm charges, an accelerated ageing program was followed by a real time storage monitoring program. The monitor program of the charges has been running since 1989.

Test procedures for the determination of shelf lives of propellants and ammunition have been developed from results obtained during small-scale studies performed on propellants as single components. In the case of 155mm charges, various propellant components are in contact with each other during storage and this should be taken into account when performing accelerated ageing studies.

This presentation will give

- a layout of the accelerated ageing program, describing the ageing conditions as well as the calculation of the shelf life of the charges;
- a layout of the monitor program conducted at 5 different storage locations in South Africa; and
- a discussion of the results of the monitor program and the correlation between the predictions from the accelerated ageing program and the real time storage results.

The final aim of this study is to use the monitor program results to refine the simulation model for the prediction of shelf lives for 155mm charges.

1 INTRODUCTION

In general, test procedures for the determination of shelf lives of propellants have been developed from results obtained during small-scale studies performed on propellants as single components. In the case of 155mm charges, various propellant components are in contact with each other during storage and this should be taken into account when performing accelerated ageing studies.

The most realistic simulation of real storage conditions, which is always as an assembled charge, should be created. In this manner additional studies regarding the migration patterns and the moisture distribution between the components can then be evaluated in the same ageing program.

During 1989 an accelerated ageing program was conducted on an experimental 155mm combustible case charge (EXP charge). From this ageing program a prediction of the chemical shelf life of each of the components of the EXP charge was calculated.

The accelerated ageing program was followed by a real time storage Monitor program, which is now in its 10th year, of the EXP charges at five different locations in South Africa.

2 ACCELERATED AGEING PROGRAM

The main propellant components of the EXP charge, namely Component A and Component B, were aged in combination at 90, 80, 70, 60, and 50°C. The stabiliser depletion was monitored for periods up to 12 weeks. The stabiliser depletion rates were determined with the aid of Zero and First Order reaction kinetics and subsequently the shelf life, $t_{1/2}$, for different storage temperatures.

2.1 COMPONENT A

Graph 1 is a graphical presentation of the results of the stabiliser depletion of Components A of the EXP charges aged at the respective temperatures.

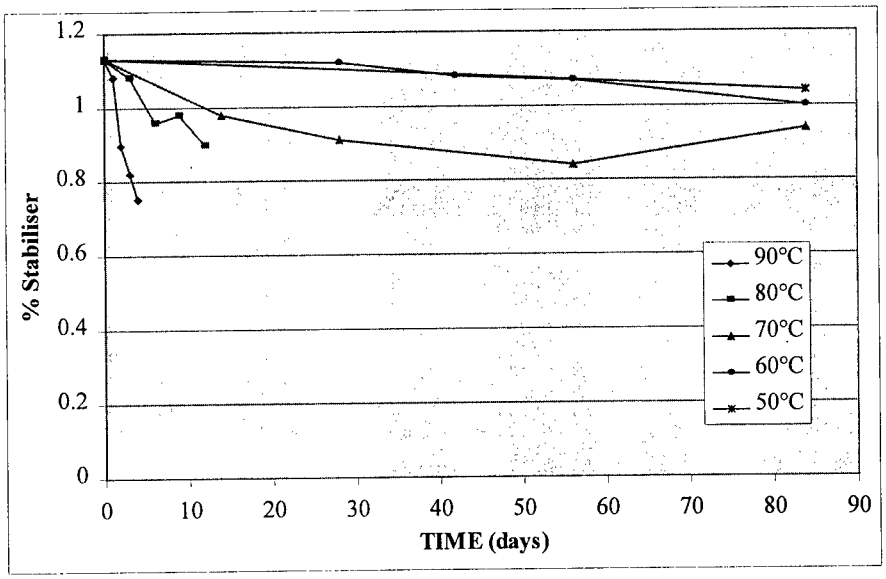

Graph 1: Stabiliser depletion results for Components A of EXP charge

The calculations and shelf life predictions according to Zero and First Order reaction kinetics for Components A of the aged EXP charges are summarised in Table 1 and shown in Graph 2.

Table 1: Calculations according to Zero and First Order reaction kinetics for Component A of EXP charge *(predicted values in Italics)*

		Zero Order Reaction Rate			First Order Reaction Rate		
TEMP. (°C)	TEMP. (1/°K)	k	ln k	$t_{1/2}$ (years)	k	ln k	$t_{1/2}$ (years)
90	0.002755	0.1020	-2.2828	0.0150	0.1095	-2.2118	0.0173
80	0.002833	0.0187	-3.9792	0.0820	0.0184	-3.9954	0.1032
70	0.002915	0.0049	-5.3185	0.3131	0.0050	-5.2983	0.3798
60	0.003003	0.0016	-6.4378	0.9589	0.0015	-6.5023	1.2660
50	0.003096	0.0011	-6.8124	1.3948	0.0010	-6.9078	1.8990
40	0.003195	*0.0001763*	*-8.6432*	*9*	*0.0001534*	*-8.7827*	*12*
30	0.003300	*0.0000429*	*-10.0558*	*36*	*0.0000356*	*-10.2424*	*53*
20	0.003413	*0.0000095*	*-11.5648*	*162*	*0.0000075*	*-11.8018*	*253*
Slope:		-13397.0			-13843.6		
Ea (J/mol):		111382.5			115095.9		

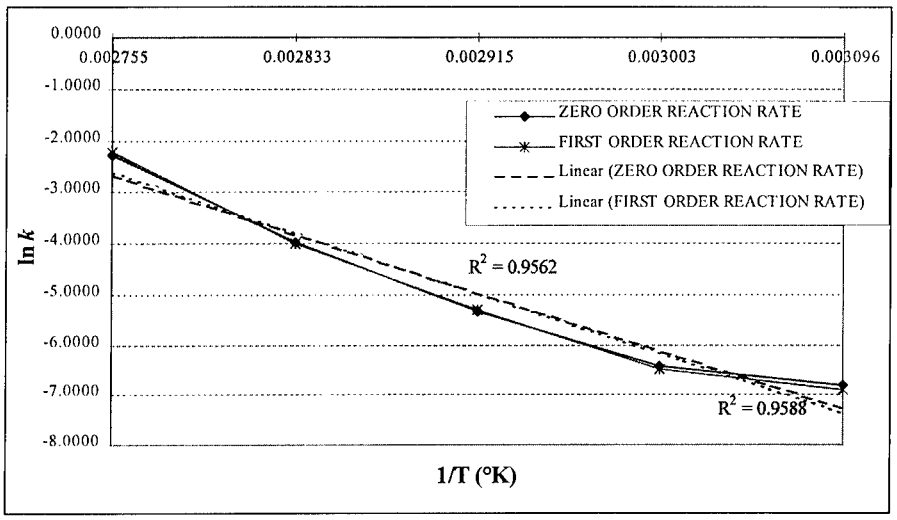

Graph 2: Graphical representation of Zero and First Order reaction kinetics for Comp A

2.2 COMPONENT B

Graph 3 is a graphical presentation of the results of the stabiliser depletion of Components B of the EXP charges aged at the respective temperatures.

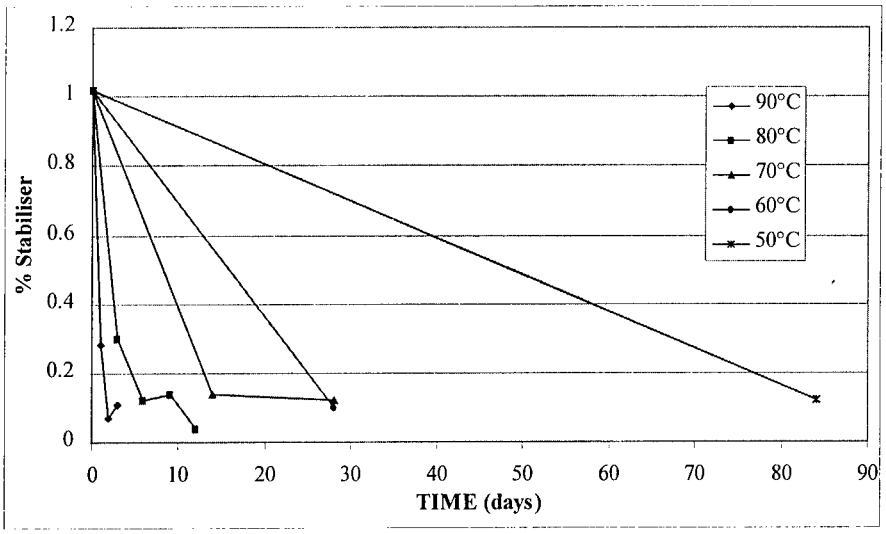

Graph 3: Stabiliser depletion results for Components B of EXP charge

The calculations and shelf life predictions according to Zero and First Order reaction kinetics for Component B of the aged EXP charges are summarised in Table 2 and shown in Graph 4.

Table 2: Calculations according to Zero and First Order reaction kinetics for Component B of EXP charge *(predicted values in Italics)*

		Zero Order Reaction Rate			First Order Reaction Rate		
TEMP. (°C)	**TEMP. (1/°K)**	***k***	**ln *k***	**$t_{1/2}$ (years)**	***k***	**ln *k***	**$t_{1/2}$ (years)**
90	0.002755	0.2940	-1.2242	0.0049	0.8068	-0.2147	0.0024
80	0.002833	0.0707	-2.6493	0.0205	0.2413	-1.4217	0.0079
70	0.002915	0.0321	-3.4389	0.0452	0.0764	-2.5718	0.0249
60	0.003003	0.0329	-3.4143	0.0441	0.0829	-2.4901	0.0229
50	0.003096	0.0107	-4.5375	0.1357	0.0255	-3.6691	0.0745
40	0.003195	*0.0044396*	*-5.4172*	*0.3*	*0.0097820*	*-4.6272*	*0.2*
30	0.003300	*0.0017901*	*-6.3255*	*0.8*	*0.0036674*	*-5.6083*	*0.5*
20	0.003413	*0.0006784*	*-7.2958*	*2.1*	*0.0012859*	*-6.6563*	*1.5*
Slope:			-8614.4			-9304.4	
Ea (J/mol):			71620.1			77356.7	

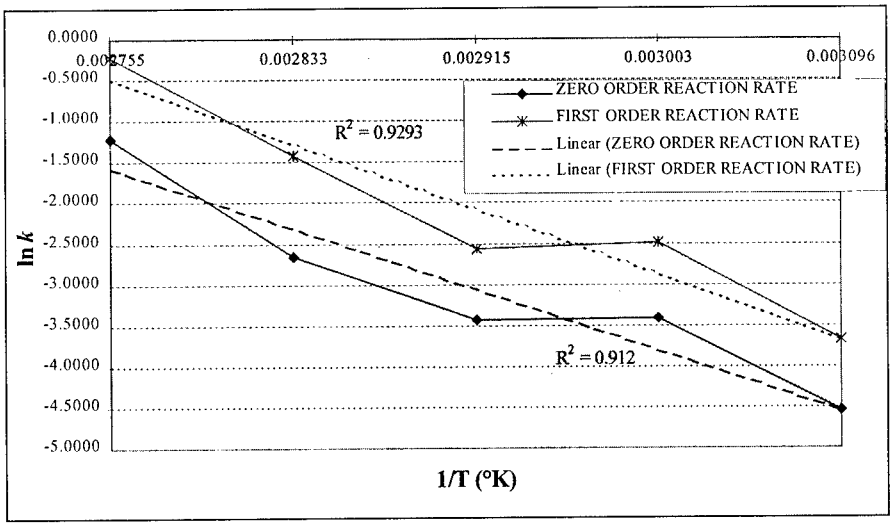

Graph 4: Graphical representation of Zero and First Order reaction kinetics for Comp B

2.3 EVALUATION OF SHELF LIFE PREDICTIONS

The shelf life predictions for Components A and B are summarised in Table 3.

Table 3: Summary of shelf life predictions

		Component A	Component B
ZERO ORDER REACTION KINETICS	Ea (kJ/mol)	111.4	71.6
	Corr. Coeff. (Ln k vs. 1/T)	0.9562	0.9120
	$t_{1/2}$ at 40°C	9	0.3
	$t_{1/2}$ at 30°C	36	0.8
	$t_{1/2}$ at 20°C	162	2.1
FIRST ORDER REACTION KINETICS	Ea (kJ/mol)	115.1	77.4
	Corr. Coeff. (Ln k vs. 1/T)	0.9588	0.9293
	$t_{1/2}$ at 40°C	12	0.2
	$t_{1/2}$ at 30°C	53	0.5
	$t_{1/2}$ at 20°C	253	1.5

The stabiliser depletion results fit into both the zero and the first order reaction rate graphs. Therefore no definite decisions can be taken on whether the break down of the stabiliser is zero order or first order. The question of the type of reaction order of the stabiliser depletion has been widely asked in literature with no definite answer.

All the predictions that have been made assume a linear plot of ln$k$ vs. $1/T$. From the graphs (Graphs 2 and 4) it can be seen that this is not completely true. For example in Graph 2, ln$k$ vs. $1/T$ was plotted for Component A according to zero order reaction kinetics and Ea was calculated from the slope of the graph. This slope is obtained from a linear fit through the five temperature points.

However, if the same plot is used and the Ea is determined between every two temperature points, i.e. between 90 and 80, 80 and 70, 70 and 60 and 60 and 50°C, it is apparent that the Ea changes as the ageing temperature changes. Refer to Graph 5.

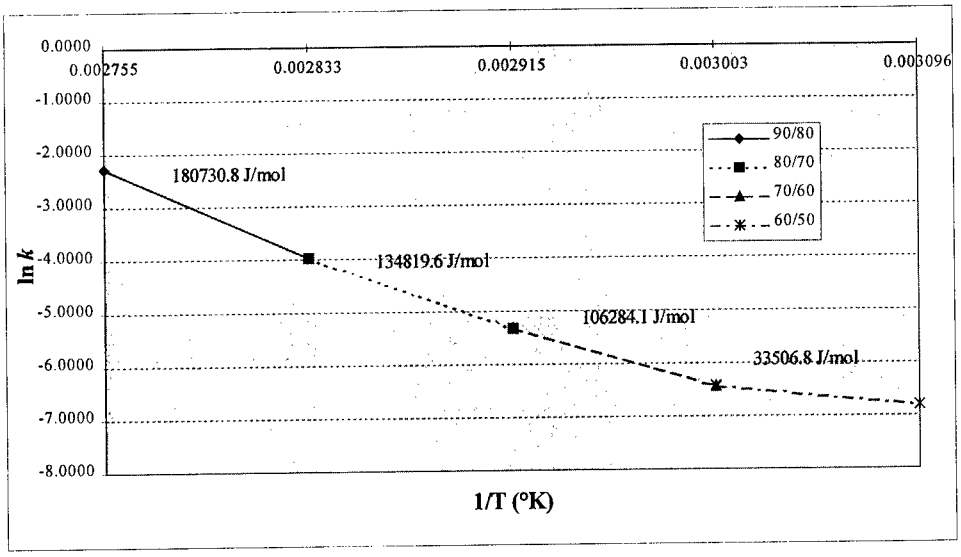

Graph 5: Graphical representation of Zero Order reaction kinetics for Component A indicating the change in *Ea* with change in ageing temperature

This observation highlights the difficulties of shelf life prognosis. To save time accelerated ageing programs are performed at high temperatures and predictions are made for general storage conditions, but the reaction rates and activation energies could differ at these conditions.

The interaction that takes place between the components of a charge can also influence the reaction rates and activation energies. This can be seen from the results obtained when Component B is aged on its own at the same temperatures. Refer to Graph 6 for a graphical presentation of the stabiliser depletion results and Table 4 for the shelf life predictions.

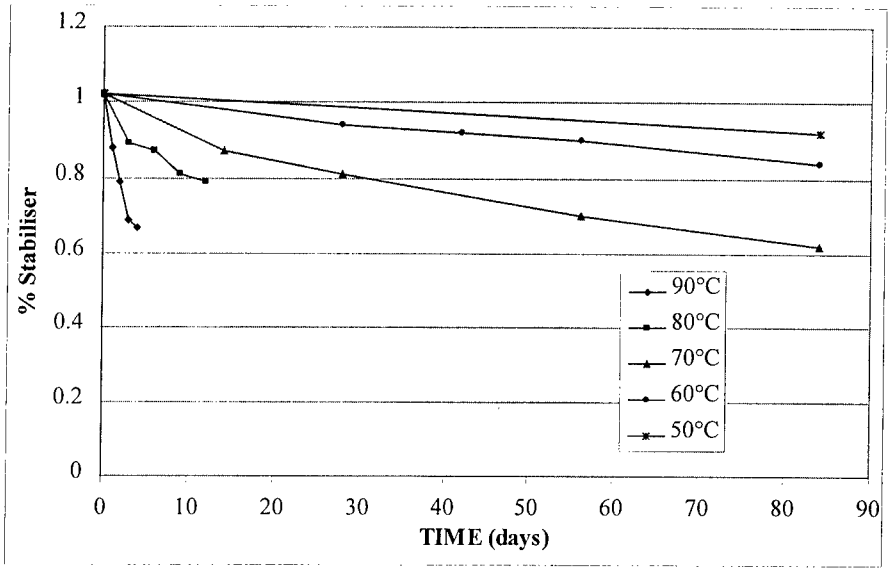

Graph 6: Stabiliser depletion results for Component B aged on its own

Table 4: Calculations according to Zero and First Order reaction kinetics for Component B aged on its own *(predicted values in Italics)*

		Zero Order Reaction Rate			First Order Reaction Rate		
TEMP. (°C)	**TEMP. (1/°K)**	***k***	**ln *k***	**$t_{1/2}$ (years)**	***k***	**ln *k***	**$t_{1/2}$ (years)**
90	0.002755	0.0890	-2.4191	0.0163	0.1084	-2.2219	0.0175
80	0.002833	0.0180	-4.0174	0.0807	0.0202	-3.9021	0.0940
70	0.002915	0.0044	-5.4262	0.3300	0.0056	-5.1850	0.3391
60	0.003003	0.0021	-6.1658	0.6915	0.0022	-6.1193	0.8632
50	0.003096	0.0012	-6.7254	1.2100	0.0012	-6.7254	1.5825
40	0.003195	*0.0002281*	*-8.3857*	*6*	*0.0002211*	*-8.4169*	*9*
30	0.003300	*0.0000610*	*-9.7052*	*24*	*0.0000557*	*-9.7946*	*34*
20	0.003413	*0.0000149*	*-11.1149*	*98*	*0.0000128*	*-11.2664*	*148*
Slope:		-12514.8			-13066.1		
Ea (J/mol):		104047.7			108631.2		

Comparing the results of Component B aged in the EXP charge and aged on its own (Table 2 and Table 4) there is a difference in the ageing behaviour and therefore the shelf life predictions of the component. These results show clearly, that when conducting ageing programs with 155mm charges, the complete charges and not separate components must undergo the accelerated ageing. In this manner the most realistic simulation of real storage conditions is created and the influence that the various components have on each other during storage is taken into account.

In order to verify the results from the accelerated ageing program and to develop a test procedure suitable for the specific determination of shelf lives of 155mm charges the above-mentioned predictions are compared with the real time storage results obtained from the Monitor Program.

3 MONITOR PROGRAM

The EXP charges were placed into standard plastic bags into cardboard containers, which in turn were stacked into wooden wire-bound crates and stored at five different locations in South Africa.

The average storage relative humidities and temperatures measured over 24 hours of the different locations for the past ten years are as follows:

Table 5: Relative Humidities and Temperatures at the different storage locations

- average values over 24 hrs
- *absolute minimum/maximum values*

LOCA-TION	RELATIVE HUMIDITY IN MAGAZINE - %			TEMPERATURE IN MAGAZINE - °C			TEMPERATURE OF ENVIRONMENT - °C		
	minimum	average	maximum	minimum	average	maximum	minimum	average	maximum
AP	58.88	70.45	78.96	20.16	23.46	26.38	15.09	21.88	29.33
	36.25		*94.00*	*13.74*		*33.69*	*7.01*		*37.54*
BP	50.84	66.17	77.18	15.47	18.01	20.76	10.20	17.74	27.12
	20.88		*95.70*	*5.15*		*31.30*	*2.46*		*38.80*
CP	41.03	47.17	54.07	19.78	21.92	24.41	9.91	20.32	32.81
	25.52		*69.03*	*6.30*		*30.93*	*0.46*		*39.31*
DV	15.67	38.01	80.27	5.42	18.68	32.46	3.97	17.93	31.42
	3.47		*99.60*	*-1.51*		*47.52*	*-6.43*		*45.53*
EP	24.08	31.93	43.65	13.37	17.87	22.08	3.38	15.03	27.24
	8.53		*60.34*	*-4.51*		*35.52*	*-6.76*		*41.19*

During the monitor program charges are withdrawn on a yearly basis for chemical evaluation. The charges are dismantled and the stabiliser depletion of the propellant components, i.e. Component A and B, are determined. The results for the different storage locations are given in the following paragraphs and the correlation with the predictions is discussed.

3.1 COMPONENT A

The results of the stabiliser depletion of Component A stored in assembled charges at different locations are represented graphically in Graph 7.

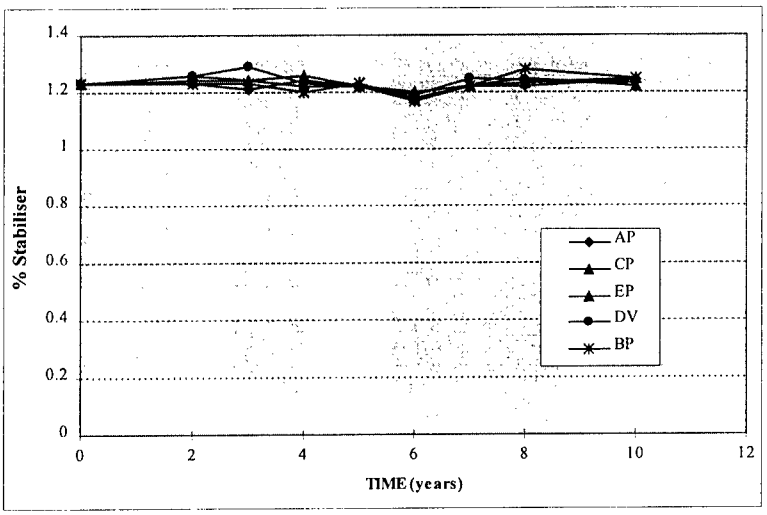

Graph 7: Plot of %Stabiliser vs. time for Component A from stored EXP charges

The half life, $t_{1/2}$, of Component A in the charges of the Monitor program has not been reached. Looking at the Graph 7 it is not reliable to make any extrapolations or calculate any values, as the stabiliser content of Component A has remained nearly constant over the last ten years.

But referring back to the shelf life predictions as shown in Table 1, it becomes clear that there is a good correlation between the predictions and the storage results, as the predicted $t_{1/2}$ at 20°C for Component A is >100years. Therefore no major change is expected during the first 10 years of storage.

3.2 COMPONENT B

The results of the stabiliser depletion of Component B stored in assembled charges at different locations are represented graphically in Graph 8.

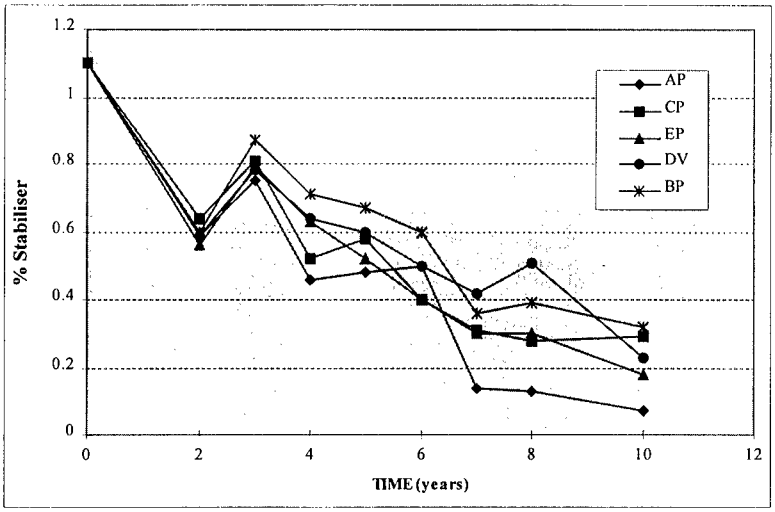

Graph 8: Plot of %Stabiliser vs. time for Component B from stored EXP charges

In contrast to Component A, the half life of Component B of the charges has been reached and the $t_{½}$ values as supplied in Table 6 for the different storage locations are compared to the predicted $t_{½}$ values in Table 2.

Table 6: Comparison of predicted and real time chemical shelf lives for Component B from stored EXP charges

Predicted $t_{1/2}$ for 20°C from Accelerated Ageing Program (years)		Real Time Storage Results	
Zero Order	First Order	Location	$t_{1/2}$ (years)
2.1	1.5	AP	4.3
		BP	5.8
		CP	5.0
		DV	5.5
		EP	4.8

From these results it can be seen that both the zero and the first order reaction kinetics give a more pessimistic prediction of the shelf life than the real time storage results reveal. It would therefore be possible to use either of the methods for future shelf life predictions.

4 SUMMARY

It is important to note that predictions made from accelerated ageing programs only give an indication of the real storage life and should not be regarded as exact values. One of the main aims of any accelerated ageing program should be to simulate the storage conditions in the best possible way and thus optimising the shelf life predictions.

The results that have been obtained to date from the Monitor Program of the 155mm EXP charges in comparison to the accelerated ageing results indicate that:

- ageing studies be conducted at temperatures not exceeding 70°C, as different reaction rates take place at higher temperatures;

- ageing studies on 155mm charges should be conducted on assembled charges, thus incorporating the influence of the components on each other into the calculations and therefore obtaining more realistic results.

This presentation gives some of the evaluations taking place between the accelerated ageing and the monitor program of the 155mm EXP charges. Further studies are conducted on the following parameters:

- the influence of humidity in addition to temperature;

- the migration of nitrate esters between the components of the charge;

- the ballistic performance of the charge.

The final aim of the study is to refine the simulations model for the prediction of the shelf lives of 155mm charges taking into account all of the above mentioned parameters.

31 st International Annual Conference of ICT June 27 – June 30, 2000

ENERGY MEASUREMENT AND CHARACTERIZATION OF INSENSITIVE MUNITIONS (IM) AS AN EXPERIMENTAL METHOD FOR DETERMINATION OF IM TERMINAL EFFECTIVENESS FOR VARIOUS FORMULATIONS.

Gideon J Ellis
Naschem, Division of Denel, Private Bag X1254,
Potchefstroom, 2520, RSA

ABSTRACT

Technological advances in the design of explosive ordnance are making possible the development of a range of munitions termed Insensitive Munitions (IM) which are less vulnerable to accidental and combat stimuli than previous weapons. Such munitions remain effective in their intended application, but are less sensitive than their predecessors to extreme environments such as heat, shock or impact.

The objective of this study was to compare the lethal effectiveness of artillery shells filled with various IM -based explosive formulations.

Fragmentation pit and arena data, including fragment velocity results, were used to quantify the terminal effectiveness of the explosive fillings in 76 mm and 155 mm caliber shells.

The flyer plate method was also used to determine explosive detonation parameters of various IM explosive formulations. Aspects of this well-known elementary test method were investigated in order to establish a reliable, but cost effective way to characterize the explosive filling of an IM fragmentation warhead.

The correlation between the detonation energy and the terminal effectiveness of the warhead, in terms of the lethal area, was finally established.

Fragmentation pit data (which is sensitive for characterizing explosive fillings) as well as static arena tests were used to verify the flyer plate test data as a reliable indicator of the terminal effectiveness of the IM fragmentation warhead as a function of the type of IM high explosive filling.

The terminal effectiveness of a fragmentation warhead is quantified by calculating the perforation capability of the fragments as function of mass and distance. The flux of lethal fragments was determined as function of distance by taking into account the fragment spread angle as measured experimentally in the static arena tests. By setting a fixed lethality criterion, comparisons were made between the different terminal effectiveness (lethal) areas, obtained for various IM explosive fillings such as various NTO and PBX formulations.

THE EFFECT OF FUEL'S CALORICITY ON IMPACT SENSITIVENESS OF BINARY OXIDIZER-FUEL COMPOSITIONS

V.A.Teselkin, A.V.Dubovik

Semenov Institute of Chemical Physics RAS

117977. Kosygin Str., 4. Moscow, Russia

The results of experimental investigations on impact sensitivity of binary oxidizer-fuel compositions as-a functions of fuel's caloricity and oxidizer's chemical activity are presented. The sensitivities of all investigating compositions increase when caloricity of fuels increase also. Maxima of composition's sensitivities depends poorly on physico-chemical nature of oxidizers.

In developing of new Solid Propellants it is necessary to have a positive information about its sensitivity to mechanical actions (impact, friction etc.). This information may be obtained on the base of reliable data on sensitivities of main SP-components and its combinations, in particular an oxidizer-fuel (OF) compositions. Generally speaking an OF-compositions may be considered as elementary SP

According to [1] the impact initiation OF-compositions are taking place due to chemical interaction between the oxidizer's decomposition products and fuel component during «hot spots» formation in deformable explosive charge. The heat generation and maximal temperature in this chemical reaction depend on fuel caloricity. The increasing of fuel caloricity will increase the sensitivity OF-composition

In this work the experimental study OF-sensitivity to impact is fulfilled for different combinations of fuels and oxidizers. As a fuel we used the polymers PMMA, fluoroplastic, powder metals Al, B, organoboron compounds (carboranes). Its caloricities changes from q=8 to q=60 MJ/kg. We used the oxidizers with different chemical activity - nitrates, chlorates, perchlorates of ammonium, potassium, sodium and ADN. AP chemical activity depends on the particle defects. The last character determines the index of AP low-temperature decomposition's depth. Oxidizer-Fuel ratio is set up 9:1 It corresponds near to zeroth oxygen balance for all compositions.

Experimental determination of the impact sensitivity for OF-compositions has been carried out by critical pressure method [2]. We have used drop-weight machine with the weight mass 10 kg and

dropping height 0,25 m (mechanical stiffness of the loading system 2,7 MN/cm) The sample under study was made in form of thin pressed disc, which was placed between the plane ends of cylindrical rollers in diameter 10 mm. The roller apparatus afforded a free scatter of failing sample during the impact. The impact pressure was measured with aid of fast-response strain gauge and dual-trace oscillograph (2-nd trace we used for recording of explosion initiation time). It may see a characteristic drop in impact pressure and (under specific conditions) an explosion initiation when the charge is failed.

By way of the sensitivity characteristic OF-compositions we took a critical pressure of explosion initiation P_c. This value corresponds to the boundary between the charge failures with and without explosions under impact (we did not consider the low-probable explosions under repeating failures of the charge). The more the value P_c than lower the OF-sensitivity to impact.

Experimental functions $P_c(q)$ are presented in Figure. All exhibited curves behaves in an unique manner: the increasing in q brings to the decreasing in P_c. However the tempo of P_c decreasing is unequal for different oxidizers. It is maximal for the nitrates of ammonium and it is minimal for ADN. At great q the sensitivities of all compositions is equal approximately.

Let's discuss the results. High sensitiveness for ADN-compositions is explained by high-level sensitivity ADN itself (P_c=0,56 GPa). In all compositions ADN behaves as oxidizer and high-explosive simultaneously. Low-caloricity fuels may be considered approximately as an inert for ADN-compositions. Only with high-caloricity fuels the ADN behaves as active oxidizer. The competing properties of ADN explain a weak dependence $P_c(q)$ for ADN-composition.

On the contrary the oxidizers $KClO_3$, $KC10_4$, $NaNO_3$ are not exploded in the small-scale drop-weight experiments (P_c>l,2 GPa). They may explode only in a tight contact with high-reducing agent (reductant). The more reducing ability of the fuel then greater the sensitivity of OF-composition. This reason explains a strong dependence $P_c(q)$ with unexploded oxidizers. As one would expect the curve $P_c(q)$ for AP-compositions takes up an intermediate place between the curve $P_c(q)$ for ADN-compositions and the curves $P_c(q)$ for the compositions with unexploded oxidizers, as AP is low-sensitive explosive (P_c=0,85 GPa).

The functions $P_c(q)$ on Figure establish only general tendency to increasing the composition's sensitiveness when the value q is increased. However some important factors (catalyst activity and thermostability of the fuel, chemical activity of oxidizer etc.) may strongly effect on sensitivity OF-compositions. We have observed an essential deviation from obtaining curves for some OF-

compositions. For example we consider the sensitiveness of (AP-Ferrocene) -composition. The caloricity of Ferrocene (FC) approximately equal to PMMA one. It is known that Ferrum-containing substances are active catalysts in AP-decomposition in a broad interval of the pressures and temperatures [3]. In result of catalyst effect we observe the decreasing of P_c by the value 0,15 GPa from the basic AP-curve (see the point f_1 at Figure).

The most sensibility effect on the sensitivity (AP-FC)-composition has been observed when we used AP with high-depth low-temperature decomposition η.. Point f_2 at Figure has been obtained for AP with η =0,21 (basic AP-curve has been obtained with η|=0,11). In last case the sensitivity (AP-FC) -composition is close to maximal sensitivities OF-compositions (under maximal q).

Maximal sensitiveness OF-compositions has been observed for boron- and carborane-containing fuels with the caloricities up to 60 MJ/kg. As one can see from Figure the values P_c for these compositions depend poorly on the oxidizer's nature. It is explained by the strong reducing ability of these fuels, which form a high-reaction-capability pairs with any oxidizer. The sensitiveness of compositions carborane with NH_4ClO_4 and $KC10_4$ are characterised by the values P_c=0,20-0,25 GPa. These values P_c are characterised the sensitiveness of some primary explosives (P_c=0,26 GPa for lead azide).

LITERATURE

1. V.A.Teselkin at al. Fiz. Goren. Vzryva. 1971, v.7, N2, pp. 261-264.
2. G.T.Afanasjev, V.K.Bobolev. Sensitiveness of Solid Explosives to Impact. M., Nauka, 1968.
3. P.W.M.Jacobs, H.M.Whitehead. Chem. Rev. 1969, N4, p.551.

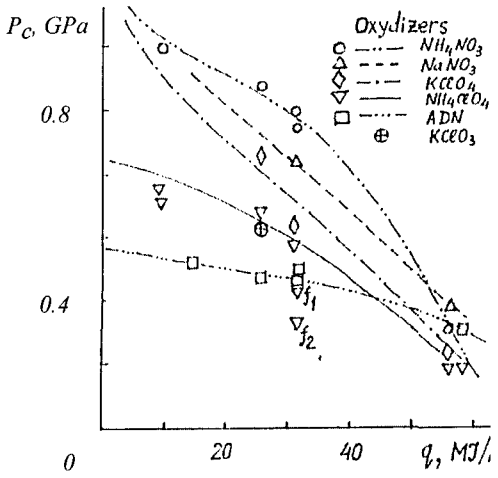

FIGURE. $P_c(q)$-dependencies for studying OF-compositions

Shock Compression of Liquid Hydrazine. Estimation of Detonability and Sensitivity to Shock Loading of Its Solutions

I. M. Voskoboinikov and O. I. Voskoboinikova.

Semenov Institute of Chemical Physics, Russian Academy of Sciences,
ul. Kosygina 4, Moscow, 117977 Russia

The possibility of calculation of the parameters of a shock compression of liquid hydrazine within the frameworks of the schemes developed for description of the compression of organic liquids and liquefied gases is shown. In the case when the mass velocities behind shock fronts do not exceed the value equals 3.1 mm/μs, it may be managed under assumption of the retention of the initial compound (hydrazine, in our case) behind a shock front. The detonation velocities of hydrazine solutions with such explosives as nitromethane and hydrazinenitrate correspond to the destruction of hydrazine up to ammonia and nitrogen that is accompanied by a noticeable energy release. The estimates performed demonstrate a possibility of the detonation of a liquid hydrazine with the velocity equals 8 mm/μs, during which the heating up of the substance behind a shock front (equals approximately 2000 K) is comparable with those observed behind a shock front during detonation of liquid explosives. The large values of the critical diameter of detonation up to the value equals 1 m are expected because of a large activation energy of hydrazine decomposition equals 53.2 kcal/mol, which is almost 1.4 times larger than the activation energy of decomposition of usual explosives. They are decreased up to the values equal 20—50 mm on addition of a certain amount of liquid explosives. In this case, their more rapid decomposition behind a shock front gives rise to the temperature increase that is sufficient for destruction of hydrazine in a time less than 0.1 μs.

Liquid hydrazine and water under normal conditions have similar initial densities and compressibility that may suppose a similarity of their Hugoniots expressed with respect to the variables pressure--mass velocity if the initial compounds do not react behind a shock wave. However, it is known from the available literature that solutions of explosives with hydrazine and water detonate with noticeably differed velocities under equal concentrations, although, the detonation pressures may not exceed the ones attained at a shock wave compression of hydrazine and water. The most probable reason of this may be the destruction of hydrazine behind shock front of the detonation wave in the solutions. It due to higher temperatures attained because of decomposition first of all an explosive and which have not been attained behind a shock front in hydrazine in the set of the experiments conducted for determination of its Hugoniot. Below, we present the results of certain estimates of this phenomenon.

Hugoniots of Hydrazine and Water

Hugoniot of liquid hydrazine was determined for the mass velocity values U_P which did not exceed 3.1 mm/μs [1]. The experimental velocities U_S of shock wave propagation determined in this work are plotted on the graph (Fig. 1) as squares. In the same figure the values obtained in [2, 13] for Hugoniot of water are plotted for comparison as triangles and rhombus. At U_P value, which does not exceed 2 mm/μs, Hugoniot of hydrazine one can describe by the dependence for liquefied gases [3], taken in the form $U_S = C_0 + 1.9\ U_P - 0.08\ U_P^2/C_0$, where C_0 is the sound velocity at the initial state. This value is equal to 1.95 mm/μs in hydrazine at the density equals 1.01 g/cm^3. A noticeable discrepancy from the calculated dependence (the upper curve in the Fig. 1) is observed for the mass velocity values equal approximately 3 mm/μs. The results of calculation for water (C_0 = 1.5 mm/μs) are presented in the same figure by a lower curve. They are fitted with the experimental values better than in the case of hydrazine. For the mass velocity

values up to 2 mm/μs one can observe an expected displacement of experimental values from water to hydrazine on the value as large as 0.45 mm/μs due to a difference of initial sound velocities.

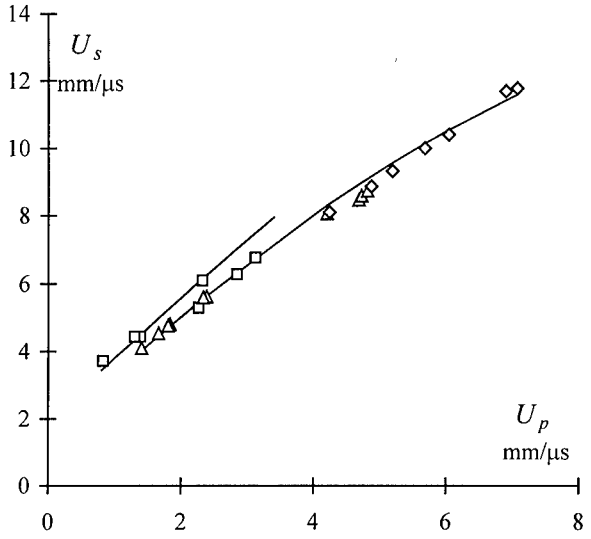

Fig. 1. Hugoniots of hydrazine and water.

The temperatures of a shock wave compression of hydrazine, calculated by the scheme of [4], within a considered range of the mass velocities may be described by the following linear expression: $T = 400 + 50\ P$, where T is the temperature in degrees of Kelvin, P is the pressure in GPa. The following equation, obtained within the frameworks of the model of a molecular crystal (the structural unit is a molecule but not an atom, the energies of intermolecular bonds remain unchangeable with the increase of a compression ratio), was solved

$c_V(\frac{dT}{dU_p}) = U_p - (C_0 + aU_p^2)(U_p - c_{V1}\Gamma_0 T/U_S)/U_S$, where c_V is the total heat capacity, c_{V1} is the heat capacity connected with the intermolecular interaction (equals 5R and 6R per mole for diatomic and polyatomic molecules, correspondingly). Γ_0 is the Gruneisen coefficient (in performed calculations the

ratio of the Gruneisen coefficient to a specific volume was assumed to be constant) at the initial state, $U_S = C_0 + b\ U_P - a\ U_P^2$.

According to [5], a decomposition of hydrazine vapors in the reaction of the first order at the temperatures equal 1100—1400 K may be described by the Arrhenius expression with the activation energy equals 53.2 kcal/mol and the logarithm of a pre-exponential factor equals 13.6. Based on these values, one should expect a destruction of liquid hydrazine behind a shock front during typical times of usual experiments for determination of Hugoniot under the temperatures larger than 1500—1650 K. According to performed calculations the mass velocities 2.9—3.25 mm/μs correspond to these temperatures. This is not contradict to the fact that the data [1] (the mass velocities up to 3.1 mm/μs) can be described under assumption of the lack of hydrazine transformations behind a shock front, although, for several large values of U_P the situation would apparently be changed.

Detonation of the solutions of explosives with hydrazine and water

It has long been observed [6] that at dilution of nitromethane by hydrazine a detonation velocity D not only does not decrease, but even noticeably increases from the value 6.3 mm/μs for pure nitromethane up to 7.3 mm/μs for a solution with 0.75 weight content of hydrazine. The detonation velocities of solutions of hydrazinenitrate with hydrazine in the ratios equal 79/21 and 30/70 are smaller than the detonation velocity of a pure hydrazinenitrate only on 0.1 and 0.8 mm/μs, correspondingly [7]. Detonation velocities of the solutions of nitromethane with methanol [6] and hydrazinenitroform with water (the weight content of methanol and water equals to 0.35 and 0.3) on 1.1 mm/μs and 1.5 mm/μs smaller than the detonation velocity of nitromethane and hydrazinenitroform. Because Hugoniot of hydrazine is similar with Hugoniot of water, then, by analogy with these data should expect a noticeable decrease of a detonation velocity at dilution of a sufficiently powerful explosive by hydrazine. This was not observed, although, at

dilution of the solution hydrazinenitrate-hydrazine in the ratio equals 93.2/7.8 with water, the weight content is 0.241, the detonation velocity of the initial solution is decreased as large as 0.8 mm/μs [7]. A possible reason of the above mentioned phenomenon is the destruction of hydrazine behind a shock front.

Hugoniot of hydrazine during its destruction behind shock wave

Calculated by the scheme [8] under assumption of hydrazine destruction up to ammonia and nitrogen the shock wave velocities were on 2—3 mm/μs larger than measured in [1] at the mass velocities U_P equals up to 3 mm/μs ones. At U_P = 2 mm/μs shock wave velocity U_S is equal to 8.06 mm/μs and the sound velocity C behind a shock front is equal to 6.06 mm/μs (the Chapman—Jouget condition for a stationary detonation wave $U_P + C = U_S$ is satisfied). The temperature of the products of destruction is approximately 2000 – 3000 K and the pressure is 16.3 GPa. The following set of equations, obtained under assumption of additivity of a specific volume of the mixture and the specific volumes of the components under equal pressures and temperatures and additivity of the internal energy of the mixture and the internal energies of the components, was solved:

$$P_{Hi} = [P - c_{V1i}\,\Gamma_{0i}(T - T_{0i})/V_{0i}]/(1 - c_{V1i}\Gamma_{0i}k_i/V_{0i}),\quad P_{Hi} = U_{Si}U_{Pi}/V_{0i},$$

$$V_i = V_{0i}(1 - U_{Pi}/U_{Si}),\quad T_{Hi} = k_i P_{Hi} + T_{0i},\quad \Gamma_i/V_i = \Gamma_{0i}/V_{0i},$$

$$(\partial V_i/\partial P)_H = -V_{0i}^2(C_{0i} + a_i U_{Pi})/(C_{0i} + 2b_i U_{Pi} - 3a_i U_{Pi}^2)/U_{Si}^2,$$

$$(\partial V_i/\partial P)_T = (\partial V_i/\partial P)_H/(1 - c_{V1i}\Gamma_{0i}k_i/V_{0i}),$$

$$(\partial V_i/T)_P = -(\partial V_i/\partial P)_H\, c_{V1i}k_i\Gamma_{0i}/V_{0i}/(1 - c_{V1i}\Gamma_{0i}k_i/V_{0i}),$$

$$(\partial V_i/\partial P) = \sum_{i=1}^{n}\alpha_i(\partial V_i/\partial P)_T,\ V = \sum_{i=1}^{n}\alpha_i V_i,\ (\partial V/\partial T)_p = \sum_{i=1}^{n}\alpha_i(\partial V_i/T)_p,$$

$$(\partial V_i/\partial P)_T = \sum_{i=1}^{n}\alpha_i(\partial V_i/\partial P)_T,$$

$$0.5P(V_0 - V) + Q = 0.5\sum_{i=1}^{n}\alpha_i P(V_{0i} - V_i) + \sum_{i=1}^{n}\alpha_i c_{Vi}(T - T_{Hi}),$$

$$-C^2/V^2 = (\partial P/\partial V)_S = (\partial P/\partial V)_T[1 - T/c_V(\partial V/\partial T)_P^2/(\partial V/\partial P)_T]$$

$$c_v = \sum_{i=1}^{n} \alpha_i c_{Vi},\ U_S^2 = V_0^2 P/(V_0 - V),\ U_P^2 = P(V_0 - V),$$

For the chosen P value one can find the T value and, then, all the other values in question. Here, α_i is the weight fraction of the i-th component, n is the number of components.

Note that the measured detonation velocities of the solutions of explosives with hydrazine are close to the expected ones derived from the additiveestimates of the component content. For the solutions of nitromethane with hydrazine this is illustrated in the Fig. 2, where the experimental values of detonation velocities$D$ from [6] for various weight contents of nitromethane$m$ are plotted by squares (the rectangles denote the values for the solutions of nitromethane with methanol which are shown for a comparison). As the pressure behind a shock front is increased twice as much, the temperature of the products is increased on 500 K, and the velocity of a wave propagation up to 9.45 mm/μs at the mass velocity equals 3.4 mm/μs.

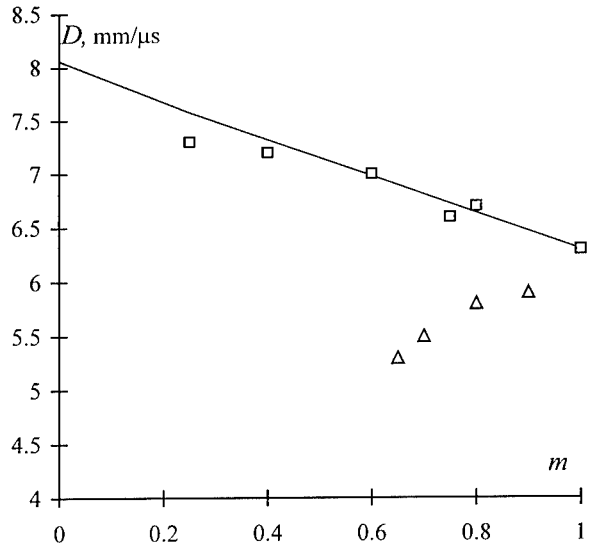

Fig. 2. Detonation velocities in nitrometane - hydrazine mixtures.

In calculations by the scheme [8] it is assumed the additivity of a specific volume and internal energy of a solution at equal temperatures and pressures with respect to a corresponding values of the components of a solution. Consequently, it is assumed the possibility of a description of a shock wave compression of the components of the destruction products of the initial compound. Hugoniot of a liquid nitrogen calculated with the use of a generalized dependence [3] at the initial sound velocity equals 0.88 mm/μs describes outstandingly well the experimental values from [9, 10] (the lower line in fig.3). The temperatures, calculated according to [4] (T = - 160 + 197 P) under the pressures behind a shock wave front up to 18 GPa, are in a complete accordance with the results of measurements [11].

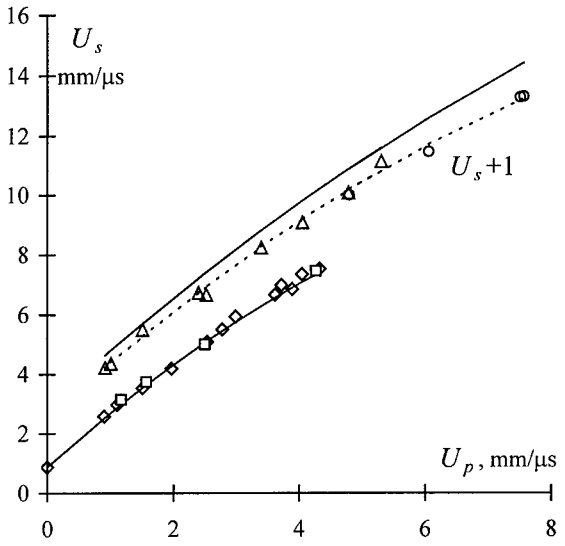

Fig. 3. Hugoniots of liquid nitrogen and ammonia.

Hugoniot of a liquid ammonia within a considered range of pressures was calculated with the use of a generalized dependence [3] for the value of sound velocity in the initial state equals 1.95 mm/μs (the upper solid line in Fig. 3). It is in a satisfactory accordance with the experimental data [12, 13] at the mass velocities values equal up to 5 mm/μs. The temperature of a shock wave compression of ammonia calculated by the scheme [8] may be described by the

relationship $T = 460 + 64\ P$. It is possible that the discrepancies between calculated and experimentally measured values at high intensities of shock waves are connected with the reliability of the value of sound velocity in the initial state, taken from [12]. For instance, the estimates of a sound velocity in a liquid ammonia from the contributions of chemical bonds do not give the values exceeded 1.55 mm/μs. Hugoniot calculated with such C_0 value (a dotted line in Fig. 3) is considerably better agree with the experimental values under practically the same temperatures of the substance behind a shock front.

The calculation with offered in [13] Hugoniot of a liquid ammonia U_S= 3.221+1.201U_P promise more high detonation parameters of hydrazine (D=8.32 mm/μs, U_P=2.74 mm/μs, C=5.62 mm/μs, P=23 GPa, T=2260 K). This is because noticeably smaller sound velocities behind shock fronts in ammonia and accordingly in products of destruction of hydrazine, which were calculated with the linear expression of Hugoniot. The distinction between calculated in different variants of velocities of the detonation not essential for evaluations as a whole, however quantities calculated with quadratic relation of Hugoniot for ammonia seem more realistic. Calculated temperatures of ammonia behind shock front were averaged by the expression T= 198 + 71 P and, either as quantities with other relation of Hugoniot, agree closely with measured in [14] temperatures of shock front (3550 K and 4330 K for 47.6 GPa and 61.3 GPa).

The temperature of hydrazine behind a shock front, propagated with the velocity equals 8.06 mm/μs, when the Chapman—Jouget condition is satisfied for a stationary detonation wave, is approximately equal to 1800 K (nearly the same as behind a shock front in nitromethane and nitrates of spirits). The activation energy of hydrazine decomposition is approximately in 1.4 times larger than, for instance, the activation energy of nitrates of spirits and nitromethane in the aci-form at nearly the same value of the pre-exponential factor. For this reason the detonation of liquid hydrazine for a realistic diameters of the charges is possible at the

temperature of initial compound behind a shock front approximately equals 2500 K. At the hydrazine temperatures behind shock front equals 1800 K the critical diameters of detonation equal approximately 1.5 m are expected. Such temperatures behind a shock front of a stationary detonation wave cannot be maintained only due to hydrazine destruction. However, they are quite attainable at a more rapid destruction of the other components of a solution (nitromethane and hydrazinenitrate in the above mentioned observations) than hydrazine destruction at smaller temperatures immediately behind a detonation shock front. When the content of the component, which is responsible for the transformation of the substances behind a shock front, is as large as one third of the total mass of the mixture, one may neglect of the main component decomposition (for instance, hydrazine) in the initial stage of the process. The decomposition of the components proceeds in independent reactions. Higher temperatures of hydrazine behind shock front may be always achieved at the use of a more powerful wave generator.

The results of estimates carried out confirm the possibility of description of high detonation velocities of solutions of explosives with hydrazine under assumption of hydrazine destruction in a shock wave up to nitrogen and ammonia. At hydrazine destruction in a shock wave the time pressure dependence behind a shock front will be similar to the dependence observed in a detonation wave. Hydrazine destruction behind a shock wave has not been observed in the experiments conducted and it is expected at rather higher intensities of waves than ones attained in [1]. The study of shock wave compression of liquid hydrazine is of interest methodically because of a relative simplicity of expected composition of destruction products and possibility of a description of its components at high temperatures and pressures.

REFERENCES

1. Garsia G.O., Persson P.= A. , *Khim.Fiz.***17,** № 1, 153 (1998)

2. Walsh J.M., Rice M.H., *J. Chem. Phys.* **26,** 815 (1957).

3. Voskoboinikov I. M., Bogomolov V. M., *Teplofizika Vysokikh Temperatur.***8,** № 1,81 (1970).

4. Voskoboinikov I. M., Gogulya M. F., *Fiz. Goreniya Vzryva,* № 5, 105 (1978).

5. Genich A. P., Zhirnov A. A., Manelis G. B. *Zh. Fiz. Khim.,* **48**, № 3, 728 (1974).

6. Forshey D.R., Cooper J.C., Doyak W. J., *Explosivestoffe,* № 6, 125 (1969).

7. Finger M., Lee E. Et al., *VI Symp. on detonation,* 172 (1976).

8. Voskoboinikov I. M., *Khim.Fiz.***10,** № 5, 672 (1991).

9. Zubarev V. N., Telegin G.S., *Dokl. Akad. Nauk SSSR,* **142**, № 2, 309 (1962)

10. Dick R. D., *J. Chem. Phys.,* **52**, № 12, 6021 (1970).

11. Voskoboinikov I. M., Gogulya M. F., Dolgoborodov A. Ya., *Dokl. Akad. Nauk SSSR,* **246,** № 3, 579 (1979).

12. Dick R. D., *J. Chem. Phys.,* **74**, № 7, 4053 (1981).

13. Mitchell A. C. and Nellis W.J., *J. Chem. Phys.,* **72**, № 12, 6273 (1982).

14. Radousky H. R., Mitchell A. C., Nellis W.J. // *J. Chem. Phys.,* **93**, № 11, 8235 (1990)

Prof. Dr. Held/gö <measurem>

Measurement of the Detonation Velocity of Infinite Diameter with Small Samples

M. Held

Abstract

The detonation velocity of infinitely large charges D_∞ is typically extrapolated by the diagram of the detonation velocity D as a function of 1/R, where R is the radius of the high explosive charge. If this value is wanted for less sensitive HEs or for propellant charges large or extremely large charges, up to several 100 kgs <1> are used. This value can be experimentally defined with a novel and tricky technique, where the charge under test is in direct contact to a donor charge which has much higher energy resp. power and detonation velocity. This charge initiates the investigated charge which creates a bow wave. This bow wave is measured as a phase velocity of the end surface of both - the donor and the acceptor charge.
Test setup with test results will be presented.

<1> Jon L. Maienschein, E.L. Lee, J.E. Reaugh and A.L. Nichols III, C.E. Mervill, R.R. Lambert, „Characteristics in Large Failure - Diameter Materials", 11th Int. Detonation Symposium, Snowmass, USA, 1998

A STUDY ON DETONATION CHARACTERISTICS OF PRESSED NTO

Stanisław Cudziło and Waldemar Andrzej Trzciński
Military University of Technology
Kaliskiego2, 00-908 Warsaw, POLAND

Abstract: *NTO is an explosive of current interest. It has been evaluated as an insensitive component to replace RDX in some explosive and propellant compositions. In our work, efforts were made to determine NTO detonation pressure and JWL equation of state of NTO detonation products. With this end in view, pressed NTO cylinders were studied experimentally by measuring the detonation velocity versus the diameter, by performing the cylinder expansion test and a water test using a SCANDIFLASH X-ray set. The results of measurements and numerical modelling of the process of copper tube expansion as well as the process of detonation of NTO charges inside a cylindrical layer of water were the basis for determining the detonation pressure and the JWL constants.*

1. Introduction

3-Nitro-1,2,4-triazol-5-on (NTO) is widely accepted as an useful explosive combining comparatively high performance and insensitivity comparable to TATB. Since the early 1980s when NTO was recognised as a potential explosive molecule, it has been a subject of many experimental and theoretical investigations [1÷10]. NTO has been found to be far less sensitive to impact and shock than RDX and HMX whereas its explosive output is comparable to that of RDX. For these reasons NTO has appeared to be very useful for systems in which its insensitivity and stability are more important than maximum performance. Now, it is manufactured on an industrial scale being one of the most effective insensitive high explosives [9].

The main objective of the study was to characterise thoroughly explosive properties of NTO synthesised in our laboratory. To this end, we measured detonation velocity, carried out the water test and the cylinder test. Results of the experiments were the basis for determining such important characteristics of NTO as its detonation pressure, acceleration abilities, effective exponent of isentrope and JWL equation of state for its detonation products.

2. NTO Synthesis and Main Properties

Synthesis of NTO was carried out in two steps including condensation of semicarbazide hydrchloride and formic acid to triazolone (TO) and its nitration to form NTO [1], Fig. 1.

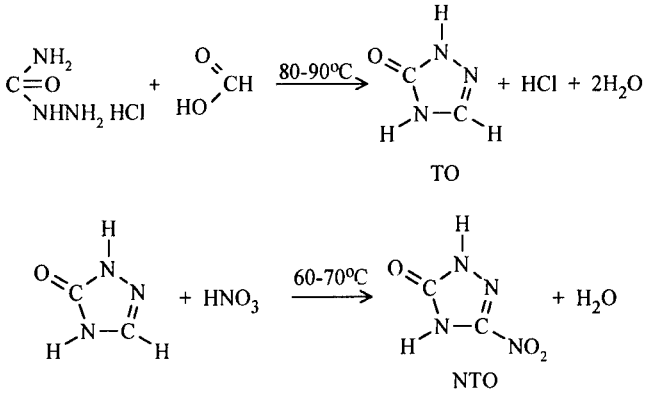

Fig. 1. TO Synthesis and TO Nitration Reactions

The final product of the synthesis was obtained by crystallisation from water. Its purity was at least 98% what was determined by both HPLC analysis and potentiometric technique according to testing methods proposed in [11].

The recrystallised NTO was ground and sieved in order to ensure the same grain size distribution in all tests. The mean particle size was about 130 μm and they had cuboid shape, Figs 2 and 3.

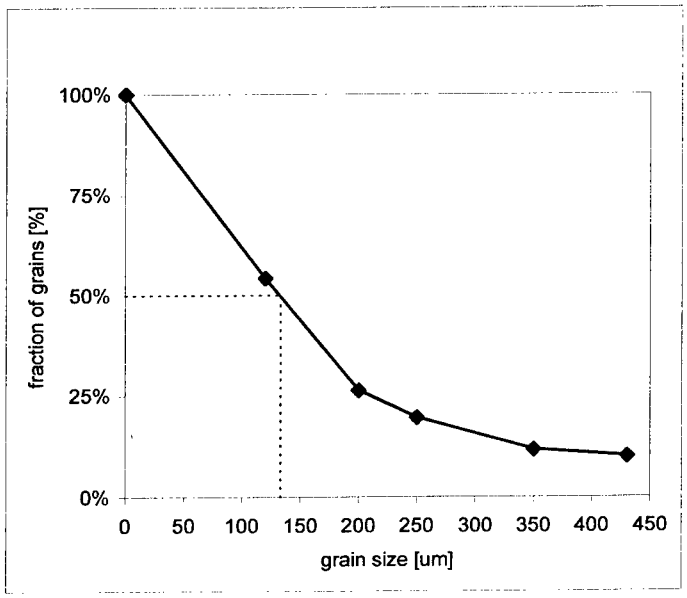

Fig. 2. NTO Grain Size Distribution

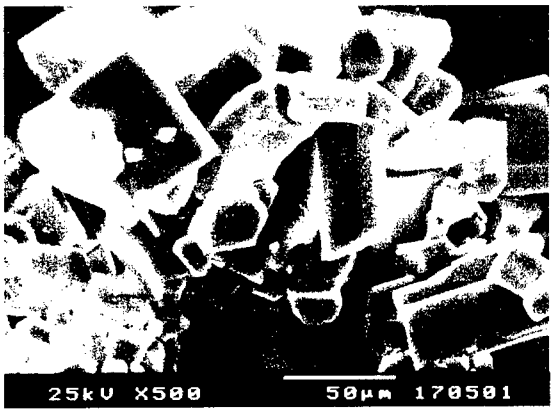

Fig. 3. SEM Photograph of NTO Particles Used in Experiments

3. NTO Detonation Velocity (VOD)

NTO was pressed at a density of 1.80±0.01 g/cm^3 in the form of cylindrical pellets with a diameter to length ratio of one. The pellets were 14.5 mm, 16.0 mm, 20 mm, 25.0 mm and 30.0 mm in diameter. For each diameter, a charge was made from a minimum of seven pellets. The experimental charges were initiated with a booster made of phlegmatised RDX that had the charge diameter and length of twice the diameter. Between the NTO pellets, short-cirquit sensors, consisting of two thin insulated wires, were located. Electrical signals from the sensors were recorded with 10-channel chronometer at accuracy of 10 ns. The distance between two sensors was measured with an accuracy of 20 µm so the average error for any one datum of detonation velocity was ±30 m/s. Results of the measurements are given in Tab. 1. Each value is an average of three experimental results.

Tab. 1. Results of Detonation Velocity Measurements

Diameter [mm]	Density [g/cm^3]	Detonation Velocity VOD [m/s]
14.5	1.81	No Go
16.0	1.80	7650
20.0	1.81	7800
25.0	1.80	7820
30.0	1.80	7860

The values of VOD obtained in this work are close to the results for coarse NTO published in [7], where it was shown that the detonation velocity was always higher for fine NTO than for coarse one. Comparatively high critical diameter of NTO (16 mm) indicates that the time needed to destroy its molecular structure and to create molecules of detonation

products is relatively long. Low rate of chemical reactions in detonation wave signifies also low shock sensitivity of NTO.

4. NTO Detonation Pressure

To determine the detonation pressure of NTO, a variant of the aquarium test was applied [12]. In this method, profiles of an oblique shock wave propagating in a cylindrical layer of water during detonation of a cylindrical charge of an explosive tested is recorded with a X-ray set. The experimental profiles are then compared with results of numerical modelling of the expansion process which are in a form of relation between the position of the front of oblique shock wave in water and the exponent of isentrope (γ) of detonation products. The value of γ corresponding to the solution that overlaps the experimental profile is accepted as the exponent sought. Having determined γ, the detonation pressure is calculated according to the following equation:

$$p_{CJ} = \frac{\rho_0 D^2}{\gamma + 1} \tag{4.1}$$

where D, p_{CJ} denote the detonation velocity and pressure, respectively, and ρ_0 is a density of the explosive tested.

The scheme of the experimental arrangement, used in this study, is shown in Fig. 4. A cylindrical NTO charge of 23.6 mm in diameter and 250 mm in length was placed inside a PCV tube with an inner diameter of 71 mm and wall thickness of 2 mm. The tube was filled with water. Short-cirquit sensors were located in the charge to measure detonation velocity and trigger the X-ray apparatus.

An exemplary radiograph of an initial stage of the acceleration of the water envelope is presented in Fig. 5. In each X-ray photographs, we observed a curved detonation wave front. This is a characteristic feature of explosives with a wide zone of chemical reactions that also means a low rate of the reactions. Therefore, it can be stated that the rate of chemical reaction in NTO detonation wave is fairly low if compared to other high explosives.

The density and detonation velocity of the NTO charges used in the water tests and results of the tests are given in Tab. 2. The detonation pressure was determined by comparison of measured and calculated positions of the shock wave front in a plane section located on a distance of one charge radius from the front of detonation wave. Table 2 also contains some theoretic values of the parameters calculated with the thermochemical code CHEETAH [13]. The BKWC set of coefficients of the Becker-Kistiakovski-Wilson equation of state was applied.

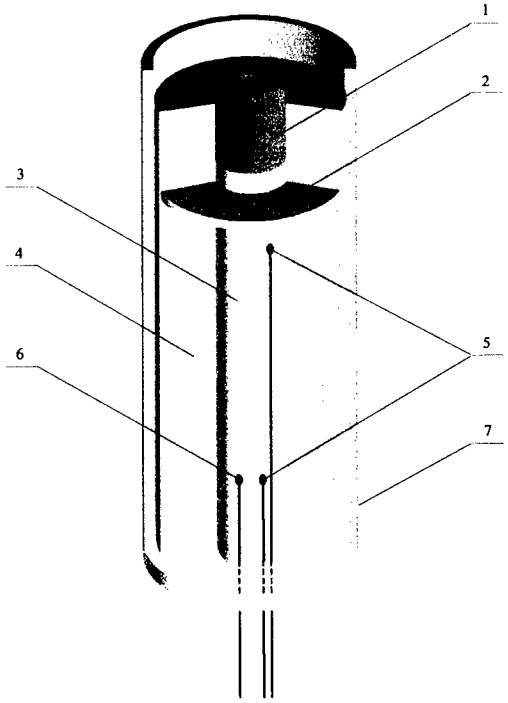

Fig. 4. Water Test – Experimental Arrangement, 1 – booster, 2 – centring ring, 3 – NTO charge, 4 – water, 5 – sensors to measure VOD, 6 – sensor to trigger the X-ray set

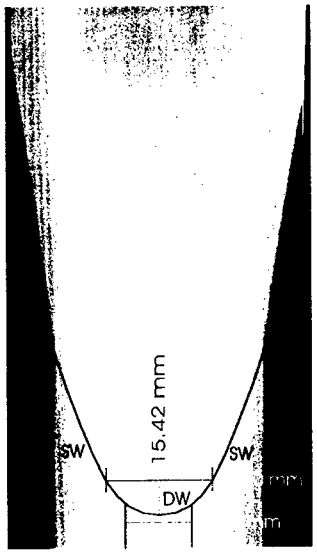

Fig. 5. Typical Radiograph of Detonation of a NTO Charge in Water

Tab. 2. Experimental and Calculated Detonation Properties of NTO

Shot No	Density [g/cm^3]	VOD[m/s]		Exponent γ		p_{CJ} [GPa]	
		Water Test	Calc.	Water Test	Calc.	Water Test	Calc.
1	1.78	7790	8000	3.40	3.48	24.6	24.98
2	1.78	7800	8000	3.40	3.48	24.6	24.98

The consistence of experimental and theoretic values is quite good. However, the theoretical values of VOD and p_{CJ} are still a bit higher than experimental ones. This fact implies that the conditions of detonation wave propagation in NTO charges confined with water do not enable to achieve the ideal regime of detonation.

5. NTO Acceleration Abilities

The cylinder test results were the basis for determination of acceleration abilities of NTO detonation products. The process of acceleration of copper tube by detonation products was recorded with the impulse X-ray apparatus. The tube was 250 mm long with internal diameter of 25 mm and wall thickness of 2.5 mm. To determine the radial velocity of the copper tube, the data obtained from the cylinder test were recalculated using the method proposed in [14]. A short description of the theoretical model of the cylindrical-liner driving process, published in that article, is given below.

A diagram of a copper tube accelerated by the detonation products is shown in Fig. 6

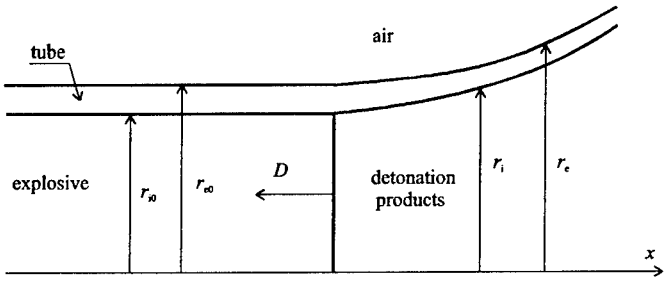

Fig. 6. Diagram of Copper Tube Accelerated by Detonation Products

A plane detonation wave propagates at a velocity D in a cylindrical charge of explosive. The gaseous detonation products expand, thus driving the tube. It is assumed that the time of detonation wave propagation is long enough to neglect the influence of the initiation of detonation. Then the motion of the detonation products and the tube material may be treated as stationary. Therefore, the axis co-ordinate and time are associated by the following relation

$$x = D \cdot t. \tag{5.1}$$

First, the position of the central cylinder surface is determined. Assuming a complete incompressibility of the tube material, this position can be established from the relation

$$r_{\mathrm{m}} = \sqrt{r_{\mathrm{e}}^2 - \frac{1}{2}\left(r_{\mathrm{e0}}^2 - r_{\mathrm{i0}}^2\right)}, \tag{5.2}$$

where r_{e0} and r_{i0} denote the initial radii of external and internal surfaces of the tube, respectively, r_{e}, and r_{m} mean the radii of external and central surfaces of the tube for given value of co-ordinate x, respectively.

By using the relation (5.1) we can replace the dependence of the tube radius on axis co-ordinate by the time function of this radius. The time dependence of central position of the tube is approximated by the following function

$$r_{\mathrm{m}} = r_{\mathrm{m0}} + \sum_i a_i \left\{b_i \left(t - t_0\right) - \left[1 - \exp\left(-b_i \left(t - t_0\right)\right)\right]\right\}, \tag{5.3}$$

where a_i, b_i, t_0 are parameters. In Ref. [14], it was proved that sufficient accuracy of approximation of the experimental results was achieved by assuming $i = 2$ in (5.3).

For the function (5.3), the radial velocity of the central part of the tube can be expressed by the relation

$$u_{\mathrm{m}} \equiv \frac{d\,r_{\mathrm{m}}}{d\,t} = \sum_i a_i\, b_i \left[1 - \exp\left(-b_i \left(t - t_0\right)\right)\right]. \tag{5.4}$$

To determine the kinetic energy of the tube, the magnitude of velocity of the tube element must be calculated. From geometrical relations it follows that the deflection angle Θ (the angle between the line being tangential to the trajectory of the central surface of the tube and the x-axis) are specified by the relation:

$$\Theta = \operatorname{arc\,tg}\left(\frac{u_{\mathrm{m}}}{D}\right). \tag{5.5}$$

On the other hand, the magnitude of velocity of the central part of the tube (a cylindrical liner) is expressed by the equation

$$u_{\mathrm{L}} = 2\,D \sin\left(\frac{\Theta}{2}\right). \tag{5.6}$$

The acceleration ability of explosive can be described by so-called *Gurney energy*, which is defined as a sum of kinetic energies of driven tube and detonation products related to unit mass of explosive. For cylindrical envelopes, the Gurney energy is expressed by the following relation [14]

$$E_G = \left(\mu + \frac{1}{2}\right)\frac{u_L^2}{2}, \tag{5.7}$$

where μ denotes the ratio of tube mass to explosive mass.

Applying this methodology to analyse X-ray records of expanding copper tubes, the dependence of the Gurney energy on the relative volume of detonation products of NTO, TNT, and TNT/RDX = 50/50 were constructed. The results of the analysis are presented in Fig. 7. Characteristics of the explosives tested were as follows:

NTO	ρ_0 = 1.77 g/cm^3,	VOD = 7940 m/s;
TNT	ρ_0 = 1.59 g/cm^3,	VOD = 6910 m/s;
TNT/RDX 50/50	ρ_0 = 1.64 g/cm^3,	VOD = 7610 m/s.

Charges of NTO with density 1.77 g/cm^3, placed in copper tube, detonate at 7940 m/s. This value is almost the same as a calculated one (7960 m/s), what indicates the ideal regime of NTO detonation under these conditions.

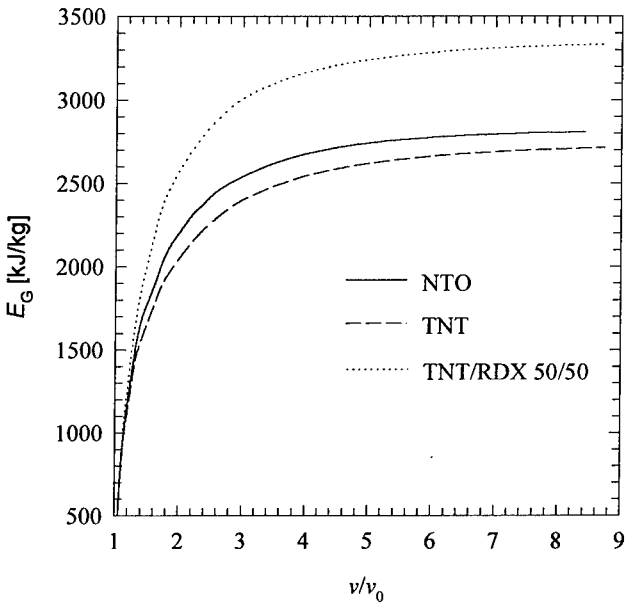

Fig. 7. Dependence of the Gurney Energy on the Relative Volume of Detonation Products

From the analysis of curves shown in Fig. 7, it follows that the changes in the Gurney energy of NTO during the tube expansion are similar to those of other high explosives. NTO acceleration abilities are only slightly higher than that of TNT.

6. NTO Detonation Energy

The results of cylinder test can also be used to estimate the detonation energy. In Ref. [14] it was shown that there was a correlation between the velocity of driven tube at the infinitive volume of the detonation products and the detonation energy of an explosive.

The relation can be written down as follows

$$\frac{E_0}{E_0^s} = \frac{\left(\mu + \frac{1}{2}\right)\rho_0}{\left(\mu^s + \frac{1}{2}\right)\rho_0^s}\left(\frac{u_L}{u_L^s}\right)^2 \tag{6.1}$$

where E_0 and E_0^s are the detonation energy of a given explosive and a standard explosive, respectively u_L and u_L^s denote the tube velocity determined at the infinitive volume of detonation products of the explosives, μ and μ_s denote the ratio of tube mass to explosive mass, ρ_0 and ρ_0^s are densities of the explosives.

In order to estimate the velocities u_L and u_L^s, the velocity of copper tube was determined from the results of cylinder test and the dependency of velocity square on reciprocal volume of detonation products was constructed. After that, the dependence was extrapolated to null and the velocities corresponding to the infinitive volume were found.

Using phlegmatized RDX as a standard explosive for which the detonation energy (E_0^s = 5263.5 kJ/kg) was taken from [15], the detonation energies of the explosives tested (E_0) was calculated from (6.1). The values obtained are given in Tab. 3

Tab. 3. Detonation Energy Estimated on the Basis of Cylinder Test

Explosive	Density ρ_0 [g/cm^3]	VOD [m/s]	Detonation Energy E_0 [MJ/m^3]
NTO	1.77	7940	7100
TNT	1.59	6910	6830
TNT/RDX 50/50	1.64	7610	8100

From Table 3, it follows that the detonation energy of NTO is a bit higher than that of TNT but considerably lower than for TNT/RDX = 50/50.

7. NTO Effective Exponent of Isentrope

So-called *effective exponent of isentrope* is often used to calculate the detonation parameters of explosives or some characteristics of the detonation products. The value of the effective exponent is not determined from the parameters in the CJ point but on the basis of the real isentrope of the detonation products, [16]. The effective exponent of isentrope can be estimated from results of the cylinder test. In Ref. [17] the effective exponent is determined

by comparing the experimental profile of the copper tube with that obtained from numerical modelling of the expansion process. The detonation products, driving the tube, are described by the constant-γ equation of state. The algorithm used to determine the effective isentropic exponent is as follows. The problem of driving the cylindrical liner is solved numerically for n values of the exponent γ_i ($i = 1, n$). For each γ_i a discrete dependence of the outer tube radius on the axial co-ordinate is derived. This dependence is interpolated by spline functions and the values of $r_{ej}(\gamma_i)$ at chosen points x_j ($j = 1, m$) are calculated. The effective exponent γ_{ef} is determined by minimising the function

$$f(\gamma) = \sum_{j=1}^{m} \left[r_{ej} - r_{ej}(\gamma) \right]^2 , \tag{7.1}$$

where r_{ej} is the experimental dependence obtained from the cylinder test.

This method was applied in present work to estimate the effective exponent of isentrope for NTO detonation products. The experimental and calculated profiles of the copper tubes driven by the detonation products of NTO and TNT (for comparison) are presented in Fig. 8. Density and detonation of the explosives are listed in Tab. 3.

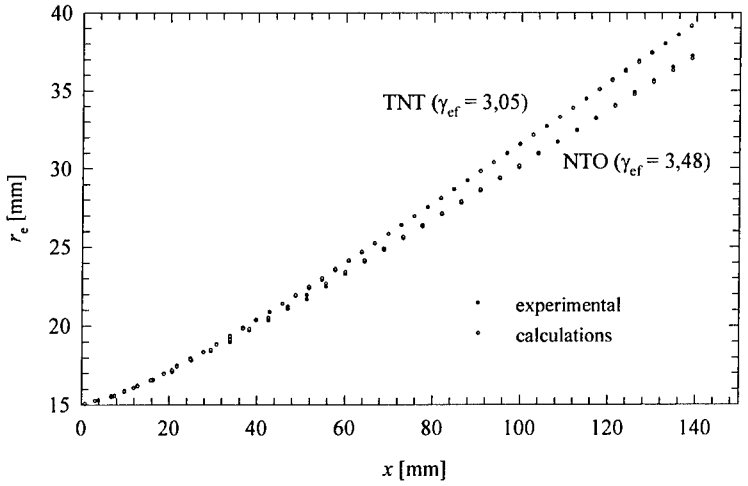

Fig. 8. Experimental and Calculated Profiles of Tubes Driven by Detonation Products of NTO and TNT

A satisfying conformity of experimental and theoretical profiles were achieved when the effective exponents (γ) were 3.48 and 3.05 for NTO and TNT, respectively. Reliable value obtained for TNT detonation products confirms correctness of the method applied.

8. NTO JWL Isentrope

Jones, Wilkins and Lee proposed the equation of the isentrope for the detonation products of explosives in the following form [18, 19]

$$p = Ae^{-R_1V} + Be^{-R_2V} + CV^{(-1-\omega)} \tag{8.1}$$

where $V=v/v_0$. The following equation of state (JWL EOS) corresponds to this isentrope

$$p = A\left(1-\frac{\omega}{R_1V}\right)e^{-R_1V} + B\left(1-\frac{\omega}{R_2V}\right)e^{-R_2V} + \frac{\omega E}{V} \tag{8.2}$$

where A, B, C, R_1, R_2 and ω are constants for given explosive. The basic method of determination of these coefficients is cylinder test. Besides it, some connections between coefficients following from the conservation laws written for the CJ point, are used in this method. As a result parameters A, B, and C are expressed as functions of R_1, R_2, ω, and ρ_0, D, E_0 and p_{CJ}, [20]. Density of explosive ρ_0 as well values of detonation velocity D, detonation energy E_0 and pressure p_{CJ} at the CJ point are established experimentally. Thus, only the constants R_1, R_2 and ω remain to be determined.

They are calculated in [20] by the method in which the experimental dependence of radial displacement of the outer tube wall on the axial co-ordinate is compared with that obtained from a numerical simulation. The set of JWL constants is chosen for which the experimental and simulated displacements are sufficiently close to each other. The R_1, R_2 and ω are obtained from comparison of the experimental and calculated radial position of the tube wall at chosen m values of the axial co-ordinate x_j. So, the values of these parameters are determined by minimising the function

$$f(R_1,R_2,\omega) = \sum_{j=1}^{m}\left[r_{ej} - r_{ej}(R_1,R_2,\omega)\right]^2, \tag{8.3}$$

where r_{ej} i $r_{ej}(R_1, R_2, \omega)$ are the experimental and calculated positions of external surface of the tube, respectively.

Using the model, proposed in [20], as well as the values of detonation velocity, detonation pressure and detonation energy of NTO, obtained with methods described in Sections 2, 4 and 6, the constants of the JWL equation of state of NTO were calculated. Results of the calculations are given in Tab. 4.

Tab. 4. JWL Isentrope of NTO

Explosive/Characteristics	JWL EOS Constants
NTO	A = 1025.489 GPa,
ρ_0 = 1.77 g/cm^3,	B = 8.4815229 GPa,
VOD = 7940 m/s,	C = 0.7041268 GPa,
P_{CJ} = 25.4 GPa,.	R_1 = 5.03, R_2 = 1.20,
	ω = 0.25, E_0 = 7.1 GPa.

A comparison of the experimental profile of copper tube driven by NTO detonation products with a calculated one, obtained at the accepted set of JWL constants, is presented in Fig. 8.

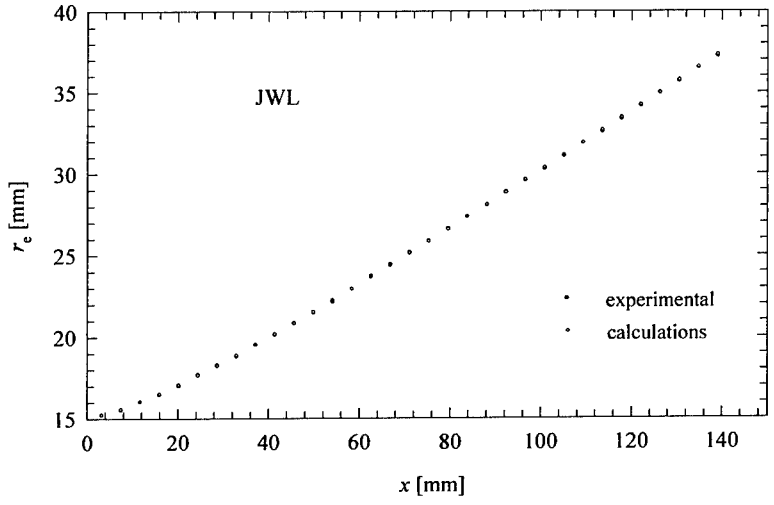

Fig. 8. Comparison of Tube Profiles Obtained Experimentally and from Calculations Using JWL EOS

After determining the JWL isentrope, the expansion work of detonation products was calculated from equation:

$$w(v) = -e_c + \int_{v_{CJ}}^{v} p_i dv, \tag{8.4}$$

where $e_c = (p_{CJ} - p_0)(v_0 - v_{CJ})/2$ denotes the energy of explosive compressed at the front of detonation wave, p_i is the pressure on the isentrope.

Dependence of the expansion work on the relative volume of detonation products is presented in Fig. 9.

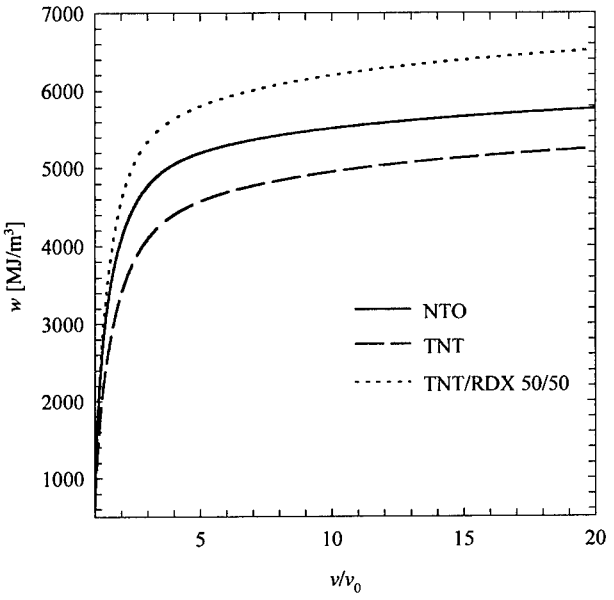

Fig. 9. Expansion Work as a Function of the Relative Volume of Detonation Products

NTO expansion work is higher than that of TNT by about 10 %, and it reaches 5800 MJ/m^3 at the relative volume of detonation products of 20.

9. Summary

1. NTO detonation velocity is quite high. It attains 7860 m/s in unconfined charges at a density of 1.8 g/cm^3. With confinement in a form of copper tube, used in the cylinder test, the velocity reaches 7940 m/s at density of 1.77 g/cm^3. Critical diameter of detonation of NTO with mean particle size of 130 μm is 16 mm in charges pressed at 1.8 g/cm^3.
2. The pressure of detonation of NTO pressed at 1,78 g/cm^3 is 25.4 GPa. This value is comparable to that of Composition B.
3. The velocity of copper tube, driven by NTO detonation products, increases rapidly in the initial stage of expansion and, then, the increase is slow. This means that a majority of energy is released in the zone of chemical reactions and in the initial stage of gaseous products' expansion. The final acceleration ability of NTO is comparable to that of TNT.
4. Detonation energy of NTO at density 1.77 g/cm^3 is a bit higher than that of TNT and reaches 7100 MJ/m^3.

5. The effective exponent of isentrope is 3.48. The set of constants of JWL EOS is as follows: A = 1025.489 GPa, B = 8.4815229 GPa, C = 0.7041268 GPa, R_1 = 5.03, R_2 = 1.20, ω = 0.25, E_0 = 7.1 GPa. The expansion work of NTO, calculated with using the JWL EOS, is higher by about 10 % than that of TNT.

References

[1] Chapman B. L., *NTO Development at Los Alamos*, Proceedings of 9th International Symposium on Detonation, Portland, Oregon, August, 28- September 1, 1989.

[2] Becuwe A., Delclos A., *Use of Oxynitrotriazole to Prepare an Insensitive High Explosive,* ibid.

[3] Ritchie P. J., Kober M. E., *Molecular Models for Explosives: Application to NTO*, ibid.

[4] Akst B. I., *Heat of Detonation, the Cylinder Test, and Performance in Munitions*, ibid.

[5] Bugaut F., Bernard S., Chirat R., *Theoretical Prediction of High Explosives Efficiency: Application to NTO*, ibid.

[6] Lee K., Gilardi R., *NTO Polymorphs*, Materials Research Society, Symposium. Proceedings, vol. 296, pp. 3-13, Structure and Properties of Energetic Materials, Pittsburgh, Pennsylvania, 1993.

[7] Gimenez P., Chabin P., Mala J., Spyckerelle C., *An Extensive Experimental Study of Pressed NTO*, Proceedings of 10th International Symposium on Detonation, Boston, Massachusetts, July, 12-16, 1993.

[8] Oxley J.C., Smiyh J. L., Yeager K. E., Rogers E., Dong X. X., *NTO Decomposition Studies*, Materials Research Society, Symposium. Proceedings, vol. 418, pp. 135-142, Decomposition, Combustion and Detonation Chemistry of Energetic Materials, Pittsburgh, Pennsylvania, 1996.

[9] M. Golfier, H. Graindorge, Y. Longevialle, H. Mace, *New Energetic Molecules and their Applications in Energetic Materials*, Proceedings of 29th International Annual Conference of ICT, Karlsruhe, Germany, June 30 - July 3, 1998.

[10] Mukundan T., Purandare G. N., Pansare S. M., Sinha R. K., Tadas V. V., Bahat V. K., *Investigations on Explosive and Propellant Nitrotriazolone Formulates*, Proceedings of 2nd International High Energy Materials Conference and Exhibit, Madras, Chennai, India, December, 8-10, 1998.

[11] STANAG 4543, Explosives, Specification for NTO, January 31, 1999.

[12] Cudziło S., Trzciński, W. A., Szymańczyk L., *Determination of the Detonation Pressure from a Water Test*, Proceedings of 30th International Annual Conference of ICT, Karlsruhe, Germany, June 29 – July 2, 1999.

[13] Fried L. E., *CHEETAH 1.39 User's Manual*, Lawrence Livermore National Laboratory, 1996.

[14] Trzciński W. A., *Use of a Cylinder Test for Determining Energetic Characteristics of Explosives* (in Polish), paper submitted to Biul. WAT, 2000.

[15] Cudziło S., Trębiński R., Trzciński W. A., Wolański P., *Comparison of Heat Effects of Combustion and Detonation of Explosives in a Calorimetric Bomb Filled with Inert Gas or Air* (in Polish), Biul. WAT, 48, 11, 1998.

[16] Włodarczyk E., *Introduction into Mechanics of Explosion* (in Polish), PWN, Warsaw 1994.

[17] Cudziło S., Trębiński R., Trzciński W., *Determination of the Effective Exponent of Isentrope for the Detonation Products of High Explosives*, Chemical Physics Reports, 16, 9, 1997.

[18] Kury J. W., Horning H. C., Lee E. L., McDonnel J. L., Ornellas D. L., Finger M., Strange F. M., Wilkins M. L., *Metal acceleration by Chemical Explosives*, Proceedings of 4th Symposium (International) on Detonation, White Oak 1965.

[19] Lee E. L., Horning H. C., Kury J. W., *Adiabatic Expansion of High Explosive Detonation Products*, Lawrence Livermore National Laboratory Report UCRL-50422, 1968

[20] Trębiński R., Trzciński W. A., *Determination of an Expansion Isentrope for Detonation Products of Condensed Explosives*, Journal of Technical Physics, 40, 4, 1999.

DETONATION OF TNT-DINA AND DNT-PETN CAST CHARGES

G.D. Kozak, B.N. Kondrikov, and Zhou Lin.
Mendeleev University of Chemical Technology
Miusskaya Sq.9, Moscow, 125047

Cast TNT-DINA and DNT-PETN and pressed HMX-paraffin charges are investigated as the systems capable of propagating a detonation in the spin-pulsating mode. Detonation parameters of the similar systems investigated earlier are compared with those measured in this work. All of these systems are appeared to have a calculated detonation velocity D_J=7.3-7.4 km/s and practically the same explosion heat Q_v=5.40±0.01 MJ/kg. Failure diameters of detonation for the systems under study are also compared and the unusual peculiarities of the d_f versus composition lines are connected with implementation of the spin detonation regime.

INTRODUCTION

Spin detonation of the cast charges TNT-RDX and TNT-PETN was discovered in Mendeleev University in 1987 [1]. Quite distinct inhomogeneity of the detonation front was found at detonation of cast charges, narrow dents or furrows of 1-2 mm wide and 0.5-1 deep at a 45-60° angle to the charge axis covered the surface of copper or brass witness-plate over which the charge was fixed. The dents directions were rather arbitrary figures in some sense, sometimes the systems of parallel strips were observed, sometimes intersecting furrows were noted. The traces of light irradiated by the detonation front on the streak camera records were also rather inhomogeneous, the bright jets of glowing detonation products altercating with the dark sections departed from the line of the detonation front. The distance between the jets measured along the charge axis corresponded as a whole (although with a large scatter) to the distance between the furrows on the witness-plates. The fine structure of the surface waves was clarified by the tests conducted as follows. Charges were inserted in a thick-walled brass ring whose diameter was 15-20 mm greater than the charge diameter. The sheet of the copper witness-plate was placed inside the ring close to its wall. The light irradiation in the gap between the copper ring and the lateral surface of the charge was recorded by means of the streak camera with a mirror surrounded under the assembly. After the test the witness-ring was withdrawn from the bushing, straightened and photographed. The test results undoubtedly indicated that a system of the surface waves was propagated in the spin-fluctuating mode. The comparison of streak camera record with photographs of the straightened witness-ring

permitted us to clear the mechanism of the spin detonation process. The overall picture of the phenomenon was described in the papers [1-2]. The mechanism of spin detonation consists of consecutive propagation of damping wave along the lateral surface of a charge, reinitiation of detonation and propagation of super compressed detonation wave in the thin subsurface layer. Some later spin detonation was found also in liquids: Nitromethane, Diethelenеglycoldinitrate and melted Dinitrotoluene-DINA solutions [3].

The objective of this work is to extend the number of explosive systems capable of a propagation detonation in the spin-pulsating regime. Cast TNT-DINA and DNT-PETN and pressed HMX-paraffin charges were investigated.

EXPERIMENTAL TECHNIQUES

The experiments were carried out with conventional high explosives. The solidification point (dry point T_S) of individual explosives and mixtures was measured according to the method [4]. The dependencies of solidification point vs. composition of TNT-DINA and DNT-PETN systems are presented in Fig.1a,b. Solidification points of TNT and DINA in our experiments were 78.5°C and 50.5° C. The TNT-DINA mixtures containing 15-45% DINA were homogeneous compositions and T_S of the mixtures decreased at DINA content augmentation. The dependence of the point of solidification T_S vs. concentration DINA in DNT-DINA solutions described in [5] is presented in Fig 1a for comparison. The results of the DNT-PETN systems T_S measurements are shown in Fig.1b. One can see that the eutectic point, T_S=63 ^{0}C, corresponds to the content of about 10% PETN. Analysis of the T_S versus C_{PETN} dependence leads to conclusion that a limit of solubility of PETN in DNT at T=90-95 ^{0}C seems to be close to 36%. The mixtures containing more than 30% PETN were prepared with the finely dispersed (5 μm) PETN.

The cast charges were prepared by pouring of the melt into cylindrical glass tubes. The charges after crystallization and cooling were removed out of the shell, the upper and lower parts of the castings were cut off and the butt-ends were polished using the fine sand paper. The charge lengths were 100-150 mm. The porosity of the castings ranged from 2 to 5%.
Manual mixing of the components at T≈60^{0}C was used to prepare the mixtures investigated. The small portions of the hot blends were placed consequently into the glass tube and pressed

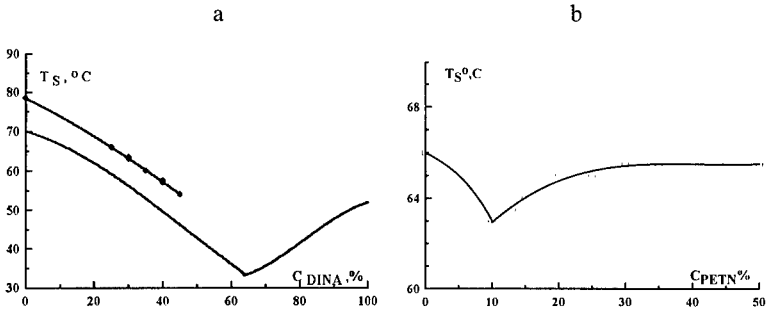

Fig.1. The solidification point (T_S) versus concentration of DINA for TNT-DINA compounds (a) and of PETN for DNT-PETN mixtures (b). Dotted line in Fig. 1a is T_S line of DNT-DINA solutions from the work [5]

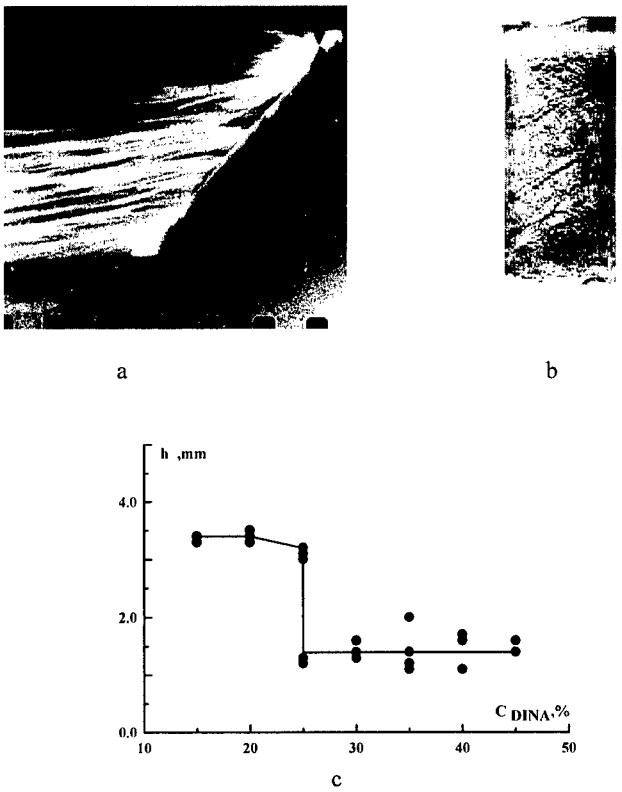

Fig.2. Typical streak-camera record (a),the traces of the spin waves on the witness plate (b) and step of detonation pulsation *versus* content of DINA (c) at detonation of TNT-DINA cast charges. (*a* and *b* – DINA content is 25%, diameter of the charge is 10 mm).

manually with a plastic punch. After cooling to the room temperature the charges were extracted from the tube. The porosity of the charges was usually in the limits of 4 to 7%.

Every charge was fastened to the copper or brass witness-plate so that a 4-5 mm clearance remained between the lateral surface of the charge and the plate. A pressed flegmatized RDX charges of 1.65-1.67 g/cm^3 density, 2-4 g mass were used as boosters. The streak camera records were taken by means of ZhFR-3 device. Velocity of detonation was measured usually in charges without confinement but sometimes (HMX-paraffin) in the steel tubes (diameter was 10 mm, wall thickness 13 mm, and length 160 mm, the small holes of d=2 mm diameter were drilled in the walls to make streak camera records). The failure diameter of detonation was determined at a room temperature with the cylindrical charges without confinement by the GO-NO GO method. The results of the test were evaluated by careful investigation of the "footprints" of the lateral detonation waves on the surface of the witness-plate and traces of light irradiation on the streak camera records.

Characteristics of ideal detonation for every composition under investigation were calculated by means of the SD computer code [6].

RESULTS

TNT-DINA

Fluctuations (Fig. 2a) are registered on the streak camera records at $C_{DINA} \leq 25\%$ as alternating of bright jets and dark zones emanating from the line of detonation front. The fluctuations of the detonation also stamped on the surface of the witness-plates as small dents of 1-2 mm wide and 0.5-1 deep located at an angle of 45-60° to the charge axis (Fig. 2b). The distance between the jets (h is the step of pulsations) in the streak camera records corresponds on an average to the distance between the dents on the plate. The dependence of pulsation steps versus composition is plotted in Fig.2c. When DINA content in the system increases over 25% the sharp reduction of step of the pulsation from 3.5 mm to ~1 mm is observed.

The dependence of the critical detonation diameter (d_f) of TNT- DINA compositions versus DINA content is presented in Fig. 3a. The curve is not so smooth, detailed investigation demonstrated that in the range of DINA concentration in the limits of 25-30% d_f does not depend on C_{DINA}.

Velocities of detonation (D_e) registered in these runs are compared with calculated figures (D_c) in Fig.3b. One can see that a difference between experiment and calculation is

a

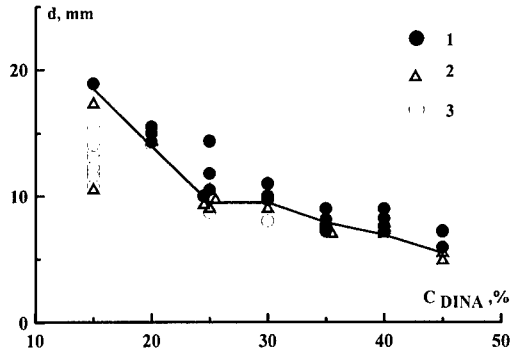

1 –detonation, 2 – extinguishment of detonation, 3 –detonation failure

b

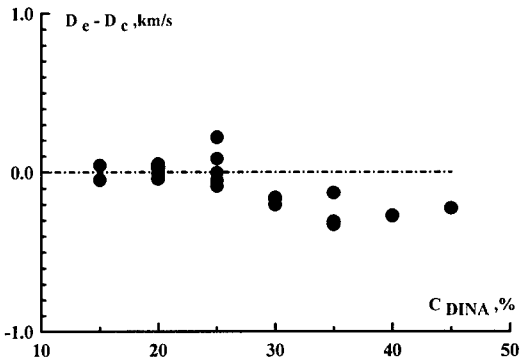

c

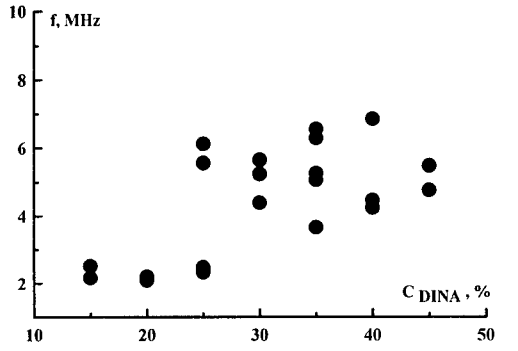

Fig. 3. TNT-DINA cast charges. Influence of the mixture composition on failure diameter of detonation (a), on difference between experimental and calculated velocity of detonation (b), and on frequency of detonation pulsation (c).

closing to zero at a content of DINA C_{DINA}<30%. At C_{DINA}>30% all of the experimental velocities are lower than the calculated ones.

DNT-PETN.

The dependence d_f on PETN content in the mixture is shown in Fig. 4a. Contrary to the $d_f(C_{DINA})$ it is a smooth line. The majority of the cast compositions detonate with no low frequency pulsations. They are registered neither by streak camera device nor by the witness plates method. The steps of pulsations on the witness plates, h=2 mm, were observed in three successive runs with the composition containing 52.5% of PETN. Velocities of detonation registered in the runs with DNT-PETN are compared with calculated values in Fig.4b. In the majority of the runs the experimental velocities are lower than the calculated ones. But at a content of C_{PETN}=50-55% the difference is close to zero.

HMX-paraffin.

The HMX-paraffin is not a solution of two explosives but a mechanical mixture of a high explosive and an inert substance. The dependence d_f versus HMX content is shown in Fig. 5a. It is a smooth line. The comparison of experimental detonation velocities with calculated ones is shown in Fig. 5b. One can see that the experimental values are always lower than the calculated figures. The fluctuations of detonation front are not seen in the streak camera records. There are weak furrows (step is about 1 mm) perpendicular to the detonation front propagation on the witness plates in some trials, but one can not exclude that they appear as a result of the charges production that is carried out by manual pressing of the discreet portion of mass. One can take into account that the step of fluctuation, h≤1, mm is close to a resolving power of the registration methods. In any case the character of dents differed essentially from the furrows that the spin detonation has stamped. The distance between dents does not depend on composition of the HMX-paraffin mixture.

DISCISSION

The main experimental results of the investigation are collected in Fig. 3-5. They have shown the influence of the mixtures composition on failure diameter of detonation, on the difference between experimental and calculated velocity of detonation, and on the frequency of detonation pulsations (f=D/h where D is detonation velocity and h is averaged step of the pulsation). One can see that these dependencies in the case of TNT-DINA charges undergo some aberration at C_{DINA}=25%. There are the plato on $d_f(C_{DINA})$ curve, excess of experimental detonation velocity over calculated value, and transition jump of detonation with low frequency of fluctuations (~2 MHz) to detonation with high frequency fluctuations (~6 MHz).

There

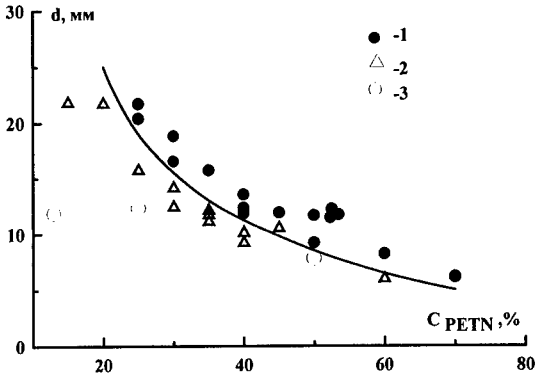

are

a

1 –detonation, 2 – extinguishment of detonation, 3 –detonation failure

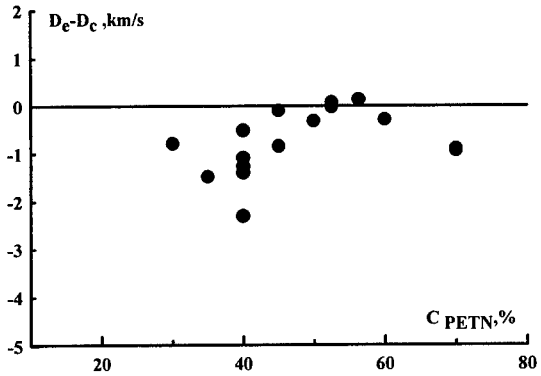

b

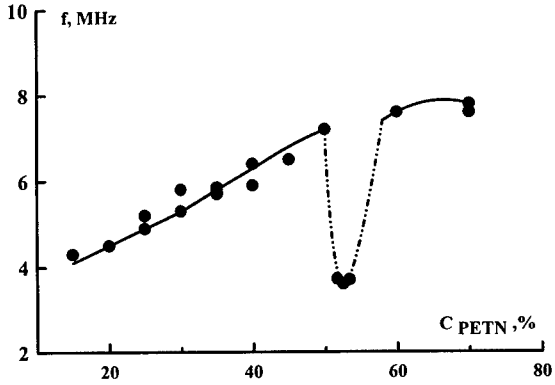

c

Fig. 4. DNT-PETN cast charges. Influence of the mixture composition on failure diameter of detonation (a), on difference between experimental and calculated velocity of detonation (b), and on the frequency of detonation pulsation (c).

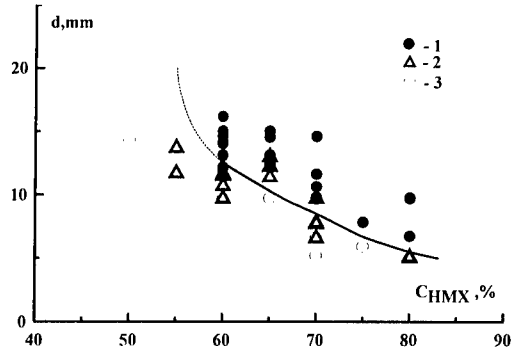

1 –detonation, 2 – extinguishment of detonation, 3 –detonation failure

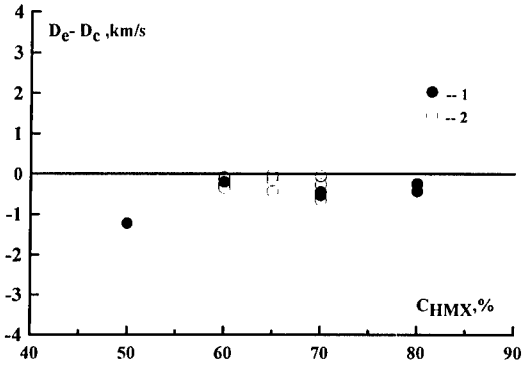

1- charges in the steel tubes, 2 – charges with no confinement.

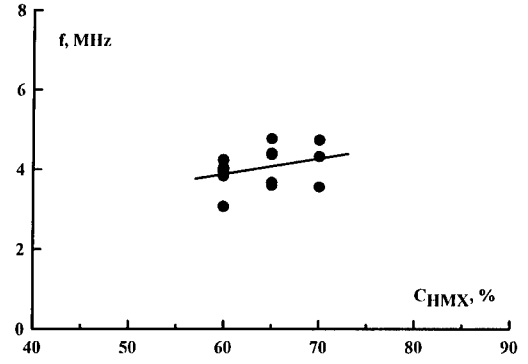

Fig. 5. HMX-paraffin pressed charges. Influence of the mixture composition on failure diameter of detonation (a), on difference between experimental and calculated velocity of detonation (b), and on frequency of detonation pulsation (c).

two points at C_{DINA}=25% when the frequency is close to 2 MHz and two points when it is about 6 MHz. One can conclude that low frequency pulsating detonation regime propagates only if concentration of DINA in mixture is less or equal to 25%.

Some tendency to propagation of detonation in low frequency spin-pulsating mode is seemed to be for the only DNT-PETN mixture, at C_{PETN}=52.5%. In spite of the smooth character of $d_f(C_{PETN})$ it is the only on the $(D_e\text{-}D_c)\text{-}C_{PETN}$ plane where experimental velocity is very close to calculated one or some higher to that. The frequency of detonation front pulsations arises (from 4 to ~8 MHz) according to C_{PETN} growth (Fig. 4c), but in three consequent runs at C_{PETN}=52.5% the frequency was near 3 MHz. We must remark that it is not more than the tendency to detonation in spin-pulsating regime.

The pulsations of detonation front for the HMX-paraffin systems are the chaotic perturbations with a mean frequency of about 4 MHz.

The comparison of dependencies d_f on sensitizer content (C_S) for all of the systems that are capable of propagation a detonation in the spin-pulsating regime with the results of our experiments is shown in Fig. 6. The plato in $d_f(C_S)$ curves is registered for any system when low frequency spin fluctuations take place. The curves plotted for TNT-RDX and TNT-PETN mixtures are close to each other whereas a line that characterizes the detonation ability of TNT-DINA charges is situated essentially higher. In the other words DINA is a weaker sensitizer than RDX and PETN are. To explain this difference the calculated velocity and pressure (P_J) of detonation versus. C_S were analyzed and shock temperatures were calculated by means of SW computer code [7,8]. Simultaneously a pressure (P_3) and a temperature (T_3)

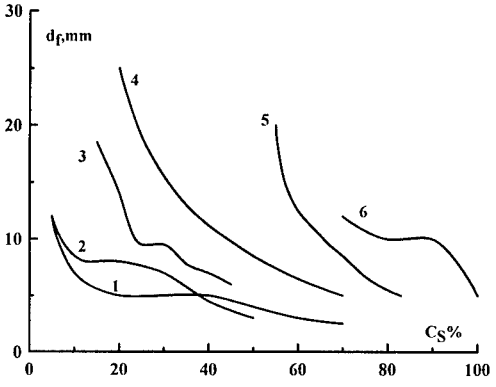

Fig.6. Comparison of dependencies d_f on the sensitizer content (C_S-is a content of the second member in every pair of the substances): 1-TNT-PETN, 2-TNT-RDX, 3-TNT-DINA, 4-DNT-PETN, 5- paraffin-HMX, 6-DNT-DINA (melt).

in the peripheral zone where damping and reinitiation of detonation take place [9] were estimated. The results of the calculations are collected in Table 1. The $P_{C\text{-}J}$ values for TNT-RDX mixtures at a content of RDX of 20, 30, and 40% are seen to be greater than the values for the TNT-DINA blends at the same content of sensitizer (RDX, on the one side, and DINA, on the other side). The corresponding differences are 1.3, 1 and 2.7 GPa. Accordingly the temperature T_3 for the former system is 60-100 K higher than for the last one. In the light of the exponential temperature dependence of the reaction rate the higher values of T_3 leads to lower d_f in the case of TNT-RDX mixtures in comparison with the TNT-DINA systems.

Table 1

Sock temperature (T_s) and temperature T_3 of TNT
and its mixtures with RDX and DINA

System	P_{cj},GPa	P_3 ,GPa	T_s, K	T_3, K
TNT	19.7	12.3	1523	1063
TNT-DINA 80/20	21.22	13.3	1622	1123
TNT-RDX 80/ 20	22.48	14.4	1706	1190
TNT-DINA 70/30	21.99	13.7	1673	1147
TNT-RDX 70/30	23.97	15.0	1806	1227
TNT-DINA60/40	22.76	14.2	1724	1178
TNT-RDX 60/40	25.44	15.9	1906	1282

The parameters of the systems capable of propagating the spin-pulsating detonation with low frequency of fluctuations (~2 MHz) investigated earlier [1-3] are shown in Table 2. They arc compared with the systems investigated in this work. The main peculiarity of the comparing is seen from the data presented in the Tabl.2. There are spin pulsation with frequency of 2-2.5 MHz at detonation of the cast charges (TNT-RDX 87.5/12.5 and 85/15, TNT-PETN 87/13), of double based propellant NB, of liquid solution DNT-DINA 30/70 and of cast mixtures TNT-DINA containing $C_{DINA} \leq 25\%$. All of them have a calculated detonation velocity D_J=7.3-7.4 km/s and practically the same explosion heat Q_v=5.4±0.01 MJ/kg. Growth of Q_v following increase of sensitizer content in cast and liquid systems leads to detonation with the high frequency (~7 MHz) and process of detonation stabilizes.

Table.2

Failure diameter of detonation, step and frequency of detonation pulsation and calculated parameters of detonation

System	Experimental parameters				Calculated parameters	
	ρ, g/cm^3	d_f, mm	h, mm	f, MHz	D_j, km/s	Q_v, Mj/kg
TNT/RDX 87.5/12.5	1.62	8	~3	~1.8	7.37	5.40
TNT/RDX 85/15	1.62	8	~3	~1.8	7.41	5.42
TNT/PETN 87/13	1.61	7	3-4	~2	7.28	5.40
DOUBLE BASED PROPELLANT NB	1.56	~9[x)]	3	2.5	7.40	5.39
DNT/DINA 30/70 (melted)	1.50	12.5	>10	~1	7.29	5.40
DINA (melted)	1.50	4.5	<1	>7.5	7.59	5.76
THT/DINA 85/15	1.612	18	3.4	2.1	7.33	5.38
THT/DINA 80/20	1.60	14	3.4	2.1	7.32	5.4
THT/DINA 75/25	1.61	9.5	3.2→1.4	2.1→5.3	7.41	5.43
THT/DINA 70/30	1.58	9.5	1.4	5.2	7.33	5.44
THT/DINA 65/35	1.564	7.8	1.4	5.2	7.31	5.46
THT/DINA 60/40	1.605	7.5	1.4	5.4	7.52	5.51
THT/DINA 55/45	1.62	5.5	1.4	5.4	7.63	5.55

[x)] at T=60°C

The Q_v and D_J numbers for the melted DINA are much greater then rhe above listed values and any fluctuation of low frequency is not detected.

The heat of explosion of investigated HMX-paraffin systems does not rich the limiting value of Q_v=5.4 MJ/kg. Correspondingly in these systems the spin-pulsating detonation regime does not develop in spite of detonation velocity at C_{HMX}= 70-75% may rich the limiting value of detonation speed D_J= 7.3-7.4 km/s. One can conclude that both of the detonation parameters (together Q_v and D_j) are essential for the spin-pulsating regime could be achieved

As it was noted above in the case of DNT-PETN mixtures at C_{PETN}=52.5% there was registered some dents on witness plate similar to the traces produced by the spin pulsating

waves. Mixture of this composition has the values of Q_v and D_j that lay precisely in the narrow region necessary to produce the spin detonation process.

ACKNOWLEDGEMENTS

The authors wish to thank Russian Foundation of Basic Research (RFBR) for partial financial support of this work (Grant 98-03-32164a).

REFERENCES

1. Kozak, G.D., Kondrikov, B.N, Oblomsky, V.B. Spin Detonation in Solid Substances Comb., Expl. & Shock Waves, Vol.25, №46 pp.459-465.
2. Kozak, G.D. Critical Diameter and Spin effect in Detonation of Cast and Liquid Explosives. Comb., Expl. & Shock Waves, Vol.31, №2, pp. 266-269.
3. Kozak, G.D., Kondrikov, B.N., Oblomsky, V.B. The spin wave and failure of detonation of liquid explosives. Comb., Expl. And Shock Waves. 1992, v.28, №2, pp.93-98.
4. Orlova, E.Yu. et al Handbook on High Explosives Preparation. Mendeleev Inst. of Chem. Technol. Moscow, 1969.
5. Kozak, G.D., Eliseenkov, M.Yu. Effect of Spin Phenomena on Critical Detonation Diameter of Liquid Explosives. Explosives and Pyrotechnics (in Russian), №№ 9-10, TCNIINTIKPK, 1994,pp.3-5.
6. Kondrikov, B.N., Sumin, A.I. Equation of State of Gases at High Pressure. Comb., Expl. & Shock Waves, 1987, vol .23, N 1, pp. 114-123.
7. Kondrikov, B.N., Raikova, V.M. Calculation of the parameters of equation of state. Mendeleev Inst. of Chem. Technol. Moscow, 1981.
8. Raikova, V.M., Kondrikov, B.N., Khalak, A. Chemical Kinetics at Detonation of Organic Compounds-Nitric Acid Mixtures. Trans. of The 30-th International Annual Conference of ICT June 29 – July 2, 1999. Karlsruhe FRG, pp. 95-1 – 95-12.
9. Dremin, A.N., Trofimov, V.S. Calculation of the failure diameters of liquid explosives. J. Appl. Mechanics and Technical Physics (Rus.), 1964, №1, p.126.

COMMON SHAPE OF DEPENDENCE OF CRITICAL DIAMETER OF DETONATION ON DENSITY FOR TATB EXAMPLE

G.T.Afanas'ev, L.N.Akimova
Semenov Institute of Chemical Phisics RAS,
Kosygin St.4, Moscow 117977 Russia

For the first time for the powder explosives the dependence of detonation critical diameter on density with distinctly marked minimum is obtained, for TATB example. According to classification of D.Price that explosive should be ranked contemporarily in two opposed groups of explosives. The new approach to an estimation of detonability of explosives - on the position of minimum and the minimum value of critical diameter is discussed. For TATB they comes to 0,90...0,93 on the relative density and 3,9±0,1 mm on the critical diameter. In a zone of the minimum is also received value of critical thickness of a detonable layer (1,94 ±0,04 mm) which is precisely equal to half of critical diameter.

Keywords: powder explosives, detonability, TATB.

Introduction

The detonability various explosives is usually compared on critical conditions of initiation, propagation or damping of a detonation. Following many researchers we shall define a critical diameter of a stationary detonation as a measure of detonability. For solid explosives the critical diameter, in a general case, essentially depends on density of a charge, particles size of explosive and initial temperature. D.Price[1] has offered to divide all granular explosives into two groups according to a kind of dependence of a critical diameter on density - falling or growing. First is characteristic for power explosives (RDX, TNT), second - for weak (nitroguanidine, hydrasine mononitrate, ammonium perchlorate). In present report results of research of steady detonation limits in cylindrical and flat charges TATB are given. TATB has calculated explosion heat 960 cal/g, intermediate between nitroguanidine (840 cal/g) and TNT(1070 cal/g), and also is the most popular object of researches during the last decades.

Experimental results and discussion

Critical conditions detonation propagation in bulk and pressed TATB charges were investigated. Measurement of detonation velocity and monitoring of damping process with the help rapid photoregister in a combination with aluminum witness plates was made. Length of charges exceeded 10 diameters. The results are shown on a fig.1. The right vertical line corresponds to density of a monocrystal (ρ_{mc}=1,938 g/cm^3). The received dependence of detonation critical diameter d_{cr} on density ρ has a distinctly marced minimum at rather high relative density ($\rho_{rel}=\rho/\rho_{mc}$). Near of a critical conditions the detonation velocity of pressed charges ($\rho\geq$1,38 g/cm^3) is equal about 0,93...0,95 from ideal D_{id}, if to accept D_{id}=0,343+3,94ρ [3].

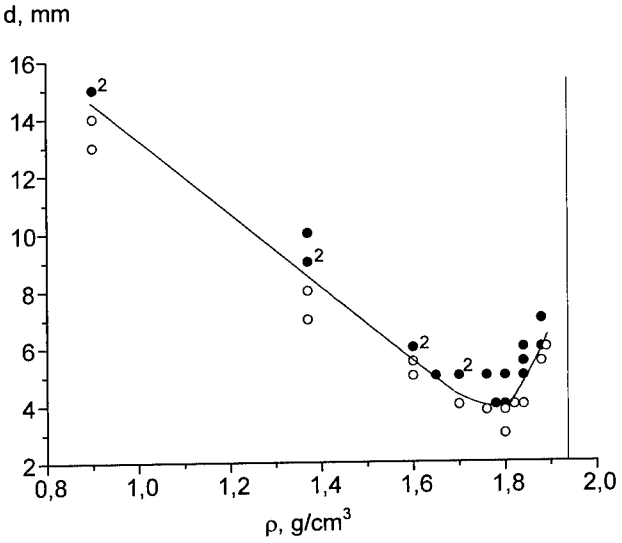

Fig.1. Critical diameter of detonation TATB *vs* density (•- steady detonation, ○- failure; figures about points - quantity of experience).

The most natural the dependence with a minimum is explained by a competition of two influences: increases of speed of combustion of particles in detonational wave with growth of pressure and reduction of initiation points quantity at decrease porosity of charges. Instead of simultaneously carrying TATB to two opposite groups, it is possible and eyen expediently to take the form of dependence $d_{cr}(\rho)$ with a minimum as common, and to use coordinates of a minimum $(d_{cr},\rho_{rel})_{min}$ for the quantitative characteristic detonability, defining the minimum as the zone of highest detonational capability(HDC)[2]. For TATB they is $3,8<d_{cr}\leq4,0$ mm and ρ_{rel}=0,90...0,93.

The right growing branch of dependence on fig.1 is rather short, so the value d_{cr} on it grows only up to 6,0 mm at limiting for pressing of density. It is close to known for high-density PBX 9502 (failure radius R_{fail}=3,88mm[4]).

The position of the HDC zone for different explosives differs. For power explosives it is approached nearly to density of a monocrystal ρ_{mc} and it fails to reveal, so far as the powerful substances have usually small $d_{НДС}$. magnitudes. To find out coordinates of the HDC zone at high density conveniently to use a method of a thin layer [2]. On an example TATB in the zone HDC (at ρ_{rel}=0,91) critical conditions of detonation propagation in rectangular charges were investigated. The charges had length 24 mm and were placed on a witness plate by the party X consistently on the area section (X×Y) decreasing with a small step. X and Y changed in limits from 2 to up 8 mm.

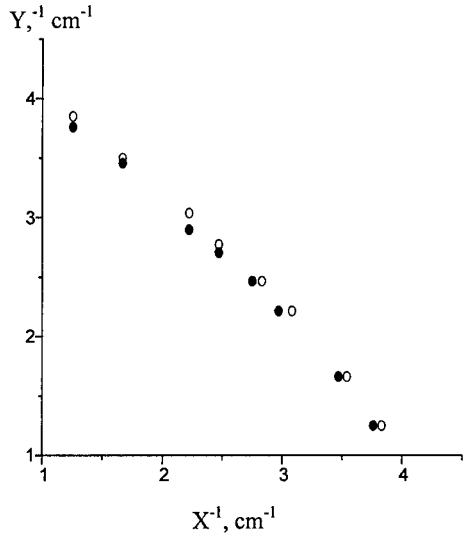

Fig.2. Critical conditions of detonation propagation in rectangular pressed charges of TATB (•- steady detonation, o- failure).

The received results(fig.2) are almost ideally described by a formula:

$$\frac{1}{Xcr}+\frac{1}{Ycr}=\frac{1}{\Delta cr}=\frac{2}{dcr}\equiv\frac{1}{Rcr},$$

where X_{cr} and Y_{cr}- party of section in critcal conditions and Δ_{cr}= 1,94±0,04 mm - critical thickness of infinite detonable layer. The received results symmetry testifies to absence of influence of an environment, apparently, from a backlash inevitable at assembly of charges on a plate. Thus $\Delta_{cr}=\Delta_{HDC}$, and with high accuracy $\Delta_{cr}=R_{cr}=d_{cr}/2$. (The last result was experimentally received earlier

by the wedge method[5], where non-stationary and multidimensional effects can be displayed[6]). It is possible to accept value R_{HDC} and equivalent to it Δ_{HDC} as the universal characteristic of detonability. The formation of the received empirically formula apparently specifies preservation of detonation front curvature in critical conditions.

Conclusions

It is offered to use coordinates of a minimum of failure diameter dependence on density for the characteristic highest detonational capability of energetic materials. For powerful explosiveves, at which the minimum is about monocristal density and the failure diameter is too small, it is recommended to measure failure thickness of a high-density pressed layer Δ_{HDC}. If then to result Δ_{HDC} values in the same grain size μ (for example, with the help of a proportion $\Delta_{cr} \sim \sqrt{\mu}$ [2]), it it is possible to compare detonability of different explosiveves. For a number of explosiveves such values are submitted in article[7] at the grain size of δ=2 μm, and for ТАТБ (Δ_{cr} = 1,8±0,2 mm) at real dispersity $\delta \approx 10$μm.

References

1. D.Price. "Contrasting patterns in the Behavior of High Explosives", 11th Symp.(Int.) on Combustion, Beckeley, CA, 1966, p.693

2. G.T.Afanas'ev, A.A.Sovko, Yu.V.Sheikov. "The Highest Detonational Capability of High Explosives", 16th Int.Coll.on Dynamics of Explosion and Reactive Systems. Cracow, Poland, 1997, p.590.

3. B.M.Dobratz. "LLNL Explosives Handbook". 1981.

4. A.W.Campbell, R.Engelke. "Diameter Effect in High-Density Explosives", Proceeding of the 6th Simposium (Int.) on Detonation, Coronado, CA, 1976,p.642.

5. J.B.Ramsay. "Effect of Confinement on Failure in 95 TATB/5 Kel-F," Proceeding of the 8th Symposium (Int.) on Detonation, Albuquerque,NM, 1985,p.372.

6. B.W.Asay, J.M.McAfee. "Temperature Effects of Failure Thickness and the Deflagration-to-Detonation Transition in PBX 9502 and TATB", Proceeding of the 10th Simp. (Int.) on Detonation, Boston, 1993,p.485.

7. G.T.Afanas'ev, T.S.Pivina, D.V.Sukhachev. "Comparative Characteristics of Some Experimental and Computational Methods for Estimating Impact Sensitivity Parameters of Explosives", Propellant, Explosives,Pyrotechnics, 1993, vol.18, p.309.

Measurement of Initiation Strength of Detonators

František Masař, Jiří Strnad, Marcela Jungová
Department of Theory and Technology of Explosives
University of Pardubice
532 10 Pardubice
Czech Republic

Abstract

A new direct method of initiation strength measurement for different construction type detonators suitable for its comparison has been developed. The determination of axial and lateral initiation strength of detonators is based on the effect of a reactive compressive shock wave on an acceptor charge.

Introduction

In order to meet the requirements of industry, Department of Theory and Technology of Explosives (DTTX), University of Pardubice (UPa), has developed a new direct method for measuring the initiation strength of detonators. The method is derived from small Gap test. Air is used as a barrier instead of PMM. The role of the acceptor is played by the plastic explosive Semtex 1A. The measuring set makes it possible to separately measure the axial and the lateral effects[1,3].

Method

The measurement of the initiation strength itself was carried out on a measuring apparatus developed at DTTX UPa[2] and assembled at Austin Detonator Ltd. The apparatus consists of a basement steel plate of 400 × 300 × 40 mm dimensions with a hole in the centre. Witness tablet (3 mm thick, steel) is put over this hole during measurement. Two pairs of lateral plates are welded to the basement leaving 4 mm gap between each pair. This gap enables vertical movement of wire carrying the tested. Delineative slider that holds the wire secures the proper distance of detonator from the charge. Leading rod that is welded to the basement behind the lateral plates enables precise movement of the slider. It is screwed to the top of these plates as well. If the axial effect is to be measured T-type wire is used. A firm attachment of the detonator and the wire is achieved by applying friction tape

to the upper part of the detonator. While securing the detonator, special care has to be taken not to apply any tape to that part of the detonator that contains ignition and base charge. In case the lateral effect is to be measured the detonator is attached directly to the straight wire again with piece of friction tape. The acceptor charge (Semtex 1A) was placed in a polyethylene tube whose dimensions were chosen in such a way as to approach the dimensions of the set for small Gap test[3]. The outer diameter was 24 mm, the inner diameter was 20 mm. The height of the acceptor charge was exactly 20 mm. The explosive was pressed into the pipe and the excess was cut off from both sides to form plane surface. Hence the weight of the charge was not constant and varied from 8.5 to 9 g Semtex 1A. The average density 1.43 g/cm^3 was found.

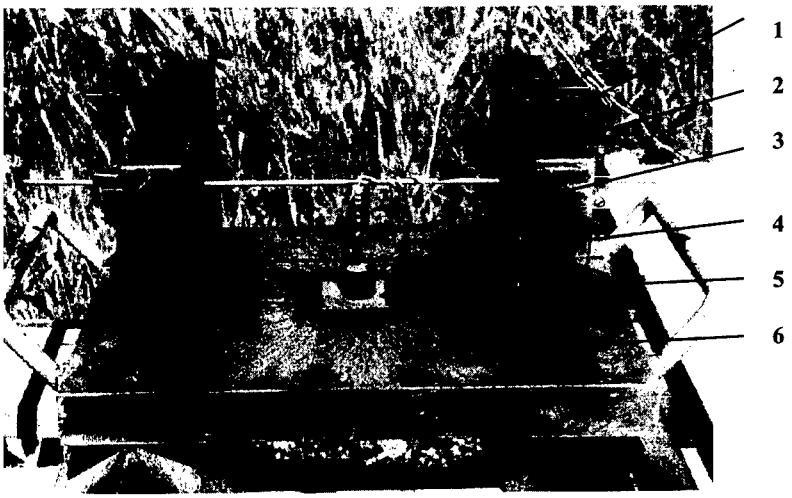

Figure 1. Measurement of initiation strength – arrangement for axial effect
1. Fixation wire 2. Leading rod for distance adjustment 3. The detonator tested 4. Acceptor explosive charge 5. Witness table 6. Apparatus for ISD measurements

In the measurements of axial initiation effect the detonator was placed over the acceptor charge in such a way that the centre of detonator was precisely above the centre of the acceptor charge. At the same time precise perpendicular position of detonator was adjusted. While measuring lateral initiation effect the centre of base charge of detonator was situated over the centre of the acceptor charge. In this case it was important to keep parallel position of the detonator with respect to the plane of charge.

The tested distance was adjusted by means of insertion gauges placed between the detonator and the charge. In this way it was possible to secure a precise dimension adjustment. The result of test was evaluated according to whether or not the witness tablet was perforated.

For determination of the mean value of H_{50} [mm] and standard deviation s [mm] we used the RUN-DOWN method. It enables a measurement of a chosen number of pieces at a single height level. The first level (height H_0) that we have included to the calculation was one step higher than the one, at which the initiation just began to appear. As the highest level was considered the one with 100% occurrence of initiations. A presumption for the application of the method given is normal distribution of the values monitored.

The detonator types used

Austin Detonator Ltd manufactured the detonators used for these measurements. The following codes were used:

-DEM-0-	the instant detonators
-Cu or Al-	the material of the detonator tube
-S-	fusehead of standard resistance
-Standard-	standard detonator filled with 0.6 g PETN
-PYX-	experimental detonator with PYX

The density of standard filling in the detonators was calculated from the measured height of the explosive. This value must be considered approximate, because of the production tolerance of the detonator tube and its deformation during pressing.

DEM-0-Cu-S-Standard

The detonator tube was made of copper, its outer and inner diameters were 6.86 ± 0.06 mm and 6.40 ± 0.05 mm, respectively, the inner diameter at the bottom of detonator tube was 6.08 ± 0.05 mm, the bottom thickness was 0.5 mm, and the tube height was 53 ± 0.5 mm. The secondary filling of the detonators was pressed in two steps: the first dose of 0.3 g PETN was pressed with a pressing mandrel of 6.25 mm diameter loaded by a pressing pressure of 180 kg/piece. The same pressure pressed the second dose of 0.3 g PETN. The height of the explosive was measured after the second pressing procedure. The calculated density was 1722 kg/m^3. The initiation element used did not contain delay charge, its outer and inner diameters were 6.25 ± 0.05 and 3.2 ± 0.1 mm, respectively.

The lead (II) azide in amount of 0.05 g covered by 0.035 g PETN was used as an ignition charge. Explosives were pressed into the priming shell under pressure of 70 kg/piece. At last assembling of detonator took place.

DEM-0-Al-S-Standard

The detonator tube was made of aluminium, its outer and inner diameters were 7.06 ± 0.05 and 6.40 ± 0.02 mm, respectively, the inner diameter at the bottom of the detonator tube was 6.13 ± 0.05 mm, thickness of the bottom was 1.0 ± 0.2 mm, and the tube height was 53 ± 0.5 mm. All the other details were identical with those of the DEM-0-Cu-S-Standard detonator described above.

DEM-0-Cu-S-PYX

The same type as the DEM-0-Cu-S-Standard detonator above, with the only difference of using 2×0.6 g PYX (sample No. 1) as a base charge. The height of the explosive column was 14 mm, its calculated density was 1460 kg/m^3. In sample No. 2, we used 2×0.34 g PYX and the pressure of 220 kg/piece. The height of base charge was15 mm, its calculated density was 1543 kg/m^3.

Results and Discussion

The effect of the material and the construction of the tube

It can be concluded from our measurement of the axial initiation strength, that does not matter what kind of material is the tube made of. The thicker wall of aluminium tube compensates the higher strength of copper here. In addition, the amount of fragments formed from the bottom section is so small, that it does not affect the result of the test.

In the measurements of the lateral IS we found a large differences in the values measured (Fig. 2). We presume that the effect of a large amount of aluminium fragments on the ISD cannot be neglected in this case. Exothermal oxidation of aluminium causes increase of the temperature of the detonation products. This according to the theory of the hot spots increases the initiation effect. In addition, aluminium extends the time of pressure impulse during detonation[4].

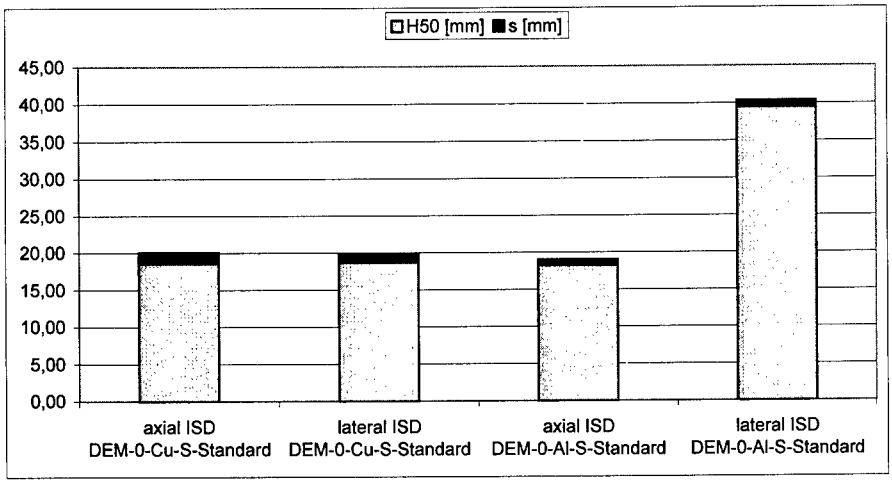

Figure 2. The effect of the material and the construction of the tube on initiation strength of detonators

Comparison of PETN and PYX in the role of base charge

As it can be seen from the H_{50} values measured (Fig. 3) that the initiation strength of PYX is lower than that of PETN. This is caused by several interrelated factors. The of PYX grains prepared by us causes a poor pressing ability resulting in low density (which in the samples was only 83 and 88% of theoretical density), which subsequently lowers the detonation velocity. The detonator with the density of base charge 1460 kg/m^3 shows slightly higher values of axial IS measured than that with 1543 kg/m^3 density. We presume that the sensitivity to initiation is lowered at higher densities of PYX repressing, which causes a slower start of detonation. In the lateral IS, on the other hand, the effect of greater amount of PYX cases, increase of the pressure impulse. Greater amount of base charge could be the right solution for higher ISR[5].

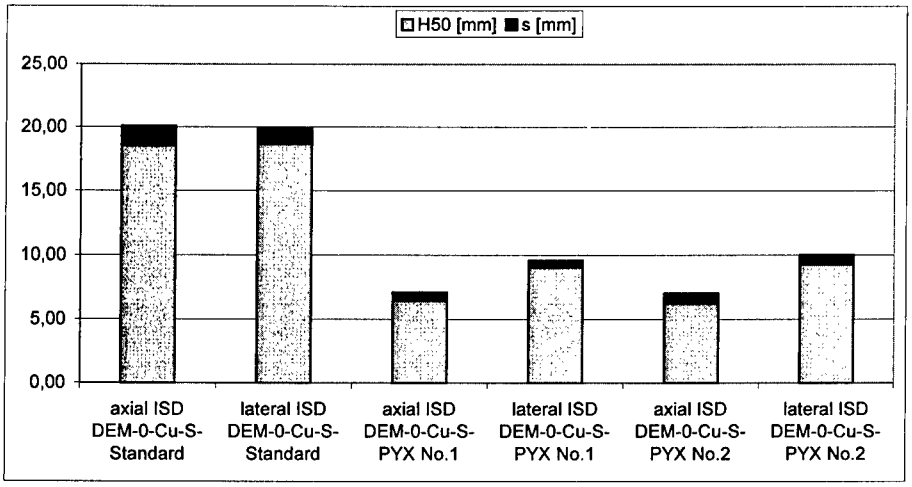

Figure 3. Comparison of PETN and PYX in the role of base charge

Conclusions

The method suggested for the measurement of initiation strength of detonators seems to be promising. The results of measurements have proved its suitability for comparison of various construction types of detonators. The setting of the detonator DEM-0-Cu-S-Standard as the reference type ensures standardisation of the method.

References

1. Jungová M.: *Effect of initial activation impulse on function of detonator* (Thesis – in Czech), University of Pardubice 1992.
2. Hes J.: *Determination of axial and lateral effect of detonators No. 8* (Thesis – in Czech), University of Pardubice 1998.
3. Buksa R., Sillinger F., Straka A.: *Analyses and tests of explosives* (In Czech), SNTL, Prague 1954.
4. Strnad J.: Private communication.
5. Wilk Z., Zygmunt B.: A new tools for oil-well perforation (In Polish) *Proceedings of the second seminar "New trends in research of energetic materials"*, University of Pardubice, April 1999.

A THEORETICAL MODEL OF DETONATION PROCESS

Hu,Shaoming
Xian Modern Chemistry Research Institute
Xian 710065, People's Republic of China
Fax: 86-29-8291307 E-mail: hu_shaoming@263.net

ABSTRACT

A new theoretical model of detonation process, called conjugate detonation model, has been proposed by the author. This model is deduced directly from conservation laws, which describes the whole process from the original reactants to the final detonation products. C-J condition (D=U+C) is a special solution of this model.

Key words: Detonation Conjugate detonation model
Conjugate state C-J theory C-J condition

1. INTRODUCTION

Since 100 years ago the hydrodynamic theory of detonation, C-J theory, came into being, it has been disputed for many reasons. The argument points mainly towards the C-J hypothesis according to which the detonation rate D is the minimum compatible with the conservation laws. It has been observed that the detonation experimental results are inconsistent with the consequences of C-J theory [1]. For example, for the gas detonation experiments, in unsupported detonations the state point although lies approximately on the calculated Hugoniot curve, but well down on the weak branch, with the pressure and density 10% to 15% below the C-J values and with the flow supersonic with a Mach number of 1.10 to 1.15. That means the C-J theory is not fully in accordance with the experimental results [2][3]. Because of lots of facts unexplained by the current detonation theory, W.C. Davis even considers the current detonation science is incomplete and has not yet reached maturity [3].

Although C-J theory has been disputed, suspected and questioned for one century, without a suitable and generally acknowledged alternative theory, it is still used in detonation study for both theoretical and practical purpose.

Assuming that a turbulence zone is behind the detonation wave front and it is composed by conjugate pairs created by released chemical energy, a new theoretical model of detonation process, called conjugate detonation model, has been deduced directly from conservation laws, which describes the whole process from the original reactants to the final products. C-J condition (D=U+C) is a special solution of this model.

2. CONJUGATE DETONATION THEORY

At 29th ICT the author announced the establishment of conjugate detonation theory [4], and the details of this theory are reported in [5].

In conjugate theory, the configuration of detonation wave is considered as being composed of detonation front, turbulence zone and final products zone as Fig 1 shows.

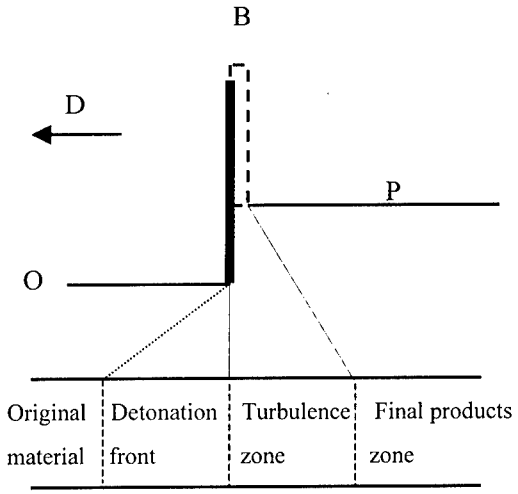

Fig.1 Configuration of steady detonation wave

Conjugate detonation theory considers the turbulence zone is composed

by two kinds of fluid sub-elements with different chemical composition and fluid characteristics, which are named as conjugate pairs. Following is the history of conjugate pairs in detonation wave.

Compressed by the detonation wave, the temperature of original material in the detonation front rises and chemical reaction quickens up. At a certain point, while the mass, momentum and energy are conservative, the strong disturbance caused by released chemical reaction energy makes the original uniform system become turbulence, i.e. the explosive element divides into two conjugate parts b and p (called "conjugate pairs") that are in different states B and P correspondingly. This conjugate pairs state also propagates at detonation velocity D. Part b (in state B) expands and changes into the final state P, and at last the turbulence disappears and whole system returns back to uniform state again, whose specific value equals to the original one but pressure and temperature are much higher.

The state change in conjugate theory is shown by Fig.2.

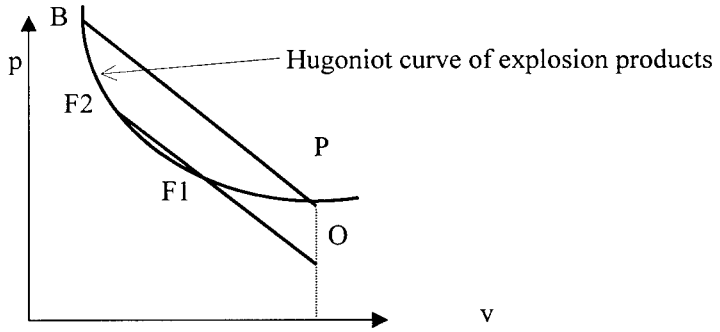

Fig.2 Hugoniot curve and Rayleigh lines in P-V plan

The process from point O to point F is described by conservation Eqs. (1)-(3) as follows [2][6]:

$$(D-U_0)/V_0=(D-U_F)/V_F \tag{1}$$

$$P_0+(D-U_0)^2/V_0=P_F+(D-U_F)^2/V_F \tag{2}$$

$$\frac{(D-U_0)^2}{2}+E_0+P_0V_0=\frac{(D-U_F)^2}{2}+E_F+P_FV_F-Q_F \tag{3}$$

State P is one of the conjugate pairs', and also is the final state of detonation products after detonation wave passes by. State P is described by Eq.(4) as follows:

$$E_P = E_0 + Q_P \tag{4}$$

The conjugate pairs zone also propagates in velocity D. During the propagation, part b (in state B) expands down the Rayleigh line BP rapidly, and changes into state P. As detonation propagates forward in stable detonation velocity D, tangent of the two Rayleigh lines OF and BP is equal, i.e. lines OF and BP are parallel ones. At last, the whole system becomes uniform as point P shows whose specific volume equals to the original one but temperature and pressure are much higher. The process from B to P is described by Eqs.(5)-(7), which are similar to Eqs.(2)-(4):

$$(D-U_P)/V_P = (D-U_B)/V_B \tag{5}$$

$$P_P + (D-U_P)^2/V_P = P_B + (D-U_B)^2/V_B \tag{6}$$

$$\frac{(D-U_P)^2}{2} + E_P + P_P V_P - Q_P = \frac{(D-U_B)^2}{2} + E_B + P_B V_B - Q_B \tag{7}$$

Before and after conjugation mutation, mass/energy/momentum conservation shall be satisfied.

It is obvious that points F,B,P locate at the same Hugoniot curve with equal energy, all of them meet the requirement of energy conservation.

Because Rayleigh lines OF and BP have the same slope (both propagate in same detonation velocity D), and same V (Vo=Vp, see Fig.2), every point, either at line OF or at line BP, has the same mass passage, i.e. for every point at them mass conservation is satisfied.

From points O and P, innumerable couples of parallel straight lines OF and BP can be drawn, but, only one couple of them is the desirable solution, which is decided upon following momentum conservation formula:

$$P_F + (D-U_F)^2/V_F = (X_B \cdot P_B + X_P \cdot P_P) + \left[Y_B \cdot (D-U_B)^2/V_B + Y_P \cdot (D-U_P)^2/V_P\right] \tag{8}$$

X and Y are volume and mass fractions separately.

As one of equations of conjugate detonation model, Eq.(8) makes parameters calculated by conjugate detonation model satisfy momentum conservation. Therefore all mass/energy /momentum conservations are satisfied in conjugate detonation theory.

There are three state equations here:

$$f_P(P_P, V_P, T_P) = 0 \quad (9)$$

$$f_F(P_F, V_F, T_F) = 0 \quad (10)$$

$$f_B(P_B, V_B, T_B) = 0 \quad (11)$$

In this way, we have totally eleven equations: mechanical equations (1)-(3) and (5)-(7), energy equation (4), momentum conservation (8), state equation (9)-(11), and the eleven unknown variables are:

P_P, T_P, P_F, V_F, T_F, U_F, P_B, V_B, T_B, U_B, D

Therefore, all of the detonation parameters can be obtained from above equations,

4. CALCULATION RESULT

Based on C-J theory, Lewis calculated the system of hydrogen and oxygen at original conditions Po=100,000Pa. and To=291K , his result is as follows[7]:

$$D = 2806 m/\sec$$

$$P_{CJ} / P_0 = 18.05$$

According to the conjugate detonation theory, at the same conditions, the result is as follows [5]:

$$D = 2876 m/\sec$$

$$P_{B+P} / P_0 = 15.87$$

Comparing with the experiment datum 2819m/sec measured by Lewis [7], the relative error of conjugate model seems a little larger. In his work that has been well known for more than half century [2][6], Lewis treats H2+O2 system as idea gas and takes specific heat above 3000K as constant, therefore, the result may be used as reference.

5. DISCUSSION

This conjugate detonation model is deduced from basic conservation laws directly (without the hypothesis D=C+U), which describes the whole process from the original reactants to the final products. Following conclusion can be drawn from conjugate detonation theory:

1). The state of final explosion products is P defined by Eq(4), whose specific volume is equal to the original explosion materials' but pressure and temperature are much higher.

2). According to conjugate detonation theory, usually, Rayeigh line is a secant of Hugoniot curve and they have two intersections F1 and F2. Under specified conditions, these two points will overlap each other and become a tangent point, which is exactly the C-J condition (D=U+C).

3). The detonation velocity obtained by the conjugate theory is higher than that one obtained by C-J theory, which can be found directly in Fig.1. Calculation shows that the average pressure at the conjugate zone is lower than so-called C-J pressure.

4). Corresponding to the two solutions F1 and F2 of uniform state F, only one couple of conjugate pair state (B+P) is obtained.

5). Conjugate theory considers the chemical reaction energy makes the system change totally, i.e. it creates turbulence in the system (describing this turbulence by "conjugate state") and this turbulence disappears during propagation, while CJ theory only simply adds enthalpy to the explosion materials.

6). The mathematical model of conjugate theory is an universally applicable one, which is suitable to simulate both high/low velocity detonation without any change in it's appearance, and also, is available to describe composition of cellular structure in detonation wave, which are in press or shall be published later [5].

REFERANCES:

1. W.C.Davis et al Phys.Fluids 8, 2169 1965
2. W. Fickett & W.C.Davis
   DETONATION University of California Press, 1979
3. W.C. Davis Sci. Am. 256(5), 106 1987
4. Hu, Shaoming
   29th International Annual Conference of ICT 111-1 1998
5. Hu Shaoming papers in press or will be published in future
6. F.A. Bom et al
   EXPLOSION PHYSICS Science Press (U.S.S.R) 1959
7. Lewis B. et al J. Am. Chem. Soc. Vol. 52 3905 1930

Detonability of tributyl phosphate and fuming nitric acid

Yoshio Nakayama, Tomoharu Matsumura, Masatake Yoshida, Shuzo Fujiwara

National Institute of Materials and Chemical Research
1-1 Higashi, Tsukuba, Ibaraki, 305-8565, JAPAN

ABSTRACT

The mixture of tributyl phosphate (TBP)/nitric acid diluted with n-dodecane has been widely used in the reprocessing of spent nuclear fuel (known as the Purex process). Therefore it is very important to understand the potential hazard of the mixtures not only under normal conditions of the reprocessing process but also under extreme conditions of pressures and temperatures. The present study report that various TBP/fuming nitric acid mixtures has detonability by the results of denting test (test for explosive strength), card gap test (test for sympathetic detonation) and detonation velocity measurement for estimation of C-J pressure. By using a plastic sample container of 20 mm inner diameter and TBP content ranging from 13 to 34 wt.% it was found that apparent crater depth created on the steel plate was 1.23 to 1.90 mm. These results showed that the mixture detonated. The detonation velocity of the stoichiometric mixture was measured optically and was found to be 6.45 km/s. The detonation pressure was estimated to be approximately 14 Gpa. The results of card gap test showed that the shock sensitivity of the mixture is lower than a pressed tetryl or petn powder but is higher than that of trinitrotoluene (TNT) or nitromethane. It was found that the mixture has relatively high shock sensitivity.

APPLICATION OF DIRECT CHEMILUMINESCENCE TO MECHANISTIC AND KINETIC STUDIES OF ENERGETIC MATERIALS

Jun-ichi Kimura

Propellants and Explosives Laboratory (PEL)
The 1st Research Center
Technical Research and Development Institute
Japan Defense Agency
2-2-1, Nakameguro, Meguro, Tokyo 153-8630, Japan

Since we firstly reported our chemiluminescence (CL) work on penthaerythryroltetranitrate (PETN) and nitrocellulose (NC) in 1989, we have reinvestigated the thermal and thermooxidative decomposition of energetic materials. All kinds of energetic materials such as nitrate esters (R-ONO_2), nitro-compounds (R-NO_2) and nitramines (>N-NO_2) exhibited CL emission when they were heated in nitrogen. Temperature dependence of the steady-state CL intensities commonly changed at the transition points such as melting (i.e., 140°C for PETN) and crystal phase transition (i.e., β to δ transition at 186°C for HMX). Their CL spectra were generally changed from blue-emission to blue- and red-emission above the transition temperature. These experimental facts implied that reaction mechanism for the thermal decomposition of energetic materials could change at the transition points. Characteristic CL peaks were observed in the early stage of heating for aged energetic materials. These CL peaks were attributed to the decomposition of hydroperoxides formed through autoxidation. The activation energy of steady-state CL emission for nitrocellulose agreed well with those obtained with micro-calorimeter and NOx analyzer. We came to conclude that chemiluminescent reactions, which are basically radical reactions, are predominant in the exoenergetic decomposition of energetic materials. Accordingly accepted decomposition mechanisms of energetic materials should be totally reinvestigated because none of them include extremely exoenergetic chemiluminescent reactions.

INTRODUCTION

For over 20 years chemiluminescence (CL) has been developed and became a powerful diagnostic method. CL techniques have become one of the most sensitive method to evaluate the aging of almost all the materials such as polymers, foods, and other organic compounds. Because of the low quantum efficiency ($\phi = 10^{-6}$ to 10^{-10}) of chemiluminescence compared to that of fluorescence and phosphorescence ($\phi = 1$ to 10^{-4}), very weak emission of light is normally not observed in routine measurements of conventional emission spectrometers. With the advent of commercially available CL apparatus, both the acquisition and the analysis of CL data have been advanced year by year. Luckily several models of photon-measuring CL apparatus are available from the Tohoku Electronic Industry Company, Sendai, Japan. In the process of autoxidation most of the organic materials can emit weak light. This type of CL has occasionally been called oxyluminescence. Origin of the CL emissions has been attributed to either disproportionation termination reaction of peroxy radicals or decomposition of hydroperoxide intermediates formed through autoxidation. Analytical method of

CL has several advantages over the other analytical methods. Numbers of CL active reactions, that is chemiluminescent reaction, and their precursors are very limited. CL emission from a chemical reaction may appear when the following two conditions are satisfied; (1) reaction products must have a double bond such as C=O, O=O and N=O: (2) heat of reaction must be high enough to excite the products electrically. Energies of CL (Ee) in the visible region (700 nm to 400 nm) fall in the range from 41 to 72 kcal mol^{-1} (170 to 300 kJ mol^{-1}). Energies of CL (Ee) should be equal to or less than the sum of the heat of reaction (ΔH) and the activation energy (Ea). Activation energies for chemiluminescent reactions are normally small (7-25 kcal mol^{-1}), so that the heat of reaction should be large. Thus only strong exoenergetic reactions could cause CL emission. The wavelength λ (nm) of a chemiluminescence can be calculated by the following equation; $\lambda = 2.86 \times 10^4 / Ee$ (Ee in a unit of kcal mol^{-1}) .

Reported chemiluminescent reactions are summarized in Scheme 1 [1, 2]. In the Reaction 1 hydroperoxide is the precursor of CL emission and electronically excited aldehydes will be the CL-emitter. It is known that hydroperoxides decompose by either unimolecular or bimolecular process. Combination of alkoxy radicals and alkyl radicals (Reaction 2) is an another chemiluminescent reaction where electronically excited aldehydes will be also the CL-emitter. Termination reaction by disproportionation of peroxy radicals (Reaction 3) is the most profoundly studied chemiluminescent reaction to cause blue-light emission from excited aldehydes and red-light emission from singlet oxygen ($^1O_2$). This reaction is named Russell mechanism

$$\mathbf{RCH_2\text{-}OOH \longrightarrow RCHO + RCHO^* + H_2O} \qquad \mathbf{(1)}$$

$$\mathbf{RCH_2O\bullet + R\bullet \longrightarrow RCHO + RCHO^* + RH} \qquad \mathbf{(2)}$$

$$\mathbf{2RCH_2\text{-}OO\bullet \longrightarrow RCHO + RCHO^* + RCH_2OH + {}^3O_2 + {}^1O_2} \qquad \mathbf{(3)}$$

$$\mathbf{RCHO^* \longrightarrow RCHO + } h\nu \textbf{ and } \mathbf{{}^1O_2 \longrightarrow {}^3O_2 + } h\nu \qquad \mathbf{(4)}$$

where * denotes electronically excited state and $h\nu$ emission of light.

Scheme 1 Representative chemiluminescent reactions and the precursors [1, 2].

Measurement of even low-resolution CL spectra are difficult because of low light intensities involved. A grating monochrometer can be used only for relatively strong CL emissions. A series of glass filters has been commonly used to obtain a CL spectrum of ultra weak CL emission. Resolution of the CL spectra obtained with the glass filter method is normally 10 nm. CL emission spectra could be useful to deduce the number of CL-emitter and the chemiluminescent reactions.

There are several non-stationary techniques in CL measurements. An example is gas-switching method, where atmosphere in a sample cell is switched from air to nitrogen or nitrogen to air. In this non-stationary CL measurement a transitional CL intensity-time curve can be obtained, which may provide a reaction order and non-stationary reaction rates. Based on a set of non-stationary reaction

rates at different temperatures one can determine the kinetic parameters such as a pre-exponential factor and an activation energy [1, 2]. One another advantage of CL is that it provides a sensitive technique for monitoring free-radical population in liquid and solid materials. The information obtained in CL measurements is complementary to studies of radical species by electron spin resonance (ESR).

Finally it should be pointed out that the technical terminology of ***chemiluminescence*** has long been misused by many investigators in the field of energetic materials. All the papers entitled "Chemiluminescence Studies----" were the research works done by using a NOx-chemiluminescence analyzer. NOx-chemiluminescence is one of chemiluminescence phenomena resulting from a reaction of nitrogen oxide (NO) and artificially generated ozone (O_3) in a quartz gas cell. All the NOx evolved from energetic materials is converted to NO with a catalytic converter prior to introduction into a NOx-chemiluminescence analyzer. This apparatus has commonly been used as a monitor of NOx pollutant gases. NOx chemiluminescence should be distinguished from (direct) chemiluminescence that is defined as the weak light emission directly from reaction products generated in highly exoenergetic reactions without addition of any chemicals into the reacting system. We have been applied direct chemiluminescence techniques to investigate the decomposition kinetics and reaction mechanism of energetic materials in these 10 years. Our first paper entitled "Chemiluminescence study on thermal decomposition of nitrate esters" appeared in the journal of *Propellants, Explosives and Pyrotechnics* in 1989 [3]. This article summarizes our CL works on energetic materials.

EXPERIMENTAL

Apparatus

The low-level intensity of CL was measured with a single-cell CL analyzer type CLD-100 (Fig. 1). CL spectra were measured with OX-70M and CLD-100FC by using glass filter method in a wavelength range between 400 and 600 nm. These CL analyzers are the products of Tohoku Electric Industry Co., Ltd., Sendai, Japan. These CL analyzers enable us to heat up the test sample to a predetermined temperature up to 200 °C under desired atmosphere or in vacuo. A test sample of approximately 3 grams was normally set into the circular sample pan made of stainless steel (50 mm in diameter and 10 mm in height). The sample pan was set into the light-tight cell equipped with a quartz window on the top. CL measurements of the decomposition of energetic materials were conducted in a flowing nitrogen at several temperatures below 90°C. Luminous intensity of CL is basically proportional to the surface area but not the sample weight. In the case of liquid nitrate esters, the CL intensities remained unchanged despite of the change in their sample thickness. It is noted that graphite-coating on gun propellants did not affect the CL intensities very much probably due to the micro-porosity of the coating.

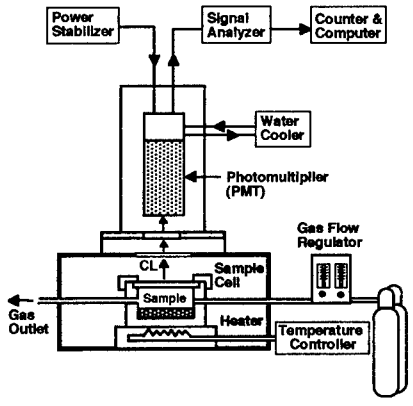

Fig. 1 Cut-view of a CL analyzer used (Tohoku Electric Industry, Type CLD-100).

RESULTS AND DISCUSSIONS

Effects of Temperature and Atmosphere

Temperature of the sample cell can be changed from one temperature to the other one within 10 minutes. Figure 2 shows an example of temperature-time profile and the corresponding CL intensity-time profile of a nitrocellulose (N = 12.6 wt. %) heated in a flowing nitrogen of 60 ml min^{-1}. It took about 40 minutes to reach a steady-state CL intensity after the onset of temperature increase. The temperature of the cell was monitored with a thermocouple embedded in the heating block under the sample pan. The time lag (ca., 30 min) would be due to low heat conductivity of a fiber-like NC because CL emission appears from the surface of a test sample.

CL intensity is strongly affected by atmosphere. A nitrocellulose sample was being heated in nitrogen and then switched to air. Changes in the CL intensities occurred very quickly but the shape of the transient curves were unsymmetrical. The CL intensities of the NC heated in air were almost 5 times higher than those in nitrogen as illustrated in Figure 3.

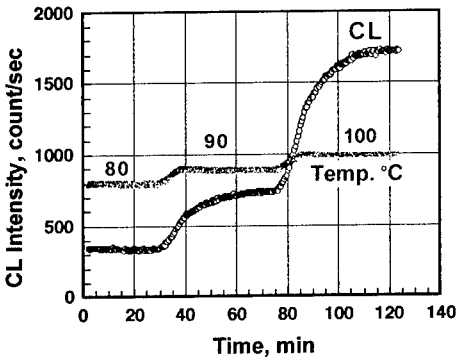

Fig. 2 Change in CL Intensity of a NC with the change in temperature in N_2 [4].

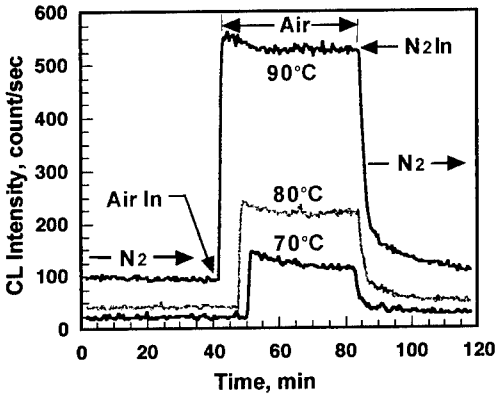

Fig. 3 Effect of cell atmosphere on CL intensity-time profiles for a NC [4].

Anomalous Initial CL Peak

In the early stage of CL measurement of energetic materials, a characteristic CL peaks frequently appeared in the CL intensity-time curves. As an example Figure 4 shows the anomalous initial CL peaks observed for a liquid nitrate ester DEGDN (diethyleneglycoldinitrate) [4,5]. Untreated DEGDN exhibited a large CL peaks as shown in Figure 4 (a). The surfaces of the untreated DEGDN was removed by attaching a potassium bromide (KBr) disk on the surface of it. The anomalous initial CL peak became smaller than that of the untreated DEGDN as shown in Figure 4 (b).

IR spectra of the surface of untreated and surface-removed DEGDN are shown in Figure 5 (a) and (b), respectively. In the wavenumber ranging from 4000cm^{-1} to 3200cm^{-1}, three major peaks observed were assigned to the following; free hydroperoxides (3680cm^{-1}): hydrogen-bonded hydroperoxides (H-bonded-OOH, 3550cm^{-1}), oximes (=NOH; 3600cm^{-1}), and peracids (-CO_3H, 3250cm^{-1}). One can

see that the CL peak height is proportional to the absorbance of hydroperoxides from comparison of the CL peak height and the absorbance of IR spectra [6]. Thus the CL peaks of DEGDN could be attributed to the thermal decomposition of thermally unstable hydroperoxides formed by autoxidation.

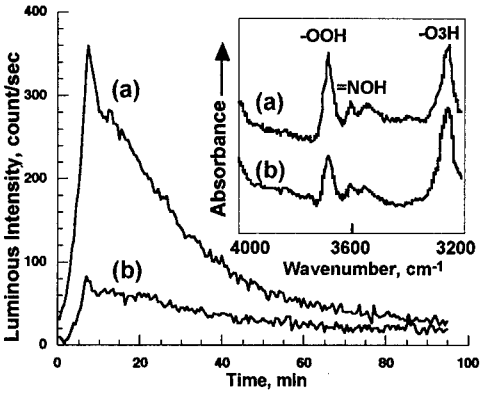

Fig. 4 (Lower) CL-time profiles of DEGDN heated at 70°C in nitrogen; (a) untreated, (b) surface-removed.

Fig. 5 (Upper) IR spectra of the surface of DEGDN corresponding to the each CL curves.

The anomalous initial CL decay curves obeyed 1st-order rate law as shown in the Figure 6 (right) [4, 5]. The slopes of the straight lines were plotted according to the Arrhenius law. Kinetic parameters obtained from Figure 6 (left) were as follows; a pre-exponential factor A of 1.16×10^{11} sec^{-1} and an activation energy E of 23.0 kcal mol^{-1} (96.1 kJ mol^{-1}). The pre-exponential factor is close to the normal value ($\approx 10^{12}$ sec^{-1}). A reported value of the activation energy for the thermal decomposition of hydrogen-bonded hydroperoxides is about 23 kcal mol^{-1} [1], which agrees well with that obtained from Figure 6. These kinetic data also support the conclusion that anomalous CL initial peaks are originated from pre-decomposition of hydroperoxides obtained with IR spectroscopy. CL initial peaks observed for nitrocellulose were also discussed in detail [5].

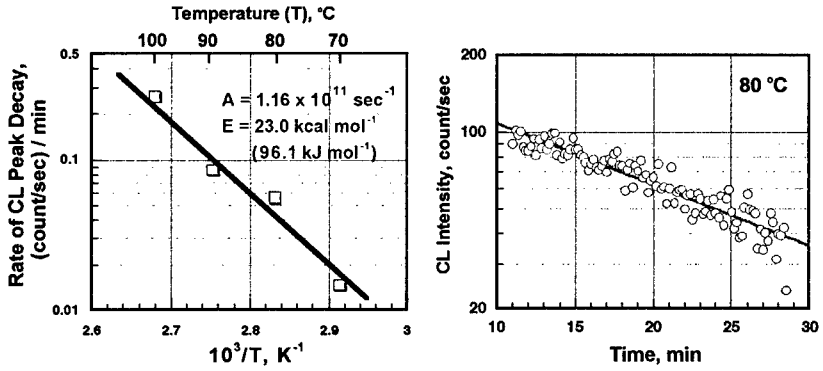

Fig. 6 First-order plots of CL peak decay curve for untreated DEGDN heated in nitrogen and the Arrhenius plot of the slopes.

Steady-state Chemiluminescence

Steady-state intensities of CL emission depend on temperature and atmosphere. Temperature dependence of a purified nitrocellulose (N = 12.6 wt.%) was measured in a temperature range from 40°C to 120°C in a flowing nitrogen of 60 ml/min. Figure 7 (Left) shows the Arrhenius plot of the steady-state CL intensities of NC. An inflection point at near 90°C was observed, which will be some kind of phase transition point of NC. The CL spectra of NC measured at a temperature above (120°C) and below (70°C) the inflection point are also shown in Figure 7 (Right). The CL spectrum below the inflection point indicates that light-emitting species might be aldehydes probably formed by the decomposition of hydroperoxides. The CL spectrum above the inflection point suggests that the light-emmitting species might be aldehydes and singlet oxygen possibly formed by disproportionation of peroxy radicals [5. 7].

The ratio of NO_2/NO for NC is illustrated in Figure 7 (Right lower), which was measured with a NOx-CL meter [4]. Surprisingly NOx gas evolved from NC below the inflection point was almost entirely nitrogen oxide NO. Above the inflection point the ratio of NO_2/NO increased with increasing temperature, that is, NO_2 became to appear. It should be pointed out that NOx gas evolved from NC has long been believed NO_2.

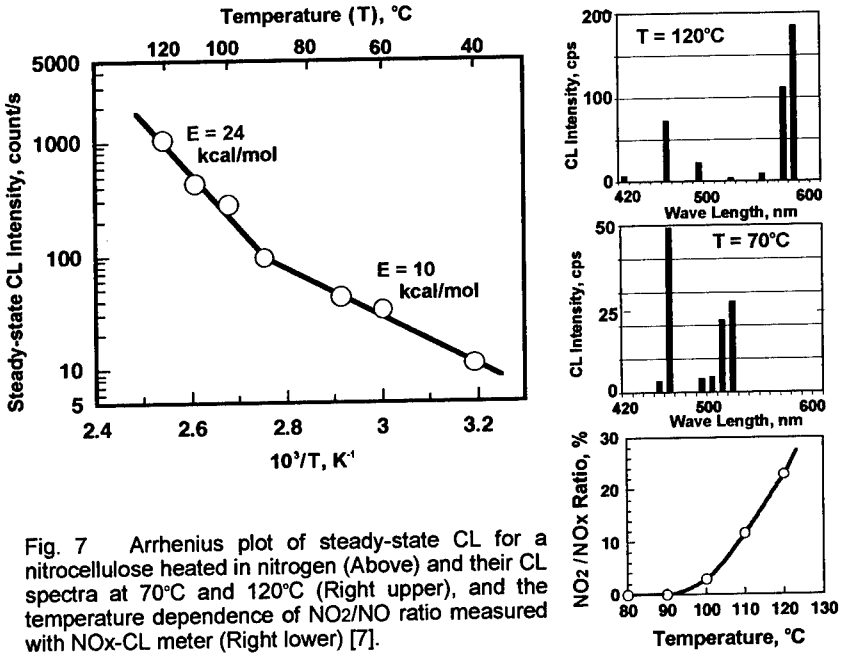

Fig. 7 Arrhenius plot of steady-state CL for a nitrocellulose heated in nitrogen (Above) and their CL spectra at 70°C and 120°C (Right upper), and the temperature dependence of NO_2/NO ratio measured with NOx-CL meter (Right lower) [7].

Change in the reaction mechanism can be explained based on Scheme 2 [3-5, 8]. NC molecule was simply expressed as $RCH_2O\text{-}NO_2$. Below the CL inflection point homolytic decomposition of NC evolves NO_2 and alkoxy radicals ($RCH_2O\bullet$). Consequently hot NO_2 molecules could oxidize alkoxy radicals ($RCH_2O\bullet$) to peroxy radicals ($RCH_2OO\bullet$). Peroxy radicals may abstract hydrogen to form hydroperoxides which could be a precursor of CL emission.

Scheme 2 Hypothetical mechanisms of thermal decomposition of NC below and above the inflection temperature shown in Fig. 7 (Left) [3-5].

Below the Inflection Point (Solid NC)

$$RCH_2O\text{-}NO_2 \longrightarrow RCH_2O\cdot + NO_2 \longrightarrow RCH_2OO\cdot + NO\uparrow$$

$$RCH_2OO\cdot \xrightarrow{[H]} RCH_2OOH \longrightarrow RCHO + RCHO^* + H_2O$$

Above the Inflection Point (Liquid-like NC)

$$RCH_2O\text{-}NO_2 \longrightarrow RCH_2O\cdot + NO_2 \qquad RCH_2OO\cdot + NO$$

$$2RCH_2\text{-}OO\cdot \longrightarrow RCHO + RCHO^* + RCH_2OH + O_2 + {}^*O_2$$

$$2NO + O_2 \longrightarrow 2NO_2\uparrow$$

We have confirmed that peroxy radicals formed in the thermal decomposition of nitrocellulose for a wide temperature ranging from room temperature to 130°C with electron spin resonance (ESR). Above the CL inflection point NC also decomposes to evolve NO_2. These NO_2 could oxidize alkoxy radicals ($RCH2O\bullet$) to form peroxy radicals($RCH_2OO\bullet$). Termination by disproportionation of these peroxy radicals would become predominant probably due to increase in mobility of polymer chain above the transition point. A part of the aldehydes and oxygen could be electrically excited states resulting in emission of blue-green CL by the aldehydes and yellow-red CL by singlet oxygen. Oxygen reacts with NO to form NO_2, which is regenerative NO_2 but not the original NO_2 formed in the initiation step. These hypothetical mechanism was confirmed by examination of a liquid nitrate ester diethyleneglycol dinitrate (DEGDN) as described below.

Figure 8 shows the CL spectrum grouping of DEGDN heated at 90°C in nitrogen. Two light-emitting species may exist; one would be excited carbonyl compounds and the other singlet oxygen. The latter was confirmed with an IR-CL spectrometer (LCD-310) at a wavelength of 1268 nm. The CL spectrum was similar to that for NC heated above the CL inflection point (Figure 7 Upper Right).

Figure 9 depicts the Arrhenius plots of NO and NO_2 of DEGDN heated in nitrogen [4, 5, 9]. Surprisingly the value of activation energy for NO_2 evolution was a negative value –2.0 kcal mol^{-1}. If the evolved NO_2 were the NO_2 generated in the homolysis of nitrate ester bonding ($RO\text{-}NO_2$) as anticipated from accepted reaction mechanism of nitrate esters, observed activation energy should be equal to the bond dissociation energy of O–N bonds, i.e., around 35 kcal mol^{-1} (146 kJ mol^{-1}).

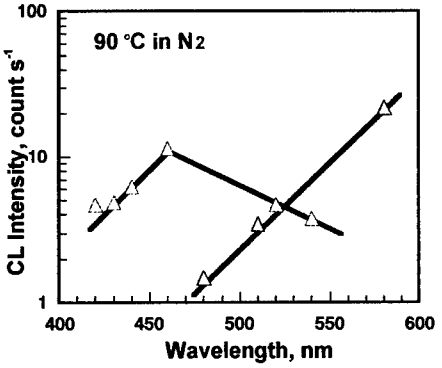

Fig. 8 CL spectrum of DEGDN at 90°C in N_2.

From the observed negative activation energy, one can tell that the evolved NO_2 was formed by the oxidation of NO with oxygen as indicated in the last step in Scheme 2. These new findings will be a strong evidence that initially generated NO_2 acts as an oxidizer and then could be regenerated. Similar results were also obtained in the case of triethyleneglycol dinitrate (TEGDN).

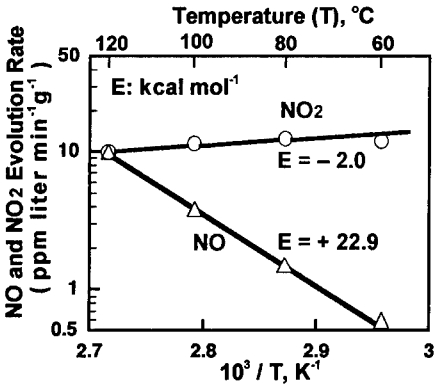

Fig. 9 Arrhenius plots for NO and NO_2 evolved from DEGDN heated in N_2 [9].

Figure 10 shows the Arrhenius plot of two nitro compounds (TNT and dimethyl dinitrobuthane (DMDNB)) in a flowing nitrogen of 60 ml min^{-1}. The latter is widely used as a tagging reagent of a plastic explosive C-4. CL activation energy for TNT changed from 6.8 kcal mol^{-1} to 64 kcal mol^{-1} at near 130°C. CL activation energy for DMDNB was obtained to be 8.2 kcal mol^{-1}. Those low activation energies for the nitro compounds at relatively lower temperatures indicate that their chemiluminescent reactions would be diffusion-controlled. The CL activation energy for TNT above 130°C was 64 kcal mol^{-1}, which is nearly equal to the bond dissociation energy of C-NO_2. Thus homolytic reaction of C-NO_2 bonds will be the rate-determining step of the thermal decomposition of TNT.

Figure 11 shows the Arrhenius plot of CL intensities for the thermal decomposition of HMX. Time interval of each measurements was 2 hours. Effect of β to δ transition of HMX on CL intensity was clearly observed. As can be seen in Figure 11, supercooled δ-HMX exhibited almost 5 times stronger CL emission than that of β-HMX at the same temperature. CL spectral change was also observed at the crystal phase transition. Detailed decomposition mechanism of HMX is in progress.

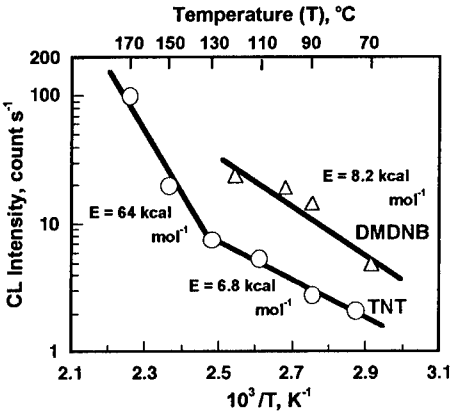

Fig. 10 Arrhenius plots of CL Intensities for TNT and DMDNB heated in nitrogen.

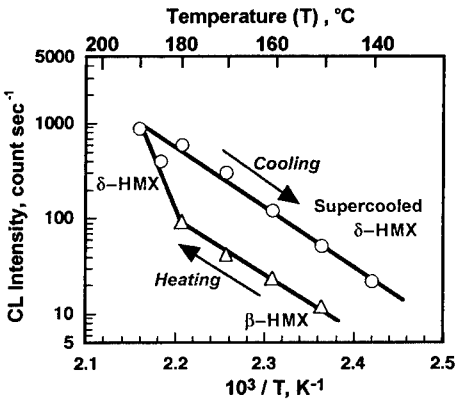

Fig. 11 Arrhenius plots for CL Intensity of HMX heated in N_2 up to 190°C; Effect of β- to δ-HMX phase transition on CL intensity.

Non-stationary Chemiluminescence (Gas Switching Method)

If an energetic material is heated in an inert atmosphere in a closed cell of a CL apparatus and then air or oxygen is admitted, there is a rapid increase in CL intensity. Conversely when the atmosphere is switched from air or oxygen to an inert atmosphere, CL intensity would decrease. Those transient CL curves enables one to derive reaction order and kinetic parameters. Those technique are called gas-switching method [1, 2]. Transient CL curves of NC for gas-switching are already shown in Figure 4, where gas-switching was applied at a flow rate of 60 ml min^{-1}. Figure 12 also illustrates the CL curves for DEGDN when the gas switching was applied at the same flow rate of 60 ml min^{-1}.

Figure 13 summarizes the results of CL gas-switching measurements for NC, PETN, and DEGDN. All the CL decay curves obeyed the 1st-order rate law. CL transient curves of NC are very steep and half-life times of the CL decay curves for a flow rate of 60 ml min^{-1} apparently remained unchanged at different temperatures as illustrated in Figure 13. This may imply that the half-times of the CL transient for NC are shorter than that for gas-switching of flow cell (approx. 1 min). Ten times faster flow rates (600 ml min^{-1}) was applied to observe the real transient curves of NC. Half-life time for gas-switching of the flow cell was reduced to one third of the time that measured at a flow rate of 60 ml min^{-1}. As the result of increase in flow rate activation energy for gas-switching from air to nitrogen was obtained to be 15 kcal mol^{-1} below 80°C.

In the case of DEGDN and PETN the CL transient curves were not so steep and the half-life times were longer than that for gas-switching. From the Arrhenius plot of the half-lives for DEGDN and PETN, activation energies were obtained to be the same value (15 kcal mol^{-1}). This value of activation energy is that for the decomposition of peracids [11], which suggests that the decomposition of an unstable intermediate peracid (RC(=O)OOH), which was identified with IR spectra in Figure 5, predominate the CL decay curves.

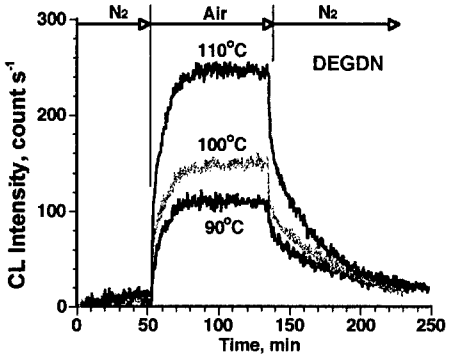

Fig. 12 CL intensity-time profiles when gas-switching method was applied at a flow rate of 60 ml min^{-1}.

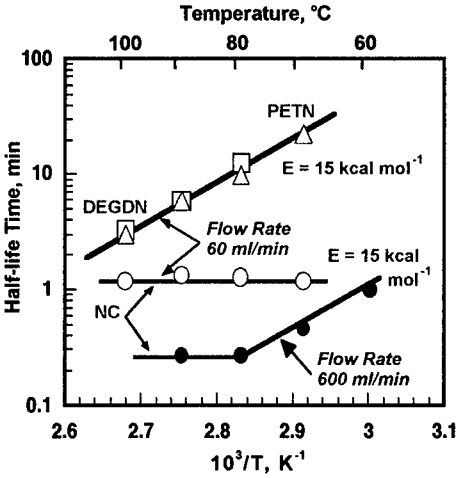

Fig. 13 Arrhenius plots of the half-life times for the CL decay of NC, PETN, and DEGDN when cell atmosphere was switched from air to nitrogen at a flow rate of 60 ml min^{-1}. Half-life times for NC obtained at a flow rate of 600 ml min^{-1} were also plotted [4, 5].

Comparison of CL, NOx and Micro Calorimetric Data

The author believes that chemiluminescent reaction must be the predominant exoenergetic reaction of energetic materials because only highly exoenergetic reactions can excite decomposition products to their electronically excited states. The strong exoenergetic reactions should be self-oxidation reactions of energetic materials by evolved NO_2. Thus it is natural to think that there is good relations between CL emission, NOx evolution and calorimetric data. Heat generation rates of NC decomposition in nitrogen were measured with Setaram micro-DSC III and the NOx evolution rates were measured with NOx-CL analyzer. These two different types of data are compared with CL data in the Arrhenius plots in Figure 14. All the kinetic parameters shown in Figure 14 agreed very well with each other [4]. These coincidence implies that self-oxidation reaction of NC by evolved NO_2 generate heat resulting in emission of light (CL).

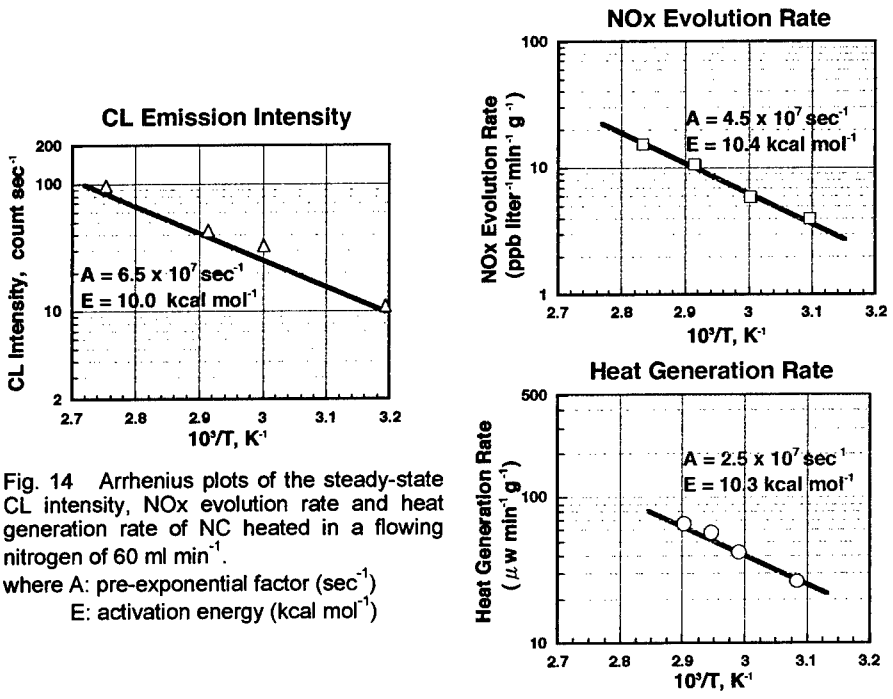

Fig. 14 Arrhenius plots of the steady-state CL intensity, NOx evolution rate and heat generation rate of NC heated in a flowing nitrogen of 60 ml min^{-1}.
where A: pre-exponential factor (sec^{-1})
E: activation energy (kcal mol^{-1})

CONCLUSION

CL techniques are demonstrated to be one of the most sensitive and promising diagnostic method to investigate the decomposition of energetic materials at relatively low temperatures. CL will be the advent of new age in the study of propellants, energetic materials and pyrotechniques.

CL emission associated with thermal decomposition of energetic materials strongly suggest that the decomposition occur via peroxide route. Hydroperoxides and peracids found in our laboratory are

unstable intermediates in the decomposition of energetic materials. We also confirmed that observable nitrogen dioxide NO_2 is not the original one generated by the homolytic cleavage of nitrate ester bonds ($RO-NO_2$) but the regenerated NO_2 formed through the reaction of NO and O_2 . Nitrogen dioxide liberated from the bond scission of $RO-NO_2$ may act as an oxidizer to convert the alkoxy radicals (R-O•) into peroxy radicals (R-OO•), which may generate oxygen through recombination reaction by disproportionation.

Totally new theory on the thermal decomposition of energetic materials must be reestablished by making the best use of advanced analytical methods such as chemiluminescence, micro calorimetry and electron spin resonance.

REFERENCES

1) S. S. Stivala, J. Kimura, and L. Reich, Chap. 1, "The Kinetics of Degradation Reactions", pp. 1-65, in "Degradation and Stabilization of Polymers", edt. H. H. J. Jellinek, Elsevier, New York (1983).

2) G. A. George, Chap. 3, "Chemiluminescence of Polymers at Nearly Ambient Conditions", in "Luminescence Techniques in Solid State Polymer Research", edt. L. Zlatkevich, Marcel Dekker, New York (1989).
3) J. Kimura,"Chemiluminescence Study on Thermal Decomposition of Nitrate Esters", 14, pp. 89-92, Prop. explos. and pyrotech. (1989).

4) J. Kimura, "New Reaction Mechanism of Thermal Decomposition of Nitrocellulose", Preprints of 4th Pacific Polymer Conference, p. 494, Kauai, Hawaii (1995).

5) J. Kimura, "Nitrocellulose", Vol. 6, pp. 4582-4587, edt. J. C. Salamone, Polymeric Materials Encyclopedia, CRC Press, Boca Raton, FL (1996).

2) J. Kimura, "Low-temperature Degradation Studies on Gun Propellants and Nitrate Esters with NOx Meter", TRDI Technical Report 6200, TRDI, Japan Defense Agency (JDA) (1991).

3) J. Kimura, H. Arisawa, and H. Hayashi, "New Finding of Hydroperoxides in Nitrate Esters as Decomposition Intermediates", TRDI Technical Report 6531, TRDI, JDA (1994).

6) J. Kimura and H. Hayashi, "Reaction Mechanism of Anomalous Initial Decomposition of Nitrate Esters", TRDI Technical Report 6657, TRDI, JDA (1998).

7) J. Kimura, "Application of Chemiluminescence to Mechanistic and Kinetic Studies of energetic materials - Nitrocellulose and Diethyleneglycol Dinitrate (DEGDN)-", 11th Symposium on Chemical Problems Connected with the Stability of energetic materials (to be published), Båstad, SWEDEN (1998).

ANALYTICAL APPLICATION OF THERMAL METHODS IN THE FIELD OF EXPLOSIVE MATERIALS

M. Sućeska, M. Rajić
Brodarski institut – Marine Research & Special Technologies
Av. V. Holjevca 20, 10000 Zagreb, Croatia

Thermal methods play important role among various measuring techniques used in the analysis of explosive materials. Although these methods are usually applied for the characterisation and determination of the thermal properties of an explosive (e.g. melting process, polymorphic transformations, thermal stability, kinetics of thermal decomposition, temperature of initiation, etc.), they can be also used for analytical purposes.

Herein we present the possibilities of applying differential scanning calorimetry (DSC) and thermogravimetry (TGA) for both qualitative and quantitative analysis. We show that these methods may be used for the identification of several standard high explosives and their mixtures, for the determination of the purity and quality of an explosive, for the identification and determination of the content of phlegmatiser and for the analysis of the multi-component systems.

The small sample size, the sample heterogeneity, the dynamic character of the processes taking place during measurements may all affect the outcome of the quantitative measurements, whereby some of the thermal methods may eventually appear less suitable for precise quantitative analysis.

1. Introduction

A group of measuring techniques in which a property of sample is monitored against time or temperature while temperature of the sample, in specified atmpsphere, is programmed, is defined as thermal analysis.[1] Differential scanning calorimetry (DSC) and thermogravimetric analysis (TGA) are thermal methods mainly used for the determination of the thermal properties,[2] while dynamic mechanical analysis (DMA) and thermomechanical analysis (TMA) are used for the determination of the mechanical properties.

Most thermal methods acquire relative information from which quantitative data may be generated by comparison of the signal from the 'unknown' with that from a 'standard' material.[3] The results obtained may differ depending upon the conditions used during the experiment – e.g. the mass of the sample, the heating rate, atmosphere surrounding the sample, etc.[4] Briefly, the differences may arose from the dynamic nature of the processes involved.[1] This eventually makes thermal methods much less "compound specific" techniques if compared to some other analytical techniques, such as infrared spectroscopy. This in turn explains why the derivation of the truly quantitative data requires precise calibration, taking into account all necessary corrections.

Due to such limitations, since recently thermal methods have been mainly used for the thermal characterisation of an explosive,[5-21] for the thermal stability determination,[22-27] and for the study of the thermal decomposition kinetics[28-47] rather than in the qualitative and quantitative analysis.[48-50] They are also used for the determination of the purity[51], the determination of the heat capacity,[52,21] the determination of the eutectic composition and temperature,[53,50] the study of the compatibility,[53,54] and others.

The precision, the sensitivity and the reproducibility of the modern instrumental thermal techniques have been improved due in part to the progress in the field of sensors and to the advancement in data acquisition and processing. The operational temperature range has been extended together with the quality of the temperature control. The reproducibility of the presently available instrumentation in quantitative analysis has become acceptable allowing its use in the field of explosive materials.

Herein we are discussing the typical examples of the possible application of differential scanning calorimetry (DSC) and thermogravimetry (TGA) for the qualitative and quantitative analysis of the explosive materials.

2. Results and Discussion

Differential scanning calorimetry and thermogravimetry were carried out under nitrogen flow, using *TA Instruments* apparatuses, model DSC 2910, and model SDT 2960,

respectively.

The heating rate was normally 10 ^{0}C/min, and samples mass was 1-10 mg. All samples were tested in unsealed, yet covered aluminium sample pans. The explosives tested were either commercially available or were the products of the small-scale synthesis.

2.1. The analysis of high explosives and of their mixtures

While heated the sample of the explosive tested undergoes both physical and chemical changes. Those include melting, polymorphic transformation, thermal decomposition, etc. Studying thermal property of an unknown explosive enables us to identify it by comparing its DSC and TGA curves with those obtained previously under identical experimental conditions for a known explosive.

The DSC and TGA curves of a high explosive are relatively simple – most often DSC curve shows the melting and the phase transition endotherm, and the decomposition exotherm (Fig. 1), while TGA curve shows the loss of the sample mass due to the thermal decomposition (Fig. 3).

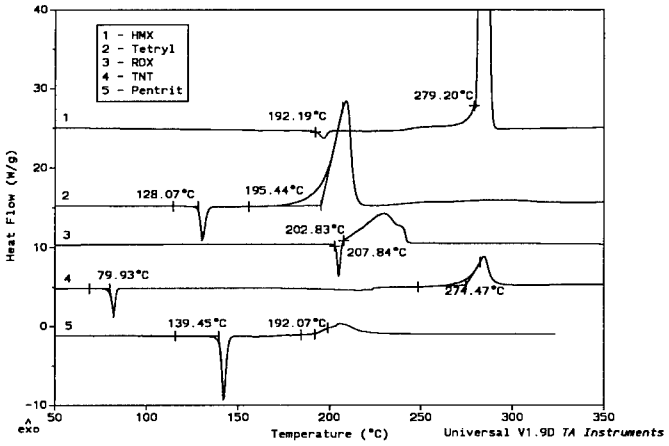

Figure 1. DSC curves of several standard high explosives

The endothermic peaks observed at 79.93 ^{0}C for TNT, at 202.83 ^{0}C for RDX, at 139.45 ^{0}C for pentrit, at 128.07 ^{0}C for tetryl, and at 279.20 ^{0}C for HMX correspond to the melting process, while endothermic peak at 192.19 ^{0}C observed for HMX corresponds to the $\beta \rightarrow \delta$ phase transition. The exothermic peaks observed in all DSC curves correspond to the thermal decomposition processes.

From DSC curves given in Fig. 1, it is obvious that each of the high explosive tested has its specific DSC curve. This fact enables the identification of an unknown explosive by comparing its DSC curve with those curves from the standard explosives, obtained under identical experimental conditions (sample mass, heating rate, surrounding atmosphere, etc.).

However, in the case of the mixtures of high explosives, and the mixtures of high explosives and non-explosive compounds DSC and TGA curves may become very complex. The main reason lies in the fact that some processes take place simultaneously (e.g. melting of one component and phase transition of the other, melting of one component and the decomposition of the other, etc.). This results in the overlap of the DSC peaks and makes the interpretation of the curves increasingly difficult.

Considering the thermal behavior, i.e. the possibility of the analytical application of the thermal methods three typical types of mixtures may exist. Their DSC and TGA curves are given in Figs. 2 and 3.

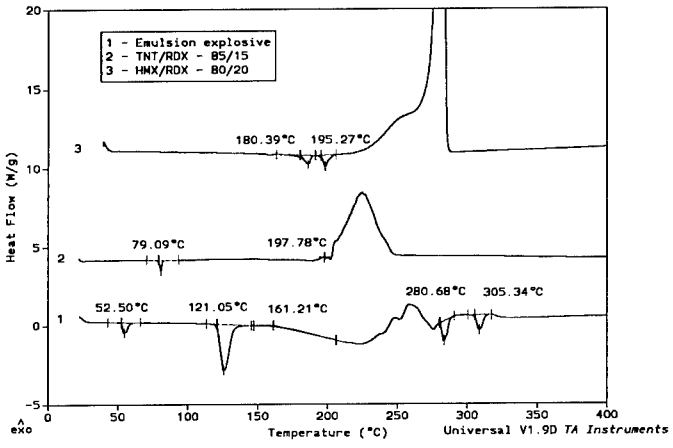

Figure 2. Three typical types of DSC curves of mixtures of explosives

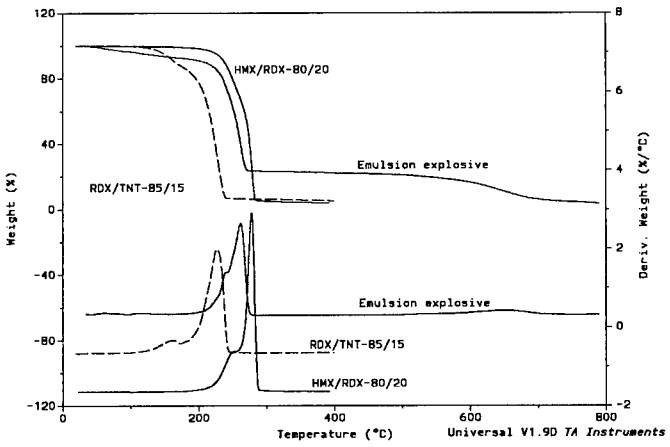

Figure 3. Three typical types of TGA and DTGA curves of mixtures of explosives

In the first case the qualitative and quantitative analysis of the mixture may be carried out from the DSC curves, i.e. from the melting endotherm of one component (e.g. melting of TNT in TNT/RDX mixture). In the second case the analysis of the mixture may be obtained from the TGA curves (e.g. in the case of emulsion explosive), while in the third case only rough quantitative analysis is possible from either the DSC or TGA curve (e.g. in case of HMX/RDX mixture).

The DSC curves of RDX/TNT mixture (Fig. 2) show two endothermic peaks. The peak at about 80 ^{0}C corresponds to the melting of TNT, while the peak at about 203 ^{0}C corresponds to the melting of RDX. From the TGA curve (Fig. 3) it is obvious that there is no mass loss until about 130 ^{0}C. That in turn means that the melting of TNT does not overlap with any other process, and may be thus used not only to detect and to identify TNT present in the mixture, but also to determine its content.

Since the enthalpy of the melting is proportional to the TNT content, its mass content in the mixture (w % TNT) can be calculated from the enthalpies of melting for pure TNT ($\Delta_m H_{TNT}$) and for RDX/TNT mixture ($\Delta_m H_{RDX/TNT}$) according to the equation [1]:[49,50]

$$w\%\text{TNT} = \frac{\Delta_m H_{\text{RDX/TNT}}}{\Delta_m H_{\text{TNT}}} \cdot 100 \qquad [1]$$

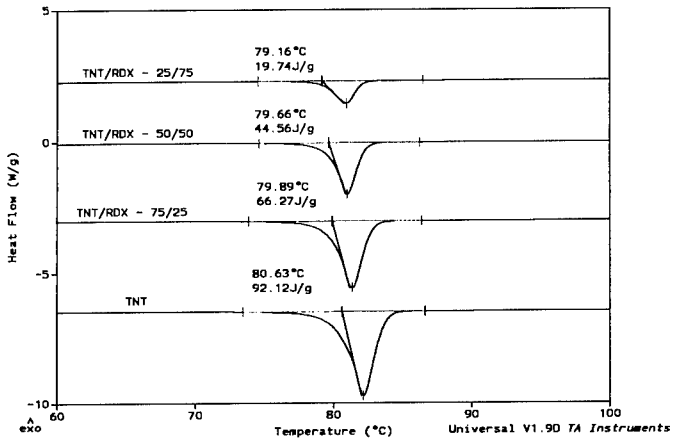

Figure 4. The temperatures and the enthalpies of melting of TNT in RDX/TNT mixtures

An extended error analysis performed in our laboratory on the samples whose weight was in the range of 3 to 5 mg, showed that the enthalpy of melting of the pure TNT could be determined inside an standard error of 2.01 J/g, (i.e. about ± 2 %). The difference between the actual and obtained TNT content was inside ± 3.

In the case of an emulsion explosive based on NH_4NO_3 and $NaNO_3$ oxidisers, the quantitative analysis based on TGA curves is possible only due to the fact that the decomposition of NH_4NO_3 and $NaNO_3$ starts at about 220 ^{0}C and 605 ^{0}C, respectively (Fig. 5). In that way, when using samples of 5-10 mg. the content of the oxidisers was determined inside the 3 % error.

In the case of HMX/RDX mixtures the melting of RDX overlaps with HMX phase transition, as well as with the decomposition process, which makes questionable the reliability of the quantitative analysis. The shape of DSC and TGA curves, i.e. the degree of overlapping depends on HMX/RDX ratio.

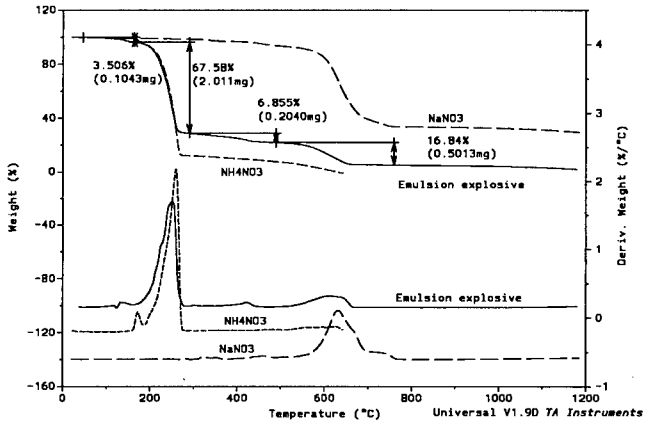

Figure 5. TGA and DTGA curves of an emulsion explosive based on NH_4NO_3 and $NaNO_3$

2.2. The determination of the phlegmatiser in high explosives

The compounds used as the phlegmatisers melt far bellow the melting or the decomposition of high explosives such as RDX, HMX, pentrit etc. This is illustrated in Fig. 6 where DSC curves of phlegmatised RDX and wax phlegmatiser are shown.

Since the melting of wax does not overlap with any other process taking place in the phlegmatised RDX, its quantitative analysis may be carried out in the way analogous to that described previously for TNT determination in RDX/TNT mixture. It means that the percentage of wax in phlegmatised RDX which DSC curve is given in Fig. 6, may be calculated according to the equation [2]:

$$w\%\text{Wax} = \frac{\Delta_m H_{\text{RDX phlegmatised}}}{\Delta_m H_{\text{Wax}}} \cdot 100 = \frac{6.034}{182.4} \cdot 100 = 3.3\% \qquad [2]$$

In the given example the actual wax content was 4 %, while the calculated content was 3.3 % (less than 1 % difference). In the same way the content of the phlegmatiser may be determined in other high explosives if the enthalpy and the temperature of melting of the pure phlegmatiser are known.

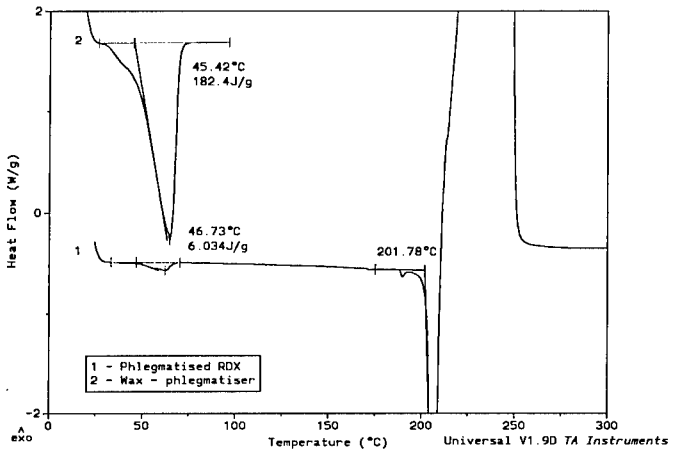

Figure 6. The DSC curves of the phlegmatised RDX and wax

2.3. The determination of the explosive purity

The melting temperature of an explosive determines its quality. It is known that small amount of an impurity, which is insoluble in the solid state but soluble in the melted state, lowers the melting temperature. Such an impurity causes the DSC melting peak to be much broader as a result of the gradual melting of an impure sample. This is clearly shown in Fig. 7 where DSC curves of crude and purified pentrit are given.

The dependence of the melting point depression (ΔT) on the molar percentage of the impurity (x_B) is given by van't Hoff equation,[1,51] which can be written it the form given by equation [3]:

$$\Delta T = (T_{m,EM} - T_{m,IET}) = \frac{RT^2_{m,EM}}{\Delta_m H_{EM}} \cdot \frac{x_B}{100} \qquad [3]$$

where: $T_{m,EM}$ – the melting temperature of the pure explosive
$T_{m,IEM}$ – the melting temperature of the impure explosive
$\Delta_m H_{EM}$ – the molar melting enthalpy of the pure explosive
x_B – the molar percentage of the impurity

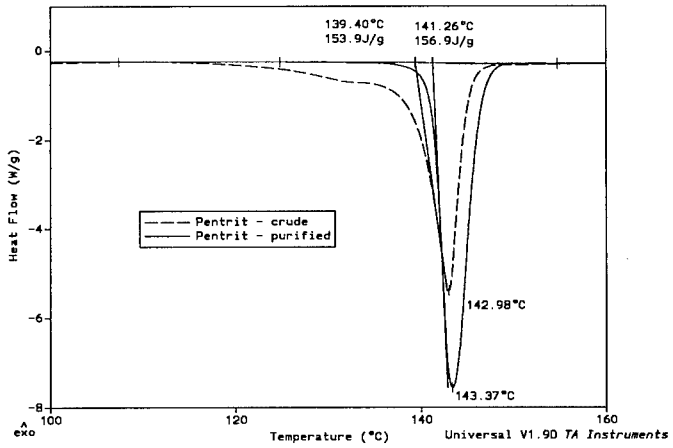

Figure 7. The DSC thermograms of the crude and purified pentrit

However, the purity could be determined more accurately from DSC melting endotherm, i.e. from its shape and from the enthalpy of the melting, according to the van't Hoff equation [4] written in the form given below:

$$T_s = T_{m,EM} - \frac{1}{F} \cdot \frac{RT^2_{m,EM}}{\Delta_m H_{EM}} \cdot x_B \qquad [4]$$

where: T_s – the temperature of the sample
F – the fraction of the molten explosive at temperature T_s

From the equation [4] the straight line should be obtained when sample temperature (T_s) is plotted versus reciprocal of the fraction melted ($1/F$), the slope being dependent upon x_B, $T_{m,ET}$, and $\Delta_m H_{EM}$. The fraction melted at a given sample temperature is obtained from the ratio of the area under the peak up to sample temperature (a), to the total peak area (A). The factors that influence the shape of the melting endotherm (e.g. pre-melting, non-equilibrium conditions, solid-solid solution, etc.) should be accounted for through an add-on correction (da) as follows:

$$F = \frac{a + da}{A + da} \qquad [5]$$

The add-on correction is obtained by the consecutively increasing its value until nice straight line $T_s = f(1/F)$ is obtained as shown in Fig. 8.

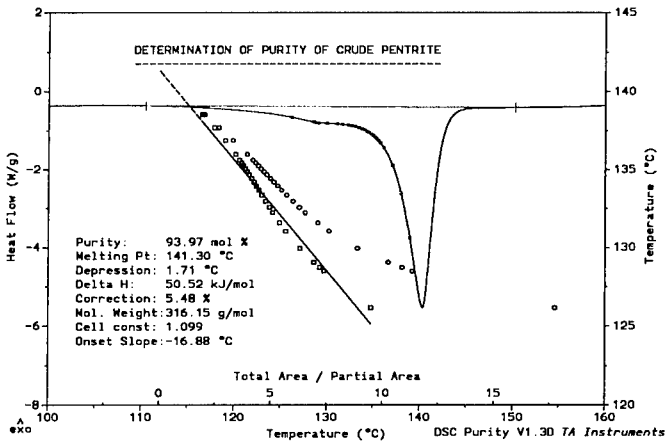

Figure 8. The determination of the purity of the crude pentrit from its DSC melting endotherm

From the data given in Figure 7 the melting point depression equals 1.9 °C, and the molar percentage of the impurity calculated according to eq. [3], taking the melting enthalpy of pure pentrit to be 50.52 kJ/mol, is 6.7 %. This is very close to the value of the molar percentage of the impurity calculated according to eq. [4] of 6.03 %.

It should be noted that the method is accurate only if purity of a substance is over 97 %.[51,1] It is also not applicable if impurity is soluble in solid state, and if explosive decomposes at its melting point or has unusually high vapour pressures.

The thermal methods would also make possible to detect, identify, and analyse certain impurities not soluble in molten state. For example, it is possible from DSC curve to detect and to analyse impurity (or additives) which melts or which has phase transition that does not overlap with melting or decomposition of the explosive. An example is given in Fig. 9.

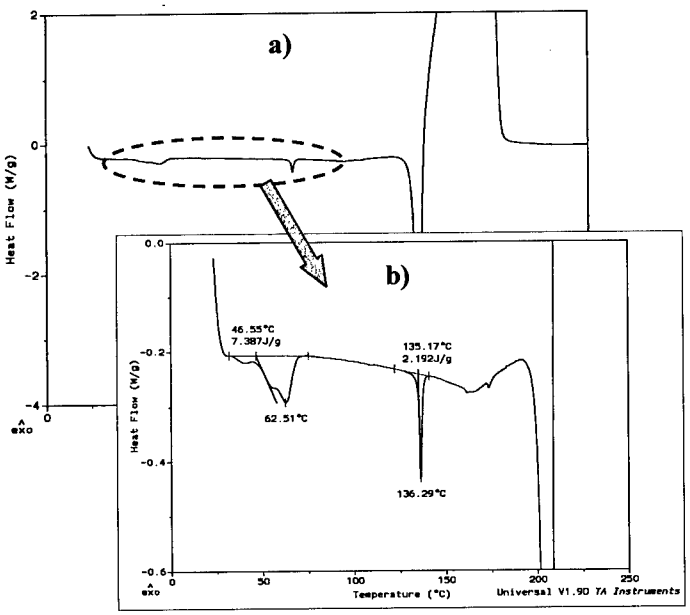

Figure 9. The DSC curves of the phlegmatised RDX contaning small amount of pentrit

After rescaling (i.e. increasing) the sensitivity of the Y-axis, two small endothermic peaks observable on the DSC curve (Fig, 9a) became much more visible (Fig. 9b). The peak at about 46 ^{0}C corresponds to the melting of the phlegmatiser, while sharp endothermic peak at about 135 ^{0}C corresponds to the melting of the pentrit. Taking into account that the enthalpy of melting of pure pentrit equals 160 J/g, it follows (from Eq. 1) that the RDX tested contains 1.4 % of the pentrit.

From the TGA curve it is possible to detect and to analyse impurities (additives) which decompose before decomposition of the explosive (e.g. volatile compounds), as well as impurities which are thermally stable and do not decompose during the decomposition of an explosive (e.g. powdered metals, sandy material, etc). An example of the determination of the water content and of the residual solvent content in nitrocellulose propellant is shown in Fig. 10.

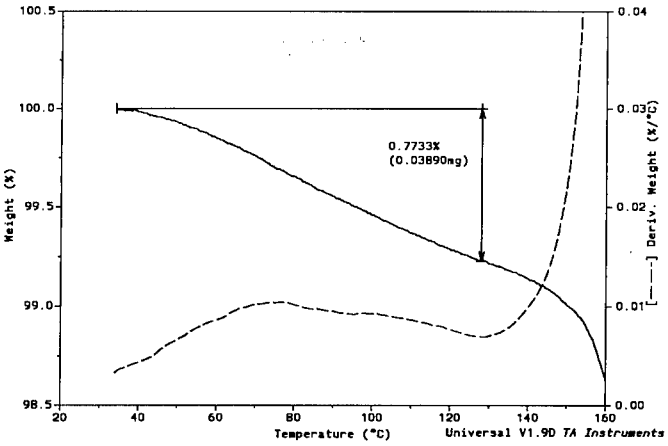

Figure 10. The determination of the water content and of the residual solvent content in the nitrocelullose propellant from TGA and DTGA curves

3. Conclusions

In this work we provide the evidence for the use of differential scanning calorimetry (DSC) and termogravimetry (TGA) in the quantitative and qualitative analysis of the explosive materials. The identification could be accomplished by comparing thermograms, while the mixture analysis could be provided either from the DSC melting endotherm or from the TGA curve. Furthermore, the purity of the explosives could be determined also based on the melting endotherm. Finally the identification and the analysis of the impurities and volatile compounds could be obtained as well.

It has to be pointed out that reliable quantitative analysis requires the precise calibration of the instruments as well as other necessary corrections.

4. References

1. P. J. Haines, Thermal methods of analysis – principles, application and problems, Blackie Academic & Proffesional, London, 1995.
2. J. Yinon, S. Zitrin, The analysis of explosives, Pergamon Press, Oxford, 1981.
3. M. J. Richardson, Standardisation and quality assurance, J. Therm. Anal. Cal. 56

(1999) 1401-1404.
4. J. C. van Miltenburg, M. A. Cuevas-Diarte, The influence of sample mass, heating rate and heat transfer coefficient on the form of DSC curve, Thermochemica Acta, 156 (1989) 291-297
5. J. R. Quintana, J. A. Ciller, F.J. Serna, Thermal behaviour of HMX/RDX mixtures, Propellants, Explos., Pyrotechn. 17 (1992) 106-109.
6. S. Zeman, Thermogravimetric analysis of some nitramines, nitrosamines and nitroesters, Thermochimica Acta 230 (1993) 191-206.
7. S. Zeman, Š. Gazda, A. Štolceva, J. Drab, New correlation of the thermogravimetric analysis data of some commercial explosives, Thermochimica Acta 230 (1993) 177-189.
8. S. Zeman, The thermoanalytical study of some aminoderivatives of 1,3,5-trinitrobenzene, Thermochimica Acta 216 (1993) 157-168.
9. R. W. Millar, N. C. Paul, D. H. Richards, P. Bunyan, P. Golding, J. A. Rpwley, "Tris-X", A new high energy polynitramine explosive: Synthesis using dinitrogen peroxide (N_2O_5) technology, characterisation, and thermal stability and hazard potential, Propellants, Explos., Pyrotechn. 18 (1993) 55-61.
10. R. L. Simpson, R. G. Garza, M. F. Foltz, D. L. Ornellas, P. A. Urtiew, Characterisation of TNAZ, Report UCRL-ID-119672, Lawrence Livermore National Laboratory, Livermore 1994.
11. B. Berger, E. L. Charsley, J. J. Rooney, S. B. Warrington, Thermal analysis studies on the zirconium/nickel alloy-potassium perchlorate-nitrcellulose pyrotechnic system, Thermochimica Acta 269/270 (1995) 687-696.
12. B. Berger, E. L. Charsley, S. B. Warrington, Characterisation of the zirconium/ potassium perchlorate/nitrcellulose pyrotechnic system by simultaneous thermogravimetry-differential thermal analysis-mass spectrometry, Propellants, Explos., Pyrotechn. 20 (1995) 266-272.
13. E. L. Charsley, S. B. Warrington, T. T. Griffiths, A. J. Brammer, J. J. Rooney, Development of thermal analysis techniques for the study of pyrotechnic systems, Proc. of 26th International Annual Conference of ICT, Karlsruhe, Germany, July 4 - 7, (Ed) Fraunhofer Institut fur Chemishe Tehnologie, 1995. pp. 23/1 – 23/14.
14. B. Berger, E. L. Charsley, J. J. Rooney, S. B. Warrington, Thermal analysis study on the zirconium-potassium perchlorate-nitrocellulose pyrotechnic system, Proc. of 26th International Annual Conference of ICT, Karlsruhe, Germany, July 4 - 7, (Ed) Fraunhofer Institut fur Chemishe Tehnologie, 1995. pp.80/1-80/14.
15. P. Simoes, P. Carvalheira, L: Dureas, A. Portugal, J. Campos, Thermal characterization of PSAN/DNAM/HTPB propellant composition, Proc. of the 22nd International Pyrotechnics Seminar, Fort Collins, 15-19 July, (Ed.) IIT Research Institut,1996, pp. 389-396.
16. A. J. Brammer, E. L. Charsley, T. T. Griffiths, J. J. Rooney, S. B. Warrington, A study of the pyrotechnic performance of the silicon-bismuth oxide system, Proc. of the 22nd International Pyrotechnics Seminar, Fort Collins, 15-19 July, (Ed.) IIT Research Institutl, 1996, pp. 447-460.
17. M. Stanković, M. Blagojević, S. Petrović, Thermal behaviour of hexogen phlegmatized with montan waxes, J. Therm. Anal. Cal. 56 (1999) 1375-1282.
18. V. Bhingarkar, H. Gandhi, P. Phawade, H. Singh, Sensitivity and thermal analysis of MTV igniter compositions, Proc. of 30th International Annual Conference of ICT,

Karlsruhe, Germany, June 29 – July 2, (Ed) Fraunhofer Institut fur Chemishe Tehnologie, 1999. pp. 72/1-72/14.
19. S. Lobbecke, A. Pfeil, H. Krause, Thermal analysis of different nitrofuroxans, Proc. of 30th International Annual Conference of ICT, Karlsruhe, Germany, June 29 – July 2, (Ed) Fraunhofer Institut fur Chemishe Tehnologie, 1999. pp. 116/1-116/12.
20. P. S. Makashir, E. M. Kurian, Spectroscopic and thermal studies on 2,4,6-trinitro toluene, J. of Thermal Analysis 55 (1) (1999) 173-185.
21. M. Rajić, M. Sućeska, Influence of ageing on nitrocelullose thermal properties and hazard potential figures-of-merit, High Temperature – High Pressure (in press).
22. D. C. Johnson, Using thermal analysis for pyrotechnic reliability predictions, Proc. of the 22nd International Pyrotechnics Seminar, Fort Collins, 15-19 July, (Ed.) IIT Research Institut, 1996, pp.227-234.
23. G. Norwitz, M. Everett, M. T. Gurbarg, Thermal and stability study of tetracene using differential scanning calorimetry, Thermochemica Acta 12 (1975) 272-232
24. X. Yi, H. Rongzu, Investigation concerning the thermal stability of HAN and HAN-based liquid propellant using DSC method, Proc. of 10th Symp. on Chem. Probl. Connected with Stabil. Explos., Margretetorp, Sweden, May 28 – June 1, 1995. pp. 339-345.
25. A. Miyake, T. Aochi, N. Oshino, Isothermal stability test of firework mixtures, Proc. of the 22nd International Pyrotechnics Seminar, Fort Collins, 15-19 July, (Ed.) IIT Research Institut, 1996, pp. 325-336.
26. G. Om Reddy, A. S. Srinvasa Rao, Stability study on pentaerythritol tetranitrate, , Propellants, Explos., Pyrotechn. 17 (1992) 307-312
27. Standard test method for assessing the thermal stability of chemicals by methods of differential thermal analysis, ASTM standard E 537 – 86, 1992.
28. R. N. Rogers, Differential scanning calorimetric determination of kinetic constants of systems that melt with decomposition, Thermochimica Acta 3 (1972) 437-447.
29. R. N. Rogers, Simplified determination of rate constants by scanning calorimetry, Analytical Chemistry 44 (7) (1972) 1336-1340.
30. R. Shaw, F. E. Walker, Estimated kinetics and thermochemistry of some initial unimolecular reactions in the thermal decomposition of 1,3,5,7-tetranitro-1,3,5,7-tetraazacyklooktane in the gas phase, The Journal of Physical Chemistry 81 (25) (1977) 2572-2576.
31. K. Kishore, Thermal decomposition studies on hexahydro-1,3,5-trinitro-s-triazine (RDX) by differential scanning calorimetry, Propellants and Explos. 2 (1977) 78-81.
32. J. W. Beckmann, J. S. Wilkes, R. R. McGuire, 2,4,6-trinitrotoluene thermal decomposition: Kinetic parameters determination by the isothermal differential scanning technique, Thermochemica Acta 19 (1977) 111-118.
33. J. Isler, D. Kayser, Correlation between kinetic properties and self-ignition of nitrocelulose, Proc. of the 6th Symp. Chem. Probl. Connected with Stabil., Kungalav, Sweden, 1982, pp. 217-237
34. Y. Oyumi, Melt phase decomposition of RDX and two nitrosamine derivatives, Propellants, Explos., Pyrotechn. 13 (1988) 42-47.
35. P. G. Laye, Kinetics by thermal analysis, Proc. of the 9th Symp. Chem. probl. Connected with Stabil. Explos. Margretetorp, Sweden, August 23 - 27, 1992. pp. 51-
36. C.C. Huang, M.D. Ger, S. I. Cheng, Study on thermal decomposition of pentolites by modified vacuum stability aparatus and differential scanning calorimetry,

Propellants, Explos., Pyrotechn. 17 (1992) 254-259.
37. H. Maruizumi, D. Fukuma, K. Shirota, N. Kubota, Thermal decomposition of RDX composite propellants, Propellants, Explos., Pyrotechn. 7 (1992) 40-45.
38. Y. Oyumi, K. Inokami, K. Yamazaki, K. Matsumoto, Thermal decomposition of BAMO/HMX propellants, Propellants, Explos., Pyrotechn. 18 (1993) 62-68.
39. G. Hussain, G. W. Rees, Thermal decomposition of RDX and mixtures, Fuel 74 (2) (1995) 273-277.
40. G. Hussain, G. W. Rees, Thermal decomposition of HMX and mixtures, , Propellants, Explos., Pyrotechn. 20 (1995) 74-78.
41. C. C. Huang, W. H. Hwu, C. S. Cheng, I. N. Shyy, K. K. Yang, Study of thermal decomposition of composite propellants containing PCP polymer or PCP-HTPB copolymer as a binder, Propellants, Explos., Pyrotechn. 20 (1995) 36-40.
42. G. Hussain, G. W. Rees, Thermal decomposition of RDX and mixtures, Propellants, Explos., Pyrotechn. 20 (1995) 74-78.
43. M. Rajić, M. Sućeska, Kinetika termičke razgradnje amonijevog perklorata u temperaturnom području 240-250 °C, Kem. Ind. 47(12) (1998) 437-441.
44. P. N. Simoes, L. M. Pedroso, A. A. Portugal, J. M. Campos, Study of the decomposition of phase stabilised ammonium nitrate (PSAN) by simultaneous thermal analysis – determination of kinetic parameters, Thermochimica Acta 319 (1-2) (1998) 55-65.
45. M. Stanković, V. Kapor, S. Petrović, The thermal decomposition of triple-base propellants, J. Therm. Anal. Cal. 56 (1999) 1383-1388.
46. A. Ksiazczak, T. Ksiazczak, Thermal decomposition of energetic materials, Proc. of the 2nd seminar "New trends in research of energetic materials", Pardubice, Czech Republik, April 14 - 15, University of Pardubice, 1999, pp. 32-42
47. M. Krupka, Thermal analysis of some selected organic nitrocompounds, Proc. of the 2nd seminar "New trends in research of energetic materials", Pardubice, Czech Republik, April 14 - 15, University of Pardubice, 1999, pp. 70-74.
48. G. Krien, Thermoanalytical determination of tetrazene in primer mixtures, Propellants, Explos., Pyrotechn. 4 (1979) 53-5.
49. M. Sućeska, M. Rajić, Termoanalitičko određivanje trinitrotoluena u smjesi s heksogenom, Kem. Ind. 47 (1) (1998) 11-16.
50. M. Sućeska, M. Rajić, M. Čuljak, Characterisation and quantitative determination of trinitrotoluene in mixtures with hexogen by differential scanning calorimetry, Proc. of 29th Int. Annual Conference of ICT, June 30 – July 3, Karlsruhe, Germany, 1998, pp. 144/1-144/12.
51. C. Plato, A. R. Glasgow, Differential scanning calorimetry as a general method for determining the purity and heat of fusion of high-purity organic chemicals. Application to 95 compounds, Analytical Chemistry 41 (1969) 330-336.
52. Standard test method for determining specificc heats capacity by differential scanning calorimetry, ASTM standard E 1269, 1994.
53. Z. R. Liu, Y. H. Shao, C. M. Yin, Y. H. Kong, Measurement of the eutectic composition and temperature of energetic materials. 1. The phase diagram of binary systems, Thermochimica Acta 250 (1) (1995) 65-76.
54. W.P.C de Klerk, M. A. Schrader, A.C. van der Steen, Compatibility testing of energetic materials, which technique?, J. Therm. Anal. Cal. 56 (1999) 1223-1331.

EFFECT OF SOME BURNING CATALYST ON THE THERMAL DECOMPOSITION BEHAVIOUR OF AN IGNITER COMPOSITION

M.A.BENMAHAMED, A.MOULOUD & N.IKENE
BP 17 EMP (ENITA), Bordj-El-Bahri, Algiers, ALGERIA

ABSTRACT

A large number of pyrotechnical compositions with varying characteristics are in use today. They have usually consisted of a rapid burning mixture of powdered fuel and oxidant, which is compressed and formed into the desired shape. The combustion characteristics of the material are highly dependent upon the conditions under which it's produced. Such factors as particle size and distribution, purity and mixing of reagents, and also the addition of metallic oxides, in very small quantity, can all have a significant effect on the properties of the material.

These metal oxide additives are known as burning catalyst and have probably a real effect on the thermal decomposition behaviour of powder pyrotechnics.

Therefore we have chosen the most common of them, as copper chromite ($Cu_2Cr_2O_5$), ferric oxide (Fe_2O_3) and ferrocen ($C_{10}H_{10}Fe$), then we have studied their possible catalytic effect on the decomposition of the selected igniter composition: B/KNO_3.

On the other hand, we have determined the thermal properties and kinetic parameters of these mixtures from Kissinger's method. The analyses were conducted employing thermoanalytical techniques as DSC.

The interest to B/KNO_3 thermal decomposition and combustion study is provoked by large pyrotechnic composition applications as an igniter for solid propellants.

So it's very important to find out this thermal decomposition mechanism as well as the kinetic characteristics of the same process.

Each of the various pyrotechnic compositions were prepared in a standard way by repetitive dry mix sieving to produce homogeneous blends of the ingredients.

The thermal properties measurements of metal oxide additives content B/KNO_3 mixtures were evaluated using a Perkin Elmer DSC 7 Differential Scanning Calorimeter operating in the non isothermal mode.

INTRODUCTION

Ignition of solid propellants stills an important problem in rocketry.
It has been investigated extensively both experimentally and theoretically.
However, the mechanism by which ignition occurs is not fully understood and seems to be more complex.
It is known that solid propellant ignition consists of a series of complex rapid events, which start on receipt of a signal (usually electric) and include heat generation, transfer of the heat from the igniter to the motor grain surface, spreading the flame over the entire burning surface area, filling the chamber free volume with gas, and elevating the chamber pressure. The igniter in a solid rocket motor generates the heat and gas required for motor ignition [1].

Ignitability of a propellant is affected by many factors, including the propellant formulation, the initial temperature of the propellant grain surface, surrounding pressure, the mode of heat transfer, grain surface roughness, the age of the propellant and the igniter composition formulation, with its characteristics.
There have been a large variety of different igniter propellants and their developments have been largely empirical.
The interest to B/KNO_3 composition, its thermal decomposition and combustion study, is provoked by its large application as an igniter for solid propellants.
To provide better understanding of this composition's mechanism and the influence of the add of burning catalyst and how they act, it's very important to find out the thermal behaviour as well as kinetic characteristics. For these purposes, several investigative techniques have been used; we have chosen the most interested of them, the DSC analysis [2], [3].
Therefore, the objective of this work is to study the possible catalytic effect of burning additives such as copper chromite, ferric oxide and ferrocen on the decomposition of B/KNO_3 composition by means of a DSC method.

EXPERIMENTAL

Sample preparation

In order to ignite the ignition unit of a solid propellant motor a multistage igniter charge is required. The main one must trigger a reliable ignition of the propellant surfaces with the shortest possible ignition delays.

B/KNO_3 in the ratio of 30/70 by weight, was a reference composition, which has been used as an igniter in various applications for propellants [4].

However, the ingredients used in the present study are amorphous boron (Fluka AG, Switzerland, with a purity of 95-97 %, and less than 50 microns of nominal size), potassium nitrate (Fluka AG, more than 99.0 % in purity, and less than 50 microns of particle size) and the three studied burning additives as:

Additive	**Molecular formula (molecular weight)**	**Purity %**	**Particle size μ**	**Origin**
Copper chromite	$Cu_2Cr_2O_5$ (311.08)	>98	Pulverulent	Fluka, CH
Ferric oxide	Fe_2O_3 (159.69)	97	Pulverulent	Fluka, CH
Ferrocen	$C_{10}H_{10}Fe$ (186.04)	97	Pulverulent	Riedel-de Haen, D

All the ingredients are passed through a 50μ sieve then weighting in the ratio of 68.5/30/1.5 (Oxidizer/fuel/burning catalyst).

For the mixing operation, the material is passed four times through a small sieve of 0.5 mm, then it's mixed for two hours in a horizontal mixer to produce homogeneous blends of the ingredients.

DSC measurements

Thermochemical measurements were obtained using a Perkin Elmer DSC7 Differential Scanning Calorimeter operating in the non isothermal mode with an appropriate thermal analysis software packages [5] which allows to perform specific tasks.

The experimental conditions are as follow:

- variety of heating rates: from 1.3 to 20°C/mn,
- sample mass: 0.6 – 1.6 mg,
- sample cell: alumina sample pans and covers (pans are crimped but not hermetically sealed),
- atmosphere: nitrogen purge gas with a flow rate of 20 cc/mn (1.4 bars),
- temperature range: all the samples are analyzed from 100 °C to 600 °C.

Meanwhile, kinetic parameters were determined from Kissinger's treatment of DSC data.

Results and Discussions

Thermal decomposition behaviours of the four igniter compositions, as measured by DSC, at heating rates from 1.3 to 20 °C/mn, are depicted in figures 1,2,3 and 4.

The characteristic peak temperatures and reaction heats of the mixtures are listed in table 1.

Table 1: Characteristic peak temperatures and reaction heats of the mixtures

Designation	Igniter composition %, in weight	Heating rate °C/mn (mass, mg)	Peak temperatures °C	Reaction heats J/g
A	KNO_3 (70.0) B (30.0)	1.3 (1.2)	466.2	641.04
		2.5 (1.4)	499.8	700.33
		5.0 (1.6)	507.5	1401.59
		10.0 (1.4)	513.9	2072.15
		20.0 (0.6)	533.8	2138.38
B	KNO_3 (68.5) B (30.0) $Cu_2Cr_2O_5$ (1.5)	1.3 (1.0)	490.7	784.00
		2.5 (1.1)	497.1	1463.09
		5.0 (1.4)	506.9	1593.34
		10.0 (0.8)	517.9	2140.10
		20.0 (0.7)	531.4	2181.30
C	KNO_3 (68.5) B (30.0) Fe_2O_3 (1.5)	1.3 (1.3)	459.2	914.98
		2.5 (1.3)	478.8	1546.94
		5.0 (1.3)	493.6	1767.31
		10.0 (0.9)	497.0	2726.00
		20.0 (0.7)	500.0	3051.79
D	KNO_3 (68.5) B (30.0) $C_{10}H_{10}Fe$ (1.5)	1.3 (1.6)	464.2	1310.78
		2.5 (1.1)	471.9	1368.82
		5.0 (1.3)	485.3	1612.23
		10.0 (1.1)	494.8	2141.82
		20.0 (0.7)	506.2	2667.98

The determination of the Arrhenius kinetic constants of the compositions is based on the Kissinger method, which has shown that the decomposition peak temperature, obtained by DSC, is dependent on the heating rate, according to the expression (1):

$$\frac{d\left[\ln\left(\beta/T_m^2\right)\right]}{d\left(1/T_m\right)} = -\frac{E_a}{R} \text{ [6]} \qquad (1)$$

and assumes that the maximum of the reaction rate corresponds to the top of the peaks. Indeed, equation (1) makes possible the determination of the activation energy, E_a, for a sample decomposition reaction regardless of reaction order by making DSC scanning analysis at different heating rates, from 1.3 to 20 °C/mn.

The main results of the studied compositions are summarized in table 2.

Table 2: Arrhenius kinetic constants using Kissinger method

Designation	Heating rate β °C/mn	T_m °C	- Ln (β/T^2_m)	1000/T_m K^{-1}	E_a kcal/mol
A	1.3	466.2	12.027	1.353	43.953
	2.5	499.8	11.512	1.294	
	5.0	507.5	10.849	1.281	
	10.0	513.9	10.181	1.271	
	20.0	533.8	9.564	1.239	
B	1.3	490.7	12.129	1.309	76.295
	2.5	497.1	11.501	1.298	
	5.0	506.9	10.847	1.282	
	10.0	517.9	10.197	1.264	
	20.0	531.4	9.555	1.243	
C	1.3	459.2	11.997	1.366	61.642
	2.5	478.8	11.426	1.330	
	5.0	493.6	10.794	1.304	
	10.0	497.0	10.114	1.299	
	20.0	500.0	9.433	1.294	
D	1.3	464.2	12.018	1.356	68.756
	2.5	471.9	11.397	1.342	
	5.0	485.3	10.760	1.319	
	10.0	494.8	10.105	1.302	
	20.0	506.2	9.458	1.283	

However, in all the thermograms, for each composition and for the five heating rates, the following can be generally observed : over the temperature range 370 – 670 K, it consists of two main features, an endothermic peak around 405 K corresponding to a crystallographic transition of potassium nitrate, and a second endothermic peak around 605 K, which corresponds to the potassium nitrate melting point.

Over the temperature range 670 – 870 K, we can observe that the thermal decomposition begins around 730 K and takes off near 820 K with an exothermic heat release; the values of the corresponding temperatures transition depend on the heating rate and on the composition.

There are two peaks in this section of the thermogram, a low temperature peak and a high temperature one which dominating the trace describing the exotherm in these cases.

As can be seen in figures 1, 2, 3 and 4, it's apparent that there exists a correlation between the maximum exothermic decomposition peak temperature and the presence of the burning catalyst. The peak temperature has a tendency to shift to a lower temperature. Since DSC measures the change in the heat content of reactions occurring in the condensed phase as well as in the gas phase nearer to the surface of the sample, it can be expected that the reactions occurring in close vicinity of the sample are responsible for the mode of the reaction process variation. Catalytic action at the B/KNO_3 interfacial surfaces might be exothermic, accelerate the condensed phase decomposition of the ingredients and alter the decomposition vapours, probably into a more reactive species [7].

As a combustion mechanism, we have:

decomposition of oxidizer : $2KNO_3 \longrightarrow K_2O + N_2 + 2.5O_2$ (2)

reduction of boron : $4B + 3O_2 \longrightarrow 2B_2O_3$ (3)

It's suggested that the reaction of B/KNO_3 proceeds with slow decomposition of the oxidizer (2) with the release of oxygen which reacts with boron for the condensed phase heat release and facilitates ignition.

Reaction (2) and (3) are responsible for the exotherms in the DSC for the condensed phase heat release. This heat release is also responsible for further decomposition of the oxidizer species in the reaction zone leading to total ignition of the sample.

Something else, is that, with fine oxidizer particles, the diffusion distances for heterogeneous surface reactions are short, i.e., all oxidizer vapour is near fuel surfaces,

and all fuel vapour is near oxidizer surfaces increasing the possible role of vapour-surface oxidizer/fuel reactions.

The presence of the burning catalyst can further enhance reactions and an additional heat release in the exotherms are expected (as we can see in table 1) due to the fact that the employed additives contain metallic atoms. The action of these additives results less from the chemical reactions than from the thermal property modifications of the burning surface. These additives allow the increasing of the heat transfer caused by the fact that the diffusion flame is being held closer to the burning surface. To assure an effective action of the catalyst, they must be uniformly dispersed in the composition, otherwise we can have, as for $\beta = 1.3$ °C/mn and 10 °C/mn, the decomposition temperature with copper chromite is higher than B/KNO_3 without catalyst.

In addition, we can observe that when the heating rate β increases, this yields an increase of the decomposition peak height (it has tendency to become more and more intense) as well as an increase of the onset (the temperature at which the reaction will proceed to completion): see figure 5.

Indeed, figure 5 shows decomposition peak temperatures obtained by DSC at heating rates of 1.3 to 20 °C/mn.

However, the Arrhenius plots calculated by the method of Kissinger are shown in figure 6. The values of activation energy, with the add of burning catalyst, are around 60 – 70 kcal/mole for ferric oxide, and 70 – 80 kcal/mole for copper chromite.

CONCLUSION

This investigation has shown that, among four candidate burning catalyst materials, it seems that ferric oxide and ferrocen were the most effective ones in terms of their effect on acceleration of thermal decomposition. In one hand, they catalytically promoted the decomposition of B/KNO_3 igniter mixtures, in the other hand, they enhance exothermic reactions and help to accelerate the combustion at the burning surface, which become an increasingly important source of heat release.

REFERENCES

[1]. G. P. Sutton, Rocket Propulsion Elements, sixth edition, John Wiley & Sons, USA 1992,

[2]. W. Hemminger, G. Hohne, Calorimetry, Fundamentals and Practice, Verlag Chemie, Germany 1984,

[3]. G. Widmann, R. Riesen, Thermal Analysis, Terms, Methods, Applications, Huthig, Germany 1987,

[4]. D. J. Whelan, M. Maksacheff, The thermal decomposition of some pyrotechnic compositions as studied by Differential scanning calorimetry, Materials research laboratories, Department of Defence, Australia,

[5]. J. L. Mc Naughton, C. T. Mortimer, Differential scanning calorimeter, Perkin Elmer, USA 1975,

[6]. W. Wendlandt, Thermal Analysis, Vol.19, John Wiley & Sons, USA 1986,

[7]. E.W. Price, R. K. Sigman, Mechanism of burning rate enhancement of composite solid propellants by ferric oxide, Journal of propulsion & power, August 1997.

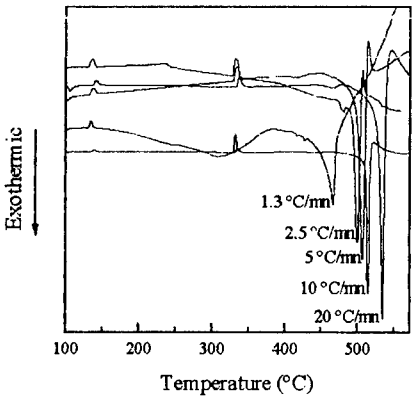

Figure 1 : No catalyst

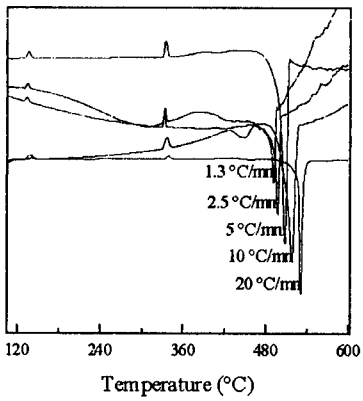

Figure 2 : Cupper chromite

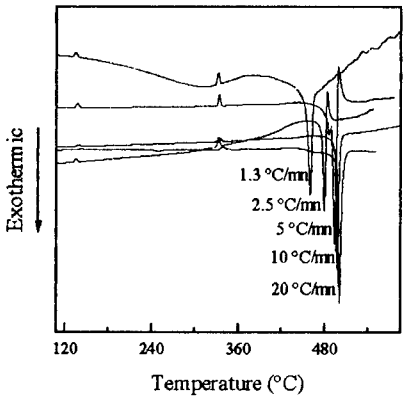

Figure 3 : Ferric oxide

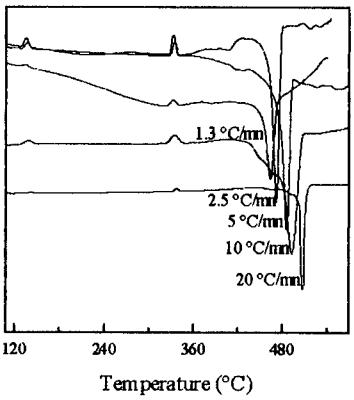

Figure 4 : Ferrocen

DSC thermograms of igniter mixtures at a variety of heating rates

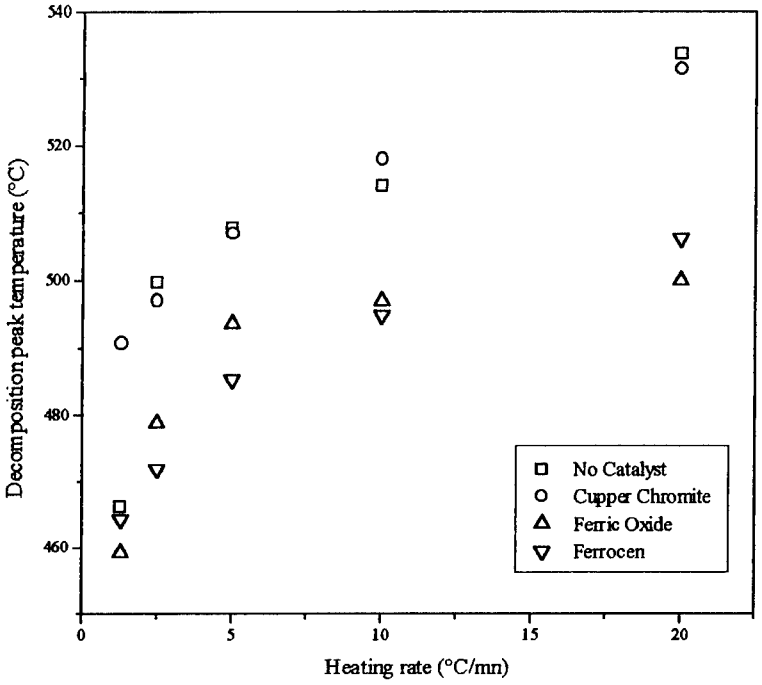

Figure 5 : DSC decomposition peak temperatures at a variety of heating rates

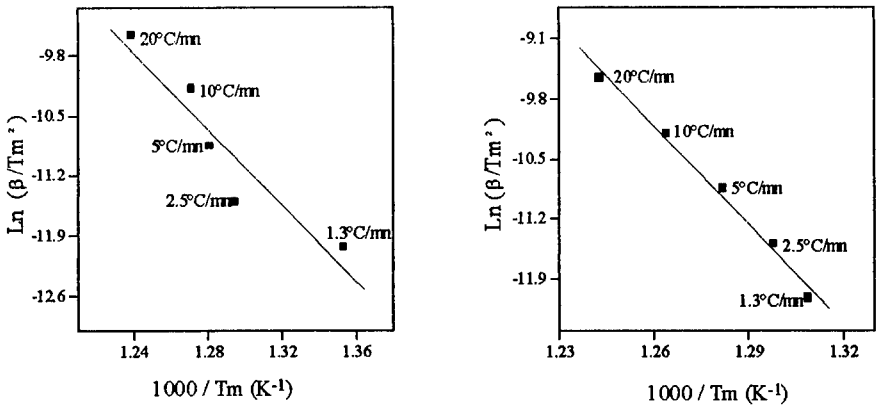

a) No Catalyst

b) Cupper Chromite

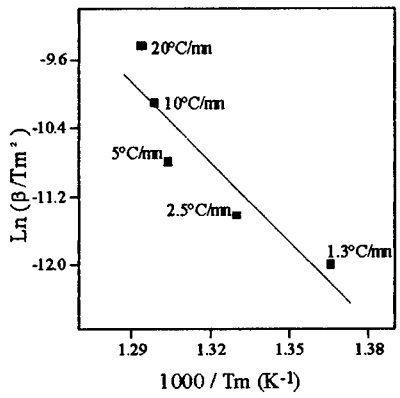

c) Ferric Oxide

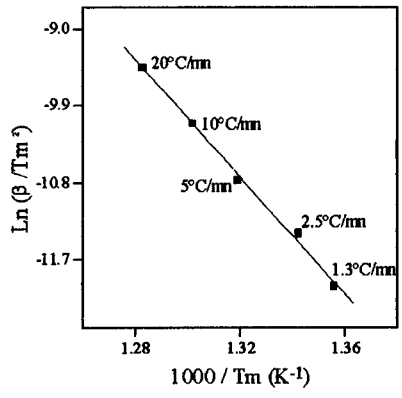

d) Ferrocen

Figure 6 : Arrhenius plots calculated by the method of Kissinger

THERMAL DECOMPOSITION OF NITRAMINE COMPOSITE SOLID PROPELLANTS (N/CSP) BASED ON POLYURETHANE BINDERS

MOHAMED A. SADEK, MOHAMED H. MOEEN, MOSTAFA A. RADWAN, AND HAMDY H. AMEEN

Egyptian Armed Forces.

ABSTRACT

Thermal decomposition of nitramine composite solid propellants (N/CSP) based on polyurethane binders was studied by differential scanning calorimetry DSC and thermogravimetric TG/DTG. DSC thermogram shows an endothermic peak at 246.8°C attributed to phase transition of Ammonium Perchlorate (AP) and sharp exothermic peak at 259.4°C. DTG thermogram shows a strong peak also at 259.4°C which reveal that complete decomposition occurs at this temperature. The activation energy "E" of decomposition was calculated by using two different techniques, TG/DTG and DSC and three different calculation methods, Ozawa, Kissinger ,and 1st order rate equation .

INTRODUCTION

The most energetic current solid propellants are composites with energetic oxidizer. Among these oxidizers, HMX is used to offer higher density, low smoke levels, high performance level, and low vulnerability propellants. HMX is introduced into the matrix of AP/CSP on the expense of small percent of AP. No studies seem to be reported in the available references concerning thermal decomposition of N/CSP.

The objective of this work is to study the thermal decomposition of N/CSP, and to determine its "E " values.

EXPERIMENTAL

N/CSP samples without metallic fuel were prepared by using Tri-modal mixture of AP having particle size 400,200 and 7-11μm (AZC ,Egypt), fine powder of HMX with average particle size 40-50μ (Rof.UK), and polyurethane fuel binder .The binder was based upon Hydroxy-terminated polybutadiene (HTPB) prepolymer crosslinked with Diisocyanate to form the urethane linkage .The ingredients were well mixed together ,poured under vacuum into the mold and cured at 55°C for 10 days.

APPARATUS AND PROCEDURE

NETZSCH model DSC-200 differential scanning calorimeter and NETZSCH model TGA-209 thermogravimetric analyzer are used. DSC-200 is calibrated using indium and zinc standards. The DSC data for N/CSP is obtained using samples of 1-2 mg weight. Heating rates of 2,5,7,10 and 15 °C /min and nitrogen gas at a rate 20ml/min are applied. TGA is recorded for samples of 2-8 mg weight using nitrogen gas at a rate of 20ml/min. Isothermal runs in TGA experiments are carried out by heating the samples to the required temperature at a heating rate of 40°C /min , then the temperature is kept constant for different periods of time.

RESULTS AND DISCUSSIONS

DSC thermogram illustrated in fig.(1) shows an endothermic peak at 246.8°C corresponding to orthorhombic - cubic phase transition of AP [1] and a strong exothermic peak at 259.4°C indicating decomposition of the sample. While in fig. (2)TG/DTG thermogram, a sharp DTG peak at 259.4°C with 96% mass loss can be observed. The two results confirm together that, complete decomposition of N/CSP takes place at 259.4°C.

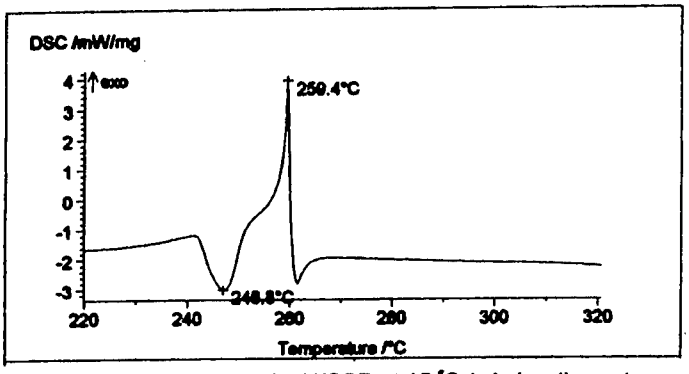

Fig 1.DSC Thermogram for N/CSP at 15 °C /min heating rate

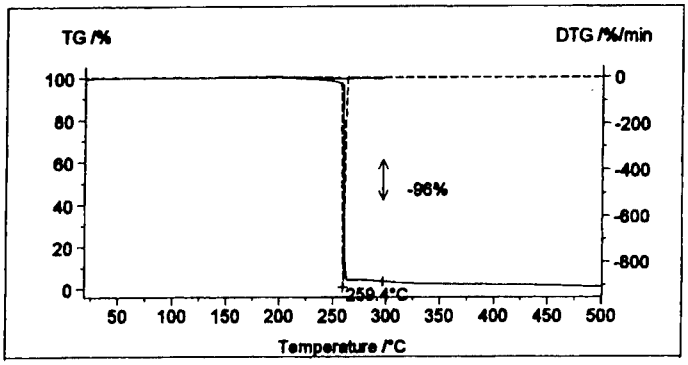

Fig 2. TG/DTG Thermogram for N/CSP at 15°C / min heating rate

Activation energy of thermal decomposition of N/CSP was determined using three different methods.

In Ozawa method[2,3], the relationship among the heating rate, temperature, and activation energy is given by equation (1).

$$\text{Log}\beta = -0.457\, E/R\, (1/T) + \text{constant} \qquad (1)$$

Thus plotting logβ against 1/T gives a straight line of slope = - 0.457 E / R, hence the activation energy could be determined.

In Kissinger method[3,4], the same relation is given by equation (2).

$$\text{Ln}\,(\beta / T^2) = -E / R\, (1/T) \qquad (2)$$

Plotting of Ln (β / T^2) against 1/T gave a straight line of slope -E/R, and the activation energy was calculated .In equation 1 and 2 , "β" is the heating rate (°C /min), "T" is the temperature(K) "E" is the activation energy (cal/mole K) and "R" is universal gas constant

(1.98 cal/mole K). Values of these parameters are illustrated in table (1) and represented graphically in fig.(3,4).

Table (1), The DSC data for N/CSP.

heating rate (β) (°C/min.)	DSC peak temp. T[K]	$(1/T).10^3$	Ln (β/T^2)	Log (β)
2	519.6	1.9245	-11.8129	0.301
5	526.9	1.8978	-10.9245	0.698
7	529.4	1.8889	-10.5975	0.845
10	531.5	1.8814	-10.2488	1
15	532.4	1.8782	-9.8467	1.176

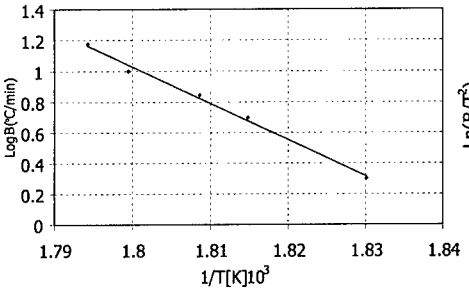

Fig 3. Ozawa plot for N/CSP from DSC data

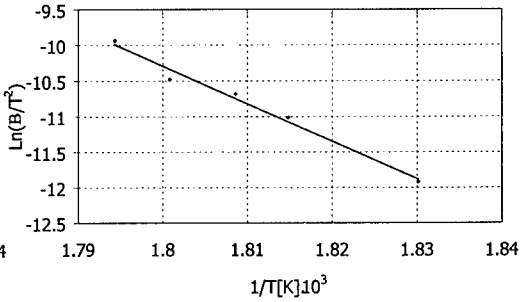

Fig 4. Kissinger plot for N/CSP from DSC data

In the third method, the decomposition reaction is considered to be a first order reaction [5],obeying the following rate equation

$$-k\,t = \mathrm{Ln}\,(C_A / C_{A^\circ}) \qquad (3)$$

Where k is the reaction rate constant, C_{A° is the initial mass of the sample in milligram and C_A is the mass of the sample at any time (t). The rate constant – k was calculated by plotting Ln (C_A /C_{A°) against t. Different k values were estimated at different temperatures. Using Arrhenius equation, the activation energy was obtained by plotting Ln k against 1/T, which give a straight line with slope [- E/R]. Data and results of the third method are illustrated in table (2) and fig.(5) and(6) . The values of activation energy determined by the three methods are given in table (3).

Table (2), Isothermal TGA data for N/CSP.

Initial mass "C_{A°"	T (K)	$(1/T).10^3$	total mass loss %	-k (slope)	$k.10^3$	Ln k
5.613	483	2.07	15.1	-0.0017	1.7	0.5306
4.100	488	2.04	14.8	-0.0029	2.9	1.0647
3.494	493	2.02	30.7	-0.0056	5.6	1.7227
7.399	498	2.00	39.0	-0.0086	8.6	2.1517
2.952	503	1.98	47.0	-0.0122	12.2	2.5014

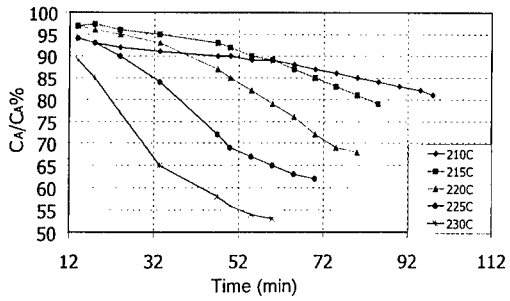

Fig 5. Mass change versus time for the isothermal run of N/CSP

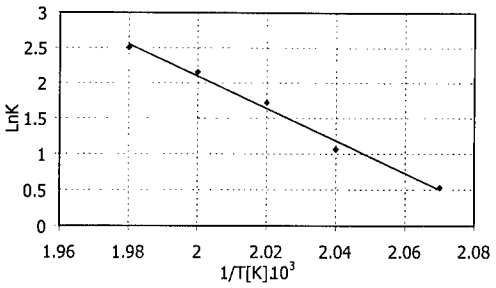

Fig 6. Arrhenius plot for N/CSP from TGA data

Table (3), "E" values calculated from DSC and TGA data.

techniques	Method	Temperature rang [°C]	E (kcal /mol)
Dynamic DSC	Ozawa	245-260	76.3
Dynamic DSC	Kissinger	245-260	78.25
Isothermal-TGA	1st order rate equation	210-230	45.12

The activation energy of thermal decomposition of N/CSP was found to be 76.3 and 78.25 kcal/mole from the DSC data (temperature range245°C -260°C) and 45.12 kcal/mole from TGA data temperature range (210°C -230°C). The difference between these values of activation energy could be attributed to the adopted techniques, as in DSC analysis the "E" value was relevant to the ignition temperature of N/CSP, while in TG analysis the 'E' value was relevant to the slow decomposition of N/CSP. For verification the obtained "E" value, Coats Redfern method (6) in case of a first order reaction given by equation (4) was applied, where "E" value was calculated from a single dynamic run of TG at 15°C /min and 20ml/min N2 flow rate as illustrated in fig.(2).

$$\text{Log}[-\text{Ln}(1-x)/T^2]=\text{Log}\,[AR/\beta E(1-2RT/E)]-E/2.3RT \qquad (4)$$

Where "X "is the fraction of the sample decompose at time "t", "β" is the heating rate (°C /min),"A" is the prexpeonanitiol factor, "T" is the temperature [°C], "E" is the activation energy and "R" is the universal gas constant (1.98 cal/mole K). The obtained data are illustrated in table (4) and represent graphically in fig. (7). The "E" value was found to be 46.5Kcol/mole and coincide well with the previous "E" value calculated from TG analysis. This result supports the previous results.

Table (4), Dynamic TGA data for N/CSP.

T[°C]	X	Log[-Ln(1-x)/T^2]	(1/T).10^3
250	0.998	-4.00	4.00
252	0.995	-4.07	3.69
254	0.991	-4.13	3.93
256	0.984	-4.19	3.90
258	0.994	-4.11	3.87
260	0.174	-5.54	3.84
262	0.060	-6.04	3.81

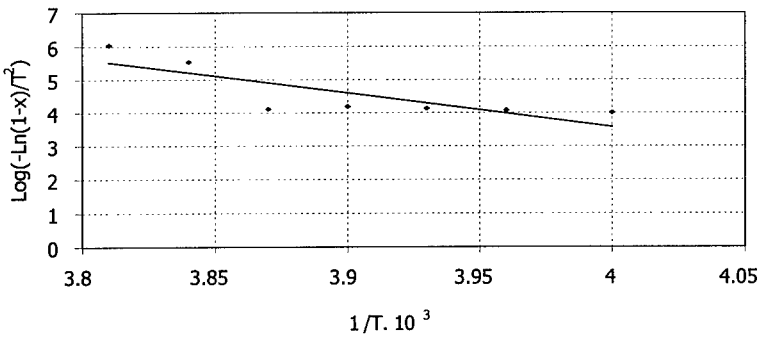

Fig 7. Coats and Redfern equation for N/CSP

CONCLUSIONS

The thermal decomposition of N/CSP was investigated by DSC and TGA techniques. The DSC thermogram shows endothermic peak at 246.8 °C attributed to orthorhombic - cubic phase transition of AP and exothermic peak at 259.4°C attributed to complete decomposition of N/CSP. This result was confirmed by sharp DTG at 259.5°C with 96% mass loss and could be considered as a finger print for N/CSP.

The activation energy of thermal decomposition of N/CSP was found to be 76.3 and 78.25 kcal/mole based on the DSC data (temperature range 245°C -260°C), 45.12 kcal/mole derived from isothermal TGA data (temperature range 210°C -230°C)and46.5kcal/mole from the dynamic TGA data(15°C /min) .In DSC analysis the "E" value was relevant to the ignition temperature of N/CSP, while in TG analysis the 'E' value was relevant to the slow decomposition of N/CSP. Therefore, to construct a burning rate model for N/CSP, the activation energy of decomposition to ignition of N/CSP could be 77.2 kcal/mole, while for establishing a chemical stability relationship (relation between storage time, temperature, and mass loss) the activation energy value of 45.12 kcal/mole could be considered.

REFERENCES

[1] T. Urbanski, Chem. and Technology of Explosives ,Vol.2,pp476-483,Pergaman Press, Oxford, New York ,Toronto,Paris,1990.
[2] E.Cohen. Nir and H. Sannier " A contribution to Study of Decomposition and Combustion of HMX, Influence of Some Additives ", Propellants, Explosives, Pyrotechnics 10: 163-169 (1985).
[3] K.N. Ninan , K. Krishnan , R. Rajeev, and G. Viswanathan " Thermoanalytical Investigations on the Effect of Atmospheric Oxygen on HTPB Resin", Propellants, Explosives ,Pyrotechnics 21: 199-202 (1996).
[4]T. Ozawa, Bull" A New Method of Analyzing Thermogravimetreic Data " Chem .Soc .Japan 38,1881(1965).
[5] M.A. BenMahamed "Determination of Reaction Kinetics Data From Thermodynamic Measurements Catalyzed Composite Propellants", 29th international Annual Conference of ICT June 30- July3, 1998.
[6] M.Hemmila,I.Niemiinen,and A.Kariniiemi " Use of Kinetic DTA and TG Methods for Compatibility Tests on 2,4,6- Trinitrotoluene ", Propellants, Explosives, Pyrotechnics 11, 91-95(1986).

Decomposition of EAK /RDX /Al Intermolecular Explosive

Zhao Shengxiang Zhang Yian Hu Huanxing Lu Chunxu*

(Xi'an Modern Chemistry Research Institute Xi'an PR China 710065)

(* Nanjing University of Science and Technology Nanjing PR China 210094)

Abstract The EAk/RDX/Al intermolucular explosive consists of EAK(Nitroguanidine-Ethylenediamine Dinitrate-Ammonium Nitrate-Potassium Nitrate eutectic), RDX and aluminium.The decomposition of this composite explosive was investigated by non-isothermal DSC and the weight loss measuring under different temperatures. It indicated that the decomposition of the Al-containing explosive was affected strongly by the thermal stability of the surfactants acting as dispersing agent for RDX. When using an alky sulphate surfactant as the dispersing agent, the decomposition reaction of the Al-containing system EAK/RDX/Al was more active than that of EAK/RDX; and when using a fluoro dispersing agent or not using any surfactant, the decomposition reaction of EAK/RDX system was somewhat similar to that of EAK/RDX/Al system.

Keywords Thermal Stability Intermolecular Explosive Eutectic Al-containing explosive EAK RDX

Zhao Shengxiang
Xi'an Modern Chemistry
Research Institute
P.O.Box 18
Xi'an 710065
P.R.China

THERMOCHEMISTRY OF COMPLEX OF TRANSITIVE METALS WITH 1,5-DIAMINOTETRAZOLE AS LIGAND

T.S.Kon'kova, Yu.N.Matyushin

Semenov Institute of Chemical Physics, Russian Academy of Sciences
117977 Kosygin Str. 4, Moscow, RUSSIA
Fax: (095) 938 2156. E-mail: ynm@polymer.chph.ras.ru

V.P.Sinditskiy, M.D.Dutov, A.F.Fogelzang

Mendeleev University of Chemical Technology
125190, Miusskaya sq.,9, Moscow, RUSSIA

ABSTRACT

By the methods of IK-spectroscopy are installed that independent of deputy positions N-substituted tetrazole enters in the co-ordination by the fourth atom of nitrogen of cycle. Purpose of given study - the determination of enthalpies of formation co-ordination compounds with 1,5-diaminotetrzole (DAT) as ligand. Complex salts of transitive metals with DAT as ligand are well dissolve in water with formation in solution the kation metal, anion and DAT. In work is experimental determined enthalpies of dissolution of DAT and perchlorates Cu, Co, Zn and Cd with DAT as ligand, that has allow to get the formation enthalpies of indicated complex salts. Required for calculations the enthalpy of formation the DAT is measured by the method of the combustion calorimetry.

INTRODUCTION

The combined calorimetric methods were used for determination of the standard formation enthalpies the complex salts ofthe transitive metals with DAT as ligand by the common formula:

$[Me(DAT)_6](ClO_4)_2$, Me = Cu, Co, Zn, Cd

The method of reaction kalorimetry was used for the determination of the heats of solution reaction in water of the complex salt compounds. This method includes the finding of conditions to reactions, as a result offlowing which under investigation complex formed finished products with known enthalpies of formation or their possible was easy define by means of other reactions.A velocity of flowing a process acceptable for calorimetric measurements of the heat effect to reactions is the necessary condition of such determination.The enthalpy of combustion DAT is determined by the method of combustion calorimetry and its standard enthalpy of formation is calculated.The standard enthalpies of formation of the complex salts are determined on the grounds of received experimental data.

EXPERIMENTAL

The complex salts received in Mendeleev University of Chemical Technology by the methods [1,2] are used in this work. Enthalpies of dissolution are measured using a swinged calorimeter with a hermetic calorimetric vessel and isotermal jacket [3]. Calibration of calorimeter carried out by transmission of an electrical current through a heater, located inside of calorimetric vessel. The accuracy of working the reaction calorimeter is

checked up on the heat of dissolution KCl in water. The heat of dissolution of KCl is received equal 4190,0 ± 2,2 kcal/mol at the concentration KCl, equal 1:1100 H_2O, which will well with the recommend value 4191,2± 2,2 kcal/mol [4]. Inaccuracy here and farther is expressed in the manner of the duplicated standard deviation from the average value under the confidential interval 0,95. Calibration of calorimeter conducted an electrical current before and after the dissolution of substance. In calculations an average value of energy equivalent are used.

The substance before the dissolution placed in beforehand weighted thinwall glass ampules with the ground joint. Ampules attached to highvacuum apparatus and placed in thermostatic heater.

After drying substances under the corresponding temperature the ampules sealled fine blaze a gas burner by means of the special protector, which prevents the substance from the influence of high temperature. At the dissolution and combustion of substance weighted on weights Bunge with accuracy 2.10^{-6} г.

Enthalpy of combustion DAT defined in the automatic calorimeter with the isotermic jacket [5]. Calibration of calorimeter realized with usereference substance - benzoic acid marks "K-1". Absence of the systematic mistake in measurements is checked by the incineration of secondary standard –hippuric acid [6]. The substance is burned under the standard pressure of oxygen in the bomb $3{\cdot}10^6$ Pa . 1,0 ml water is enterred in calorimetric bomb before the experience. At the determination of value of energy of combustion took corrections account into heat effects of forming a nitric acid,the heat exchange of the calorimetric vessel isotermic jacket, the energy of combustion of auxiliary substance and the cotton thread.

The corrections for the adduction of energy of combustion tothe standard conditions are enterred at the calculation of energy of combustion [7].

The enthalpies of formation $CO_2(g)$ and $H_2O(l)$ are accepted equal -94,051 and -68,315 kcal/mol accordingly [6].

RESULTS

Known that complex salts with DAT as ligand in the water solutions are dissociated practically completely with formation in dissolve of the metals cations, anion acid and DAT already at concentrations 0,01 mol/l.

Thermochemical cycle of reactions for the determination of the standard enthalpies of formation the under investigation complex salts in general type possible to present as follows:

$$[Me(DAT)_6](ClO_4)_{2\,(cr.)} + \Delta H^{o}_{sol} \rightarrow Me^{2+}_{(aq)} + 2ClO^{-}_{4\,(aq)} + 6DAT_{(aq)} \quad (1)$$

$$DAT_{(cr.)} + \Delta H^{o}_{sol} \rightarrow DAT_{(aq)} \quad (2)$$

$$DAT\ (cr.) + \Delta H^{o}_{c} \rightarrow CO_2(g) + 2H_2O(l) + 3N_2(g) \quad (3)$$

Reaction (1) - the dissolution of the complex salts in water; reaction (2) - the dissolution DAT in water; reaction (3) - combustion DAT in the oxygen (for the determination of enthalpies of formation DAT in the standard condition).

The standard enthalpy of formation DAT ($\Delta H^{o}_{f} = 74,18 \pm 0,24$kcal/mol) is received from experimental measured enthalpies of combustion. The enthalpies of formation of the complex salts are calculated coming from equations (1)-(3) and the measured enthalpies of reactions. The standard enthalpies of formation of the under investigation complex compounds with DAT as ligand calculated according to the equation:

$$\Delta H^{o}_{f}\,[Me(DAT)_6](ClO_4)_{(cr.)} = \Delta H^{o}_{f}[Me^{2+}]_{(aq)} + 2\Delta H^{o}_{f}[ClO_4^{-}]_{(aq)} +$$

$$+ \Delta H^{o}_{f}[DAT]_{(cr.)} + \Delta H^{o}_{sol}(1) + 6\Delta H^{o}_{sol}(2) \qquad (4)$$

The calculated enthalpies of formation in the standard condition ofthe ivestigated complex salts are presented in the Table 1.

Table 1.

Thermochemical properties the investigated compounds, 298 K, kJ/mol

COMPOUNS	ΔH^{o}_{sol}	ΔH^{o}_{f}
$[Cu(DAT)_6](ClO_4)_{2(cr.)}$	41,84 ± 0,02	403,2 ± 1,5
$[Co(DAT)_6](ClO_4)_{2(cr.)}$	40,54 ± 0,04	375,4 ± 1,5
$[Zn(DAT)_6](ClO_4)_{2(cr.)}$	41,37 ± 0,04	351,5 ± 1,5
$[Cd(DAT)_6](ClO_4)_{2(cr.)}$	40,01 ± 0,06	371,3 ± 1,5
DAT	7,66 ± 0,03	74,18 ± 0,24

Required for the calculation of enthalpies of formation the ions of zinc, cadmium, honeys and cobalt are taken equal -36,61 ± 0,48 [7], -18,15 ± 0,14 [7], 15,51 ± 0,24 [7] and -13,53 ± 0,46 [8] kcal/mol accordingly. The enthalpy of formation of the perchlorate anion was determined by us andequal -30,77 ± 0,07 kcal/mol.

Thus, offered and marketed complex method of thermochemical studies allows get precizion thermochemical data on the enthalpies of formiation of the complex salts.

REFERENCES

1. Lavreneva L.G., Larionov S.V., Grankina Z.A. *Izv. Akad. Nauk SSSR, Ser. Khim.*, **1979**, N 5, 88 (in Russian).
2. Sinditskiy V.P., Sokol V.I., Fogelzang A.E. *Jurn. Neorg. Chimii*, **1987**, 32(11), 2726.
3. Matyushin Yu. N., Vorobev A. B., Konkova T. S. et al. *Pat USSR* 726442, **1980** (in Russian).
4. R.L. Montjomery. J. Chem. Thermodynamics, **1977**, 9, 915.
5. Matyushin Yu. N.; Vorobev A. B.; Konkova T. S. et al. *Pat USSR* 1221568, **1986** (in Russian).
6. Matyushin Yu. N., Konkova T. S., Titova K.V., Rosolovskiy V.Y. *Izv. Akad. Nauk SSSR, Ser. Khim.*, **1981**, 498 (in Russian).
7. Cox J. D.; Vagman D. D.; Medvedev V. A. (Eds.) *Codata Key Values for Thermodynamics*, New-York – Washington, **1989**.
8. Thermochemical constants of substances: *Reference book under the editing Glushko V.P.* Moscow, Science, 1972-1979, VI, IX.

The Thermal Decomposition of Pentaerythritoltetranitrate Studied by GCMS & FTIR

Dr K MacDonald, Explosive Technology, AWE, Aldermaston; Mr I. Belcher, Explosive Technology, AWE, Aldermaston; Dr C. Blackman, RMCS Shrivenham, Cranfield University; Dr J. Bellerby, RMCS Shrivenham, Cranfield University

Introduction

This study was set up to assess the effect of PETN age and ageing characteristics in support of explosive device life assessment and the suitability of explosive powder storage conditions. There is considerable contradiction in the literature regarding which parameters affect PETN decomposition. This programme of work was implemented as a pilot study to investigate some of these parameters.

The gaseous and solid phase thermal decomposition products of a range of pentaerythritoltetranitrate (PETN) samples at 100°C in sealed vials were investigated. The effect of headspace (the free volume available in the sample vial) and sample mass were determined. The resulting gaseous decomposition species were identified using a novel GCMS detection technique, enabling the analysis of both NO_2 and other important gaseous species such as CO_2, CO, NO & N_2O from the same injected sample. Changes in the solid phase were monitored using FTIR and confirmed by HPLC.

Experimental

Three samples of PETN stored at approximately 20°C for 2yrs, 11yrs & 31yrs were heated in sealed glass vials at 100°C for a total of four weeks. Each powder was heated in an atmosphere of air in three different physical environments comprising two different masses (1g & 0.5g) and two different vial volumes (6ml & 20ml), see Table 1. The effect of sample mass on decomposition was studied by comparing the results from 1g sample in 6ml headspace (V1) with those from a 0.5g sample in a 6ml

headspace (V2). The effect of headspace was studied by comparing the results from the 0.5g sample in 6ml headspace (V2) with 0.5g sample in a 20ml headspace (V3).

Table 1: Ageing environments for each PETN powder sample in study

Powder age/ yrs	2	2	2	11	11	11	31	31	31
Headspace/ml	6	6	20	6	6	20	6	6	20
Sample Mass/g	1	0.5	0.5	1	0.5	0.5	1	0.5	0.5
Notation	**V1a**	**V2a**	**V3a**	**V1b**	**V2b**	**V3b**	**V1c**	**V2c**	**V3c**

The gaseous decomposition products were analysed weekly by headspace GC-MS *(Dani 3950 headspace analyser fitted with a 10 µL sample loop, products separated using a Fisons GC8000 gas chromatograph fitted with a Chrompack PoraPlot Q column. Product identification via a Fisons MD800 mass spectrometer. Initially the GC oven was cryogenically maintained at –80 ℃ for 5 minutes whereupon the temperature was increased at 15 ℃/minute up to 150 ℃. The MS was set to scan mass ions from m/z 10 to m/z 50)*. A column switching technique was employed in order to analyse NO_2 as well as CO_2, CO, N_2O, NO & H_2O.

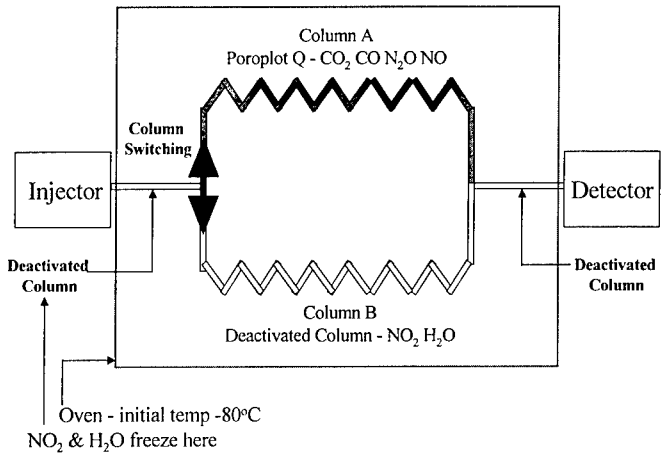

Figure 1: GC-MS experimental set up

After thermal treatment for 4 weeks the solid phase powders were analysed by FTIR *(BioRad FTS-7, 50 mg of sample ground with 300 mg of dry potassium bromide (KBr), 55 mg of the ground mixture pressed to a disk with 10 tonnes of pressure)* and HPLC *(Gilson 231 autoinjector and a Gilson 401 dilutor connected to a LDC/Milton Roy CM4000 solvent delivery system. Detection performed using a Waters 996 Photodiode Array Detector. The column used was a Waters μBondapack C18 with an internal diameter of 3.9 mm and length of 150 mm. The solvent used was 50% acetonitrile / 50% water running at 1ml/min. Processing of the resultant chromatogram was carried out at 220 nm).* The results were compared to the spectra obtained from the 'unaged' samples in order to identify any compositional changes in the solid phase of the PETN powders.

Results

The trends observed for gas evolution were consistent across all powders for all ageing environments, i.e. an increase in CO_2, CO, N_2O, NO_2 & H_2O together with significant depletion of headspace O_2. Typical results are shown in Figure 2 & 3.

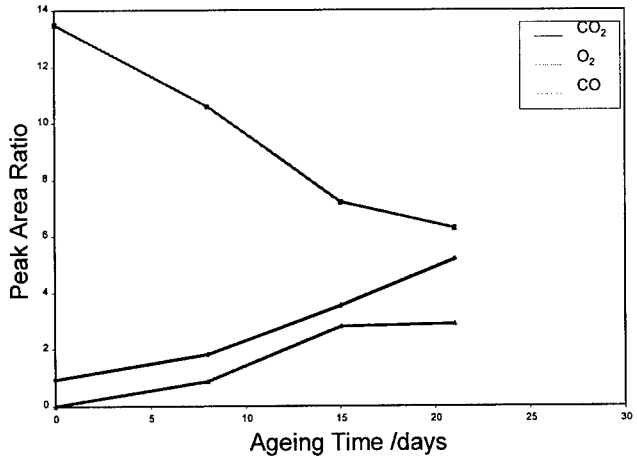

Figure 2 General trends observed for the evolution of CO_2 & CO, and the depletion of O_2 from the headspace.

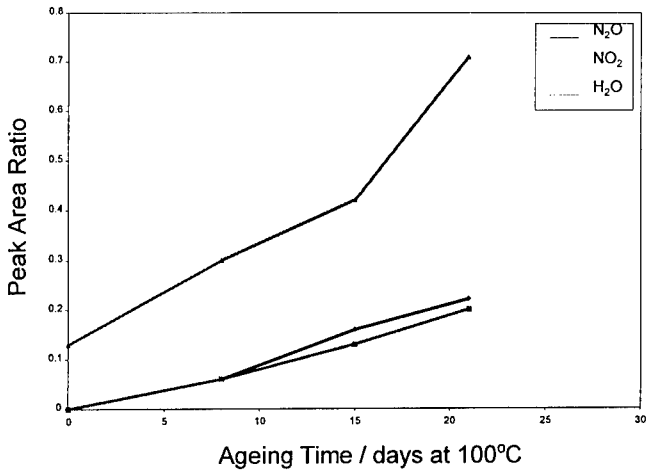

Figure 3 General trends observed for the evolution of NO_2, N_2O & H_2O.

The age related effects were evident in the gas evolution profiles of the powders with the 2yr old PETN sample evolving significantly less gas than the others, similarly the 11yr old powder produced less gas than the 31 yr old powder.

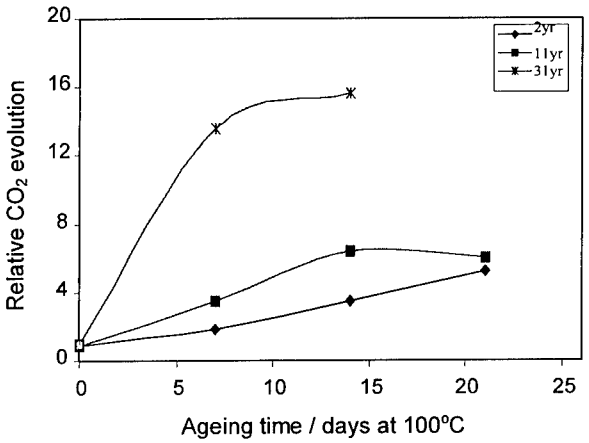

Figure 4: Trends observed for CO_2 evolution with age, 31yr > 11yr > 2yr.

The powder samples were analysed in the solid phase before and after thermal treatment, firstly to identify any differences in the chemical composition between the

three powders before thermal treatment, and secondly to identify any chemical changes that occur in the solid phase with accelerated age.

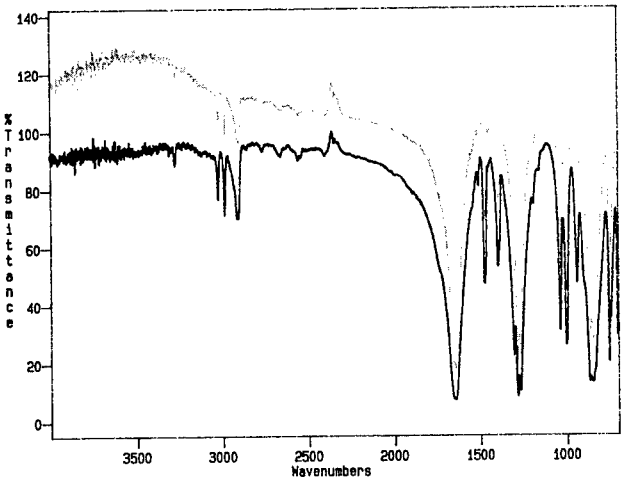

Figure 5 FTIR spectra of PETN before accelerated ageing (top/orange spectrum) & after 4 weeks ageing at 100°C (bottom/blue spectrum)

All powder samples produced spectra representative of 'pure' PETN, this was found irrespective of the original age of the powder. Similarly the spectra resulting from the thermally treated PETN suggested that there were no remaining decomposition products in the solid phase. These results were confirmed by HPLC. These results obtained from FTIR and HPLC suggest that there was no difference in the solid phase composition of the PETN samples, however the GC-MS results suggest that the powders thermally decompose at different rates.

Generally the same trends in gas evolution were observed for each of the powders, although the rates at which particular gases were evolved differed for different powders. All showed the same significant differences in gas evolution when changing the accelerated ageing environment (sample mass and vial volume). These general trends are illustrated in the Figures 6 & 7.

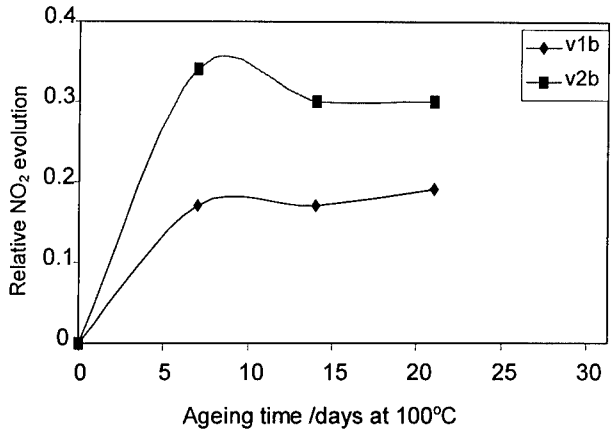

Figure 6: Effect of sample mass

It was indicated from the results for all evolved gases and all powder samples that at 100°C, smaller masses evolve more gas per unit mass. Previous work completed at AWE investigating the decomposition of PETN samples at different elevated temperatures resulted in similar observations. For a given temperature lower mass samples were shown to evolve more gas per unit mass than higher mass samples. It is suggested that this may be due to molecular diffusional issues. Further investigations are underway to support this theory.

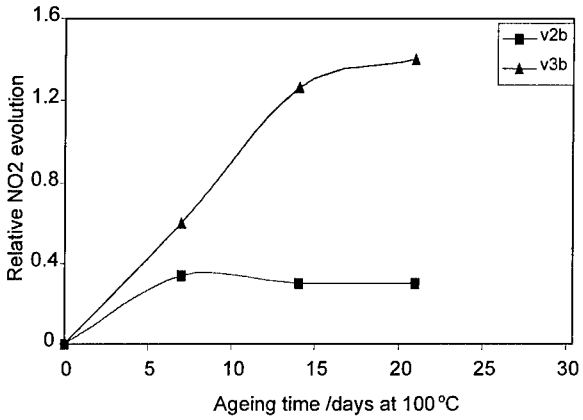

Figure 7: Effect of vial volume

It was found that a larger headspace results in significantly more gas phase decomposition products [Figure 7]. This difference was consistently greater than that observed for the mass effect [Figure 8].

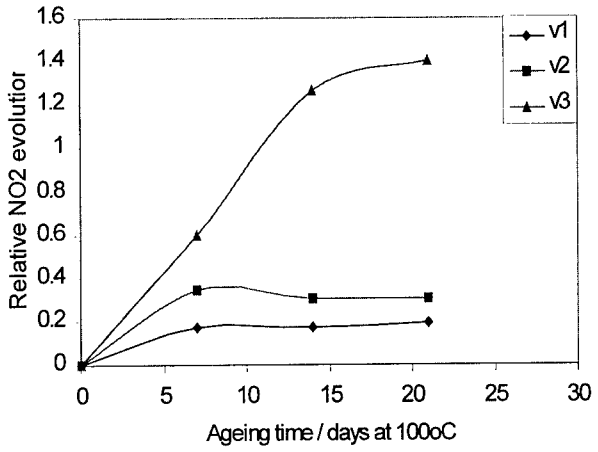

Figure 8:Effect of sample mass and vial volume

Conclusions

These results suggest that the physical experimental environment can have an effect on the extent and mechanism involved in the thermal decomposition of PETN, and have significant implications for the ageing of PETN in powder form and in explosive devices. Therefore the ageing rates and mechanisms of explosive powders may be quite different in a sealed compact with little or no free volume compared to the decomposition rate and mechanism observed for 'loose' powders.

The sensitive techniques used here for analysis of the solid phase could not distinguish between the three powder samples before heat treatment, however it was evident from the gaseous phase analysis that these powders did react differently on thermal treatment at 100°C. Further investigations are required in order to identify possible techniques of a higher sensitivity.

This study has highlighted the need for careful design of laboratory scale ageing experiments in order to represent more closely typical service environments, as well as the obvious implications for appropriate, stable storage environments.

© Crown Copyright 2000

This document is of United Kingdom origin and contains proprietary information which is the property of the Secretary of State for Defence. It is furnished in confidence and may not be copied, used or disclosed in whole or in part without the prior written consent of the Director of Contracts/Underwater Systems, Ministry of Defence, Defence Procurement Agency, Ash 2b, #88, MOD Abbey Wood, Bristol BS34 8JH, England

Thermal Analysis of Selected Pyrazines and Pyrazoles

S. Löbbecke, H. Schuppler, W. Schweikert, K. Schmid

Fraunhofer Institut für Chemische Technologie ICT,
Joseph-von-Fraunhofer Strasse 7, D-76327 Pfinztal, Germany

Introduction

In recent years nitrogen-rich substances have received an increasing interest as components for high energetic materials (explosives, propellants, gas generators, etc.). In particular, heterocyclic nitrogen-rich compounds are considered to be of interest for energetic applications because of their high molecular density, ring strain, low volatility, and mostly positive enthalpy of formation which can be significantly increased by additional substituents, for example containing nitro groups.

This paper presents first results of a thermoanalytical investigation of three new energetic heterocycles based on pyrazole and pyrazine ring structures (Fig. 1).
Since NPEX 1, NPEX 2 and NPEX 3 are considered as components for energetic applications the thermal analysis was focused on their decomposition behavior. Therefore, this work describes both the decomposition exothermicity and the time-resolved detection of thermal decomposition products. The latter allows the identification of the main decomposition pathways of the different heterocycles investigated.

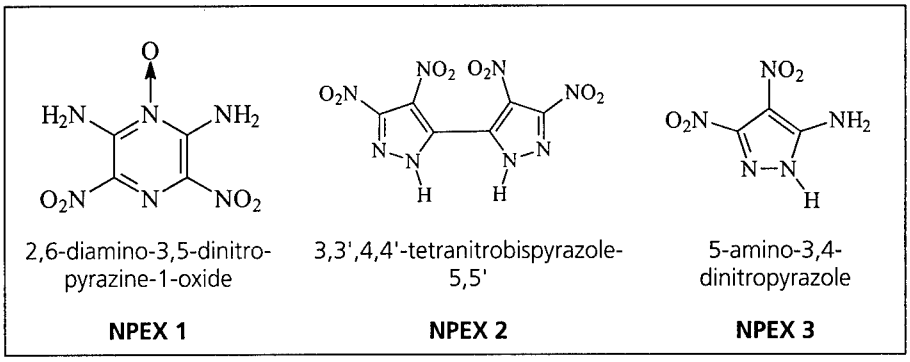

Fig. 1: energetic heterocycles investigated

Experimental

NPEX samples were supplied by the laboratories of the N.D. Zelinsky Institute of Organic Chemistry, Moscow, Russia (Prof. N. Makhova, Dr. I. Ovchinnikov).

The thermoanalytical characterization was caried out by applying DSC (TA Instruments, MDSC 2920), TGA (TA Instruments, HIRES-TGA 2950), TG-MS (Balzer Thermostar) and fast infrared spectroscopic Evolved Gas Analysis (EGA) based on a self constructed heatable optical cell adapted to a rapid scan FTIR spectrometer (Nicolet 60 SX).

Samples weighing between 0.3 mg and 3.0 mg (for EGA measurements: up to 10 mg) were analyzed under argon atmosphere by applying heating rates between 0.5 K/min and 10.0 K/min. DSC experiments were carried out in sample pans with pierced lids made of aluminum.

For statistical reasons all experiments were repeated up to five times. Characteristic temperatures of samples (e.g. onset temperature, maximum heat flow temperature) were extrapolated to a heating rate of zero.

Results

Figure 2 shows a characteristic DSC spectrum of NPEX 1 consisting of a sharp exothermicity with two heat flow maxima. The onset temperature of the exothermic decomposition is surprisingly high (300°C) and the exothermicity is spread over a relatively narrow temperature range. These features combined with a relatively high decomposition enthalpy (266.5 ± 33.5 kJ/mole) and the absence of other thermal effects like phase transitions makes NPEX 1 interesting as a new energetic compound. All its relevant thermoanalytical data are listed in Tab. 1.

Tab. 1: thermoanalytical data of NPEX 1

onset temperature of exothermic decomposition T_{onset} (HR 0)	maximum heat flow temperature T_{max1}(HR 0)	maximum heat flow temperature T_{max2} (HR 0)	decomposition enthalpy ΔH_{decomp}
297.77 ± 0.60	313.05 ± 0.50	324.71 ± 0.81	266.5 ± 33.5 kJ/mole

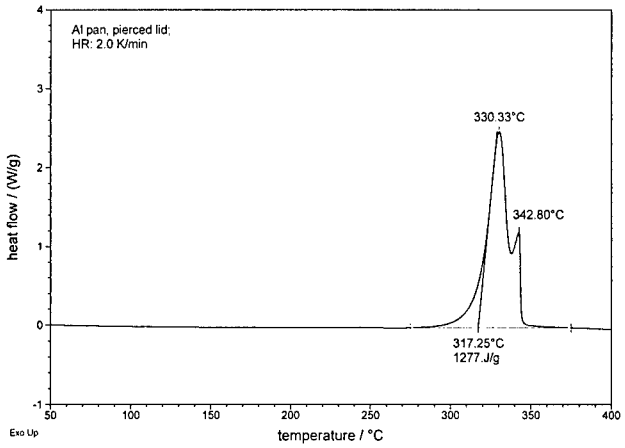

Fig. 2: DSC curve of NPEX 1 (2,6-diamino-3,5-dinitro-pyrazine-1-oxide)

In contrast to the two heat flow maxima which can be observed in DSC experiments the TGA curve of NPEX 1 (or its derivative, respectively) shows only one continual mass loss step during decomposition (Fig. 3) even if heating rate is changed. The TGA curve shows also that no residue remains after decomposition of the pyrazine oxide.

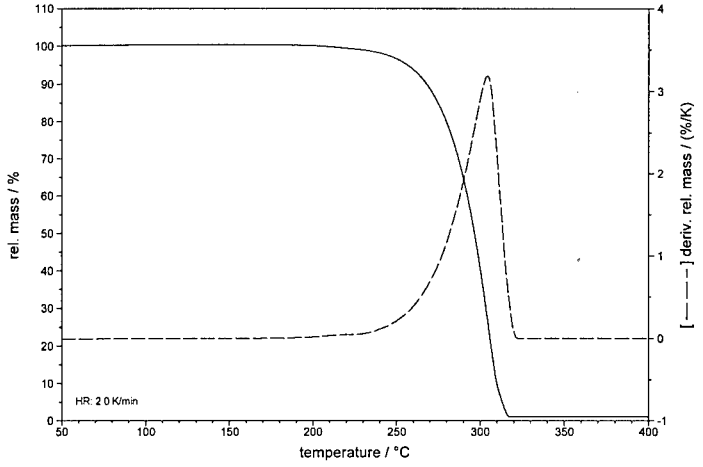

Fig. 3: TGA curve of NPEX 1 (2,6-diamino-3,5-dinitro-pyrazine-1-oxide)

IR spectroscopic EGA measurements confirm the continual degradation of NPEX 1. Figure 4 shows that the main gaseous decomposition products are CO_2, NH_3, HCN and smaller amounts of N_2O, as well. Water is not formed.

The gaseous products detected by TG-MS correspond well with those detected by EGA. Figure 5 shows the simultaneous evolution of CO_2/N_2O (44 amu), HCN (26 amu: HCN-H) and NO (30 amu). The latter is immediately formed when NO_2 is liberated from the nitro groups of the pyrazine oxide. Because of its instability at higher temperatures NO_2 can only be detected in traces by mass spectrometry (46 amu). NO which is a weak absorber in the IR spectral range can also be easier detected by mass spectrometry. Furthermore, TG-MS data show that elemental nitrogen (28 amu) is only a neglectable decomposition product of NPEX 1.

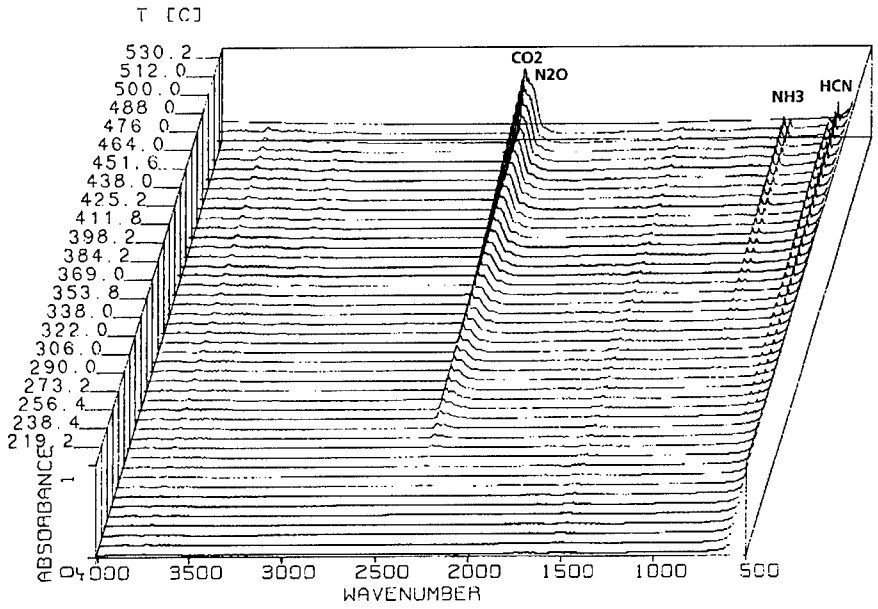

Fig. 4: EGA plot of NPEX 1 (heating rate: 5.0 K/min)

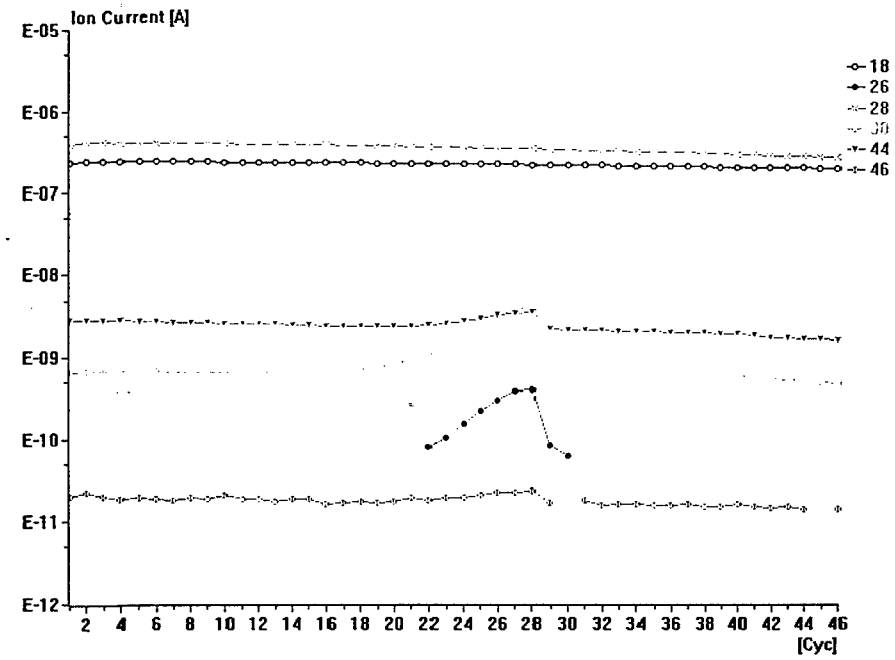

Fig. 5: mass spectrometric detection of decomposition gases from NPEX 1 during a TG-MS experiment with 10.0 K/min up to 500°C

NPEX 2 has a more complex thermal behavior. Figure 6 shows a typical DSC spectrum of NPEX 2 consisting of two main thermal effects. After the evolution of some impurities NPEX 2 melts at $\vartheta > 200°C$. The melt decomposes in two main exothermic steps with the second step being the most exothermic. Decomposition occurs in a wide temperature range and is completed at approximately 425°C. The overall decomposition enthalpy amounts to 855.7 ± 53.4 kJ/mole. Other relevant thermoanalytical data are listed in Table 2. The two-step degradation of NPEX 2 is confirmed by TGA experiments with approx. 20% mass loss in the first and approx. 60% mass loss in the second step (Fig. 7).

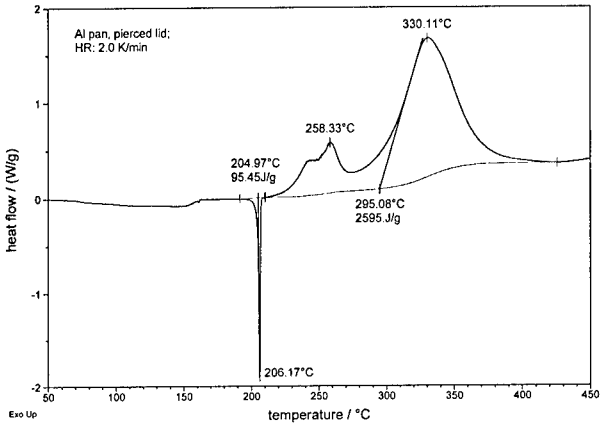

Fig. 6: DSC curve of NPEX 2 (3,3',4,4'-tetranitrobispyrazole-5,5')

Tab. 2: thermoanalytical data of NPEX 2

onset temperature of melting point T_{mp} (HR 0)	maximum heat flow temperature T_{max1}(HR 0)	maximum heat flow temperature T_{max2} (HR 0)	decomposition enthalpy ΔH_{decomp}
202.04 ± 0.18	232.85 ± 0.13	310.56 ± 0.44	855.7 ± 53.4 kJ/mole

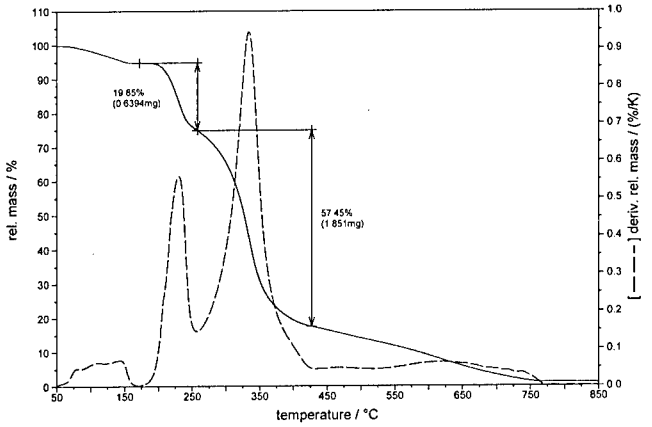

Fig. 7: TGA curve of NPEX 2 (3,3',4,4'-tetranitrobispyrazole-5,5')

Decomposition gases detected by infrared spectroscopic EGA experiments are CO_2 as the main product, small amounts of N_2O and HCN as well as CO and NH_3, particularly at higher temperatures (Fig. 8). NO_2 can be detected as an intermediate at an early stage of the decomposition (Fig. 9).

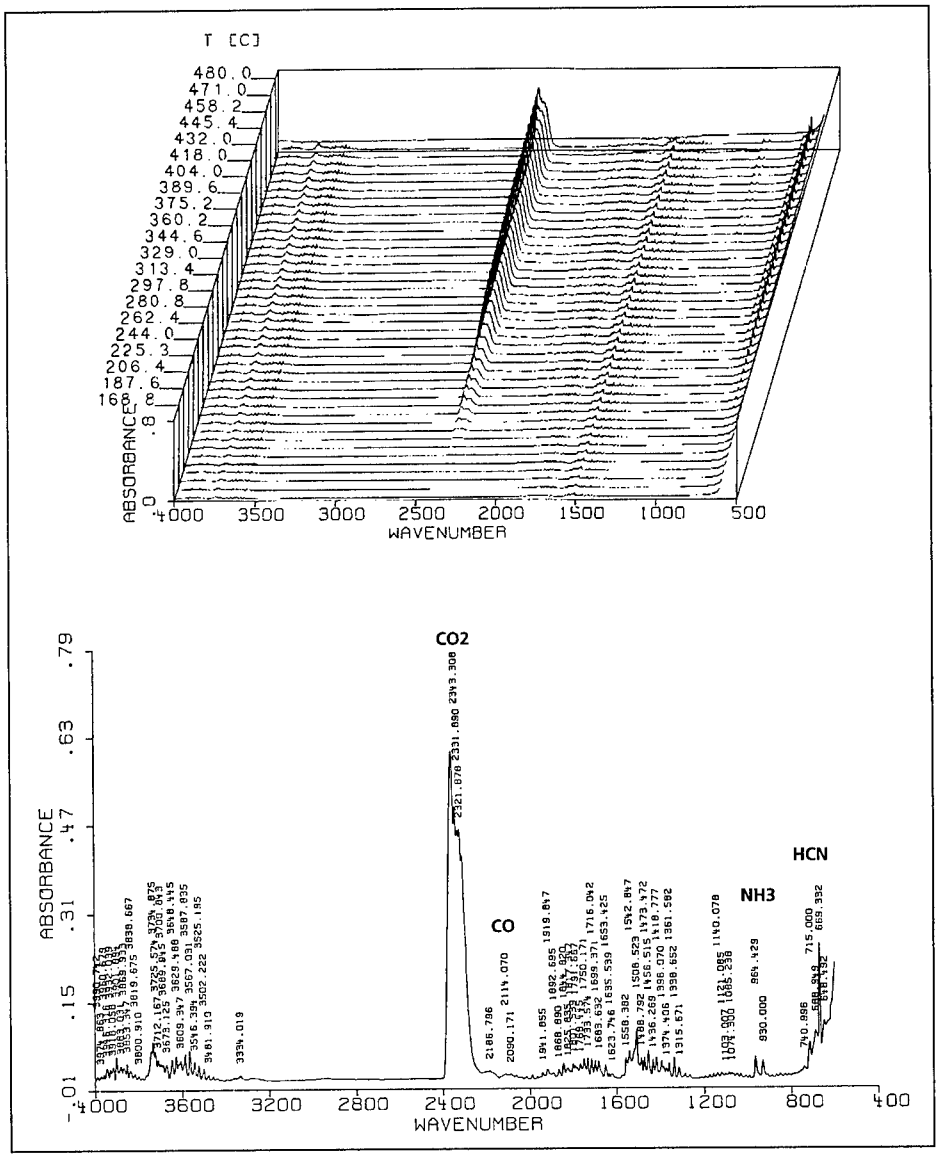

Fig. 8: EGA plot of NPEX 2 (heating rate: 5.0 K/min) with characteristic IR gas phase spectrum at 480°C

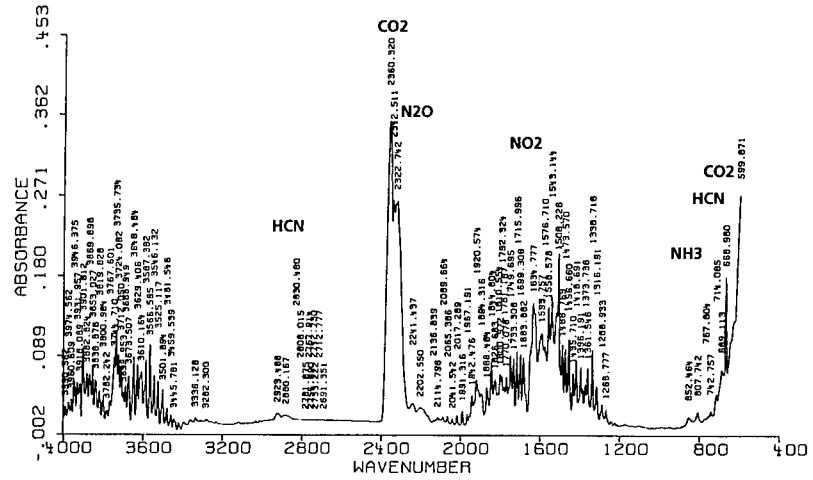

Fig. 9: gas phase spectrum detected at 270°C during EGA experiment of NPEX 2

TG-MS data confirm the multiple step decomposition showing that already the first main exothermic step in DSC consists of two overlaping effects (Fig. 10).

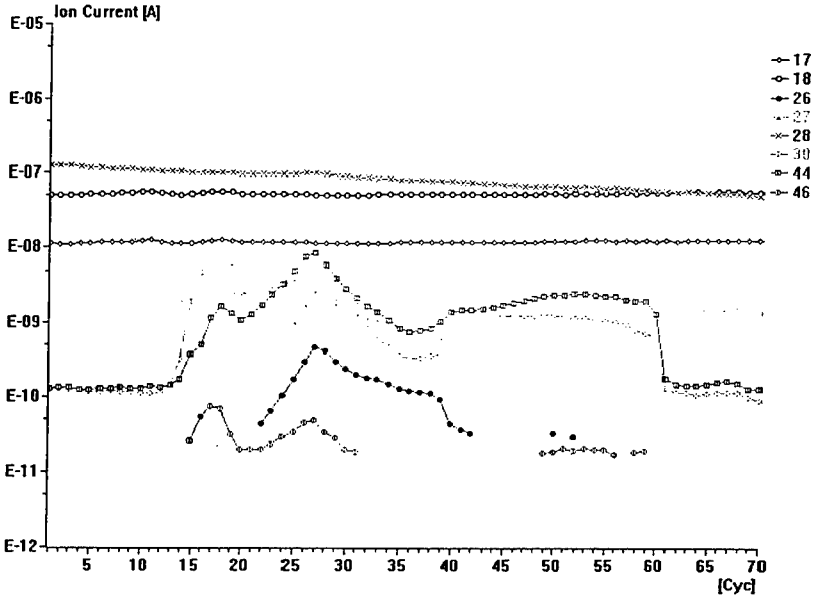

Fig. 10: mass spectrometric detection of decomposition gases from NPEX 2 during a TG-MS experiment with 10.0 K/min up to 800°C

In a first degradation step NO_2 (46 amu) is liberated from the nitro groups together with NO (30 amu), CO_2/N_2O (44 amu) and traces of ammonia (17 amu). In the second decomposition step HCN (26 and 27 amu) and traces of elemental nitrogen (28 amu) are additionally evolved indicating the quantitative degradation of the pyrazole rings. Finally, the third decomposition step is dominated by the evolution of CO_2, NO and traces of NH_3 whereas NO_2 and HCN are not detected anymore.

NPEX 3 has the sharpest exothermic decomposition behavior of the three heterocyclic compounds investigated. The DSC curve shows an intensive peak at a calculated onset temperature of 177°C spread over a narrow temperature range of approx. 30 K (Fig. 11). The decomposition enthalpy amounts to 307.1 ± 12.3 kJ/mole; other thermoanalytical data are listed in Tab. 3.

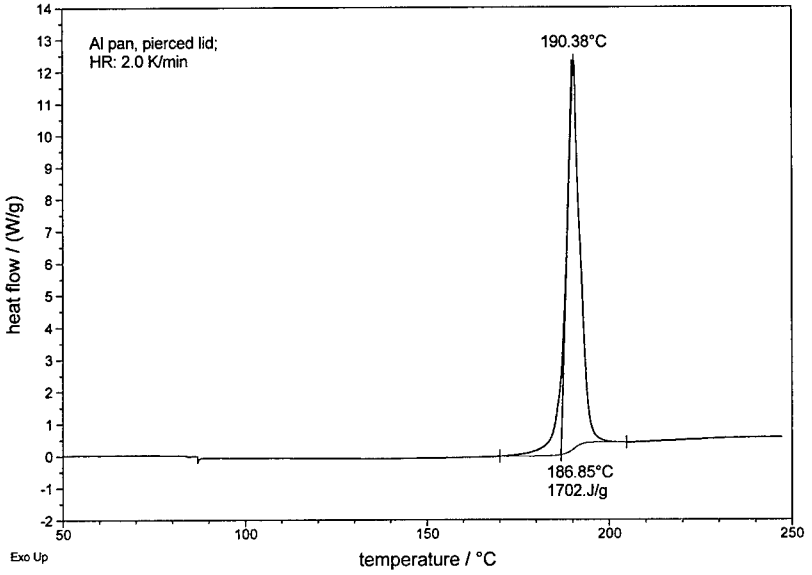

Fig. 11: DSC curve of NPEX 3 (5-amino-3,4-dinitropyrazole)

Tab. 3: thermoanalytical data of NPEX 3

onset temperature of exothermic decomposition T_{onset} (HR 0)	maximum heat flow temperature T_{max1}(HR 0)	decomposition enthalpy ΔH_{decomp}
177.01 ± 0.31	179.60 ± 0.38	307.1 ± 12.3 kJ/mole

The strong exothermic decomposition step of NPEX 3 is accompanied with a mass loss of only 41% as the TGA curve shows (Fig. 12). A complete degradation of the pyrazole occurs in two further mass loss steps distributed over a wide temperature range up to 650°C.

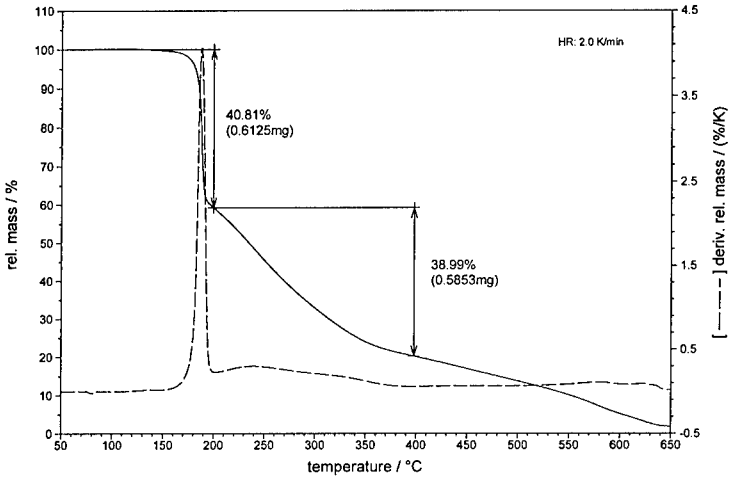

Fig. 12: TGA curve of NPEX 3 (5-amino-3,4-dinitropyrazole)

EGA experiments show that CO_2, N_2O, CO, NH_3 and HCN can be detected as gaseous decomposition products of NPEX 3 (Fig. 13). TG-MS data reveal that the first and most exothermic decomposition step is dominated by the evolution of CO_2/N_2O (44 amu), NO (30 amu) and HCN (26 and 27 amu). NH_3 (16 and 17 amu) and CO (28 amu) can be detected in this first degradation step, too (Fig. 14). During the two following broad decomposition steps of less exothermicity only CO_2 and NO are detectable.

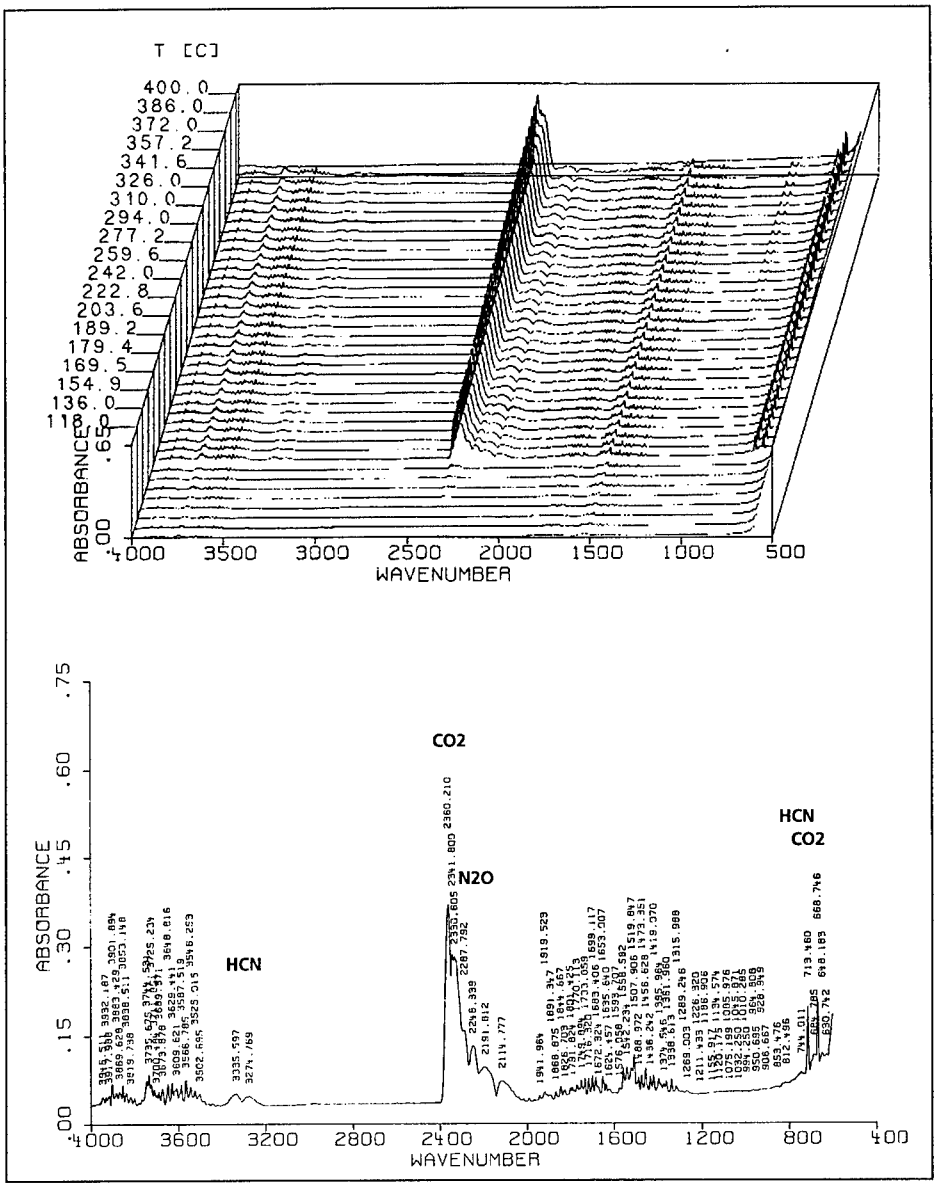

Fig. 13: EGA plot of NPEX 3 (heating rate: 5.0 K/min) with characteristic IR gas phase spectrum at 180°C

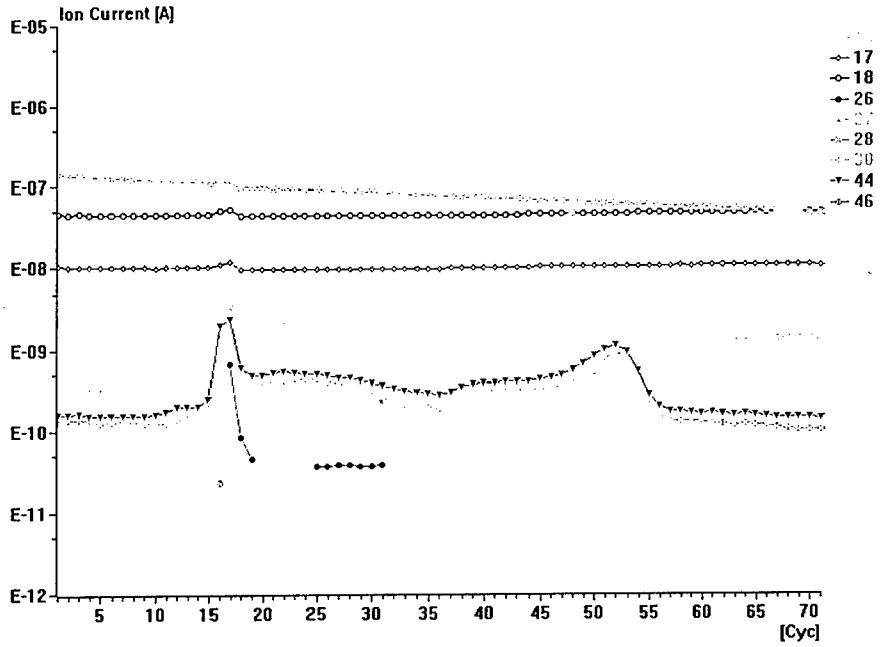

Fig. 14: mass spectrometric detection of decomposition gases from NPEX 3 during a TG-MS experiment with 10.0 K/min up to 800°C

Conclusions

First results of a thermoanalytical screening of three different heterocycles based on pyrazine and pyrazole structures have shown that their thermal decomposition behavior makes these compounds interesting as new structural components for energetic materials. Features like, partially sharp, exothermicities at high temperatures, relatively narrow decomposition intervals and no phase transitions at lower temperatures are criteria for energetic applications that are fulfilled by the NPEX compounds. The decomposition products detected during the individual degradation steps indicate the main decomposition pathways based on NO_2 cleavage, ring opening and ring destruction. By understanding the main thermal decomposition behavior of the NPEX compounds a more deliberate modification of their molecular structures will be possible giving an access to a tailoring of their thermal, respectively energetic, properties.

CHROMATOGRAPHIC DETERMINATION OF DINITRAMID ANIONS IN THE PRESENCE OF NITRATE

G. Bunte, H. Neumann, H. Krause

H. Fraunhofer-Institut für Chemische Technologie (ICT), D-76327 Pfinztal 1

Abstract

In the last years ammonium dinitramide, ADN appeared to be a promising new oxidator and a possible substitute for ammonium nitrate, AN and especially for the chlorinated oxidizer ammonium perchlorate. Among others main advantages of ADN are the higher energy input combined with a reduced pressure for decomposing. Furthermore ADN shows no phase transitions like AN.

For judging the purity of the synthesized and / or treated or aged pure or formulated ADN so far the estimated ammonium nitrate content was taken into account. AN is known as a byproduct of the ADN synthesis as well as a possible decomposition product of ADN. Under thermal treatment ADN decomposes mainly in N_2O, H_2O, NO_2 and AN which further reacts to N_2O and NH_3. So determining the nitrate contents assuming the rest is intact ADN must not lead to true values especially in cases where ADN was treated / handled at higher temperatures in open systems. Objective of this work was to develope a suitable ion chromatographic method for the direct analysis of DN^- anions.

Different ion exchanger phases were tested with organic and / or inorganic eluents. The ionic strength and flow rate of the eluent was improved to get an acceptable resolution for nitrite and nitrate combined with a short run time for the whole analysis. Detection was realized by electrical conductivity or UV absorption whereby the measurement wave lengths were optimized in order to get a small signal to noise ratio and simultaneously a suitable sensitivity especially for NO_2 and NO_3.

Under improved conditions (Ion Pac 11, 1 ml/min NaOH, 300mmol) detection limits of 0,05 to 0,01 ppm were realized for NO_3 and NO_2 respectively measured at 214 nm. Linearity range for the analysis of DN^- (285 nm) was found to be very broad (up to 700 ppm). All three anions can be analysed in one run taking maximal 30 minutes.

1. INTRODUCTION

In the last years ammonium dinitramide, ADN appeared to be a promising new oxidator /1-3/ and a possible substitute for ammonium nitrate, AN and especially for the chlorinated oxidizer ammonium perchlorate, AP. In comparison to AN there would be the advantage that ADN has a higher energy input combined with a reduced pressure for decomposing. Moreover ADN shows no phase transitions like AN meaning no critical volume / density changes under temperature stresses. Compared to AP the use of ADN-based propellants is expected to have a reduced signature plume producing no environmental hazardous halogenated gases. At the ICT several aspects concerning the potential use of ADN in new formulations are regarded. Among these the following research topics are considered:

- synthesis of ADN in a technical scale with a high purity
- recrystallisation / prilling of sperical ADN /7/
- stabilization of neat ADN
- compartibility tests for ADN and new binders and / or energetic plasticizers
- ageing / shelf life prediction of ADN-based formulation.

For judging the purity of the synthesized and / or treated pure or formulated ADN so far the estimated ammonium nitrate content was taken into account. AN is known as a by-product of the ADN synthesis as well as a possible decomposition product of ADN /6/. In former thermal decomposition studies /4-5/ it was observed that ADN's main decomposition products are N_2O, NO_2, H_2O and AN which further reacts to N_2O and NH_3 at higher temperatures. So determining the nitrate contents assuming the rest is intact ADN must not lead to true values especially in cases where ADN was treated / handled at higher temperatures in open systems. Therefore a direct characterization method for DN^- anions is needed.

2. OBJECTIVES

While the analysis of inorganic nitrate by ion chromatography is a routine method at the ICT since a long time, the possibility of a direct detection of the dinitramide ion content

was lacking. Therefore main objective of this work was to develope a suitable analytical method for the direct characterization of dinitramide anions parallel to nitrate.

3. EXPERIMENTAL

The ion chromatographic instrumentation (Alltech / GAT) used at the ICT is a so called single column ion chromatography (SCIC) technique which uses no suppressor in combination with the electrical conductivity detector. Here the ground level of the conductivity of the used eluent is compensated electronically. Alternative systems using the suppressor technique reduce the ground conductivity of the eluent chemically yielding to a greater usable detection range of the detector. For standard anions, cations and organic acids the used SCIC-system has been a well suited technique making measurements possible in the ppm or ppb level.

The used IC-system is equipped with two HPLC pumps, a column oven and a ten-port injection ventil coupled with two parallel injection loops going to two parallel IC columns. Besides the electrical conductivity detectors (one for each IC-channel) alternatively also one UV detector (Hewlett Packard) was installed instead or sometimes in series with the other. Registration and evaluation of the detector signals was performed with a FISONS chromatography software (Minichrom). Purities of the used standards and chemicals for making the eluents were p.a. or better. Different separation phases were used in this study:

- ANION-R: Wescan anion exchange material, styrene-divinylbenzene-copolymer with trimethylammonium exchanger functions, 10 µm sperical particles
- Ion Pac 11: Dionex anion exchange material, pellicular latex particles, divinylbenzene/ ethylvinylbenzene copolymer modified with alkalonol quaternary ammonium

4. RESULTS AND DISCUSSION

4.1 ANION R column with electrical conductivity detector

With a standard Wescan anion exchanger material (ANION-R) tests were made to detect dinitramide anions besides nitrate and nitrite on the same column using an electrical conductivity detector. Under standard elution conditions usually used for nitrate and nitrite no signal was detected for DN^- in a realistic analysis time. Also different ionic strengths of the eluent (p-hydroxy-benzoic acid) were tested but nothing lead to a noticable peak for

dinitramide. A possible reason for these results could be the good delocalisation of the negative charge of DN^- yielding only to a small difference in the conductivity of the pure and the dinitramide loaded eluent and moreover to a not detectable signal because of the high ground level of the eluent itself. This would be noticeable especially for high molarities of the used eluent p-hydroxybenzoic acid which should theoretically lead to a shorter retention time of the analysed anions. Otherwise the type and / or capacity of the used anion exchange material (ANION R) could be denoted as not suitable for the examination of DN^-.

4.2 ANION R column with UV detector

Therefore a different detection principle was tested in order to get a reasonable signal for the dinitramide anion. The UV spectrum of ADN shows two strong absorption bands with maxima at 214 and 285 nm (figure 1). Nitrate and nitrite show UV absorption maxima at 202 and 211 nm but with much lower sensitivity than dinitramide. Tests for the above mentioned ANION-R column were made to separate and detect dinitramide anions using p-hydroxy-benzoic acid as eluent. As the detection wave length both 285 or 214 nm were used. Nevertheless different molarities of the eluent were tested no evaluable signal was recorded in a realistic analysis time. Again it's not clear what's the main reason for these results. The separation phase generally could be not suitable for the analysis of dinitramide as well as the eluent (pHBA) which has a high UV ground absorption level.

4.3 Ion Pac 11 column with UV detector

Therefore a special IC anion exchange column from DIONEX (IonPac 11 HS) was coupled with the UV detector. This separation phase could be used with sodium hydroxide as eluent also at very high concentrations. Moreover NaOH shows really no UV absorption in the possible wavelength region. With this combination firstly a peak was registered for DN^-.

Ionic strength and flow of the eluent:

The retention time of dinitramide strongly depends on the molarity and secondly on the flow rate of the eluent which is demonstrated in Figure 2. For a flow of 0,8 ml/min DN^- eluts after 54 min when a 0,1 molar NaOH is used. Doubling the concentration shifted the to 28,3 min. Nearly the same retention time was observed with a slightly higher flow rate of 1,0 ml/min combined with a lower eluent molarity (0,15 m NaOH). Further increase of

the ionic strength of the eluent only showed a relative small decrease of the retention time. With a molarity of 0,18 the peak eluts at about 24 minutes and a 0,3 m NaOH shifted the peak to 19,6 minutes. In order to get the optimum signal to noise ratios the measuring wave lengths were varied.

Adjustment of the UV measurement wave length

Whlie a wave length of 202 or 204 for the nitrate analysis was tested to have the highest sensitivity here a very high noise of the UV base line signal was recorded. At 214 nm the signal to noise ratio was much better for the nitrate and nitrite peaks yielding also to a very high sensitivity for the dinitramide anion. For the latter a much better signal to noise ratio was observed for a measuring wave length of 285 nm leading only to a slightly loss in sensitivity. So the UV detector was adjusted at 214 nm for the analysis of NO_2^- and NO_3^- and at 285 nm for the detection of DN^-.

Concerning both the optimum retention time for dinitramide and a reasonable separation also of nitrate and possibly of nitrite a concentration of 300 mmol NaOH was tested to give the best results. While the resolution of nitrate and nitrite and therefore also the possible detection limit was slightly better when a 0,15 m NaOH-eluent was taken, the higher concentration of 300 mmol NaOH yielded to much shorter run times especially for high concentrated ADN-samples for which a long peak tailing was observed. Figure 3 shows ion chromatograms of different standard concentrations. It could be seen that the peak maximum is slightly shifted between 17 and 24 min with increasing ADN-concentrations yielding to a entire run time of 30 min in all cases.

Detection limits and calibration curves

Under improved separation conditions NO_2^- and NO_3^- elut at 2,8 and 3,1 min respectively. If measured at 214 nm the detection limit for nitrite is about 0,5 ppm and about 0,05 ppm for nitrate. These values are not quite as good as observed for the standard anion analysis method using the ANION R column in combination with pHBA and an electrical conductivity detector. While the latter method shows detection limits of about 0,1 to 0,01 ppm these high limits are not needed if realistic ADN samples, especially after thermal treatment have to be analysed. In the case of the dinitramide estimation a very broad linearity of the method was observed (figure 4). With a correlation factor of R = 0,9992 linear proportional

signal areas for DN^- were recorded in the range of 0,5 and about 750 ppm of ADN. Also the little higher detection limit for nitrite could be accepted because in thermally treated ADN samples analysed until now with the older standard anion IC-method mainly nitrate and only in very few caeses nitrite had been detected. The calibration of nitrate was found to be linear up to 20 ppm. Assuming a typical weight concentration of about 300 to 600 mg/l for a ADN sample to be analysed the detection limit enables the determination of 0,01 to 0,02 % of nitrate in one run parallel to a high dinitramide content.

Analysis of realistic treated ADN samples

Under improved measurement conditions also treated, realistic samples were analysed. Results show that the prilling of ADN does not substantially increase the low nitrate content in ADN which is contained from the synthesis of ADN. Non stabilized ADN aged under different temperatures for several periods also analysed. The results showed the trend that an increased temperature treatment and / time period yielded to an increased nitrate content besides a decreasing dinitramide part while nitrite was mostly not detected or only in spare quantities. Assuming the nitrate to be NH4NO3 and adding it's content to the ADN content lead to about 95 to 96 %. The rest could possibly be interpreted to be water.

5. LITERATURE

/1/ V. A. Tartakovsky, The design of stable high nitrogen systems, in: Decomposition, combustion and detonation of energetic materials, MRSSP v.418 B. Brill et al. (Eds.), Material Research Society, Pittsburgh, 1996, p. 15 - 24

/2/ A. Langlet, N. Wingborg, H. Östmark, ADN: A new high performance oxidizer for solid propellants, in: Challenges in propellants and combustion, K. K. Kuo (Ed.), begell house, inc., 1997, p. 616 - 626

/3/ M. L. Chan, A. Turner, L. Merwin, G. Ostrom, C. Mead, St. Wood, ADN propellant technology, in: Challenges in propellants and combustion, K. K. Kuo (Ed.), begell house, inc., 1997, p. 627 - 635

/4/ S. Löbbecke, H. Krause, A. Pfeil, Thermal behavior of Ammoniumdinitramide, 27. Intern. Anual Conf. of ICT, 25. - 28.o6.1996, Karlsruhe, P 143.1 - 143.4

/5/ S. Löbbecke, H. Krause, A. Pfeil, Thermal decomposition and stabilization of ammoniumdinitramide (ADN), 28. Intern. Anual Conf. of ICT, 24. - 27.o6.1997, Karlsruhe, P 112.1 - 112.8

/6/ Ch. Frenck, W. Janitschek, W. Weisweiler, Die Reaktion von Ammoniak mit Distickstoffpentoxid, 29. Intern. Anual Conf. of ICT, 30.06.-03.07.1998, Karlsruhe, P 50

/7/ U. Teipel, T. Heintz, K. Leisinger, H. Krause Formation of ammonium dinitramide (ADN) particles 29. Intern. Anual Conf. of ICT, 30.06. - 03.07.1998, Karlsruhe, 63.1 - 63.14

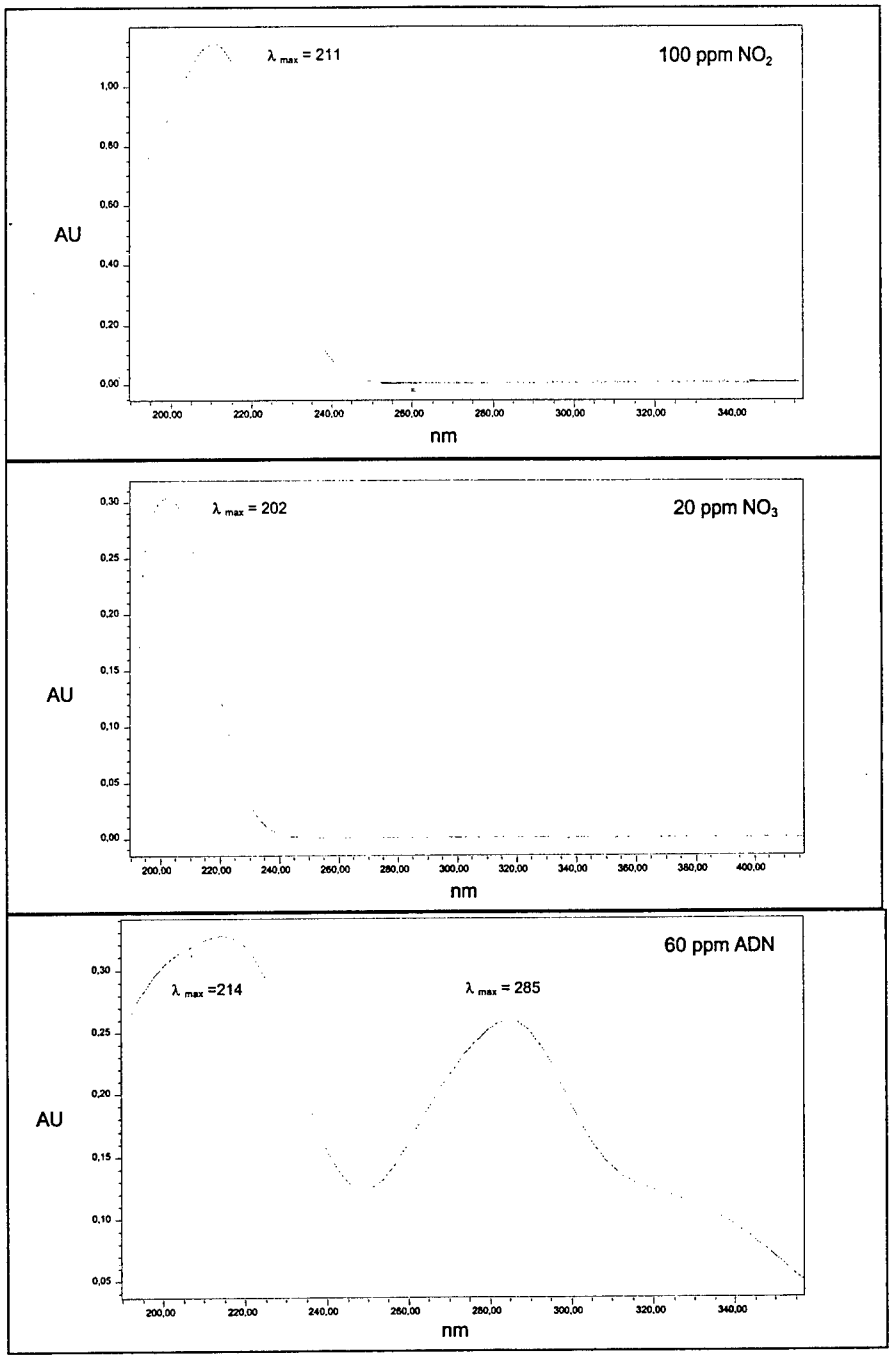

Figure 1: UV-Spectra of ADN, potassium nitrate and sodium nitrite

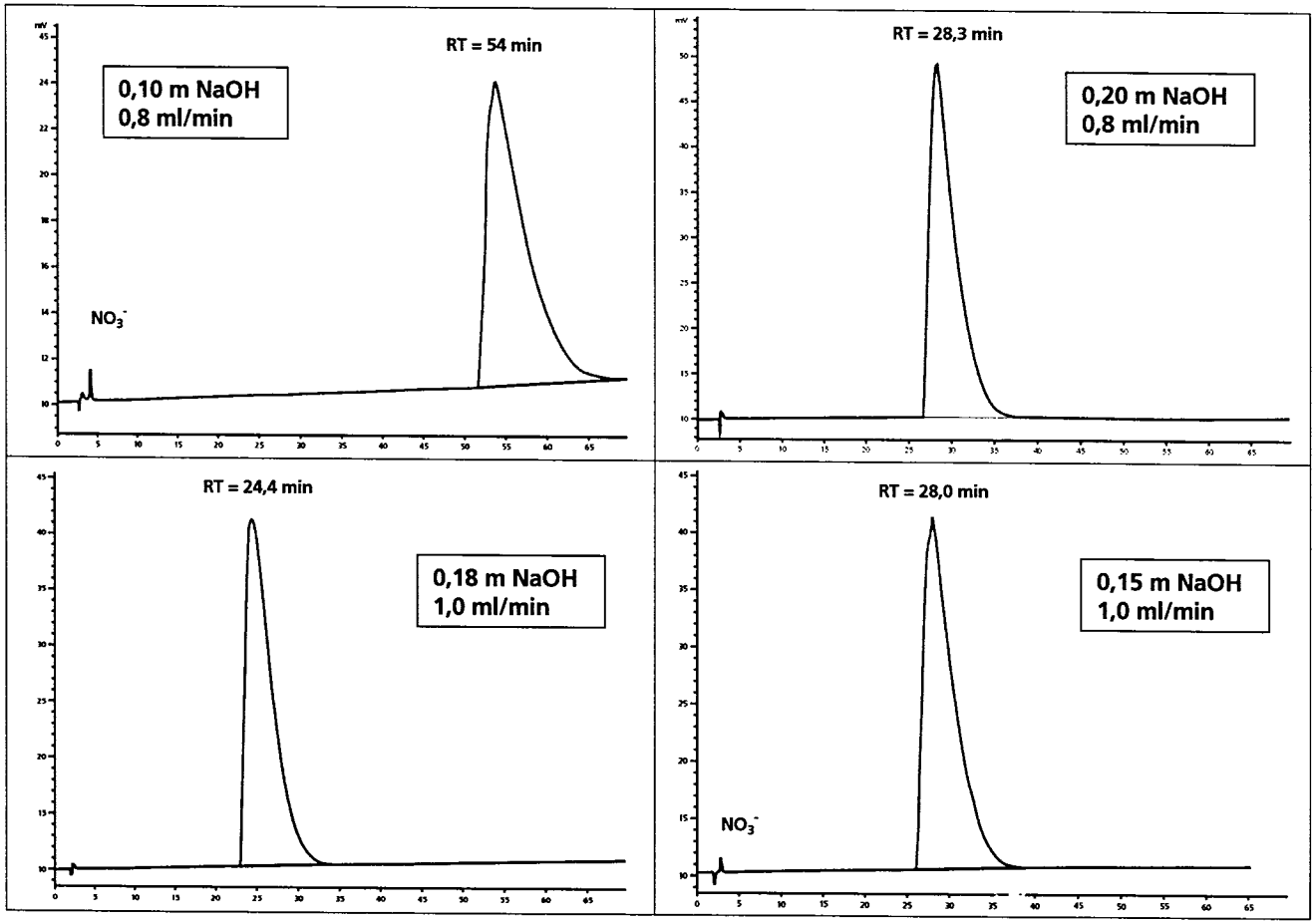

Figure 2: Influence of the ionic strength and flow of the eluent (NaOH) on the retention time (RT) of the DN^- anion (Ion Pac 11, UV-detection)

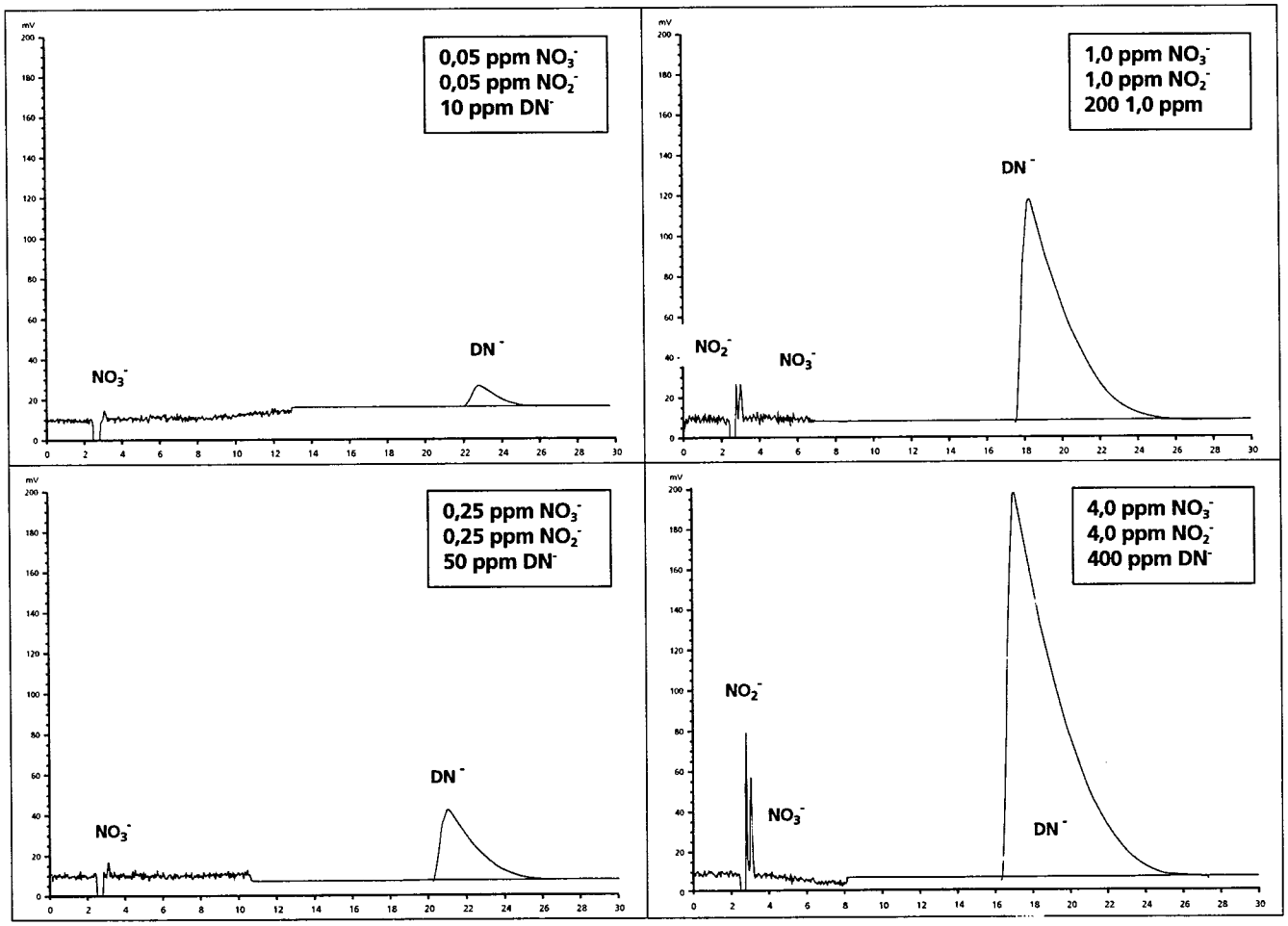

Figure 3: Different calibration standards (Ion Pac 11, 300 mmol NaOH, 1 ml/min, UV: 214 nm for NO_2^- and NO_3^- and 285 nm respectively for DN^-)

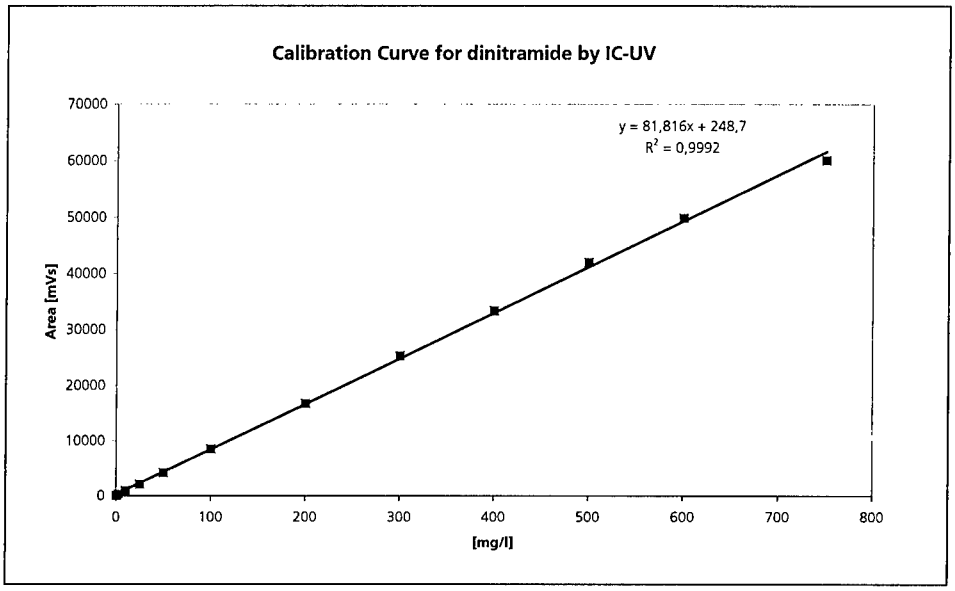

Figure 4: Calibration curve for the determination of dinitramide with Ion Pac 11

SEPARATION AND IDENTIFICATION OF NITRO AROMATIC COMPONENTS BY DIFFERENT CHROMATOGRAPHIC TECHNIQUES EXEMPLARILY FOR NITRONAPHTHALENES

G. Bunte, H. Neumann, J. Deimling, W. Schweikert

Fraunhofer-Institut für Chemische Technologie (ICT), D-76327 Pfinztal 1

Abstract

Depending on the reaction conditions the nitration of naphthalene by N_2O_5 leads to different quantities and types of mono- and multiple substituted nitronaphthalenes. As a possible co-reaction also - undesired - chlorinated nitronaphthalenes could possibly be built. In order to identify and quantify the product mixtures processed in different reactor systems respectively suitable gas and liquid chromatographic analysis routines were tested and established.

1. INTRODUCTION

The synthesis of most nitro-organic components is marked through high exothermic reaction heats needing special care for cooling devices to prevent a self-running of the reaction or possibly an explosion. In order to minimize danger potentials a new technical concept is developed at the ICT by the use of suitable micro reactors for processing nitro-organic compounds. Moreover micro reactor systems are supposed to have a positive influence to the desired product selectivity meaning the proportional product distribution as well as the selectivity of distinct nitro isomers.

For evaluating different micro reactor types for their processing characteristics and determining suitable reaction conditions e.g. the nitration of naphthalene with N_2O_5 was studied as a model reaction.

2. OBJECTIVES

Objective of this work was to provide suitable gas and liquid chromatographic analysis routines for the qualitative and quantitative determination of product mixtures of the stated model reaction produced in micro reactors and normal glass-ware lab-scale respectively.

3. EXPERIMENTAL

Gas chromatographic measurements for identifying and quantifying the produced product mixtures were performed with a Hewlett Packard GC-MSD-system (HP 5890 with 5971 MSD) equiped with a HP-5-MS capillary column. Furthermore liquid chromatographic analyses were developed using a Waters HPLC-system with a PDA detector at 225 nm. Naphthalene and the used mono- and dinitro-naphthalenes were baught in p.a. purity. A tri- and tetra-isomer were isolated from lab-scale experiment product mixtures by normal pressure column seperation.

4. RESULTS AND DISCUSSION

4.1 GC analytical method

Using the analytical possibilities existing at the ICT the identification of complex nitro organic product mixtures is preferably done by gaschromatographic techniques where identifying detectors like the infrared or the mass selective detector can be utilized. In

order to get a short analysis run time the GC temperature program firstly was optimized using a 60 m * 0,32 mm SPB-5 separation phase. As Figure 1 shows the retention time of the standards 1-nitronaphthalene (1-NN) and 1,8-dinitronaphthalene (1,8-DNN) only could be shifted to about 37 min and 46 min respectively giving no peak for 1,3,5-trinitronaphthalene (1,3,5-TNN) until 70 min. Therefore a shorter GC-column was taken. With a 30 m * 0,32 mm SPB-5 capillary column the retention times of the noted standard components were shortened very much. Figure 2 shows the total ion chromatogram of a reaction mixture produced in normal lab-scale. Here the 1,8-dinitronaphthalene elutes at about 15,5 minutes. Because the used GC-MSD system has a limit of at most 1 ml flow per minute into the vacuum recipient the required carrier gas head pressures and GC temperature program conditions lead to a nonstable operating status of the mass selective detector.

By utilizing a HP5-MS caplillary column with a smaller inner diameter (30 m * 0,25 mm, 1 film) this problem was repaired. With an optimized carrier gas flow rate and an appropriate temperature program all mono- and dinitronaphthalenes could be analysed whithin 30 minutes including possible chlorinated nitronaphthalene isomers like for the reaction mixture already demonstrated in figure 2. Although very high concentrated standard solutions of 1,3,5-TNN were injected a detection of this component couldn't be realized by GC analysis meaning this is also valid for the tetraisomer because of it's much smaller vapor pressure. A typical total ion chromatogram of the available mono- and dinitro standards is shown in figure 3. For quantitating the other isomers the assumption was made that both mono- and all dinitro-isomers respectively have the same sensitivity.

4.1 HPLC analytical method

Depending on the reaction conditions also tri- and tetranitronaphthalene could possibly be built as undesired products in the studied model reaction of N_2O_5 with naphthalene. Therefore a liquid chromatographic analysis method was established in order to judge the selectivity of the studied lab-scale and micro reactor processes respectively.

Two RP-18 phases of different manufactors were tested for this application. With optimized gradient elution conditions (CH_3OH and H_2O) the NUCLEOSIL C 18 PAH

column provided the separation of the both existing tri- and tetranitro standards at ICT while 1-nitronaphthalene and 1,3-dinitronaphthalene eluted in one peak (figure 4). On the other hand utilizing the Nova-PakC18 column a separation of the latter components was realized while the tri- and tetra-isomers couldn't be separated (figure 5).

Naturally the PDA detector does not enable a fully identification of unknown substances because of the relative unspecific UV absorption of organic components. But in the case of the noted tri- and tetranitro-compounds their absorption spectra could clearly be distinguished so that looking for the peak purity could be used to determine the absence or presence of the tetra isomer. For that reason the Nova Pak column was used for analysing possible amounts of the higher nitronaphthalenes nevertheless pure naphthalene elutes a little later than using the other column phase (about 26 minutes instead of 19 minutes).

5. CONCLUSIONS

Enabeling existing GC- and HPLC equipments at the ICT in this work chromatographic analysis routines were established to identify and quantitate the reaction products of the nitration of naphthalene with N_2O_5 used as a model reaction for the examination and optimization of the processing conditions of different micro reactor systems in relation to normal glassware lab-scale reactors. Description and results of the processing conditions and realizable product selectivities are reported in paper V 33 /1/.

6. LITERATURE

/1/ S. Löbbecke, J. Antes, T. Türcke, E. Marioth, K. Schmid, H. Krause
The potential of microreactors for the synthesis of energetic materials

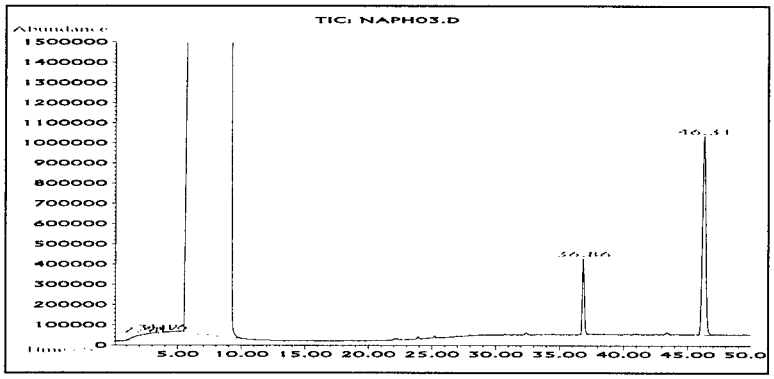

Figure 1: GC-MSD total ion chromatogram of a standard mixture of 1-nitronaphthalene (at 36,8 min) and 1,8-dinitronaphthalene (at 46,3 min)

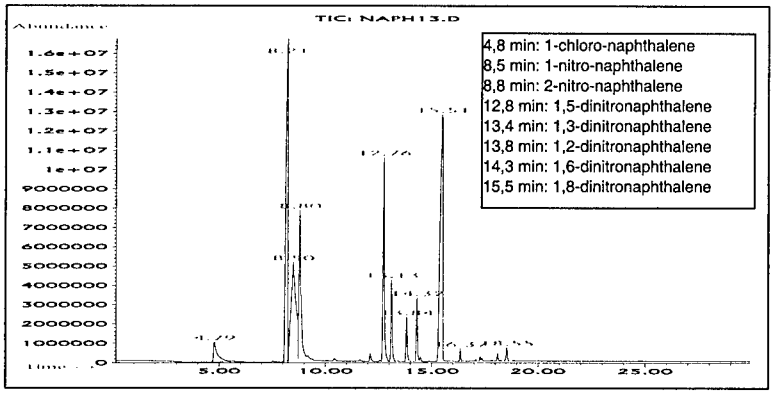

Figure 2: GC-MSD total ion chromatogram of a reaction mixture of the nitration of naphthalene with N_2O_5 in glassware reactors of normal lab-scale

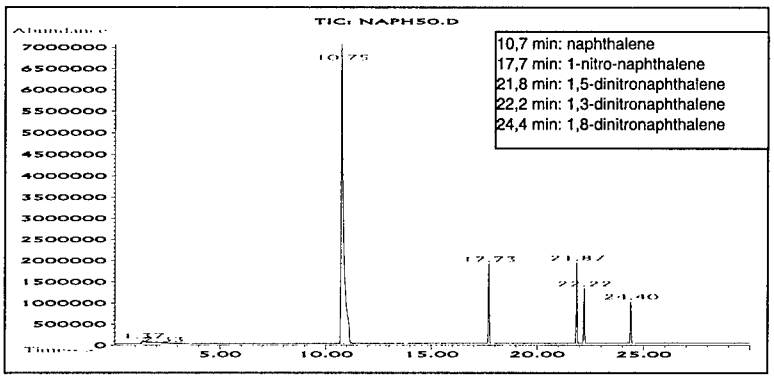

Figure 3: GC-MSD total ion chromatogram of a mixture of reference standards analysed with a 30m * 0,25mm HP5-MS column

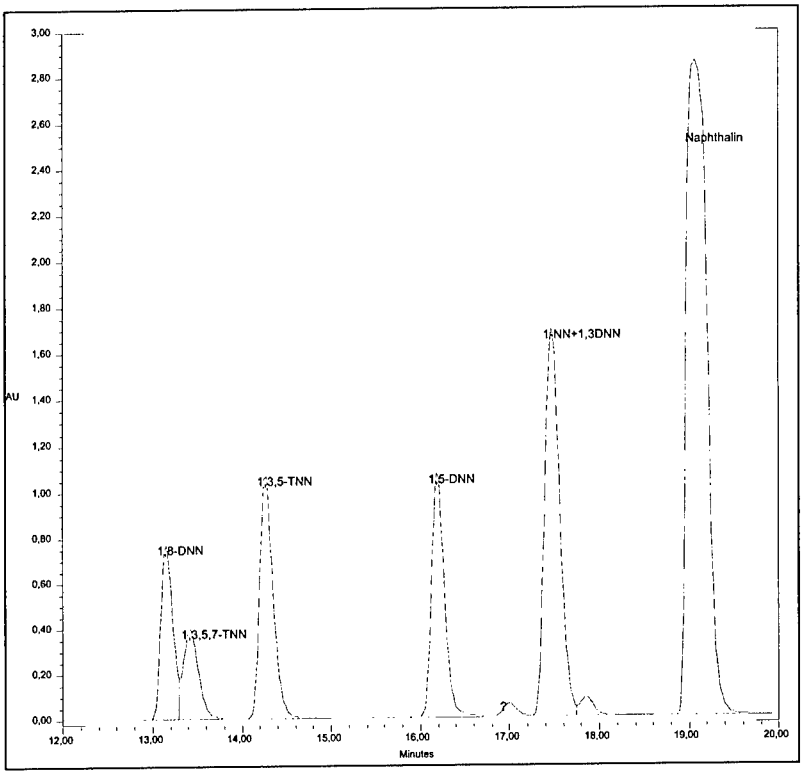

Figure 4: HPLC chromatogram of the reference standard mixture measured on the NUCLEOSIL C18 PAH column with a detection wave length of 225 nm

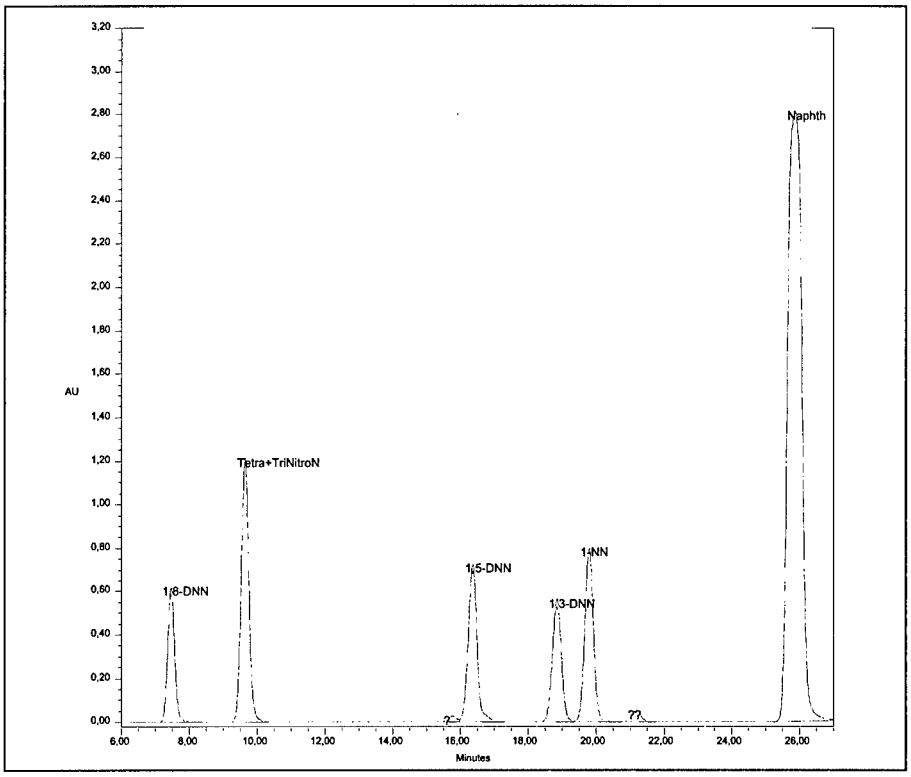

Figure 5: HPLC chromatogram of the reference standard mixture measured on the Nova-Pak C18 column with a detection wave length of 225 nm

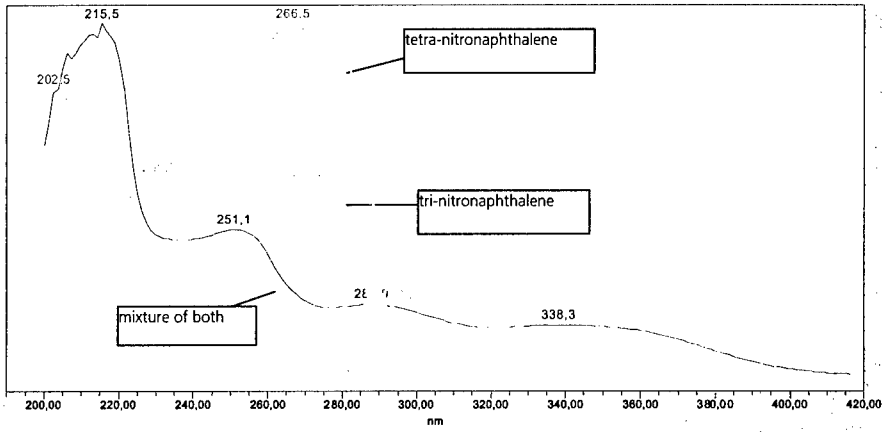

Figure 6: UV absorption spectra of pure trinitro- and tetranitronaphthalene as well as a mixture of both components

Estimation of The of Service Live of NC Propellant by HPLC

Shokry, S.A and Husseiny, M. E***

ABSTRACT

Recently HPLC has gained the popularity in tracking of the change of composition of the stabilizers and its nitration products in the propellant formulation, and so offers the best potential method for estimation of the useful lifetime of the propellants. In the present study we use single base propellant (99% NC with 13.1% nitrogen content), and stabilized by 1% DPA. We follow up the percent concentration of DPA and its derivative products as a function of time, using HPLC. The samples of the powders were subjected to thermal artificial aging at 80 C,100 C, and 110 C, also samples of powders stored at normal temperature were used. The analysis of the results with the aid of computer program in MATLAB programming allow to devise a mathematical formula govern the estimation of the useful lifetime of the used propellant as a function of the storage temperature. Considering that the propellant contains 50% from the initial concentration of DPA as a good stabilized propellant, we can estimate from the derived formula that the propellant under study can withstand safely storage life of 22 years at normal temperature. For the same propellant, we can estimate that it may be self – ignited after about 50 years of storing at normal temperature.

---

* Prof. Dr. Shokry Abd El –Sami Shokry: Technical advisor of Abu Zaabal Company for specialty chemicals (AZC),Cairo, EGYPT

** Chem. Husseiny Mohammed El- Sayed: AZC ballistic laboratory

Introduction

Propellants based on NC decomposes significantly at normal storage temperature, the products of decomposition are acids and oxides of nitrogen. These products catalyze and accelerate the decomposition process, which is exothermic and may lead to self-ignition under certain circumstances. To prevent this auto –catalytic reaction, stabilizers are added to propellant formulations, in order to react with the decomposition products before they can catalyze further decomposition.

If a propellant is correctly stabilized, it can be safely stored for many years. It is therefor most important that valid tests are devised to check that a propellant has been adequately stabilized.

In the majority of stability tests, the propellant is artificially aged by heating to simulate the storage lifetime at ambient temperature (1). These stabil. y tests are not entirely satisfactory for a number of reasons. In some tests, the time taken to carry out the test is too long (2). In others, the temperature of the test may be too high.

In recent, many investigators tracking the change in the stabilizers quantitatively during aging of propellants, using analytical methods (3). HPLC offers the best potential method for the quantitative analysis of stabilizer, and its derivatives (4), and thus for an estimation of the degree of decomposition of a propellant. This quantitative analytical method gives a fair indication of the storage ability and allows devising a suitable formula for the estimation of the so-called " safe storage lifetime" for a propellant. HPLC, as theory, practice, instrumentation and application have been widely covered in a series of books and review articles (5,6,7). In spite of that a little of these articles and publication deal with the subject of the storage lifetime determination of propellants. So a great of additional work may be done in that field and thus we suggested making this subject, the objective of our work in this paper.

Experimental work

Single base propellant was subjected to an artificial aging at temperature of 80 °C, 100 °C, and 110 °C. For the aged propellant, the consumption and decomposition of diphenyl amine (DPA), and its derivatives were studied for the estimation of the useful safe lifetime for this propellant.

The percent consumption of DPA was followed up as a function of time by the use HPLC for the aged samples of propellant and also for other samples stored at normal temperature in the range 1-22 years.

Procedure

The used samples were ten grams per each from fresh produced single base propellant, used in 9 mm. ammunition. The formulation of the propellant was 99% NC, 13.1 % nitrogen content and 1% DPA. The samples were artificially aged at different temperatures of 80 °C, 100 °C, and 110 °C, using the test tubes of the 100 °C test (international test). The temperatures used were adjusted thermostatically with error < 1 °C, sample withdrawing were performed each 24 hours intervals for the aging temperatures 80 °C and 100 °C, but at 110 °C, samples withdrawing occurred each 8 hours intervals. About one gram of the aged samples were weighed exactly and extracted by 100 ml. 1,2 dichloroethane for 48 hours. Disconnected the extractor, evaporated the solvent and dried the residue. The dry residuals were dissolved in 50 ml. Ethyl acetate and derived for quantitative analysis by HPLC. DPA and its derivatives were analyzed and were made in percent as a function of time based on initial DPA concentration. The used apparatus was Hewlett Packard 1081B HPLC, the used column was RPC18, the mobile phase was (methanol / water), detector was UV type, used at wavelength of 254 NM, and the external standard was ethyl acetate. The standard solution of DPA and its three derivatives were prepared by dissolving about .01 gram of each in 50ml. ethyl acetate. The HPLC automatically calculate the

analytical results after each analysis. It is selfcalibrated, in case that a standard mixture was used.

Results and Discussion

The kinetics of stabilizer decomposition during the self accelerating reaction accompany the storage of a propellant, have been successfully modeled by first order kinetics with respect to the amount consumed from the stabilizer (8). It has been suggested that an aging experiments combined with the kinetic analysis could be used to determine quantitatively the useful lifetime of the propellant. Typical percent mass loss of the stabilizer DPA versus time, at three different aging temperatures of 80 °C, 100 °C, 110 °C, and at normal temperature are shown in the figures (1,2,3,4).

The equation for the assumed first order reaction rate is,

$$dx/dt = k(100 - x) \qquad (1)$$

Integration of the of equation (1) gives,

$$Ln\ (100/(100 - x) = k\ t \qquad (2)$$

And the relation between reaction rate constant and temperature is obtained from the Arrhenius equation,

$$k = A\ e^{-E/RT} \qquad (3)$$

$$Ln\ k = Ln\ A - E/RT \qquad (4)$$

For the preceding equations, x is the percent weight loss of DPA, k is the rate constant (day $^{-1}$), t is the time of aging (day), T is the absolute temperature of aging, R is the gas constant, A is the preexponential factor, and E is the activation energy for the decomposition reaction (cal.).

Applying the approach of the estimated first order kinetics on the four aging experiments results the straight lines shown in the figures (5,6.7). And the rate constant calculation results with the aid of the computer program in MATLAB programming are shown in table (1). From equation (3), and with the aid of the same program, the first order kinetics parameters E and A, can be determine, table (1) and figure (8) show the results of this calculation.

According to these interpretation, and if we consider that the propellant which is still contains 50% of stabilizer as a good stabilized save propellant, then the following derived equation can gives the estimated save lifetime for the single base propellant under study as a function of the storage temperature:

$$t_u\ (year) = 1.78\ 10^{-16}\ e^{11730/T}$$

From this equation, we found that the calculated safe lifetime of the propellant under study is 22 years (50% stabilizer), and this value gives god agreement with the experimental results. To find the storage lifetime of the studied propellant as a function of both stabilizer % conversion and storage temperature we can use the following equation,

$$t_s\ (year) = 2.568\ 10^{-16}\ e^{11730/T}\ Ln\ 100/(100-x)$$

The application of this equation on the experimental results of the stabilizer analysis for the samples stored at normal temperature give an excellent agreement between the calculated storage lifetime and real one. This agreement can be shown from figure (9). Same agreement has also been found for other aging temperatures.

Conclusion

These studies indicate that the aging experiments for a propellant accompanied with the quantitative analysis by HPLC, and the proposed modeling technique, are effective tool in the estimation of the save useful lifetime for that propellant. The relative simplicity gives this method the potential for application in the propellant factories and military research centers.

Acknowledgment

We should like to express our deepest thanks to Dr. El- Amir Adel Abd El-Kader, chairman of AZC for his helpful advise and facilities given to accomplish this work..

References

1. R. J. Verhoeff, " Comparison of Several Stability Test Methods", 5Th Symposium on Chemical Problems Connected with the Stability of Explosives; Swedish National Defense Research Institute, Stockholm, Sweden, 1979.
2. A. J. Brook, " An Investigation of Some Aspects of the Stability Testing of NC Propellants.5Th on Chemical Problems Connected with the Stability of Explosives; Swedish National Defense Research Institute, Stockholm, Sweden, 1979.
3. L. Drut and M. Asselin, " A Review of Stability Test Methods for Gun and Mortar Propellant", J.of Energetic Material, Vol. 6, March and Sept. 1988.
4. S. Wart and A. Oehile, " Analysis of Stabilizer Degradation Products in Propellant Using HPLC Photodiode Array Detection", Propellant, Explosive and Pyrotechnics, 22, 1998.
5. P.D.Storey, " Predication of Propellant Stability by the Correlation of Stabilizer Depletion rate and Abel Heat Test Times", 18 Th International Annual Conference of ICT, 1987.
6. M. E. Walsh and T. F. Jenkins, " HPLC Separation of Explosives and Reduction Products." Anal. Chem. Acta., 231, 313, 1990.
7. J. Yinon and S. Zitrin, " Modern Method and Applications in Analysis of Explosives ", John Wiley & Sons Ltd, England, 1993.
8. J.Kimura, " Kinetic Mechanism of Thermal Degradation of a. Nitro Ester Propellant.", Propellants, Explosives and Pyrotechnics., 13, 1988.

Fig.(1):Conversion of DPA versus time at 80 °C

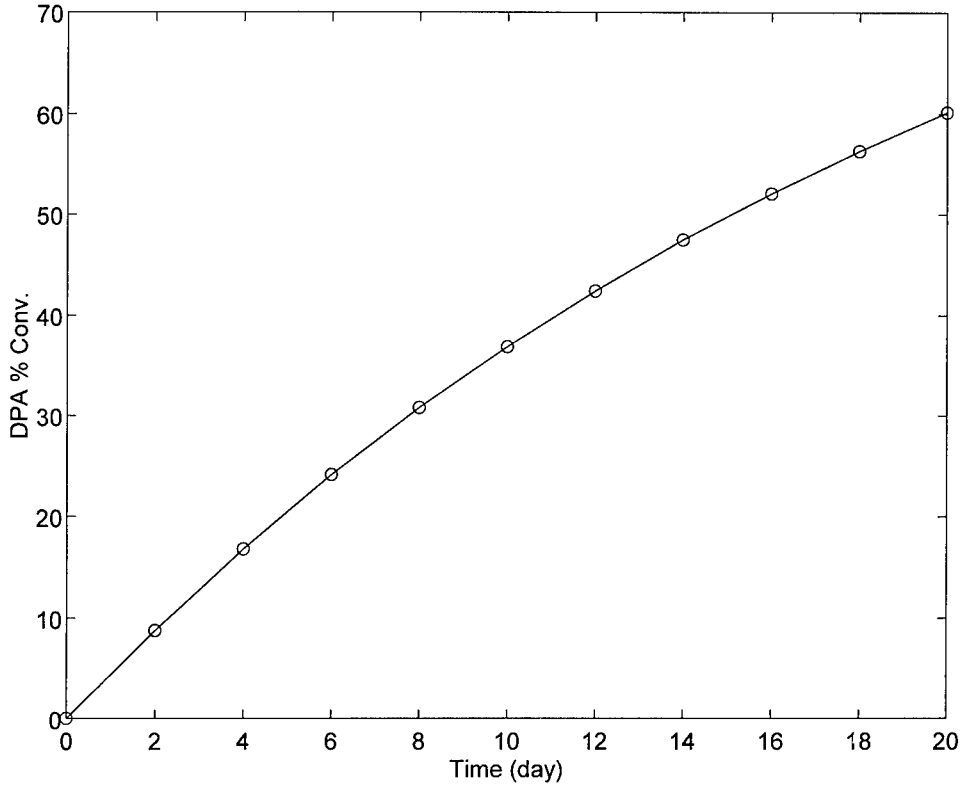

Fig.(2):Conversion of DPA versus time at 100°C

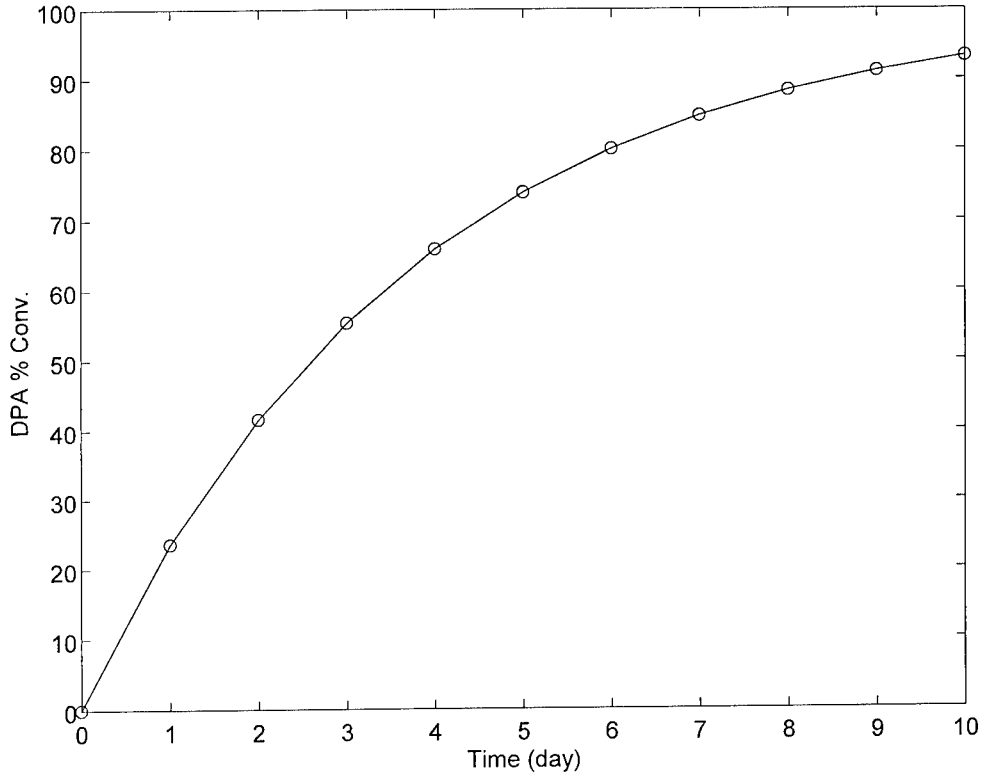

Fig.(3):Conversion of DPA versus time at 110 °C

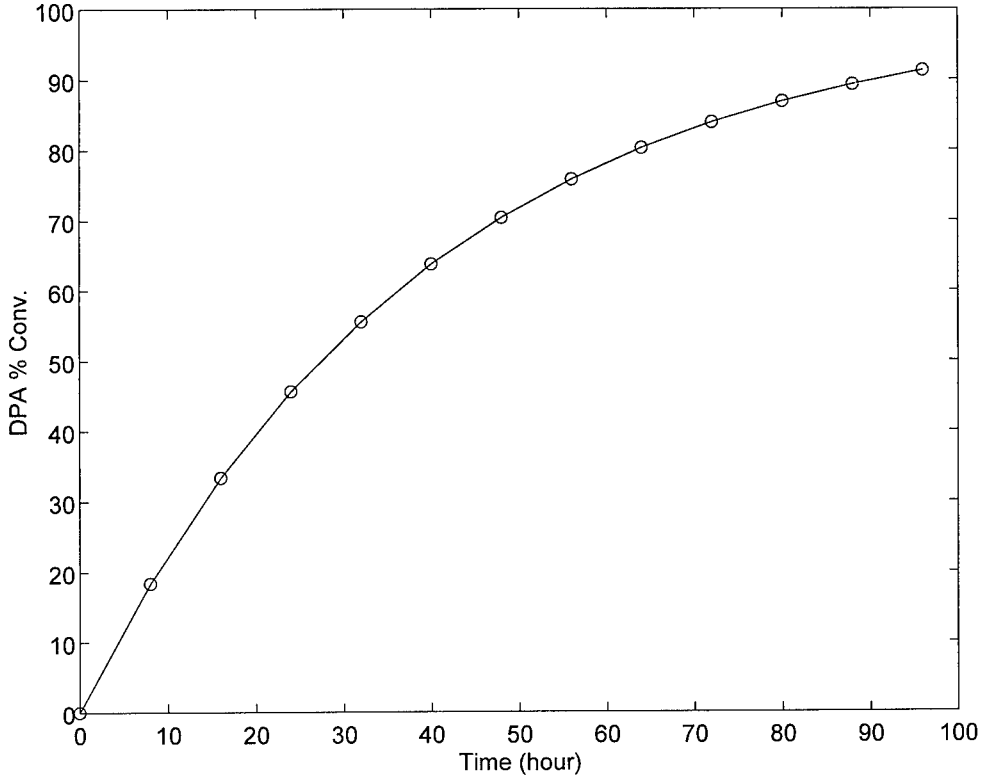

Fig.(4):Conversion of DPA versus time at normal temperature

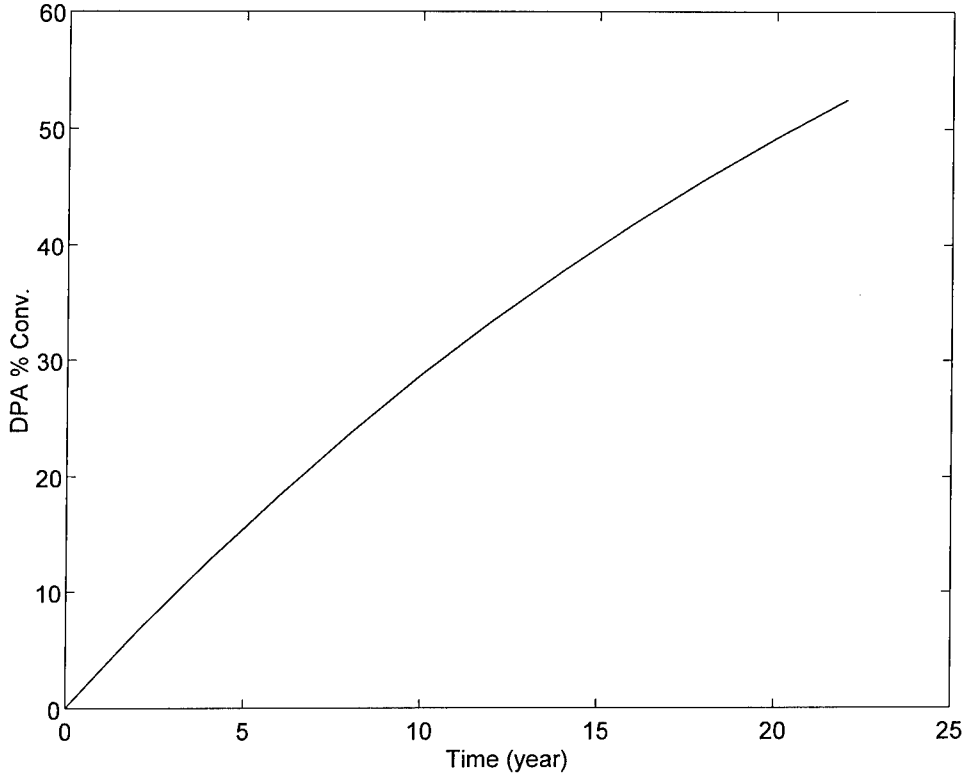

Fig.(5) Determination of the rate constant at 80℃,100℃

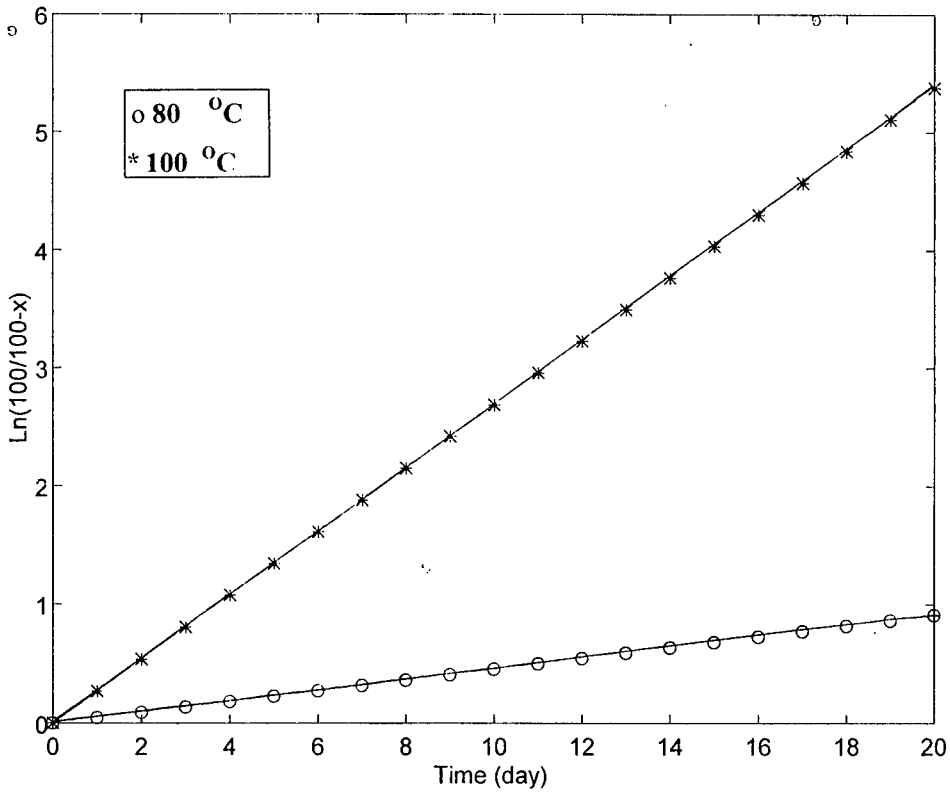

Fig.(6) Determination of the rate constant at 110 °C.

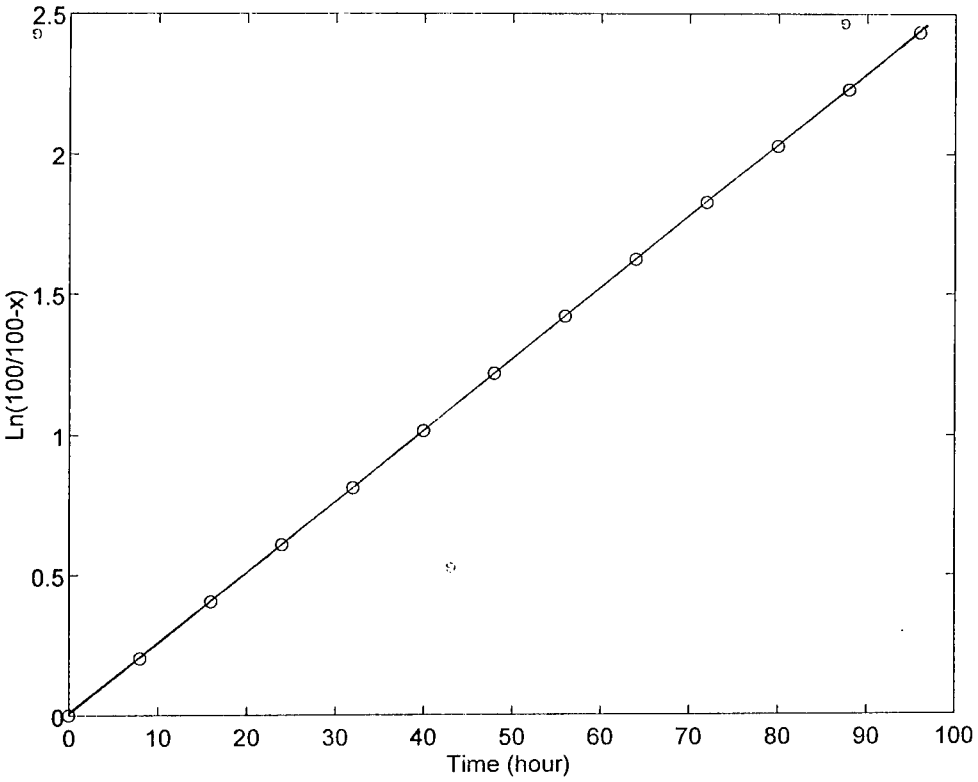

Fig.(7) Determination of the rate constant at NTC

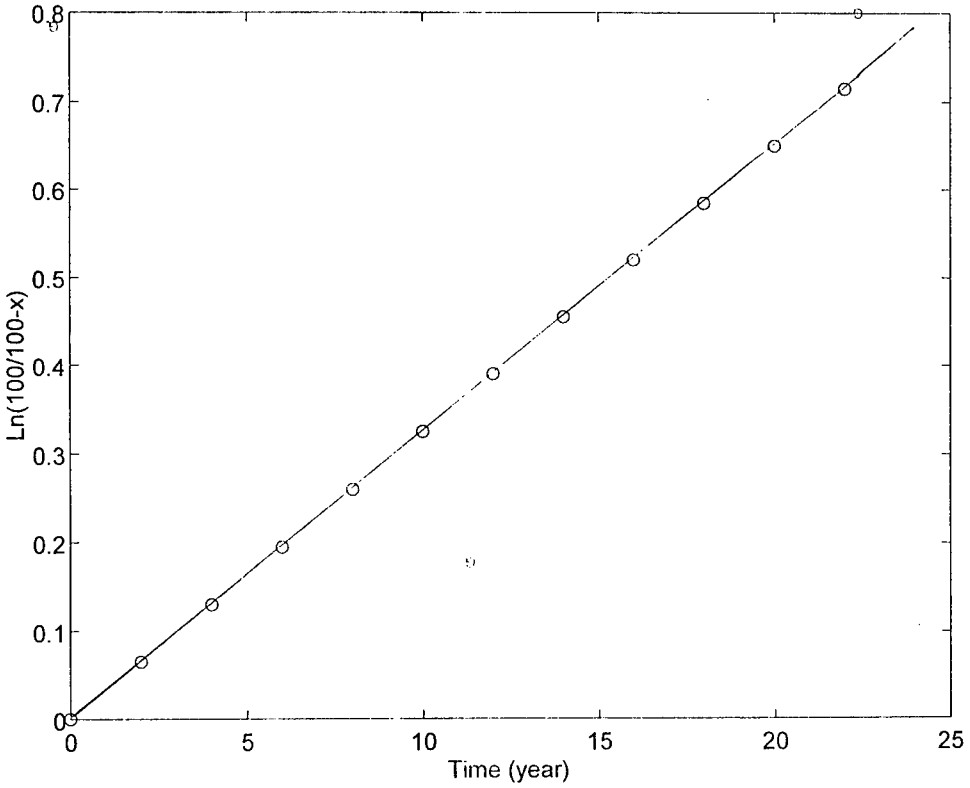

Fig.(8): Arrhenies plot

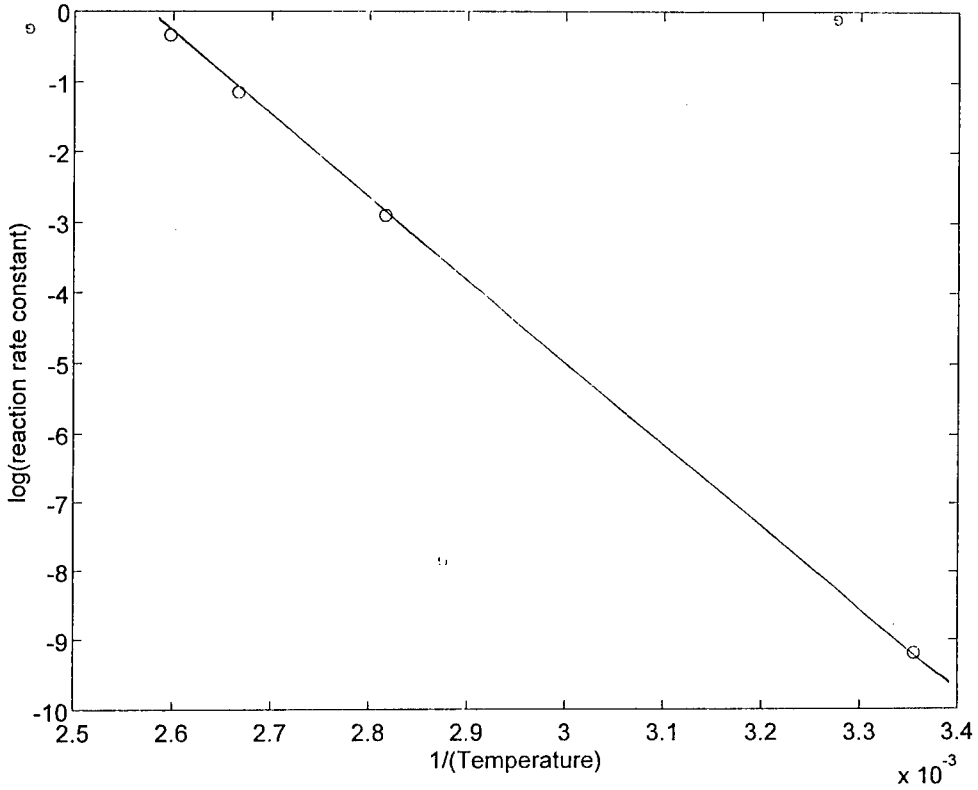

Fig.(9):Calculated and experimental DPA versus time at normal temperature

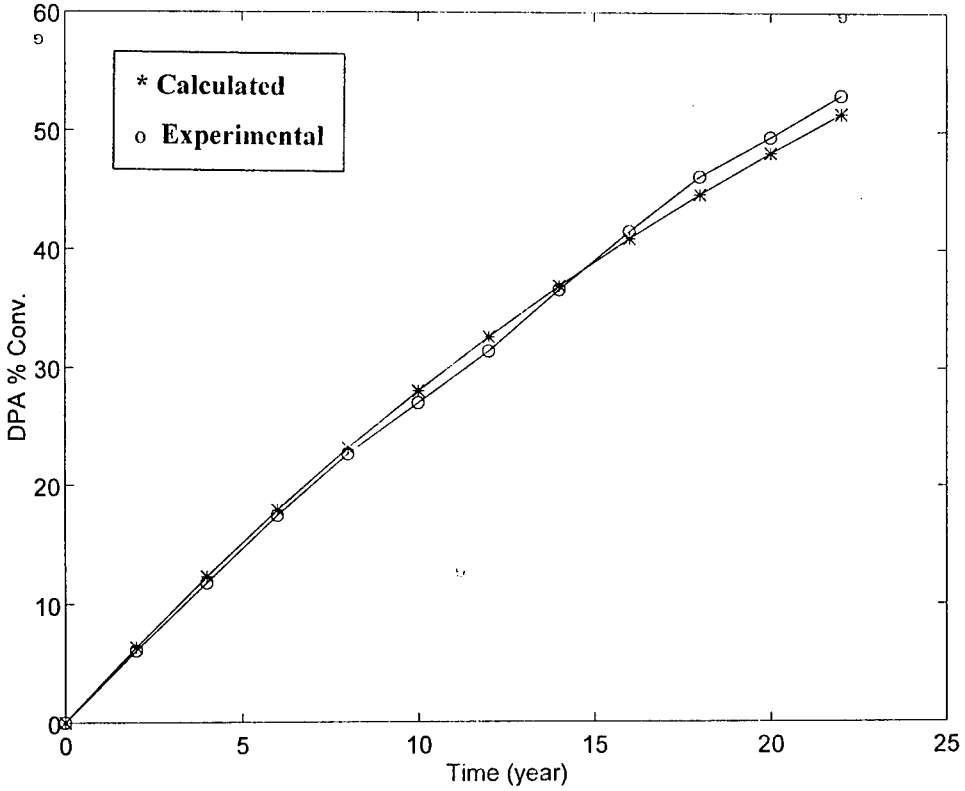

Table (1)

Temperature , K	k, (day^{-1})	E, (Cal.)	A, (day^{-1})
298	$9x10^{-5}$		
353	0.046		
373	0.268	23460	$1.0686x10^{+13}$
383	0.6089		

Charts of the HPLC output results for samples stored at normal temperature

a. 2 years storage:

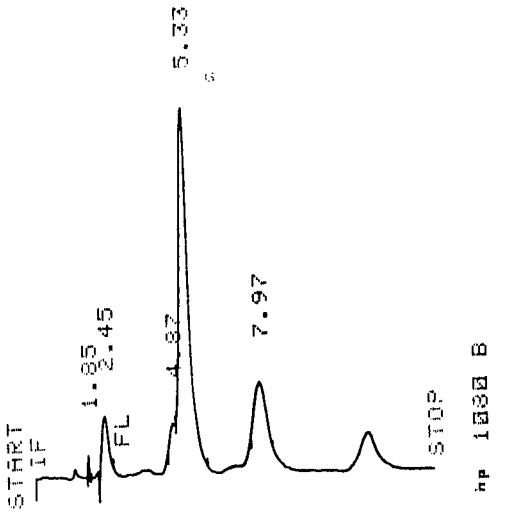

b. 21 years storage:

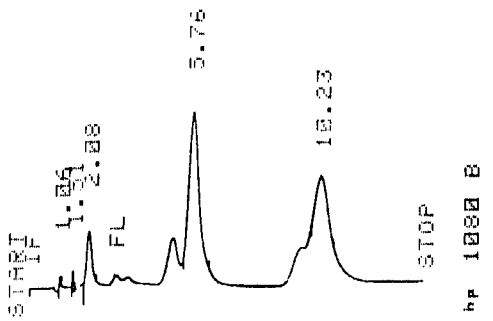

SPECTRAL OVERLAP AND ABSORBANCE RATIO METHODS FOR IDENTIFYING PEAK PURITY OF EXPLOSIVES IN HPLC

Liu Yonggang, Luo Shunhuo

(*Institute of Chemical Materials, Chinese Academy of Engineering and Physics, Mianyang, China,* 621900)

ABSTRACT

The use of spectral overlap and absorbance ratio methods is described for examining peaks of explosives for homogeneity and purity separated by reversed-phase high-performance liquid chromatography (HPLC) with a photodiode array detector. It is found that severely overlapped peaks can be identified easily using the above methods. The efficiency of both methods has been compared on a strongly overlapping model system (2,4,6-TNT and 2,4-DNT). 2,4-dinitrotoluene (2,4-DNT) is an explosive, which is a byproduct of 2,4,6-trinitrotoluene (2,4,6-TNT) and which often coelutes with it. A series of binary mixtures of 2,4-DNT and 2,4,6-TNT ($0 < R_S < 1.5$; 0-50% 2,4-DNT) was analysed. For samples where the resolution of the binary peak was 0.2, limit of detection for 2,4-DNT of 1%(w/w) were obtained using spectral overlay method. This compared with limit of detection of 5%(w/w) for the absorbance ratio method. It is shown that absorbance ratio method is the less powerful method. Limitations of both methods for identifying peak purity are also discussed.

INTRODUCTION

High-performance liquid chromatography (HPLC) methods are widely used in the explosives and other industries (1,2). Primarily due to their simplicity and specificity. These methods are inherently more specific than the more conventional method like spectrophotometer because the separation of the compounds is achieved on an efficient column prior to UV detection or other methods. However, it is possible for two or more compounds to elute together from the column, thus appearing as a single peak in the chromatogram. In methods using spectrophotometric detectors, one simple way to check the peak purity or homogeneity is by the use of a signal (absorbance) ratio method (3).

With the introduction of multiple wavelength monitoring detectors and photodiode array detectors to the market (4), it is now possible to measure absorbances simultaneously at two or more wavelengths as the compounds are eluted from the column. Devoid of instrument limitations, drifting baseline, etc., a peak due to a single component is expected to produce a corresponding absorbance ratio plot, which is rectangular in shape. A deviation from the flat-top of the plot is an indication of two or more components eluting together.

Peak homogeneity can also be checked by UV spectrum overlaying. In this technique, three or more UV spectra of the peak of interest are recorded at different times during elution. A perfect match of these spectra when overlayed signifies peak homogeneity.

The use of absorbance ratio and spectral overlap for purity check of peaks obtained from high-performance liquid chromatography (HPLC) is gaining popularity. This is evident in the many recent analytical applications of these techniques. However, few reports are available describing the use of these techniques for the analysis of explosive compounds.

The efficiency of absorbance ratio (AR) and spectral overlap techniques for explosives peak purity testing using a photodiode array detector has been evaluated. For this purpose, a strongly overlapping model system consisting of 2,4,6-TNT and 2,4-DNT has been chosen. 2,4-DNT has been selected as a model impurity since it is a byproduct in 2,4,6-TNT formulation. The relative proportions of the two explosives have been varied from 1 to 100 (w/w) within a concentration range of chemical interest.

EXPERIMENTAL

Reagents and materials.

2,4,6-TNT and 2,4-DNT were purchased from Xi'an Modern Chemistry Research Institute. All solvents used were of HPLC grade or better. High purity water was from

a Milli-Q™ system (Millipore, Bedford, MA).

Solutions

Stock solutions of 2,4,6-TNT (40.0mgl^{-1}) and 2,4-DNT (40.0mgl^{-1}) were prepared. From these solutions, five solutions containing various proportions of 2,4-DNT with respect to 2,4,6-TNT and conversely, were prepared in the mobile phase below mentioned. The concentrations were respectively 0.1, 0.4, 2.0, 10.0, 20.0 mgl^{-1} of 2,4-DNT (or 2,4,6-TNT) in the presence of 40.0 mgl^{-1} of 2,4,6-TNT (or 40.0 mgl^{-1} of 2,4-DNT). Mobile phase was acetonitrile-water (70:30) (v/v). It was filtered through a 0.45 μm Millipore filter. Flow rate was 0.6 ml/min.

Apparatus

The chromatographic system consisted of a Waters™ 600A solvent delivery system with column heater and a Waters™ 996 photodiode array (PDA) detector collecting from 200-500 nm at a spectral resolution of 1.2 nm (Waters Corporation, Milford, MA). The column used was a Nova-Pak™ C_{18} column (3.9mm×150mm).

RESULTS AND DISCUSSION

Absorbance ratio is the ratio of absorbances at two different wavelength obtained when the component of interest is in the detector flow cell. According to Beer's law, it is expressed by the following equation:

$$\text{Absorbance ratio} = \frac{\varepsilon_1 bc(t)}{\varepsilon_2 bc(t)} = \varepsilon_1/\varepsilon_2 = \text{constant}$$

$\varepsilon_1/\varepsilon_2$ are the molar absorptivity at wavelengths 1 and 2, b is the path length, and C(t) is the concentration of the component of interest at time. This ratio can have a value from zero to infinity depending on the nature of the peak and the wavelengths selected.

The absorbance ratios obtained were characteristic of each explosive in a given mobile phase, regardless of solute concentration, column efficiency, lamp energy, peak shape, flow rate and retention time. A distortion and alteration of both the

spectrum and ratiogram indicate any impurities that co-eluted or overlapped with the peak of interest.

The dependence of the absorbance ratio and UV-VIS spectra on the mobile phase has been considered to be a major practical limitation of the techniques. However, we feel that this drawback may be turned into an advantage, because upon changing the mobile phase new ratio values are obtained, which give additional information on the purity and identity of the explosives under investigation.

Typical retention times were 3.03 and 3.09 min for 2,4,6-TNT and 2,4-DNT respectively, yielding a resolution (R_S) of 0.20 for equal concentrations of 2,4,6-TNT and 2,4-DNT ($40mgl^{-1}$).

Selection of the wavelengths for AR

A critical issue for AR is the selection of a pair of wavelengths for selectivity and sensitivity. Since both compounds are known, the optimum pair of wavelengths could be approached from ratioing the spectra of the pure compounds in the mobile phase. The plot of the ratio of the spectrum of 2,4,6-TNT (Fig.1a) and 2,4-DNT (Fig.1b) is shown in Fig.2.

A maximum and minimum absorbance ratio is observed at 280 nm and 220 nm respectively. At these wavelengths, the absorbance ratios differ most and moreover, these wavelengths are very close to the maximum absorbance wavelengths of 2,4,6-TNT and 2,4-DNT, respectively. Therefore, they were selected in the further stages of the method.

Absorbance ratio plot

AR was plotted for comparison. The absorbance ratiogram at A_{280}/A_{220} plotted along the elution profile allows to detect easily 5% (w/w) 2,4-DNT with respect to 2,4,6-TNT but the detection of 1% (w/w) of 2,4-DNT is more problematic (Fig.3).

Spectral overlay

The sensitivity of spectral overlay was also considered. Spectra acquired at the upslope, the apex and at the downslope of the peak were normalized and overlayed. Fig.4 shows that 1% of 2,4-DNT in 2,4,6-TNT are easily detected.

Sensitivity

As the sensitivity of a detector plays a major role in monitoring explosives or decomposition products at trace levels, the sensitivity of the photodiode array detector used in the present study was compared to that of a conventional variable wavelength detector (Waters 486 model). The study was carried out on 2,4,6-TNT and three of its isomeric impurities. The compounds were separated on the same C_{18} stationary phase with an acetonitrile-water (60:40) (v/v) mobile phase at a flow rate of 0.8ml/min.

Under the same chromatographic conditions, the limit of detection was about one time lower using a conventional detector relative to the diode array detector. This shows that spectral information on contemporary diode array detector is not gathered at the expense of detector sensitivity (5).

CONCLUSION

It has been show that absorbance ratio and spectra overlap methods provide two very useful identification of HPLC peak purity of explosives. The two techniques are easily applied to explosives quality control and detection of impurities chromatographically unsolved.

The sensitivity of the AR method depends both on the chromatographic resolution and the magnitude of difference in the absorptivities of the compounds at the selected wavelengths. When it is included in the software of a diode array detector, AR can be easily applied on a routine basis.

Spectral overlay technique has sensitivity comparable to AR, does not require information on the spectra.

ACKNOWLEDGEMENTS

We wish to thank Miss Zhao Yingbin for her help in the experimental.

RRFERENCES

1. Jehuda Yinon, Shmuel Zitrin. The Analysis of Explosives, New York: Pergamon Press, 1981.108
2. J.B.F. Lloyd, Adv. Chromatogr., 32, 17300261(1992)
3. K.H.Law and N.P.Das, J. Chromatogr., 388(1987)225-233
4. Huber 1. Application of diode-array detection in HPLC. Product literature. France: Hewlett-packward Co, 1989
5. H.Fabre and A.F.Fell, J.Chromatogr., 15(17),3031-3043(1992)

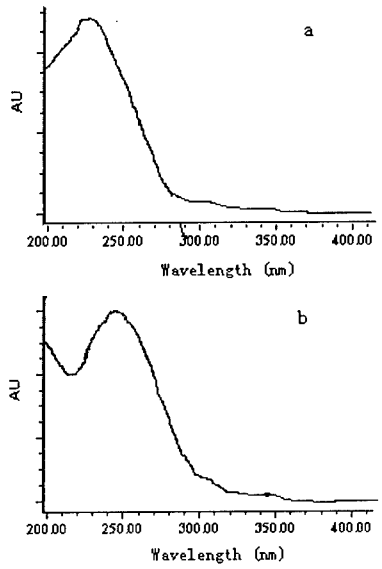

Figure 1. Absorbance spectrum by HPLC-UV detection.
a : 40.0 mgl^{-1}2,4,6-TNT solution injected.
b : 40.0 mgl^{-1}2,4-DNT solution injected.

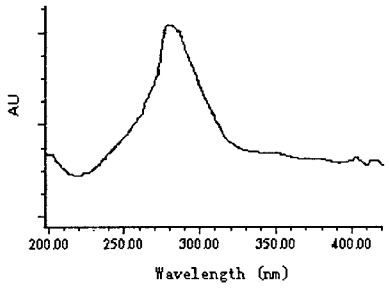

Figure 2. Graph of absorbance ratio of 2,4-DNT / 2,4,6-TNT vs wavelength

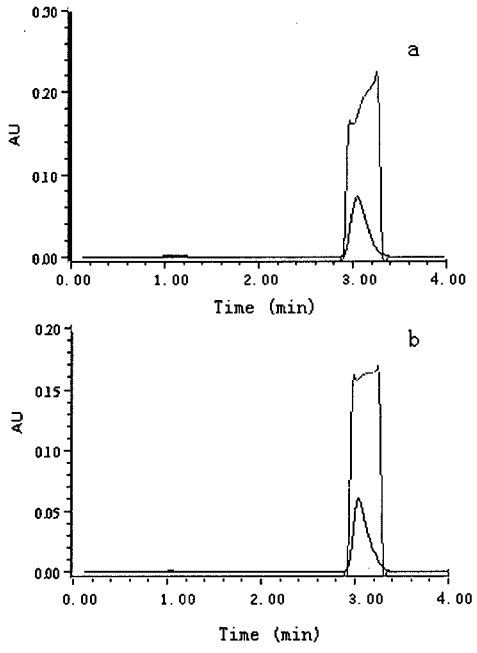

Figure 3. Absorbance ratio plots from a mixed solution of 2,4,6-TNT (40.0 mgl^{-1}) and 2,4-DNT.
a : 2.0 mgl^{-1} of 2,4-DNT.
b : 0.4 mgl^{-1} of 2,4-DNT.
Chromatograms recorded at 230 nm. Other conditions, see text.

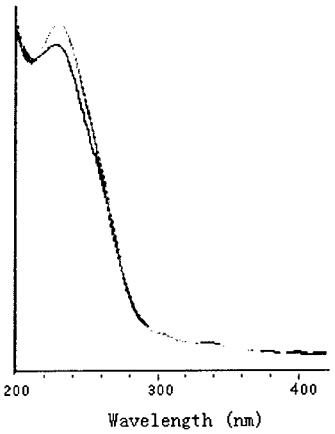

Figure 4. Spectral overlay from a mixed solution of 2,4,6-TNT (40.0 mgl^{-1}) and 2,4-DNT (0.1mgl^{-1}).

Detection of α-HMX in β-HMX with FTIR Diffuse Reflection Technique.

Richard Gjersøe
Dyno ASA, Defence Products. Norway

ABSTRACT

Detection of α-HMX polymorphs in HMX is an important quality parameter in most HMX-specifications. Common analytical methods are X-ray diffraction, microscopy with polarized light and IR using sample mull or KBr-pellets.

A rapid method for detecting α-HMX with FT-IR instrument has been established. The analytical technique Diffuse Reflection Fourier Transformation has been used. This technique allows analysis of dry samples with a minimum of preparation. Standards from 0.1 % to 1.0 % α-HMX in β-HMX were mixed and analysed by measuring the absorbance at 714-712 cm^{-1}. The absorbance showed a good linearity with the α-HMX concentration. Repeated measurements show that a concentration down to 0.1 % is detected. The total analysing time for routine samples is 2 min. per sample.

Keywords: HMX, Polymorphs, FTIR

Introduction

The high explosive Cyclotetramethylene-tetranitramine (Octogen, HMX) is known in four polymorphic forms, α, β, γ and δ (1). The β-form is the least sensitive and the most stable form at room temperatures and is used extensively in various military applications. During the nitration process the α-polymorphs is formed and the product therefore needs to be recrystallised to the β-form. The β-HMX is then checked for absence of α-HMX.

Commonly used methods for detection of the α-HMX form have been: X-ray (2), IR (3) and microscopy with polarized light (4). The IR-method was based on a traditional IR instrument (dispersive type) with the sample dispersed in paraffin or in hexachlorobutadiene. The

analytical principle is based on the absorption of energy at 713-715 cm^{-1} (14 μm) for α-HMX. β-HMX has no absorption in this region. The detection limit is only 0.3 % α-HMX with the dispersive type instrument, in addition the preparation method is time consuming and involves chemicals dangerous to health. The FT-IR instrument (Fourier Transform IR) is far more sensitive than the dispersive IR-type and therefore gives the possibility to analyse on dry samples, based on reflection techniques in the same way as for X-ray diffraction. **Figure 1** shows IR-spectra (diffuse reflection) of the two HMX-polymorphs from 1500-400 cm^{-1}. FT-IR compared to X-ray is an easier instrument to handle and has a lower cost. Another benefit of the IR-method is that RDX gives no interference in the α-HMX-analysis.

The purpose of this work was to find the detection limit for α-HMX in β-HMX based on Diffuse Reflection technique.

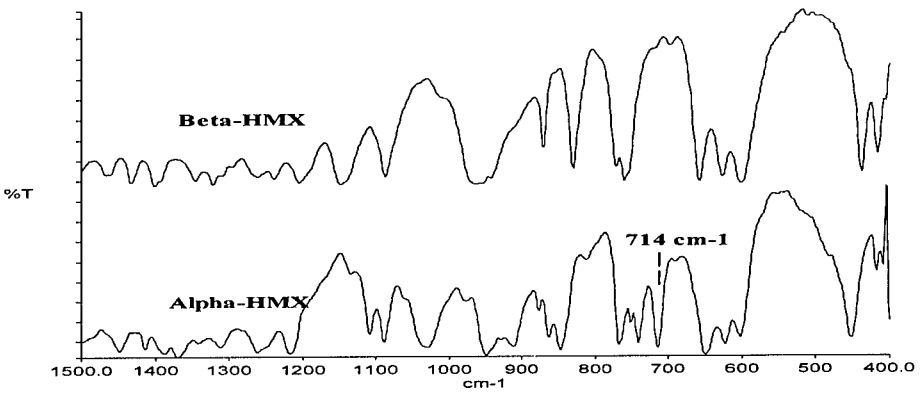

Figure 1. IR-spectra of β-HMX (upper) and α-HMX, diffuse reflection scans.

Experimental

Apparatus

Perkin Elmer model Spectrum 1000 FTIR-instrument.

Sample unit: DRIFT (Diffuse Reflectance Infrared Fourier Transform) unit which is based on reflectance of the IR-beams at the sample surface concurrently with the absorption of energy. The reflected beams are concentrated and directed into the detector.

Sample materials

Potassium Bromide (pa) from Merck, grinded in mortar.

β-HMX, recrystallized at Dyno Defence Products.

α-HMX: Sample taken from nitration process before recrystallization at Dyno Defence Products. Dried and examined in microscope for absence of β-HMX.

Mixing of α-HMX-standards: Weighed quantities of α-HMX and β-HMX was grinded together in a mortar. Following standards were blended: 0.12 %, 0.20 %, 0.28 %, 0.41 %, 0.53 %, 0.72 % and 1.0 % α-HMX in β-HMX.

Sample preparation

The DRIFT sample cup is filled with the sample. The surface is levelled off by tapping the cup gently on the bench, and placed in the holder. The sample surface should not be pressed (as with X-ray diffraction preparations) to avoid specular reflectance. Neither is KBr needed as a sample dilutor. The energy level of the reflected beam is optimised by levelling the cup holder. Scan range may be limited to 730-700 cm^{-1}, number of scans: 10.

Measurement

KBr was first run as a background for pure β-HMX. After running β-HMX and checking for absence of α-HMX, it was run as a new background for the α-HMX standards. **Figure 2** shows the IR-spectra of the smallest and the largest α-HMX standards.

The IR-absorbance at 712-714 cm^{-1} was calculated automatically by the instrument's software. No Kubelka-Munk recalculations were made.

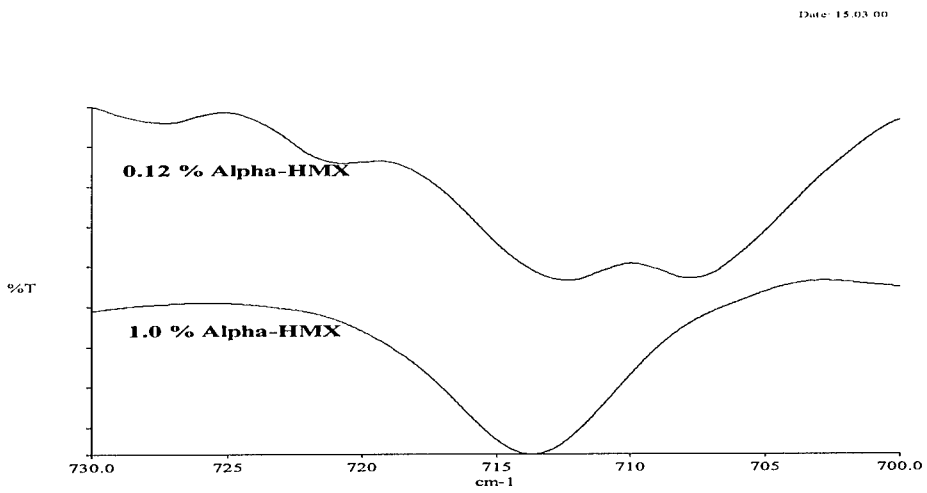

Figure 2. FTIR-spectra of standard mixtures of α-HMX in β-HMX. The IR-absorbance is measured at 712-714 cm^{-1}.

Results

The absorbances of the α-HMX standards:

α-HMX	Absorbance at 712-714 cm^{-1}
0.12 %	0.0027 - 0.0018
0.20 %	0.0032 - 0.0058
0.28 %	0.0089 - 0.0094
0.41 %	0.0146 - 0.0132
0.53 %	0.0159 - 0.0157
0.72 %	0.0229 - 0.0232
1.00 %	0.0301 - 0.0299

The results are presented graphically in **figure 3**.

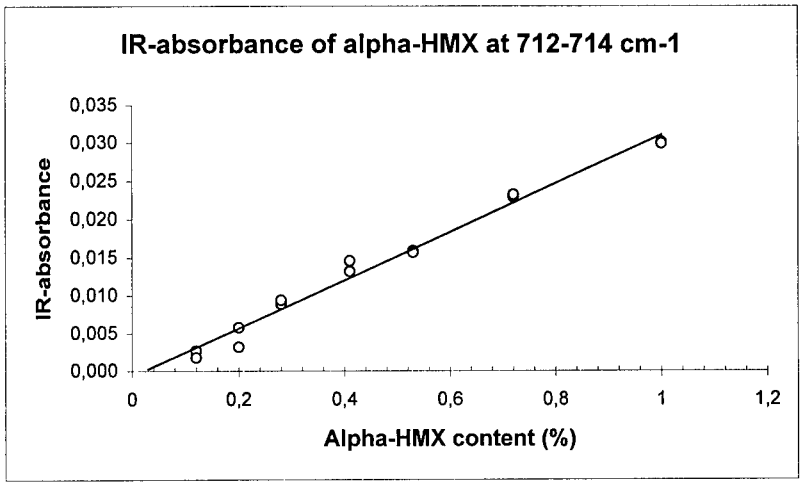

Figure 3 Infrared absorbance of different alpha-HMX mixtures at 712-714 cm^{-1}. Measured with FT-IR instrument and Diffuse Reflectance method.

The correlation between the standards is fairly good (0.98), considering the difficulties of weighing and mixing the samples homogeneously. Generally reflection techniques are not very good quantitative methods. This is, however, not very important in this analysis, since the main task is to *detect* any α-HMX. The results show that it is possible to detect 0.1 % α-HMX, which is the maximum allowed in US-spec. for HMX (2).

Conclusion

The use of Diffuse Reflectance Infrared Fourier Transform technique allows the detection of α-HMX in β-HMX with a detection limit of 0.1 %. The technique is fast and easy to perform and sensitive enough to meet the requirements in HMX-specifications.

Acknowledgements

The participation and assistance of Ms. Trine Granby at Defence Product's R&D-laboratory is gratefully acknowledged.

References

1. Cady, H.H., Smith, L.C.; "Studies on the Polymorphs of HMX", Los Alamos Scientific Laboratory, LAMS-2652, 1962.

2. US military specification MIL-DTL-45444C

3. US military specification MIL-H-45444A

4. Royal Ord. Factory, Ammunition Group (UK), Method No. BM 17

LATTICE IMPERFECTIONS OF HMX MEASURED WITH X-RAY DIFFRACTION

Michael Herrmann, Walter Engel

Fraunhofer Institut für Chemische Technologie / Joseph-von-Fraunhofer-Straße 7
D-76327 Pfinztal / Berghausen

Abstract

Lattice imperfections play an important role in the production and quality assurance of energetic materials, as they influence the mechanical sensitivity. However, their quantitative detection is difficult. Direct methods measure small areas often not representative. Integral methods characterize larger volumes and deliver average values useful for a quantitative detection.

Significant methods are based on the strong effects of lattice imperfections on the diffraction phenomena especially by X-ray diffraction. These methods are well established for metallic materials. Their application to energetic materials could raise problems caused by low symmetries and poor orientation statistics of coarse crystals obtained by usual crystallization procedures. But special preparation techniques as grinding induce defects and sophisticate the characterization of the original crystals.

The detection of micro strain in energetic materials was tested with HMX, one of the most important energetic nitramines. It was crystallized under varying conditions to obtain different defect concentrations. The samples were measured by X-ray diffraction and scanning electron microscopy, and the density and sensitivity of the samples were determined. For reducing the effects of poor orientation statistics on the diffraction patterns, modern X-ray optics combined with a rotating sample holder were tested.

The diffraction data were evaluated by means of a Williamson Hall plot and the micro strain was correlated with crystallization conditions, density and sensitivity.

Monitoring of Nitration Reactions in Microreactors with FTIR Microscopy

W. Schweikert, T. Türcke, S. Löbbecke

Fraunhofer-Institut für Chemische Technologie ICT
P.O. Box 12 40, 76318 Pfinztal, Germany

Introduction

In recent years microreactors have received an increasing interest as useful devices for chemical reactions and processes. In comparison to conventional scales the application of microfluidic devices give the opportunity to change significantly selectivity, product spectrum and yield of chemical syntheses [1].

Up to now, the analysis of products synthezised in microreactors is usually carried out offline by chromatographic and/or spectroscopic techniques. As a consequence, both the evaluation of experimental data and the assessment of the overall reactor performance is relatively time-consuming.

To improve the application of microreactors for chemical processes fast analytical techniques are required allowing a monitoring of the process simultaneously while the reaction is taking place. Such online resp. inline analysis will give an access to an increased through-put and automation of microreactor systems.

Application of FTIR microscopy

This poster shows the application of FTIR microscopy as a fast online analytical tool for the monitoring of nitration reactions carried out in microreactors.

Since many microreactors are based on microstructures made of silicon, infrared spectroscopy is a suitable method to analyse chemical processes within those structures because of the transparency of silicon in the mid-IR spectral range. Furthermore, by applying microscopic techniques it is possible to carry out IR spectroscopic analysis

ensuring a high spatial resolution (≥ 10 µm). As a consequence, educts and products of chemical reactions can be identified and quantified at different positions inside the microreactor. By focusing the IR beam consecutively on different reaction zones, both final products and intermediates of chemical reactions can be IR spectroscopically detected. Hence, the progress of a reaction can be monitored.

Furthermore, the quality of reactant mixing and contacting can be assessed and compared with theoretical approaches, for example arising from CFD simulations (CFD: Computional Fluid Dynamics). Therefore, FTIR microscopy can be a helpful tool for optimizing design and fluidic structures of silicon microreactors.

Setup and exemplary results

The setup of the IR spectroscopic microprocess monitoring is schematically shown in figure 1. The flat silicon microreactor [2] is mounted on a positionable stage and connected with the reactants supply. The reactor can be applied for both gas and liquid phase reactions.

A video camera on the top of the microscope [3] allows a computer controlled viewing and positioning of the reactor. The IR beam can thus be focused on different parts of the microreactor. Furthermore, the video-controlled computer allows a pre-programmed collection of IR spectra along a designated line or even a complete IR spectroscopic mapping of the continuously operating microreaction process.

The nitration of naphthalene with dinitrogen pentoxide was used as a test reaction. From macroscopic batch reactions it is known that - depending on the process conditions applied - a large number of products can be obtained differing in the number and position of their nitro groups (Fig. 2).

By applying continuously operating microreactors short residence times combined with good mass transfer performances are achievable for nitration processes [1,4,5]. Therefore, main nitration products obtained from microreaction experiments were mono- and dinitro naphthalenes in contrast to a significantly broader product spectrum obtained from macroscopic batch reactions containing also tri- and tetranitrated products beside numerous isomers of lower nitrated naphthalenes.

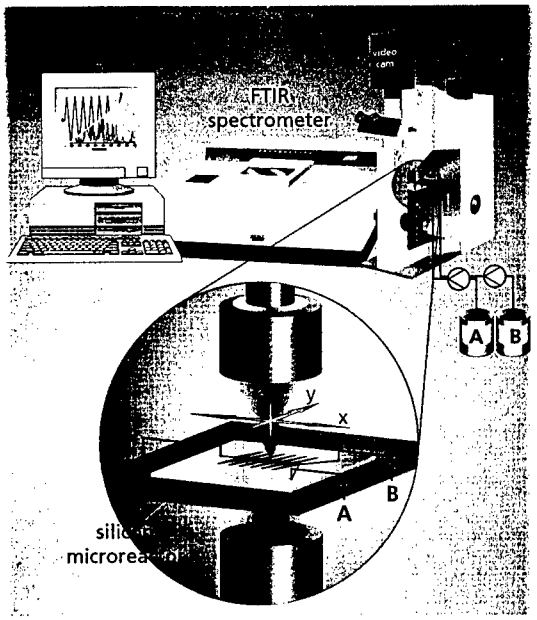

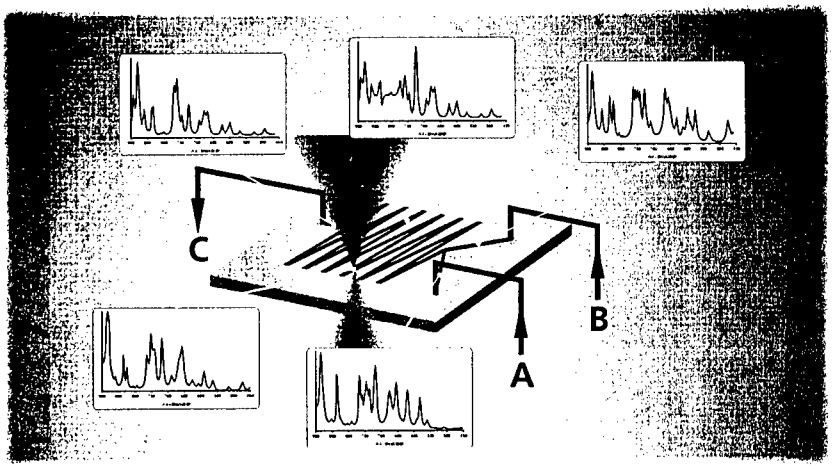

Fig. 1: Scheme of experimental setup for FTIR microscopic monitoring of chemical processes in microreactors

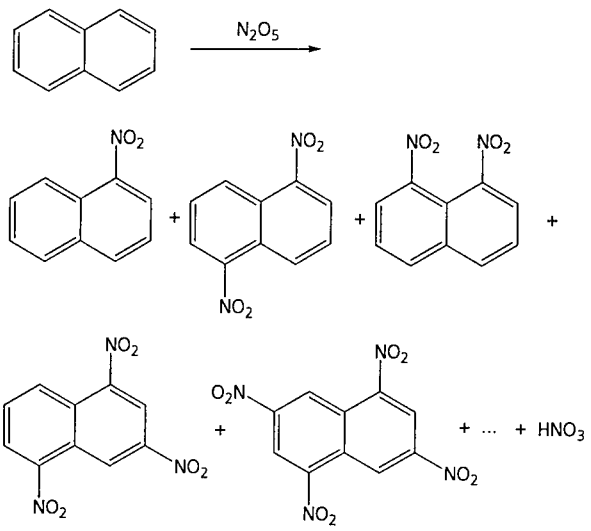

Fig. 2: nitration of naphthalene: possible reaction products

Figure 3 shows as an example IR spectra detected at the entrance and in the center of the microreactor during the continuous nitration of naphthalene. Dichloromethane solutions of naphthalene and dinitrogen pentoxide were mixed in the silicon microreactor by using programmable syringe pumps.

Although solvent, nitrating agent, educt and product(s) are all IR active substances causing a large number of, partly overlapping, absorption bands in the IR spectral range 1,5-dinitro naphthalene could be IR spectroscopically identified as the favoured reaction product. The selective production of the dinitro isomere could be also confirmed by conventional offline analytical methods (HPLC and GC-MS).

Beside identification of reaction products FTIR microscopy permits also semi-quantitative information about the reaction progress by means of absorption band intensities measured at different positions inside the reactor structure. The fast kinetics of the nitration reaction can be realized by the weak absorption bands of 1,5-dinitro naphthalene detected already after the first contact of the educts at the reactor entrance.

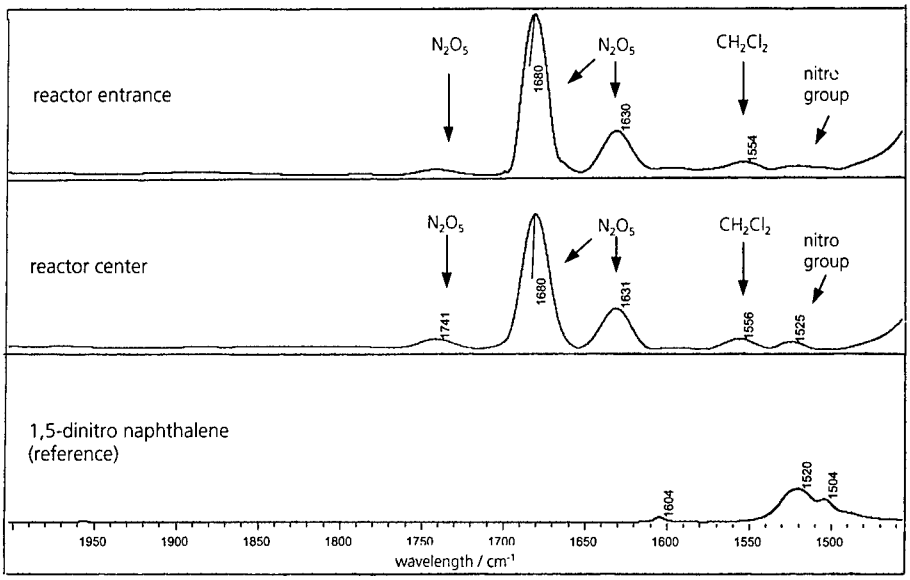

Fig. 3: IR spectroscopic detection of the reaction product 1,5 dinitro naphthalene inside of the silicon microreactor

Conclusions

The feasibility of applying FTIR microscopy for the monitoring of chemical reactions inside of silicon microreactors was proved. This technique allows the identification of reaction products besides educts and solvents with a high spatial resolution. The progress of chemical processes can thus be investigated on very small dimensions.

References and annotations

1 see also V 33 in this proceedings

2 manufactured by the Technical University of Ilmenau, Germany

3 Nicolet Magna-IR 750 spectrometer with NIC-Plan IR microscope

4 J.R. Burns, C. Ramshaw, P. Harston, 2nd Int. Conference on Microreaction Technology (IMRET 2), 8-12 March 1998, New Orleans, USA

5 J. Antes, T. Türcke, E. Marioth, K. Schmid, H. Krause, S. Löbbecke, 4th Int. Conference on Microreaction Technology (IMRET 4) , 5-9 March 2000, Atlanta, GA, USA

IR Spectroscopic Analysis of Energetic Materials Dissolved in Highly Compressed Gases

S. Panić, W. Schweikert, H. Krause, S. Löbbecke

Fraunhofer-Institut für Chemische Technologie ICT
P.O. Box 12 40, 76318 Pfinztal, Germany

Introduction

In recent years the development of processes using highly compressed gases, especially sub- and supercritical CO_2, have risen to a mayor research-field. These developments have led to a large number of applications, particularly in food, pharmaceutical and textile industries. Due to its chemical inertness and inflammablity compressed CO_2 is an interesting solvent for research on energetic materials, as well. A lot of investigations focusing on particle formation processes and supercritical fluid extractions (SFE) of energetic materials already exist. Current research is focusing more on the advantages of compressed CO_2 as a solvent for reactions so that CO_2 may serve in future as a serious substitute for conventional organic solvents. Especially in processes involving energetic materials the use of compressed CO_2 may prevent or minimize the risk of serious harm or damage. To control and monitor such processes analytical techniques are highly required.

In this work a measuring device is presented, which allows the FTIR spectroscopic on-line detection of substances dissolved in compressed CO_2 by applying a so-called high-pressure "Lightpipe" cell. This device provides a comfortable monitoring, controlling and regulation of high-pressure processes as they proceed.

Experimental setup

The centerpiece of the experimental setup applied in this study is a specially developed optical high-pressure cell ("Lightpipe") which permits IR spectroscopic investigations at pressures up to 250 bar and temperatures up to 100°C (Fig. 1). The lightpipe consists of

a 150 mm glass capillary with golden insert positioned in a heatable high pressure housing. Two optical windows made of zinc selenide are mounted on each side of the capillary to use the lightpipe cell for transmission spectroscopic measurements.

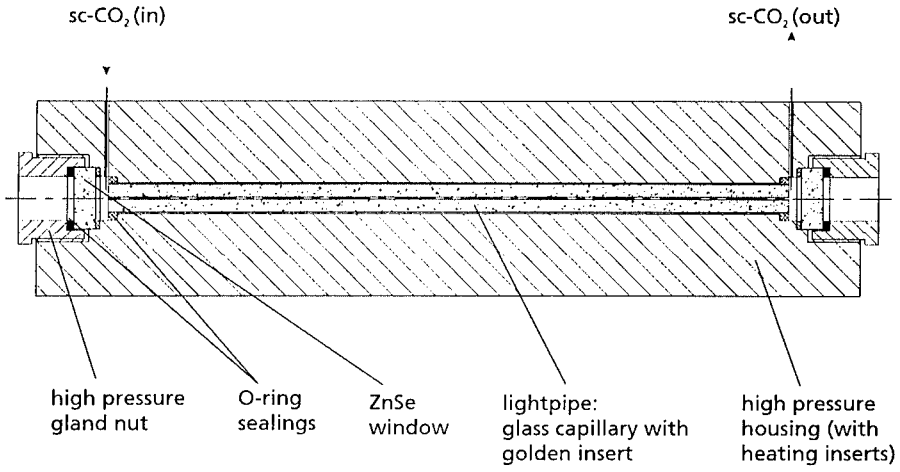

Fig. 1 "Lightpipe" - high pressure optical cell for IR spectroscopy

The Lightpipe is positioned in a specific GC-interface for FTIR spectrometers (here: Nicolet 60 SX). The GC interface is directly connected with the high pressure process which supplies solutions of energetic materials in compressed CO_2. Figure 2 shows how the IR beam is passed through the lightpipe to the detector of the spectrometer using different mirrors and lenses.

In this work all measurements were made under static conditions, but in principal, the optical high-pressure cell could be also used for investigations under dynamic process conditions.

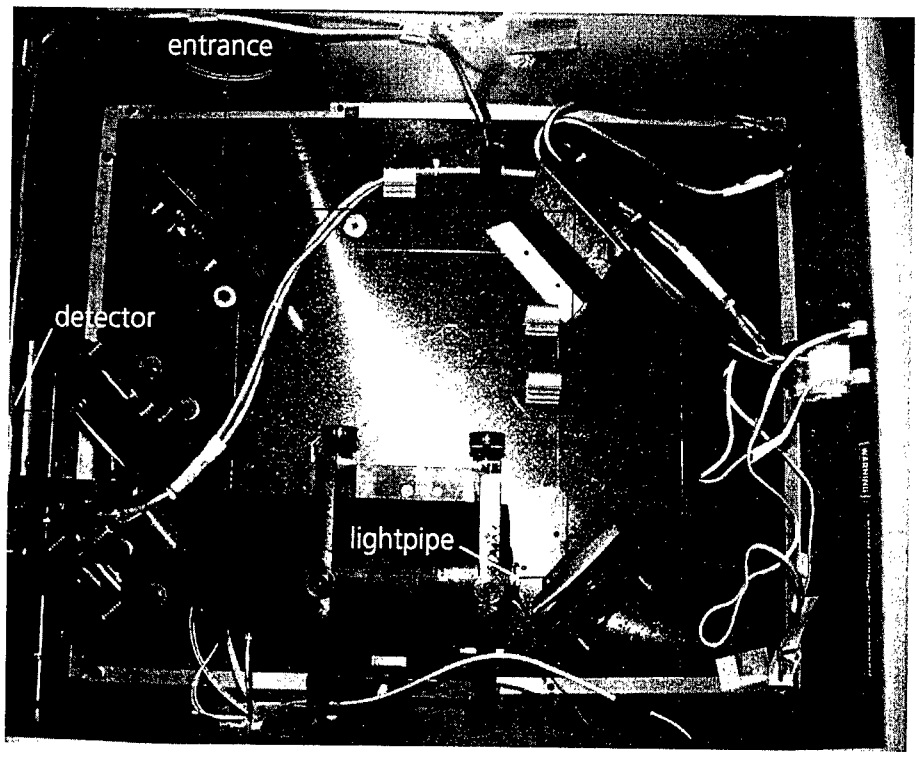

Fig. 2 optical setup for IR Lightpipe experiments

Exemplary results

The IR spectroscopic behavior of pure compressed CO_2 was systematically investigated at a constant temperature of 70°C and pressures varied between 80 and 200 bar. Figure 3 shows the individual IR absorption bands of pure CO_2. By applying the high pressure lightpipe cell the broadening of these absorption bands can be significantly reduced in comparison to conventional transmission cells. Therefore, even at high pressures spectral windows are remaining in the IR spectral range which make the detection of analytes dissolved in CO_2 possible, whenever their specific absorption bands are located in the spectral windows of the solvent.

To demonstrate the feasibility of detecting energetic materials being dissolved in compressed CO_2 IR spectroscopically, two series of measurements were performed using TNT and CL 20 as model compounds.

For these measurements a heated and stirred vessel, which contained a surplus amount of TNT and CL 20 respectively, was integrated in the high pressure CO_2 supply system. The vessel was pressurized for approximately 30 minutes before dissolved TNT resp. CL 20 was passed to the lightpipe cell.

Figure 4 and 5 show the detection of TNT and CL 20, respectively, by means of their typical NO_2 absorption bands (TNT at 1560 cm^{-1}; CL20 at 1605 cm^{-1}). Due to increasing solubility of the solutes the NO_2 bands are becoming more intensive with increasing pressure. (For comparison, spectra of pure compounds are shown as well.)

Conclusions

This work shows the successful application of an optical high pressure lightpipe cell as an analytical tool for detecting energetic materials dissolved in compressed CO_2.

The successful application of this measurement device depends on following conditions:

1. Analytes must have a sufficient solubility in compressed CO_2, or even in other compressed gases.
2. Their specific IR absorption bands must be located in spectral ranges where the solvent (here: compressed CO_2) is not IR active (no individual absorption bands).

These conditions are fulfilled by a large number of energetic materials since many of them have NO_2 groups, which are detectable within the spectral windows of CO_2. Furthermore, many of them are non- or less polar substances thus possessing a sufficient solubility in the non-polar solvent CO_2.

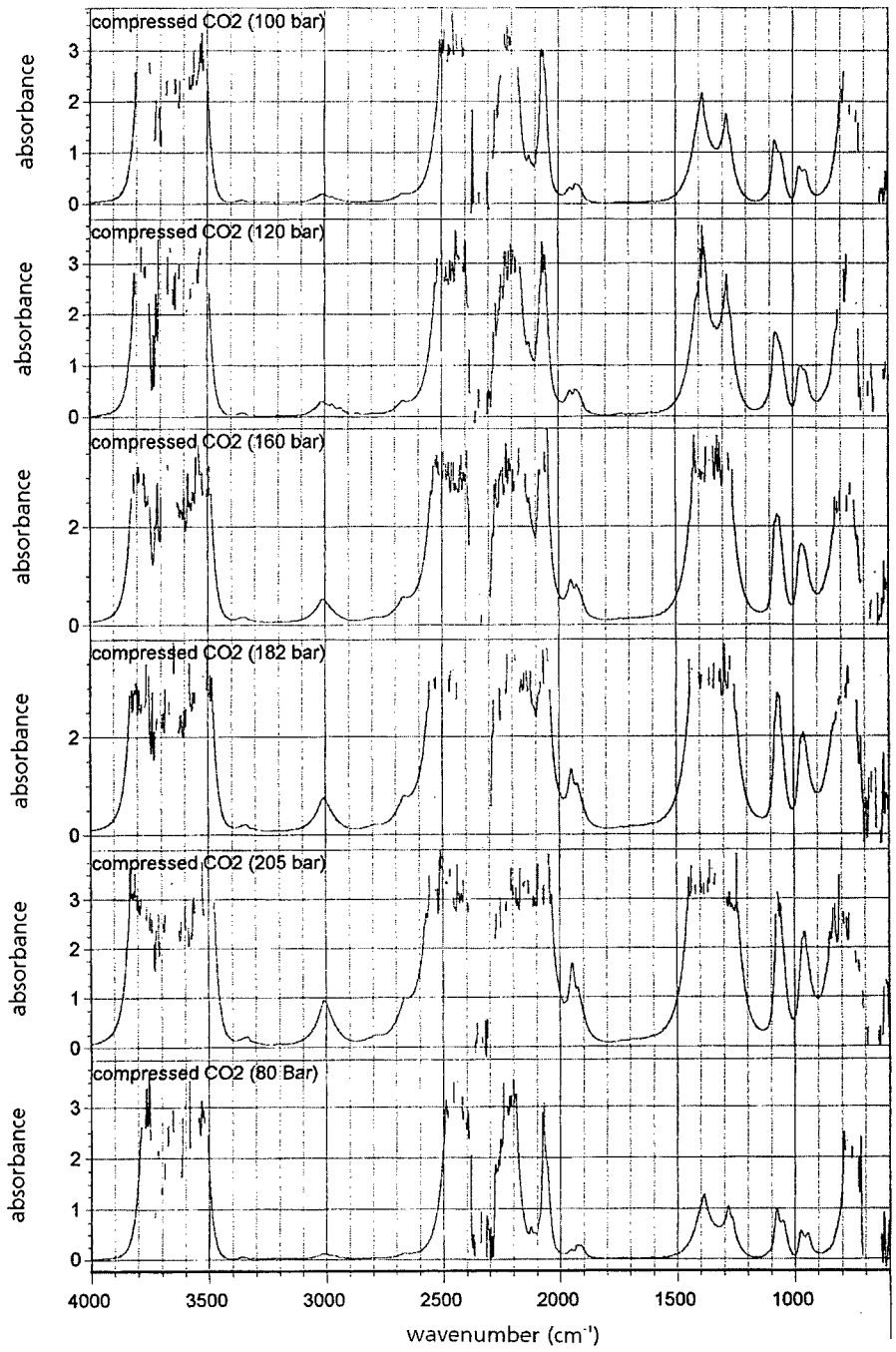

Fig. 3 spectra of compressed CO_2 at different pressures (T = 70°C)

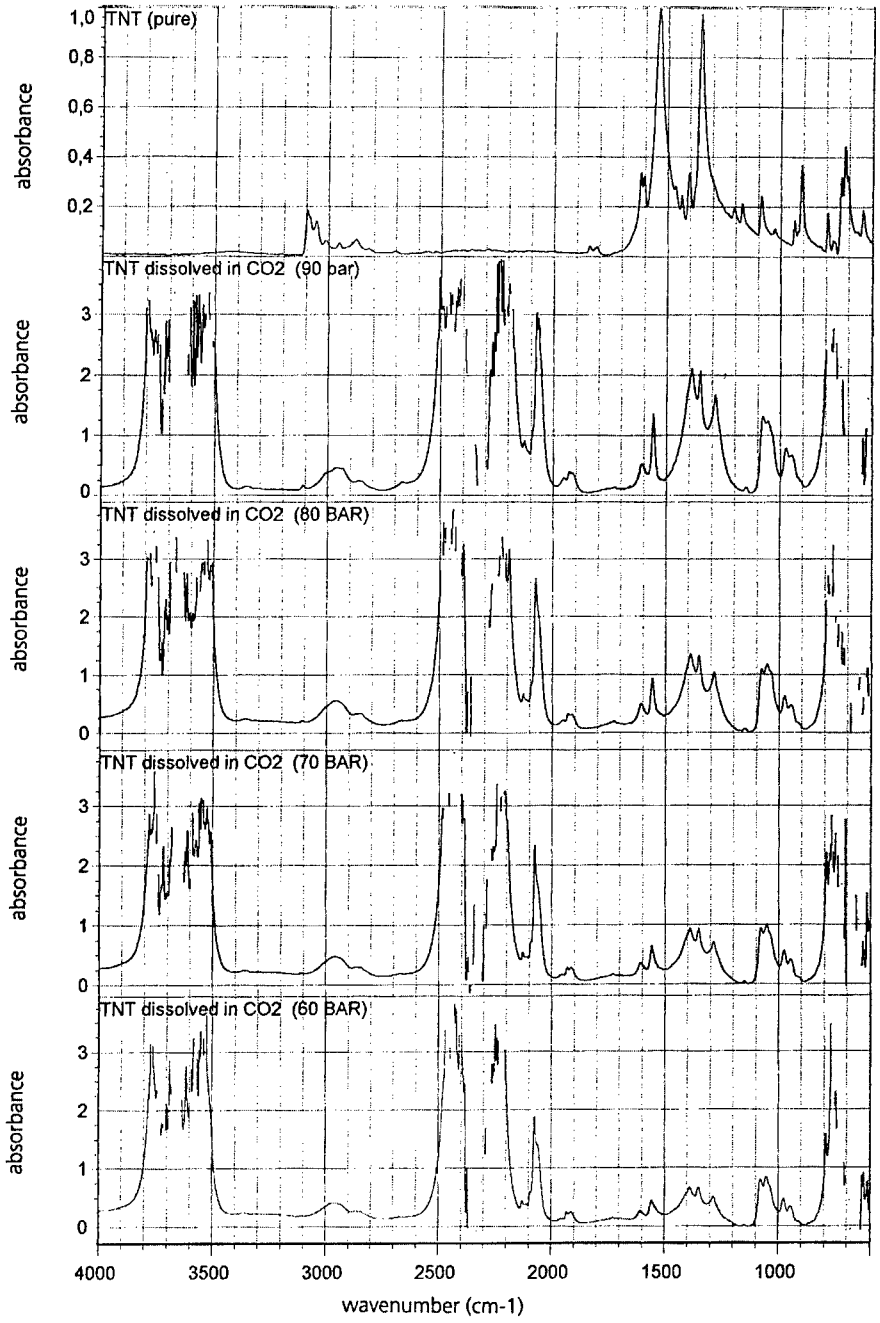

Fig. 4 spectra of TNT dissolved in compressed CO_2 (T = 70°C)

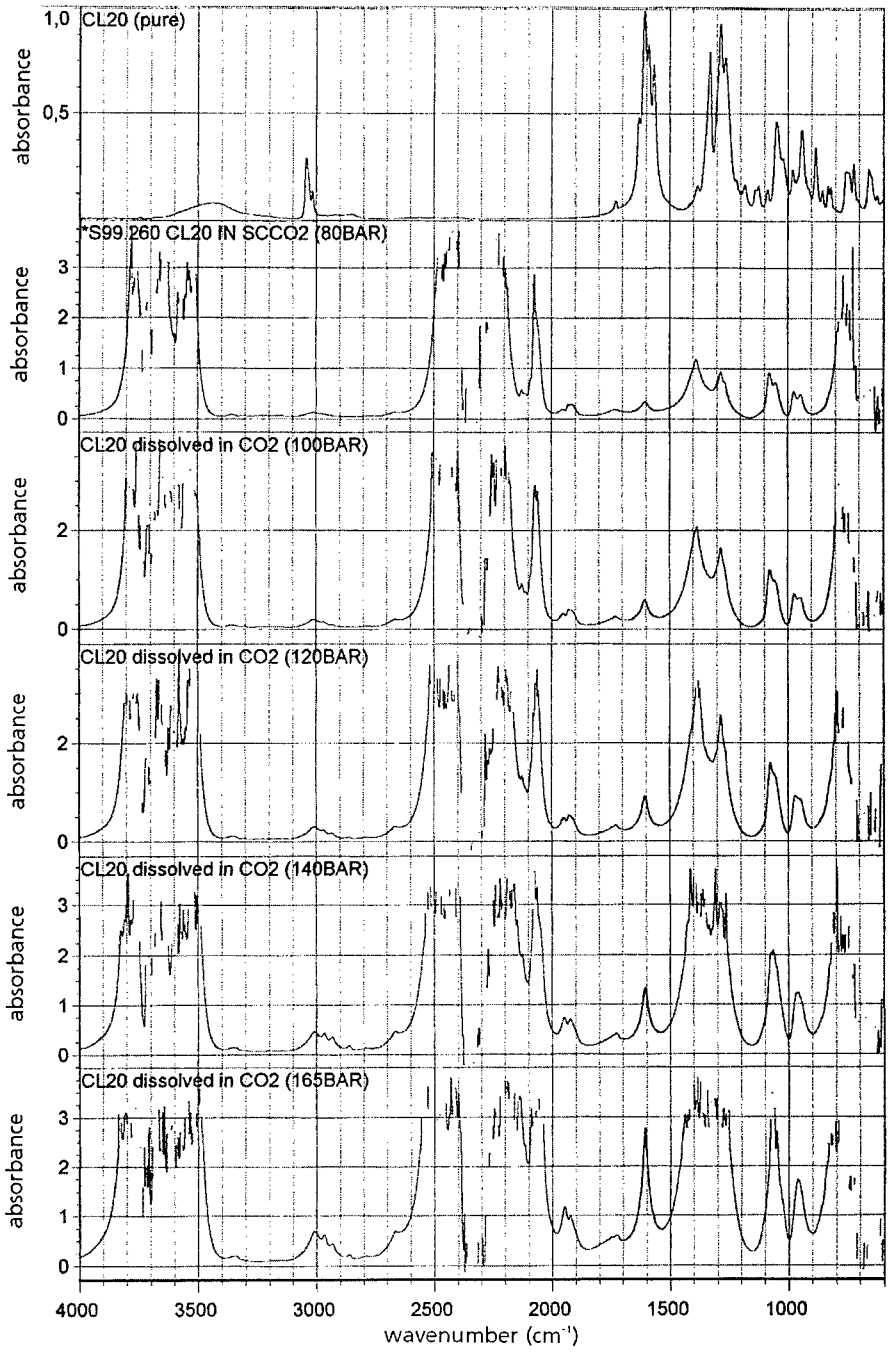

Fig. 5 spectra of CL20 dissolved in compressed CO_2 (T = 70°C)

MECHANICAL CHARACTERISATION OF ENERGETIC MATERIALS BY APPLYING WLF THEORY

Gaynor M. Kavanagh, David A. Tod & John. Theobald

DERA, Fort Halstead, Sevenoaks, Kent, TN14 7BP, UK

ABSTRACT

Dynamic Mechanical analysis has been shown to be a very efficient method of mechanical assessment. It is generally used to provide a reference point by which ageing trends can be established. A further use of this technique is to determine the time-temperature superposition of energetic materials. This relationship is an essential requirement for various analysis codes such as finite element analysis. The use of DMA as opposed to tensile data would be a very significant cost saving in terms of time and material.

Unaged and aged energetic materials were selected and tested using dynamic mechanical analysis (DMA) experiments. Master curves were produced from this data by applying the WLF theory. A comparison was made with the current methodology obtained following Stanag 4540. The advantages and disadvantages of the two methods were contrasted.

Keywords:

Dynamic mechanical analysis (DMA)

WLF

Stanag 4540

Abstract for 31st International Annual Conference of ICT

Effects of Surface Interactions on the Mechanical Properties of PBXs : Part I. Surface Free Energy of Solids

Hyoun-Soo Kim, Jung-Seob Shim, Keun-Deuk Lee and Bang-Sam Park

Agency for Defense Development (ADD)
Yuseung P.O.Box 35-5, Taejon, Korea

Plastic bonded explosive(PBX) is mainly composed of the nitramine explosives, RDX and HMX, and polymer binders. PBX is characterized by high velocity and pressure of detonation, low vulnerability and good thermal stability. Many important applications of PBX require the good adhesion between nitramine crystals and the binder. For PBXs as well as propellants, where good mechanical properties are of great importance, dewetting therefore must be prevented by strong adhesion between filler-binder. Adhesion depends on surface characteristics of filler and binder. In order to design for better adhesion, an understanding of te surface properties of solid is required. Surface free energy determined from wettability data is a proper method to described the properties of a solid surface. The surface free energy of solids cannot be measured directly. So the contact angles of filler and binders are measured by Wilhelmy plate method or wicking method. And then the surface free energies are calculated from contact angle values by the method of Kaelble. Critical surface tension of solids are calculated by Zisman plot. Critical surface tension is a useful parameter for characterizing the wettability of solid surface. In this study, RDX and 5 kinds of ethylene vinyl acetate copolymers are selected, since they are widely used in many plastic bonded explosives. The technical objective of this investigation is to predict the interaction between filler and binder from their surface free energies.

Key Words : PBX, Surface free energy, Mechanical property

STUDY ON THE LOW TEMPERATURE(-40℃) MECHANICAL PROPERTIES OF HIGH BURNING-RATE HTPB PROPELLANTS (Ⅱ) DESIGN AND APPLICATION OF THE SURFACTANTS

Du Lei
The Fourth Academy CASC
P.O. Box 120, Xian 710025
P.R.China

Xiao Jinwu Yin Ruikang
HuBei Redstar Chemical Institute
P.O. Box 156, Xiangfan, 441003
HuBei, P.R.China

ABSTRACT

This paper focuses the research on improving the low temperature(-40℃) mechanical properties(LTMP) and processing properties of propellant with high content of fine AP based on HTPB/IPDI. Samples used in this study are the propellant with a solid content of 83%, weight of which fraction 42% is fine AP which particle size is about 5μm. The burning-rate of the propellant is about 35mm/s at the combustion pressure of 7MPa.

New multi-functional surfactants are designed, synthesized and used to improve the LTMP and processing properties. The experimental results indicate that these new surfactants are of high efficiency and the maximum elongation of experimental propellants at -40℃ increase distinctly from about 40% to 50～70%. The dynamic mechanical analysis (DMA) and the diffuse reflection infrared(DRIR) spectral analyze are used to study the action mechanism.

1 INTRODUCTION

It is a common knowledge that the mechanical property is one of the most important properties of propellants. For improving the mechanical properties, A.E.Oberth[1] advanced the three design principles of bonding agents early, C.S.Kim[2] put forward the method how to design neutral polymeric bonding agents lately, which provided theoretical direction for choice and synthesis of bonding agents. In common high burning-rate HTPB propellants, fine AP is filled in a higher content. It results in poorer processability and mechanical property at low temperature. Thus researchers turn to seek for processing aid to improve processability. PA-2 was a high efficient processing aid. But it led to worsen mechanical property at -40℃. In our work early[3], we studied the influences of the content of fine AP and processing aid PA-2 on LTMP, and came to the significant conclusions. In this paper, we investigate the design

principles of surfactants and try to raise the maximum elongation at -40℃ of propellant with high content fine AP based on HTPB/IPDI as well as improve the processing properties.

2 EXPERIMENT

2.1 Material

Samples used in this study are HTPB/IPDI propellant with a solid content of 83%, among which 42% is fine AP, whose particle size is about 5 μ m, 25% is coarse AP with particle size about 230 μ m, and 15% is aluminum powder. The burning rate is about 35mm/s at the pressure of 7MPa in combustion chamber.

The propellant was processed with a standard procedure described in literature everywhere, and then cured 7 days at 70℃. The cured propellant was prepared mechanically into specimens according to standard JANNAF and stored in a desiccate for use.

2.2 Measurements

The uniaxile tensile test was conducted with Instron (JINDAO IM100) according to the standard described in literature everywhere. The dynamic mechanical analysis (DMA), model 7000 (Perkin-Elmer, USA) was used at 1HZ in disc. compression, the test temperature ranged from -100 to 100℃ at the heating rate 1℃/min. The Diffuse Reflection Infrared (DRIR) spectral analysis used NICOLET-170SX Fourier transfer infrared instrument with diffuse reflection platform HARRICK-1.

3 DESIGNING PRINCIPLE OF SURFACTANTS

In consideration of the new interface features of propellant with high content of fine AP, according to the basic requirements of rheology and the fundamental physical-chemistry of filler/binder interface, the design principles of surfactants molecule are advanced as follows:

i) For good LTMP, the designed surfactants, in addition to following the design principles of bonding agent advanced early by A.E.Oberth[1], should have good flexibility, moderate content of polar groups and suitable acid-base property, which ensure to form an interface layer with good flexibility and fairly toughness between filler and matrix, and effectively to restrain the stress concentration in the course of uniaxile tensile test at low temperature, and make sure that after reacting with AP, there are enough reacting capacity with curing agent to form a effective chemical bond.

ii) In order to improve the processing properties, the surface tension matched principle (STMP) is proposed to design surfactants for propellant.

According to the STMP, once the surfactants adhere to the surface of filler, a new liquid/liquid interface will be formed between adhesive layer and HTPB binder. If surface tension

of a surfactant and solubility index are matched with or close to that of binder, there is not liquid/liquid interface to form. The filler with adhesive layer of surfactants will be easy to disperse in binder. Therefore, the surfactants should change the surface tension of filler and make the surface tension match with or close to that of binder.

The surface tension γ of organic compounds can be calculated by isotonic specify volume[4].

$$\gamma = (P_s / V)^4 \quad \text{.....(1)}$$

Where P_s is isotonic specific volume and V is molar volume.

The approach of Lee Lienghuang can be used to calculate the surface tension γ of polymer with end groups[5].

$$\gamma^{1/4} = \gamma_R^{1/4} + \frac{2K}{m+2K} \cdot (\gamma_E^{1/4} - \gamma_R^{1/4}) \quad \text{.....(2)}$$

Where γ_R is the surface tension of repeated unit in polymer structure, γ_E is the surface tension of end group of polymer, m is the number of repeated unite, and $k=V_E/V_R$, wherein, V_E is the molar volume of end group, V_R the molar volume of repeated unit in polymer, V_E and V_R are calculated by addition of molar volume values contributed by groups in polymer[4], γ_E adopted the surface tension value of the hydroxyl terminated group provided by literature[5].

New multi-functional surfactants, AO-1,,AO-2 and AO-3, are designed and synthesized according to the principles mentioned above. All of these three surfactants are more flexible molecular structure than the used processing aid PA-2. The basicity, the polar groups content and the surface tension values reduce gradually from PA-2, AO-1, AO-2 to AO-3. Herein, the surface tension values of PA-2 and AO-1 are closest to that of the binder HTPB. The surface tension values of several substances are calculated and list in table 1.

Table 1 Surface tension value calculated of several substances

Compound	Surface tension value , dyn/cm
HTPB	42.29
PA-2	42.01
AO-1	38.67
AO-2	37.27
AO-3	35.81

4 RESULTS

4.1 The efficiency of new surfactants

In this section, the propellants were of similar formulation, differing only in the kinds of surfactants. The result of uniaxile tensile test is shown in table 2.

Table 2 mechanical properties of propellant with new surfactants

Absolute Humidity $G_{water}/kg_{dry\ air}$	surfactant	Mechanical Properties	
		25℃,R=100mm/s	-40℃,R=100mm/s
		σ m,MPa/ ε m,%/ ε b,%	σ m,MPa/ ε m,%/ ε b,%
11.8	AO-3	0.90/73.7/89.3	2.98/73.5/85.1
11.8	AO-3	0.95/76.9/88.5	2.71/71.3/81.2
19.1	AO-3	1.10/69.8/82.0	2.50/63.3/77.7
15.2	AO-3	0.96/74.9/87.7	2.78/67.3/84.3
23.0	AO-3	0.94/84.3/96.5	2.83/69.4/84.4
4.30	AO-2	1.08/67.7/75.9	2.53/58.2/68.7
11.8	AO-2	1.03/66.7/73.9	3.09/62.7/76.5
11.8	AO-2	1.00/70.6/80.9	3.13/73.1/84.3
4.30	AO-1	1.19/62.4/65.0	3.08/56.0/70.6
9.60	AO-1	1.17/67.1/76.6	3.12/62.7/71.4
19.4	AO-1	1.36/65.3/71.7	3.00/64.6/75.1
21.5	AO-1	—	2.56/59.1/80.4
4.3	PA-2	0.98/59.8/68.9	3.05/43.4/63.0
4.5	PA-2	1.17/59.7/64.7	3.27/39.3/59.3
15.2	PA-2	1.25/57.8/65.9	3.02/32.8/53.4

From table 2, it is easy to find that the new surfactants are of high efficacy and the maximum elongation at -40℃ increase distinctly from about 40% to 60%, and even if on the condition of high humidity (> 22gwater/kgdry air), the maximum elongation can keep at 60% or more.

4.2 The results of DMA

Fig.1 give the DMA spectrogram of propellant specimens incorporated with PA-2 or AO-3.

Table 3 DMA results of propellant

Surfactant	Tg_{β},℃	$\tan\delta_{\beta}$	T_{α},℃	$\tan\delta_{\alpha}$
PA-2	-79.7	0.2992	5.10	0.3347
AO-3	-79.7	0.3076	22.5	0.4407

The results shown in table 3 indicate that the $\tan\delta_m$ and T_g of propellant specimens with AO-3 is higher than that with PA-2.

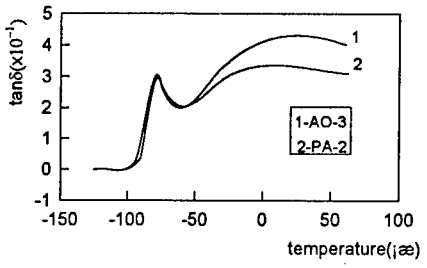

Fig.1 DMA spectrogram of propellant with different surfacants

4.3 Results of the DRIR

The results of the DRIR are shown in figure 2, wherein figure 2A stands for the reactor of AP and PA-2, figure 2B notes to the reactor of AP and AO-3, figure 2C for the reactor of AP+PA-2 and IPDI, and figure 2D for the reactor of AP+AO-3 and IPDI.

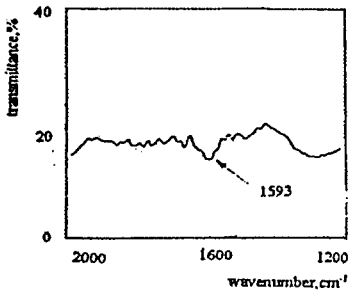

Fig.2A Reactor of PA-2/AP

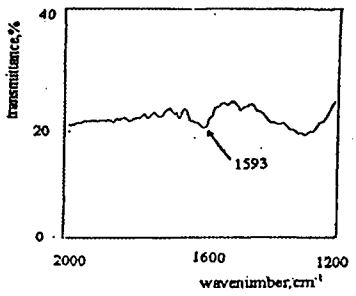

Fig.2B Reactor of AO-3/AP

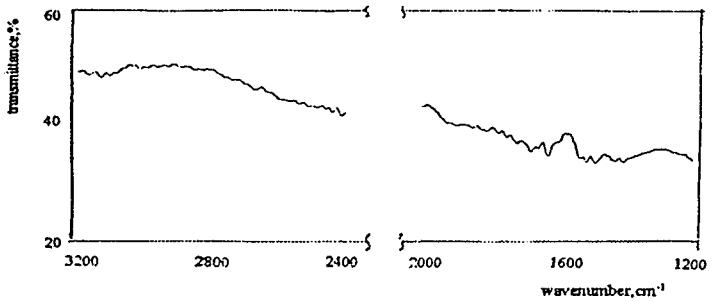

Fig.2C Reactor of (AP+PA-2)/IPDI

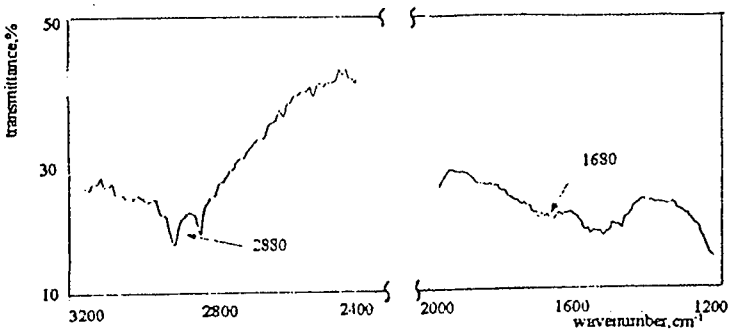

Fig.2D Reactor of (AP+AO-3)/IPDI

Fig.2 DRIR differential spectral

In figure 2A and 2B, there are new peaks in 1593cm^{-1}, which indicates that PA-2 and AO-3 have covered on the surface of AP by chemical reaction.

Figure 2C shows that there is no new peak, which states clearly that the reactor of PA-2 and AP is failure to react with IPDI.

In figure 2D, two new peaks appear, one in 2880cm^{-1}, the other in 1680cm^{-1}. The former stands for the stretch vibration of C-H of IPDI, and the later notes to the stretch vibration of -NC (O)-N- produced by the reaction of AO-3 with IPDI. DRIR spectra indicate that indicate that the reactor of AO-3 and AP can continue to react to IPDI.

4.4 Effect of new surfactants on processing properties

At 50℃, the initial viscosity, yield value of propellant slurry with different surfactants are measured by Harker viscometer. The test results are shown in table 4. Wherein the initial viscosity was measured at 50℃, shear velocity γ =1m/s. The pot-life of the propellant slurry with surfactants was given by the Falling Ball Viscometer measurement. Fig.3 shows the curves of viscosity value vs. Time.

Table 4 effect of new surfactants on processing properties

Surfactant	$\eta_{50℃}$,Pa•s(γ =1m/s)	$\tau_{y50℃}$,Pa
PA-2	395.2	34.8
AO-1	527.4	91.0
AO-3	771.0	257.4

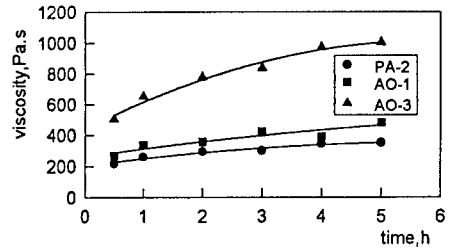

Figure 3 curves of propellant with different surfacants viscosity vs. time

From table 4 and figure 3, we can see:

i) The initial viscosity and the growth of viscosity value of propellant slurry with new surfactants is slow, the fluidity of propellant slurry is excellent;

ii) The viscosity values and yield values increase gradually from PA-2, AO-1 to AO-3, which is well correspondent with surface tension aforementioned (see table 1). Clearly, the more matched the surface tension of surfactants with that of HTPB, the better the rheological properties of propellant slurry.

5 DISCUSSION

5.1 Analysis of new surfactants improving LTMP

a. Improving the bonding strength of interface

As is well known, once the bonding strength of interface of filler/matrix is too low to afford the stress created by stress concentration, the dewetting will occur in the course of uniaxile tensile test. The secondary bond force, for example, H-bond action and Van der Waals attraction, makes the modulue of matrix and bulk strength of propellant increases greatly at low temperature (-40℃), it aggravates the dewetting. Therefore it is necessary to improve the LTMP to increase the bonding strength of interface of filler/matrix. The results of DMA show that tan δ α of propellant with AO-3 is higher than that with PA-2 (see table 3), which indicate that the bonding strength is increased[6]. Moreover, the results of DRIR (see figure 2) state clearly that PA-2 improves bonding properties by physical adhesion while AO-3 improves the interface properties by effective chemical bond.

b. Inhibiting effectively the stress concentration

According to the results of stress field analysis by A.E.Oberth[1], the stress concentration is the strongest in the direction of the applied load slightly away from the surface of filler. Fig.10 illustrates the interface microstructure of filler/matrix. Region D is the interface of bonding agent/matrix.

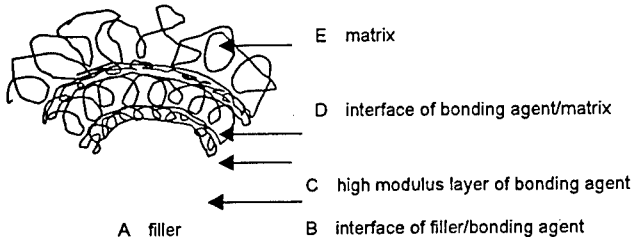

Figure 4 Diagrammatic sketch of filler/matrix interface microstructure

In region D, if there is a strong enough and quite flexible molecular layer, it will constrain effectively stress concentration in the course of uniaxile tensile.

In the three surfactants, there are long flexible side chains, which play important roles. The first is to increase the bonding strength. The second is to form a tough interface with high modulus on the surface of AP.

The flexible side chains can weaken the hindrance of the polar interface to the movement of matrix main chains and increase the flexibility of matrix. As has been mentioned above, it is an effective method for improving LTMP of HTPB/IPDI with high AP content.

5.2 Analysis of new surfactants improving the processing properties

The test results of viscosity aforementioned indicated that the more matched the surface tension of surfactants with that of HTPB, the better the processing properties of propellant slurry.

A brief discussion on the reason are had as follows:

In the view of surface chemistry, a necessary condition of AP infiltrated by HTPB is $\gamma_{AP}^{d} > \gamma_{HTPB}$[7]. Uncovered AP is hydrophilic, it is easy to form a thin film of water on the surface of AP. The dispersed surface tension section of AP, γ_{AP}^{d}, is contributed by that of water, 22dyn/cm, which is far less than that of HTPB, 42.39dyn/cm. Therefore the adhesion of HTPB on the surface of AP is poor. It is hard for AP fillers to disperse in HTPB well, which causes the bad processing properties. The three surfactants do change the surface tension of AP and make it matched with that of the bind HTPB. As a result, they improve the processing properties of propellant.

6 CONCLUSION

6.1 New surfactants are of high efficiency in improving maximum elongation of experimental propellants at -40℃ distinctly from about 40% to 50～70%. The reproducibility of LTMP is good and the environmental humidity has few effects on the results.

6.2 The test results reveal that the new surfactants work well by means of improving the bonding properties of filler/matrix interface and restraining the stress concentration around the filler in the course of uniaxile tensile test. Good flexibility, moderate content of groups and suitable acid-base property are of great advantage to improve the LTMP of HTPB/IPDI propellants with high content of AP.

6.3 Surface tension matched principle is applied to molecular design of propellant aids. The rheological properties state clearly that the more matched the surface tension value of surfactants and that of HTPB is, the better the processing properties of propellant slurry, which confirm experimental the validity of the STMP put forward in this paper

REFERENCES

[1] A.E.Oberth, Principle of Strength Reinforcement in Filled Rubber, Rubber chem. technol. 40(5), 1337(1967).

[2] C.S.Kim, The Mechanism of Filler Reinforcement from Addition of Neutral Polymeric Bonding Agents to Energetic Polar Propellants, Propellants, Explosives, Pyrotechnics, 17,51 ~58(1992).

[3] Xiao Jinwu, Study on Improving The Low Temperature(-40℃) Mechanical Properties of HTPB/IPDI Propellant With High Burning-rate, Master's degree thesis of Hubei Redstar Chemical Institute,1995.4

[4] Osborne R.Quayle,Chem. Rev.,53,439(1953).

[5] Lienghuang Lee, Adhesion and Adsorption of Polymers, 1979, Symposium on Adhesion and Adsorption of Polymers, p15(1979).

[6] DuLei, PengSong and Wang Hongfan, Accelerated Aging Study of strained HTPB propellant by mechanical Measurements,

[7] Zhang Jinchun, The chemistry and Process of solid propellant, p142 (1987) and Process of solid propellant, p142 (1987)

HYDROXYFURAZANS: Outlook to using.

Aleksei B. Sheremetev,* Elena V. Mantseva, Nataly S. Aleksandrova,

Igor L. Yudin, Tatyana S. Novikova

N.D.Zelinsky Institute of Organic Chemistry, Russian Academy of Sciences, 47, Leninsky Prosp., 117913 Moscow, RUSSIA
Fax: +7 (095) 135 5328, E.mail: sab@ioc.ac.ru

Efforts directed toward the synthesis of energetic materials utilizing hydroxyfurazans as the major building blocks are described. The main emphasis on the program is on the synthesis of hydroxyfurazan salts and furazanic ethers.

Key words: furazans, hydroxyfurazans, furazanic ethers, hydroxyfurazan salts

Furazans bearing *O*-bridged substituents have attracted considerable attention, with examples including linear 3,3'-dinitrodifurazanyl ether (**FOF-1**)[1,2], bis-3,3'-(nitro-*NNO*-azoxy)-difurazanyl ether (**FOF-9**)[3], bis-3,3'-(1-fluoro-1,1-dinitromethyl)-difurazanyl ether (**FOF-13**)[4], cyclic ether (**FOF-7**)[5], and others[6-9].

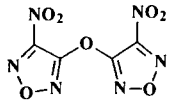

FOF-1 ($C_4N_6O_7$)

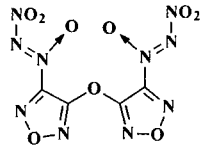

FOF-9 ($C_4N_{10}O_9$)

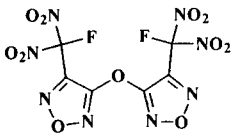

FOF-13 ($C_6F_2N_8O_{11}$)

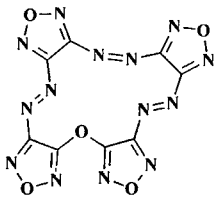

FOF-7 ($C_8N_{14}O_5$)

Many of them possess very attractive performance and are potential candidates as ingredients in castable high energetic compositions. For example, **FOF-1** has received extensive synthetic research in the Russian explosive synthesis community for more than 15 years. The low-melting material has energy content and density slightly higher than those of **TNAZ**.

In addition to continuing efforts in preparing higher performance materials for military and space application, recent research in energetic compounds at our laboratory was focused on less sensitive high explosives and propellant ingredients.

A potentially interesting class of compounds, analogs to **NTO**, which the predictive techniques suggest as being dense and energetic is hydroxyfurazans. Moreover, these compounds are building blocks for construction of a set of other explosives. In particular, we were interested in the unsymmetrical derivatives of furazanyl ethers.

We have prepared a large number of hydroxyfurazans[10,11] for preliminary evaluation. Some of the more energetic examples are shown below:

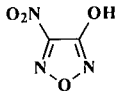

HNF ($C_2H_1N_3O_4$)

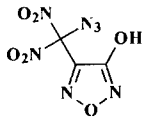

HF-5 ($C_3H_1N_7O_6$)

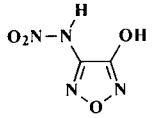

HF-11 ($C_2H_2N_4O_4$)

We investigated these compounds and found them to be very attractive high energetic candidates. Although **HNF** is more energetic than **NTO**, it however is much less stable than **NTO**.

It turned out that dihydroxyfurazans, such as **HF-2** and **HF-14**, had moderate thermal stability, with performance a little better than that of **NTO**.

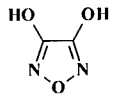

HF-2 ($C_2H_2N_2O_3$)

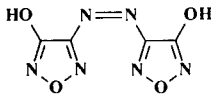

HF-14 ($C_4H_2N_6O_4$)

The acidity of hydroxyfurazans allowed the preparation of a large variety of salts.[3,7,11] The first compound prepared under this program was ammonium salt of HNF. The salt formed eutectics with NH_4NO_3 and ADNA. The fact impelled us to investigate the ammonium, hydrazinium, hydroxylammonium, and other salts of some of hydroxyfurazans.

The next approach we investigated involved a utilization of alkali-metal salts of these hydroxyfurazans, which were useful building blocks in the synthesis of oxyfurazanyl-modified energetic materials, as shown in Scheme.

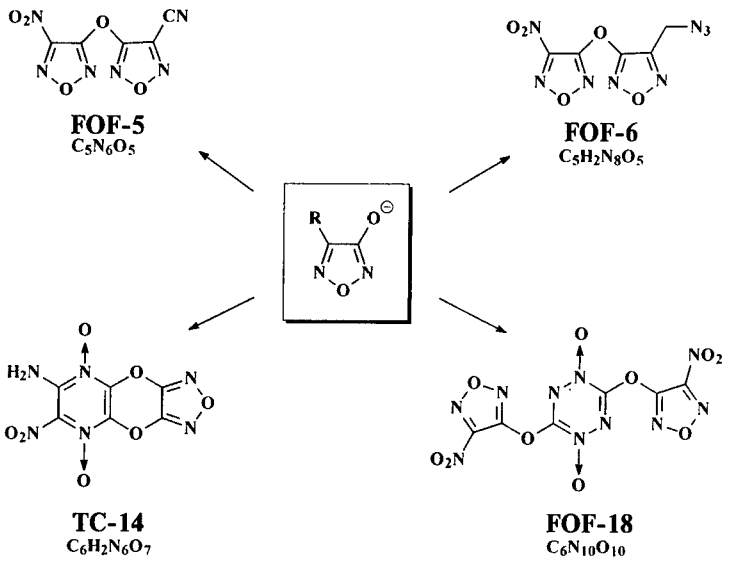

These compounds were found to be quite dense and have high thermal stability and performance. The compound **FOF-5** formed eutectics with common explosives and high energetic furazans that gave reduction of the sensitivity. **TC-14** is as insensitive as **TATB**, and its performance is much better than that of **RDX**. The properties of **FOF-18** are compared with those of **CL-20**. The **FOF-6** is beautiful plasticizer and has not analogs on performance.

REFERENCES

1. **Sheremetev, A. B.** and **Pivina, T. S.** "Nitrofurazanyl Moiety as an Alternative to Picryl One for High Energetic Materials Construction". *Proc. 27th International ICT-*

Conference, Energetic Materials - Technology, Manufacturing and Processing, June 25 - June 28, **1996**, Karlsruhe, FRG, 30/1-13.

2. **Sheremetev, A. B.; Kharitonova, O. V.; Melnikova, T. M.; Novikova, T. S.; Kuzmin, V. S.** and **Khmelnitskii, L. I.** "Synthesis of Symmetrical Difurazanyl Ethers", *Mendeleev Commun.*, **1996**, (4), 141-143.
3. **Sheremetev, A. B.; Semenov, S. E.; Kuzmin, V. S.; Strelenko, Yu. A.** and **Ioffe, S. L.** "Synthesis and X-ray Crystal Structure of Bis-3,3`-(nitro-NNO-azoxy)-difurazanyl Ether". *Chemistry-European Journal*, **1998**, *4*, (6), 1023-1026.
4. **Sheremetev, A. B.** "3,3-Bis(1-Fluoro-1,1-dinitromethyl)difurazanyl Ether". *Proc. 29th International ICT-Conference, Energetic Materials - Production, Processing and Characterization*, June 30 - July 3, **1998**, Karlsruhe, FRG, 58/1-13.
5. **Sheremetev, A. B.; Kulagina, V. O.** and **Ivanova, E. A.** "Zero-Hydrogen Furazan Macrocycles with Oxy and Azo Bridges". *J.Org.Chem.*, **1996**, *61*, (4) 1510-1511.
6. **Sheremetev, A. B.** and **Shatunova, E. V.** "Furazanyl Ethers of Pentaerythritol Derivates". *Proc. 28th International Annual ICT-Conference, Combustion and Detonation*, June 24 - June 27, **1997**, Karlsruhe, FRG, 94/1-8.
7. **Sheremetev, A. B.; Yudin, I. L.; Aleksandrova, N. S.; Andrianov, V. G.** and **Starchenkov, I. B.** "High Nitrogen Furazan Derivatives for Gas Generators" *Proc. Twenty-Third International Pyrotechnics Seminar*, Sept.30-Oct.4, **1997**, Tsukuba, Japan, 377-388.
8. **Sheremetev, A. B.; Kulagina, V. O.; Aleksandrova, N. S.; Dmitriev, D. E.; Strelenko, Yu. A.; Lebedev, V. P.** and **Matyushin, Yu. N.** "Dinitro Trifurazans with Oxy, Azo, and Azoxy Bridges". *Propellants, Explosives, Pyrotechnics*, **1998**, *23* (3), 142-149.
9. **Sheremetev, A. B.; Aleksandrova, N. S.; Melnikova, T. M.; Novikova, T. S.; Strelenko, Y. A.** and **Dmitriev, D. E.** "Synthesis of Difurazanyl Ethers from 4,4'-Dinitroazoxyfurazan", *Heteroatom Chem.*, **2000**, *11*, (1), 48-56.
10. **Sheremetev, A. B.** and **Aleksandrova, N. S.** "Efficient Synthesis of Hydroxyfurazans", *Mendeleev Commun.*, **1998**, (6), 238-239.
11. **Sheremetev, A. B.; Kharitonova, O. V.; Mantseva, E. V.; Kulagina, V. O.; Shatunova, E. V.; Aleksandrova, N. S.; Melnikova, T. M.; Ivanova, E. A.; Dmitriev, D. E.; Eman, V. A.; Yudin, I. L.; Kuzmin, V. S.; Strelenko, Y. A. Novikova, T. S.; Lebedev, O. V.** and **Khmelnitskii, L. I.**. "Nucleophilic Displacement in Furazan Series. Reactions with O-Nucleophiles". *Zh. Org. Khim.*, **1999**, *35*, (10), 1555-1566.

ANALYSIS OF HYDRAZINIUM NITROFORMATE (HNF)

J.M. Bellerby; C.S. Blackman

Cranfield University, Royal Military College of Science (RMCS), Shrivenham, Swindon, Wiltshire SN6 8LA, United Kingdom

M. van Zelst†; A.E.D.M. van der Heijden

TNO- Prins Maurits Laboratory, Researchgroup Pyrotechnics and Energetic Materials, P.O. Box 45, 2280AA Rijswijk, The Netherlands

ABSTRACT

Several methods of analysis have been applied to the study of the high performance oxidiser, hydrazinium nitroformate ($[N_2H_5^+][C((NO_2)_3)^-]$ or HNF). These include thermo gravimetric analysis combined with gas chromatography (TG-MS), headspace gas chromatography combined with mass spectrometry (GC-MS), nuclear magnetic resonance (NMR), Fourier transform infra red spectroscopy (FTIR) and differential scanning calorimetry (DSC).

The measurements were performed on HNF that had been subjected to temperatures between 40 °C and 80 °C. The GC-MS measurements were undertaken as a function of time.

† Corresponding author.

1. INTRODUCTION

A number of methods of analysis have been applied to the oxidiser hydrazinium nitroformate (HNF) by Cranfield University and by TNO. HNF is an oxidiser that is very promising for application in high performance solid rocket propellants. It performs better than conventional oxidisers like ammonium perchlorate (AP) HNF contains no chlorine, which makes it more environmentally acceptable and results in a low rocket exhaust signature (no hydrochloric acid). The goal of the investigations was to get insight in the behaviour of HNF at elevated temperatures, ultimately to try to identify the decomposition mechanism.

At Cranfield University samples of HNF were aged over different periods of time and at various temperatures. The headspace above these samples was analysed by GC-MS as a function of time. Subsequently the solid residues were analysed using TG, DSC and NMR.

At TNO the following experiments were performed: NMR measurements on HNF that was aged up to 4.2 wt% mass loss, and experiments in which the gas phase above decomposing HNF in a TG apparatus was analysed.

2. TG-MS

The mass spectrometer used at TNO for the TG-MS was a IPAG 421/430/260 and the TG apparatus was a TGDSC 111 Setaram type 31/1550. Two types of TG measurements were conducted: scanning and isothermal. For the scanning experiments amounts of 1.8 to 4.5 mg of HNF were put into an aluminium cup in the apparatus. After that the temperature of the TG apparatus was raised from 25 °C with a heating rate of 2 °C/min until a temperature of 160 °C had been reached. During the course of this process the mass spectrometer was continuously recording the spectra between 1- and 60 atomic mass units (amu) of the evolved gasses from the sample. For the isothermal measurements the TG apparatus was held at a constant temperature of 100 °C. The products in the gas phase above the HNF sample were analysed with the mass spectrometer.

The results of the experiments are summarised in Table 1. The observed mass fragments can be assigned to different molecular fragments or molecules. Gaseous products have only been observed during the fast decomposition at high temperatures. The molecules to which the observed molecular weights may be assigned are listed in Table 2.

Table 1: Results of TG-MS experiments on HNF.

Experiment:	Tot. Mass decrease (wt%)	Decomposition at (°C):	Weight of observed gaseous products (amu):
Scanning 1	84	120 - 125	16,17,18, 28, 30, 32, 44
Scanning 2	100	120 - 125	16,17,18, 28, 30, 32, 44
Scanning 3	94	120 - 125	16,17,18, 28, 30, 32, 44
Isothermal	95		16,17,18, 28, 30, 32, 44

Table 2: Gaseous compounds and molecular fragments detected by means of TG-MS during fast decomposition (120 °C) of HNF.

Molecular weight (amu)	Possible compound or fragment
16	Oxygen atom
17	NH_3 or OH^- fragment of H_2O
18	H_2O
28	CO or N_2
30	NO or formaldehyde
32	O_2
44	N_2O or CO_2

(No NO_2 (m = 46 amu) has been observed)

3. HEADSPACE GC-MS

The headspace GC-MS analysis was carried out using a Dani 3950 headspace analyser fitted with a 10 µL sample loop. The separation was achieved using a Fisons GC8000 gas chromatograph (GC) and identification was via a Fisons MD800 mass spectrometer (MS). The GC and MS were controlled via a PC running Masslab software.

To produce samples for analysis small amounts (0.500 g ± 0.005 g) of HNF were placed into several 20 cm^3 crimp top vial (Chromacol 20-CV) and sealed with an aluminium crimp cap and butyl rubber/PTFE septum. The prepared vials were then placed in pre-drilled holes in an aluminium block which was maintained at the appropriate ageing temperature by a Grant BT3 block heater. Periodically (depending on the ageing temperature) vials were removed from the heating block and analysed.

The ageing temperatures examined were 40 °C, 60 °C, 70 °C and 80 °C.

The aged vials were placed in the Dani headspace analyser and maintained at 40 °C. The headspace sample was taken and passed into the GC-MS. Initially the GC oven was cryogenically maintained at –80 °C for 5 minutes whereupon the temperature was increased at 15 °C/min up to 150 °C which was maintained for a further 5 minutes. The column used for the separation was a Chrompack PoraPlot Q (25 m long, 0.25 mm internal diameter, 8 µm film thickness). The MS was set to scan mass ions from m/z 10 to m/z 50. It was found that under these conditions the chromatographic separation of N_2, O_2, Ar, CO, NO, CO_2, N_2O and H_2O was achieved. The separation of argon allows it to be used as an inert internal standard to give semi-quantitative data about the increase or decrease in concentration of other gases in the headspace.

A series of 6 air 'blanks' was analysed before each set of samples in order to provide baseline values for the N_2/Ar, O_2/Ar, CO_2/Ar and H_2O/Ar ratios. From these values the error associated with the measurement of each ratio was calculated using twice the standard deviation. The values obtained for the amount of gas

evolved is a relative value within one measurement series. They cannot be used for comparison of the amount of different gases evolved.

For ageing at 40 °C, 15 vials were prepared and periodically removed from heating up to a maximum ageing time of 1100 hours (~ 46 days). Only trace levels of N_2O were detected after 307 hours (12.8 days) but this amount scarcely increased up to 1081 hours at which time the test was terminated. No other change in the composition of the headspace was detected and no physical change in the HNF was observed.

Similar results were obtained at 60 °C up to a maximum ageing time of 600 hours (25 days). Only nitrous oxide (N_2O) was measurable after 200 hours (~ 8 days) of ageing and the amount detected continued to increase slowly with time. An examination of the HNF after 600 hours showed no obvious physical change in the appearance of the solid.

The following graphs show the different gaseous species levels in the headspace during ageing at 70 °C: nitrogen (Figure 1), oxygen (Figure 2), carbon dioxide (Figure 3), nitrous oxide (N_2O) (Figure 4) and water (Figure 5).

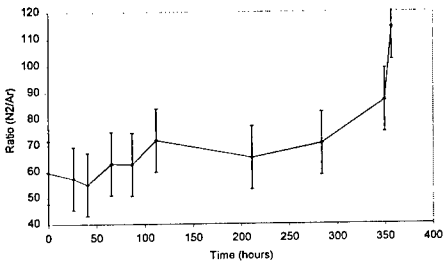

Figure 1: A graph to show headspace nitrogen for HNF aged in air at 70 °C.

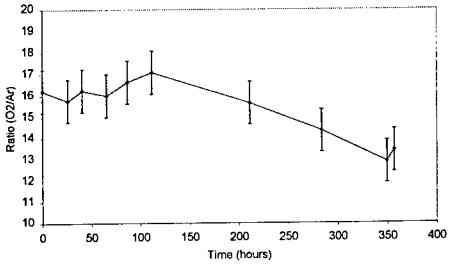

Figure 2: A graph to show headspace oxygen for HNF aged in air at 70 °C.

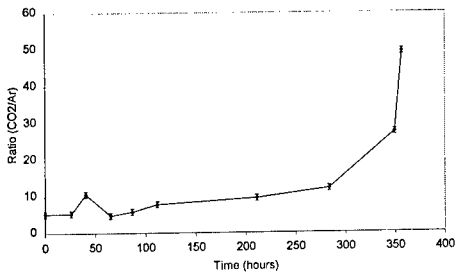

Figure 3: A graph to show headspace carbon dioxide for HNF aged in air at 70 °C.

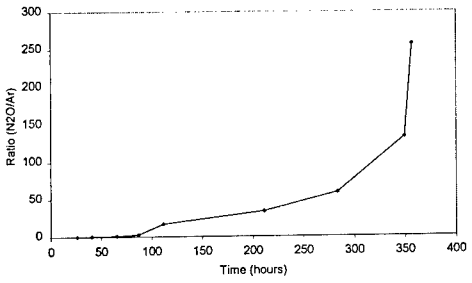

Figure 4: A graph to show headspace nitrous oxide for HNF aged in air at 70 °C.

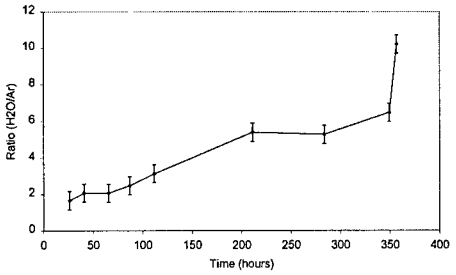

Figure 5: A graph to show headspace water for HNF aged in air at 70 °C.

It is seen that the headspace nitrogen level (Figure Figure 1) remains approximately constant until 300 hours after which it is seen to increase, particularly after 350 hours. For oxygen (Figure 2) there is a slight downwards trend between 100 and 350 hours. The level of carbon dioxide (Figure 3) stays approximately constant through the first 100 hours of ageing but then a slow increase is observed up to ~ 300 hours. After this time the rate of CO_2 evolution increases dramatically. The results for nitrous oxide (Figure 4) show a similar rapid increase with time. In the result for water (Figure 5) it is seen that there is a steady increase in the amount of water present in the headspace.

The physical appearance of the HNF changed dramatically during the course of this experiment. No obvious change was observed until about 200 hours at which time the HNF in the vials stopped being completely free flowing and small clumps of solid formed. By around 300 hours the HNF was completely immobile and had formed a single 'biscuit' like clump, although the individual crystals were still apparent. By 350 hours the HNF had a completely different appearance, having changed to a wet amorphous solid that looked like a slurry (perhaps not surprising given the dramatic increase in the water content (Figure 5)) and changing colour from yellow to brown. Small gas pocket 'voids' were also visible in the slurry matrix. After a further few hours of ageing the HNF appeared to have turned more red than brown.

The results for the GC-MS analysis at 80 °C for ageing times up to 100 hours were similar to those found at 70 °C for ageing times up to 400 hours. The change in the physical appearance of the HNF at 80 °C matched that seen at 70 °C.

The results from the GC-MS analysis of the headspace gases above aged HNF show some similarities with the work of Koroban et al [2].

4. NMR

Cranfield University and TNO have performed ^{1}H- and ^{14}N-NMR experiments on aged and unaged HNF. At Cranfield University a number of samples of aged HNF were kept for further analysis during the course of the ageing experiments for the GC-MS experiments. The visual examination of HNF ageing revealed two significant times of change. The first change takes place when the HNF loses its free flowing nature, which is accompanied by a slight change of colour from orange to yellow. The second change takes place when an amorphous, wet slurry begins to form. This slurry has been seen to take on several colours from a bright orange, through a deep red to a dark brown. The cause of this is not yet known. The samples were prepared such that the unaged HNF sample contained 30 mg of solid per cm^3 of DMSO-d6 and the aged sample contained 30 mg of solid per 0.7 cm^3 of DMSO. Sixteen scans were used to gather the data. The instrument used at was a Bruker Advance 250 with the data being gathered on a Silicon Graphics workstation running Icon-NMR software.

For the measurements by TNO two samples of HNF were aged at 80 °C until one had lost 1.4 wt% and the other sample 4.2 wt% in mass.

4.1 H-NMR

4.1.1 TNO RESULTS

Spectra were recorded of the 1.4 wt% aged sample, the 4.2 wt% aged sample and the 4.2 wt% aged sample with ammonium nitrate (AN) added. The AN was added to obtain a positive identification of peaks which were supposed to relate to NH_4^+. An additional spectrum was recorded of a brown water-insoluble residue that is left after ageing. All samples were dissolved in DMSO-d6†.

The spectrum of 1.4 wt% aged HNF (Figure 6) shows two broad peaks (at ~4.5 ppm and ~8.5 ppm) with a relative proportion of 2:3. These are caused by the two types of hydrogen atoms bound to the two nitrogen atoms in hydrazinium; each give a separate signal in the spectrum. The reason that these signals can be resolved (as opposed to N-NMR, see furtheron) is because of the shorter acquisition time‡ that is used in H-NMR. Furthermore, because an aprotic solvent is used in these measurements, exchange of hydrogens between the two nitrogens of HZ^+ is difficult. This results in two separate signals.

Yet the hydrogens did not produce the typical duplet (for the two "neighbouring" hydrogens at one side of the HZ^+ ion) and triplet (for the three hydrogens at the other side); customary for NMR signals of atoms with neighbouring atoms of the same 'kind'. The reason for this is that the intermolecular exchange of hydrogens

† DMSO = DiMethyl Sulfoxide (O=S(CH3)3). The 'd6' denotes that the hydrogens are all replaced by deuterium. DMSO is a widely used solvent in NMR spectroscopy because of the large variety of compounds that dissolve in it.

‡ Amount of time in which the radio wave emission from the nuclei is measured.

on one and the same nitrogen atom in HZ^+ is still faster than the acquisition time. This is opposed to the exchange of hydrogens between the two different nitrogens in hydrazinium, which is a relatively slow process.

The ^{1}H-NMR spectrum of the 4.2 wt% aged HNF sample (Figure 7) shows a big, broad peak centered at approx. 7 ppm with three sharp peaks superimposed on this broad peak. The broad peak is from water; the little peaks appear to be from NH_4^+ after comparison with a spectrum of the same sample with deliberately added AN (spectrum not shown). The peak at 2.25 ppm is from the solvent, DMSO.

The amount of NH_4^+ appeared to be 0.3 wt% (3.2 mole%). This is in very good accordance with the N-NMR measurements and the Cranfield University results (see section 4.1.2).

The additional spectrum of the brown water-insoluble residue (Figure 8) showed the same NH_4^+ triplet as the aforementioned aged samples. The spectrum also showed a very large peak area centred at approx. 3.5 ppm. It is not known to what species this signal should be assigned.

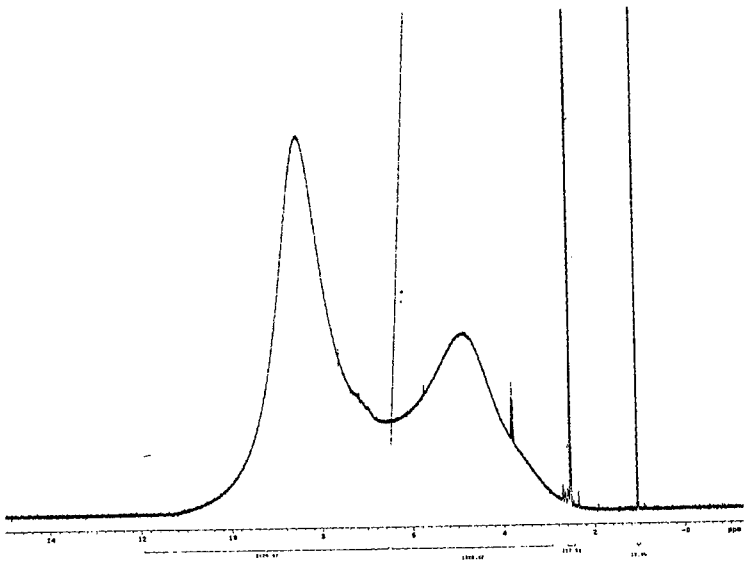

Figure 6: ^{1}H-NMR spectrum of HNF aged at 80 °C up to 1.4 wt% mass loss, dissolved in DMSO-d6 (TNO).

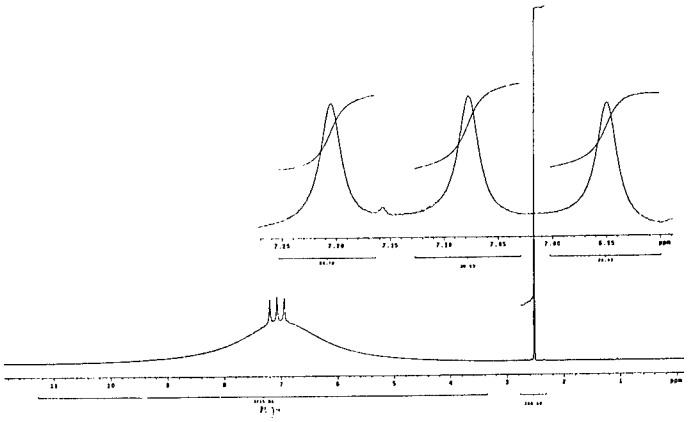

Figure 7: ^{1}H-NMR spectrum of HNF aged at 80 °C up to 4.2 wt% mass loss, dissolved in DMSO-d6 (TNO).

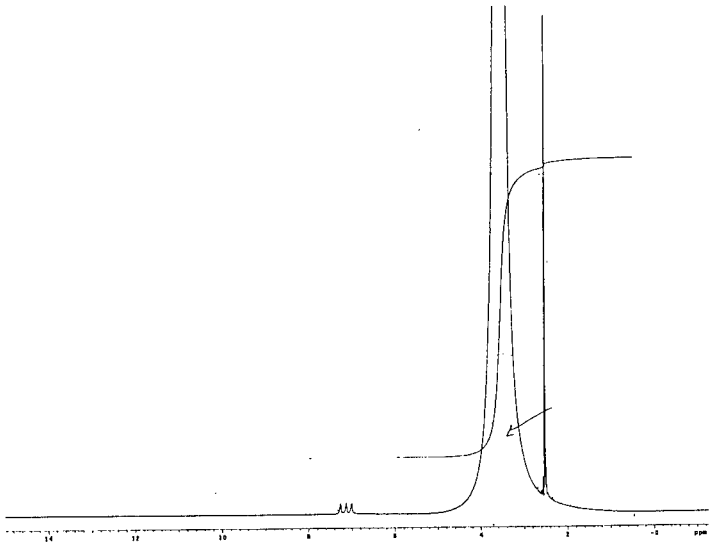

Figure 8: ^{1}H-NMR spectrum of the residue that is left after ageing of HNF, dissolved in DMSO-d6 (TNO).

4.1.2 CRANFIELD UNIVERSITY RESULTS

The samples examined using ^{1}H-NMR at Cranfield University were unaged HNF (Figure 9) and a sample of HNF aged at 80°C in air until it had formed a brown slurry which is about 94 hours (Figure 10).

The peak at ~ 1 ppm in Figure 9 is assigned to iso-propyl alcohol (IPA) which is also indicated by the fine structure of bands seen to the left of the large peak at ~ 3 ppm (this is the residu of a processing liquid). The peak at ~ 2 ppm is due to the solvent, DMSO. The 2 remaining peaks at ~ 7 ppm and 3 ppm, when integrated by hand (in the spectra shown the integrations were performed by the software) have a ratio of approximately 3:2. These peaks were therefore assigned to $-NH_3^+$ and $-NH_2$ in the hydrazinium ion, respectively.

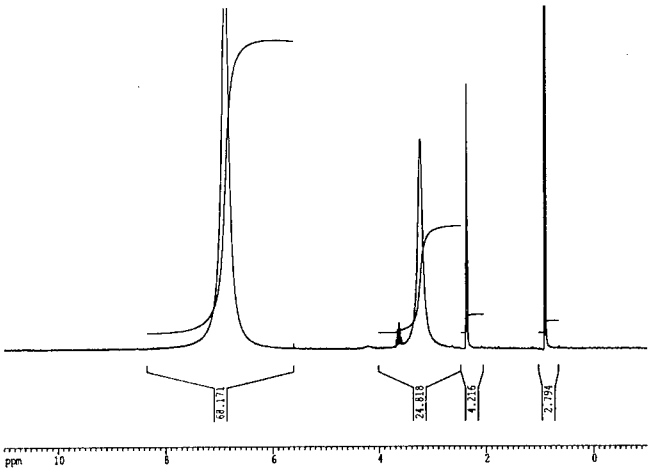

Figure 9: ^{1}H-NMR spectrum of unaged HNF (Cranfield University).

The NMR spectrum of the aged HNF (Figure 10) shows a dramatic change. The principal feature of the spectrum is the 1:1:1 triplet seen at ~ 7 ppm. This pattern is characteristic of ammonium, NH_4^+ (see previous discussion). The peaks assigned to $-NH_3^+$ and $-NH_2$ in the unaged spectrum (Figure 9) are not visible. The peak seen previously at ~ 1 ppm (IPA) is no longer present while the peak due to DMSO (~ 3 ppm) is still present but diminished due to the higher sample concentration used.

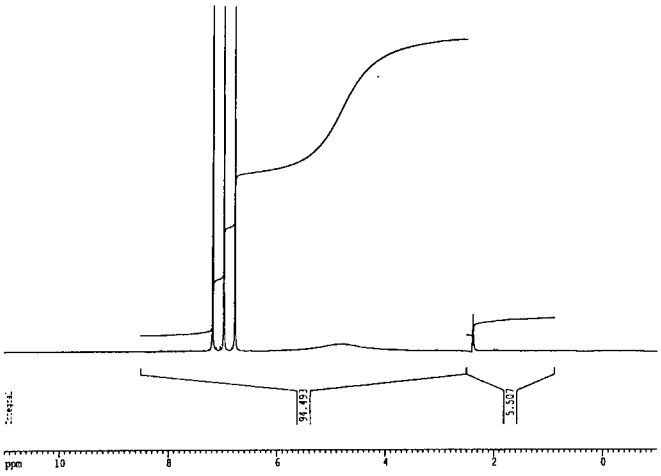

Figure 10: ^{1}H-NMR spectrum of aged HNF (Cranfield University).

4.2 N-NMR

At TNO ^{14}N-NMR spectra were recorded of unaged HNF (reference sample), the reference after 6 days in D_2O/H_2O (to inspect possible influence of the solute), the 4.2 wt% aged sample and the 4.2wt% aged sample with an acid added. The addition of acid is a method to see if the supposed NH_4^+ peak indeed is NH_4^+ [3]. All samples were dissolved in H_2O/D_2O. A fact worth noting is that during the dissolution of the 4.2 wt% aged sample in water for the N-NMR experiments, gas was observed to evolve from the solution.

The spectrum of pure HNF (Figure 11) showed a sharp peak from the three nitrogroups at 346 ppm and a broad peak around 47 ppm from the two $N_2H_5^+$ nitrogens. The nitro-group nitrogens are chemically indistinguishable from each other and therefore produce one signal with a relative intensity (integral) of approx. 3. The nitrogens from HZ^+ are in principle different from each other and therefore distinguishable because one nitrogen has three hydrogens bound to it and the other two. A long acquisition time was used to obtain a high-resolution spectrum. The interchange time of hydrogens between the nitrogens in HZ^+ (better known as Lewis-structures or resonance) is, however, shorter than the acquisition time, producing one broad signal instead of two sharp ones.

In the spectrum of the 4.2 wt% aged sample an extra signal is clearly apparent. This peak appears at 18.4 ppm. Upon addition of acid (CF_3COOH) this peak splits up into several others, implying that the signal is from NH_4^+ (as opposed to NH_3).

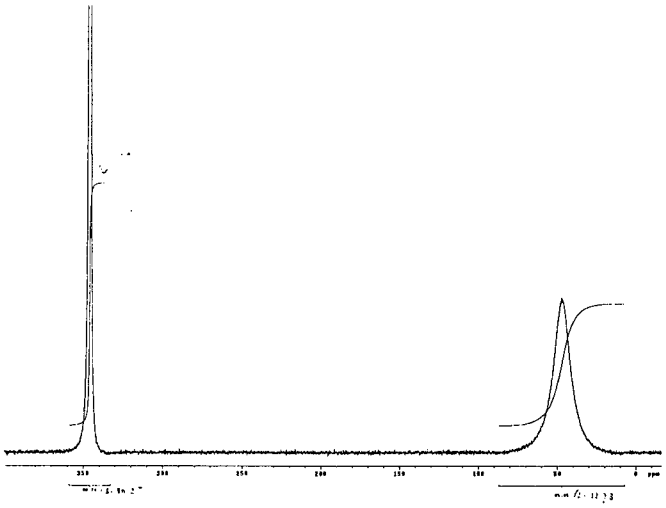

Figure 11: ^{14}N-NMR spectrum of pure HNF, dissolved in a D_2O/H_2O mixture (TNO).

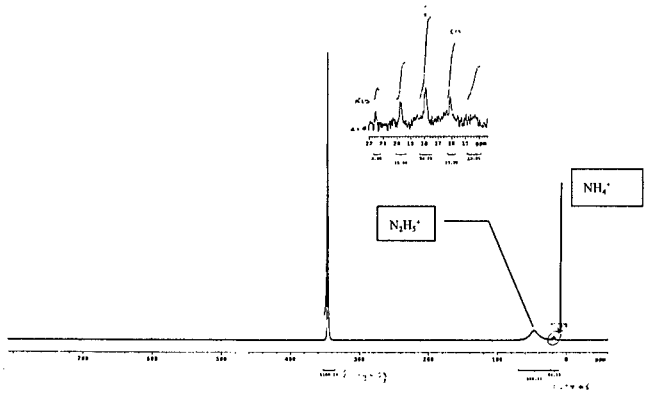

Figure 12: ^{14}N-NMR spectrum of HNF aged at 80 °C up to 4.2 wt% weight loss, dissolved in a D_2O/H_2O mixture with an acid added (CF_3COOH) to enhance the ammonium peaks (TNO).

5. FTIR

Samples for IR analysis were prepared by taking 50 mg of the solid to be examined and grinding with 300 mg of dry potassium bromide (KBr). 55 mg of the ground mixture was then poured into a die and pressed into a disk under 10 tons of pressure. The samples analysed comprised an unaged sample of HNF and a sample of HNF aged at 80 °C until it had become a slurry (around 90-95 hours).

Figure 13 shows the FTIR spectrum obtained of unaged HNF in the region 700 cm^{-1} to 1700 cm^{-1}. The FTIR spectrum of HNF after ageing is shown in Figure 14.

There are several obvious differences between the FTIR spectra of the aged and unaged materials. The changes include an additional peak (with a shoulder) at 825 cm^{-1}, the broadening and loss of intensity of the peaks at 964 cm^{-1} and 989 cm^{-1} (N-N stretch) and the loss of the peaks between 1082 and ~ 1100 cm^{-1} (N-C-N asymmetrical stretch).

The broadening of the peaks at 964 cm^{-1} and 989 cm^{-1} to a single peak was observed by Williams and Brill [1]. It was a reversible process caused by heating HNF but in the case of the present study it appears to be a non-reversible process. The peak at 1241 cm^{-1} in the spectrum of unaged HNF is lost (NO_2 symmetrical stretch and NH_2 rock) and there is a dramatic change between aged and unaged spectra at ~ 1400 cm^{-1} (NH_3^+ bend region). Additionally the peaks after 1512 cm^{-1} (NH_3^+ deformation) are no longer present in the aged sample. It is stated by Williams and Brill [1] that, "the 1400 – 1550 cm^{-1} region containing – NO_2 antisymmetric stretching strongly depends on the counter ion in $C(NO_2)_3^-$ salts". Ammonium nitroformate was suggested as a HNF decomposition product by Koroban et al [2] and also by Brill and Williams [1] and was indicated by NMR experiments carried out during the present study (see section 4). The formation of ANF may account for the observed changes in the 1400 – 1550 cm^{-1} region of the FTIR spectrum of HNF during ageing.

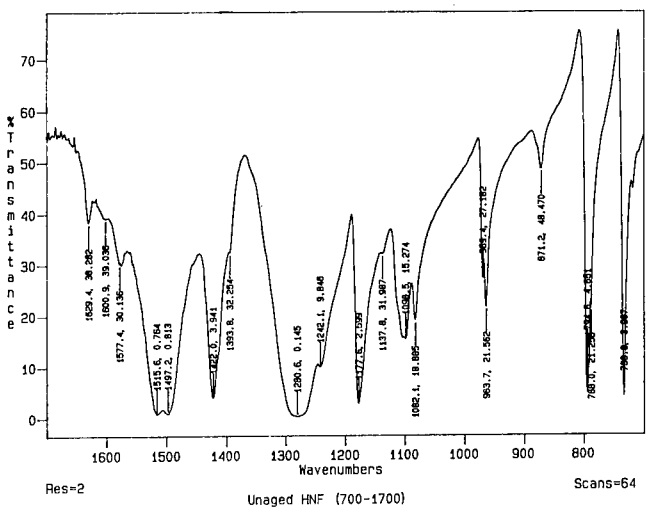

Figure 13: FTIR spectrum of unaged HNF.

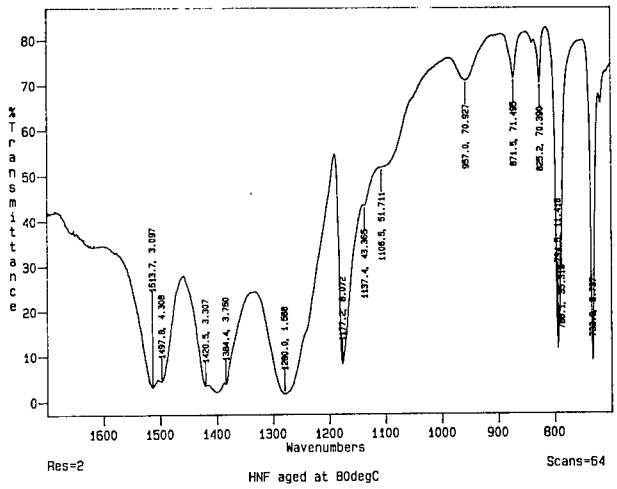

Figure 14: FTIR spectrum of aged HNF.

6. DSC

3.4 mg of unaged HNF and 1.8 mg of HNF aged at 80 °C (slurry) were analysed using DSC (Mettler TA4000 Thermal Analysis System). The heating rate was 10 °C/min. The DSC curve of the unaged sample is shown in Figure 15 and that of the aged sample in Figure 16.

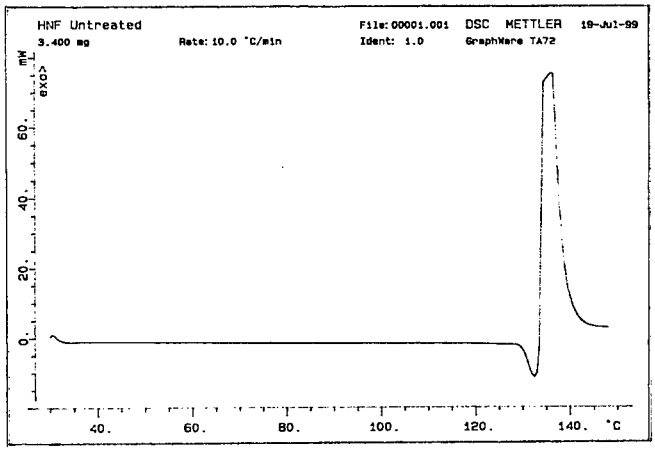

Figure 15: DSC of unaged HNF.

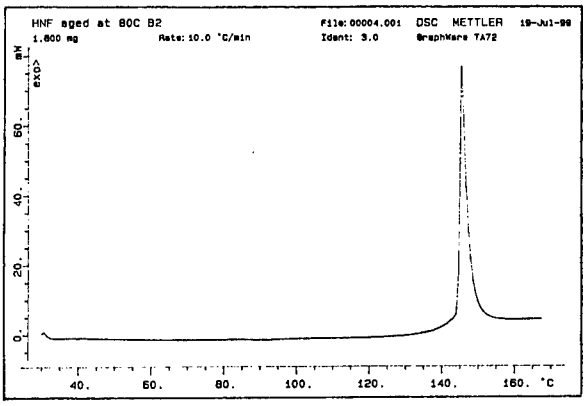

Figure 16: DSC of aged HNF.

The temperature of the onset of the exotherm for unaged HNF (Figure 15) is ~ 135 °C. A DSC of unaged HNF performed by Hatano et al. [4] showed two exothermal peaks between 130 °C and 140 °C. The heating rate is not given but it is thought that the broad peak shape seen in Figure 15 may be due to the presence of the two peaks observed by Hatano [4] but hidden due to a higher heating rate.

The temperature of exotherm onset for the aged HNF (Figure 16) is ~ 145 °C. It is acknowledged that the difference in mass analysed (3.4 mg for unaged HNF and 1.8 mg for aged HNF) may have had some effect on the temperature of onset. However the shape of the peak for aged HNF is dramatically different to that of unaged HNF. It may be concluded fron DSC that aged HNF contains no measurable amount of HNF.

7. CONCLUSIONS

From the TG-MS experiments it may be concluded that during the fast decomposition at 120 - 125°C no NO_2 (m = 46 amu) is being generated from HNF. Note that the headspace GC-MS at Cranfield University does not detect NO_2. From TNO results one may conclude that during the *fast* decomposition no NO_2 evolves, but whether it is present, or not, in the decomposed gaseous phase above HNF cannot be stated with certainty.

The conclusion from the headspace GC-MS experiments is that the major gaseous species evolving from ageing HNF is N_2O. Koroban et al. [2] state that, "One of the major hydrazine oxidation products coinciding with the decomposition of HNF, as established by our analysis, is ammonia", although no evidence is given. The analysis of the headspace of aged HNF samples revealed no detectable presence of ammonia. It is difficult to reconcile these results with those of Koroban et al.

From the results from the H-NMR experiments it can be concluded that in the HNF sample aged up to 4.2 wt% mass loss, 0.3 wt% (= 3.2 mole%) NH_4^+ is present. This observation is supported by the H-NMR measurements at Cranfield as well as the results from the N-NMR experiments at TNO. Also aged HNF dissolved in DMSO-d6 may attract water. This conclusion may be combined with the results of FTIR measurements on ageing HNF. It appears that ammonium nitroformate (ANF) is formed. The FTIR signals stemming from the hydrazinium part of the molecule seem to disappear faster than the nitroform signals. Ammonium has been observed, which in combination with nitroformate may produce ANF.

From the DSC measurements it may be concluded that the slurry that has been observed to form during ageing contains no measurable amount of HNF.

8. ACKNOWLEDGEMENTS

The authors acknowledge the European Space Agency (ESA) for financial support of this work (Estec contract nr. 13.239/98/NL/PA(SC)), Mr. S.H. van Krimpen (TNO-PML) for performing the NMR analyses and Mr. E.A. Bal (TNO-PML) for performing the TG-MS analyses.

9. REFERENCES

[1] G.K. Williams, T.B. Brill, *Thermal decomposition of energetic materials 67. Hydrazinium nitroformate (HNF) rates and pathways under combustionlike conditions*, Combustion and Flame, 102, pp. 418-426, 1995

[2] V.A. Koroban, T.I. Smirnova, T.N. Bashirov, B.S. Svetlov, *Kinetics and mechanism of the thermal decomposition of hydrazin trinitromethane*, Tr.-Mosk. Khim.-Tekhnol. Inst. Im. D. I. Mendeleeva, 104, pp38-44, 1979 (in Russian)

[3] S.H. van Krimpen, personal communication, TNO-PML (1999)

[4] H. Hatano, T. Onda, S. Kiname, S. Suzuki, *Characteristics of HNF*, Proceedings of the 20th International Pyrotechnics Seminar, pp397-402, 1994

CHARACTERIZATION OF A COMMERCIAL GRADE CL-20: MORPHOLOGY, CRYSTAL SHAPE, SENSITIVITY AND SHOCK INITIATION TESTING BY FLYER IMPACT

R.H.B. Bouma, W. Duvalois, A.E.D.M. van der Heijden, A.C. van der Steen
TNO Prins Maurits Laboratory, P.O. Box 45, 2280 AA Rijswijk, The Netherlands

Abstract

CL-20 is a new energetic molecule. Its high detonation velocity and pressure make it a suitable candidate for replacing HMX. In literature, data is shown on the impact and friction sensitivity of CL-20 with figures not too far from acceptable limits. These data may direct research to improve the crystal shape by changing the process conditions during production, in order to decrease the sensitivity.

Results will be shown on a commercial grade CL-20 obtained from SNPE. For the characterization of the crystals various techniques have been used: infrared spectroscopy and X-ray diffraction for the CL-20 polymorph, liquid pycnometry for the crystal density, electron microscopy for crystal shape and aspect ratio, and TG/DTA and DSC for the transition temperatures.

Sensitivity and stability testing includes impact and friction testing, electrostatic discharge and vacuum stability test.

Based on the tap density a polyurethane based, monomodal PBX has been cast with a solid load of 62 wt% of the studied CL-20. Results will be shown on the shock sensitivity (and pressure profile), determined by the impact of a 125 micrometer thick Kapton flyer on CL-20-based PBX charges with diameter and length of 20 mm.

Introduction

CL-20 is a relatively new explosive molecule, with a caged structure [1]. Due to its high density, detonation velocity and pressure, it may become a replacement for HMX in AT applications, a high energy constituent in shock insensitive explosive compositions for deformable warheads [2], or a constituent in propellant formulations [3].

At the TNO Prins Maurits Laboratory the properties of CL-20 are studied. At the moment the sensitivity of CL-20 is considered to be relatively high. The sensitivity may be decreased for example by changing crystal shape and removing crystal defects. In order to study the effectiveness of these measures a comparison of the properties of such less sensitive crystals with a commercial grade CL-20 will be made. The properties of a CL-20 batch, procured from SNPE, is subject of this paper.

Material

A commercial grade CL-20 (hexanitro-hexaaza-isowurtzitane or abbreviated as HNIW) with a specified particle size range of 100-150 µm, has been obtained from SNPE, batch n° A1113. The TNO code for this sample is TL 256/98. Various physical properties of the molecule have been studied. Furthermore, the shock initiation of a polyurethane based PBX containing CL-20 is investigated. The measured tapdensity of TL 256/98 is 0.874-0.877 g/cm^3. The value is relatively low and due to the irregular shape of the crystal agglomerates, see figure 1. Based on the tapdensity a polyurethane based PBX has been made with 62 wt.% CL-20 and 38 wt.% of a cured binder system. Its Theoretical Maximum Density is 1.386 gcm^{-3}.

Characterization of CL-20

Scanning electron microscopy

In figure 1 one can see the scanning electron micrograph of a typical agglomerate of the as-received CL-20. All the agglomerates have very sharp edges and one may expect from their shape a low tap density of the crystals. At large magnification one can observe that some of the surfaces contain submicron pores, whereas other surfaces do not show these pores at all.

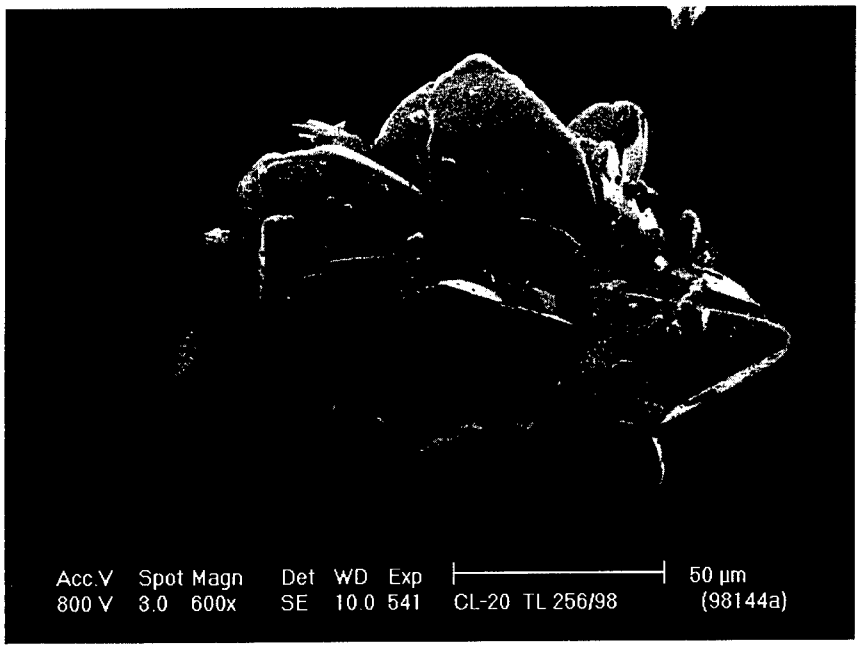

Figure 1: Detailed SEM picture of a single CL-20 agglomerate.

With SEM and a software tool to analyse the individual particles one can calculate particle size distribution, aspect ratio, surface roughness, etc... One has to prepare SEM samples in which the CL-20 agglomerates are deposited on a substrate with a minimum distance in between them in order to make sure that the software is observing separate particles. As an example of such an SEM analysis the surface roughness distribution is shown in figure 2. The surface roughness is defined here as the perimeter (the number of contour pixels) divided by the CVX perimeter (the convex perimeter), and for a sphere it equals one.

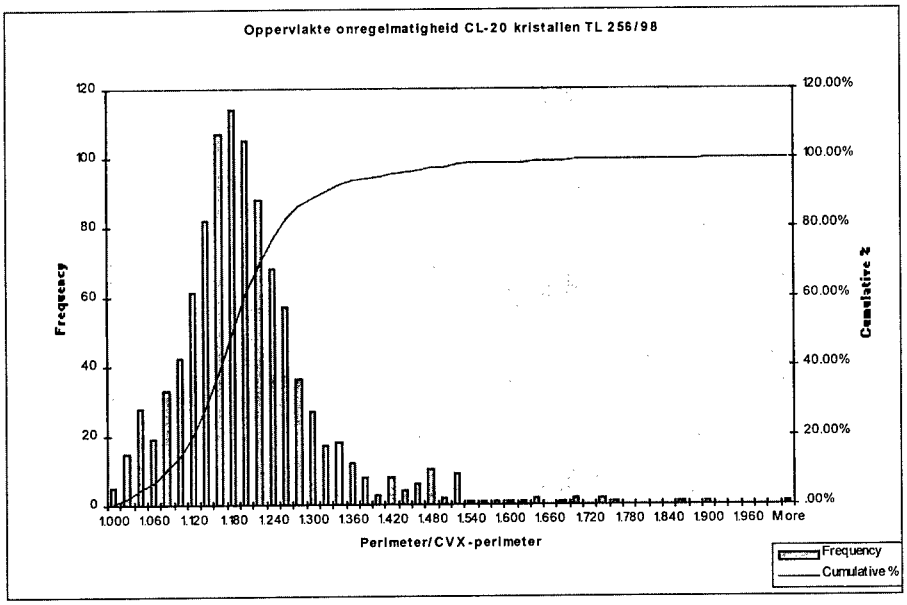

Figure 2: Frequency distribution and cumulative distribution versus surface roughness.

The particle size distribution determined with the software tool has been compared with the particle size distribution as determined with a Malvern particle size analyser. The differences in shape of respective distributions, although in the same range of particle size, is inherent to the analyses; the former takes into account a particle size and shape, the latter determines the size distribution from a light scattering experiment, assuming spherical particles.

FTIR

The IR spectrum of the CL-20 has been measured and agrees with the spectrum of the epsilon polymorph of CL-20 as presented in STANAG 4566 [4]. In figure 3 one can see the expanded spectrum of sample TL256/98. The differences of the IR spectra corresponding to the various polymorphs of CL-20 are relatively small [4] and therefore one cannot distinguish impurities of other polymorphs at levels lower than 20%.

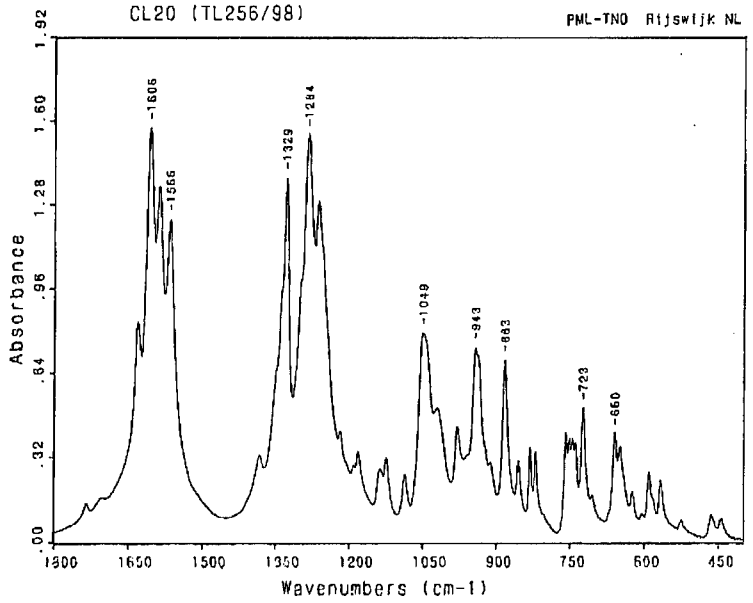

Figure 3: Expanded FTIR-spectrum (absorbance versus wavenumber) in the range of 450 to 1800 cm^{-1}.

X-ray diffraction

As the XRD spectra for the CL-20 polymorphs have not been found in literature, the XRD spectrum of the studied ε-CL-20 has been measured with a Philips PW3710 X'Pert system, see figure 4. The XRD spectra of other CL-20 polymorphs has been studied as well. Different lines (2θ) show up in the various polymorphs which give the opportunity to quantify the amount of impurities of other polymorphs in ε-CL-20 at levels much lower than possible with FTIR, typically at impurity levels down to 1 %.

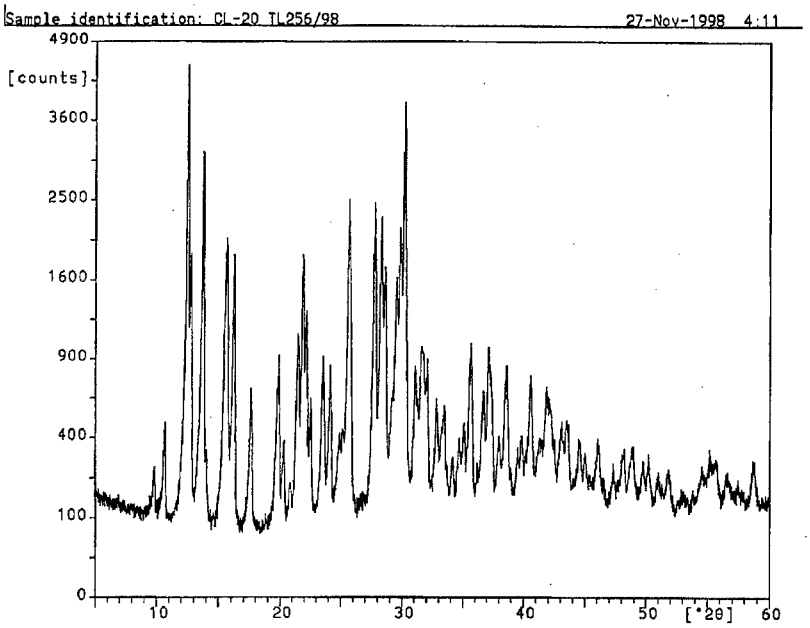

Figure 4: X-ray diffractogram (counts versus 2θ) of CL-20 batch TL 256/98.

Liquid pycnometry and crystal inclusions

The crystal density has been determined with liquid pycnometry using dodecane saturated with CL-20, at 25 °C. The density, measured in duplo, equals 2.017 and 2.018 g/cm^3, which is below the Theoretical Maximum Density of 2.05 g/cm^3.

The CL-20 crystals have been dispersed in a I-benzene and Br-benzene mixture with 1.60 refractive index. Under an optical microscope one can study directly the nature of inclusions in the crystals. The crystals of batch TL 256/98 show small air inclusions to a minor extent.

TG/DTA and DSC

The thermal properties of CL-20 have been determined with combined thermogravity (TG) / differential thermal analysis (DTA) and differential scanning calorimetry (DSC). Experiments have been performed in the temperature range 25 – 350 °C, at an heating rate of 10 °C/min (both in nitrogen and air atmosphere) and at a heating rate of 2 °C/min (nitrogen atmosphere). All the experiments have been performed in duplo and results are given in tables 1 and 2.

Table 1: DTA, onset and maximum of observed endotherm and decomposition.

heating rate °C/min	atmosphere	onset endotherm °C	max endotherm °C	onset decomp. °C	max decomp. °C
10	N_2	116	129	215	233
2	N_2	113	119	202	220
10	air	113	128	209	232

Table 2: DSC, onset and maximum of observed endotherm and decomposition.

heating rate °C/min	atmosphere	onset endotherm °C	max endotherm °C	onset decomp. °C	max decomp. °C
10	N_2	111	126	216	239
2	N_2	107	116	205	223
10	air	112	126	217	238

Sensitivity and stability testing of neat CL-20

The impact and friction sensitivity of dry CL-20 have been determined with the BAM Fallhammer and BAM friction apparatus, according to the UN SERIES 3 Test 3(a)(i) and Test 3(b)(i), respectively [5]. The measured impact sensitivity of CL-20 batch TL 256/98 is 3 J, which is only slightly higher than 2 J, the value at which the material is considered too dangerous for transport in the form it was tested, i.e. dry.

The measured friction sensitivity is 84 N. When the friction sensitivity is less than 80 N, the material is again considered too dangerous for transport in the form it was tested, i.e. dry.

However, with other batches of CL-20 impact sensitivities of 2 J and friction sensitivities in the range of 54 – 84 N have been measured thus far at TNO. This compares well with data given in reference 6. Wetting CL-20, coating it with IDP [6], or making a PBX with CL-20 [7], will significantly lower the sensitivity.

The sensitivity towards electrostatic discharge has been measured using three different capacitors. A positive reaction has been noted at a level of 0.45 J.

A vacuum stability test of neat CL-20 has been done in duplo with test samples of 1.0 gram, for 40 hrs at 100 °C. The gas evolution, recalculated to 2.5 gram sample, is 1.58 and 1.52 mliter.

Flyer impact initiation behaviour of a CL-20 based PBX

Flyer impact initiation has been studied with the TNO MegaAmpere Pulser. By the discharge of a capacitor bank (10-40 kV) into an aluminium bridge, a aluminium plasma is created which accelerates a 250 μm Kapton polyimide flyer with a diameter of 21.4 mm. At the end of a 5 mm long PVC barrel the flyer impacts a sample of the CL-20 based PBX, with diameter and height of 20 mm. A so-called Fiber Optic Probe [8] has been placed at the central axis to monitor the Shock-to-Detonation Transition or decay of input shock wave, as function of the impact velocity. Experimental results are given in figure 5 and table 3.

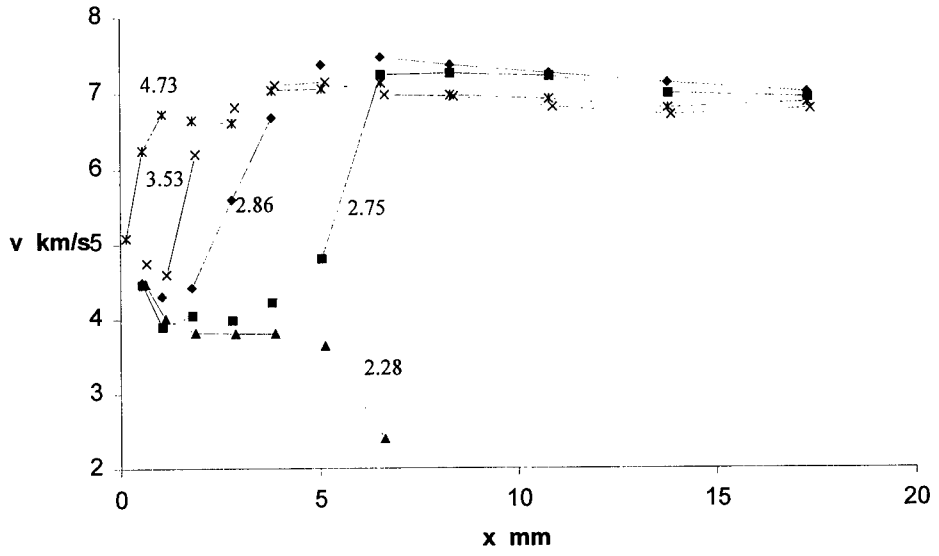

Figure 5: Shock wave velocity versus distance in PBX with 62 wt.% CL-20, after flyer impact at indicated velocities.

Table 3: Experimental result of Kapton flyer impact on PBX with 62 wt.% CL-20; initiation distance as function of flyer impact velocity, and detonation velocity (measured at the end of 20 mm charge).

number	flyer velocity km/s	result	initiation distance mm	detonation velocity km/s
CL01-1	2.86	detonation	ca. 4	7.0
CL02-1*	2.53	no initiation	-	-
CL03-1	2.75	detonation	> 6	6.95
CL04-1*	2.28	no initiation	-	-
CL05-1	3.53	detonation	ca. 3.5	6.8
CL06-1	4.73	detonation	1	6.9

** Due to low light intensity of Fiber Optic Probe only a bad and a weak signal have been recorded for experiments CL02-1 and CL04-1, respectively.*

The experiments CL03-1 and CL04-1 are just above and below the shock initiation threshold of the CL-20 PBX, respectively. One can observe a constant value of the shock wave velocity in the first 4 mm of the explosive. This effect may occur only near the initiation threshold; usually a continuous increase or decrease in shock wave velocity with distance is observed.

The observed plateau value is not correlated to the release wave coming from the back side of the impacting flyer. This has been verified by analysis of shock and release waves in flyer and explosive. For this purpose one needs to know the densities and Hugoniots of flyer and explosive. The density and Hugoniot of Kapton are 1.414 gcm^{-3} and Us = 2.893 + 1.19 up, respectively, with Us the shock wave velocity and up the particle

velocity [9]. For the density of the PBX the TMD value of 1.386 gcm^{-3} is taken. Unfortunately, no Hugoniot of the PBX is available, and no Hugoniot of CL-20 based explosives has been found. In figure 10 of reference 10, pressure histories of LX-14 and its CL-20 analog LX-19 are shown. Based on this graph, the Hugoniot of CL-20 is assumed to be similar to the Hugoniot of HMX, the data of which are found in reference 11. Applying a mixture rule based on weight fraction of the constitutive components, the Hugoniot of a 62 wt.% CL-20 PBX is approximated by Us = 2.75 + 1.87 up. The shock and release wave analysis is demonstrated graphically in figure 6 in case of impact with a 250 µm thick Kapton flyer at a flyer velocity of 2.6 km/s, i.e. near the initiation threshold.

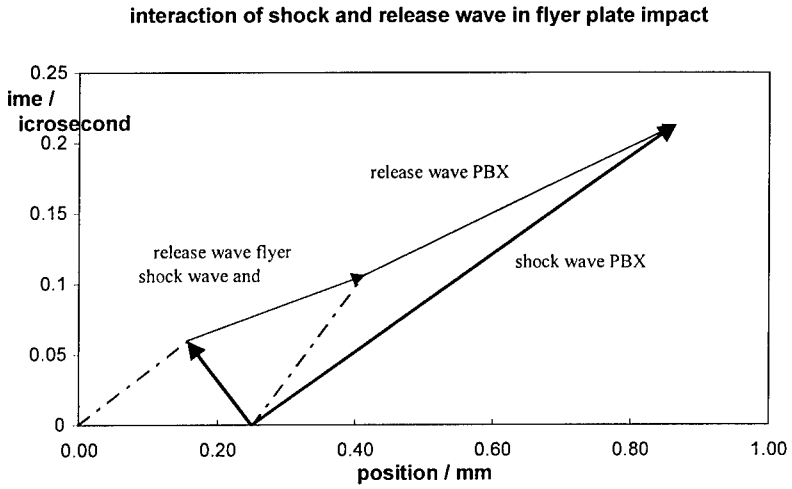

Figure 6: Shock waves and release waves in flyer and PBX, after impact at 2.6 km/s of 250 µm flyer.

In the range of Kapton impact velocities of 2.0 – 4.0 km/s, the release from the back of the flyer will overtake the shock wave in the PBX within 0.56 – 0.70 mm. Near the impact velocity of 2.6 km/s, at an estimated input shock strength in the PBX of 6.2 GPa, there must be a delicate balance between the strong release wave (typical for the flyer plate impact configuration) and the growth to detonation.

In literature one can find typical shock sensitivities of 27.7 kbar (PBXW-131, 88% CL-20, NOL large scale gaptest), 24.5 kbar (PBXW-132, 90% CL-20, NOL gaptest) [6], 260 cards (LX-19, 95% CL-20, IHE card gaptest) [7], 20.7-22.0 kbar (PAX-12, 90%, NOL gaptest) [12]. The initiation pressure of 6.2 GPa of the studied PBX is relatively high and due to the low explosive content of the PBX and the short duration of the input pulse.

References

1 Caged polynitramine compound, A.T. Nielsen, US Patent 5693794.

2 Preparation of fine particulate CL-20, M.L. Chan, A.D. Turner, US Patent 5712511.

3 New molecules for high energetic materials, B. Finck, H. Graindorge, 27th International Annual Conference of ICT, 25-28 June 1996, Karlsruhe, Germany.

4 Explosives, specification for ε-CL-20 (hexanitrohexaazaisowurtzitane) for deliveries from one NATO nation to another STANAG 4566, edition 1, 4th draft,.

5 Recommendations on the transport of dangerous goods, manual of tests and criteria, United Nations.

6 Hazard properties of Cl-20 based explosives, Y. Tran, J. Kelly, K. Burrows, D. Boyd, IM&EM symposium, 6-9 October 1997, Tampa (Fl), USA.

7 Performance and hazard characterization of CL-20 formulations, M.J. Mezger, S.M. Nicolich, D.A. Geiss Jr., 30th International Annual Conference of ICT, 29 June-2 July 1999, Karlsruhe, Germany.

8 Fibre-optical techniques for measuring various properties of shock waves, W.C. Prinse, R.J. van Esveld, R. Oostdam, M.P. van Rooijen, R.H.B. Bouma, 23rd International Congress on High-Speed Photography and Photonics, 20-25 September 1998, Moscow.

9 LASL shock Hugoniot data, ed. S.P. Marsh.

10 CL-20 performance exceeds that of HMX and its sensitivity is moderate, R.L. Simpson, P.A. Urtiew, D.L. Ornellas, G.L. Moody, K.J. Scribner and D.M. Hoffman, Propellants, Explosives, Pyrotechnics 22, 249-255 (1997).

11 LASL explosive property data, ed. by T.R. Gibbs, A. Popolato.

12 Additional characterization of high performance CL-20 formulations, D.A. Geiss Jr., S.M. Nicolich, M. Mezger, K.E. Lee, L. Hatch, 1999 Insensitive Munitions and Energetic Materials symposium, 29 November – 2 December 1999, Tampa (Fl), USA.

SUBJECT : IDENTIFICATION AND ANALYSIS OF IMPURITIES OF HNIW

AUTHORS: G. JACOB; G. LACROIX; V. DESTOMBES
SNPE Propulsion- CRB BP N°2
F-91710 VERT LE PETIT (France)

Abstract

Synthesis of HNIW is now performed by different manufacturers according to several modifications of the same general route. In order to compare different qualities of HNIW, analytical tools are required. Apart from titration methods which are absolute, others are normalized versus standards. Purity is best expressed if one is able to quantify amount of impurities. This work present isolation and spectrometric characterizations of some of them followed by chromatographic assessment.
Purity of HNIW is determined by high performance liquid chromatographic technique (HPLC), by using the internal normalization method. This method calculates chromatographic peak area of impurities by including the response factor correction of each impurity isolated by the chromatographic method, and it adds all the peak areas of the chromatogram and calculates the ratio between HNIW peak area and total corrected area.
With this corrected internal normalization method, systematic impurities and HNIW calibration is useless; the error caused by variability of impurities response factors is minimized by the corresponding correction.

Introduction

Different routes to HNIW are described in literature (1, 2, 3). Up to now, all of them start from hexabenzyl-isowurtzitane cage HBIW (4). The next step involves hydrogenolysis into acetylated or formylated compounds. After transformation into nitroso derivatives if required, the last step is nitrolysis to get HNIW.
All these steps lead to impurities which may alter final properties of HNIW. It is then valuable to be able to analyze and quantify these impurities to distinguish different qualities of HNIW and to correlate the amount of them with other data.
Analytical methods offer two types of purity determination : " absolute " methods such as titration afford gross purity but, due to precision, are not suited to high level of purity. More sophisticated ones, like chromatography, lead to good precision if one is interested in the amount of each impurity. Indeed, standardization with an authentic sample of pure material is questionable too for very high purity HNIW.
Identification of several intermediates (2) or residual impurities (5) are described while some other remain unknown at the beginning of this work.
SNPE turned towards selection of major impurities, isolation and characterization to be able to normalize their amount to HNIW and so to obtain a reliable quantitative analysis of HNIW.
This paper will describe these procedures from isolation to HPLC separation and quantitative assessment.

1) Experimental

Preparative liquid chromatography was performed with a Büchi column model B685 (50 mm diameter and 460 mm long), Gilson 305 pump and 117 UV-detector followed with a Gilson 201 fraction collector. Stationary phase was Amicon Matrex Silica 60 Å, 20-45 µm. Eluants are indicated in following section.
Control of separation was achieved by HPLC chromatography on Si 60 column with dichloroethane as eluant.
NMR spectra were collected on a Bruker AC 200 spectrometer with a 5 mm QNP or 10 mm multinuclear probe or AC 400 when mentioned. Chemical shifts were referenced to TMS using acetone deplacement as 2.2 for proton and 30.2 for ^{13}C. Multipulses sequences were manufacturer's ones. For 1D spectra, resolution was set at 0.2 Hz/pt for ^{1}H and 0.3 Hz/pt for ^{13}C ; for 2D spectra it was 0.3 Hz/pt for COSY and 0.2 and 3 respectively for ^{1}H and ^{13}C dimension. Program PANIC was used for simulation.
Mass spectra were collected on a Nermag R10 spectrometer with a ionisation potential of 70 eV.

2)Separation of impurities

Separation of impurities has been performed by two different ways:

- crude HNIW contains impurities that are observable on the proton NMR spectrum as complex signals located at the bottom of low-field signals of HNIW. Impurities have been separated from such a product by semi-preparative chromatography using dichloroethane for elution.
- by quenching nitrolysis medium before completion, other impurities have been separated (eluant is ethyl acetate 20 / methylene chloride 80).

3) Identification

Pentanitromonooxopentaazaisowurtzitane

4,6,8,10,12-pentanitro-2-monooxo-4,6,8,10,12-pentaazaisowurtzitane (**1**) was isolated from crude HNIW.
Mass spectrometry indicates molecular weight of 394.
Carbon NMR spectrum shows six peaks at 71.7, 72.4, 72.45, 76.3, 84.6 and 90.1 ppm.
Proton NMR spectrum consists of a complex pattern split into two parts integrating each of them for the same number of protons. At 400 MHz, the structure of the low field pattern is simplified and suggests a decomposition into three H designated as X, Y and Z protons. The high field part accounts therefore for three protons T, U, V.
Structure elucidation is performed via 2D COSY experiments. Magnitude (fig. 1) and phased 2D spectra allow determinations of coupling constants (table 1).

Table 1 : *Coupling constants (Hz) and ^1H chemical shifts (ppm) observed in compound **1***

	X	Y	Z	T	U	V
X	/					
Y	2.48	/				
Z	8.10	0	/			
T	1.01	0	1.04	/		
U	0	7.65	2.86	0	/	
V	0	1.28	0	6.00	0	/
δ	8.430	8.345	8.281	7.860	7.742	7.658

Structure is consistent with the following formula

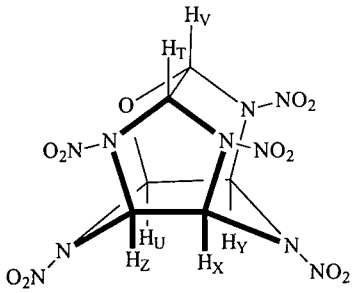

Oxygen atom is obviously located at the place of one of the four equivalent N-NO_2 groups of HNIW in order to have no symmetry to lead to such a spectrum.
Highest couplings values are typical of three A-B systems (V-T, Z-X, U-Y). All ^4J W couplings through nitramino groups are observed ; the couplings between atoms belonging to the six membered ring ((U-Z, X-Y) are of higher magnitude than the couplings in the seven member rings (T-Z, T-X, V-Y). Linkages with oxygen atom do not transmit U-V coupling.
Simulation of spectrum using chemical shifts and couplings constants of table 1 without refinement shows good agreement between calculated and observed spectra (fig 2).
Assignment of ^{13}C chemical shifts was done by heteronuclear 2D correlation. Using the same formalism as for H designation, attribution is as follow (table 2):

Table 2 : *^{13}C Chemical shifts in compound **1***

Carbon atom	chemical shift (ppm)
C_V	90.1
C_U	84.6
C_T	76.3
C_X	72.45
C_Y	72.40
C_Z	71.7

Tetranitrodioxotetraazaisowurtzitane

4,6,8,10-tetranitro-2,12-dioxotetraazaisowurtzitane (**2**) was also isolated from crude HNIW. Mass spectrometry (IC CH_4) indicates a molecular mass at 350, corresponding to HNIW in which two nitramino groups have been replaced by oxygen atoms.
^{13}C NMR spectrum consists of four peaks at 102, 83.5, 79.1 and 72 ppm.
Among the six possible isomers, only the following structure has the symmetry leading to four different signals

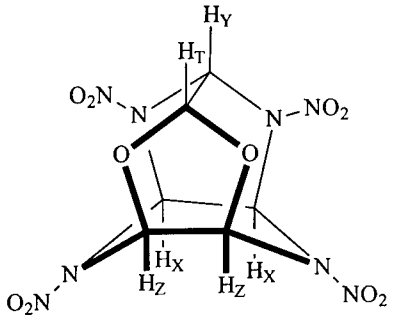

^1H spectrum affords three patterns centered at 8.25, 7.5 and 6.75 ppm (fig. 3) integrating respectively for 2, 3 and 1 protons. Signal at 7.5 ppm is composed of a doublet and two triplets.

Phased COSY experiments affords determination of couplings and chemical shifts (table 3) :

Table 3 : *Coupling constants (Hz) and ^1H chemical shifts (ppm) observed in compound* ***2***

	X	Y	Z	T
X	/			
Y	1.14	/		
Z	2.55	0	/	
T	0	4.8	0	/
δ	8.25	7.50	7.48	6.75

As in compound **1**, no scalar ^4J coupling is observed trough oxygen atoms whereas ^4J coupling appears through nitramino groups. ^3J coupling magnitude between H_T and H_Y has a smaller value (4.8 Hz) than corresponding ones in compound **1**, probably due to a greater deformation of the cage.

Because of very low quantity of product available, it has not been possible to record 2D H-C correlation spectrum. Assignment of ^{13}C signals has been done by inverse gated decoupled technique to integrate peaks and by heteronuclear selective decoupling to determine connection of C to H atoms (table 4) :

Table 4 : ^{13}C *chemical shifts in compound* ***2***

Carbon atom	chemical shift (ppm)
C_X	72.0
C_Y	79.1
C_Z	83.5
C_T	102.0

Monoacetylpentanitrohexaazaisowurtzitane

2-acetyl-4,6,8,10,12-pentanitro-2,4,6,8,10,12-pentaazaisowurtzitane (**3**) was isolated from partially nitrated mixture.
Mass spectrum (electronic impact) shows peaks at m/e = 436 (M+1), 347 (M+1 - NO_2 - $COCH_3$) ; 301 (M+1 - 2 NO_2 - $COCH_3$) ; 209 (M+1 - 4 NO_2 - $COCH_3$).
^1H NMR (fig. 4) is in accordance with previously described structure (5)

Diacetyltetranitrohexaazaisowurtzitane

Two different diacetyltetranitrohexaazaisowurtzitane have been separated from partially nitrated reaction medium.
Mass spectra are quite similar for the two isomers, showing only changes in relative intensity of peaks.
Only one of them, designated as "tetra 2" (**4**), was pure enough to try to elucidate structure. The other will be designated as "tetra 1" or compound (**5**).
^1H spectrum consists of a singlet at 2.4 ppm (6H, CH_3), a doublet at 8.23 ppm (2H, J = 7.6 Hz), a doublet at 7.92 ppm (2H, 7.6 Hz) and a singlet at 7.62 ppm.

Because of the synthetic route, we know that N4 and N10 bear nitro groups. Among the three possible isomers of diacetyl-tetranitro- derivatives

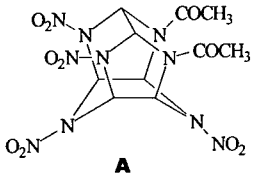
A

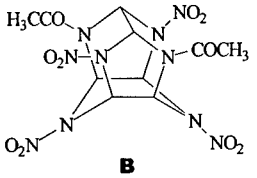
B

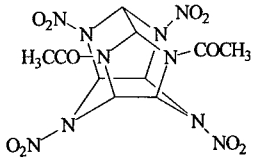
C

we tentatively assign the structure of "tetra2" as **A**, with no ^4Jcouplings even through the nitramino group due to a large deformation of the cage.

Tetraacetyldinitrohexaazaisowurtzitane

2,6,8,12-tetraacetyl-4,10-dinitrohexaazaisowurtzitane was obtained by oxidation of dinitroso corresponding derivative with nitric acid (2).

Tex

Tex (2,6,8,12-tetraoxo-4,10-dinitrohexaazaisowurtzitane) was prepared by the one-pot procedure of Boyer (6).

4) HPLC separation

Topic of the study

HNIW purity is determined by high performance liquid chromatography (HPLC) because of the high separation performance of this technique towards HNIW and its impurities. It allows to determine HNIW purity with a good precision (0.5% relative precision).
The first HPLC method development was an external HNIW and impurities calibration method, with HNIW and impurities standards, qualified by internal normalization HPLC method. This method was too long, heavy and expensive because it required making again periodically impurities, which wasn't realistic. So, we have developed a corrected internal normalization HPLC method, able to suppress HNIW and impurities external calibration, while keeping accurate results.

Application field

The corrected internal normalization HPLC method developed here quantitatively determines only main impurities:

- 2-monoacetyl pentanitrohexaazaisowurtzitane (**3**)
- diacetyl tetranitrohexaazaisowurtzitane (**5**)
- 2,6 diacetyltetranitrohexaazaisowurtzitane (**4**)
- TEX.

The other products described above are separated but not precisely quantified.
It doesn't measure others impurities such as salts, solvents, water or any other impurities which wouldn't be detected by here above HPLC conditions.

Measurement principle

The originality of this internal normalization HPLC method is the determination of response factors of each known impurity versus HNIW response. Then, these response factors are included in the final purity measure relationship to minimize errors due to factor variability .
The principle consists in:
1/ calculating peak area / injected weight ratio of each impurity and HNIW.
2/ multiplying this ratio by a chromophore factor F, related to the number of NO_2 groups, in the impurity and HNIW molecules:

- 1 /2 for TEX
- 1 /4 for tetranitrodiacetyl. impurities
- 1/5 for pentanitromonoacetyl impurity
- 1/6 for HNIW

3/ comparing those product results for each constituant : fact that an impurity (S/W*F) value is similar to HNIW (S/W*F) value , means that correction factor is related to number of NO_2 groups and can be included in purity measure relationship.
Table n°5 presents the response factors (S/W*F) obtained on HNIW and the four analyzed impurities.

Table n°5 *: Response factors (S/W*F) of HNIW and four impurities*

	S/W (1) Arbitrary units	**CORRECTING FACTOR F** (2)	**R. factor S/W x F**
HNIW	2531	1 /6	422
2-acetylpentanitro	2096	1 /5	419
"tetra 1"	1515	1 /4	378 (3)
"tetra 2"	1659	1 /4	415
TEX	1244	1 /2	622 (*)

(1) peak area / injected product weight

(2) F is related to the number of NO2 groups in the molecule

(3) Impure standard

(*) Only TEX presents a response which can't be related to its number of NO_2 groups. This impurity does not exist in actual HNIW samples.

Description of instrumentation and experimental conditions of analysis

- Apparatus

We use a high performance liquid chromatograph (HPLC) equipped with a variable wavelength UV detector and an integrator link up to a data acquisition system. The whole instrumentation is from Waters Corporation.

- Materials

- analytical column Microsorb C-18, L=15 cm, particule size = 5 µm
- eluent is a mixture of acetonitrile (HPLC grade), water (HPLC GRADE) and 85% phosphoric acid (H_3PO_4).

- Experimental conditions

- eluent : 40/60 acetonitrile / water + 0.1% H_3PO_4
- flow rate : 1 ml per minute
- injection volume : 20 µl
- UV detector wavelength : 230nm
- Concentration : 2 mg/ml
- Injection of impurity standards to verify their retention times and comparison with impurities detected in HNIW sample to be analyzed.

Figure n° 5 shows the typical chromatogram of an impurity standards + HNIW mixture, in these analytical conditions.

- Calculation

Taking only in account compounds (**3**), (**4**) and (**5**), the HNIW purity rate relationship, using response factors based on the number of nitramines groups, is as follows:

$$[\text{ HNIW }]\ \text{mol \%} = \frac{S\ (\text{HNIW})}{\sum S + [\ S_c\,(p) + S_c\,(t)\ ] - [\ S\,(p) + S\,(t)]}$$

where :

S (p) = pentanitromonoacetyl (**3**) peak area (not corrected)
S (t) = tetranitrodiacetyl (**4** + **5**) peak area (not corrected)
S_c (p) = S (p) x 6/5 = corrected pentanitro impurity peak area
S_c (t) = S (t) x 6/4 = corrected tetranitro impurities peak area
S(HNIW) = HNIW peak area
$\sum$ S = total chromatogram area of concerned compounds
= S(HNIW) + S (p) + S (t)

The simplified calculation lead to the following final relationship:

$$[\text{ HNIW }]\ \text{mol \%} = \frac{S\ (\text{HNIW})}{\sum S + (1/5 \times S\ (p)) + (1/2 \times S\ (t))}$$

Results

Table n°6 presents purity rate results of 3 HNIW samples produced at SNPE.

Table n°6 *: HNIW samples purity results.*

HNIW produced at SNPE Reference n°:	PURITY RATE (mol %)	Pentanitro-impurity rate (mol %)
916 S 99	99	0.7
573 S 98	99.5	0.2
99 A 1282	99.2	0.6

Figure n° 6 shows typical chromatogram of a HNIW sample produced at SNPE (ref. 916 S 99).

Figure n° 7 presents a zoomed area of impurities zone of this chromatogram.

We can observe the presence of some HNIW impurities, including well identified ones, tetranitrodiacetyl. and pentanitromonooxowurtzitane, at very low rate (estimated inferior to 0.3%).

Conclusion

Preparative separation and identification of the impurities in HNIW allow attribution of the main peaks in HPLC chromatogram.
A new quantitative method based on the response of the chromophore NO_2 at a selected wavelength have been developed and validated. It does not required large amount of by-product for calibration.
This purity determination is well suited for high purity HNIW ans seems more precise than conventional chemical titration.

Acknowledgments

Financial support of French DGA is gratefully acknowledged.

Bibliography

1 B. Wardle; W. Edwards WO 97/20758 (1996)
2 T. Kodama; M. Tojo; M. Ikeda EP 0 753 519 A1 (1996)
3 P. Bescond; H. Graindorge; H. Macé EP 913347 (1999)
4 A. T. Nielsen et al. J. Org. Chem. 1990, 55, 1459-1466
5 M. Kaiser; B. Ditz Proceedings of the 30th Annual Conference ICT 1999, 94-1 – 94-16
6 V. T. Ramakrishnan; M. Vedachalam; J. H. Boyer Heterocycles 1990, 31, 479

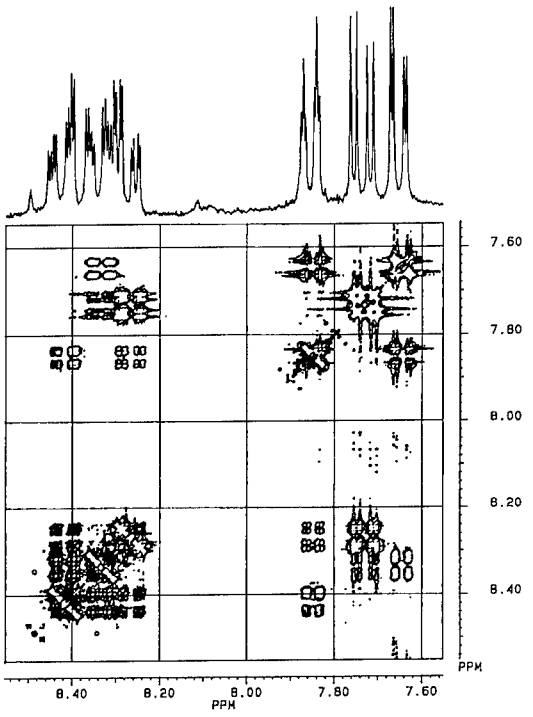

Fig. 1 : DQF COSY Spectrum of pentanitromonooxopentaazaisowurtzitane (**1**)

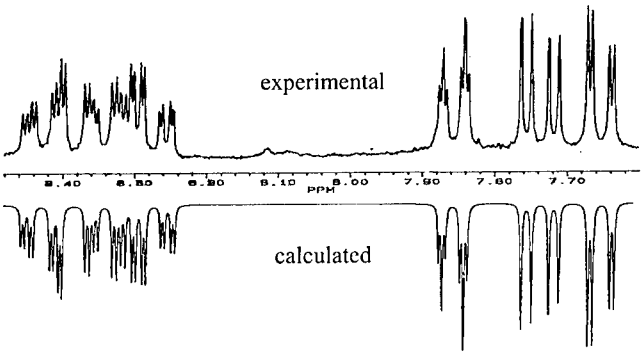

Fig. 2 : comparison of experimental vs calculated spectra of compound (**1**)

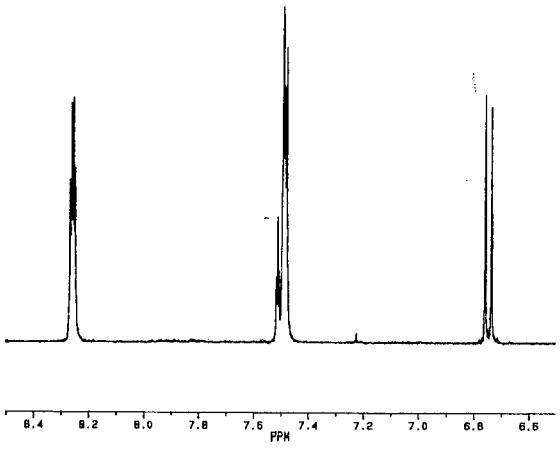

Fig. 3 : ^{1}H spectrum of tetranitrodioxotetraazaisowurtzitane (**2**)

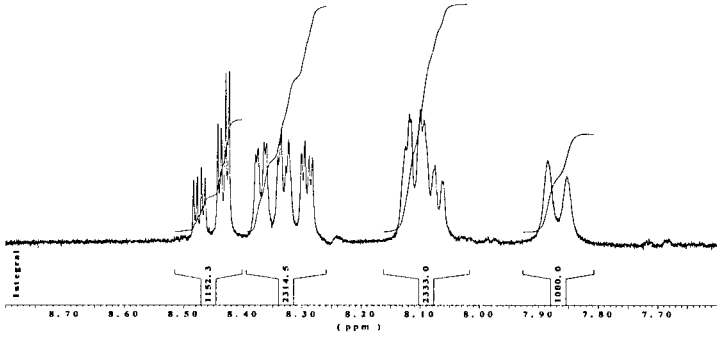

Fig. 4 : ^{1}H spectrum of acetylpentanitrohaxaazaisowurtzitane (**3**)

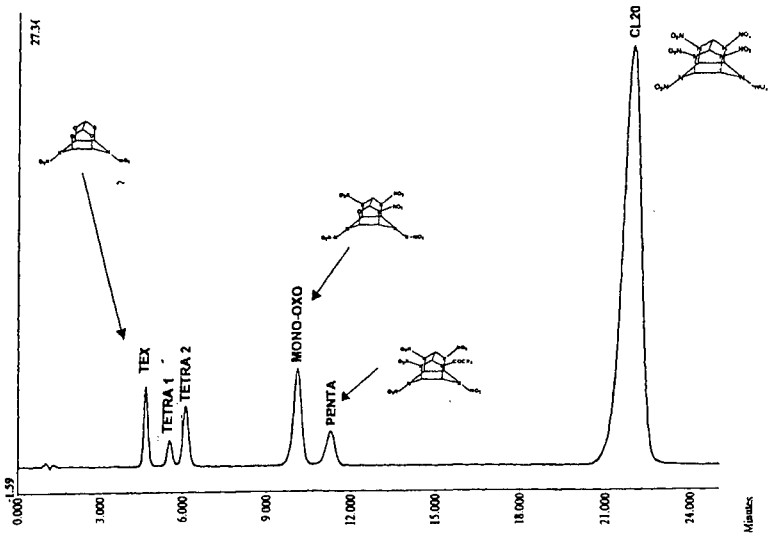

Fig. 5 : typical chromatogram of impurity standards

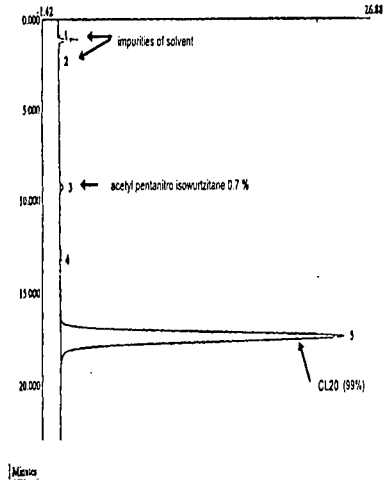

Fig. 6: : typical chromatogram of HNIW sample produced at SNPE (ref.916S99)

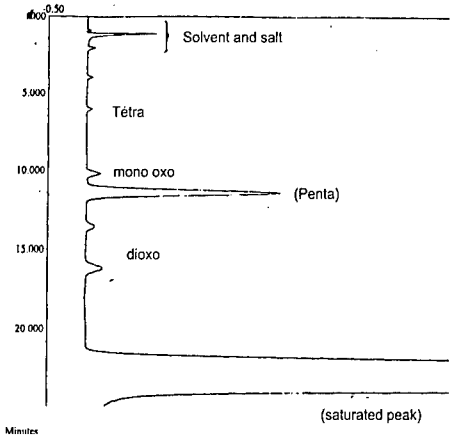

Fig. 7 : zoomed area of impurities zone of HNIW chromatogram

Polymorphism and Solubility of CL20 in Plasticisers and Polymers

Simon Torry, Anthony Cunliffe

DERA, Fort Halstead, Sevenoaks, Kent TN14 7BP, UK.

Abstract

The most powerful commercially available explosive, 2,4,6,8,10,12-hexanitro hexaazaisowurtzitane (CL20) can exist in at least four phases. The preferred polymorph is the epsilon phase as it is morphologically stable at room temperature and has the highest density of the CL20 polymorphs. In this work, DERA has been investigating CL20 solubility and the rate of polymorph conversion at various temperatures in different plasticisers and polymers.

Solubility was measured using variable temperature proton nuclear magnetic resonance spectroscopy. The rate of polymorph conversion was quantified by partial least squares analysis of infra red spectroscopy data. CL20 polymorph conversion was found to be a complex process. There was evidence that 1:1 mixes of epsilon and gamma CL20 obeyed Ostwald's Rule of Stages. At temperatures above the epsilon to gamma phase transition, the meta-stable epsilon polymorph was formed in excess before it converted into the stable gamma phase. In this work, the epsilon to gamma phase transition temperature was estimated to be 56.5±1.5°C.

1. INTRODUCTION

The continuously improving threats faced by UK forces require ongoing technical advances in the performance of UK weapons systems. In the case of plastic bonded explosives and propellants, this can be achieved by improving formulations or by developing new energetic materials. Formulations with RDX and HMX tend to be fully developed, hence a substantial body of work has been devoted to the creation of new energetic materials. One of the most promising explosives to date is hexanitrohexaazaisowurtzitane, (CL20). The explosive performance of CL20 is greater than that measured for the equivalent RDX and HMX compositions. Volume for volume, CL20 exhibits 14% more energy than HMX when using the cylinder test [1].

As with a number of crystalline solids, CL20 can exist as one of several types of polymorphs. Polymorphism is a condition whereby a solid can exist in more than one crystalline form. That is to say, the molecules are packed within the crystal structure in different ways. Consequently, the thermodynamic and solid state properties of polymorphs can differ appreciably. Properties such as density, solubility, hardness, melting point, crystal shape, colour, and chemical reactivity can vary from polymorph to polymorph.

At a certain temperature and pressure, one polymorph tends to be thermodynamically more favoured than others. However, in some circumstances, a polymorph may be meta-stable. That is to say, the rate at which the unstable polymorph transforms to the more stable polymorph may be so slow that the unstable structure persists indefinitely. Some workers try to exploit this effect by introducing stabilisers or by-products into the crystalline structure [2]. In the case of plastic bonded explosives, it is important that the phase transition temperature of a polymorphic system should not occur in normal deployment environments. When temperature cycling induces phase transitions, there are often undesirable changes in physical properties such as the density and crystallite size of the solid filler. This can cause solid/binder de-bonding and lead to cracking of the composite.

Although, the ε form of CL20 has been identified as being stable at room [3] temperature, there has been some debate about the ε to γ polymorph phase transition temperature. In this work, the rates at which CL20 polymorphs inter-convert in the presence of common energetic plasticisers are studied using Fourier transform infrared spectroscopy (FTIR). The ε to γ phase transition temperature has been

identified. Additionally, the solubility of CL20 in some plasticisers and binders has been measured using nuclear magnetic resonance (NMR) spectroscopy.

2. EXPERIMENTAL

Preparation of CL20 Polymorphs

ε-CL20 was used as received (SNPE, CL2089 Lot A1049, UN0475).

β-CL20 was prepared by dissolution of ε-CL20 (7g) in 21g of ethyl acetate (distilled from calcium hydride). The solution was rapidly injected, under nitrogen, into 170g of dry chloroform (distilled from calcium hydride) seeded with a few β-CL20 crystals.

γ-CL20 was prepared by dissolving of ε-CL20 in acetic acid at 115°C. The solvent was allowed to boil off until material crystallised of solution. The sample was washed repeatedly with water until neutral.

1.38g ε-CL20 was dissolved in 3.77g acetone. When all CL20 was in solution distilled water was added to produce a precipitate. The excess liquid was removed with a pipette and the precipitate was dried in a vacuum oven at 45°C.

Polymorph type was confirmed by X-ray diffraction.

Nuclear Magnetic Resonance (NMR) Spectroscopy

NMR spectroscopy was performed on a Bruker MSL300 fitted with a 5mm $^{13}C/^{1}H$ dual NMR probe. Temperature control was achieved by use of the Bruker VTEC09 controller (calibrated by insertion of a thermocouple into the sample coil). Data processing was performed using WINNMR (version 6.0, Bruker).

Solubility Measurements

0.2±0.1 g of CL20 was mixed with 0.7±0.2 cm3 of plasticiser in a 5mm NMR tube. The sample was shaken several times and allowed to equilibrate at 72°C in an oil bath overnight. At all times during the masurement, there was an excess of solid CL20 in the sample.

The NMR tube was transferred to the heated spectrometer and allowed to equilibrate for a further 60 minutes before measurement took place. The temperature was ramped down from 70°C to room temperature automatically. At each temperature, the sample was equilibrated for 1 hour and then shimmed automatically (Z1, Z2, X and Y shim groups).

Polymorph Equilibration Measurements

Two systems were studied:

- the ε/γ system (mass ratio 1:1); and
- the ε/γ/β systems (mass ratio 1:1:1).

Approximately 0.1g of CL20 mix was placed in a sample vial (8mm diameter by 45mm height) with 0.14g of plasticiser. The sample was stirred and heated in an enclosed oil bath at various temperatures.

Approximately 0.05 g of CL20 was withdrawn from the plasticiser mix at known periods. The sample was filtered over 0.5μm nylon filter paper and washed with dichloromethane.

Fourier Transform Infrared (FTIR) Spectroscopy

FTIR measurements were performed on a Nicolet 760 spectrometer fitted with DTGS and MCT detectors. 0.005±0.003g of CL20 was crushed with 0.172±0.03 g of potassium bromide (spectroscopic grade). The solid was loaded into a die and dried in vacuo for five minutes before applying pressure (up to 8 tons) to the sample cell. Clear pellets were obtained.

Quantitative analysis of the CL20 was performed using the Partial Least Squares method as supplied in the Nicolet TurboQuant software suite.

3. RESULTS AND DISCUSSION

FTIR Characterisation of CL20

The most commonly observed CL20 polymorphs are the α, β, ε and γ phases. ε-CL20 is the preferred phase due to its stability at room temperature and its high density. Foltz et al [3] has suggested that there are probably thirteen polymorphs in total. The eleven remaining polymorphs are unlikely to stable due to strong steric hindrances in the theoretical structures.

In this work, the four common CL20 polymorphs have been characterised. The IR spectra of the α, β, ε and γ polymorphs are reported in Figure 1.

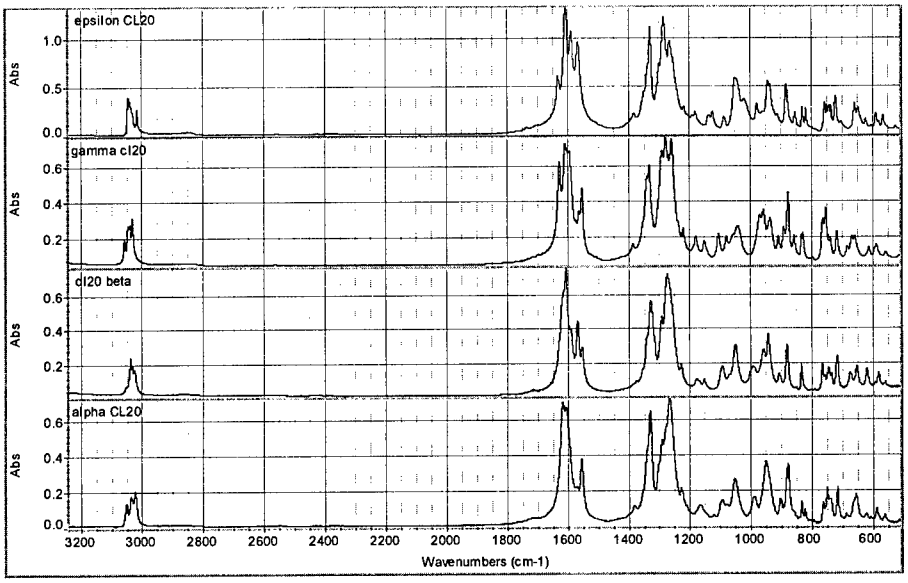

Figure 1. FTIR spectrum of CL20 polymorphs.

Solubility

Liquid state NMR spectroscopy is ideal for solubility measurements. Only dissolved materials are observable using liquid state NMR probes – signals due to solid material are either unobservable or at best exist as very broad peaks on the base line. Hence, dissolved solid can be measured without disturbing the liquid/solid phase equilibrium. A prerequisite condition of this method is well-understood CL20/plasticiser NMR spectra.

Table 1 summarises the solubility of CL20 in various liquids at 30°C. It is noted that CL20 has a high solubility in MEN42 - 16g per 100cm^3 of plasticiser (Figure 2). Similarly, CL20 is reasonably soluble in phthalates. Materials containing nitrate ester groups do not facilitate the dissolution of CL20. As expected, the solubility of CL20 in HTPB and polyNIMMO pre-polymers is very low (not measurable using the NMR process). Surprisingly, CL20 is slightly soluble in polyGLYN (Figure 3).

Over the range studied, temperature did not affect the solubility of CL20 in plasticisers to any large extent.

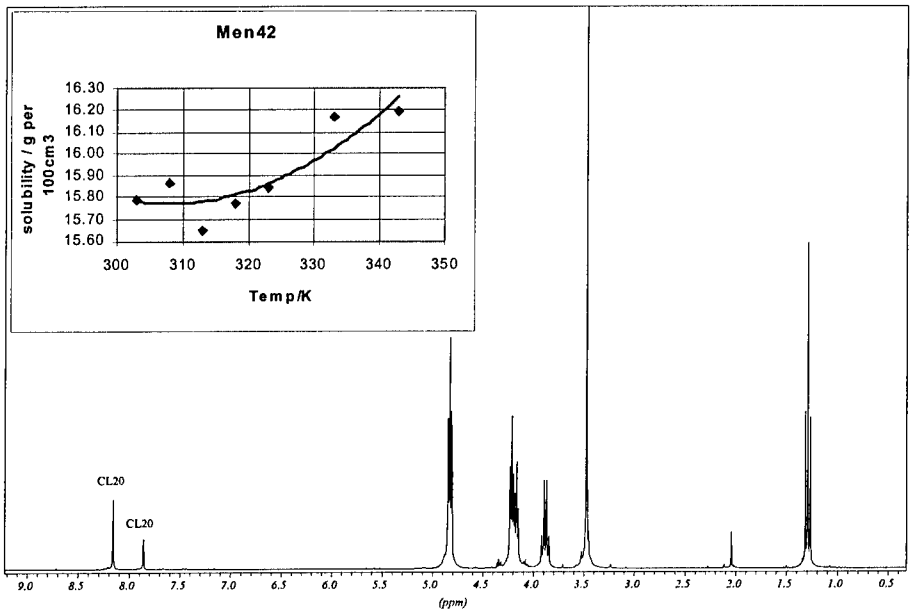

Figure 2. ^{1}H NMR spectra of CL20 dissolved in MEN42 plasticiser at 70°C.

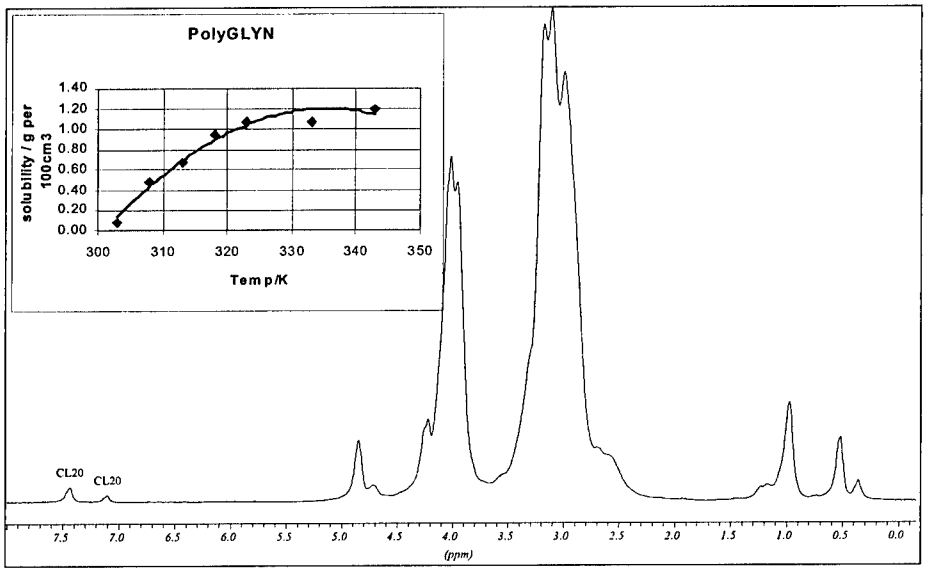

Figure 3. ^{1}H NMR spectra of CL20 dissolved in polyGLYN binder at 70°C.

Plasticiser	CL20 Solubility at 30°C (g per 100g of solvent)
MEN42 (methyl/ethyl nitratoethylnitramine)	15.8
DBP (dibutyl phthlate)	4.9
DOP (dioctyl phthalate)	4.5
BuNENA (butyl nitratoethylnitramine)	3.5
DOS (dioctyl sebacate)	2.8
BTTN (1,2,4-butanetrioltrinitrate)	1.5
MTN (metriol trinitrate)	1.1
BDNPA/F (bisdinitropropyl acetate/formate)	1.0
K10 (trinitro/dinitro ethyl benzene)	0.7
PolyGLYN (polyglycidol nitrate)	0.12
HTPB (polybutadiene)	<0.1
PolyNIMMO (poly3-nitratomethyl-3-methyloxetane)	<0.1

Table 1. The solubility of CL20 in plasticisers.

Solubility in Binder Mixtures.

As expected, the addition of polymer to the plasticiser decreased the quantity of soluble explosive. PolyNIMMO/Men42/Cl20 measurements at 70°C suggest that the mol fraction versus solubility relationship is non-linear (Figure 4). Solubility measurements were performed on CL20/PolyGLYN/BTTN/MTN mixtures. These materials are being developed as part of a new propellant formulation [4]. Unlike the polyNIMMO/Men42 mixtures there was no discernible trend between the plasticiser content and the solubility of CL20. This may be due to errors associated with NMR measurement. At low temperatures, the NMR peaks were broad – it was difficult to fit a reliable baseline to the NMR spectrum. Additionally, the CL20 solubility in the both the pure nitrate esters and the pure polymer was small – large errors are generated when measuring the ratio of small CL20 peaks to a large plasticiser/polymer peaks. Even though large errors are expected in calculating the CL20 content, it is however clear that addition of the plasticisers to the polyGLYN did not change the CL20 solubility to any large extent (Figure 5).

Polymer	Plasticiser	Mass ratio of polymer:plasticiser	CL20 solubility at 70°C.
PolyNIMMO(PP600)	K10	1:1	2.0
PolyNIMMO(PP600)	Men42	1:1	5.3
PolyNIMMO(PP600)	Men42	1:2	11.7
PolyNIMMO(PP600)	Men42	2:1	2.3
Polybutadiene	DOS	1:1	0.9
PolyGLYN	BTTN:MTN (1:1)	1:1	1.4
PolyGLYN	BTTN:MTN (1:1)	1:0.4	1.5
PolyGLYN	BTTN:MTN (1:1)	1:1.6	1.3

Table 2. Solubility of CL20 at 70°C in polymer/plasticiser mixtures.

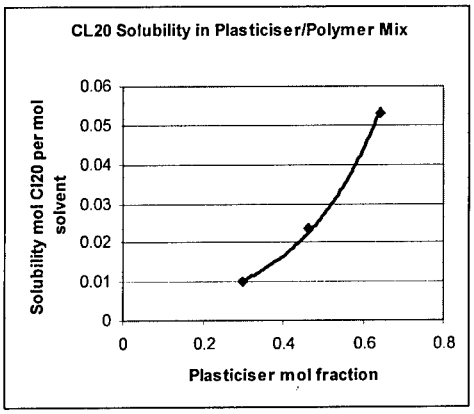

Figure 4. CL20 solubility in polyNIMMO/Men42 mixtures.

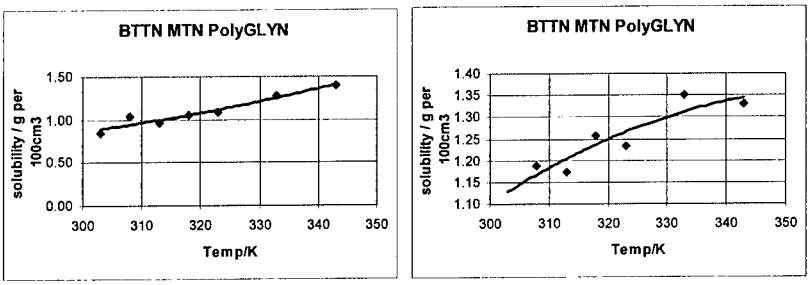

Figure 5. Solubility of CL20 in PolyGLYN:BTTN:MTN mixes (left 1:0.5:0.5 polyGlyn:BTTN:MTN by mass, right 1:0.2:0.2 polyGLYN:BTTN:MTN.

Polymorphic Phase Change – ε/γ CL20

ε-CL20 is the preferred polymorph as it has the highest density of the CL20 phases. Previous work [3] has suggested that at temperatures above 64±1°C, the ε phase transforms to the γ phase. This temperature is similar to that employed during the preparation of polyurethane based plastic bonded explosives and propellants. Hence, the rates of polymorphic inter-conversion of 50:50 ε:γ CL20 mixtures in MEN42 plasticiser were investigated in the temperature range of 54 to 70°C.

Quantitative analysis was performed using the partial least squares method supplied in the Nicolet Turbo software. The calibration curve consisted of thirteen standards and two validation samples. Three out the seven factors were used in the partial least squares calculation. Both the mean centering and the variance scaling techniques were used in the partial least squares calculation. Five spectrum areas were used in the calibration method (no baseline, 986-953, 730.1-714.60, 3035.4-3029.5,3020.2-3014.1, 3064.7-3054.3 cm^{-1}). All peaks were normalised against the nitrate ester area (1612.2 to 1603.52 cm^{-1}, two point baseline 2010.43-1462.74 cm^{-1}). The calibration line was not forced through the zero point. As received "pure" ε-CL20 material was calculated to be 98% by mass thereby suggesting that 2% by mass of other CL20 phases/impurities are present.

The phase composition error tended to vary from 2 to 10 %. Although this method is eminently suitable for measuring large changes in the CL20 phase composition, it is not precise enough to measure small quantities of undesirable phases in as received ε-CL20.

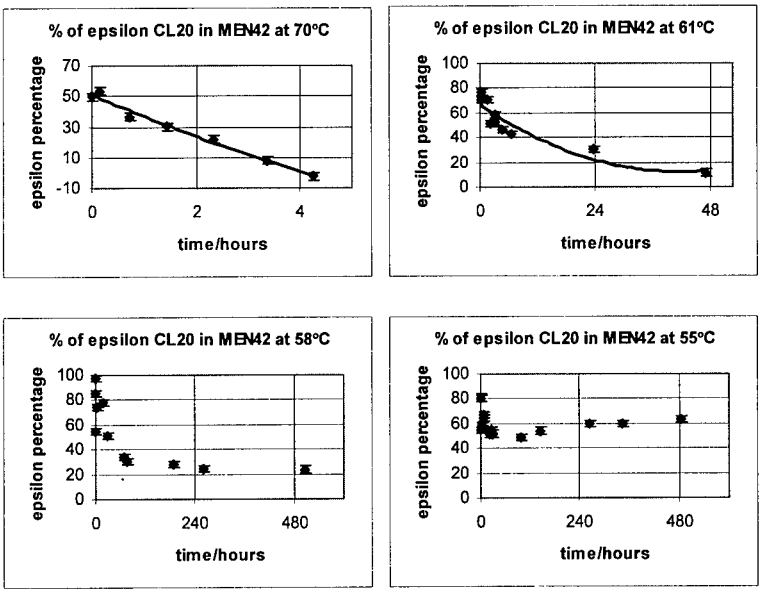

Figure 6. The mass % of ε-CL20 in MEN42 equilibrated at various temperatures.

CL20 ε/γ mixtures stirred at 70°C (Figure 6) converted to γ phase within five hours in MEN42 plasticiser. Although the rate of conversion of the ε phase is quick, there ought not be a problem in real life PBX/propellant preparations.

Re-crystallisation and polymorphic inter-conversions are complex processes. Although the inter-conversion of CL20 at 70°C appears to demonstrate simple behaviour, the polymorphic conversion of ε/γ phases at lower temperatures is more complicated.

Despite being below the reported ε to γ transition temperature (64°C), the equilibration of γ/ε-CL20 mixes at 61.1°C (Figure 6) clearly shows that the γ-CL20 is the preferred species at 61.1°C. Equilibration studies at 58 and 55°C suggest that the γ/ε transition temperature is 56.5 ±1.5°C. The equilibration curves are complex: they do not follow the simple behaviour as seen in the 70°C equilibration study. Initial measurements at 55, 58 and 61.1°C suggest that γ phase is rapidly converted to ε phase. That is to say, the initial concentration of the ε material increased from 54% to 97% (at 58°C). Thereafter, the concentration of the ε material decreased slowly at temperatures above 56.5°C. Increase in the concentration of the metastable ε phase may be a consequence of Ostwald's rule of stages [5]. Re-crystallisation processes proceed with the lowest loss of free energy. That is to say, the metastable species may crystallise out before the more thermodynamically stable phase.

Alternatively, the dissolution rate of the γ crystals may be greater than the ε crystals, thereby increasing the apparent concentration of the metastable phase. Additionally, very small crystals (eg γ-CL20) may be washed through the 0.45 micron filter. Consequently, FTIR measurements may not observe the stable γ nuclei crystals.

At the lower temperatures, the rate of change from the ε phase to the γ phase is slow. At 55°C, the γ-CL20 phase is initially favoured in the first 120 hours of measurement. After a prolonged induction

period, the γ phase was slowly transformed to the ε phase. The nature of this complex phenomenon is not known and may be another example of Ostwald's rule of stages.

Polymorphic Phase Change – ε/β/γ in Various Plasticisers

The calibration curves for the ε/β/γ CL20 mixes were measured using thirty-one standards and three validation samples. The relative peaks were normalised against the spectral area between 1778 and 1196 cm^{-1} (two-point baseline 2034 to 1196 cm^{-1}). Eight spectral areas were used to characterise the polymorphic content.

The rate of polymorph consumption/production was followed for 1:1:1 mixes of β:ε:γ CL20 in various plasticisers (DOS, MEN42, BTTN, K10, MTN, DOP, and BDNPA/F). In this paper, we illustrate CL20 phase transformation in BTTN and MEN42. Phase composition measurements in all plasticisers suggested that the β phase was consumed within thirty minutes. The errors associated with calculating low concentration of β phase are large. Nevertheless, close inspection of the IR spectra confirmed that little or no β phase is present in the sample.

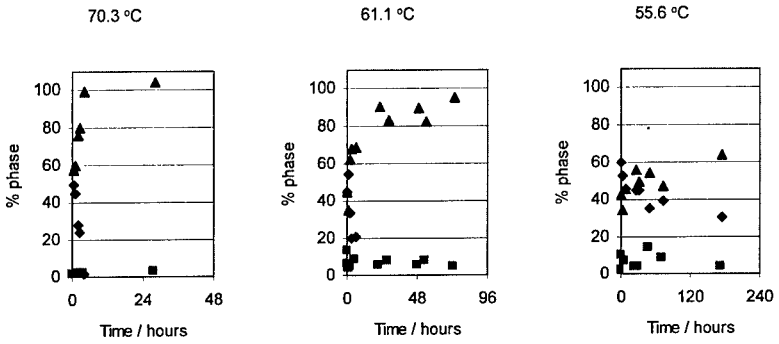

Figure 7. Equilibration of gamma (▲), epsilon (◆) and beta (■) CL20 in BTTN.

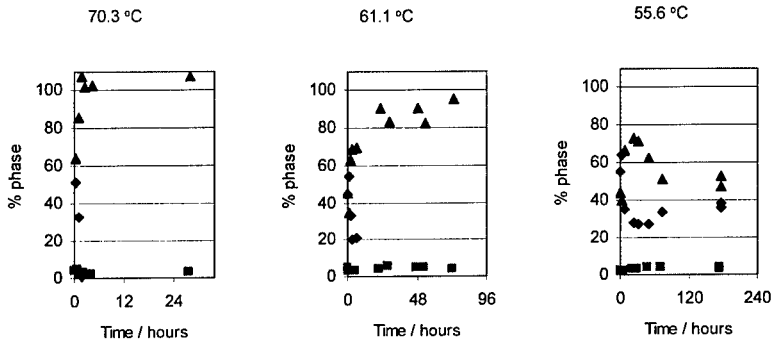

Figure 8. Equilibration of gamma (▲), epsilon (◆) and beta (■) CL20 in MEN42.

The β phase is either consumed by preferential dissolution or phase transformation. At 70.3°C, the CL20 mixes are γ rich in most solvents, which may suggest that the β phase rapidly transforms to the γ species. At the lower temperature (55.6°C), some of the mixes appeared to be ε rich. That is to say the β sample may have transformed to the ε phase. Alternatively, the preferential production of some CL20 phases may be associated with the phase's solubility at the measured temperature. That is to say, the metastable β phase is preferentially dissolved thereby forming super-saturated metastable solutions. However, depending on the solvent, ε-CL20 solubility varies from 1 to 16 g CL20 per 100cm^3 of solvent (about 1g to 19g of CL20 per 100g of plasticiser). The ratio of CL20 to solvent in the phase transformation measurements was 1:1.36. If the β-CL20 preferentially dissolved, then concentration of CL20 in the solvents would be at least 1g per 4g of solvent - a very high solubility.

Generally, the low temperature CL20 phase measurements (55.6°C) suggested that the γ phase was the thermodynamically stable polymorph (eg BTTN - Figure 7). However, close inspection of the MEN42 data (Figure 8) shows that the concentration of the γ phase decreases before it slowly increases. That is to say, there appears to be induction period before the epsilon phase is produced. This may be another manifestation of Ostwald's rule of stages. Therefore, it is the opinion of the authors, that below 55.6°C, the epsilon phase is the most thermodynamically stable phase. The solubility of CL20 in all the plasticisers other than MEN42 is low. Hence, the rate of production of ε-CL20 is kinetically slow due to dissolution rates limited by solubility constraints.

Phase Equilibration in Plasticised Binders.

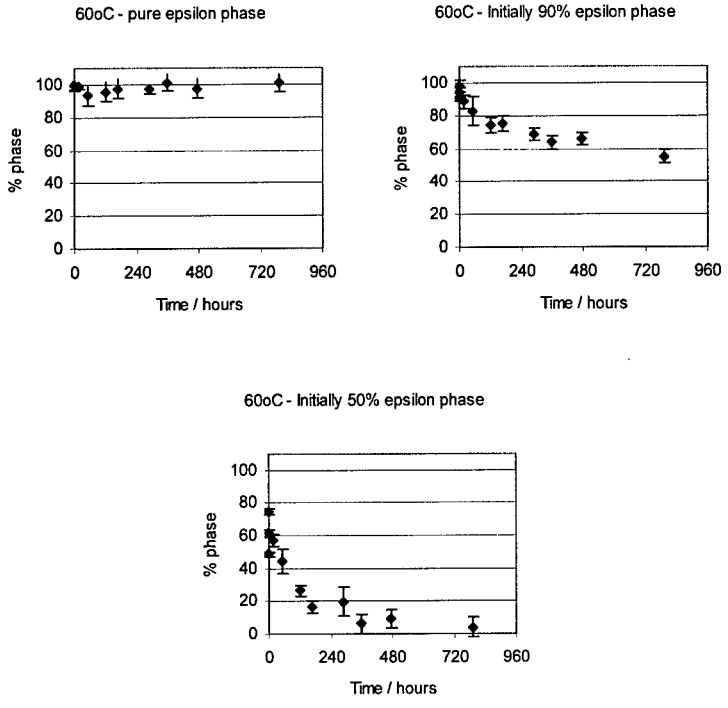

Figure 9. The inter-conversion of CL20 phases at 60°C in polyGLYN/MTN/BTTN mixes.

CL20 is reasonably soluble in polyGLYN plasticised with 25% BTTN and 25% MTN, Hence, the inter-conversion of CL20 polymorphs was measured in this potential propellant binder system. Three mixtures were studied at 60°C and 70°C:

- 50% ε-CL20 50% γ-CL20;
- 90% ε-CL20 10% γ-CL20;
- as received ε-CL20.

At 60°C, the mixtures containing 90% and 50% ε-CL20 slowly converted to the γ phase (Figure 9). The pure, as received ε-CL20, remained as the ε phase throughout the experiment. In the absence of γ-CL20 crystals, ε-CL20 appears to be meta-stable at 60°C.

As in previous experiments, the concentration of the ε phase in the 1:1 ε:γ CL20 mix appeared to increase to 80% by mass before it decreased to 0% by mass.

At 70°C, ε-CL20 converted to γ-CL20 (Figure 10) in the presence of γ-CL20 seeds. The 'pure' ε-CL20 appeared to be metastable at 70°C in the polyGLYN/BTTN/MTN mix during the time scale studied. This may not be the case for other pre-polymer/plasticiser mixtures. Additionally, other CL20 batches may contain appreciable quantities of undesirable phases, which could seed phase transformation processes. At this moment in time, a method to accurately characterise small quantities of CL20 phases does not exist.

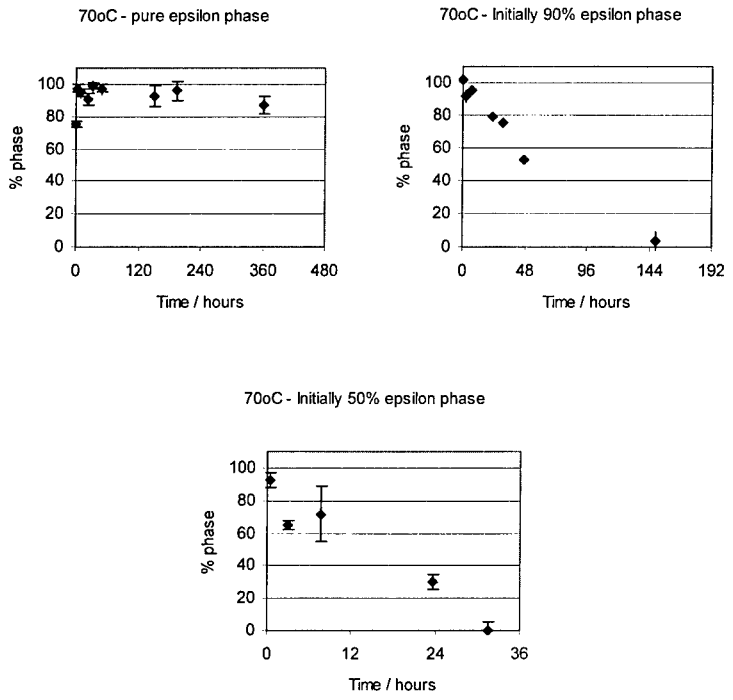

Figure 10. The inter-conversion of CL20 phases at 70°C in polyGLYN/MTN/BTTN mixes.

4. General Discussion and Conclusions

The rate at which polymorphs inter-convert is complicated. It depends on a number of factors including:

- the nature of the solvent;
- the polymorph's solubility;
- diffusion/transport at the crystal face;
- the crystal size;
- the surface energy of each crystal face;
- the impurities/additives adsorbing at the crystalline face; and
- the nucleation rates and re-crystallisation processes of competing crystals.

This work demonstrates that CL20 is soluble in a number of common energetic plasticisers. CL20 is reasonably soluble in the NENA and phthalate plasticisers at room temperature. Plasticisers containing only nitrate functional groups appear to solvate CL20 the least.

Although addition of binder lowers the explosive's solubility, there may still be potential for re-crystallisation of the fine explosive crystals in the composite. This could lead to the composite hardening in a similar manner observed in the moist ageing of ammonium perchlorate based propellants [6]. Generally, temperature did not greatly affect the CL20 solubility in plasticisers/binders. This will moderate the effect of temperature cycling in accelerating CL20 recrystallisation.

A number of authors have made the observation that solvents accelerate the polymorphic inter-conversion rate of crystals. In the absence of solvent, γ-CL20 is meta-stable for years at room temperature. However, when placed in contact with a solvent below 56.5±1.5°C, the γ phase slowly converts to the ε phase. The γ to ε phase transition temperature reported in this work 56.5±1.5°C is lower than previously reported values (64°C) [3]. Previous authors have measured the transition temperature using pure phases (eg pure ε CL20). However, in this work, the CL20 was stirred in equilibrium with seed crystals. Consequently, the CL20 ε to γ phase transition temperature was lowered by 7°C.

However, it should be noted that 'pure' ε-CL20 appeared to be stable at 70°C in polyGLYN/BTTN/MTN. That is to say, the ε-CL20 to γ-CL20 phase transition probably requires the presence of a nucleation species. In the absence of γ-CL20, ε-CL20 may be stable at temperatures above 57°C for several days in polyGLYN/BTTN/MTN mixes. This may not be the case for all plasticisers and solvents. Some work on other crystal systems has shown that additives can kinetically slow down the re-crystallisation process thereby apparently stabilising the metastable species.

An important feature of this work is that the CL20/plasticiser mixtures were stirred at all times. This helps to negate any CL20 diffusion effects. In propellants and plastic bonded explosives, CL20 diffusion is likely to play an important part in potential phase transformation/re-crystallisation processes.

Although γ-CL20 could not be detected in the material used in this project, future batches and other sources of CL20 may be contaminated with enough γ-CL20/β-CL20 so as to cause potential problems. Therefore, on a practical level, it is important that 'pure' ε-CL20 composites are not exposed to temperatures above 57°C. If this temperature is exceeded, ε-CL20 (seeded with γ-CL20) will convert to γ-CL20 thereby changing the density of the crystal and possibly causing cracking of the plastic bonded explosive. If the material is contaminated with γ-CL20, the mixing and storage temperature should not exceed 56°C.

5. Conclusions

Re-crystallisation is a very complex process. This work presents a practical study on some of the conditions for processing and storing CL20 composites.

ε-CL20 is soluble in a number of common energetic and non-energetic plasticisers. The highest CL20 solubility measurements were observed in phthalate esters and nitratoethylnitramine compounds. CL20 was least soluble in compounds containing nitrate just nitrate ester functional groups.

CL20 exhibited little or no solubility in polyNIMMO and polybutadiene pre-polymer binders. CL20 was slightly soluble in polyGLYN.

Addition of plasticiser to the pre-polymer increased the solubility of CL20 in a non-linear manner.

CL20 phases were characterised using FTIR spectroscopy. Partial least squares analysis of FTIR data was used to quantitatively characterise the CL20 phase percentage.

Above 57°C, ε/γ and ε/γ/β CL20 mixtures converted to γ-CL20. The rate of conversion depended on the nature of the solvent. There was no correlation between the solubility of the CL20 and the rate of polymorph conversion in the plasticisers studied. β-CL20 was not observed after twenty minutes immersion in plasticiser – it was rapidly consumed during the re-crystallisation processes.

Unusual, consistent anomalies in the CL20 polymorphic inter-conversion processes suggest that Ostwald's rule of stages apply to the CL20 system. The metastable species appeared to increase in concentration before the more thermodynamically stable species crystallised.

'Pure' ε-CL20 appeared to be metastable in polyGLYN/BTTN/MTN mixtures above the ε to γ phase transition temperature. This suggests that conversion of ε-CL20 above the high temperature phase transition require γ nucleation species/seeds. At this moment in time, a method for measuring small quantities of polymorphic impurities does not exist.

5. References

1 RL Simpson, PA Urtiew, DL Ornellas, GL Moody, KJ Scribner, DM Hoffman, Propellants, Explosives, Pyrotechnics, 22, 249-255, (1997).
2 N Blagden, R Davey, Chemistry in Britain, 35(3), 44-47, 1999.
3 MF. Foltz, C.L. Coon, F. Garcia, A. L. Nichols III, Propellants, Explosives, Pyrotechnics, **19**, 19-25 and 133-144, 1994.
4 AV Cunliffe, C Leach, Private Communication, Fort Halstead, Jan 2000,
5 W Ostwald, Z. Phys. Chem. (Liepzig), 289, 22, 1897.
6 SA Torry, AV Cunliffe, Humid Ageing of Composite Propellants: Part 2, Unpublished results, 1999.

© British Crown Copyright 2000/DERA

Published with the permission of the Controller of Her Britannic Majesty's Stationary Office.

PROCESS IMPROVEMENTS IN CL-20 MANUFACTURE

Rao Surapaneni; Reddy Damavarapu
U.S. Army Armament Research, Development and Engineering Center
Picatinny Arsenal, NJ 07806-5000
Rajagopal Duddu; Ajay Kumar and Paritosh R. Dave
GEO-CENTERS, INC. @ ARDEC
Bldg. 3028, Picatinny Arsenal, NJ 07806-5000

Abstract:
CL-20 is a highly powerful new energetic material with a variety of potential applications. There are two generally utilized approaches to CL-20, that start with common reagents. This paper presents the results of our investigations aimed at process improvements to provide for an economical, environmentally friendlier process for the preparation of CL-20.

Hexanitrohexaazaisowurtzitane, (CL-20), first synthesized by Nielsen, is a high energy density material of considerable current interest for a variety of applications. Following several years of process development, two slightly different methods have emerged. Both methods start with the condensation of benzylamine with glyoxal to form hexabenzylhexazaisowurtzitane, HBIW. Replacement of the benzyl groups by nitro groups is achieved by different routes.

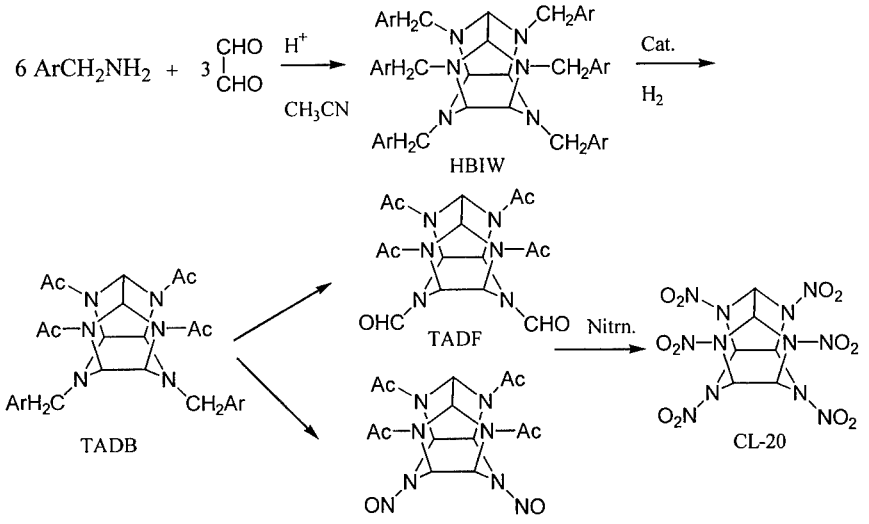

In one method, HBIW is subjected to a two-step catalytic hydrogenation to produce tetraacetyldiformyhexazaisowurtzitane, TADF, which is then nitrolyzed by standard method to obtain CL-20.

In another method, HBIW is subjected to hydrogenation in acetic anhydride to replace four of the six benzyl groups, to give tetraacetyldibenzylhexaazaisowurtzitane, TADB. Nitrosation of TADB then results in the formation of tetracetyldinitrosohexaazaisowurtzitane, which is then nitrolyzed to obtain CL-20.

A common drawback of both approaches is the necessity to use benzylamine in the condensation step. It has been found that only benzylic amines give the isowurtzitane skeleton in this condensation. In the subsequent steps, more than 90% of the weight of benzylamine is discarded. Based on atom economy and cost of starting material, the use of a lower molecular weight aliphatic type amine would be desirable. Additionally, removal of the benzyl groups requires hydrogenolysis, which on an industrial scale has its own drawbacks. Finally, the nitration of the penultimate intermediate, produces spent acid waste as well as other impurities in the product that are believed to form due to the heat released upon quenching of the nitration reaction.

Addressing some or all of the above issues in the preparation of CL-20 would result in a more economical process that is environmentally less harmful. We have investigated alternatives to each step in the process with this view and the results are presented herein.

As an alternate to benzylamine, the condensation of a number of amines and amides with glyoxal has been investigated, using different organic acid and mineral acid catalysts under a variety of conditions (solvent, temperature, etc.). However, in no cases was the formation of isowurtzitane detectable.

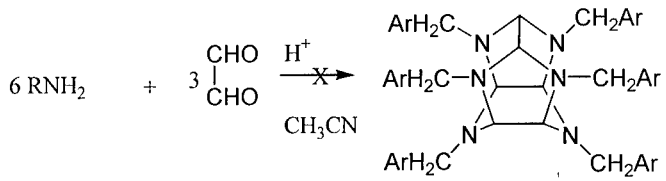

R = tert-Bu; CH_3CO etc.

We therefore focused our attention on developing non-hydrogenolytic methods for the removal of the benzyl groups of HBIW. Recently, we have successfully developed and demonstrated the Lewis acid catalyzed acylation of tertiary amines bearing carbocation stabilizing substituents such as tert-butyl, isopropyl and benzyl groups on tertiary amines. It was therefore of interest to investigate the acylative debenzylation of HBIW. HBIW was thus treated with acylating agents such as acetic anhydride, acetyl chloride, chloroformates etc. in the presence of various Lewis acid catalysts under different conditions. In most cases, products from the decomposition of the cage system or partial acylation were observed. The reaction of HBIW with acetyl chloride in the presence of $TiCl_4$ resulted in the formation of a triacetyltribenzylisowurtzitane, based on the integration of the proton NMR spectrum of the reaction product. Nitration of the reaction product led to the formation of CL-20 isolable in very low yields. Further optimization of this sequence is necessary before it becomes useful as a non-hydrogenolytic route to CL-20.

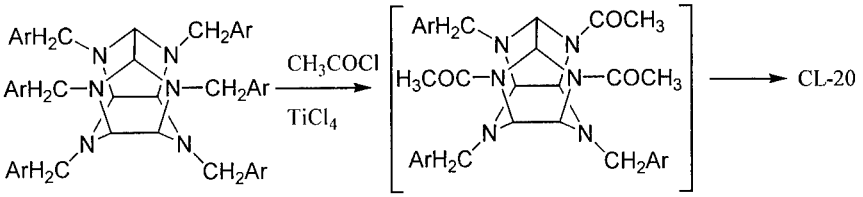

Possible Structure From NMR

It has been observed that the nitration of TADF is not successful with nitric acid alone. Noting that simple N-acyl amines can be cleanly nitrated with conc. Nitric acid we decided to investigate the nitration of TADF. The advantages of a single acid nitration would be lower reagent cost as well as a simplified waste stream. In our initial studies we subjected TADF to nitric acid nitration in the presence of solid acid catalysts. Nafion-H was found to promote the formation of CL-20 with nitric acid at 85 ^{0}C, in very modest yields. In varying the conditions it was found that the use of higher temperatures promoted the reaction even further, even in the absence of Nafion-H. Thus, at an external temperature of 125 ^{0}C, nitric acid nitration of TADF produced CL-20 in 90-97 % yields. This procedure is advantageous in that concentrated nitric acid is inexpensive and the waste stream is simplified in that it constitutes of only dilute nitric acid.

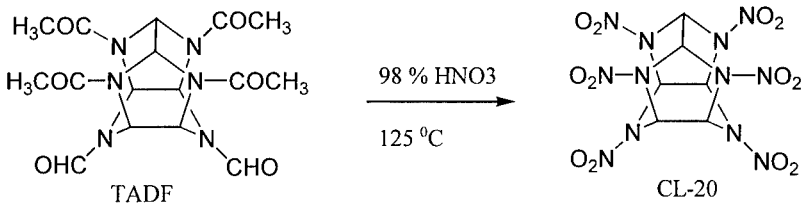

TADF CL-20

The CL-20 thus produced is always obtained as the gamma polymorph, which was converted to the higher density epsilon polymorph by recrystallization.

POLYNITROHEXAAZAISOWURTZITANE DERIVATIVES RELATED TO HEXANITROHEXAAZAISOWURTZITANE (HNIW, WN_6)

Anthony J. Bellamy
Department of Environmental and Ordnance Systems,
Cranfield University/ RMCS,
Shrivenham, Swindon SN6 8LA, UK

Abstract.
Incomplete nitrolysis of 2,6,8,12-tetraacetyl-4,10-diformylhexaaza-isowurtzitane has been shown to leave predominantly monoformylpentanitro- and diformyltetranitro-hexaazaisowurtzitane, nitrolysis of the N-acetyl groups occurring much more rapidly than that of the N-formyl groups.

Chemical reduction of hexanitrohexaazaisowurtzitane has been shown to give predominantly the 2-H mono-amine, which is then reduced further to *inter alia* the 2-H,4-H and 2-H,10H di-amines. The isomeric mono- and di-amines may also be formed.

Products from the under-nitration of 2,6,8,12-tetraacetyl-4,10-diformyl-hexaazaisowurtzitane (WA_4F_2)

The nitration of WA_4F_2 with 20vol% 98% H_2SO_4 in 90% HNO_3 (80°C/4h) gives 97+% pure HNIW, but nitration with 10wt% 98% H_2SO_4 in 99.5% HNO_3 (75°C) gives incomplete nitration even after 6h, with the product consisting of a mixture of HNIW and 2 intermediates (isolated by medium-pressure chromatography and characterised by ^1H and ^{13}C NMR), 4,10-diformyl-2,6,8,12-tetranitrohexaazaisowurtzitane (WF_2N_4) and 4-formyl-2,6,8,10,12-pentanitrohexaazaisowurtzitane (WFN_5). The isolation of these intermediates indicates that the formyl groups in WA_4F_2 are nitrolysed more slowly than the acetyl groups, the reaction sequence being: $WA_4F_2 \rightarrow WF_2N_4 \rightarrow WFN_5 \rightarrow WN_6$. This accounts for the usual presence of WFN_5 as a minor impurity in HNIW manufactured by nitration of WA_4F_2 [1].

Experimental details

(i) WA_4F_2 (0.5g) was added to 10wt% 98% H_2SO_4 in 99.5% HNO_3 (5.0ml) at room temperature and stirred until the solid had dissolved. The solution was then heated at 75°C during 6h. Samples were removed at 2, 3, 4, 5 and 6h, and the isolated products were analysed by HPLC:

RT/min time/h	0.82	2.83 WF_2N_4	3.22	3.74 WFN_5	4.53 HNIW
2	1.4	59.7	0.1	32.8	5.9%
3	1.1	49.1	-	39.9	9.9%
4	1.2	39.8	-	44.3	14.8%
5	1.1	30.7	-	46.8	21.4%
6	1.4	25.3	-	46.8	26.6%

(ii) The products from i (4, 5 and 6h; 0.18g) were combined and nitrated with 20vol% 98% H_2SO_4 in 90% HNO_3 (6.1ml) at 80°C/4h. The product was isolated to give HNIW (0.16g; HNIW-content 97.1%).

(iii) WA_4F_2 (2.0g) was added to 10wt% 98% H_2SO_4 in 99.5% HNO_3 (49ml) with cooling in ice/water and then heated at 75-80°C during 4h. The hot solution was poured onto ice (166g) and diluted to 400ml with water. The mixture was left for 30min before the product was filtered off. The material was washed with water and dried. Yield 0.92g. HPLC analysis:

RT/min	0.82	2.83 WF_2N_4	3.22	3.74 WFN_5	4.53 HNIW
	0.5	18.4	0.5	47.0	33.1%

TLC analysis (heptane/ethyl acetate 3/2): R_f 0.60 (HNIW), 0.42 (WFN_5) and 0.16 (WF_2N_4). The components were separated by medium-pressure chromatography (Biotage Flash 12): column KP-Sil 32-64µm, 60Å silica - 8g; solvent heptane/ethyl acetate 3/2; sample 100mg; fractions 5ml. Isolated products: HNIW (R_f 0.60 – fraction A), WFN_5 (R_f 0.42 – fraction B, 98.4% pure), and WF_2N_4 (R_f 0.16 – fraction C, 97.5% pure).

Characterisation of WFN_5 and WF_2N_4

^1H and ^{13}C NMR spectra: Bruker DPX 250 (MHz), solvent acetone-d_6.

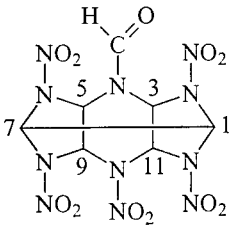

WFN_5

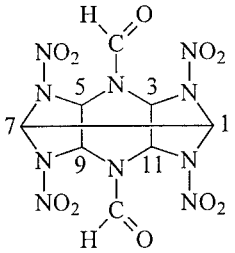

syn-WF_2N_4

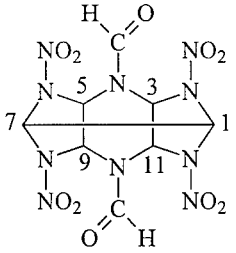

anti-WF_2N_4

WFN_5

^1H NMR: Figure 1. ^{13}C NMR: 66.57 (C-5), 71.10 (C-9), 71.24 (C-3), 72.33 (C-11), 74.69 (C-1), 75.16 (C-7) and 161.60ppm (NCHO). These data are in good agreement with those reported by Kaiser and Ditz [1] (Bruker DPX 400).

WF_2N_4

^1H NMR at 20°C (Figure 2): 7.10-7.14 (dd, 1.34H, H-3 + H-9 in *anti*), 7.20 (br s, 0.69H, H-3 + H-11 in *syn*), 7.70 (br s, 0.70H, H-5 + H-9 in *syn*), 7.76-7.80 (dd, 1.30H, H-5 + H-11 in *anti*), 7.82-7.84 (d, 0.35H, H-1 in *syn*), 7.93 (s, 1.28H, H-1 + H-7 in *anti*), 8.06-8.09 (m, 0.34H, H-7 in *syn*), 8.58 (s, 0.73H, NCHO in *syn*) and 8.60ppm (s, 1.27H, NCHO in *anti*).

^1H NMR at 55°C (Figure 3): the NCHO-absorption became a single broad peak at 8.55ppm, with further changes in the CH-absorptions. The NCHO-absorption changed back to a double peak when the temperature was lowered to 20°C.

^{13}C NMR at 20°C: 65.21, 66.53, 69.65, 71.28, 74.19, 74.66, 75.36, 162.04 and 162.11ppm.

According to Kaiser and Ditz [1], NCHO gives a ^{13}C-absorption at 161.6ppm (4-WFN_5) and $NCOCH_3$ a ^{13}C-absorption at 167.9ppm (2-WAN_5). Therefore ^{13}C-absorptions at both 162.04 and 162.11ppm indicates that there are 2

NCHO groups in this intermediate, and no $NCOCH_3$ group (CH_3 absorptions – ^1H at 2.25ppm and ^{13}C at 21ppm – are also absent).

If the formyl groups are at C-4 and C-10, they are formally equivalent, but the amide group has a planar geometry. Therefore one can expect 2 conformational isomers, *syn* and *anti* (see diagram above), which at 20°C interconvert rather slowly. This is reflected in the ^1H NMR spectrum as a double peak for NCHO with unequal heights (~35 and ~65%), and much more complicated absorptions in the CH region. This also applies to the ^{13}C-absorptions. At 55°C the *syn*- and *anti*-conformers interconvert faster and the NCHO ^1H-absorptions become averaged to a single broad peak.

Due to the symmetry in the molecules, *anti*-WF_2N_4(~65%) exhibits no H-H coupling between H-1 and H-7 (equivalent protons), but coupling between H-3 and H-11 (and H-5 and H-9), whilst *syn*-WF_2N_4 (~35%) exhibits no coupling between H-3 and H-11 (and H-5 and H-9; equivalent protons), but coupling between H-1 and H-7.

Figure 1. ^1H NMR spectrum of WFN_5

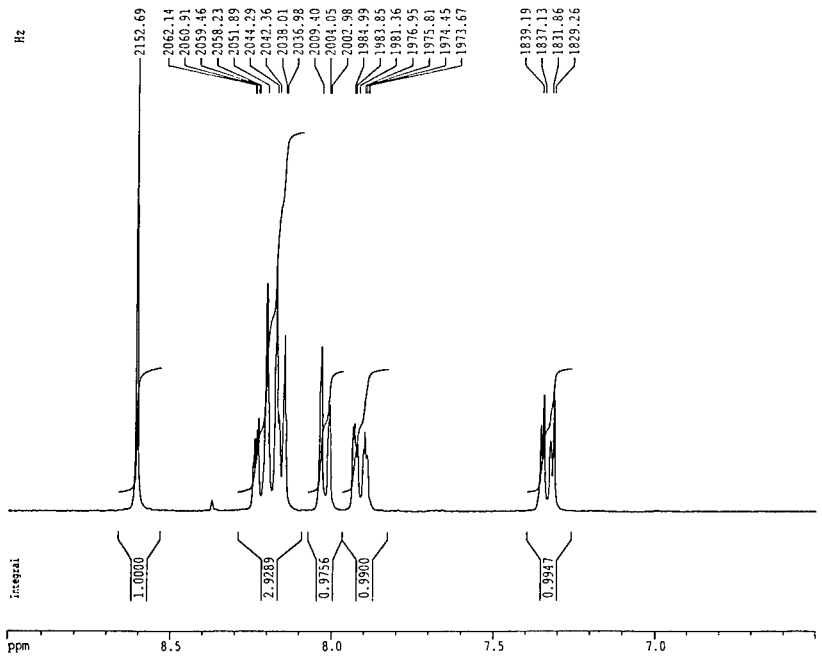

Figure 2. ^1H NMR spectrum of WF_2N_4 at 20°C

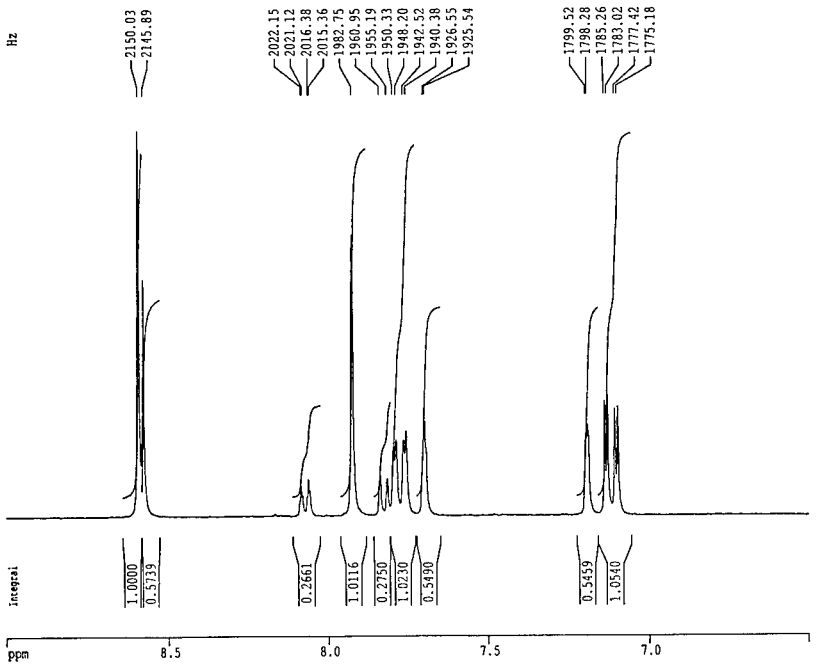

Figure 3. ^1H NMR spectrum of WF_2N_4 at 55°C

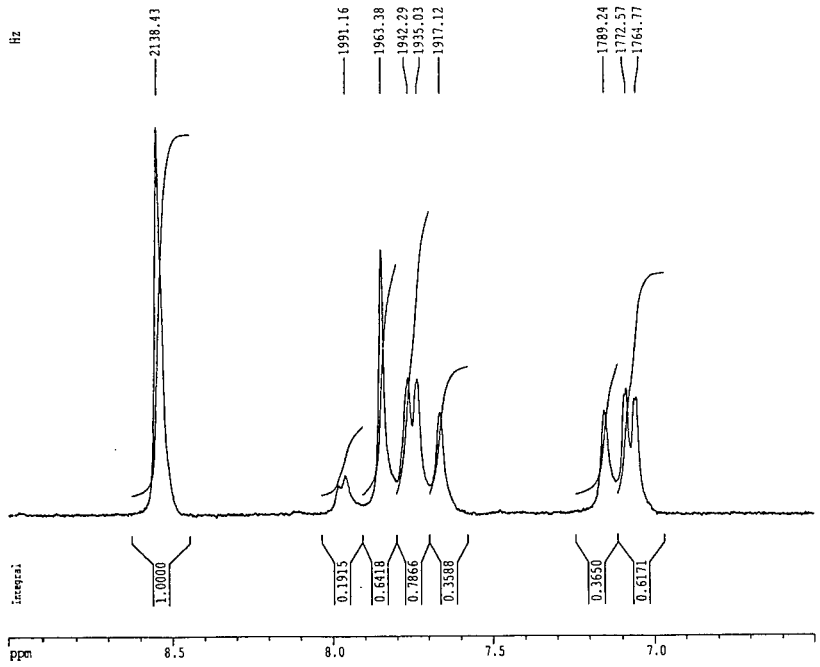

Products from the chemical reduction of hexanitrohexaaza-isowurtzitane (HNIW, WN_6)

Nitramines may be chemically reduced to the corresponding amine using a variety of reagents [2]. These reagents have been used mostly for deprotecting N-nitroarginine derivatives, but we have found them to be also useful for the selective removal of 1 or 2 nitro groups from HNIW. The following reagents were used under roughly the same conditions as had been applied to the original N-nitroarginine derivatives, the progress of the reaction being followed by TLC (silica gel, heptane/EtOAc 3/2):

(i) cyclohexa-1,4-diene/ Pd-C/EtOH or MeOH or CH_3CN [3],

(ii) formic acid/Pd black/MeOH [4],

(iii) $SnCl_2.2H_2O/HCO_2H$–MeOH or H_2O or MeOH [5],

(iv) hydrazine/Pd black/CH_3CN [used previously on HMX, 6].

Most reactions were run at room temperature. The behaviour with all reagents was broadly similar, with the spot for HNIW (R_f 0.60 – spot A) decreasing, a primary product appearing at R_f 0.44 (spot B), followed by 2 secondary products appearing at R_f 0.35 (spot C) and 0.18 (spot D). A significant amount of material appeared near to the origin. Reagents (i) and (iii) appeared to be the most selective, and $SnCl_2.2H_2O$ in MeOH was used in larger scale preparations.

A mixture containing all of the main components (spots A-D) was dissolved in EtOAc and shaken with 3M HCl; this removed the slow running material on the TLC. The components were then separated by medium-pressure chromatography and characterised by ^1H and ^{13}C NMR spectroscopy (see below). All 3 reduction products could be converted back to HNIW by nitration with 20vol% 98% H_2SO_4 in 90% HNO_3 (80°C/4h), demonstrating that the hexaazaisowurtzitane moiety was retained in all three products.

The product with R_f 0.44 (B) was identified as 4,6,8,10,12-pentanitro-hexaazaisowurtzitane (NH at position 2), since only 1 NH group was visible in the ^1H NMR spectrum, the N-H stretch in the IR spectrum appeared as a single absorption, it was transformed into 2-acetyl-4,6,8,10,12-pentanitrohexaazaisowurtzitane, a known impurity in HNIW synthesised from 2,6,8,12-tetraacetyl-4,10-dibenzylhexaazaisowurtzitane [1], on treatment with

Ac_2O/AcCl, and it was transformed into a monoformylpentanitrohexaaza-isowurtzitane on treatment with HCO_2H which was not 4-formyl-2,6,8,10,12-pentanitrohexaazaisowurtzitane, a known impurity in HNIW synthesised from 2,6,8,12-tetraacetyl-4,10-diformylhexaazaisowurtzitane [1].

The products with R_f 0.35 (C) and 0.18 (D) were identified as di-amines (both exhibited double N-H stretch absorptions in the IR spectrum, and both exhibited 2 NH signals in the ^1H NMR spectrum), and, since they were derived from the primary product, must have 1 NH group at position 2. The position of the second NH group in each product was determined from the ^1H-^1H correlation NMR spectrum (COSY45). The product with R_f 0.35 was identified as 4,6,8,12-tetranitrohexaazaisowurtzitane (NH groups at positions 2 and 10) since the 2 NHs were not coupled to the same CH), whilst the product with R_f 0.18 was identified as 6,8,10,12-tetranitrohexaazaisowurtzitane (NH groups at positions 2 and 4) since the 2 NHs were coupled to the same CH (H-3).

Although only some of the reduction products have been isolated and characterised, it appears that initial reduction of HNIW occurs preferentially at the nitro groups attached to nitrogen in the 5-membered rings giving product B. Further reaction then occurs at the nitro groups attached to nitrogen in the 6-membered ring to give products C and D. However, a more detailed analysis of the course of the reaction by HPLC (see Table 1 and Graphs 1 and 2) indicates that another primary product (presumably the 4-H mono-amine) is also formed, but to a smaller extent (initial rate about 0.2 of that for formation of the 2-H mono-amine), and that this intermediate then disappears faster than the 2-H mono-amine (by the more rapid reaction at N-2 etc). Furthermore, two other secondary products are observed, one being more abundant than C and D, and the other intermediate between C and D. These unidentified secondary products are probably di-amines with both NH groups in the 5-membered rings. It is possible that some degradation of the isowurtzitane moiety also occurs leading to strongly polar materials that have not yet been characterised. In contrast to HNIW, reduction of HMX with hydrazine/Pd black (reagent iv) leads to extensive degradation via methyleneimine [6].

Experimental details

HNIW (0.5g) was dissolved in MeOH (25ml) at room temperature and a 0.25g portion of $SnCl_2.2H_2O$ (total 1 equivalent) was added every 15min for 1h. [Reaction after each addition was complete within 5min.] The MeOH was evaporated, the residue was dissolved in EtOAc (35ml) and the solution was washed with 3M HCl (2x5ml), water (3x) and brine (2x). Rotary evaporation gave a white solid, 0.32g. TLC analysis (heptane/ethyl acetate 3/2): R_f 0.60 (HNIW), 0.44, 0.35, 0.18. The components were separated by medium-pressure chromatography (Biotage Flash 12): column KP-Sil 32-64µm, 60Å silica - 8g; solvent heptane/ethyl acetate 3/2; sample 100mg; fractions 5ml. Isolated products: HNIW (R_f 0.60 – fraction A), WHN_5 (R_f 0.44 – fraction B), WH_2N_4 (R_f 0.35 – fraction C) and WH_2N_4 (R_f 0.18 – fraction D).

The above reduction was also followed by HPLC analysis of the residue obtained from samples taken before each addition of $SnCl_2$ i.e. after reaction of the previous portion of $SnCl_2$. The results from these analyses are presented in Table 1, and displayed in Graphs 1 and 2.

Characterisation of reduction products

^1H and ^{13}C NMR spectra: Bruker DPX 250 (MHz), solvent acetone-d_6.

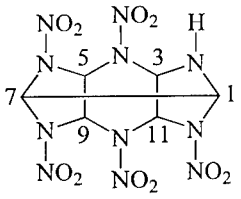

WHN_5 (B)

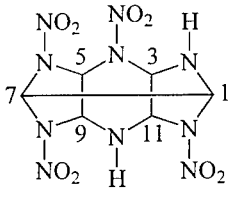

WH_2N_4 (C)

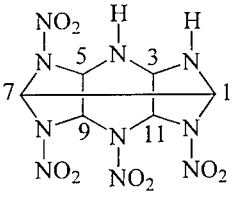

WH_2N_4 (D)

Fraction B (R_f 0.44)

FTIR (KBr): 3362cm^{-1}. ^1H NMR: Figure 4. ^1H-^1H correlation (COSY45) – Figure 5 (NH coupled to 2 CHs). ^{13}C NMR: 70.21, 70.94, 71.77, 72.85, 76.19 and 76.64ppm.

Fraction C (R_f 0.35)

FTIR (KBr): 3362 and 3346cm^{-1}. ^{1}H NMR: Figure 6. ^{1}H-^{1}H correlation (COSY45) – Figure 7 (each NH coupled to 2 different CHs). ^{13}C NMR: 69.43, 70.73, 70.83, 70.92, 71.00, 73.76, 73.84, 74.77, 74.86 and 76.05ppm.

Fraction D (R_f 0.18)

FTIR (KBr): 3370 and 3338cm^{-1}. ^{1}H NMR: Figure 8. ^{1}H-^{1}H correlation (COSY45) – Figure 9 [each NH coupled to the same CH (5.53, H-3) and to one other]. ^{13}C NMR: 69.89, 70.04, 70.11, 71.60, 71.69, 72.24, 75.80, 75.93 and 75.99ppm.

Acknowledgments

I wish to thank Dr B.Ringrose (Cranfield University) for the medium-pressure chromatographic separations, and Drs J.Matley and S.Trussell (AWE) for some of the NMR spectra.

References

1 M.Kaiser and B.Ditz, Characterisation of impurities in CL-20 by NMR spectroscopy, ICT Conference 1999, 94-1 – 94-16.

2 T.W.Greene and P.G.M.Wuts, Protective groups in organic synthesis, 2nd ed., Wiley 1991, p374.

3 A.M.Felix, E.P.Heimer, T.J.Lambros, C.Tzougraki and J.Meienhofer, *J.Org.Chem.*, 1978, **43**, 4194.

4 B.ElAmin, G.M.Anantharamaiah, G.P.Royer and G.E.Means, *J.Org.Chem.*, 1979, **44**, 3442.

5 T.Hayakawa, Y.Fujiwara and J.Noguchi, *Bull.Chem.Soc.Japan*, 1967, **40**, 1205.

6 R.D.Chapman, R.A.O'Biren and P.A.Kondracki, *J.Energetic Materials*, 1998, **16**, 147.

Figure 4. ^{1}H NMR spectrum of fraction B (WHN_5) from the reduction of HNIW

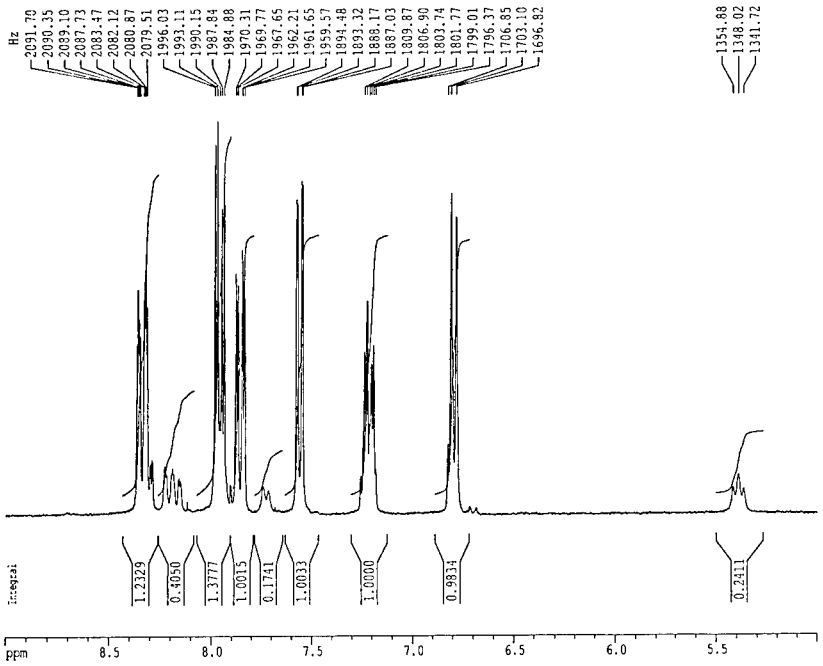

Figure 5. ^{1}H-^{1}H correlation (COSY45) of fraction B (WHN_5) from the reduction of HNIW

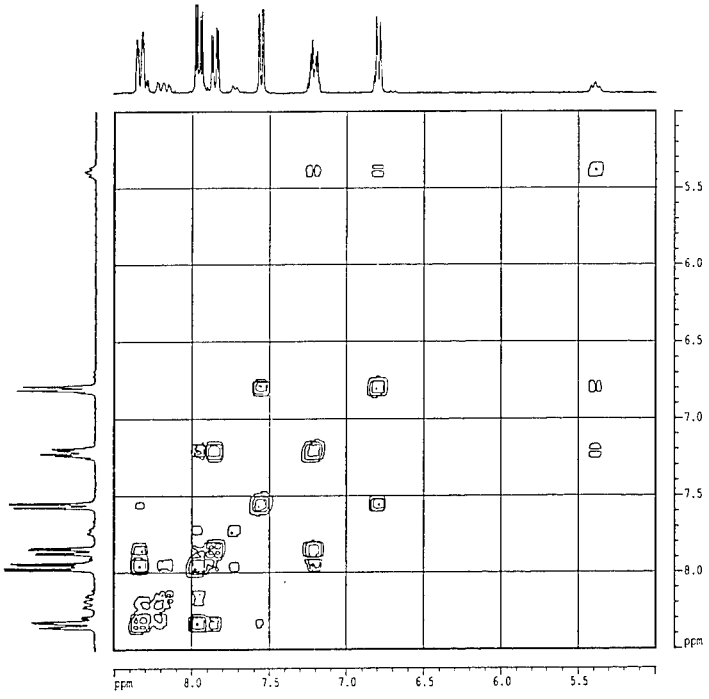

Figure 6. ^{1}H NMR spectrum of fraction C (WH_2N_4) from the reduction of HNIW

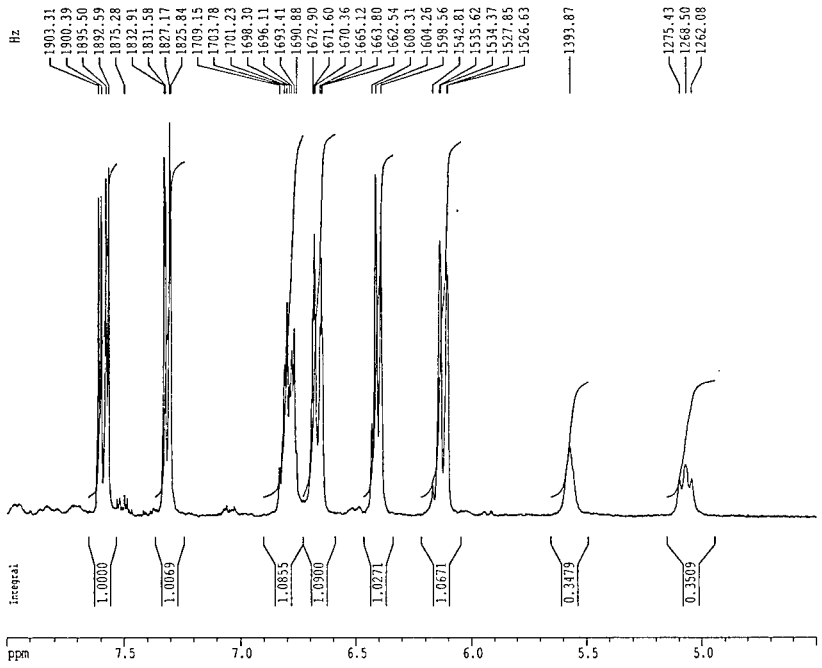

Figure 7. ^{1}H-^{1}H correlation (COSY45) of fraction C (WH_2N_4) from the reduction of HNIW

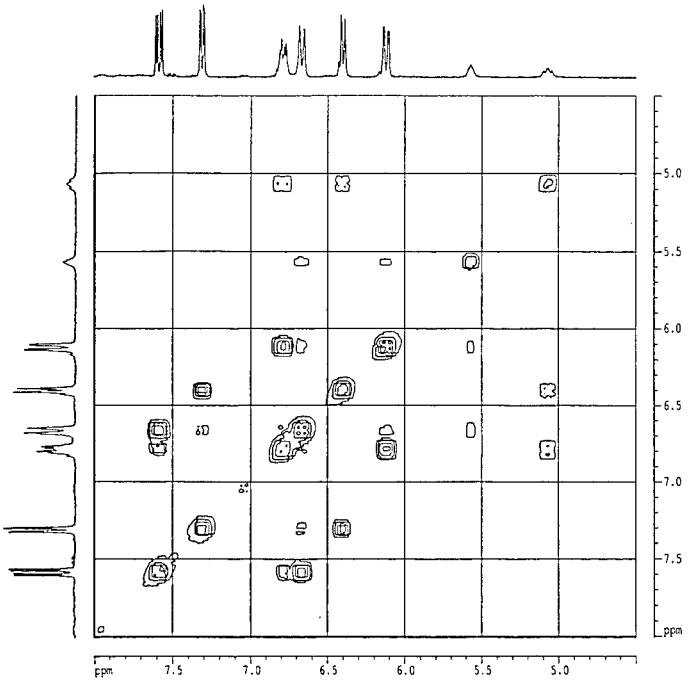

Figure 8. ^{1}H NMR spectrum of fraction D (WH_2N_4) from the reduction of HNIW

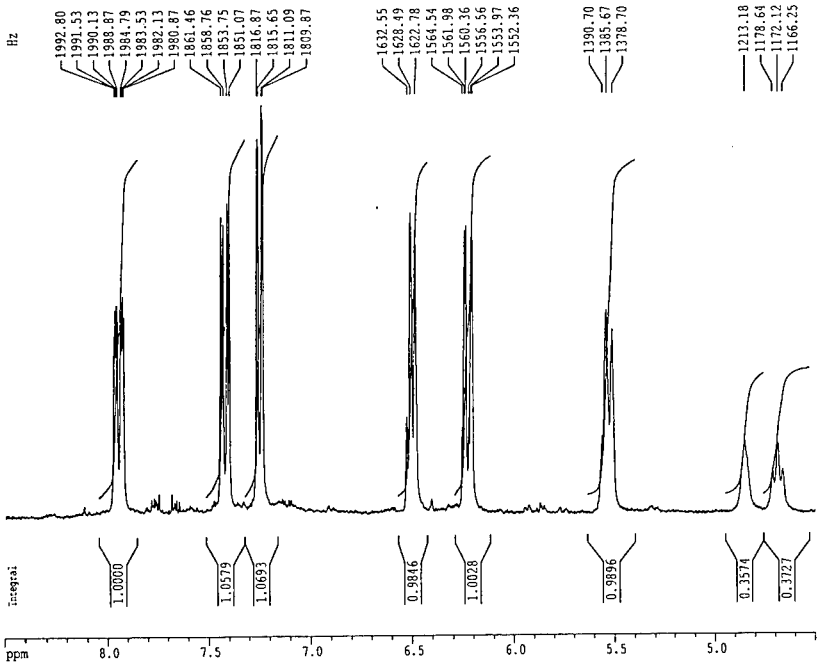

Figure 9. ^{1}H-^{1}H correlation (COSY45) of fraction D (WH_2N_4) from the reduction of HNIW

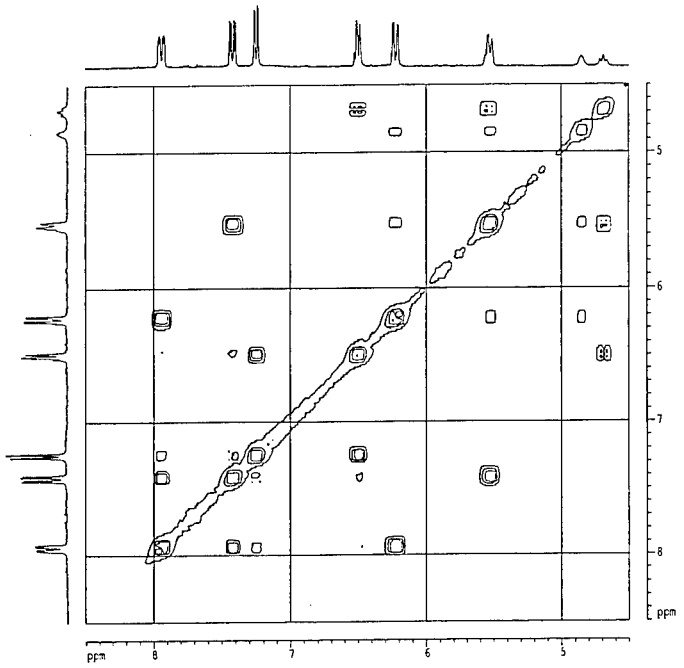

Table 1. HPLC analysis of samples removed during $SnCl_2$ reduction.

Sample	RT/min Identity*	1.15 SP	2.04 SP(C)	2.40 SP(D)	2.79	2.96 PP(B)	3.44 SP	4.15 PP	4.44 HNIW
0		-	-	-	-	-	-	-	100.0
1		1.8	1.9	1.3	-	28.4	2.5	5.7	57.3
2		4.3	4.6	3.3	-	37.2	9.3	5.2	35.5
3		7.2	8.0	6.8	-	37.6	17.0	2.6	20.0
4		10.1	11.2	9.2	5.9	29.9	21.2	1.6	10.2
5		12.5	14.8	11.0	6.1	26.8	22.4	0.8	4.7

* SP = secondary product; PP = primary product

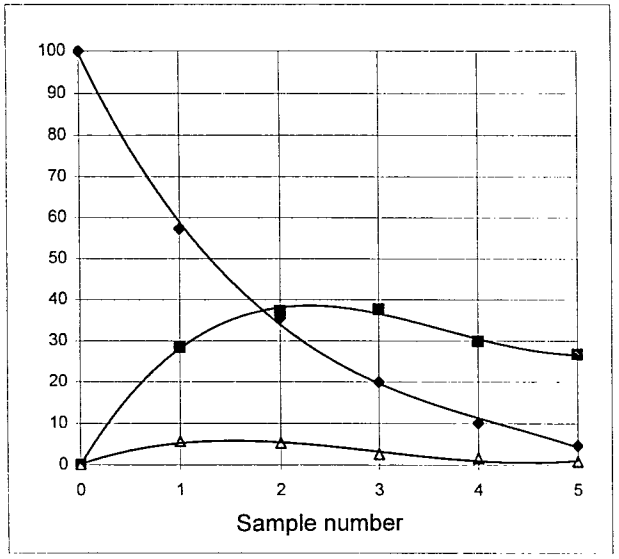

Graph 1. HPLC analysis of reduction of HNIW – HNIW and primary reduction products.

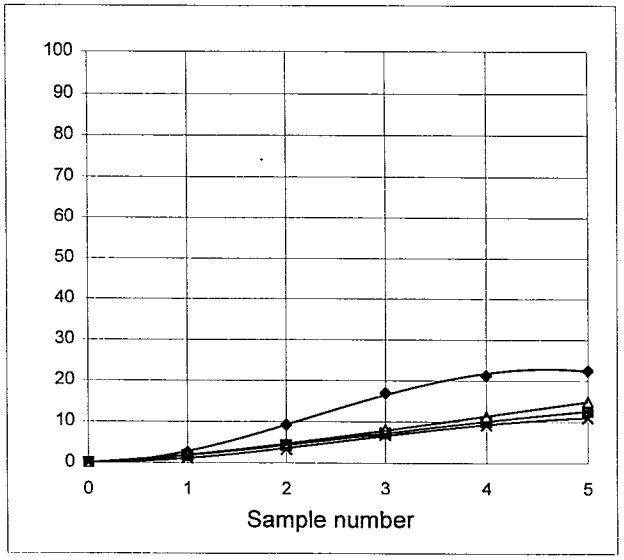

Graph 2. HPLC analysis of reduction of HNIW – secondary reduction products.

LABORATORY TESTING OF HNIW MIXTURES

Kamil Dudek, Pavel Mareček
ALIACHEM a.s., Division Synthesia
Research Institute of Industrial Chemistry
Pardubice-Semtin, CZ-532 17
Czech Republic

Pavel Vávra
University of Pardubice
Department of Theory and Technology of Explosives
Pardubice, CZ-530 10
Czech Republic

Abstract

Preliminary testing of HNIW mixtures with active and passive components has been performed in laboratory scale. The evaluated parameters were sensitivity to impact, and shock wave and also compatibility. The results are discussed especially with regard to utilization of HNIW as a component of explosive charges.

Introduction

Great attention has been paid lately to utilization of hexanitrohexaazaisowurtzitane (HNIW) as an high explosive(HE)[1,2,3] and also as an oxidant in propellants[4,5]. This is a well-founded interest; unlike octogen (HMX), so far the most powerful explosive used in practice, HNIW offers by 17% more energy. It is, however, necessary to consider the fact that HNIW is more sensitive than HMX and full use has not been made of the possibilities of its utilization yet. There is a series of other, energetically also very rich explosives as dinitroazofuroxane, hexanitrobenzene or octanitro-

cubane. These compounds are too sensitive, however, their preparation is not simple and moreover further improvement of HNIW preparation can be expected. It is therefore possible to presume that HNIW may become a very important component of many formulations.

Compatibility, sensitivity and some other properties have been measured at the selected HNIW mixtures with 1,3,3- trinitroazetidine (TNAZ), dinitraminotetraoxaiso-wurtzitane (TEX), hydroxyl terminated polybutadiene (HTPB), and trinitrotoluene (TNT) and compared with analogous HMX based mixtures.

Experimental

The ε-HNIW compatibility with TNAZ, TEX, HTPB, and TNT in mixtures has been tested by means of vacuum test at 110°C for 20 hours. As the reference substance β-octogen (HMX) has been used in analogous mixtures with TNAZ, TEX, HTPB, and TNT of the same weight ratios . The results are given in Table 1.

TABLE 1 - Vacuum test of HNIW and HMX mixtures at 110°C for 20 hours

	ε-HNIW	HMX	TNAZ	TEX	TNT
Density ($g.cm^{-3}$)	2.02	1.90	1.84	1.99	1.65
Volume of gas (cm^3)	0.02	0.06	0.01	0.00	0.01

	HNIW/TNT 40/60	HNIW/TNAZ 40/60	HMX/TNAZ 40/60	HNIW/TEX/HTPB 32/48/20	HMX/TEX/HTPB 32/48/20
Density ($g.cm^{-3}$)	1.732	1.858	1.808	1.595	1.560
(% TMD)	96.9	97.0	97.0	98.9	98.6
Volume of gas (cm^3)	0.06	0.37	0.18	0.44	0.04

Next parameter to be determined has been sensitivity to impact (2 and 5 kg hammer). The results are given in Table 2.

TABLE 2 - Sensitivity to impact of HNIW and HMX mixtures

	HNIW	HMX	TNAZ	HMX/TNAZ 40/60
h_{50} (cm)/ 2kg hammer	28	30	26	67

	TNT	TEX	HNIW/TNT 40/60	HNIW/TEX/HTPB 32/48/20	HMX/TEX/HTPB 32/48/20
h_{50} (cm)/ 5kg hammer	60	50	44	45	60

Sensitivity to shock wave has been determined by means of the so-called "small" GAP-Test (ϕ 21 mm). The results are given in Table 3.

TABLE 3 - GAP-Test of HNIW and HMX mixtures

	Density ($g.cm^{-3}$)	TMD (%)	p_i^* (GPa)
HNIW/TEX/HTPB 32/48/20	1.595	98.9	5.6
HMX/TEX/HTPB 32/48/20	1.560	98.6	10.2

	Density ($g.cm^{-3}$)	TMD (%)	p_i^* (GPa)
HNIW/HyTemp/DOA 96/1/3	1.901	98.3	2.60
HMX/HyTemp/DOA 96/1/3	1.792	98.0	3.56

* p_i - initiation pressure

Detonation velocity of pressed charges (ϕ 21 mm) is given in Table 4.

TABLE 4 - Detonation velocity of HNIW and HMX mixtures

	Density ($g.cm^{-3}$)	TMD (%)	Detonat. Velocity ($m.s^{-1}$)
HNIW/HyTemp/DOA 96/1/3	1.901	98.3	9018
HMX/HyTemp/DOA 96/1/3	1.817	98.9	8748

To assess the possibility of casting, TNAZ density has been measured at temperatures above melting point (micro pycnometric determination). The results are given in Table 5.

TABLE 5 - TNAZ density at 105°C and 120°C

Temperature (°C)	105	120
Density ($g.cm^{-3}$)	1.554	1.522

Discussion

The results of vacuum test do not show a very good HNIW compatibility in some samples. This fact is especially reflected at castable mixtures with TNAZ and also at HNIW/TEX/HTPB mixture. At octogen the deterioration has been observed only in case of HMX/TNAZ mixture. It is possible to assume that more significant dissolving occurs of HNIW in TNAZ (in less measure also HMX) and decrease in stability of individual molecules. In case of TNT this phenomenon is not too conspicuous. In case of HNIW/TEX/HTPB mixture we have no explanation for the time being, especially if the fact is considered that the analogous mixture with HMX shows a very good compatibility.

The values of sensitivity to impact are, on the contrary, in accordance with the expectations in spite of the fact that this test is considered to be a little disputable. The value of drop test rather deviates at HMX/TNAZ mixture, where a lower sensitivity has been expected than at HNIW/TNAZ mixture. In accordance with the expectations a higher sensitivity has been observed at the sample with HNIW content compared to HMX mixtures.

Even more markedly the higher sensitivity of HNIW has reflected itself at GAP-Test. It emerged that even in the presence of TEX as a considerably insensitive substance and fairly high content of binder (cross-linked, vacuum casting) a low sensitivity has not been achieved, unlike the analogous mixtures with HMX, in spite of the fact that the charges have been of considerably high relative density (with regard to theoretical maximum density - TMD). At these mixtures, however, the sensitivity to shock wave can be lowered by means of further proceeding.

Experimental values of detonation velocity are in accordance with the calculated values although the diameter of the charges has not been large. This type of HNIW mixture is well utilizable.

The value of density of melted TNAZ is by 15% lower than the value of density of crystalline TNAZ (1,84 g . cm^{-3}).

In addition, certain vapour tension has been found at the melted TNAZ. This fact, and the above mentioned observations bring us to certain circumspection in considerations on substitution of TNT with TNAZ for castable mixtures although the performance and stability parameters are fully acceptable.

Conclusion

The given results are of preliminary nature. The future work will be aimed at optimum composition of HNIW mixtures so that the full use is made of HNIW excellent performance properties and its increased sensitivity is suppressed.

References

1. Mezger, M.J. et al.: „Performance and Hazard Characterization of CL-20 Formulations" , Ann. Int. Conf. of ICT, Karlsruhe, 1999, p.4-1
2. Braithwaite, P.C. et al: „Development of High Performance CL-20 Explosive Formulations", Ann. Int. Conf. of ICT, Karlsruhe, 1998, p. 4-1
3. Wallace, I.A. et al.: „ Evaluation of a Homologous Series of High Energy Oxetane Thermoplastic Elastomer Gun Propellants" , Ann. Int. Conf. of ICT, Karlsruhe, 1998, p. 87-1
4. Bircher, H.R. et al.: „Properties of CL-20 Based High Explosives", Ann. Int. Conf. of ICT, Karlsruhe, 1998, p. 94-1
5. Mueller, D.: Propel. , Expl., Pyrotech., 24, 1999, 176

Foamed Propellants with Energetic Binders

Geschäumte Treibladungen mit energetischen Bindern

A. Messmer, A. Pfatteicher
K. Schmid, Kuglstatter

Fraunhofer Institut für Chemische Technologie - ICT
76327 Pfinztal

Abstract

Foamed polymerbonded propellants show variable material characteristics and performance on a high energy level. Specific energy and burning behaviour can be optimised by choosing energetic binders instead of inert polymers. First results of examinations on foamed propellants containing nitramine/glycidyl azide polymer/polyurethane are reported in this paper. Foamed propellants can be produced by reaction injection moulding with a very high reproducibility. The pore size distribution of the propellants can be controlled by using special additives and processing parameters. Material and burning characteristics of the foamed propellants can be adjusted independently of the shape of the charge by combining different energetic components and suitable porous structures.

Kurzfassung

Geschäumte polymergebundene Treibladungen besitzen bei hohem Energiegehalt ein sehr variables Leistungsprofil. Durch den Einsatz energetischer Binder können Energieinhalt und Abbrandeigenschaften optimiert werden. Untersucht wurden dazu geschäumte Treibladungen auf Nitramin/GAP/Polyurethan-Basis. Die Porosität der geschäumten Ladungen läßt sich im Reaktionsschaumguß-verfahren mit hoher Reproduzierbarkeit herstellen. Bei konstanter Gesamtdichte lassen sich durch die Wahl der Inhaltsstoffe und der Verarbeitungsparameter unterschiedliche Porenstrukturen einstellen. Durch Inhaltsstoffe und Porosität kann somit auch unabhängig von der äußeren Geometrie ein gewünschtes Leistungsprofil erreicht werden.

Introduction

Compared to conventional solid propellants, foamed charges based on nitramine/polyurethane have several advantages like high energy content, variable burning characteristics and low vulnerability. The burning characteristics of the foamed propellants can be adjusted independently of the shape of the charge using different energetic components and porous structures. Therefore, foamed propellants can be used for example as combustible cases or for caseless ammunition. Since foamed propellants can be easily produced even in very complex shapes, further applications like modular charges, fixing of ammunition components by surrounded foam and gradient charges are possible.

Foamed propellants with inert polymeric binders have good mechanical properties, but compared to energetic systems performance data like force and oxygen balance are decreased. This disadvantage can be balanced by using energetic binders. Therefore foamed propellants with glycidyl azide polymers (GAP) were examined, since GAP shows good performance data combined with high thermal and chemical stability. In order to achieve sufficient mechanical properties GAP was blended with other binders like polyurethane.

Experimental

In order to examine properties and processibility, samples of foamed propellants based on nitramines (RDX) and GAP/polyurethane blends were produced manually according to the reaction injection moulding process. Samples with variations of the following parameters were produced: Porosity and densitiy, respectively, ratio of energetic polymers and of energetic fillers like RDX, nitroguanidine, TAGN and ammonium nitrate. Additives and processing parameters were adjusted in order to achieve charges with smooth surface and closed-cell porous structure.

Porous structure

Burning characteristics and mechanical properties of foamed propellants are determined by components and additives, but also by porosity (pore size distribution) and internal

surface. The porous structure can be varied in a wide range by additives like catalysts, foaming agents, foaming initiators and stabilisers and by processing parameters like temperature. Using reaction injection moulding, foamed propellants can be produced with reproducible porosity. Foamed propellants with different pore size distributions but constant density (charge mass / charge volume) can be achieved by varying additives and parameters like the amount of foaming agent (fig. 1). In this way, propellants with constant loading density but varied internal surface and varied burning characteristics are possible.

For most tests samples with different shapes are needed. Since foamed propellants can be produced easily in one step – even with complex shapes, the different samples were made without further cutting treatment. In order to achieve a comparable internal structure, the pore size distribution has to be adjusted by additives and processing parameters independently from the shape of the samples. Figure 2 shows the pore size distribution of foamed propellants with constant formulation and density. In spite of different sample geometries, the pore size distribution of both samples are comparable.

Thermodynamical data

The specific energy of foamed propellants is determined by the ratio of energetic binder as well as the ratio of energetic fillers or components. Figures 3, 4 and 5 show the influence of different energetic substances on the thermodynamical performance data. Specific energy and oxygen balance can be improved by higher filler content (fig. 3), by alternative explosives like CL20 or TNAZ (fig. 4), or by replacing inert binders by energetic polymers (fig. 5).

Further thermodynamical data of foamed propellants developed and produced by ICT are shown in table 1.

Thermal stability and sensitivity

Foamed propellants with good thermodynamical data and mechanical properties as well as high stability and low sensitivity can be achieved by combining different energetic substances and binders. Table 2 shows some data on stability and sensitivity of foamed RDX/GAP propellants.

Tab. 2: Stability and sensitivity data of foamed RDX/GAP propellants.

DSC (5 K / min)	190°C (Onset)
TGA (5 K / min)	193°C (Onset)
Deflagration point	197°C
Impact sensitivity	6 Nm
Friction sensitivity	240 N

Burning Characteristics

The burning behaviour of foamed propellants was examined using a closed vessel. Cubic samples (10^3 mm^3) were produced and tested with different loading densities in a 100 ml vessel with reduced volume. Whenever suitable igniters were used, the tests showed a very good reproducibility. Some results of these tests are represented in the figures 6 – 8.

The burning rate of foamed propellants decreases with growing charge density. The dynamic vivacity decreases in an equivalent manner (fig. 6). Besides, burning rate and vivacity of the foamed propellants are influenced by the content of energetic filler (fig. 7). The less energetic filler (RDX) is contained, the lower is the dynamic vivacity. The burning behaviour of foamed propellants with constant energetic filler content and constant density can be varied in a wide range by combining different energetic substances. In order to examine this effect, GAP/polyurethane propellants containing 65% of energetic fillers were tested. Figure 8 shows the results of GAP/polyurethane propellants with mixtures of RDX and alternative energetic substances like nitroguanidine, ammonium nitrate and nitrocellulose.

Since the density of the charge and the ratio of energetic fillers can influence the burning characteristics in an opposite manner, burning rate and specific energy can be adjusted independently from each other. For example, increasing the density of foamed propellants causes a higher energy density while decreasing the burning rate at the same time.

Summary

Foamed propellants can be produced with a high reproducibility by reaction injection moulding. The properties of foamed propellants can be varied in a wide range by changing the formulation as well as by adjusting the internal porous structure. Therefore a special internal ballistic behaviour can be achieved without changing the shape of the propellant. Foamed propellants with suitable components have good chemical and thermal stability, low sensitivity and good mechanical properties. Using energetic binders instead of inert polymers, foamed propellants with high specific energy and good burning characteristics are possible. The mechanical properties required for foamed propellants are achieved by combining different energetic and inert binders.

Literature

[1] T. S. Fischer, A. Meßmer, G. Langer, Geschäumte polymergebundene Treibladungen, Wehrtechnisches Symposium: Innenballistik der Rohrwaffen, BAkWVT Mannheim, 25.-27.05.1999

[2] F. Schedlbauer, A. Meßmer, U. Steffens, I. Reuter, Combustible Cases for RMK 30, 29th International Annual Conference of ICT, Karlsruhe, Federal Republic of Germany, P103, 1998

[3] T. S. Fischer, W. Koppenhöfer, G. Langer, M. Weindel, Modellierung von Abbrandphänomenen bei porösen Ladungen, 30th International Annual Conference of ICT, Karlsruhe, Federal Republic of Germany, P98, 1999

(4] A. Meßmer, A. Pfatteicher, F. Schedlbauer, Herstellung und Charakterisierung von geschäumter hülsenloser Munition, Bericht 10/98, Fraunhofer Institut für Chemische Technologie, 1998

[5] A. Meßmer, F. Schedlbauer, Konzeption einer Herstellungsanlage für geschäumte polymergebundene Treibladungen, Bericht 12/97, Fraunhofer Institut für Chemische Technologie, 1997

[6] J. Schwörer, J. Böhnlein-Mauß, Untersuchung des Einflusses von Verfahrensparametern auf die Schäumungsstruktur von gefüllten Kunststoffen, Bericht 3/96, Fraunhofer Institut für Chemische Technologie, 1996

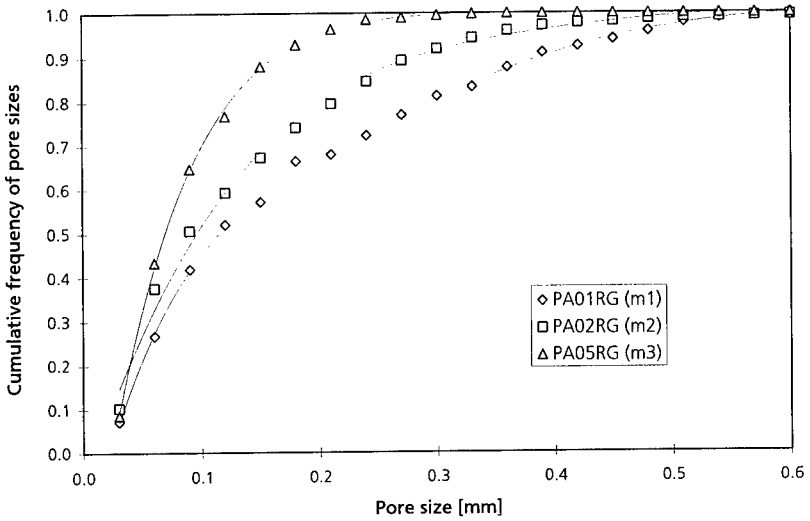

Fig.1: Pore size distribution of foamed propellants based on RDX/polyurethane with constant density (0.88 g/cm³) and varied amount of foaming agent m_i ($m_1 > m_2 > m_3$).

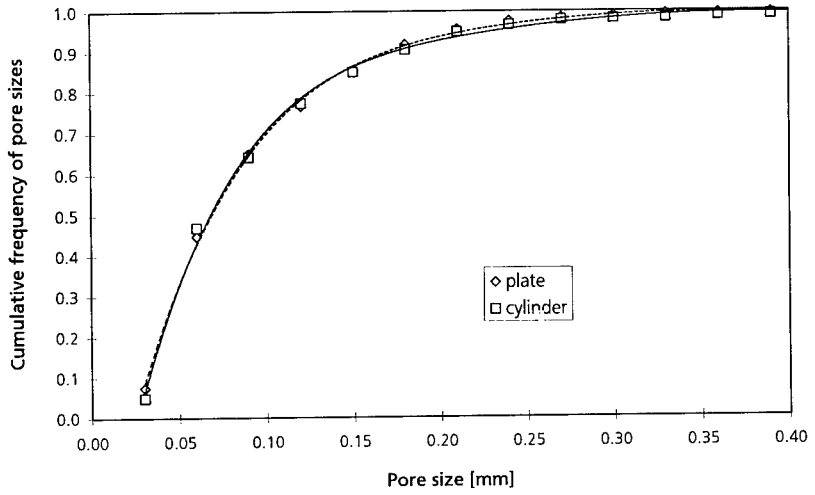

Fig. 2: Pore size distribution of foamed RDX/polyurethane propellants (0.88 g/cm³) with constant formulation and varied shape.

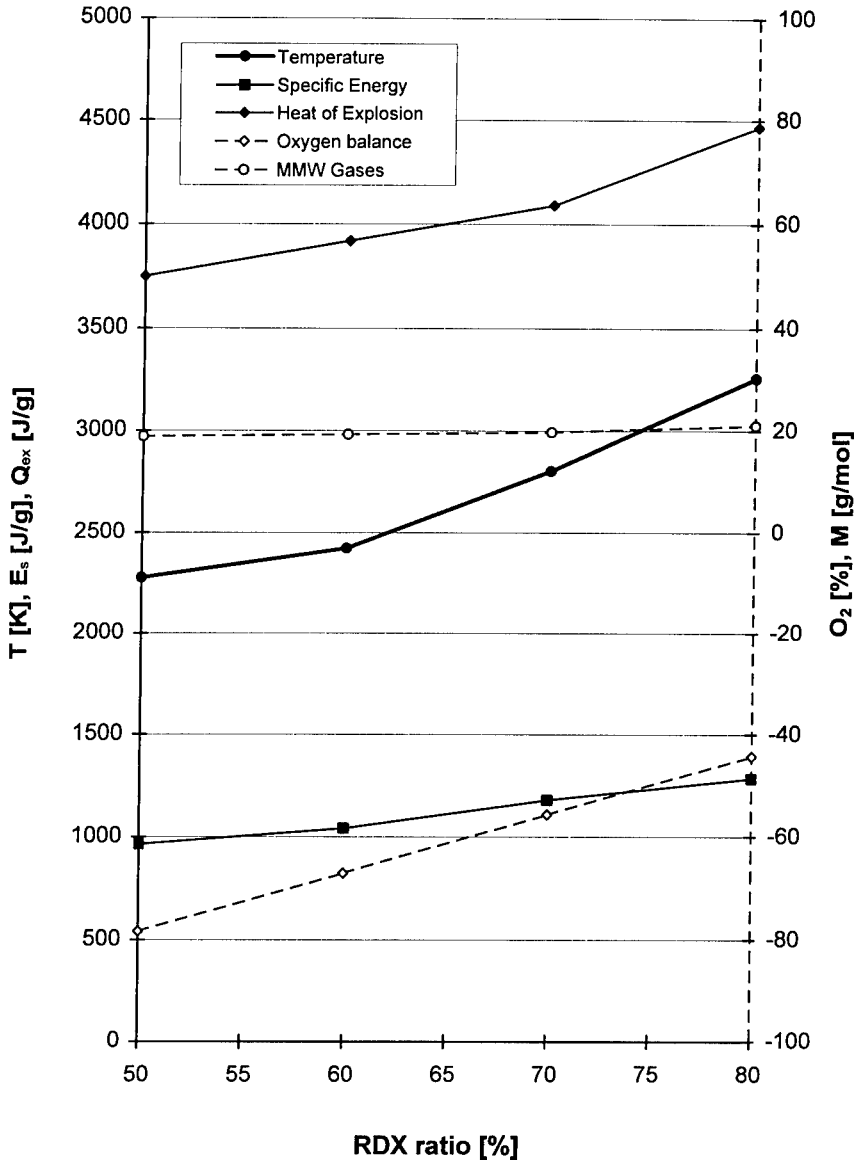

Fig. 3: Thermodynamical calculations of foamed RDX/GAP propellants: Influence of the RDX ratio on burning temperature T, specific energy E_s, heat of explosion Q_{ex}, oxygen balance O_2, mean molecular weight MMW.

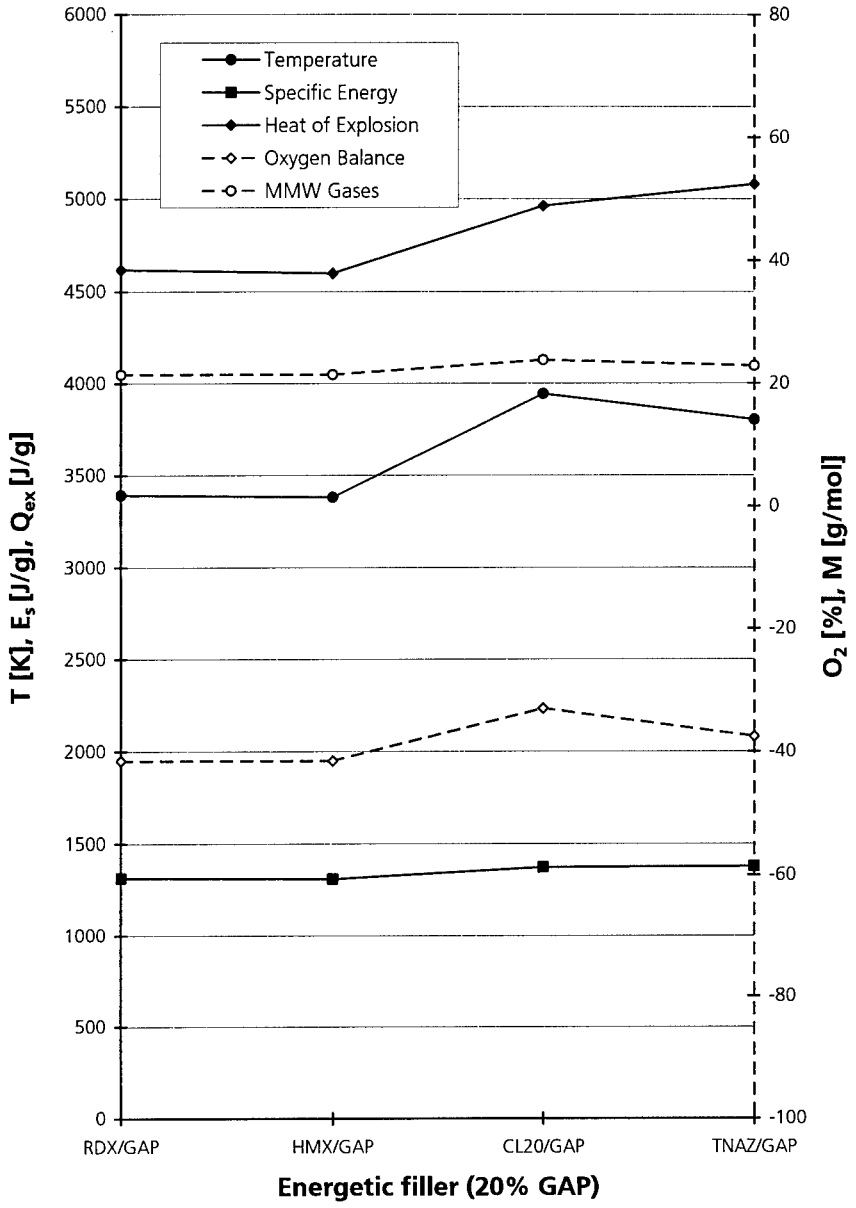

Fig. 4: Thermodynamical calculations of foamed GAP propellants: Influence of the energetic filler on burning temperature T, specific energy E_s, heat of explosion Q_{ex}, oxygen balance O_2, mean molecular weight MMW.

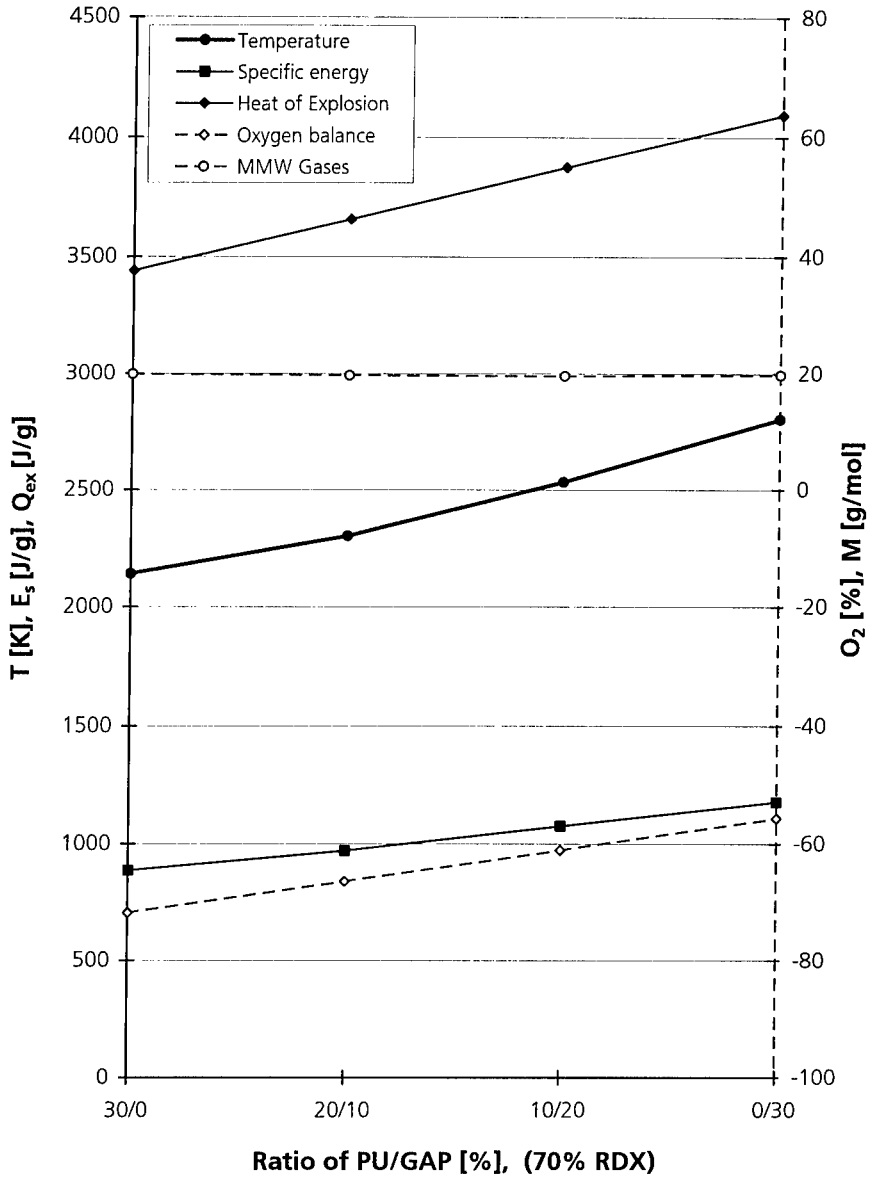

Fig. 5: Thermodynamical calculations of foamed propellants based on RDX/GAP/polyurethane: Influence of the content of energetic binder (GAP) compared to inert binder (polyurethane) on burning temperature T, specific energy E_s, heat of explosion Q_{ex}, oxygen balance O_2, mean molecular weight MMW.

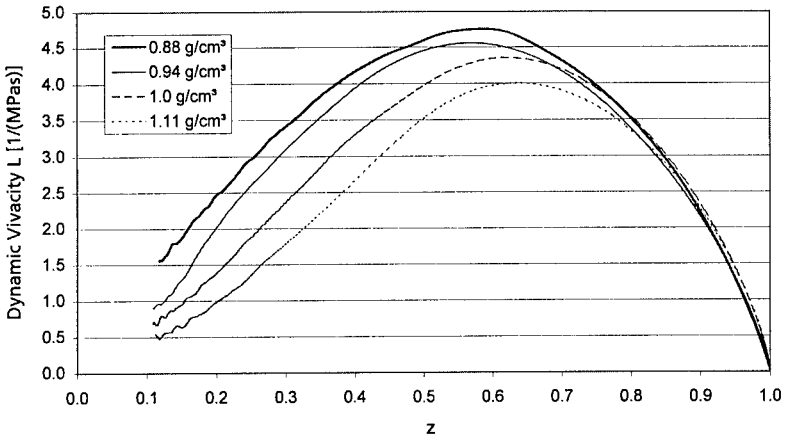

Fig. 6: Dynamic vivacity of foamed RDX/GAP/polyurethane propellants as a function of the charge density. Closed vessel with reduced volume, 112 ml, loading density 0,2 g/cm³, 21°C (z: fraction of mass of propellant burnt).

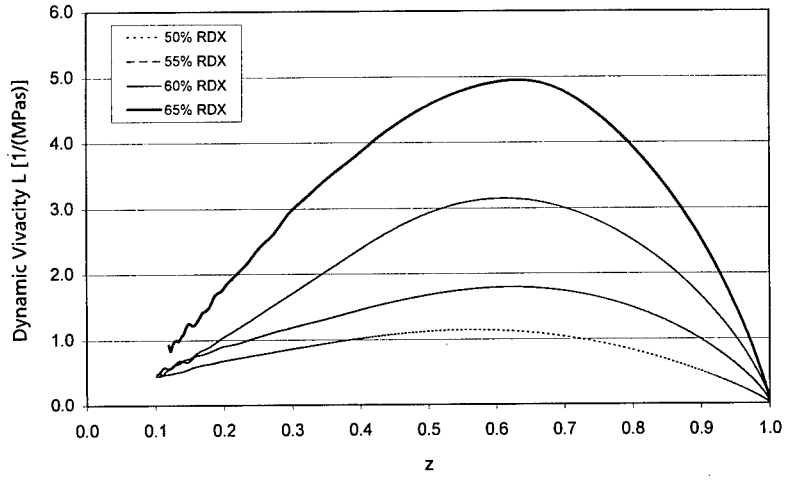

Fig. 7: Dynamic vivacity of foamed RDX/GAP/polyurethane propellants as a function of the RDX ratio. Closed vessel with reduced volume, 112 ml, loading density 0,2 g/cm³, 21°C (z: fraction of mass of propellant burnt).

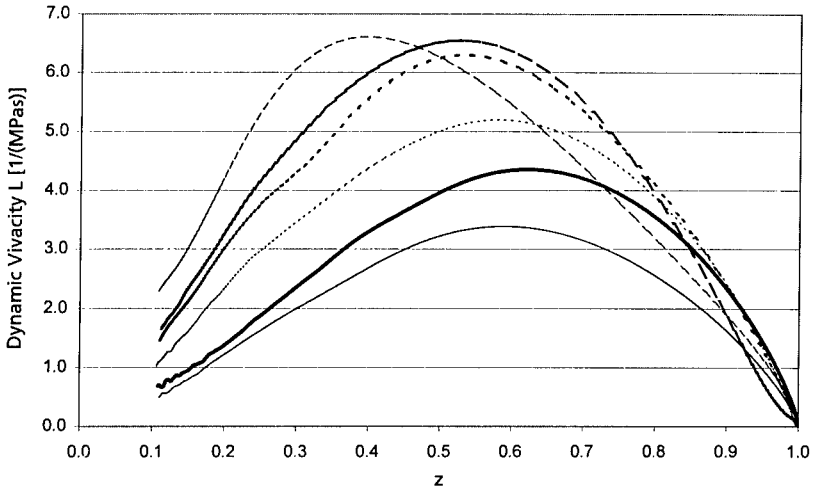

Fig. 8: Dynamic vivacity of foamed GAP/polyurethane propellants as a function of the type of energetic filler (65% of mixtures of different energetic fillers, 35% GAP/polyurethane, 1,0 g/cm³). Closed vessel with reduced volume, 112 ml, loading density 0,2 g/cm³, 21°C (z: fraction of mass of propellant burnt).

Tab. 1: Thermodynamical calculations of foamed propellants: oxygen balance (*O_2 balance*), mean molecular weight (*MMW*), burning temperature (T_{ex}), specific energy (E_s), volume of produced gases without H_2O (*Gas vol.*).

Energetic fillers: RDX, CL20, ammonium nitrate (AN), nitrocellulose (NC)
Energetic binder: Glycidyl azide polymer (GAP)
Energetic plastiziser: EGBAA

Formulation	RDX [%]	CL20 [%]	AN [%]	GAP [%]	EGBAA [%]	NC (13,2%) [%]	O_2-balance [%]	MMW [g/mol]	T_{ex} [K]	E_s [J/g]	Q_{ex} [J/g]	Gas vol. without H_2O, 298 K [ml/g]
1	70			30			-55,65	19,8	2804	1179	4091	1001
2	80			20			-44,3	21,1	3258	1284	4467	960
3	70			20	5	5	-47,9	20,8	3048	1219	4186	975
4	50		20	30			-47,3	20,0	2676	1115	3858	977
5	55		20	15	5	5	-33,9	21,8	3131	1194	4348	876
6	35	35		20	5	5	-44,2	21,8	3295	1259	4325	954
7		70		30			-48,19	21,6	3297	1271	4385	953

WATER-IMPREGNATED EXPLOSIVES CONTAINING UP TO 90% FINELY DISPERSED ALUMINUM

Boris N. Kondrikov, Vladimir E. Annikov

Mendeleev University of Chemical Technology, Moscow, Russia

Water-impregnated metal-containing compositions are safe explosive materials characterized by very low levels of mechanical and heat sensitivity. Those with a high content of aluminum possess a very high explosion heat, per se, and especially when afterburning of excess of aluminum at the expense of environmental occurs. A series of water-impregnated explosives, mostly of the gelled type, containing different quantities of finely dispersed aluminum were developed and investigated. The weight percent of aluminum in the formulations ranged from about 5 to 90%. If afterburning is included, the compositions containing 80-90% aluminum have heat evolution level up to 23 MJ per kilogram of explosive, which is four to five times more than is available with standard TNT-like explosives.

Introduction

Water-impregnated aluminum-containing compositions are used as commercial explosives for rock blasting, seismic investigations and other purposes [1-3]. Those with a high content of aluminum possess a very high explosion heat, per se, and especially when afterburning of excess of aluminum at the expense of environmental oxygen occurs (Fig. 1). They are safe explosive materials, characterized by very low levels of mechanical and heat sensitivity. Nonetheless, explosives of this type are sufficiently sensitive to initiating stimuli to be reliably initiated, and they are capable of propagating a detonation under the prevailing conditions of possible applications. When initiated by a detonating cap or other initiating device, the release of energy involves reaction of a small part of the metal in the detonation wave, while most of the metal is burned behind the detonation front in the ambient atmosphere or other oxidation media. It is obvious that the problems of composition of the explosives, the technology of their production and application, calculation of thermodynamic parameters and chemical kinetics of the processes both in detonation wave and in the ambient media are of great importance.

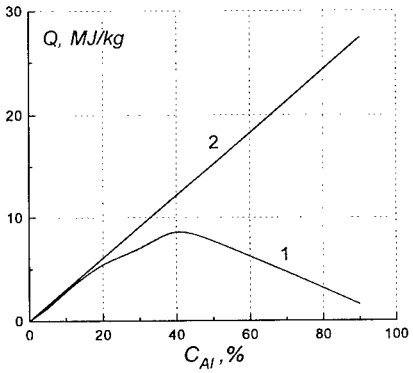

Fig.1. Heat evolution at detonation of water-impregnated compositions containing aluminum;
1 – in an inert atmosphere; 2 – in air

In this work we have developed and

investigated a series of water-impregnated explosives, mostly of the gelled type, containing different quantities of finely dispersed aluminum. The weight percent of aluminum in the formulations ranged from about 5 to 90%. The detonation velocity as a function of density, the dependence of the velocity on the charge diameter, the failure diameter, as well as the critical density for propagationof a detonation were measured. The chemical composition and thermodynamic characteristics of the products of reaction in the detonation wave and the chemical kinetics of the explosives considered were calculated by means of the computer package SGKR. The general computer codes ASTRA and REAL were used to calculate the heat released upon burning of the remaining metal in an oxidizing atmosphere. If afterburning is included, the compositions containing 80-90% aluminum have heat evolution up to 23 MJ per kilogram of explosive, which is four to five times more than is available with standard TNT-like explosives.

It was stated above that all the compositions investigated have good detonation properties. Some of the compositions are constructed in such a manner that they do not exhibit the phenomenon of critical density of detonation. Correspondingly they may detonate at every reasonable conditions of ambient pressure, particularly at great depth under the sea, with evolution of the excess of energy from the reaction of the metal with water.

Experimental

Water-impregnated compositions containing up to 90% powdered aluminum were prepared by mixing the aluminum powder with a water-gel matrix containing ammonium nitrate, sodium nitrate and polyacrylamide. The ratios of the masses of water, ammonium nitrate, and sodium nitrate were chosen to be 2:3:1. The polyacrylamide content was very small, 0.3%, to avoid an excessive viscosity increase that could prevent blending of the relatively small volume of the water-gel base with the large mass of the aluminum powder. Several domestic types of aluminum powders were used. The trade names, a brief description of their characteristics, and the mean dimensions of the powder particles are presented in Table 1.

Table 1. Characteristics of aluminum powders used in this work

Trade mark of aluminum	Mean dimensions of particles, μm	Notes
PP-1 PP-2 PP-3		Aluminum powders of the pyrotechnic type
PA-1 PA-2 PA-3 PA-4	250-450[a] 140-250[a] 100-160[a] <100 (85%)[b]	Relatively crude aluminum powder, mostly for commercial explosives used in the boreholes of large diameter
ASD-1 ASD-4	13-15 5-6	Spherical powder, predominantly for compositions of rocket propellants
PAP-1 PAP-2	0.4 x 50 x 50 0.2 x 50 x 50	Pigment grade flaked aluminum powder

Notes:

[a]Mean particle dimensions relate to about 70% of whole mass of the powder. About 10% of the mass has dimensions greater than the upper limit given in the column, and about 20% has dimensions less than the lower limit.

[b]About 15% of the whole mass of the powder have dimensions from 100 to 140 μm.

For some of the experiments the commercial batches of the powders of the type PA were sieved to give relatively narrow fractions (see Table 1 and text).

Detonation experiments were carried out in steel tubes about 200 mm long, with 10 mm inner diameter and 36 mm outer diameter, as well as in glass tubes of different diameters with walls of 1-2 mm thick. Small orifices, ~ 2 mm diameter, were drilled in the walls of the steel tubes for measurements of detonation velocity by means of a streak camera. It is well-known that water-gel explosives containing pigment grade aluminum, particularly of PAP-1 or PAP-2 type, may have a very high detonation ability, critical diameter at a weak confinement up to 2 mm, critical density at a moderate diameter charge up to 90% TMD. Addition of only 3% aluminum is very effective in sensitization of the water-gel matrix. This effect is obviously connected with the small characteristic dimension of the particles, i.e. the thickness of the aluminum flakes, which is about 0.4 μm for PAP-1 and 0.2 μm for PAP-2. However, the concentration of aluminum in the mixture is limited to a maximum of 20-30%, precisely because of the small particle diameter and correspondingly large specific surface of the material. Thus, one should use the crude powders to produce mixtures with higher aluminum content.

Pyrotechnic grade aluminum powders (PP-1, PP-2, PP-3) have the smallest particle dimensions of the powders given in Table 1, with the exception of the pigment grade aluminum (PAP-1, PAP-2). They may exert a sensitizing effect on the water-impregnated compositions (Fig. 2). Quite naturally, a very narrow region of detonation ability is detected. The water-gel matrix mixed with the powder was detonable in the steel tubes at a relatively high concentration of the metal, 50-80% (Table 2, Fig. 2-3).

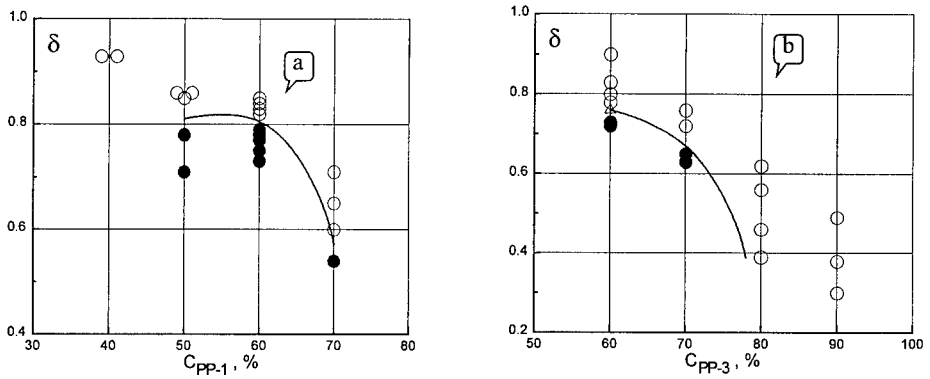

Fig.2. Critical relative density (mass % of TMD) for detonation of water-impregnated compositions based on the water-gel matrix and pyrotechnic aluminum powder PP-1 (**a**) and PP-3 (**b**). Experiments in the glass tubes of 14-15 mm diameter. Solid points correspond to detonation of the charges, open circles are failures, and a triangle is a run where detonation extinguished in the middle of the charge length.

The peak of detonation ability appears to correspond to 60% aluminum. The smaller particle dimensions of PP-3 powder seem to be responsible for the highest critical density of the charges based on the powders of the PP-type at a concentration of the metal of 60% in the mixture (Fig. 3). Aluminum powder sintered at 1100 K in granules of 1.5 – 2.5 mm diameter gave formulations of very low density, 1.28 g/cm^3, 66% TMD when the granule concentration in the composition was 60%. It detonated in the steel tubes even when initiated only by a detonating cap № 8.

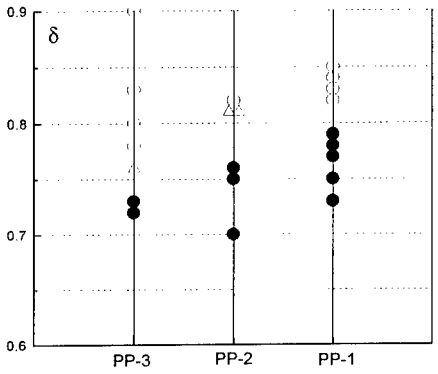

Fig.3 Comparison of the relative critical densities of the mixtures on the base of the pyrotechnic powders in the glass tubes. For explanation of the symbols, see fig. 2.

Crude powders of six other sorts listed in Table 1 demonstrated a very weak ability to sensitize the water-gel matrix. Only powder PA-2 out of the other 6 produced a composition that was capable of propagating a detonation with no additional sensitizer. At a concentration of 60%, the composition containing 60% PA-2 detonated in the steel tubes at a density of 1.75 g/cm^3, or 90 % of TMD, when initiated by a booster consisting of two pressed 2 g pellets the Russian explosive A-1X-1 (RDX phlegmatized with 5-6% paraffin/ceresine mixture). One pellet gave no steady state process.

The ability of the water-gel compositions to propagate a detonation was enhanced substantially by the addition of pigment grade aluminum to the crude metal powder. A composition containing 60% aluminum in the form of a mixture of PA-3 (125-200 μm) and PAP-2 was used first. The composition with 5% PAP-2 was detonable in the steel tubes at a density of 1.67 g/cm^3, 86% TMD, (Fig. 4). Increasing the pigment grade material concentration from 5 to 15 % resulted in the further detonation ability augmentation. It should be noted that, with respect to its influence on detonation ability, PA-3 itself behaves in these compositions approximately as an inert material. Substitution of the crude metal with sand of about the same particle size (200-250 μm) made no difference in the critical density of the mixture (see the relative placement of the circles (PA-3) and the rhombs (sand) in Figure 5). With the same mass fractions of aluminum powder and water-gel solution as in the experiments with the mixture of PAP-2 and PA-2 (15/45 in Fig. 4), it is possible to achieve a detonation in the water-impregnated system at a sand concentration level as high as 60%. The critical density of this blend was 1.63

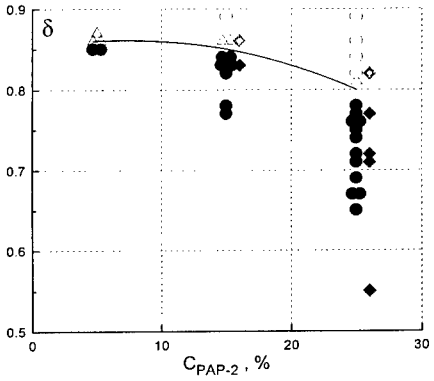

Fig.4. Critical density of the water-impregnated compositions based on PAP-2/PA-3 blends, at an overall aluminum content of 60%. For designations of the points with the exception of rhombs see fig. 2. The rhombs are experiments with sand instead of PA-3

g/cm^3. Suspensions containing 70 and 80% sand were not capable of propagating a detonation. It is likely that those containing 90 and 100% sand would also not propagate a detonation.

Table 2. Results of the experiments with water-gel compositions containing relatively crude aluminum powders (steel tubes 36/10 mm)

Trade mark of aluminum	Content of aluminum in the mixture, %	TMD, g/cm^3	Density of the charge ρ, g/cm^3	Relative density δ (% TMD)	Initiator, g of A-IX-I	Result[a]
PA-2	60	1.95	1.75	90	4	+
			1.75	90	4	+
			1.75	90	4	+
			1.75	90	4	+
			1.75	90	4	-
			1.75	90	2	-
PA-1	60	1.95	1.65	85	4	-
			1.65	85	4	-
PA-4	60	1.95	1.87	96	4	-
			1.87	96	4	-
PA-2 PA-4	36 24	1.95	1.82	93	4	-
			1.82	93	4	-
PA-2 PA-4	40 24	2.01	1.84	92	4	-
			1.84	92	4	-
PA-1 PA-4	42 25.5	2.06	1.86	90	4	-
			1.86	90	4	-
PA-2 ASD-1	48 17.5	2.03	1.90	94	4	-
			1.90	94	4	-
ASD-4	30	1.61	1.57	98	4	-
			1.57	98	4	-
Sintered Fraction 1.5-2.5mm	60	1.95	1.28	66	4	+
			1.28	66	4	+
			1.28	66	DC#8[b]	+
			1.28[c]	66	DC#8	-

Notes:
[a] + detonation, - detonation failure;
[b] DC#8 is detonating cap number 8;
[c] Experiment was carried out in a glass tube 14.3 mm diameter.

A small but quite definite influence of the aluminum particle dimensions on detonation ability of the mixtures containing crude aluminum and PAP-2 is observable. Figure 5 shows the

effect of the use of ASD-1 spherical particles of about 30 μm diameter and five relatively narrow fractions of the powders PA-3 and PA-1, specially sieved from the commercial batches. There is a noticeable increase in critical density of the compositions containing 45% crude powder and 15% PAP-2 with increasing size of the crude particle.

Table 3. Results of experiments with water-gel compositions containing PAP-2 and PA-3 aluminum powders at a different water concentrations (Glass tubes, 14-15 mm diameter, 1 mm wall thickness, initiator DC#8)

Content of water in mixture, %	TMD, g/cm^3	Density of the charge ρ, g/cm^3	Relative density δ (% TMD)	Result
13	1.95	1.51	77	+
		1.53	78	+
		1.59	82	+
		1.61	83	+
		1.61	83	+
		1.62	83	+
		1.63	84	+
		1.64	84	Extinction
		1.67	86	Extinction
		1.68	86	Extinction
		1.73	89	-
20	1.86	1.37	74	+
		1.39	75	+
		1.45	78	Extinction
		1.47	79	Extinction
		1.55	83	-
25	1.79	1.32	74	-
		1.40	78	-
		1.47	82	-
		1.41	79	+[a]
		1.41	79	+[a]
30	1.71	1.34	78	-
		1.33	78	-
		1.34	78	+[a]
		1.34	78	+[a]
		1.34	78	+[a]

Note:

[a] Experiments were carried out in the steel tubes 36/10 mm, l = 250 mm with two pellets of A-IX-I, 2 g each, as a booster.

Using a blend of PAP-2 and PA-3 the maximum content of aluminum in the mixture capable of propagating a detonation, 90%, was reached. The main parameter was assumed to be the relation between the amounts of PAP-2 and the water-gel matrix. The maximum occurred at the same ratio as in the mixture of PA-3 and PAP-2 of the greatest detonation ability (PA-3/PAP-2 = 45/15; see Fig. 4), i.e. when the mass ratio of PAP-2 to water was 3 to 8. The experimental results in the glass tubes of 14-15 mm diameter are presented in Fig.6. The mixture containing 90% of the dispersed aluminum consists of 86.25% PA-3, 3.75% PAP-2 and 10% water-gel matrix.

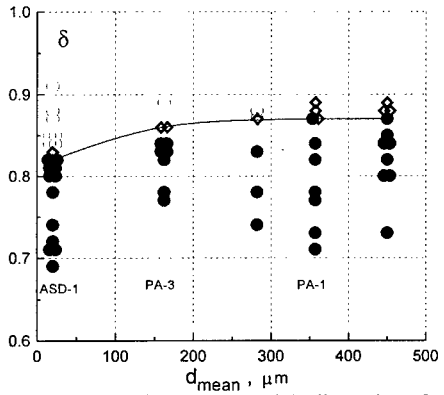

Fig.5. Influence of the mean particle dimension of the crude aluminum powder on the relative critical density of water-gel composition containing 15% of PAP-2 and 45% of the crude powder. Experiments are performed in the glass tubes 14-15 mm in diameter.

The critical density of the mixture in the glass tubes of 14-15 mm diameter (Fig. 6) tends to increase with increasing overall concentration of the aluminum blend in the mixture from 50 to 70 %. (Four points at the concentration of 80% correspond to a blend containing 7% PAP-2, 15% PP-2 and 58% PA-2). At a higher aluminum content a very interesting peculiarity of the mixture was observed. When the concentration of the crude powder of PA-3 was 70% or higher, the overall density of the charge was defined by the bulk density of the crude powder and could not be surpassed without special pressing. This is, in fact, impossible in the preparation of charges of small diameter in weak confinement such as the glass tubes). The limiting density is shown in Fig.6 by line 2. All the trials at a density lower than those corresponding to lines 1 and 2 are detonations. It should be noted that the line 1 is the absolute limit of detonation ability of compositions of this sort, whereas line 2 corresponds to the relative limit.

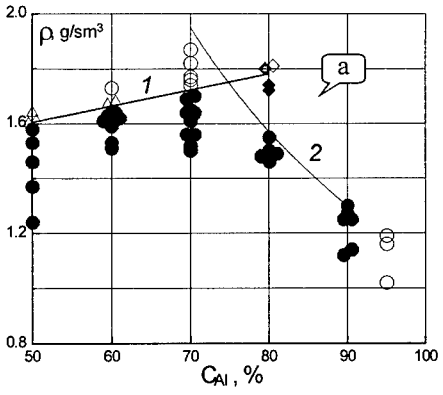

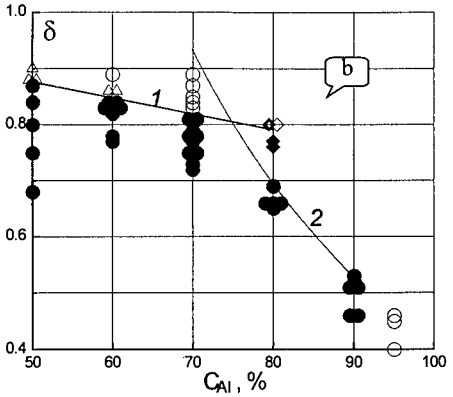

Fig. 6. Critical density (a, real, and b, relative) of the compounds, containing a blend of aluminum powders PAP-2 and PA-3 (125-250 μm). Mass relation of the PAP-2 and the watergel matrix (3 to 8) is a constant. Experiments are carried out in the glass tubes of 14-15 mm diameter. Line 1 is the limit of detonation ability. Line 2 is the largest density of the mixture that might be reached at preparation of the charges.

If it were possible to manufacture a charge of greater density than that which line 2 represents, it would probably be possible to increase the limit. Of course, this is a rather arbitrary conclusion. Under actual conditions of application of charges of this sort it is almost impossible, or at least very difficult, to reach a density exceeding that corresponding to line 2. In this sense, line 2 is the absolute limit.

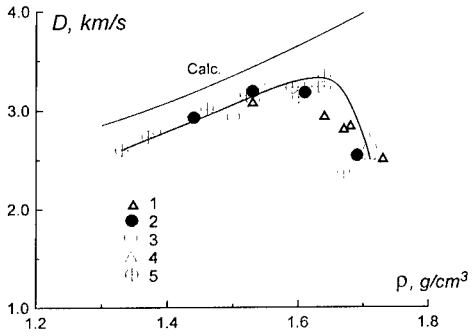

Fig. 7. Detonation velocity vs density for the mixtures containing 15% PAP-2 and 45% of the crude aluminum powder of the dimensions (μm): 1 – 125-200, 2 – 250-300, 3 – 315-400, and 4 – 400-630. The points 5 correspond to the polydispersed powder PA-2 (mean particle size 250 μm). *Calc.* is the line calculated in SD computer code at 15% active aluminum and 45% inert additive.

To produce an explosion of water-gel explosives at great depth under the sea or in deep wells filled with water or drilling solution, the main obstacle is over-compression of the explosive, resulting in a density exceeding the critical value. It is evident that for the systems described here this obstacle at least is assumed to be strongly suppressed.

The influence of the overall water concentration on detonation ability of the composition with a high (but not extremely high) aluminum content in shown in table 3. A base formulation containing 15% PAP-2, 45% PA-2, 20% AN and 7% SN and 3% water (Fig.4) detonated at densities of 1.67 g/cm^3 (86% TMD) and lower. A similar composition containing 15 % PAP-2 and 45% PA-3 (fraction of 125 – 200 μm) in the glass tubes 14-15 mm diameter, with 1 mm wall thickness, with concentration of water equal to 20 % detonated only in the charges of 1.39 g/cm^3 (75% TMD) and less. The critical density diminished very strongly. At 25% water in the glass tubes, a detonation was not propagated at the relative density of 94% TMD (1.32 g/cm^3, TMD is 1.79 g/cm^3 for this concentration of water). However, a steady state detonation was propagated in the steel tubes at 79% TMD (1.41 g/cm^3), when initiated by 2 phlegmatized RDX pellets. The composition containing 30% water did not detonate even in these experimental conditions.

The dependence of detonation velocity on charge density in systems containing 60% of the aluminum blend (15% PAP-2 and 15% PA-3) is presented in Fig. 7. The velocities are relatively low because the PA-3 does not participate in the heat evolution process in the detonation wave. Accordingly the calculations

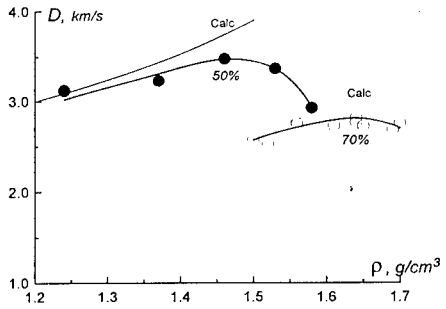

Fig. 8 Detonation velocity vs density for the mixtures containing 50 and 70% of the PAP-2/crude powder (125-200 μm).

with the SD code were performed with the assumption that PA-3 is an inert ingredient having about the same density, compressibility and specific heat as aluminum. With this assumption, the results of the computations (line marked "Calc." in Fig. 7) appear to be close to the linear part of the experimental curve. The difference between calculated and experimentally measured data is about 0.3 km/s. It should be taken into account also that the experimental detonation velocities are measured in the glass tubes of relatively small diameter, and the difference of several meters per second connected with the energy loss eventually is unavoidable.

The maximum on curve 1 in Fig. 7 is connected with the lack of reactivity of the pigment grade aluminum resulting in a long reaction time at high charge density. Two curves for the overall aluminum content of 50 and 70% (15% PAP-2, Fig. 8) support the assumption of inertness of the crude powder is valid, and may explain the decreasing detonation rate with increasing crude powder content.

Acknowledgements

Financial support of Russian Foundation of Basic Research (Grants 98-03-32164a and 98-03-32167a) of B.N.K. and V.E.A. is highly appreciated. The authors are indebted to P.P. Kapustin who had participated in carrying out of the experiments.

References

1. V.E. Annikov, B.N. Kondrikov, N.P. Smagin, L.P. Parfenov, The study of detonation of aluminum containing watergel explosives, (Problems of theory of explosives), Mendeleev Institute of Chemical Technology, Moscow, 1974, v. 83, 147 – 153
2. V.E. Annikov, B.N. Kondrikov, Watergel explosives on the base of disperse aluminum, "Vzryvnoe delo", 75/32, 1975, 151 – 158
3. V.E. Annikov, M.N. Borzykh, B.N. Kondrikov, Detonation of water-gel explosives, Detonation, Akad. Sci. USSR, Chernogolovka, 1978, 19-23

CONFINED EXPLOSIONS OF ALUMINIZED HIGH EXPLOSIVES

Waldemar A. Trzciński, Józef Paszula

Military University of Technology
Kaliskiego 2, 00-908 Warsaw, POLAND

Abstract

Effects of turbulent combustion of the detonation products of aluminized high explosives were determined and compared with those of non-aluminized ones. Heat effects of explosions of the mixtures of TNT and TNT/RDX with Al were measured in a calorimetric bomb of 3.6-liter volume. The bomb was filled with nitrogen, argon or air at a pressure of 1.5 MPa. Overpressure histories were recorded in an explosion chamber of 150-liter volume. The chamber was filled with nitrogen and air under normal conditions. Energy effects of detonation and combustion of the detonation products in air were also estimated. Finally, the degree of after-burning was calculated for the explosive mixtures tested.

On the basis of the results presented in Refs. [1÷5] and those obtained in this work, the dependence of the mean overpressure in closed vessels on the loading density of TNT was determined. TNT equivalent loading densities of the explosive tested were also established for confined explosions.

1. Introduction

Effects of turbulent combustion of TNT detonation products in confined explosions have been studied recently in works [1÷5]. In papers [1-2], the heat effects were measured in a calorimetric bomb of 3.6-liter volume. The bomb was filled with argon, air or oxygen at a pressure of 1 MPa. Experiments indicated the heat effects of 3929 kJ/kg and 15108 kJ/kg in argon and air (or oxygen) atmosphere, respectively. Other experiments were conducted in Refs. [2-3], in which an explosion chamber of 150-liter volume was applied. The chamber was filled with argon, air or oxygen enriched air at one atmosphere pressure. Measured pressure histories in the chamber filled with oxygen contained atmosphere showed enhancements due to after-burning effects. In the work [4], effects of turbulent combustion induced by explosion of a 0.8 kg charge of TNT in a 17 m^3 chamber filled with air were investigated. Mixing and after-burning of TNT detonation products in a steel vessel were

recorded in work [5] by the use of the Schlieren vizualization system and high-speed photography. Overpressure histories were also measured at the vessel wall by using pressure transducers.

Behaviour of an aluminium admixture in the reaction zone of detonation wave and in expanding detonation products was investigated in many works, for example, in Refs. [6÷9]. The influence of aluminium ingredient of high explosives on their ability of metal acceleration was determined in paper [6] by streak camera recording of radial motion of a copper tube. Composition B and a cast RDX/TNT based explosives with 15 % aluminium or lithium flouride additives were used in the cylinder test. It was established that the first sign of aluminium reaction appeared at about 4 μs behind the detonation front. However, the cylindrical data obtained did not give any information on the degree of this reaction.

In Ref. [7], the early time rate of energy release from detonating PETN and TNT explosives filled with 5 to 20 % of either 5 μm or 18 μm spherical aluminium was determined by using Fabry-Perot interferometry techniques. From the measured particles velocity data, the reaction rate of aluminium with the detonation products was inferred. All of the metal in PETN formulations filled with 5 % or 10 % of either 5 μm or 18 μm aluminium reacted within 1.5 μs, resulting in an increase of 18-20 % in energy compared to pure PETN. For TNT formulations, between 5 to 10 % aluminium reacts completely within the same timeframe.

The compositions of detonation products for several explosives containing RDX, NQ and HMX with different binders and varying Al content were measured in Refs. [8-9]. Experiments were done in a stainless steel chamber of a volume of 1.5 m^3 filled with argon under different pressures up to 0.3 MPa. In work [9], explosives with different Al content were also detonated under water in a plastic balloon. The gaseous products and the solid residue were analyzed with regard to the formation of carbon soot and unreacted aluminium. The content of unreacted aluminium found in the residue depended strongly on the oxygen balance of explosive and the argon pressure.

In this work, a series of experiments for charges of TNT and TNT/RDX containing aluminium additive has been conducted in a calorimetric bomb and in an explosion chamber. The heat effects of detonation in the bomb filled with argon, nitrogen and air under pressure of 1.5 MPa were measured. Signals of overpressure were recorded after detonation of a charge in the chamber filled with nitrogen or air under normal conditions. The results of gasdynamical modelling and thermochemical calculations were compared with the overpressure histories. In consequence, the energies released during the closed detonation of explosives tested in nitrogen and air were determined. Moreover, TNT equivalents for these explosives were determined for confined explosions.

2. Explosives tested

Crystalline RDX, flaked TNT, aluminium powder (size of grains < 0.15 mm) and flaked aluminium (specific surface about 3000 cm^2/g) were used to prepare explosive mixtures. Charges of the mixtures were pressed from the granulate products obtained in the following way.

- TNT dissolved in acetone was mixed with RDX and/or Al.
- After homogenization the mixture was granulated and acetone was evaporated.

Compositions of the mixtures, their densities and detonation velocities are given in Table 1.

Table 1. Characteristics if mixtures tested

Mixture	Composition	Density [kg/m^3]	Detonation velocity [m/s]
Tritonal_5	TNT/Al $_{flaked}$ 95/5	1610±20	6740±40
Tritonal_10	TNT/Al $_{flaked}$ 90/10	1620±20	6680±40
Tritonal_20	TNT/Al $_{flaked\ r}$ 80/20	1640±20	6480±40
Tritonal_15$_{powder}$	TNT/Al $_{powder}$ 85/15	1690±20	6710±40
Tritonal	TNT/Al $_{flaked}$ 85/15	1630±20	6590±40
Hexatol	TNT/RDX 50/50	1660±20	7560±40
Hexatonal	TNT/RDX/Al $_{flaked}$ 42.5/42.5/15	1740±20	7300±40

3. Heat effects of detonation

A spherical steel bomb of a volume of 3.6 l was used to measure heat effects of detonation ([1]). The bomb was filled with argon, nitrogen or air under the pressure of 1.5 MPa. Weighed samples of the explosive mixtures were pressed in matrices of inner diameter of 16 or 20 mm. Detonation of the charge was initiated by an electrical fuse. The energy released by the fuse was estimated by the method described in Ref. [10]. The results of measuring the heat effects of detonation in different gases are presented in Table 2.

Comparison of measured heats in inert atmosphere shows that the heats of detonation in argon filler of the bomb are smaller than those obtained for nitrogen. This means that some exothermic reactions between nitrogen and the detonation products took place in the bomb.

Thermochemical calculation was performed by using TIGER – Ref. [11]. The set of values of the parameters $\alpha = 0.50$, $\beta = 0.298$, $\kappa = 10.50$ and $\Theta = 6620$ for the BKW equation of state and covolumes factors for gaseous species were taken from Ref. [12]. Calculated heat effects are presented in Table 2. The compositions of the detonation products frozen at the temperature 1800 K on the CJ isentrope were used to calculate the detonation heat of the explosive tested [13]. The mixture of air and combustion products (the explosion products) cooled to the same temperature was the basis for calculation of the heat effect.

Calculated detonation heats are close to those obtained in calorimetric experiments with argon filler. Measured heats of detonation in air atmosphere are higher than calculated heats of explosion the mixture of air and the charge of explosive. Calculated heats of detonation and those of explosion were used to estimate the energetic TNT equivalents for the mixture tested.

Table 2. Measured and calculated heat effects of detonation in the bomb filled with different gases

Explosive	Gaseous filler	Mass of sample [g]	Heat effect [kJ/kg]	Averaged heat [kJ/kg]	Calculated heat [kJ/kg]
TNT	Argon*	10.3182	4053	4019 ± 46	4507
	Nitrogen	6.0253 7.0454 7.9709 10.0798 11.8944	4168 4266 4511 4498 4540	4430 ± 175	4507
	Air*	9.0066	15088	15106 ± 380	14923
Tritonal	Argon	6.1507 8.0875 10.0598 12.0247	4893 5026 5089 5226	5059 ± 140	5057 (30 % Al inert)
	Air	6.1124 7.4490 8.1829 8.9557	17465 17771 17973 18114	17831 ± 280	16938
Hexatol	Argon	6.1376 7.8914 10.0821 11.9810	4685 4684 4937 4829	4785 ± 125	4835
	Nitrogen	6.0108 8.0578 10.1010 12.1160	4791 4920 5019 5100	4958 ± 135	4835
	Air	6.0945 6.5192 7.1842 8.2830 8.8270 9.6672	13312 13318 13169 13500 13574 13901	13462 ± 260	12180
Hexatonal	Argon	6.1013 7.9075 10.0154 12.0497	5481 5744 5902 6049	5795 ± 242	5677 (20 % Al inert)
	Nitrogen	6.0629 7.9507 10.0302 11.9450	5806 5897 6144 6256	6027 ± 207	5677 (20 % Al inert)
	Air	6.0633 6.9588 7.0484 8.0376 8.0491 9.0264 9.0832	15997 14546 14670 15453 15369 15296 15311	15235 ± 495	14577

* Data taken from Ref. [10]

4. Explosion chamber tests

Overpressure histories of the afterburning process of the detonation products were measured in a chamber which schematic diagram is shown in Fig. 1.

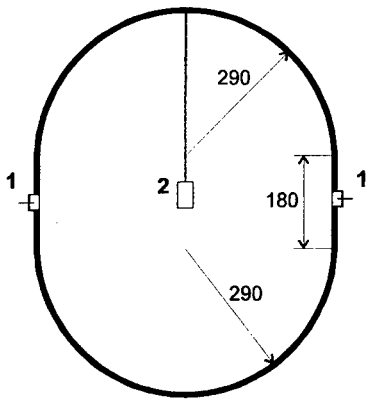

Fig. 1. Schematic diagram of an explosion chamber; 1- pressure gauges, 2 - explosive charge.

The chamber of volume of about 0.15 m^3 was filled with nitrogen or air under the pressure of 0.1 MPa. The charge with a fuse was placed in the centre of the chamber. Signals of overpressure from two piezoelectric gauges located at opposite walls of the chamber (see Fig. 1) were recorded. Selected overpressure records (dotted lines) from the chamber are presented in Figs. 2 and 3. The time-axis of the figures starts from nonzero values, because the storage scope had recorded signals during a period of time, before the first reverberation of the shock wave at the chamber wall took place.

The overpressure records have the oscillating nature due to the gasdynamical processes (acceleration, reflection and reverberation of shock waves, turbulence flow) occurring in the vessel. The averaged overpressure was obtained by using the following formula – Ref. [14]:

$$\Delta p_{\text{aver}}(t) = \frac{1}{\tau} \int_{t-\frac{\tau}{2}}^{t+\frac{\tau}{2}} p(t)dt \tag{1}$$

Chosen value of τ was about two times longer than the time-duration of a main peak of overpressure recorded in the chamber. The results of averaging are presented in Figs. 2 and 3 by solid lines.

From analysis of the averaged pressure histories it follows that, initially, the gasdynamical processes proceeding in the gaseous medium and the afterburning process influence strongly the average pressure at the chamber wall. After the first reverberations of shock waves at the vessel wall, the decrease of mean value of overpressure is caused mainly by the heat losses to the wall. Thus, the mean overpressure was determined for the time when the influence of the gasdynamical processes could be neglected. It was assumed that the first dynamical stage of shock wave reverberations at the wall lasted about 20 ms. After that period of time, the time-dependence of the mean overpressure can be approximated by the following function

$$\Delta p_{mean}(t) = p_0 e^{-a(t-t_0)}, \tag{2}$$

in which t_0 is the time of the first reflection of the shock wave at the chamber wall (t_0 = 10.25), p_0 and a are constants. To determine those constants, the averaged overpressures for all shots (from 3 to 5) for given type of gas filling the chamber were used.

For the initial phase of records (10.25<t<30 ms), all values of the average overpressures for given gascous filler are approximated by the function

$$\Delta p_{mean}(t) = p_0 e^{-a(t-t_0)} + p_1\left(\frac{t}{t_0}\right)^{-b} + p_2 \ln[c\,(t-t_0)], \tag{3}$$

in which t_0 p_0, a are taken from the function (2) and p_1, p_2, b and c are constants. The functions approximating averaged overpressures were used in the procedure of determining the kinetics of the afterburning processes.

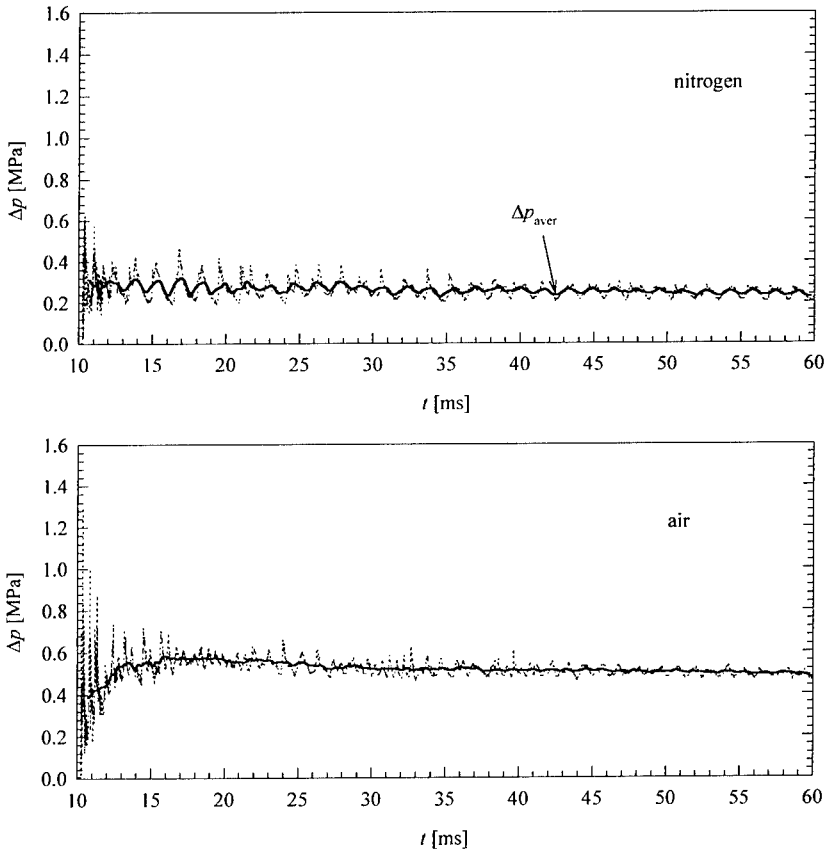

Fig. 2. Overpressure records in the chamber filled with nitrogen and air for a 25 g charge of hexatol

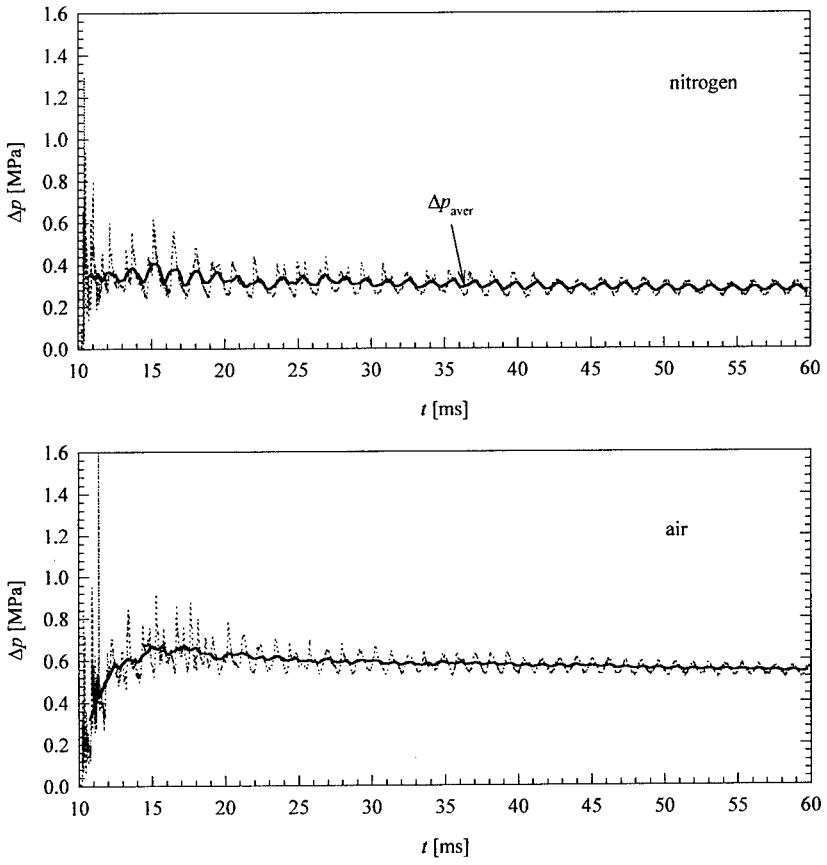

Fig. 3. Overpressure records in the chamber filled with nitrogen and air for a 25 g charge of hexatonal

5. Characteristics of afterburning

Characteristics of the afterburning process were determined with the method described in Ref. [3]. The mean overpressure histories from the chamber filled with nitrogen and air are the basis of this method. Moreover, the results of thermochemical calculations are applied to estimate the heat effect of afterburning. The procedure for determining the energy released in the chamber in the course of time is as follows. From the experimental time-dependence of mean pressure at the wall in the chamber filled with nitrogen, the hypothetical equivalent volume of gases for given time can be obtained by using the adiabate of the mixture of nitrogen and detonation products. It is assumed that at that moment the reactive mixture of detonation products and air occupies the same volume. Knowing the equivalent volume and the average pressure for a given time, we can fit the value of the fraction of active oxygen,

i.e., the mass of oxygen taking part in reactions. We choose the value for which pressure of reaction products compressed adiabatically from the chamber volume to the equivalent volume is equal to the mean pressure. Then, the chemical energy corresponding to this fraction can be obtained. In this way the energy can be calculated as a function of time (Figs. 4÷5). From Figs. 4 and 5 it follows, that the process of afterburning of the detonation products of TNT in air filling the explosion chamber of 150 l in volume proceeds about 1-3 ms for charges of 50 and 100 g and 3-6 ms for small charges (10 and 25 g).

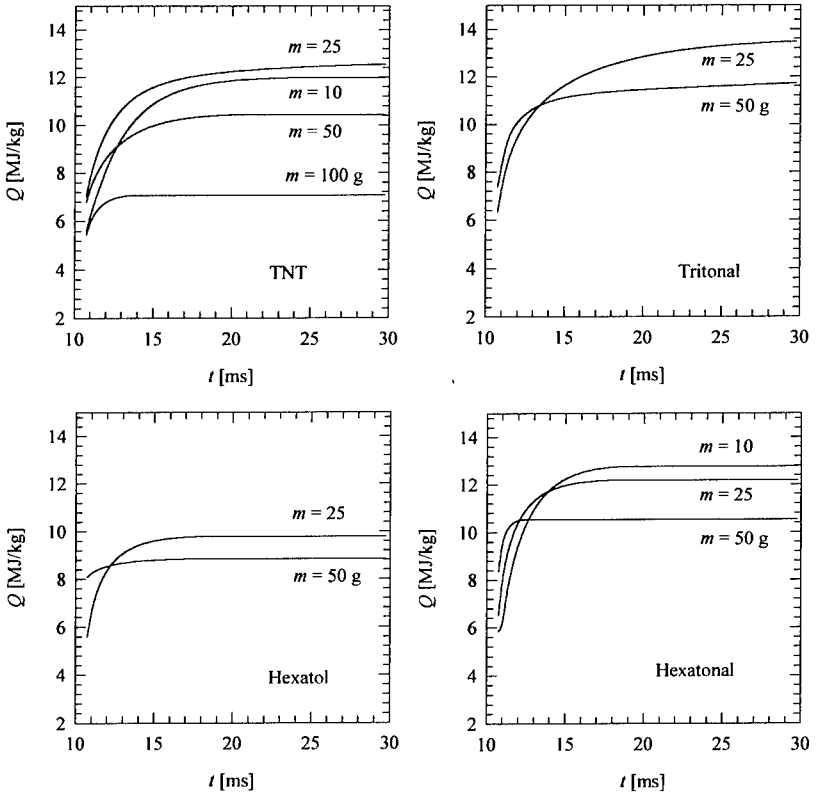

Fig. 4. Time-dependence of the energy released in the chamber filled with air after detonation of charges of different explosives

From Fig. 5 it follows that the increase of aluminium content in tritonal charges from 0 to 20 % effects higher rate of heat release during the first stage of combustion following the detonation. The final values of the specific heat differ less than 10 %. The high energy of reaction of the detonation products with air was estimated for the mixture with 15 % of flaked aluminium.

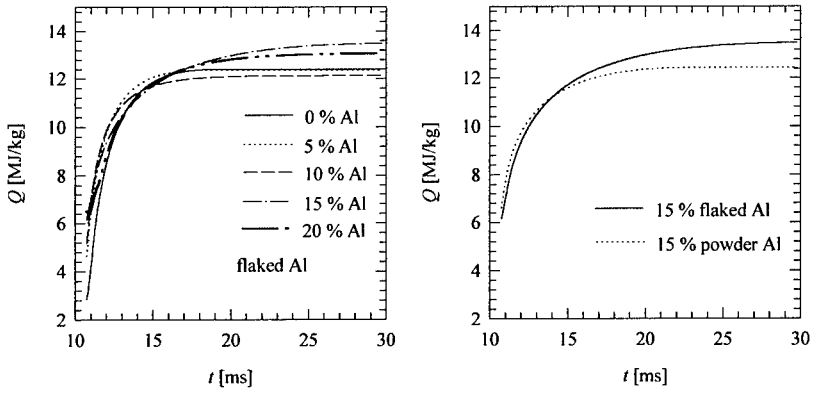

Fig. 5. Time-dependence of the energy released in the chamber filled with air after detonation of charges of TNT with different admixtures of Al.

The values of maximal mean overpressure and the temperature, fraction of active oxygen, products composition and the heat effect corresponding with the maximal overpressure are presented in Table 3 for selected charges of explosive tested. Parameter τ is a period of time, during which this maximal value is achieved. The data for TNT are taken from Ref. [3].

Table 3. Calculated characteristics of afterburning of the detonation products of explosives tested

Explosive	TNT				Tritonal	Hexatol	Hexatonal
Mass of charge [g]	10	25	50	100	25	25	25
p_0 [MPa]	0.30	0.65	1.01	1.33	0.69	0.54	0.63
T [K]	1098	1926	2520	2497	2072	1636	1895
η [%]	13.75	35.37	57.02	60.00	33.36	20.75	22.75
$\tau(p_0)$ [ms]	12.25	11.50	7.00	1.25	19.25	7.00	5.00
Products [mol/kgm]							
N_2	25.766	24.377	22.448	19.648	24.257	24.794	24.629
CO	0.487	1.094	3.418	9.505	1.437	0.918	1.044
Ar	0.304	0.282	0.252	0.207	0.282	0.282	0.275
CO_2	1.227	2.728	3.313	1.498	1.827	1.858	1.329
H_2	0.093	0.061	0.189	1.358	0.090	0.108	0.112
H_2O	0.568	1.348	2.254	2.604	1.119	1.452	1.225
O_2	5.875	4.083	2.427	1.855	4.224	5.007	4.877
NO			0.028	0.003	0.001		
Al_2O_3					0.309		0.308
Heat effect [kJ/kg]	11966	12345	10297	6392	13496	8899	12003

The results given in Fig. 4 and in Table 3 show that the specific energy released in the chamber during the first stage of detonation and combustion increases with increasing mass of explosive.

However, for most explosives tested, the final value of the heat effect diminishes for greater mass of given explosive.

The degree of afterburning is defined by the formula

$$\delta \equiv \frac{Q_r - Q_{det}}{Q_{com} - Q_{det}} 100\%, \tag{4}$$

in which Q_r, Q_{det} and Q_{com} denote the heat effect of afterburning, the detonation heat and the combustion heat, respectively. Calculated degrees for the explosives tested are shown in Fig. 6 as a function of the loading density ρ_l, i.e., the ratio of the charge mass to the chamber volume. The values of the degree do not differ more than 7 % for given charge mass. So, the dependence of the degree of afterburning on the loading density is approximated by the following function

$$\delta = -8.221 \cdot 10^{-7} \rho_l^2 - 3.550 \cdot 10^{-4} \rho_l + 0.7754, \tag{5}$$

in which ρ_l is expressed in g/m^3.

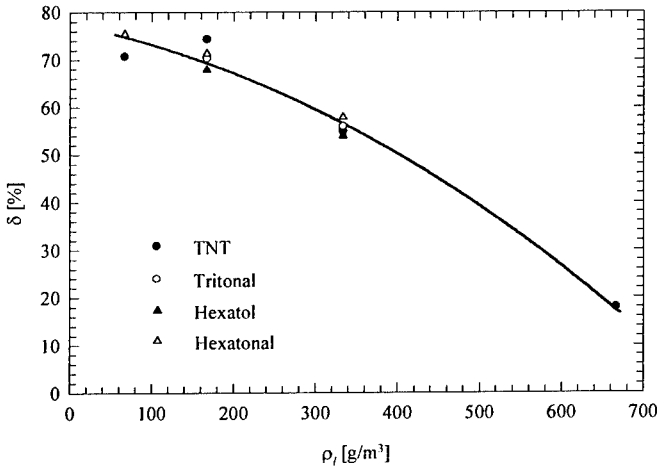

Fig. 6. Dependence of the degree of afterburning on the loading density

6. TNT equivalent of explosives for confined explosions

The dependence of the mean overpressure in the chamber on the loading density of TNT is presented in Fig. 7 for nitrogen and in Fig. 8 for air in a closed vessel. The data given in works [3÷5] were taken into considerations. The experimental relation between Δp and ρ_l was approximated by a function

$$\Delta p = A \cdot \rho_l^k \tag{6}$$

The values of coefficients A and k are given in Table 4.

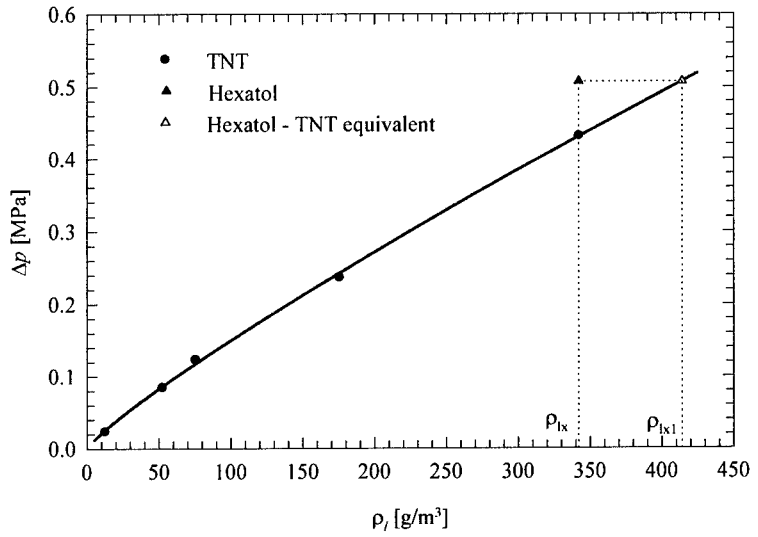

Fig. 7. Dependence of overpressure in the chamber filled with nitrogen on the loading density of TNT

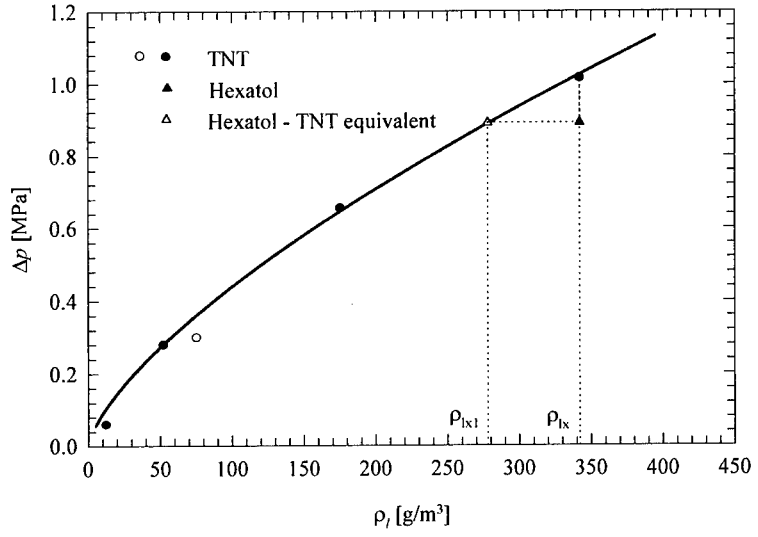

Fig. 8. Dependence of overpressure in the chamber filled with air on the loading density of TNT

Table 4. Values of coefficients A and k from the function (6)

Gaseous filler	A	k
Nitrogen	0.002874	0.858489
Air	0.01828	0.6895

The function (6) can be used for determining the TNT equivalent of given explosive for confined explosion. The TNT equivalent is the loading density of TNT charge causing the same overpressure in confined explosion like the charge of given explosive of a unit of loading density. For the examples shown in Figs. 7 and 8, the TNT equivalent for confined explosion is expressed in the following way

$$\alpha_{TpV} = \frac{\rho_{lxl}}{\rho_{lx}} \tag{7}$$

Taking into account the function (6), we obtain

$$\alpha_{TpV} = \frac{1}{\rho_{lx}} \left(\frac{\Delta p}{A} \right)^{1/k} \tag{8}$$

The values of α_{TpV} for explosives tested are presented in Table 5. For comparison, the values of energetic TNT equivalents are also given. The energetic TNT equivalent α_{TQ} is expressed in the following manner

$$\alpha_{TQ} = \frac{Q_{\text{det}}}{Q_{\text{det.TNT}}}, \tag{9}$$

and the energetic TNT equivalent for confined explosions α_{TQV}

$$\alpha_{TQV} = \frac{Q_{\text{com}}}{Q_{\text{com.TNT}}}, \tag{10}$$

Table 5. TNT equivalents for explosives tested

Explosive	Mass [g]	α_{TpV} (nitrogen)		α_{TQ}	α_{TpV} (air)		α_{TQV}
TNT	-	1.00		1.00	1.00		1.00
Tritonal	25	1.14	1.16 ± 0.02	1.12	1.11	1.08 ± 0.04	1.13
	50	1.17			1.05		
Hexatol	25	1.17	1.19 ± 0.03	1.07	0.78	0.81 ± 0.03	0.82
	50	1.21			0.82		
Hexatonal	10	1.36	1.39 ± 0.03	1.26	0.79	0.91 ± 0.10	0.97
	25	1.41			0.96		
	50	1.41			0.96		
Tritonal_5	25	1.13		-	0.97		1.04*
Tritonal_10		1.12		-	1.00		1.09*
Tritonal_20		1.11		-	1.06		1.18*
Tritonal_15$_{\text{powder}}$		1.10		-	1.01		1.15*

(*) The heats of combustion obtained from of thermochemical calculations are the basis for estimation of α_{TQV}

From Table 5 it follows that the values of α_{TpV} determined from the mean overpressures for the chamber filled with nitrogen are slightly smaller than the values of α_{TQ}. Analogously, the values of α_{TpV} obtained for the chamber filled with air are slightly smaller than the values of α_{TQV}. It must be underlined that the TNT equivalents of hexatol and hexatonal for confined explosions are less than 1 and only those estimated for tritonal are greater or comparable to 1.

Summary

1. Heats of detonation measured in argon atmosphere are smaller than those obtained for nitrogen filling the calorimetric bomb. In our opinion, there are some exothermic reactions between nitrogen and detonation products in the bomb.
2. Quite good agreement between the heats of detonation measured in argon and those calculated are obtained when 30 and 20 % of inert aluminium were assumed for tritonal and hexatonal, respectively.
3. The specific energy released in the chamber of 0.15 m^3 volume during the first stage of detonation and combustion increases with enlarging mass of explosive charge. However, the final specific heat effect decreases with increasing that mass.
4. Differences in the final values of the heat effect of tested mixtures of TNT and aluminium do not exceed 10 %.
5. Estimated degrees of the afterburn process for the explosives tested do not differ themselves more than 7 % for given loading density.
6. Determined TNT equivalents for confined explosions in air are close to the energetic TNT equivalents calculated on the basis of the combustion heat of explosives tested.
7. Among the explosives used, only the mixtures of TNT and aluminium have the TNT equivalents for confined explosions greater or comparable to 1.

This paper was accomplished within the framework of the Project 0 T00A 020 16 financed by the State Committee for Scientific Research.

References

[1] S. CUDZILO, R. TRĘBIŃSKI, W. A. TRZCIŃSKI, P. WOLAŃSKI, *Comparison of heat effects of combustion and detonation of explosives in a calorimetric bomb,* 29th International Annual Conference of ICT, Karlsruhe 1998.

[2] J. PASZULA, R. TRĘBIŃSKI, W. A. TRZCIŃSKI, P. WOLAŃSKI, *Afterburning of TNT detonation products in an explosive chamber,* 29th International Annual Conference of ICT, Karlsruhe 1998.

[3] W. A. TRZCIŃSKI, J.PASZULA, *The influence of TNT mass on the afterburn of detonation products in an explosion chamber*, 30th International Annual Conference of ICT, Karlsruhe 1999.

[4] A. L. KUHL, J. FORBES, J. CHANDLER, A. K. OPPENHEIM, R. SPECTOR, R. E. FERGUSON, *Confined combustion of TNT explosion products in air*, Colloquium on Gas, Vapor, Hybrid and Fuel-Air Explosions, September, 1998, Schaumburg, Illinois, USA.

[5] P. WOLAŃSKI, Z. GUT, W. A. TRZCIŃSKI, J. PASZULA, L. SZYMAŃCZYK, *Visualization of turbulent combustion of TNT detonation products in a steel vessel*, 17th International Colloquium on the Dynamics of Explosions and Reactive System, Heidelberg 1999.

[6] G. BJARNHOLT, *Effects of aluminium and lithium fluoride admixtures on metal acceleration ability of Comp B*, Sixth Symposium (International) on Detonation, Coronado, CA, USA 1976.

[7] W. C. TAO, C. M. TARVER, J. W. KURY, C. G. LEE, D. L. ORNELLAS, *Understanding composite explosive energetics: IV. Reactive flow modelling af aluminium reaction kinetics in PETN and TNT using normalized products equation of state*, Tenth Symposium (International) on Detonation, Boston, MA, USA 1993.

[8] F. VOLK, *Analysis of the detonation products of insensitive high explosives,* 25th International Annual Conference of ICT, Karlsruhe 1994.

[9] F. VOLK, F. SCHEDLBAUER, *Detonation products of less sensitive high explosives formed under different pressures of argon and in a vacuum*, Ninth Symposium (International) on Detonation, Portland, Oregon, USA 1989.

[10] S. CUDZILO, J. Paszula, R. TRĘBIŃSKI, W. A. TRZCIŃSKI, P. WOLAŃSKI, *Studies of afterburning of TNT detonation products in confined explosions*, Colloquium on Gas, Vapor, Hybrid and Fuel-Air Explosions, September, 1998, Schaumburg, Illinois, USA.

[11] CH. L. MADER, *Numerical modelling of detonations*, University of California Press, Berkeley-Los Angeles-London, 1979.

[12] M. L. HOBBS, M. R. BAER, *Nonideal thermoequilibrium calculations using a large product species data base*, Shock Waves (1992), 2: 177-187.

[13] D.L. ORNELLAS, *Calorimetric determinations of the heat and products of detonation explosives*, Lawrence Livermore Laboratory, Livermore 1982.

[14] P. NEUWALD et al., *Self-similar combustion of turbulent fuel jets in air*, Fraunhofer Institut für Kurzzetdynamik, 1997.

The Development of High Explosives in CAEP

Dong Haishan

(Institute of Chemical Materials, China Academy of Engineering Physics, 621900, Mianyang, Sichuan)

Abstract

The study on synthesis of high energy explosives and their formulations started at the begining of 60s of 20th century. Since the late of 70s the study direction were changed to synthesize and formulate less sensitive and insensitive high explosives.

In this paper, the properties (performance, sensitivity, stability and mechanical strength) of about 20 explosive compounds and about 30 formulations (cast explosives, pressed PBX and composite explosives) were represented, and some regularities of phlegmatization and plastification technique were described.

Key words: explosive, property, phlegmatization, plastification, formulation.

ALTERNATIVE OPTION FOR HIGH-PERFORMANCE, IM-COMPLIANT, METAL ACCELERATING WARHEAD FILLINGS: PRESSED PBX TECHNOLOGY

T.T. Nguyen
Weapons Systems Division
Defence Science and Technology Organisation (DSTO)
P.O. Box 1500 Salisbury, South Australia 5108

Abstract

An overview is presented of pressed PBX formulations suitable for application as IM-compliant, high-performance, metal accelerating warhead fillings.

The review is focussed on recently developed pressed formulations with potential for Service qualification and application into weapons systems. The processing procedures are described with important experimental parameters highlighted. Results from small-scale sensitivity testing (e.g. impact sensitivity, friction sensitivity, vacuum thermal stability, etc.) and vulnerability testing (e.g. slow cook-off, fast cook-off, bullet impact, etc.) are discussed. Explosive performance (indicated by detonation velocity, detonation pressure, and shaped charge penetration results) of selected representative formulations are reported and analysed.

Future trends and potential applications of pressed formulations as shaped charge and fragmentation charge fillings in advanced weapons systems are discussed.

GLOSSARY

ARDEC	Armament Research Development and Engineering Center
ASRAAM	Advanced Short Range Air-to-Air Missile
BDNPA/F	Eutectic mixture (50/50) of bis(2,2-dinitropropyl)acetal and bis(2,2-dinitropropyl)formal
CAB	Cellulose acetate butyrate
CD	Charge diameter
DOA	Dioctyladipate
ERGM	Extended Range Guided Munition
HAAP	Holston Army Ammunition Plant
HMX	Cyclotetramethylene tetranitramine
IM	Insensitive munition
LLNL	Lawrence Livermore National Laboratory
MBD	Matra BritishAero Dynamics
NAVORDSTA	Naval Ordnance Station Detachment Yorktown
NSFS	Naval Surface Fire Support
NSWC	Naval Surface Warfare Center
NTO	3-Nitro-1,2,4-triazol-5-one
PBX	Plastic bonded explosive
PEG	Polyethylene glycol
RDX	Cyclotrimethylene trinitramine
TMD	Theoretical maximum density
TNT	Trinitrotoluene

INTRODUCTION

A current major driver for design of modern-day weapon systems is the increasing demand both for improved performance to defeat new or perceived future targets, and for improved insensitiveness of the weapon system to unplanned, accidental stimuli. There has been a growing trend among western countries over the past decade for compliance with the requirements of Insensitive Munitions (IMs). Australia has also adopted an IM Policy which was promulgated in the Australian Defence Instructions General DI(G)-LOG 07-10 in 1993 [ref 1].

Insensitive Munitions (IMs), by definition [ref 1], are those munitions which reliably fulfill their performance and operational requirements on demand, but in which the violence of response to unplanned stimuli is restricted to an acceptable level determined by prescribed tests and criteria.

Several approaches have been proposed for achieving IM compliance. They include weapon design, mitigation devices, storage and transport strategies, and use of appropriate warhead fillings. The last mentioned, i.e. fillings of warhead with increased-performance, improved-insensitiveness explosive formulations constitute an important (and perhaps the most obvious) approach.

Recently, considerable effort has been put into cast-cured polymer bonded explosive (PBX) research, which can be quite applicable to IM-compliant underwater and air-blast explosives. Essentially cast-cured technology involves the use of a suspension of an explosive (e.g. RDX or HMX) in a polymeric binder, which is cast into a munition and allowed to cure *in situ* to obtain an elastomeric charge. The binder acts as an inert matrix surrounding the explosive particles thus helping to reduce their vulnerability against shock and thermal stimuli. However the requirement for large binder contents to allow casting makes high-performance explosives for metal accelerating applications difficult to obtain by this means.

An alternative approach involves coating the explosive particles with an inert polymeric material, which acts as both binder and desensitiser. These formulations, which typically contain over 90% solid loadings (which are important to achieve high performance), cannot be cast. Instead they are pressed into high-density solid charges, having typically more than 97% of their theoretical maximum density.

PROCESSING PROCEDURES

1. Formulation

As mentioned, compared with cast PBXs, pressed PBXs usually contain higher solid loadings (90-95%) of high explosives (HMX, RDX, and others), and consequently smaller amounts (5-10%) of binders.

Although present in only a small percentage, the binder plays a key role in determining the pressed charge density, thermo-mechanical, and vulnerability characteristics of the resultant explosive formulation. The binder also has a significant effect on explosive performance. In general, a higher density binder was found to produce formulations with higher theoretical maximum densities that should lead to fillings with higher detonation pressures. However, the denser binders are more difficult to press and, in some cases, the higher density binders did not give rise to formulations with significantly higher detonation pressures. This was reported in a UK study on RF 44, a composition containing a high density fluoropolymer binder Hostaflon, and RF 42 a composition containing a thermoplastic elastomer binder Kraton [ref 2].

Basically, the formulation procedure consists of three principal steps. The first step involves the preparation of a lacquer solution by dissolving the binder in a suitable solvent and adding a plasticiser, if required. The second step involves making a slurry or suspension of the explosive particles in water. The final step involves adding the lacquer to the slurry with agitation at ambient or elevated temperature before evaporation of the solvent to precipitate the binder onto the surface of the explosive solid [ref 3].

When NTO was combined with HMX as the explosive solid, the water slurry method was found to be complicated by the poor solubility of NTO in water. This was circumvented by adding the lacquer to the dry explosive and evaporating the solvent by stirring [ref 4]. However, caution must be exercised when manipulating dry explosive crystals, and this approach is only suitable for preparing small amounts of moulding powders for laboratory studies. Further, this approach may give rise to higher impact sensitivities of the moulding powders, when compared with powders prepared by the water slurry method, probably because of poorer coating efficiency [ref 4].

In some instances, the use of an anionic surfactant (e.g. Alipal CO-433) has been recommended [ref 3]. It was added to an HMX/water slurry before adding the lacquer, to enhance the coating of the explosive particles by the lacquer due to the wetting action of the surfactant and also to help prevent the binder from sticking to the internal surfaces of the mixer.

Large amounts of water (three times the total explosive batch weight) are recommended for the HMX slurry solution in order to help agglomerates of HMX particles separate more readily during mixing and encouraging more complete granulation [ref 3].

At the heart of the mixing process is the mixer. The capacity of the mixer dictates the size of the batch (small scale, medium scale, or large scale) which can be prepared. Table 1 shows a list of the small-scale mixers, with indicated capacity, features, final pressed PBX products and the organisations using them. Other mixers of medium and larger capacities are also included in Table 2 for future reference.

Table 1. "Small-Scale" Mixers Used in Preparing the Moulding Powders

	Small-Scale Mixing				
Capacity	1.5-litre steam pot	2-litre kettle	7.6-litre mixer (2-gallon)	12-litre still	40-litre kettle
Features	High-speed propeller with agitator	Four baffles; 3-membered blade glassed-steel impeller /agitator	Baker-Perkins vertical planetary mixer	bottom-discharged; unpitched, high-speed agitator;	Eight baffles; eight-membered glassed-steel
PBX product	300-g batches of PBXW-9	300-g batches of PBXW-17	PBXW-9	PBXW-9	PBXW-17
Organisation	NAVORDSTA[a]	NSWC[b] Indian Head	NSWC White Oak	HAAP[c]	NSWC Indian Head

[a] Naval Ordnance Station Detachment Yorktown, MD, USA;
[b] Naval Surface Warfare Center ; [c] Holston Army Ammunition Plant, Kingsport, TN, USA

2. Pressing

The next stage is pressing of the resultant moulding PBX powder into billet charges. This is an important stage because pressing determines the density of the charge which affects the sensitiveness, performance, and vulnerability of the explosive filling.

Table 2. Medium and Large Scale Mixers Used in Preparing the Moulding Powders

	Medium Scale	Large Scale	
Capacity	114-litre (30 gallon) kettle	121-litre still (32-gallon)	1893-litre (500-gallon) vacuum still
Features	Anchor-blade tilt kettle; having removable or hinged lids for complete internal access to decant the content.	Bottom discharge; having solvent traps to condense and capture solvent vapour; medium-speed agitator.	Heating HMX slurry to 65 C; with agitation; To produce 240-kg batches of PBX
PBX product	PBXW-9	PBXW-9	LX-1
Organisation	NSWC[a] and NAVORDSTA[b]	NAVORDSTA	LLNL[c]

[a] Naval Surface Warfare Center, Indian Head, MD, USA

[b] Naval Ordnance Station Detachment Yorktown, MD, USA

[c] Lawrence Livermore National Laboratory, California, USA

Conventional mechanical pressing using axially loaded dies, and hydrostatic or isostatic pressing in which pressure is applied uniformly from all directions, have been used [ref 2,5]. For small-scale laboratory studies, an "Instron" Universal Testing Machine in the compression mode was used as a press to produce small RDX/wax pellets weighing about 2.5 g [ref 6].

A number of experimental factors are important. The consolidation pressures and the press dwell times need to be determined for the particular material being pressed and for a desired size of the resultant pellet. Further, the temperature of the moulding powder and the die set, and the amount of vacuum and vacuum dwell times should be tested before selecting the optimised conditions.

Formulations containing Cariflex and Estane as binders had to be pressed at elevated temperatures, but some Hytemp formulations were pressed at ambient temperatures [ref 7].

Another important parameter to be determined is whether single pressing or multiple pressing is more effective in producing higher density pellets. Multiple pressing was reported to produce very high density HMX-based pellets containing as little as 1% binder Estane [ref 8]. However, in a more recent study for PBXW-17 formulation, the best conditions involved single pressing at about 138 MPa (or 20 kpsi) pressure with minimal press dwell time (30 seconds) [ref 9].

Several options were reported as pressing techniques to filling generic test vehicles [ref 2]. They included: single end pressing from the liner end, single end pressing from the initiation end, double end pressing and isostatic pressing. Alternatively, the explosive charges could be pressed directly into the case and the liner assembled to the case. This technique, however, may give rise to distortion of the case in some instances [ref 2].

CURRENT PRESSED EXPLOSIVE FORMULATIONS

Recent R&D has led to the development of explosive formulations which offer improved IM compliance and high performance, and some of which could have potential for qualification and application into advanced

weapon systems. Most formulations are based on HMX as explosive fillers, although some are based on RDX fillers. In some formulations, NTO is used as a partial replacement for HMX to lower sensitivity, but at the expense of reduced performance [ref 4].

In Table 3, recently reported HMX-based and RDX-based formulations (developed and tested in the past 5 to 7 years) are compiled. LX-14, PBXN-9, and a melt cast Octol 85/15, although developed earlier, are also included as references.

Table 3. Formulations of recently developed pressed explosives

Formulation Designation	HMX (%)	RDX (%)	NTO (%)	(%) Binder	(%) Plasticiser
PBXN-9	92			(6.0) Hytemp	(2.0) DOA
PBXW-9 (Type II) [a]	92			(2.0) Hycar 4054	(5.9) DOA
PBXW-11	96			(3.0) Hytemp	(1.0) DOA
DXD-59	92			(2.0) Hytemp	(6.0) DOA
PAX-2A	85			(6.0) CAB	(9) BDNPA/F
PBX-P31	96			(4.0) Silicone	
PBX-P32 [b]	95			(3) [c]	
PBX-P33 [b]	95			(2.5) [c]	(0.5) [c]
PBX-P11		96		(4.0) Silicone	
PBXW-17		94		(1.5) Hytemp	(4.5) DOA
LX-14	95.5			(4.5) Estane	
Octol	85.0			(15.0) TNT	
GD-7	86.0			(5.0) Cariflex1101	(9.0) BDNPA/F
GD-8	92.5			(7.5) Cariflex 1107	
GD-9	47.5		47.5	(2.4) Cariflex 1101	(2.4) BDNPA/F
GD-11	48		48	(4) Cariflex 1101	
GD-12	48		48	(4) Cariflex 1107	
GD-13	48		48	(2) Hytemp	(2) DOA
GD-14	48		48	(4) Estane	
No designation		92		(8) P(n-BA)g(PS) [d]	
No designation		92		(7.5) P(n-BA)g(PS)[d]	(0.5) DOA
No designation		92		(7.0) P(n-BA)g(PS)[d]	(1.0) DOA

[a] original PBXW-9 formulation contained: 92%HMX, 1.9% Hycar; 5.7% DOA; 0.4% lecethin; and 0.05% carbon black. Bimodal HMX Class1/Class 5 ratio 55.2/36.8

[b] also containing 2% carbon black

[c] plasticiser not disclosed

[d] graft copolymers of poly(n-butyl acrylate) and polystyrene

Some of the important formulations shown in Table 3 are discussed in the following.

PBXN-9

This pressed formulation contained 92% HMX, 6% Hytemp binder and 2% DOA plasticiser. It had been used as replacement for PBXN-106 as main charge filling for the US Navy 5"/54 caliber gun Mk 64 projectile. Note that PBXN-106 is a cast cured formulation containing 75% RDX, 18.5% BDNPA/F plasticiser, and 6.5% PEG binder.

However the rising cost of HMX used in PBXN-9 created a funding problem which prompted the US Navy to look for alternative filling options. Furthermore, while PBXN-9 showed acceptable vulnerability characteristics, its output did not meet the requirements for

shaped charge and metal accelerating applications [ref 10]. This led to the development of PBXW-17 and PBXW-11. See below.

PBXW-17

This is the RDX analogue of the PBXN-9 formulation that contains HMX. With the successful development of PBXW-17, its cost was estimated to be about one-fifth the cost of PBXN-9 and about half that of PBXN-106 [ref 9].

PBXW-17 was being under the scale-up program by the US Navy for the 5"/54 Mk 64 ammunition. It was also predicted to have applications for the Naval Surface Fire Support (NSFS) Extended Range Guided Munition (ERGM) 5"/62 gun ammunition [ref 9].

PBXW-11

The main objective for the development of PBXW-11 was to increase the performance of PBXN-9. In PBXW-11 the HMX content was increased to 96%, (compared to 92% HMX in PBXN-9), while maintaining the same ratio for the binder and plasticiser [ref 10].

PBXW-11 was found to have shock and bullet impact sensitivity, cook-off behaviour, detonation pressure, and armour penetration performance either meeting or exceeding the acceptance requirements for US Navy qualifications. It was qualified for US Navy use as a main charge explosive in October 1995 [ref 10]. The formulation was renamed PBXN-10. It was intended for use as fillings for the JSOW/BLU 108 and the XM-80 sub-munitions of ERGM for the NSFS Program [ref 11].

PBX-P31 and PBX-P11

PBX-P31 contains 96% HMX and 4% silicone binder. This pressed formulation was manufactured by a German company, TDW (Schrobenhausen). It was originally intended for use as warhead filling for the Advanced Short Range Air-to-Air Missile (ASRAAM) developed by the UK Ministry of Defence (MoD). The majority of IM tests on ASRAAM components, i.e. warhead and rocket motor sections, have been completed, and testings for system all-up-round qualifications were reported to be in progress [ref 12].

If it passes all system tests, ASRAAM would be the first UK weapon system to be successfully developed by the UK MoD with strong initiatives to comply with IM requirements. Note that Matra BritishAero Dynamics (MBD) was the prime contractor with TDW as sub-contractor for the energetic systems.

TDW also reported an RDX analogue version of PBX-P31, named PBX-P11, containing 96% RDX and 4% silicone binder [ref 13].

PAX-2A

PAX-2A, a pressable formulation, contains 85 % HMX, 6% CAB (cellulose acetate butyrate) and 9% BDNPA/F. It was developed for the US Army by ARDEC, with intended applications for use as shaped charge warhead fillings in the Hellfire anti-tank guided missiles.

PAX-2A can be pressed loaded into Hellfire warheads at a wide range of temperatures from ambient to 71°C [ref 14]. Furthermore, performance tests of the Hellfire II warheads assembled using a shrink fit loading technique of the PAX-2A billet into the warhead body showed improved penetration when fired at the low temperature of - 43°C (- 45°F) [ref 14].

HMX/NTO Containing Formulations

These formulations were developed under a Switzerland/Norway collaborative program, and could have potential for shaped charge warhead application [ref 4,7]. The series incorporated NTO as partial replacement for HMX, and several different binders (Cariflex, Hytemp, and Estane) and plasticisers (BDNPA/F and DOA). Their vulnerability characteristics and shaped charge warhead performance data have been reported [ref 7].

Formulations Containing Graft Copolymer Acrylate/Styrene Binders

The philosophy of using as binder the graft copolymer acrylate/styrene containing poly(n-butyl acrylate) backbone with polystyrene side chain was to combine the beneficial properties of polystyrene (e.g. Kraton binder) for desensitising impact stimuli and of polyacrylate binders (e.g. Hycar binder) for desensitising shock and thermal stimuli [ref 15].

Formulations containing 7% copolymer acrylate/styrene binder and 92% RDX (Bimodal Class 1/Class 5 ratio 3:1) with 1% DOA plasticiser were prepared [ref 15]. It is noted that this work appeared to be in the preliminary stage.

DXD-59

DXD-59 was a Korean formulation developed as an improved alternative to their DXD-57 for use in shaped charge warhead applications [ref 16]. Although similar in composition to the US Navy's PBXW-9, DXD-59 contained a different bimodal HMX (Class1/Class 5 ratio 3/1) and a different binder Hytemp-4404. Note that PBXW-9 contained 92% HMX (bimodal HMX Class1/Class 5 ratio 55.2/36.8), and 1.9% Hycar binder. These formulation differences were reported to lead to DXD-59 having a higher press density than PBXW-9 (by about 0.03 g/cm^3), which gave rise to a higher detonation velocity (8.63 km/s at 1.76 g/cm^3 compared to 8.49 km/s at 1.73 g/cm^3 for PBXW-9) and higher detonation pressure (33.4 GPa compared to 31.0 GPa for PBXW-9) [ref 16].

SMALL-SCALE SENSITIVITY DATA

In Table 4, available small-scale sensitivity data are summarised. The differing sensitivity tests used and lack of sufficient information reported limited a meaningful comparison.

Nevertheless, both PBXW-17 and PBXW-11 exhibited overall improved sensitivity characteristics over PBXN-9, and these characteristics are within the acceptable range of the US Navy qualifications.

EXPLOSIVE DETONATION DATA

The calculated detonation velocities and detonation pressures of some explosives are summarised in Table 5. PBXW-11 and LX-14 exhibited the best performance in terms of detonation properties, which were followed by PBX-P31 and DXD-59, and, in the order of decreasing performance, PBXW-17, DXD-57, Octol 85/15, and PBXW-9, DXD-53, PAX-2, and finally PBXN-106.

In another study, where HMX was partially replaced by NTO, calculated detonation velocities were reported [ref 4]. See Table 6.

Table 4. Small-scale sensitivity data of selected formulations.

	PBXW-17	PBXW-11	PBXN-9	DXD-59	LX-14	Octol (85/15)
Impact (cm)	38-43 [a]	25	34	[b]	26	25
ABL Friction (psig)	[c]	315	420	[d]	750	315
Electrostatic Discharge (J)	1.72 [e]	4.20	8.75	Not reported	12.5	0.25
Vacuum Thermal Stability (ml/g)	0.10	0.12	0.13	0.08	0.21	0.14
Large Scale Gap Test (cards)	205 (ρ = 1.69 g/cm^3)	205 (ρ = 1.80 g/cm^3)	201 (ρ = 1.73 g/cm^3)	139 (ρ = 1.76 g/cm^3)	199 (ρ =1.80 g/cm^3)	236 (ρ = 1.81 g/cm^3)

[a] reported against RDX standard = 17 cm; [ref 9].

[b] 23.3 J with reference to HMX = 6.5 J; [ref 16].

[c] reported as 120 N in BAM Friction test, against RDX standard of 84 N; [ref 9].

[d] 36.1 kgf by Julius Peter's BAM friction test, with reference to HMX = 10.6 kgf; [ref 16].

[e] ABL Electrostatic discharge; RDX standard 0.095 J; [ref 9].

Table 5. Detonation Properties of Selected Explosives

Formulation	Density (g/cm^3)	Detonation Velocity (km/s) (calc)	Detonation Pressure (GPa) (calc)
PBXN-9	1.73	8.43	31.0
PBXW-11	1.80	8.82	35.4
PBXW-17	1.72	8.50	31.2
PBX-P31	1.83	8.56	33.0
PBXW-9 Type II	1.76	8.49	29.6
PAX-2A	1.74	8.35	30.0
DXD-59	1.76	8.63	33.4
DXD-57	1.80	8.62	31.4
DXD-53	1.64	8.33	29.5
PBXN-106	1.66	7.97	26.3
Octol 85/15	1.86	8.34	31.5
LX-14	1.82	8.83	35.1

Partial replacement of HMX in GD-8 with NTO should have the effect of reducing the detonation velocity of GD-10. The effect of the energetic plasticiser BDNA/F should be to increase the detonation velocity of GD-9 over GD-11 and GD-12; the use of Hytemp/DOA in GD-13 and Estane in GD-14 is predicted to have a similar effect.

Table 6. Calculated Velocities of Detonation of some HMX/NTO Formulations [ref 4].

Formulation	Composition	Designation	Velocity of detonation (km/s) (calc)
HMX/Cariflex 1101/BDNPA/F	86/5/9	GD-7	8.320
HMX/Cariflex	92.5/7.5	GD-8	8.490
NTO/HMX/Cariflex1101/BDNPA/F	47.5/47.5/2.4/2.4	GD-9	8.280
NTO/HMX/Cariflex 1101	48.8/48.8/2.4	GD-10	8.352
NTO/HMX/Cariflex 1101	48/48/4	GD-11	8.187
NTO/HMX/Cariflex 1107	48/48/4	GD-12	8.174
NTO/HMX/Hytemp/DOA	48/48/2/2	GD-13	8.275
NTO/HMX/Estane	48/48/4	GD-14	8.268

SHAPED CHARGE WARHEAD PENETRATION DATA

The depth of shaped charge jet penetration into stacks of rolled homogeneous armour was used as a direct measurement of warhead explosive performance. Penetration tests were conducted using an 81 mm-diameter generic shaped charge test unit (GSCTU) containing a 42° copper cone liner [ref 17]. The GSCTU was placed at stand-off distances of two, five, seven and nine charge diameters (CD).

As shown in Table7, at stand-offs of two, five and seven CDs, the performance of PBX-P31 in armour penetration exceeded that of all other formulations tested including LX-14 and Octol 85/15. The performance of PBXW-11 was remarkably similar to that of LX-14 through out all the stand-off distances tested.

Table 7. Penetration Data for Selected Pressed Explosives as a Function of Stand-Off Charge Diameter (CD) Distance [ref 17].

Formulation	Average Penetration Depth (mm) at Various Stand-Off Distance (CD)			
	2CD	5CD	7CD	9CD
PBX-P31	496	620	612	559
PBXW-9 Type II	467	552	560	538
PBXW-11	475	550	593	567
PAX-2	470	575	551	556
Octol 85/15	477	583	525	628
LX-14	467	557	575	597

The order of decreasing armour penetration at 7 CD stand-off distance was as follows.

PBX-P31>PBXW-11>PBXW-9 Type II>PAX-2>LX-14>Octol 85/15.

In another investigation, the penetration depth into a steel target of some selected HMX/NTO explosives were measured by firing a 50 mm-diameter shaped charge with a 50° copper cone liner at stand-off distance of 5 CD. Penetration losses were measured against LX-14 as a reference [ref 7].

As shown in Table 8, replacing HMX with NTO or lowering the total filler content resulted in loss in penetration. The penetration loss for the HMX/NTO/Cariflex/Edward oil formulation was found to be 15.5%.

The same loss was found for the HMX/NTO/Hytemp/DOA. Estane as a binder among the three used in HMX/NTO formulations tested, gave rise to the minimum loss (10.5%) [ref 7]. It was also found that PBXN-9, containing 92% HMX, 6% Hytemp and 2% DOA inert plasticiser, exhibited only 5.5% penetration loss, but the formulation containing HMX/Cariflex (92.5%/7.2%) suffered 8% loss [ref 7]. RF 42, a formulation containing 95%HMX and Kraton a thermoplastic elastomeric binder, was reported to produce significant improvement (nearly 40%) over Octol 75/25 in shaped charge penetration depth at 14 CD [ref 2]. This formulation is noted to possess a pressed density of 1.81 g/cm^3 at 99.4% TMD.

VULNERABILITY DATA

Vulnerability tests for some HMX/NTO formulations have been conducted, using a monobloc steel tube (length 20 cm; inner diameter 4.70 cm; wall thickness 0.41 cm) screwed by end caps with a torque of 204 Nm [ref 9].

As shown in Table 8, the HMX/NTO/Cariflex/Edward oil formulation exhibited the best vulnerability properties, i.e. responses as burning reactions for all the tests conducted. All other formulations showed at least one response at a level more violent than a burning reaction. PBXN-9 responded as a partial detonation to the fragment impact test. The energetic plasticiser BDNPA/F compensated for the loss in energy when replacing HMX with NTO, but it gave rise to worse responses to slow cook-off and fragment impact tests; no further work was performed with the formulation containing this plasticiser [ref 7]. Pressing at elevated temperatures resulted in surface inhomogeneities, and the charges containing the Hytemp binder/DOA was found to be very brittle, whereas the Cariflex binder system was temperature sensitive [ref 7].

Table 8. Vulnerability Behaviour and Warhead Penetration Performance Loss Measured at 5 Charge Diameter (CD) Stand-Off Distance [ref 7]

Composition	Designation	Slow Cook-off	Fast Cook-off	Bullet Impact	Fragment Impact	Penetration Loss in (%) at 5 CD [a]
HMX/NTO/ Hytemp/DOA	GD-13	Burn	Burn	No reaction	Partial detonation	15.5
HMX/NTO/ Cariflex/Edward Oil	not designated	Burn	Burn	Burn	No reaction	15.5
HMX/NTO/ Estane	GD-14	Deflagration	Burn	Deflagration	Deflagration	10.5
HMX/Cariflex	GD-8	Burn	Deflagration	Explosion	Detonation	8.0
HMX/Hytemp/DOA	PBXN-9	Burn	Burn	Burn	Partial detonation	5.5

[a] Compared with LX-14 as reference

In a separate study, the vulnerability characteristics of PBX-P31, PBXW-11, PAX-2, PBXW-9 Type II, and PBXN-9 were determined [ref 17]. See Table 9. The slow cook-off, fast cook-off, and bullet impact tests were conducted using the GSCTU described earlier [ref 17].

Only PBXN-9, PBXW-11, and PBXW-9 Type II passed the slow cook-off test. With the exception of the melt cast Octol 85/15, which reacted violently (partial detonation), the remainder of the formulations tested passed the fast cook-off tests. Only PBXN-9 and PBXW-9 Type II passed the bullet impact tests. LX-14,

PBXW-11, PAX-2 and PBX-P31 all exhibited impact sensitivity by showing responses more violent than burning reactions.

Table 9. Vulnerability Behaviour of Some Recently Developed Explosives [ref 17].

Formulation	Slow Cook-off	Fast Cook-Off	Bullet Impact
PBXN-9	Burn (2x)	Burn (2x)	Burn (2x)
PBXW-11	Burn (2x)	Burn (2x)	Burn (1x) Deflagration (1x)
PAX-2	Explosion (2x)	Burn (2x)	Burn (1x) Deflagration (1x)
PBXW-9 Type (II)	Burn (2x)	Burn (2x)	Burn (2x)
PBX-P31	Partial detonation (2x)	Burn (2x)	Deflagration (2x)
Octol 85/15	Detonation (2x)	Burn (1x) Partial detonation (1x)	Deflagration (1x) Detonation (1x)
LX-14	Detonation (2x)	Burn (2x)	Deflagration (2x)

FRAGMENT IMPACT CRITICAL VELOCITY

Single fragment impact (SFI) tests were performed using some selected explosive formulations [ref 17]. The tests were conducted by firing a 1.4 cm-diameter cylindrical flat-nosed steel projectile at a 7.6 cm-diameter cylindrical explosive charge at normal impact. The critical velocity of impact was determined by varying the projectile velocity until a violent reaction was witnessed.

Table 10 shows the highest no-detonation and lowest detonation impact velocity data for some selected explosives, including LX-14 as a reference and PBXN-110, a cast cured formulation for comparison. [ref 17].

The pressed explosive least sensitive to fragment impact was found to be PBX-P31. Note that this formulation was pressed to a density in excess of 99% TMD. The order of increasing fragment impact sensitivity was as follows, with the cast cured PBXN-110 being the least sensitive.

$$\text{PBXN-110} < \text{PBX-P31} < \text{PAX-2} < \text{PBXW-9} < \text{PBXW-11} < \text{LX-14}$$

All the candidate pressed explosives were found to show improved vulnerability to fragment impact as compared to the base line explosive LX-14.

Table 10. Highest No-Detonation Velocity and Lowest Detonation Velocity for Selected Explosives [ref 17]

Formulation	Highest No-Detonation Impact Velocity (m/s)	Lowest Detonation Impact Velocity (m/s)
PBXW-9 Type II	933	947
PBXW-11	862	884
PBX-P31	969	1103
PAX-2	923	964
LX-14	813	847
Octol 85/15	1051	1082
PBXN-110	1359	1418

DISCUSSION

1. Binder Coating and Shock Sensitivity

There is experimental evidence that, in the PBXW-17 moulding powder, the RDX particles have no sharp corners, and the polyacrylic binder is homogeneous with a coating thickness of greater than 2 μm [ref 9]. It is reasonable to believe that other moulding powders are similar. During pressing, the polymer binder coating becomes a matrix that imparts mechanical strength to the powder. The polymer may function as a lubricant that reduces sensitivity to accidental initiation, presumably by dissipating and distributing the energy of an impact throughout a larger volume of the explosive. A plasticiser may help maintain the elasticity and deformability of the material after pressing and also enhances the ability of the binder to distribute input shocks and to absorb and conduct heat away rapidly from hot-spots.

Nevertheless, pressed formulations tend to be more shock sensitive than cast cured formulations. This can be attributable to several factors. First, pressed compositions normally contain higher levels of sensitive explosive solids such as HMX (typically more than 90%) than do cast compositions (typically less than 85%). Secondly, initiation occurs at hot-spots, locations of discontinuity, and one type of discontinuity is provided by voidage. Cast compositions are virtually void-free, and are close to 100% theoretical maximum density (TMD), but this is much harder to achieve with pressed compositions. It is noted that the explosive least sensitive to initiation by fragments was PBX-P31, for which a density exceeding 99% TMD was achieved [ref 17].

Hot spot sites are also created by discontinuities of the explosive solid. The effect of surface discontinuities can be mitigated by efficient coating by the binder/desensitiser, but internal crystal imperfections such as voids, cracks or twinning are not affected. Thus formulations prepared from large particle sizes may be more sensitive than those using finer material. However fine materials with small particle sizes have much larger surface area and require higher concentrations of binder to achieve desensitisation and to give manageable moulding powders. A compromise is reached by the use of bimodal and trimodal particle size distributions. An additional benefit is that the finer particles tend to fill the voids between the larger crystals, enabling a decrease in voidage, an increase in density and an increase in explosive performance.

An alternative approach to reducing sensitivity to thermal and shock stimuli is the use of binders which decompose endothermically, thus absorbing the energy of the stimulus. Performance of pressed explosives has

been improved by the use of energetic plasticisers such as BDNPA/F, and presumably could be further enhanced by energetic binders.

2. Improved Performance of Shaped Charge Warheads

In general, pressed explosives can give rise to improvement in shaped charge penetration but the advantages achievable depend on a number of factors such as solid loadings, pressing method, loading assembly technique to warhead body, choice of optimum stand-off distance, and choice of base line reference (i.e. LX-14 or a specified Octol formulation).

Improvement in penetration of shaped charge warhead at 7 CD have been discussed [ref 17], and more significant enhancement at longer stand-offs (nearly 40% at 14 CD) has been reported [ref 2]. This was attributed to the homogeneity of the pressed fillings, or at least the symmetrical density distribution about the shaped charge axis, which leads to lower lateral jet drift velocities than for shaped charges containing melt cast fillings [ref 2].

By optimising pressing conditions to increase the pressed charge density closer to the TMD, improved detonation properties can be obtained. However, as has been noted earlier, higher density charges may not always give rise to formulations with significantly higher detonation pressures [ref 2].

3. Direct Pressed Loading of Shaped Charge Warheads

Another area of shaped charge warhead penetration improvement resulted from the direct pressed loading of the charges into warheads at low temperatures. This was demonstrated by the shrink fit assembly loading of PAX-2A into the Hellfire shaped charge warhead [ref 14].

The fit between the explosive billet and warhead body can have a significant effect on shaped charge warhead penetration. The explosive performance was shown to increase through elimination or reduction of gaps at the explosive billet and warhead body interface. It is thought these gaps introduce asymmetry into detonation mechanics especially at low temperatures, thus causing loss in penetration performance [ref 14].

CONCLUSION

An overview of current developments in pressed PBX formulations has been provided in this Review. Small-scale sensitivity data, explosive detonation properties, shaped charge warhead penetration depths, and vulnerability characteristics, were compiled and analysed, and a number of important observations highlighted.

Pressed explosive formulations are in general more shock sensitive than cast cured and melt cast formulations, but this problem may be circumvented by several options: choice of appropriate binder and plasticiser, increasing the finer particle fraction, and increasing the pressed charge density. The choice of appropriate binder/plasticiser/particle size distributions can lead to improved vulnerability characteristics and performance of the solid charges.

References

1. DI(G)-LOG-07-10, Australian Department of Defence, Canberra, November 1993.
2. WEAG Technical Area 25, CTP 25.2 Working Group, and A.S. Cumming, "Collaboration on Pressable Explosives for Shaped Charges.- A European Success Story", *Propellants, Explosives, Pyrotechnics*, 24, 46-49 (1999); delivered at the 28th International Conference of ICT at Karlsruhe in 1997.
3. M. Lowell, "PBXW-9 Explosive Moulding Powder Scale-Up", Indian Head Technical Report, IHTR 1338, 29 March 1990.
4. O'Hammer Johansen, E. Skjold, K.K. Samuelsen, R. Gjersoe, J. Mathieu, B. Berger, P. Mader, and H.R. Bircher, "Formulations of NTO-Based Compositions", Proceedings of IM and EM Technology Symposium, NDIA, Tampa, Florida, 6-9 October 1997.
5. M.W. G. Burt, "The Effect of HMX Particle Size on the Hazard Properties of Pressed HE Charges", ADPA Symposium on "Compatibility and Processing of Plastic Materials", Missouri, 31 October 1983.
6. W.S. Wilson, "RDX/Polyethylene Wax Compositions as Pressed Explosives" Material Research Laboratory Report, MRL-R-722, Sept 1978.
7. H.R. Bircher, J. Mathieu, B. Berger, P. Mader, E. Skjold, K. K. Samuelsen, R. Gjersoe, and O. Hammer Johansen, "Vulnerability and Performance of NTO-Based High Explosives", Proceedings of IM and EM Technology Symposium, NDIA, Tampa, Florida, 6-9 October 1997.
8. Humphrey, J.R., "LX-14: A New High-Energy Plastic Bonded Explosive", Lawrence Livermore Laboratory, UCRL-52350, 21 Nov 1977.
9. K. Newman and S. Brown, "Development of PBXW-17: An RDX Filled Polyacrylic Elastomer", Proceedings of IM and EM Technology Symposium, NDIA, Tampa, Florida, 6-9 October 1997.
10. L.J. Montesi, and K.E. Alexander, "Development of the High Performance Metal Accelerating Explosive, PBXW-11", IM Technology Symposium, NIMIC Meeting #655, San Diego, 18-21 March 1996.
11. A.Duong, "IM Advanced Development - High Explosives Program: An Overview", IM and EM Technology Symposium, NDIA, Tampa, 6-9 October ,1997.
12. C.J. Brown, D.M. Francey, I.H. Maxey, D. Turner, A. Whitehouse, "Advanced Short Range Air-to-Air Weapon (ASRAAM)- Insensitive Munitions Aspects of Rocket and Warhead (The Development and Proving of an Insensitive Munition)", IM Technology Symposium, NIMIC Meeting #655, San Diego, California, 18-21 March 1996.
13. H. Rosner, "Test Results Achieved with LOVA Explosive Charges", IM Technology Symposium, NIMIC Meeting #655, San Diego, California, 18-21 March 1996.
14. D. Geiss, A. S. Daniels, S. M. Nicolich, and A.L. Larson, "Performance of IM Explosives in Advanced Shaped Charge Warhead", IM Technology Symposium, NIMIC Meeting #655, San Diego, California, 18-21 March 1996.
15. Y.G. Cheun, Y.H. Kwon, J.K. Kim, K.B. Lee, K.D. Lee, "A Study on Acrylate/Styrene Binders for Pressable Explosives", IM Technology Symposium, NIMIC Meeting #655, San Diego, California, 18-21 March 1996.
16. H.S. Kim, B.S. Park, "Development of the Insensitive Pressed Plastic Bonded Explosive DXD-59", Proceedings of IM and EM Technology Symposium, NDIA, Tampa, Florida, 6-9 Oct 1997.
17. S.L. Collignon, W.P. Burgess, W.H. Wilson, and K.D. Gibson, "Insensitive Munitions for the Development and Evaluation of Metal-Accelerating Explosives", Proceedings of Symposium on "IM Technology Advances to Reduce Sensitivity and Maintain Performance", ADPA and Joint Ordnance Commanders Group, Williamsburg, Virginia, 15-18 June 1992, pp.136-158.

HIGH-ELASTIC FIRECONDUCTIVE CORDS

Dmitry L. Rusin, Dmitry B. Mikhalev, Dmitry V. Vetrov

D.Mendeleyev University of Chemical Technology,
9, Miusskaya sq., 125047 Moscow, Russia

ABSTRACT

The composite polymeric materials based on copolymer of vinylidene fluoride with trifluorchloroethylene, filled by aluminium powder or by its alloys with a magnesium, as a fundamentals, for manufacturing by a method of through passage pressing of fireconductive cords with the improved physico-mechanical and ballistic parameters are considered.

The adequate mathematical models of a type «structure - property» for internal and external friction, physico-mechanical and ballistic parameters are obtained, the role of separate components in shaping of structural - mechanical also of ballistic properties of samples is revealed .

Developed fireconductive cords are characterized high strength properties - up to 25 MPa stretching durability and up to 350 % break deformation and possibility of variation of a transfer impulse rate at atmospheric pressure from 3 up to 3000 mm/s as at the expense of change of chemical structure of samples, and its form and geometrical sizes.

INTRODUCTION

Known fireconductive cords for actuating various pyrotechnic systems [1, 2], on the one hand have the restrictions on a impulse transfer rate (10-30 mm / c), and on the other hand - are not capable to ignition in any point on length, since have external cover; used for the same purposes stopin, representing a cotton filament, impregnated solution of an oxidizer, is astable in work and after several inflections on 90 degrees loses serviceability. Therefore development of the small-sized (diameter of 1-3 mm) elastic fireconductive cords on a polymeric basis without external cover which is capable to stable burning at pressure close to atmospheric, and to transmit thermal impulse in more broad of band rates, it is represented rather actual. Such cords should be produced by a high-productive method of through passage pressing. Therefore problem of their development includes optimization not only structural - mechanical also ballistic, rheological and technological characteristics.

EXPERIMENTAL SECTION

In the present paper are considered the fireconductive cords produced by a method of through passage pressing from a composite polymeric material based on copolymer of vinylidene fluoride with trifluorochlorethylene (SRF-32), filled by aluminium powder or by its alloys with a magnesium.

Is established, that structural - mechanical characteristics of the high filled compositions on the basis of various binding are essentially improved with modifying them with the help polytetrafluoroethylene (PTFE, f-4). This modifier, being entered in a composition in quantity 1-4 % instead of a part binding is raised by durability of samples to various deformation kinds (stretching (S_b, fig.1), cutting (fig.3) in 1.5 - 12 times, and simultaneously size of break deformation (E_b) in 1.5-9 times grows (fig.2).

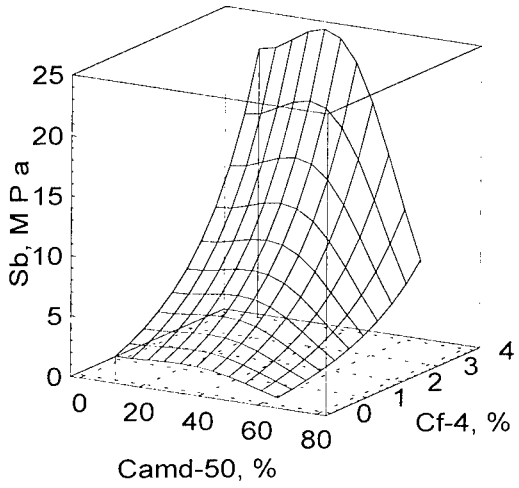

Figure 1 Influence of AMD-50 and f-4 concentration in compositions on the single-axis stretching durability (293K)

On figures 1, 2 there are shown the influence of quantity of the modifier and metal filler AMD-50 on the single-axis stretching durability (S_b) and size of break deformation (E_b) at the room temperature for compositions on a basis SRF-32.

The magnification of the metal filler (AMD-50) contents for account SRF-32 results in decrease of the cutting durability, if the filler contents exceeds 40 % mass.(fig.3).

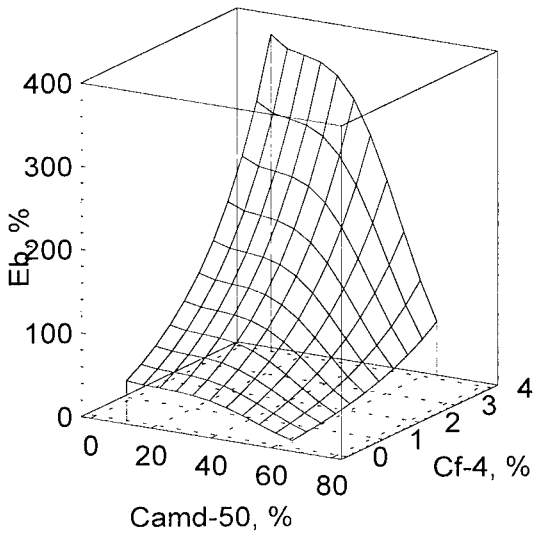

Figure 2 Influence of AMD-50 and f-4 concentration in compositions on the break deformation (293K)

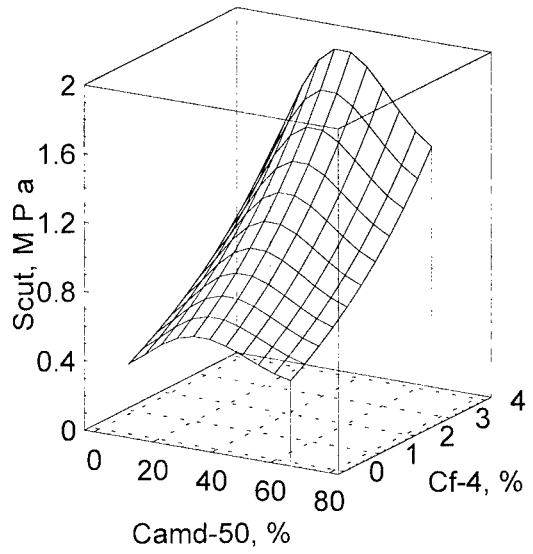

Figure 3 Influence of the AMD-50 and f-4 concentration in compositions on the cutting durability of composition containing 4% f-4 (343K)

The presence of the modifier in compositions provides simultaneously decrease of size of their external friction (T_m) up to ~2 times (fig.4) and improvement of technological characteristics of samples with their through passage pressing.

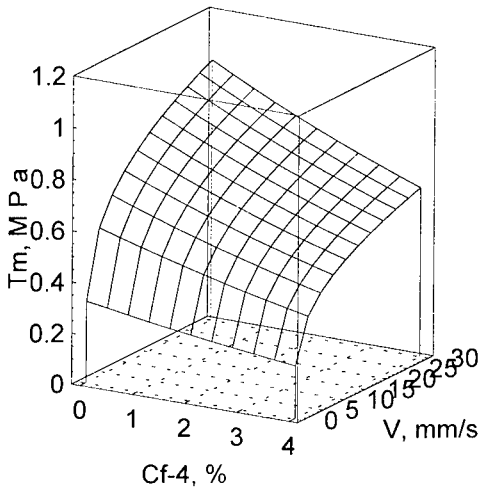

Figure 4 Dependence of the external friction of compositions on the f-4 concentration and the slide velocity (343K, 40%AMD-50)

It is known, that for deriving qualitative finished products for through passage pressing it is required that the internal friction exceeded external one at 2-10 times, a quantitative measure it is factor of adaptability to processing equal to the attitude cutting durability to a specific force of external friction : $K_t = S_{cut} / T_m$.

If thc $K_t = 1$, then equal probability of processes of a sliding and flow stipulates emerging spoilage which is known as "stick-slip" [3], the deriving of qualitative sumples for the case of $K_t < 1$ is possible only at very small velocities.

From fig.5 follows, that only use 2-4 % of the modifier f-4 ensures necessary characteristics of compositions containing 20-65 % metal filler. From the compositions which are not containing of the modifier is impossible to receive qualitative finished products by through passage pressing method at the high velocities of forming.

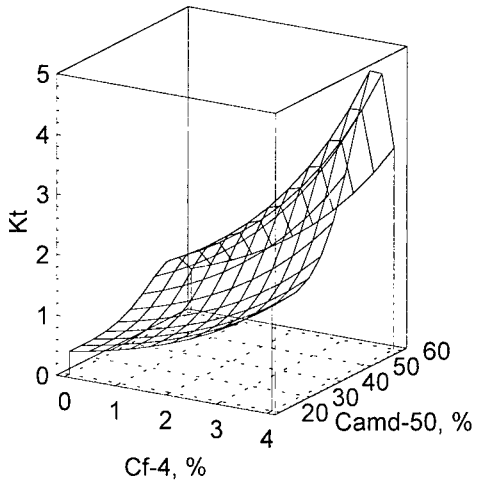

Figure 5 Influence of f-4 and AMD-50 percentage in compositions on the factor of adaptability to processing (343K, V=2 mm/s).

The similar action of the modifier is caused by that with thermomechanic influence on a composition at stages rolling and pressing in volume of a material the spatial structure f-4 - its initial particles by the size 100-300 microns will be formed 0.1-2 microns turn to the most thin mixed strings by a diameter. The mixture is fibrillated in situ into a lattice network of omni-directional fibers that reinforce the elastomeric binder, containing fillers. Intensity and duration of influence the structures, necessary for such change, are defined by a kind of binding and by the conditions of processing. For the majority of the investigated compositions containing up to 80 % fillers, the structure with optimum structural - mechanical parameters is formed with total deformation (product of shear speed on impact time) order 1000-2000.

At the processing of compositions not containing of the modifier or containing as the modifier polytrifluorochlorethylene (PTFCE), similar structural modifications does not happen and, as a concequence, such samples differ in the worse technological and physico-mechanical properties. For example, cutting durability at 353K for sumples, distinguished only by quality, (PTFE, PTFCE and without the modifier), are accordingly equal: 1.99 MPa, 0.79 MPa, 0.84 MPa.

It is established that the modification of a filler chemical nature, form and sizes of its particles with other things being equal, renders essential influence to physico-mechanical, technological and ballistic characteristics of compositions (tab. 1). For example, the replacement of

spherical particles of aluminium on a plate-like magnesium results in decreaseas of the deformation-structural properties in 3-3.5 times, and the burning rate of cords without cover- in 4.2 times.

Table1

Influence of metal filler quality and f-4 quantity on the properties of compositions

Peculiar properties of the metal filler	C_{f-4}, %	ε_b,%	σ_b, MPa	P^l, MPa	U_{cord}, mm/s	U_{tube}, mm/s
100% Al, (10-30 mkm), sphere	2	450	13.9	29.9	14.3	290
100% Mg (100-150 mkm), plate	2	130	4.9	39.9	3.3	-
mixture (50% Al + 50% Mg)	2	230	9.4	32.7	13.0	240
alloy (95% Al +3% Mg+2%Zn), 10-50 mkm, sphere	2	335	10.1	29.4	5.1	-
alloy (91% Al +5% Mg+3%Pb+1%Cu), 10-50 mkm, sphere	2	420	11.6	24.9	13.3	-
alloy (94% Al +5% Mg+1%Fe),100-150 mkm, sphere	2	280	7.0	28.3	4.5	-
alloy (92% Al +7% Mg+1%Fe), 100-150 mkm, sphere	2	240	7.0	27.7	2.8	-
MgB_{12} (10-50 mkm),plate	2	225	10.1	36.6	25.0	710
alloy(90% Al + 10% Mg), 30-100 mkm, sphere	2	340	10.8	29.9	8.5	-
alloy(50% Al + 50% Mg), 10-50 mkm, sphere	2	295	9.8	27.7	45.0	1900
alloy(50% Al + 50% Mg), 10-30 mkm, plate	0	270	3.2	19.4	29.0	900
alloy(50% Al + 50% Mg), 10-30 mkm, plate	1	287	7.9	21.1	39.0	1500
alloy(50% Al + 50% Mg), 10-30 mkm, plate	2	336	8.9	26.0	47.0	2000
alloy(50% Al + 50% Mg), 10-30 mkm, plate	3	310	14.6	37.7	50.1	2200
alloy(50% Al + 50% Mg), 10-30 mkm, plate	4	340	16.3	39.9	57.0	2750
alloy(50% Al + 50% Mg), 10-30 mkm, sphere	4	320	17.3	30.0	49.0	2200
alloy(50% Al + 50% Mg), 10-30 mkm, plate	5	360	16.8	53.2	61.7	3200

All samples contain 52 mass.% metal fillers

The properties of compositions containing particle of an alloy (50/50) aluminia with a magnesium of the spherical form (AMD-50) or as plates (PAM-4) differ from properties of a sample containing a mechanical mixture, similar on structure, of powders of aluminium and a magnesium, especially on value of a burning rate of a cord without cover (U_{cord}) and tube with the central aperture and longitudinal cut on whole length (U_{tube}). One from the reasons of difference U_{cord} and U_{tube} for compositions containing Al, Mg and Al_3Mg_4 can be difference of melting points of indicated individual metals and their alloy, that changes flammability of compositions also ability to distribution of burning on their surface. So according to [4] melting points of aluminium, magnesium and their alloy (50/50) are accordingly equal 933K, 924K, 736K.

The difference of values U_{cord} and U_{tube} for same compositions is stipulated, as shown in [5, 6], by increasing of pressure inside a tube with the central aperture and longitudinal cut and by its erosive burning, and U_{tube} is about proportional to value $U_{cord}^{1.6}$.

The modifier f-4 (tab.1) renders influence not only the structural - mechanical properties of compositions, but also influences its ballistic characteristics. The magnification of the contents of the modifier (C_{f-4}) up to 5 % instead of SRF-32 stipulates increase of a of burning rate of cords in 1.3-1.5 times.

The much greater influence to ballistic parameters renders C_{mg} - contents of a magnesium in compositions (fig. 6, 7), which settled up as a product of a filler share in samples on the contents of a magnesium in aluminium-magnesium alloys. Used powders of alloys containing 3-50 % of a magnesium with a size of particles 10-50 microns, and their mass share in compositions made 0.30-0.65.

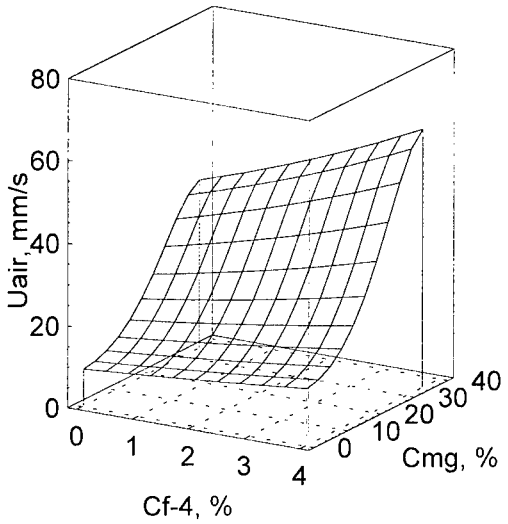

Figure 6 Dependence the transfer rate of thermal impulse in air medium on f-4 concentration and magnesium quantity in compositions (cords without cover)

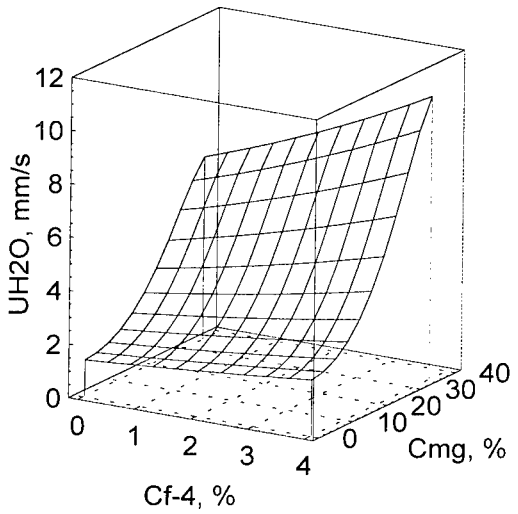

Figure 7 Dependence the transfer rate of thermal impulse in water medium on f-4 concentration and magnesium quantity in compositions (cords without cover)

The magnification in 5-7 times of a burning rate of compositions with increase C_{mg} from 0.2 up to 30 happened, despite of decrease (approximately on 400K) of its settlement burning temperature. Simultaneously according to thermodynamic accounts in burning products there is sharp (in 5.2 times) the vaporous magnesium content (up to 10 mole/kg) has increased, which interaction with oxygen of an air or water, can be the main reason of increasing of a burning rate of the coverfree cord. It is established that the burning rate of the coverfree cords by a diameter of 3 mm on an air (U_{air}) exceeds those similar covered cords (U_{cover}) at 6-11 times (fig.8), and for burning in water (U_{H2O}) - up to 1.7 times (fig.9).

The figures 1-9 represent graphic interpretation of analytical dependences of a type "structure - property", received as a result of statistical processing of experimental data.

The dependence of structural - mechanical and ballistic properties of compositions from the structure peculiarities is approximated as follows:

$$S_b = \exp (0.961 + 0.6088*C_{f-4} - 0.1507*\mathrm{Ln}(1+C_{amd}) + 0.00084*C_{amd}^2 - 0.00002*C_{amd}^3)$$

$$E_b = \exp (4.351 + 0.5189*C_{f-4} - 0.2249*\mathrm{Ln}(1+C_{amd}) + 0.00068*C_{amd}^2 - 0.000015*C_{amd}^3)$$

$$S_{cut} = \exp(-6.2186 + 1953.4/T + 0.2753*C_{f-4} + 0.1482*C_{amd} + 0.049*\mathrm{Ln}(1+P) + 0.00002*C_{amd}^3 - 0.0027*C_{amd}^2 - 0.7515*\mathrm{Ln}C_{amd})$$

$$T_m = \exp(-4.682 + 588.7/T + 0.2504*LnV + 3.5646*LnC_{amd} - 0.772*C_{amd} + 0.03*C_{amd}^2 - 0.0006*C_{amd}^3 + 0.000004*C_{amd}^4 - 0.1067*C_{f-4})$$

$$U_{cover} = 0.2946 + 0.4071*C_{f-4} + 0.1248*C_{mg}$$

$$U_{H2O} = \exp(0.2914 + 0.1098*C_{f-4} + 0.0034*C_{mg}^2 - 0.00006*C_{mg}^3)$$

$$U_{air} = \exp(2.1982 + 0.1077*C_{f-4} + 0.0035*C_{mg}^2 - 0.00007*C_{mg}^3)$$

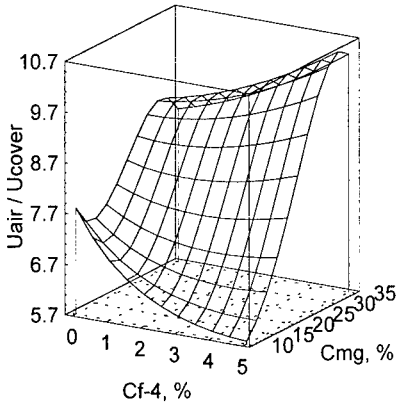

Figure 8 Comparison of burning rates coverfree cord and covered one in air medium for pyrotechnic compositions, distinguished by the contents of the modifier f-4 and a magnesium

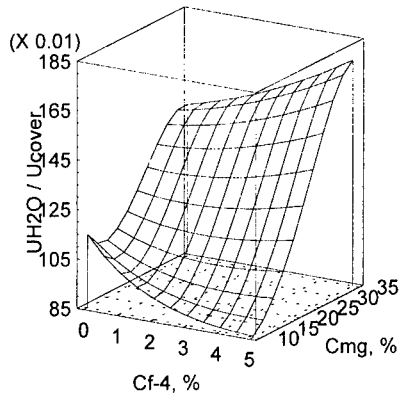

Figure 9 Comparison of burning rates coverfree cord in water medium and covered one on an air for pyrotechnic compositions, distinguished by the contents of the modifier f-4 and a magnesium

CONCLUSIONS

The complex structural - mechanical and ballistic characteristics of pyrotechnic compositions on the basis of SRF-32 filled by various metal powders is investigated. Is shown, that structural - mechanical characteristics of any compositions are essentially improved with modifying samples with the help 2-5 % polytetrafluoroethylene. Such compositions have high strength properties - up to 25 MPa stretching durability and up to 350 % break deformation

Is established, that the thermal impulse transfering rate of a fireconductive cords on a polymeric basis can be varied over a wide range (3-3000 mm/s) as at the expense of change of chemical structure of samples, and their form and geometrical sizes.

NOMENCLATURE

SRF-32	copolymer trifluorochlorethylene with vinylidenefluoride
PTFE, f-4	polytetrafluoroethylene
PTFCE	polytrifluorochlorethylene
S_{cut}	cutting durability
AMD	aluminium-magnesium alloy powder
T_m	external friction
S_b	single-axis stretching durability
E_b	break deformation
$C_{f\text{-}4}$	f-4 contents
C_{amd}	AMD contents
U_{cord}	burning rate of a coverfree cord without aperture
U_{tube}	pulse transfering rate of a cord-tube with longitudinal cut
U_{cover}	burning rate of a cover cord without aperture
P	pressure
P^1	pressure of forming
V	slide velocity

LIST OF REFERENCES

1. Gorst A.G. Gunpowders and explosives. M.: Mashinostroenie, 1972 , p.117.
2. USA Patient No. 2863353, 1958.
3. Tordella J.P., J.Appl.Polymer Sci.,v.7, 1963, p.215
4. Pokhil P.F., Belyaev A.F., Frolov Yu.V., Logachov V.S., Korotkov A.I. The burning of metal powders in active medium. M. Nauka, 1972, p.294
5. Rusin D.L., Kozhuch M.S., Mikhalev D.B., et al. Pyrotechnical cord and composition for its processing. Patient of Russian Federation No. RU 2026277 C1, 1995.
6. Rusin D.L, Mikhalev D.B., Vetrov D.V. Fireconductive cords on a polymeric basis. The Proceedings of EuroPyro-99, France, 1999

Development of Cure Cast High Loaded HMX IHE's

Daniel Cohen, Shlomo Mandelbaum, Evgeny Dreerman, Moshe Gil
Rafael, Manor - Propulsion & Explosive Division, P.O.B. 2250, Haifa, Israel, 31021

A new family of high loaded HMX cure cast explosive was developed. 88 – 91.5 wt.% load of HMX was introduced to a HTPB based explosive. This high solids content was achieved by introducing of new self developed wetting agents to the explosive and improving the mixing procedure.

The developed explosives have a low end-of-mix viscosity (0.7 to 6.5 kPs) and no residual shear stress. The mechanical properties are excellent: (σ_m = 5 – 7 kg/cm^2, ε_m = 10 – 45%, E_0 = 40 - 90 kg/cm^2).

The safety properties of the explosive were measured and they are very good: impact sensitivity more than 31 N*m, friction sensitivity 165 – 250 N, decomposition temperature 250 °C.

The detonation velocity was elevated from 8380 m/s for the 88% HMX composition to 8510 m/s for the 91% HMX composition.

The density of the explosive is almost equal to TMD: 1.68 g/cm^3 for the 88% HMX composition to 1.73 g/cm^3 for the 91% HMX composition.

THE INFLUENCE OF SIZE AND SHAPE OF THE EXPLOSIVE PARTICLES ON A CURE-CAST EXPLOSIVE PROPERTIES

Daniel Cohen, Shlomo Mandelbaum, Evgeny Dreerman, Moshe Gil
Rafael, Manor - Propulsion & Explosive Division, P.O.B. 2250, Haifa, Israel, 31021

Abstract

It is known for a long time that the size and the shape of the explosive's powder (HMX, RDX) introduced to an explosive have an effect on the rheological, mechanical and safety properties of cure-cast explosives based on HTPB binder.

This study had three goals: (1) development of explosives with high loading of only grounded particles (monomodal packaging) of the size 4 – 15 μ, (2) study of explosives with packaging of 70/30 and 34/66 coarse-to-fine particles at a total solids loading of 88 wt.%, and (3) study of the influence of the HMX particle's shape (60 μ size) at a total solids loading of 88%.

The main result is that developed explosives with small monomodal particle size are characterized by better impact and friction sensitivities. Moreover, the formulations with bimodal particle size distribution demonstrate improved safety characteristics when the greater part of filler's particles have small size.

Introduction

Development of Insensitive Munitions (IM) technology was a significant step in energetic materials area in the last decade. PBX's (plastic bonded explosives) can serve as a good example of energetic materials which combine relatively high performance with good safety characteristics. Typical cast-cure PBX formulation consists of explosive powder (e.g., nitramines RDX, HMX) incorporated in rubbery polymer matrix. As a rule, filler particles of different sizes used in these formulations to enable maximal solids content (bi- or trimodal packaging).

It is known that the size and the shape of the explosive powder have a strong effect on the rheological, mechanical and safety properties of an explosive. The main objective of this study was development of PBX formulations with improved safety properties (mainly, impact and friction sensitivities) and improved (or at least not significantly deteriorated) mechanical and rheological properties. The number of ways to achieve such formulations were examined:

(a) development of explosives with high loading of only grounded filler particles (with median size of 5 – 15 μ) without coarse fraction (i.e., monomodal package);

(b) development of PBX formulations with inverse filler bimodal package of 34/66 coarse-to-fine particles at a 88 wt.% total solids loading;

(c) examination of effect of filler particle's shape (60 μ size) on explosive's characteristics. At this stage of the study HMX particles were treated by a special treatment (developed in Rafael) to round particles and reduce the internal defect content.

Experimental

Formulations

All PBX formulations prepared in this study were compared with two reference explosives developed in Rafael: PX-80 (based on HMX filler) and PX-599 (with RDX filler). These reference formulations shown in Table 1.

Table 1. Composition of Reference Formulations (weight %)

Ingredient	PX-80 (88% solids)	PX-599 (85% solids)
coarse HMX (300 μ)	61.6	-
super fine HMX (5 μ)	26.4	-
coarse RDX (150 μ)	-	59.5
super fine RDX (5 μ)	-	25.5
HTPB	6.14	7.78
IPDI	0.65	0.79
Inert Plasticizer	4.80	6.00
Antioxidant	0.06	0.08
Wetting agent	0.24	0.24
Bonding agent	0.10	0.10
Curing catalyst	0.015	0.015

The composition of examined PBX formulations chosen for this study, shown in Table 2.

Table 2. Composition of Examined Formulations (weight %)

Ingredient	PX-G-730 PX-G-748-1	PX-G-733	PX-G-738 PX-D-763	PX-G-748-2	PX-G-751	PX-G-752	PX-G-753	PX-G-755 PX-G-757
coarse HMX (300 μ)	-	-	29.92	-	-	-	-	-
HMX (60 μ)	-	-	-	-	61.6	61.6	61.6 (rounded)	-
HMX (15 μ, wide span)	-	-	-	-	-	-	-	88.0
super fine HMX (5 μ)	-	86.0	58.08	-	26.4	26.4	26.4	-
super fine RDX (5 μ)	85.0	-	-	86.6	-	-	-	-
HTPB	7.87	7.29	6.21	6.97	6.21	6.21	6.21	6.17
IPDI	0.74	0.67	0.58	0.63	0.58	0.58	0.58	0.62
Inert Plasticizer	6.00	5.60	4.80	5.36	4.80	4.80	4.80	4.80
Antioxidant	0.08	0.07	0.06	0.07	0.06	0.06	0.06	0.06
Wetting agent A	0.22	0.28	0.24	0.27	0.24	-	-	-
Wetting agent B	-	-	-	-	-	0.24	0.24	0.24
Bonding agent	0.07	0.09	0.10	0.09	0.10	0.10	0.10	0.10
Curing catalyst	0.02	-	0.015	0.01	0.015	0.015	0.015	0.005

Preparation of PBX formulations

In general, preparation processes of cast-cure explosives are well known and proven in the industry of explosives. Mixing of the components was performed in 1 gallon Baker-Perkins planetary mixer. Uncured explosives were cast under vacuum into moulds to produce explosive blocks of any desired shape. Curing of the explosive was at 65 °C in a designated explosive oven.

Characterization of Compositions

Rheological characteristics. The viscosity and residual shear stress of the uncured explosive were measured by a Brookfield viscometer, HAT model, with T-C spindle, at rotation speed of 2.5 RPM. The measurement took place at constant temperature bath at 65 °C. The measured viscosity values are end-of-mix viscosity (η_0) and initial viscosity one hour after introduction of curing agent (η_1). Pot life was determined according the time in which the viscosity reaches 15 kPs.

Mechanical properties were measured by Instron testing machine at uniaxial tensile mode according to JANNAF standard. The PBX specimens tested at ambient temperature, at the tensile rate of 5 cm/min. The measured parameters are initial elasticity modulus, maximal engineering and real stresses and strain at maximal stress.

Impact sensitivity tests were performed according to the BAM (*Bundsanstalt fur Material Prefung*) procedure by "Julius Peters" falling hammer device. The tests were performed according to Bruceton method. 25 tests were conducted to evaluate the height of 50% probability for explosive reaction.

Friction sensitivity tests were performed according to the BAM procedure by "Julius Peters" friction apparatus. The reported value of load refers to the largest load on the pistil in which the material does not react for 10 successive tests (10 N.F.).

Decomposition (ignition) temperature tests were performed by a TGA (Thermogravimetric Analyzer). The used TGA machine is Mettler, model TA3000. The tests were performed under air flowing at a rate of 200 ml/min and a heating rate was 10 °C/min.

Results and Discussion

Formulations with monomodal filler package

At this stage of the study formulations with only grounded fine filler particles were developed. These formulations include 85% (PX-G-730, 748-1) and 86.6% (PX-G-748-2) RDX filled explosives and 86% HMX filled PBX (PX-G-733). The mean particle's size of nitramine fraction was 5 μ. Likewise, formulations with 88% HMX (15μ) (PX-G-755, 757) in wide monomodal particle size distribution were prepared and characterized. All formulations make use of fine HMX/RDX grounded by fluid energy mill.

The values of end-of-mix viscosity of the above formulations are compared in Figure 1.

Figure 1. Comparison of End-of-Mix Viscosities of Monomodal Formulations

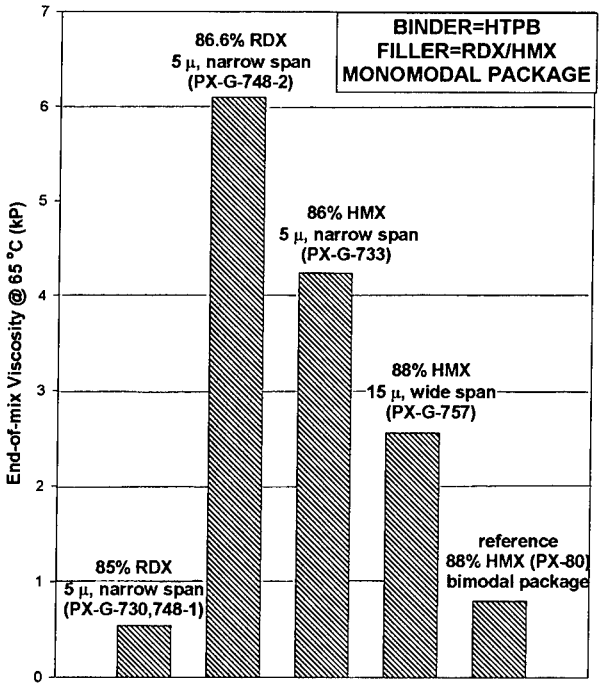

Generally speaking, all formulations showed good or sufficient end-of-mix viscosities and were easily mixed and readily cast into molds. As it was expected, widening of particle size distribution enabled to increase total solids loading and to decrease end-of-mix viscosity.

Table 3 represents main safety characteristics of the monomodal explosives.

Table 3. Safety Characteristics of Monomodal Formulations

Characteristic	88% HMX		85% RDX	
	PX-G-755 (monomodal)	PX-80 (bimodal)	PX-G-730 (monomodal)	PX-599 (bimodal)
Impact Sensitivity (kg*cm)	**421**	**300**	**265.4**	**85.7**
Friction Sensitivity (kg)	**28.8**	**21.6**	**28.8**	**25.2**
Decomposition Temperature (°C)	**244.3**	**247**	**214.2**	**215**

There is a significant improvement in impact sensitivity of PBX when all coarse particles replaced by fine ones. The improvement in friction sensitivity is more moderate. The obtained correlation is expected because it has been shown that the smaller the particle's size, the higher the crystal quality and the lower sensitivity of the explosive. There is no evidence that the decomposition temperature is affected by the nitramine particle's size.

The mechanical properties of the studied formulations in comparison with the references are shown in Table 4.

Table 4. Mechanical Properties of Monomodal Formulations

Characteristic	88% HMX		85% RDX	
	PX-G-757 (monomodal)	PX-80 (bimodal)	PX-G-730 (monomodal)	PX-599 (bimodal)
Maximal Real Stress, σ^R (kg/cm^2)	**15.0**	**8.6**	**14.7**	**7.7**
Maximal Real Strain, ε^R (%)	**31.7**	**25.0**	**38.9**	**31.0**
Initial Elasticity Modulus, E^0 (kg/cm^2)	**63**	**55**	**38.5**	**59**

The mechanical properties of developed "monomodal" formulations are much better than of appropriate reference compositions due to improved wetting of the filler particles by polymeric matrix.

Formulations with "inverse" filler package

At this part of the research the formulations with 34/66 coarse-to-fine packaging ratio were developed and characterized. Rheological, mechanical and safety properties were tested and compared to reference explosives with 70/30 ratio, as represented on Figure 2 and Tables 5-6.

Figure 2. Viscosity Test Results of "Inverse" Formulations in Comparison with PX-80

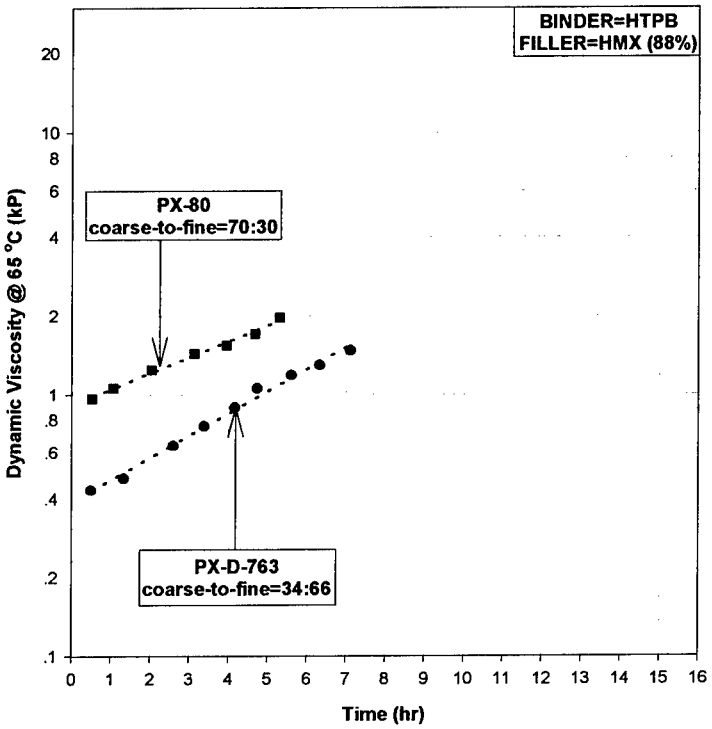

Table 5. Safety Characteristics of PBX with Inverse Particle Packaging

Characteristic	PX-G-738 (300μ:5μ=34:66)	PX-80 (300μ:5μ=70:30)
Impact Sensitivity (kg*cm)	**374.9**	**300**
Friction Sensitivity (kg)	**28.8**	**21.6**
Decomposition Temperature (°C)	**243.7**	**247**

Table 6. Mechanical Properties of PBX with Inverse Particle Packaging

Characteristic	PX-D-763 (300μ:5μ=34:66)	PX-80 (300μ:5μ=70:30)
Maximal Real Stress, σ^R (kg/cm^2)	**9.3**	**8.6**
Maximal Real Strain, ε^R (%)	**26.3**	**25.0**
Initial Elasticity Modulus, E_0 (kg/cm^2)	**45.2**	**55.0**

The formulations with inverse coarse-to-fine particle ratio are characterized by improved rheological characteristics, namely very low end-of-mix viscosity making possible increase of total solids loading.

The expected improvements in safety and mechanical characteristics are more moderate than in monomodal compositions with only fine nitramine particles.

Influence of particle's shape on explosive properties

It is known that one of the most important factors affecting PBX sensitivity is the internal quality of the nitramine crystals. The special technique rounding filler's particles was developed at Rafael. The effect of this treatment on explosive's characteristics was studied.

Figure 3 represents SEM micrographs of HMX particles (mean size of 60μ) after the treatment.

The HTPB/HMX formulations at 88% solids loading were prepared using treated HMX and compared with formulations based on untreated HMX.

Figure 4 represents the results of end-of-mix viscosities measurements of the formulations.

Figure 3. Treated HMX particles

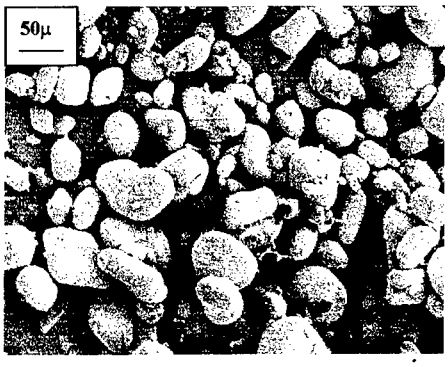

Figure 4. Comparison of End-of-Mix Viscosities of PBX Formulations with Treated and Treated HMX filler

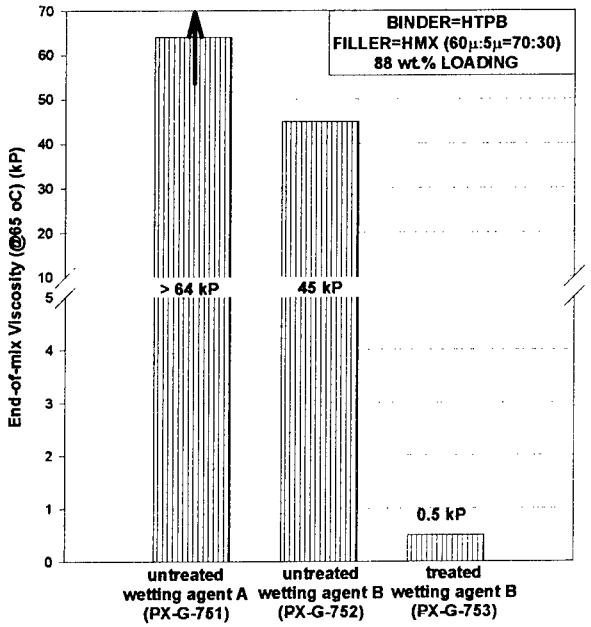

Dramatic drop in viscosity (from 45 to 0.5 kP) was observed. Practically, it was impossible to cast the explosive slurry with untreated HMX, while the formulation with treated explosive powder was easily mixed and cast.

Safety characteristics of the prepared PBX represented in Table 7.

Table 7. Safety Characteristics of PBX with Rounded HMX Particles in Comparison with Untreated HMX

Characteristic	PX-G-752 (untreated HMX)	PX-G-753 (rounded HMX)
Impact Sensitivity (kg*cm)	**>500 (10 NF)**	**>500 (10 NF)**
Friction Sensitivity (kg)	**25.2**	**19.2**
Decomposition Temperature (°C)	**240**	**246**

Unfortunately, it is impossible to reach a conclusion about influence of HMX particles shape on impact sensitivity since in both cases there was no observed any reaction. It is seen that there is slight increase in friction sensitivity as a result of the treatment.

Conclusions

PBX formulations based on HTPB/HMX or HTPB/RDX with only fine or 34/66 coarse-to-fine particles at total solids loading of 85-88% were developed and characterized. The significant improvement in impact and friction sensitivities was observed. The mechanical properties of the formulations were much better than "classical" bimodal formulations. The end-of-mix viscosities were good.

Special HMX particles treatment caused dramatic drop in slurry viscosity and in this way significantly improved explosive's processability. There was no observed clear evidence of effect of this treatment on mechanical or safety properties.

Acknowledgements

This study was performed at Solid Propulsion Department, Propulsion & Explosive Division of Rafael. The authors wish to thank MoD (Maf'at) for financial support of this study. The authors are greatly thankful to Mrs. Tamar Kaoli and Mrs. Orly Dekel from Explosive's Research Department, Rafael for development and carrying out of HMX particles rounding.

Screening units for particle formations of explosives using supercritical fluids

E. Marioth, S. Löbbecke, H. Krause

Fraunhofer Institut für Chemische Technologie, P.O. Box 1240, D-76318 Pfinztal

Abstract

Particles of explosives need to have a defined particle size and a narrow particle size distribution. One promising and nowadays applied technique to produce such defined particles uses a supercritical fluid as the main process fluid during the crystallisation. The objective of this work are screening units which allow to determine suitable process parameters (pressure, temperature and sc-fluid) for the particle formation of explosives. First results were achieved with the Rapid Expansion of Supercritical Solutions (RESS) of CL 20 using CHF_3 as the sc-fluid. The used set up is a small scale RESS unit basing on a supercritical fluid chromatograph.

Introduction

During the last decade, particle formation processes using supercritical fluids (scf) became more and more subject of interest. The most common techniques are the RESS process (Rapid Expansion of Supercritical Solution) and the PCA process (Precipitation with a Compressed Antisolvent). The most obvious advantages of these techniques bases on the achievable small particle sizes and the narrow particle size distributions. Other interesting properties of the particles formed by supercritical fluid processes are based on the small amounts or the completely absence (if using the RESS technique) of organic solvents in the particles. As important parameters of the scf processes temperature, pressure, co- or antisolvent and the supercritical fluid itself can be changed and in consequence may have influence on the particle size, particle size distribution, morphology, etc..

Processes applying sc-fluids under high pressure and increased temperature are cost intensive and have to deal with high safety standards, especially if they are applied to explosives. To reduce the costs for experiments and keep the risks as small as possible, small bench scale screening units for these techniques are introduced which need very small amounts of explosive material for every run.

The screening strategy is divided into two steps depending on the amount of material available:

1. < 100 mg: RESS
2. <1 g RESS and PCA

The first screening unit is already set up and subject of this paper. To determine the particle size and shape the crystallised particles were collected on an adhesive tape and prepared for SEM or optical microscopy. The second screening step will be set up this year and will produce sample amounts which allow a characterisation of the particles by REM/optical microscopy, particle size and particle size distribution, IR spectroscopy, XRD, DSC, etc.. The second screening step will start running at the end of 2000.

Set up

The smallest screening unit was set up on the basis of a supercritical fluid chromatograph from Dionex. For crystallisation purposes, several changes have been made concerning the fluidics, particle collection device and the expansion nozzle. For the first experiments capillary nozzles (a glass capillary with an internal diameter of 15 µm and different lengths) were applied.
During the process the sc-fluid is pressurized by a syringe pump, passes a heatable extraction cell containing the explosives and expands as a free jet.

Results and Discussion

First experiments were carried out with ε-CL 20. The most used sc-fluid for industrial applications is CO_2. To have a more polar fluid enabling a more efficient extraction of CL 20 supercritical CHF_3 was used. The critical data of CHF_3 (T_c=26.2 °C, P_c=4.86 MPa) are similar to those of CO_2.
For this first experiments an oven temperature of 100°C, an extraction cell temperature of 80°C and a process pressure of 15 MPa were used. The length of the glass capillary nozzle was fixed at 2 cm. The received particles were analysed by SEM (figure 1).

Figure 1: SEM picture of CL20 processed by the RESS technique

The sizes of the particles are between 1 µm and 10 µm. A more detailed view on the particles (figure 2) shows that bigger particles seem to be agglomerates of smaller ones. This effect may happen if the particle formation takes place while passing the capillary nozzle. For more detailed information the second screening step must be set up. The second screening step allows to change the nozzle diameter in order to vary the retention time in the nozzle.

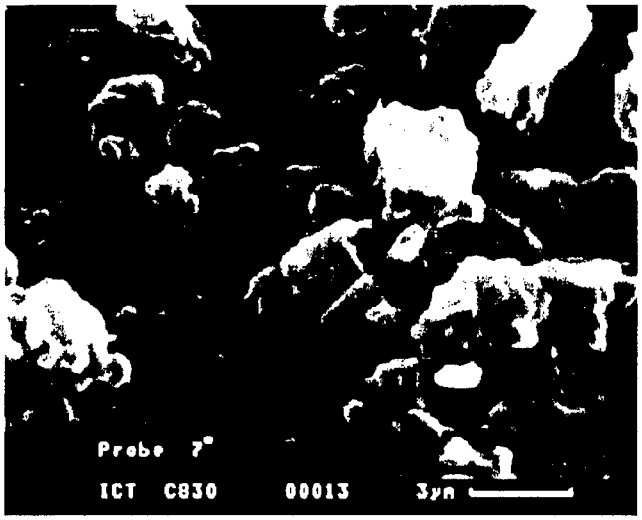

Figure 2: Detailed picture of CL20 after RESS processing

Conclusion and Outlook

First studies have shown that particles of CL 20 can be formed by the RESS technique using CHF_3 as the supercritical fluid. The set up of the second step will be helpful to investigate if the particle size is influenced by pressure or temperature and if the morphology of the formed particles depends on the polarity of the solvent. If further investigation of CL 20 will show that the polarity of the used sc-fluid influences significantly the morphology and crystallinity of the particles, mixtures of CHF_3 and CO_2 will be investigated.

COATING OF PARTICULATE ENERGETIC MATERIALS
BESCHICHTUNG VON PARTIKULÄREN ENERGETISCHEN MATERIALIEN

T. Heintz, U. Teipel

Fraunhofer-Institut für Chemische Technologie (ICT)
Joseph-von-Fraunhofer-Str. 7, 76327 Pfinztal
Germany

Abstract

The microencapsulation of particulate energetic materials aims in the improvement of the product quality regarding to processing, stability and compatibility. Adjusted to the properties of the core (energetic) materials, several coating materials and suitable solvents are investigated. In this paper only chemical and physico-chemical microencapsulation processes, which are working in liquid phase, are considered. So far, ammonium dinitramide (ADN), CL 20, HMX and RDX have turned out to be appropriate core materials for microencapsulation.

1 Zusammenfassung

Die Mikroverkapselung von partikelförmigen Treib- und Explosivstoffen dient der Produktverbesserung hinsichtlich der Weiterverarbeitung, der Stabilität und der Kompatibilität. Angepaßt an die Eigenschaften der zu beschichtenden, energetischen Materialien wurden verschiedene Stoffsysteme eingesetzt. In dieser Arbeit werden die chemische Mikroverkapselungsverfahren vorgestellt, bei welchen die Abscheidung des Wandmaterials auf dem Kernmaterial in einer flüssigen Phase erfolgt. Es haben sich bislang folgende Stoffpaarungen, bestehen aus Kernmaterial und Wandmaterial, als geeignet erwiesen:

- Ammoniumdinitramid (ADN) beschichtet mit Ethylcellulose
- Ammoniumdinitramid (ADN) beschichtet mit Celluloseestern
- CL 20 beschichtet mit Celluloseestern
- HMX beschichtet mit Aminoharz

2 Einleitung

Die Technologie der Mikroverkapselung von partikulären Materialien wird häufig, z.B. bei pharmazeutischen und agrartechnischen Produkten, zum Zweck der kontrollierten Wirkstofffreigabe eingesetzt. Hierbei wird um die einzelnen Wirkstoffpartikel eine Schicht erzeugt, welche z.B. semipermeabel gestaltet sein kann, so daß der Wirkstoff in Abhängigkeit von der Zeit durch die Coatingschicht permeiert. Eine andere Möglichkeit der kontrollierten Freigabe besteht darin, Beschichtungen derart herzustellen, daß diese bei bestimmten Umgebungseinflüssen durchlässig werden, bzw. sich auflösen. Als Beispiel sei hier die magensaftresistente Beschichtung von Medikamenten genannt, deren Stabilität vom pH-Wert abhängt. Eine weitere technische Anwendung ist die Mikroverkapselung von Farb- oder Klebstoffen, wobei eine undurchlässige Beschichtung durch gezielte mechanischer Belastung zerstört wird und somit ihren Inhalt freigibt.

Bei der Beschichtung von Treib- oder Explosivstoffpartikeln stehen folgende Anforderungen im Vordergrund. Eine Steigerung der Produktqualität, der meist durch unterschiedliche Kristallisationsverfahren erzeugten Partikel, soll durch folgende Verbesserungen erreicht werden:

- Desensibilisierung, z.B. Verringerung der Reib- und Schlagempfindlichkeit
- Erhöhung der Kompatibilität mit polymeren Binderwerkstoffen
- Schutz vor Umwelteinflüßen, z.B. Feuchtigkeit, Strahlung

3 Grundlagen der Mikroverkapselung

Unter Mikrokapseln versteht man Partikel mit einem mittleren Durchmesser von 1 – 5000 µm, die aus einem Kern und einer festen Hülle bestehen [1]. Der Kern kann ein Gas, eine Flüssigkeit oder ein Feststoff sein. Die feste Hülle wird vor allem aus natürlichen oder synthetischen Polymeren aufgebaut.
Die äußere Form der Mikrokapseln ist vom Kernmaterial und der Abscheidungsart des Wandmaterials abhängig. Mikroverkapselte Flüssigkeiten behalten in der Regel ihre sphärische Form, während bei beschichteten Feststoffe, z.B. Kristallen, deren äußere Gestalt weitgehend erhalten bleibt, wenn die Wandstärke der Kapsel gering ist.

3.1 Verfahrensvarianten:

Es werden mechanisch-physikalische und chemische Verfahren der Mikroverkapselung unterschieden. Bei den mechanisch-physikalischen Verfahren werden Füssigkeits- oder Feststoffteilchen im Gasraum verkapselt [1]. Die chemischen Verfahren arbeiten in flüssiger (kontinuierlicher) Phase, also in Emulsionen oder Suspensionen. Die Verkapselung erfolgt hierbei durch Abscheidung des im Kontinuum gelösten Wandmaterials an der Grenzfläche zwischen Kernmaterial und kontinuierlicher Phase.
In Abbildung 1 sind verschiedene Verfahren bzw. Kapselbildungsmechanismen aufgeführt. Bei den Coatingverfahren in der Gasphase muß das zu beschichtende Partikelkollektiv fluidisiert werden, wobei das flüssige Beschichtungsmaterial (Schmelze oder Lösung) mittels Zerstäubung auf die bewegten Partikel aufgebracht wird. Zur Erzeugung und Erhaltung einer Wirbelschicht werden großen Gasvolumenströme benötigt, wobei je nach Auslegung der Abluftfilter Feinanteile des Partikelkollektivs in den Abluftstrom mitgerissen werden. Dies ist bei sicherheitstechnisch und ökologisch unproblematischen Stoffen unbedenklich, stellt aber, z.B. bei der Be-

schichtung von Explosivstoffpartikeln, erheblich höhere Anforderungen an die Staubabscheidungsvorrichtungen im Abgasstrom.

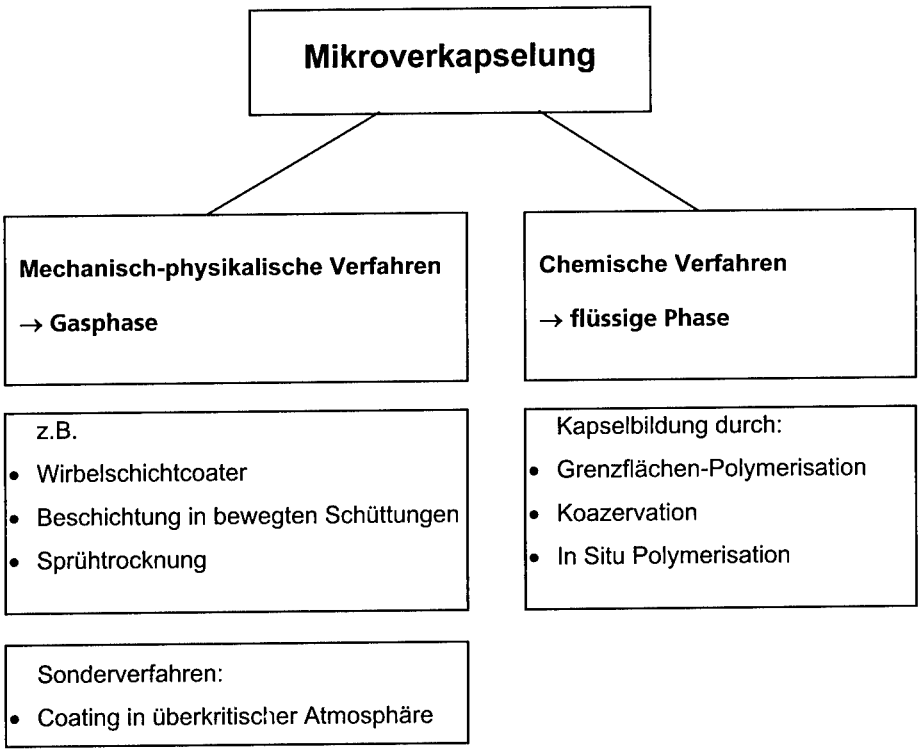

Abb. 1: Verfahrensvarianten der Mikroverkapselung

Betrachtet man den Aggregatzustand des Trägermediums als Unterscheidungsmerkmal zwischen chemischen und mechanisch-physikalischen Verfahren (Abb. 1), so stellt die Beschichtung von energetischen Materialien in einer Wirbelschicht unter Anwendung überkritischer Fluide, wie sie in [2] am Beispiel von verdichtetem CO_2 beschrieben wird, ein Sonderverfahren zur Erzeugung sehr dünner Schichten dar.

Im folgenden wird näher auf die chemischen Verfahren eingegangen, da sich diese zur Bearbeitung von energetischen Materialien im Batch-Betrieb sehr gut eignen. Je nach der Art des Abscheidungsmechanismus des Wandmaterials unterscheidet man folgende Verfahren [1]:

- Wandbildung durch Polykondensation oder –addition:

Die Grenzflächen-Polymerisation beinhaltet eine Reaktion von verschiedenen Monomeren an der Grenzschicht zwischen zwei nicht mischbaren flüssigen Phasen, wobei ein Polymerfilm entsteht [3]. Das Verfahren wird bei Emulsionen eingesetzt, wobei jeweils die kontinuierliche und die disperse Phase eine Monomerkomponente enthält, die beim Zusammentreffen an der Genzfläche polymerisieren und somit die disperse Phase einschließen.

- Verkapselung mittels In-Situ Polymerisation:

Der Prozeß der In-Situ Polymerisation unterscheidet sich von der Grenzflächen-Polykondensation darin, daß nur ein Monomer oder Vorkondensat in der dispersen oder der kontinuierlichen Phase vorliegt. Ausgelöst durch einen Katalysator bildet sich eine unlösliche Polymerschicht , die das Kernmaterial einschließt [3, 4].

- Koazervation, Phasenseparation [4]:

Während der Begriff Koazervation für die Phasentrennung in wäßrigem Medium gebraucht wird, versteht man üblicherweise unter Phasenseparation die Polymerentmischung (Koazervation) in nichtwäßrigen Medien [5]. Es können unterschiedliche Prinzipien zur Einleitung der Phasentrennung eingesetzt werden, wie die Wechselwirkung inkompatibler Stoffe, die Zugabe eines Nichtlösungsmittels oder das Aufprägen eines Temperaturgradienten [6]. Ein Koazervat kann als Zwischenprodukt bei der Überführung eines gelösten bzw. kolloidal verteilten Polymers in ein festen Präzipitat entstehen, wobei das Koazervat eine noch lösungsmittelhaltige Phase ist, in welcher sich die gelösten Moleküle, bzw. kolloiden Anteile anreichern und zu größeren Verbänden verknüpfen. Das Koazervat ist dann in der verbleibenden Restlösung (Gleichgewichtsphase), die wenig kolloide Anteile des Polymers enthält, nicht mehr lösbar.

Abbildung 2 zeigt die für ein Koazervationsverfahren typischen Schritte:

(a) Das Kernmaterial wird in einer Lösung des polymeren Beschichtungsmaterials dispergiert.

(b) Beginn der Koazervation durch Zugabe von Hilfsstoffen oder Änderung der Versuchsparameter.

(c) Allmähliche Abscheidung der Koazervattropfen an der Kernmaterialoberfläche.

(d) Koaleszenz der Koazervattropfen zu einer geschlossenen Mikrokapsel.

(e) Vernetzung und Trocknung der Koazervatschicht zu einer festen Kapsel.

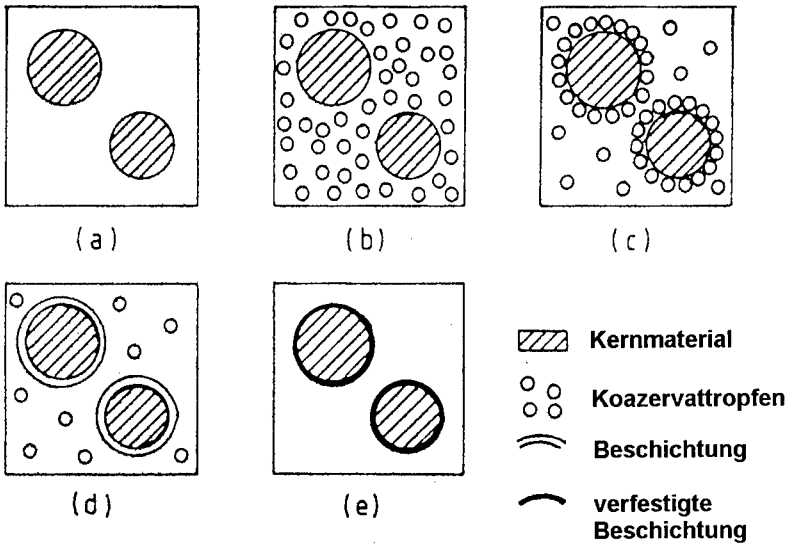

Abb. 2: Verfahrensschritte bei der Mikroverkapselung durch Koazervation [3]

4 Versuchsduchführung

Im Rahmen dieser Arbeit wurden Machbarkeitsuntersuchungen zur Mikroverkapselung von ADN, RDX, HMX und CL 20 in der flüssigen Phase durchgeführt. Bei den chemischen Verfahren ist vor allem die Auswahl geeigneter Stoffsysteme maßgeblich. Diese Stoffsysteme bestehen aus Kernmaterial, Wandmaterial, Träger-Flüssigkeit (Lösungsmittel für das Wandmaterial), evtl. Fällmittel für das Wandmaterial und Hilfsstoffen zum Erhalt der Partikelstuktur.

Die Mikroverkapselungsverfahren in der flüssigen Phase (chemischen Verfahren) haben den Vorteil, daß die Versuchsapparaturen im Vergleich zu den physikalischen Verfahren einfach aufgebaut sind, da die Partikel nicht in einem Gasstrom fluidisiert werden müssen, wie z.B. bei den Wirbelschichtverfahren.

Eine Versuchsanlage besteht aus folgenden Hauptkomponenten:

- temperierbares Doppelmantelgefäß
- Thermostat mit Regelung
- Rührer mit Drehzahlregelung
- Bürette zur exakt dosierbaren Zugabe von flüssigen Hilfsstoffen

Zunächst wird das zu beschichtende Kernmaterial in der Flüssigkeit, in welcher das Beschichtungsmaterial bereits gelöst sein kann, dispergiert. Danach wird unter ständigem Rühren die eigentliche Beschichtung mittels Abscheidung des gelösten (prä-)polymeren Materials auf dem Kernmaterial durchgeführt. Ausgelöst wird der Abscheidungsvorgang (z.B. Polykondensation oder Phasentrennung) des Wandmaterials durch die Zugabe von Hilfsstoffen und/oder einem bestimmten Temperaturverlauf. Die Rührerdrehzahl muß hierbei den Gegebenheiten angepaßt werden, da zu heftiges Rühren zu scherungsbedingten Verformungen der noch flüssigen Kapseln führt [5]. Wenn sich geschlossene Schichten mit ausreichender Festigkeit gebildet haben, kann die Trennung der Mikrokapseln von der Restlösung und die anschließende Trocknung erfolgen.
Die Temperaturregelung ist aus folgenden Gründen erforderlich:

- Am Anfang des Verfahrens ist eine konstante Temperatur, bei welcher das Beschichtungsmaterial vollständig gelöst wird, erforderlich.
- Durch die Abkühlung des Stoffsystems, bestehend aus Lösungsmittel, Beschichtungsmaterial und Kernmaterial, kann die Phasentrennung bei den Koazervationsverfahren, oder das Ausfällen von gelösten Polymeren gezielt ausgelöst werden.

5 Ergebnisse

5.1 Beschichtung von Ammoniumdinitramid (ADN)

Zur Mikroverkapselung von sphärischen Ammoniumdinitramid (ADN)-Partikeln eignet sich die Phasenseparation (Koazervation) durch Abkühlen einer Lösung von Ethylcellulose in Cyclohexan. Um die Agglomeration der Partikel während des Prozesses zu vermeiden, ist es erforderlich dem Lösungsmittel geeignete Schutzkolloide zuzusetzen. Hierzu kommen makromolekulare Verbindungen in Betracht, die in den zur Verkapselung notwendigen unpolaren Kohlenwasserstoffen löslich sind [6].
Abbildung 3 zeigt die unbeschichteten, sphärischen ADN-Partikel hergestellt mittels Emulsions-Kristallisation [7]. Das noch lösungsmittelhaltige Koazervat bildet auf der ADN Oberfläche eine geschlossene Schicht, wobei die Phasengrenze zur umgebenden Restlösung sichtbar ist (Abbildung 4). Nach dem Separieren und Trocknen der Partikel erhält man voneinander getrennte, rieselfähige und beschichtete ADN-Partikel (Abbildung 5).

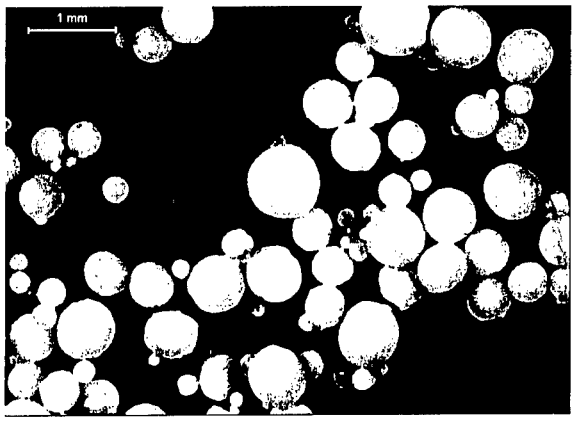

Abb. 3: Unbeschichtete ADN-Prills

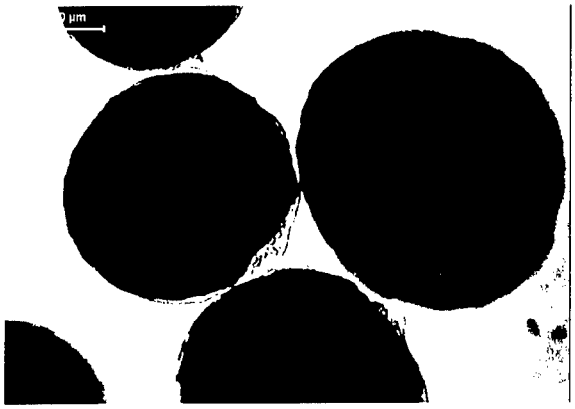

Abb. 4: ADN-Prills mit Koazervatschicht in Lösungsmittel

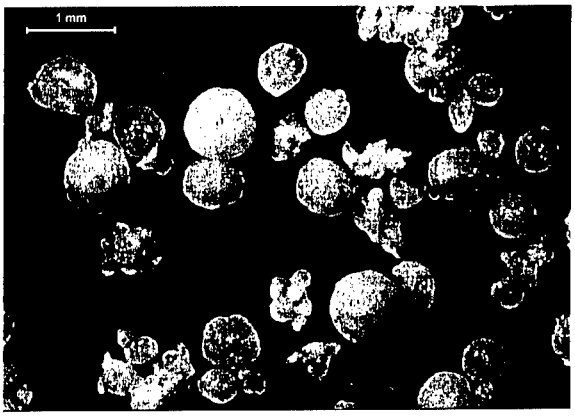

Abb. 5: Mikroverkapselte ADN-Prills

Zur Mikroverkapselung von ADN eignen sich neben hochverätherter Ethylcellulose mit einem Ethoxylgehalt von 48,0 – 49,5 % [8], welche zu den Celluloseäthern [9] gehört, auch noch bestimmte Celluloseester, die in Abhängigkeit von ihrem Veresterungsgrad verschiedene Lösungseigenschaften besitzen. Mit abnehmendem Gehalt an gebundener Essigsäure, bzw. abnehmendem Veresterungsgrad, steigt die Löslichkeit in polaren Lösungsmitteln an, während die Löslichkeit in unpolaren abnimmt [8]. Somit haben sich hochveresterte Celluloseester für die Mikroverkapselung ADN als geeignet erwiesen, da sie eine hinreichende Löslichkeit in unpolaren organischen Lösungsmitteln haben, in welchen ADN nahezu nicht löslich ist. Abbildung 6 zeigt die noch lösungsmittelhaltige Koazervatphase eines solchen Celluloseesters, die die kugelförmigen ADN-Partikel umhüllt.

Abb. 6: Sphärische ADN-Partikel mit einer Koazervatschicht in Lösungsmittel

5.2 Beschichtung von HMX und CL 20

Zur Mikroverkapselung von nicht-wasserlöslichen energetischen Materialien, wie HMX, RDX und CL 20, können wäßrige Lösungen als Trägerfluide für die Verfahren eingesetzt werden. Diese Verfahren haben den Vorteil, daß die Veränderung des pH-Wertes der wäßrigen Phase als wichtiger Parameter zur gezielten Beeinflussung des

Lösungs- und Abscheidungsverhaltens des Beschichtungsmaterials zur Verfügung steht. Nach [8, 10] gibt es bestimmte Celluloseester (Mischester), welche im Sauren unlöslich und im Alkalischen löslich sind. Diese Eigenschaft wurde zur Mikroverkapselung von CL 20 genutzt, wobei der gelöste Celluloseester durch Verringerung des pH-Wertes koazerviert wurde. Abbildung 7 zeigt die von einer celluloseesterhaltigen Koazervatschicht eingehüllten CL 20 Kristalle, welche sich noch im wäßrigen Medium befinden.

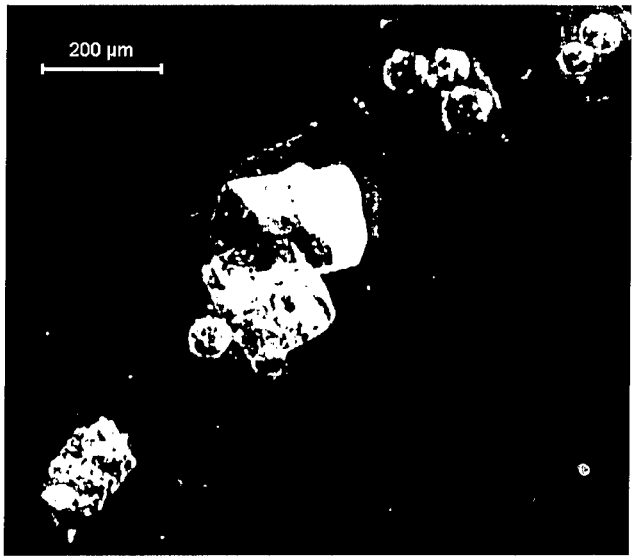

Abb. 7: Mikroverkapselte CL 20 Kristalle in wäßriger Phase

Die Mikroverkapselung von HMX mit Aminoharzen kann mittels In-Situ Polykondensation [3, 4] durchgeführt werden. Ein ähnliches Verfahren ist für die Mikroverkapselung von Wirkstoffen, zum Zweck der kontrollierten Freigabe, in der Patentschrift [11] beschrieben. Zur Beschichtung von HMX Kristallen werden diese in eine wäßrige Lösung eines Aminoharzpräkondensates unter Rühren eingetragen. Die Suspension wird anschließend mit einem sauren Katalysator auf einen pH-Wert im Bereich 5 bis 3,5 eingestellt und bei einer Temperatur im Bereich von 50 bis 70 °C gehalten, wobei das Präpolymer polykondensiert. Während der fortschreitenden Polykondensation bildet sich ein partikuläres, kolloidales Gel, das sich im Grenzbereich der HMX Partikel anreichert, dort koalesziert und zu einer Polymerwand vernetzt. In Abbildung 8 sind die beschichteten und getrockneten HMX Partikel dargestellt.

Abb. 8: Mikroverkapselte HMX Kristalle

6 Schlußfolgerung

Es stehen mehrere Stoffsysteme zur Verfügung, die sich zur Mikroverkapselung von partikelförmigen energetischen Materialien eignen. Zur Beurteilung der Qualität dieser Beschichtungen hinsichtlich der gewünschten Eigenschaften und zur Weiterentwicklung der Verfahren, ist eine ausführliche Charakterisierung notwendig. Hierbei ist unter anderem die Messung der Schichtdicke von großen Interesse, was meßtechnisch derzeit eine noch ungeklärte Aufgabe darstellt.

7 Literatur

[1] Ullmanns Encyklopädie der technischen Chemie, 4. Auflage, Band 16, Verlag Chemie, Weinheim, 1975

[2] Niehaus, M., Teipel, U., Krause, H.: Verfahren zum Mikroverkapseln von Partikeln, DE 197 11 393 (1), 1998

[3] Deasy, P. B.: Microencapsulation and Releated Drug Processes, Marcel Dekker Inc. New York and Basel, 1984

[4] Kondo, A.: Microcapsule Processing and Technology, Marcel Dekker Inc. New York and Basel, 1979

[5] Weiß, G.: Mikroverkapselung von Ibuprofen mit magensaftresitenten Polymeren durch einfache Koazervation, Dissertation, Universität Regensburg, 1991

[6] Merkle, H.P.: Zur Mikroverkapselung fester Arzneistoff mittels Koazervation, Dissertation EHT Zürich, 1972

[7] Teipel, U. , Heintz, T., Leisinger, K., Krause, H.: Verfahren zur Herstellung von Partikeln schmelzfähiger Treib- und Explosivstoffe, DE 198 16 853 A1, 1999

[8] Ullmanns Encyklopädie der technischen Chemie, 4. Auflage, Band 9, Verlag Chemie, Weinheim, 1975

[9] Morrison, R.T., Boyd, R. N.: Lehrbuch der Organischen Chemie, Verlag Chemie Weinheim, 1978

[10] Römpp Chemie Lexikon, 9. Auflage, Band 1, Georg Thieme Verlag, Stuttgart New York, 1989

[11] Nastke, R., Rafler, G.: Mikropartikel, enthaltend einen Wirkstoff und ein polymeres Kapselwandmaterial, ein Verfahren zu deren Herstellung und deren Verwendung, WO 97/27939, 1997

SCALE-UP OF CRYSTALLIZER FOR PRODUCING SPHERICAL CRYSTALS OF NTO

Kwang-Joo Kim[1], Kap-Mo Kim[1], Jung-Min Lee[1], Hyoun-Soo Kim[2], Bang-Sam Park[2] and Jun-Wung Lee[2]

1 Chemical Process & Engineering Center, Korea Research Institute of Chemical Technology, P.O.BOX 107, Yusung, Taejeon 305-600, Korea

2 Agency for Defense Development, P.O. BOX 35, Yusung, Teajeon 305-600, Korea

Abstract

Spherical crystallization for producing NTO crystals was carried out by cooling mode in two laboratory-scale and bench-scale crystallizers. The effect of scale-up of crystallizers on mean size of crystals of NTO at batch cooling crystallization was studied. Optimum conditions for crystallizing spherical NTO were set through the operations. Depending on the concentration, the temperature, and the additives as well as the operating conditions, crystallization led to spherical shape with acceptable hardness and narrow crystal size distribution. The morphology of the NTO crystals was strongly dependent on the composition of solvents and independent of production scale. Comparison of the crystals obtained from the laboratory-scale and from the bench-scale operations showed that the hydrodynamic condition in crystallizer affects crystal size distribution(CSD). Eventually, no scale-up effect on product crystal size distribution, average crystal size and shape was observed if composition of cosolvent was set optimally and scale-up of crystallizer was reasonable.

Introduction

The irregular and agglomerate explosives cause the mixing of the explosive formulations to be highly viscous and difficult to process and to pour. As a result, the amount of NTO which can be used in a processable explosive composition is limited, the performance of the explosive is reduced, and explosives eventually becomes very sensitive to unintentional shock. Formation of spherulite depends on solvent, crystallization methods and compositions. We reported previously novel spherulitic crystallization techniques that produce a compacted spherical crystal using mixed solvents[1]. Our recent works enclosed spherulites of NTO by rapid cooling crystallization with mixed solvents[2]. It was found

that spherical crystals have insensitivity toward sudden shock, have high performance, and have high packing density compared to polygonal crystals.

In explosives manufacture, crystallization from organic solvent or mixtures of solvents is often used. The composition of solvent determines the solubility of the substance and thus strongly influences the choice of supersatuation generation method. Furthermore, the solvent composition may have an effect on the nucleation rate as well as on the crystal growth rate, and thus affects the shape of the product crystals and the size distribution of crystalline mass.

Batch cooling crystallization using cosolvent is used in the production of spherical NTO crystals. For the purposes of the highly qualified production, product crystals with narrow crystal size distribution are wanted to improve downstream processing efficiency, insensitivity toward a sudden shock. For the purpose of production of crystalline particles, the size of product should be controlled as desired.

In this study, batch cooling crystallization tests were conducted with linear cooling mode by using a bench-scale DTB crystallizer equipped with marine propeller agitator. The results are compared with those of laboratory-scale test using crystallizer equipped with a geometrically similar stirrer. Additionally the effect of some other operational conditions on the performance of batch crystallization was examined with the laboratory-scale crystallizer.

Experimental Study

The laboratory jacketed crystallizer(300 ml) used in this study is shown in Figure 1. It was made of Pyrex and is equipped with a stainless-steel marine stirrer(SUS 304) and sensors. Draft tube and inner baffles are included. Agitation speed was fixed at 350 min^{-1} to ensure well-mixed crystal suspension.

The bench-scale-jacketed crystallizer(50l) used in this study is shown in Figure 1 together with the laboratory-scale crystallizer. It was made of stainless steel(SUS 304), and is equipped with a geometrically similar marine propeller stirrer(SUS 304) and temperature sensors. Draft tube type and baffles are included. Agitation speed was fixed at 350 min^{-1} to ensure well-mixed crystal suspension. To critically assess the scale up effect of the product crystal size, the experimental conditions of the laboratory experiments were basically the same as those of the bench-scale experiments. The dimensionless group for scale-up crystallizer is calculated by basis on the laboratory-scale operation : Newton number of 0.5,

Flow number of 0.4, Reynolds number of 90000 and Froude number of 0.81, at which tip speed of agitator is 1.6m/s[1]. These conditions make well suspended crystals, temperature profiles and cooling rates similar to bench-scale crystallizer.

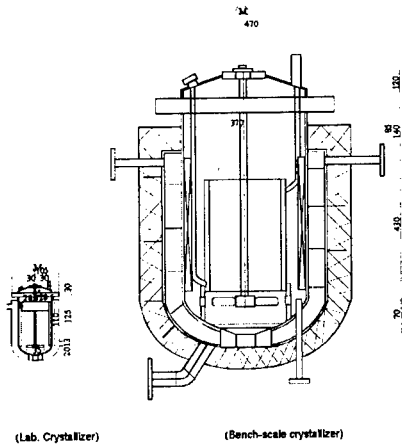

Fig 1. Crystallizers used in laboratory-scale and bench-scale experiments

Mixture of NTO-NMP-water was prepared, charged into the feed. The solution was maintained at 10°C above the saturation temperature for 30 min. The temperature was adjusted to the desired initial value and then the solution was cooled according to a constant cooling rate. Experiments were carried out with various compositions of ternary mixture, cooling rates and agitation. After crystallization, the resultant crystals were collected by filtration, washed with the saturated NTO solution and dried in an oven at 80 °C for 5hrs. Crystal slurry was withdrawn from the crystallizer to the crystal analysis system in order to measure crystal size, shape, and crystal size distribution. At the same time, samples were taken for analyzing purity and yield. The sampled crystals were filtered from the residual solution.

Results and discussion

The crystal size and crystal size distribution of explosives are parameters of importance in the performance of explosion in that they determine both packing density and true density of explosive. They are complex functions of nucleation and crystal growth rates, which are themselves functions of process variables as agitation rate, feed composition, and

production rate. The composition and the temperature were also important factors in determining the spherulite size and its distribution in the crystallization of NTO in cosolvent[1].

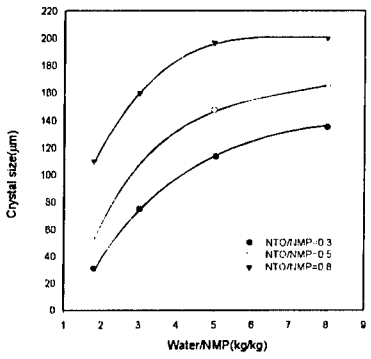

Fig. 2 Effect of composition on crystal size.

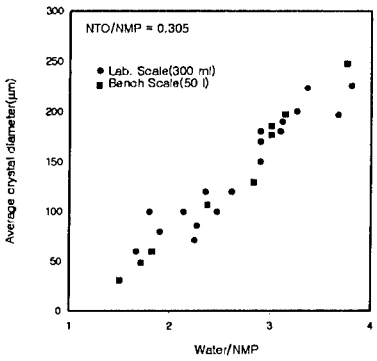

Fig. 3. Comparison of laboratory-scale and bench-scale results

Figure 2 shows the relationship between the crystal size of spherical spherulites and ratio of water/NMP. The experiments were carried out at the NTO/NMP ratio ranging from 0.3 to 0.8 and the cooling rate of 10 K/min, in which spherical crystals was obtained. It was found that crystal size increases with increasing the water/NMP ratio and increasing NTO/NMP ratio. The crystal size increases with increasing content of water in cosolvent.

Eventually, we can control the crystal size of spherulite in the range from 20 μm to 250 μm by adjusting the composition of ternary mixture.

Figure 3 shows the average size of crystals obtained from laboratory-scale and bench-scale experimentals at the NTO/NMP ratio of 0.3. It was found that product mean size at constant ratio of NTO/NMP was completely in agreement with the laboratory-scale products.

Figure 4 shows the effect of crystal size on agitation rate. Note than an increase in agitation resulted in a reduction in crystal

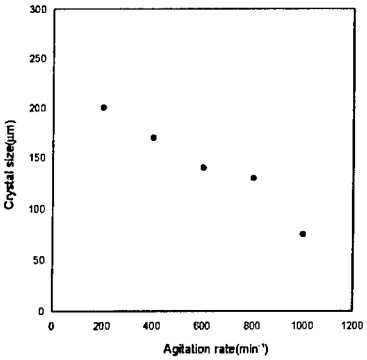

Fig. 4. Effect of agitation rate

size. As an illustration, the size of NTO crystals was reduced by 40% when agitation rate was increased by a factor of 5 with ternary composition maintained at a constant value. Figures 5a and 5b show the CSDs obtained from laboratory and bench-scale experiments, respectively. The final suspension density was 85 kg/m^3, which is not so high. Composition of solution fed and agitation speed was same. The cooling rate was controlled as a 10 K/min. The same CSD behavior was observed in both experiments although crystal size distribution is found to be wide slightly in bench-scale crystallizer. It can be expected that no scale-up factor except water/NMP ratio and NTO/NMP ratio will be considered in cosolvent system. The distribution curves were shifted to the right with decreasing NTO concentration.

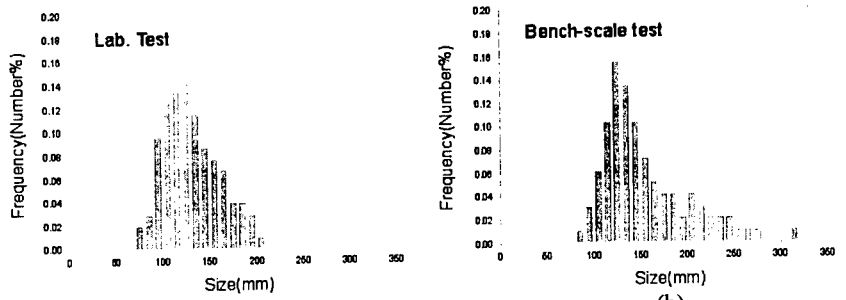

Fig. 5. Crystal size distributions of laboratory-scale(a) and bench-scale(b) tests.

Conclusion

The morphology of the NTO crystals was strongly dependent on the composition of cosolvent and independent of production scale. Comparison of the crystals obtained from the laboratory-scale and from the bench-scale operations showed that the hydrodynamic condition in crystallizer affects slightly CSD. No scale-up effect was observed in terms of CSD, shape and average size if the composition of cosolvent is set optimally in ternary system.

References

1. K.J. Kim, M.J. Kim, J.M. Lee, KRICT report IG-0649, 1998
2. K.J. Kim, M.J. Kim, Spherical crystallization of NTO in cosolvent, 14th International Symposium of Industrial Crystallization, Robinson Cambridge Univ., UK, 1999.

RECYCLING AND REUSING OF AN AGED AMINE BASED LIQUID ROCKET PROPELLANT FUEL

M. H. Sammour

Armed Forces, Cairo, Egypt

ABSTRACT

Hypergolic or spontaneous ignition of liquid rocket propellants is very desirable property which improves the reliability of starting the rocket motor. The chemical and physical characteristics of liquid propellant fuels based on mixtures of aliphatic and aromatic amines deteriorate during normal aging due to the susceptibility of amines, specially the aromatic ones, to oxidation by the atmospheric oxygen. The deterioration of fuel component properties results in increasing the ignition delay, which significantly affect the smooth combustion of the rocket motor.

As a result of extensive processing experience and experimentation at the laboratory scale we designed, fabricated, and installed a unit for recycling and reusing of aged fuel, with a capacity of about 8 tons/month and 95% recovery of pure fuel. The method is based on separation of the main fuel components from the other unuseful products and impurities formed during normal aging. The principle of the method is based on the wide difference between the boiling points of the fuel components. The regenerated main fuel components are remixed to form the required fuel composition which meets the military specification in this respect. Since all the necessary safety elements have been introduced, it is clear that the recycling process is clean and environmentally friendly process.

ERZEUGUNG VON PARTIKELWOLKEN MIT DRUCKGAS UND MIT GASGENERATOREN

Andrea Baier, Norbert Eisenreich, Volker Hell, Helmut Schmid, Helmut Schneider

Fraunhofer Institut Chemische Technologie
Joseph von Fraunhoferstr. 7
76327 Pfinztal – Berghausen
DEUTSCHLAND

Abstract

The controlled release and dispersion of particles into the surrounding atmosphere is of interest in several research projects at ICT. In each case a particle cloud with special geometry and particle concentration should be generated within a short time scale of a few milliseconds to about 100 ms. The basic idea is a realization by means of gas generators. In this context tests on a realistic scale with pressurized gas were performed. The modelling of the propagation of the cloud (geometry, volume) can be achieved by simple assumptions.

1. Einleitung

Die Beherrschung der kontrollierten Freisetzung und Verteilung von Partikeln in die umgebende Atmosphäre ist bei mehreren im ICT durchgeführten Forschungsvorhaben von Bedeutung.
Im wehrtechnischen Bereich gilt dies für die Herstellung hybrider Sprengstoffsysteme, d.h. für die Weiterentwicklung der früher unter der Bezeichnung Fuel Air Explosives bekannten Waffensysteme / 1/, deren Anwendung nicht nur für den konventionellen Einsatz sondern auch neuerdings für die Abwehr von in der oberen Atmosphäre freigesetzten chemischen oder biologischen

Kampfstoffen angedacht ist. Es gilt auch für die Entwicklung von Nicht Lethalen Waffen / 2/, wobei die hier erzeugten Partikelwolken nicht wie im vorigen Beispiel unbedingt aus energetischen Partikeln bestehen müssen; in diesem Fall kommen vorwiegend solche Substanzen zum Einsatz, die in irgendeiner Weise die Sensorik der betreffenden Personen beeinträchtigen.
Im zivilen Sektor besteht im Bereich der Sicherheitstechnologie ebenfalls Know-How-Bedarf, da hier die Untersuchung von Staubexplosionen und die Entwicklung von Löschgasgeneratoren Forschungsthemen sind.
In allen Fällen muß die Partikelfreisetzung in relativ kurzer Zeit erfolgen, d.h. je nach Einsatzzweck im Bereich von einigen Millisekunden bis zur Größenordnung von 100 ms. Das Ziel ist die Herstellung einer Partikelwolke mit einer bestimmten Geometrie und Partikelkonzentration innerhalb der Wolke in der vorgegebenen Zeit.
Diese Anforderungen können möglicherweise durch die Verwendung von für den entsprechenden Anwendungsfall maßgeschneiderten Gasgeneratoren erfüllt werden. Durch entsprechende Konzeption der chemischen Formulierung, durch welche die wesentlichen Parameter wie Verbrennungsgeschwindigkeit und –temperatur und Gasausbeute festgelegt werden können sowie durch geeignete Gestaltung der mechanischen Konstruktion, die die Strömungsverhältnisse bestimmt, erscheint ein kontrollierter Materialaustrag und die Erzeugung einer definierten Wolkengeometrie möglich.
Im Folgenden wird über Austragversuche berichtet, die zunächst mit Druckgas im Realmaßstab durchgeführt wurden.

2. Konzeption der Experimente

Die einzelnen Komponenten des Gesamtsystems, nämlich der Gasgenerator, die Behälterkonstruktion und die Art der auszutragenden Substanz müssen in ihren Eigenschaften sorgfältig aufeinander abgestimmt sein. Zur Untersuchung dieser Zusammenhänge sind eine Vielzahl von Versuchen notwendig, so daß sich Versuche im Kleinmaßstab anbieten. Vorläufige Versuche dieser Art wurden auch durchgeführt. Allerdings ist es aus verschiedenen Gründen auch notwendig, Versuche im Realmaßstab durchzuführen: Das Ausbreitungsverhalten von Partikeln ist bei großen auszutragenden Massen anders als bei kleinen und die Bewertung der

Reaktion einer Partikelwolke aus energetischen Teilchen in Form einer Verbrennung oder Detonation nur ab einer gewissen Größe möglich.
Im Folgenden werden im Realmaßstab durchgeführte Versuche beschrieben. Dabei wurden keine Gasgeneratoren sondern zunächst Druckgas verwendet. In solchen Anwendungsfällen, in denen möglichst großflächige bzw. großvolumige Wolken erzeugt werden sollen, ist es naheliegend kreiszylindrische Behälter zu verwenden. Aus Gründen der Rationalisierung und einer möglichst geringen Druckbelastung der Umgebung wurde bei den Versuchen jedoch nur ein "Segment" eines solchen Behälters untersucht.

3. Aufbau und Durchführung der Versuche

Die Apparatur wurde im Raketenprüfstand des ICT aufgebaut. Sie besteht aus einem Rohrsystem von 200 mm ∅ mit Volumina von ca. 20 l und 40 l (Abb. 1). An der Frontseite des Rohres ist ein Behälter mit dem zu dispergierenden Staub angebracht. Er hat trapezförmigen Querschnitt mit einem Öffnungswinkel von 45^0. An seiner Vorder- und Rückseite ist er mit dünnen Glasplatten abgeschlossen. Zwischen dem Rohr mit Druckgas und dem Staubbehälter befindet sich eine Berstscheibe und ein "Adapter", der das Rohr auf den Rechteckquerschnitt des Behälters (200 x 20 mm^2) anpaßt. Das Staubmaterial bestand aus 120 µm KCl-Partikeln, die zur Verbesserung der Rieselfähigkeit mit ca. 1% TiO_2 versetzt wurden. Entsprechend der Tabelle waren 8 Versuche geplant, wobei die Versuchsparameter Volumen V (ca. 20 l und 40 l), Druck P (ca. 50 bar und 100 bar) und auszutragende Staubmasse M (1,26 kg und 2,52 kg) variiert wurden.

Test Nr.	10	11	12	17	14	15	13	16
V (l)	35,2	35,2	35,2	35,2	18,5	18,5	18,5	18,5
P (bar)	48,7	91,2	48,6	---	48,7	93,1	48,8	95,0
M (kg)	1,26	1,26	2,52	2,52	1,26	1,26	2,52	2,52
D (s^{-1})	20,88	18,78	16,20	---	25,44	21,61	17,26	(22,65)
U_0 (m/s)	200	218	154	---	201	222	148	(157)
α (Grad)	9,4 ±0,3	10,1 ±0,5	11,2 ±0,6	---	12,2 ±0,7	13,1 ±0,6	10,8 ±0,8	---

Bei Versuch 16 erfolgte eine Zerlegung des Staubbehälters, so daß diese Ergebnisse irregulär sind. Versuch 17 konnte nicht durchgeführt werden, da hier der gleiche Staubbehälter verwendet werden sollte. Das Rohrsystem wurde durch Öffnen eines elektromagnetischen Ventils mit Luft aus einer Preßluftflasche gefüllt, wobei der Druckanstieg im Rohr mit einem Druckaufnehmer P_1 gemessen wurde. Nach dem Aufplatzen der Berstscheibe wurde über den Druckanstieg eines zweiten Druckaufnehmers P_2 auf der Ausblasseite das Schließen des Ventils und eine High Speed Video Kamera (1000 B/s) mit Ringspeicher getriggert, die die Ausbreitung der Staubwolke von der Seite aufnahm. Ergänzend wurde die Wolke auch von vorne mit einer normalen Video-Kamera (25 Hz) aufgenommen.

4. Ergebnisse

4.1. Druckverlauf im Rohrsystem

Die Abb.2 zeigt den Druck/Zeit- Verlauf der beiden Druckaufnehmer P_1 (Rohrrückwand) und P_2 (kurz hinter der Berstscheibe ausblasseitig) beispielhaft für den Versuch 10. Den Druckabfallkurven sind Schwingungen überlagert, die für Ausblasvorgänge dieser Art typisch sind. Der zeitliche Abstand aufeinander folgender Maxima entspricht dabei der Zeit, die eine Schallwelle zum zweimaligen Durchlaufen der Rohrsystemlänge (Distanz Rohrrückwand bis Staubbehälter) benötigt.
Die Ausströmzeiten, d.h. die Zeitdifferenz zwischen dem Platzen der Berstscheibe und dem Druckabfall auf Umgebungsdruck im Rohr liegen bei den Versuchen – abhängig vom Ausgangsdruck und –Volumen zwischen ca. 100ms und 200 ms. Die Werte stimmen mit den nach / 3 / mit Hilfe der Beziehung

$$P / P_a = \{(F / V)\, 40{,}28\, t + 1\}^7 \qquad (1)$$

P Druck im Rohr beim Platzen der Berstscheibe

P_a Umgebungsdruck

F Ausströmfläche (Querschnittsfläche Staubbehälter auf der Einströmseite)

V Volumen mit Druck P (Rohrrückwand bis Berstscheibe)

t Ausströmzeit

berechneten gut überein.
Wird der Berechnung das Volumen des gesamten Rohrsystems (also einschließlich "Adapter") und der auf dieses Volumen entspannte Druck zugrunde gelegt, so sind die erhaltenen Ausströmzeiten ebenfalls in guter Übereinstimmung mit den experimentellen Werten. Im ersten Fall sind die berechneten tendenziell etwas kürzer und im zweiten Fall etwas länger als die experimentellen.

4.2. Qualitative Beschreibung der Wolkenausbreitung

Die Abb.3 zeigt beispielhaft die Ausbreitung der Partikelwolke von Versuch 10 bei 20 ms, 50 ms und 80 ms nach Platzen der Berstscheibe. Aus den Aufnahmen gewinnt man den Eindruck, daß die Partikelmasse zunächst sozusagen als Ganzes aus dem Behälter ausgestoßen wird und erst daran anschließend die Verteilung der Partikel in der Luftströmung beginnt. Dies wird durch Modellrechnungen /4/ bestätigt. Nach einiger Zeit bekommt die Wolke Bodenkontakt, während sich an der Oberseite immer wieder Wirbel bilden, die sich ablösen. Die Frontal-Video-Kamera registriert zunächst einen ziemlich kreisförmigen Querschnitt der Wolke, der sich dann in einen Rechteckquerschnitt ändert (betrachtet wird der Zeitraum bis 200 ms). Bei den Versuchen mit doppelter Masse (2,52 kg) ist allerdings bereits nach 120 ms eine Veränderung vom Rechteck- zum Halbkreisquerschnitt erkennbar.
Die Abb.4 und 5 zeigen beispielhaft die Weg/Zeit-Diagramme der Wolkenspitze für die Versuche 10/11 und 10/12. Qualitativ stellt man fest:

1. Vergeich 50 bar / 100 bar
   Die Wolkenspitze erreicht bei Versuchen mit P_1 =100 bar wesentlich schneller eine bestimmte Entfernung als bei Versuchen mit 50 bar.
2. Vergleich 18,5 l / 35,2 l
   Die Kurven unterscheiden sich nur geringfügig. Der Effekt ist wesentlich kleiner als bei 1.
3. Vergleich 1,26 kg / 2,52 kg

Bei Versuchen mit größerer Masse wird diese zunächst verzögert beschleunigt; ansonsten sind auch hier die Unterschiede in der Ausbreitung eher gering.

4.3. Datenauswertung und Diskussion der Ergebnisse

Die Weg/Zeit Diagramme (Abb.4,5) wurden mit dem Ansatz

$$x(t) = U_0/D \{ 1 - \exp(- D t) \} \qquad (2)$$

gefittet, der aus der Integration der Bewegungsgleichung

$$m \ddot{x} + m D \dot{x} = 0 \qquad (3)$$

folgt. Die sich ergebenden Werte für die Anfangsgeschwindigkeit U_0 und die Konstante D sind in der Tabelle angegeben.
Für die mit 100 bar Ausgangsdruck durchgeführten Versuche erhält man ca 220 m/s und für die Versuche mit 50 bar ca 200 m/s (bei jeweils gleicher Masse von 1,26 kg). Für die beiden mit doppelter Masse durchgeführten Versuche ergeben sich deutlich geringere Geschwindigkeiten von ca 150 m/s. Die aus den experimentellen Daten abgeleiteten inkrementellen Geschwindigkeiten zeigen eine starke Streuung und liegen zum Teil erheblich über den oben genannten. Dies resultiert aus den Pulsationen im Druck/Zeit-Verlauf beim Entleerungsvorgang des Behälters, die sich im Geschwindigkeits/Zeit- Verlauf widerspiegeln. Der Ausbreitungsvorgang wird – abgesehen von der ersten Beschleunigungsphase – durch das Modell recht gut beschrieben.
Ein wesentliches Ziel der Auswertung der Versuchsergebnisse ist neben der Beschreibung der Wolkenausbreitung (Wolkengeometrie, Wolkenradius als Funktion der Zeit) die Kenntnis der Partikelkonzentration innerhalb der Wolke. Wird diese innerhalb der Wolke als konstant vorausgesetzt, so kann sie aus der (bekannten) ausgebrachten Masse und dem Wolkenvolumen bestimmt werden. Daher wurden zunächst aus den Filmaufnahmen Wolkenvolumina zu verschiedenen Zeiten ermittelt. Dabei wurde so vorgegangen, daß unter Berücksichtigung der Information über die Wolkengeometrie aus den Bildern der Frontalkamera den jeweiligen Wolkenbildern der Digital-Video-Kamera einfache geometrische Figuren (Kegelstumpf, Kreiszylinder, etc.) einbeschrieben wurden, wobei im allgemeinen Rotationssymmetrie der Wolke in Ausbreitungsrichtung vorausgesetzt wurde.

Stark vereinfacht kann für die Wolkenkontur eine Geometrie entsprechend der unten stehenden Figur angenommen werden. Wird Rotationssymmetrie um die Ausbreitungsachse angenommen, so ergibt sich für das Volumen des Körpers:

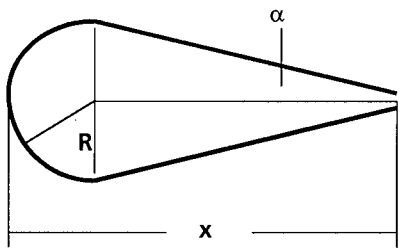

$$V = \pi/3 \{2 + k^{-1}\} \{ k/(1+k) \}^3 \; x^3 \qquad (4)$$

mit $k = \tan \alpha$ und $\tan \alpha = R/(x - R)$

Mit dieser Beziehung wurden die Daten gefittet, woraus sich die in der Tabelle angegebenen Werte für den (halben) Öffnungswinkel α ergaben.
Die Tatsache, daß bei Versuch 10 und 11 die Winkel am kleinsten sind resultiert möglicherweise daraus, daß diese bei bedecktem Himmel, die anderen jedoch bei Sonnenschein durchgeführt wurden, so daß die Grenzen der Wolkenkonturen anders bewertet wurden. Theoretisch ergibt sich nach / 5/ für den Fall eines stationären Jets eines inkompressiblen Fluids für den halben Öffnungswinkel $\alpha \approx 12{,}5^0$ im Bereich der "main region", d.i. der mittlere Bereich des Jets, der ja auch hier vorwiegend von Interesse ist. Experimentelle Untersuchungen an instationären Jets / 6/ ergaben einen Wert von $(11{,}8 \pm 0{,}3)^0$.
Das bedeutet, daß – unter den gegebenen experimentellen Bedingungen - für die Beschreibung des Ausbreitungsvorgangs die verwendeten, einfachen Modellvorstellungen ausreichend sind.
Unter der Annahme, daß sich die Partikel innerhalb der Wolke homogen verteilen, kann nun auch eine mittlere Partikelkonzentration in der Wolke angegeben werden, da ja die dispergierte Masse bekannt ist.

Wie eingangs erwähnt, wird ein einsatzfähiges System evtl. aus einem rotationssymmetrischen Behälter bestehen, der nach seiner Öffnung die Partikelwolke in einem Winkel von 360^0 verteilt. In diesem Falle ergibt sich das Volumen aus einer Rotation der in obiger Figur dargestellten Fläche um die Vertikale (z - Achse). Somit kann auch für diesen Fall abgeschätzt werden, welche Partikelmasse dispergiert werden muß, um eine gewünschte Partikelkonzentration zu erhalten.

5. Literatur

1. N. Eisenreich, H. Schneider
   Entwicklungsmöglichkeiten künftiger Fuel Air Explosives Systeme
   Int. Annual Conf. ICT, Karlsruhe (1999)
2. W. Liehmann, H. Schneider
   FAE – Perspektiven zum Einsatz als Nicht Lethales Wirkmittel
   Workshop "Neue Technologien – NLW- Wirkmittel"
   FhI Chemische Technologie, 19./20.10.1999
3. E. Schmidt
   Ausströmen von Gasen aus Behältern hohen Innendrucks
   Chemie-Ing.-Techn. 37, Nr. 11 (1965)
4. M.W. Glass
   Far-Field Dispersal Modeling for Fuel-Air-Explosive Devices
   Sandia Nat. Labs., Albuquerque, Report SAND90-0528 (1990)
5. G.N. Abramovich
   The Theory of Turbulent Jets
   MIT Press, Massachusetts (1963)
6. R.S. Scorer
   Environmental Aerodynamics
   Ellis Horwood Ltd, Chichester (1978)

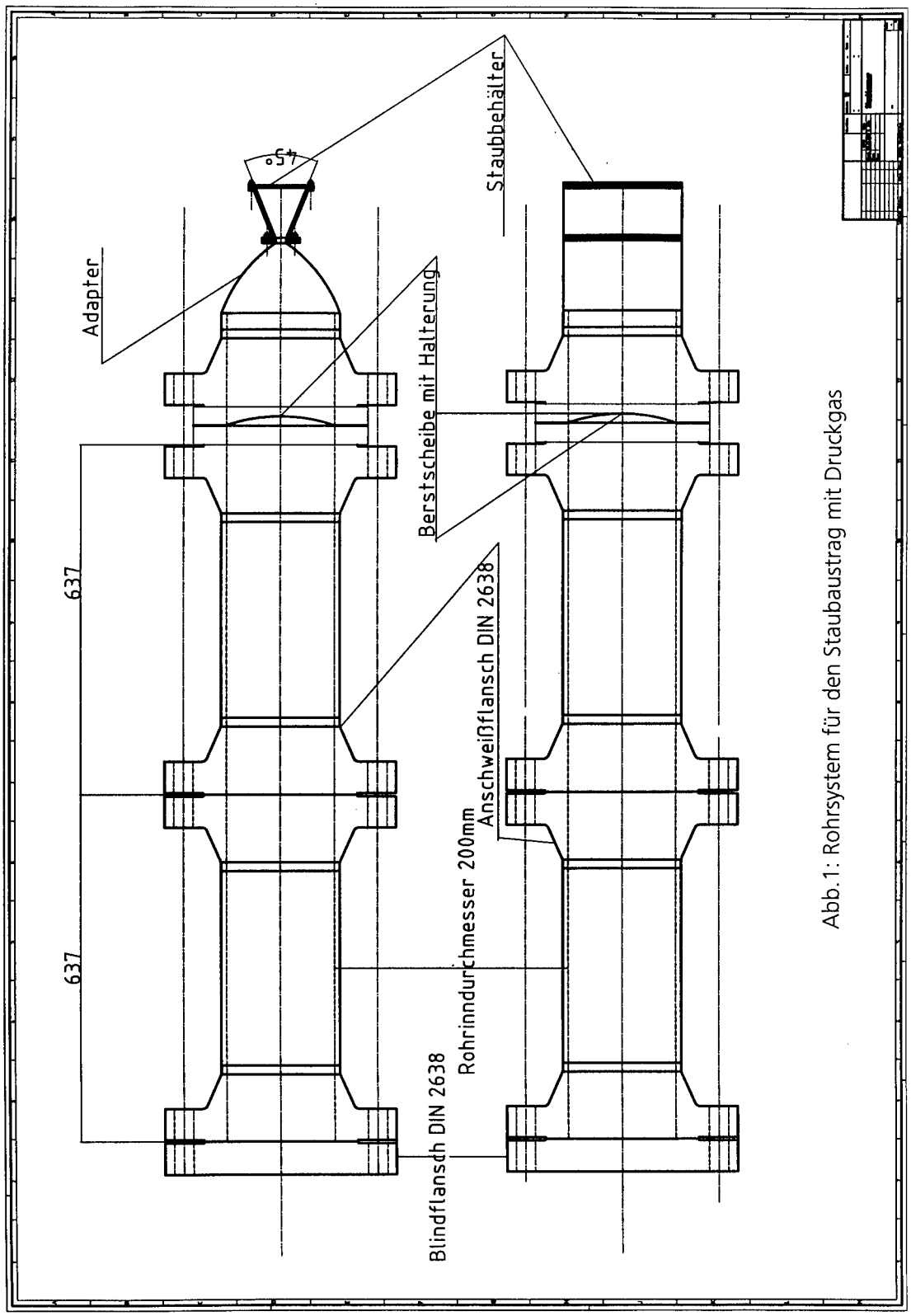

Abb.1: Rohrsystem für den Staubaustrag mit Druckgas

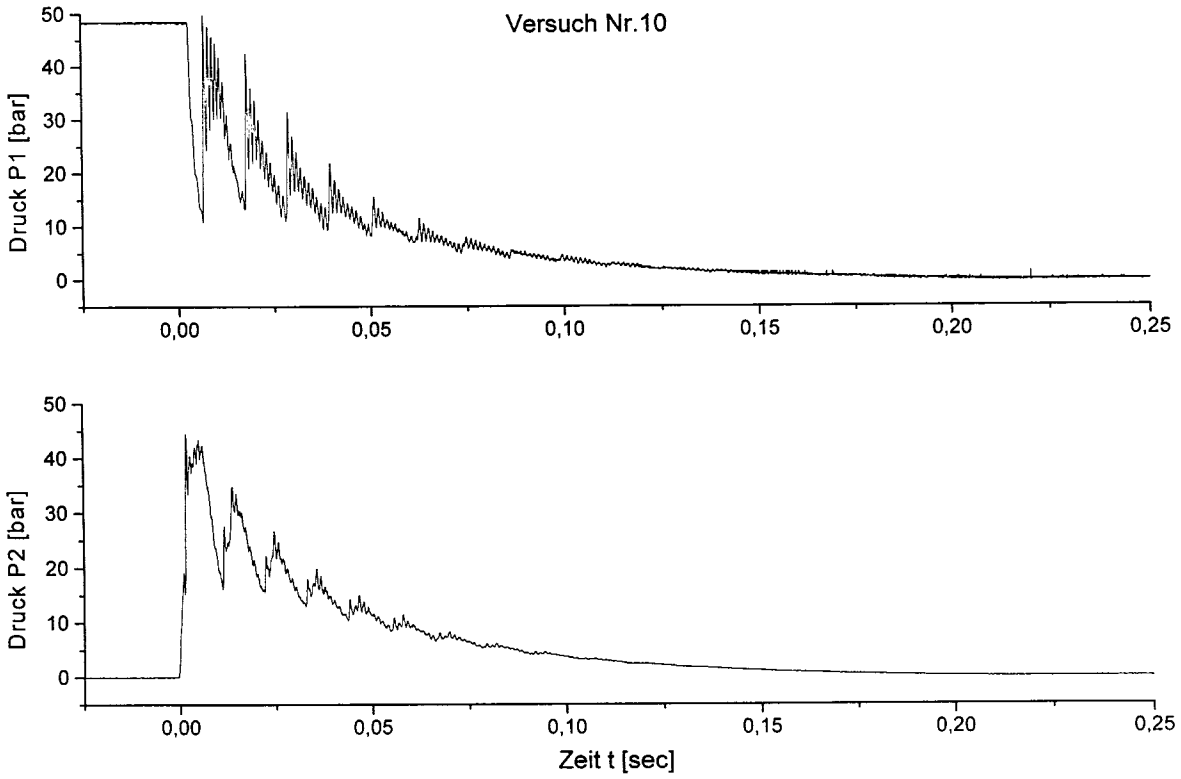

Abb.2: Im Rohrsystem gemessene Druck/Zeit-Verläufe

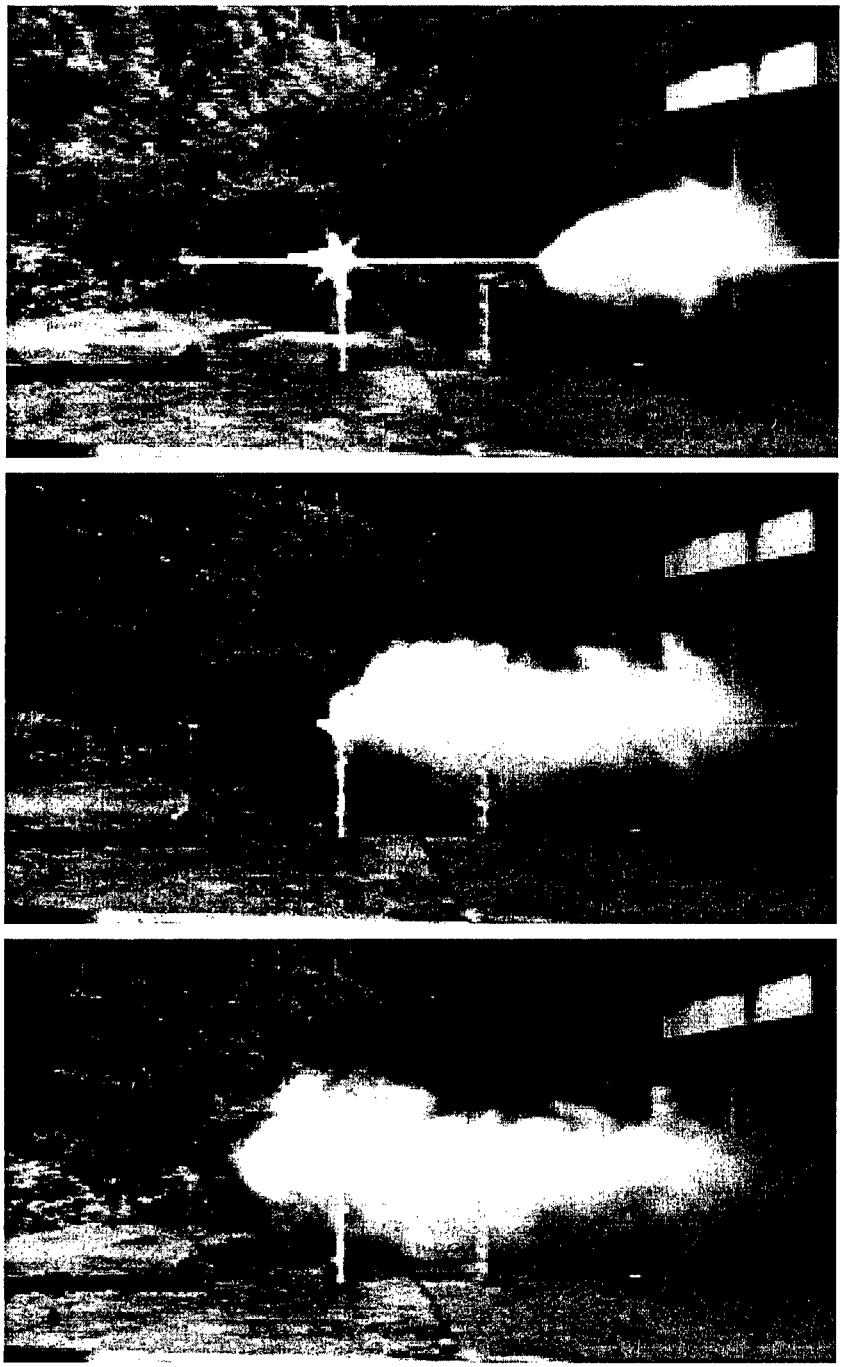

Abb.3: Wolkenausbreitung bei Versuch 10: 20 ms, 50 ms und 80 ms nach Behälteröffnung; Abstand zweier Markierungen: 2 m

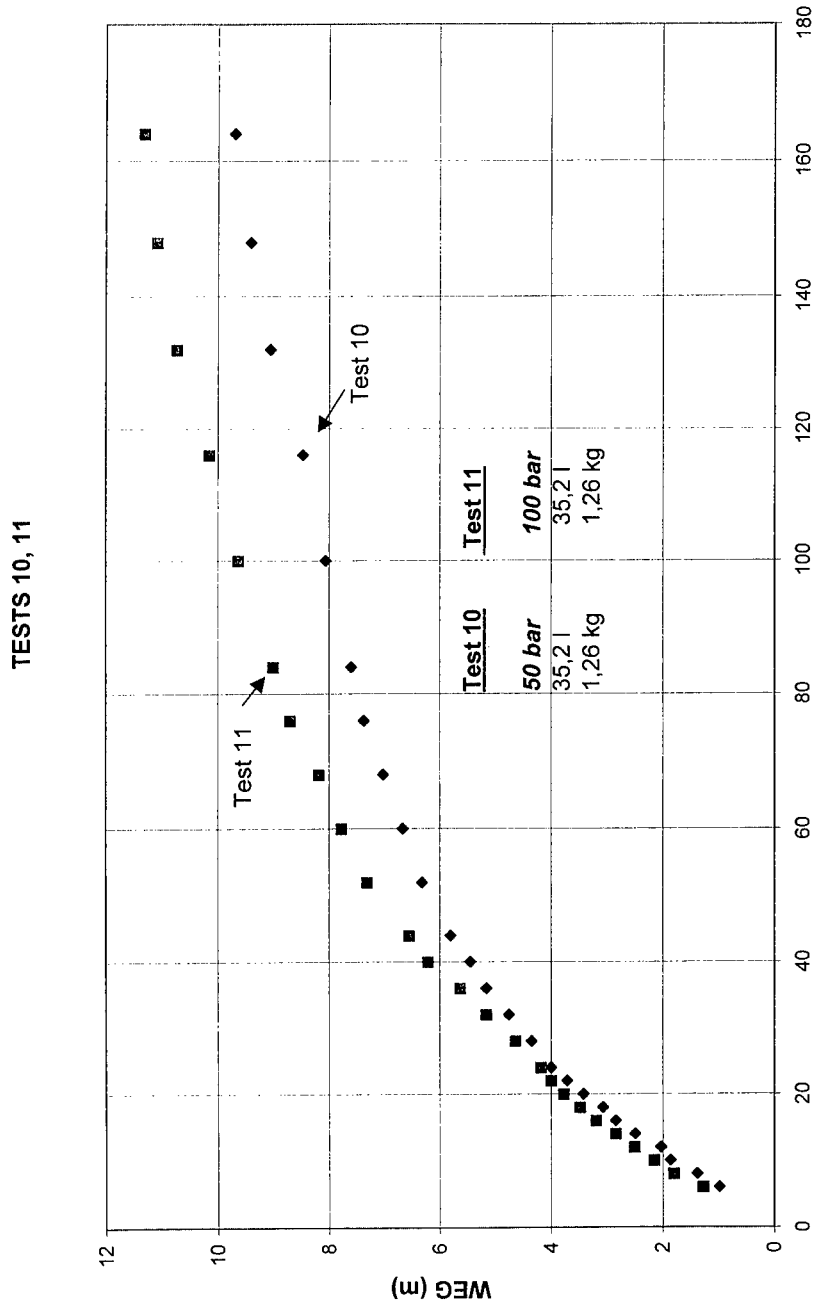

Abb.4: Ausbreitung der Wolkenfronten (Versuche 10/11)

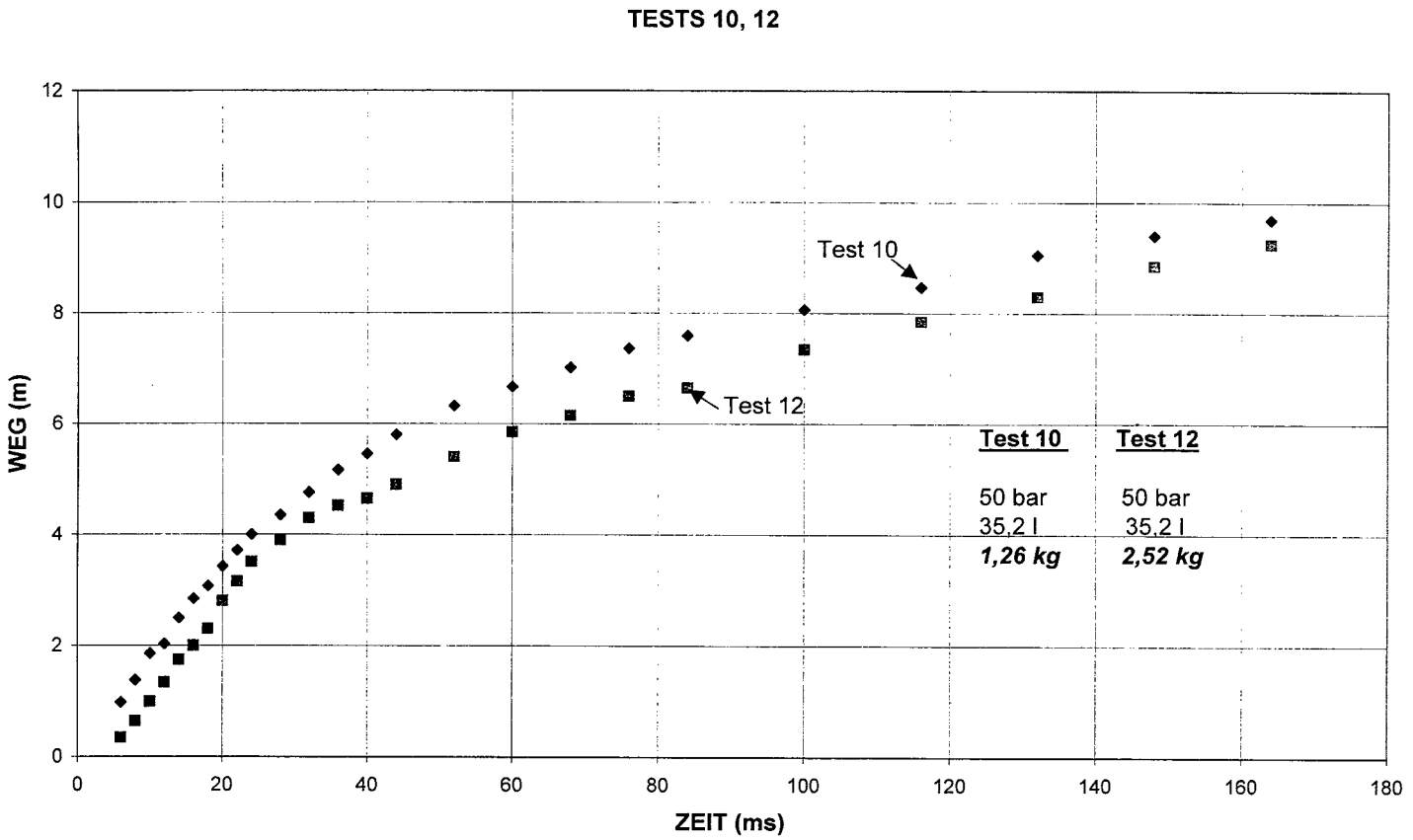

Abb.5: Ausbreitung der Wolkenfronten (Versuche 10/12)

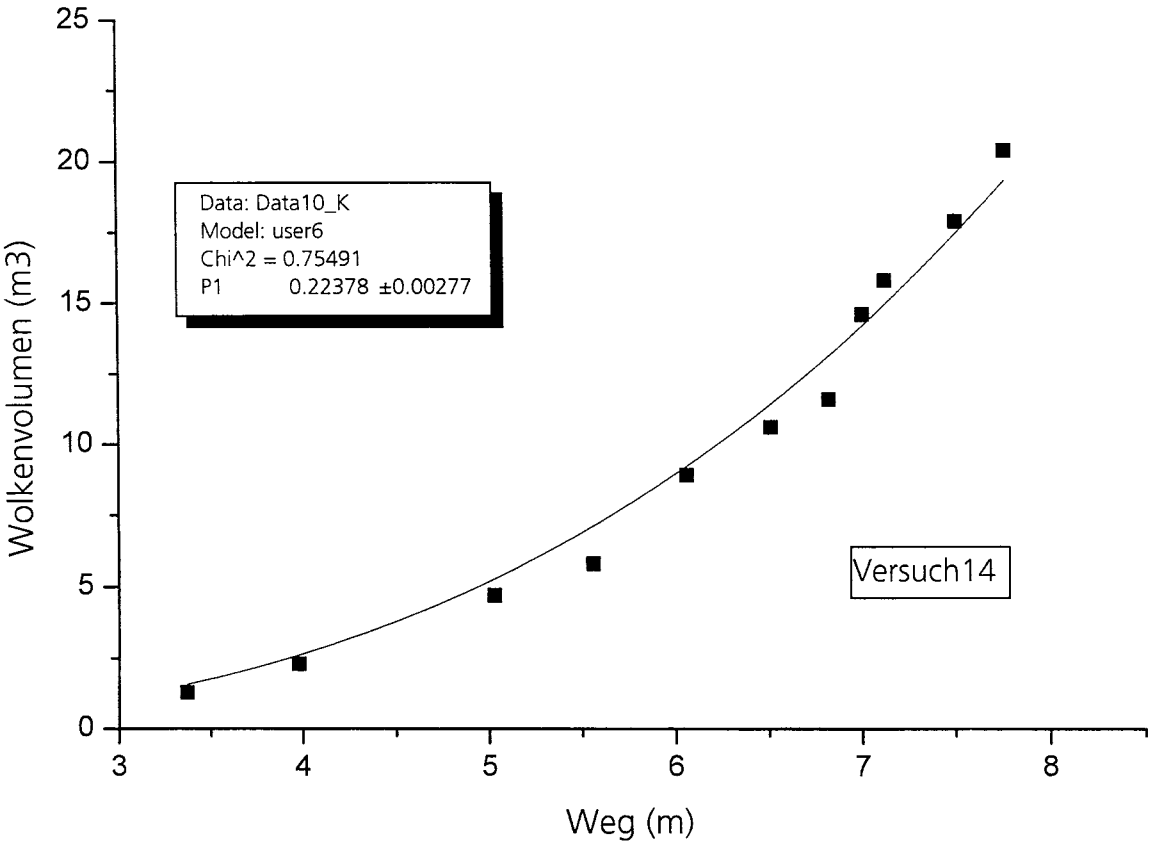

Abb. 6: Wolkenvolumen in Abhängigkeit von der Entfernung vom Austragsort

ENVIRONMENTAL QUALIFICATION OF GAS GENERATOR SYSTEMS FOR AUTOMOBILES

Thomas Reichert, Thomas Hirth, Richard Jakob, Joachim Cäsar

Fraunhofer-Institut für Chemische Technologie ICT,
Joseph-von-Fraunhofer-Str. 7, D-76327 Pfinztal

Abstract
For the new non azide gas generator types nowadays the gas generator qualification program according AK LV 03 is applied for estimation the pressure curve and the particle concentration before and after the artificial ageing. For the determination of the gaseous emissions of the gas generant material, the AK ZV 01 test specification is used, because of the interaction of different gas generator emissions in a car and the decreasing influence of the bag and car interior material to the gas and particle concentrations. Therefor the measurements of the gaseous emissions were done additional to the can tests in the 2.5 m³ airbag test chamber of the ICT with three gas generators, preconditioned by -35°C, RT. and + 85°C. This paper describes the complete test program of a gas generator system.

1. Investigations

For the gas generator qualification program according AK LV 03, the listed investigations have to be done /1/:

A. Airbag inflator module environmental test programme

1. Drop test 1±0,2 m RT. (23±5°C) 6x
2. Mechanical impact test at -35°C, 23°C and 85°C
   36 Shocks pro AGG (2x6Ax3T) X 6 AGG (airbag gas generators)
3. Low pressure test 6 AGG
4. Simultaneous vibration temperature test
5. Thermal humidity cycling test 6 AGG

B. Performance test programme

5. Electrostatic discharge test
6. Electromagnetic compatibility
7. Performance 9 AGG
7.1 Tank test at -35°C, RT. and 85°C
7.2 Analysis of gaseous emissions
7.3 Analysis of solid emissions
8. Bonfire test 3 AGG

2. Environmental test programme

The gas generators were numbered, weighted and the igniter resistance was measured before the tests. Typical values of gas generators are depicted in table 2.1. The difference in mass was estimated after the artificial ageing program.

Gas generator Nr.	Mass (g)	Resistance (Ω)	Mass (g) after ignition	Δ Mass (g)
1	360.101	2.1	338,391	21,71
2	360.668	2.0	338,324	22,344
3	360.174	2.0	336,233	23,941
4	360.633	2.0	340,956	19,677
5	361.029	2.0	337,943	23,086
6	358.847	2.0	334,893	23,954
7	360.910	2.1	341,634	19,276
8	360.810	2.1	338,880	21,93
9	360.151	2.0	336,526	23,625
...	...	...	...	...

Table 2.1 Igniter Resistance before tests

	test	environmental testing parts						reference parts									
Nr.		1	2	3	4	5	6	7	8	9	10	11	12	13	14	15	16
1	drop test	X	X	X	X	X	X										
2	mechanical shock	X	X	X	X	X	X										
3	low pressure	X	X	X	X	X	X										
4	simultaneous vibration	X	X	X	X	X	X										
5	climatic change	X	X	X	X	X	X										

Table 2.2 Environmental testing program

	test	environmental testing parts						reference parts									
Nr.		1	2	3	4	5	6	7	8	9	10	11	12	13	14	15	16
5	electrostatic discharge										X	X	X				
6	electromagnetic compatibility													X	X	X	
7	performance - 35° + 23° + 85°	X	X	X	X	X	X	X	X	X							
7.1	can test	X	X	X	X	X	X	X	X	X							
7.2	gas analysis	X	X	X	X	X	X	X	X	X							
7.3	particle analysis	X	X	X	X	X	X	X	X	X							
8	bonfire test										X	X	X				
9	reserve																X

Table 2.3 Performance test program

	Drop direction								
GG Nr.	a	b	c	d	e	f	damage	resistance [Ω] before	after
1	x						no	2.1	2.1
2		x					no	2.0	2.0
3			x				no	2.0	2.0
4				x			no	2.0	2.0
5					x		no	2.0	2.0
6						x	no	2.0	2.0

Table 2.4 Resistance after drop tests (Remark: Drop high 1,1 m , Temperature 21° C)

Nr.	low pressure 0.875 bar, 23° C, 1h	climate cycling test 30 cycles	damage	resistance [Ω]
GG Nr. 1	23° C, 1 h	30 Cycles	no	2,1
GG Nr. 2	"	"	no	2,0
GG Nr. 3	"	"	no	2,1
GG Nr. 4	"	"	no	2,0
GG Nr. 5	"	"	no	2,0
GG Nr. 6	"	"	no	2,1

Table 2.5 Resistance after low pressure test and climatic cycling test

The gas generator environmental test program was completely fulfilled for all gas generators. No damage or failure occurs during the tests. The frequency spectrum for the vibration test and an example for the mechanical shock test are depicted in Figure 1 and 2.

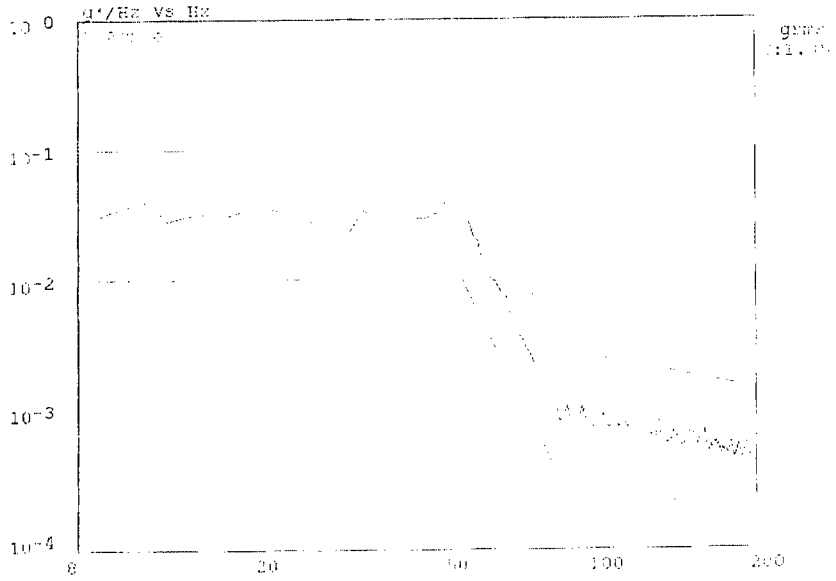

Figure 1 Frequency spectrum for vibration test of gas generators

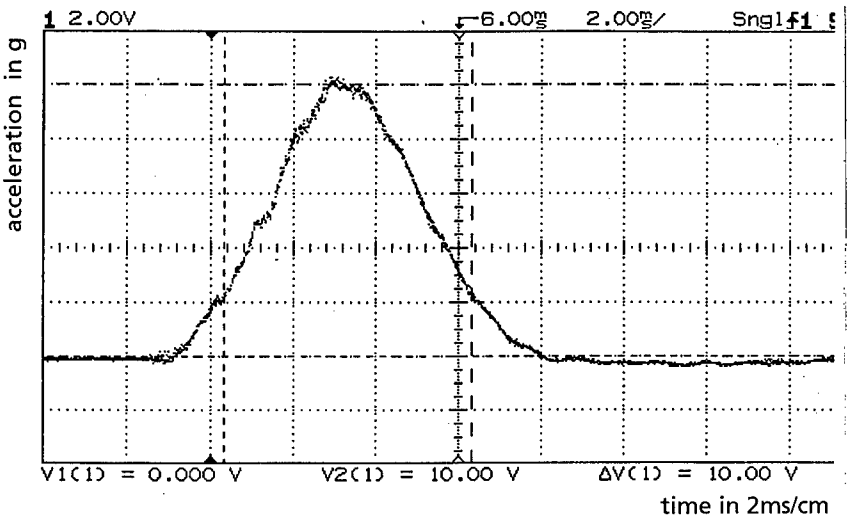

Figure 2 Mechanical shock test curve for gas generator tests

3. Results for performance tests

An example for the pressure curve during the can test are depicted in Figure 3. The ignition time for the bonfire tests are listed in table 3.1. A video normally is made of the bonfire test and attached to the test results.

Generator Nr:	Orientation	Ignition time (examples)
10	igniter towards burner	95 sec
11	igniter away from burner	58 sec
12	right angle to burner	77 sec

Table 3.1 Typical ignition times for gas generators during bonfire test

3.1 Gaseous emissions from performance tests according AK ZV 01:

The objection of the experiments described as follows was to determine the gaseous- and solid reaction products after common deployment of driver inflators into an airbag test chamber (2,5 m³). The following parameters have to be measured:

I Gaseous reaction products

a) Carbon Monoxide (CO)
b) Carbon Dioxide (CO_2)
c) Nitrogen Monoxide (NO)
d) Nitric-Oxides (NO_X)
e) Hydrocyanic Acid (HCN)
f) Ammonia (NH_3)

II Solid reaction products

g) Concentration

III Other Parameters

i) Temperature
j) Relative Humidity
k) Ambient pressure

3.2 Analysis of the reaction products

For the continuous determination of CO and CO_2 a NDIR-instrument BINOS 1.2 was used, the determination of both NO and NO_X happened with a ROSEMOUNT Model 951 A chemiluminescence analyser. At several times HCN and NH_3 were estimated with a DRAEGER-Tube.
Temperature and relative humidity have been measured together with a TESTO 601 equipment.
The particles were sucked onto a filter (PALIFLEX, 47mm dia., type T60A20) housed in a MILLIPORE filter holder with a vacuum pump (ILS-Schäfer, type HSG 12) at a flow adjusted to 5 SLM. A VACUUBRAND manometer was used for the ambient pressure measurement.

For the continuous determination of the gaseous products three PTFE-tubes[1] (o.dia. 6mm, i. dia. 4 mm) were mounted at the middle left side of the chamber. The first tube has been used for the CO/CO_2 -measurements, the second one for the measurements of NO/NO_X .The third line was the sample line for gases estimated with a DRAEGER-tube, e.g. HCN and NH_3 .
To protect the analytical equipment from generated dust it was necessary to put polysulfone-filterholders with PTFE-filters (Ø 25 mm, pore size 0,45 µm) into the sampling tubes. All values of the gas-analysis were computed.

For the sampling of particles the MILLIPORE filter holder was placed in the middle of the left side of the chamber and connected with a PTFE-tube (left side) to the pump. This arrangement prevents certain particle-losses inside the tube before collecting onto the filter. The sensor for the measurements of temperature and relative humidity was located in the middle of the chamber. Resulting gaps were fitted with tape.

All results of the gas analysis are shown in table 3.2. The values of NO and also of NO_2 are corrected according to H_2O- and CO_2 concentration[2].

[1] PTFE = Poly Tetra Fluoro Ethylene

Before collecting all filters have been dried at 105 °C and weighted with a analytical balance. During the measurements they were kept in petri dishes inside a dessicator. After collecting they have been dried altogether at 105 °C and weighted to constancy. The flow was also observed during the collections. Table 3.2 shows the amount of the dust on the filters multiplied with the gas volume and enables a comparison of the gas generator emissions.

Specimen NR.	GG - Nr. 2 (Ref.)		GG - Nr. 3 (Ref.)		GG - Nr. 1 (Ref.)		AK ZV 01 Values
Temperature storage [°C]	+ 23 ° C		+ 85 ° C		- 35 ° C		
Gas analysis A = GC -Analysis (Vol.%) B = NDIR/Dräger (ppm)	A	B	A	B	A	B	B
H_2							
O_2							
N_2							
CH_4							
CO							
CO_2							
C_2H_2/C_2H_4							
CO NDIR		29 - 31		39 - 41		31 - 35	500
CO_2 NDIR		1500		1500		1400	20000
NO/NO_x - Analyzer		28		34		29	50
NO2		2		3		2	10
NH_3 „		13 -14		18 - 21		2 - 5	150
HCN „		2 -3		2 - 3		2 - 3	25
HCHO „		< 0,5		< 0,5		< 0,5	10
HCl		< 1		< 1		< 1	25
$COCl_2$ „		< 0,25		< 0,25		< 0,25	1
Cl_2 „		< 0,2		< 0,2		< 0,2	5
SO_2 „		< 1		< 1		< 1	50
H_2S „		< 0,2		< 0,2		< 0,2	50
Particle mass (mg)		413		523		518	

Table 3.2
Examples for gaseous emissions for +85°C, -35°C and +23°C preconditioned gas generators in the 2,5 m³ chamber in comparison to the limit values for the total vehicle. The gas concentrations are all below the limit values.

3.3 Particle measurements in the 60 l can

For the analysis of the particles in the 60 l - can, the test can was washed out with 1000 ml dest. water. The disolutions were filtered with G3 glass fritts and dried with 120°C to mass constancy. The analysis were done for water soluble and non soluble particles and have had the results depicted in table 3.3.

Examples for analysis of disolutions:

Specimen	pH - value	K (mg/l)	Na (mg/l)	Mo (mg/l)	Cl (mg/l)	mass mg/l
1	7,15	10,30	384,3	0,58	628	1023,2
2	7,29	12,44	359,3	0,23	809	1181,0
3	7,00	12,36	583,9	0.56	648	1244,8
4	6,58	11,95	411,6	0,10	731	1154,7
5	7,31	12,33	496,5	0,77	848	1357,6
6	7,00	< 0,05	87,1	< 0,05	163	250,1
7	6,46	9,90	347,4	0,06	615	972,36
8	6,85	12,81	421,4	0,05	650	1084,3
9	6,76	9,70	396,1	0,18	742	1148,0

Examples for analysis of dry residues:

Specimen GG	Residue (mg)	C (mg)	H (mg)	N (mg)	Si (mg)	Mo (mg)	mass (mg)
1	157,4	3,27	6,14	4,93	0,92	1,13	16, 4
2	188,4	3,30	6,36	3,90	1,40	0,85	15,8
3	216,8	2,12	4,96	4,04	1,45	2,40	15,0
4	227,9	1,80	5,48	5,44	1,18	2,40	16,3
5	204,0	3,18	5,88	4,83	0,94	1,15	16,0
6	42,8	0,52	1,37	1,05	< o,05	0,24	3,2
7	192,7	1,29	4,26	4,36	0,72	2,07	12,7
8	299,3	4,62	12,51	7,29	0,09	1,00	25,5
9	188,4	2,63	6,30	4,79	0,99	1,75	16,5

Table 3.3
Examples of soluble and non soluble solid emissions of the gas generators after the can test. The amount of solid emissions from the gas generators are all below the limit value of 2 g according to AK LV 03.

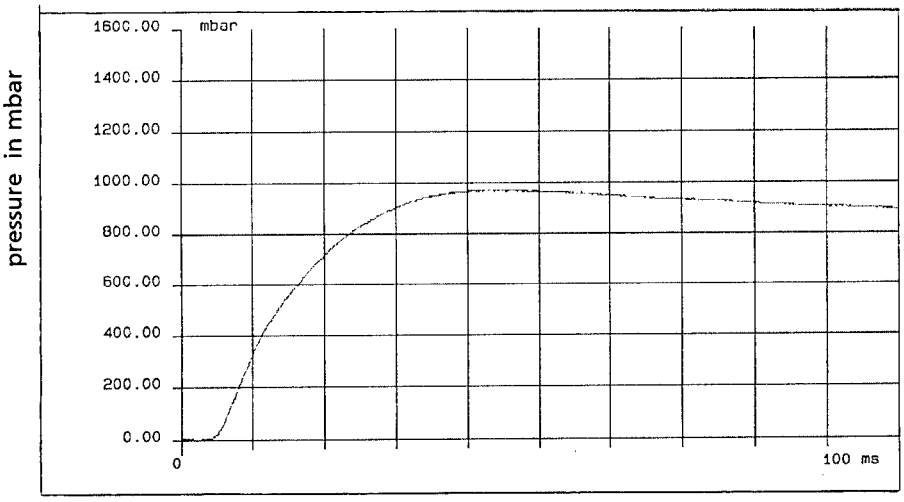

Figure 3 Example for a can pressure curve

4. Conclusions

In order to determine the gaseous and solid reaction products of airbag gas generators before and after the artificial ageing program, investigations have been done within the 2,5 m³ airbag chamber of the ICT and the 60 l can.
The results have shown, that the extremely interesting gaseous reaction compounds such as CO and NO_2 had average values below the limit values according AK ZV 01. Also the other gaseous emissions and the amount of particle emissions were below the limit values.

5. References

/1/ AK-LV 03 Airbag System , inflator assemblies, Requirements and test procedures (January 1995)

/2/ AK ZV 01 Airbag System, pyrotechnical restraint system in the total vehicle (February 1997)

/3/ R.D. Matthews, R.F. Sawyer and R.W. Schefer: Interferences in Chemiluminescent Measurement of NO and NO_2 Emissions from combustion Systems, *Envir. Sci. & Tech.* 11 (1977), 1092-1096

/4/ *CRC Handbook of Chemistry and Physics, 75th Edition* (1995), CRC Press Boca Raton, 6-15

MATHEMATICAL SIMULATION OF AIR BAG INFLATION BY LOW TEMPERATURE GAS GENERATOR PRODUCTS

A.Vorozhtsov, S.Bondarchuk, A.Salko, O.Kondratova
Tomsk State University, Lenin Ave., 36, Tomsk, 634034, Russia
fax 7 - 3822- 553836, e-mail tnk@post.tomica.ru

The system of safety for cars has in the structure air bags. It is important to know how to simulate supercharge with the purpose of maintenance correct and optimum on temporary parameters of process of deployment of an air bag at the moment of emergency, to eliminate a capability of their gap etc.

In the present work the outcomes of the analysis of process of air bag supercharge by products of low temperature gas generators developed in FRPC "Altai" are submitted [1]. The mass gas flow rate is constant, and temperature of generated gas does not exceed 300K. The volumetric structure of gases in nitrogen generated compositions of various compounds actuates 96÷99% N_2, 1÷4% H_2+CH_4, and less than 0,05% NH_3, i.e. the generated gas is not capable to form inflammable and explosive mixture with an air. The combustion products of the low temperature gas generator go in a cavity of an elastic envelope (air bag) and inflate an air bag up to volume determined by its design. The schemes of computational models are adduced on fig.1.

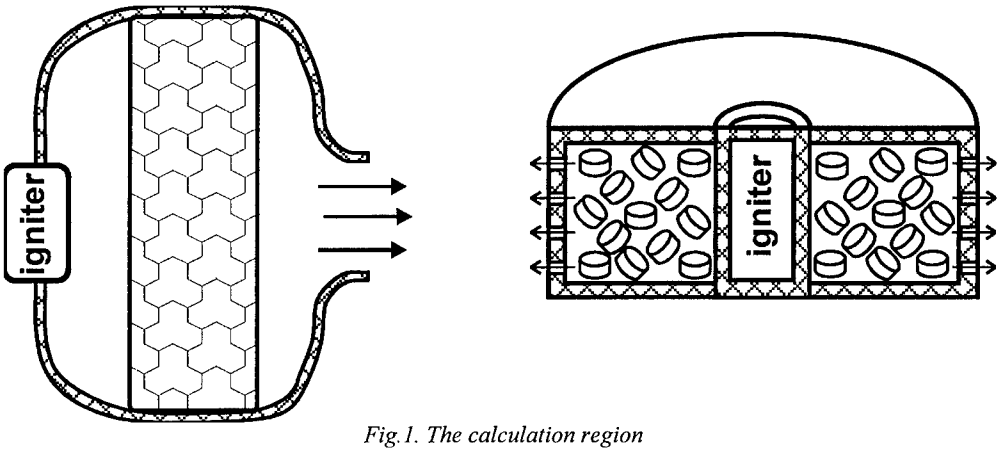

Fig.1. The calculation region

The mathematical model of the processes described above is based on the integral equations of the gasdynamics derived from the laws of mass, momentum and energy conservation. The thermodynamics of the gas mixture in the igniter and in the air bag is described by averaged parameters. The gasdynamics in the gas generator combustion chamber – within the framework of the one-dimensional, two-dimensional or average descriptions of the characteristics changes [2,3].

The thermodynamics of the gas mixture in the igniter (indestructible perforated casing) is described by averaged parameters. In this case, the mathematical model describing the variation of gas dynamic parameters in the volume of the igniter casing is a system of lumped or non-dimensional dif-

ferential equations for interior free volume, W. It is also assumed that the entire surface, $\Im$, of the igniter grains is instantaneously ignited and that the perforated casing prevents the escape of these grains.

The system of equations for the conservation of mass and energy and for variation in the free interior volume in the igniter then becomes:

$$\begin{aligned}
&\frac{d}{dt}(\rho \cdot W) = \sum_{i=1}^{\Im}(1 - z_{vi}) \cdot M_i \; - \; M_*, \\
&\frac{d}{dt}(\rho \cdot R \cdot W) = \sum_{i=1}^{\Im}(1 - z_{vi}) \cdot R_i \cdot M_i \; - \; R \cdot M_*, \\
&\frac{d}{dt}(\rho \cdot C_p \cdot W) = \sum_{i=1}^{\Im}(1 - z_{vi}) \cdot C_{pi} \cdot M_i \; - \; C_p \cdot M_*, \qquad (1) \\
&\frac{d}{dt}\left(\frac{p \cdot W}{\gamma - 1}\right) = \sum_{i=1}^{\Im}(1 - z_{vi}) \cdot C_{pi} \cdot T_{pi} \cdot M_i \; - \; \frac{1}{\gamma - 1} \cdot \frac{p}{\rho} \cdot M_*, \\
&\frac{dW}{dt} = -\sum_{i=1}^{\Im} \frac{d\omega_i}{dt}, \qquad M_i = -\rho_{oi} \frac{d\omega_i}{dt}, \qquad i = 1,2,\ldots,\Im.
\end{aligned}$$

Here t – time;

p, ρ – pressure and density;

R, , γ – gas "constant" and adiabatic index (ratio of specific heats);

C_p, T_p – specific heat of gas components or mixture and isobaric combustion temperature;

z_v – portion of condensed phase in combustion products.

The gas flow, $M*$, through the perforation holes is calculated by the familiar quasi – stationary equations through external (in the gas generator chamber) pressure [4]. The instantaneous volume of the pyrotechnic grains depends on the flame depth ($m_o/\rho_o \geq \omega \geq 0$, m_O, ρ_O – mass and powder density) and is the function of the grain shape. For a wide spectrum of shapes, the relationship between the instantaneous volume of these grains, ω, and their sizes is very simple

$$\omega_i = \frac{m_{oi}}{\rho_{oi}} \cdot \frac{\prod_{j=1}^{3}(e_i^j - e_i)}{\prod_{j=1}^{3} e_i^j}, \qquad (2)$$

where e_{ij} $(j=1,2,3)$ is the initial geometric characteristic features of the i-grain.

The variation of typical sizes of a grain as a result of burning is described through the burn rate and depth, u_g, e_i, is defined by the equations

$$\frac{de_i}{dt} = u_{gi}, \qquad i = 1,\ldots,\Im. \qquad (3)$$

The mathematical model of the processes in the combustion chamber of gas generator is based on the integral equations of the gas dynamics derived from the laws of mass, momentum, and energy conservation. Additional special equations define the thermal and physical properties of the multicomponent combustion products from the igniter charge and the air that initially fills the chamber. This system of equations is applied to a reference volume, V, bounded by a closed surface comprised of both gas-permeable (A) and gas-impermeable (S) materials. Heat and mass are exchanged between gas flow and gas generator elements. The change in the mass, momentum and energy in the control volume is connected through volume interactions, the influence of the external surroundings on every of the mentioned quantities, and their transfer through A. This system of conservation equations is written below in the integral form with a generalized co-ordinate system.

$$\frac{\partial}{\partial t}\int_V \rho dV + \int_V \rho \cdot N dA = \int_S \sum_{j=1}^{L} M_j dS,$$

$$\frac{\partial}{\partial t}\int_V \rho \cdot \mathbf{u} dV + \int_V \mathbf{\Pi} dA + \int_S \mathbf{\Pi} dS + \int_S \rho \cdot \mathbf{f} dS = 0,$$

$$\frac{\partial}{\partial t}\int_V E dV + \int_V (E+p)\cdot N dA + \int_S q dS = \int_S \sum_{j=1}^{L} H_j \cdot M_j dS, \qquad (4)$$

$$\frac{\partial}{\partial t}\int_V \rho \cdot R dV + \int_V \rho \cdot R \cdot N dA = \int_S \sum_{j=1}^{L} R_j \cdot M_j dS,$$

$$\frac{\partial}{\partial t}\int_V \rho \cdot C_p dV + \int_V \rho \cdot C_p \cdot N dA = \int_S \sum_{j=1}^{L} C_{p_j} \cdot M_j dS.,$$

$$E = \frac{p}{\gamma - 1} + \frac{\rho \cdot |\mathbf{u}|^2}{2},$$

where $\boldsymbol{u}$ - vector of velocity;

N - normal velocity to the surface determined by scalar product normal to a surface of a vector of the velocity **u** on the unit external vector **n**, $N=(\boldsymbol{u}, \boldsymbol{n})$;

$\boldsymbol{\Pi}$ - flow of impulse, $P \cdot \mathbf{n} + p \cdot \mathbf{u} \cdot N$;

M - mass supply density;

H - enthalpy of flow products;

$\boldsymbol{f}$ - friction stress;

q - heat flux density.

For granular charges of sizes of the area A, free for flow of gases, are determined in volumetric gravimetric density, and the surface S is considered as total for elementary volume V. Time histories of these parameters, and also mass supply and the enthalpy in volume are determined on ratios which are similar used for igniter in the supposition, that granules of propellant are immobilised. For a porous charge of solid propellant the set of equations (4) is supplemented by a heat conduction equation circumscribing change of charge temperature owing to a filtration through it of combustion products. The particular values of sizes of surfaces A and S are determined by a porosity coefficient.

The ignition time is calculated in terms of the condensed – phase ignition theory developed by V.Vilyunov[5]. The mathematical model of a problem of ignition of condensed substance – hard fuel – actuates a heat conduction equation with allowance for of exothermal responses and equation of a chemical kinetics [5].

The set of equations circumscribing change of averaged thermodynamic parameters in a cavity of air bag (volume V), has a kind:

$$\frac{d}{dt}(\rho \cdot V) = M^+ - M^-,$$

$$\frac{d}{dt}(\rho \cdot R \cdot V) = M^+ \cdot R^+ - M^- \cdot R,$$

$$\frac{d}{dt}(\rho \cdot C_p \cdot V) = M^+ \cdot C_p^+ - M^- \cdot C_p, \qquad (5)$$

$$\frac{d}{dt}\left(\frac{p \cdot V}{\gamma - 1}\right) = M^+ \cdot H^+ - M^- \cdot \frac{\gamma}{\gamma - 1} \cdot \frac{p}{\rho} - Q_\Sigma.$$

Here M^{-} – density of the consumption from volume stipulated by diffusion of gas through an envelope of air bag; the parameters with a superscript "+" mark total supplies in volume V mass, enthalpy and properties of gas R and C_p from the gas generator or cool unit.

The total thermal losses Q_{Σ} were determined by means of the solution of a one – dimensional heat conduction equation for a material of an envelope of an air bag.

The essential specificity for solution is represented by calculation of change of current volume of an air bag V. Thus three stages of process are considered:

- before reaching a rupture pressure of a container envelope volume is considered constant and equal initial;
- after a gap the change of air bag volume up to its design value is calculated at constant value of pressure equal atmospheric;
- after a full deployment of an air bag on base of the previously solved thermos strength problem of an elastic envelope change of volume (the deformation of air bag) is calculated on a current pressure differential between the chamber of an air bag and atmosphere.

Appropriate initial and boundary conditions close the mathematical statement of a problem. The systems (1) – (3), (5) of ordinary differential equations circumscribing change of averaged parameters, are solved by the fourth order accuracy schemes; the 3D flow of gas (4) is calculated by a modified S.Godunov method [6]. For implementation of an equation of ignition the adapted computational grid varying depending on conditions of a warm – up [7] is used.

On submitted model the numerical researches were made. In computational versions the parameters of charges were selected so that the identical dynamic characteristics of process of pressurization of an air bag were provided approximately. On fig.2 the relations «pressure – time» for charges of the various shape of granules are adduced at an identical initial surface of combustion:

1 – Spherical granules in diameter 5mm;

2 – Tablets of diameter 5.8mm also height 2.9mm;

3 – Tablet of diameter 5.7mm with a central hole 1.4mm and height 2.8mm.

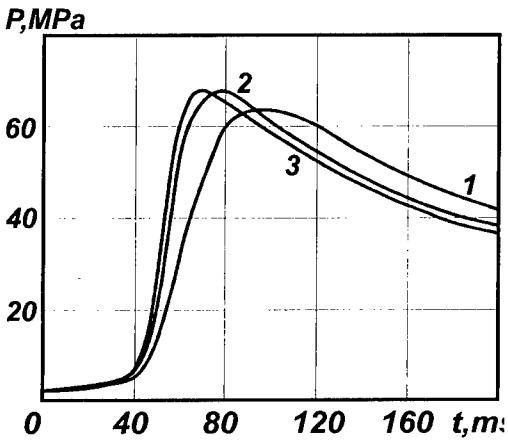

Fig.2The dependencies «pressure – time» for charges of the various shape of granules

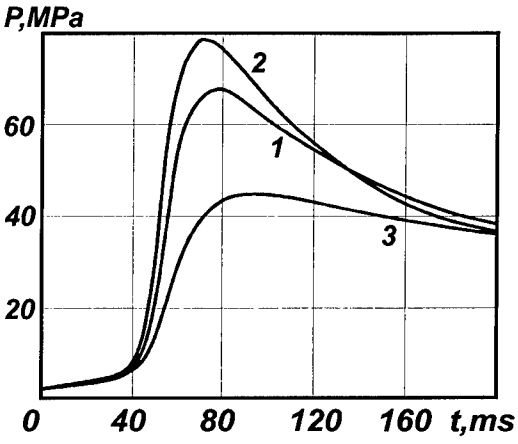

Fig.3. Dependence pressure from initial volumes of the combustion chamber

The physics – chemical characteristics of compounds and combustion products were selected close to parameters solid rocket propellants. The maximum difference of curves on a quasi – stationary period does not exceed 9%; the much greater difference is observed on a segment at high gradient rise of pressure, that is stipulated by difference of moment of a beginning of ignition. On fig.3 for granules of a charge of tablet shape are adduced curves «pressure – time» on a segment of rise for initial parameters of gas generator (curve 1); for reduced on 20% (curve of 2) and double initial volumes of the combustion chamber(curve of 3). The difference of curves is stipulated, as well as in the previous case, difference of times of a beginning of ignition.

On fig.4 for a porous charge with the characteristics taken from paper[1], the relations of pressure profile in various instants on relative length of a charge are adduced. The maximum pressure differential will be realized at t≈70ms and makes 3.5MPa. The relation of pressure to time in a head part of gas generator for the given design is adduced on fig.5.

From the analysis of results it is visible, that at qualitative conformity of process of pressurization of a cavity by combustion products of granular and porous propellant charges in the last necessary effect is reached at a much lower level of pressure in the gas generator, though in design it will have, apparently, large sizes for maintenance adequate mass supply despite of the order higher rates of linear burning of propellant.

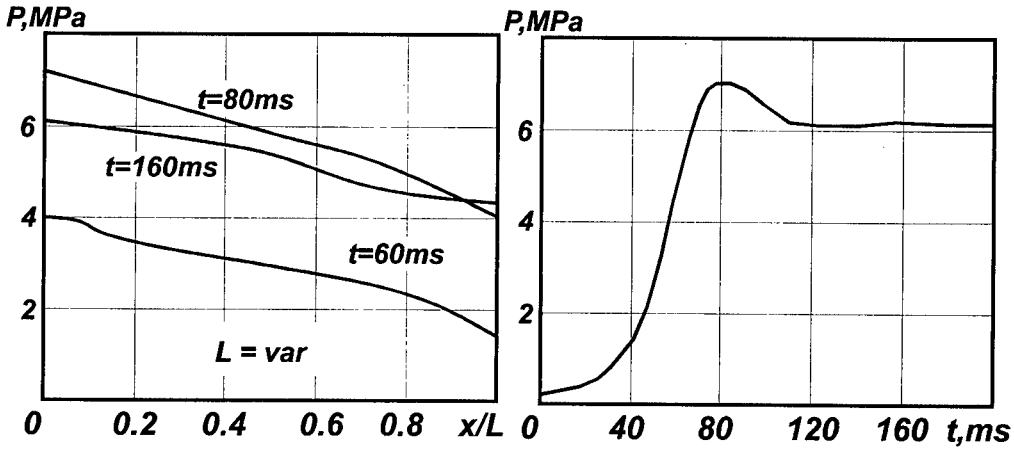

Fig.4. The dependencies of pressure profile in various instants on relative length of a charge

Fig.5. The dependence of pressure to time in a head part of gas generator

In summary we shall mark, that the given problem should is put and to be decided as optimization, when for a specific first passage time of required pressure in air bag the necessary relation of the mass flow rate characteristics of the gas generator to time in conditions of limitations (stipulated

strength parameters of air bag materials) on a gradient and dynamics of rise of pressure in an air bag, it final value is determined.

References

1. V.Shandakov, V.Puzanov, V.Komarov, V.Borochkin The method of low temperature generating in solid gas generators / Fizika goreniya i vzryva, 1999, V.35, No.4.
2. S.S.Bondarchuk, O.N.Kondratova, A.B.Vorozhtsov. Propellant conversion use for supercharge elastic cases / The third International Symposium "Application of the Conversion Research Results for International Co-operation" (SIBCONVERS' 99). Proceedings. - Tomsk: Tomsk State University of Control Systems and Radioelectronics. – Pp.264.
3. Bondarchuk S.S., Vorozhtsov A.B., Kozlov E.A., Feshchenko Y.V. Analysis of Multidimensional and Two-Phase Flows in Solid-Rocket Motors // Journal of Propulsion and Power, Vol.11, No.4, July-August 1995. –P .593-599.
4. Orlov B.V., Mazing G.G. Thermodynamic and ballistic fundamentals of designing SPRM. - Mashinostroenie, Moscow, 1979. –392c.
5. Vilyunov V.N., and Zarko V.E. Ignition of Solids. - Elsevier, Amsterdam, 1989.
6. Godunov, S.K. (ed), Numerical Solution of Multidimensional Problems of Gas Dynamics, Nauka, Moscow, 1982.
7. Borovskoy, I.G., Bondarchuk, S.S., Kozlov E.A., and Vilunov, V.N. Solution of the Problem of Condensed System Ignition Based on a Difference Scheme with Time – Dependent Grid / Fizika Gorenia i Vzryva, Vol. 22, No. 3, 1986, –pp.14-19.

Gasgeneratorentwicklung für Feuerlöschanwendungen

Neutz, J.; Schmid, H.; Schröter, D.; Weiser, V.

Fraunhofer Institut für Chemische Technologie, Joseph von Fraunhofer Strasse 7, D-76327 Pfinztal

Abstract:

The development of gasgenerators for fire extinguishing purpose is presented exemplary with two mixtures. The results of the thermogravimetric investigations, the interior ballistic characterisation in the optical bomb and the tests in the burning test device are presented as an selection of the multitude of characterisation methods. The decomposition kinetics of the used fuels Guanidinium - Aminotetrazolat (GA) and 5,5´ - Guanidinium - Azotetrazolat (GZT) and of the oxidizer strontiumnitrate are evaluated and presented. The measured burning rates are presented and evaluated with Vieille's law. Results of the extinguishing tests are temperature measurements in the gas jet, gas concentrations and the evaluation of the extinuishing process done with isopropanol flames.

Kurzfassung:

Es wird anhand von zwei ausgewählten Mischungen exemplarisch die Entwicklung von Gasgeneratoren für die Feuerlöschung dargestellt. Aus der Vielzahl von Untersuchungsmethoden werden die Ergebnisse der thermogravimetrischen Untersuchungen, der innenballistischen Charakterisierung in der optischen Bombe und der Löschversuche im Brandstand dargestellt. Die Zersetzungskinetik der eingesetzten Brennstoffe Guanidinium - Aminotetrazolat (GA) und 5,5´ - Guanidinium - Azotetrazolat (GZT) und des Oxidators Strontiumnitrat wird ausgewertet und dargestellt. Die gemessenen Abbrandraten werden vorgestellt und mit Hilfe des Gesetzes von Vieille ausgewertet. Bei den Löschversuchen im Brandstand werden die Ergebnisse der Temperaturmessung im Gasstrahl, die zeitliche Entwicklung der Konzentrationen der einzelnen Gasspezies und der Löschvorgang bei Isopropanolflammen vorgestellt.

1 Einleitung:

Das Verbot von Halonen als Feuerlöschmedien hat einen starken Bedarf für einfach zu handhabende, gasförmige Feuerlöschsysteme ausgelöst. Die bisher verwendeten Ersatzsysteme,

wie z. B. CO_2 oder INERGEN, zeichnen sich durch systeminhärente Nachteile aus. Als Beispiel dafür wäre die Speicherung der Gase unter Druck zu nennen. Diese Systeme müssen regelmäßig geprüft und gewartet werden und haben ohne Regelung keine zeitlich konstante Massenstromcharakteristik. Zusätzlich kommt bei der Verwendung von CO_2 die toxische Wirkung in geschlossenen Räumen hinzu.
Daraus resultierend wurde ein neues Konzept für Gasgeneratoren auf der Basis von stickstoffreichen Brennstoffen vorgeschlagen [1]. Im folgenden werden die zur Charakterisierung der Gasgeneratormischungen verwendeten Untersuchungsmethoden exemplarisch an drei Beispielen dargestellt.

2 Untersuchungsmethoden:

Eine Gliederung der zur Verfügung stehenden Untersuchungsmethoden bei der Gasgeneratorentwicklung ist in Abbildung 1 dargestellt. Die einzelnen Schritte werden aufeinanderfolgend oder parallel durchlaufen. Sollten die Ergebnisse aus einer der Charakterisierungsmethoden unzureichend sein, muss die Gasgeneratormischung abgeändert werden und der ganze Entwicklungszyklus oder Teile dessen wiederholt werden. Aus der Vielzahl an Untersuchungen wurden die thermograviemetrischen Untersuchungen, die innenballistische Charakterisierung in der optischen Bombe und der Prototypentest im Brandstand ausgewählt. Für die Versuche wurden die stickstoffreichen Brennstoffe Guanidinium 5,5´ Azotetrazolat (GZT) und Guanidinium Aminotetrazolat (GA), sowie Strontiumnitrat als Oxidator verwendet.

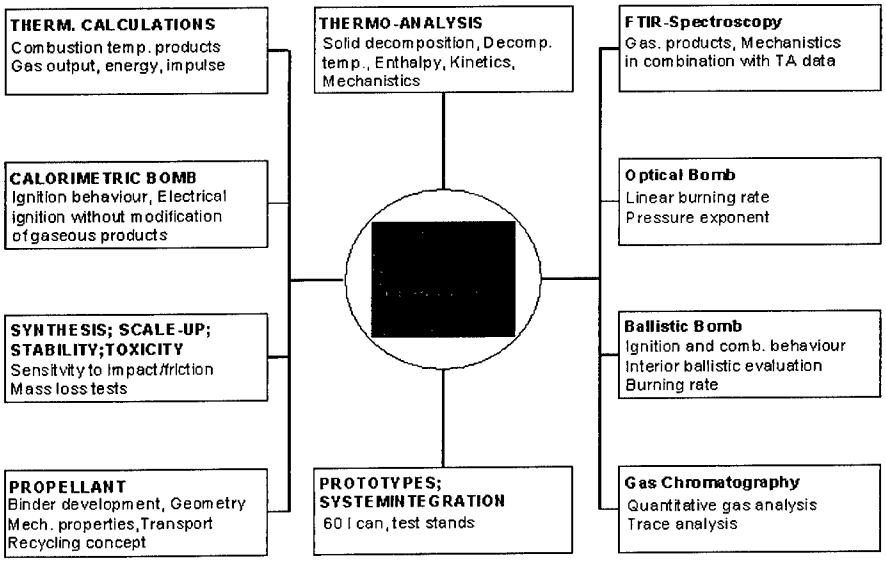

Abbildung 1: Übersicht über die Untersuchungsmethoden

2.1 Thermogravimetrische Untersuchungen

Die Untersuchungen an der Thermowaage dienen der Ermittlung der Zersetzungstemperatur und der Zersetzungskinetik. Sie wurden mit einem HI-RES TGA 2950 Thermogravimetric Analyzer der Firma TA Instruments durchgeführt und für die untersuchten Substanzen sind die Kurven der Massenverluste über die Temperatur bei unterschiedlichen Heizraten in den Abbildungen 2 bis 4 dargestellt. Die Auswertung der Messdaten erfolgte mit dem Softwarepaket KINETICS der Firma Netzsch. Es ermöglicht die multiple nicht lineare Regression mehrer Kurven mit bis zu vier Kinetikstufen.

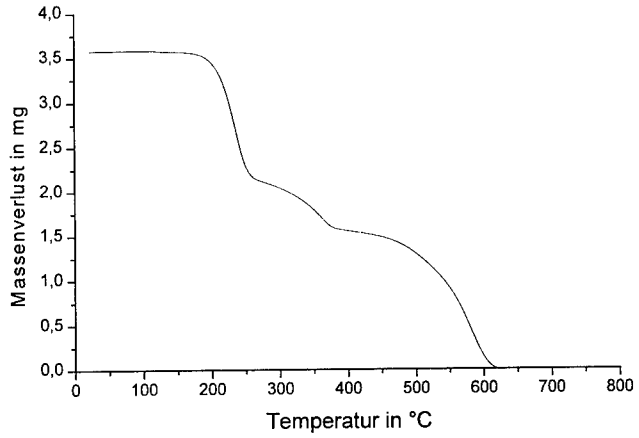

Abbildung 2: Zersetzung von GA bei einer Heizrate von 5 K/min

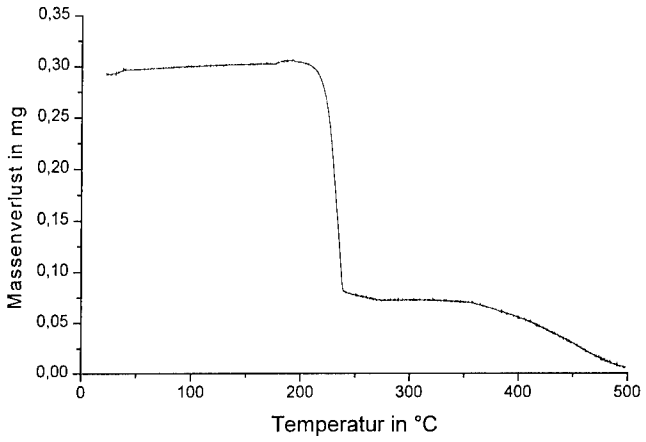

Abbildung 3: Zersetzung von GZT bei einer Heizrate von 1K/min

Für die Zersetzung von GA wurde eine 3 Stufen Kinetik angesetzt, wobei die erste und dritte Reaktion als erster Ordnung und die zweite Reaktion als n-ter Ordnung angenommen wurde. Die Ergebnisse stellen sich für die erste Reaktion folgendermaßen dar. Der Logarithmus des Vorfaktors beträgt 9,96 1/s und die Aktivierungsenergie 119,64 kJ/mol. Für die zweite Reaktion ergibt sich eine Reaktionsordnung von 1,66, ein Logarithmus des Vorfaktors von 5,27 1/s und eine Aktivierungsenergie von 93,04 kJ/mol. Der logarithmierte Vorfaktor der dritten Reaktion beträgt 6,75 1/s und die Aktivierungsenergie 152,02 kJ/mol.
Die Auswertung der Zersetzung von GZT ergab eine einfache Reaktion in erster Ordnung. Der Logarithmus des Vorfaktors beträgt 34,12 und die Aktivierungsenergie 355,28 kJ/mol. Der Korrelationskoeffizient der Anpassung ist mit 0,999654 sehr gut. Nur im unteren Bereich der Kurve weicht die Simulation von den Messwerten ab. Dies liegt an der Überlagerung mit der einsetzenden Pyrolysereaktion, die zur Vereinfachung der Kinetik bei dieser Anpassung vernachlässigt wurde.
Die Kinetik der Zersetzung von Strontiumnitrat wird durch eine einstufige Reaktion mit zweidimensionaler Grenzflächenreaktion beschrieben. Der Logarithmus des Vorfaktors beträgt 11,49 und die Aktivierungsenergie 239,14 kJ/mol. Auch hier wurde zur Vereinfachung der kinetischen Auswertung die einsetzende Pyrolysereaktion vernachlässigt.

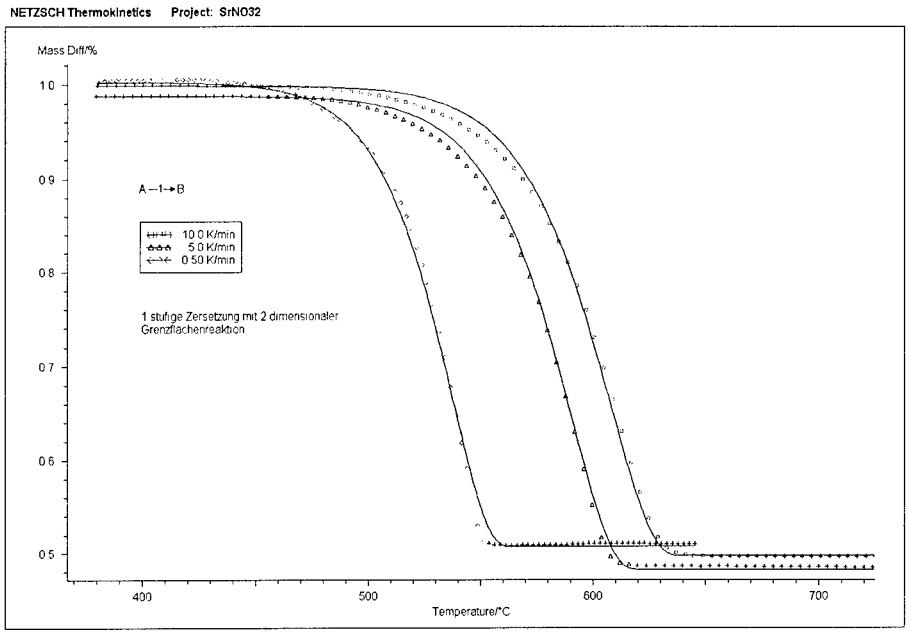

Abbildung 4: Zersetzung von Strontiumnitrat bei Heizraten von 0,5, 5 und 10 K/min

2.2 Untersuchungen in der optischen Bombe

Die optische Bombe ermöglicht die direkte Beobachtung und Untersuchung des Abbrandverhaltens eines Strands bis zu einem Druck von 150 bar. Dabei besteht die Möglichkeit gleichzeitig zwei Messmethoden einzusetzen, wobei in der Regel die Messung der Abbrandraten mit Hilfe einer CCD Kamera und die Charakterisierung der Spezies in der Reaktionszone mit Hilfe eines Emissionsfilterradspektrometers erfolgt.

Die isobare Messung der Abbrandrate basiert auf der Auswertung eines mit Hilfe einer CCD - Kamera aufgenommenen digitalen Films. Dabei werden zunächst die Lichtintensitäten der einzelnen Bilder integral verrechnet. Mit Hilfe eines vorher aufgenommen Kalibriergitters und der verwendeten Aufnahmefrequenz kann aus dem Verlauf der Lichtintensitäten die Abbrandgeschwindigkeit berechnet werden. Bei den verwendeten Mischungen kam es infolge der schlackebildenden Eigenschaft des Strontiumnitrats zu Schwierigkeiten bei der Auswertung, da Schlacketropfen zum einen durch seitliches Herabfließen den Strand auf der ganzen Länge seitlich anzündeten oder zum anderen beim Herabfallen durch die hohe Lichtintensität den Auswertungsalgorithmus teilweise störten, da kein lokales Intensitätsmaximum gefunden wurde. Ein Bildsequenz, die den Vorgang verdeutlicht, ist in Abbildung 5 dargestellt. Dort wird deutlich, wie sich der Schlacketropfen langsam aufbaut und anschließend herabtropft.

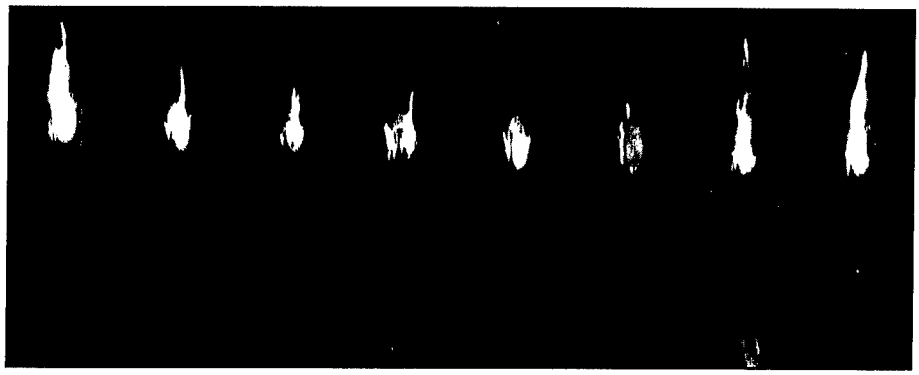

Abbildung 5: Ablösung eines Schlacketropfens von der Strandoberfläche

Für die beiden vorgestellten Mischungen wurden die Abbrandraten bei 5, 10, 20, 40 und 70 bar bestimmt. Die Auswertung nach dem Gesetz von Vieille ergab für M1 (Abbildung 6) einen Vorfaktor von 0,43 mm/s und einen Exponentialfaktor von 0,73. Für M5 (Abbildung 7) ergab die Auswertung der Messwerte einen Vorfaktor von 0,42 mm/s und einen Exponentialfaktor von 0,85. Für die Anwendung im Bereich der Feuerlöschgasgeneratoren ist die Mischung M1 aufgrund der innenballistischen Daten besser geeignet, da hier ein konstanter Gasstrom über eine längere Zeit ($\approx$ 60 s) gefordert ist.

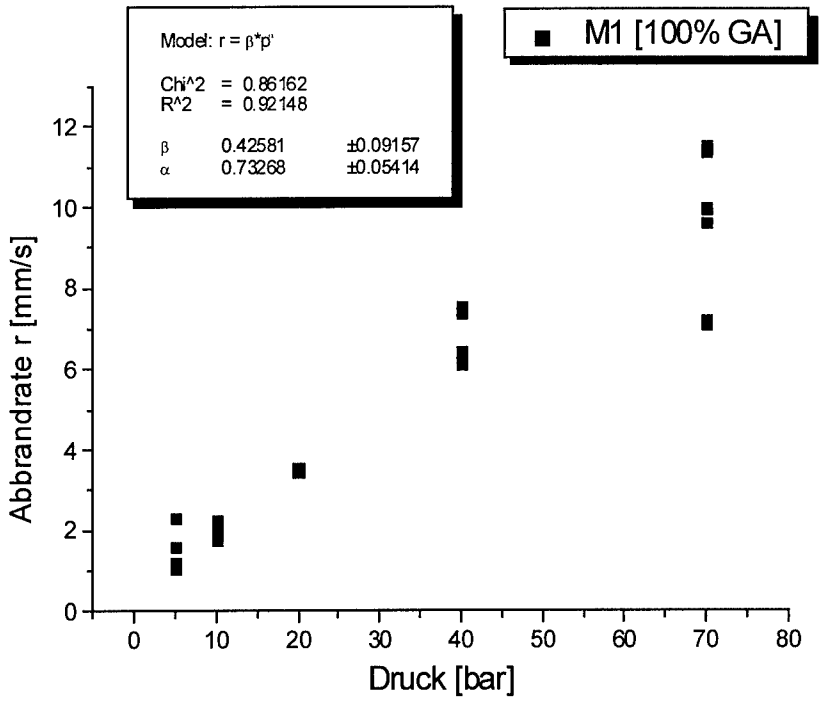

Abbildung 6: Auswertung der Abbranddaten von M1

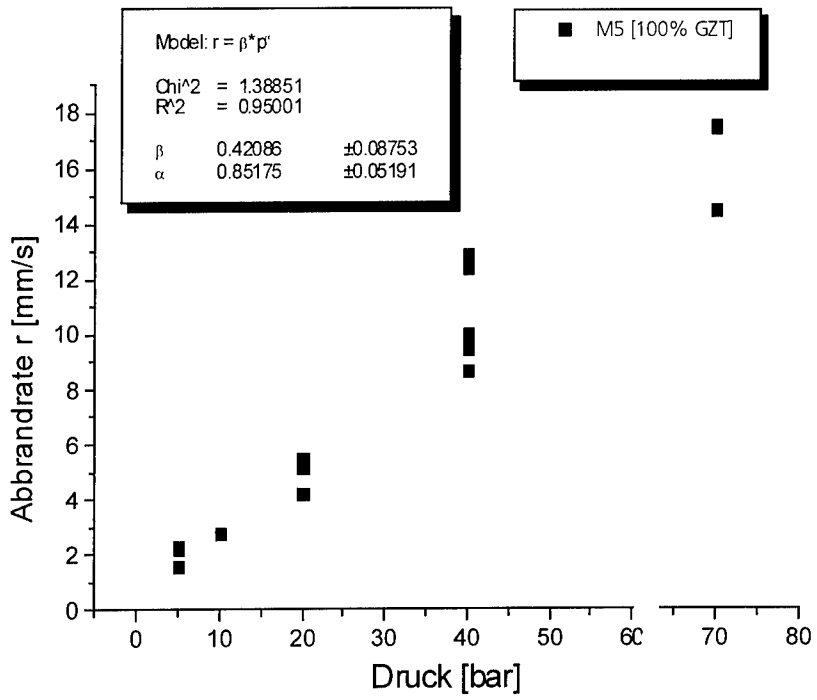

Abbildung 7: Auswertung der Abbranddaten von M5

2.3 Löschversuche am Brandstand

Die Löschversuche im Brandstand wurden bisher nur mit der Mischung M5 durchgeführt. Der Brandstand ist ein Stahlkubus mit einem Innenvolumen von 1,2 m³, der auf einer Seite durch Fenster optisch zugänglich ist.

Im Rahmen der Experimente wurden zunächst die Temperaturen im Austrittstrahl des Gasgenerators bestimmt, um zu entscheiden, ob ein zusätzliches Kühlmittel für die Rauchgase implementiert werden muss. Die Temperaturen wurden in einem Abstand von 10 cm (T2), 20 cm (T3), 40 cm (T4) mit Hilfe von Thermoelementen gemessen. Zusätzlich wurde die Außentemperatur des Gehäuses (T1) gemessen. Die Ergebnisse sind in Abbildung 8 dargestellt. Die maximale Temperatur im Gasstrahl betrug 192 °C in 10 cm Abstand und verringert sich auf etwa 130 °C in 40 cm Abstand. Die Gehäusetemperatur stieg auf 91 °C an.

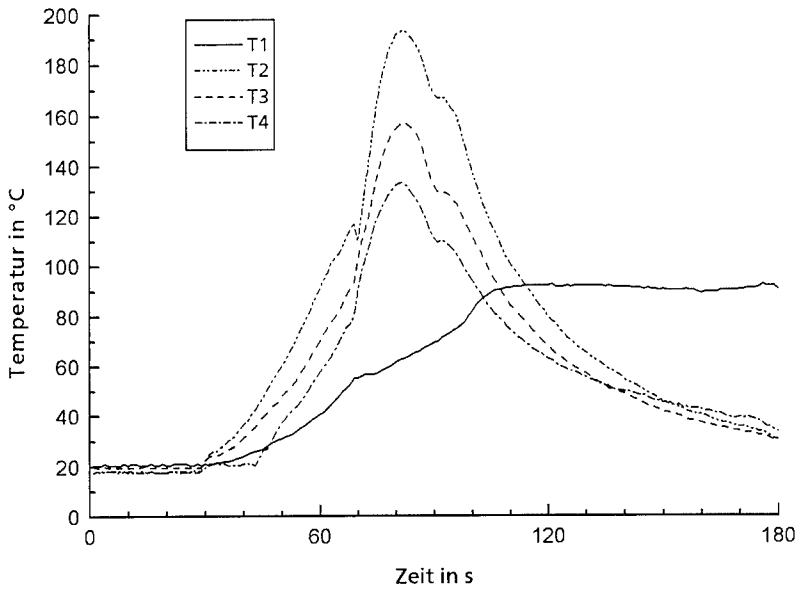

Abbildung 8: Temperatur des Gasstrahles in verschiedenen Abständen

Für die Untersuchung der Löschwirkung wurde eine Isopropanolflamme verwendet, wobei der Pooldurchmesser 300 mm betrug. Vor Zündung des Gasgenerators wurde eine Vorlaufzeit von 2 Minuten eingehalten, damit sich die Flamme voll ausbilden und stabilisieren konnte. Der Löschvorgang wurde mit Hilfe einer Videokamera dokumentiert (Abbildung 9). Bei allen drei Versuchen war der Löschvorgang nach etwa 30 Sekunden erfolgreich abgeschlossen und es kam zu keiner Rückzündung der schon gelöschten Flamme.

Die integralen Konzentrationen der einzelnen Gaskomponenten wurden im Abgaskamin des Brandstandes gemessen und sind in Abbildung 10 dargestellt. Auffallend sind die konstant hohen NO Konzentrationen von bis zu 9000 ppm und die zu Anfang bis zu 10 Vol% hohen CO Konzentrationen, die zum Ende des Löschvorgangs hin auf unter 1 Vol% abfallen. Ein Großteil der CO Konzentrationen wird zu Beginn von der Flamme selbst erzeugt und kann somit zur Kontrolle der Löscheffizienz genutzt werden. Zur genauen Klärung der NO Konzentrationen sind noch weitere Versuche ohne Poolflamme notwendig. Die alleinige Verursachung durch die Gase des Gasgenerators ist anzuzweifeln.

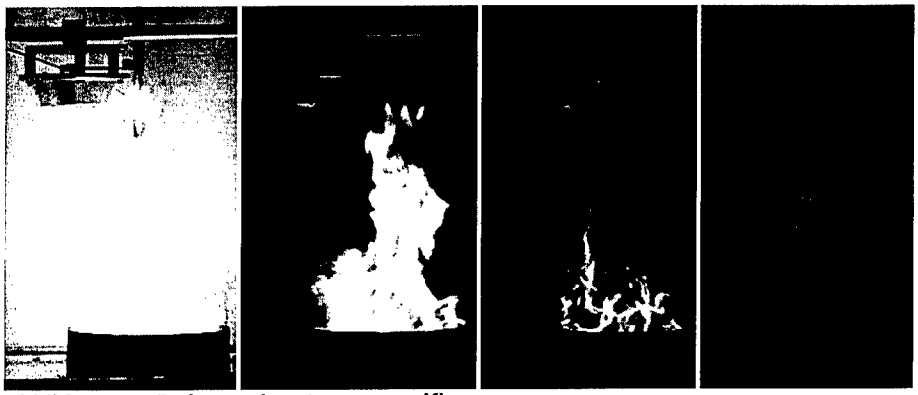

Abbildung 9: Löschung einer Isopropanolflamme

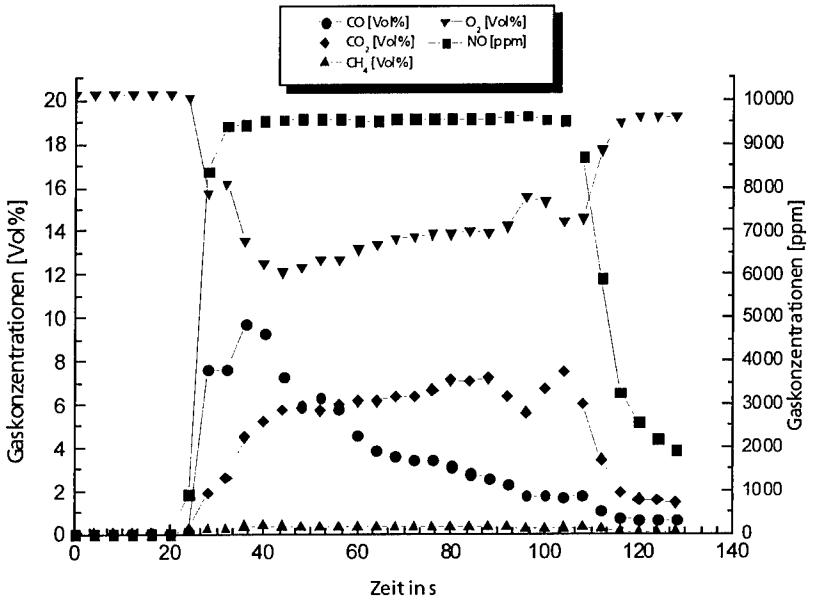

Abbildung 10: Verlauf der Gesamtkonzentrationen im Brandstand

3 Zusammenfassung:

Die thermogravimetrischen Untersuchungen ergeben für GZT eine einstufige Zersetzungskinetik (1. Ordnung), für GA eine dreistufige Zersetzungskinetik (1.Ordnung, n - ter Ordnung, 1.Ordnung) und für Strontiumnitrat eine zweistufige Zersetzungskinetik, wobei hier nur die erste Stufe (1.Ordnung) betrachtet wurde. Die Ergebnisse stimmen mit den Messwerten auch bei der , Verwendung mehrerer Heizraten gut überein.

Die innenballistische Charakterisierung der beiden Mischungen in der optischen Bombe ergab für die Mischungen M1 und M5 einen ähnlichen präexponentiellen Faktor von etwa 0,42 mm/s und für M1 einen Druckexponenten von 0,73 und für M5 einen Druckexponenten von 0,85. Der Unterschied in den Druckexponenten lässt sich durch das unterschiedliche Zersetzungsverhalten der beiden Brennstoffe erklären. GA hat durch seine dreistufige Zersetzung mit breitem Temperaturintervall einen verlangsamenden Einfluss auf die Umsetzungsraten in der Abbrandzone und ist somit aus innenballistischer Sicht für die Anwendung als Brennstoff für Feuerlöschgasgeneratoren besser geeignet.

Die Untersuchungen im Brandstand ergaben einen im Verhältnis zur Isopropanolflamme relativ kalten Gasstrom. Die Erwärmung des Gehäuses muss je nach Anwendungsfall durch Zusatzmaßnahmen begrenzt werden, um eine Entzündung der Umgebung zu verhindern. Die globalen Gaskonzentrationen zeigten einen relativ hohen Anteil an Stickoxiden, der über die gesamte Abbrandzeit des Gasgenerators konstant blieb. Ob die gesamte Menge an NO durch den Gasgenerator erzeugt wird muss durch zusätzliche Untersuchen geklärt werden. Die drei Löschversuche waren in allen Fällen erfolgreich und es wurde eine Rückzündung des noch heißen Brennstoffes verhindert.

DIE NACHPRÜFUNG DER I-BRENNER METHODE FÜR DIE ABSCHÄTZUNG DER VERBRENNUNGSINSTABILITÄT IN FESTSTOFFRAKETEN

Kiyoshi Matsui
Daicel Chemical Industries, Ltd., Harima Plant, Ibogawa-cho, Ibo-gun,
Hyogo-ken, 671-1665 Japan

Abstract

Iwama invented a method for the investigation of combustion instability of the solid propellant rockets (the I-burner method, ICT Conference Proceedings, 1994). He reported that pressure oscillation can be excited in a thcik-walled rocket (the I-burner) by the application of a propellant grain having a particular perforation and of soft ignition. This method is experimentally studied. Two I-burners are used: one has a case 1208 mm long (the short I-burner), and the other 2240 mm (the long I-burner). The grain (817 mm long, 65 mm in diameter) is perforated with a diameter of 20 mm (from the fore end, 657 mm long) and of 42 mm (successively, 160 mm long). First, occurrence of pressure oscillation is investigated for two kinds of ordinary HTPB-composite-propellant: one contains aluminum powder, and the other not. Pressure oscillation is always excited for the aluminized propellant, but never, in 30 experiments, for the non-aluminized propellant. Second, the characteristics of pressure oscillation are investigated. The oscillation is longitudinal and acoustic; the frequencies are those for the acoustic oscillation occurring in a tube with both ends rigidly closed. The oscillation occurs in two successive periods. In the first period the fundamental wave with comparatively small amplitudes prevails; in the second the waves of higher orders coexist and the amplitudes are large. An amplitude of 2.2 MPa is observed in the short I-burner at a chamber pressure of 22 MPa. Last, it is attempted to change the oscillation characteristics by attachment of variously shaped plates at the fore end of the I-burner. For example, it is found that attachment of a plate, whose shape is designed so as to scatter the incident waves, perfectly suppresses the pressure oscillation.

(English title: A Study of the I-Burner Method for the Investigation of the Combustion Instability of Solid Propellant Rockets)

1. EINLEITUNG

Wenn man eine Rakete entwickelt, muß man die Verbrennungsstabilität der Rakete abschätzen. Für die Abschätzung der Verbrennungsstabilität der Feststoffraketen oder deren Treibsätze gibt es einige Methoden. Strand und Brown haben sechs Methoden angeführt [1]: T-Brenner (T-burner), Rotierende Absperrvorrichtung (rotating-valve apparatus), Impedanzrohr (impedance tube), Düsenmodulation-Nachabklingen Brenner (modulated throat-acoustic damping burner), Mikrowelle Brenner (microwave burner), und Magnetischer Durchflußmesser (magnetic flowmeter). Jede der Methoden hat eigentümliche Stärke. Leider lassen sich diese Methoden leicht benutzen, weil besondere Geräte oder spezielle Techniken gebraucht werden. Zum Beispiel ist es nicht leicht, die Druckschwingung im T-Brenner zu erregen.

Iwama erdachte im Jahre 1994 eine neue Methode für die Äbschätzung der Verbrennungsinstabilität in Feststoffraketen; die Methode nannte er die I-Brenner Methode [1]. Man braucht keine spezielle Vorrichtung, um die Methode zu verwenden; die nötige Vorrichtung ist nur eine dickwadige, festgelegte Rakete. Druckschwingungen in der Rakete (dem I-Brenner) sollen durch die einfachen Verfahren erregt werden, und durch die Analyse der Druckschwingungen sollen wichtige Informationen über die Verbrennungsinstabilität des Treibstoffs oder des Raketensystems herausgezogen werden. Es wurde gedacht, daß die Methode ausführliche Prüfung wert ist. Deshalb haben wir die Methode experimentell eingehend nachgeprüft.

2. EXPERIMENTELLES

2.1 I-Brenner

Bild 1 zeigt den Aufbau unsres I-Brenners. Der I-Brenner ist nichts anderes als eine dickwandige Rakete. Zwei I-Brenner, die sich voneinander nur in der Länge des Gehäuses unterscheiden, wurden benutzt: ein Brenner hat die Gehäuselänge von 1208 mm (genannt der kurze I-Brenner), und der andere die von 2240 mm (der lange I-Brenner). Für Druckaufnahme ist ein Loch (8 mm im Durchmesser) in der Mitte der internen Fläche des Vorderschlusses gebohrt, und zwei Löcher (6 mm im Durchmesser, jedes auf der anderen Seite des Zentrums) an der internen Wand des Hinterverschlusses.

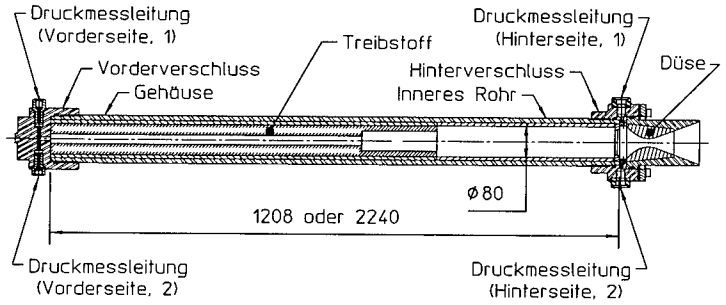

Bild 1. Aufbau des I-Brenners

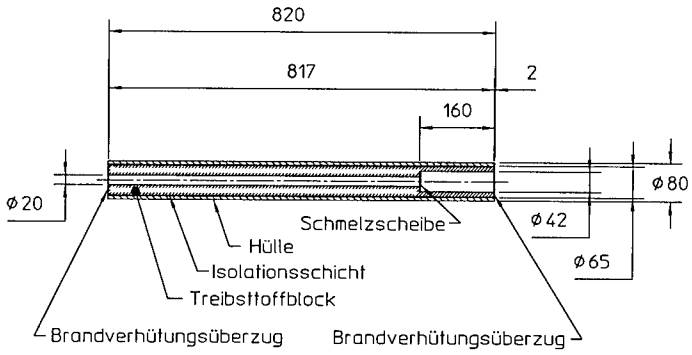

Bild 2. Einzelheiten des Treibstoffs

Die Einzelheiten des Treibstoffs sind in Bild 2 angegeben. Die Schemelzscheibe (aus Polykarbonat) ist 1 mm dick und hat in der Mitte ein Loch mit einem Durchmesser von 3 mm. Zwei Arten gewöhnliche Komposit-Festtreibstoffe wurden gebraucht: der eine enthält Aluminiumpulver (HTPB, 9,1%; AP, 69,8%; Al-Pulver, 17,9%; die andere, 3,2%), und der andere nicht (HTPB, 15,2%; AP, 79,6%; die andere, 5,2%).

2.2 Meßverfahren

Der Treibstoff wird von einem Stückchen Glut an seiner hinteren Bohrung sanft gezündet; ein kleiner Würfel Treibstoff, gezündet von einem erhitzten Nickelchromdraht, dient als die Glut. Darauf tritt die Druckschwingung in dem I-Brenner für den Aluminiumpulver enthaltenden Treibstoff auf. Die Schmelzscheibe soll zum Auftreten der Druckschwingung beitragen, indem sie erst die

Flammenverbreitung hindert und dann (beim Schmelzen) plötzliche Flammenverbreitung in die vordere Bohrung ermöglicht. Der Druck im Brenner wird an dem vorderen und dem hinteren Ende des Brenners von sowohl den Piezoelektrischen Druckmessern als auch den Dehnungsmeßstrefen-Druckmessern gemessen; siehe Bild 1. Der Druck wird auf einem Oszyllographen und in einem Datenregistrierapparat (Magnetband Typ) registriert. Das aufgenommene Druckzeichen wird mit einem FFT Analysator ausgewertet.

3. ERGEBNISSE

3.1 Auftreten der Druckschwingen

Wenn Aluminiumpulver enthaltenden Treibstoffe gebrannt wurden, traten immer die Druckschwingungen auf, deren Eigenschaften unten eingehend diskutiert werden. Wenn ein von Aluminiumpulver freier Treibstoff erst gebrannt wurde, konnte eine Druckschwingung nicht beobachtet werden. Iwama berichtete, daß die Druckschwingungen in dem I-Brenner leicht erregt werden. Deshalb ist das Auftreten der Druckschwingung für den von Aluminiumpulver freien Treibstoff natürlich zu erwarten. Wir wendeten deshalb einige Mittel an, um die Druckschwingung im I-Brenner zu erregen. Der kurze I-Brenner wurde dabei gebraucht. Erstens ließen wir den Verbrennungsdruck in dem Brenner (Brennkammerdruck) sich verändern. Zweitens änderten wir die Länge der hinteren Bohrung in dem Treibstoffblock. Drittens verwendeten wir dreistufig durchgebohrte Treibstoffblöcke. Diese letzten zwei Mittel wurden deshalb angenommen, weil geändertes Druckverhalten, das diese zwei Mittel verursachen, die Druckschwingung wohl erregegen mochte. Letztens addierten wir S_rCO_3 (0.5%, nach Gewicht) zu dem Treibstoff, weil solch ein Katalysator auch die Druckschwingung auslösen mochte. Insgesamt Dreißig Versuche wurden durchgefürt. Trotz all dieser Versuche trat keine Druckschwingung für den von Aluminiumpulver freien Treibstoff auf. Aus diesem Resultat läßt sich folgern, daß Druckschwingung in dem I-Brenner nicht immer geregt werden kann.

3.2 Druckschwingungen in dem kurzen I-Brenner

Bild 3 zeigt das Verhalten des Brennkammerdrucks bei einer Verbrennung. Der durchscnittliche Brennkammerdruck hat zwei lokale Maxima. Die Druckschwingungen fangen auf dem Wege der anfänglichen Kammerdruckzunahme an. Sie ereignen sich in zwei aufeinanderfolgenden, klar unterschiedbaren Zeitabschnitten.

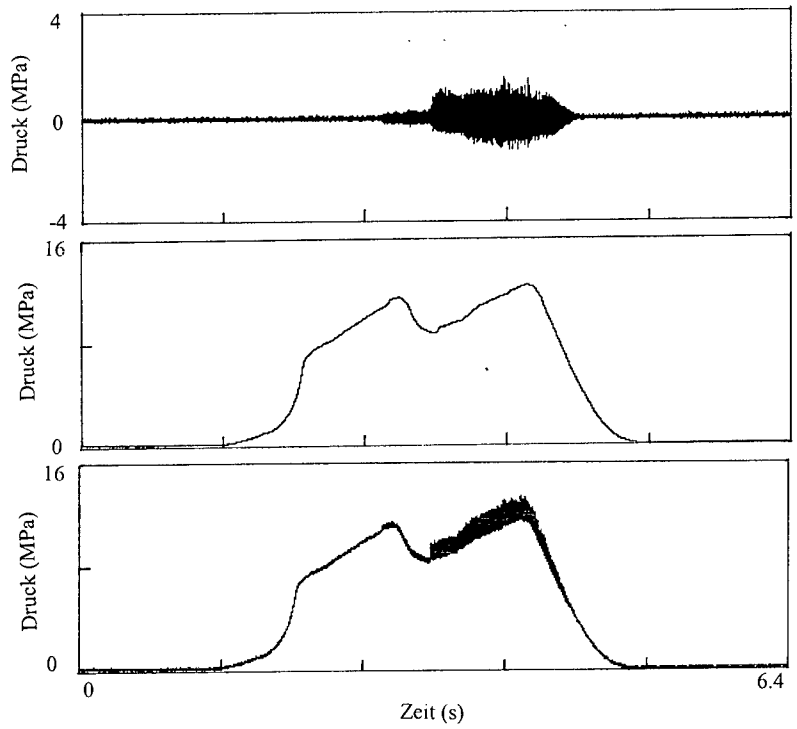

Bild 3. Druckverlauf in dem I-Brenner (höchster Kammerdruck von 11,8 MPa): überlagernder, schwingender Druck (oben), durchschnittlicher Kammerdruck (mitten), wirklicher Kammerdruck (unten)

In dem ersten Abschnitt sind die Druckamplituden klein, und in dem zweiten groß. Die in dem ersten Abschnitt auftretenden Wellenformen und das entsprechenden Frequenzspektrum sind in Bild 4 angegeben. Aus dem Spektrum ergibt sich, daß eine Welle mit der Freqenz von 400 Hz überwiegend ist; auch die Wellen von 800 Hz, 1200 Hz, und 1600 Hz sind auch vorhanden.

Die Formen der überwiegenden Welle, die zugleich an dem vorderen und dem hinteren Ende des Brenners aufgenommen wurden, sind in Bild 5 dargestellt. Die beiden Wellen haben gleiche Freqenz von 400 Hz, und deren Phasen verschieben sich einander ungefähr eine halben Periode. Daraus ergibt sich, daß die in dem I-Brenner

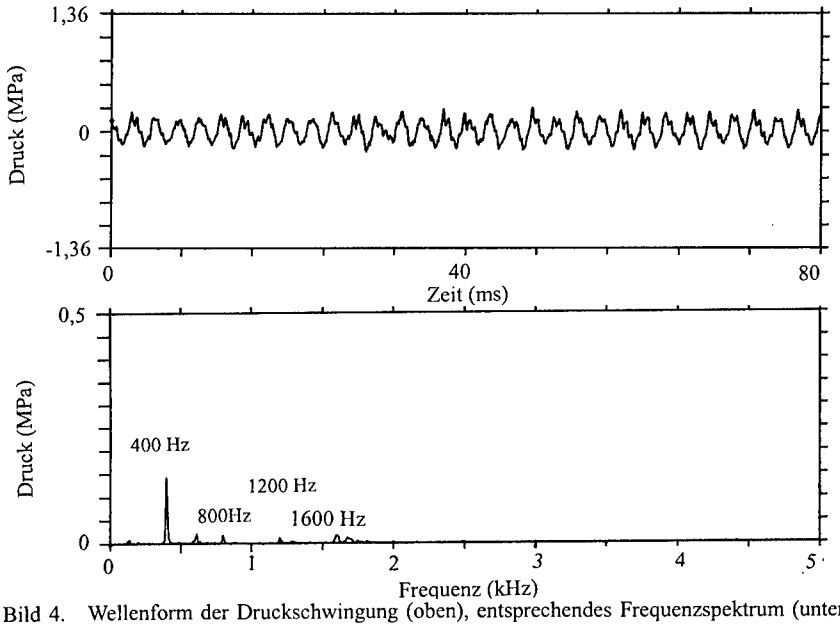

Bild 4. Wellenform der Druckschwingung (oben), entsprechendes Frequenzspektrum (unten) in dem ersten Zeitabschnitt (höchster Kammerdruck von 11,8 MPa)

auftretenden longitudinalen Wellen sind stehend und linear (akustisch); die Randbedingungen der Wellengleichung sind null Teilchenschnelle an den beiden Enden. Die Frequenzen f_n sind durch

$$f_n = nc/2l$$

gegeben, wobei c die Schallgeschwindigkeit, l die Kammerlänge, und n die Ordnungszahl bedeutet.

Die radialen oder tangentialen akustischen Wellen mögen in diesem zylindrischen I-Brenner auftreten; die Grundfrequenz der radialen Wellen wird auf 20,6 kHz geschätzt, und die der tangentialen auf 9,91 kHz, unter der Voraussetzung der Schallgeschwindikeit von 1100 m/s. Auftreten der radialen oder tangentialen Wellen wurde untersucht, indem die radialen und tangentialen Kammerdruckänderungen bewertet wurden. Der Kammerdruck wurde an dem Zentrum der inneren Seite des Vorderschlusses und an einer vom Zentrum radial 28 mm entfernten Stelle gemessen; zugleich wurde Kammerdruck an vier tangential 90 Grade entfernten Stellen am Rand des Hinterschlusses gemessen. Radiale oder tangentiale Wellen wurden nicht beobachtet.

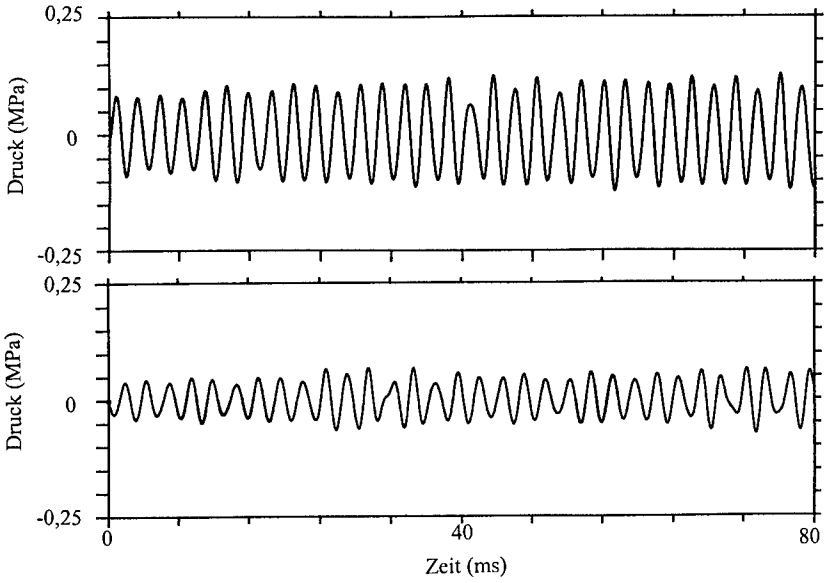

Bild 5. Wellenform der Druckschwingung (gefiltert, 400~600 Hz), aufgenommen an der Vorderseite (oben) und an der Hinterseite (unten) (höchster Kammerdruck von 11,8 MPa)

Bild 6 zeigt die Wellenformen und das entsprechende Freqenzspektrum in dem zweiten Zeitabschnitt der Druckschwingung. Die Amplituden sind bei weitem größer als die in dem ersten Abschnitt. Im Gegensatz zu den Wellen in dem ersten Abschnitt finden sich ziemlich starke Wellen der höheren Ordnungen; vergleiche dieses Spektrum mit dem in Bild 4. Die Grundfrequenz steigert sich von 400 Hz in dem ersten Abschnitt bis 450 Hz in diesem zweiten Abschnitt, vermutlich wegen des Steigens der durchschnittlichen Gastemperatur im Brennkammer (also des Steigens der Schallgeschwindikeit). Die höchsten Frequenzen der einzelnen Spektren sind immer nicht die ganzzahligen Vielfachen der Grundfrequenz (450 Hz), und die Formen der einzelnen Spektren nicht vollständige gleichschenklige Dreiecke. Dies bedeutet, daß die einzelnen Wellen nicht korrekt sinusförmig sind.

Bild 7 zeigt die Veränderung der Frequenzspektren im Verlauf der Zeit in dem zweiten

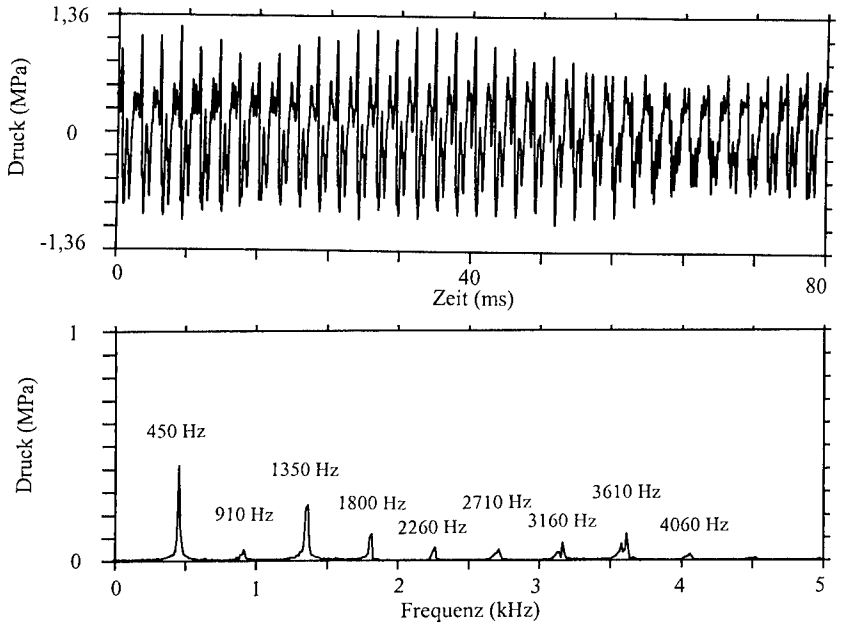

Bild 6. Wellenform der Druckschwingung (oben), entsprechendes Frequentspektrum (unten), in dem zweiten Zeitabschnitt (höchster Kammerdruck von 11,8 MPa)

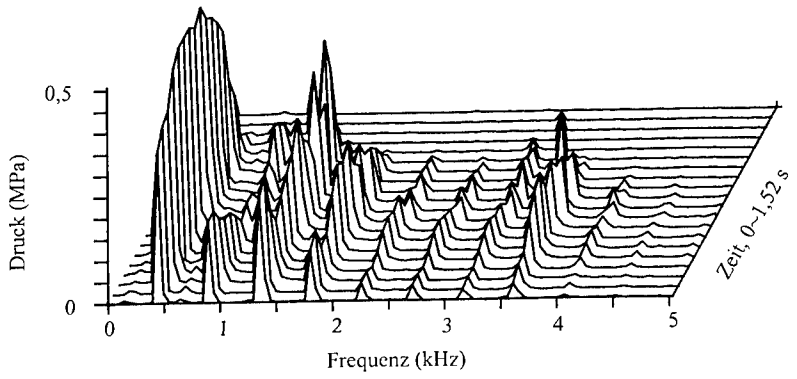

Bild 7. Veränderung des Frequenzspektrums im Verlauf der Zeit, in dem zweiten zweiten Zeitabschnitt (höchster Kammerdruck von 11,8 MPa)

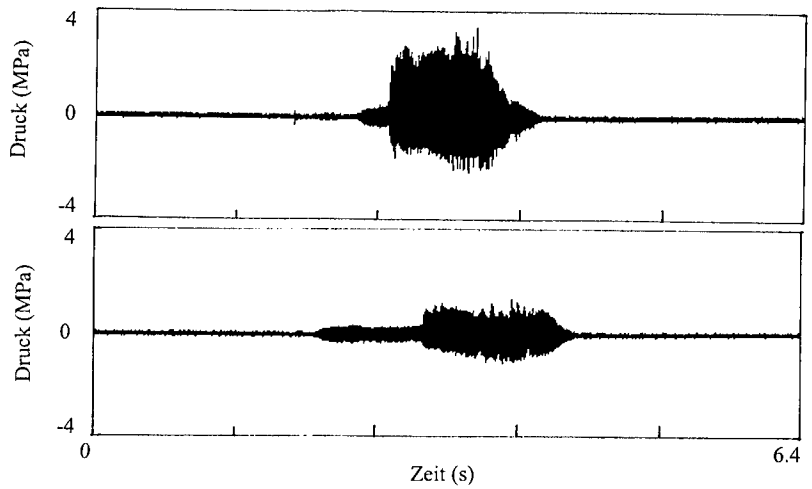

Bild 8. Schwingender Druck bei einem hohen Kammerdruck (oben, höchster Kammerdruck von 27,5 MPa) und bei einem niedrigen Kammerdruck (unten, höchster Kammerdruck von 9,81 MPa)

Zeitabschnitt der Druckschwingung. Daraus geht hervor, daß das Frequenzspektrum sich allmählich im Verlauf der Zeit ändert. Zum Beispiel ist die Intenstät der Welle der zweiten Ordnung in Bild 6 äußerst schwach, aber sie ist beträchtlich in der anfänglichen Zeitdauer in Bild 7.

Die Druckschwingengen bei einem höhen und einem niedrigen Brennkammerdruck sind in Bild 8 angegeben. Die wichtige Eigenschaft der Druckschwingung, daß die Schwingung in den zwei aufeinanderfolgenden Zeitabschnitten auftritt, ist hier auch zu erkennen. Die Druckamplituden in dem zweiten Abschnitt beim hohen Kammerdruck sind größer als die beim niedrigen. Eine Welle, deren Amplitude 2,2 Mpa erlangt, wird beobachtet (bei einem Kammerdruck von 22 Mpa).

3.3 Druckschwingungen in dem langen I-Brenner

Bild 9 zeigt die in dem langen I-Brenner auftretenden Druckschwingungen. Die Druckschwingungen erscheinen in zwei Zeitabschnitten. Aus der Wellenform und dem entsprechenden Frequenzspektrum in dem ersten Zeitabschnitt (Bld 10) ergibt sich, daß die Grundwelle hier auch vorherrscht. Die Wellen der mehrereren Ordnungengen überlagern sich in dem zweiten Abschnitt (Bild 11); sogar die Welle fünfzehnter

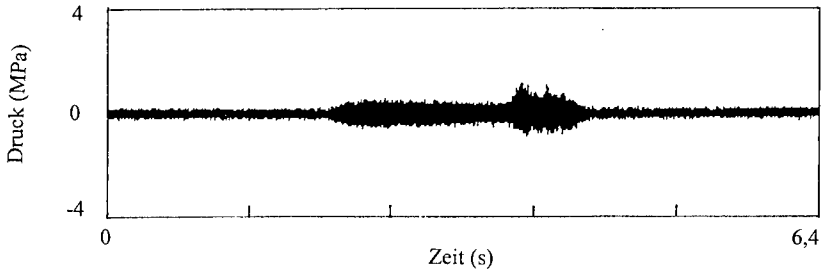

Bild 9. Schwingender Druck (höchster Kammerdruck von 11,8 MPa)

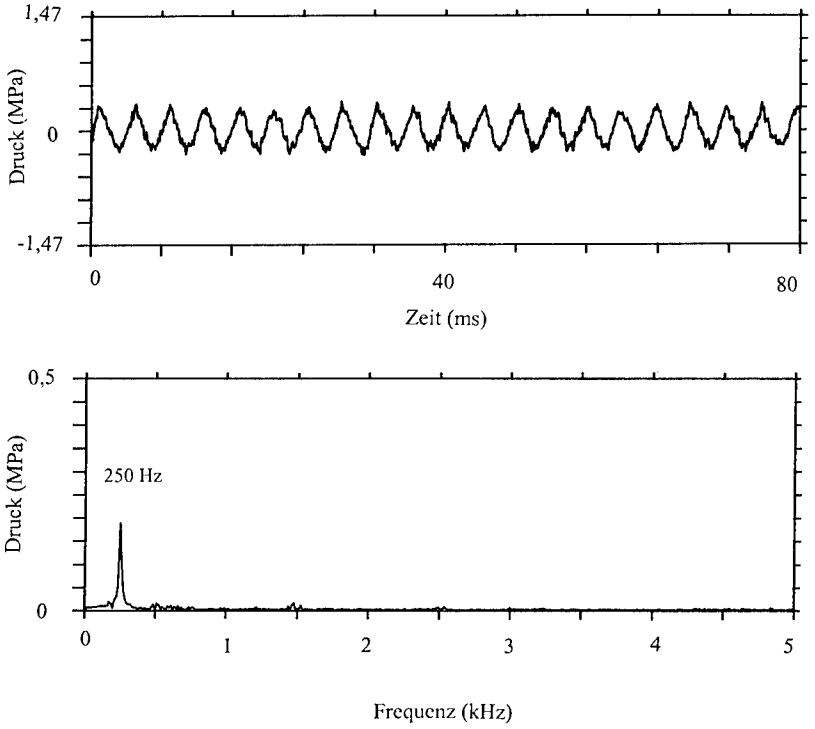

Bild 10. Wellenform der Druckschwingung (oben), entsprechendes Frequenzspektrum (unten), in dem ersten Zeitabschnitt (höchster Kammerdruck von 11,8 MPa)

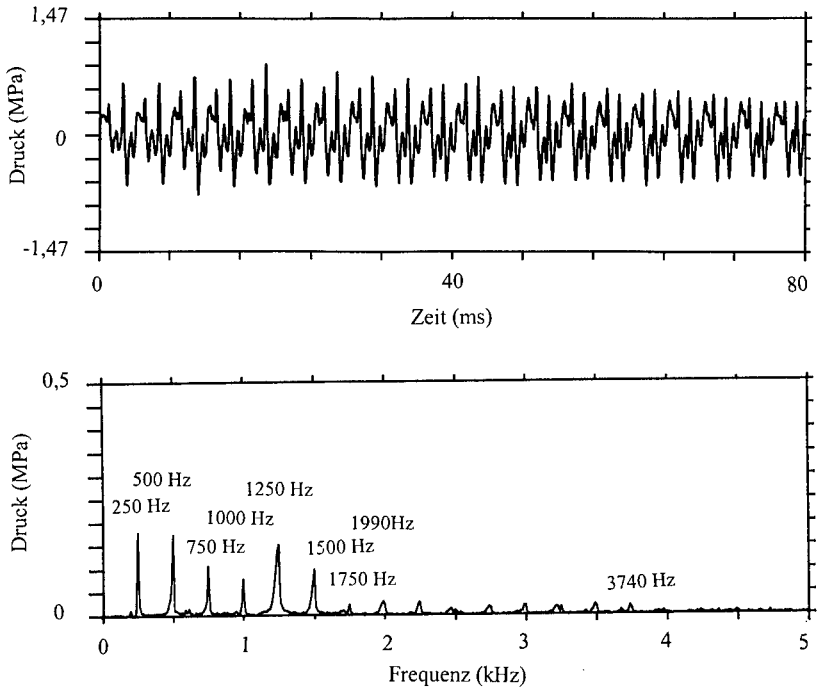

Bild 11. Wellenform der Druckschwingung (oben), entsprechendes Frequenzspektrum (unten), in dem zweiten Zeitabschnitt (höchster Kammerdruck von 11,8 MPa)

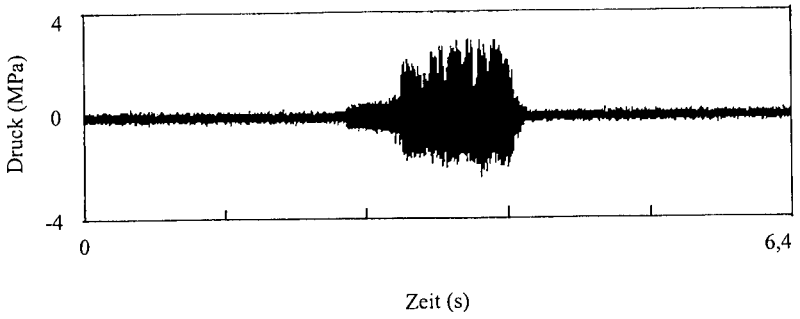

Bild 12. Schwingender Druck bei einem hohen Kammerdruck (höchster Kammerdruck von 27,0 MPa)

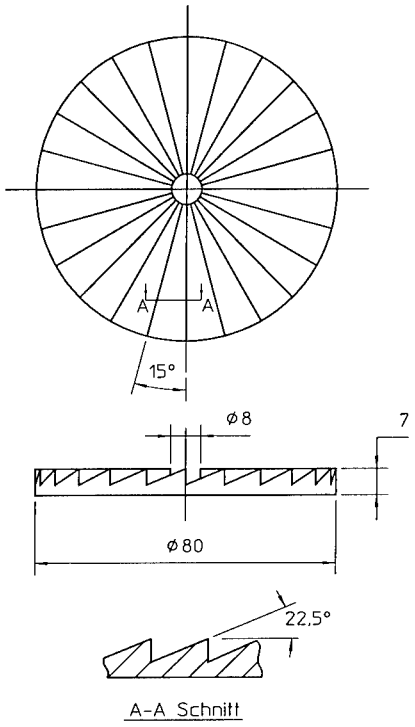

Bild 13. Form der Scheibe

Ordnung ist zu erkennen. Bild 12 zeigt die Druckschwingungen bei einem hohen Kammerdruck. Die Druckamplituden betragen höheren Werte in dem zweiten Abschnitt. Eine Amplitude von 0,77 MPa wird bei einem Kammerdruck von 28 MPa erkannt. Im allgemeinen sind die Druckschwingungszustände in dem langen Brenner diejenigen in dem kurzen Brenner gleich.

3.4 Einflüsse der Form eines Ende des I-Brenners auf die Druckschwingungen

Starke, longitudinale, akustische Wellen lassen sich in dem I-Brenner anregen. Man kann deshalb diesem Brenner zweckmäßig benutzen, um den Einfluß der Form (das heißt, der akustischen Admittanz) eines Brennkammerendes auf die Druckschwingugszustände zu untersuchen. Zum Beispiel wurden zwei Versuche durchgeführt. In dem ersten Versuch wurde eine Scheibe, deren Form in Bild 13 gezeichnet ist, an der Vorderseite des I-Brnners angelegt, und in dem zweiten eine

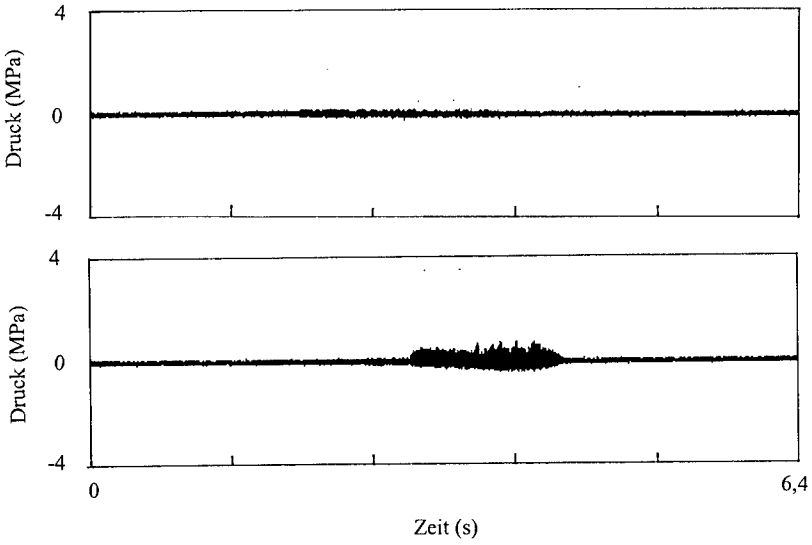

Bild 14. Schwingender Druck in dem I-Brenner mit in Bild 16 gezeichneten Scheibe (oben, höchter Kammerdruck von 10,4 Mpa), mit der flächen Scheibe (unten, höchster Kammerdruck von 11,2 Mpa). In beiden Versuchen ist die Düsenfläche 2,27 cm^2.

flache Scheibe. (In dem zweiten Versuch ist die Randbediungung an dem Vorderende des Brenners die Bedingung für bisher ausgeführten Versuche gleich.) Der Einfluß der Änderung der akustichen Admittanz ist auffallend. Anlegen der Scheibe hält völlig Auftreten der Druckschwingungen auf (Bild 14).

4. SCHLUSSFOLGERUNG

1. Die Druckschwingungen treten jedesmal in dem I-Brenner für den Aluminiumpulver enthaltenden Treibstoff, aber nie für den von Aluminiumpulver freien Treibstoff.
2. Die Druckwellen, die in dem I-Brenner angeregt werden, sind longitudinal und stehend, und deren Frequenz sind diejenigen für die akustischen Wellen im mit den

beiden Enden starr geschlossenen Rohr.

3. Die Schwingungen treten in zwei aufeinanderfolgenden Zeitabschnitten auf. In dem anfänglichen Zeitabschnitt herrscht die Grundwelle mit einer relative kleinen Amplitude vor; in dem folgenden Zeitabschnitt liegen die Wellen der höheren Ordnungen übereinander, und deren Amplituden sind größer.

4. Der I-Brenner kann zweckmäßig benutzt werden, um den Einfluß der Form eines Rohrendes auf die akustischen Druckschwingungszustände zu untersuchen.

Literatur

1. D. Strand und R. S. Brown, „ Laboratory Test Methods for Combustion Instability Properties of Solid Propellants", SS. 689-718, in Nonsteady Burning and Combustion Stability of Solid Propellants, Progress in Astronautics and Aeronautics, Volume 143, AIAA, 1992.

2. A. Iwama, T. Saito, K. Hori, T. Takahashi, und K. Kato, „Novel Method for Evaluating Acoustic Combustion Stability of Solid Propellant", ICT Tagungshandbuch, Absch. 26, 1994.

THERMODYNAMICAL PREDICTION OF COMBUSTION AND DETONATION PROPERTIES USING MODIFIED THOR CODE

Luisa Durães*, José Campos** and António Portugal*

Laboratory of Energetics and Detonics
**Chem. and **Mech. Eng. Departments - Fac. of Sciences and Technology*
University of Coimbra – Polo II - 3030 Coimbra - PORTUGAL

Abstract

The existing reactions in pyrolisis, combustion or detonation processes, generating intermediary chemical species and compounds, are very hard to follow by experiments, because these processes are very fast with increasing pressure and temperature. The proposed method of predicting reaction path and final composition of combustion products, as a function of temperature and pressure, uses a thermochemical computer code, named THOR, now modified, in order to calculate the composition and thermodynamic properties of explosive and pyrotechnic compositions, for isobar and isochor adiabatic combustion and Chapman-Jouguet detonation. The reaction path is estimated theoretically, assuming the thermodynamic equilibria for all the possible compounds, including intermediary molecules, as a function of temperature and pressure conditions, for the minimum Gibbs free energy at the equilibrium. The used equation of state, H_L , is supported by a Boltzmann equation of state type, but now based on physical intermolecular potential of gas components, instead of correlations from final experimental results. It takes α=13.5 to the exponent of the intermolecular potential and θ=1 to the adimensional temperature. The applied examples of thermal decomposition procedure, as case studies, are mixtures based in Ammonium Nitrate and Nitromethane. Detonation velocities, using the modified THOR code, are also presented for other 48 explosive molecules, proving its validity.

1. INTRODUCTION

The existing reactions in pyrolisis, combustion or detonation processes, generating intermediary chemical species and compounds, are very hard to follow by experiments, because these processes are very fast and proceed with increasing pressure and temperature. The method, here presented, of predicting reaction path and final composition of combustion products, as a function of temperature and pressure, uses a thermochemical computer code, named THOR, presented in previous works (Campos, 1991, Durães et al, 1995, 1996). It is based on theoretical work of Heuzé et al., 1985, Heuzé, 1989, in order to calculate the composition and thermodynamic properties of combustion products, assuming

an isobar or isochor adiabatic combustion, or a Chapman-Jouguet detonation. Several equations of state (EoS) may be used. In our particular case, the H_L EoS (Durães et al., 1995, 1996) is supported by a Boltzmann EoS, based on physical intermolecular potential of gas components, instead of correlations from final experimental results. This EoS takes α=13.5 to the exponent of the intermolecular potential and took θ=1.4 to the adimensional temperature. Modified THOR code uses the same α value but now takes θ=1 to the adimensional temperature. Also the reaction path, using this code, was revised (vd. Durães et al., 1997). It assumes the thermodynamic equilibria for all the possible compounds, including intermediary molecules, as a function of temperature and pressure conditions for the minimum Gibbs free energy at the equilibrium. The applied examples of thermal decomposition procedure, as an example of case studies, are mixtures based in Ammonium Nitrate and Nitromethane. Detonation properties, using modified THOR code, are also presented for other 48 explosive molecules.

2. SUMARIZED DESCRIPTION OF THOR CODE

A classical combustion system is generally a CHNO system. It is possible to consider up to *m* atomic species and form *n* chemical components. The mass balance yields a linear system involving *m* equations. The *n-m* equilibrium equations, necessary to solve the problem, are determined by the method of Lagrange multipliers or the equilibrium constants. To determine the chemical concentration of *n* components, for imposed P and T conditions, it can been used the chemical affinity method, proposed by Heuzé et al.,1985, or solving first the system composed by the *m* "basic" components, and secondly adding one by one more components, optimising the relative concentration inside the group related to the same atomic species, for the minimum value of global Gibbs free energy, $G = \Sigma\, x_i\, \mu_i$, being the Gibbs free energy of each component $\mu_i = G_{Oi}(T) + R\,T\,\ln P + R\,T\,\ln(x_i)$.

The selection of components is dependent of atomic initial composition. For a classical CHNO system it is assumed an equilibrium composition of CO_2, CO, H_2O, N_2, O_2, H_2, OH, NO, H, N, O, HCN, NH_3, NO_2, N_2O, CH_4 gases and two kinds of solid carbon (graphite and diamond). When the initial mixture includes Cl species, HCl and Cl_2 are expected in final products.

Consequently the solution of composition problems (Duraes et al.,1995) involves simultaneously:

- the thermodynamic equilibrium for $G=G_{min}$ (P,T,x_i), applying to the condensed phase the model proposed by Tanaka, 1983,

- the thermal equation of state (EoS) and the energetic equation of state, related to the internal energy $E = \Sigma\, x_i e_i(T) + \Delta e$, $e_i(T)$ being calculated from JANAF Thermochemical Tables, 1971, and polynomial expressions of Gordon and McBride, 1971,

- the combustion condition regime, assumed like an isobar or isochor adiabatic combustion, or a Chapman-Jouguet detonation.

3. MODIFIED H_L EQUATION OF STATE

In the earlier work (vd. Durães et al., 1995) H_L equation of state was proposed. This equation takes the general expression

$$\frac{PV}{nRT}=\sigma(V,T,X_i) \tag{1}$$

where V represents the volume, T the temperature and X_i the mole number of i compound in reaction gaseous products. The second term, σ, presented by Heuzé et al., 1985, for H_α equations of state, is a fifth order polynome obtained from virial expansion. It represents very well the behaviour of gaseous mixtures at high temperature and pressure:

$$\sigma(V,T,X_i)=1+x+0.625x^2+0.287x^3-0.093x^4+0.014x^5 \tag{2}$$

with

$$x(V,T,X_i)=\frac{\Omega}{VT^{3/\alpha}} \tag{3}$$

$$\Omega=\sum_{i=1}^{s} X_i\omega_i \tag{4}$$

The α represents the exponent of the repulsive part of the intermolecular potential. Heuzé et al., 1995, has proposed for α the values 9 and 12 (to deduce H_9 and H_{12} equations of state), based on theoretical and experimental final correlations. This parameter has great influence on the results and the preceding values are too low to represent the detonation gaseous products, which co-exist in equilibrium at very high pressure. In H_L equation of state, the intermolecular potential function considered is the Buckingham α-exp-6 function and α takes the value 13.5, in agreement with bibliography (vd. Brown and Braithwaite, 1989, Brown and Horton, 1987, Bugaut et al., 1989, Chirat and Pittion-Rossilon, 1981,

Jones, 1981, Jones and Zerilli, 1993, Stiel et al., 1993, 1996, Van Thiel at al., 1993, Zerilli and Jones, 1989). The ω_i values are dependent of each gas component. Replacing equation (4) in (3):

$$x = \frac{\sum_{i=1}^{n} X_i \, \omega_i}{V \, T^{3/\alpha}} \tag{5}$$

and considering the Boltzmann EoS, it can be possible

$$\frac{\sum_{i=1}^{n} X_i \, \omega_i}{V \, T^{3/\alpha}} = \frac{\sum_{i=1}^{n} X_i \, B_i}{V} \, , \tag{6}$$

being B_i the covolume of component i in reaction products. This is a valid procedure because, at low densities, the terms of higher order (fourth and fifth) in σ expression are negligible, and then, numerically, H_L EoS reduces to a Boltzmann EoS.

Using a simplified rigid sphere model (vd. Heuzé, 1985, Montanelli, 1978, Percus and Yevick, 1958, Xiong, 1991),

$$B_i = \frac{2}{3} \pi r_{0i}^3 N_{AV} \, , \tag{7}$$

where r_{Oi} is the intermolecular distance at minimum value of the intermolecular potential and N_{AV} the Avogadro number, it can be obtained:

$$B_i = \frac{2}{3} \pi r_{0i}^3 N_{AV} \, , \tag{8}$$

$$T = \theta \frac{\varepsilon}{k} \tag{9}$$

In these equations, θ is the adimensional temperature, k the Boltzmann constant (k = 1.380 x 10^{-23} J/K) and r_{Oi} and ε_i/k the parameters of the Buckingham α-exp-6 intermolecular potential function, for each reaction gaseous product in pure state. The values of r_{Oi} and ε_i/k parameters are usually obtained, for each gas in the products, by agreement between experimental and theoretical Hugoniot curves; since they have low influence in obtained theoretical results, in the present work, H_L EoS is not used to fit their values; the applied values are listed in the literature (vd. Finger at al., 1976, Heuzé et al., 1985, Stiel et al., 1993) for JCZ3 EoS. Several θ values have been evaluated. They have great influence on predicted dynamic characteristics of products of condensed reactive mixtures (Durães at al.,

1995). Initially, the value $\theta = 1.4$ has been considered the best-adopted constant value (Durães et al., 1996), by comparison of experimental and theoretical detonation results. In this work a new θ value is proposed - $\theta = 1$, omiting the referred comparison and meaning that ε_i/k is a good measure of each pure compound temperature in shock experimental tests, which is theoretically more consistent than taking any other value. Calculated values of ω_i for H_L EoS are presented in Table 1.

	θ = 1.4	θ = 1		θ = 1.4	θ = 1		θ = 1.4	θ = 1
CO_2	326.8	303.2	**N_2**	261.5	242.7	**NO**	239.1	221.9
CO	261.5	242.7	**H_2**	112.9	104.8	**CH_4**	328.6	304.9
H_2O	152.7	141.7	**O_2**	208.7	193.7	**NH_3**	181.7	168.6

Table 1. Calculated ω_i (10^{-6} m^3 $K^{3/\alpha}$ / mole) for H_L EoS, with $\theta = 1.4$ and $\theta = 1$.

4. THERMODYNAMIC MODELLING CONDITIONS

The thermodynamic modelling conditions are based in the calculation of the thermodynamic properties of the products of combustion, first, of a theoretical adiabatic combustion, assuming P and T conditions, and secondly, evaluating the decomposition reaction path, based in heat loses to the exterior.

4.1 Isobar and Isochor Adiabatic Combustion and CJ Detonation Conditions

The **isobar adiabatic combustion** is the basic theoretical combustion condition (Durães et al., 1997) where dP=0 and dQ=0 imply dH=0, i.e. equal initial and final total enthalpy $Hb^{Tb}=Ho^{To}$. This expression is equivalent to $Hb^{Tb} - Hb^{To} = -(Hb^{To} - Ho^{To})$, also equivalent to $H_b\Big|_{To}^{Tb} = -\Delta_r^{To}H$ (the total enthalpy from burned gases is equal to the module of the enthalpy of reaction). Considering now a global isobar adiabatic process, formed by one reactive system enclosed in a non resistant wall, working like an enthalpy absorber of value ΔH, the preceding equation takes the form $H_b\Big|_{To}^{Tl} + \Delta H = -\Delta_r^{To}H$, where the enthalpy of reaction is distributed to the heated burned gas and the wall, being always $P=P_o$. Consequently, it is possible to consider $T_o < T_l < T_b$. The corresponding products composition can then be changed from the "basic" chemical components, when $T_l = T_o$, to

the final components, when $T_1 = T_b$, isobar adiabatic combustion temperature with the preceding condition. The Gibbs free energy, taking its minimum relative value for a (V,T,X_i) group, is also reduced with increasing values of T_1, from T_o to T_b.

The **isochor adiabatic combustion** implies a constant total volume ($dV=0$) and also an non existing heat transfer from the reactive system to the exterior ($dQ=0$), verifying equal initial and final total internal energy $E_b^{Tb}=E_O^{To}$. The isochor adiabatic combustion regime needs the calculation of the internal energy E_i^T, for a specified (V,T,X_i), where V represents the volume, T the temperature and X_i the mass fraction. This E_i^T can be expressed as a function of the enthalpy, H_i^T, and of PV for the same conditions, being $PV=\sigma NRT$ obtained from the used EoS, ($E_i^T=H_i^T-\sigma N_i RT_i$). This expression allows to solve the calculation of values for isochor adiabatic combustion from the obtained values of the corresponding isobar adiabatic combustion, for the same P and T conditions, but needs an interactive method to find the solution.

The **Chapman-Jouguet detonation** condition (mass, momentum and energy balances and $dp/dV]_S = ((P-P_O) / (V-V_O))$ for the detonation regime, is based on the assumption that the detonation velocity D is obtained adding sound velocity a_o with particular velocity u_p ($D = a_o + u_p$).

4.2 Reaction path conditions

The reaction path can now be explained, in a decomposition process, (vd. Duraes et al., 1997) by the mechanism of heat loses, from the original adiabatic combustion condition, (where there are no heat loses). The calculation can start, from one initial reactive composition A, to a final products composition C, assuming an intermediary composition B, being this B the composition that decomposes in final products C. The reactions can be presented in a simple way like: $A \rightarrow C$, being $A \rightarrow B$ and $B \rightarrow C$. Taking the example of the isobar combustion regime, the total enthalpy released by any reaction is converted to increase the temperature of the products of reactions. Assuming the preceding reaction scheme, from the initial temperature T_0, to the final temperatures T_b, T_b', T_b'', respectively, it can be written, for the total enthalpy: $H_A^{T0} = H_C^{Tb}$; $H_A^{T0} = H_B^{Tb'}$ and $H_B^{T0} = H_C^{Tb''}$. The preceding equations are equivalent to $H_A^{T0}-H_C^{T0}=-\Delta H_{A-C}^{T0}=H_C^{Tb}-H_C^{T0}$, $H_A^{T0}-H_B^{T0}=-\Delta H_{A-B}^{T0}=H_B^{Tb'}-H_B^{T0}$ and $H_B^{T0}-H_C^{T0}=-\Delta H_{B-C}^{T0}=H_C^{Tb''}-H_C^{T0}$. So,

$\Delta H^{T0}_{A-B} + \Delta H^{T0}_{B-C} = H^{T0}_{C} - H^{T0}_{A} = \Delta H^{T0}_{A-C}$. Then, if the reaction is incomplete, the intermediary final products are B, and $\Delta H^{T0}_{A-B} = \Delta H^{T0}_{A-C} - \Delta H^{T0}_{B-C} = H^{Tb''}_{C} - H^{Tb}_{C}$. Obtaining the theoretical results of reactions A-C and B-C, the necessary data to calculate ΔH^{T0}_{A-B} is then obtained.

The calculation mechanism for isochor adiabatic combustion is similar, but now changing all the equations from enthalpy to the internal energy values.

5. THEORETICAL RESULTS – CASE STUDIES

5.1 Decomposition path of Ammonium Nitrate and Ammonium Nitrate-Fuel Oil

Applying the preceding scheme, as a revised process of a previous work (Duraes et al., 1997), the thermal decomposition can be obtained for pure ammonium nitrate (AN) and for ammonium nitrate-fuel oil explosive ANFO (94.4%, in mass, of AN, for 5.6% of fuel oil - FO), assuming the intermediary components, shown in Tables 2 and 3. The graphic representation of the three main points of the adiabatic Crussard curves (Figure 1) proves the importance of the decomposition of pure AN in NH_3+HNO_3, and the small influence of this decomposition in ANFO (all the points are almost in the same position). Experimental results, from decomposition processes of pure ammonium nitrate, show significant influence of (Kolaczkowski, 1980, Durães et al., 1986, 1987) endothermic dissociation above 169 °C ($NH_4NO_3 \rightarrow HNO_3 + NH_3$); exothermic elimination of N_2O on careful heating at 200 °C ($NH_4NO_3 \rightarrow N_2O + 2H_2O$); exothermic elimination of N_2 and NO_2 above 230 °C ($4\ NH_4NO_3 \rightarrow 3N_2 + 2NO_2 + 8H_2O$); and exothermic elimination of nitrogen and oxygen, sometimes accompanied by detonation ($NH_4NO_3 \rightarrow N_2 + 1/2\ O_2 + 2\ H_2O$), in a good agreement with theoretical predictions.

Products of Reaction	AN	ANFO
NH_3+HNO_3	184.3	176.1
N_2+O_2+H_2O	-97.4	-115.8
N_2O+H_2O	-39.3	-37.5
N_2+NO+H_2O	-30.5	-29.1
N_2+NO_2+H_2O	-103.5	-100.9
N_2+HNO_3+H_2O	-97.4	-124.3

Table 2. Enthalpy of reaction of Ammonium Nitrate and ANFO decomposition, as a function of selected products (kJ mol-1).

Products of Reaction	AN	ANFO
NH_3+HNO_3	179.5	171.4
N_2+O_2+H_2O	-129.3	-123.6
N_2O+H_2O	-46.6	-44.5
N_2+NO+H_2O	-39.1	-37.3
N_2+NO_2+H_2O	-112.2	-107.2
N_2+HNO_3+H_2O	-133.5	-127.5

Table 3. Internal energy of reaction of Ammonium Nitrate and ANFO decomposition, as a function of selected products (kJ mol^{-1}).

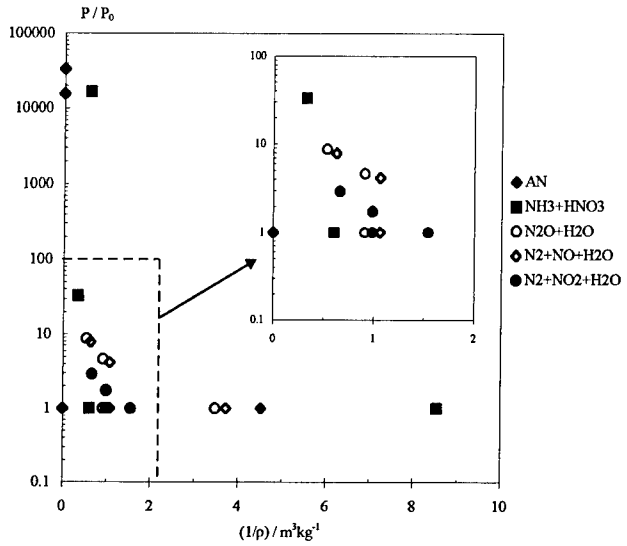

Figure 1. Represented states of the isobar and isochor adiabatic combustion and CJ detonation of AN, as a function of selected decomposition products.

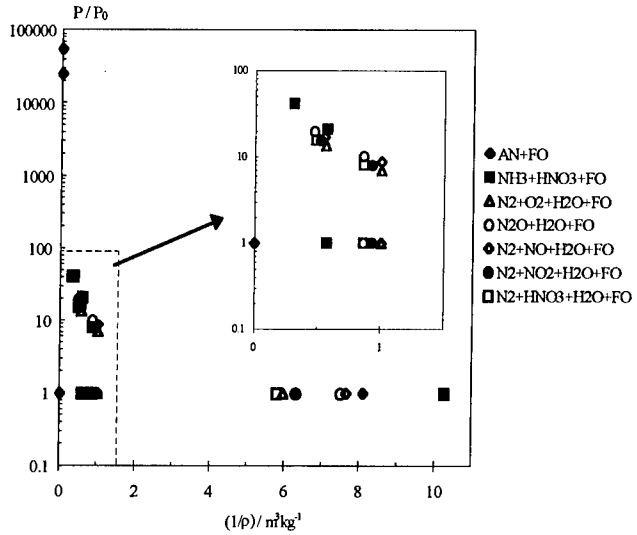

Figure 2. Represented states of the isobar and isochor adiabatic combustion and CJ detonation of ANFO, as a function of selected decomposition products.

5.2 Decomposition path and detonation of Nitromethane

In a similar way, results from NM decomposition are presented in Table 4 and Figure 3. The obtained results prove the main influence of CH_3+NO_2, $2CH_3O+2NO$ and $2CH_2O+2HNO$ as decomposition products. The thermal decomposition of nitromethane can be expressed (Ornelas, 1982), using a calorimetric bomb, by $2CH_3NO_2 \rightarrow H_2O + CO + N_2 + O_2 + CH_4$, with $H_2O + CO \rightarrow H_2 + CO_2$; $CH_4 \rightarrow C(s) + 2H_2$; $2H_2 + O_2 \rightarrow 2H_2O$; $3H_2 + N_2 \rightarrow 2NH_3$, with final main products composition of H_2O, CO, N_2 , H_4, CO_2 , C(s) and NH_3. These mechanisms have been also analysed by Bardo, 1985. Other intermediary products were proposed by Shaw, 1976, Haskins, 1985, ($CH_3 + NO_2$) and Agnew, 1989, ($N_2O + CO_2 + H_2O + CH_4$). These results are in good agreement with predictions.

Products of Reaction	$\Delta_r H$	$\Delta_r E$
$2CH_3+2NO_2$	291.8	287.0
$2CH_3O+2NO$	161.2	156.3
$2CH_2O+2HNO$	96.7	91.9
$H_2O+CO+N_2+O_2+CH_4$	-101.1	-107.3
$N_2O+CO_2+H_2O+CH_4$	-201.8	-206.7

Table 4. Enthalpy of reaction and internal energy of reaction of Nitromethane decomposition, as a function of selected products (kJ mol^{-1}) .

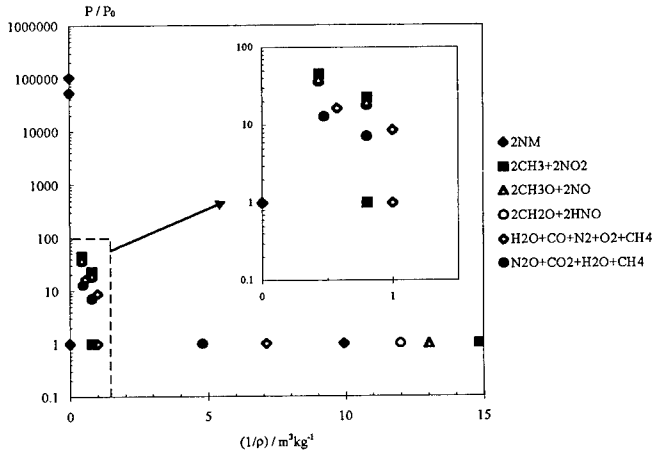

Figure 3. Represented states of the isobar and isochor adiabatic combustion and CJ detonation of NM, as a function of selected decomposition products.

The fundamental detonation study case is based in nitromethane (NM), a pure chemical, liquid, very known homogeneous explosive, that allows to change its initial density by adding small percent of glass microballoons (GMB), used generally to sensitize emulsion explosives (vd. Gois et al, 1993). The used GMB (of type C15/250, supplied by 3M Corporation) have 1 μm wall thickness and an effective density about 150±3 $kg.m^{-3}$. They can be sieved in different granulometric classes (vd. Table 5), allowing the precise experimental evaluation of detonation velocity, as a function of initial density, by the change of its concentration in final composition (presented, in mass %, in Table 5). The presented value of detonation velocity is referred to an infinite diameter, obtained by extrapolation (vd. Gois et al, 1993). It decreases linearly with the increasing of GMB concentration. As it can be seen in Figure 4, for low GMB concentration, its values show an excellent correlation with theoretical predictions using H_L EoS. For high GMB concentration the influence of GMB is more important.

dp_{50} (μm) **dp_{10}-dp_{90} (μm)** Conc. (mass %)↓	**45** **37-50**	**75** **25-110**	**100** **34-154**
0	1.13	1.13	1.13
0.5	-	1.09	-
1	1.09	-	-
1.44	-	-	0.95
2	1.04	0.97	-
3	1.00	-	-
4.36	0.96	-	-
5	-	0.79	0.68
6.5	0.90	-	-

Table 5 - Density of NM/PMMA-GMB mixtures as a function of mass fraction (X) and the mean particle size of GMB (dp_{50}).

5.3 Detonation results of other energetic molecules

The validation of preceding formulations and H_L EoS have been done calculating the detonation velocities of 49 different condensed energetic molecules and correlating them to the experimental values. The observed error, in percent, (Figure 5) proves the validity of used equation of state, H_L , with α=13.5 to the exponent of the intermolecular potential and θ=1 to the adimensional temperature.

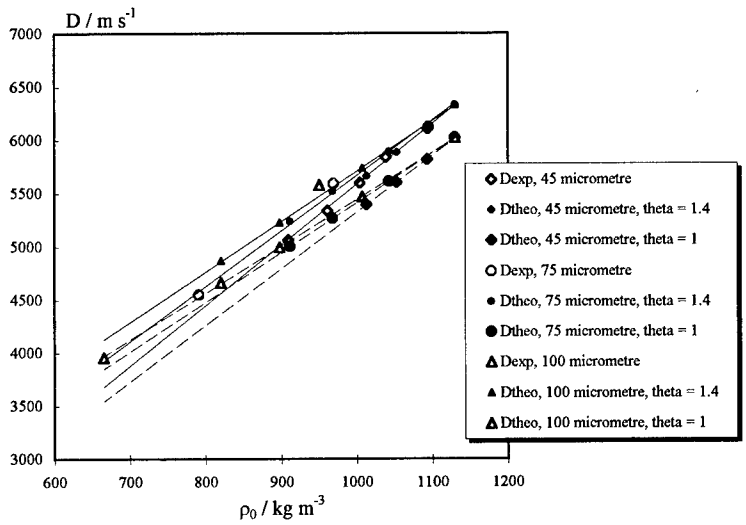

Figure 4. Experimental and calculated detonation velocity as a function of initial density of NM base mixtures, with GMB of indicated diameter.

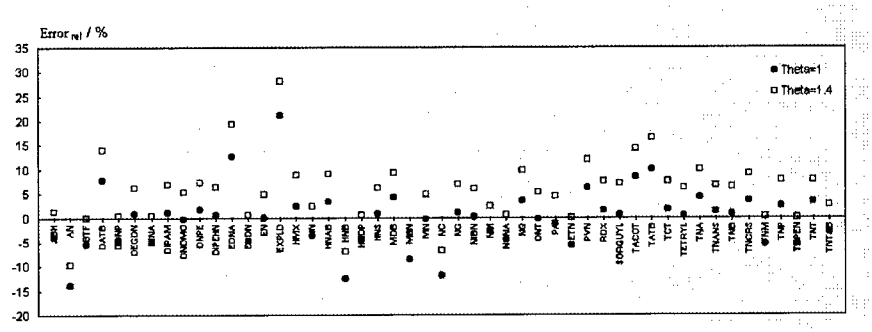

Figure 5. Exp. and theoretical *D* deviation, for 49 different energetic molecules, using H_L EoS with $\theta=1$ and $\theta=1.4$ values.

6. CONCLUSIONS

The method of predicting reaction path, using modified THOR code, allows for isobar and isochor adiabatic combustion and CJ detonation regimes, the calculation of the thermodynamic properties of reaction products. The reaction path is estimated theoretically, assuming the thermodynamic equilibria for all the possible compounds, including intermediary molecules, as a function of temperature and pressure

conditions, for the minimum Gibbs free energy at the equilibrium. The used equation of state, H_L , takes α=13.5 to the exponent of the intermolecular potential and θ=1 to the adimensional temperature. The applied examples of thermal decomposition procedure, mixtures based in Ammonium Nitrate and Nitromethane, as case studies, are in good agreement with experimental values and prove the validity of proposed method. Detonation velocities, using the modified THOR code, are also presented for other 48 explosive molecules, proving its validity.

REFERENCES

Agnew, S. F. et al., "Chemistry of Nitromethane at Very High Pressure", *Proc. of the 9th Symposium (International) on Detonation*, Portland, Oregon, pp. 1019-1026, 1989.

Bardo, R., "Calculated Reaction Pathways for Nitromethane and Their Role in the Shock Initiation Process", *Proc. of the 8th Symposium (International) on Detonation*, Albuquerque, New Mexico, pp. 855-863, 1985.

Brown, W. B.; Braithwaite, M. - "Sensitivities of Adiabatic and Gruneisen Gammas to Errors in Molecular Properties of Detonation Products", in *Proc. of the 9th Symposium (International) on Detonation*, Vol. I, Portland (OR), USA, 1989, p.513-24.

Brown, W. B.; Horton, T. V. - "Analytical Representation of the Excess Thermodynamic Equation of State for Detonation Products Based on Statistical Mechanics", in *Proc. of the 3e Congrès International de Pyrotechnie Spatiale & 12th International Pyrotechnics Seminar*, Juan-les-Pins, France, 1987, p.71-8.

Bugaut, F.; Bernard, S.; Chirat, R. - "Theoretical Prediction of High Explosives Efficiency: Application to NTO", in *Proc. of the 9th Symposium (International) on Detonation*, Vol. I, Portland (OR), USA, 1989, p.489-97.

Campos, J., "Thermodynamic Calculation of Solid and Gas Combustion Pollutants Using Different Equations of State", *Proc. of 1st International Conference on Combustion Technologies for a Clean Environment*, Vilamoura, Algarve, Portugal, pp. 30.4-1-30.4-11, 1991.

Chirat, R.; Pittion-Rossilon, G. - "A New Equation of State for Detonation Products", *The Journal of Chemical Physics*, 74 (8), 1981, p.4634-42.

Chirat, R.; Pittion-Rossilon, G. - "Detonation Properties of Condensed Explosives Calculated with an Equation of State Based on Intermolecular Potentials", in *Proc. of the 7th Symposium (International) on Detonation*, Annapolis (MD), USA, 1981, p.703-15.

Durães, L.; Campos, J.; Gois, J. C. - "Deflagration and Detonation Predictions Using a New Equation of State", in *Proc. of the 26th International Annual Conference of ICT*, Karlsruhe, Federal Republic of Germany, 1995, p.67.1-13.

Durães, L.; Campos, J.; Gois, J. C. - "New Equation of State for the Detonation Products of Explosives", in *Proc. of 1995 APS Topical Conference on Shock Compression of Condensed Matter*, The American Institute of Physics, Seattle (WA), USA, 1996, p.385-8.

Durães, L.; Campos, J.; Portugal, A., "Combustion and Detonation Modeling Using THOR Code", *Proc. of the 28th International Annual Conference of ICT*, pp. 89.1-89.10, 1997.

Finger, M.; Lee, E.; Helm, F. H.; Hayes, B.; Hornig, H.; McGuire, R.; Kahara, M.; Guidry, M. - "The Effect of Elemental Composition on the Detonation Behavior of Explosives", in *Proc. of the 6th Symposium (International) on Detonation*, Coronado (CA), USA, 1976, p.710-22.

Gois, J. C.; Campos, J.; Mendes, R. - "Shock Initiation of Nitromethane-PMMA Mixtures with Glass Microballoons", in *Proc. of the 10th International Detonation Symposium*, Boston (MA), USA, 1993, p.758-65.

Gordon, S., McBride, B.J., "Computer Program for Calculation of Complex Chemical Equilibrium Compositions, Rocket Performance Incident and Reflected Shocks and Chapman-Jouguet Detonations", *Report NASA SP 273*, NASA Lewis Research Center, 1971.

Haskings, P. J. and Cook, M. D., "Quantum Chemical Studies of Energetic Materials", *Proc. of the 8th Symposium (International) on Detonation*, Albuquerque, New Mexico, pp. 827-838, 1985.

Heuzé O., *Cálculo Numérico das Propriedades das Misturas Gasosas em Equilíbrio Termodinâmico*, Universidade de Coimbra, Portugal, 1989.

Heuzé, O. - "Equations of State of Detonation Products: Influence of the Repulsive Intermolecular Potential", *Physical Review*, 34 (1), 1986, p.428-32.

Heuzé, O.; Bauer, P.; Presles, H.-N.; Brochet, C. - "The Equations of State of Detonation Products and Their Incorporation into the Quatuor Code", in *Proc. of the 8th Symposium (International.) on Detonation*, Albuquerque (NM), USA, 1985, p.762-9.

Janaf, *Thermochemical Tables*, 2nd Edition, National Bureau of Standards, Washington DC., 1971.

Jones, H. D. - "Theoretical EoS for Reaction Products of RDX", in *Proc. of the 7th Symposium (International) on Detonation*, Annapolis (MD), USA, 1981, p.716-20.

Jones, H. D.; Zerilli, F. Z. - "Multipole Effects on the Equation of State for Reaction Products of Explosives", in *Proc. of the 10th International Detonation Symposium*, Boston (MA), USA, 1993, p.449-55.

Kolaczkowski, A., *Samorzutny Rozklad Saletry Amonowej*, Wydawnictwo Politechniki Wroclawskiej, Wroclaw, 1980.

Montanelli, T. - *Calcul de la Composition de Mélanges Gaseux dans le Cas de Mélanges de Gaz Réels à l'Aide des Seconds Coefficients du Viriel*, Laboratoire d'Énergétique et de Détonique de L'Université de Poitiers, France, 1978.

Ornelas, D. L., "Calorimetric Determinations of the Heat and Products of Detonation for Explosives", *LLNL Report*, UCRL - 52821, 1982.

Percus, J. K.; Yevick, G. J. - "Analysis of Classical Statistical Mechanics by Means of Collective Coordinates", *The Physical Review*, 110 (1), 1958, p.1-13.

Shaw, R., "Discussion on Nitromethane Decomposition Kinetics", *Proc. of the 6th Symposium (International) on Detonation*, Coronado, California, pp. 98-101, 1976.

Stiel, L. I.; Gold, V. M.; Baker, E. L. - "Analysis of Hugoniots and Detonation Properties of Explosives with JCZ3 Equation of State", in *Proc. of the 10th International Detonation Symposium*, Boston (MA), USA, 1993, p.433-40.

Stiel, L. I.; Rotondi, P.; Baker, E. L. - "Optimization of Parameters for JCZ3 Equation of State", in *Proc. of 1995 APS Topical Conference on Shock Compression of Condensed Matter*, The American Institute of Physics, Seattle (WA), USA, 1996, p.389-92.

Tanaka, K., "Detonation Properties of Condensed Explosives Computed Using the Kihara-Hikita-Tanaka Equation of State", *Report from National Chemical Laboratory for Industry*, Ibaraki, Japan, 1983.

Van Thiel, M.; Ree, F. H.; Haselman Jr., L. C. - "The Significance of Interaction Potentials of Water With Other Molecules in EoS of High Explosive Products", in *Proc. of the 10th International Detonation Symposium*, Boston (MA), USA, 1993, p.425-32.

Xiong, W. - "Progress in VLW Equation of State of Detonation Products", in *Proc. of the 17th International Pyrotechnics Seminar Combined with the 2nd Beijing International Symposium on Pyrotechnics and Explosives*, Vol. II, Beijing, China, 1991, p.871-5.

Zerilli, F. J.; Jones, H. D. - "Calculations of Detonation Pressures for Homologous Series of Polynitroaliphatic Explosives Using a Fluid Perturbation Equation of State and a New Chemical Equilibrium Computer Program", in *Proc. of the 9th Symposium (International) on Detonation*, Vol. I, Portland (OR), USA, 1989, p.461-8.

AGGLOMERATE AND OXIDE PARTICLES GENERATED IN COMBUSTION OF ALEX CONTAINING SOLID PROPELLANTS

O. G. Glotov, V. E. Zarko,

INSTITUTE OF CHEMICAL KINETICS AND COMBUSTION,

Russian Academy of Sciences, Novosibirsk 630090, Russia

and M. W. Beckstead

BRIGHAM YOUNG UNIVERSITY, Provo, Utah 84602, USA

ABSTRACT

The characteristics of the condensed combustion products (CCP) were studied via sampling technique at pressure 46 atm (nitrogen or argon) for 7 formulations of metalized propellant based on well characterized ingredients. All formulations contained 18% of aluminum (commercial grade and ultra fine particles in various proportions), AP or mixtures of AP and HMX, and 20% of energetic binder. The replacement of commercial aluminum by electrically exploded aluminum (Alex) led to an increase in the burning rate, a decrease in agglomerates mass and an increase in the metal conversion completeness. All propellant formulations exhibited rather effective aluminum conversion (total unburned aluminum content in CCP did not exceed 9%). The observed trends were most pronounced in the combustion of HMX containing propellants where even small additives of Alex (Alex/Al = 8.3/91.7) produced a noticeable effect. For oxide particles of 0.5-15 μm size a typical three-peak pattern of the mass size distribution function has been observed. The mass size distribution function for different formulations was not changed significantly by the partial replacement of aluminum by Alex, and an increase in the metal combustion completeness was achieved mainly by a decrease of the mass fraction of agglomerates that contained the major portion of unreacted aluminum. The higher the extent of aluminum conversion, the greater the contribution of oxide mass in the total mass of CCP. The effect of environmental gas on the CCP characteristics (both agglomerate and oxide particles) was studied by using argon instead of nitrogen as pressurizing gas. The gas environment did not change significantly the CCP size distribution.

INTRODUCTION

Agglomeration of metal in the combustion wave of composite propellants as one of the main processes that control the efficiency of aluminum conversion still remains unsolved problem because of great complexity of the physicochemical processes and the lack of data on behavior of metal particles under fast heating in oxidizing media. Using ultra fine metal particles gives additional possibility to affect the process of agglomeration and metal combustion completeness due to enhancement of chemical reactivity of metal and resulting increase of heat release in the vicinity of

the burning surface. Thus the study of propellant formulation with additives of different kind ultra fine metal powders is of undoubted interest.

At present time several methods for producing the ultra fine aluminum powders are known: evaporation and condensation of Al in argon [1], electrical explosion of Al wire [2] (this material under name of Alex is commercially distributed by Argonide Corp., USA [3]), and electrical arc plasma re-condensation [4]. The first attempts to explore combustion behavior of ultra fine Al loaded propellants have been undertaken in Russia about 30 years ago. A brief literature survey concerning Alex properties characterization and Alex containing formulations combustion as well as some our previous results have been reported in [5]. It was shown that the Alex addition results in modification of ballistic characteristics – by increasing the burning rate, decreasing pressure exponent in the burning law, etc. These features seem to be caused by the low threshold temperature when the Alex chemical reacting starts as compared with ordinary commercial aluminum powder. However, no data on the effect of the ultra fine aluminum powders on condensed combustion products (CCP) are available in the literature.

The objective of the present work was to evaluate particle size distribution and free aluminum content both for agglomerates and fine oxide particles formed in combustion at elevated pressure of AP/HMX based propellants that contain ultra fine aluminum and commercial aluminum in different proportions. In most cases the Alex [2] was used as ultra fine aluminum component but one formulation contained the powder named "UFA", produced via electrical arc plasma re-condensation [4]. All experiments have been performed using original sampling method [6] at the pressure approximately equal to 46 atm. Two different gases (argon or nitrogen) were used for the bomb pressurization to evaluate the gas environment effect.

EXPERIMENTAL TECHNIQUE

Propellant formulations

Totally seven compositions of aluminized propellants were studied in the present work, see Table 1. They can be divided into two "lines" – propellants based on pure AP (batches # 1-3) and that on the mixture of AP and HMX (batches # 4-7). In each line the proportion of ultra fine and commercial aluminum has been varied. In batch #7 (shadowed cell) an UFA powder was used instead of Alex. All propellants

contained energetic binder (EB) made of butadiene-nitryl rubber plastisized with diethylene glycol dinitrate (DEGDN).

Mixing of components was performed in the teflon mortar by summary propellant weight about 100 g per batch. Curing of cylindrical propellant samples was performed individually in teflon forms with open ends in air at 70°C during 170 hours. Samples for the firing tests had cylindrical shape with diameter of 7.8 mm and length of 16-18 mm.

It has to be noted that the production of Alex containing propellant meets considerable difficulties due to large specific area of the Alex powder that results in poor mixing of components. Therefore, the acetone was used in the mixing process as a liquefying agent. The acetone has been evaporated during curing. In this case one may expect the presence of porosity in the bulk of propellant. The cavities with size up to 0.7 mm were observed on the lateral surface of cured samples. The propellant density was determined on cured propellant samples and served for indication of propellant porosity. Due to the porosity, the burning rate data obtained in sampling bomb tests have relatively high scatter and should be treated only as an illustration for the formulation effects.

Table 1. Propellant formulation

Batch #	ρ, g/cm^3	Alex/Al	EB	AP1	AP2	HMX	Al	Alex
1	1.62±0.04	0/100	20	41	21	-	18	-
2	1.59±0.02	30/70	20	41	21	-	12.6	5.4
3	1.52±0.04	100/0	20	41	21	-	-	18
4	1.59±0.02	0/100	20	18	9	35	18	-
5	1.64±0.03	30/70	20	18	9	35	12.6	5.4
6	1.56±0.02	8.3/91.7	20	18	9	35	16.5	1.5
7*)	1.56±0.03	30/70	20	18	9	35	12.6	5.4*)

Comment: *) In batch #7 UFA powder was used instead of Alex.

Propellant ingredients

The results of particle size distribution analysis for commercial AP, HMX, and Al are presented in Table 2 in the form of mean diameters D_{mn}. In the cases when commercial sizer Malvern 3600E was employed, the suspension of particles in the carrier liquid was subjected to ultrasound treatment during 40 second before measurement and the mechanical mixer was in action during measurement. For Alex and UFA powders the curves of cumulative mass size distribution function, obtained

by Malvern sizer, are presented in Fig. 1. The data have meaning of estimate only, because the size of particles is too small for this analysis method. However, it shows that Alex and UFA powders have similar size distribution and contain ~80% by mass of particles with size smaller than 5 μm. It should be underlined that obtaining the correct data on size distribution for ultrafine powders is a difficult technical task. In fact, using optical techniques – visible light microscopy or automatic sizers based on light scattering – faces the restrictions caused by the finite value of the light wavelength. In order to determine the particle size distribution function by means of electron microscope it is necessary to measure thousands of particles because of the wide size range – from 0.01 μm to 10 μm – of their population. This statement is illustrated by Fig. 2 where typical overview of Alex powder is presented made by microscope JEM-100SX at magnification 5600^X. One can see individual round shape particles with size about 1 μm and large number of small (<0.1 μm) particles.

The chemical analysis indicates the following content of active (metallic) aluminum in used for the propellant manufacturing powders – Alex: 82.2±0.3%, UFA: 85.5±0.7%, ordinary commercial Al: 97.8±0.9%.

Table 2. Mean size D_{nm} (μm) for propellant ingredients

Com-ponent	Grain size or surface area	Analysis method	D_{10}	D_{20}	D_{30}	D_{32}	D_{43}	D_{53}
AP1	160-315 μm	optical microscope	282	285	288	294	301	304
AP2	6700 cm^2/g	Malvern, hexane	4.5	5.4	6.6	9.6	13.1	14.8
HMX	> 315 μm	optical microscope	211	236	264	330	402	434
Al	~ 15 μm	Malvern, water	4.2	4.8	5.9	8.8	15.2	18.7

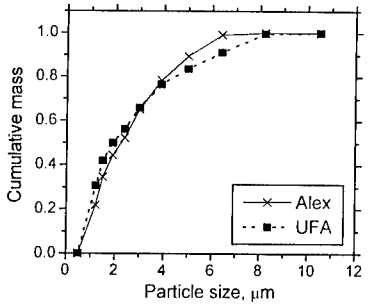

Fig. 1. Cumulative mass size distribution for Alex and UFA powders.

Malvern 3600E data, acetone as carrier liquid.

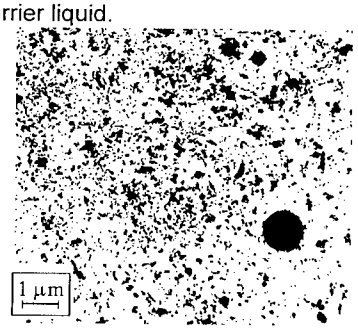

Fig. 2. Typical electron microscope image of Alex powder.

The experimental procedure and data treatment

The original technique designed for simultaneous sampling of agglomerates and fine oxide particles followed by size distribution and chemical analyses has been described previously [6-10]. Briefly, when small size propellant specimen burns inside the blow through bomb, the combustion products are diluted and quenched via mixing with inert gas and trapped with wire mesh screens and aerosol filter installed in the gas outlet. Below we present only specific features of approach used in this work.

• Each experimental series consisted of 3 propellant samples with total mass about 4 g which were consecutively combusted under identical conditions that provided generation of 1.4-2 g of CCP used for subsequent analyses. The lateral surface was inhibited by the vacuum oil Alcaren®. Additionally, the weak gas blowing (~ 1 cm/s) was arranged along the lateral sample surface directed from the cold to hot end. Obviously, the oil drops were trapped by wire mesh screens and by filter but special tests have shown that oil did not make effect on particle size distribution and on chemical analysis results.

• The thin (~ 1 mm) layer of pliant non-metalized propellant was attached to the ignited butt end of studied propellant specimen to make easier its ignition.

• The initial pressure in all experiments was 41 atm. The maximum rise of pressure during the combustion run was 11-12 atm. The characteristic pressure in the individual run was taken as a half of sum of initial and final pressures. The characteristic pressure and burning rate for given series were chosen as arithmetical mean values of characteristic pressure and burning rate for individual runs.

• The nominal mesh sizes of wire screens in the stack installed inside the bomb were 130, 150, 300, and 450 μm.

• The sampled particles were divided into fractions via dry and wet sieving in acetone by using sieves with the same mesh sizes. The particles caught by the filter were added to the sieve fraction <130 μm. All sieved fractions of particles were weighed after drying with accuracy of no less than 0.00015 g and then were subjected to the particle size and permanganatometric analysis [11] to determine the free aluminum content.

• The fine (< 130 μm) particles were analyzed with Malvern 3600E sizer using acetone as the carrier liquid after 40 seconds treatment with ultrasound and with

continuous mechanical mixing of suspension. 16 channels were employed with exponential incrementing width in the size range 0.5-118.4 μm.

• Particle size analysis for fractions >130 μm was performed using optical microscope. The accuracy of size measurement estimated as a half of histogram sub-range was equal to 9 μm for fractions in the size range 130-300 μm, and 22 μm for fractions 300-450 μm. These values may be treated as an estimate for the accuracy of the data on mean diameters reported below.

• The density of particles of <130 μm size was assumed to be equal to 3.71 g/cm^3 while the mean density of particles in fractions >130 μm was determined experimentally.

Based on the results of particle size analysis and chemical analysis of sieved fractions particles, the mass size distribution functions and the set of parameters that characterize the CCP particles were calculated using original computer codes.

The definitions of used characteristics are as follows:

Mass size distribution function for CCP particles, $f(D)$, or distribution of relative mass of CCP, is defined as $f_i(D) = m_i / (M_{prop} \cdot \Delta D_i)$, where m_i is the mass of CCP in the i-th histogram sub-range, and ΔD_i is the width of i-th size interval.

Mass size distribution function for unburned aluminum in CCP, $f_i^{Al}(D)$, is defined as $f_i^{Al}(D) = f_i(D) \cdot \varepsilon_j^{Al}$, where $f_i(D)$ is the histogram of relative mass of CCP, ε_j^{Al} is the mass content of aluminum in the j-th sieve fraction. Index i is omitted below.

D_L and D_R bound sizes. The whole population of CCP particles can be treated as consisting of *coarse* ($D>D_L$) and *fine* ($D<D_L$) condensed combustion products that correspond to *agglomerate* and *oxide* particles. For propellants under study bound size D_L can be easy established as a local minimum in a mass size distribution function $f(D)$, because there is the size interval in the range of 33-127 μm, where $f(D) \approx 0$.

When calculating the mean diameters for agglomerates, the upper limit size D_R was used. This size is the maximal size of agglomerates that is determined as the right end of monotonous portion of the normally filled with CCP particles $f(D)$ curve. Actually, single particles with the size greater than D_R were excluded from calculation of the characteristic mean sizes D_{mn} of agglomerates. The formation of several extra

large particles in each test can be caused by transient combustion of the propellant sample, when burning surface reaches sample holder plate, and/or destroying the igniting nichrome wire in the flow of hot combustion products.

The following *dimensionless characteristics of CCP* were calculated for fine and agglomerate particles on the basis of experimental mass size distribution functions $f(D)$ and $f^{Al}(D)$. The characteristics are scaled by the total mass of propellant burned M_{prop}. (For example, $m_f = M_f/M_{prop}$, where M_f is the mass of fine particles).

m_f – dimensionless mass of fine particles,

m^{Al}_f – dimensionless mass of free aluminum in fine particles,

m_{ag} – dimensionless mass of agglomerates,

m^{Al}_{ag} – dimensionless mass of free aluminum in agglomerates,

$m_{ccp} = m_f + m_{ag}$ – total dimensionless mass of CCP,

$m^{Al}_{ccp} = m^{Al}_f + m^{Al}_{ag}$ – total dimensionless mass of aluminum in CCP,

m^{Al}_{prop} – dimensionless initial mass of aluminum in propellant,

m_{ag}/m_{ccp} – relative mass fraction of agglomerates in CCP,

m_f/m_{ccp} – relative mass fraction of fine particles in CCP,

$[Al]_f = (m^{Al}_f/m_f)\cdot 100\%$ - percentage of free aluminum in fine particles,

$[Al]_{ag} = (m^{Al}_{ag}/m_{ag})\cdot 100\%$ - percentage of free aluminum in agglomerates,

$[Al]_{ccp} = (m^{Al}_{ccp}/m_{ccp})\cdot 100\%$ - percentage of free aluminum in CCP,

m^{Al}_f/m^{Al}_{prop} - relative quantity of free aluminum in fine particles,

$m^{Al}_{ag}/m^{Al}_{prop}$ - relative quantity of free aluminum in agglomerates,

$m^{Al}_{ccp}/m^{Al}_{prop}$ - total incompleteness of aluminum combustion,

$m_f : m_{ag}$ - mass ratio of fine particles and agglomerates in CCP,

$m^{Al}_f : m^{Al}_{ag}$ - mass ratio of free aluminum in fine particles and in agglomerates.

EXPERIMENTAL RESULTS

The performed 13 experimental series are listed in Table 3. The series identifier consists of letters A (Argon) or N (Nitrogen), which correspond to gaseous environment, and the number, which represents batch number # from Table 1. The experimental conditions in series N7D (the letter "D" means "duplicate") were the same as in series N7. Thus, the comparison between the results of N7 and N7D

series gives the notion about general reproducibility of experimental and treatment procedures.

The data in Table 3 show that the propellants studied exhibit very effective aluminum conversion and low intensity of the agglomeration process. Actually, the agglomerate formation is relatively rare event that brings low contribution of the agglomerates mass into total CCP mass. However, for most propellants the main portion of non-consumed aluminum is presented in agglomerates. Detailed data on the content of unburned aluminum in CCP are reported in Table 4.

Table 3. Pressure P, burning rate r and total CCP characteristics

Series	P, atm	r, mm/s	m_{ccp}	m^{Al}_{ccp}	$m_f:m_{ag}$	$m^{Al}_f:m^{Al}_{ag}$	$m^{Al}_{ccp}/m^{Al}_{prop}$
A1	49	39±10	0.514	0.0104	97:3	10:90	0.058
N1	46	48±9	0.371	0.0146	89:11	7:93	0.081
A2	49	61±6	0.374	0.0066	96:4	14:86	0.037
N2	44	60±6	0.289	0.0093	90:10	6:94	0.052
A3	50	290±40	0.442	0.0015	98:2	80:20	0.008
N3	46	290±50	0.542	0.0029	99:1	76:24	0.016
N4	46	22±2	0.297	0.0347	69:31	4:96	0.193
A5	46	41±4	0.365	0.0129	91:9	15:85	0.072
N5	46	46±7	0.433	0.0154	88:12	7:93	0.085
N6	46	35±3	0.306	0.0271	80:20	7:93	0.150
A7	47	40±6	0.288	0.0124	90:10	16:84	0.069
N7	46	40±4	0.452	0.0148	90:10	12:88	0.082
N7D	46	50±6	0.370	0.0150	88:12	9:91	0.084

Table 4. Chemical analysis data on unburned aluminum for individual sieve fractions of CCP particles and averaged over all sampled CCP (% mass.)

Series	< 130 μm	130-150 μm	150-300 μm	> 300 μm	$[Al]_{ccp}$
A1	0.21	57.0	57.4	~2	2.0
N1	0.30	33.4	39.7	7.7	3.9
A2	0.26	47.0	37.0	0	1.8
N2	0.22	35.0±1.2	39.4	5.2	3.2
A3	0.27	2.8	3.1	~4	0.3
N3	0.42	8.0	~14	~6	0.5
N4	0.63	37.4±1.0	38.2±0.5	33.8±1.6	11.7
A5	0.58	36.5	33.4	0	3.5
N5	0.30	24.5±0.5	31.2±0.3	~5.6	3.5
N6	0.78	39.4±0.5	43.8±0.3	24.0	8.9
A7	0.79	40.0	39.6	3.7	4.3
N7	0.32	25.1±0.1	39.4±0.2	4.7	3.3
N7D	0.42	29.3	33.2±0.5	6.7	4.1

Comments:

1. In most cases the data presented correspond to the mean result of analyses of two independent probes. The figure after sign ± corresponds to standard error of determined value. This figure is not written if mass of given fraction of CCP was too small to repeat an analysis and only one determination was made.
2. The sign ~ corresponds to low accuracy data due to small absolute mass of the probe (fraction).

Due to pronounced boundary between coarse and fine CCP particles we will discuss below their characteristics separately.

Agglomerate characteristics

The major part of coarse (>D_L) CCP particles is "classical" nearly spherical shape agglomerates covered with hard surface oxide layer. In most series mean agglomerate density was found to be equal to about 2.1÷2.3 g/cm^3, except series A3 and N3 (formulations with 100% Alex). In these series sampled agglomerates had rough surface, coated with attached flakes, and agglomerate density was equal to 1.3÷2.0 g/cm^3. One may propose that during combustion of this formulation #3 a partial destruction of the burning surface (dispersion) does occur, and some part of agglomerates finish their formation not in the condensed but later in the gas phase. That is why the appearance and density of these agglomerates have distinctive features. There are two facts indicating the disturbance of layer-by-layer character of combustion of the formulation #3 based on pure Alex. 1) The extremely high burning rate has been measured during combustion of such samples that was accompanied by loud sound (like explosion) and damages of some interior bomb constructions.
2) The sampled condensed combustion products partially consisted of powder that looked like crushed propellant specimen material. This powder can be dissolved in acetone and in water. The chemical and RFA analyses show the presence of AP (up to 27% mass) in this powdered material.

The main mass and size characteristics of agglomerate particles are presented in Table 5. Before analyzing the data it should be remarked that comparison between series N7 and N7D gives the notion about scatter or reproducibility of presented parameters. Unfortunately, the larger the Alex fraction, the worse sample quality. "Bad" samples have the porosity that causes scatter in the burning rate data and causes the roughness and caverns on the lateral sample surface. The oil used for inhibiting the lateral surface filled these caverns and then was dispersed in the course of combustion. The oil drops, being trapped by screens and filter,

contaminated sampled products, especially their fine fraction. That is why the scatter of mass parameters is relatively high because the oil mass depends on the roughness of the sample surface. However, one can see in Table 6 that values m_{ag}, m^{Al}_{ag}, m^{Al}_{ccp} in series N7 and N7D have fairly good reproducibility.

The basic tendencies in agglomerate characteristics behavior are as follows.

In all series the mass size distribution function has a typical shape and therefore it is not pictured here. The position of maximum practically coincides with the mean size D_{10}. The "width" of the distribution can be characterized by the ratio D_{10}/D_{43}.

The effect of replacement of commercial Al by Alex has been studied in series consequence A1-A2-A3 and N1-N2-N3 for the propellant formulations without HMX and in series N4-N6-N5 (A6) for the propellant formulations containing HMX.

Analysis of experimental data reported in Tables 5-6 shows that such replacement leads to increase in the burning rate, decrease of agglomeration intensity and decrease of the metal combustion incompleteness. For propellants without HMX the characteristic sizes D_{mn} for different formulations do not differ significantly and decrease of the metal combustion incompleteness is achieved mainly due to decrease of the mass fraction of agglomerates. In other words, the shape of size distribution curve is not changed while its amplitude decreases. The most pronounced example of such behavior demonstrates propellant #3 where ratio m_f:m_{ag} amounts 99:1 (series N3) and 98:2 (series A3).

Propellant formulations containing HMX initially exhibit the higher agglomeration intensity as compared with pure AP based propellants. For instance, free aluminum percentage in CCP in series N4 is 3 times higher ($[Al_{ccp}]$=11.7%) than that in series N1 ($[Al_{ccp}]$=3.9%). The listed above trends are most expressed in the combustion of HMX containing formulations. Indeed, the higher incompleteness is the result of the bigger mass of agglomerates. The mean sizes D_{mn} slightly decrease with replacement of Al by Alex (the maximum of size distribution function moves left). It is noteworthy to underline that in the case of HMX containing propellants even small amount of Alex in the propellant formulation produces sizable effect on the agglomeration behavior (propellant #6).

It is interesting to note that for all studied propellants the one of the main parameters that characterize the agglomerate intensity, namely, dimensionless mass

of agglomerate m_{ag}, demonstrates practically inversely proportional dependence to the burning rate, Fig. 3.

Regarding the influence of gaseous environment it was revealed that in most cases the experiments in argon give smaller value of agglomerate mass as compared with the experiments in nitrogen though the propellant burning rates in both gases practically coincide. However, a noticeable difference in agglomerate sizes was not observed. The nature of this phenomenon is not clear yet.

The experimental series N6 and N7 were performed to estimate fine aluminum type effect. For this end an UFA was used in formulation #7. Actually, no considerable difference in agglomerate behavior has been observed, and no specific features of different chemical reactivity of Alex and UFA were detected.

Table 5. Mass and size characteristics of agglomerate particles. Mean size D_{nm} was calculated in size interval D_L-D_R. The values D_{nm}, D_L, D_R are given in μm.

Series	D_L-D_R	m_{ag}	m^{Al}_{ag}	$[Al]_{ag}$	D_{10}	D_{30}	D_{32}	D_{43}	D_{53}	D_{43}/D_{10}
A1	34-289	0.018	0.0094	52.5%	167	170	174	179	181	1.07
N1	100-289	0.040	0.0136	34.2%	165	170	174	180	182	1.09
A2	24-433	0.015	0.0057	38.0%	172	176	181	186	190	1.08
N2	118-238	0.026	0.0087	33.5%	162	164	166	169	170	1.04
A3	34-433	0.010	0.0003	2.9%	188	202	217	237	248	1.26
N3	24-306	0.007	0.0007	10%	162	167	173	180	184	1.11
N4	118-736	0.093	0.0334	35.9%	212	230	250	274	288	1.29
A5	34-306	0.033	0.0110	33.3%	183	189	195	201	205	1.10
N5	118-325	0.052	0.0143	27.5%	174	180	186	193	196	1.11
N6	118-605	0.061	0.0252	41.3%	186	195	205	218	225	1.17
A7	34-736	0.030	0.0104	34.7%	171	179	188	212	239	1.24
N7	118-303	0.043	0.0135	31.4%	170	175	181	187	190	1.10
N7D	118-306	0.047	0.0136	28.9%	171	177	183	189	192	1.11

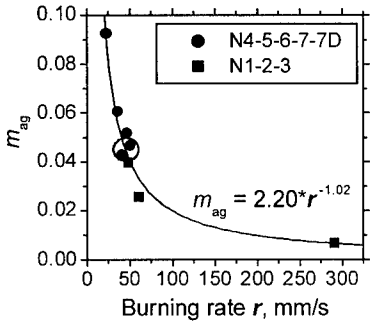

Fig. 3. Unified dependence of dimensionless agglomerate mass on burning rate.

Two round shape circled points corresponding to series N7 and N7D performed under identical conditions give estimate for reproducibility of experimental data.

Characteristics of the fine CCP particles.

The main mass characteristics of particles with size smaller than D_L and their contribution into total CCP mass are shown in Table 6. First of all it should be noted that in all cases the unburned aluminum content $[Al]_f$ does not exceed 0.8%. Thus, the fine CCP particles consist mainly of oxide formed in course of aluminum burnout. The ratio of the fine particle and agglomerate masses m_f:m_{ag} varies from (69:31) to (99:1). At the same time the ratio of free aluminum mass contained in fine particles and in agglomerates, (m_f:m_{ag}), for most series varies from (6:94) to (16:84). The propellant sample with total replacement of commercial aluminum by Alex (series A3 and N3, shadowed lines in Table 6) exhibit exceptional behavior due to extremely low agglomerate mass and mass contribution of agglomerates into total mass of CCP: m_f:m_{ag} = 98:2 and m_f:m_{ag} = 99:1 for series A3 and N3, respectively.

Table 6. Mass characteristics of fine particles

Series	D_L, μm	m_f	$m^{Al}{}_f$	$[Al]_f$	m_f:m_{ag}	$m^{Al}{}_f$:$m^{Al}{}_{ag}$
A1	34	0.497	0.0010	0.2%	97:3	10:90
N1	55	0.331	0.0010	0.3%	89:11	7:93
A2	24	0.359	0.0009	0.3%	96:4	14:86
N2	55	0.263	0.0006	0.3%	90:10	6:94
A3	34	0.432	0.0012	0.3%	98:2	80:20
N3	24	0.535	0.0022	0.4%	99:1	76:24
N4	118	0.204	0.0013	0.6%	69:31	4:96
A5	34	0.332	0.0019	0.6%	91:9	15:85
N5	118	0.381	0.0011	0.3%	88:12	7:93
N6	118	0.245	0.0019	0.8%	80:20	7:93
A7	55	0.258	0.0020	0.8%	90:10	16:84
N7	118	0.409	0.0013	0.3%	90:10	12:88
N7D	118	0.324	0.0014	0.4%	88:12	9:91

The features of the mass size distribution function behavior (in the range from 0.5 μm to D_L) can be summarized as follows.

- In all cases the mass size distribution of fine particles has three characteristic peaks or local maxima which were previously observed for other aluminized propellants [6, 8-10]. Typically these peaks are located in 2nd (1.2-1.5 μm), 6th (3-3.9 μm) and 9th (6.4-8.2 μm) Malvern sizer histogram size intervals.
- For both propellant types – with HMX and without HMX – the higher aluminum conversion degree, the greater oxide mass in total mass of CCP. In other words, m_f

increases with reduction of agglomerate mass m_{ag} and with reduction of incompleteness of aluminum combustion $[(m^{Al}_{ccp})/(m^{Al}_{prop})]$. The last quantity decreases with the burning rate. In the case of experimenting in nitrogen, with consecutive replacement of aluminum by Alex the incompleteness of aluminum combustion $[(m^{Al}_{ccp})/(m^{Al}_{prop})]$ decreases monotonously and mass size distribution *f(D)* transforms so as at first the *f(D)* right tail becomes shortly and then the magnitude of function *f(D)* increases in the size range 0.5-1.9 μm.

- For the propellant composition #7 based on UFA the mass size distribution function *f(D)* has elongated right hand side tail (D_L up to 118 μm) as compared with another series. The reason for such behavior is not clear at present time.
- When the combustion experiments are carried out in argon instead of nitrogen, the function *f(D)* changes. Namely, in most cases right hand side tail becomes shorter and the magnitude of function *f(D)* increases in the size range 0.5-1.9 μm. The mechanism of this influence in not clear too. Analysis of the thermodynamic calculation data on combustion product characteristics and comparison of the physical properties of argon and nitrogen show no sizable distinctions which may induce the disparity in the combustion mechanism or in the freezing rate for aluminum particles.

CONCLUSIONS

Ultra fine metal (like aluminum exploded Alex) powders seem to be promising additive to the propellant formulation to diminish agglomeration intensity especially for HMX containing formulations. The experiments have shown that the replacement of commercial aluminum by Alex leads to increase in the burning rate, decrease of the agglomeration intensity and increase in the metal conversion completeness. The aluminum combustion incompleteness correlates with the mass of agglomerates. For all propellants the dimensionless mass of agglomerate varies inversely as the burning rate. In the case of HMX containing propellants even small amount of Alex (Alex/Al = 8.3/91.7) in the propellant formulation gives sizable effect. In future work it should be estimated the minimal concentration of Alex that may affect agglomeration and combustion efficiency of metalized propellant.

ACKNOWLEDGMENTS

This work has been sponsored in part by United States Air Force through its European Office of Aerospace Research and Development under Contract F61708-97-W0197.

The authors are grateful to V. N. Simonenko (propellant preparation), O. N. Zhitnitskaya, V. L. Bizyaev, T. D. Fedotova, A. G. Kir'yanova (particle size and chemical analyses), and especially G. V. Ivanov, V. Surkov, A. E. Salko, A. B. Vorozhtsov who supplied us with Alex and UFA powders.

REFERENCES

1. Gen M. Ya., Ziskin M. S., Petrov Yu. I. "Study of size distribution of Al aerosol in dependence of operational conditions". *Doklady AN SSSR*, v.127, 1959, p.366 - 368.

2. Ivanov G.V., Tepper F. "Activated Aluminum as a Stored Energy Source for Propellants". In: Challenges in Propellants and Combustion 100 Years after Nobel, edited by K. K. Kuo et al. Begell House, 1997, pp. 636-645.

3. Internet WEB Site: ARGONIDE NANO METAL POWDER TECHNOLOGIES <http://www.argonide.com/mainframe.htm>.

4. Sal'ko A. E. "Certain Aspects of Development and Use of Ultrafine Powdered Materials". In: Int. Workshop on Chemical Gasdynamics and Combustion of Energetic Materials TW95, Book of Abstracts, Report P8. Tomsk, 1995, p. 10-12.

5. V. N. Simonenko, V. E. Zarko. (1999). "Comparative studying the combustion behavior of composite propellants containing ultra fine aluminum". In: *Energetic materials. 30th Int. Annual Conf. of ICT*, Karlsruhe, Germany. Report 21, 14 pages.

6. Glotov O. G., Zyryanov V. Ya. (1991). "The Effect of Pressure on Characteristics of Condensed Combustion Products of Aluminized Solid Propellant". *Archivum Combustionis*, Vol. 11, No. 3-4, pp. 251-262.

7. Glotov O. G., Zyryanov V. Ya. (1995). "The Condensed Combustion Products of Aluminized Solid Propellants. I. The Method of Quenching at Various Distances from Burning Surface for Studying the Evolution of Particles". *Combustion, Explosion and Shock Waves*, Vol. 31, No. 1

8. Glotov O. G., Zarko V. E., Karasev V. V., Beckstead M. W. (1997). "Effect of Binder on the Formation and Evolution of Condensed Combustion Products of Metalized Solid Propellants", In: *Combustion and Detonation. 28th Int. Annual Conf. of ICT*, Karlsruhe, Germany, Report 75, 14 pages.

9. Glotov O. G., Zarko V. E., Karasev V. V., Beckstead M. W. (1998). "Condensed combustion products of metalized propellants of variable formulation". *AIAA Paper 98-0449*, 6 pages.

10. O. G. Glotov, V. E. Zarko, V. V. Karasev, M. W. Beckstead. (1998). "Aluminum Agglomeration in Solid Propellants: Formulation Effects". In: *Propellants, Explosives, Rockets, and Guns.* Proceedings of the 2nd Int. High Energy Materials Conference and Exhibit, December 8–10, 1998, IIT Madras, Chennai, India, pp. 131-137.

11. T. D. Fedotova, V. V. Malachov, O. G. Glotov, A. G. Kir'yanova. "Permanganatometric Determination of Metallic Aluminum in Condensed Combustion Products", *Siberian Chemical Journal*, No. 2, pp. 37-38 (1992). *(In Russian).*

REGULARITIES OF COMBUSTION OF ENERGETIC SYSTEMS CONTAINING POTASSIUM NITRATE

Anatoly P. Denisjuk, Dmitry L. Rusin, Yuri G. Shepelev

D.Mendeleyev University of Chemical Technology,
9, Miusskaya sq., 125047 Moscow, Russia

Abstract

It is established, potassium nitrate (PN) influences on the ballistite powders combustion in various zones of the burning wave. On the one hand, PN introduces the negative contribution to powders c-phase thermal balance because of the cost of heat on its heating and melting. On the other hand, PN introduces also positive contribution increasing a heat flow into c-phase from a zone above burning surface. The ratio of these contributions depends on a PN quantity in compositions, therefore PN can both increase, and reduce its burning rate.

The burning rate of powders with PN will increase essentially on introduction to composition of aluminium or carbon black (CB). It happens because of its intensive combustion in a zone above burning surface riched by oxidizer evolved at PN decomposition. PN considerably reduce efficiency of catalysis even it presence in a small content (3-5%). It limits the possibilities of burning rate regulation of such powders.

The propellants containing 70 % PN differ by reduced ability to combustion in case of they contain polymeric binder incapable of independent combustion. The addition to such compositions of 5-10% CB or phenoloformaldehide resin (iditol) results in sharp intensification of burning process and reduces dependence of the burning rate on pressure.

Introduction

It is known, the first powder which named "black" or "smoky" was invented on basis of PN and was used during many centuries. Then, as missile explosive, it was completely superseded by smokeless (pyroxylin and ballistite) powders.

Recently the interest in PN as a component of modern powders has essentially increased. On its basis the fire-suppressing compounds [1,2] and also plasma powder for magnetohydrodynamic generators [3] are created. PN is added to a powders for an elimination of fire- and explosion dangerous gases (CO and H_2) from burning products [4] and apply as

inhibitor of a secondary flame of artillery and rocket shots and as component of low temperature rocket propellants.

For an effective use of compositions, containing PN, the knowledge of regularities of their burning is necessary. In the literature there are only data on the combustion of black powder [5] and some fire-suppressing propellants [6].

Experimental section

Powders and propellants, containing PN, can be divided into 2 groups:

1. Compositions, containing the binder (without PN) capable to independent burning. Ballistite powders refer to this group.

2. Composite propellants, in which PN is an oxidizer. In this case the combustion of other components of propellant is impossible in the absence thereof PN. Besides, PN can execute and other functions. The fire-suppressing propellants based on inert binders can be refer to this group.

The peculiarities of the 1st group propellants combustion

The investigations were carried out on powders with various burning heat (Q_I) and temperature (T_f) (tab. 1). The size of PN particles in powder samples were of 10-20 microns. The burning rate determined in a Crowford bomb with photoregistration of burning process. The samples by a diameter of 7 mm were used.

The addition of 5 up to 60% PN to a powder No.1 increases coefficient of oxidizer surplus (α) from 0.787 up to 1.058, but the value of T_f decreases from 3120 K up to 2735 K.

The main experimental results are:

1. At the region of pressure 1-20 MPa PN renders qualitatively identical influence upon the burning rate of investigated powders irrespective of whether calculated burning temperature is increased or it is decreased as result of PN addition.

2. The dependence U(% PN) has an extreme character (fig. 1). Addition of 20-30% PN result in poorly burning rate increasing and futher PN addition - to sharply its decreasing. For high-energy powders the burning rate is increased upon 10% and for middle-energy propellants - upon 20%. The region of burning rate decreasing for middle-energy propellants begins at greater content of PN (~30%), than for high-energy one (~20%). For the last value U is reduced faster (fig. 2).

The combustion of high-energy propellant, containing ~30% PN, at pressure less than 1 MPa is unstable and it is accompanied by formation of a melting stratum on a powder surface and hard residual as small-sized balls, that is evidence of combustion incompleteness and, as result, partial evolving of energy.

Table 1

Peculiarities of investigated ballistite compositions

Basis of powder, R=plasticizer/NC, Q_l, kJ/kg	PN, %	α	T_f (P = 4 MPa)	Value ν at P, MPa	
				0.3 - 1	2 - 20
NG/NC	0	0.761	3139	0.60	0.70
R = 1,5	10	0.813	3092	0.58	0.70
Q_l = 5490	30	0.864	3053	0.57	0.70
Sample No.1	60	1.058	2735	0.35	1.00
NG/NC	0	0.785	3057	0.7	0.70
R = 1,3	31,1	0.951	2939	0.6	0.76
(3,3 % MgO)					
Q_l = 5322					
Sample No.2					
NG/NC	0	0.731	3030	0.76	0.76
R = 1	12.5	0.771	3011	0.65	0.79
Q_l = 5121	16.6	0.796	2999	0.61	0.81
Sample. No.3	23	0.821	2986	0.6	0.95
	33	0.869	2954	0.62	1.0
Powder N	0	0.553	2316	0.71	0.71
28 % NG, 11 % DNT	3.8	0.569	2328	0.42	0.80
Q_l = 3572	9.1	0.592	2345	0.42	0.80
Sample. No.5	20	0.638	2380	0.43	0.81
	37.5	0.711	2436	0.58	0.82
DEGDN/NC	0	0.559	2236	0.82	0.82
R = 0,8	10	0.601	2270		
Q_l = 3645	30	0.684	2338		
Sample No.4	50	0.764	2404		
	55	0.783	2420	0.66 (1-7)	0.98 (p> 2)
NG/NC	60	1.058	2735		
R = 1,5	60 (+4.25% CB)	0.923	2822		
	60 (+8.5% CB)	0.826	2680		

At pressure more than 4 MPa PN increases dependence of the burning rate on pressure, increasing a parameter ν in the law of burning ($U = BP^{\nu}$) from 0,1 up to 0.8-1. At the pressure less than 2-4 MPa the using of PN results in decrease value of ν, for example, for a powder N from 0.67 up to 0.42.

These features of burning of a powder with PN can be explained as follows. It is known [7], on the one hand the burning rate of powders is determined in main by heat release directly in a reaction zone of a condensed phase (c-phase) at the temperature of 600-800 K (depending on pressure). On the other hand it is determined by heat arriving from a zone above powder surface. The last is the result of partial reducing of NO_2 (formed at disintegration NC and NG) up to NO, which completely reacts with CO and H_2 only in a zone of a secondary flame at increased (4-6 MPa) pressure. The PN in c-phase is diluent of a powder and absorbs heat not only on the heating, but also on melting (T_m=609 K) and partial own decomposition ($T_d \geq 673$ K). The oxygen formed at PN decomposition, reacts in zones above a burning surface and increases a stream of heat in to c-phase. At contents PN of 20-30% this stream exceeds endothermic effects on heating, melting and partial decomposition of PN in c-phase and the burning rate of powders with PN is a little bit higher, than initial compounds without PN.

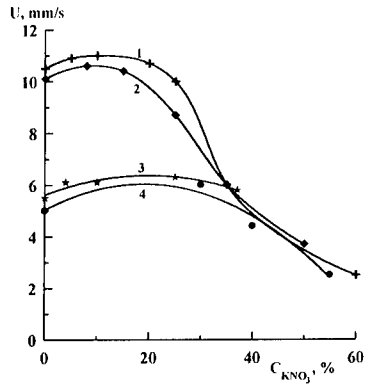

Fig. 1. The dependence of the burning rate of different powders upon percentage of PN:
1 - sample No. 1;
2 - sample No. 3;
3 - sample No. 4;
4 - sample No. 5.

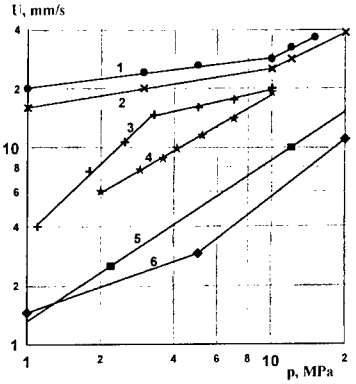

Fig. 2. The dependence of the burning rate of different powders upon pressure:
1 - No.1 + 60% PN + 8.5% CB, 2 - No.1 (based on DNDEG) + 60% PN + 8.5% CB, 3 - No.1 + 30% PN + 18% Al, 4 - No.1 without PN and CB, 5 - No.1 (based on DNDEG) without PN and CB, 6 - No.1 + 60% PN without CB

In result of adding of PN over 40-50% the quantity of heat evolved in a zone above a surface, probable, increase unsignificantly, and the heat consumption in c-phase are increased and the burning rate of compounds containing PN becomes lower than for initial powders.

For understanding of PN influence on a processes in a zone above burning surface the distribution of temperature in a burning wave of powder N and one with 5% PN was determined by microthermocouples [8]. It is visible (tab. 2) introduction 5% PN in a powder N results in a modification of a temperature profile:

- maximum burning temperature (T_{max}) increased;
- height (L) of the smoke-gas zone 2.5 times as less decreased;
- a temperature gradient at a surface sharply increased.

It results in part of heat supply in to c-phase from gas 1.5 times as much increases, therefore the surface temperature and the burning rate increases.

Table 2

Some performances of powder N combustion zones at P = 1 MPa

Sample	U, mm/s	T_s, K	dT/dx, K/cm	L, microns	T_{max}, K
N	2.3	576	3.8	265	1155
N + 5% PN	3.25	600	10.2	102	1523

Despite of increasing of intensity of reactions in a hiss zone, the full evolving of energy of PN powders happens, as well as for powders without PN at pressure higher 4 MPa. It follows from results of determination of products composition and burning temperature.

The measurements of T_f carried out with using of thermocouples, which placed in a quartz capillary for prevention of adhering of melt PN drops. Without capillary the break of the thermocouple happened or the pulsings of temperature were observed. Experimental value of T_f at all pressures considerably differs from calculated one. It occur owing to heat dissipation by the thermocouple by means of a radiation [8].

In the region of reduced pressure the difference between experimental and calculated temperature values is higher, than at pressure greater than 4 MPa (fig. 3). At pressure variation from 4 up to 1 MPa measured values of T_f decreases by 520 K, while the calculated temperature - by 70 K. At the pressure above 4 MPa the growth rates of experimental and calculated temperatures of combustion are about identical. Thus, at pressure approximately up to 4 MPa take place incomplete burning. It conforms to results of the gas analysis - at pressure less than 6 MPa in the burning products occur NO, CO and H_2, but in calculated composition of products (α= 1) these gases are absent.

Aluminium and its alloys with magnesium render strong influence on the burning of considered powders. Thus, addition of 22% (over 100%) aluminium ASD-4 (the average size of

particles ~ 6 mkm) into compound No.1, containing 33% PN, lead to increasing of a burning rate (for example, at P = 4 MPa up to 4.5 times) and decreasing of the value ν up to ~ 0.4.

The metal influences on the burning rate of initial samples without PN (burning with higher rates) very weakly (the increase is 10-20%). Strong influence of metals on the burning of propellants with PN is conditioned by higher concentration of oxidizing gases (CO_2, H_2O and O_2) in zones above a burning surface, in which the diffusion combustion of particles of metal happens.

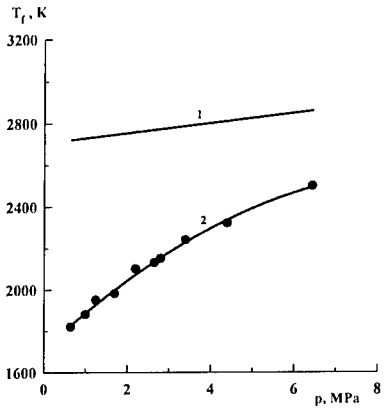

Fig. 3. The dependence of the flame temperature of the sample No.2 upon pressure:
1 - calculation, 2 - experiment.

The carbon black renders strong influence on the burning of ballistite powders with PN, increasing a burning rate, especially in the range of reduced pressure. The burning rate is weakly ($\nu < 0.2$) depends on pressure in a range from 2 up to 10 MPa. Thus, samples containing 8.5% CB in the propellant composition both based on NG and one on DEGDN (contents PN ~ 60%) at pressure 0.1-1 MPa burn 10-15 times as much faster than compositions without carbon black. The addition of carbon black into a basis of these powders without PN decreases the burning rate.

The increasing of a burning rate of propellants with high PN contents in result of addition of carbon black, despite of significant decrease of Q_l and T_f, can be explained by a changing of burning mechanism. A zone above a burning surface becomes a leading zone. In this zone in a diffusion mode take place intensive interaction between superfine particles of carbon black ($S_{specific}$ ~ 100 m^2/g) and oxygen, formed as result of PN decomposition. Thereof dependence U(P) sharply decreases and becomes close to those for a black powder or mixture PN with wood coal or soot. Thus, at pressure approximately up to 10 MPa the burning rate of propellant is

determined by a subsystem PN - CB. With an increase pressure above 10 МПа dependence U(P) increase, probable, owing to transition of burning to a kinetic mode, at which the role of gas reactions, for example, CO and H_2 with NO intensifies.

The powders, containing PN, at P > 2 MPa have high dependence of the burning rate on pressure, but it is extremely undesirable. It is important to know, whether it is possible to change the burning rate of powders, containing PN, by catalysts and reduce the dependence U(P), as it is done for powders in the absence of PN. The catalyst efficiency were estimated by value of $Z = U_k/U_0$, where U_k and U_0 - the burning rate of a sample with the catalyst and without it accordingly. In case of addition of PN to powder the value of Z essentially decreases. The higher contents PN results in the more weak catalysis (fig. 4).

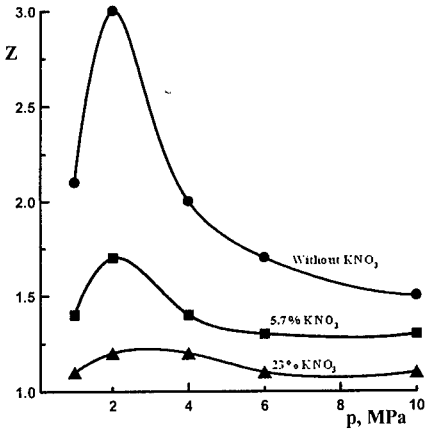

Fig. 4. The influence of PN on efficiency (Z) of complex catalyst of combustion (3% lead phthalate + 1% CB) in a powder "A" (sample No.3) at various pressures

In case of powders, containing PN, the value of Z at pressure above 4 MPa does not decrease almost, in contrast to powders without PN, and coefficient ν is not reduced (tab. 3). Thus, PN renders negative influence on catalysis of powders combustion.

It is shown in [7], the catalysis of combustion of powders take place, if on a burning surface a soot sceleton is formed, on which the particles of the catalyst are accumulated without its aglomeration. The PN accelerates reactions above a burning surface and considerably increases a gradient of temperature (tab. 2). It, probable, decreases a possibility of formation of a sceleton and decreases catalysts efficiency also, that have confirmed by results of researches of surface state of extinguished powder N.

The surface of extinguished initial powder N is covered with a sceleton (height of the order 100 microns), consisting of carbon in the main. On a surface of extinguished catalyzed powder sample there is a sceleton also, on which the particles of the catalyst are located.

Table 3

The influence of PN on catalyst efficiency on the combustion of different powders

Powder	Z at P = 4MPa	ν	P, MPa
N	-	0.71	2 - 20
N + catalyst			
N + catalyst + 4% PN	1.25	0.3 0.7	2 - 6 6 - 20
No.3	-	0.76	2 - 20
No.3 + catalyst	2	0.33	1-15
No.3 + catalyst + 5.7% PN	1.4	0.6	2 - 20
No.3 + catalyst + 50% PN	1.3	0.6 1.2	2 - 6 6 - 20

The surface of catalyzed powder, containing PN, is plane in the main, a soot sceleton practically is absent, only separate unregulated soot formations and the particles of PN also are visible.

The peculiarities of the 2nd group propellants combustion

Two types of fire-suppressing propellants were investigated:

1. Low-temperature propellants ($T \leq 1500$ K). The reduced temperature was reached by low (0.4-0.5) value of α.

2. Ecologically safe propellants ($\alpha \sim 1$), not containing fire- and explosive dangerous gases (CO and H_2) in the burning products.

Regularities of combustion of low-temperature compositions

Two kinds of propellants were investigated: sample No.6 [NC+TAC (or DBP) = 24.9%, PN - 62.5, CB - 8.9%, technological and other additives - 3,7%]; sample No.7 [PVB - 10,5%, TAC - 4,5%, DBP - 4.5%, PN - 68.5%, CB - 10%, technological additives - 2%].

For decrease of α and T_f in the composition of propellants the carbon black were entered. The magnitudes of α and T_f depend on a ratio PN/CB (η) and on an amount of this mixture in propellant. Basis propellants contained PN and CB in quantities ensuring the absence of free carbon in calculated composition of the burning products. For these propellants the special components permitting to supply its stable burning at atmospheric pressure were found.

For compositions based on PVB the burning rate at atmospheric pressure is about 2.5-2.8 mm/s and for one based on NC - 3-4 mm/s.

If carbon black to exclude from compound based on NC-TAC, the sample begins to burn at pressure about 3 MPa only (curve 3, fig. 5), its burning rate at pressure 4 MPa almost in 10 times less than for a sample, containing CB. The sample without CB has very high dependence U(P) - value of ν=1,1. The sample based on PVB without CB does not burn up to high pressure. Thus, the carbon black as well as in case of ballistite powders, containing PN, plays the special role in the burning of propellants based on inactive binder. Samples of both propellants with CB have low dependence of a burning rate on pressure ($\nu \sim 0$) at wide interval of pressure (fig. 5).

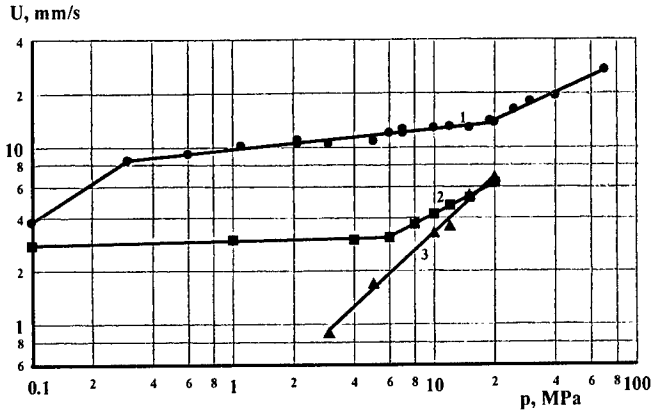

Fig. 5. The dependence of the burning rate of fire-suppressing powders upon pressure:
1 - NC-TAC + 62.5% PN + 8.9% CB, 2 - PVB-DBP + 68.5% PN + 10% CB,
3 - NC-TAC + 62.5% PN without CB

At pressure in the range higher 6 (20) MPa (curve 1 and 2, fig. 5) the dependence U(P) is increased ($\nu \sim 0.5$–0.7). Such strong changing of dependence U(P) with pressure increasing can be stipulated for transition of burning from a diffusion mode (combustion of soot with O_2) to kinetic mode at the expense of interaction gaseous fuel (formed in result of decomposition of binder) with oxygen.

Variation of a ratio between plasticizer and polymer in limits (0.8 - 1.25) renders small influence on the burning rate both propellants.

The burning rate of propellants depends also on an amount of a mixture PN+CB (at its constant ratio). Carbon black with a specific surface 75 m^2/g and fine-dyspersated PN (size of particles ~10 microns) were used.

The value of η especially hardly influences a rate and stability of burning of compounds at atmospheric pressure. Propellants with η = 5 and 6,5 at atmospheric pressure burn with a high rate - 7.0 and 3.8 mm/s accordingly (tab. 4). Propellants with η= 7.5-10 (diameter of charge is 6 mm) after ignition burn unstable and extinguish. At the increasing of pressure and decreasing of η in limits from 10 up to 5 the burning rate increase. All samples have weak dependence U(P). Thus, the ratio PN-CB is the factor, defining magnitude of a burning rate and combustion stability at atmospheric pressure.

The influence of a dispersibility of CB on the burning rate of propellants (η = 7.5; PN+C=75%; CB with $S_{specific}$ = 250, 100 and 75 m^2/g) were investigated.

Table 4

The burning rate of propellants with a various ratio PN/C

η	α	T_f, K	U, mm/s at pressure, MPa			ν at P, MPa	
			0.1	0.3	3.0	0.1-0.3	0.3-3.0
5.0	0.59	1270	7.0	9.0	9.0	0.25	0
6.5	0.68	1435	3.8	6.5	9.5	0.5	0.16
7.5	0.72	1486	Don't burn	6.5	10.3		0.20
10.0	0.8	1515	Don't burn	4.3	10.5		0.40

It is visible (tab. 5), samples with large-dispersed CB does not burn at atmospheric pressure, though, since pressure 0.3 MPa they burn at high rate (6 mm/s).

In the range of pressure 0.3-3 MPa the propellants burning rate increases with rising of CB specific surface. With growth of pressure this dependence weakens. At pressure 0.3MPa the burning rate of the sample with superfine-dispersed CB in 2.15 times higher, than for the sample with the largest-dispersed CB and at pressure 3 MPa - in ~ 1.4 times.

Table 5

The influence of CB dispersibility on the propellants burning rate

$S_{specific}$ of CB, m^2/g	U, mm/s, at pressure, MPa			ν at pressure interval, MPa	
	0.1	0.4	3.0	0.1-0.4	0.4-3
250	3.9	14.0	14.0	1.0	0
100	Don't burn	8.2	11.8	-	0.15
75	Don't burn	6.5	10.3	-	0.20

The burning rate of a sample with fine-dispersed CB does not depend on pressure in an investigated interval. For compounds, containing CB with $S_{spesific}$ = 100 and 75 m^2/g, value of U is weakly increased with growth of pressure (ν are equal 0.15 and 0.2 accordingly).

The burning temperature of propellants, containing potassium hexacianoferrate (HCFP), the largest-dispersed CB ($S_{spesific}$ = 75 m^2/g, tab. 6) and 1.7 % of the technological adds is determined experimentally. The technological adds ensures stability of burning of propellants at atmospheric pressure even without the catalyst.

Table 6

The burning temperature of propellants

P, MPa	Without the catalyst		With the catalyst		Z
	T_{calc}, K	T_{exp}, K	$T_{calc.}$, K	T_{exp}, K	
0.1	1375	1490±25	1343	1315±10	1.47
1.1	1478	1645±20	1417	1535±5	0.94
2.1	1493	1635±7	1424	1635±8	0.98

For a sample without HCFP the experimental and calculated values of T_f increase depending on pressure (from atmospheric up to ~1 MPa) and at pressure above 1 MPa it is practically constant. The calculated T_f is lower, than experimental in all an investigated range of pressure: the difference between T_{calc} and T_{exp} at atmospheric pressure is 110 K and at 2MPa - 140 K.

For samples with the catalyst calculated and experimental values of burning temperature in an investigated interval of pressure (tab. 6) is lower, than for a sample without HCFP. At atmospheric pressure, when HCFP considerably accelerates the combustion of propellants (by ~50%), value of experimental and calculated temperatures are close. At pressure above 0.5 MPa, when the HCFP does not accelerate burning, experimental T_f is higher, than calculated one. It can be explained by following: thermodynamic equilibrium at the propellant combustion is not reached and the burning products contain a carbon (as initial CB or formed as result of decomposition of propellant components), which has no time to react in a burning wave completely correspondingly to the following endothermic reactions:

$$C + H_2O \rightarrow CO + H_2 \qquad \Delta H = + 132{,}7 \text{ kJ/mol},$$

$$C + CO_2 \rightarrow 2CO \qquad \Delta H = + 172{,}6 \text{ kJ/mol}$$

Acknowledgement of this assumption are the calculation of T_f under condition of fixation of the contents of carbon in burning products. At presence in the burning products of 3.6% of carbon the calculated meaning of temperature (1632 K) practically equal to experimental one, the contents of H_2O and CO_2 in burning products simultaneously changes.

Low temperature of combustion of propellants was reached by small value α (0,3-0,6), at which main products of combustion are CO and H_2. It is inherent almost in all propellants,

developed by variuos authors and used in modern fire-suppressing generators. The use of such propellants is undesirable, as the carbon oxide is poisoning gas and, besides it, as well as the hydrogen, derivate explosive- and fire-dangerous mixtures with an air.

The regularities of burning of high-temperature propellants

We developed ecological and fire-explosive safe propellants, in burning products of which are absent CO and H_2. It was supplied by arrangement of propellants with value of α, close to 1. In this case amount of propellant binder is about 16% and oxidizer ~84%. As binder used iditol, plasticized by DBP. For regulation of various properties of propellant part of PN was substituted by $KClO_4$. The burning temperature of these compounds is 1700-2100 K, that on 300-700 K higher, than for low-temperature one.

After partial replacement (up to 20%) of PN by $KClO_4$ the burning rate at atmospheric pressure increases, and at content above 20% it decreases. The sample, containing $KClO_4$, burns in 2.5 times slower than sample, containing PN.

Samples based on PN or mixtures KNO_3+$KClO_4$ have very weak dependence of the burning rate on pressure in the range of low pressure (0.1–0.4 MPa). At further increasing of pressure the value of ν is increased up to 0.4 (tab. 7).

Table 7

The dependence of burning rate on pressure for high-temperature fire-suppressing propellants

$KNO_3/KClO_4$	ν at P, MPa	
	0.1 - 0.4	1 - 10
84/0	0.1	0.4
64/20	0.1	0.4

For propellants with constant ratio (64/20) of oxidizers in compounds the modification of a ratio iditol-DBP (from 1.96 up to 1.43) results in decrease in 1.6 times of the burning rate and aggravation of a burning completeness.

Thus, experimental contents CO is increased from ~ 1 up to 15.7%, whereas on calculated concentration of CO is equal approximately 0.1%.

References

1. Denisjuk A.P., Zhukov B.P., Alferov V.G., Shepelev Yu.G., Baloyan B.M., Rusin D.L., Sedov S.A. Development of solid propellants for effective fire-extinguishing systems. "Conversion Concepts for Commercial Applications and Disposal Technologies of Energetic Systems". Proc. of the NATO Advanced Research Workshop, Moscow, 17-19 May 1994. NATO

ASI Series. Ser. 1: Disarmament Technologies. Vol. 14. Kluwer Acad. Publishers. Dordrecht / Boston/ London, 1997, p. 99-112.

2. Ewing C.T., Hughes I.T., Carhart H.W. Fire and materials, 1984, v. 8, No. 3.

3. Zhukov B.P. Powder based MHD-generators. Principle of operation and application area in economy. Proc. of 21st Int. Pyrotech. Seminar, Moscow, 11-15 Sept. 1995, p. 977-1017.

4. Denisjuk A.P., Zyambaev M.N., Rusin D.L., Shepelev Yu.G. Ecologically safe propellants for aerosol fire-suppressing. Fire-and-Explosion Hazard of Substances and Venting of Deflag-rations. Proc. of 2nd Int. Seminar, Moscow, 11-15 Aug. 1997, p. 817-823.

5. Bakhman N.N., Belyaev A.F. The combustion of heterogeneous condensed systems. Moscow, Nauka, 1967.

6. Zhukov B.P., Denisjuk A.P., Zyambaev M.N., Rusin D.L., Shepelev Yu.G. High-effective fire-suppressing propellant. Proc. of 21st Int. Pyrotech. Seminar, Moscow, 11-15 Sept., 1995, p. 1018-1032.

7. Denisjuk A.P., Margolin A.D., Tokarev N.P., Khubaev V.G., Demidova L.A. Role of carbon black at the burning of ballistite powders with lead-containing catalysts. Combustion, Explosion, and Shock Waves, 1977, Vol. 13, No. 4, p. 576-584.

8. Zenin A.A. About heat exchange of microthermocouples at the condensed substances combustion. J. Appl. Mechanics and Eng. Physics (ПМТФ), 1963, No. 5, p. 125-131.

BURNUNG WAVE STRUCTURE AND COMBUSTION MECHANISM OF DLYCIDYL-AZIDE/NITRAMINE MIXTURES.

Anatoli A.Zenin, and Sergej V.Finjakov
Semenov Institute of Chemical Physics, Russian Academy of Sciences.
Moscow 117977, Kosygin Str. 4. Russia. 5195.g23@g23.relcom.ru

Abstract

Combustion wave structures of mixtures of glycidyl azide with HMX and RDX were studied by microthermocouple technique and by data processing. Pellets of the mixtures burned in nitrogen atmosphere at pressures 5-60 atm and at normal ambient temperature. Temperature profiles and the following burning wave parameters were obtained: burning rates, burn-surface temperatures, heat feedback from gas to solid, heat release in solid, distributions of heat release rate along the gas phase of the combustion waves, zone sizes and temperatures in solid and gas. Characteristic features of physics of the combustion were established. Location of burning rate control region in the combustion waves was found. Macrokinetic laws of solid gasification and gas phase combustion were determined. The obtained data can be useful in modelling of glycidyl azide - nitramine mixture combustion.

1. Introduction

Glycidyl azides are new energetic binders for composite propellants and cyclic nitramines HMX and RDX are new oxidizes for the propellants having improved ballistics and mechanical performance, reduced vulnerability and corrosivity of exhaust products. Many investigations of burning behaviour of HMX, RDX and their additions to different propellants and investigations of combustion of various energetic binders were performed during last years[1-11].

Burning wave structures of HMX and RDX and nitramine containing propellants were studied in Refs. 12-16. Burn-surface temperatures, heat release in solid and heat feedback from gas to solid were found in combustion waves of the nitramines in wide pressure and ambient temperature ranges. Combustion mechanisms of chemical family of glycidyl azides - monomer, olygomer and copolymer of glycidyl azide with polyurethane - were studied in Ref. 17. Temperature profiles, burning wave parameters, macrokinetics laws and rate constants in solid reaction layer were determined and burning rate control stages were indicated. Characteristic features of physics of the combustion were established.

This work continues the combustion mechanism investigation by the approach of Refs. 12-17. The objects of the investigation here are the mixtures of HMX and RDX with glycidyl-azide-monomer. The paper has the following sections: subject of investigation, experimantal techniques, results of measurements and date processing, burning rate control region, macrokinetics and conclusions.

2. Subject of Investigations

The aim of the paper is to study the combustion mechanism of two mixtures: HMX with glycidyl azide monomer (GA) and RDX with GA. The mixtures have ratio 80:20 (by weight) of GA:nitramine. Oxidizer paritle sizes were 300-150 μm (50%) and <50 μm (50%). The monomer GA consists of $C_3H_5N_3O$. It is a pale yellow fluid of density 1.22 g/cm^3. The mixtures were prepared under vacuum condition at 60°C by mixing during about 6 ours in a special mixing device.

The obtained propellant mixtures had density 1.3 g/cm^3.Thermodynamic temperatures were 2400°C for HMX/GA and 2420°C for RDX/GA.

3. Experimental Techniques.

Temperature profiles of combustion waves and the burning surface temperatures were obtained by microthermocouple methods. The profiles were obtained by microthermocouples imbedded into mixtures. Thermocouples went through combustion waves when the waves propagated through the mixtures and recorded temperature profiles[12-18]. The ribbon U-shaped thermocouples made of alloys W+5%Re/W+20%Re of 2-7mkm thick were imbedded into the mixtures. Every sample had inside 2-3 thermocouples placed one above the other. Distances between the junctions were 2-4 mm. The mixtures burned in ceramic or glass tubes, havig inner diameter of 8 mm. Experiments were performed in a bomb of constant pressure in atmosphere of nitrogen at pressures 5 -60atm and at sample initial temperature T_o=+20°C. Samples were ignited by electrically heated wire. Thermocouple signals were recorded by oscillograph. Burning rate was measured by time delay between the thermocouple signals, by photoregistrations of sample combustion and by pressure increase during the sample combustion. Photoregistration of sample combustion allows also the type of combustion to be established. Burning surface temperatures were measured by thermocouples that are being pressed to the surface during sample combustion and by establishing the locations of slope breaks on temperature profiles registered by thermocouples (see below: method of "slope break").

Thermocouple Measurement Validations.

As a rule, temperature gradients in combustion waves close to the burning surface has a very high value. It implies that thermocouple measurements can give temperature profiles with significant errors due to thermocouple heat inertia. A special work was performed to minimize errors of the microthermocouple measurements[18-20]. Conditions have been found under which thermocouple measurements in combustion waves will introduce small errors. The thermocouple partially absorbs the heat of the thermal layer and decreases the temperature at the point of the measurement. The requirement of the small temperature decreasing (less than 10%) is indicated by the following formula:

$$h<0.2\,\chi/r_b; \qquad (1.3)$$

Here: h - thermocouple thickness (in cm), χ- heat diffusivity of the solid (in cm^2/s), r_b - linear burning rate (in cm/s). $\chi/r_b=l$ where l is thickness of heat layer of the condensed phase. There is another requirement for correct measurements by thermocouples in combustion waves: the thermocouples have to have U-shape form. It is necessary because of a very high difference between heat conductivity coefficients of metallic thermocouple wire and that of solid or gas. The junctions do not experience large temperature decrease if U-shaped thermocouple is used for that measurements. Modelling experiments and numerical simulations show that the decrease of junction temperature will be small (≤3%) if the horizontal part of the U-shaped thermocouple is about one hundred times more than thermocouple thickness h. Thermal inertia of the thermocouple in the gas phase can be taken into consideration and eliminated by a correction procedure. The procedure implies the use of the following equation:

$$dT_{ex}/dx=(r_b\cdot\tau_o)^{-1}\cdot(T - T_{ex}); \qquad (2.3)$$

Here: T - the real temperature of gas in the combustion wave; T_{ex} - the temperature obtained by thermocouple; τ_o - time response of the thermocouple in gas. Time response is known function of mass burning rate m ($m=\rho\cdot r_b$) and T. The temperature profiles in gas were corrected by this equation. The theory of thermocouple measurements in combustion waves of solids was created

and confirmed by measurements of combustion wave temperature profiles by thermocouples with sequentially decreased thickness (method of "zero diameter"). All the above mentioned requirements have been met in the investigations. Different types of metal wires for thermocouples were used (We,Re and Pt,Rh) to test the catalytic effect on thermocouples. The catalytic effect was not observed. The method of burning surface temperature measurement by determining locations of slope breaks on temperature profiles registered by thermocouples (method of "slope break") is based on the existence of the delay ($r_b \cdot \tau_0$) on the temperature profiles when thermocouples go through the burning surface. The delay is due to change of heat exchange between environment and thermocouple: contact heat exchange in solid is replaced by convective heat exchange in gas.

4. Results of Measurements and Date Processing

Figs. 1-4 show the obtained at 5-60 atm averaged temperature profiles for mixtures GA/HMX and GA/RDX. Averaging was performed by using about 6-12 temperature curves recorded for every regime of combustion. Temperature profiles for both mixtures have nonpulsating character, only at 5 atm can exist weak irregular pulsations.

As a rule, the gas phase of the combustion waves of the investigated mixtures is comprises of two zones: the first one is a relatively low-temperature zone and the second one is the flame zone. At elevated pressures the gas phase zone merged into one zone; for GA/HMX it is observed at p>20at and for GA/HMX it takes place already at 20 atm. Figs. 5-8 show also the obtained due to temperature profiles (see below) distributions of heat release rates Φ along the gas phase.

Table 1 shows the averaged burning wave parameters obtained by experiments and by processing experimental data (see below).

Mass burning rate.

Table 1 shows that mass burning rate m increases when pressure increases for both mixtures. Values of m comprise 0.13 - 0.88 g/cm^{2}s for mixture GA/HMX and 0.17 - 1.07 g/cm^{2}s for mixture GA/RDX in pressure interval 5-60 atm. Standard deviation of the mass burning rate measurements is ϑm=±5%.

Burn-Surface Temperature.

It can be seen from Table 1 that burn-surface temperature T_s always increases when m and pressure increase. Values of T_s grow from 380°C at 5 atm up to 540-570°C at 60 atm. Standard deviation of the burn-surface temperature measurements is ϑT_s=±5%.

The obtained values of T_s for mixture GA/HMX are higher than those for mixture GA/HMX at the same values of m. Values of T_s for investigated mixtures are also higher than those for burning pure HMX and RDX at the same values of m.

Geometric Structure of the Temperature Profiles in Gas.

It was mentioned already that the gas phase of the combustion waves has two-zone structure. The end of the first zone has zone temperatures T_1 and the second zone (flame zone) has final zone temperatures T_f. Both zones merge at p≥20atm into one zone of the gas phase. Table 1 shows that values of T_1 are equal to 1000-1100°C. Thermodynamically calculated values of T_f are observed at 60 atm. Distances L_1 from the burning surface up to beginning of the flame zone at pressures 5-20 atm are very small and comprise 130-250 μm (in fact, L_1 is the length of the first flame). Distances L from the burning surface up to the end of the flame (up to 0.99 T_f) comprise 1.2 - 0.9 mm. In fact, L is the length of the gas phase reaction zone. Standard deviations of L_1 and L estimations are equal to ±10-20%.

Table 1: Burning wave parameters of mixtures GA/HMX and GA/RDX
(above - values for GA/HMX / below - for GA/RDX)

p, atm	5	10	20	60
r_b, cm/s	0.10/0.13	0.16/0.2	0.31/0.39	0.68/0.82
m, g/cm^{2}s	0.13/0.17	0.21/0.39	0.40/51	0.88/1.07
T_s, °C	380/380	420/450	480/470	570/540
$\varphi \cdot 10^{-4}$, K/cm	4.5/3.8	5.2/4.8	6.6/6.2	11.0/9.0
q, cal/g	80/52	59/30	41/30	34/22
q_r, cal/g	19/15	13/7.4	7.4/6.3	4.0/3.3
Q, cal/g	64/101	107/158	155/167	202/206
l, μm	150/115	125/100	90/72	53/44
l_m, μm	60/80	60/80	50/60	40/40
$\lambda_s \cdot 10^4$, cal/cm·s·K	7.8/7.8	10.4/10.4	14.5/14.6	18.7/18.7
$\chi \cdot 10^3$, cm^2/s	1.5/1.5	2.0/2.0	2.8/2.8	3.6/3.6
T_l, °C	1000/1000	1050/1100	1100/-	-/-
T_f, °C	2200/2200	2250/2280	2300/2350	2400/2420
L_1, μm	150/250	150/230	130/-	-/-
L, mm	1.0/1.2	1.0/1.0	1.0/1.0	0.9/1.0
Λ, μm	77/32	27/15	15/12	7.2/6.0
$\lambda_g \cdot 10^4$, cal/cm·s·K	2.3/2.3	2.4/2.4	2.5/2.5	2.7/2.6

Characteristic Sizes in Gas and Solid.
Characteristic thickness l and l_m in solid were obtained by temperature distributions in solid. Experimentally obtained thickness of heat layer in solid l is a distance between the burning surface and a section in solid with the temperature:

$$T^*=(T_s-T_o)/e - T_o; \qquad (1.4)$$

Thickness l_m of melt layer for nitramines in solid were obtained by temperature distributions in solid, taken into consideration nitramine melt temperatures T_m which are equal to 200°C for RDX and 280°C for HMX. It can be seen from Table 1 that values of l and l_m decrease when pressure increases and that $l > l_m$. Values of l are equal to 150-53 μm and of l_m - 60-40 μm for mixture GA/HMX. Mixture GA/RDX has l=115-44 μm and l_m=80-40 μm. Standard deviations of estimations of l and l_m are equal to ±20%.
Conductive sizes Λ of the gas phase were obtained by the formula:

$$\Lambda=\lambda_g/mc_p; \qquad (2.4)$$

where λ_g is the heat conductivity coefficient and c_p is the specific heat coefficient of the gas phase.

Values of λ_g and c_p were estimated by content of the combustion products and they are presented in Table 2 as function of temperature. Table 1 shows that values of Λ decrease when pressure increases and comprise 77-7.2 μm for mixture GA/HMX and 32-6 μm for mixture GA/RDX. It is important to stress that the values of Λ are significantly less than the values of L_1 and L. It implies that the gas phase of GA/HMX and GA/RDX combustion wave has wide reaction zone.

Table 2: Heat coefficients λ_g and c_p of the gas phase

T,K	700	1000	1500	2000	2600
c_p, cal/g·K	0.420	0.433	0.477	0.510	0.560
$\lambda_g \cdot 10^4$, cal/cm·s·K	2.4	3.2	4.6	6.3	11.8

Heat Diffusivity and Heat Conductivity Coefficients of Heat Layer in Solid.
Solid heat diffusivity coefficient χ was estimated by formula $\chi = l \cdot r_b$. Table 1 shows that χ increases when pressure increases. Values of χ grow for both mixtures from $1.5 \cdot 10^{-3}$ cm^2/s at 5 atm up to $3.6 \cdot 10^{-3}$ cm^2/s at 60 atm. That are normal values of χ for many propellant mixtures. Solid heat conductivity coefficient λ_s was obtained by the formula:

$$\lambda_s = \chi \cdot c \cdot \rho; \qquad (3.4)$$

It was assumed that solid specific heat coefficient c=0.4 cal/g·K. Table 1 shows that values of λ_s increase from $7.8 \cdot 10^{-4}$ cal/cm·s·K at 5 atm up to $18.7 \cdot 10^{-4}$ cal/cm·s·K at 60 atm.
Heat Release in Solid and Heat Feedback from Gas to Solid.
The obtained temperature profiles and burning surface temperatures allow the parameters of the thermal burning wave structure to be received. Heat flux from gas to solid q·m by heat conduction is as follows:

$$q \cdot m = -\lambda_g(T) \cdot (dT/dx)_o; \qquad (4.4)$$

Here: $(dT/dx)_o = \varphi$ is the temperature gradient in gas close to the burning surface which can be obtained by temperature slope on temperature profiles at x=0. Heat feedback q from gas into solid by heat conduction is as follows:

$$q = -\lambda_g(T) \cdot \varphi / m; \qquad (5.4)$$

Heat release in the reaction layer of the condensed phase (or on the burning surface) Q is as follows:

$$Q = c \cdot (T_s - T_o) - q - q_r + q_m; \qquad (6.4)$$

here q_r is the radiant heat supply from gas into solid and q_m is heat of nitramine melting. It was assumed that heat of HMX's melting is equal to 24 cal/g and that of RDX to 29 cal/g. It implies that q_m=19.2 cal/g for GA/HMX and q_m=23.2 cal/g for GA/RDX. The radiant heat supply was estimated by formula: $q_r = k_o \cdot k_1 \cdot T_f^4/m$, where k_o is the coefficient of the burning surface absorption of the radiation from the flame and $\cdot k_1$ is the degree of the flame blackness. It was assumed that k_o=0.5, k_1=0.1. Table 1 shows that a detectable radiant heat supply from gas into solid is observed at 5-10 atm. Table 1 also shows that the temperature gradient φ in gas close to the burning surface has very large values: it can be at 60 atm as much as 10^5 K/cm. However a very small heat conductivity coefficient λ_s leads to a relatively low heat supply from gas to solid.
Table 1 shows that the sum $q+q_r$ is larger than heat release in solid Q only at 5 atm and only for mixture GA/HMX. At p>5 atm the relation $Q>(q+q_r)$ is observed for both mixtures. It is important to stress that Table 1 shows that Q increases when burning rate increases, but the values

$q+q_r$, on the contrary, decrease when m increases.

Distributions of Heat Release Rate in Gas.

Distributions of the heat release rates $\Phi(x)$ along the gas phase were found by using of the temperature profiles T(x), values of λ_g, m and c_p and heat conduction equation. Functions of Φ shows, obviously, the intensity of chemical reactions in gas. The heat conduction equation for the gas phase, connected with the burning surface of stable propagated combustion wave, is as follows:

$$d/dx\cdot(\lambda_g dT/dx)-m\cdot c_p\cdot dT/dx+\Phi(x)=0; \qquad (7.4)$$

Hence:

$$\Phi(x) = m\cdot c_p\cdot dT/dx - d/dx\cdot(\lambda_g dT/dx); \qquad (8.4)$$

The derivatives $d/dx\cdot(\lambda_g dT/dx)$ and dT/dx were obtained as function of x from the experimentally obtained temperature profiles T(x) in gas - see Figs. 1-4. The obtained distributions $\Phi(T)$ are presented on Figs. 5-8. It can be seen that values of Φ are very high: up to $(6\text{-}9)\cdot10^3$ cal/cm^{3}s at 5 atm and up to $4\cdot10^4$ cal/cm^{3}s at 60 atm. Figures 5-7 show that between two zones in gas a significant drop of Φ is observed. But when zones of the gas phase merge, functions $\Phi(T)$ change monotonically. The obtained functions $\Phi(T)$ show that the heat release is not located close to maximal temperature of the gas phase but it is distributed along this zone.

5. Burning Rate Control Region

The results of measurements of $q+q_r$ and Q and the investigations of the gas phase zone behaviour show that burning rate of the mixtures are caused by the heat release in solid (or on solid surface) and, in a smaller degree, by the heat feedback from the gas layer which is close to the surface. It was mentioned above also that the values of of $q+q_r$ decreases when the burning rate increases. An important conclusion can be made from the analysis of the obtained data: the high temperature region of the burning waves cannot affect the burning rate. The influence of the heat release in the gas phase on the burning rate can be estimated by the following formula obtained as a solution of the heat conduction equation:

$$m\cdot q=\int_0^\infty \Phi\cdot\exp(-x/\Lambda)\cdot dx; \qquad (1.5)$$

This formula shows that influence of heat release in gas on m decreases very quickly when $x>\Lambda$. Table 1 shows that values Λ are small and they are significantly smaller than gas zone size L (Λ=77-6 μm, L=0.9-1 mm). It implies that, indeed, high temperature region of the burning waves cannot affect the burning rate.

Thus the obtained results show that the burning rate control regions in the combustion waves for all regimes of GA/HMX and GA/RDX combustion are the regions of heat release in solid just under the burning surface (or immediately on the burning surface) and thin low-temperature gas layers close to the burning surface. High temperature gas regions cannot influence the burning rate in fact because of a very large heat resistance of the gas phase of the both mixtures.

6. Macrokinetics

Gasification Laws.

The following equation connects burning rate of solid with burn-surface temperature and macrokinetic characteristics of solid gasification(obtained by Haikin, B. I.):

$$m^2=\lambda_s\rho/Q^2\cdot\Re T_s^2/E\cdot k_o Q^*\cdot 1/N\cdot\exp(-E/\Re T_s); \qquad (1.6)$$

where $N=1/\eta_s+(1-\eta_s)/\eta_s\cdot\ln(1-\eta_s)-(q/Q)\cdot[\ln(1-\eta_s)]/\eta_s$; $\eta_s=Q/Q^*$; Q^* is the maximum of the heat release in solid E is activation energy of limiting stage of the gasification process, T_s in K. For studied combustion waves $N\cong1$. The expression was obtained by solution of the system of two equations for the steady propagated burning wave: the heat conduction equation for solid phase and the equation of diffusion of reagents. The burning wave propagates due to heat release in solid Q and heat feedback from gas to solid q. Function of the volumetric heat release rate Φ_s in solid was assumed as follows:

$$\Phi_s(\eta, T)=Q^*k_o\cdot\rho\cdot(1-\eta)\cdot\exp(-E/\Re T); \qquad (2.6)$$

Here η is the reaction completeness ($\eta=\eta_s$ on the burning surface), k_o is the preexponent multiplier.

The member $\exp(-E/\Re T_s)$ plays the most important role in formula (1.6). Because of that the connection m and T_s can be presented by the following simplified expression:
$m=A\cdot\exp(-E/2\Re T_s)$; This expression has been designated "gasification law". The results of measurement, presented in Table 1, allow the following gasification laws to be obtained:
for mixture GA/HMX:

$$m=0.83\cdot10^3\cdot\exp(-23000/2\Re T_s);\ g/cm^3s\ ; \qquad (3.6)$$

for mixture GA/RDX:

$$m=1.3\cdot10^3\cdot\exp(-23000/2\Re T_s);\ g/cm^3s\ ; \qquad (4.6)$$

Here T_s in K, m in g/cm^2s.
One of the merits of these laws is the possibility of T_s estimations under different conditions by use of the experimentally obtained values of the mass burning rates m.
Reaction Rate Constants in Solid.
It is interesting toobtain constants of reaction rate in solid k_o for the investigated mixtures. The results of measurement, presented in Table 1, allow the following expressions for k_o to be obtained (it was assumed that $Q^*=220$ cal/g):
for mixture GA/HMX:

$$k_o=1.6\cdot10^3\cdot\exp(-27000/\Re T_s);\ s^{-1}; \qquad (5.6)$$

for mixture GA/RDX:

$$k_o=1.6\cdot10^3\cdot\exp(-27000/\Re T_s);\ s^{-1}; \qquad (6.6)$$

The obtained here activation energy - 27 kcal/mole - a bit more than that obtained above in gasification laws (23 kcal/mole). Obviously the last value is more correct for solid reaction process.
Laws for Heat Release Rates in the Gas Phase.
Distributions of heat release rates $\hat{O}$ along the gas phase presented on Figs. 5-8 can be discribed by the following expression:

$$\Phi(\eta_g,T)=C\cdot p^k\cdot(1-\eta_g)^n\cdot\exp(-E/\Re T); \qquad (7.6)$$

Here C, k and n are constant values and $\eta_g=(T-T_s)/(T_f-T_s)$;
The best fitting of experimentally established functions $\Phi(\eta,T)$ was received at n=1, k=0.8, and E=6 kcal/mole. The following dependencies can approximately describe functions $\Phi(\eta,T)$,
(T in K):
for mixture GA/HMX:

$$\Phi(\eta_g,T)=15\cdot p^{0.8}\cdot(1-\eta_g)\cdot\exp(-6000/\Re T);\ kcal/cm^3s\ ; \qquad (8.6)$$

for mixture GA/RDX:

$$\Phi(\eta_g,T)=20\cdot p^{0.8}\cdot(1-\eta_g)\cdot\exp(-6000/\Re T);\ \text{kcal/cm}^3\text{s}\ ; \qquad (9.6)$$

It can be seen that the functions of heat release rate in gas are described by a very low activation energy. It is obviously that eqs.(8.6), (9.6) are only formal descriptions of very complex gas phase chemical and diffusional processes.

7. Conclusions.

Combustion mechanisms of mixtures of HMX / glycidyl azide monomer (GA) and RDX / GA were studied by obtaining burning wave parameters at pressures 5 - 60 atm. The parameters were found by temperature profile and burn-surface temperature measurements and date processing. Temperature measurements were performed by microthermocouple techniques. Burn-surface temperatures comprise 380 - 570 °C and they increase with pressure and burning rate. Gas phase of the burning mixtures has two-zone structure up to 20 atm and one zone at elevated pressures. Significant heat release in solid is observed for both mixtures. The heat release increases from 64 - 101 cal/g at 5 atm up to 202 - 206 cal /g at 60 atm. Heat feedback from gas to solid decreases from 80 - 52 cal/g at 5 atm up to 34 - 32 cal/g at 60 atm. Heat feedback from the flame by heat radiation comprises 19 - 15 cal/g and quickly decreases when pressure increases. Thickness of the heat layer in solid and nitramine melt layer, thickness of the first and the second flame zone in gas were found. Values of heat diffusivity and heat conductivity coefficient in solid during combustion were estimated. It was found that the reaction layer in solid is very thin, but the reaction zone in the gas phase is very wide. Distributions of heat release rate in gas were obtained. Parameters of macrokinetics of reactions in gas and solid were estimated. Activation energy of solid gasification comprises 23 - 27 kcal/mole for both mixtures. Expressions for constants of reaction rates in solid are presented. Formal activation energy in the gas phase comprises about 6 kcal/mole.
Burning rate control region in combustion waves of the investigated mixtures is located in solid just under the burning surface (or immediately on the burning surface) and in thin low-temperature gas layers close to the burning surface. High temperature gas regions cannot influence the burning rate.

In future work mixtures of polymerized GAP with nitramines will be investigated by the presented methods.

Acknowledgement

This work was supported by the Russian Found of the Basic Research, grant No. 97-03-32076a. This support is much appreciated.

References

1. Boggs, T. L., "The Thermal Behaviour of Cyclotrimethylenetrinitramine (RDX) and Cyclotetramethylenetetranitramine (HMX)," *Fundamentals of Solid-Propellant Combustion*, edited by K. K. Kuo and M. Summerfield, Vol. 90, Progress in Astronautics and Aeronautics, AIAA, New York, 1984, pp.121-175.

2. Kubota, N., "Physicochemical Process of HMX Propellant Combustion", *Nineteenth (International) Symposium on Combustion*, The Combustion Inst., Pittsburgh, PA, 1982, pp. 777-785.

3. Cohen, N. S., and Price, C. F., "Combustion of Nitramine Containing Propellants", AIAA Paper 81-1582, 1981.

4. Yano, Y., and Kubota, N., Combustion of HMX-CMDB Propellants", *Propellants, Explosives, and Pyrotechnics*, Vol. 10, No. 6, 1985, pp. 192-196.
5. Zhao, B.-C., and Zhao, Z. J., "High Pressure Combustion Characteristics of RDX Based Propellants", *Twenty-Second (International) Symposium on Combustion*, The Combustion Inst., Pittsburgh, PA, 1988, pp. 1835-1842.
6. Kubota, N., and Sakamoto, S., "Combustion Mechanism of HMX", *Propellants, Explosives, and Pyrotechnics*, Vol. 14, No. 6, 1989, pp. 6-11.
7. Raman, K. V., and Singh, H., "Ballistic Modification of RDX-Based CMDB Propellants", *Propellants, Explosives, and Pyrotechnics*, Vol. 13, No. 5, 1988, pp. 149-151.
8. Beckstead, M. W., "A Model for Composite Modified Double Base Propellant Combustion," *26th JANNAF Combustion Meeting*, Vol. IV, CPIA 529, 1989, pp. 239-254.
9. Kubota, N., and Sonobe, T., "Conbustion Mechanism of Azide Polymer", *Propellants, Explosives, and Pyrotechnics*, Vol. 13, 1989, pp. 172-177.
10. Hori, K., and Kimura, M., "Combustion Mechanism of Glycidyl Azide Polymer", *Propellants, Explosives, and Pyrotechnics*, Vol. 21, 1996, pp. 160-165.
11. Kubota, N., et al., "Burning Rate Characteristics of GAP Propellants", *Journal of Propulsion and Power*, 1990, Vol. 6, p. 686.
12. Puchkov V. M., and Zenin, A. A., "Thermal Structure of HMX Combustion Waves", *Twenty-Fifth (International) Symposium on Combustion, Proceedings of Work-in-Progress Posters*, The Combustion Inst., Pittsburgh, PA, 1994, p. 326.
13. Zenin, A. A., "HMX and RDX: Combustion Mechanism and Influence on Modern Double-Base Propellant Combustion", *Journal of Propulsion and Power*, 1995, Vol. 11, No. 4, pp. 752-758.
14. Zenin, A. A., Puchkov V. M., and Finjakov, S. V., "Combustion Mechanism of Nitramines as Monopropellants and as Additives to Double-Base Propellants", *Aerotecnica, Missile, Spazio*, Rome, Vol. 74, No. 3-4, pp. 80-92.
15. Zenin, A. A., Puchkov V. M., and Finjakov, S. V., "Characteristics of HMX Combustion Waves at Various Pressures and Initial Temperatures", *Combustion, Explosion, and Shock Waves*, Vol.34, No.2, 1998, pp. 170-176.
16. De Luca, L., Cozzi, F., Germinasi, G., Ley, I., and Zenin, A. A., "Combustion Mechanism of an RDX-Based Composite Propellant", *Combustion and Flame*, Vol. 118, 1999, pp. 248-261.
17. Zenin, A. A., and Finjakov, S. V., "Physics of GAP Combusstion", AIAA Paper 2000-1032, 2000.
18. Zenin, A. A., "Experimental Investigations of Burning Mechanisms of Solid Propellants and Movements of Burning Products", *D.Sc. Thesis, Inst. of Chem. Phys., USSR Acad. of Sc.* Moscow, 1976, (in Russian).
19. Zenin, A. A., "About Heat Exchange of Thermocouples Under Conditions of Solid Combustion Waves", *Journal of Applied Mathem. and Technical Phys.*", No.5, 1963. pp. 125-131. (in Russian).
20. Zenin, A. A., "About Errors of Thermocouple Measurements Inside Flames", *Ingeneerno-Physical Journal*, Minsk, Vol.5, No. 5, 1962, pp. 67-74, (in Russian).

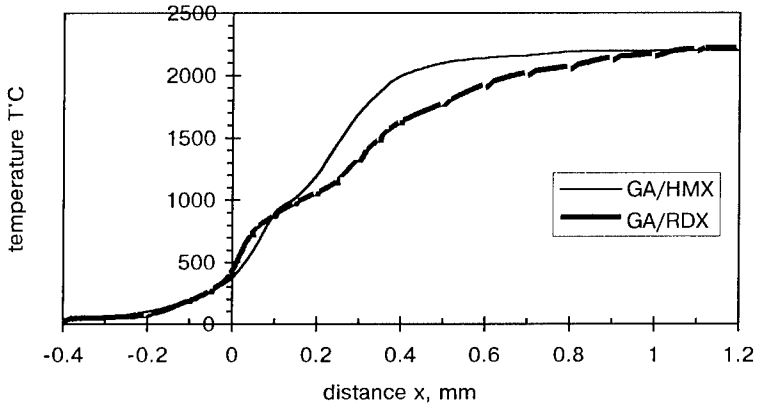

Figure 1: Averaged temperature profiles of GA/HMX and GA/RDX at 5 atm, To=20°C.

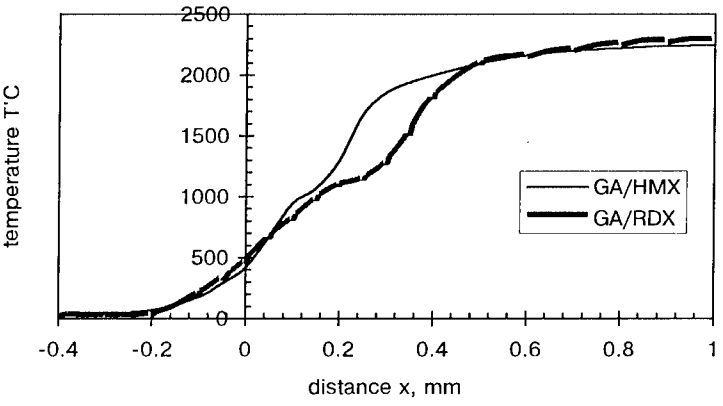

Figure 2: Averaged temperature profiles of GA/HMX and GA/RDX at 10 atm, To=20°C.

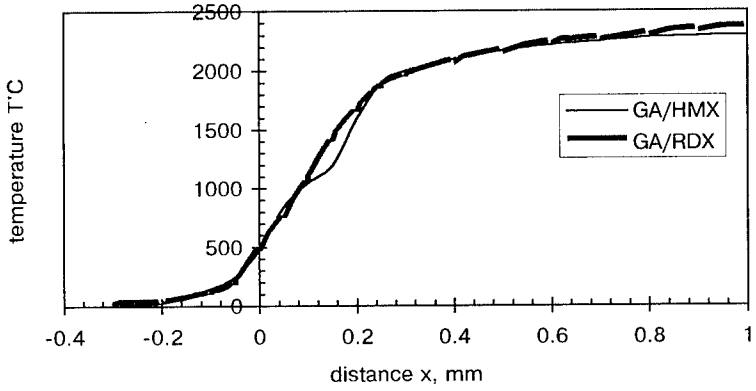

Figure 3: Averaged temperature profiles of GA/HMX and GA/RDX at 20 atm, To=20°C.

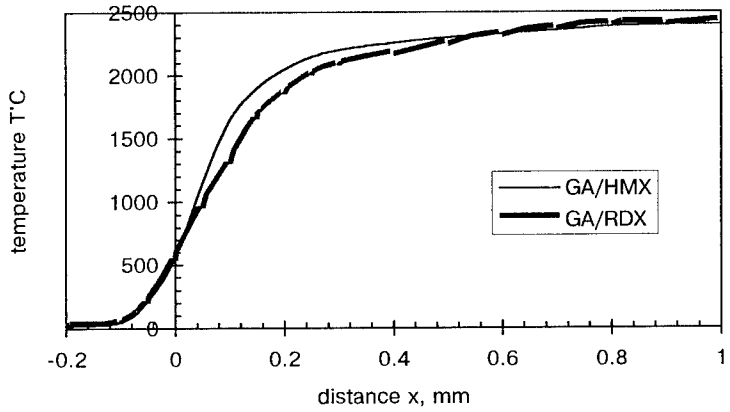

Figure 4: Averaged temperature profiles of GA/HMX and GA/RDX at 60 atm, To=20°C.

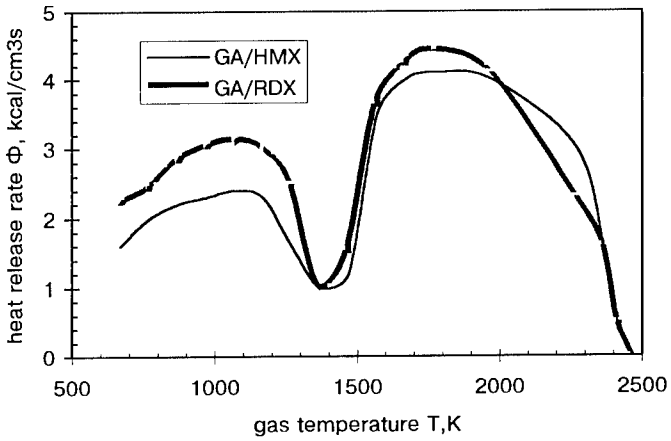

Figure 5: Distributions of Φ(T) for the gas phase of GA/HMX and GA/RDX at 5 atm, To=20°C.

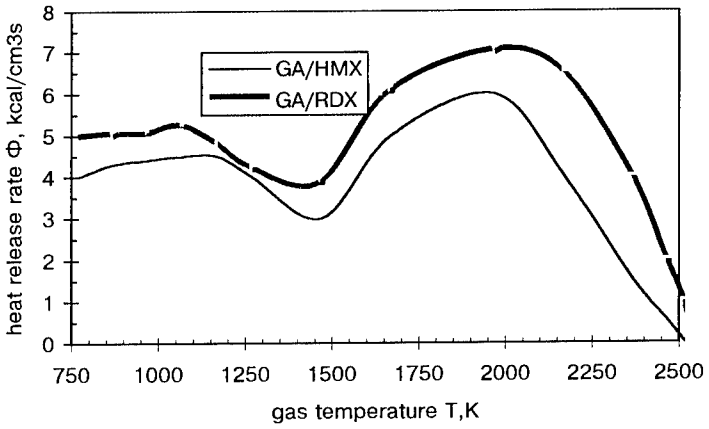

Figure 6: Distributions of Φ(T) for the gas phase of GA/HMX and GA/RDX at 10 atm, To=20°C.

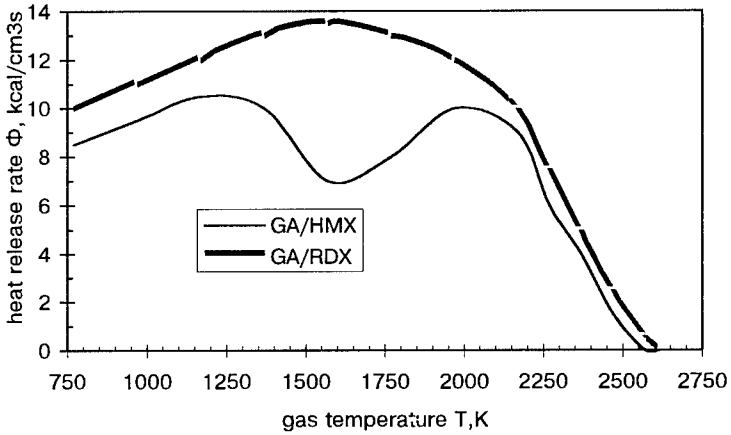

Figure 7: Distributions of Φ(T) for the gas phase of GA/HMX and GA/RDX at 20 atm, To=20°C.

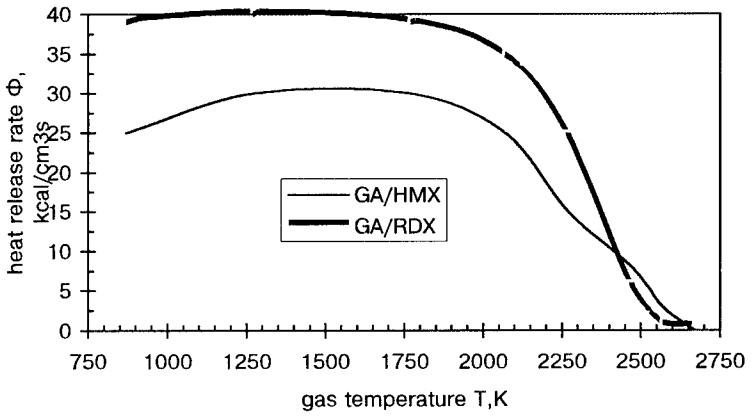

Figure 8: Distributions of Φ(T) for the gas phase of GA/HMX and GA/RDX at 60 atm, To=20°C.

MECHANISM OF VORTEX FORMATION IN FLAME AT NON-STATIONARY COMBUSTION

Victor P. Samsonov, Elena N. Petrova,
Natalya N. Sergeeva, Ludmila A. Shilnikova

Chuvash State Pedagogical University,
K.Marx st. 38, 428000, Cheboksary, RUSSIA

The numerical investigation of the diffusion «singing» flame hydrodynamics has been developed. The stationary combustion in the vertical cylindrical furnace (tube) and the conditions of the excitement of the acoustic oscillations have been studied. The results of the visualization of the burning products in the physical experiments were compared. It was shown that the excitement of the acoustic oscillations is always accompanied by the vortex formation near the mouth of the gas-burner.

The calculations of the fields of the stream-function and the velocity rotation allowed to find 4 mechanisms of the vortex structure formation. The first of them is connected with the viscous dissipation of the mechanical energy. The second can be described by the thermal expansion of the gas in the burning zone (because of the refraction of the stream-lines). The third is caused by the gas circulation under the influence of geometry of the burning chamber. The fourth is stipulated by the different influence of the free convection in the center of the burning chamber and also near its walls.

It was shown that the vortex structures are the multi-pole sources of the acoustic oscillations which are the reason of the non-stationary regime of the combustion. They provide the back connection between the heat-release rate in the flame and the pressure oscillations.

It is obvious now that only the visualization of the flow without the numerical experiment does not provide the full information for describing the connection of the vortex formation and the acoustic oscillations.

UPPER COMPOSITION LIMIT OF BURNING OF AP-FUEL MIXTURES

Nikolai N.Bakhman and Victor V.Evdokimov
Institute of Chemical Physics, Russian Academy of Sciences
117977 GSP-1, Kosygin str. 4, Moscow, Russia
FAX (007 095) 9382156, e-mail: bakhman@center.chph.ras.ru

ABSTRACT

The upper (rich) composition limit (UL) was determined for AP-fuel mixtures burning in inert atmosphere. UL was calculated as $\alpha_{ul} = (m_{ox}/m_f)_{ul}/(m_{ox}/m_f)_{st}$ where m_{ox} and m_f are mass fractions of oxidizer and fuel and index st means stoichiometric. For AP-PMMA mixtures UL is 2-5 times higher than that for AP-PS mixtures. Further, it was determined that coarse mixtures can burn at higher fuel content (and thus at smaller UL) than fine mixtures. The influence of soot and Fe_2O_3 additives on UL was also investigated. The meaning of experimental data is discussed.

INTROLUCTION

For most part of oxidizer-fuel mixtures both lower (lean) and upper (rich) composition limits (CL) of burning are observed. For homogeneous gaseous mixtures the CL are investigated during many tens of years, however a number questions remains debatable [1] . The CL for fuel aerosols are examined to a very limited extent due to considerable experimental difficulties so that disagreements in the data obtained by diverse authors are very appreciable [2] . The data concerning CL of mixtures: solid oxidizer- solid fuel burning in inert atmosphere are very scarse. Meanwhile, this problem is of definite interest for the stability of burning of composite solid propellants and pyrotechnic mixtures. In this paper our experimental data are presented relevant to upper composition limit (UL) of burning of ammonium perchlorate (AP) - polymethylmethacrylate (PMMA) and AP-polystyrene (PS) mixtures at various AP particle size, d_{AP} , and various pressure. The effect of soot and Fe_2O_3 additives on UL was also investigated.

EXPERIMENTAL

Specimens (8 or 15 mm dia and ~10 or ~18 mm high, respectively) were pressed from mixtures of powdered AP (d = var) and PMMA (~3 mcm) or PS (~5 mcm). In two series of experiments additives of soot or Fe_2O_3 (~2 mcm) were used. Specimens were inhibited by a layer of epoxy resin. The burning of specimens was investigated in nitrogen atmosphere. To describe the upper limit of burning the value $\alpha_{ul} = (m_{ox}/m_f)_{ul}/(m_{ox}/m_f)_{st} = 1/\varnothing_{ul}$ was used where α and $\varnothing$ are stoichiometric coefficients, m_{ox} and m_f are mass fractions of oxxidizer and fuel and index st means stoichiometric. The experimental value α_{ul} was calculated as $\alpha_{ul} = (\alpha_+ + \alpha_-)/2$ where α_+ is relevant to the most rich mixture capable to burn completely in nitrogene atmosphere and α_- is relevant to just mentioned mixture plus some small additional amount of fuel such as composition burn only in part. A layer (1-2 mm thick) on the top end of each specimen was pressed from the same composition as main part of specimen but with more favorable oxidizer-fuel ratio. Specimens were ignited from the top end by electrically-heated wires.

RESULTS.

The experimental data obtained in this work (Table 1) show that α_{ul} for AP-PMMA mixtures are 2-5 times higher than α_{ul} for AP-PS mixtures (Table 2). So, AP-PS mixtures capable to burn can contain more additional fuel* than AP-PMMA mixtures. Further, the data presented in Table 1 show that α_{ul} decreases (and $(m_f)_{ul}$ increases) with increasing AP particle size. In other words, coarse mixtures can burn at higher fuel content than fine mixtures. Thus, for AP-PS mixtures at p = 70 atm the value α_{ul} is equal 0.0675 for AP fraction <50 mcm and 0.0525 for 140-320 mm fraction (the values $(m_f)_{ul}$ are equal 62.1 and 67.9%, respectively). For AP-PMMA mixtures this effect is more pronounced and at p = 70 atm the transition from AP fraction <50 mcm to

---

* with respect to stoichiometric composition

140-320 mcm decreases α_{ul} from 0.32 to 0.11 and increases $(m_f)_{ul}$ from 35.7 to 61.7 %.

It is seen also from Table 1 that for all mixtures studied the value α_{ul} decreases (and $(m_f)_{ul}$ increases) with pressure increasing, i.e. at high pressure can burn more rich mixtures than those at low pressure. For AP-PMMA mixtures the effect of pressure is stronger than that for AP-PS mixtures. For example, at d_{AP} = 140-320 mcm the transition from 10 atm to 100 atm decreases α_{ul} 2.4 times for AP-PMMA mixture and 2.1 times for AP-PS mixture (the value $(m_f)_{ul}$ increases 1.54 and 1.35 times, respectively).

The data presented in Table 1 were obtained for specimens 8 mm dia. Besides, some part of experiments was performed with specimens 15 mm dia. It is natural to expect that the value α_{ul} can decrease (and $(m_f)_{ul}$ can increase) with increasing of specimer diameter. Really, in a ~50 % of experiments the increase of specimen diameter from 8 to 15 mm resulted in the decrease of α_{ul} by 6 to 10 % (Table 3). However, in the rest of experiments no change of α_{ul} was observed.

The linear- and mass-burning rate (u_+ and $(\rho u)_+$, respectively) of specimens at $\alpha = \alpha_+$ was measured at various d_{AP} (Table 4) and various pressure (Table 5). Tables 4 and 5 show that the value u_+ for AP-PMMA mixtures is greater than that for AP-PS mixtures. It seems rather logical taking into account that the value α_+ for AP-PMMA mixtures is sufficiently greater than that for AP-PS mixtures. The value u_+ for AP-PS mixtures depends rather slightly on d_{AP} and pressure (and is equal to 0.9-1.4 mm/s for the range tested). The value u_+ for AP-PMMA mixtures in the same interval of d_{AP} and p is equal to 1.2-3.8 mm/s and decreases with d_{AP} or pressure increasing.

DISCUSSION

It was shown above that the value α_{ul} for AP-PS mixtures is much smaller than that for AP-PMMA mixtures. It seems to be probable that this fact can be explained in the following way. Decomposition of PS proceeds with the formation of considerable amount of soot. The burning of soot is rather slow

process as compared with burning of gaseous products of decomposition of PS. So, the mixture AP-PS really reacting in the flame velocity controlling zone (FVC-zone) [3] contains smaller quantity of fuel than it formally follows from the value α_{ul} calculated for the fresh AP-PS mixture. In contrast, decomposition of PMMA gives little if any soot and the value α_{ul} calculated for fresh AP-PMMA mixture is nearly the same as the value α for the mixture reacting in the FVC-zone.

A second factor, namely a greater stability of burning of AP-PS mixtures (as compared with AP-PMMA mixtures) may be also considered to explain why $(\alpha_{ul})_{AP-PS} < (\alpha_{ul})_{AP-PMMA}$. The burning of (100-x)% AP(63-100mcm) + PMMA($\sim$3mcm) + x % soot was investigated. The following results were obtained at p = 40 atm:

x	0	0.45	1.5	1.75	2.25	3 ÷ 25
α_{ul}	0.33	0.30	0.27	0.25	0.22	α_{ul} = const = 0.21

It is necessary to underline that the value α_{ul} was calculated here only for AP-PMMA mixture. If we calculate α_{ul} taken into account also soot as a fuel, the value α_{ul} will decrease monotonously with x increasing in all the range x studied. The possibility to increase the amount of PMMA in the mixtures AP-PMMA capable to burn using the additives of soot may be explained in the following way: hot agglomerates of soot ignite the products of gasification of AP-PMMA mixture at α smaller than α_{ul} in the absence of soot**. In contrary, no effect of soot additives (0.5; 1; 5 or 10 %) was observed for AP(63-100mcm) + PS ($\sim$5mcm) mixture. This result seems to be quite natural as decomposition of PS leads to the formation a lot of "own" soot.

** The additives of Fe_2O_3 act on the burning of AP-PMMA mixtures in the similar way as additives of soot. Thus, the value α_{ul} for pure mixture AP(63-100mcm) + PMMA (3 mcm) is equal 0.33 and that for mixture containing 15 % Fe_2O_3 is equal 0.155.

REFERENCES

1. L.A.Lovachev, V.S.Babkin, V.A.Bunev et al. Combust.Flame, 1973, Vol.20, No 2, pp.259-289
2. K.J.Mintz. Combust.Flame, 1993, Vol.94, No 1-2, pp.125-130
3. N.N.Bakhman and A.F.Belyaev - Gorenie geterogennykh condensirovannykh sistem. Moscow, Nauka, 1967. English translation: Combustion of Heterogeneous Condensed Systems, Rocket Propulsion Establishment, Westcott, England, RPE-Trans-19, 1967

Table 1.

p atm	Characteristics of upper limit at d_{AP}, mcm				
	<50	50-63	63-100	100-140	140-320
AP - PS mixtures					
10	$(m_f)_{ul}$	0.13	0.13	0.125	0.115	0.11
	α_{ul}, %	46.0	46.0	47.0	49.1	50.2
40	$(m_f)_{ul}$	0.0825	0.0825	0.0775	0.0775	0.0775
	α_{ul}, %	57.3	57.3	58.8	58.8	58.8
70	$(m_f)_{ul}$	0.0675	0.0675	0.0625	0.0575	0.0525
	α_{ul}	62.1	62.1	63.9	65.8	67.9
100	$(m_f)_{ul}$	0.0575	0.0575	0.0525	0.0525	0.0525
	α_{ul}, %	65.8	65.8	67.9	67.9	67.9
AP - PMMA mixtures						
10	$(m_f)_{ul}$	0.475	0.375	0.315	0.265	0.265
	α_{ul}, %	27.2	32.1	36.0	40.1	40.1
40	$(m_f)_{ul}$	0.46	0.385	0.315	0.15	0.15
	α_{ul}, %	27.8	31.6	36.0	54.2	54.2
70	$(m_f)_{ul}$	0.32	0.225	0.175	0.15	0.11
	α_{ul}, %	35.7	44.1	50.4	54.2	61.7
100	$(m_f)_{ul}$	0.185	0.185	0.14	0.14	0.11
	α_{ul}, %	49.0	49.0	55.9	55.9	61.7

Table 2.

p atm	$(\alpha_{ul})_{AP-PMMA}/(\alpha_{ul})_{AP-PS}$				
	d_{AP} <50 mcm	50-63	63-100	100-140	140-320
10	3.65	2.88	2.52	2.30	2.41
40	5.58	4.67	4.06	1.94	1.94
70	4.74	3.33	2.80	2.61	2.10
100	3.22	3.22	2.67	2.67	2.10

Table 3

Fuel	PS		PMMA					
d_{AP}, mcm	63-100		<50				50-63	63-100
p, atm	40	70	10	40	70	100	10	100
$(\alpha_{ul})_1$	0.0775	0.0625	0.475	0.46	0.32	0.185	0.375	0.14
$(\alpha_{ul})_2$	0.0725	0.0575	0.425	0.42	0.32	0.185	0.375	0.14

Note: $(\alpha_{ul})_1$- specimens 8 mm dia; $(\alpha_{ul})_2$- specimens 15 mm dia

Table 4

p_-, atm	10			70			
d_{AP}, mcm	<50	63-100	140-320	<50	63-100	100-140	140-320
AP - PS mixtures							
u_+, mm/s	1.4	1.2	1.1	1.3	1.0	1.4	-
$(\rho u)_+$, g/cm^{2}s	0.18	0.16	0.15	0.16	0.12	0.16	-
AP - PMMA mixtures							
u_+, mm/s	3.8	2.2	-	3.2	1.4	-	1.4
$(\rho u)_+$, g/cm^{2}s	0.62	0.34	-	0.50	0.21	-	0.20
Ratio $(u_+)_{AP-PMMA}/(u_+)_{AP-PS}$ (1); $[(\rho u)_+]_{AP-PMMA}/[(\rho u)_+]_{AP-PS}$ (2)							
Ratio (1)	2.7	1.8	-	2.5	1.4	-	-
Ratio (2)	3.4	2.1	-	3.1	1.8	-	-

Table 5

d_{AP}, mcm	<50				63-100			
p, atm	10	40	70	100	10	40	70	100
AP - PS mixtures								
u_+, mm/s	1.4	1.0	1.3	-	1.2	0.9	1.0	1.0
$(\rho u)_+$, g/cm^{2}s	0.18	0.12	0.16	-	0.16	0.11	0.12	0.12
AP - PMMA mixtures								
u_+, mm/s	3.8	3.6	3.2	1.4	2.2	2.6	1.4	1.2
$(\rho u)_+$, g/cm^{2}s	0.62	0.58	0.50	0.21	0.34	0.40	0.21	0.17
Ratio $(u_+)_{AP-PMMA}/(u_+)_{AP-PS}$ (1); $[(\rho u)_+]_{AP-PMMA}/[(\rho u)_+]_{AP-PS}$ (2)								
Ratio (1)	2.7	3.6	2.5	-	1.8	2.9	1.4	1.2
Ratio (2)	3.4	4.8	3.1	-	2.1	3.6	1.8	1.4

UV -spectral analysis of NO in the mixture with other gases.

Boris Lurie, Alexey Mikhno, Victor Seregin, Sergey Smirnov.

Mendeleev University of Chemical Technology,
Miusskaya sq. 9, 125047, Moscow, Russia
lurie @ iht.rhtu.msk.ru

Abstract

The intensity of the gaseous NO absorption in UV-spectrum on the its three main peaks in region 200-230 nm can be significantly increased under the action of the inert gas excess. The change of the NO optical density has been studied in dependence on variation of NO and inert gas amounts. The main quantitative dependence has been established of mixtures of NO with helium. The influence of He is compared with the action of another gases. Their influence is qualitatively analogous. The effect is the more, the higher a molecule mass of inert gas. The temperature dependence of the alteration of NO optical density is estimated at the range 20-100^{o}C. The optical density falls very slightly at a temperature increasing.

Introduction

The intensity of NO absorption in the UV-spectrum can significantly increase due to action of the inert gas - He [1]. This growth of the NO optical density on the all three double peaks with maximums at the wave lengths 205, 215 and 226,5 nm was described quantitatively and explained by forming of the induced form of NO* responsible for observed absorption.

The further more careful spectral investigations show that the single-line dependence of the relative increase of NO optical density ($\Delta D/D_{NO}$) (at wave length 226,5 nm) upon the relative pressure of He (P_{He}/P_{NO}) in logarithmic co-ordinates:

$$\lg(\Delta D/D_{NO}) / \lg(P_{He}/P_{NO}) = 0{,}5$$

is not quite exact. In this expression the increase of the optical density is: $\Delta D = D - D_{NO}$, where D - optical density of NO in presence of He and D_{NO} - in absence of He. In reality the exponent in dependence of $(\Delta D/D_{NO})$ - (P_{He}/P_{NO}) is some higher. Therefor the corresponding straight line is more steep in the logarithmic coordinate. It means that an effect of the He presence in the gas mixture is a little stronger.

A main cause of the mistake in previous measurements [1] is permeation of the air traces into the adding inert gas. This admixture of air is not influences almost on the NO-spectrum at the relatively small amounts of the injected He (P_{He} : P_{NO} < 2-3). But when amount of He becomes significantly (P_{He} : P_{NO} > 5), the admixture of air in helium begins to reduce the NO content through its oxidising to NO_2. The appearance of the NO_2 traces looks in spectrum as dimerization of NO to the $(NO)_2$ [2]. A "background" absorption increases a little in all considered region of spectrum and the height of NO peak is some reduced. The pressure of He polluted by the air traces is the higher, the stronger an effect of NO transformation into NO_2, the smaller the exponent in the expression describing a growth of ΔD.

A main cause of the air trace permeation in He was connected with the using of a rubber football bladder for keeping gas before adding it to NO. Sometimes this bladder stayed in the air atmosphere up to ~30 hours. During this time air diffused slowly through a rubber wall in the inner volume of bladder and polluted He gradually. Usually helium was added to NO repeatedly from small to greater amounts. Its maximal excess in respect to NO is realised in the final part of the experiments when bladder with He was keeping maximum time at the external atmosphere conditions and He was polluted by air much more.

When this demerit was found we repeated the quantitative measurements of the NO-spectrum in helium and replaced a rubber football bladder on a glass bottle with two glass vacuum crans. We paid special attention to the clearness of the inert gas which was controlled by chromatography and to the tightness of the all connecting lines from the primary source of the gas to the place of its adding to NO. Together with He we studied an influence of another gases: Ar, Xe, N_2, CO_2, H_2 and $(C_2H_5)_2O$. We determined a temperature influence on the NO UV-absorption at the range 20-100 °C in two model mixtures with He and H_2.

Experimental

The experiments have been carried out into the special glass vacuum circulating installation in flow of He with UV-VIS spectrum control of reagents content in gas phase (Fig. 1). The circulating contour includes the optical cell and is thermostated at necessary temperature. The spectral measurements were made by the "Specord" (GDR) spectrophotometer with speed of the spectral sweep 12,5 mm/1000 sm^{-1}. Usually onl·· c .e

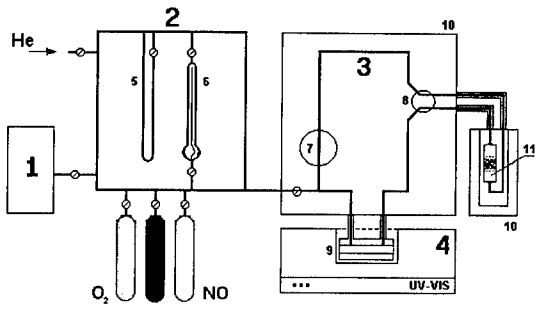

Fig. 1.
Scheme of the glass vacuum circulating installation.
1- vacuum post;
2- block for preparation and quantitative measuring of gaseous components;
3- circulating contour;
4- spectrophotometer;
5- mercury manometer;
6- Burdon type manometer with a calibrated volume;
7- circulating pump;
8- crane;
9- photometer cell;
10- thermostat;
11- reactor

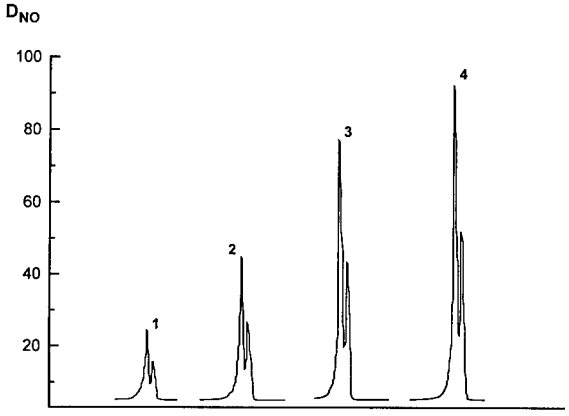

Fig. 2.
Increase of the NO absorption (P_{NO} =10 mm Hg) in the vicinity of maximum at 226,5 nm in dependence on He pressure in gaseous mixture:
1 -0,
2 -73,
3 -355,
4 -610 mm Hg.

double peak of NO with maximum at 226,5 nm was recorded. But sometimes two neighbour or all three NO peaks were recorded in order to control a raising a "background" absorption (between the peaks) as a result of NO_2 formation because of an ingress of the trace oxygen in to gaseous mixture. In a doubtful situation the NO_2 presence was checked by the change of its visible spectrum and also by a freezing out of circulation gas into the special trap in a contour by means of a liquid nitrogen. In the last case NO_2 causes a blue painting of the white condensate by reason of the forming of N_2O_3 traces.

The experiment included the initial NO injection into the circulation contour and the further repeated adding an another gas which effect was studied. The amount of gas in the contour after adding is estimated by its pressure which was measured by means of the glass

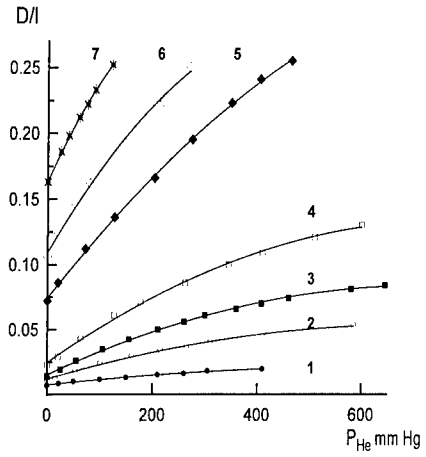

Fig. 3.
Change of the NO specific optical density (D/l) under action of He in experiments with different initial pressure of NO: 1 -1,4; 2 -3,5; 3 -5,5; 4 -10,5; 5 -23; 6 -36; 7 -54 mm. Hg.

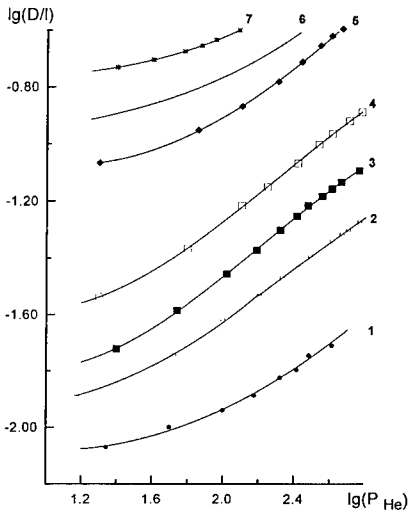

Fig. 4.
Logarithmic dependence of the NO specific optical density for deferent initial amount of NO. Figure signs correspond to Fig. 1.

compensation manometer of Burdon type in the auxiliary part of the installation [3]. The real pressure of the adding gas in the circulating contour is counted as $P_{\Sigma} - P_{NO}$.

Results

The initial pressure of NO in the experiments with He is changed from 1,4 to 54 mm Hg. The obtained values of the optical density for clear NO (without He) well correspond to literary data [1,2]. The growth of the intensity of NO absorption under the effect of He is described by a convex curve (Fig.3). The greatest growth of the observed NO optical density attained 5–6 times during the experiments at P_{NO}= 5 -10 mm and P_{He} ~600 mm Hg. In large He excess, when ratio P_{He}/P_{NO} >5, the dependence: lg D = f (lg P_{He}) is linear. The tangent of its slope is 0,5, it means that D is proportional to $P_{He}^{0,5}$ (Fig.4). If (P_{He}/P_{NO}) ratio is smaller this dependence is weaker and is described as a concave curve.

The obtained results allow to produce dependence of the NO optical density on its amount under constant pressure of helium (Fig.5). In this case the maximum effect of the He takes place at the rather low NO pressure (below 10 mm Hg), i. e. at the large He excess. If for the clear NO (without He), variation of the optical density is linearly proportional to its pressure: D/ l = 0,0029 P_{NO}, (where P- mm Hg), that in the He medium

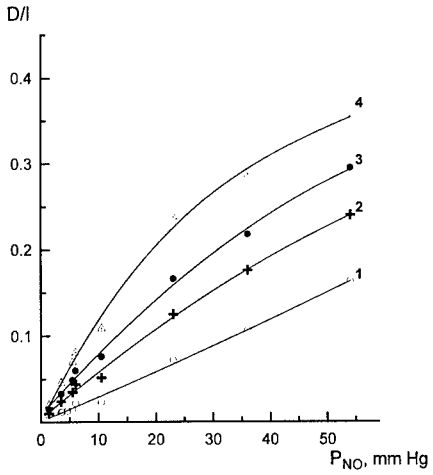

Fig. 5.
Change of the NO specific optical density (D/l) depending on NO quantity in different pressure of He:
1 -0, 2 -100, 3 -200, 4 -400 mm. Hg.

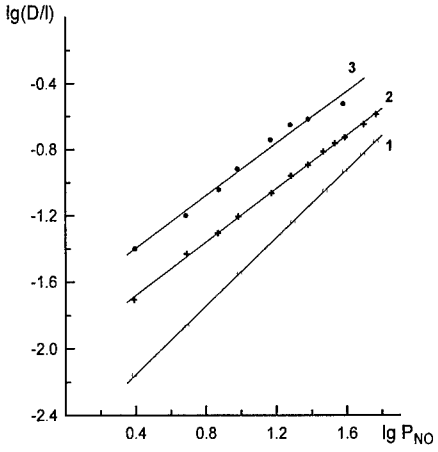

Fig. 6
NO specific optical density versus its pressure in logarithmic co-ordinate for different P_{He}: 1 -0, 2 -100, 3 -200 mm. Hg.

this dependence is weaker (Fig.6). It is characterised by the exponent 0,75 which does not depend from P_{He}. The bigger is pressure of He the more magnitude of NO optical density (D), the higher the straight line is in the co-ordinates: lg(D/ l) - lg(P_{NO}). With the growth of NO pressure the straight line which describes NO absorption in He are gradually closing to the straight line typical for the clear NO. When the He pressure equal 100 mm Hg they are crossed in the point where the P_{NO} is 400 mm Hg. A small amount of introduced helium (at $P_{He}/P_{NO} < 1/4$) is not influence on the UV-absorption of NO. For P_{He} = 400 mm Hg the calibrated dependence of D_{NO} - P_{NO} is: $(D/l) = 0{,}017\ P_{NO}^{0{,}75}$.
This He pressure was used usually in the kinetic experiments researching the NO_2 reduction in the circulating installation [3].

The carried out measurements show that the relative growth of the NO optical density ($\Delta D/D_{NO}$) under the effect of inert gas is proportional to relative pressure of this inert gas (P_{gas}/P_{NO}) with exponent 0,75 (Fig.7). It is interesting that magnitude of ($\Delta D/D_{NO}$) is increased strongly with the rise of NO pressure at its small content in gaseous mixture (P_{NO} <10 mm Hg). For example, it is raised in three times at the change of P_{NO} from 1,5 to 5,5 mm Hg. On the contrary the growth of the relative optical density is changed negligible at the P_{NO} is above 10 [mm Hg].

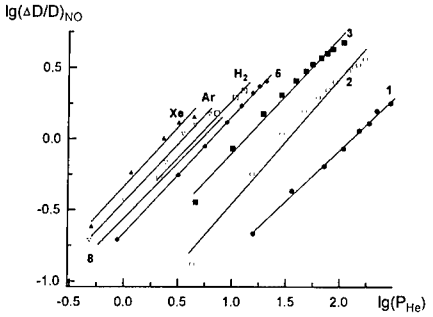

Fig. 7.

Influence of the relative "content" of inert gas (P_{gas}/P_{NO}) on the relative increase of NO absorption $(\Delta D/D_o)_{NO}$. In experiments with Xe the NO pressure is 58, Ar -59, H_2 -37, He -60 mm Hg. Results of measurements in case of other P_{NO} present in comparison: 1 -1,4; 2 -3,5; 3 -5,5; 5 -23 mm Hg.

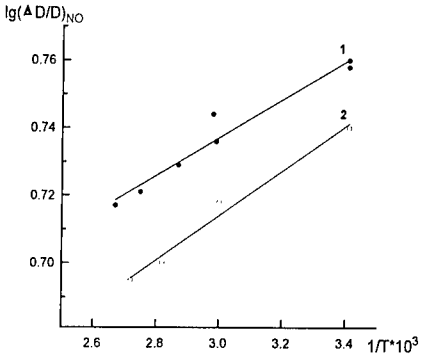

Fig. 8.

Temperature dependence of the relative increase of the NO optical density under influence of He (1) and H_2 (2).

The another gases influence on the NO absorption like He. Hydrogen shows very close quantitative dependence of the variation of NO optical density to He. Absorption of NO is stronger a little in the medium of N_2, CO, Ar, CO_2, Xe (Fig.7). The efficiency of their influence in this row is increased slightly from left to right. Xenon exceeds helium in 1,8 times. At the identical conditions diethyl ether acts in two time stronger in comparison with He. All this experiments on the influence of the gas nature were made at the NO pressure equal ~ 35 mm Hg.

The temperature influence was estimated by two gas mixtures with He and H_2 at range 20-100 ^oC and a large excess of inert gas when its effect on the NO spectrum absorption is high. In the mixture with He the ratio (P_{gas}/P_{NO}) is ~100 and ~30 with H_2, the NO pressure is equal P_{NO} = 7 and 17 mm Hg correspondingly. In the researching interval of temperature the changing of NO optical density is small extremely. With the growth of the temperature D_{NO} falls a little from 0,76 to 0,72 for He and from 0,46 to 0,43 for H_2. The formal Arrenius dependence of the changing ($\Delta D/P_{NO}$) value from the temperature (Fig.8) is characterised by the magnitude of ΔH ~1 kJ / mole (1,1 for the mixture with He and 1,35 - with H_2).

The found phenomenon of the growth of NO optical density under the action of another gas excess is very specific and is not observed for NO_2, which absorbs in the same

spectrum zone. It should take into consideration for UV-spectral analysis of NO in the gaseous mixtures, especially when NO presents in small amounts. This situation is typical for analysis of gaseous emission from chemical and energetic stations and engines.

References

1 Lurie B.A., Seregin V.V. // J. Appl. Spectr. (USSR). 1990. V.53. N 2. P. 221.

2. Forte E., Van Den Berg H. // Chem. Phys. 1978. V.30. N 4. P. 325.

3. Lurie B.A., Mikhno A.V. // Kinet. and Catal. 1997. V. 38. N 4. P. 535.

ON FLAME TEMPERATURE DETERMINATION BY THERMAL RADIATION

Igor S. Altman[1], Donggeun Lee[2], Yuriy L. Shoshin[1], Jae Dong Chung[2], Mansoo Choi[2]

[1]Institute of Combustion & Advanced Technologies, Odessa State University, Dvoryanskaya 2, Odessa, 65026, Ukraine, e-mail: ialtman@tm.odessa.ua

[2]National CRI Center for Nano Particle Control, School of Mechanical and Aerospace Engineering, Seoul National University, Seoul 151-742, Korea

The work is devoted to the discussion on the principle possibility of flame diagnostics by its thermal radiation. It is shown that the temperature usually obtained by the multi-color method is incorrect particle temperature. It is due to the strong spectral dependence of the flame emissivity.

The detail study of radiation of the silica particle within flame irradiated by a laser is carried out. The laser irradiation allows to control the particle temperature. The new spectral method of particle temperature change is developed.

INTRODUCTION

The knowledge of the combustion temperature is very important for understanding the processes occurring within flame. In particular, the interest is caused by the synthesis of oxide particles within flame, which has attracted considerable research attention in these days [1]. There exist many different methods of the determination of the combustion temperature. These methods could be separated into two groups: 1) the gas temperature determination, and 2) the condensed particle (CP) temperature determination. Usually it is assumed that there is no the difference between the temperatures obtained by these methods, when the sizes of CP are small ($\leq 0.1\mu m$), i.e. that the gas temperature and the condensed phase one are the same. However, according to the new result, it recently appeared [2,3] the difference between CP and gas temperatures could be essential. At least for the metal containing flames, where the oxide particles are formed, CP temperature can be above and below the gas temperature, depending on the stage of the oxide particle growth [3]. In this case the gas temperature measurement methods (which often are more exact and simpler) are not applicable for CP temperature determination.

CP temperature determination methods are based on the comparison of flame continuous radiation spectrum with the Planck function. This comparison requires the assumption about flame emissivity to restore CP temperature. Usually the assumptions about this emissivity have no physical reason, although they seem to be obvious. For instance, the two-color or more advanced the multi-color method assume the grayness of the light source. However, even if this assumption might be correct with a few limitations for soot containing flame, it is wrong (as we will see) for flame radiation emitted by the oxide particles. Indeed, the oxide particle is a wide gap dielectric as a rule. Due to this the spectral properties of the emitting particle strongly depend in the visible upon the wavelength. This may lead to the wrong result on CP temperature restoration. The objective of present work lies in analysis of possibility of CP temperature determination by the radiation spectrum in general case when spectral dependence of flame emissivity is not known *a priori*.

FLAME THERMAL RADIATION

As a rule, the radiation from optical thin flame is studied. In this case the registered radiation I_λ is the sum of radiation emitted by single particles within flame. According to the Kirchhoff law we can write for flame containing spherical nano particles:

$$I_\lambda = A\lambda^{-5} f_V \int_{T_{\min}}^{T_{\max}} g(T) q(\lambda,T) \left[\exp\left(\frac{hc}{k_B \lambda T} \right) - 1 \right]^{-1} dT \qquad (1a)$$

here A is the constant containing solid angle of the collection optics and the constant $2\pi hc^2$, f_V is the particle volume fraction, $g(T)$ is the function describing the temperature distribution of emitting particles, T_{min} and T_{max} are minimal and maximal particle temperatures and the ratio of nano particle emissivity to its radius [4]

$$q(\lambda,T) = \frac{24\pi}{\lambda} \frac{\varepsilon''}{(\varepsilon' + 2)^2 + (\varepsilon'')^2} \qquad (2)$$

here $\varepsilon(\lambda,T) = \varepsilon'(\lambda,T) + i\varepsilon''(\lambda,T)$ is the complex dielectric function of particle substance.

In visible region the unity in brackets in Eq.(1a) can be neglected and flame luminosity can be written as

$$I_\lambda = A\lambda^{-5} f_V \int_{T_{\min}}^{T_{\max}} g(T) q(\lambda,T) \exp\left(-\frac{hc}{k_B \lambda T} \right) dT \qquad (1b)$$

In the simplest case of the gray source of light when $q(\lambda,T)=const$ and for the

isothermal system when $g(T)=\delta(T-T_p)$, which is often considered, we obtain

$$I_\lambda = const\lambda^{-5}\left(-\frac{hc}{k_B\lambda T_p}\right) \qquad (3)$$

and particle temperature T_p can be restored by the slope of $ln(I_\lambda\lambda^5)$ upon inverse wavelength. The processing of experimental data according to this way lies in the basis of multi-color method. However, it is not believable that all particles have the same temperature within reacting system. The constancy of value $q(\lambda)$ is also physical unreasonable in general. Due to this Eq.(3) allows obtain only the "average" temperature. In the case of narrow particle temperature distribution $g(T)$ and if the value $q(\lambda)$ slightly depends on the wavelength this "average" temperature has a physical meaning. But, even if $g(T)=\delta(T-T_p)$ and, for instance, $q(\lambda,T)=exp(hc/k_B\lambda(1/T_p-1/T_*))$ the use of Eq.(3) gives the temperature T_* instead the correct temperature T_p. Note that exponential behavior of $q(\lambda)$ just might correspond to light absorption mechanism in oxides, where absorption in the visible occurs due to the transition between tails in the forbidden band [4]. The latter illustrates the principle impossibility to obtain the particle temperature using direct spectral measurements. This conclusion contradicts the paper [5] where it claims that it is possible to restore temperature from the flame spectrum. But the assumption about flame luminosity made in [5] excludes its exponential behavior that is why we believe the result [5] has no the physical generality. Therefore, to make conclusion about the possibility of flame diagnostics it is necessary to carry out the special experiment on study the flame luminosity when the CP temperature is known *a priori*. It may allow to restore the correct behavior of $q(\lambda)$.

EXPERIMENTAL METHOD

The experiment is carried out on the burner described in [6]. A co-flow oxy-hydrogen diffusion flame is used for $SiCl_4$ conversion to silica particles. The flow rate of $SiCl_4$ is chosen by the two orders of magnitude smaller than those of oxygen and hydrogen in order to avoid the change of gas temperature during the phase change of silica. The flame is irradiated by the CO_2 laser (Bystronic, BTL 2800) beam to change the temperature of silica particles. The laser power can be changed up to 1500 W with an approximate 40 W for each step. The gas temperature of the flame region irradiated by the laser is measured by a thermocouple. The gas temperature T_g without a laser irradiation is about 2000 K. At this point combustion

of $SiCl_4$ is completed that is why the silica particle temperature distribution is narrow and the average particle temperature is close to the gas one. The signal from the photomultiplier (Hamamatsu, R 928) (PMT) is fed into a lock-in amplifier (Stanford Research System, SR 830) to register the flame radiant emittance at a certain wavelength λ. The wavelength is defined by a color filter whose transparence band is about 10 nm. The self-radiation I_λ from the silica particles within flame is determined as the difference between the flame radiant emittance with and without $SiCl_4$ flow. The flame is optically thin for all measurements. In this case the registered self-radiation from silica particles is the sum of radiation emitted by the single silica particle. Note that the flame radiation without $SiCl_4$ flow is smaller than the flame radiation with silica particles as much as 20 times in case of no laser irradiation and 200 times in case of the highest laser power considered, 1220 W. Also note that the registered flame luminocity without $SiCl_4$ injection is the same at all laser powers.

RESULTS AND DISCUSSIONS

Fig.1 shows the dependence of $\ln(I_\lambda\lambda^5)$ upon the inverse wavelength of radiation λ for without laser power and for laser power W=1220 W.

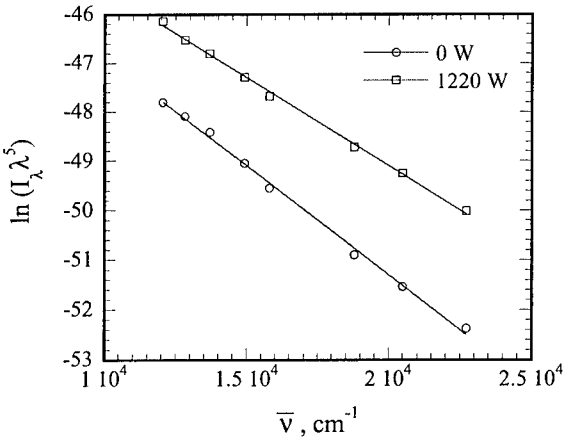

Figure 1

The particle temperature obtained in assumption of the flame grayness is 3260 K for the case without laser irradiation and 4000 K for the highest laser power. It is obvious that these temperatures are non-realistic. Indeed, the particle temperature without laser irradiation can not be larger than the gas temperature due to the particle cooling by self-radiation. Besides the particle temperature can not be larger than the boiling point of silica (3220 K) at atmospheric pressure. So, this discrepancy between the particle temperature obtained from the radiation spectrum and possible temperature without laser irradiation, for instance, corresponds to the non-grayness of silica particles and proves the above conclusion on the principle impossibility of the direct temperature diagnostics by the multi-color method.

The radiant emittance measured by PMT is given by formula

$$I_\lambda = 3q(\lambda, T_p) V f_V R_B(\lambda, T_p), \tag{4}$$

where V is the volume from which the radiation goes into the hole of PMT, f_V is the particle volume fraction, $R_B(\lambda, T_g)$ is the Planck function. Particle volume fraction can be estimated by the known flow rate of $SiCl_4$ injected in the burner, and volume V can be calculated using the parameters of optics. In this case it is possible to restore the particle absorption coefficient $q(\lambda)$. Fig. 2 shows the spectral dependence of the particle absorption coefficient restored by the Planck function $R_B(\lambda, T_g)$ at gas temperature.

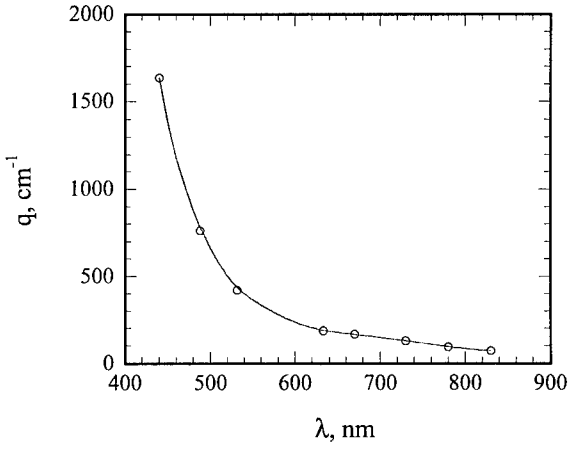

Figure 2

Note that the error in the estimation of f_V and V does not effect the spectral character of this dependence. A choice of the gas temperature in the Plank function is conditioned by the proximity of the gas and particle temperatures without a laser irradiation. As one can see the absorption coefficient of silica particles generated within flame strongly depends on the wavelength and this dependence is close to the exponential one. The exponential fitting of $q(\lambda)$ gives in the energy scale $q \sim exp(E/E_0)$ with $E_0 \sim 0.45$ eV. Note again that just this exponential behavior leads to the wrong particle temperature.

Let us dwell on the reason of the oxide particle non-grayness. Using Eq. (4) we calculated the imaginary part of dielectric function of silica particle substance. The obtained value is about 0.0015 at the wavelength 830 nm and about 0.02 at the wavelength 440 nm for particle temperature 2000 K. Such a large [4] values of imaginary part of dielectric function in visible region corresponds to the sufficient difference of the absorption properties of our particles and bulk silica. This difference might be caused by a high carrier concentration due to the large depth of the tails in forbidden band. The value of E_0 also indicates on the large tails depth [7]. Therefore the possible reason of the particle non-grayness may be related to the tailing in the forbidden band. Moreover, taking into account the large values of q, ε'' and E_0 we claim that the experimentally observed behavior of the particle absorption coefficient $q(\lambda)$ corresponds to the high carrier concentration at the forbidden band, which is comparable with the carrier concentration in the valence band. In this case, forbidden band loses its meaning. Note that possible reason of the disappearance of forbidden band may be connected with a large energy evolved during oxide particle formation from a gas (about 6 eV per a molecule). Since such a large energy is evolved during formation of ***all oxide*** particle we claim that the flame diagnostics by a multi-color method leads to the wrong result for ***all*** flames containing oxide particles. It is obvious that the difference between the correct particle temperature and the temperature obtained by multi-color method decreases with E_0 increase. That is why, it is possible for this difference to be small. But also it is possible to obtain the non-realistic value of temperature.

Let us consider the temperature behavior of the particle absorption coefficient. Using the Wien limit of the Planck function we can obtain the ratio of the intensities of radiation with and without laser irradiation:

$$\ln\left(\frac{I_\lambda}{I_{\lambda 0}}\right) = \ln\left(\frac{f_V}{f_{V0}}\right) + \frac{hc}{k_B\lambda}\left(\frac{1}{T_{p0}} - \frac{1}{T_p}\right) + \ln\left(\frac{q(\lambda, T_p)}{q(\lambda, T_{p0})}\right) \qquad (5)$$

Subscript "0" denotes the values corresponding to no laser irradiation.

The experimentally obtained values of $\ln(I_\lambda/I_{\lambda 0})$ at the different laser powers are plotted in Fig. 3 as a function of the inverse wavelength.

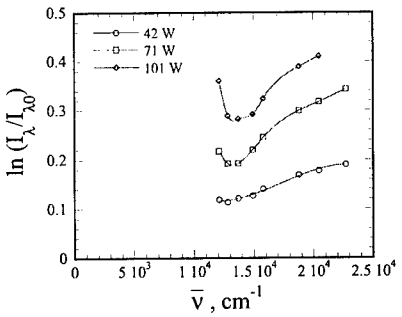

Figure 3.a

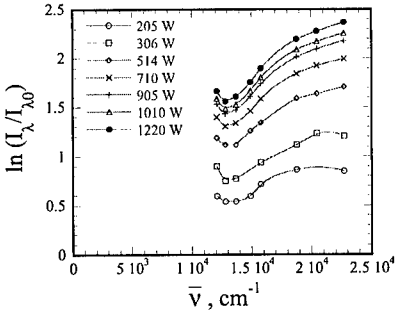

Figure 3.b

Regardless of laser power, a similar pattern with an inflection point is found. The non-linear behavior of $\ln(I_\lambda/I_{\lambda 0})$ stems from the variation of the value of $q(T_p)/q(T_{p0})$ according to the change of the wavelength, i.e. different dependence of the absorption coefficient upon the temperature at the different wavelengths.

It is possible to explain the spectral behavior of the value $q(T_p)/q(T_{p0})$ if the particle absorption is due to the tailing in the forbidden band and spectral dependence of absorption is given by a formula similar to $q \sim exp(h\nu/E_0)$. With the increase of the particle temperature due to a laser irradiation, the depth of state in the forbidden band E_0 might increase. Then the value $q(T_p)/q(T_{p0})$ is a monotonous (increasing) function of the wavelength.

The monotonous dependence of $q(T_p)/q(T_{p0})$ upon the wavelength gives a possibility to obtain a lower estimation of the particle temperature as the slope of the inflection tangent to a plot of $ln(I_\lambda/I_{\lambda 0})$. Indeed, if

$$\frac{1}{T_{p0}} - \frac{1}{T_p} \geq \frac{k_B}{hc} \left. \frac{d \ln(I_\lambda / I_{\lambda 0})}{d(1/\lambda)} \right|_{\inf l.p.} \qquad (6)$$

there are no different wavelengths with the same values of $q(\lambda, T_p)/q(\lambda, T_{p0})$. In the opposite case these wavelengths appear. Fig.4 shows the dependence of the lower estimation of non-dimensional inverse particle temperature change z_l ($z = T_g^*(1/T_{p0} - 1/T_p)$) upon the laser power.

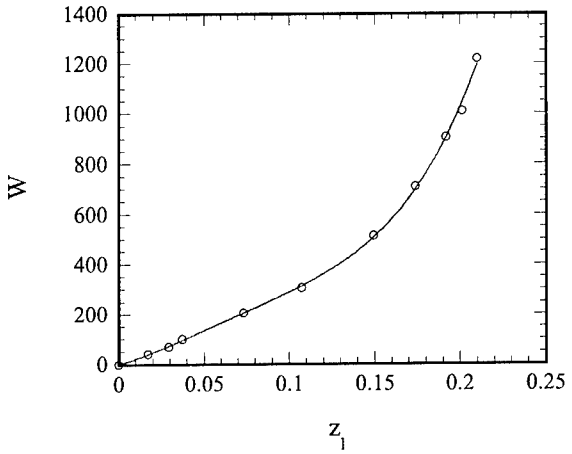

Figure 4

This dependence may be used for the estimation of the silica particle heat and mass transfer with the surrounding gas. However the discussion about this lies outside the scope of the present work.

CONCLUSIONS

For the temperature restoration of a particle within flame from the flame thermal radiation spectrum it is necessary to know the spectral dependence of the flame emissivity. This dependence is defined by the particle substance electronic properties. Since these properties depend on the rate of particle formation process within flame, they can not be calculated *a priori*. That is why the temperature of an oxide particle within flame can not be correctly restored in principle from the flame thermal radiation spectrum

ACKNOWLEDGEMENTS

The authors are grateful to P.V.Pikhitsa for helpful discussions. This work was partially funded by INTAS (grant #96-2334) and by National CRI Center for Nano Particle Control supported by the Ministry of Science and Technology, Korea.

REFERENCES

1. S. E. Pratsinis, Flame Aerosol Synthesis of Ceramic Powders, *Prog. Energy Comb. Science*, 1998, **24**, p. 197-219.
2. S. Altman, High-Temperature Estimation of Energy Accommodation Coefficient of Gas-Molecules on The Surface, *Journal of Physical Studies (Ukraine)*, 1999, **3(4)**, p.456-457.
3. I. S. Altman, On Condensation Growth of Oxide Particles during Gas-Phase Combustion of Metals. 17-th ICDERS, Heidelberg, Germany, July 25-30, 1999, CD p.107, submitted in *Combust. Sci. Technol.*
4. C. F. Bohren, D. R. Huffman, Absorption and Scattering of Light by Small Particles. Wiley, New York, 1983.
5. B. Block, W. Hentschel, W. Ertmer, Pyrometric Determination of Temperature in Rich Flames and Wavelength Dependence of Their Emissivity. Combustion and Flame, 1998, 114, p.359-369.
6. D. Lee, M. Choi, Control of Size and Morphology of Nano Particles Using CO_2 Laser During Flame Synthesis, *Journal of Aerosol Science*, accepted for publication.
7. J. I. Pankove, Optical Processes in Semiconductors, Prentice-Hall, New Jersey, 1971.

BESTIMMUNG DER TEMPERATUR VON H_2O_2/BRENNSTOFF-FLAMMEN AUS DEN EMITTIERTEN NIR-WASSERBANDEN

W. Eckl, V. Weiser, C. Besnard

Fraunhofer-Institut Chemische Technologie (ICT)
Joseph-von-Fraunhoferstr. 7
D-76327 Pfinztal (Berghausen), Germany

Abstract

The emitted near infrared band radiation of water has been used for non-intrusive spectroscopic temperature determination in H_2O_2 fuel flames. The applied spectrometer system has a high detector sensitivity combined with a excellent signal to noise ratio and reproducibility. The absorption coefficient in the near infrared is in a range where hot emitter (e.g. flame molecules) show a strong signal and cold absorber (e.g. air) can be neglected in the data analysis. Time and spatial resolved temperature and concentration profiles of water and soot are determined.

H_2O_2 / methanol and 2-propanol systems have been investigated as liquid- and cryo-propellants (CSP). The CSP showed a lower burning rate than the corresponding liquid fuels. The deviation can be explained by the lower starting temperature and the additional phase transition. The flame temperature of the CSP's is about 100 K lower. The measured water is suitable to describe the kinetics and in practical investigations as an indicator substance for the combustion precedence.

Kurzfassung

Zur berührungslosen Bestimmung der Temperatur von H_2O_2/Brennstoffflammen wurden die emittierten NIR Wasserbanden spektroskopisch erfaßt und ausgewertet. Das verwendete Spektrometersystem ist einfach zu bedienen, hat eine hohe Detektorempfindlichkeit, mit einem guten Signal/Rausch-Verhältnis und Reproduzierbarkeit. Die Größe des Absorptions-koeffizienten im nahen Infrarot erlaubt eine Auswertung ohne Berücksichtigung der Selbstabsorption der kalten Umgebungsatmosphäre. Als Ergebnis erhält man zeit- und ortsaufgelöste Temperatur- und Konzentrationsprofile von Wasser und Ruß.

Untersucht wurden Mischungen von H_2O_2 mit Methanol und 2-Propanol als Flüssigtreibstoff und als gefrorener Kryofesttreibstoff (CSP). Die CSPs brannten langsamer ab als die entsprechenden Flüssigtreibstoffe, diese Abweichung läßt sich aus der niedrigeren Anfangstemperatur und der zusätzlichen Phasenumwandlung erklären. Die Flammentemperatur der CSPs liegt etwa 100 K unter jener der Flüssigtreibstoffe. Das gemessene Wasser eignet sich sowohl für die kinetische Beschreibung als auch für die praktischen Untersuchung als Indikatorsubstanz des Verbrennungsfortschritts.

Einleitung

Die Abbrandrate von chemischen Treibstoffen steht in engem Zusammenhang mit der Flammenstruktur, d. h. der Profile von Temperatur und Gaskonzentration senkrecht zur Abbrandoberfläche. Sie charakterisiert die Gasreaktionen in der Treibstoffflamme und beschreibt die Wärmerückführung von der Gasphase auf den Treibstoff, die wiederum maßgeblich die Abbrandrate bestimmt. Eine Messung des Temperaturprofils gibt zusätzlich Hinweise auf die tatsächliche Leistungsfähigkeit der Brennkammergase vor der Expansionsdüse.

So ist ein schnelles und einfaches On-Line-Screening der Flammenstruktur zur Beurteilung einer, in Entwicklung befindlichen, Treibstoffformulierung wünschenswert. Vorgestellt wird ein Spektrometersystem im NIR-Bereich, daß es erlaubt während eines einzigen Strandabbrands die Temperaturverteilung zeitgleich mit der Konzentrationslänge des Hauptverbrennungsproduktes Wasser und der Festkörperstrahlung von Abbrandoberfläche und Partikeln in der Flammenzone zu bestimmen. Bei gleichzeitiger visueller Messung der Abbrandgeschwindigkeit ist es möglich die zeitaufgelösten Daten der ortsaufgelösten Flammenstruktur zuzuordnen.

Eingesetzt werden vorgemischte Modelltreibstoffe mit H_2O_2 und Methanol verschiedener Zusammensetzungen, als ein denkbar einfaches chemisches Treibstoffsystem, daß ausgehend von seinem spezifischen Impuls von >2600 Ns/kg als Flüssig- oder Geltreibstoff eingesetzt werden kann. Zur Simulation eines Festtreibstoffes wird das System in flüssigem Stickstoff gefroren. Solche Systeme werden zur Zeit für das neuartiges Raketensystem mit Kryofesttreibstoffen (CSP) diskutiert [1,2].

Experimentelles

Zur Aufnahme der Spektren im nahen Infrarot wurde ein Gitterspektrometer HGS 1700 basierend auf dem Zeiss System MCS 511 verwendet, daß speziell für Flammgasmessungen modifiziert wurde. Dieses Gerät ist mit einem InGaAs Diodenarray (256 Elemente) ausgestattet und deckt den Spektralbereich von 0.9 bis 1.7 µm ab. Die erreichbare spektrale Auflösung liegt bei 15 nm bei einer Scanrate von 300 Spektren pro Sekunde [3]. Als Eingangsoptik wurde eine spezielle Sonde verwendet, die auf das Glasfaserbündel nur Licht aus einem engen Öffnungswinkel von etwa 5° einkoppelt und auf den Spektrometerbaustein lenkt. Dadurch erhält man eine relativ gute Ortsauflösung 4 bis 5 mm.

Zur Abbrandratenmessung wurde eine Digitalvideokamera (Panasonic NV-DX100) mit Framecrabber und Bildverarbeitungssoftware eingesetzt. Das Verfahren wird in [4] genauer beschrieben.

Untersucht wurden Treibstoffmischungen von H_2O_2(85%) mit Isopropanol und Methanol in Glasröhrchen. Sie brannten in vertikaler Stirnbrenneranordnung (Strand burner) ab (vgl. Abbildung 1). Das Glasrohr zeigte keine Absorptionsbanden im untersuchten Spektralbereich. Eingesetzt wurden Mischungen in verschiedenen Zusammensetzungen nahe dem maximalen spezifischen Impuls. Vorteil von Methanol ist die Verfügbarkeit eines Modells des reaktionskinetischen Zersetzungsmechanismus, der für eine Abbrandmodellierung unerläßlich ist [5].

Die Verbrennungsfront durchläuft von unten den optischen Meßpunkt, so daß bei einem beobachteten stationären Abbrand die gesamte Reaktionszone abgetastet wird. Die

Scanrate betrug 100 Spektren/s. Durch Multiplikation mit der Abbrandrate wird der Zeitverlauf in ein Ortsprofil umgerechnet.

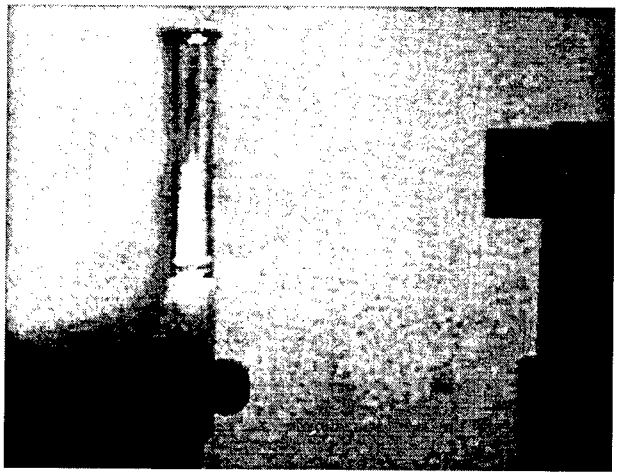

Abbildung 1 Versuchsanordnung: Abbrand eines homogenen Methanol/H_2O_2-Kryofesttreibstoffes im Glasrohr mit Eingangsoptik des NIR-Spektrometers (Heißgassensors HGS, rechts)

Datenauswertung

Das Modellierungsprogramm für die Nahinfrarotspektren basiert auf den Daten des 'Handbook of Infrared Radiation from Combustion Gases' [6]. Es erlaubt die Berechnung von Emissions- und Transmissionsspektren im Temperaturbereich 600 bis 3500 K. zusätzlich kann eine vorhandene kontinuierliche Strahlung von z. B. Ruß oder heißen Metallpartikeln mit in die Rechnung einbezogen werden. Die eigentliche Temperaturbestimmung erfolgt durch den Vergleich der gemessenen Spektren mit den berechneten Intensitätsverteilungen wobei Effekte der Selbstabsorption und Druckverbreiterung in die Rechnung integriert sind. Im hier genutzten Spektralbereich emittiert vornehmlich Wasser, das sowohl bei der Zersetzung von H_2O_2 als auch in den meisten Treibstoffen gebildet wird und als Indikator für den Reaktionsfortschritt der Treibstoffreaktion genutzt werden kann. Bei der Auswertung wird jedes einzelne Spektrum mit Hilfe eines mathematischen Least-Squares-Fits mit dem theoretischen Spektrum verglichen. Anpassungsparameter sind Temperatur und optische Dichte der Gaskomponente [Konzentration × Länge]. Ein Beispiel für die Datenauswertung ist in Abbildung 2 dargestellt.

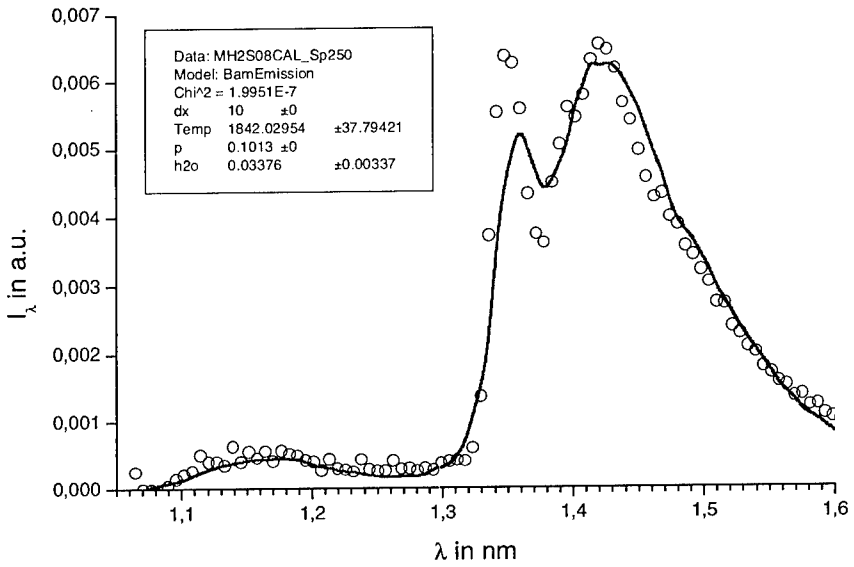

Abbildung 2 Vergleich einer gemessenen mit der berechneten Wasserbande beim Abbrand von Methanol mit H_2O_2 (85%)

Ergebnisse

Spektrometersystem und Anwendbarkeit

Die Anwendung des HGS 1700 erweißt sich als sehr einfach und benutzerfreundlich. Die Empfindlichkeit ist sehr hoch und die Spektren weisen ein geringes Signal/Rauschverhältnis auf. Der Untergrund, der durch eine Dunkelmessung bestimmt und dann automatisch vom Spektrum abgezogen wird, blieb nach einer Aufwärmphase des Spektrometers von etwa 60 min äußerst stabil.

Nach der Kalibrierung des Spektrometersystems an einem technischen Schwarzstrahler wurden an dem gleichen Strahler und einer geeichten Wolframbandlampe Referenzspektren bei verschiedenen Temperaturen zwischen 1200 K und 2000 K aufgenommen und mit der gleichen Kalibrierdatei analysiert. Dabei ergaben sich unüblich hohe Genauigkeiten nur sehr geringe Temperaturabweichungen von kleiner 0.5% (<10 K) beim Schwarzstrahler und 1% (<20 K) bei der Wolframbandlampe.

Bei den Abbrandversuchen passiert die stetig absinkende Flammenfront den Meßfleck. Dabei wird die gesamte Flammenlänge abgetastet. Trotz der relativ einfachen Eingangsoptik an der Glasfaser konnten deutlich aufgelöste Spektrenserien aufgenommen werden (Abbildung 3). Trotz der z. T. umfangreichen Anzahl von mehreren Spektren, betrug die Auswertedauer weniger als eine Minute.

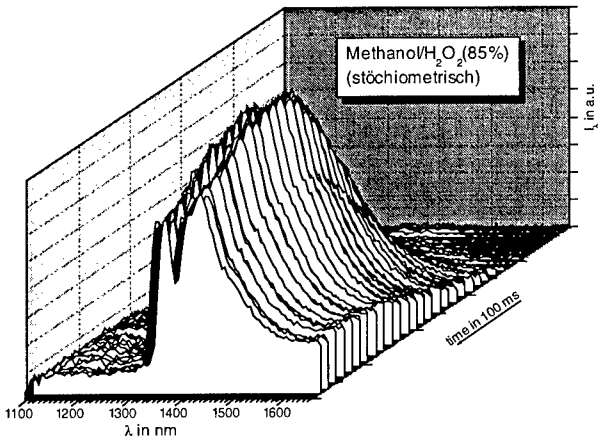

a)

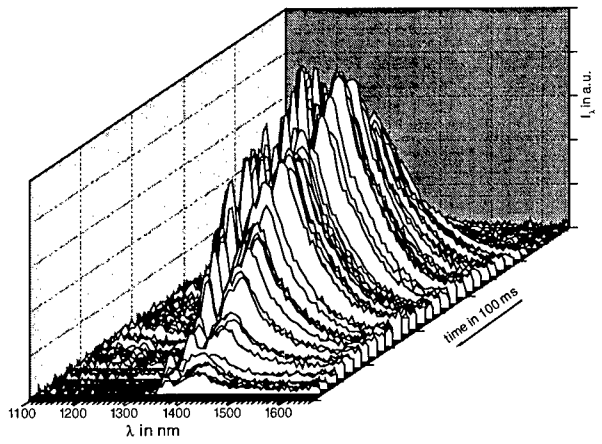

b)

Abbildung 3 Serien von NIR-Emissionsspektren der CSP-Flammen beim passieren des Detektionsfensters. Die Flammenspitze befindet sich im vorne, der CSP hinten. a) 20% Methanol, b) 15% Methanol in H_2O_2 (85%)

Abbrandverhalten

Alle Mischungen ließen sich leicht mit einer Propanflamme anzünden und brannten stationär ab. Bei den gefrorenen Mischungen bildete sich je nach Mischung eine konstante Schmelzschicht von 1 bis 5 mm Stärke. Die Regression verlief streng linear, so daß man von einer konstanten Abbrandrate sprechen konnte. Abbildung 4 zeigt ein Beispiel der

numerischen Videoauswertung einer H_2O_2/Methanol-CSP-Mischungen. Die helle Linie beschreibt die Abbrandoberfläche, darunter befindet sich der Brennstoff.

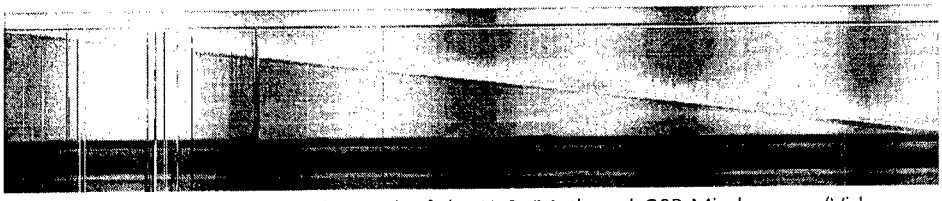

Abbildung 4 Linearer Regressionsverlauf der H_2O_2/Methanol-CSP-Mischungen (Videoauswertung). Die Abbrandfront verläuft von links oben nach rechts unten. Unter der Linie ist der CSP, darüber die Flamme. Die waagrechten Linien stammen vom Glasrand (oben) und der Halterung (unten)

Eine Zusammenstellung der Abbrandraten findet sich in Tabelle 1. Die Werte waren gut reproduzierbar. Die Abbrandraten der gefrorenen Mischungen liegen etwa 2 mm/s niedriger, als die der Proben bei Raumtemperatur. Diese Größenordnung läßt sich ausschließlich durch die um etwa 150 K niedrigere Anfangstemperatur und die zusätzliche endotherme Umwandlungswärme bei Schmelzen erklären. Die Zusammenhänge werden in [7] ausführlich dargestellt. Die höchsten Abbrandraten ergeben magere Mischungen mit Brennstoffunterschuß. Man kann vermuten, daß die Zersetzungsreaktion des H_2O_2 die Reaktion dominiert. Der Zusammenhang soll durch Modulieren der Reaktionskinetik und der Abbrandphänomene analysiert werden, wie in [7-9] dargestellt.

Tabelle 1 Abbrandraten der Mischungen im Glasrohr unter Atmosphärendruck. Vergleich zwischen Flüssigtreibstoffen (T_0=290 K) und CSPs (ca. T_0=140 K) bei verschiedenen Mischungsverhältnissen

Mischung	Verhältnis	Abbrandrate	
		gefroren	flüssig
Methanol/H_2O_2 (85%)	15/85	0,46	0,72
(stöchiometrisch)	20/80	0,35	0,52
	25/75	0,33	0,44
2-Propanol/H_2O_2 (85%)	10/90	0,32	0,72
(stöchiometrisch)	14.3/85.7	0,34	0,69
	20/80	0,31	0,42

Spektroskopische Untersuchungen

Die Spektren der untersuchten Proben zeigen klare Wasserbanden, die teilweise einem Kontinuum überlagen. Man kann einzelne Reaktionszonen in der Flamme unterscheiden. Die Spektren unterscheiden sich je nach Brennstoff und Mischungsverhältnis deutlich in den Intensitäten der Wasserbande in Relation zum kontinuierlichem Rußspektrum. Abbildung 5 zeigt eine Auswahl der gemessen Spektren. Erwartungsgemäß weisen die Spektren der Mischungen mit dem längerkettigen 2-Propanol einen höheren Rußanteil auf. Die überstöchiometrischen Mischungen mit Methanol zeigen dagegen keinen Untergrund. Hier unterdrücken die

oxidativen Bedingungen durch den Sauerstoffüberschuß in der Abbrandzone jegliche Rußbildungsneigung. Signifikante Unterschiede zwischen den flüssigen Mischungen und den CSP sind nicht zu beobachten.

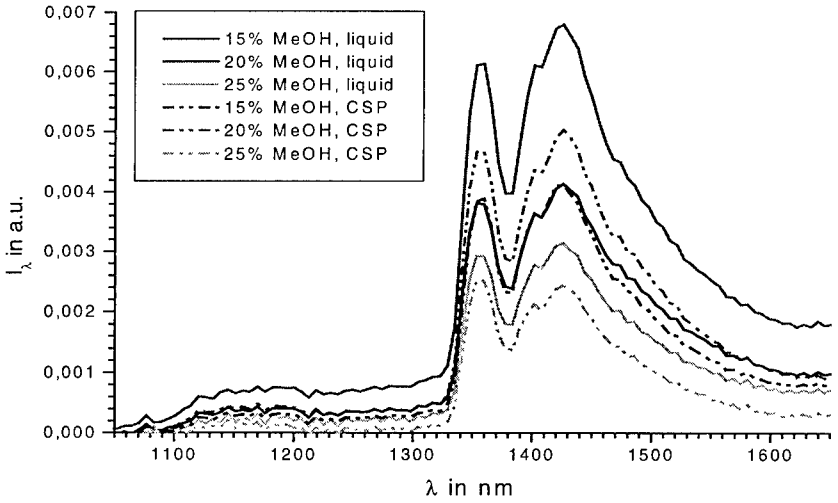

Abbildung 5 Emissionsspektren der CSP-Flammen (20% Methanol in H_2O_2) im NIR. Gemessen mit HGS.

Alle Spektren lassen sich mit einer mit einer großen Güte anfitten. Die Reproduzierbarkeit bei verschiedenen Messungen gleicher Bedingungen in Relation zu anderen Flammenmessungen sehr hoch. Die Kontinuumsstahlung bei gleichzeitiger Anwesenheit der Wasserbande lies sich am besten mit den Absorptionskoeffizienten von Ruß anpassen. War keine Wasserbande mehr zu erkennen sank die gleichzeitig die Gesamtintensität des Spektrum schlagartig ab und die Anpassung lieferte Temperaturen, die mehrere hundert Kelvin niedriger als zuvor lagen. In diesen Fällen gelang eine etwas bessere Fitanpassung mit einem konstanten Emissionsgrad (Graustrahler). Vergleiche mit den Videoaufnahmen ergaben, daß man sich hierbei über dem Flammenende befand und die Strahlung ausschließlich von der aufgeheizten Glaswand herrührte.

Beispielmessungen des Verlaufs von Temperatur und H_2O-Kurve zeigt Abbildung 6. Der Zeitverlauf wurde mit Hilfe der Abbrandrate in Ortsprofile umgerechnet. Nahe der Abbrandoberfläche bzw. Phasengrenze steigt die Temperatur in wenigen Millimetern rasch auf Werte zwischen 1700 K und 1800 K an, bleibt aber über die gesamte Flammenlänge etwa konstant. Ein Verhalten, das typisch für viele selbstkontrollierte Flammen ist [4,10]. Danach sinkt die Temperatur schlagartig auf 1000 K bis 1200 K ab. Ein Vergleich mit dem in diesem Bereich ebenfalls abbrechenden Wassersignal zeigt, daß es sich hierbei um das obere Flammenende handelt. Die niedrigeren Temperaturwerte stammen von der Glaswand. In einem kurzen Übergangsbereich am Ende der Flamme findet man sowohl hohe Verbrennungstemperaturen als auch niedrigere Temperaturen Glaswandtemperaturen. Hier verhält sich die Flamme nicht

mehr ganz stationär sondern flackert ein wenig. Dadurch trifft abwechselnd Strahlung von Flamme und Glaswand auf den Detektor und die Temperatur wird entsprechend der Strahlungsspektren richtig berechnet. Das Wassersignal steigt langsamer als die Temperatur auf einen etwa konstanten Wert an. Es wird entsprechend des Verbrennungsfortschritts in der Flamme gebildet. Da die Reaktionen der Wasserbildung schneller verlaufen, als die Oxidation des Kohlenstoffs [5], findet sich im oberen Flammenbereich ein Plateau. Hier sinkt die Wasserkonzentration scheinbar leicht ab. Dieser Effekt erklärt sich dadurch, daß in diesem Bereich die Flamme schmäler. Da die beschriebene Meßmethode nur optische Dichten, daß heißt das Produkt von Wasserkonzentration mal strahlungsaktiver Weglänge mißt sinkt hier das Signal ab.

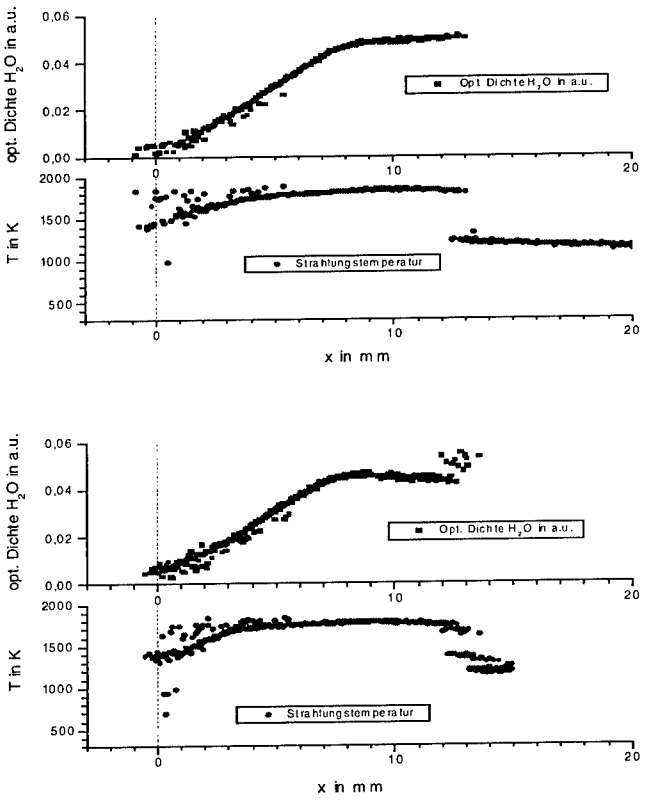

Abbildung 6 Profile von Temperatur und Wasser bei : homogen gemischten stöchiometrischen Mischungen von Methanol in H_2O_2(85%); oben: Flüssigtreibstoff, unten: CSP

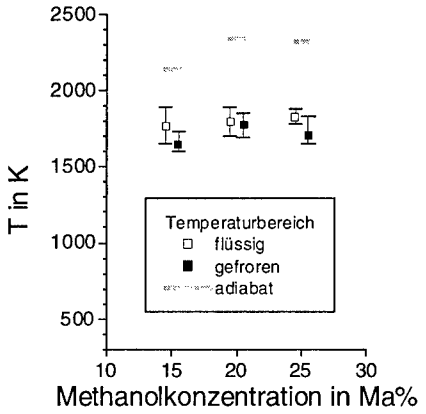

Abbildung 7 Temperaturmessungen in den Methanol/H_2O_2(85%)-Flammen verschiedener Zusammensetzung; Vergleich zwischen den entsprechenden Flüssigtreibstoffen und adiabat berechneten Verbrennungstemperaturen

Literatur

[1] Lo, R. E.; Modular Dissected Cryogenic Solid-Rocket Propellant Grains; 49th International Astronautical Congress; Sept. 28 – Oct.2., 1998, Melbourne, Australia; IAF-98-S.3.10

[2] Lo, R.; Adirim, H; Voronetzky, A; Weiser, V.; Eisenreich, N.; Kelzenberg, S.; Poller, S; Weiterführende und ergänzende Untersuchungen zur Kryofeststoff Triebwerks-technologie; BMBF-Bericht zu Projekt PA-FA/RD-JR 50 TT 9812; März 2000

[3] Eckl, W.; Weiser,V.; Weindel; M.; Determination of the Temperature in an Isopropanol Diffusion and a Premixed Propane-Air Flame; Application Note - HGS-1700 der Fa. WMM Sensorik Gmbh & Co.KG

[4] Weiser, V.; Eisenreich, N.; Baier, A.; Eckl, N.; Burning Behaviour of ADN Formulations; Propellants, Explosives, Pyrotechnics 24; 163-167 (1999)

[5] Warnatz, J., Maas, U.; Technische Verbrennung; Springer, 1993

[6] Ludwig, C. B.; Malkmus, W.; Reardon, J.E.; Thomson, J. A. L.; Handbook of Infrared Radiation from Combustion Gases, NASA SP-30980 (1973)

[7] W. Eckl, S. Kelzenberg, V. Weiser, and N. Eisenreich, "Einfache Modelle der Anzündung von Festreibstoffen", 29th Int. Annual Conference of ICT, Karlsruhe, June 30 – July 3, 1998, Germany, pp. 154.

[8] Kelzenberg, St.; Eisenreich, N.; Eckl, W.; Weiser, V.; Modelling Nitromethane Combustion; Propellants, Explosives, Pyrotechnics 24; 189-194 (1999)

[9] Kelzenberg, S.; Weiser, V.; Eisenreich, N.; Baier, A.; Eckl, W.; Burning Mechanisms of New Energetic Compounds; ; 30th International Annual Conference of ICT, 1999, Karlsruhe, pp. 14-(1-12)

[10] Weiser, V.; Weindel, M.; Eisenreich, N.; Eckl, W.; Influence of Transient Flame Phenomena on the Radiation from hazardous Fires; Eurofire'98, Brussels, 11 to 13 March 1998

[11] F. Volk, H. Bathelt, "User's Manual for the ICT-Thermodynamic Code; Vol. 2", ICT-Bericht 1/1991

Anwendung der digitalen Particle-Image-Velocimetry zur Vermessung turbulenter Strömungen im Inneren einer luftdurchströmten Brennkammer

Application of the Digital-Particle-Image-Velocimetry (DPIV) on turbulent airflows in a combustion chamber

J. Backhaus, A. Brock, L. Deimling

Fraunhofer Institut für Chemische Technologie (ICT), Joseph-von-Fraunhofer-Straße 7, D-76327 Pfinztal

Kurzfassung

Diese Arbeit befaßt sich mit der Lösung der Problemstellung, PIV für Strömungen in optisch schwer zugängliche Bereiche innerhalb einer luftdurchströmten Brennkammer anzuwenden. Die Versuche finden im isothermen Betriebszustand statt, wobei die Untersuchungen der Durchmischung einer Gegenstromeindüsung mit dem Hauptstrom im Vordergrund steht. Ein Vergleich der PIV-Meßergebnisse mit den Werten aus einer LDV-Messung soll die Aussagekraft der aufgenommenen Strömungsmessungen erhöhen. Die gemessenen zweidimensionale Strömungsfelder sind anhand der gebräuchlichsten Wirbelmodellen zu diskutieren.

Abstract

This paper deals with the solution of problematic nature to apply PIV for airflows inside the combustion chamber, which optical entrance is not very accessible. The experiments takes place in isothermic state in which the investigation of mixture upstreamed jet of flow with the main flow is to the fore. PIV-measurements compared with the results of LDV should improved the meaningfulness of flow measurements. The measured two-dimensional flowfields are discussed in context with vortex models.

1 Einleitung

Die Entwicklung und Erprobung von festen Brennstoffen für neue Antriebskonzepte ist eines der Forschungsthemen am Fraunhofer Institut für Chemische Technologie. In diesem Zusammenhang wird auch die Einsatzfähigkeit von Festbrennstoffen in luftatmenden Kombinationsantrieben, die eine Weiterentwicklung des Staustrahlkonzeptes darstellen, untersucht.

Bei der Staustrahlverbrennung zeigte sich, daß die Strömungs- bzw. Mischungsverhältnisse in der Brennkammer von großem Einfluß sind. Zur Erhöhung der Verweilzeit der Brennstoffpartikel in der Brennkammer erfolgte eine Gegenstromeindüsung des Brennstoffvolumenstroms in die Luftströmung. Um Brennstoff und Verbrennungsluft vollständig zu verbrennen, müssen beide Stoffströme im richtigen Verhältnis zueinander stehen. Dabei soll die Mischung beider Ströme im Idealfall so vollkommen sein, daß bis in die kleinsten Raumelemente in der Größenordnung der freien Weglänge der Moleküle stöchiometrische Mischungsverhältnisse herrschen. Hinsichtlich dieser Zielvorgabe ist es deshalb wichtig, die Brennkammergeometrie dahingehend zu verändern, um im Verbrennungsraum ein möglichst hoher Turbulenzgrad zu erreichen. Für einen solchen Schritt ist es eine unabdingbare Notwendigkeit, den Strömungszustand unter den gegenwärtigen Randbedingungen zu kennen und zu beschreiben.

Der Einsatz der bestehenden Turbulenzmodelle bietet zwar eine kostengünstige und schnellere Möglichkeit im Vergleich zu Modellversuchen, erfordert jedoch genauere Anfangs- und Validierungswerte aus dem Experiment. Aufgrund dieser Notwendigkeit kommen ausschließlich nicht intrusive Verfahren in Betracht.

Zur Charakterisierung instationärer Strömungen eignen sich besonders Ganzfeldmethoden wie die Particle-Image-Velocimetry (PIV). Das Prinzip dieser zweidimensionalen Meßmethode besteht in der Abbildung von Partikeln in einer Beobachtungsebene im Meßraum. Zur Eliminierung der Richtungszweideutigkeit sind zwei einzelne Aufnahmen des Partikelfeldes zu machen. Die nachfolgende Auswertung der Aufnahmen liefert mittels lokaler Kreuzkorrelationsfunktionen ein momentanes zweidimensionales Geschwindigkeitsfeld. Das Beobachtungsfeld ist dabei groß genug zu wählen für die Betrachtung makroskopischer Abläufe und muß gleichzeitig über eine ausreichende räumliche Auflösung zur Erfassung mikroskopischer Strömungsstrukturen verfügen.

Die vorliegende Arbeit befaßt sich mit der Lösung der Problemstellung, PIV zur Vermessung von Strömungen im Inneren einer luftdurchströmten Brennkammer anzuwenden. Die Versuche finden im kalten Betriebszustand statt, wobei die Untersuchung der Brennkammerinnenströmung mit Gegenstromeindüsung im Vordergrund steht.

2 Kenngrößen zur Beschreibung turbulenter Strömungen

Die Turbulenz ist eine Erscheinung mit starken Wirbelbewegungen. Bei einer Momentaufnahme des Strömungszustandes lassen sich deshalb die Turbulenzen in Form einer Wirbelstärke unmittelbar aus den benachbarten Vektoren am Meßort ermitteln. Die PIV-Methode erfaßt auf der Grundlage eines Lichtschnitts im Beobachtungsbereich ein zweidimensionales Strömungsfeld. Die dadurch gemessenen Geschwindigkeitskompo-

nenten in der Ebene ermöglichen die Berechnung der Rotationskomponente in Betrag und Drehsinn senkrecht zur Meßebene nach der folgenden Gleichung:

Gl. 2-1

$$\omega_z = \frac{\partial u_y}{\partial x} - \frac{\partial u_x}{\partial y}$$

Die partiellen Ableitungen in Gl. 2-1 berechnen sich mit dem in /1, 2, 3/ beschriebenen Auswerteverfahren.

Das Fehlen der senkrechten Geschwindigkeitskomponente läßt sich am zweidimensionalen Vektorfeld teilweise kompensieren mittels Berechnung der Streckungsrate senkrecht zur Meßebene. Ausgangspunkt dafür ist das Kontinuitätsgesetz. Unter der Bedingung, daß eine inkompressible Strömung vorliegt, vereinfacht sich diese Gleichung zu:

Gl. 2-2

$$e_{zz} = \frac{\partial u_z}{\partial z} = -\left(\frac{\partial u_x}{\partial x} + \frac{\partial u_y}{\partial y}\right)$$

Die Streckungsrate e_{zz} gibt Aufschluß über die lokalen Zu- bzw. Abströmungen des Fluids. Es ist jedoch zu beachten, daß diese Größe lediglich die Anwesenheit der Strömungsbewegung senkrecht zum Lichtschnitt nachweist. Die dazugehörige Geschwindigkeitskomponente läßt sich nicht daraus ermitteln.

Die Schwankungsgeschwindigkeiten enthalten die charakteristischen Eigenschaften der Turbulenz, die sich aus der Wurzel des mittleren Fehlerquadrates berechnen läßt. Dies führt zur Bestimmung der Standardabweichung nach Gl. 2-3:

Gl. 2-3

$$u' = \sqrt{\frac{\sum_{i=1}^{n} (u_i - \overline{u})^2}{(n-1)}}$$

3 Versuchsaufbau

Der Aufbau in Abb. 3-1 ermöglicht eine flexible Anpassung des Versuchsstandes auf verschiedene optische Meßverfahren und Versuchsobjekte. Dieses Kapitel beschreibt im wesentlichen die wichtigsten Bestandteile und Kenndaten des Versuchstands, deren Aufbau in /4/ ausführlich behandelt ist.

Ein Hochdruckradialgebläse erzeugt einen Hauptluftstrom und ist in der derzeitigen Konfiguration in einem Volumenbereich von 50 bis 280 l/s durch eine saugseitig angebrachte Drosselklappe einstellbar. Nach dem Gebläse folgt ein Meßrohrsegment zur Messung der Strömungsparameter Temperatur, Volumenstrom, Druck. Weiter stromabwärts befindet sich die zentrale Zufuhr der Streuteilchen.

Das zu untersuchende Objekt des Versuchstands in Abb. 3-1 besteht in diesem Fall aus einer luftdurchströmten Brennkammer, die optisch zugänglich ist. Deren Konzeption ist in den Arbeiten von Liehmann /5, 6/ dargestellt. Die Treibstoffzufuhr erfolgt bei regelbarer Luftzufuhr entgegengesetzt der Hauptluftströmung. Im Bereich des konischen Lufteinlasses der Brennkammer befindet sich ein axial verstellbarer Staukörper.

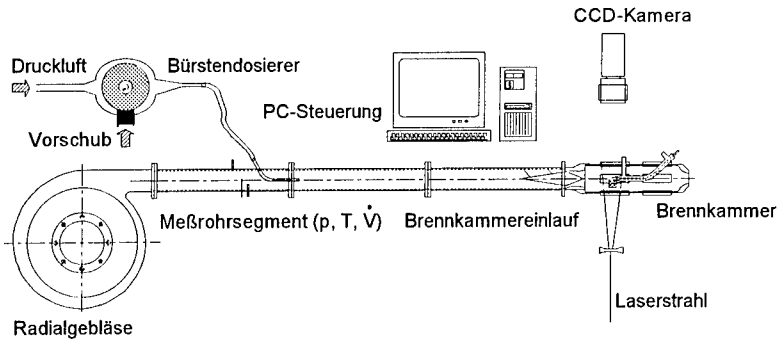

Abb. 3-1: Versuchsstand

3.1 Partikeldosierung

Bei der PIV als partikelgestützte Ganzfeldmethode hängt die Qualität der Meßergebnisse maßgeblich von der Dosierung der Streuteilchen ab. Außer einem guten Folgeverhalten ist die gleichmäßige Verteilung der Streuteilchen über dem Meßfeld Voraussetzung für zuverlässige und auswertbare Ergebnisse. Die Partikelzugabe, die im vorliegenden Aufbau bereits in der Luftzufuhr der Brennkammer erfolgt, bewirkt eine gleichmäßige räumliche Partikelverteilung im Brennkammerinneren. Die Zuführung über einer ausreichend langen Beruhigungsstrecke gleicht die räumlichen Konzentrationsschwankungen der Partikel weitgehend aus.

Die Dotierung großer Beobachtungsfelder mit Streuteilchen in Verbindung mit hohen Strömungsgeschwindigkeiten benötigt leistungsfähige Partikelgeneratoren, die einen großen und konstanten Massenstrom an Streupartikel produzieren. Der in dieser Arbeit verwendete Bürstendosierer, entwickelt im Engler-Bunte-Institut, erfüllt diese Bedingung und erzeugt die für PIV-Geschwindigkeitsmessungen notwendigen Streupartikel. Ausgangsmaterial für die Streuteilchen ist kommerziell erhältliches Magnesiumoxydpulver. Unter Anwendung eines speziellen Verfahrens /7/ werden daraus feste zylinderförmige Blöcke hergestellt. Eine rotierende Metalldrahtbürste trägt den Magnesiumoxydkörper mechanisch ab. Die hohe Umfangsgeschwindigkeit der rotierenden Bürste und der sehr langsame Vorschub der Magnesiumoxydblöcke erzeugen Partikelkollektive einer kleinen Korngröße. Der Partikelstrom des Dosierers ist über den Vorschub des MgO-Blocks gegen die rotierende Drahtbürste steuerbar. Um einen spürbaren Einfluß der Streuteilchen auf die Strömungseigenschaften zu vermeiden, ist darauf zu achten, daß die Beladung von Partikelmaterial 0.5g auf $1m^3$ nicht überschreitet.

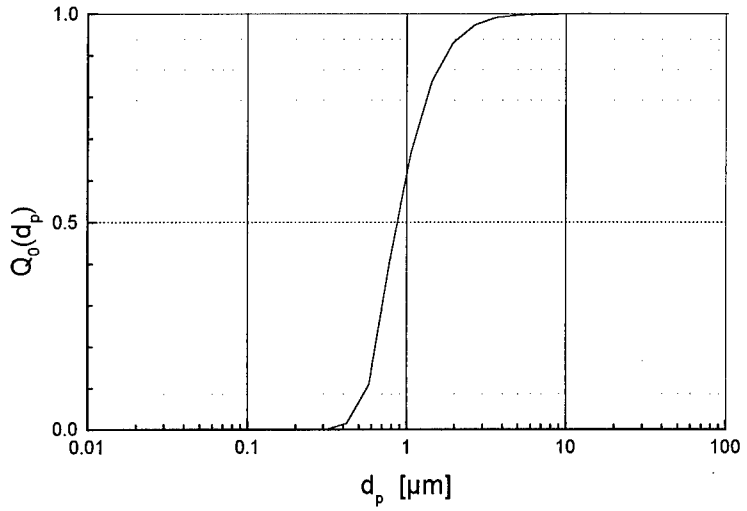

Abb. 3-2: Summenverteilung der Korngröße von Magnesiumoxydteilchen

Die massengewichtete Partikelgrößenverteilung wurde mittels eines Laserbeugungsverfahrens /8/ gemessen und nach Gl. 3-1 unter Annahme einer logarithmischen Gaußverteilung in eine Anzahlgrößenverteilung umgerechnet /9/:

Gl. 3-1

$$q_0(d_p) = \frac{1}{d_p \sigma \sqrt{2\pi}} \exp\left\{-\frac{1}{2}\left[\frac{\ln\left(d_p / d_{p,50,3}\right)}{\sigma} + 3\sigma\right]^2\right\}$$

Als Ergebnis stellt Abb. 3-2 die anzahlgewichtete Summenverteilung $Q_0(d_p)=\Sigma q_0(d_p)d_p$ im logarithmischen Maßstab dar.

3.2 Brennkammer

Die Brennkammer besteht aus einem Brennkammerrohr mit acht rechteckigen Öffnungen, an welche die Meßfenster angeschweißt sind. Im ungenutzten Zustand werden diese mit Blindblenden verschlossen, deren Innenfläche exakt der Kontur des Brennkammerrohres entspricht. Die in dieser Arbeit verwendete Brennkammer enthält am unteren Meßfenster eine wasserkühlbare Brennstoffzufuhr. An diese ist die Gegenstrombrennstoffdüse aufgeschraubt, durch die der Brennstoff in einem Winkel von 160° gegenüber der Hauptströmungsachse durch acht Bohrungen in die Verbrennungsluft eintritt.

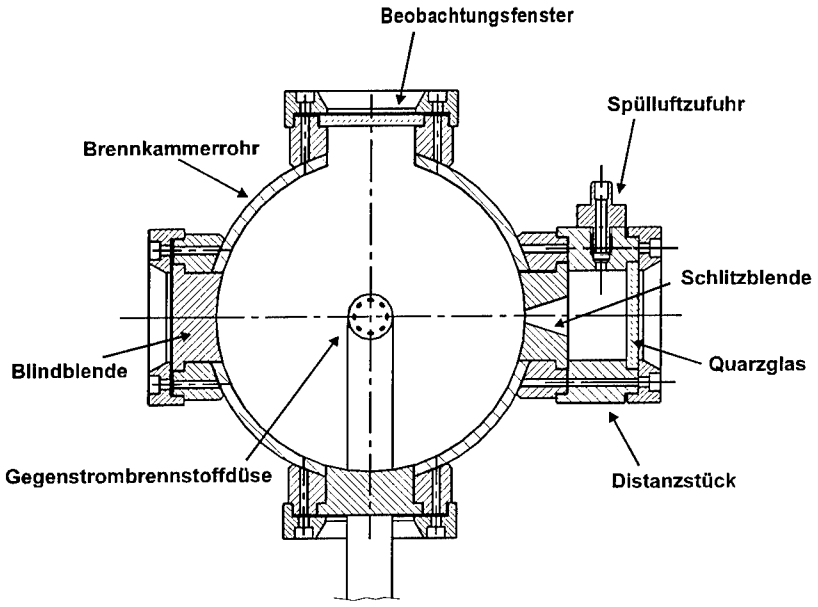

Abb. 3-3: Optische Zugänglichkeit der Brennkammer (im Vertikalschnitt)

Zur Beobachtung von Gegenstromverwirbelungen ist für das verwendete PIV-System ein Meßbereich der Größe von ca. 40mm x 40mm in unmittelbarer Umgebung der Gegenstromdüse vorgegeben, die sich im Lichtschnitt befindet. Dieser Bereich ist optisch von zwei Seiten zugänglich.

Bei den Versuchen mit Zugabe von Streupartikel ist die Blindblende an der zum Lichtschnitt zugewandten Brennkammerseite ersetzt durch eine Schlitzblende, wie bei den LDV-Versuchen beschrieben in /4, 10/. Die Schlitzblende in Abb. 3-3 ermöglicht den Zugang des Laserlichtschnitts. Um ein Ausblocken der Laserstrahlen an Schlitzkanten zu vermeiden, verbreitert sich die Schlitzöffnung nach außen hin. Auf der Kammerinnenseite hat die Blindblende wieder die Wölbung des Kammerrohres, womit die Störung der Kammergeometrie auf ein Minimum reduziert ist. Um Ablagerungen von Streuteilchen auf der Quarzglasscheibe zu verhindern, befindet sich zwischen Fenster und Fensterrahmen ein Distanzstück, durch welches hinter dem Schlitz ein Totvolumen entsteht. Eine Spülluftzufuhr erzeugt einen schleichenden Spülstrom in die Hauptströmung, der das Eindringen von Partikel an die Quarzglasscheiben erschwert.

Das der Kamera zugewandte Brennkammerfenster ist mit einer weiteren Quarzglasscheibe versehen. Das PIV-Verfahren benötigt jedoch einen optischen Beobachtungszugang, an dem sich möglichst wenig Streuteilchen ablagern. Ein Zurücksetzen des Beobachtungsfensters vermindert zwar die Verschmutzung, aber infolge der benötigten größeren optischen Weglänge auch das Beobachtungsfeld der Kamera. Aus diesem Grund besteht der Lösungsweg zu diesem Problem in der Zuführung von Spülluft über einen schmalen Schlitz am Fensterrahmen an die Innenseite des Fensters, wie in Abb. 3-4 dargestellt.

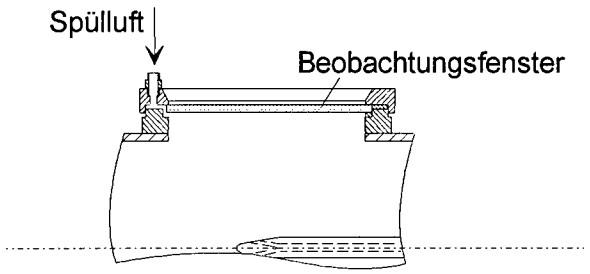

Abb. 3-4: Spülluftvorrichtung zur Reinhaltung des Beobachtungsfensters

3.3 Kamerasystem

Die für die Bearbeitung der Aufgabenstellung verwendete digitale Kamera vom Typ Kodak-Megaplus ES 1.0 ermöglicht mittels eines Interline-Transfere-Sensors die Aufnahmen von zwei aufeinanderfolgenden Bildern mit einem zeitlichen Abstand bis in den Größenbereich von 1µs. Die CCD-Auflösung beträgt 1024 x 1024 Pixel. Die Abbildung erfolgt über ein Makroobjektiv vom Typ Zeiss Makro-Planar mit einer Brennweite von 100mm.

Das Signalverlaufsschema in Abb. 3-5 stellt den Vorgang bei der Erfassung von zwei aufeinanderfolgenden Aufnahmen dar. Ein vom Anwender vorgegebenes Triggersignal aktiviert per Schließkontakt den Nd-YAG-Doppelpulslaser /11/, der zu zwei verschiedenen Zeiten einen kurzen intensiven Lichtpuls erzeugt. Der erste Lichtpuls liegt innerhalb des Zeitfensters der ersten Kamerabelichtung. Aufgrund der sehr kurzen Lichtpulse ist eine Belichtungszeit von 1µs vollständig ausreichend. Innerhalb einer vom Benutzer vorgegebenen Übertragungszeit von 2µs (Transferpulsbreite ≤ 5µs) erfolgt eine Verschiebung des aufgenommenen ersten Bildes vom Pixelfeld in das vertikale Schieberegister. Die zweite Aufnahme erfolgt in einer fest vorgegebenen Zeit von 66ms, aufgrund der Tatsache, daß das erste Bild vom vertikalen Schieberegister nur zeilenweise ausgelesen und seriell in den Bildspeicher einer Bilderfassungskarte verschoben werden kann. Innerhalb dieser Zeitspanne befindet sich der zweite Lichtpuls. Nachdem das erste Bild vollständig in den Bildspeicher verschoben ist, erfolgt die Verschiebung des zweiten Bildes in den Bildspeicher der Bilderfassungskarte. Die Verwendung eines Interferenzfilters ermöglicht die Bildaufzeichnung auch bei hellem Umgebungslicht.

Die Beobachtung von optisch schwer zugänglichen Bereichen im Brennkammerinneren benötigt eine Aufnahmevorrichtung, bei der die Kamera unter einem Winkel abweichend von 90° zur Objektebene auch Bereiche von Strömungsfeldern aufzeichnet, die bei senkrechter Betrachtung durch die Rohrwand verdeckt sind. Die zusätzlichen Anforderungen nach einer kleinen Blendenzahl ist verknüpft mit einer kleinen Schärfetiefe.

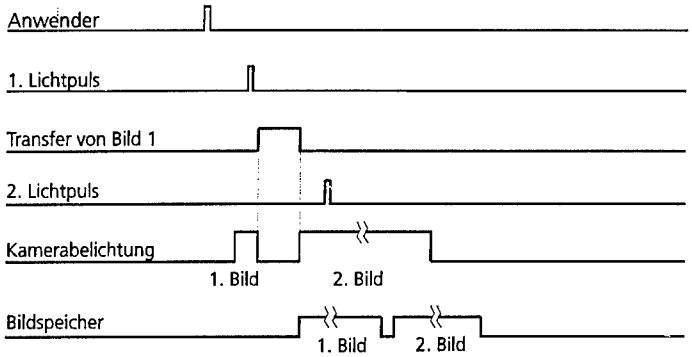

Abb. 3-5: Zeitlicher Signalverlauf beim Einlesen von zwei Bildern

Um die Partikel im gesamten Beobachtungsbereich gleich scharf abzubilden, ist eine Aufnahmeanordnung zu wählen, die dem Scheimpflug-Kriterium genügt. Dieses Kriterium beinhaltet folgende Forderung: Die Verlängerungslinien von Abbildungs-, Linsen- und Objektebene müssen sich an einem Punkt schneiden (vgl. Abb. 3-6).

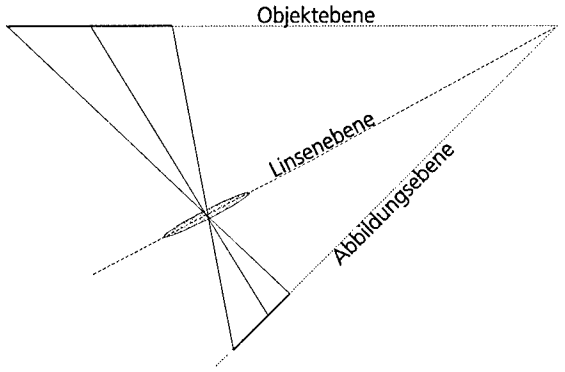

Abb. 3-6: Aufnahmeanordnung nach Scheimpflug

Als unerwünschter Nebeneffekt tritt jedoch bei einer solchen Anordnung eine perspektivische Verzerrung auf, welches ein Quadrat in ein Trapez transformiert. Der Abbildungsmaßstab ist dann nicht mehr konstant über dem gesamten Abbildungsfeld und verlangt deshalb nach einer zusätzlichen Bildentzerrung.

Die Entzerrungsparameter lassen sich am besten anhand eines Millimeterpapiers, aufgenommen mit einer in Scheimpflug-Anordnung angebrachten CCD-Kamera, bestimmen. Das Millimeterpapier erscheint, wie oben beschrieben, in Form eines Trapezes verzerrt. Der Vergrößerungsfaktor läßt sich anhand des Millimeterrasters für jeden beliebigen Bildpunkt berechnen und für das Entzerren mit Hilfe der perspektivischen Projektion verwenden.

4 Ergebnisse

Die Untersuchung der Brennkammerinnenströmungen erfolgten im isothermen Betriebszustand unter Verwendung der folgenden Parameter:

Spülluftstrom am Meßfenster	$\dot{V}_S = 2\ \frac{m_N^3}{h}$
Hauptströmung	$\dot{V}_L = 468 \frac{m_N^3}{h}$
Düsenvolumenstrom	$\dot{V}_D = 12\ \frac{m_N^3}{h}$ Luft
Umgebungstemperatur	T = 15°C
Dosierung	MgO mit Dosierzahl DZ = 20

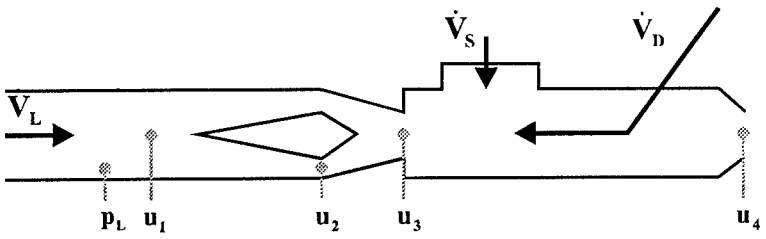

Abb. 4-1: Versuchsparameter bei Strömungsmessung in der Brennkammer

In Abb. 4-1 ist die Brennkammer schematisch dargestellt. Mit den Querschnittsflächen und unter Anwendung der Kontinuitätsgleichung lassen sich die zu erwartenden mittleren Geschwindigkeiten für den verwendeten Volumenstrom vor dem Brennkammereinlauf u_1, am Ringspalt u_2, am Kammereintritt u_3 und an der Austrittsdüse u_4 abschätzen:

$\dot{V}_L$ / $\frac{m_N^3}{h}$	p_L / mmWS	u_1 / ms^{-1}	u_2 / ms^{-1}	u_3 / ms^{-1}	u_4 / ms^{-1}
468	17	9,1	43	20	46

In Abb. 4-2 ist die Lage der Beobachtungsbereiche des LDV- und des PIV-Systems innerhalb der Brennkammer dargestellt. Aufgrund der Vorgabe, Strömungsbereiche mit hoher Wirbelstärke zu untersuchen, konzentriert sich der Beobachtungsbereich von PIV in unmittelbarer Umgebung der Gegenstromdüse.

Im folgenden werden die Ergebnisse der LDV-Vermessung und der Messungen mit dem PIV-System jeweils für die isotherme Brennkammerinnenströmung mit Gegenstromeindüsung beschrieben.

Die Versuche erfolgten mit einer Gegenstromeindüsung von ca. 12 m_N^3/h. Um eine gleichmäßige räumliche Verteilung der Streupartikel zu gewährleisten, erfolgte die Zugabe der Streupartikel über den Hauptstrom (Hauptstromdotierung).

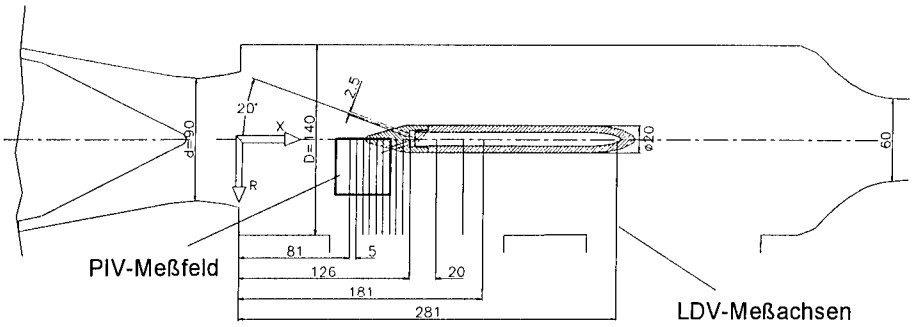

Abb. 4-2: Meßfeld bei isothermer Gegenstromeindüsung

Abb. 4-3 zeigt die Geschwindigkeitsprofile und ihre Standardabweichungen aus einer LDV-Vermessung. Am Düsenaustritt bei x=111mm sind starke negative Geschwindigkeiten von ca. 50m/s zu erkennen. Mit zunehmendem axialen Abstand nimmt der Betrag der negativen Strömungsgeschwindigkeiten ab. Gleichzeitig verschiebt sich das lokale Geschwindigkeitsminimum zu größeren Radien. Die Standardabweichungen der Strömungsgeschwindigkeit nehmen an diesen Positionen einen lokalen maximalen Wert an. Dies läßt auf eine erhöhte Turbulenz in diesen Bereichen schließen.

Die PIV-Auswertung aus zwei einzelbelichteten Momentaufnahmen in Abb. 4-4 ergibt den augenblicklichen Zustand der Hauptströmung mit Gegenstromeindüsung. Die Abbremsung und Ablenkung des Düsengegenstroms durch die Hauptströmung führt zu einem parabelförmigen Verlauf der Gegenströmung. Die Verwirbelungen befinden sich angereiht zu beiden Seiten mit entgegengesetztem Drehsinn in den Schubspannungsbereichen zwischen Gegenströmung und Hauptströmung, wobei die linksdrehenden Wirbel stärker ausgeprägt sind.

Aus einer Mittelung von 50 PIV-Einzelauswertungen bleibt, wie in Abb. 4-5 dargestellt, ein linksdrehender Wirbel übrig. Diese makroskopische Struktur ist auf die überlagerten Bewegungen von Haupt- und Gegenströmung zurückzuführen.

Die Divergenz der mittleren Streckungsraten e_{zz} senkrecht zur Meßebene sind am stärksten in der Gegenströmung am Auslaß der Gegenstromdüse ausgeprägt (vgl. Abb. 4-6). Dies läßt sich mit einem freistrahlähnlichem Verhalten der Gegenströmung erklären. Abb. 4-7 zeigt, daß die Gegenströmung deutlich turbulenter im Vergleich zu ihrer Umgebung ist.

Abb. 4-9 beinhaltet das radiale Profil des gemittelten Gegenstromwirbels bezogen auf die in Abb. 4-8 eingezeichnete Meßachse. Diese Betrachtung bezieht sich dabei auf einen x-Achsenabstand von 13mm relativ zum Auslaß der Gegenstromdüse in einem radialen Bereich r von 12mm bis 35mm. Die gemessenen Werte der Wirbelstärke lassen sich mittels einer Gaußfunktion annähern. Dies wiederum entspricht dem Wirbelmodell von Hamel-Oseen.

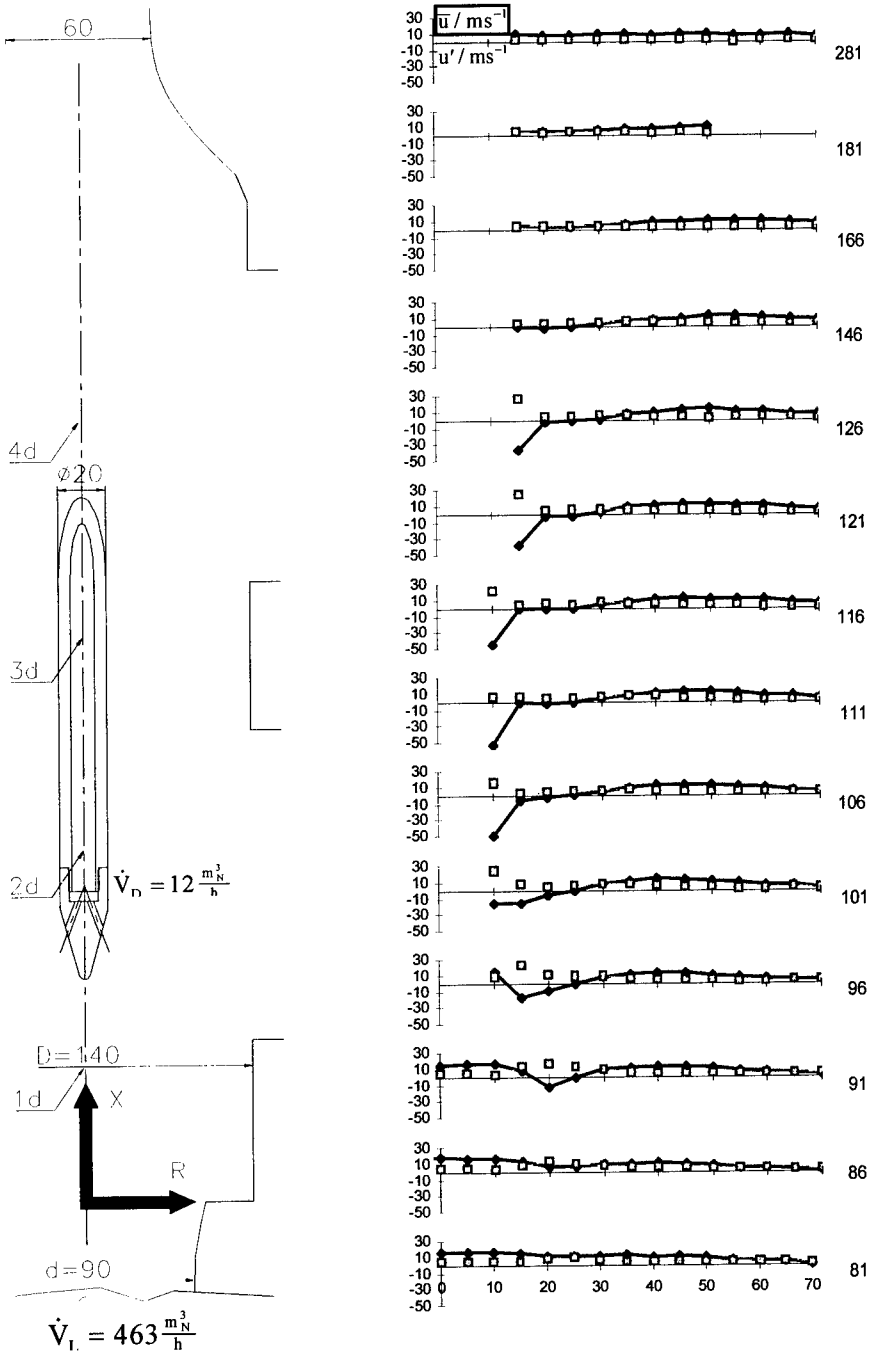

Abb. 4-3: LDV-Messung der Geschwindigkeit und Standardabweichung bei Gegenstromeindüsung

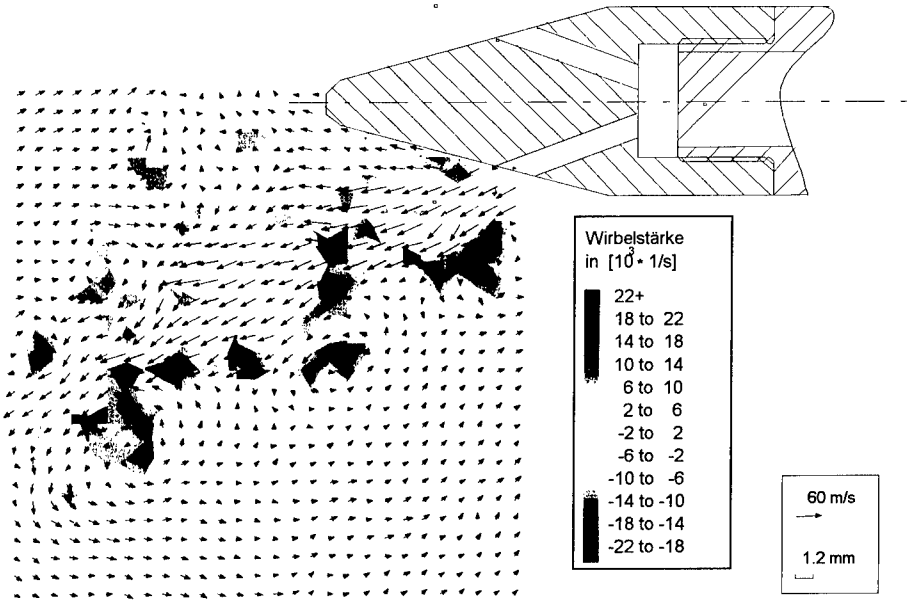

Abb. 4-4: PIV-Messung der Geschwindigkeit und Wirbelstärke bei Gegenstrom-eindüsung

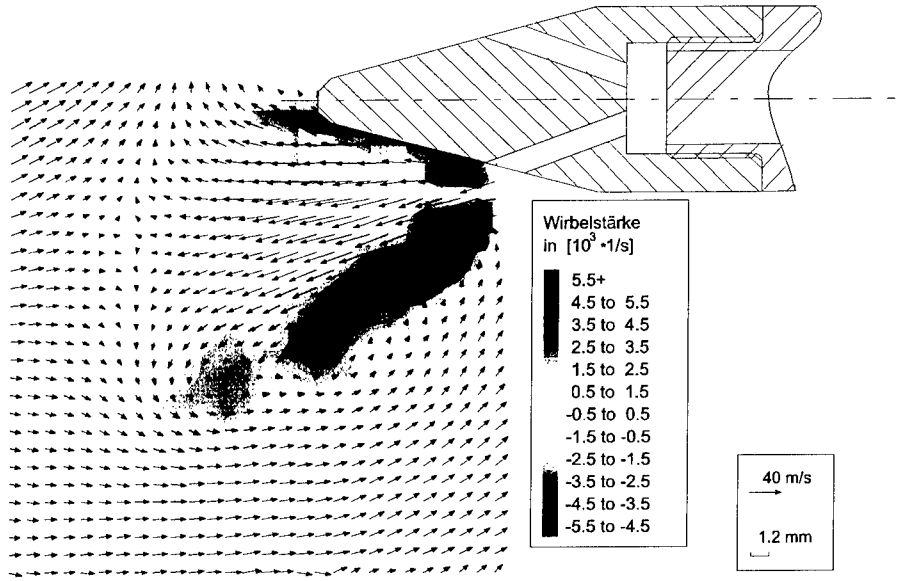

Abb. 4-5: Gemitteltes Geschwindigkeits- und Wirbelstärkefeld aus 50 PIV-Auswertungen der Gegenströmung

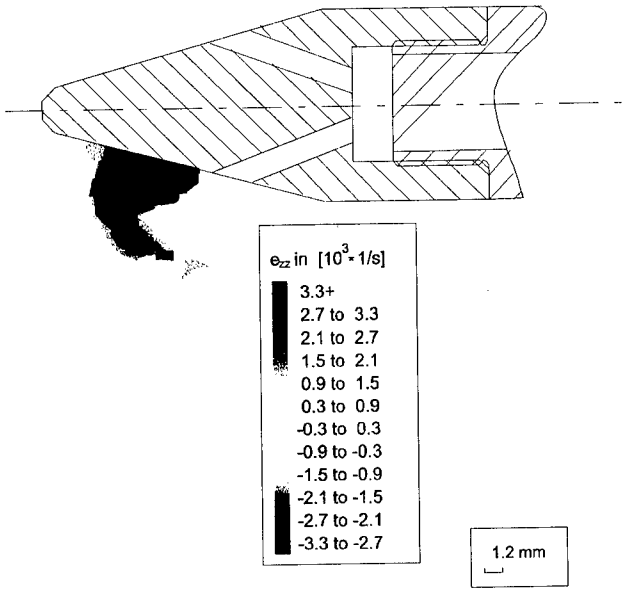

Abb. 4-6: Gemittelte Streckungsraten e_{zz} aus 50 PIV-Auswertungen der Gegenströmung

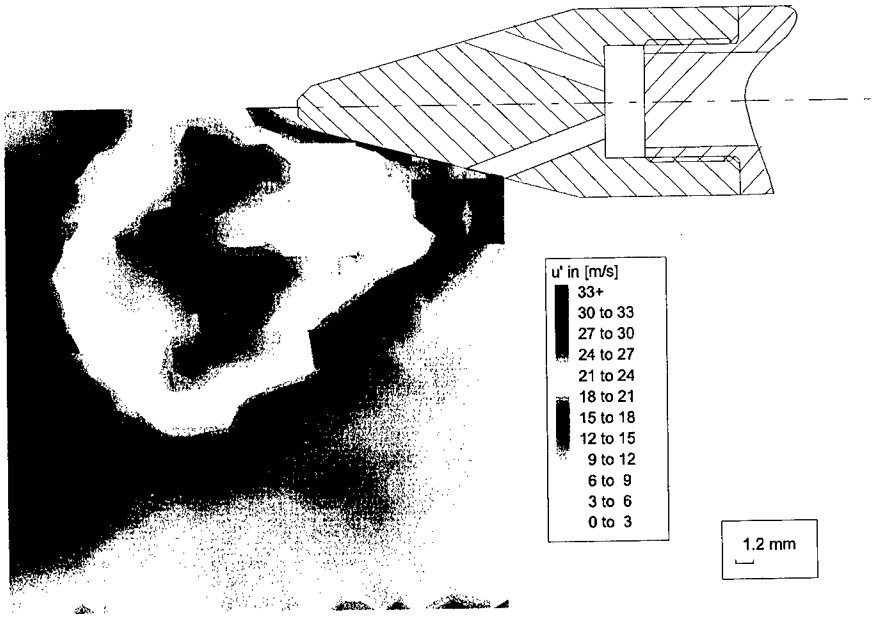

Abb. 4-7: Standardabweichung der axialen Geschwindigkeit aus den PIV-Messungen bestimmen das Turbulenzprofil

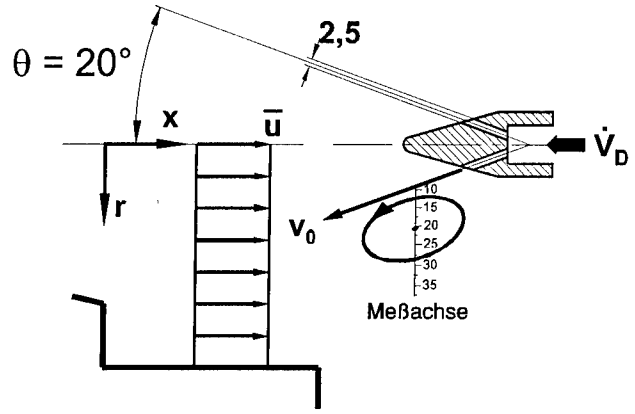

Abb. 4-8: Meßachse zur Betrachtung des Wirbelstärkeprofils

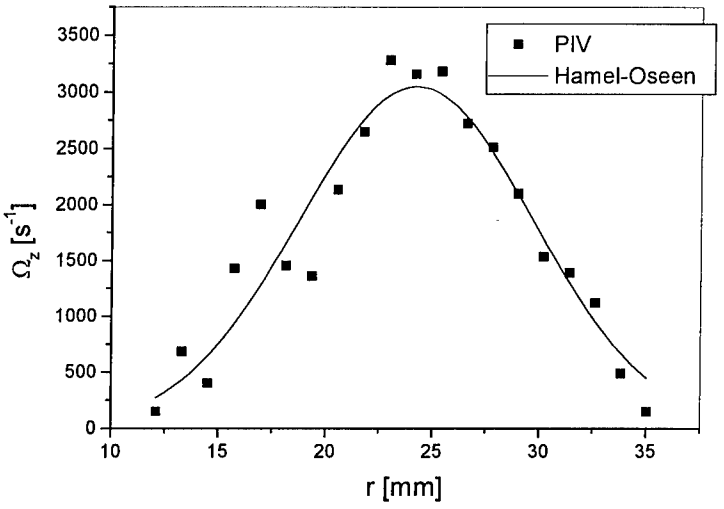

Abb. 4-9: Vergleich des aus 50 PIV-Auswertungen gemittelten Profils mit dem Oseen'schen Wirbelmodell in einem Achsenabstand von 13mm zum Ausgang der Gegenstromdüse.

5 Diskussion der Meßergebnisse

Die Momentaufnahmen von PIV beinhalten Informationen über den momentanen Strömungszustand, so daß prinzipiell Abweichungen von den gemittelten Geschwindigkeitswerten aus den LDV-Messungen auftreten. Erst eine Mittelung von mehreren Geschwindigkeitsfeldern aus den PIV-Messungen ermöglicht einen quantitativen Vergleich mit der LDV-Methode. Hinsichtlich dem Ablenkverhalten und der Eindringtiefe der Ge-

genströmung entsprechen die gemittelten Auswerteergebnisse von PIV den mittleren Strömungsprofilen aus den LDV-Messungen. Ein Vergleich der Turbulenzgradverläufe von Abb. 4-7 mit den Werten aus dem LDV-Verfahren bestätigen die Richtigkeit der PIV-Messungen.

Beim Ausströmen von Gas aus der Öffnung der Gegenstromzuführung entsteht infolge des im Vergleich zur Gegenstromdüse sehr großen Brennkammerquerschnitts eine freistrahlähnliche Gegenströmung, die bereits nach einer kurzen Lauflänge ein voll ausgebildetes turbulentes Profil besitzt. Die erhöhte Turbulenz in der Gegenströmung (vgl. Abb. 4-7) resultiert wiederum aus den instationären Wirbeln, die in den Scherschichten zwischen Haupt- und Gegenströmung entstehen. Diese Verwirbelungen verursachen einen turbulenten Austausch von Impuls, Energie und Masse über den gesamten Querschnitt des Gegenstroms.

Die instationären Verwirbelungen von hoher Wirbelstärke konzentrieren sich mit dem entsprechenden Drehsinn zu jedem Zeitpunkt zu beiden Seiten der Gegenströmung (vgl. Abb. 4-4) und bilden dadurch eine mehr oder weniger stark ausgeprägte Doppelscherschicht. Aufgrund dieser turbulenter Schubspannung verändern sich die Bewegungen von Haupt- und Gegenströmung. Der im Bezug zur Hauptströmungsrichtung schräge Einlaß der Gegenstromdüse gibt im Mittel den parabelförmigen Verlauf der Gegenströmung vor. Dies beeinflußt wiederum die Verwirbelungen derart, daß die linksdrehenden Wirbel im Durchschnitt höhere Rotationsbetragswerte besitzen. Bei der Bestimmung eines durchschnittlichen Strömungsfeldes aus mehreren momentanen Strömungsfeldern mitteln sich die turbulenten Schwankungen aus. Übrig bleiben die regulären Bewegungen von Haupt- und Gegenströmung, aus deren Überlagerung ein stationärer linksdrehender Gegenstromwirbel hervorgeht (vgl. Abb. 4-5). Aus diesem Grund läßt sich das gemessene Wirbelstärkeprofil in Abb. 4-9 gut mit dem Hamel-Oseen-Modell annähern, obwohl dieses Modell lediglich die Ausbreitung von kreiszylindrischen Wirbeln in laminaren Strömungen beschreibt. Diese Anschauung entspricht der „Reynold'schen Beschreibung turbulenter Strömungen" /12/.

6 Zusammenfassung

In dieser Arbeit wurde das PIV-System zur Untersuchung von Strömungen im Inneren der Brennkammer ausgerichtet. Die Brennkammer befand sich dabei im isothermen Betriebszustand. Hinsichtlich der optischen Zugänglichkeit gab es jedoch zwei Schwierigkeiten zu überwinden:

Zum einen verdeckte die Rohraußenwand den größten Teil des Beobachtungsfeldes im Inneren der Brennkammer. Die Kamera zeichnete deshalb abweichend zum Lot der Meßebene die Strömungen auf. Um die Objektebene innerhalb der Schärfetiefe zu halten, befand sich die CCD-Kamera in einer Scheimpflug-Anordnung. Der Abbildungsmaßstab war bei diesen Aufnahmen nicht mehr konstant, weshalb die Bilder mittels Bildverarbeitung nachträglich entzerrt wurden. Die Ermittlung der Parameter zur Bildentzerrung erfolgte anhand von Rasteraufnahmen.

Zum anderen bestand die Schwierigkeit darin, die Fenster der zwei optischen Zugänge von Streupartikeln und anderen Staubteilchen freizuhalten. Die Erzeugung einer schlei-

chenden Spülluft verminderte diese Ablagerung und steigerte dadurch erheblich die Qualität der Aufnahmen.

Wie aus Abb. 4-5 - Abb. 4-7 ersichtlich ist, charakterisieren die gemittelten Strömungszustandswerte den Durchmischungsbereich zwischen Haupt- und Gegenströmung. Als Ergänzung dazu liefert der momentane Strömungszustand die Information über den augenblicklichen Vermischungsvorgang. In unserem Fall ist dieser Vorgang durch eine Doppelscherschicht (vgl. Abb. 4-4) geprägt.

Letztendlich liefern die Meßergebnisse als Anfangs- und Validierungswerte einen wertvollen Beitrag für den verbesserten Einsatz bestehender Turbulenzmodelle, die für eine systematischen Optimierung der Brennkammergeometrie unerläßlich sind.

7 Literatur

/1/ Brock A., Deimling L.: *Zweifarben-PIV zur Strömungsvisualisierung in Verbrennungszonen*, Combustion and Detonation, 28th Int. Ann. Conf. of ICT, 1997

/2/ Brock, A.: *Bestimmung der Wirbelstärke aus der Kreuzkorrelation*, Lasermethoden in der Strömungsmeßtechnik (6. Fachtagung), 1998

/3/ Brock A., Deimling L.: *Direkte Kreuzkorrelation zur hochauflösenden PIV-Auswertung von Wirbelstrukturen*, Energetic Materials, 30th Int. Ann. Conf. of ICT, 1999

/4/ Backhaus J. M.: *Aufbau und Inbetriebnahme einer luftatmenden Versuchsbrennkammer und Vermessung der Strömungsverhältnisse im unbefeuerten und befeuerten Zustand*, Diplomarbeit Karlsruhe, FB Chemieingenieur, ICT-Eigenverlag, 1997

/5/ Liehmann W.: *Combustion of Boron-based Slurries Ramburner*, Combustion and Reaction Kinetics, 22. Int. Ann. Conf. of ICT, 1991

/6/ Liehmann W.: *Entwicklung einer Versuchsanlage zur Simulation von Luftströmungen für den transsonischen Bereich*, Bericht 6/92, ICT-Eigenverlag, 1992

/7/ Zeyen C.: *Geschwindigkeitsmessungen an einer eingeschlossenen konzentrischen Flamme mit Hilfe der Laser-Doppler-Anemometry*, Studienarbeit, Lehrstuhl für Feuerungstechnik, Universität Karlsruhe, 1982

/8/ Förter-Barth U. et al: *Verfahren der Partikelmeßtechnik - Ein Überblick*, ICT-Eigenverlag, 1998

/9/ Löffler F., Raasch J.: *Grundlagen der Mechanischen Verfahrenstechnik*, Vieweg, 1992

/10/ Backhaus J., Brock A., Deimling L.: *LDV-Vermessung reaktiver Strömungsfelder in einer Brennkammer*, Combustion and Detonation, 29th Int. Ann. Conf. of ICT, 1998

/11/ Deimling L.: *Aufbau eines Doppelpulslasers hoher Leistung als Lichtquelle der Particle-Image-Velocimetry*, ICT-Bericht 9/93, ICT-Eigenverlag, 1993

/12/ Rotta J.: *Turbulente Strömungen*, Teubner, Stuttgart, 1972

Strahlungsbeeinflussung der Anzündung und Verbrennung von festen Treibstoffen

N. Eisenreich, W. Ehrhardt, S. Kelzenberg, A. Koleczko, H. Schmid
Fraunhofer-Institut für Chemische Technologie, ICT
Joseph-von-Fraunhofer Str.7, D-76327 Pfinztal

Kurzfassung

Anzündung und Verbrennung fester Treibmittel kann durch Strahlung intensiv beeinflußt werden. Die Strahlung aus der eigenen Flamme und oder aus konventionellen pyrotechnischen Mitteln reicht jedoch nicht zu entscheidenden Veränderungen. Um deutliche Effekte zu erzielen, werden intensive Emissionsquellen wie Plasmen benötigt.

Die vorgestellte Arbeit beschreibt einige grundlegende Vorgänge der Wirkung von Strahlung und sehr heißen Gase auf energetische Materialien. Es wird experimentell und theoretisch untersucht, wie inerte und reaktive Festkörper auf entsprechende Energieübertragung reagieren. Unter vereinfachenden Annahmen werden Anzündverzugszeiten und Abbrandgeschwindigkeiten berechnet, sowie das dynamische Verhalten von Temperatur- und Konzentrationsprofilen untersucht. Die Folgerungen werden mit Ergebnissen aus Experimenten mit transparenten und nicht transparenten Treibstoffen verglichen und diskutiert. Die gezielte Anwendung der Effekte erfolgt im Hinblick auf Strahlungsfragmentierung durch Plasma-Emission.

1 Einleitung

Beschreibung des Abbrandes über empirische Gesetze basiert im wesentlichen auf dem Vielle'schen Gesetz: $\mathbf{r} = \mathbf{A} \cdot \mathbf{p}^{\mathbf{n}}$.
Neue Treibladungskonzepte erfordern neue Abbrandmodelle. Beispiele sind:

- Poröse, geschäumte Pulver: Hot Spots
- Temperaturunabhängige Pulver: Abhängigkeit von Anfangstemperatur
- ETC-Anzündung, -Verbrennung /1-9/: Strahlungswirkung, Hot Spots

Im folgenden wird der Einfluß der Strahlung, insbesondere Plasmastrahlung auf die Abbrand von festen Rohrwaffentreibmittel untersucht.

2 Physikalisch-chemische Modelle

Folgende Punkte sollten für die kondensierte Phase der Verbrennung energetischer Materialien berücksichtigt werden:

- Wärmeleitung mit Phasenumwandlungen
- Zersetzungskinetik

- Strahlungsausbreitung und Absorption

In der Gasphase und in der Flamme sollten berücksichtigt werden
- Wärme- und Stofftransport
- Reaktionskinetik entweder über Elementarreaktionen oder über reduzierte Mechanismen
- Molekülstrahlung und Strahlungstransport

Vereinfacht zeigt Bild 1 die Grundlage des Verständnisses der Abbrandphänomene.

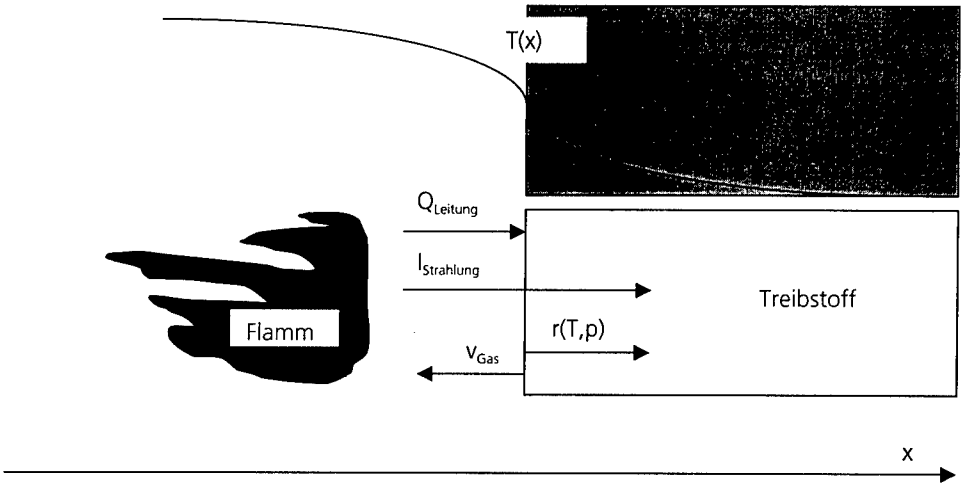

Bild 1: Vereinfachte Darstellung der Verbrennung eines Festtreibstoffes

3 Wärmeleitung im Feststoff

Wärmeleitungsgleichung im Feststoff lautet wie folgt (siehe im Detail /10,11/):

$$\rho c_p \frac{\partial T}{\partial t} - \lambda \frac{\partial^2 T}{\partial x^2} = \dot{Q}[x,t]$$

Die Lösung mittels Green'scher Funktion erlaubt eine Berechnung von Temperaturprofilen, die für verschiedene Wärmequellen flexibel handhabbar ist. Für den einfachen Fall einer zeitlich konstanten Energieübertragung von außen (Anzündung) läßt sich analytisch das Temperaturprofil berechnen (Bild 2):

$$T[x,t] = \dot{Q}_R \cdot \left(2 \cdot \sqrt{\frac{t}{\pi \lambda \rho c_p}} \cdot e^{-\frac{\rho c_p x^2}{4\lambda t}} - \frac{x}{\lambda} \cdot \mathrm{Erfc}\left[x \cdot \sqrt{\frac{\rho c_p}{4\lambda t}} \right] \right)$$

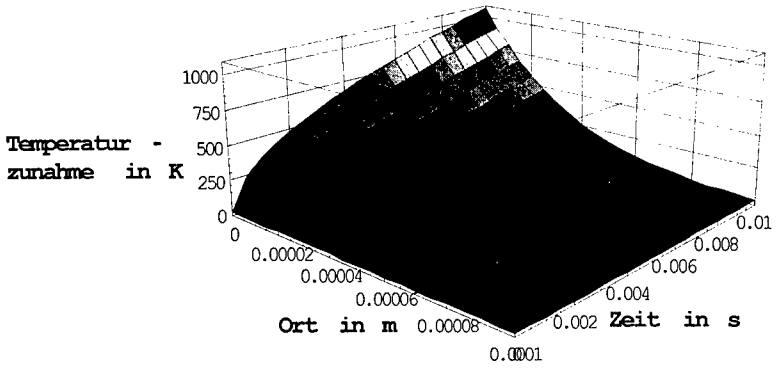

Bild 2: Temperaturverlauf im Festkörper bei konstanter Energieübertragung auf die Oberfläche durch Leitung

Der Temperaturverlauf an der Oberfläche hat folgende Gestalt:

$$T[0,t] = 2\dot{Q}_R \sqrt{\frac{t}{\pi\lambda\rho c_p}}$$

Häufig beansprucht die Zeit zum Aufheizen der Oberfläche auf eine bestimmte Temperatur durch externe Quellen, bei der Feststoff- oder/und Gasphasenreaktionen einsetzen den wesentlichsten Teil der Anzündverzugszeit. Deshalb ist in einfachster Näherung die Anzündverzugszeit durch folgende Formel gegeben:

$$t_{ign} \approx \frac{\pi\lambda\rho\, c_p (T_p - T_0)^2}{4\dot{Q}_R^2}$$

Der Energieübertrag durch Strahlung wird durch folgenden Quellterm beschrieben:

$$\dot{Q}[x,t] = \dot{Q}_R \cdot b \cdot e^{-bx}$$

Die Lösung ist in Bild 3 dargestellt:

$$T[x,t] = \frac{\dot{Q}_R}{2b\lambda}\left(e^{b\left(\frac{b\lambda t}{\rho c_p} - x\right)} \left(\operatorname{Erfc}\left[\sqrt{\frac{\lambda t}{\rho c_p}}\, b - \frac{x}{2}\sqrt{\frac{\rho c_p}{\lambda t}} \right] \right) - 2bx \cdot \operatorname{Erfc}\left[\frac{x}{2}\sqrt{\frac{\rho c_p}{\lambda t}} \right] + e^{b\left(\frac{b\lambda t}{\rho c_p} + x\right)} \left(\operatorname{Erfc}\left[\sqrt{\frac{\lambda t}{\rho c_p}}\, b + \frac{x}{2}\sqrt{\frac{\rho c_p}{\lambda t}} \right] \right) + 4b\sqrt{\frac{\lambda t}{\pi\rho c_p}}\, e^{-\frac{\rho c_p x^2}{4\lambda t}} - 2e^{-bx} \right)$$

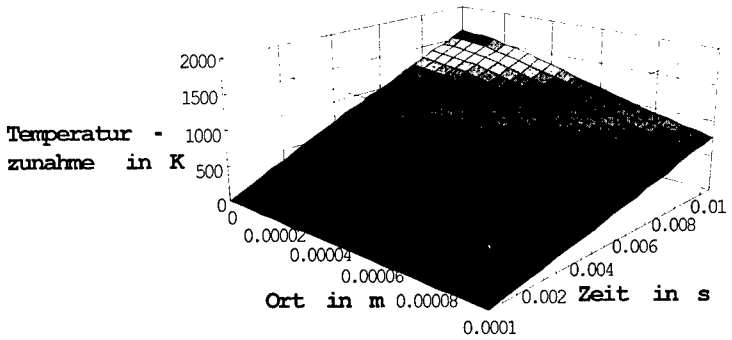

Bild 3: Temperaturprofil bei tief eindringender Strahlung

Stationärer Abbrand

Nach einer Anfangsphase der Feststoffaufheizung durch extern zugeführte oder intern durch Reaktion entstandene Energie stellt sich ein stationärer Reaktionsfortschritt ein, wenn gewisse Bedingungen erfüllt sind. D.h., die Reaktionsfront bewegt sich als stationäres Temperaturprofil mit einer konstanten Geschwindigkeit r in den Feststoff hinein. Wegen der konstanten Geschwindigkeit kann das Koordinatensystem so transformiert werden, daß das Temperaturprofil ruht. Es ergibt sich folgende gewöhnliche Differentialgleichung:

$$\rho c_p r \frac{dT}{dx} + \lambda \frac{d^2T}{dx^2} = -\dot{Q}[x] + r\sum_i q_i \frac{dc_i}{dx}$$

$$r = \frac{\dot{Q}_o + \dot{Q}_R}{\rho\left(c_p \cdot (T_s - T_\infty) + L - \sum_i q_i\right)}$$

Unter der Annahme, dass sich Q_0 entsprechend dem Veille'schen Gesetz verhält, kann man diese Gleichung auch schreiben als:

$$r = \frac{A \cdot p^n + \dot{Q}_R}{\rho\left(c_p \cdot (T_s - T_\infty) + L - \sum_i q_i\right)}$$

Diese Annahme wird gestützt durch Ergebnisse aus Ref. /10/.

Eine realistischere Berechnung mit Einbeziehung der Gasphase mit Stofftransport und Reaktionskinetik liefert im wesentlichen eine Bestätigung der vereinfachten Modelle, bringt aber auch dynamische Effekte (berechnet nach /12,13/). Diese sind in den Bildern 4 und 5 dargestellt, in denen der Einfluß eines konstanten aber in 2 Stufen veränderten Wärmeübertrages auf die Anzündung und die Verbrennung zu erkennen ist.

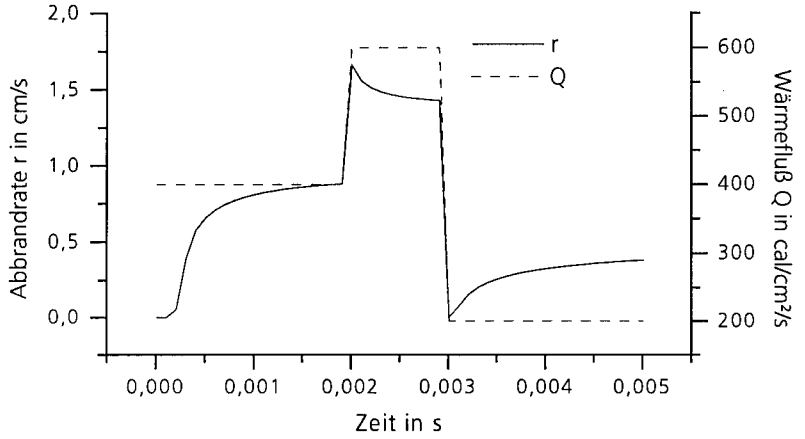

Bild 4: Instationäre Abbrandrate bei externer, stufenförmiger Energiebeaufschlagung an der Oberfläche, erhalten durch numerische Lösung

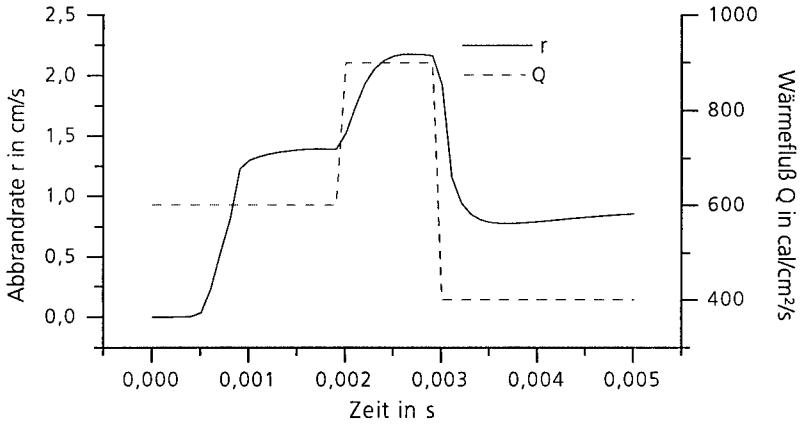

Bild 5: Instationäre Abbrandrate bei externe stufenförmiger, tief eindringender Strahlungsbeaufschlagung an der Oberfläche, erhalten durch numerische Lösung

Hot Spots

Wenn Strahlung an Schichten oder Zentren absorbiert wird, entstehen Hot Spots im Treibstoff, die entweder zu Poren oder direkt zur Anzündung führen. Bei absorbierenden Schichten der Dicke x_d würde folgende Quellfunktion entstehen:

$$\dot{Q}[x,t] = \sum_{i=1}^{I} \dot{Q}_R \cdot b \cdot e^{-b \cdot i \cdot d} \cdot \sqrt{\frac{\rho \cdot c_p}{2\pi\lambda t}} \cdot e^{\frac{\rho \cdot c_p \cdot (x - i \cdot x_d)^2}{2\lambda t}}$$

In den Bildern 6 und 7 ist die Lösung der 3-dimensionalen Wärmeleitungsgleichung mit einer 0.ter Ordnungsreaktion bei verschiedenen Zeiten zu sehen (siehe /14-16/).

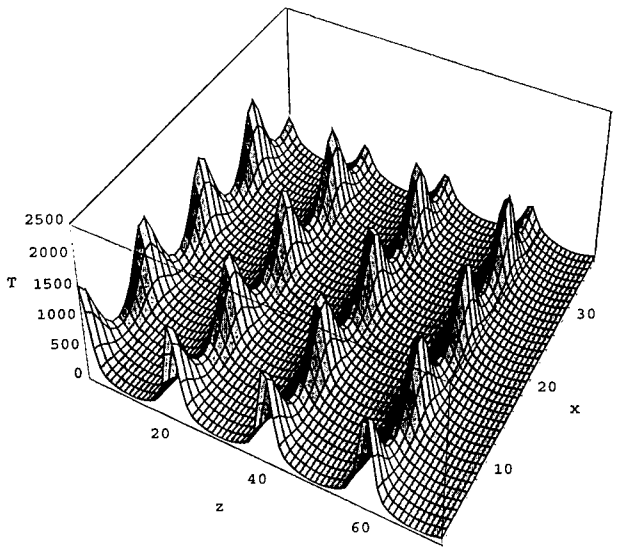

Bild 6: Lösung der 3-d Wärmeleitungsgleichung mit Reaktion bei Energieabsorption an regelmäßig angeordneten Zentren zur schnelleren Umsetzung.

Erwartungsgemäß wird der Treibstoffblock deutlich schneller umgesetzt als bei Anzündung nur an den Außenflächen.

4 Untersuchung der Plasma/Pulver-Wechselwirkung

Zur Untersuchung der Plasma/Pulver-Wechselwirkung stand eine 100 kJ EVA zur Verfügung, die in Kombination mit einer offenen Plasmaapparatur und der Plasma-Bombe

(V=100 ml) betrieben wurde (Bild 8). Variiert wurden die Art der Anzündung, sowie Größe und Pulsverlauf der elektrischen Energie.

Als Proben wurden transparente NC-Pulver in Form von Platten (h = 3 mm) oder Zylindern vorgelegt. Die Platten waren in der ETC-Bombe zylindrisch angeordnet, so daß reproduzierbare Bedingungen für Abstand und Kontaktfläche zum Lichtbogen gegeben waren.

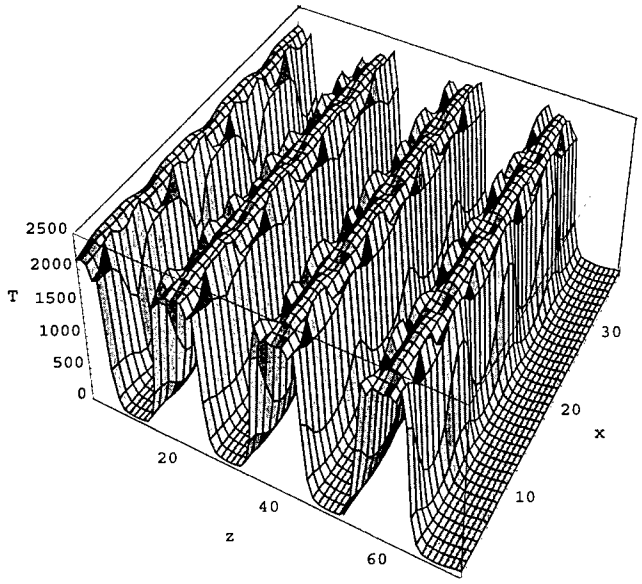

Bild 7: Lösung der 3-d Wärmeleitungsgleichung mit Reaktion bei Energieabsorption an regelmäßig angeordneten Zentren (Weiterentwicklung von Bild 6).

Der theoretisch zu erwartende Effekt einer Verbesserung der Anzündung mit Verkürzung der Anzündverzugszeit konnte für NC-Pulver experimentell nachgewiesen werden.

Ferner wurde für transparente NC-Pulver eine Vergrößerung der Umsetzungsgeschwindigkeit in Abhängigkeit von der Menge der elektrischen Energie erzielt. Außer den Effekten der Energiemenge und des Energietransports durch Strahlung sind Anzündung und Fragmentierung in der Tiefe des Pulvers bestimmend.

Zur detaillierten Untersuchung der Anzündphänomene wurden Experimente in der 100 ml Plasma-Bombe bei gleicher Ladedichte von 0,117g/cm^3 (T=293K) durchgeführt. Variiert

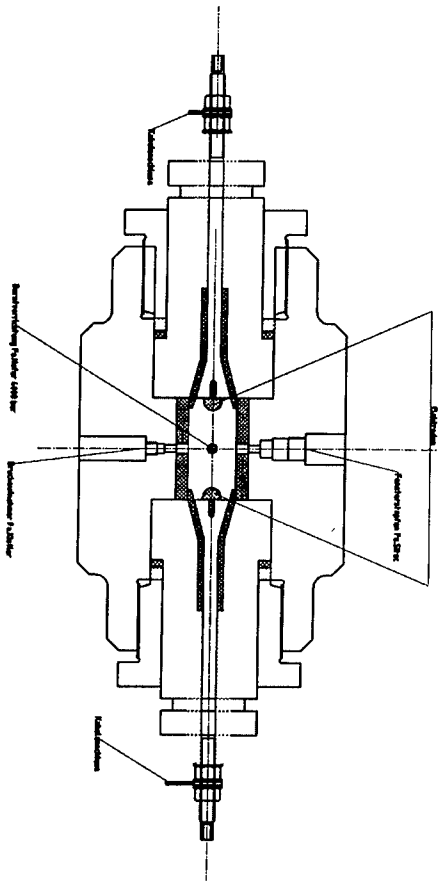

Bild 8:Schematische Darstellung der Plasma-Bombe (V = 100 ml) mit der gewählten Elektrodenform und Anordnung.

wurde die Art der Anzündung (konventionell, Plasma) in Kombination mit graphitierten und transparenten JA2-Proben. Die Ergebnisse sind in Bild 9 dargestellt. Erkennbar ist der flache Verlauf der Druck/Zeit-Kurve bei konventioneller Anzündung einer transparenten JA2-Platte mit B/KNO_3 (schwarz). Ein steilerer Verlauf wird bei Plasma-Anzündung einer graphitierten JA2-Probe erhalten (rot). Der steilste Druckanstieg zeigt sich bei Verwendung der Plasma-Anzündung in Kombination mit transparenten NC-Proben (grün).

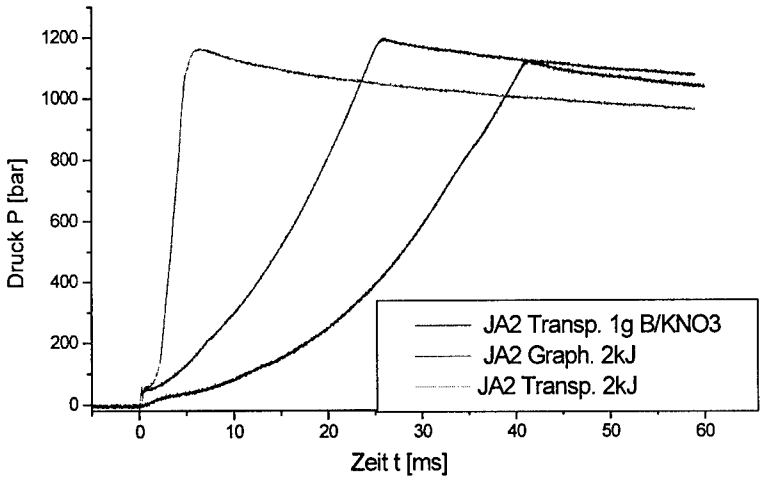

Bild 9: Druckbombenexperimente mit konventioneller und Plasmaanzündung

Diese Ergebnisse werden folgendermaßen interpretiert:
Bei Verwendung von B/KNO_3 liegt eine konventionelle Partikelanzündung vor. Die Plasmaanzündung der graphitierten NC-Probe liefert eine größere Energiemenge und einen höherer Energiefluß auf die Pulveroberfläche und schnellere Anzündung. Transparente Proben zeigen zusätzlich Energieabsorption, Anzündung und Fragmentierung im Innern.

Einen weiteren Nutzen bei der Verwendung von Plasmen liegt in der Initiierung schwer anzündbarer Pulver. Konventionell war es schwierig, ausgewählte Nitraminpulver unter den gewählten Randbedingungen reproduzierbar anzuzünden (Bild 10). Mit Hilfe der Plasmaenergie war in jedem Fall eine effektive und reproduzierbare Anzündung mit reduzierter Anzündverzugszeit möglich.

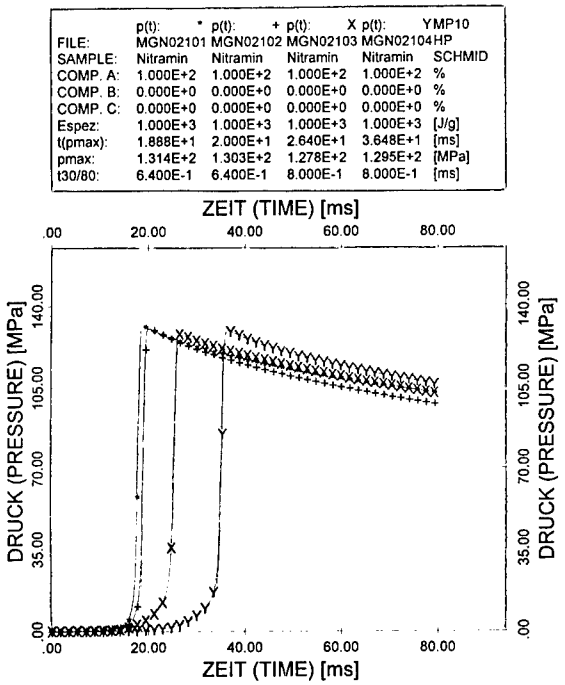

Bild 10: Vergleich der in der ballistischen Bombe (Volumen: 100 ml) experimentell ermittelten Druck/Zeit-Diagramme des Nitraminsystems MGN02000.100, das als Pulver (Symbole: *, +) und als zylindrische Formkörper [d = 5 mm, h = 5 mm] (Symbole: X, Y) vorgelegt wurde. Eingesetzt wurde die Zündpille T7 in Kombination mit 0.75 g B/KNO_3. Es ist erkennbar, daß bei konventioneller Anzündung sich eine reproduzierbare Initiierung schwierig gestaltet. Bei Anwendung der Plasmazündung wird die Reproduzierbarkeit verbessert und die Anzündverzugszeit verkleinert.

Gemäß theoretischer Überlegungen ergibt sich ein Zusammenhang zwischen eingekoppelter Energiemenge und der Umsetzungsrate. Dies wurde in der Plasma-Bombe experimentell überprüft, in dem der Reaktionsverlauf transparenter JA2-Pulver als Funktion abgestufter elektrischer Energiemengen verfolgt wurde. Die Ergebnisse sind in BILD 11 dargestellt und bestätigen den postulierten Zusammenhang. Damit werden Möglichkeiten zur Abbrandsteuerung eröffnet.

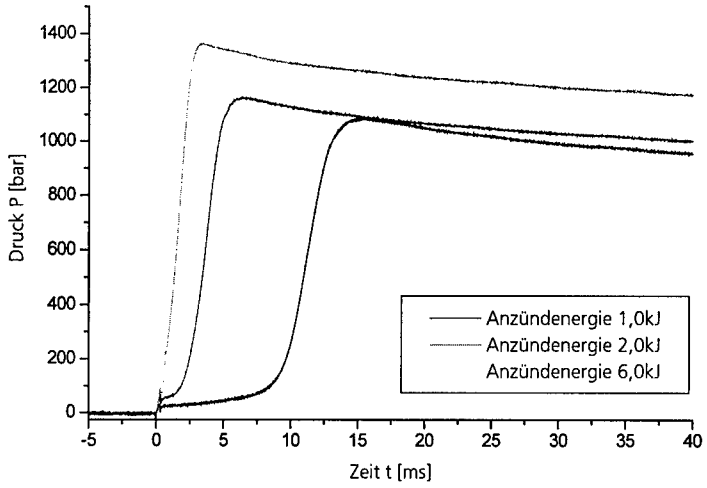

Bild 11: Experimentell in der Plasmabombe (V = 100 ml) ermittelte Druck/Zeit-Diagramme für transparente JA2-Platten (Ladedichte 0,117g/cm^3, Temperatur 293K).
E_{el} = 1 kJ (schwarz):
Längste Anzündverzugszeit, langsamste Umsetzungsgeschwindigkeit.
E_{el} = 2 kJ (rot):
Deutlich verkürzte Anzündverzugszeit, beschleunigte Umsetzungsgeschwindigkeit.
E_{el} = 6 kJ (grün):
Minimale Anzündverzugszeit, höchste Umsetzungsgeschwindigkeit.

Zur detaillierten Charakterisierung des Umsetzungsverhaltens auf Grund der Fragmentierung wurden entsprechende Proben in der optischen Bombe (siehe /17,18/) untersucht. Mit Hilfe der Pulsar-Methode (/19/, Bildauswertung gemäß BILD 12) wurde die Abbrandgeschwindigkeit als Funktion des Drucks für mit Plasma beaufschlagte und unbeaufschlagte JA2-Platten gemessen. Die Ergebnisse sind in Bild 13 zusammengestellt. Graphitierte und ungraphitierte Proben zeigen unter diesen Bedingungen kaum Unterschiede. Eine signifikante Vergrößerung der Abbrandgeschwindigkeit ergibt sich bei den vorbehandelten Proben, sofern die Poren senkrecht zur Flammenfront angeordnet sind. In diesem Fall wird das Eindringen der Reaktionsfront in die Poren begünstigt.

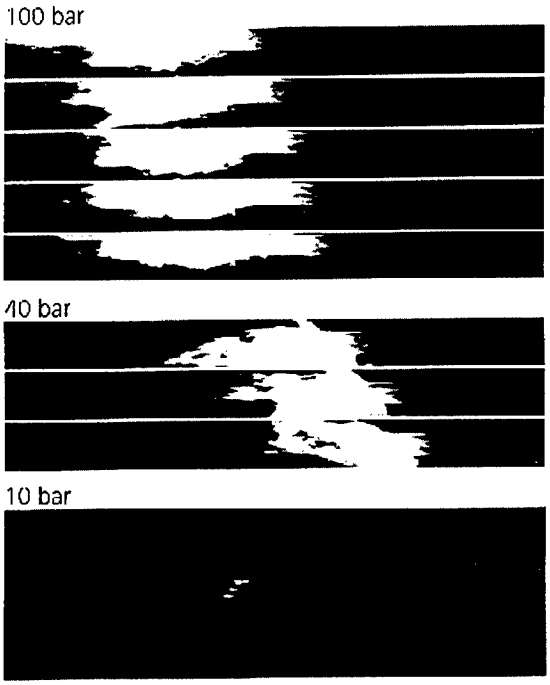

Bild 12: Aufnahmen der Reaktionsfront von mit Plasma beaufschlagten JA2-Proben in der optischen Bombe als Funktion des Drucks. Bei einer Porenstruktur senkrecht zur Flammenfront ergibt sich außer der Erhöhung der scheinbaren Abbrandgeschwindigkeit eine Verbreiterung der Reaktionszone.

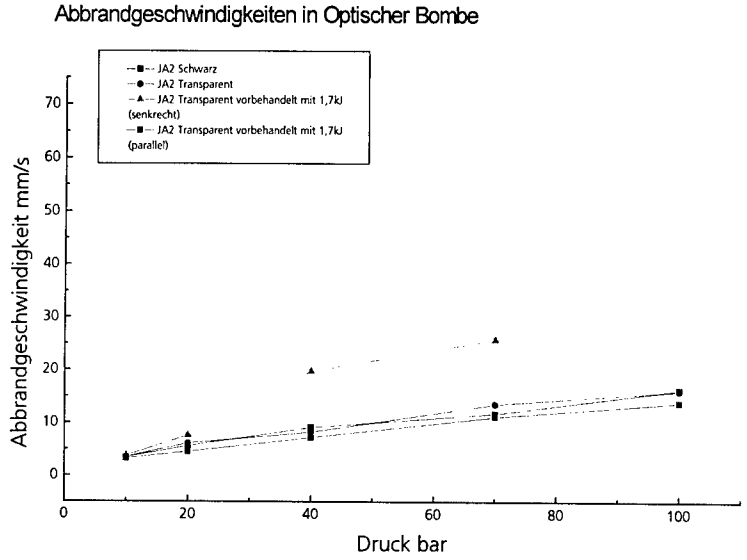

Bild 13: Experimentell in der optischen Bombe ermittelte Daten für die Abbrandgeschwindigkeit als Funktion des Drucks für mit Plasma beaufschlagte und unbeaufschlagte JA2-Platten.

5 Untersuchungen zum Absorptionsverhalten ausgewählter Pulver und Komponenten

Die Transmission der eingesetzten JA2-Platten unterschiedlicher Wandstärke wurde im Bereich von 200 bis 1100 nm spektroskopisch untersucht. Die Ergebnisse sind in Bild 14 dargestellt. Im UV-Bereich bis 390 nm beträgt die Transmission 0 %; die Strahlung wird vollständig absorbiert. Im VIS-Bereich zwischen 390 bis 770 nm steigt ab 450 nm die Transmission an. Eine weitere Zunahme der Transmission im IR-Bereich ab 770 nm bis zum Ende des Meßbereichs bei 1100 nm ist deutlich erkennbar. Bei transparentem JA2 wird somit nur der VIS/IR-Strahlungsanteil zur Energieeinkopplung in der Tiefe der Probe genutzt. Eine Verringerung der Oberflächenrauhigkeit bewirkt eine Reduktion von Streueffekten und führt zu einer Erhöhung der Transmission (rote Kurve). Hier wurde die JA2 Platte mit Aceton angelöst und zwischen zwei Glasscheiben einige Wochen gelagert. Daß es sich tatsächlich um den VIS/IR-Strahlungsanteil handelt, der die Tiefenwirkung in den JA2-Proben auslöst wurde in weiteren Experimenten nachgewiesen, in denen ein Plexiglasfilter zum Einsatz kam (Bild 15 und Bild 16).

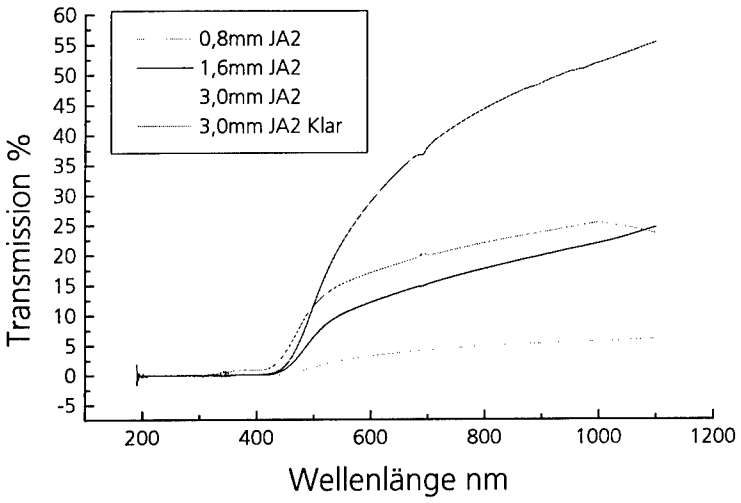

Bild 14: Transmissionsspektren transparenter JA2-Platten; Hersteller: WNC.

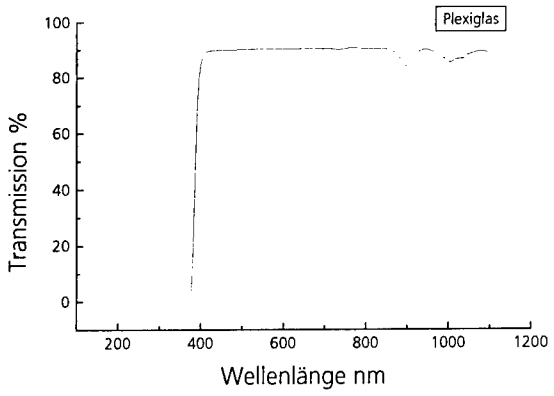

Bild 15: Transmissionsspektrum einer 10mm starken Plexiglasplatte

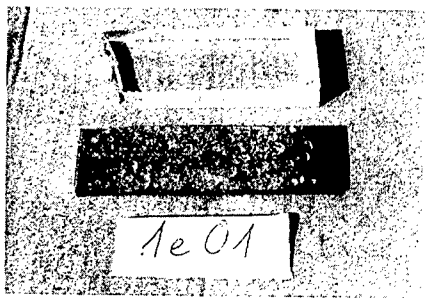

Bild 16: Schuppenbildung der transparenten JA2-Platte, die zur Hälfte mit einem Plexiglasfilter abgedeckt wurde. Die Schuppenstruktur ist vergleichbar, was dahingehend interpretiert wird, daß nur der VIS/IR-Strahlungsanteil im Innern wechselwirkt.

Auch die Schwadenabsorption kann den Strahlungstransport wesentlich behindern. Unter diesem Aspekt sind N_2-Anteile im Treibgas wünschenswert, die durch N-reiche Brennstoffkomponenten, wie Guanidinium-5,5'-azotetrazolat erzeugt werden können.

Ein weiterer Schwerpunkt bestand darin, bei transparenten JA2-Platten Fragmentierungseffekte als Funktion struktureller Aspekte der Proben und der eingesetzten elektrischen Energiemenge zu untersuchen. Dazu wurde eine offene Plasmaapparatur eingesetzt, die bezüglich der Geometrie dem Versuchsaufbau der Plasmabombe entsprach . Für JA2-Hohlzylinder ergab sich stets eine Fragmentierung längs der Vorzugsrichtung der NC-Fasern (Bild 17). Die Vergrößerung der elektrischen Energie führte zu einem feineren Raster kleinerer Schuppen (Bild 18). Dies deckt sich mit den Ergebnissen der Druckbombenexperimente (Bild 11).

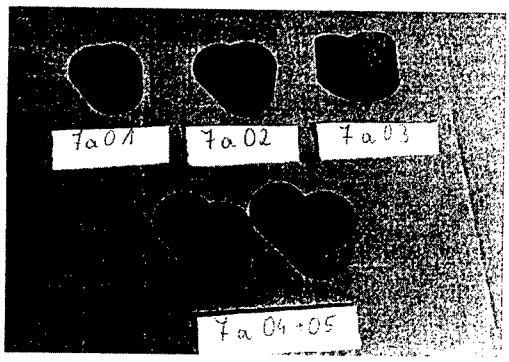

Bild 17: Darstellung der mit dem offenen Plasmaversuchsaufbau untersuchten JA2-Hohlzylinder.

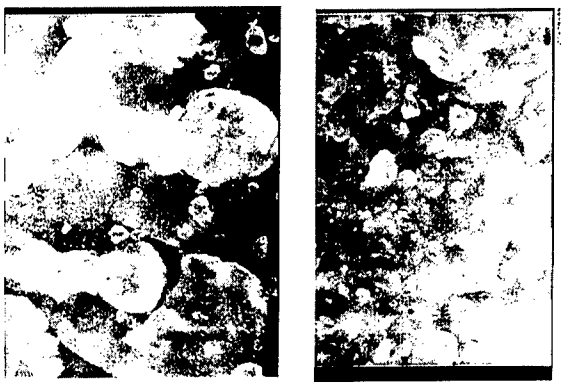

Bild 18: Lichtmikroskopische Aufnahme der Proben. Die mit höherer Energie beaufschlagte Probe zeigt vermehrt kleinere Schuppen. Links 0,8kJ Rechts 1,55kJ .

Mit Hilfe von REM wurde die Porenstruktur detaillierter untersucht. Als Nullprobe diente eine JA2-Platte, die mit 1.8 kJ Plasmaenergie vorbehandelt war (Bild 19). Die REM-Untersuchung nach Durchführung des Druckbombenexperiments mit Abbrandunterbrechung bei 20 MPa (Umsatz 59 %) brachte den Beweis, daß eine Reaktion auch im Innern der Poren stattgefunden hat, was an den vergrößerten und abgerundeten Poren erkennbar ist (Bild 20).

Bild 19: REM-Aufnahme (Vergrößerungsfaktor 66) einer mit 1.8 kJ Plasmaenergie vorbehandelten JA2-Platte, die Poren längs der Vorzugsorientierung der NC-Fasern aufweist.

Bild 20: REM-Aufnahme (Vergrößerung 66) einer mit 1.8 kJ Plasmaenergie vorbehandelten transparenten JA2-Platte nach Durchführung eines Druckbombenexperiments mit Abbrandunterbrechung bei 20 MPa.

6 Gezielte Strahlungsfragmentierung

Im Zuge der Entwicklung kompakter Ladungsaufbauten in Kombination mit Plasmaanzündung konnten in transparente Pulverplatten schwarze rußhaltige Schichten auf NC-Basis eingebracht werden (Bild 21). In Versuchen mit offenen Plasmalichtbögen konnten solche Pulverplatten an der schwarzen Schicht aufgesprengt werden. Der Mechanismus dieses Vorgangs kann so erklärt werden, daß die Strahlung durch die erste transparente Schicht durchdringt und diese je nach Energiemenge mehr oder weniger fragmentiert. Der Rest der Strahlung wird an der schwarzen Schicht vollständig absorbiert und in Wärme umgewandelt. Dies führt so zur Zersetzung der NC-Moleküle an der schwarzen Grenzschicht und zur Abtrennung der oberen Schicht. Anhand der Oberflächenstruktur der Proben im Bild 22 ist der Vorgang leicht nachvollziehbar.

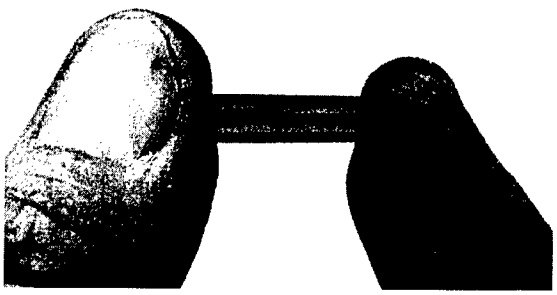

Bild 21: JA 2 Platten mit Rußhaltige Schicht auf NC Basis

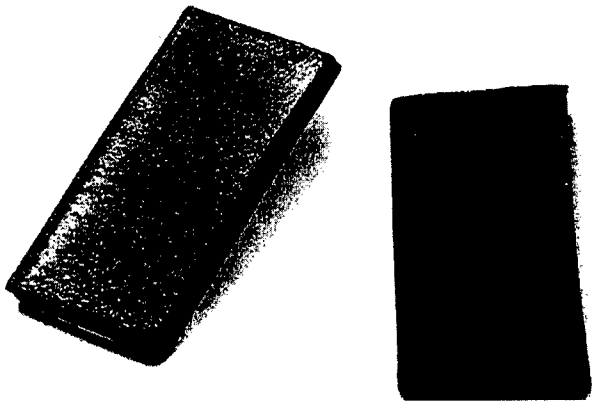

Bild 22: Transparente JA2 Platten mit rußhaltiger Schicht nach dem offenen Plasmaversuch. Deutlich sichtbar ist die Kraterbildung.

7 Literatur

(1) C. R. Woodley and S. Fuller, "Apparent Enhanced Burn Rates of Solid Propellants Due to Plasmas", *16th International Symposium on Ballistics*, San Francisco, CA, 23-28 September 1996, pp. 153-162.

(2) W. G. Proud. and N. K. Bourne, "The Electrothermal Enhancement of Propellant Burning by Plasma Injection", *Propellants, Explosives, Pyrotechnics. 22*, 212-217 (1997).

(3) H. K. Haak, A. M. Voronov, and Th. H. G. G. Weise, "The Interaction of Electrothermally Supplied Energy with Compact Solid Propellants", *9th EML Symposium*, Edinburgh Scotland, May 13-15, 1998.

(4) W. F. Oberle and G. P. Wren, "Radiative and Convective Heat Loss in Electrothermal-Chemical (ETC) Closed Chambers", *35th JANNAF Combustion Subcommittee Meeting*, Tucson, AZ, December 1998, Vol I, pp. 229-236.

(5) D. E. Kooker, "Burning Rate Deduced from ETC Closed-Chamber Experiments: Implications for Temperature Sensitivity of Gun Systems", *35th JANNAF Combustion Subcommittee Meeting*, Tucson, AZ, December 1998, Vol. II, , pp. 201-217.

(6) P. J. Kaste et al., ETC Plasma-Propellant Interactions, 29th *International Annual Conference of ICT, Karlsruhe*, Germany, P125, (1998)

(7) Birk, M. Del Guercio, A. Kinkennon, D. E. Kooker, and P. Kaste, "Interrupted-Burning Tests of Plasma-Ignited JA2 and M30 Grains in a Closed Chamber", *Propellants, Explosives, Pyrotechnics 25*, 3 (2000).

(8) A.Koleczko, W. Eckl, T. Rohe, "Untersuchungen zur Einkopplung elektrischer Energie in flüssige Energieträger und deren Verbrennungsprodukte" 27th *International Annual Conference of ICT, Karlsruhe*, Germany, P142, (1996)

(9) A. Voronov, A, Koleczko*, H. Haak**, Th. Weise, N. Eisenreich*,"Energy Criteria for Combustion control in a large caliber gun".

(10) N.Eisenreich, "*Vergleich theoretischer und experimenteller Untersuchungen über die Anfangstemperaturabhängigkeit von Festtreibstoffen*", ICT-Bericht 8/77, (1977), Fraunhofer-Institut für Chemische Technologie ICT, Pfinztal, Germany.

(11) W. Eckl, S. Kelzenberg, V. Weiser, and N. Eisenreich, "Einfache Modelle der Anzündung von Festreibstoffen", *29th Int. Annual Conference of ICT*, Karlsruhe, June 30 – July 3, 1998, Germany, pp. 154.

(12) V. E. Zarko, L. K. Gusachenko, and A. D. Rychkov, "Simulation of Combustion of Melting Energetic Materials" Defence Science Journal; 46, 425 - 433, (1996).

(13) L. K. Gusachenko, V. E. Zarko, and A. D. Rychkov, "Modeling of Gasification of Evaporated Energetic Materials under Irradiation" INTAS Workshop, Milan, July (1996).

(14) N. Eisenreich, "Successively Initiated Arrays of Hot Spot in a Reactive Medium"in: *BMVg-FBWT 98-1*, FIZBw, Bonn,(1998), *Proceedings: Physics of Explosives*, Berchtesgaden, (October 29th 1997).

(15) G. Langer, N. Eisenreich, "Entwicklung von Hotspots in energetischen Materialien", *29th International Annual Conference of ICT, Karlsruhe*, P157, (1998).

(16) G. Langer, N. Eisenreich, "Hot Spots in Energetic Materials", *Propellants, Explosives, Pyrotechnics*, 24 (1999) 113

(17) N. Eisenreich, "A Photographic Study of the Combustion Zones of Burning Double Base Propellant Strands", *Propellants and Explosives 5*, 141-146 (1978).

(18) N. Eisenreich, H. P. Kugler, and F. Sinn, "An Optical System for Measuring the Burning Rate of Propellant Strands", *Propellants, Explosives, Pyrotechnics 12*, 78-80 (1987).

(19) V. Weiser, N. Eisenreich, A. Bayer, M. Weindel, K. Menke, „Abbrandverhalten von ADN-Mischungen"; 28th International Annual Conference of ICT, 1997, Combustion and Detonation; Karlsruhe.

THE BURNING PROPERTY OF DOUBLE-BASE PROPELLANT BY USING THREE KINDS OF COMMON PLASTICIZER AND THE PROSPECT FOR THE NEW TYPE PLASTICIZER

Wang Jiang-Ning, Xu Yu, Wang Ning-Fei

XI'AN MODERN CHEMISTRY RESEARCH INSTUTE

P.O.BOX 18 XI'AN P.R.CHINA (710065)

ABSTRACT

Three kinds of formulation with different energy level that were studied the rule of burning property of three kinds of the plasticizer, which are DINA, DNT and DEP. The burning rate and plateau range is same as the formulation of containing DINA and DNT, and the burning rate of the formulation of containing DEP is higher than that of the formulation of containing DINA and DNT, and the plateau range of the formulation of containing DEP is wider than that of others. This mechanism is relation to the carbon which born in the burning surface. A wider plateau and energetic plasticizer from the point of view about enhancing energy is presented in this paper.

1. Introduction

DINA, DNT and DEP were the common plasticizer for DB and CMDB propellant, and it's self-property is different from each other that lead to the energetic and burning property is also different. It had being not discoved any reference for the different, and this paper had made a systematic study for them, and prospect a new type of plasticizer.

2.The Basic Properties of the Three Kinds of Plasticizer

Table 1.The Basic Properties of the Three Kind Plasticizer

Name	Code name	Structural formula	Molecular weight	Melting or solidifying point
N-Nitro-digydroxyethylamie diitrate	DINA	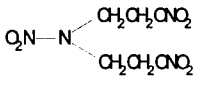	240.14	49.5~51.5□
Dinitorotluene	DNT	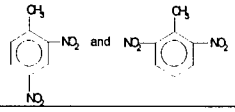	182.14	50~54□
Diethyl Phthalate	DEP	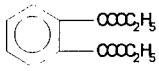	222.23	-40.5□

3.The Experimentation of Burning Property

3.1 Experimental Formulation and Sample Preparation

Table 2. Experimental Formulation, %

Code	DB binder	RDX	Vaseline	catalyst	Plasticizer
1	61.7	30	0.5	4.8	3.0
2	90.4	0	0.5	6.4	2.5
3	65.8	25	0.5	3.8	4.9

The process of sample preparation is absorbing, sooth rolling and screw extrusion, and the burning rate-pressure curve can be measured by standard constant pressure instrument.

3.2 Result of Burning Rate

3.2.1 The Burning Rate of □ Formulation

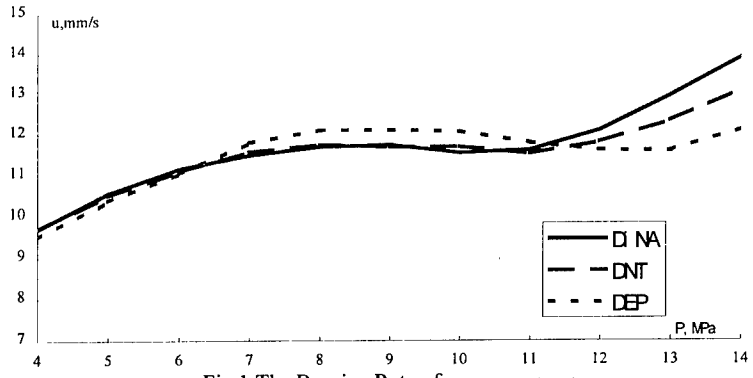

Fig.1 The Burning Rate of ¢ ñFormulation

From Fig.1 we could discoved the DINA's and DNT's super and plateau burning rate and plateau range is correspond to each other. But the DEP's plateau burning rate is higher than that

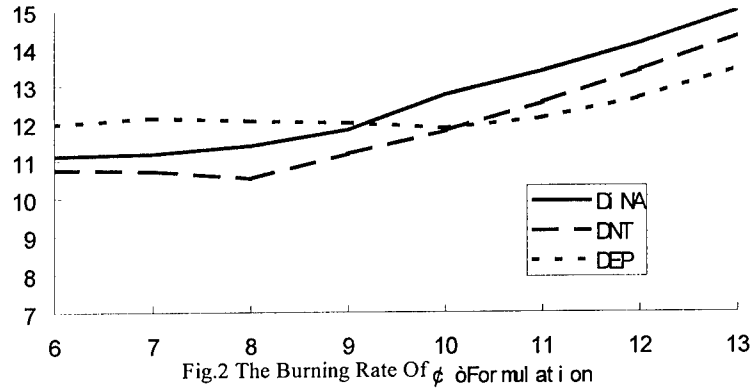

Fig.2 The Burning Rate Of ¢ òFormulation

of DINA and DNT, and the plateau range is wider than their.

3.2.2 The Burning Rate Of □ Formulate

From Fig.2, we could find DINA's plateau burning rate is slightly higher than that of DNT, and it's plateau is same as DNT's, but DNT's plateau range is showing a tendency to wide DINA's, and DEP's burning rate is higher than them, and the plateau range is wider than them.

3.2.3 THE BURNING RATE OF□ FARMULATION

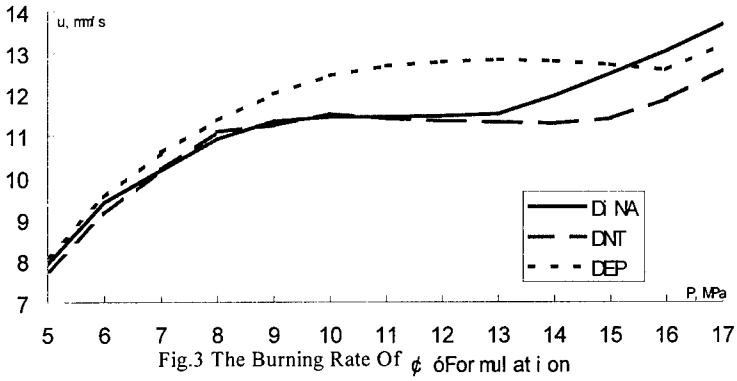

Fig.3 The Burning Rate Of ¢ óFor mul at i on

In this Fig., the DINA's super and plateau burning rate is same as DNT's, but the DNT's plateau range is slightly wider than DINA's, DEP's plateau burning rate is higher than their, and it's plateau range wider than their or moving to high pressure range.

4 CONCLUSION

4.1 The DEP's plateau burning rate is higher than that of DINA and DNT, but the DINA and DNT's plateau burning rate is almost same with each other.

4.2 The DEP's plateau range is wider than DINA and DNT's, or moving to high-pressure range. DINA's plateau range is almost same as DNT's, but the DNT's plateau range is showing a tendency to wide DINA's constantly in this study.

5 MECHANISM STUDY

It's well know that DINA and DNT's energy lever is higher than that of DEP, but the burning rate of DEP's formulation is high, this couldn't explain that according to the theory, which is the higher of the energy, the higher of the burning rate. But discussed from the Carbon-unit Theory, under the condition of equal weight of catalyst, the more the carbon that born in burning surface, the higher the burning rate is, and the plateau range will move to high pressure. It could discover that from the molecular structural of the three plasticizer in table 1, when it's

discomposed to molecule pieces of DINA, It couldn't easily born some carbon-carrier with a long carbon-chain, DNT is a mixture. It also could not easily born some carbon-carrier with a long carbon-chain. And the carbon just on DEP's benzene-circle easily formed a long chain carbon-carrier, this is advantageous to adsorbed of catalyst. Please see the reference about the production regular of carbon on burning-surface of DB and CMDB propellant.

6 PROSPECT

With the background for increasing energy lever of solid propellant, and the wide plateau range is still a technical index for the new type weapon, from this will produce a idea that retain the DEP's wide plateau range, and increase the DEP's energy, that is adding 1~2 –NO2 group to DEP's benzene-circle, this will form a new type plasticizer, $(O_2N)_{1-2}$ there is the intermediate to sell.

REFERENCE.

1. Wang Jiang-Ning, Carbon-unit Theory Hypothesis on Combustion Surface of Double Base Propellant (Physical Model I), 22nd International Annual Conference of ICT, July 2-July 5, 1991

2. Wang Jiang-Ning, Study and Calculate the Carbon Weight of Boring on Combustion Surface of DB and Nitro-amine Modified Propellant. (in published)

3. Catalog Handbook of Fine Chemicals, Aldrich Chemical Company, Inc. 1992-1993

The Influence of Composite Catalyst on Combustion of Al/HMX/CMDB Propellant

Lu.Shuanchang Xu Yu

Xi'an Morden Chemical Research Institute

Box 18 Xi'an china (710065)

Subject: Composite Catalyst. CMDB Propellant. Combustion

Here researched is the combustion law of lead stannate-TDI pyrolysis products. lead methylene-di-salicylate. lead tannate .lead phthalate. lead 2.4-dihydroxybenzoate. cupric pyromellitic. cupric phthalate and carbon black in Al/HMX/CMDB propellant. By optimization composite catalyst which consists lead stannate-TDI pyrolysis products. cupric phthalate and carbon black can improve the combustion of Al/HMX/CMDB propellant. The pressure exponent of burring rate is lowered from 0.6 to 0.24,and the temperature sensitivity of burring rate is reduced. This is an effective method to lower the pressure exponent of burring rate of Al/HMX/CMDB propellant.

ABBRANDMODELLE FÜR ROHRWAFFENTREIBMITTEL: ABBRANDVERHALTEN DES ROHRWAFFENTREIBMITTELS JA2 UND ABBRANDPHÄNOMENE PORÖSER LADUNGEN

BURNING RATE MODELS OF GUN PROPELLANTS:
BURNING BEHAVIOUR OF JA2 GUN PROPELLANT AND
COMBUSTION PHENOMENA OF POROUS CHARGES

Thomas S. Fischer, Norbert Eisenreich, Stefan Kelzenberg,
Gesa Langer, Angelika Messmer

Fraunhofer Institut für Chemische Technologie, Joseph-von-Fraunhofer-Str. 7,
D 76327 Pfinztal

Abstract

The linear burning rate of gun propellants governs the design of charges by interior ballistic simulations. Recent efforts to increase performance led to innovative propellants. The later comprise e.g. porous and foamed charges and formulations exhibiting a temperature independent burning. A simplified model able to describe the dependence of the burning rate on initial temperature is presented. It is based on the heat flow equation and can be considered as a modification of Vieille's law. To apply the model experimental data of standard gun propellant JA2 is used. In addition experimental and model results describing combustion phenomena of porous charges are presented.

Kurzfassung

Die Kenntnis der linearen Abbrandrate ist Grundlage für die Auslegung von Ladungen auf Basis innenballistischer Simulationen. Arbeiten zur Leistungssteigerung führten zu neuartigen Rohrwaffentreibmitteln. Diese umfassen unter anderem poröse und geschäumte Ladungen und Formulierungen, die einen sogenannten temperaturunabhägigen Abbrand zeigen. Ein vereinfachtes Modell, das die Abhängigkeit der Abbrandrate von der Ausgangstemperatur beschreibt, wird präsentiert. Es basiert auf der Wärmeleitungsgleichung und kann als eine Modifizierung des Vieilleschen Gesetzes dargestellt werden. Das Modell wird dazu auf experimentell ermittelte Daten des Standardrohrwaffentreibmittels JA2 angewandt. Desweiteren werden Ergebnisse aus Experimenten und Simulationsrechnungen präsentiert, die den Abbrand poröser Ladungen beschreiben.

1. EINLEITUNG

Die Kenntnis der linearen Abbrandrate ist essentiell für die Simulation des innenballistischen Verhaltens eines Rohrwaffentreibmittels. Experimentell kann sie durch Untersuchungen in der ballistischen Bombe ermittelt werden [1,2].

Diese Simulationen benutzen das Vieillesche Gesetz (1), das empirisch aus experimentell ermittelten Druckkurven gemäß der vereinfachten Relation (2) abgeleitet wurde.

$$r(P) = aP^n \qquad (1)$$

$$\frac{dP}{dt} \propto A(P) r(P) \qquad (2)$$

Das Vieillesche Gesetz beschreibt die experimentell gefundene Abhängigkeit der Abbrandrate vom Druck trotz seiner Einfachheit für eine sehr große Anzahl von Festtreibstoffen über drei Größenordnungen. Durch Modifikationen wie

$$r(P) = aP^n + \gamma \qquad (3)$$

konnte die Übereinstimmung zwischen experimentellen Daten und dem Modell für weitere Festtreibstoffe erreicht werden. Jüngste Entwicklungen im Bereich der Festtreibstoffe betreffen u.a. temperaturunabhängige Treibmittel, Strahlung absorbierende Formulierungen und kompakte Ladungen mit porösen Strukturen. Zur Beschreibung des Abbrandverhaltens dieser Ladungen werden Modifikationen des Vieilleschen Gesetzes benötigt oder es müssen komplett neue Ansätze in Betracht gezogen werden. Wünschenswert sind dabei Abbrandgesetze, die auf physikalisch-chemischen Modellen beruhen. Diese sollten den Einfluß von physikalischen und chemischen Stoffdaten aufzeigen: dazu gehören Dichte, spezifische Wärme und Wärmeleitungskoeffizienten. Sie sollten außerdem aufzeigen, wie Phasenumwandlungen und chemische Reaktionen bei der Pyrolyse in der kondensierten Materie bzw. in der Gasphase wirken. Bei Raketenfesttreibstoffen hat die Modellierung der Abbrandrate für Composites und Double Base Formulierungen zu neuen Beschreibungen geführt [3-7].

In diesem Beitrag werden Modifikationen des Vieilleschen Gesetzes aufgezeigt, mit deren Hilfe

a) die Anfangstemperaturabhängigkeit der Abbrandrate für Rohrwaffentreibmittel auf Basis der Analyse des Wärmeflusses im Festkörper bzw.
b) die besonderen Abbrandeigenschaften poröser Ladungen durch explizite Berücksichtigung der inneren Struktur

beschrieben werden kann. Detailliertere Modelle, die u.a. Reaktionsmodelle, Wärmefluß und Diffusion in der Gasphase berücksichtigen sind in [8] kurz zusammengestellt.

2. TEMPERATURABHÄNGIGKEIT DER ABBRANDRATE VON JA2

Die Verbrennung eines Festtreibstoffs wird durch den Übergang der kondensierten Phase in die Gasphase dominiert. Dies bedeutet, daß der kalte Festkörper durch den Energieübertrag aus der Flamme auf die Temperatur der brennenden Oberfläche erwärmt wird. Phasenumwandlungen können auftreten, z.B. in die Flüssigphase. Der Übergang in die Gasphase kann durch endotherme Verdampfung, exotherme Pyrolyse oder durch heterogene Reaktionen erfolgen, die aus dem Energieübertrag aus einer hier nicht näher spezifizierten Energiequelle (Q (x,t) aus der Flamme) in der Gasphase herrührt (Abb. 1).

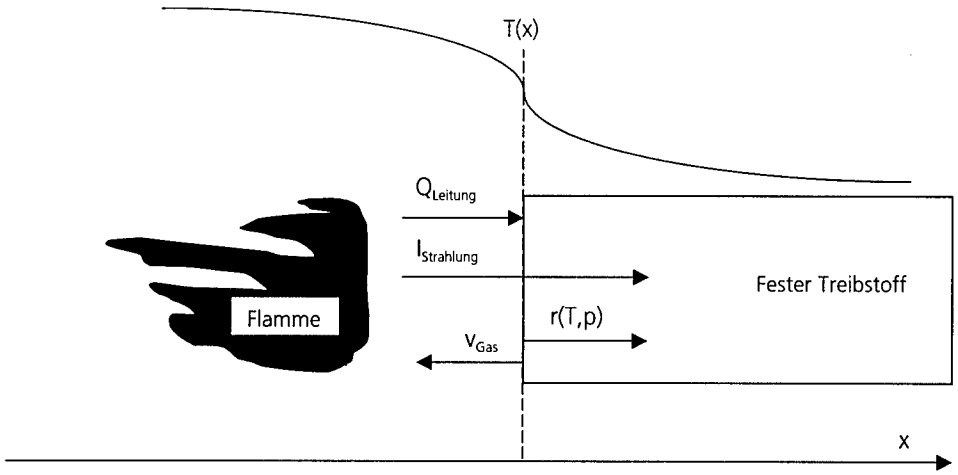

Abb. 1: Vereinfachtes Modell eines brennenden Festtreibstoffs

Diese Effekte können in der Wärmeleitungsgleichung im Feststoff (4) berücksichtigt werden. Vernachlässigt werden dabei Diffusionsvorgänge und auch alle Vorgänge in der Gasphase bzw. Flamme wie: Wärme- und Stofftransport, Reaktionskinetik entweder über Elementarreaktionen oder über reduzierte Mechanismen, Molekülstrahlung und Strahlungstransport.

$$\rho c_p \frac{\partial T}{\partial t} - \lambda \frac{\partial^2 T}{\partial x^2} = \lambda Q[x,t] + \lambda \sum_i q_i \frac{\partial c_i}{\partial t} \qquad (4)$$

Für die Umsatzrate $\frac{\partial c_i}{\partial t}$ benutzt man für gewöhnlich den Arrhenius-Ansatz:

$$\frac{\partial c_i}{\partial t} = -\sum_j A_{i,j} e^{-\frac{E_{i,j}}{RT}} f[c_i, c_j] \qquad (5)$$

Die Herleitung der Formeln, die benutzten Transformationen, Näherungen und Lösungen für die Aufheizung eines Feststoffes sind detailliert in [7,9] beschrieben, die hauptsächlich zum tragen kommende Mathematik (u.a. Greensche Funktionen) in [10].
Das Modell für die Abhängigkeit der Abbrandrate von der Ausgangstemperatur benutzt den Fall des stationären Abbrandes. Nach einer Anfangsphase der Feststoffaufheizung durch extern zugeführte oder intern durch Reaktion entstandene Energie stellt sich ein stationärer Reaktionsfortschritt ein, d.h., die Reaktionsfront bewegt sich als stationäres Temperaturprofil mit einer konstanten Geschwindigkeit r in den Feststoff hinein. Wegen der konstanten Geschwindigkeit kann das Koordinatensystem so transformiert werden, daß das Temperaturprofil ruht. Es ergibt sich folgende gewöhnliche Differentialgleichung [9]:

$$r\rho c[T]\frac{dT}{dx} + \lambda\frac{d^2T}{dx^2} = -\lambda Q[x] + r\sum_i \lambda q_i \frac{dc_i}{dx} \qquad (6)$$

Diese Gleichung kann unter Berücksichtigung folgender Randbedingungen integriert werden.

$T[\infty] = T_\infty$; $T[0] = T_s$

$\lambda dT/dx = -Q_0$, bei $x = 0$ (Wärmeübertragung von der Flamme)

$\lambda dT/dx = 0$ für $x \rightarrow \infty$

$c_i[0] = 1$ und $c_i[\infty] = 0$; (vollständiger Stoffumsatz)

Eine Phasenumwandlung wird dabei als Polstelle beschrieben und die Strahlung wie ein Quellterm behandelt.

$c(T) = c + L\delta[T-T_L]$

$Q[x] = ble^{-bx}$; Strahlungsaufheizung

Diese führt zu folgender Gleichung:

$$r = \frac{Q_0 + I}{\rho\left(c\cdot(T_s - T_\infty) + L - \sum_i \lambda q_i\right)} \qquad (7)$$

Diese zeigt, daß Wärmeübertragung durch Wärmeleitung und durch Strahlung die Abbrandrate gleichartig beeinflussen. Endotherme Phasenumwandlungen führen zu einer Verringerung der Abbrandrate, exotherme chemische Reaktionen zu einem Anstieg.
Formeln vom Typ (7) wurden von Landau bzw. Masters [11, 12] für durch Wärmezufuhr abschmelzende Oberflächen hergeleitet und von Glick [13], Ewing und Osborn [14]

benutzt, um die Abhängigkeit des Abbrandes von Raketenfesttreibstoffen von der Ausgangstemperatur zu beschreiben.

Vernachlässigt man Phasenumwandlungswärmen, chemische Reaktionen und Strahlung, vereinfacht sich Gleichung (7) zu:

$$r = \frac{Q_0}{\rho c \cdot (T_s - T_\infty)} \qquad (8)$$

Diese Gleichung ermöglicht es, Q_0 und T_S zu bestimmen, wenn die Abbrandgeschwindigkeit aus Messungen bei verschiedenen T_∞ bekannt ist. Für JA2 wurden Messungen in einer Ballistischen Bombe mit einem Volumen von 302 cm^3 durchgeführt. Die Anfangstemperatur wurde in 10° Schritten von –233 K bis +333 K variiert. Die Ladedichte betrug 0,2 g/cm^3. Aus den Druck-Zeit-Verläufen und der bekannten 7-Loch Geometrie wurde dann jeweils die lineare Abbrandrate nach den in [1] und [15] beschriebenen Verfahren bestimmt.

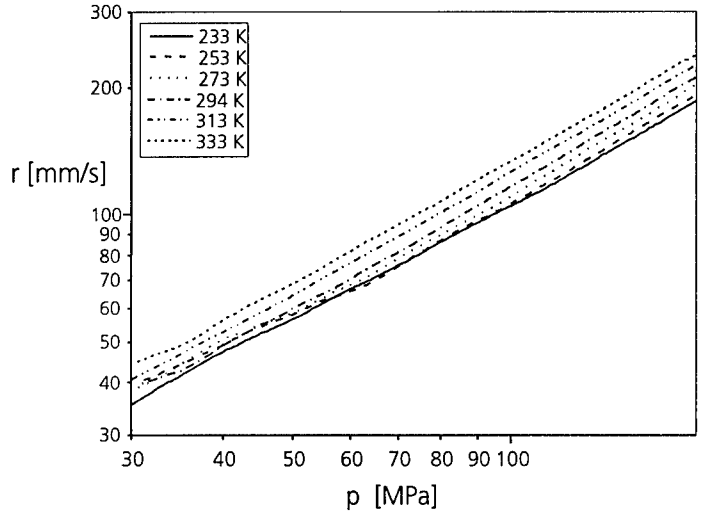

Abb.2: Abbrandraten des JA2 in Abhängigkeit vom Druck für verschiedene Ausgangstemperaturen

In Abb. 2 sind diese Abbrandraten in logarithmischer Form für den Druckbereich zwischen 30 und 175 MPa für 6 der 11 Ausgangstemperaturen dargestellt. Die Druckexponenten liegen zwischen 0,9 und 1. Dabei werden die Abbrandraten in

Abhängigkeit vom Druck quasi-kontinuierlich bestimmt. In Abbildung 3 sind sie für 5 ausgewählte Drücke in Abhängigkeit von der Ausgangstemperatur dargestellt.

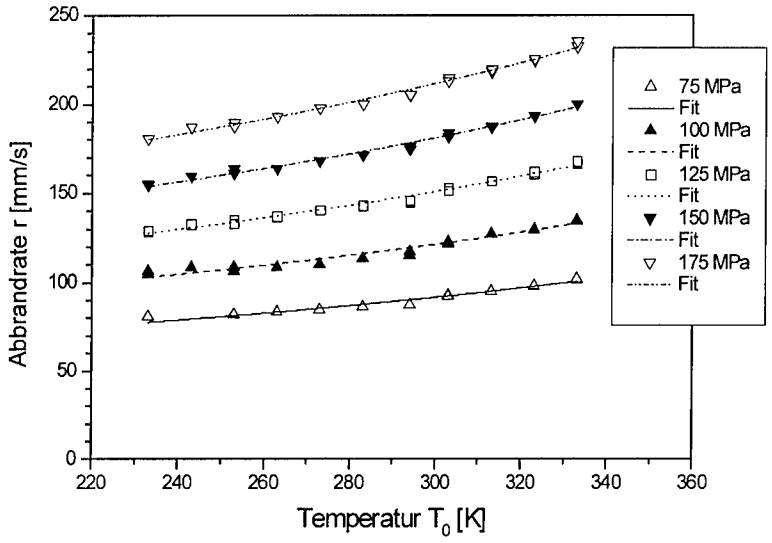

Abb. 3: Abbrandraten des JA2 in Abhängigkeit von der Ausgangstemperatur bei verschiedenen Drücken

Bei allen Drücken steigt die Abbrandrate mit steigender Ausgangstemperatur. Diese Daten bestätigen die Gültigkeit von Gleichung (8) für JA2, die entsprechenden Fits mit den Parametern Q_0 und T_s sind in Abb. 3 ebenfalls dargestellt. Für T_s ergibt sich ein Mittelwert von 675 Kelvin, die Schwankung ist dabei sehr gering (Abb. 4). Für Q_0 ergibt sich eine systematische Abhängigkeit vom Druck. Sie korrespondiert mit der Druckabhängigkeit der linearen Abbrandrate und reproduziert den Druckexponenten n. Dies ist in Abbildung 5 dargestellt. Dabei korreliert der starke Anstieg des Wärmeflusses aus der Gasphase zur brennenden Oberfläche mit der exponentiellen Verringerung des Abstandes der Flamme von der Oberfläche [16].

Daher kann Gleichung (8) zu einer Modifikation des Vieillesche Gesetzes umformuliert werden, wobei der Term I in diesem Fall für zusätzlich von außen eingestrahlte Energie steht:

$$r = \frac{a^{*} P^{n} + I}{\rho c \cdot (T_s - T_\infty)} \qquad (9)$$

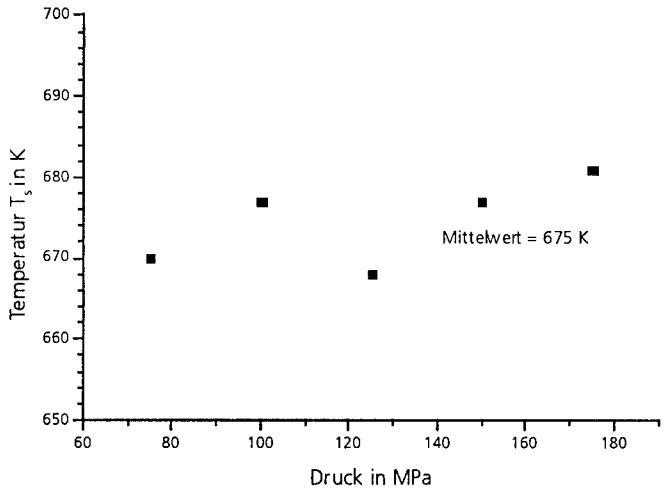

Abb. 4: Abhängigkeit der Temperatur der brennenden Oberfläche vom Druck

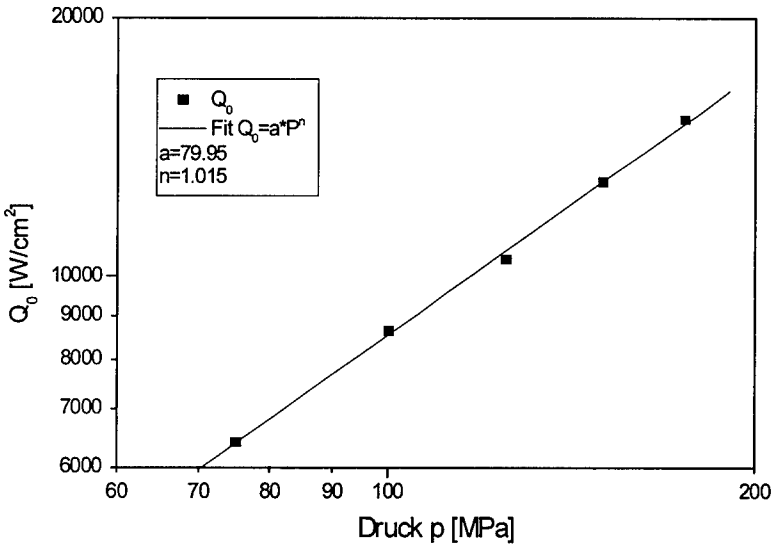

Abb 5: Least Square Fit des Wärmerückflusses Q_0 in Abhängigkeit vom Druck

Unter Vernachlässigung dynamischer Effekte kann Gleichung (9) dazu benutzt werden, die Möglichkeiten abzuschätzen, die Abbrandrate mit Hilfe eines zusätzlichen Strahlungswärmeflusses zu steigern. Dies ist besonders für die ETC Technologie von Bedeutung. Für JA2 würde man eine Verdoppelung der Abbrandrate bei 110 MPa mit einem zusätzlichen Strahlungswärmefluß aus dem Plasma von 9400 W/cm^2 erreichen. Weiterführende Untersuchungen und Abschätzungen sind in [16,17] dokumentiert.

Fazit: Für JA2 wurde eine sehr gute Übereinstimmung des vereinfachten Modells mit experimentellen Daten festgestellt. Damit kann die im niedrigen Druckbereich der Raketenfesttreibstoffe gefundene Gesetzmäßigkeit der Abhängigkeit der Abbrandrate von der Ausgangstemperatur auf den hohen Druckbereich der Rohrwaffentreibmittel übertragen werden. Dies führt auf Basis eines physikalisch-chemischen Modells zu einem modifizierten Vieilleschen Gesetz.

3. ABBRANDPHÄNOMENE PORÖSER LADUNGEN

Poröse und geschäumte Treibmittel besitzen auf Grund der großen inneren Oberfläche der Poren im Vergleich zu kompakten Treibladungen eine sehr hohe Abbrandgeschwindigkeit. Bei der Bestimmung der Abbrandrate aus Experimenten in der Ballistischen Bombe ist aber der Formfaktor der porösen Ladung im Gegensatz zu den Standardgeometrien unporöser Treibmittel nicht einfach herleitbar. Benutzt man zur Auswertung nur die Geometrie der makroskopischen Form (und vernachlässigt damit den Einfluß der inneren Struktur), so erhält man eine Ladedichteabhängigkeit der Abbrandgeschwindigkeit. In Abbildung 6 ist dieses Verhalten für 3 Ladedichten dargestellt. Die Treibladungskörper hatten Würfelgeometrie mit 1 cm^3 Volumen und eine Dichte von 0,765 g/cm^3. Eine identische unporöse Formulierung hat eine theoretische Dichte von 1,56 g/cm^3. Im Gegensatz zu dem in Abb. 6 dargestellten Verhalten, findet man bei unporösen Standardrohrwaffentreibmitteln, daß die berechneten Kurven der Abbrandgeschwindigkeiten bei gleichem Druck nahezu unabhängig von der Ladedichte sind. Die auf diese Weise für poröse Ladungen ermittelten Werte sind daher keine Stoffkenngröße mehr. Eine formale Auswertung nach Vieille ist für jede einzelne Ladedichte möglich, aber das innenballistische Verhalten

in der Waffe kann auf Basis dieser Abbrandkoeffizienten nicht adäquat simuliert werden.

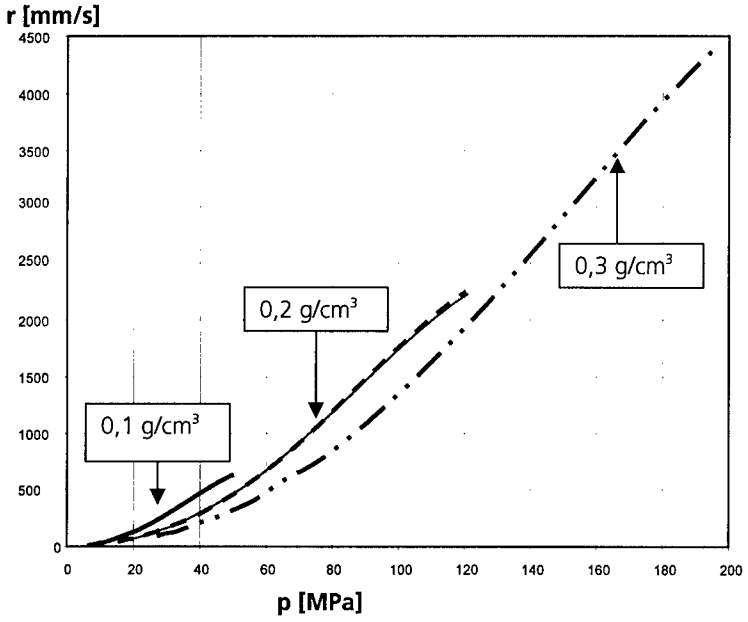

Abb. 6: Effektive lineare Abbrandgeschwindigkeit eines porösen Rohrwaffentreibmittels bei drei Ladedichten

Es werden aber Abbrandgeschwindigkeiten erreicht, die über eine Zehnerpotenz größer sind als die von Hochleistungspulvern. Damit wird es mit Hilfe poröser Treibmittel möglich, großvolumige Körper schnell genug abzubrennen, um neuartige Ladungskonfigurationen zu verwirklichen (ein Beispiel hierfür ist teleskopierte Munition auf Basis einer verbrennbaren Hülse für RMK 30 [30]). Daher wurde in Experimenten in der Ballistischen Bombe die Auswirkungen von systematischen Parametervariationen der porösen Ladungen untersucht. Dies umfaßte u.a. Dichte, Porenverteilung (nach Größe und Anzahl der Poren) und Zusammensetzung [18,19,20]. Abbildung 7 zeigt den Einfluß der Porengröße auf den maximalen Druckanstieg bzw. die $t_{30\text{-}80}$ Zeit. Bis auf den mittleren Porendurchmesser wurden alle anderen Parameter nicht verändert. Die Ladedichte betrug 0,3 g/cm³ und die Dichte 0,88 g/cm³. D.h., das innere Volumen (Summe über alle Poren im Würfel) blieb konstant, es änderte sich aber die Art und Anzahl der Poren und damit die innere Oberfläche. Ein kleinerer mittlerer

Porendurchmesser führt zu einer größeren inneren Oberfläche und damit zu einem höheren Massenumsatz. Dies führt zu einem schnelleren Druckanstieg und damit zu einer höheren effektiven Abbrandrate.

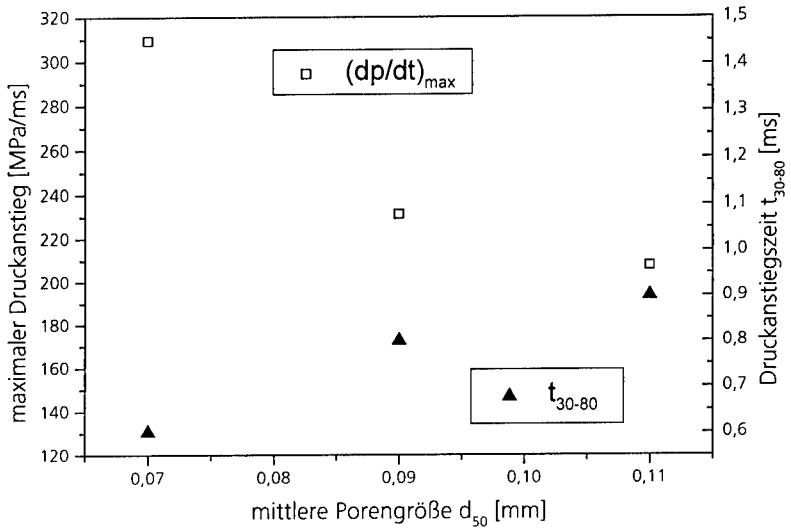

Abb. 7: Abhängigkeit des maximalen Druckanstiegs und der Druckanstiegszeit von der mittleren Porengröße

In diesen Experimenten werden also eindeutige empirische Zusammenhänge zwischen der inneren Struktur der porösen Ladungen und den Druck-Zeit Verläufen gefunden, die in der Ballistischen Bombe gemessen werden. Solange die poröse innere Struktur und die äußere Form der Proben identisch ist, stellt man bei porösen Ladungen dieselben Zusammenhänge bei systematischer Variation von Formulierung, Korngröße etc. fest wie bei kompakten Formkörpern.

Dies führte zur Entwicklung eines phänomenologischen Modells auf Basis von Zellulären Automaten (weitere Modelle auf physikalischer Basis sind in [8,21-24] beschrieben). Details des phänomenologischen Modells sind in [20] erläutert. Kurzgefaßt werden über eine formale Prozedur die Formfunktionen komplexer zweidimensionaler Körper berechnet und auf Basis der Nobel-Abel Gleichung dann der adiabatische Druckaufbau in einer Ballistischen Bombe simuliert. Experimentelle Daten aus Ballistischen

Bombenuntersuchungen und optische Untersuchungen zur Bestimmung der inneren Struktur der Treibladungsformkörpern dienen zur Modifizierung der Modellparameter. Diese explizite Berücksichtigung der inneren Struktur der porösen Ladungen in diesem Modell ermöglicht die qualitative Beschreibung der in Experimenten gefundenen Abbrandphänomene [19,20]. Auch die in Abbildung 6 aufgezeigte Ladedichteabhängigkeit kann beschrieben werden. Abbildung 8 zeigt die theoretische Berechnung der linearen Abbrandrate in Abhängigkeit von der Ladedichte für eine poröse und eine unporöse Ladung.

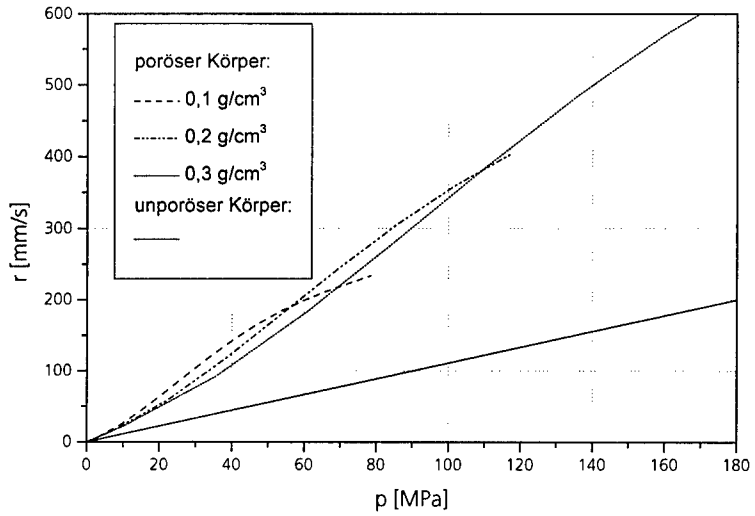

Abb. 8: Einfluß der Ladedichte auf die Abbrandrate

Ein weiteres Beispiel ist der Einfluß von Änderungen der inneren Struktur auf den Druckanstieg in einer Ballistischen Bombe (Abbildung 9). Dabei wurde das Leerraumvolumen bzw. die Dichte der porösen Ladung konstant gehalten (auf 60% der theoretischen Dichte). Die Treibladungskörper hatten Würfelgeometrie (1 cm^3 Volumen) und ihre Porosität wurde durch Poren mit jeweils identischem Durchmesser simuliert. Die Berechnungen wurden für drei verschiedene Porendurchmesser und eine unporöse Ladung durchgeführt, alle bei der Ladedichte 0,2 g/cm^3. Wie in Abbildung 7 führt ein kleinerer Durchmesser zu einem höheren maximalen Druckanstieg.

Quantitative Berechnungen werden durch eine weitere Einflußgröße stark erschwert: die Eindringtiefe der Wechselwirkung. Die Reaktionszone beim Abbrand homogener unporöser Treibladungskörper ist nur wenige µm dick. Bei porösen Systemen kann der Abbrand auch in größerer Tiefe initiiert werden. Der außenanliegende Druck kann z.B. die Wand zwischen zwei Poren durchstoßen oder aber durch Strahlungswirkung kann die Oberfläche tieferliegender Poren angezündet werden. Für drei Eindringtiefen wird dieser Einfluß in Abbildung 10 dargestellt. Dabei wird angenommen, daß die Oberfläche von Poren, die innerhalb dieses Abstandes von der Oberfläche liegen, angezündet werden.

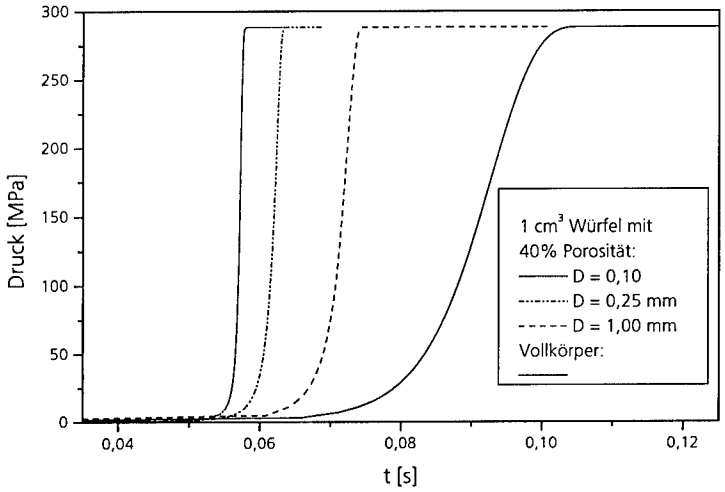

Abb. 9: Einfluß der Porengröße (D = Durchmessser) auf die Druck-Zeit-Kurve

Ansätze, die Eindringtiefe der Wechselwirkung theoretisch näher zu fassen, beruhen auf der Annahme, daß das Eindringen der heißen Gase der Flamme in die Poren des Festkörpers mit dem Darcyschen Gesetz beschrieben werden könnte. Dabei ist die Geschwindigkeit der heißen Gase dem Druckgradienten und der Permeabilität des Materials proportional [25,26,27]. Andere Ansätze berücksichtigen den Effekt des druckabhängigen Flammenabstandes von der Abbrandoberfläche [28, 29].

Fazit: Die explizite Berücksichtigung der inneren Struktur poröser Ladungen ermöglicht eine Anwendung des Vieilleschen Gesetzes für die Simulation des innenballistischen

Verhaltens in ballistischen Bomben auch im Bereich poröser Ladungen. Dies ermöglicht die modellhafte Beschreibung der Abbrandphänomene, die bei porösen Treibmitteln in der Realität beobachtet werden.

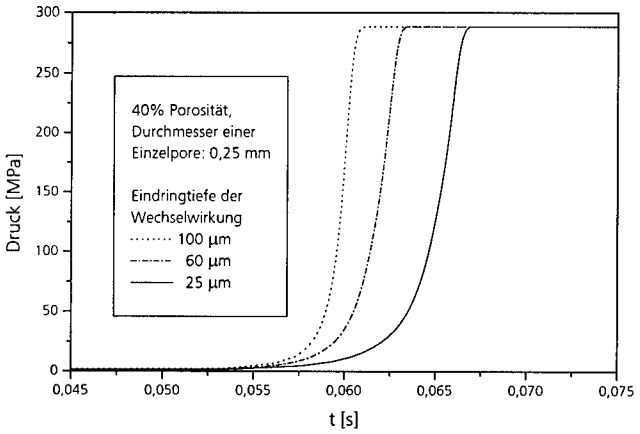

Abb. 10: Einfluß der Eindringtiefe der Wechselwirkung auf den Druckaufbau

4. NOMENKLATUR

T	Temperatur (T_s Temperatur an der Abbrandoberfläche, T_∞ Ausgangstemperatur)
E	Aktivierungsenergie
Z	exponentieller Vorfaktor
r	lineare Abbrandrate
p	Druck
a	Faktor
n	Druckexponent
I	Strahlungsintensität
b	Absorptionkoeffizient
L	Phasenumwandlungswärme
T_L	Temperatur der Phasenumwandlung
Q(x,t)	Wärmefluß von einer externen Quelle
Q_0	Wärmefluß an der brennenden Oberfläche
q_i	Wärmeumsatz der Spezies c_i
λ	Wärmeleitfähigkeit
ρ	Dichte
c	spezifische Wärme
c_i	Konzentration
v_{gas}	Geschwindigkeit der heißen Gase

5. LITERATUR

[1] H. Krier, S.A. Shimpi, "Predicting Uniform Gun Interior Ballistics Part I: An Analysis Of Closed Bomb Testing", Aeronautical and Astronautical Engineering Department University of Illinois at Urbana-Champaign, Technical Report AAE 74-5, (1974)

[2] B. Baschung, D. Grune, "The Closed Vessel, Still an Essential Experimental Device for Interior Ballistics in the Future?", *European Forum on Ballistics of Projectiles,* French-German Research Institute of Saint-Louis (ISL), Saint-Louis, pp. 105 – 115, (April 2000)

[3] M. Summerfield, G. Sutherland, M. Webb, H. Taback, K. Hall, *Techn. Rept. PR-87-P,* Princeton University, New Jersey, (1958)

[4] M. W. Beckstead, R. L. Derr, C. F. Price, "A Model of Composite Solid Propellant Combustion Based on Multiple Flames", *AIAA Journal,* Vol. 8, pp. 2200-2207, (December 1970)

[5] Y. B. Zeldovich, *J.Phys. Chem.,* U.S.S.R, 22 (1948) 27

[6] R.G. Parr, B.L Crawford, *J. Coll. Phys. Chem.,* 54 (1950) 929

[7] N.Eisenreich, "Vergleich theoretischer und experimenteller Untersuchungen über die Anfangstemperaturabhängigkeit von Festtreibstoffen", *Bericht 8/77,* ICT (1977) Pfinztal

[8] N. Eisenreich, T. S. Fischer, G. Langer, "Burning Rate Models of Gun Propellants", *European Forum on Ballistics of Projectiles,* French-German Research Institute of Saint-Louis (ISL), Saint-Louis, pp. 117 – 127, (April 2000)

[9] W. Eckl, S. Kelzenberg, V. Weiser, N. Eisenreich, "Einfache Modelle deer Anzündung von Festreibstoffen", *29th International Annual Conference of ICT,* Karlsruhe, Federal Republic of Germany, P154, (1998)

[10] H.S. Carslaw, J.C. Jaeger, *Conduction of Heat in Solids, 2. Edition,* Oxford University Press, London, (1973)

[11] H.G. Landau, *Quart. Appl. Math.,* 8 (1950) 81

[12] J.I. Masters, *J. Appl. Phys,.* 27 (1956) 477

[13] R. L. Glick, *AIAA J.,* 5 (1967) 586

[14] D.L. Ewing, J. R. Osborn, *J. Spacecraft Rockets,* 8 (1971) 290

[15] M. Hund, N. Eisenreich, "Determination of Interior Ballistic Parameters of Solid Propellants by Different Methods", *Proceed. 6th Int. Symp.on Ballistics,* Orlando, pp. 77-84, (1981)

[16] N. Eisenreich, W. Eckl, Th. Fischer, V. Weiser, S. Kelzenberg, G. Langer, A. Baier, "Burning Phenomena of the Gun Propellant JA2", *Propellants, Explosives, Pyrotechnics, accepted for publication (3 / 2000)*

[17] N. Eisenreich, S. Kelzenberg, A. Koleczko, H. Schmid, "Strahlungsbeeinflussung der Anzündung und Verbrennung von festen Treibstoffen", *31st International Annual Conference of ICT,* Karlsruhe, Federal Republic of Germany, P139, (2000)

[18] A. Meßmer, T. S. Fischer, ISL, (March 1999)

[19] T.S. Fischer, A. Meßmer, G. Langer, "Geschäumte polymergebundene Treibladungen", *23. Wehrtechnisches Symposium – Innenballistik der Rohrwaffen,* Bundesakademie für Wehrverwaltung und Wehrtechnik, Mannheim, (25.05.- 27.05.1999)

[20] T. S. Fischer , W. Koppenhöfer, G. Langer, M. Weindel, "Modellierung von Abbrandphänomenen bei porösen Ladungen", *30th International Annual Conference of ICT,* Karlsruhe, Federal Republic of Germany, P98, (1999)

[21] N. Eisenreich, A. Pfeil, "Pyrolysis Craters Produced by Laser Pulse Irradiation on Propellant Solids", *Appl. Phys.,* 15 (1978) 47

[22] N. Eisenreich, "Successively Initiated Arrays of Hot Spot in a Reactive Medium"in: *BMVg-FBWT 98-1,* FIZBw, Bonn,(1998)
Proceedings: Physics of Explosives, Berchtesgaden, (29 October 1997)

[23] G. Langer, N. Eisenreich, "Entwicklung von Hotspots in energetischen Materialien", *29th International Annual Conference of ICT, Karlsruhe,* Federal Republic of Germany, P157, (1998)

[24] G. Langer, N. Eisenreich, "Hot Spots in Energetic Materials", *Propellants. Explosives, Pyrotechnics*, 24 (1999) 113
[25] B.N. Kondrikov, "Theory of Hydrodynamic Burning Instability of Granular Porous Energetic Materials", *28th Annual Int. Conf. of ICT*, June 24 -27 (1997)
[26] D.A. Schult, B.J. Matkowsky, V.A, Volpert, A. C. Fernandez-Pello, "Forced Forward Smolder Combustion", *Comb. Flame*, 104 (1996) 2
[27] N. Ishchenko, Yu. P.Khomenko, "Effect of Force Interphase Interaction on the Characteristics of Convective Combustion of Porous Media", *Combustion, Explosion and Shockwaves*, 93 (1997) 448
[28] N. Eisenreich, "A Photographic Study of the Combustion Zones of Burning Double Base Propellant Strands", *Propellants and Explosives*, 3 (1978)141-146
[29] N. Kubota, T.J. Ohlemiller, L.H. Caveny, M. Summerfield, *AIAA J.*, 12 (1974) 1709
[30] F. Schedlbauer, A. Meßmer, U. Steffens, I. Reuter, "Verbrennbare Hülse für RMK 30", *29th International Annual Conference of ICT, Karlsruhe*, Federal Republic of Germany, P103, (1998)

ABBRANDVERHALTEN VON CL-20/GAP UND HMX/GAP-FESTTREIBSTOFFEN

Volker Weiser, Norbert Eisenreich, Wilhelm Eckl,
Siegfried Eisele, Klaus Menke

Fraunhofer-Institut Chemische Technologie (ICT)
Joseph-von-Fraunhoferstr. 7
D-76327 Pfinztal (Berghausen), Germany

Abstract

BURNING BEHAVIOUR OF CL-20/GAP AND HMX/GAP ROCKET PROPELLANTS
The burning rate and flame structure of two GAP propellants with the same mass fractions of HMX and CL-20 were compared. CL-20 leads a strong increase of the burning rate combined with a lower pressure exponent. Reasons seems to be a higher surface temperature combined with a longer flame zone of the CL-20 propellant.

Zusammenfassung

Verglichen wurde die Abbrandrate und Flammenstruktur zweier GAP-Modelltreibstoffe mit jeweils gleichen Massenanteilen von HMX und CL-20. CL-20 führt zu einer Verdopplung der Abbrandrate bei einem deutlich niedrigeren Druckexponenten. Dieser Treibstoff weist eine deutlich höhere Oberflächentemperatur und längere Reaktionszone auf.

Einleitung

Neue leistungsstarke Festtreibstoffe mit einem gesteigerten spezifischem Impuls basieren auf hochenergetischen Abbrandzusätzen. Beispiel dafür ist CL-20 (Hexanitrohexaazaisowurtzitan), das erst in jüngster Zeit in ausreichenden Mengen verfügbar ist. Es weist mit einer Bildungswärme von 964.39 kJ/kg und einer Sauerstoffbilanz von -10.95% ein sehr hohes Leistungspotential auf. Da die Verbindung nur aus den Elementen C, H, O, N besteht eignet sie sich für signaturarme Treibstoff-formulierungen.

Allerdings gelingt es vielen solcher energetischen Materialien nicht ihren gesamten Energieinhalt so umzusetzen, daß ihr ganzes Potential in raketentechnischen Anwendungen genutzt werden kann. Z.B. kann eine zu schnelle Gasbildung nahe der Abbrandoberfläche die Stand-Off-Distanz so weit erhöhen, daß zu wenig Energie für die weitere Pyrolyse zum Treibstoff zurückgeführt wird und trotz hoher Verbrennungstemperatur eine niedrige Abbrandrate mit hoher Druckabhängigkeit resultiert.

Derartige Effekte lassen sich leicht an Strand-Proben durch Bestimmung der druckabhängigen Abbrandrate und Erfassung der Flammenstruktur (Temperatur und Konzentrationsprofile senkrecht zur Abbrandoberfläche) überprüfen. Dies wurde an einem CL-20/GAP-Modelltreibstoff in Vergleich zu einem Nitramintreibstoff durchgeführt, in dem HMX durch die gleiche Menge an CL-20 ersetzt wurde.

Experimentelles

Untersuchte Treibstoffe

Verglichen wurden zwei GAP/BDNPF-Modelltreibstoffe mit 70% Füllstoffgehalt an a) HMX und b) CL-20. Die theoretischen und gemessen Leistungsdaten sind in der Tabelle 1 zusammengefaßt. Der Ersatz von HMX durch CL-20 führt schon bei diesen einfachen und nicht optimierten Modelltreibstoffen zu einer Leistungssteigerung von 100 Ns kg^{-1}, die allerdings mit einer starken Erhöhung der adiabaten Verbrennungstemperatur auf über 3000 K einher geht, die zu Problemen bei der Triebwerksauslegung führen könnte.

Meßtechnik und Auswertung

Abbrandrate:

- Untersuchung in der Crawfordbombe mit Schmelzdrähten
  (Druck: 2 bis 25 MPa, Anfangstemperatur: 295 K)
- Referenzmessungen in der optischen Bombe beobachtet mit einer CCD-Kamera. Automatische Bildauswertung des digitalen Films
  (Druck: 2 bis 25 MPa, Anfangstemperatur: 295 K)

Fotografie:

- Einzelbilder: Spiegelreflexkamera mit Makrovorsatz
- Abbrandverlauf: CCD-Kamera

Temperatur und Gaskomponenten:

- 2-Farbenpyrometrie: Si/Ge-Sandwichdetektor (900 und 1500 nm),
  Samplerate: 1000 s^{-1}
- UV/Vis-Spektroskopie: Gitterspektrometer, Samplerate: 200 s^{-1}
  Rotationsspektren 2-atomiger Moleküle im UV
  Kontinuumsstrahlung bei 400 bis 700 nm
- Filterradspektroskopie: rotierendes Interferenzfilter (2600 bis 8000 nm, CaF_2-Optik),
  Samplerate: 100 s^{-1}
- Heißgassensor: NIR-Gitterspektrometer (900 bis 1700 nm) mit automatischer Auswertung von Temperatur der Rußstrahlung und Wasserbande bei 1.6 µm,
  Samplerate: 100 s^{-1}

Alle optischen Untersuchungen fanden in einer Optischen Bombe mit zwei gegenüberliegenden Fenstern bei 1 bis 10 MPa in Stickstoff statt. Die Anlage ist ebenso wie die eingesetzten Untersuchungsmethoden z. B. in [1] und [2] genauer beschrieben. Weitere Informationen zu den Messungen mit dem Heißgassensor finden sich [3].

Ergebisse und Diskussion

Bilder der Abbrandzonen bei 1 und 7 MPa finden sich in Abbildung 1. Die Flammen beginnen sehr nahe der Oberfläche. Eine Dunkelzone deutet sich nur an. Die Flammenzone des CL-20/GAP-Treibstoffs ist etwa doppelt so lang, wie die des HMX/GAP-Treibstoffs. Bei niedrigem Druck finden sich nur nahe der Abbrandoberfläche intensiv leuchtende Flammenzonen. Die Flammen entstehen an einzelnen Zentren der Oberfläche und verlaufen in Strähnen nach oben. Bei hohem Druck sind die Flammen deutlich länger und leuchten intensiver.

Die gesteigerte Leistungsfähigkeit des CL-20/GAP-Treibstoffes schlägt sich nicht nur in den theoretischen Leistungsdaten, sondern auch in der Abbrandrate nieder (Tabelle 1, Abbildung 2). Sie ist bei 7 MPa mit 15 mm s^{-1} doppelt so hoch, wie beim HMX/GAP-Vergleichstreibstoff. Dabei weist sie mit 0.57 einen deutlich niedrigeren Druckexponenten auf. Bei beiden Treibstoffen deutet sich im einsatzrelevanten Druckbereich zwischen 4 und 9 MPa ein Plateau mit deutlich geringerer Druckabhängigkeit an. Das Abbrandverhalten erwies sich als gut reproduzierbar.

Die Temperaturmessungen bestätigen die erwarteten hohen Flammentemperaturen speziell bei dem CL-20/GAP-Treibstoff nicht (Tabelle 1). Sie liegen mit maximal 2500 K in einem für Hochleistungstreibstoffe üblichen Bereich. Die zeitaufgelösten Spektren zeigen weiterhin, daß der Grund für die hohe durch CL-20 bedingte Abbrandrate auf eine sehr hohe Zersetzungstemperatur an der Abbrandoberfläche zurückzuführen ist (ebenfalls in Tabelle 1 aufgeführt), die auf eine stark exotherme Zersetzungsreaktion hindeutet. Dadurch ergibt sich ein sehr hoher Wärmetransport in Richtung des Feststoffes der die Zersetzung begünstigt [4].

Literatur

[1] Weiser, V.; Eisenreich, N.; Baier, A.; Eckl, N.; Burning Behaviour of ADN Formulations; Propellants, Explosives, Pyrotechnics 24; 163-167 (1999)

[2] Eckl, W.; Weiser, V.; Langer, G.; Eisenreich, N.; Burning Behaviour of Nitramine Model Formulations; Propellants, Explosives, Pyrotechnics 22; 148-151 (1997)

[3] Eckl, W.; Weiser, V.; Eisenreich, N.; Spectroscopic Flame Diagnostics by Analyzing NIR Water Bands; accepted at "Combustion of Energetic Materials"; Stresa (Lake Maggiore area), Italy, 19-22 June 2000

[4] N. Eisenreich, T. Fischer, and G. Langer, "Burning Rate Models of Gun Propellants", European Forum on Ballistics of Projectiles, Saint-Louis, France, April 11-14, 2000, French-German Research Institute of Saint-Louis (ISL), pp. 117-127

Tabellen und Abbildungen

Tabelle 1 Theoretische und gemessene Leistungsdaten der HMX/GAP und CL-20/GAP-Modelltreibstoffe

	HMX/GAP	CL-20/GAP
Zusammensetzung		
GAP+BDNPF	20%+10%	20%+10%
energetischer Füllstoff	70%	70%
Sauerstoffbilanz	-44.5%	-37,0%
theor. spezifischer Impuls	2363 s kg-1	2462 s kg-1
adiab. Temperatur	2567 K	3023 K
Abbranddrate (7MPa)	7.5 mm s-1	15 mm s-1
Druckexponent	0.74	0.57
2-Farbentemperatur	1900-2200 K	2000-2500 K
NIR-Messungen	1700-2100 K	1900-2200 K
IR-Messungen	1700-2500 K	2000-2600 K
Oberoberflächentemperatur	1350 K	1900 K

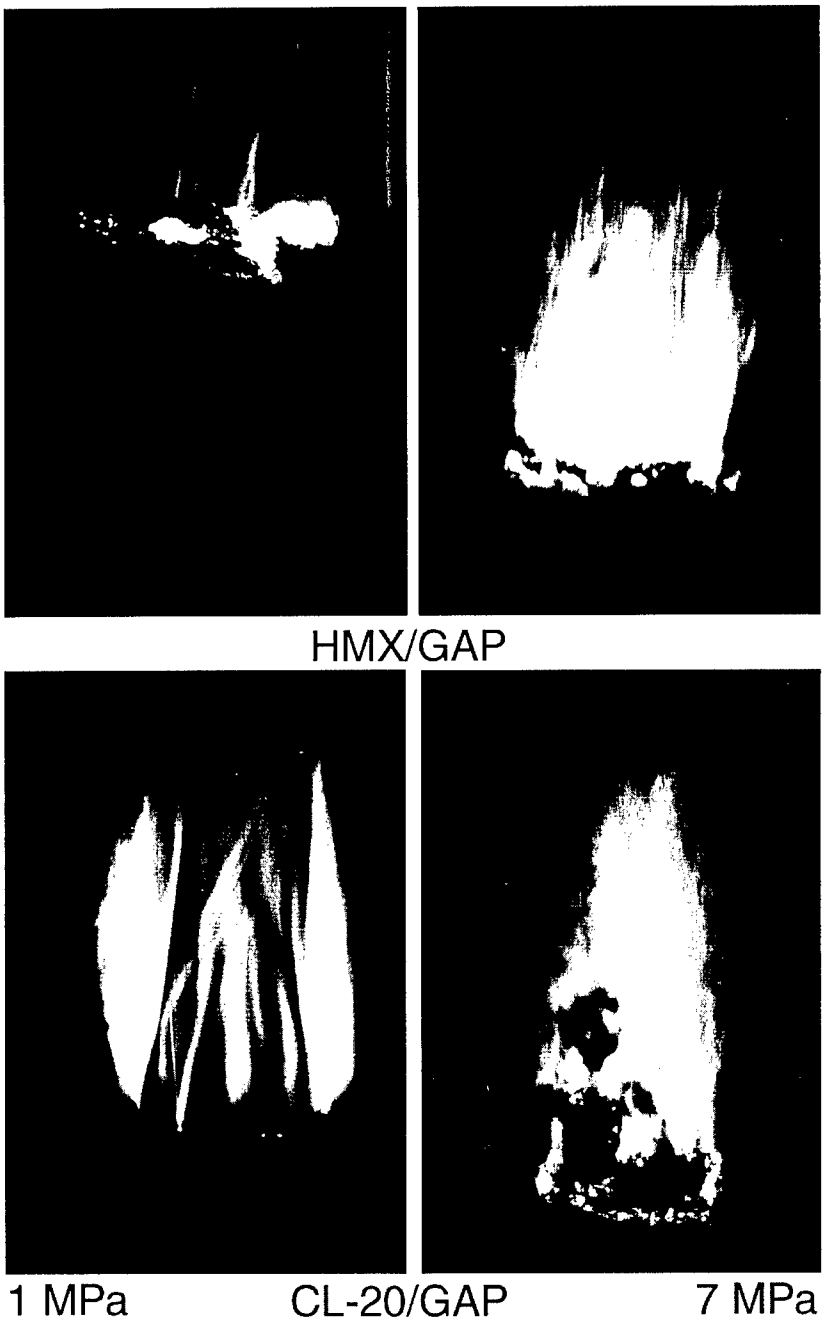

Abbildung 1 Abbrandfotos der Modeltreibstoffe von HMX/GAP (oben) und CL-20/GAP (unten)

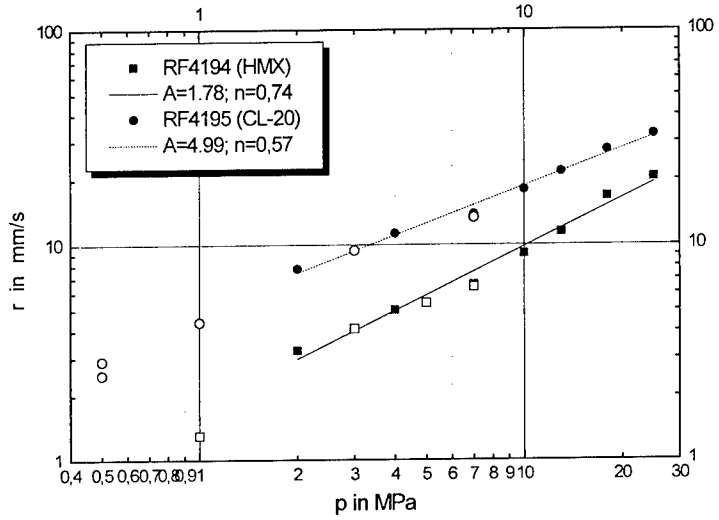

Abbildung 2 Abbrandrate der untersuchten Modelltreibstoffe gemessen nach Crawford und in der Optischen Bombe mit einer CCD-Kamera

ABBRANDVERHALTEN VON KRYOFESTTREIBSTOFFEN

V. Weiser*, S. Poller, St. Kelzenberg, N. Eisenreich
Fraunhofer Institut Chemische Technologie (ICT), Pfinztal, D

R. Lo, H. Adirim
TU Berlin IRTS, Berlin, D

Abstract

BURNING BEHAVIOUR OF CRYOGENIC SOLID PROPELLANTS

A new approach for more powerful rocket motors is the Cryogenic Solid Propellant (CSP) technology. It combines the advantages of classical weight saving solid propellants with the power efficiency and safety of modern liquid propellants. The idea of CSP-grains is to freeze liquid or gaseous fuels and/or oxidisers. CSP-technology can be realised in two versions: 1. Mono-CSP follow the burning behaviour of solid propellants. Experiments with mono-CSPs have been carried out under inert pressure conditions in a window bomb. Mono-CSPs show stable burning behaviour with a constant regression rate which obeys the exponential Law of Vieille under varying pressure conditions. 2. Another approach is to arrange oxidiser and fuel as separate grains. This gives the advantage of high safety and provides influencing the burning behaviour by grain geometry. Two versions have to be distinguished: externally controlled systems (e. g. by heat from an external gas generator) and self-sustained systems (e.g. a rod-in-matrix burner). This particular system shows self sustained combustion in an inert pressure atmosphere with overall burning rates in a similar range as corresponding solid rocket propellants which obey also a Vieille-type pressure law.
The recent experiments with CSPs resulted in encouraging combustion behaviour showing no serious technical obstacles and open a broad spectrum of applications in rocket propulsion.

Zusammenfassung

Die Kryofesttreibstofftechnologie eröffnet neue Wege zu Raketenantrieben mit deutlich gesteigerter Leistung. Die Idee flüssige Treibstoffe gefroren in einem Raketentriebwerk einzusetzen kombiniert die Vorteile von leichten Feststoffmotoren mit der Leistung und Sicherheit von Flüssigtriebwerken. Man unterscheidet vorgemischte Mono-CSP, die ähnlich konventioneller Festtreibstoffe abbrennen, von modularen Systemen bei denen Oxidator und Brennstoff getrennt angeordnet sind. Die Verbrennung verläuft entweder selbstkontrolliert oder unter dem Heißgasstrom eines Gasgenerators. Als Beispiel brennt ein selbstkontrollierter Rod-In-Matrix-Brenner unter Druck stabil mit typischen Abbrandraten von konventionellen Festtreibstoffen ab, die einem potentiellen Druckgesetz gehorchen. Die bisherigen Untersuchungen des Abbrandverhaltens weisen auf keine ernsten Probleme bei der Realisierung von CSP-Motoren hin.

* Corresponding Author: vw@ict.fhg.de

Einleitung

Raketentriebwerke mit festen Treibstoffen zeichnen sich durch große Zuverlässigkeit und hohe volumenspezifische Leistungsdaten aus. Wegen der sehr beschränkten Auswahl an geeigneten festen Oxidatoren und Bindern erreichen Feststofftriebwerke nur vergleichsweise niedrige spezifische Impulse, die erheblich unter jenen von Flüssigkeitsantrieben liegen. Bei Flüssigkeitsraketenantrieben besteht dagegen eine große Vielfalt verfügbarer Brennstoffe und Oxidatoren, sie erfordern jedoch eine deutlich aufwendigere Verfahrenstechnik beim Antrieb. Die spezifischen Impulse reichen bis in den hochenergetischen Bereich von 4000 Ns/kg und mehr [1].
Ein Ansatz diese günstigen Eigenschaften von festen Treibstoffen mit denen von flüssigen zu kombinieren sind Kryofesttreibstoffe (Cryo Solid Propellants „CSP"). Die Idee der CSP beruht auf folgenden zwei Prinzipien:

- Alle Treibstoffe und ihre Komponenten werden durch entsprechende Kühlung ausschließlich im festen Aggregatzustand eingesetzt
- Die Reaktionsgeschwindigkeit der beteiligten Stoffe wird nötigenfalls durch makroskopische Trennung innerhalb der Brennkammer kontrolliert.

Dadurch werden im Prinzip alle in Praxis oder Theorie bekannten Raketentreibstoffkombinationen als Feststoffantrieb realisierbar. Damit vereinigen sie wichtige Vorteile der festen und flüssigen Treibstoffe miteinander, nämlich einfachen Aufbau einerseits, hohe spezifische Impulse andrerseits. Insbesondere Großtriebwerke mit festem Schub-Zeit Verlauf (Booster) können vorteilhaft mit dieser Technologie ausgelegt werden und sind bei geeigneter Treibstoffauswahl nicht nur leistungsfähiger, sondern auch erheblich umweltfreundlicher als herkömmliche Festtreibstoffe. CSP können in zwei grundlegende Konfigurationen vorliegen:

1. homogen, vergemischter CSP (mono-CSP), entsprechend dem klassischen Festtreibstoff
2. Anordnung mit getrennten Modulen von Oxidator und Brennstoff unterschiedlichster Geometrie (modularer CSP)

Die Bedeutung und der Entwicklungsstand der CSP-Technologie wird in [1-3] ausführlich dargestellt.

Dieser Beitrag beschränkt sich auf die Untersuchung der Besonderheiten des Abbrandverhaltens von CSP. Der Treibstoffabbrand unter Einsatzbedingungen bestimmt entscheidend: Einsatz, Leistung, Aufbau und Auslegung eines Raketenmotors. So setzt die Konzeption und Entwicklung eines CSP-Triebwerks fundierte Kenntnisse über das Abbrandverhalten (Umsatzgeschwindigkeit, Flammentemperaturen/-struktur, geometrische Verhältnisse ...) gefrorener Festtreibstoffe voraus. In einem ersten Schritt wurden folgende Ziele angestrebt:

- Reproduzierbare Anzündung
- Demonstration brennender Kryofesttreibstoffe
- Charakterisierung des Abbrandverhaltens

Theoretische Grundlagen

Zwei wichtige Kenngrößen für die Charakterisierung eines Teibstoffes sind seine Abbrandrate und die Anzündverzugszeit. Sie sind stark von der Treibstofftemperatur abhängig, die bei CSPs bis weit in den Helium-Kryostaten-Bereich reichen kann. Beide Größen sind weiterhin abhängig vom Energiefluss aus der Verbrennungszone $\dot{Q}$, den Stoff- und Reaktionseigenschaften und dem Druck.
Ausgangspunkt für die theoretischen Überlegungen ist die Differentialgleichung für den Wärmetransport in einem Feststoff.

$$\rho c_p \frac{\partial T}{\partial t} - \lambda \frac{\partial^2 T}{\partial x^2} = \dot{Q}[x,t] \qquad (1)$$

Wird Wärme auf die Oberfläche des Festkörpers übertragen, so kann für $\dot{Q}[x,t]$ als Dirac-Impuls beschrieben werden:

$$\dot{Q}[x,t] = \dot{Q}_0 \cdot \delta[x - x_0]$$

Dafür ergibt sich folgende Lösung für die Temperaturzunahme:

$$T[x,t] = \dot{Q}_0 \cdot \left(2 \cdot \sqrt{\frac{t}{\pi \lambda \rho c_p}} \cdot e^{\frac{\rho c_p x^2}{4\lambda t}} - \frac{x}{\lambda} \cdot \mathrm{Erfc}\left[x \cdot \sqrt{\frac{\rho c_p}{4\lambda t}} \right] \right) \qquad (2)$$

Häufig beansprucht die Zeit zum Aufheizen der Oberfläche (bei x=0) von der Anfangstemperatur T_0 bis zum Erreichen der Pyrolysetemperatur T_p den überwiegenden Teil der Anzündverzugszeit. Damit ergibt sich aus Gleichung (2):

$$t_{ign} \approx \frac{\pi \lambda \rho c_p (T_S - T_0)^2}{4 \dot{Q}_0^2} \qquad (3)$$

D.h. die Anzündverzugszeit t_{ign} ist quadratisch von der Differenz zwischen Oberflächentemperatur T_s (Pyrolyse- oder Verdampfungstemperatur) und der Anfangstemperatur T_0 abhängig. Eine schnelle und stabile Anzündung benötigt einen hohen Wärmeübertrag, der am einfachsten durch eine heiße Anzündung erreicht wird. Gl. (3) gilt jedoch nur, wenn während des Aufheizvorgangs keine Phasenumwandlung eintritt, was vor allem dann erfüllt ist, wenn der Brennstoff pyrolysiert, bevor er flüssig wird oder verdampft. Viele Stoffe müssen aber erst schmelzen und verdampfen, bevor sie in eine chemische Reaktion eintreten. Um Phasenumwandlungen zu berücksichtigen erweitert man Gl. (1):

$$\rho \left(c_p + \frac{\Delta_f h}{\sqrt{2\pi}\sigma_T} \cdot \mathrm{Exp}\left[-\frac{(T - T_m)^2}{2\sigma_T^2} \right] + \frac{\Delta_v h}{\sqrt{2\pi}\sigma_T} \cdot \mathrm{Exp}\left[-\frac{(T - T_s)^2}{2\sigma_T^2} \right] \right) \frac{\partial T}{\partial t} - \lambda \frac{\partial^2 T}{\partial x^2} = \dot{Q}_0 \cdot \frac{2}{\sqrt{2\pi}\sigma_x} \cdot \mathrm{Exp}\left[-\frac{x^2}{2\sigma_x^2} \right] \qquad (4)$$

In der obigen Differentialgleichung wurden die Phasenübergänge mit Hilfe von Gaußfunktionen (Halbwertsbreite σ -> 0) beschrieben. Auch die Energieübertragung auf die Oberfläche wurde hier mit einer Gaußfunktion beschrieben, da bei der numerischer Lösung der Differentialgleichung eine Deltafunktion unberücksichtigt bliebe. Abbildung 1 zeigt eine solche Lösung für Nitromethan. Die Lösung der Differentialgleichung kann nur die Aufheizphase bis zum Erreichen der Siedetemperatur T_s an der Oberfläche beschreiben, da sich beim Übergang in die Gasphase die Stoffparameter wesentlich ändern. Aus der numerischen Lösung der Differentialgleichung (4) läßt sich die Zeit bis zum Erreichen der Siedetemperatur ermitteln.

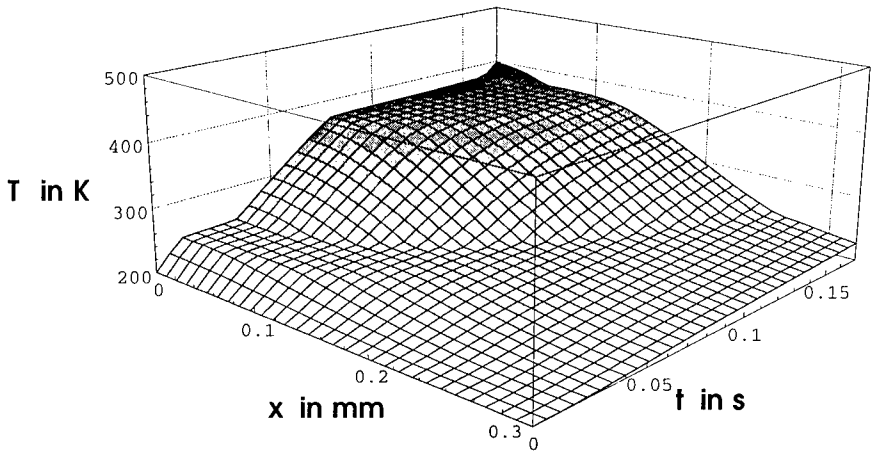

Abbildung 1: Dreidimensionale Darstellung der numerischen Lösung der Differentialgleichung mit Phasenumwandlung am Beispiel Nitromethan (ρ = 1130 kg/m³, c_p = 1710 J/kg/K, λ= 0.2165 W/m/K, T_m = 244 K, L_m = 159000 J/kg, T_s = 374 K, L_s = 548 000 J/kg, Δ_T = 1 K, Q_R = 1 000 000 W/m², σ_x = 10^{-4} m)

Beim stationären Abbrand kann die Zeitableitung $\partial T/\partial t$ in Gl. (1) über eine Koordinatentransformation durch den Term $-r \cdot dT/dx$ ersetzt werden. Damit ergibt sich dann folgende gewöhnliche lineare Differentialgleichung:

$$\rho r c_p[T]\frac{dT}{dx} + \lambda\frac{d^2T}{dx^2} = -\dot{Q}[x] + r\sum_i q_i\frac{dc_i}{dx}$$

Die Gleichung kann direkt integriert werden, wenn folgende zusätzlichen Bedingungen berücksichtigt werden:

- $T[\infty] = T_0$ Anfangstemperatur;
- $T[0] = T_s$ Temperatur an der Oberfläche (x = 0)
- $c_p = c_p + \Delta_f h \cdot \delta[T_s - T] + \Delta_v h \cdot \delta[T_m - T]$; (Phasenumwandlungen als Polstellen)
- $\lambda dT/dx = -Q_0$, bei x = 0 und
- $\lambda dT/dx = 0$ für $x \to \infty$
- $\dot{Q}[x] = b\,I\,e^{-bx}$; Strahlungsaufheizung
- $c_i[0] = 1$ und $c_i[\infty] = 0$; (vollständiger Stoffumsatz)

Aufgelöst nach der Abbrandrate r ergibt sich:

$$r = \frac{Q_o + I}{\rho\left(c_p \cdot (T_s - T_0) + \Delta_f h \cdot \theta[T_f - T_0] + \Delta_v h - \sum_i q_i\right)}$$

In Abbildung 2 wurden die nach dieser Formel bestimmten Abbrandraten in Abhängigkeit von der Anfangstemperatur T_0 für die Brennstoffe Isopropanol, Methanol und Nitromethan sowie für die Oxidatoren Wasserstoffperoxid, Distickstofftetroxid und Salpetersäure berechnet. Dazu wurden die Werte aus Tabelle 1 benutzt. Der auf den

Brennstoff rückgeführte und als konstant angenommene Wärmestrom Q_0 wurde unter Luft an Tankflammen der reinen Stoffe bestimmt und dürfte die bei Kryotreibstoffmischungen zu erwartenden Werte deutlich unterschreiten [4]. Die Ergebnisse sind daher exemplarisch für das zu erwartende Abbrandverhalten zu verstehen und sollen nicht die zu erwartenden absoluten Regressionsraten vorhersagen. Allerdings findet sich zumindest im Bereich über 270 K - für die am ICT Vergleichsmessungen durchgeführt wurden [4] - sowohl im Kurvenverlauf, als auch in der Größenordnung qualitative Übereinstimmung. Man erkennt, daß zumindest nach diesen einfachen Abschätzungen die Abbrandrate bei niedrigeren Temperaturen deutlich absinken kann.

Tabelle 1: Parameterwerte für die Berechnung der Abbrandraten. Die Q_0-Werte für Isopropanol, Methanol und Nitromethan [5]

Stoff	**Q_0 in W/m³**	**ρ in kg/m³**	**c_p in J/kg/K**	**T_v in K**	**$\Delta_v h$ in J/kg**	**T_f in K**	**$\Delta_f h$ in J/kg**
Isopropanol	24 000	782,7	2600	355	663 100	183	89 448
Methanol	32 000	787,2	2350	337,7	1 098 900	175	99 182
Nitromethan	37 000	1131,3	2440	374,4	629 050	244,6	159 063
H2O2	100 000	1442,5	2620	423,4	1 320 000	272,5	359 417
N2O4	100 000	1446,8	1550	294,3	414 500	252,0	156 352
Salpetersäure	100 000	1503,9	1745	358,5	569 355	231,5	166 308

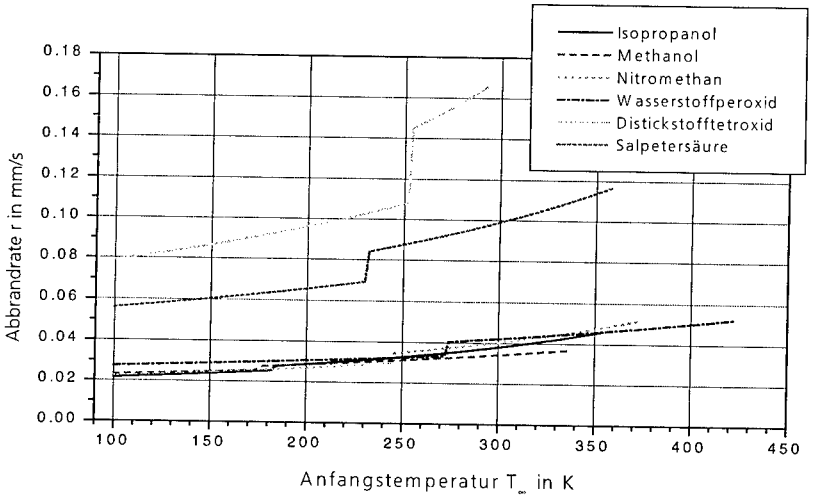

Abbildung 2: Verhalten der Abbrandrate r in Abhängigkeit von der Anfangstemperatur T_0 für Isopropanol, Methanol und Nitromethan. Die Abbildung zeigt den deutlichen Einfluß der Anfangstemperatur auf die Abbrandrate

Experimentelles

Stoffauswahl

Zur Leistungs- und Kostenoptimierung wird für reale Raketen angestrebt, Brennstoffe wie Wasserstoff oder Paraffine mit gefrorenem Sauerstoff zu oxidieren [2]. Diese Experimente sind allerdings wegen der hierfür benötigten aufwendigen Kryotechnik aus Kostengründen derzeit nicht durchführbar. Deshalb mußte bei den beschriebenen Untersuchungen auf Modelloxidatoren ausgewichen werden. Da sie bei tiefen Temperaturen die ähnliche physikalische Eigenschaften aufweien wie niedrige Anfangstemperatur im LN_2-Bereich, hohe Schmelz- und Verdampfungswärme, ausgeprägter Flüssigphasenbereich (große Differenz zwischen Schmelz- und Siedepunkt) erlauben auch diese Substanzen die Besonderheiten von CSP-Abbränden zu untersuchen. Auswahlkriterien für geeignete Oxidator/Brennstoff-Paare waren:

- Handhabbarkeit (Gefrierpunkt, Toxizität, Verfügbarkeit)
- thermodynamische Leistung ähnlich konventioneller FTS
- Gefrierpunkt höher als LN_2 (Flüssigstickstoff)
- Mischbarkeit, Verträglichkeit (speziell mono CSPs)
- Verträglichkeit (speziell mono CSPs)

Als Testsubstanzen wurden ausgewählt:

Brennstoffe: Methanol, Isopropanol, Isooktan, Nitromethan, Isopropylnitrat (IPN) Paraffin (flüssig und Wachs),
Oxidatoren: HNO_3, N_2O_4, H_2O_2 (70%), H_2O_2 (85%), Tetranitromethan (TNM)

Versuchsmuster und Durchführung

Mono-CSPs wurden in Stirnbrenneranordnung untersucht. Die Stoffe wurden flüssig vorgemischt, in PP-Hülsen ($Ø_i$=5 mm, L=40 mm) oder Glasrohre ($Ø_i$=6 mm, L=70 mm und $Ø_i$=20 mm, L=50 mm) eingefüllt und durch langsames Eintauchen in Flüssigstickstoff (LN_2) tiefgefroren. Zur Anzündung diente ein 5 mm langer Festtreibstoff, der mit einem Glühdraht angezündet wurde.

Als modulare Anordnungen wurden untersucht (Abbildung 3):

- 2- und 3-fach Sandwich mit horizontaler Abbrandoberfläche (Modulbreite 2 und 5 mm)
- mehrfach Sandwich (Organ-Pipe) in horizontaler und vertikaler Anordnung (Modulbreite 2 und 5 mm)
- Rod-In-Matrix mit horizontaler Abbrandoberfläche: 3 bis 7 Brennstoffstäbe (Ø=5 mm) eingebettet in Oxidatormatrix

Die einzelnen Module von Oxidator und Brennstoff waren meist, gegenseitig mit Kunststofffolien abgeschirmt (PP, PE, PET), standen aber bei manchen Versuchen auch in direktem Kontakt (besonders Rod-In-Matrix in der Druckbombe).
Zur Anzündung bzw. als Stützflamme diente ein Propanbrenner. Die Rod-In-Matrix-Anordnungen wurde in der Druckbombe über eine Anzündkaskade von Glühdraht, Composite-FTS und Mono-CSP angezündet.

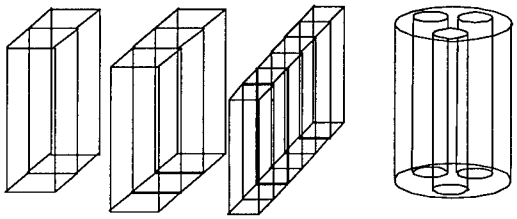

a) b) c) d)

Abbildung 3 Skizze der untersuchten modularen Anordnungen: a) 2-fach Sandwich, b) 3-fach Sandwich, c) Organ Pipe, d) Rod-In-Matrix

Alle Muster blieben nach der Entnahme aus dem LN_2-Kryostaten für etwa 5 bis 10 min gefroren. Durch Routine gelang es die Proben in einer Zeit von etwa 1 bis 2 min nach der Entnahme anzuzünden, so daß reproduzierbare Bedingungen erreicht wurden, in denen die Versuchsmuster noch ausreichend tiefgefroren waren.

Bei den Untersuchungen unter Umgebungsatmosphäre verhinderte die Ummantelung und der Stützbrenner einen nennenswerten Lufteintrag in die Reaktionszone.
Die Mono-CSPs und die modularen Rod-In-Matrix-Anordnungen wurden zusätzlich in einer Optischen Bombe unter Stickstoffdruck (bis 10 MPa) untersucht. Das System ist z.B. in [6] genauer beschrieben.

Ergebnisse

Mono-CSPs

Auch bei Temperaturen im LN_2-Bereich können CSP-Mischungen angezündet werden und es bildet sich eine stabile Verbrennungsfront aus. Bei den Versuchen gelang es viele Mischungen, die meist in etwa stöchiometrisch vorlagen, stabil anzuzünden. Dies galt ins besondere für fast alle Mischungen mit H_2O_2 (85%). Abbildung 4 zeigt Beispiele bei Mischungen von N_2O_4 mit IPN und TNM mit einem Paraffin. Mischungen mit HNO_3 waren sehr schlecht anzündbar. Eine stabile Anzündung erreicht man am leichtesten bei Mischungen deren Komponenten einen ähnlichen Siedepunkt aufweisen. Beim Abbrand bildet sich eine wenige Millimeter dicke Schmelzschicht konstanter Stärke.

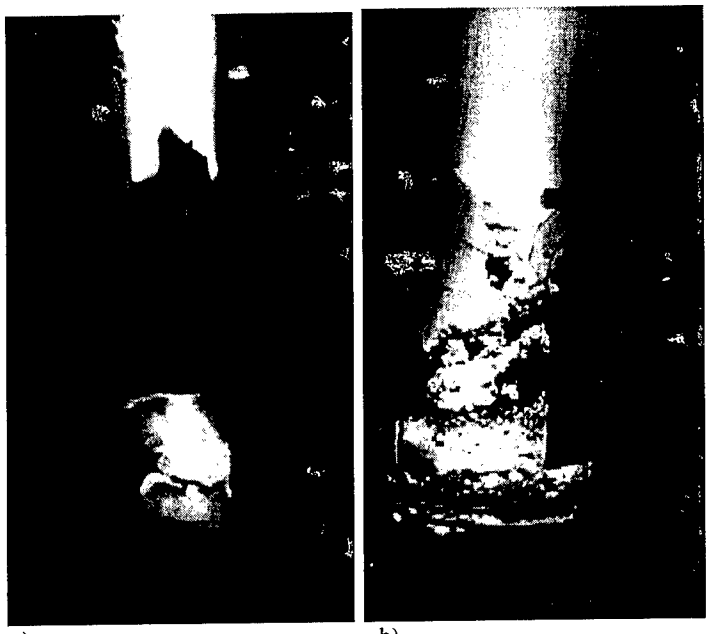

a) b)

Abbildung 4 CSP-Abbrand von gefrorenen Mono-CSP-Mischungen; a) N_2O_4/IPN, b) TNM/Isooktan

Auch in der Optischen Bombe lassen sich viele Mischungen unter N_2-Druck bis 10 MPa stabil anzünden. Abbildung 5 zeigt Beispiele mit H_2O_2 und Methanol. Es ergab sich ein linearer Abbrand mit konstanter Regressionsrate (Abbildung 6). Diese Abbrandraten waren bei Einhalten der Versuchsparameter (bes. T_0) sehr gut reproduzierbar und stiegen bei allen untersuchten Mischungen in einem potentiellen Druckgesetz mit konstantem Druckexponenten (nach Vieille) an. Abbildung 7 zeigt die Druckabhängigkeit der Abbrandrate für eine stöchiometrische Mischung von H_2O_2 (85%) mit 2-Propanol. Nur bei hohen Drücken kam es versuchsbedingt zu Ablösungen zwischen CSP und Behälterwand, was zu einem scheinbar überpotentiellen Druckanstieg führte. Auch unter Druck bildet sich an der Oberfläche eine Schmelzschicht konstanter Dicke, deren Stärke mit wachsendem Druck abnimmt

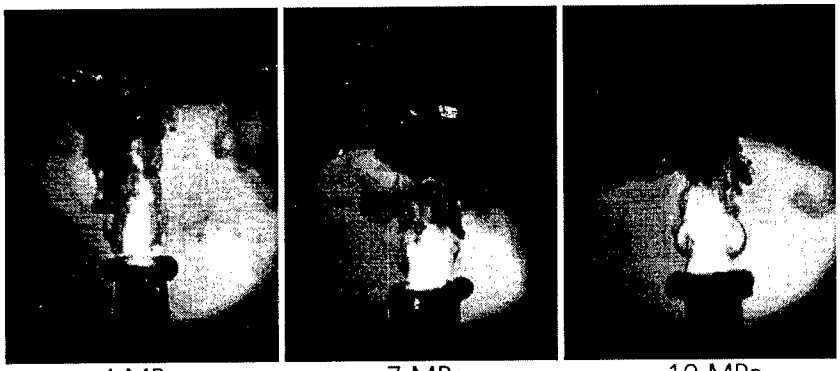

Abbildung 5 Abbrand von gefrorenen Mischung H_2O_2 (70%)/Methanol in der optischen Bombe bei 4, 7, 10 MPa in Stickstoff

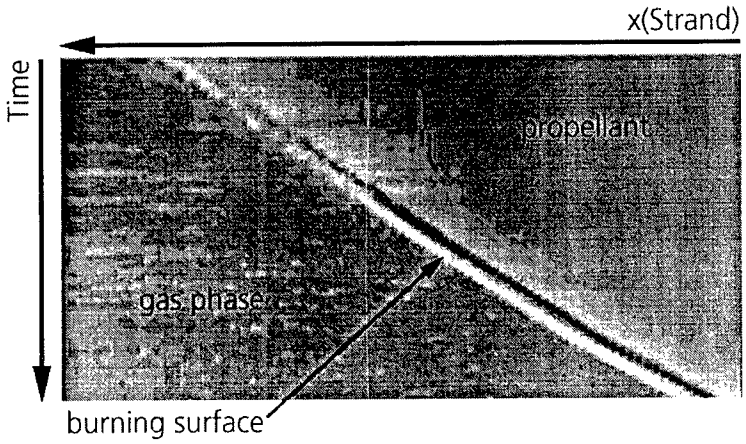

Abbildung 6 Zeitlicher Verlauf der Abbrandoberfläche am Beispiel von N_2O_4/IPN (2 MPa); Bildschirmausgabe der Bildanalysesoftware PULSAR

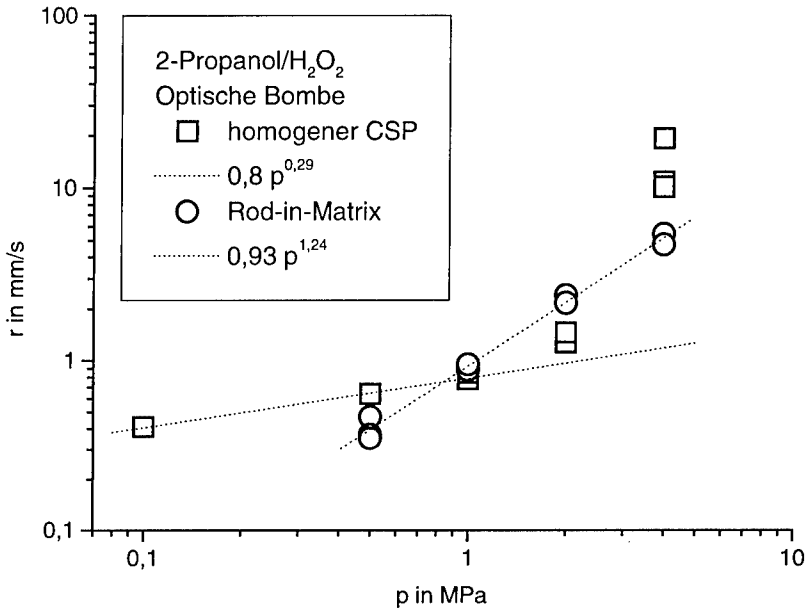

Abbildung 7 Druckabhängigkeit der Abbrandraten der stöchiometrischen Mischung von Isopropanol in H_2O_2 (85%) a) als Mono-CSP b) in einer modularen Rod-In-Matrix-Anordnung

Modulare Anordnungen

Auch modulare Anordnungen liesen sich stabil anzünden und brannten selbstkontrolliert mit einer linearen Regressionsrate ab. Dies galt sowohl für einfache Sandwich-anordnungen vom Typ Oxidator-Brennstoff und Oxidator-Brennstoff-Oxidator als auch für die Rod-In-Matrix-Anordnungen. Dabei bilden sich je nach Mischbarkeit der flüssigen Komponenten eine weitgehend einheitliche Flammenfront über der gesamten Treibstoffoberfläche (Abbildung 8a) oder einzelne Diffusionsflammen über der Unterschußkomponente (Abbildung 8b) aus.

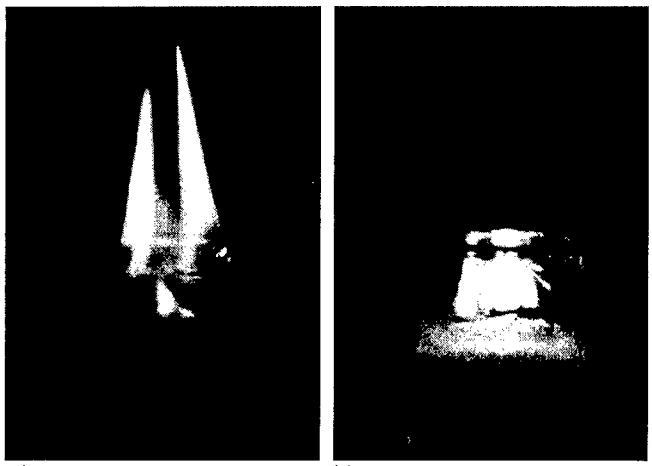

a) b)

Abbildung 8 Modulare CSP-Abbrände in Rod-in-Matrix-Anordnung mit jeweils 3 Brennstoffstäben.
a) flüssig mischbare Modulkomponenten bilden eine gemeinsame Flamme über der gesamten Abbrandoberfläche aus (Isopropanol/H_2O_2)
b) bei nicht mischbaren Komponenten stabilisieren sich einzelne Diffusionsflammen (Isooktan und H_2O_2)

Rod-In-Matrix unter Druck

In der Optischen Bombe wurden Rod-In-Matrix Anordnungen von 3 Isopropanolstäben in H_2O_2 (85%) unter Stickstoff-Druck untersucht. Die Overall-Bilanz der Mischung lag etwa beim stöchiometrischen Wert. Beim Abbrand bilden sich eine intensiv leuchtende Verbrennungszone ähnlich dem Abbrand von Composit-Treibstoffen. Mit steigendem Druck nähert sich die Flamme der Abbrandoberfläche (Abbildung 9), parallel dazu verringert sich die Dicke der Schmelzschicht an der Brennstoffoberfläche. Auch hier ergaben sich lineare Regressionsraten (Abbildung 10), die z. T. über denen der entsprechenden Mono-CSP lagen. Die Werte folgten einem Druckgesetz nach Vieille. Der Druckexponent lag über dem des entsprechenden Mono-CSPs (vgl. Abbildung 7)

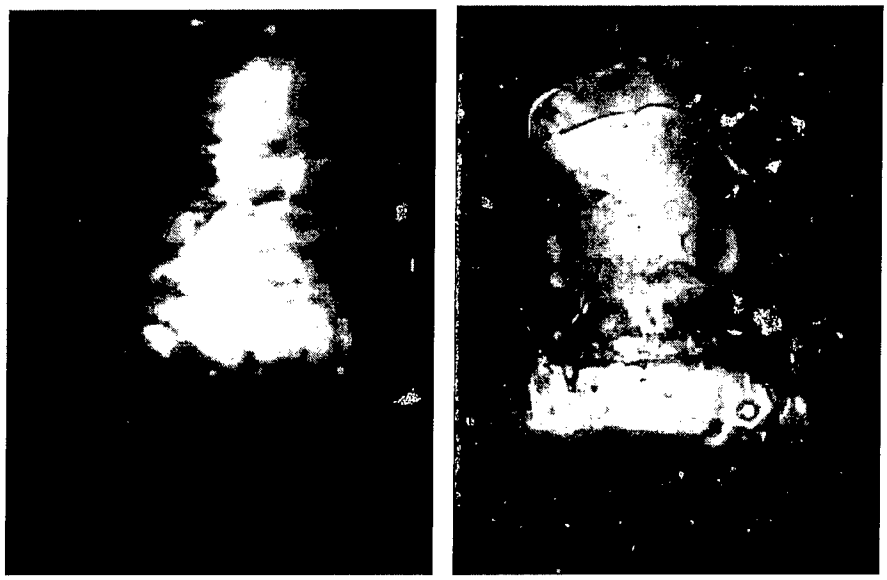

0.5 MPa 1 MPa

Abbildung 9 Rod-in-Matrix Abbrand mit 3 Isopropanol-Stäben in H_2O_2 unter Stickstoffdruck.

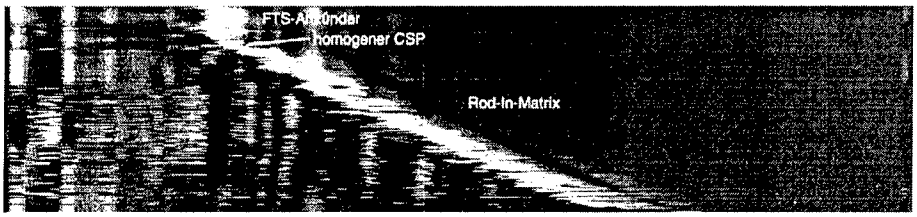

Abbildung 10 Regressionsverlauf mit Anzündkaskade eines Rod-In-Matrix-CSP-Brenners mit H_2O_2 und Isopropanol unter 0.5 MPa Stickstoff. (Pulsarauswertungen des CCD-Films). Die Abbrandfront verläuft von links oben nach rechts unten. Rechts der Linie ist der CSP. Man kann deutlich die Anzündkaskade mit Festtreibstoff und Mono-CSP vom Rod-In-Matrix-Abbrand unterscheiden. Auch dieser verläuft mit linearer Regressionsrate

Fremdkontrollierter Abbrand

Ein weiteres, angedachtes Scenario zum CSP-Abbrand ist, mit den heißen Schwaden eines Gasgenerators modular angeordnete CSPs definiert zu verdampfen und damit den Abbrand im Raketenmotor zu kontrollieren. Zur Untersuchung der Wirkung heißer Flammgase auf CSPs wurde ein Linearbrenner gebaut (Abbildung 11).
Grundsätzlich ergab sich der Nachweis, daß vertikal angeordnete CSP-Module durchaus über extern erzeugte Heißgase kontrolliert abbrennen können. An den Modulgrenzen bilden sich teilweise intensive Flammenzonen aus, die allerdings selbstkontrolliert

abbrennen. Für definierte Untersuchungen soll eine Brennkammer aufgebaut werden, die auch die Untersuchung des Druckabbrands erlaubt.

Abbildung 11 CSP-Abbrand in einer vertikal angeordneten Linearbrennkammer. Die CSP-Module werden mit den heißen Gasen eines Propanbrenner beflammt

Folgerungen und Ausblick

Das Abbrandverhalten sowohl von homogen vorgemischten als auch modular angeordneten CSP-Treibstoffen zeigt keine prinzipiellen Einschränkungen für die Verwirklichung realer Treibstoffmotoren. Für eine konkrete Auswahl eines technisch einzusetzenden CSP wird man ähnlich umfangreichen Forschungs- und Entwicklungsaufwand aufbringen müssen, wie er für die gegenwärtig eingesetzten flüssigen und festen Treibstoffe notwendig war. Dafür verspricht die CSP-Technologie deutlich effizientere Antriebssysteme.
Nächste Schritte bedürfen einerseits konkrete physikalische Modellierungen und den Aufbau einer realistischen Modellbrennkammer, die es erlaubt speziell modulare Systeme anwendungsbezogen zu testen.

Acknowledgment

Diese Arbeiten wurden dankenswerterweise vom Deutschen Zentrum für Luft- und Raumfahrt e.V. (DLR) und dem Bundesministerium für Bildung und Forschung (BMBF) gefördert.

Literatur

[1] Lo, R. E.; „A Novel Kind of Solid Rocket Propellant", Aerospace Science and Technology, Elsevier, 1998.

[2] Lo, R.; Adirim, H; Voronetzky, A; Weiser, V.; Eisenreich, N.; Kelzenberg, S.; Poller, S; Weiterführende und ergänzende Untersuchungen zur Kryofeststoff Triebwerkstechnologie; BMBF-Bericht zu Projekt PA-FA/RD-JR 50 TT 9812; März 2000

[3] Lo, R.; Adirim, H; Poller, S.; Eisenreich, N.; Weiser; V.; Kelzenberg. St; Advances in cryogenic solid rocket propulsion; 31st International Annual Conference of ICT, 2000, Karlsruhe, Paper 15 (accepted)

[4] Kelzenberg, St.; Eisenreich, N.; Eckl, W.; Weiser, V.; Modelling Nitromethane Combustion; Propellants, Explosives, Pyrotechnics 24; 189-194 (1999)

[5] Weiser, V.; Eisenreich, N.; Krause, H.; Experimentelle Untersuchungen von Flammengeometrie, Temperaturverteilung und Konzentrationsfeldern in Modell-Tankflammen verdampfender, flüssiger Brennstoffe; 22nd International Annual Conference of ICT 1991, S. 101-(1-14)

[6] Weiser, V.; Eisenreich, N.; Baier, A.; Eckl, N.; Burning Behaviour of ADN Formulations; Propellants, Explosives, Pyrotechnics 24; 163-167 (1999)

TI-NANOPARTIKEL ZUR ANZÜNDUNG VON ROHRWAFFENTREIBMITTELN

Volker Weiser, Andreas Koleczko, Stefan Kelzenberg,
Norbert Eisenreich, Dietmar Müller
Fraunhofer-Institut Chemische Technologie (ICT)
Joseph-von-Fraunhoferstr. 7
D-76327 Pfinztal (Berghausen), Germany

Abstract

TI-NANOPARTICLES TO IGNITE GUN POWDERS
The modelling of gun powder ignition using a hot-spot-model shows that smaller particles of the same temperature and mass fraction lead to a more effective ignition. Experiments with and without nano-particles of titan show the opposite effect. We conclude that inside the hot gas stream small particles vaporise before hitting the surface of the powder. So nano-particles with higher boiling point should be used.

Zusammenfassung

Die Modellierung von Anzündvorgängen bei Rohrwaffentreibmitteln mit einem Hot-Spot-Modell ergibt, daß bei gleicher Temperatur und Gewichtsbeladung viele kleine Schwadenpartikel zu einer effektiveren Anzündung führen. Vergleichende Experimente mit zwei Anzündmischungen gleicher Zusammensetzung mit und ohne Ti-Nanopartikel ergeben einen entgegengesetzten Effekt. Anscheinend muß auf Metallpartikel zurückgegriffen werden, deren Siedepunkt über der Verbrennungstemperatur des AZM liegt.

Einleitung

Neue, wenig empfindliche Treibmittel unterscheiden sich in ihrem Anzündverhalten zum Teil erheblich von eingeführten Treibladungspulvern. So vermindert bei Nitraminen die höhere Pyrolysetemperatur und die Phasenumwandlung die Anzündfreudigkeit der Pulver. Dies erfordert eine intensive Charakterisierung des Anzündverhaltens neuer Rohrwaffentreibmittel und die Anpassung und Optimierung der pyrotechnischen Anzündsätze, um ein schnelles und definiertes Anzünden des Treibladungspulvers zu gewährleisten. Als beeinflußbare Wirkparameter des Anzündmittels (AZM) gelten Temperatur, Gaszusammensetzung, Schwaden/Partikelverhältnis sowie Größe und Anzahl der Partikel [1], [2].
In diesem Beitrag steht die Untersuchung der Wirkung von Größe und Anzahl der auf die TLP-Oberfläche auftreffenden Schwadenpartikel im Vordergrund.

Hot-Spot-Modell

Ausgangspunkt für die Beschreibung ist die Wärmeleitungsgleichung (vgl. [3],[4]):

$$\rho c_p \frac{\partial T}{\partial t} - \lambda \cdot \Delta T = \dot{Q}[\vec{x}, t] + \sum_i q_i \frac{\partial c_i}{\partial t}$$

In einem inerten Medium ohne chemische Reaktionen können Lösungen für eingebrachte Wärmequellen $\dot{Q}[\vec{x}, t]$ durch Integration mit der Green'schen Funktion [5] gefunden werden:

$$T[\vec{x}, t] = \int_0^t \int_{-\infty}^{\infty} \left(\frac{\rho c_p}{4\pi\lambda(t-t')} \right)^{3/2} \cdot e^{-\frac{\rho c_p (\vec{x}-\vec{x}')^2}{4\lambda(t-t')}} \cdot \frac{\dot{Q}[\vec{x}', t']}{\rho c_p} d^3x' dt'$$

Wärmequellen sind in dem hier zu betrachtenden Fall die verschiedenen Partikel. Da sie den größten Teil ihrer Energie erst dort abgeben, wo sie zur Ruhe kommen, können sie als Hot-Spots angesehen und durch Dirac'sche Deltafunktionen beschrieben werden:

$$\dot{Q}[\vec{x}', t'] = \sum_i Q_i \cdot \delta[\vec{x}' - \vec{x}_i] \cdot \delta[t' - t_i]$$

Für die so beschriebenen Hot-Spots kann eine analytische Lösung angegeben werden. Für $t > t_i$ ergibt sich:

$$T_{hs}[\vec{x}, t] = \sum_i \left(\frac{\rho c_p}{4\pi\lambda(t-t_i)} \right)^{3/2} \cdot \frac{Q_i \cdot e^{-\frac{\rho c_p (\vec{x}-\vec{x}_i)^2}{4\lambda(t-t_i)}}}{\rho c_p} \qquad (1)$$

In einem reaktiven Medium muß zusätzlich der Umsatzmechnanismus beschrieben werden. Benutzt man dazu den Ansatz nach Arrhenius,

$$\frac{\partial c_i}{\partial t} = -\sum_j A_{i,j} \cdot e^{-\frac{E_{i,j}}{RT}} f[c_i, c_j]$$

lassen sich die entstehenden Integrale nur noch numerisch lösen. Im vorliegenden Modell wird dazu die Green'sche Funktion genutzt. Aus der anfänglichen Verteilung der Hot-Spots berechnet sich die Anfangstemperaturverteilung $T_0[x,0]$ gemäß Gl. (1). Während eines Zeitschritts Δt verteilt sich die Wärme der Hot-Spots. Gleichzeitig wird Wärme durch die chemischen Reaktionen des Mediums freigesetzt und verteilt sich ebenfalls. Daraus ergibt sich für den n-ten Zeitschritt folgendes Integral Gl. (2), das numerisch berechnet wird.

$$T_n[\vec{x}, t_n] = \int_{-\infty}^{\infty} \left(\frac{\rho c_p}{4\pi\lambda(t-t_n)} \right)^{3/2} \cdot \frac{e^{-\frac{\rho c_p (\vec{x}-\vec{x}')^2}{4\lambda(t-t_n)}}}{\rho c_p} \cdot \left(\sum_i Q_i \delta[\vec{x}' - \vec{x}_i] + \Delta t_n \sum_j q_j \frac{\partial c_j[T_{n-1}[\vec{x}', t_{n-1}]]}{\partial t} \right) d^3x' \qquad (2)$$

Dabei wird die Temperaturverteilung aus dem (n-1)-ten Zeitschritt verwendet den Reaktionsfortschritt zu berechnen. Die Abbildungen 1a und 1b zeigen Momentaufnahmen nach 15 Zeitschritten. In Abbildung 1a wurden mehrere kleine Partikel und in Abbildung 1b wenigere große Partikel angenommen. Der Gesamtenergieeintrag durch die Partikel war in beiden Fällen gleich. Es ist deutlich erkennbar, daß bei den kleinen Partikeln (Abbildung 1a) die Reaktion gleichmäßiger verläuft als bei den großen (Abbildung 1b).

Die Modellierung der Anzündvorgänge mittels des beschriebenen Hot-Spot-Modells ergibt, daß bei gleicher Temperatur und Gewichtsbeladung viele kleine Schwadenpartikel zu einer gleichmäßigeren und schnelleren Anzündung führen als wenige grobe. Feine Partikel führen schneller zu einer stetigen Umsatzgeschwindigkeit (Abbildung 1c).

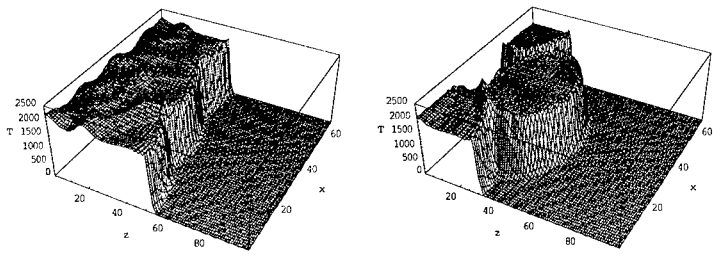

a) b)

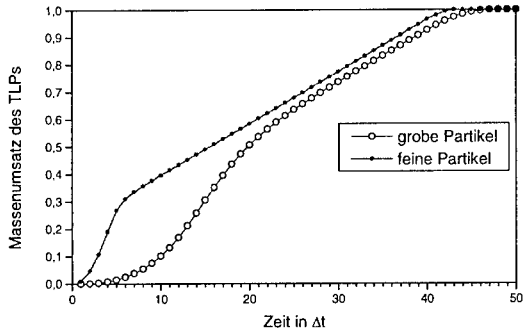

c)

Abbildung 1 Momentaufnahme des Verlaufs der Reaktionsfront in einem TLP, angezündet durch a) viele kleine und b) wenige große Partikel. c) Zeitlicher Verlauf des Massenumsatzes des Pulvers.

Experimentelle Untersuchungen

Erst seit jüngster Zeit stehen von einigen für die Anzündung interessanten Metallen wie Titan, Wolfram und Zirkon feinste Partikel (sog. Nanopartikel) in definierten Korngrößen mit ≤1 µm in ausreichender Menge zur Verfügung [6]. Untersuchungen in einer Mikrosonde ergaben:

- Die Partikelgröße liegt in einem Bereich von <200 bis 2000 nm
- Die Gestalt der Partikel ist annähernd kugelförmig (Abbildung 2)
- Trotz der großen spezifischen Oberfläche ist der Oxidanteil ähnlich oder z. T. sogar geringer als bei konventionellen Vergleichsproben

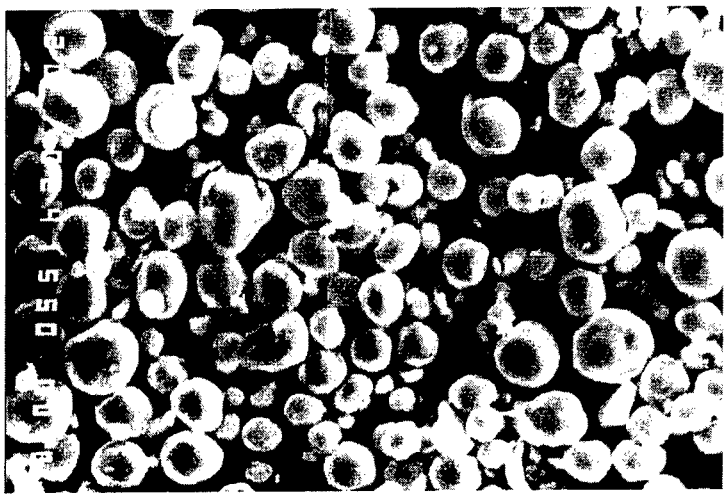

Abbildung 2 Feinste kugelförmige Titanpartikel

So sind die Voraussetzungen für den Einsatz in einem AZM gegeben, die eine gleichmäßigere Anzündung und einen besseren Partikeldurchgriff erwarten lassen.
Hergestellt wurde ein als AZ-1F bezeichnetes AZM, das diese feinen Titan-Partikel enthält, dessen Zusammensetzung sich schon früher zur Anzündung von neuen TLPs bewährt hat [7]. AZ-1 besteht aus KNO_3, Ti und GAP. Als Referenz wurde ein AZM gleicher Zusammensetzung mit einem Sauterdurchmesser von 15 µm hergestellt (AZ-1G). Beide AZM wurden im Vergleich zu Schwarzpulver und B/KNO_3 geschossen.
Leider liegen die Nanopartikel immer noch in begrenzten Mengen vor, so daß nur Untersuchungen im Kleinmaßstab durchgeführt werden konnten. Untersucht wurden:

- Verbrennungstemperatur, Schwadenstrahl:
  2-Farbenpyrometrie und Spektroskopie (Analyse der Kontinuumsstrahlung im UV/Vis und NIR)
- Qualität der auftreffenden Partikel:
  Schwadenstrahl trifft auf einen kalten, polierten Kupferblock. Mit einer Mikrosonde werden die erstarrte Schlacke und die Einschlagkrater auf der gereinigten Kupferoberfläche untersucht
- Druckaufbau des AZM in einer Anzündbombe (Δ=0.3)
- Anzündwirkung auf TLP (JA-2, NENA-TLP, GAP-TLP und Semi-Nitramin TLP):
  Druck/Zeit-Kurve, Anzündverzugszeit

Die beiden letzten Untersuchungen fanden in einer speziell modifizierten Minibombe mit zwei getrennten Kammern für AZM und TLP statt (Abbildung 3). Sie erlaubt wahlweise die optische Beobachtung der Schwaden oder die Messung des Druckaufbaus in der TLP-Kammer.

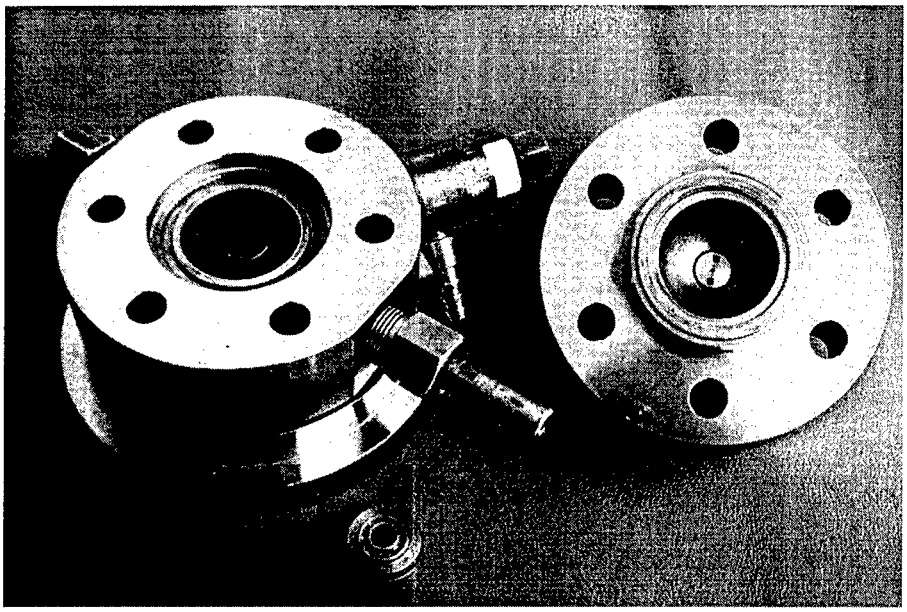

Abbildung 3 Minibombe zur Untersuchung der Wirkung von Anzündmittel auf Treibladungspulver

Ergebnisse

Die Druck/Zeit-Kurven zeigen, daß beide AZ-1 ähnlich schnell abbrennen, wie SP oder B/KNO_3. Der Maximaldruck wird reproduzierbar bei allen AZM nach 2.5 bis 5 ns erreicht. Bei Schüssen ohne TLP liefert AZ-1F einen um etwa 30% höheren Maximaldruck als das AZM mit gröberem Titan.

Das Anzündverhalten wurde an 4 verschiedenen TLPs: NENA-TLP, GAP-TLP und Semi-Nitramin TLP untersucht. Als Referenz diente JA-2.

Der Verlauf der Druck/Zeit-Kurve zeigt sehr schön getrennte Stufen zwischen dem Druckaufbau des AZM und dem des TLPs (Abbildung 4). Damit war eine Ermittlung der Anzündverzugszeit möglich. Alle AZM ergeben eine ordentliche Anzündung nach 40 bis 120 ns. B/KNO_3 lag meist zwischen den Anzündverzugszeiten von AZ-1G und AZ-1F. Bei allen TLPs benötigte SP die längste Anzündzeit.

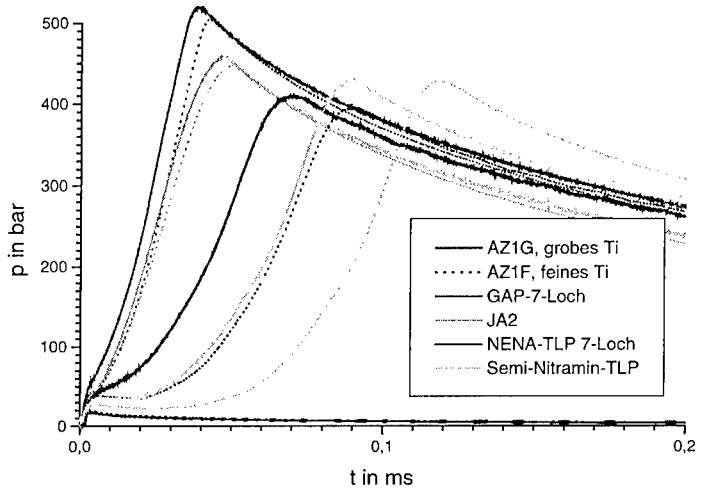

Abbildung 4 Druckverlauf in der Minibombe bei der Anzündung verschiedener TLPs mit und ohne Ti-Nanopartikel

AZ-1F mit Nanopulver zündet die TLPs etwa 10 bis 20 ns langsamer an als das grobkörnige AZ-1G. Dies steht im Widerspruch zu den Erwartungen und den in sich schlüssigen Modellberechnungen.
Die adiabate Verbrennungstemperatur von AZ-1 liegt nahe dem Siedepunkt von Titan bei 3533 K und der Titanoxide. Die pyrometrischen Messungen der Schwadentemperatur bestätigen dies. So muß vermutet werden, daß sich die Nanopartikel aufgrund ihrer kleinen Abmessungen schneller vollkommen aufheizen und dadurch sofort im heißen Schwadenstrahl verdampfen, bevor sie auf das TLP auftreffen und daher nicht mehr als Partikel für die Anzündvorgänge zur Verfügung stehen. Eine Verdampfung der feinen Ti-Partikel erklärt auch den höheren Maximaldruck in der Minibombe bei AZ-1F ohne TLP. Diese Vermutung wurde auch durch die Kupferblockschüsse bestätigt. Sie zeigen bei AZ-1F deutlich mehr geschmolzene Schlacken als AZ-1G. Die Einschlagkrater durch AZ-1F sind kleiner als bei den anderen untersuchten AZMs, aber auch seltener.

Weiterführung

Will man die Idee einer schnellen und gleichmäßigen Anzündung durch Nanopartikel weiter verfolgen, muß man auf Metalle zurückgreifen deren Siedepunkt höher ist als die Verbrennungstemperatur des AZM. Dabei ist geplant Wolfram und Zirkon-Partikel einzusetzen, die mit 5830 K und 4680 K einen wesentlich höheren Siedepunkt aufweisen und ebenfalls als Nanopulver verfügbar sind.

Literatur

[1] Rochat, E.; Berger, B.; Unempfindliche Anzündmittel für moderne Treibladungspulver; 30th International Annual Conference of ICT, 1999, Energetic Materials; Karlsruhe, pp. 24-1 – 75-15

[2] V. Weiser, D. Kuhn, R. Ludwig, H. Poth; Einfluß der Partikelgröße auf das Abbrandverhalten von B/KNO3-Anzündmischungen; 29th International Annual Conference of ICT, 1998, Energetic Materials; Karlsruhe, pp. 75-1 – 75-12

[3] G. Langer, N. Eisenreich; Hot-Spots in Energetic Materials; Propellants, Explosives, Pyrotechnics, Vol. 24, Nr. 3/99 pp.113-118 (1999).

[4] N. Eisenreich; Successively Initiated Arrays of Hot Spots in a Reactive Medium; Proceedings Physics of Explosives, DEA-AF-71-F/G-7304, Berchtesgaden, Sept. 29-Oct. 1, 1997.

[5] H. S. Carslaw, J. C. Jaeger; Conduction of Heat in Solids, 2nd ed.; Clarendon Press, Oxford (1973).

[6] Ivanov, G. V.; Ivanov, V. G.; Surkov, V. G; Gawrilyuk, O. V.; Nonosize eloctro-explosion powders: assessment of safety in the production and application; Prevention of Hazardous Fires and Explosions – The Transfer to Civil Applications of Military Experiences; NATO Science Series; – Vol. 26, Kluwer Academic Publishers; p.329-340

[7] Müller, D.; Weiser, V.; Ebeling, H.; Eisenreich, N.; Neue Anzündmittel für TLANZ Kal. 76 mm, ICT-Bericht 9/95

[8] Baier, A.; Weiser, V.; Eisenreich, N.; Halbrock, A.; IR-Emissionsspektroskopie bei Verbrennungsvorgängen von Treibstoffen und Anzündmitteln; 27th International Annual Conference of ICT, 1996, Karlsruhe, pp. 84-(1-12)

SYNTHETIC MACROMOLECULAR COMPOUNDS

Dr. M.J. Freiría Gándara
Fernández Areal nº 50
Porriño, Pontevedra (Spain)

SUMMARY

Synthetic macromolecular compounds include: elastomers, which have the particular kind of elasticity characteristic of rubber; fibers, long, thin, and thredlike, with the great strength along the fiber that characterizes cotton, wood, and silk; and plastics, which can be extruded as sheets or pipes, painted on surfaces, or molded to form countless objects.

Low-density polyethylene (density lower than 0.94 gmL^{-1}) had a total annual production in the United States of 4.7 MT in 1988. Half of this production goes into the manufacturing of films, half of which are used for packages in different forms (50% for industrial and commercial use, 50% for food packaging and litter bags).

High-density polyethylene (density higher than 0.94 gmL^{-1}) was produced in the range of 3.4 MT in 1987 (US). Its major use is to manufacture containers: bottles for milk, orange juice, non-gaseous drinks, antifreeze, motor oils, etc.

Polypropilene (total US production in 1988: 3.8 MT) is used mainly for packaging: mold injection stoppers, capsules, etc., meant for containers made from other plastics; for the manufacture of fibres and filaments. The latter are used in textiles and rugs.

Polyvinyl chloride (PVC: total US production in 1988: 3.8 MT) is used mainly as a construction material, siding, pipes, etc. But there are numerous other uses, from records to toys. Its production has stagnated for several reasons: carcinogenic monomer; overcapacity; recession of the building industry; difficulty in recycling as compared to other polymers such as polyesters.

Polystyrene (annual US production in 1988: 2.3 MT) has applications similar to polyethylene. Polystyrene and copolymers are used in the packaging, building and furniture industries.

ADN – A NEW OXIDIZER FOR SMOKELESS ROCKET PROPELLANTS

Christer Lagerstam, Dr. Per Sjöberg
NEXPLO Bofors AB
SE-691 86 Karlskoga
SWEDEN
E-mail: per.sjoberg@nexplo.se

Abstract:

ADN has now been tested by a large number of rocket formulaters. It is today regarded as the most likely oxidizer for the next generation of signature free and high impuls rocket motors. The applicability for ADN and the production capacity at NEXPLO Bofors will be described in this poster.

DADNE (FOX7) – a new high explosive for IM. NEXPLO Bofors will this year start to produce diaminodinitroethene in the scale from 10 – 100 kilo. The applicability for DADNE as a high explosive will be described in this poster.

Welcome to our poster for technical discussions as well as quantities and delivery times for samples.

Analysis and Test Methods for Service Life Prediction of Energetic Materials

Geißler, Egon; Eisenreich, Norbert; Geißler, Adam; Hübner, Christof

Fraunhofer-Institut für Chemische Technologie ICT
Joseph-von-Fraunhofer-Str. 7
D-76327 Pfinztal

Summary

Aging behaviour of energetic materials is correlated with a change in mechanical properties. The aging process e. g. leads to a decrease in stiffness and an embrittlement of the material. Background of the aging process are micromechanical phenomena. Therefore the characterization and understanding of micromechanical phenomena like matrix-filler detachment are the key to the understanding of aging behaviour of energetic materials. These micromechanical phenomena influence both the mechanical behaviour and the sensitivity to impacts of energetic materials. In this paper different methods to study the aging behaviour of energetic materials and the correlation to micromechanical phenomena are described. Furthermore the influence on the macroscopic observable mechanical properties and the service life time is discussed.

1. Introduction

Modern solid rocket propellants, gun powder or special kinds of explosives are made of composite materials. These energetic materials are composed in the same way: relative hard particles are dispersed in a relatively soft matrix material. The matrix material has to fulfil two main tasks: (1) it burns during the service of the propellant and (2) it gives the mechanical stability to the compound. The particles deliver the oxygen for the burning and contribute to the production of energy by containing burnable substances. Therefore the composition of the energetic material is strongly influenced by the demand of their energetic properties. On the other side a suitable mechanical stability of the system is necessary for proper service. Mechanical failure of energetic materials can cause catastrophic failures of rocket motors or guns.

During service life the rocket propellant, the gun powder or other kinds of explosives have to survive the rigors of the environmental loads through mechanical and climatic conditions. The energetic material in the system is loaded by impacts, vibrations, temperature cycles and humidity.

These loads lead to a change in the microscopic structure of the energetic material. Matrix-filler debonding happens. These causes an increase in surface due to cracks or matrix-filler-debonding which could lead to an unwanted extreme increase in burning rate. This increase in burning rate causes a pressure rise and could lead to a catastrophic failure.

2. The Effect of Matrix-Filler Debonding

The most important phenomena which can cause severe problems during the service of energetic materials is the detachment of the matrix and filler surface [7,16,17]. This detachment does not only lead to a weakening of the material, a decrease of the modulus and an increased inclination to break, but can also produce vacuoles in the material. Breakage which occur when the propellants or the gun powder burn can cause an immediate pressure rise and therefore lead to a catastrophic failure in the system.

The vacuoles which are formed by a detachment increase the impact sensitivity even if no breakage occur. They are filled with gases which sort from the matrix or the filler e. g. absorbed humidity. At the event of a strong mechanical impact due to rough handling or a projectile, these gases are very rapidly compressed and as a consequence heat up to temperatures which can ignite the energetic material.

Due to this big importance, the interface of matrix and filler deserves a special attention. Therefore in the next chapter, modern methods for detection of cracks in the matrix-filler interface are reported and discussed in view of their applicability for energetic materials.

3. Detection of Matrix-Filler debonding

3.1. Detection of Matrix-Filler Debonding by Measurement of the Material Properties

The process of aging is correlated to a change in material properties. Cracks can be detected in a standard tensile test due to their weakening of the material. Whether the weakening is really due to cracks, has to be determined by separate methods.

In the Fraunhofer ICT the Poisson Ratio was measured with a non contact laser optical system. In this experiments composite propellants which were predamaged by matrix-filler detachment where tested. The specimen with matrix-filler detachment show a decrease in Poisson Ratio [22,23,24,25,26].

3.2. Finite Element Modelling of the Matrix-Filler Debonding

For the simulation of the effect of debonding of the matrix material from the filler surface on Poisson's Ratio, a three-dimensional FEM model of a elementary cell of a composite propellant was developed by Fraunhofer ICT [1,2,3,4,5,6]. It consists of a rigid filler particle modelled as a sphere enclosed in an elastic matrix material, representing the smallest repeating unit of the microstructure of the material. The filler content was modelled by different ratios of the diameter of the sphere to the size of the elementary cell. The composite propellant is thought to be built up by an assembly of these elementary cells. In the calculations the sides of the elementary cell were forced to stay plane during deformation. This is a necessary prerequisite, because a deformation of the side planes would hinder a combination of several elementary cells to a composite material. With this condition, the result for a single elementary cell is valid for the complete material consisting of many elementary cells, which stands for a composite material with a spherical monomodal and uniformly distributed filler. For the calculation only 1/8th of the total cell was modelled due to symmetry in order to save calculation time. In figure 1, the described eighth of the undeformed elementary cell with 15% filler content can be seen. The dark grey area is the rigid filler and the light grey area is the matrix material.

Four states in view of the detachment of the matrix from the filler surface were defined:

- Perfect adhesion (The matrix adheres perfectly on the filler surface)
- Onset (The matrix has detached from 25% of the filler surface)
- Dewetting (The matrix has detached from 50% of the filler surface)
- Total dewetting (The matrix has detached completely from the filler surface)

For these four stages of dewetting calculations of Poisson's Ratio for the elementary cell were performed. The matrix material was modelled by material properties depending on the prestrain, the filler material was regarded as rigid [8]. The deformation was performed by a force acting in Y-direction uniformly on the upper surface of the cell.

As can be seen, an onset of dewetting leads at a given strain to a decrease of Poisson's Ratio (Figure 2). This principle result was already measured with sample propellants of the respective filler contents [22,23,24,25,26]. The explanation for this result is the decrease of the load carrying cross section of the stressed material and the increased production of volume due to the higher amount of detached filler surface in the materials with higher filler contents during elongation.

3.3. Microscopy

Microscopy is a classic method for the detection of cracks in composite materials [20]. The materials must be prepared for the detection of the failures which in many cases causes artefacts. Especially in elastometric materials, cracks which occurred between filler and matrix during loading can close again when the material is unloaded again (Figure 3). Furthermore in most cases, the investigation is only possible in the surface of the material.

3.4. NMR Imaging of Energetic Materials

NMR imaging has become a common method in medical diagnostics for years. The application of NMR imaging in material science is very new. NMR allows a view through the surface into the material. If these method is coupled with tomography, a 3-D picture of the bulk material is possible in special cases. Nowadays the spatial resolution of NMR imaging (10μm and more) is limited compared to other imaging and microscopic methods. The matrix-filler debonding of single particle could not be resolved. But it is possible to observe the agglomerates of the filler particles (Figure 4). NMR imaging is extremely useful to map local variations in composition, matrix filler interaction and cross-link density.

4. Constitutive Equations for Finite Element Modelling of Dynamic Loads

To analyse the aging behaviour of energetic materials numerically, the finite element method (FEM) is used. For this purpose suitable constitutive equations must be developed with respect to their special loading conditions. The mechanical behaviour under vibration conditions of these compounds is characterized by a dynamic moduli which depend on the static preload [10,11,12,13,14,15,18,19].
When a viscoelastic material like a solid propellant is deformed dynamically, one part of the deformation energy is stored and an the other part is dissipated as heat. This material behaviour for a given prestrain and an excitation frequency f_0 can be described by a complex modulus:

$$E(\varepsilon_{xx}, f_0) = E'(\varepsilon_{xx}, f_0) + i\, E''(\varepsilon_{xx}, f_0)$$

With an absolute value of

$$|E(\varepsilon_{xx}, f_0)| = (E'(\varepsilon_{xx}, f_0)^2 + E''(\varepsilon_{xx}, f_0)^2)^{1/2}$$

where $E'(\varepsilon_{xx}, f_0)$ is the storage moduli which describes the reversible material behaviour; and the irreversible behaviour is described by $E''(\varepsilon_{xx}, f_0)$, the loss moduli. The quotient of these values

$$\tan[\delta(\varepsilon_{xx}, f_0)] = E''(\varepsilon_{xx}, f_0) / E'(\varepsilon_{xx}, f_0)$$

is an expression for the damping behaviour of the material. The dynamic behaviour of the investigated viscoelastic material was characterized through this material properties. In [10,11,12] is shown that the basic parameters needed to obtain sufficient material description for dynamic analysis of nonlinear viscoleastic structures. With this constitutive law the frequency response of structure can be calculated.

5. Conclusions

The measurement of material properties is a quick simple and valuable method to examine the aging behaviour of energetic materials [9]. Especially the determination of Poisson's Ratio is a powerful method for the determination of dewetting in energetic materials. It is relatively simple to perform and gives additional information for the use of FEM methods for the development of energetic systems. The use of FEM methods for the calculation of the mechanical properties of energetic materials is a meaningful support of the determination of the mechanical properties of energetic materials in view of a correct interpretation of the measured values.

NMR imaging and microscopy deliver valuable information of the morphology of energetic material during aging. Especially NMR imaging offers new aspects of examining aging behaviour.

The macroscopic behaviour of the material can be described by constitutive equations which are used to calculate the dynamic behaviour with a finite element programme.

References

[1] Geißler, Egon; Hübner, Christof
Einsatz der Methode der Finiten Elemente zur Berechnung des Deformationsverhaltens von gefüllten Polymeren.
MARC Benutzertreffen, 28.-29. Oktober 1999, München, Paper 16, 1999.

[2] Hübner, Christof; Geißler, Egon
Finite element modelling of matrix-filler debonding of energetic materials.
Fraunhofer-Institut Chemische Technologie, Pfinztal, D-76327, Germany, 30th International Annual Conference of ICT 1999, p 99.1-99.15, 1999.

[3] Hübner, Christof; Geißler, Egon; Elsner, Peter; Eyerer, Peter
The importance of micromechanical phenomena in energetic materials.
Propellants, Explosives and Pyrotechechnics, (1999), 24(3), 119-125, 1999.

[4] Geißler, Egon; Hübner, Christof
A finite element based unit cell model to analyse the deformation behaviour of filled polymers.
International Union of Pure and Applied Chemistry, 1998 Prague Meetings on Macromolecules, 18th Discussion Conference, Paper PC 7, 1998.

[5] Geißler, E.; Hübner, C.
Finite-element simulation of the micromechanics of solid propellants and gun propellants.
Fraunhofer-Institut Chemische Technologie, Pfinztal, D-76327, Germany, 29th International Annual Conference of ICT 1998, p 83.1-83.11, 1998.

[6] Geißler, Egon; Hübner Christof
Finite Elemente Modellierung der Mikromechanik von gefüllten Polymeren.
MARC Benutzertreffen, 28.-29. Oktober 1999, München, Paper 9, 1998.

[7] Lohrmann, M.; Hübner, Ch.
The influence of the matrix-filler-interaction on the mechanical properties of filled elastomers.
Fraunhofer-Inst. Chemische Technologie (ICT), Pfinztal-Berghausen, D-76327, Germany, 27th International Annual Conference of ICT 1996, p140.1-140.12, 1996.

[8] Hübner, Christof
Ermittlung eines zweidimensionalen zeit- und deformationsabhängigen Materialgesetzes für gefüllte Elastomere unter Berücksichtigung von Phasengrenzflächenphänomenen.
Diss., Universität Karlsruhe (T. H.), 1994.
In wissenschaftlicher Schriftenreihe des ICT, Bd. 10, Pfinztal, 1994.

[9] Husband, D. Mark
Use of dynamic mechanical measurements to determine the aging behaviour of solid propellant.
Propellants, Explosives and Pyrotechnics, v 17 n 4 Jul 1992, p 196-202, 1992.

[10] Geißler, Adam; Geißler, Egon
Dynamic behavior of composites under preloading.
Propellants, Explosives and Pyrotechnics, v 17 n 4 Jul 1992, p 211-213, 1992.

[11] Geißler, Egon
Anwendungung eines speziellen Stoffgesetzes für nichtlinear viskoelastische Werkstoffe in einem Finite Elemente Programm.
Diss., Universität Karlsruhe (T. H.), 1992.
In wissenschaftlicher Schriftenreihe des ICT, Bd. 3, Pfinztal, 1992.

[12] Geißler, Adam
Dynamische Verhalten von compoundierten Kunststoffen unter Vorbelastung, dargestellt am Beispiel eines geschlossenzelligen Schaumstoffes und eines hochgefüllten Kunststoffes.
Diss., Universität Karlsruhe (T. H.), 1991.
In wissenschaftlicher Schriftenreihe des ICT, Bd. 2, Pfinztal, 1992.

[13] Geißler, E.; Geißler, A.; Weber, H.
Ein Stoffgesetz für nichtlinear viskoelastische Werkstoffe unter großer statischer und überlagerter dynamischer Belastung.
ZAMM – Z. angew. Math. Mech. 71 (1991) 4, T 248- T251.

[14] Weber, H.; Geißler, E.
Safe Cushion Design for sensitive products.
6th IAPRI World conference on Packaging '89, Hamburg 27.-29. September 1989.

[15] Geißler, Egon; Weber, Herbert
Constitutive equations for dynamically loaded polymer solids and their application in a finite element program.
3rd European Rheology Conference and Golden Jubilee Meeting of the British Society of Rheology, Edinburgh, UK, 3.-7. September 1988, p 171-173, 1988.

[16] Hübner, Ch.; Stacer, R. G.
Recovery of strain-induced damage in filled and unfilled elastomers.
3rd European Rheology Conference and Golden Jubilee Meeting of the British Society of Rheology, Edinburgh, UK, 3.-7. September 1988, p 226-228, 1988.

[17] Stacer, R. G.
Autohesion in the presence and absence of interfacial mass transfer.
3rd European Rheology Conference and Golden Jubilee Meeting of the British Society of Rheology, Edinburgh, UK, 3.-7. September 1988, p 465-467, 1988.

[18] Geißler, Adam; Weber, Herbert
Dynamic material properties of a closed-cell polyethylene foam.
3rd European Rheology Conference and Golden Jubilee Meeting of the British Society of Rheology, Edinburgh, UK, 3.-7. September 1988, p 552-554, 1988.

[19] Weber, H.; Geißler, A.; Kugler, H.-P.
Einsatz der experimentellen Mechanik in der statischen und dynamischen Prüfung unverstärkter Kunststoffe.
Experimentelle Mechanik in Forschung und Praxis. Düsseldorf: VDI-Verlag, VDI-Bericht 679, 1988

[20] Geißler, Adam; Schmitt, Waltraud
Investigations of a closed-cell foam with scanning electron microscopy.
3rd European Rheology Conference and Golden Jubilee Meeting of the British Society of Rheology, Edinburgh, UK, 3.-7. September 1988, p 555-557, 1988.

[21] Eisenreich, N.; Fabry, C.; Fischer, R.; Geißler, A.; Kugler, H.P.; Sinn, F.
Strain distribution in the uniaxial tensile test up to high strain rates.
Propellants, Explosives and Pyrotechnics, v 12 n 3 Jun 1987, p 101-104, 1987.

[22] Geißler, A.; Schmitt, D.; Ziegahn, K.-F.
Materials science and environmental qualification applied on solid chemical energetics.
Propellants, Explosives and Pyrotechnics, v 12 n 3 Jun 1987, p 92-96, 1987.

[23] Eisenreich, Norbert; Geißler, Adam; Kugler, H. Peter; Weinkötz, Christoph
Volume change measurements of filled polymers due to humidity changes.
Proc. - Inst. Environ. Sci. (1986), 32nd, 141-4, 1986.

[24] Eisenreich, N.; Geißler, A.; Fabry, K.; Kugler, H. P.
Tensile test of solid propellants by the use of optical techniques.
1985 Proceedings, 31st Annual Technical Meeting - Institute of Environmental Sciences: Improve Your Odds with Sound Basic Science and Creative Engineering.
Inst of Environmental Sciences, Mount Prospect, IL, USA, Las Vegas, NV, USA
30 Apr 1985-02 May 1985, Proceedings, Annual Technical Meeting - Institute of Environmental Sciences 31st.Publ by Inst of Environmental Sciences, Mount Prospect, IL, USA, p 452-457, 1985.

[25] Eisenreich, N.; Fabry, K.; Geißler, A.; Kugler, H.-P.
Messung der Querkontraktionszahl an Kunststoffen im Hinblick auf die Beurteilung der Füllstoffhaftung.
Deutscher Verband für Materialprüfung E. V., Vortag in der Tagung Werkstoffprüfung 1985,
3.-4- Dezember 1988, Bad Nauheim, S. 391-398, 1988.

[26] Kugler, H.-P.; Eisenreich, N.; Pielka, C.; Geißler, A.
Messung der Querkontraktionszahl unter einachsiger dynamischer Beanspruchung.
Vorträge der Tagung Werkstoffprüfung 1984, DVM.

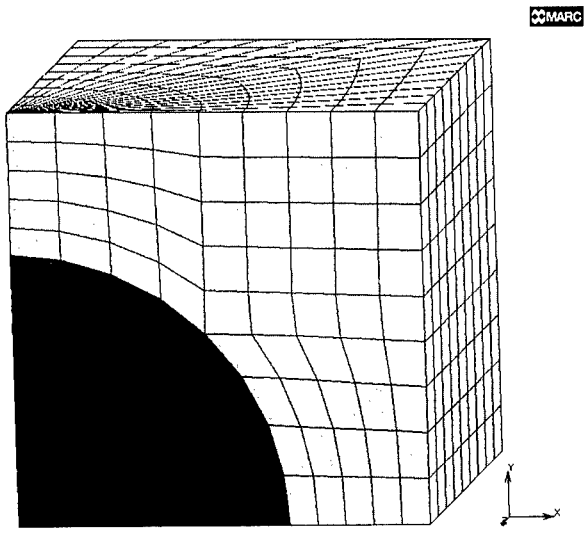

Figure 1: View on 1/8th of the elementary cell for a 15vol.-% filled material in the undeformed state

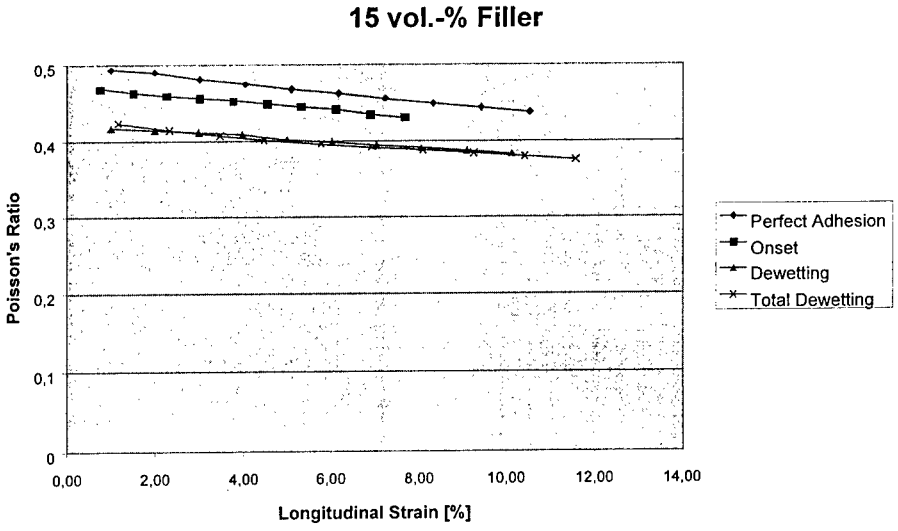

Figure 2: The calculated results for Poisson's Ratio as a function of strain for a 15 vol% filled material with the state of detachment as parameter.

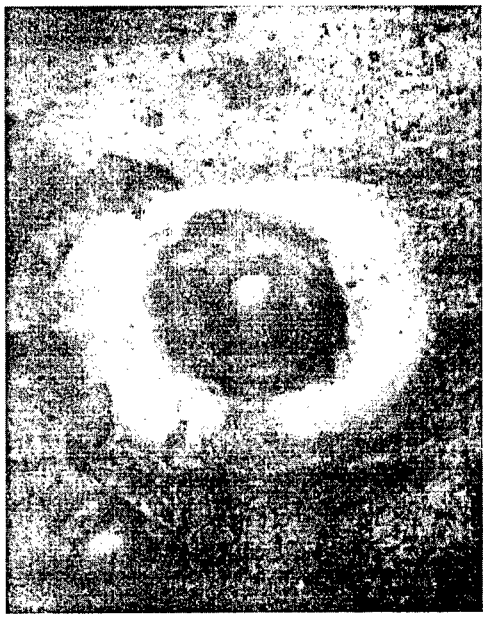

Figure 3: Matrix-filler debonding of polybutadiene matrix and filler particle

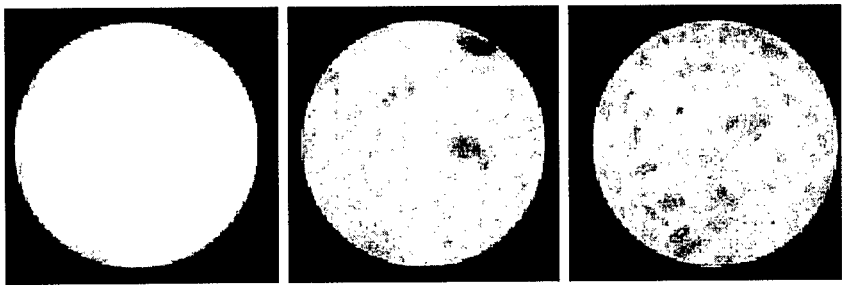

0 weight-% Carbon black 5 weight-% Carbon black 30 weight-% Carbon black

Figure 4: NMR-image of elastomer matrix with different content of carbon black

Methylsubstituted Hydrazinium Azide Derivatives

T. Habereder,[a] A. Hammerl,[a] G. Holl,[b] T.M. Klapötke*,[a], J. Knizek,[a] P. Mayer,[a] H. Nöth [a]

[a] *Department of Chemistry, University of Munich (LMU), Butenandtstrasse 5-13 (D), D-81377 Munich (Germany)*

[b] *Wehrwissenschaftliches Institut für Werk-, Explosiv- und Betriebsstoffe (WIWEB), Swisttal-Heimertsheim, D-53913 Swisttal (Germany)*

* *corresponding author, e-mail: tmk@cup.uni-muenchen.de fax: intl. + 49 89 2180 7492*

Introduction

Hydrazinium azide, first reported by Curtius in 1891,[1] is a powerful explosive that produces nitrogen, hydrogen and ammonia after explosion.[2]

$$[N_2H_5]^+ [N_3]^- \xrightarrow[30\ bar]{\Delta} 2.18\ N_2 + 1.52\ H_2 + 0.65\ NH_3$$

We investigated hydrazinium azide for use as an highly energetic material.[3,4,5,6,7]

Hydrazinium azide is hygroscopic and volatile and therefore not in commercial use. We attached methyl groups to the hydrazine molecule and investigated the effects of this substitution on the physical and explosive properties of hydrazinium azide.

Syntheses

Hydrazine azide derivatives were prepared by reacting the anhydrous hydrazine derivative with a solution of hydrazoic acid in ether. We report the

synthesis of methyl- , N,N-dimethyl, N,N′-dimethyl, N,N,N′-trimethyl- and N,N,N′,N′-tetramethylhydrazinium azide.

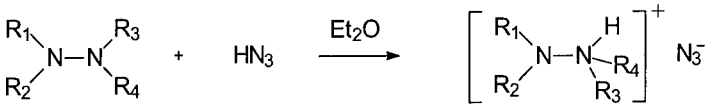

HN_3 was prepared from a neat mixture of molten stearic acid ($C_{18}H_{36}O_2$, Aldrich) and sodium azide (NaN_3, Aldrich) (vessel I, Scheme 1). The generated HN_3 was then carried with a constant flow of dry nitrogen directly into a solution of the corresponding hydrazine derivative in dry ether (vessel II, Scheme 1).

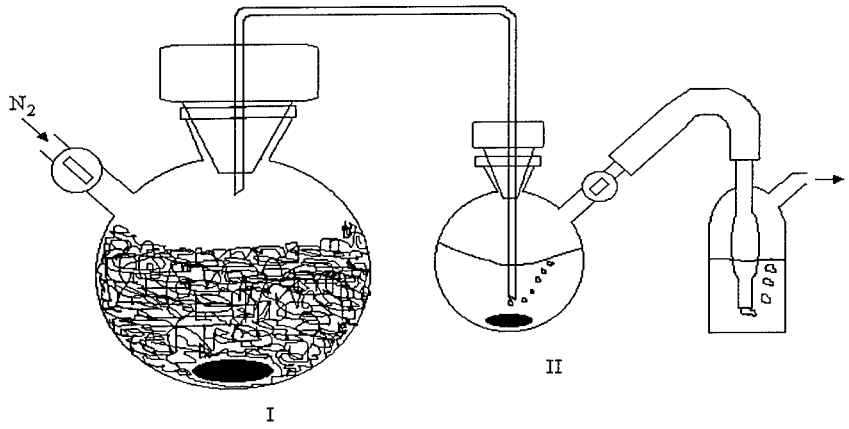

Scheme 1 Preparation of hydrazinium azides
vessel I: neat stearic acid / NaN_3 melt (140 - 165°C)
vessel II: hydrazine derivative dissolved in dry ether

Caution: Most hydrazinium azide salts are explosive and thermally unstable species. Pure HN_3 very explosive is highly toxic and appropriate safety precautions should be taken.

Hydrazine azide derivatives with permethylated nitrogen atoms could not be prepared by the reaction of a hydrazine derivative with methyl azide. They were made via anion exchange from the corresponding hydrazinium iodide with silver azide. We report the syntheses of N,N,N-trimethyl-, N,N,N,N´-tetramethyl and pentamethylhydrazinium azide.

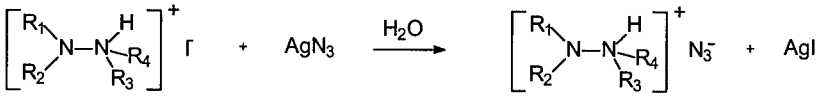

X-Ray-structure determination

The crystal structures of methyl, N,N-dimethyl, N,N´-dimethyl and N,N,N-trimethylhydrazinium azide were determined. All crystal structures show strong hydrogen bonds between hydrazine and azide units.

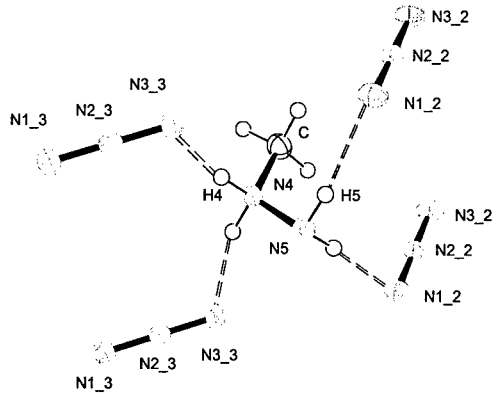

Figure 1: Hydrogen bonds of methylhydrazinium azide

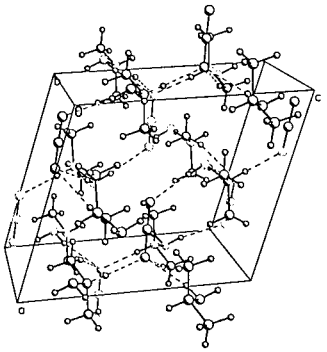

Figure 2: Hydrogen bonds in N,N-dimethylhydrazinium azide

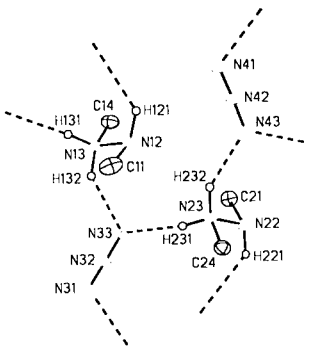

Figure 3: Hydrogen bonds in N,N´-Dimethylhydrazinium azide

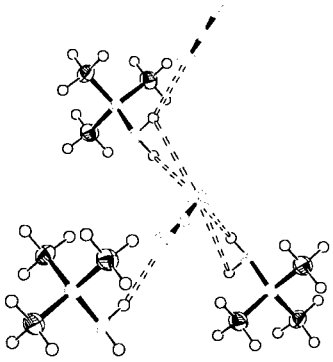

Figure 4: Hydrogen bonds in trimethylhydrazinium azide

DSC investigation

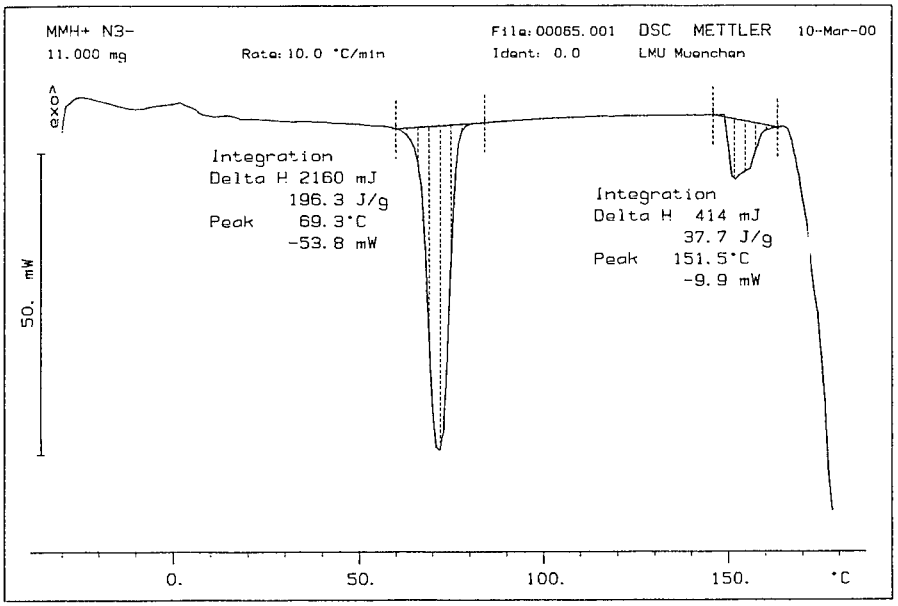

Figure 5:DSC of Methylhydrazinium azide

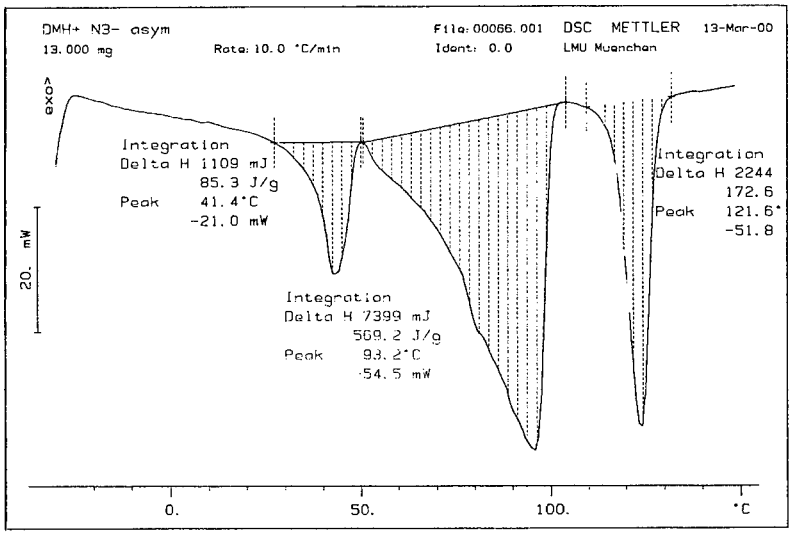

Figure 6: DSC of N,N-dimethylhydrazinium azide

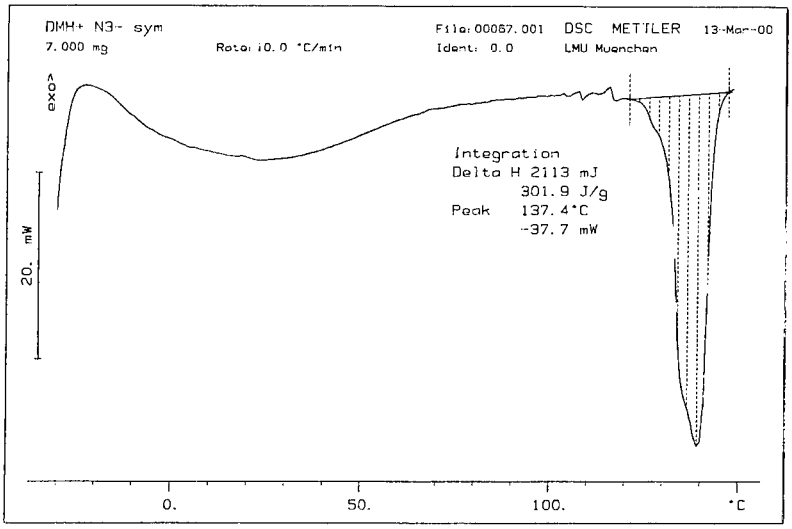

Figure 7: DSC of N,N´-dimethylhydrazinium azide

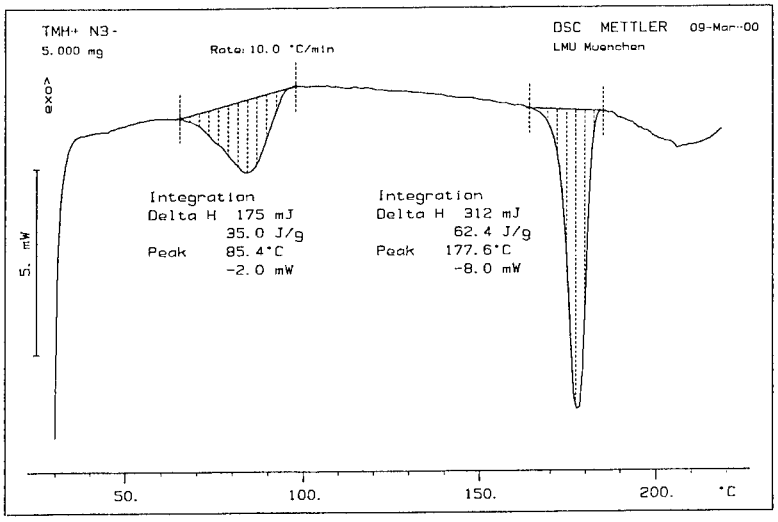

Figure 8: DSC of N,N,N-trimethylhydrazinium azide

Conclusion

As more methyl groups are attached to hydrazine , the melting point of the HN_3 salt decreases. The volatility of the compound increases. With more methyl groups the elimination of HN_3 from the molecule gets easier. Compound $[Me_2N\text{-}NMe_2H]^+[N_3]^-$ eliminates HN_3 at room temperature.

If a permethylated nitrogen atom is present, the molecule can no longer eliminate HN_3. Compounds $[Me_3N\text{-}NH_2]^+[N_3]^-$, $[Me_3N\text{-}NMeH]^+[N_3]^-$ and $[Me_3N\text{-}NMe_2]^+[N_3]^-$ have melting points over 150°C.

Acknowledgment

Financial support of this work by the University of Munich, the Fonds der Chemischen Industrie and the Wehrwissenschaftliche Institut für Werk-, Explosiv- und Betriebsstoffe is gratefully acknowledged.

References

1 T. Curtius, *Ber.* **1891**, *24*, 3341.

2 E. P. Kirpichev, A. P. Alekseev, Yu. I. Rubtsov and G. B. Manelis, *Russian Journal of Phys. Chem.* **1973**, *47*, 1654

3 H. Holfter, T. M. Klapötke, A. Schulz, *Eur. J. Solid State Inorg. Chem.* **1996**, *33*, 855.

4 T.M. Klapötke, P.S. White, I. C. Tornieporth-Oetting, *Polyhedron* **1996**, *15*, 2579.

5 W.-H. Walther, T. M. Klapötke, G. Holl, *29th Annual Conference of ICT* **1998**, P134, Fraunhofer Institut für Chemische Technologie (ICT), Karlsruhe.

6 T. M. Klapötke, H. Nöth, H. Schwenk-Kircher, W. –H. Walther, *Polyhedron* **1999**, *18*, 717-719.

7 T. Habereder, A. Hammerl, G. Holl, T.M. Klapötke, J. Knizek, H. Nöth, *Eur. J. Inorg. Chem.* **1999**, 849-852.

Author index

A

Adirim, H. V 15, P 145
Afanasev, G.T. P 79
Akhavan, J. P 59
Akimova, L.N. P 79
Aleksandrova, N.S. P 103
Altman, I.S. V 41, P 136
Ameen, H.H. P 86
Annikov, V.E. P 112
Antes, J. V 33
Arnold, W. V 27
Asano, N. P 67
Astachov, A.M. V 13
Axenrod, T. V 38

B

Backhaus, J. P 138
Baier, A. P 123
Bailey, A. P 70
Bakhman, N.N. P 134
Bales, C. V 2
Beckstead, M.W. P 130
Belcher, I. P 89
Bellamy, A.J. P 109
Bellerby, J.M. V 22, P 89, P 104
Benmahamed, M.A. P 85
Bergman, H. P 45
Besnard, C. P 137
Birk, A. V 44
Blackman, C. P 89, P 104
Bohn, M.A. P 62, P 63
Bondarchuk, S. P 125
Boniuk, H. V 39, P 46, P 47
Bouma, R.H.B. P 69, P 105
Brill, T.B. V 6
Brock, A. P 138
Bunte, G. P 57, P 92, P 93
Bunyan, P.F. V 4

C

Cäsar, J. P 124
Campos, J. V 43, P 129
Cannizzo, L.F. V 36
Cates, M. V 37
Chabin, P. V 29
Charskii, V.V. P 56
Chauhan, N. V 34
Cheng, H. P 68
Choi, M. P 136
Chukanov, N.V. V 9, P 56
Chung, J.D. P 136
Chunxu, L. P 87
Cieslowska-Glinska, I. V 39
Claridge, R.P. V 34
Coburn, M.D. V 37
Cohen, D. P 117, P 118
Colclough, M.E. V 34, P 59
Cudzilo, S. P 77
Cui-Mei, Y. P 58
Cunliffe, A. V 25, P 107

D

Damavarapu, R. P 48, P 108
Das, K.K. V 38
Dave, P.R. V 38, P 48, P 108
Debenham, D. V 1
DeGraaw, K. P 70
Deimling, J. P 93
Deimling, L. P 138
Denisjuk, A.P. P 131
Destombes, V. P 54, P 106
Dong, Y. P 58
Dreerman, E. P 117, P 118
Drees, D. P 52
van Driel, C.A. V 3
Dubikhin, V.V. V 7
Dubovik, A.V. P 74
Duddu, R. P 108
Dudek, K. P 110

Duraes, L. P 129
Dutov, M.D. P 88
Duvalois, W. P 105

E

Eckl, W. P 137, P 144
Ehrhardt, W. P 139
Eisele, S. P 144
Eisenreich, N. V 15, P 62, P 123, P 139,P 143, P 144, P 145, P 146, P 149
Ellis, G.J. P 73
Engel, W. P 64, P 97
van Esveld, R.J. P 69
Evdokimov, V.V. P 134

F

Fedorov, B.C. P 56
Feng-Qi, Z. P 58
Finjakov, S. P 132
Fischer, T. P 143
Flippen-Anderson, J.L. V 38
Fogelzang, A.F. P 88
Forohar, F. V 38
Fude, N. P 68
Fujiwara, S. P 82

G

Gandara, M.J. P 147
Gash, A. V 35
Geißler, A. P 149
Geißler, E. P 149
Gerber, P. V 19
Gil, M. P 117, P 118
Gilardi, R.D. V 38
Gjersoe, R. P 96
Glotov, O.G. P 130
Goede, P. V 11, P 45
Groux, J. V 29
del Guercio, M. V 44
Guillaume, P. V 2

H

Habereder, T. P 150
Haishan, D. P 114
Hajik, R. M. V 36
Hamid, J. V 34
Hamilton, R.S. V 21
Hammerl, A. P 150
Hasegawa, K. V 32
van der Heijden, A.E.D.M. V 8, V 22, P 69, P 104, P 105
Heintz, T. P 120
Held, M. V 26, P 71, P 76
Hell, V. P 123
Herrmann, M. P 64, P 97
Highsmith, T.K. V 36
Hirth, T. P 124
Holl, G. P 150
Hordijk, A.C. V 40
Hori, K. V 32
Hrubesh, L. V 35
Huanxing, H. P 87
Hübner, C. V 19, P 149
Hui, H. P 68
Hunter, R. P 53
Husseiny, M.E. P 94

I

Ikene, N. P 85
Inozemcev, Y.O. P 51

J

Jacob, G. P 106
Jakob, R. P 124
Jayasurya, K. P 48
Jiang-Ning, W. P 140
Jinwu, X. P 102
Jungova, M. P 80

K

Kaiser, M. V 2, V 24, P 65
Kaschmieder, D. V 10
Kaselj, M. V 38
Kaste, P. V 44
Kavanagh, G.M. V 18, V 23, P 100
Keicher, T. V 30
Kekin, Y.V. V 13
Kelzenberg, S. V 15, P 57, P 139, P 143, P 145, P 146
Kempa, P.B. P 63, P 64
Kermarrec, J.-Y. V 1
Keßler, A. P 66
Kim, H.-S. P 101, P 121
Kim, K.-J. P 121
Kim, K.-M. P 121
Kimura, J. P 83
Kinkennon, A. V 44
Klapötke, T.M. P 150
de Klerk, W.P.C. V 3
Knizek, J. P 150
Koleczko, A. P 139, P 146
Kondratova, O. P 125
Kondrikov, B.N. P 78, P 112
Konkova, T.S. P 88
Korsounskii, B.L. V 9
Kosowski, B.M. V 12
Kostikova, L.M. P 50, P 51
Kozak, G.D. P 78
Kramer, J.F. V 20
Krause, H. V 33, P 92, P 99, P 119
Kronfli, E. P 59
Kruglyakova, L.A. V 13
Künstlinger, M. P 65
Kuglstatter, W. P 111
Kumar, A. P 108
Kuzaev, A.I. P 56

L

Lacroix, G. P 54, P 106
Lagerstam, C. P 148
Langer, G. P 143
Langlet, A. V 11
Larikova, T.S. V 9
Latypov, N.V. V 11, P 45
Leach, C. V 1
Lebedev, V.P. P 51
Lecume, S. V 29
Lee, D. P 136
Lee, G.S. V 37
Lee, J.-M. P 121
Lee, J.-W. P 121
Lee, K.-D. P 101
Lei, D. P 102
Licht, H.H. V 14
Lieb, R. V 44
Lin, Z. P 78
Ling, Z. P 68
Lo, R. V 15, P 145
Löbbecke, S. V 33, P 90, P 98, P 99, P 119
Löffel, D. P 52
Lurie, B. P 135

M

MacDonald, K. P 89
Makhov, M.N. V 42
Mandelbaum, S. P 117, P 118
Manelis, G.B. V 7
Mang, J.T. V 20
Mantseva, E.V. P 103
Manzara, T. P 53
Marecek, P. P 110
Marioth, E. V 33, P 119
Martins, L.J. V 36
Masar, F. P 80
Matei, M. P 70
Matsui, K. P 128

Matsumura, T. P 82
Matyushin, Y.N. P 50, P 51, P 88
Mayer, P. P 150
van der Meer, N. V 2
Menke, K. V 19, P 144
Messmer, A. P 52, P 111, P 143
Meyers, C. V 12
Mikhalev, D.B. P 116
Mikhno, A. P 135
Millar, R.W. V 34
Miroshnichenko, E.A. P 50, P 51
Mitchell, A.R. V 37
Moeen, M.H. P 86
Mouloud, A. P 85
Müller, D. P 146

N

Nakayama, Y. P 82
Nazin, G.M. V 7, P 56
Nedelko, V.V. V 9
Neumann, H. P 92, P 93
Neutz, J. P 126
Newberry, J. V 44
Nguyen, T.T. P 115
Nicklas, B. V 30
Niehaus, M. P 57
Ning-Fei, W. P 140
Nöth, H. P 150
Novikova, T.S. P 103

O

Ossola, B. V 5
Ouazzani, J. V 17

P

Pagoria, P.F. V 37
Panić, S. P 99
Pantel, G. V 2, V 24, P 61
Park, B.-S. P 101, P 121
Paszula, J. P 113
Pei, C. P 58
Pesce-Rodriguez, R. V 44
Petrova, E.N. P 133
Petrzilek, J. P 61
Pfatteicher, A. P 111
Philbin, S.P. V 34
Phillips, D.S. V 20
Pilecki, W. P 46
du Plessis, M. V 16
Poller, S. V 15, P 145
Portugal, A. V 43, P 129
Portugal, P. V 43
Prokudin, V.G. P 56

Q

Quinlan, W.T. V 37

R

Radwan, M.A. P 86
Rajic, M. P 84
Redecker, K. P 65
Reichert, T. P 124
Ritter, H. V 14
Robitelle, D. V 12
Rochat, E. V 28
Rodgers, M.I. V 22
Roos, B.D. V 6
Ruebner, A. V 12
Ruikang, Y. P 102
Rusin, D.L. P 116, P 131

S

Sabel, H.W.R. V 40
Sadek, M.A. P 86
Salko, A. P 125
Sammour, M.H. P 122
Samsonov, V.P. P 133
Sanderson, A.J. V 21, V 36
Schäfer, M.R. V 14
Scheunemann, W. P 65

Schimansky, H.G. P 72
Schmid, H. P 123, P 126, P 139
Schmid, K. V 10, V 33, P 52, P 90, P 111
Schmidt, R.D. V 37
Schneider, H. P 123
Schoolderman, C. V 40
Schroeder, M. V 44
Schröter, D. P 126
Schuppler, H. P 90
Schweikert, W. P 90, P 93, P 98, P 99
Seregin, V. P 135
Sergeeva, N.N. P 133
Shang-Wen, L. P 58
Shaoming, H. P 81
Shengxiang, Z. P 87
Shepelev, Y.G. P 131
Sheremetev, A.B. P 103
Shilnikova, L.A. P 133
Shim, J.-S. P 101
Shimoda, M. V 32
Shimose, S. V 32
Shokry, S.A. P 94
Shoshin, Y.L. V 41, P 136
Shu, Y. V 7
Shuanchang, L. P 141
Shunhuo, L. P 95
Simmons, R.L. P 49
Simpson, R.L. V 35
Sinditskiy, V.P. P 88
Sjöberg, P. P 148
Skidmore, C.B. V 20
Skladal, J. P 61
Smirnov, S. P 135
Statton, G.L. V 12
Stawinski, T. P 46, P 47
van der Steen, A.C. P 105
Stein, W. P 66
Stepanov, R.S. V 13
Stottmeister, L. P 61
Strnad, J. P 80
Suceska, M. P 84
Sun, J. V 38, P 68
Surapaneni, R. P 48, P 108
Syczewski, M. V 39, P 46, P 47

T

Takahashi, K. P 67
Teipel, U. P 64, P 120
Teselkin, V.A. P 74
Theobald, J. V 18, V 23, P 100
Thome, V. P 63, P 64
Thorpe, R. V 37
Ticmanis, U. V 2, V 24, P 65
Tillotson, T. V 35
Tod, D.A. V 4, V18, V 23, P 100
Tormo, C. V 1
Torry, S. V 25, P 107
Trivedi, N.J. V 38
Trzcinski, W.A. P 77, P 113
Türcke, T. V 33, P 98

V

Vavra, P. P 110
van der Velde, I. V 40
Veltmans, W.H.M. V 22
Vetrov, D.V. P 116
Vogelsanger, B. V 5
Volk, F. V 9
Vorozhtsov, A. P 125
Voskoboinikov, I.M. P 75
Voskoboinikova, O.I. P 75

W

Wanders, B. V 14
Wardle, R.B. V 21, V 36
Waring, S.C. P 59
Warner, K.F. V 21
Weiser, V. V 15, P 126, P 137, P 144, P 145, P 146

Wellmar, U.	V 11
Wild, R.	V 30
Wilker, S.	V 2, V 24, P 61
Williams, M.	P 70
Wingborg, N.	P 45

X

Xenhai, Y.	P 68

Y

Yamaya, T.	V 32
Yeh, T.-F.	P 55
Yian, Z.	P 87
Yonggang, L.	P 95
Yoshida, M.	P 82
Yu, X.	P 140, P 141
Yudin, I.L.	P 103

Z

Zarko, V.E.	P 130
van Zelst, M.	V 8, P 104
Zenin, A.	P 132

Topics of previous conferences:

1982	Use of Plastic Materials for Propellants and Explosives
1983	Production Control and Surveillance of Propellants and High Explosives
1984	Technology of Propellants and High Explosives
1985	Pyrotechnics: Basic Principles, Technology, Application
1986	Analysis of Propellants and Explosives - Chemical and Physical Methods
1987	Technology of Energetic Materials - Manufacturing and Processing, Valuation of Product Properties
1988	Combustion and Detonation Phenomena
1989	Environmental Testing in the 90's
1990	Technology of Polymer Compounds and Energetic Materials
1991	Combustion and Reaction Kinetics
1992	Waste Management of Energetic Materials and Polymers
1993	Energetic Materials - Insensitivity and Environmental Awareness
1994	Energetic Materials - Analysis, Characterization and Test Techniques
1995	Pyrotechnics - Basic Principles, Technology, Application
1996	Energetic Materials - Technology, Manufacturing and Processing
1997	Combustion and Detonation
1998	Energetic Materials - Production, Processing and Characterization
1999	Energetic Materials - Modelling of Phenomena, Experimental Characterization, Environmental Engineering